TOOTH ENAMEL: FRONTIERS IN MINERAL CHEMISTRY AND BIOCHEMISTRY, INTEGRATIVE CELL BIOLOGY AND GENETICS

EDITED BY: Steven Joseph Brookes, Ariane Berdal, Sylvie Babajko and Alexandre Rezende Vieira

PUBLISHED IN: Frontiers in Physiology

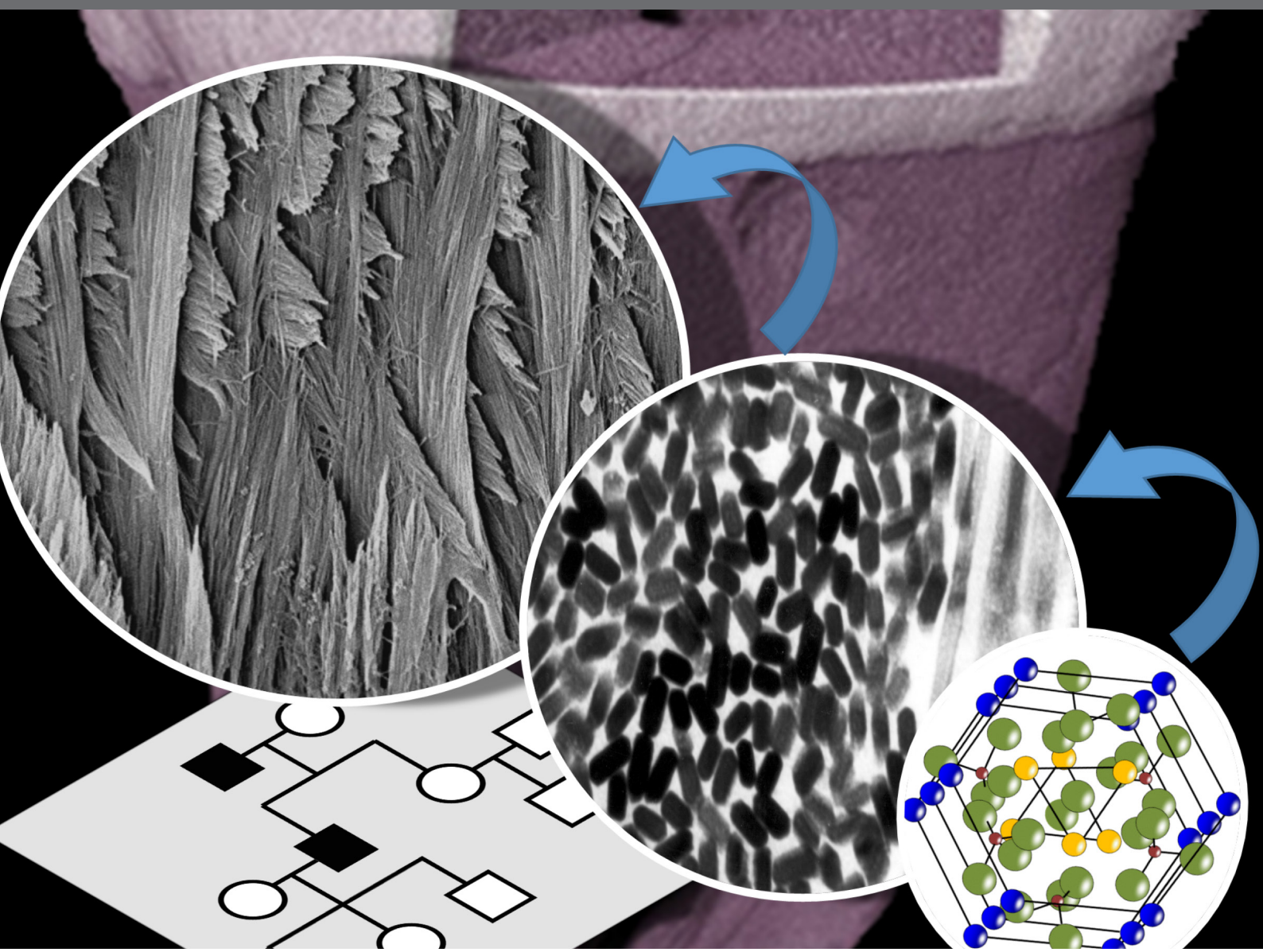

frontiers Research Topics



frontiers

Frontiers Copyright Statement

© Copyright 2007-2019 Frontiers Media SA. All rights reserved.

All content included on this site, such as text, graphics, logos, button icons, images, video/audio clips, downloads, data compilations and software, is the property of or is licensed to Frontiers Media SA ("Frontiers") or its licensees and/or subcontractors. The copyright in the text of individual articles is the property of their respective authors, subject to a license granted to Frontiers.

The compilation of articles constituting this e-book, wherever published, as well as the compilation of all other content on this site, is the exclusive property of Frontiers. For the conditions for downloading and copying of e-books from Frontiers' website, please see the Terms for Website Use. If purchasing Frontiers e-books from other websites or sources, the conditions of the website concerned apply.

Images and graphics not forming part of user-contributed materials may not be downloaded or copied without permission.

Individual articles may be downloaded and reproduced in accordance with the principles of the CC-BY licence subject to any copyright or other notices. They may not be re-sold as an e-book.

As author or other contributor you grant a CC-BY licence to others to reproduce your articles, including any graphics and third-party materials supplied by you, in accordance with the Conditions for Website Use and subject to any copyright notices which you include in connection with your articles and materials.

All copyright, and all rights therein, are protected by national and international copyright laws.

The above represents a summary only. For the full conditions see the Conditions for Authors and the Conditions for Website Use.

ISSN 1664-8714
ISBN 978-2-88945-734-2
DOI 10.3389/978-2-88945-734-2

About Frontiers

Frontiers is more than just an open-access publisher of scholarly articles: it is a pioneering approach to the world of academia, radically improving the way scholarly research is managed. The grand vision of Frontiers is a world where all people have an equal opportunity to seek, share and generate knowledge. Frontiers provides immediate and permanent online open access to all its publications, but this alone is not enough to realize our grand goals.

Frontiers Journal Series

The Frontiers Journal Series is a multi-tier and interdisciplinary set of open-access, online journals, promising a paradigm shift from the current review, selection and dissemination processes in academic publishing. All Frontiers journals are driven by researchers for researchers; therefore, they constitute a service to the scholarly community. At the same time, the Frontiers Journal Series operates on a revolutionary invention, the tiered publishing system, initially addressing specific communities of scholars, and gradually climbing up to broader public understanding, thus serving the interests of the lay society, too.

Dedication to Quality

Each Frontiers article is a landmark of the highest quality, thanks to genuinely collaborative interactions between authors and review editors, who include some of the world's best academicians. Research must be certified by peers before entering a stream of knowledge that may eventually reach the public - and shape society; therefore, Frontiers only applies the most rigorous and unbiased reviews.
Frontiers revolutionizes research publishing by freely delivering the most outstanding research, evaluated with no bias from both the academic and social point of view. By applying the most advanced information technologies, Frontiers is catapulting scholarly publishing into a new generation.

What are Frontiers Research Topics?

Frontiers Research Topics are very popular trademarks of the Frontiers Journals Series: they are collections of at least ten articles, all centered on a particular subject. With their unique mix of varied contributions from Original Research to Review Articles, Frontiers Research Topics unify the most influential researchers, the latest key findings and historical advances in a hot research area! Find out more on how to host your own Frontiers Research Topic or contribute to one as an author by contacting the Frontiers Editorial Office: researchtopics@frontiersin.org

TOOTH ENAMEL: FRONTIERS IN MINERAL CHEMISTRY AND BIOCHEMISTRY, INTEGRATIVE CELL BIOLOGY AND GENETICS

Topic Editors:
Steven Joseph Brookes, University of Leeds, United Kingdom
Ariane Berdal, Centre de Recherche des Cordeliers, France
Sylvie Babajko, Centre de Recherche des Cordeliers, France
Alexandre Rezende Vieira, University of Pittsburgh, United States

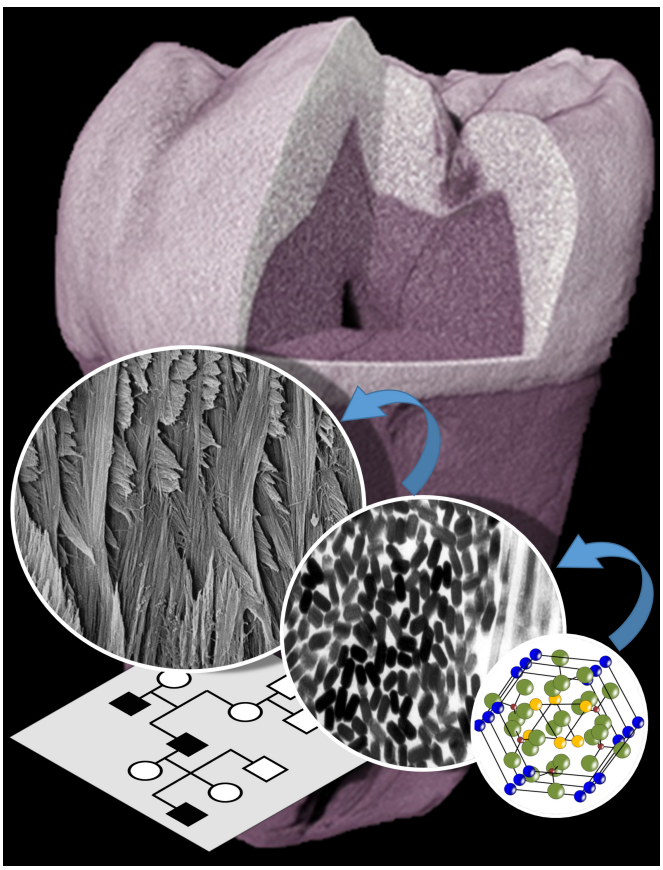

The hierarchical structure of rodent enamel structure illustrated using a collage of electron micrographs and a cartoon representation of the structure of hydroxyapatite. A X-ray μCT reconstruction of a carious human molar and a simple genetic pedigree complete the cover to emphasize the importance of enamel research to human health and well being.
Image: Dr. Sylvie Babajko and Dr. S. J. Brookes. The cartoon of the lattice structure of hydroxyapatite is derived from: Brunton, P.A., Davies, R.P.W., Burke, J.L., Smith, A., Aggeli, A., Brookes, S.J., and Kirkham, J. (2013). Treatment of early caries lesions using biomimetic self-assembling peptides – a clinical safety trial. BDJ 215, E6. It is reused here under the CC BY 3.0 license (https://creativecommons.org/licenses/by/3.0/).

"Tooth Enamel: Frontiers in Mineral Chemistry and Biochemistry, Integrative Cell Biology and Genetics" incorporates the proceedings of the 9th International Enamel Symposium (Enamel 9) hosted in the UK and chaired by Professor Jennifer Kirkham and Professor Ariane Berdal. The topic covers cellular and molecular aspects of the development, pathology, evolution and repair or regeneration of dental enamel. The original research papers and reviews will be of interest to all enamel and biomineralization researchers. Clinicians will find up-to-date thinking and opinion on the aetiology of enamel pathologies and their potential future treatment via novel strategies for preventing, repairing and regenerating enamel.

ACKNOWLEDGMENTS

We acknowledge the support provided by The University of Leeds, Paris Diderot University, National Institute of Dental and Craniofacial Research, Colgate-Palmolive, Bruker and Credentis for the 9th International Enamel Symposium (Enamel 9). Travel bursaries for the 9th International Enamel Symposium (Enamel 9) were awarded by Colgate and NIH.

Citation: Brookes, S. J., Berdal, A., Babajko, S., Vieira, A. R., eds. (2019). Tooth Enamel: Frontiers in Mineral Chemistry and Biochemistry, Integrative Cell Biology and Genetics. Lausanne: Frontiers Media. doi: 10.3389/978-2-88945-734-2

Table of Contents

08 ***Editorial: Tooth Enamel: Frontiers in Mineral Chemistry and Biochemistry, Integrative Cell Biology and Genetics***
Steven J. Brookes, Ariane Berdal, Alexandre R. Vieira, Sylvie Babajko and Jennifer Kirkham

1. ENAMEL FORMATION: STEM CELLS AND DIFFERENTIATION

10 ***Ameloblastin Peptides Modulates the Osteogenic Capacity of Human Mesenchymal Stem Cells***
Øystein Stakkestad, Ståle P. Lyngstadaas, Jiri Vondrasek, Jan O. Gordeladze and Janne Elin Reseland

2. CELL BIOLOGY OF AMELOGENESIS

18 ***Intravesicular Phosphatase PHOSPHO1 Function in Enamel Mineralization and Prism Formation***
Mirali Pandya, Lauren Rosene, Colin Farquharson, José L. Millán and Thomas G. H. Diekwisch

27 ***Endocytosis and Enamel Formation***
Cong-Dat Pham, Charles E. Smith, Yuanyuan Hu, Jan C-C. Hu, James P. Simmer and Yong-Hee P. Chun

41 ***Claudin Loss-of-Function Disrupts Tight Junctions and Impairs Amelogenesis***
Claire Bardet, Sandy Ribes, Yong Wu, Mamadou Tidiane Diallo, Benjamin Salmon, Tilman Breiderhoff, Pascal Houillier, Dominik Müller and Catherine Chaussain

45 ***Multiple Calcium Export Exchangers and Pumps are a Prominent Feature of Enamel Organ Cells***
Sarah Y. T. Robertson, Xin Wen, Kaifeng Yin, Junjun Chen, Charles E. Smith and Michael L. Paine

57 ***Deletion of* Slc26a1 *and* Slc26a7 *Delays Enamel Mineralization in Mice***
Kaifeng Yin, Jing Guo, Wenting Lin, Sarah Y. T. Robertson, Manoocher Soleimani and Michael L. Paine

3. ENAMEL MATRIX PROTEINS

70 ***Dose-Dependent Rescue of KO Amelogenin Enamel by Transgenes* in Vivo**
Felicitas B. Bidlack, Yan Xia and Megan K. Pugach

81 ***Posttranslational Amelogenin Processing and Changes in Matrix Assembly During Enamel Development***
Mirali Pandya, Tiffani Lin, Leo Li, Michael J. Allen, Tianquan Jin, Xianghong Luan and Thomas G. H. Diekwisch

96 ***Phosphorylation Modulates Ameloblastin Self-assembly and Ca^{2+} Binding***
Øystein Stakkestad, Ståle P. Lyngstadaas, Bernd Thiede, Jiri Vondrasek, Bjørn S. Skålhegg and Janne E. Reseland

106 ***Protein Phosphorylation and Mineral Binding Affect the Secondary Structure of the Leucine-Rich Amelogenin Peptide***
Hajime Yamazaki, Elia Beniash, Yasuo Yamakoshi, James P. Simmer and Henry C. Margolis

118 ***Preparative SDS PAGE as an Alternative to His-Tag Purification of Recombinant Amelogenin***
Claire M. Gabe, Steven J. Brookes and Jennifer Kirkham

129 ***Optimizing Immunostaining of Enamel Matrix: Application of Sudan Black B and Minimization of False Positives From Normal Sera and IgGs***
Xu Yang, Alexander J. Vidunas and Elia Beniash

4. ENAMEL BIOMINERALIZATION

137 ***Integrative Temporo-Spatial, Mineralogic, Spectroscopic, and Proteomic Analysis of Postnatal Enamel Development in Teeth With Limited Growth***
Mirali Pandya, Hui Liu, Smit J. Dangaria, Weiying Zhu, Leo L. Li, Shuang Pan, Moufida Abufarwa, Roderick G. Davis, Stephen Guggenheim, Timothy Keiderling, Xianghong Luan and Thomas G. H. Diekwisch

152 ***Beyond the Map: Enamel Distribution Characterized From 3D Dental Topography***
Ghislain Thiery, Vincent Lazzari, Anusha Ramdarshan and Franck Guy

164 ***Difference in Striae Periodicity of Heilongjiang and Singaporean Chinese Teeth***
Sharon H. X. Tan, Yu Fan Sim and Chin-Ying S. Hsu

171 ***Crystal Initiation Structures in Developing Enamel: Possible Implications for Caries Dissolution of Enamel Crystals***
Colin Robinson and Simon D. Connell

5. BIOMIMETICS

176 ***Elastin-Like Protein, With Statherin Derived Peptide, Controls Fluorapatite Formation and Morphology***
Kseniya Shuturminska, Nadezda V. Tarakina, Helena S. Azevedo, Andrew J. Bushby, Alvaro Mata, Paul Anderson and Maisoon Al-Jawad

6. ENAMEL EVOLUTION AND DEVELOPMENT

188 ***Co-option of Hair Follicle Keratins into Amelogenesis is Associated With the Evolution of Prismatic Enamel: A Hypothesis***
Elia Beniash

191 ***Evolutionary Analysis Predicts Sensitive Positions of MMP20 and Validates Newly- and Previously-Identified* MMP20 *Mutations Causing Amelogenesis Imperfecta***
Barbara Gasse, Megana Prasad, Sidney Delgado, Mathilde Huckert, Marzena Kawczynski, Annelyse Garret-Bernardin, Serena Lopez-Cazaux, Isabelle Bailleul-Forestier, Marie-Cécile Manière, Corinne Stoetzel, Agnès Bloch-Zupan and Jean-Yves Sire

7. ENAMEL PATHOLOGY

202 ***No Change in Bicarbonate Transport but Tight-Junction Formation is Delayed by Fluoride in a Novel Ameloblast Model***
Róbert Rácz, Anna Földes, Erzsébet Bori, Ákos Zsembery, Hidemitsu Harada, Martin C. Steward, Pamela DenBesten, Antonius L. J. J. Bronckers, Gábor Gerber and Gábor Varga

214 ***Fluoride Alters Klk4 Expression in Maturation Ameloblasts Through Androgen and Progesterone Receptor Signaling***
Michael H. Le, Yukiko Nakano, Dawud Abduweli Uyghurturk, Li Zhu and Pamela K. Den Besten

224 ***The Unfolded Protein Response in Amelogenesis and Enamel Pathologies***
Steven J. Brookes, Martin J. Barron, Michael J. Dixon and Jennifer Kirkham

236 ***Molar Hypomineralisation: A Call to Arms for Enamel Researchers***
Michael J. Hubbard, Jonathan E. Mangum, Vidal A. Perez, Garry J. Nervo and Roger K. Hall

242 ***Disruption of Steroid Axis, a New Paradigm for Molar Incisor Hypomineralization (MIH)***
Sylvie Babajko, Katia Jedeon, Sophia Houari, Sophia Loiodice and Ariane Berdal

247 ***4-phenylbutyrate Mitigates Fluoride-Induced Cytotoxicity in ALC Cells***
Maiko Suzuki, Eric T. Everett, Gary M. Whitford and John D. Bartlett

8. AMELOGENESIS IMPERFECTA

256 ***Amelogenesis Imperfecta; Genes, Proteins, and Pathways***
Claire E. L. Smith, James A. Poulter, Agne Antanaviciute, Jennifer Kirkham, Steven J. Brookes, Chris F. Inglehearn and Alan J. Mighell

278 ***A Fourth* KLK4 *Mutation is Associated With Enamel Hypomineralisation and Structural Abnormalities***
Claire E. L. Smith, Jennifer Kirkham, Peter F. Day, Francesca Soldani, Esther J. McDerra, James A. Poulter, Christopher F. Inglehearn, Alan J. Mighell and Steven J. Brookes

289 **FAM20A** ***Gene Mutation: Amelogenesis or Ectopic Mineralization?***
Guilhem Lignon, Fleur Beres, Mickael Quentric, Stephan Rouzière, Raphael Weil, Muriel De La Dure-Molla, Adrien Naveau, Renata Kozyraki, Arnaud Dessombz and Ariane Berdal

297 ***Analyses of* MMP20 *Missense Mutations in Two Families With Hypomaturation Amelogenesis Imperfecta***
Youn Jung Kim, Jenny Kang, Figen Seymen, Mine Koruyucu, Koray Gencay, Teo Jeon Shin, Hong-Keun Hyun, Zang Hee Lee, Jan C.-C. Hu, James P. Simmer and Jung-Wook Kim

9. CARIES

304 ***A Novel Kinetic Method to Measure Apparent Solubility Product of Bulk Human Enamel***
Linda Hassanali, Ferranti S. Wong, Richard J. M. Lynch and Paul Anderson

313 **In-vitro** ***Thermal Maps to Characterize Human Dental Enamel and Dentin***
Paula Lancaster, David Brettle, Fiona Carmichael and Val Clerehugh

321 In Vitro *Acid-Mediated Initial Dental Enamel Loss is Associated With Genetic Variants Previously Linked to Caries Experience*
Alexandre R. Vieira, Merve Bayram, Figen Seymen, Regina C. Sencak, Frank Lippert and Adriana Modesto

10. ANIMAL MODELS

328 *A microCT Study of Three-Dimensional Patterns of Biomineralization in Pig Molars*
Susanna S. Sova, Leo Tjäderhane, Pasi A. Heikkilä and Jukka Jernvall

11. OPINION PIECE ON THE PRIORITIES AND FUTURE DIRECTIONS IN ENAMEL RESEARCH

335 *Enamel Research: Priorities and Future Directions*
Jennifer Kirkham, Steven J. Brookes, Thomas G. H. Diekwisch, Henry C. Margolis, Ariane Berdal and Michael J. Hubbard

frontiers in Physiology

EDITORIAL
published: 28 August 2018
doi: 10.3389/fphys.2018.01153

Editorial: Tooth Enamel: Frontiers in Mineral Chemistry and Biochemistry, Integrative Cell Biology and Genetics

Steven J. Brookes[1]*, *Ariane Berdal*[2]*, *Alexandre R. Vieira*[3], *Sylvie Babajko*[2] and *Jennifer Kirkham*[1]

[1] Oral Biology, School of Dentistry, Faculty of Medicine and Health, University of Leeds, Leeds, United Kingdom, [2] INSERM U1138 Centre de Recherche des Cordeliers, Paris, France, [3] School of Dental Medicine, University of Pittsburgh, Pittsburgh, PA, United States

Keywords: amelogenesis, enamel (mature and developing), enamel pathology, enamel 9 symposium, ameloblast

OPEN ACCESS

Edited by:
Thimios Mitsiadis,
Universität Zürich, Switzerland

Reviewed by:
Timothy C. Cox,
University of Washington, United States
Giovanna Orsini,
Università Politecnica delle Marche, Italy

***Correspondence:**
Steven J. Brookes
s.j.brookes@leeds.ac.uk
Ariane Berdal
ariane.berdal@crc.jussieu.fr

Specialty section:
This article was submitted to Craniofacial Biology and Dental Research, a section of the journal Frontiers in Physiology

Received: *02 July 2018*
Accepted: *31 July 2018*
Published: *28 August 2018*

Citation:
Brookes SJ, Berdal A, Vieira AR, Babajko S and Kirkham J (2018) Editorial: Tooth Enamel: Frontiers in Mineral Chemistry and Biochemistry, Integrative Cell Biology and Genetics. Front. Physiol. 9:1153. doi: 10.3389/fphys.2018.01153

Editorial on the Research Topic

Tooth Enamel: Frontiers in Mineral Chemistry and Biochemistry, Integrative Cell Biology and Genetics

This Frontiers research topic, Tooth Enamel: Frontiers in Mineral Chemistry and Biochemistry, Integrative Cell Biology and Genetics, was hosted under the Craniofacial Biology and Dental Research speciality. The speciality covers cellular and molecular aspects of the development, pathology, and repair or regeneration of craniofacial tissues and organs; each and all of these aspects are covered in this topic as they relate to dental enamel. The topic was initially conceived as the vehicle by which manuscripts arising from the Enamel 9 International Symposium (held in November 2016 at Rudding Park, Harrogate, UK) would be disseminated but the topic was also open to all enamel researchers to contribute their findings irrespective of their attendance at the Symposium.

The topic presents 34 manuscripts from 15 different countries that together convey the breadth and scope of enamel research across the globe. The research themes of the Enamel 9 Symposium provided the framework on which the topic was based. The themes comprise: (i) Enamel Formation: Stem Cells and Differentiation, (ii) Cell Biology of Amelogenesis, (iii) Enamel Matrix Proteins, (v) Enamel Biomineralization & Biomimetics, (vi) Enamel Evolution and Development, (vii) Enamel Pathology, (viii) Amelogenesis Imperfecta (AI), (ix) Caries, and (x) Animal Models in Enamel Research. The articles are mostly in the form of original research papers but accepted papers also included reviews, perspectives, opinion pieces, and methodological papers.

It is impossible, in this short editorial, to highlight each of the papers submitted to this topic, which span the full breadth of enamel research. We therefore have chosen to take an objective approach and highlight here the top three *original research papers* with the most viewings at the time of writing, along with the most viewed *review*, *perspective, opinion piece,* and *methodological paper*. Stakkestad et al. report how different ameloblastin processing products, and splice variants thereof, might influence gene expression and proliferation in human mesenchymal stem cells in an autocrine fashion, highlighting the increasing interest in tissue regeneration and stem cell biology amongst enamel researchers. Focusing on amelogenesis imperfecta (AI), Lignon et al. report on the detailed characterization of enamel in enamel renal syndrome caused by a *FAM20A* mutation and conclude that while initial enamel formation is unaffected by the mutation, subsequently secreted enamel is abnormal. The authors discuss the pathological etiology involved by correlating the

observed phenotype to loss of FAM20A function. The paper exemplifies the need to move from the phenomenological to the mechanistic if we are to further our knowledge base of the etiology of inherited conditions. The role of amelogenin phosphorylation in enamel biomineralization has long been debated. Yamazaki et al., investigating the role of amelogenin phosphorylation in enamel matrix function, report data indicating that amelogenin (LRAP) phosphorylation on serine 16 influences protein secondary structure and enhances the ability of amelogenin to stabilize mineral precursor phases. It is clear that future functionality work using recombinant amelogenin, for example, must take this post-translational modification in to account. The global research effort to further our understanding of amelogeneisis imperfecta has contributed towards our knowledge of the fundamental biology of enamel biomineralization and will increasingly inform clinical treatment of those affected. Smith et al. review the genes and mutations underlying non-syndromic AI and present a Leiden Open Source Variation Database (LOVD) used to identify trends in genes and mutations causing AI in some 270 families, together with a discussion of how translation of AI genetics can benefit patient care. Molar hypomineralization (MH) is a "silent public health problem" on a global scale, affecting the dental health of up to 1 in 6 children. Hubbard et al. provide a state-of-the-art perspective on MH and argue the need for awareness building and a greater collaborative research effort to tackle this emerging issue while Babajko et al. provide an opinion piece on the potential role of environmental endocrine disrupting chemicals in MH etiology through disruption of endocrine signaling via ameloblast steroid receptors. Finally, the technical aspects of amelogenin research are still of high interest to our research community, as evidenced by those accessing the report by Gabe et al. on the use of a preparative polyacrylamide electrophoretic methodology for amelogenin protein purification.

Space precludes a wider description of the articles published but readers are urged to peruse the on line contents list to view and quickly access the full range of topic articles published. We are confident that the contents will be of interest to all enamel and biomineralization researchers. Clinicians will find up-to-date thinking and opinion on the etiology of enamel pathologies and their potential future treatment via novel strategies for preventing, repairing and even regenerating enamel. Industry-based colleagues will have access the latest advances in translational enamel research.

LOOKING TO THE FUTURE

Proceedings arising from the Enamel Symposia reach back over 50 years of enamel research and provide a rich archive offering access to state of the art understanding of all things enamel at that point in time. We are confident that the manuscripts within this research topic continue that tradition, illustrating our current understanding of enamel development, structure and pathology and signposting the future direction of enamel research. The final session of the Enamel 9 Symposium comprised an open forum where enamel researchers from across the world came together to discuss the future priorities and directions for enamel research, identifying the key questions remaining to be answered and highlighting the methodological, technical and clinical challenges that need to be addressed. These views were captured and are presented in an opinion article (Kirkham et al.) published alongside the other articles comprising the topic. Key points raised included: a call for stronger outcomes through interdisciplinary, integrative and translational approaches, a call for a better standardization of experimental variables, better collaboration for a stronger collective voice and outputs and increased and more effective communication. This was a very positive message from the enamel research community and indicates a genuine desire to increase collaboration for the benefit of advancing the field. Increased cross-collaboration between research groups can be challenging given the competition for increasingly scarce funding but advancement of our science and the solving of complex problems demands that we cross disciplinary and geographical boundaries to work together. We look forward to the Enamel 10 Symposium to evidence how enhanced collaboration and interdisciplinarity has shaped enamel research in the intervening period since Enamel 9.

This is the first time that an Enamel Symposium has been associated with Frontiers Media SA and we thank the team at Frontiers for their help with the process, bringing with it the benefits of full open access to the papers as soon as they are accepted for publication following full peer review. We are especially grateful to Thimios Mitsiadis who, as Specialty Chief Editor for Craniofacial Biology and Dental Research, provided invaluable support and advice throughout.

Finally, we owe a huge thank you to all the contributors whose hard work and dedication to their science brought this research topic to fruition. We are all waiting eagerly to see how the research presented here continues to develop and advances our understanding of this amazing tissue: dental enamel.

AUTHOR CONTRIBUTIONS

All authors listed have made a substantial, direct and intellectual contribution to the work, and approved it for publication.

Conflict of Interest Statement: The authors declare that the research was conducted in the absence of any commercial or financial relationships that could be construed as a potential conflict of interest.

Copyright © 2018 Brookes, Berdal, Vieira, Babajko and Kirkham. This is an open-access article distributed under the terms of the Creative Commons Attribution License (CC BY). The use, distribution or reproduction in other forums is permitted, provided the original author(s) and the copyright owner(s) are credited and that the original publication in this journal is cited, in accordance with accepted academic practice. No use, distribution or reproduction is permitted which does not comply with these terms.

frontiers in Physiology

ORIGINAL RESEARCH
published: 07 February 2017
doi: 10.3389/fphys.2017.00058

Ameloblastin Peptides Modulates the Osteogenic Capacity of Human Mesenchymal Stem Cells

*Øystein Stakkestad[1], Ståle P. Lyngstadaas[1], Jiri Vondrasek[2], Jan O. Gordeladze[1] and Janne Elin Reseland[1]**

[1] Department of Biomaterials, Institute of Clinical Dentistry, University of Oslo, Oslo, Norway, [2] Department of Bioinformatics, Institute of Organic Chemistry and Biochemistry, Czech Academy of Sciences, Prague, Czechia

During amelogenesis the extracellular enamel matrix protein AMBN is quickly processed into 17 kDa (N-terminus) and 23 kDa (C-terminus) fragments. In particular, alternatively spliced regions derived by exon 5/6 within the N-terminus region are known to be critical in biomineralization. Human mesenchymal stem cells (hMSC) also express and secrete AMBN, but it is unclear if this expression has effects on the hMSC themselves. If, as suggested from previous findings, AMBN act as a signaling molecule, such effects could influence hMSC growth and differentiation, as well as promoting the secretion of other signaling proteins like cytokines and chemokines. If AMBN is found to modulate stem cell behavior and fate, it will impact our understanding on how extracellular matrix molecules can have multiple roles during development ontogenesis, mineralization and healing of mesenchymal tissues. Here we show that synthetic peptides representing *exon 5* promote hMSC proliferation. *Interestingly,* this effect is inhibited by the application of a 15 aa peptide representing the alternatively spliced start of *exon 6*. Both peptides also influence gene expression of RUNX2 and osteocalcin, and promote calcium deposition in cultures, indicating a positive influence on the osteogenic capacity of hMSC. We also show that the full-length AMBN-WT and N-terminus region enhance the secretion of RANTES, IP-10, and IL-8. In contrast, the AMBN C-terminus fragment and the exon 5 deleted AMBN (DelEx5) have no detectable effects on any of the parameters investigated. These findings suggest the signaling effect of AMBN is conveyed by processed products, whereas the effect on proliferation is differentially modulated through alternative splicing during gene expression.

Keywords: ameloblastin, biomineralization, bone growth, exon 5, human mesenchymal stem cells, osteogenesis, proliferation

OPEN ACCESS

Edited by:
Ariane Berdal,
Inserm and University Paris-Diderot, France

Reviewed by:
Anne Poliard,
Paris Descartes University, France
Ana Angelova Volponi,
King's College London, UK

***Correspondence:**
Janne Elin Reseland
j.e.reseland@odont.uio.no

Specialty section:
This article was submitted to Craniofacial Biology and Dental Research, a section of the journal Frontiers in Physiology

Received: *09 November 2016*
Accepted: *23 January 2017*
Published: *07 February 2017*

Citation:
Stakkestad Ø, Lyngstadaas SP, Vondrasek J, Gordeladze JO and Reseland JE (2017) Ameloblastin Peptides Modulates the Osteogenic Capacity of Human Mesenchymal Stem Cells. Front. Physiol. 8:58. doi: 10.3389/fphys.2017.00058

INTRODUCTION

Ameloblastin (AMBN) is an extracellular matrix protein expressed in mesenchymal and epithelial cells (Fong et al., 1998). Epithelial-mesenchymal interactions initiate tooth development and has been shown to induce the expression of AMBN (Takahashi et al., 2012). AMBN is also involved in biomineralization in other tissues than teeth, and is expressed and secreted from cultured human mesenchymal stem cells (hMSC) and osteoblasts (Tamburstuen et al., 2011). Expression of AMBN (Spahr et al., 2006; Tamburstuen et al., 2010) in cells bordering bone defects suggest a role for

AMBN in the recruitment, growth and differentiation of hMSC, and is a potential target for clinical interventions for bone healing.

AMBN is known to modulate proliferation and differentiation of ameloblasts, periodontal ligament cells (PDL), pulp cells (Nakamura et al., 2006) and hMSC; (Fukumoto et al., 2004; Sonoda et al., 2009; Tamburstuen et al., 2010; Zhang et al., 2011). AMBN splice variants are widely distributed in time and location, and have several roles during dental biomineralization. During early tooth development in mice, the predominant splice variant is 15 aa shorter than the splice variant expressed in later stages. These 15 aa (*Q9NP70)* derive from the start of *exon 6* (Cerný et al., 1996; Fong et al., 1996; Hu et al., 1997; Lee et al., 2003; Ravindranath et al., 2007). However, spatial distribution and post-translational modification of the splice variants present in mesenchymal tissues like bone still needs to be investigated.

Extracellular full-length AMBN has not been identified *in vivo*. This is most probably due to rapid degradation by co-secreted specific matrix metalloproteases like MMP-20 (Uchida et al., 1997). Thus, it is important to understand the dynamics of AMBN processing and the biological role of the processed products. It is interesting that recombinant full-length AMBN has been found to enhance the secretion of cytokines and chemokines involved in inflammation and recruitment of progenitor cells (Tamburstuen et al., 2010). This effect is evident in the healing of critical-size defects in the jawbone of rats (Spahr et al., 2006; Tamburstuen et al., 2010) and in pulpal wound healing in pigs (Nakamura et al., 2006). These findings suggest that the full-length product has a biological (or at least pharmacological) effect on its own or that the full-length molecule act as a founding source for shorter, active, peptides.

Unprocessed ameloblastin (AMBN-WT) is a two-domain protein where the amino- and carboxyl ends are differently organized with opposing chemical properties (Vymetal et al., 2008). The N-terminus is defined by the first 10 exons encoding 222 aa (human). Both the unprocessed ameloblastin and the N-terminus may form fibrils through self-assembly supported by the *exon 5* derived region (Wald et al., 2013). The C-terminus is defined by the last three exons encoding 225 aa (Toyosawa et al., 2000). It has been suggested that parts of the porcine N-terminus (17 kDa fragment) is active in mineralization and regeneration (Fukae et al., 2006; Stout et al., 2014), whereas the C-terminus product may have a role in cell surface attachment (Sonoda et al., 2009).

In silico modeling of AMBN-WT folding, suggests that some discrete peptide-sequences are exposed on the surface of the folded protein structure (Vymetal et al., 2008). It is reasonable to assume these domains have biological functions that are presently unknown. Whether these domains act in concert or have individual activities also need assessment. Based on *in silico* modeling, we have designed synthetic peptides from exons 2–13 (without signal peptide) representing these exposed domains. In an attempt to look for biological effects of AMBN and the processing products as suggested by Tamburstuen et al. and others (Nakamura et al., 2006; Spahr et al., 2006; Tamburstuen et al., 2011), these peptides and various other AMBN fragments were added to cultures of hMSC, and the cells were monitored for changes in growth and differentiation as well as effects on levels of selected cytokine and chemokine secretion.

MATERIALS AND METHODS

Experimental Design

Human mesenchymal stem cells (hMSC; Cat.no: PT-2501, Lonza Walkersville, MD, USA) were maintained in growth medium [GM; Cat.no: PT-3238 supplemented with MSCGM SingleQuots, Cat.no: PT-4105, Lonza (http://www.lonza.com/products-services/bio-research/stem-cells/adult-stem-cells-and-media/human-mesenchymal-stem-cells-media.aspx)] and changed every 3rd day. These hMSC cells are isolated from normal (non-diabetic) adult human bone marrow withdrawn from bilateral punctures of the posterior iliac crests of healthy volunteers.

The recombinant AMBN protein, fragments, and peptides, presented in **Figure 1**, were produced and purified as described by Wald et al. (2013).

Human MSC were incubated with 0.1 μM and 0.2 μM of AMBN-WT, AMBN-WT without Exon 5 (DelEx5), N-terminus of AMBN, C-terminus of AMBN, or 0.2 μM of exon 5 related peptides [Ex5 (AA62-98), Ex5-18 (AA62-80), Ex5-36 (AA81-98), Ex5|Q9NP70 (AA62-113), and Q9NP70 (AA99-113)]. Untreated hMSC were used as control at each time point tested. Cells and culture medium were harvested after 1, 3, 7, 14, 21, and 28 days of incubation.

Proliferation Assay

hMSC (6000 cells/well) were seeded in 48 well plates and incubated with the various test fragments or controls for 24 h. New DNA produced in the cells was labeled with 0.1 μCi [^{3}H]-thymidine in a 12 h pulse prior to harvesting. The cells were then washed twice in PBS and then twice in 5% TCA to remove excess thymidine, and the remaining pellet dissolved in 1 M NaOH. Optifluor Scintillation liquid (Lumagel LSC GE BV, Groningen, Netherlands; 4 ml) was added, and radioactivity was measured

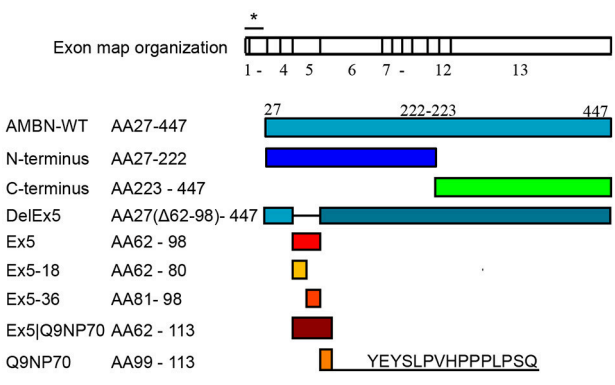

FIGURE 1 | Overview of recombinant ameloblastin (AMBN) proteins and derivatives of the N-terminus region. Signal sequence of the 26 amino acids is indicated with asterisk in the exon map that is scaled according to the stretch of residue length in each exon.

in a Packard 1500 TRI-CARB liquid scintillation counter (Perkin Elmer, Shelton, CT, USA).

Measurements of Secreted Biomarkers

Harvested cell-culture-medium samples were concentrated 5-fold in spin columns with a 3 kD cut-off (Pall Life Science, Ann Arbor, MI, USA).

The concentrations of Eotaxin, granulocyte-colony stimulating factor (G-CSF), interferon (IFN) α2, IFNγ, interleukin (IL)-1α, IL-1β, IL-1 Receptor Antagonist (RA), IL-2, IL-4, IL-5, IL-6, IL-7, IL-8, IL-10, IL-12, IL-13, IL-15, IL-17, interferon gamma-inducible protein (IP-10), monocyte chemoattractant protein-1 (MCP-1), macrophage inflammatory protein-1 alpha (MIP-1α), macrophage inflammatory protein-1 beta (MIP-1β), regulated upon activation normal T-cell expressed and secreted (RANTES), tumor necrosis factor alpha (TNFα), vascular endothelial growth factor (VEGF), as well as adreno-corticotrophic hormone (ACTH), Dickkopf-1 (DKK1), Insulin, Leptin, osteoprotegerin (OPG), osteocalcin (OCN), osteopontin (OPN), sclerostin (SOST), fibroblast growth factor-23 (FGF-23), respectively, were measured using HCYTOMAG-60K and HBNMAG-51K assays (MILLIPORE corporation, Billerica, MA, USA), respectively, and analyzed with the Luminex xPONENT version 3.1.871 or MILLIPLEX^{TM} Analyst version 5.1 software in the Luminex-200 system (Luminex Corp., Austin, TX, USA). Only the cytokines and chemokines that showed significant change are discussed here.

mRNA Isolation

hMSC were washed in PBS and lysed, and the mRNA was isolated using magnetic beads according to manufacturer's instructions (Dynabeads Oligo $(dT)_{25}$, Life Technologies, Gaithersburg, MD, USA). The mRNA was separated from the beads by heat treatment (80°C for 2 min), and quantified using a nano-drop spectrophotometer (ND-1000, Thermo Scientific, Wilmington, DE, USA, with software version 3.3.1.).

Real Time PCR

cDNA was generated from mRNA using Revertaid First Strand cDNA synthesis kit (Fermentas, Burlington, Ontario, Canada) according to the producer's instructions. Real time PCR was performed using Ssoadvanced SYBRGreen Supermix (Bio-rad, Hercules, CA, USA) in a reaction mix of 20 μl (1 ng cDNA) in 96 well plates using the CFX Connect^{TM}-system. Gene expression was normalized to reference housekeeping genes β-actin and glyceraldehyde phosphate (GADPH) using the ΔΔCT method with Bio-Rad CFX Manager software version 2.1. The primer sequences used are listed in **Table 1**.

Mineralization

Cells were cultured to confluence in 12-well plates and then treated with AMBN or its fragments in either GM or osteogenic differentiation media (DM; Cat.no: PT-3924, supplemented with hMSC osteogenic SinglequotsTM) for up to 28 days. Medium was changed every 3rd day. Upon harvest, the cells were washed three times with PBS, fixed in 95% ethanol for 30 min, and then stained with 1% alizarin red for 5 min as described elsewhere (Dahl, 1952). To quantify mineralization, the alizarin red deposition was extracted with cetyl pyridinium chloride (Sigma-Aldrich, St. Louis, MO, USA) at room temperature, and measured at 562 nm in (EL × 800 Absorbance Reader, BioTek instruments, Winooski, VT, USA).

Statistics

Student *t*-test was used to evaluate the effect of AMBN and its fragments compared to untreated controls at each individual time point. The Mann-Whitney U- Test was used if the results were not normally distributed. The significance level was set to $P \leq 0.05$.

RESULT

Proliferation of hMSC is Influenced by Peptides Derived by *exon 5* and *Q9NP70*

AMBN-WT (0.1 μM) enhanced cell proliferation of hMSC to 1.8-fold ($P = 0.002$) of the control. DelEx5 was found to enhance proliferation to 1.5-fold ($P = 0.004$), whereas no effects were observed from the C-terminus or the N-terminus fragments alone at the time points tested (**Figure 2A**). Among the tested peptides, Ex5 enhanced the proliferation to 2.6-fold ($P = 0.004$) while Q9NP70 and Ex5|Q9NP70 both inhibited proliferation to 0.5-fold of control ($P = 0.015$ and $P = 0.003$, respectively; **Figure 2B**).

TABLE 1 | Description of human primers used in experiments.

Genes	Forward primer	Reverse primer
OCN	5′-GAAGCCCAGCGGTGCA	3′-CACTACCTCGCTGCCCTCC
Col1α1	5′-AAGGGACACAGAGGTTTCAG	3′-TAGCACCATCATTTCCACGA
RUNX2	5′-CCAGATGGGACTGTGGTTACC	3′-ACTTGGTGCAGAGTTGAGGG
Osterix	5′-GCCAGAAGCTGTGAAACCTC	3′-GCTGCAAGCTCTCCATAACC
β-Actin	5′-CTGGAACGGTGAAGGTGACA	3′-AAGGGACTTCCTGTAACAATGCA
GADPH	1′–TGCACCACCAACTGCTTAGC	2′-GGCATGGACTGTGGTCATGAG
RANKL	5′-CGGGGTGACCTTATGAGAAA	3′-GCGCTAGATGACACCCTCTC
OPG	5′-TGGGAGCAGAAGACATTGAA	3′-GTGTCTTGGTCGCCATTTTT

OCN (osteocalcin), Col1α1 (collagen type 1 α1), RUNX2 (Runt-related transcription factor 2), GAPDH (glyceraldehyde 3-phosphate dehydrogenase), RANKL (Receptor Activator of Nuclear Factor κ B), OPG (osteoprotegerin).

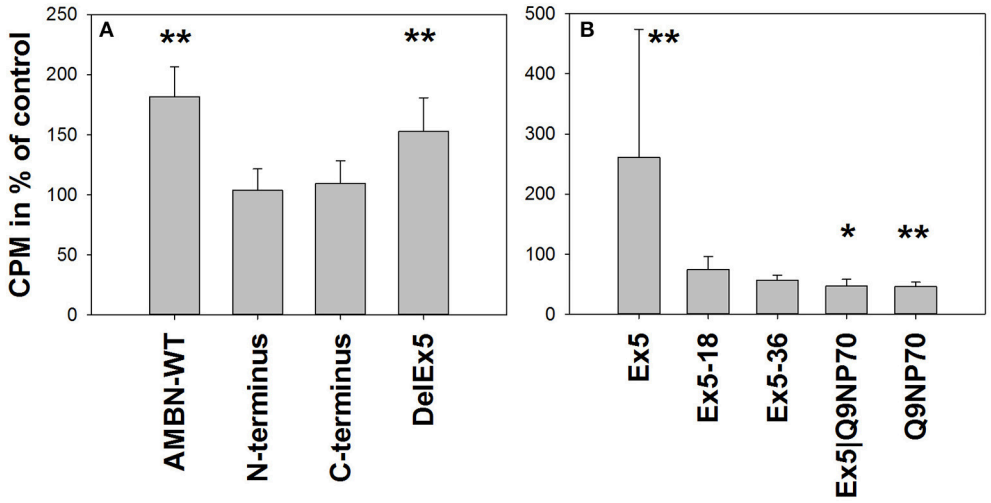

FIGURE 2 | Proliferation measured as [^{3}H]-thymidine incorporation in hMSC exposed to (A) 0.1 μM AMBN-WT, N-terminus, C-terminus or DelEx5 ($n = 6$). **(B)** 0.2 μM Ex5, Ex5-18, Ex5-36, Ex5|Q9NP70, or Q9NP70 ($n = 12$). ^{3}H-thymidine incorporation (CPM) was calculated relative to untreated control cells (%), and presented as mean ± *SD*. *Indicate $P < 0.05$, **Indicate $P < 0.01$.

Cytokine and Chemokine Secretion is Enhanced by AMBN-WT and N-Terminus

AMBN-WT (0.2 μM) enhanced the secretion of RANTES 19 and 21-fold at day 7 and 14 respectively ($P = 0.015$ and $P = 0.019$). The secretion of IP-10 was enhanced 22-fold and 24-fold at day 1 and day 14, respectively ($P = 0.029$ and $P = 0.047$). Finally AMBN-WT enhanced the secretion of MIP-1α 8-fold at day 1 ($P = 0.043$) and 12-fold at day 14 ($P = 0.001$; **Table 2**). Lower concentration (0.1 μM) of AMBN-WT produced only a slight increase in secretion of MCP-1 and IL-6 at day 1 (values not shown).

N-terminus (0.2 μM) enhanced the secretion of RANTES 2.5, 4.5, and 3-fold at days 1, 7, and 14 respectively ($P = 0.036$, $P = < 0.001$, $P = 0.003$). The secretion of IP-10 was enhanced 5.5 and 2.7-fold at day 1 and 14, respectively ($P = 0.003$ and $P = 0.037$). N-terminus enhanced the secretion of MIP-1α 2.6-fold at day 14 ($P = 0.004$). The N-terminus also significantly enhanced secretion of IL-8 2.5-fold at day 3 ($P = 0.038$; **Table 2**).

The C-terminus and DelEx5 did not have any significant effects on the secretion of cytokines or chemokines, nor did they influence any differentiation markers tested.

TABLE 2 | Cytokine/chemokine secretion from hMSC.

Chemokine	Days	AMBN-WT	DelEx5	N-term	C-term
RANTES	1	10 ± 6	1.5 ± 0.8	2.5 ± 1.3*	0.9 ± 0.2
	3	0.9 ± 0.4	0.7± 0.04	1.3 ± 1	0.9 ± 0.4
	7	19 ± 7*	1 ± 0.3	4.5 ± 0.6***	1.3 ± 0.3
	14	21 ± 9*	1 ± 0.5	3 ± 0.7**	0.9 ± 0.3
IP-10	1	22 ± 13*	2 ± 1	5.5 ± 0.8**	1 ± 0.4
	3	1.6 ± 0.08	2 ± 0.2	1 ± 0.5	2 ± 0.3
	7	24 ± 14*	1.5 ± 0.4	5.8 ± 5	1.7 ± 1
	14	21 ± 7.9	1.8 ± 0.7	2.7 ± 0.5*	1.2 ± 0.3
IL-8	1	2 ± 1.3	1.6 ± 113	2.3 ± 2.1	1 ± 0.8
	3	3 ± 0.5	1.3 ± 0.4	2.5 ± 1.3*	1.2 ± 0.04
	7	4 ± 0.8	1.7 ± 0.6	3.9 ± 0.8	1.6 ± 0.6
	14	3 ± 0.6	2 ± 0.7	3 ± 0.3	1.7 ± 0.6
MIP-1α	1	8 ± 5.5*	1 ± 0.5	2.4 ± 1.3	0.7 ± 0.4
	3	n/a	n/a	n/a	n/a
	7	14 ± 6	3 ± 0.6	4.7 ± 0.7	1.5 ± 0.05
	14	12 ± 2***	1.3 ± 0.6	2.6 ± 0.3**	0.8 ± 0.1

*Secretion of RANTES, IL-8, IP-10, and MIP-1α from human mesenchymal stem cells (hMSCs) grown in standard growth media containing 0.2 μM of AMBN-WT, DelEx5, C-terminus, or N-terminus. Data are presented as –fold change mean ± SD (n = 2–6). *Indicate P < 0.05, **Indicate P < 0.01, ***Indicate P < 0.001. n/a means data not available.*

Differentiation of hMSC are Stimulated by Peptides Derived by *exon 5* and *Q9NP70*

The N-terminus and the Ex5, Ex5-18, and Ex5|Q9NP70 peptides all stimulated the mRNA expression of RUNX2 (3-fold ($P = 0.008$), 1.9 -fold ($P = 0.016$), 2.1-fold ($P = 0.004$), and 1.5-fold ($P = 0.019$)), respectively (**Figure 3A**). Ex5 stimulated the mRNA expression of OCN 2.5-fold ($P = 0.009$; **Figure 3B**), however no significant effect was observed on the secretion of OCN to the cell culture medium (results not shown). AMBN-WT stimulated the mRNA expression of RANKL; however neither AMBN nor its fragments had any significant effect on mRNA expression of OPG at the time-point analyzed (**Figures 3C,D**, respectively).

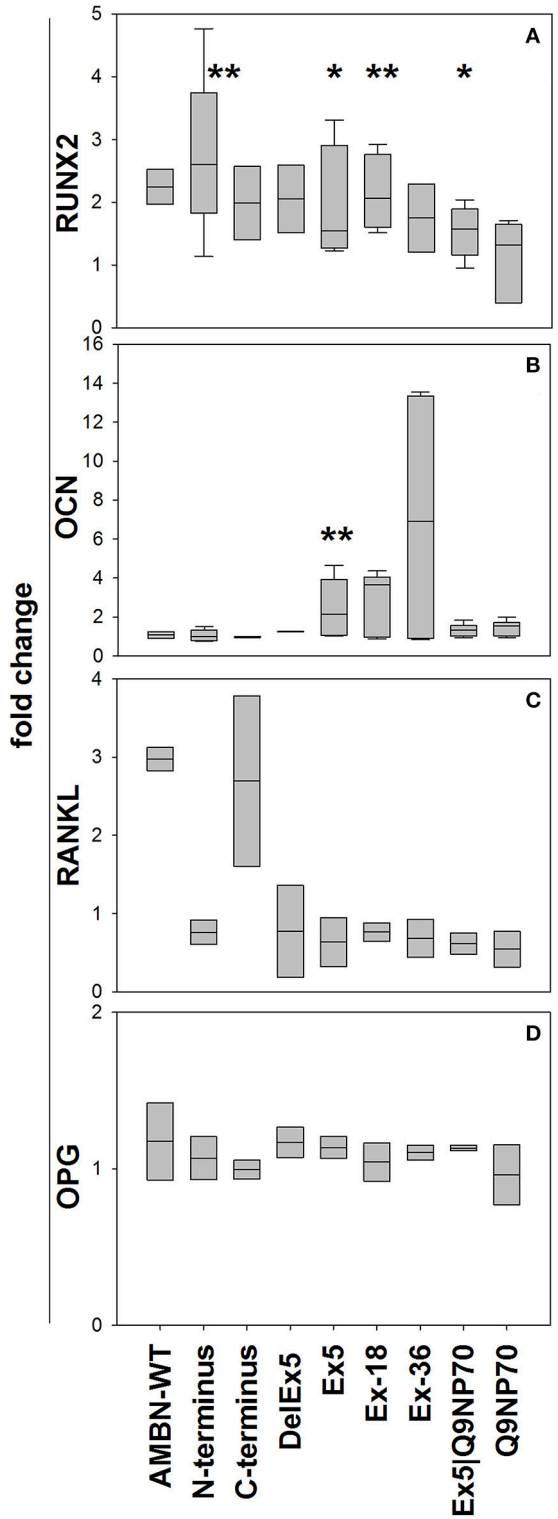

FIGURE 3 | Gene expression of RUNX2 (A), OCN **(B)**, RANKL **(C)**, and OPG **(D)** in human hMSCs at 72 h. Expression was normalized against the reference genes Glyceraldehyde-3-Phosphate Dehydrogenase (GADPH) and Beta Actin using the ΔΔCT method. Data are calculated relative to untreated control as fold-changes and presented as mean ± *SD* ($n = 5$) (%). *Indicate $P < 0.05$, **Indicate $P < 0.01$.

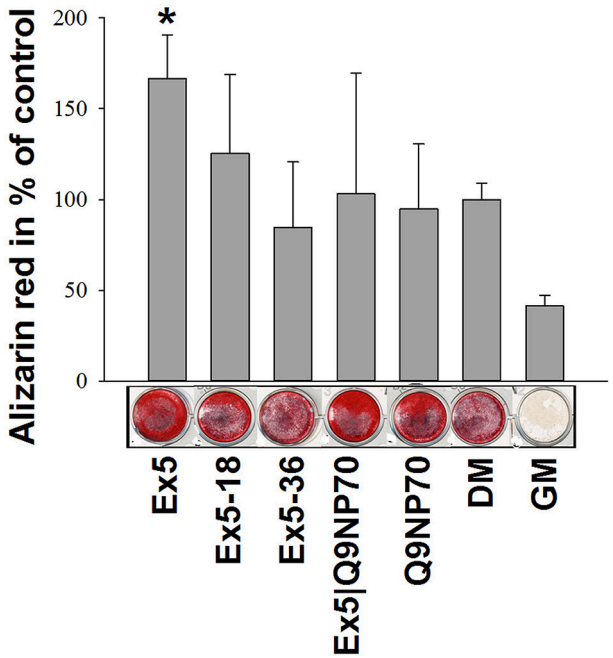

FIGURE 4 | Extracted alizarin red from mineralized surfaces of hMSC after 28 days incubation with Ex5, Ex5-18, Ex5-36, Ex5|Q9NP70, or Q9NP70 (0.2 μM). Data are presented as mean ± *SD* ($n = 5$) (%). *Indicate $P < 0.05$.

Mineralization of hMSC is Mostly Influenced by *exon 5* Derived Peptides

In initial tests with hMSC growing in regular medium for 21 days, none of the larger fragments AMBN-WT, N-terminus, C-terminus, or DelEx5, promoted *in vitro* mineralization. However, *exon 5* and *Q9NP70* derived peptides had a visible but not statistically significant, effect on the formation of mineralized nodules in hMSC cell cultures (results not shown). Only when a combination of Ex5 peptide and osteogenic medium (DM) was used did the mineralization increase significantly to 1.7-fold over the DM-only control ($P = 0.029$; **Figure 4**).

DISCUSSION

AMBN is first and foremost an extra cellular matrix protein, and may as such constitute a slow-release depot for biological signals. AMBN has not been identified as an intact soluble protein *in vivo* (Brookes et al., 2001; Iwata et al., 2007), and no complete information is available on the processing of AMBN in tissues other than in teeth. In other tissues, fragments are probably released into solution from the self-assembled AMBN complex, but little is known about the nature and the function of these fragments. Here we have shown that some selected fragments have discrete and significant effects on cultured hMSC.

To be able to compare different peptides and fragments we performed the experiments with equimolar concentrations. The recombinant proteins and peptides were administered to hMSC

in a dosage (0.2 μM) to reflect the levels previously shown to be secreted from cultured hMSC (Tamburstuen et al., 2011) and that has been shown to have effects in other experiments with hMSC (Tamburstuen et al., 2010). We also included a lower concentration of AMBN to test the responsiveness to concentration levels similar as found in mature osteoblasts (0.1 μM; Tamburstuen et al., 2011). Both concentrations induced effects on proliferation and secretion of chemokines, suggesting that the AMBN secreted from progenitor cells and osteoblasts (Tamburstuen et al., 2011) indeed can have an effect as a signaling molecule in mesenchymal tissues.

Proliferation of hMSC Were Modulated by AMBN-WT and Regions Derived by *exon 5* and *Q9NP70*

Proliferation of stem cells is a key feature in healing and tissue homeostasis. Here we have shown that AMBN-WT and peptide Ex5 stimulate hMSC proliferation. In fact Ex5 alone is more efficient as a signal for proliferation for these cells than the whole WT molecule, most probably due to superior bioavailability and/or a more favorable structural conformation. Interestingly, when exon 5 was deleted out of the full length AMBN there was little effect on proliferation, suggesting that Ex5 is a key element for this process. This was further demonstrated by the fact that additional processing of Ex5 into smaller fragments minimizes the effect on proliferation. The other fragments tested here did not significantly alter proliferation of hMSC. This is also supported by other studies, where a 15 aa peptide derived by *exon 2* and *exon 3* was shown not to influence proliferation (Kitagawa et al., 2011, 2016). Moreover, overexpression of AMBN lacking *exon 5* and *exon 6* in mice resulted in reduced bone growth, femur length, and higher fracture rate (Lu et al., 2016a,b) indirectly suggesting the importance of *exon* 5 in cell proliferation.

The regions derived by *exon 5* and *exon 6* have been shown to be vital for proper development of enamel (Smith et al., 2009; Wazen et al., 2009). Interestingly, the upstream part of *exon* 6 encodes a peptide (Q9NP70) that was found to inhibit proliferation of hMSC. This inhibition is probably stronger than the positive signal from Ex5 since the combination of the two (Ex5|Q9NP70) has a net inhibitory effect. However, this may also be due to steric inhibition or interfering pathways. The *exon 6* derived Q9NP70 has been found *in vivo* during post-natal tooth development (Lee et al., 2003; Ravindranath et al., 2007) and thus may contribute by inhibiting cell proliferation at a stage where differentiation probably is more developmentally desired than proliferation.

The C-terminus fragment of AMBN showed no effect on hMSC proliferation. This fragment has however, been found to inhibit the proliferation of PDL and dental follicle cells (Zhang et al., 2011). This suggests that the effect of the various processed AMBN fragments might be tissue specific in real life situations.

Cytokines/Chemokines Secretion Enhanced by AMBN Fragments

Several reports suggest that AMBN can play a role in regeneration of bone (Nakamura et al., 2006; Spahr et al., 2006; Tamburstuen et al., 2010; Lu et al., 2016a,b). Overexpression of AMBN has been found to increase osteoclastogenesis (Lu et al., 2013). Osteoclastogenesis and inflammation are both critical processes influencing the early stages in regeneration of bone (Mountziaris and Mikos, 2008). Here we have demonstrated that AMBN-WT significantly enhanced the secretion of MCP-1, IL-6, RANTES, MIP-1α, and IP-10. All these factors have been associated with osteoclastogenesis (Kotake et al., 1996; Watanabe et al., 2004; Kim et al., 2005, 2006) in addition to inflammatory processes (Schall et al., 1990; Dufour et al., 2002). Interestingly, again, this effect is only observed from peptides derived from the N-terminus part of the AMBN molecule. Moreover, when the N-terminus fragment was tested alone it also enhanced the secretion of IL-8.

None of the other fragments, DelEx5, C-terminus, Ex5, Ex5-18, Ex5-36, Ex5|Q9NP70, or Q9NP70, had any effect on the markers analyzed here. Relevant for bone formation is the fact that IL-8 so far is the only chemokine known to enhance secretion of MMPs (Li et al., 2003).

Both the N-terminus and AMBN-WT self-assemble into fibrils (Wald et al., 2013). It is a surprising but striking feature that only these fibril forming regions affected the secretion of cytokines / chemokines from hMSC. Receptor oligomerization (George et al., 2002) has been shown to enhance secretion of chemokines (Martinez-Martin et al., 2015). Fibril formation of AMBN may be a way to expose multiple signaling motifs in close proximity, which in turn could bind several motifs at once and thus initiating chemokine associated receptor oligomerization.

The AMBN-WT includes the C-terminus that has been suggested to provide cell anchoring (Fukumoto et al., 2004) through DGEA binding motifs (Cerný et al., 1996). AMBN has also been shown to bind integrin β1 (Iizuka et al., 2011; Lu et al., 2013), and Integrin β1 ligands have been shown to enhance secretion of RANTES (Peng et al., 2005). This may explain the observation that AMBN-WT is more potent in enhancing secretion of cytokines and chemokines than its processed products.

Expressed Markers for Differentiation and Mineralization

The expression of RUNX2, a transcriptional factor for extracellular matrix proteins like collagen and OCN (Ducy et al., 1997; Kern et al., 2001), has been found to be enhanced by AMBN and synthetic peptides derived from its 17 kDa fragment in PDL (Kitagawa et al., 2011, 2016). Enhanced hMSC expression of RUNX2 and OCN by the N-terminus, *exon 5*, and *Q9NP70* peptides presented here, support the idea that AMBN has effect on bone differentiation and mineralization.

This is further underlined by AMBN knockdown experiments that show reduction in alizarin red deposition during mineralized nodule formation (Iizuka et al., 2011). In the initial experiments on hMSC grown in GM we here found effects on mineralization only with the *exon 5* and the *Q9NP70* derivedpeptides. *Exon 5* and *exon 6* (including Q9NP70) have previously been shown to be important in enamel mineralization

(Smith et al., 2009; Wazen et al., 2009). Accordingly, we confirmed that the Ex5 peptide stimulates calcium deposition under mineralizing conditions (DM) as visualized by alizarin staining.

CONCLUSION

AMBN-WT enhances the proliferation of hMSCs and secretion of cytokines/chemokines. Moreover, the two main AMBN processing fragments and derived peptides have markedly diverse effects. The N-terminus portion seems to enhance secretion of cytokines/chemokines, whereas peptides derived by *exon 5* and *Q9NP70* modulate proliferation, enhance secretion of markers for hMSC differentiation and extracellular mineralization. In contrast the C-terminus fragment shows no discernible effect on hMSC differentiation or proliferation and is probably only involved in cell attachment.

AUTHOR CONTRIBUTIONS

ØS contributed in experimental design, performed and analyzed experiments, drafted and wrote the manuscript, SL contributed in experimental design, drafting and finalizing the manuscript. JV provided essential materials and contributed in experimental design. JG contributed in experimental design and in drafting of the manuscript, JR contributed in experimental design, drafting and finalizing the manuscript.

ACKNOWLEDGMENTS

This work was supported by grants from EU (QLK3-CT-2001-00090) and the Research Council of Norway (231530) The authors are grateful for the skillful technical assistance of Aina-Mari Lian, Oral Research Laboratory and Rune Hartvig, Department of Biomaterials. The authors declare no conflict of interest.

REFERENCES

Brookes, S. J., Kirkham, J., Shore, R. C., Wood, S. R., Slaby, I., and Robinson, C. (2001). Amelin extracellular processing and aggregation during rat incisor amelogenesis. *Arch. Oral Biol.* 46, 201–208. doi: 10.1016/S0003-9969(00)00121-7

Cerný, R., Slaby, I., Hammarstrom, L., and Wurtz, T. (1996). A novel gene expressed in rat ameloblasts codes for proteins with cell binding domains. *J. Bone Miner. Res.* 11, 883–891. doi: 10.1002/jbmr.5650110703

Dahl, L. K. (1952). A simple and sensitive histochemical method for calcium. *Proc. Soc. Exp. Biol. Med.* 80, 474–479. doi: 10.3181/00379727-80-19661

Ducy, P., Zhang, R., Geoffroy, V., Ridall, A. L., and Karsenty, G. (1997). Osf2/Cbfa1: a transcriptional activator of osteoblast differentiation. *Cell* 89, 747–754. doi: 10.1016/S0092-8674(00)80257-3

Dufour, J. H., Dziejman, M., Liu, M. T., Leung, J. H., Lane, T. E., and Luster, A. D. (2002). IFN-gamma-inducible protein 10 (IP-10; CXCL10)-deficient mice reveal a role for IP-10 in effector T cell generation and trafficking. *J. Immunol.* 168, 3195–3204. doi: 10.4049/jimmunol.168.7.3195

Fong, C. D., Cerny, R., Hammarstrom, L., and Slaby, I. (1998). Sequential expression of an amelin gene in mesenchymal and epithelial cells during odontogenesis in rats. *Eur. J. Oral Sci.* 106(Suppl. 1), 324–330. doi: 10.1111/j.1600-0722.1998.tb02193.x

Fong, C. D., Slaby, I., and Hammarstrom, L. (1996). Amelin: an enamel-related protein, transcribed in the cells of epithelial root sheath. *J. Bone Miner. Res.* 11, 892–898. doi: 10.1002/jbmr.5650110704

Fukae, M., Kanazashi, M., Nagano, T., Tanabe, T., Oida, S., and Gomi, K. (2006). Porcine sheath proteins show periodontal ligament regeneration activity. *Eur. J. Oral Sci.* 114(Suppl. 1), 212–218. discussion: 254–216, 381–212. doi: 10.1111/j.1600-0722.2006.00309.x

Fukumoto, S., Kiba, T., Hall, B., Iehara, N., Nakamura, T., Longenecker, G., et al. (2004). Ameloblastin is a cell adhesion molecule required for maintaining the differentiation state of ameloblasts. *J. Cell Biol.* 167, 973–983. doi: 10.1083/jcb.200409077

George, S. R., O'Dowd, B. F., and Lee, S. P. (2002). G-Protein-coupled receptor oligomerization and its potential for drug discovery. *Nat. Rev. Drug Discov.* 1, 808–820. doi: 10.1038/nrd913

Hu, C. C., Fukae, M., Uchida, T., Qian, Q., Zhang, C. H., Ryu, O. H., et al. (1997). Sheathlin: cloning, cDNA/polypeptide sequences, and immunolocalization of porcine enamel sheath proteins. *J. Dent. Res.* 76, 648–657. doi: 10.1177/00220345970760020501

Iizuka, S., Kudo, Y., Yoshida, M., Tsunematsu, T., Yoshiko, Y., Uchida, T., et al. (2011). Ameloblastin regulates osteogenic differentiation by inhibiting Src kinase via cross talk between integrin beta1 and CD63. *Mol. Cell. Biol.* 31, 783–792. doi: 10.1128/MCB.00912-10

Iwata, T., Yamakoshi, Y., Hu, J. C., Ishikawa, I., Bartlett, J. D., Krebsbach, P. H., et al. (2007). Processing of ameloblastin by MMP-20. *J. Dent. Res.* 86, 153–157. doi: 10.1177/154405910708600209

Kern, B., Shen, J., Starbuck, M., and Karsenty, G. (2001). Cbfa1 contributes to the osteoblast-specific expression of type I collagen genes. *J. Biol. Chem.* 276, 7101–7107. doi: 10.1074/jbc.M006215200

Kim, M. S., Day, C. J., and Morrison, N. A. (2005). MCP-1 is induced by receptor activator of nuclear factor-{kappa}B ligand, promotes human osteoclast fusion, and rescues granulocyte macrophage colony-stimulating factor suppression of osteoclast formation. *J. Biol. Chem.* 280, 16163–16169. doi: 10.1074/jbc.M412713200

Kim, M. S., Magno, C. L., Day, C. J., and Morrison, N. A. (2006). Induction of chemokines and chemokine receptors CCR2b and CCR4 in authentic human osteoclasts differentiated with RANKL and osteoclast like cells differentiated by MCP-1 and RANTES. *J. Cell. Biochem.* 97, 512–518. doi: 10.1002/jcb.20649

Kitagawa, M., Ando, T., Subarnbhesaj, A., Uchida, T., Miyauchi, M., and Takata, T. (2016). N-terminal region of human ameloblastin synthetic peptide promotes bone formation. *Odontology* 105, 116–121. doi: 10.1007/s10266-016-0243-8

Kitagawa, M., Kitagawa, S., Nagasaki, A., Miyauchi, M., Uchida, T., and Takata, T. (2011). Synthetic ameloblastin peptide stimulates differentiation of human periodontal ligament cells. *Arch. Oral Biol.* 56, 374–379. doi: 10.1016/j.archoralbio.2010.10.012

Kotake, S., Sato, K., Kim, K. J., Takahashi, N., Udagawa, N., Nakamura, I., et al. (1996). Interleukin-6 and soluble interleukin-6 receptors in the synovial fluids from rheumatoid arthritis patients are responsible for osteoclast-like cell formation. *J. Bone Miner. Res.* 11, 88–95. doi: 10.1002/jbmr.5650110113

Lee, S. K., Kim, S. M., Lee, Y. J., Yamada, K. M., Yamada, Y., and Chi, J. G. (2003). The structure of the rat ameloblastin gene and its expression in amelogenesis. *Mol. Cells* 15, 216–225.

Li, A., Dubey, S., Varney, M. L., Dave, B. J., and Singh, R. K. (2003). IL-8 directly enhanced endothelial cell survival, proliferation, and matrix metalloproteinases production and regulated angiogenesis. *J. Immunol.* 170, 3369–3376. doi: 10.4049/jimmunol.170.6.3369

Lu, X., Fukumoto, S., Yamada, Y., Evans, C. A., Diekwisch, T. G., and Luan, X. (2016a). Ameloblastin, an extracellular matrix protein, affects long bone growth and mineralization. *J. Bone Miner. Res.* 31, 1235–1246. doi: 10.1002/jbmr.2788

Lu, X., Ito, Y., Atsawasuwan, P., Dangaria, S., Yan, X., Wu, T., et al. (2013). Ameloblastin modulates osteoclastogenesis through the integrin/ERK pathway. *Bone* 54, 157–168. doi: 10.1016/j.bone.2013.01.041

Lu, X., Li, W., Fukumoto, S., Yamada, Y., Evans, C. A., Diekwisch, T., et al. (2016b). The ameloblastin extracellular matrix molecule enhances bone

fracture resistance and promotes rapid bone fracture healing. *Matrix Biol.* 52–54, 113–126. doi: 10.1016/j.matbio.2016.02.007

Martinez-Martin, N., Viejo-Borbolla, A., Martin, R., Blanco, S., Benovic, J. L., Thelen, M., et al. (2015). Herpes simplex virus enhances chemokine function through modulation of receptor trafficking and oligomerization. *Nat. Commun.* 6, 6163. doi: 10.1038/ncomms7163

Mountziaris, P. M., and Mikos, A. G. (2008). Modulation of the inflammatory response for enhanced bone tissue regeneration. *Tissue Eng. Part B Rev.* 14, 179–186. doi: 10.1089/ten.teb.2008.0038

Nakamura, Y., Slaby, I., Spahr, A., Pezeshki, G., Matsumoto, K., and Lyngstadaas, S. P. (2006). Ameloblastin fusion protein enhances pulpal healing and dentin formation in porcine teeth. *Calcif. Tissue Int.* 78, 278–284. doi: 10.1007/s00223-005-0144-2

Peng, Q., Lai, D., Nguyen, T. T., Chan, V., Matsuda, T., and Hirst, S. J. (2005). Multiple beta 1 integrins mediate enhancement of human airway smooth muscle cytokine secretion by fibronectin and type I collagen. *J. Immunol.* 174, 2258–2264. doi: 10.4049/jimmunol.174.4.2258

Ravindranath, R. M., Devarajan, A., and Uchida, T. (2007). Spatiotemporal expression of ameloblastin isoforms during murine tooth development. *J. Biol. Chem.* 282, 36370–36376. doi: 10.1074/jbc.M704731200

Schall, T. J., Bacon, K., Toy, K. J., and Goeddel, D. V. (1990). Selective attraction of monocytes and T lymphocytes of the memory phenotype by cytokine RANTES. *Nature* 347, 669–671.

Smith, C. E., Wazen, R., Hu, Y., Zalzal, S. F., Nanci, A., Simmer, J. P., et al. (2009). Consequences for enamel development and mineralization resulting from loss of function of ameloblastin or enamelin. *Eur. J. Oral Sci.* 117, 485–497. doi: 10.1111/j.1600-0722.2009.00666.x

Sonoda, A., Iwamoto, T., Nakamura, T., Fukumoto, E., Yoshizaki, K., Yamada, A., et al. (2009). Critical role of heparin binding domains of ameloblastin for dental epithelium cell adhesion and ameloblastoma proliferation. *J. Biol. Chem.* 284, 27176–27184. doi: 10.1074/jbc.M109.033464

Spahr, A., Lyngstadaas, S. P., Slaby, I., and Pezeshki, G. (2006). Ameloblastin expression during craniofacial bone formation in rats. *Eur. J. Oral Sci.* 114, 504–511. doi: 10.1111/j.1600-0722.2006.00403.x

Stout, B. M., Alent, B. J., Pedalino, P., Holbrook, R., Gluhak-Heinrich, J., Cui, Y., et al. (2014). Enamel matrix derivative: protein components and osteoinductive properties. *J. Periodontol.* 85, e9–e17. doi: 10.1902/jop.2013.130264

Takahashi, K., Shimonishi, M., Wang, R., Watanabe, H., and Kikuchi, M. (2012). Epithelial-mesenchymal interactions induce enamel matrix proteins and proteases in the epithelial cells of the rests of Malassez *in vitro*. *Eur. J. Oral Sci.* 120, 475–483. doi: 10.1111/j.1600-0722.2012.01002.x

Tamburstuen, M. V., Reppe, S., Spahr, A., Sabetrasekh, R., Kvalheim, G., Slaby, I., et al. (2010). Ameloblastin promotes bone growth by enhancing proliferation of progenitor cells and by stimulating immunoregulators. *Eur. J. Oral Sci.* 118, 451–459. doi: 10.1111/j.1600-0722.2010.00760.x

Tamburstuen, M. V., Reseland, J. E., Spahr, A., Brookes, S. J., Kvalheim, G., Slaby, I., et al. (2011). Ameloblastin expression and putative autoregulation in mesenchymal cells suggest a role in early bone formation and repair. *Bone* 48, 406–413. doi: 10.1016/j.bone.2010.09.007

Toyosawa, S., Fujiwara, T., Ooshima, T., Shintani, S., Sato, A., Ogawa, Y., et al. (2000). Cloning and characterization of the human ameloblastin gene. *Gene* 256, 1–11. doi: 10.1016/S0378-1119(00)00379-6

Uchida, T., Murakami, C., Dohi, N., Wakida, K., Satoda, T., and Takahashi, O. (1997). Synthesis, secretion, degradation, and fate of ameloblastin during the matrix formation stage of the rat incisor as shown by immunocytochemistry and immunochemistry using region-specific antibodies. *J. Histochem. Cytochem.* 45, 1329–1340. doi: 10.1177/002215549704501002

Vymetal, J., Slaby, I., Spahr, A., Vondrasek, J., and Lyngstadaas, S. P. (2008). Bioinformatic analysis and molecular modelling of human ameloblastin suggest a two-domain intrinsically unstructured calcium-binding protein. *Eur. J. Oral Sci.* 116, 124–134. doi: 10.1111/j.1600-0722.2008.00526.x

Wald, T., Osickova, A., Sulc, M., Benada, O., Semeradtova, A., Rezabkova, L., et al. (2013). Intrinsically disordered enamel matrix protein ameloblastin forms ribbon-like supramolecular structures via an N-terminal segment encoded by exon 5. *J. Biol. Chem.* 288, 22333–22345. doi: 10.1074/jbc.M113.456012

Watanabe, T., Kukita, T., Kukita, A., Wada, N., Toh, K., Nagata, K., et al. (2004). Direct stimulation of osteoclastogenesis by MIP-1alpha: evidence obtained from studies using RAW264 cell clone highly responsive to RANKL. *J. Endocrinol.* 180, 193–201. doi: 10.1677/joe.0.1800193

Wazen, R. M., Moffatt, P., Zalzal, S. F., Yamada, Y., and Nanci, A. (2009). A mouse model expressing a truncated form of ameloblastin exhibits dental and junctional epithelium defects. *Matrix Biol.* 28, 292–303. doi: 10.1016/j.matbio.2009.04.004

Zhang, Y., Zhang, X., Lu, X. Y., Atsawasuwan, P., and Luan, X. H. (2011). Ameloblastin regulates cell attachment and proliferation through RhoA and p27. *Eur. J. Oral Sci.* 119, 280–285. doi: 10.1111/j.1600-0722.2011.00887.x

Conflict of Interest Statement: The authors declare that the research was conducted in the absence of any commercial or financial relationships that could be construed as a potential conflict of interest.

Copyright © 2017 Stakkestad, Lyngstadaas, Vondrasek, Gordeladze and Reseland. This is an open-access article distributed under the terms of the Creative Commons Attribution License (CC BY). The use, distribution or reproduction in other forums is permitted, provided the original author(s) or licensor are credited and that the original publication in this journal is cited, in accordance with accepted academic practice. No use, distribution or reproduction is permitted which does not comply with these terms.

frontiers in Physiology

ORIGINAL RESEARCH
published: 17 October 2017
doi: 10.3389/fphys.2017.00805

Intravesicular Phosphatase PHOSPHO1 Function in Enamel Mineralization and Prism Formation

Mirali Pandya[1,2], *Lauren Rosene*[1,2], *Colin Farquharson*[3], *José L. Millán*[4] and *Thomas G. H. Diekwisch*[1,2]*

[1] Department of Periodontics, Texas A&M College of Dentistry, Dallas, TX, United States, [2] Center for Craniofacial Research and Diagnosis, Texas A&M College of Dentistry, Dallas, TX, United States, [3] Division of Developmental Biology, The Roslin Institute and The Royal (Dick) School of Veterinary Studies, University of Edinburgh, Edinburgh, United Kingdom, [4] Sanford Children's Health Research Center, Sanford-Burnham Institute for Medical Research, La Jolla, CA, United States

OPEN ACCESS

Edited by:
Steven Joseph Brookes,
Leeds Dental Institute,
United Kingdom

Reviewed by:
Pierfrancesco Pagella,
University of Zurich, Switzerland
Janet Moradian-Oldak,
University of Southern California,
United States
Amel Gritli-Linde,
University of Gothenburg, Sweden

***Correspondence:**
Thomas G. H. Diekwisch
diekwisch@tamhsc.edu

Specialty section:
This article was submitted to Craniofacial Biology and Dental Research, a section of the journal Frontiers in Physiology

Received: 22 June 2017
Accepted: 29 September 2017
Published: 17 October 2017

Citation:
Pandya M, Rosene L, Farquharson C, Millán JL and Diekwisch TGH (2017) Intravesicular Phosphatase PHOSPHO1 Function in Enamel Mineralization and Prism Formation. Front. Physiol. 8:805. doi: 10.3389/fphys.2017.00805

The transport of mineral ions from the enamel organ-associated blood vessels to the developing enamel crystals involves complex cargo packaging and carriage mechanisms across several cell layers, including the ameloblast layer and the stratum intermedium. Previous studies have established PHOSPHO1 as a matrix vesicle membrane-associated phosphatase that interacts with matrix vesicles molecules phosphoethanolamine and phosphocholine to initiate apatite crystal formation inside of matrix vesicles in bone. In the present study, we sought to determine the function of *Phospho1* during amelogenesis. PHOSPHO1 protein localization during amelogenesis was verified using immunohistochemistry, with positive signals in the enamel layer, ameloblast Tomes' processes, and in the walls of ameloblast secretory vesicles. These ameloblast secretory vesicle walls were also labeled for amelogenin and the exosomal protein marker HSP70 using immunohistochemistry. Furthermore, PHOSPHO1 presence in the enamel organ was confirmed by Western blot. *Phospho1*$^{-/-}$ mice lacked sharp incisal tips, featured a significant 25% increase in total enamel volume, and demonstrated a significant 2-fold reduction in silver grain density of von Kossa stained ground sections indicative of reduced mineralization in the enamel layer when compared to wild-type mice ($p < 0.001$). Scanning electron micrographs of *Phospho1*$^{-/-}$ mouse enamel revealed a loss of the prominent enamel prism "picket fence" structure, a loss of parallel crystal organization within prisms, and a 1.56-fold increase in enamel prism width ($p < 0.0001$). Finally, EDS elemental analysis demonstrated a significant decrease in phosphate incorporation in the enamel layer when compared to controls ($p < 0.05$). Together, these data establish that the matrix vesicle membrane-associated phosphatase PHOSPHO1 is essential for physiological enamel mineralization. Our findings also suggest that intracellular ameloblast secretory vesicles have unexpected compositional similarities with the extracellular matrix vesicles of bone, dentin, and cementum in terms of vesicle membrane composition and intravesicular ion assembly.

Keywords: amelogenesis, PHOSPHO1, ameloblast, enamel, matrix vesicle

INTRODUCTION

Amelogenesis is a complex process that involves a multitude of proteins and proteinases to facilitate the orderly assembly of elongated calcium phosphate apatite crystals into enamel prisms. Early studies have established that proline/glutamine-rich enamel proteins such as amelogenin, ameloblastin, and enamelin control enamel crystal shape and habit by facilitating enamel crystal growth in c-axis dimension and limiting their expansion in width (Diekwisch et al., 1993; Masuya et al., 2005; Hatakeyama et al., 2009; Gopinathan et al., 2014). During the secretion of these structural proteins, two enamel proteases, MMP20 and KLK4, are involved in the processing and degradation of the proline-rich enamel matrix (Ryu et al., 2002; Shin et al., 2014). Through the step-wise removal of the organic protein matrix, the MMP20 and KLK4 enamel proteases facilitate inorganic crystal nucleation and growth resulting in an overall increase of enamel hardness (Lu et al., 2008). In addition, MMP20 appears to have additional functions related to the stability of the dentin-enamel junction, ameloblast retreat during enamel thickening, and ameloblast differentiation (Hu et al., 2016).

Enamel proteases not only affect enamel crystal growth by processing matrix proteins such as amelogenins that are directly in contact with the growing crystal surface. Enzymes also play a role as components of the vesicular transport machinery that facilitates the orderly movement of ions, notably calcium and phosphate, from the blood vessels of the enamel organ into the enamel layer. The secretory cells of bone, dentin, and cartilage connective tissues contain small vesicles surrounded by a lipid bilayer that in addition to small calcium phosphate crystals contain a number of enzymes that are important for their function in tissue mineralization, including tissue non-specific alkaline phosphate (TNAP), nucleotide pyrophosphatase phosphodiesterase (NPP1/PC-1), annexins (ANX), and other matrix metalloproteinases (MMPs; Hsu and Anderson, 1978; Anderson, 1984; Bonucci, 1992; Dean et al., 1992; Wuthier et al., 1992). These unique proteases have been implicated in the mineralization of bone and dentin (Golub, 2009).

One of the matrix vesicle enzymes involved in initiation of bone, dentin, and cartilage mineralization is the matrix vesicle phosphatase PHOSPHO1 (Millán, 2013). PHOSPHO1 has been identified in the matrix vesicles of osteoblasts, odontoblasts, and chondrocytes (Houston et al., 2004; Roberts et al., 2007; McKee et al., 2013). Biochemical studies have characterized PHOSPHO1 as a haloacid dehalogenase family member that interacts with matrix vesicle molecules phosphoethanolamine and phosphocholine to initiate apatite crystal formation inside of matrix vesicles (Millán, 2013; Cui et al., 2016). PHOSPHO1 has also been localized in ameloblasts (McKee et al., 2013), and enzyme replacement therapy has verified the essential role of the matrix vesicle alkaline phosphate TNAP for enamel formation (Yadav et al., 2012), but according to textbook knowledge, enamel mineralization occurs without the involvement of matrix vesicles (Nanci, 2008).

We thus conducted the present study to characterize the role of PHOSPHO1 during amelogenesis and to determine the function of PHOSPHO1 as a component of the ameloblast secretory vesicle wall in its effect on enamel structure and mineralization. We hypothesized that the loss of PHOSPHO1 would affect enamel structural integrity through a delay in intravesicular mineralization initiation, and we used light and electron microscopy as well as elemental mapping and von Kossa staining to characterize the effects of loss of PHOSPHO1 on the enamel layer. Our data not only provide a structural characterization of the *Phospho1* deficient enamel but also give insights into the function of the matrix vesicle phosphatase PHOSPHO1 related to enamel ion transport in vesicles.

MATERIALS AND METHODS

Animal Models and Biosafety

Animals were sacrificed in accordance with guidelines of the Animal Care and Use Committee at the Sanford Burnham Prebys Medical Discovery Institute and National Institutes of Health (NIH). Breeding, genotyping, and characterization of *Phospho1*$^{-/-}$ mice has been described previously (Yadav et al., 2011; Zweifler et al., 2016). Eleven mandibles each from control and *Phospho1*$^{-/-}$ mice were chosen for histology and microscopy studies. All research involving biohazards and toxins has been carried out according to Texas A&M institutional biosafety standards.

Ultrathin Ground Sections of Control and *Phospho1*$^{-/-}$ Mouse Mandibles

Thirty day old hemi-mandibles of control and *Phospho1*$^{-/-}$ were fixed in 10% formalin and processed for ground sections. The mandibles were subjected to a series of different gradients of alcohol as well as mixture of ethanol/technovit as per the EXAKT company standard protocol for preparation of tissue samples for ground sections. Once the samples were in 100% light cure technovit (Technovit 7200, EXAKT), they were polymerized and embedded. The samples were grossly sectioned using a diamond bandsaw (EXAKT 300 CP), ground and polished to produce 30 μm thin sections (Liu et al., 2016). Two of the four ground sections were stained with alizarin red for 90 min and the other two for von Kossa staining.

Radiographs

Thirty day old hemi-mandibles were analyzed using a Faxitron MX-20 specimen radiography system (Faxitron X-ray Corp., IL) at 20 kV for 20 s.

Micro-CT Analysis

Three WT and three *Phospho1*$^{-/-}$ mouse mandibles were imaged individually and analyzed using a Micro-CT 20 Scanco Medical Scanner (Zürich, Switzerland). Specimens were scanned in standard resolution mode, with *x*-, *y*-, and *z*-axis resolution of ∼10 μm. The level of X-ray exposure was 55 kVp energy and 800 ms exposure time. After the scanning was completed, 3-D data were generated by segmenting specimens at a threshold chosen to only include enamel tissue based on a morphological match with normal tooth histology. For each mandible, 70 slices were assembled and analyzed to perform a 3-D reconstruction of the incisors, and the total enamel volume fractions of the incisors were calculated and compared between the WT and *Phospho1*$^{-/-}$ samples.

Scanning Electron Microscopy (SEM) and Energy Dispersive X-ray Spectroscopy (EDS)

Thirty day old hemi-mandibles for control and *Phospho1*$^{-/-}$ mice were fixed in 10% formalin and treated gently with 4.5% EDTA for 15 min. The etched samples were dried and sputter coated with Au/Pd alloy for 90 s. These mandibles were further analyzed using a scanning electron microscope (JEOL JSM-6010LA). For EDS analysis, the samples were fixed, dried, and analyzed by selecting five random points in the enamel region. The elemental mapping at the selected points was recorded and the mass percent amount of calcium and phosphorous was compared between the control and PHOSPHO1 samples.

Transmission Electron Microscopy

E16 tooth organs were cultured for 12 days, and thereafter fixed in Karnovsky's fixative as previously described (Diekwisch, 1998), dehydrated and embedded in Eponate 12 (Ted Pella, Redding, CA). Following polymerization of the Eponate, ultrathin sections were cut on a Leica Ultracut UCT ultramicrotome. After drying, sections were contrasted using uranyl acetate and Reynold's lead citrate for 15 min each. Stained sections were examined using a JEOL 1220EX transmission electron microscope at the UIC Research Resources Center (Chicago, IL).

Paraffin Sections and Immunohistochemistry

Three days old hemi-mandibles of three wild-type mice were fixed in 10% formalin, decalcified with 4.5% EDTA for 1 week, and then processed for regular paraffin sectioning after dehydrating through graded series of ethanol and xylene. Alternatively, a second set of 3-days old wildtype mandibles was fixed in Bouin's fixative and also processed into 5 μm thin paraffin sections. For antigen retrieval, the paraffin fixed samples were incubated in 10 mM sodium citrate buffer for 30 min at pH 6 and boiling temperature. Alternatively, the samples fixed in Bouin's fixative were treated with 8M guanidine HCl overnight at 4°C and pH 8 to unmask the PHOSPHO1 antigen sites as suggested by McKee et al. (2013). Following antigen retrieval, samples were incubated using human recombinant Fab monoclonal anti-PHOSPHO1 primary antibody (AbD Serotec, Morphosys AG) or polyclonal anti-PHOSPHO1 antibody (GeneTex, USA) for PHOSPHO1 identification. Other vesicle associated proteins such as amelogenin or HSP70 were labeled using a polyclonal anti-amelogenin antibody or a mouse monoclonal anti-HSP70 antibody (Abcam, Cambridge, MA). Immunohistochemistry was performed using a broad spectrum IHC staining kit and an AEC substrate kit (Life Technologies, Carlsbad, CA) and stained sections were analyzed using a Leica DMR light microscope (Nuhsbaum, IL).

Western Blot

Enamel organs were immediately harvested from unerupted mandibular molars of 3 months old pigs sacrificed at a local animal farm. The enamel organs were subjected to extraction with 0.5% sodium dodecyl sulfate (SDS) lysis buffer with subsequent extraction with 4M guanidine HCl (pH 7.4). Initially, the proteins from enamel organ were extracted using SDS lysis buffer for 5 days. The supernatant was collected after centrifugation at 2,400 g and 4°C. The residue after SDS extraction was subjected to extraction with 4M guanidine (Gu) HCl buffer for 5 days. The supernatant from Gu-based extract was collected and processed following the same procedure as the SDS based extract. The extracted protein lysate from SDS and Gu-based extracts were dialyzed against double distilled water for 1 week. Equal amounts of protein extracts were loaded for both groups in a 10% SDS polyacrylamide gel and was subjected to gel electrophoresis at 150 V for 58 min. A semi-dry transfer system was used to transfer proteins from the gel to a polyvinylidine difluoride (PVDF) membrane at 18 V for 40 min. The PVDF membrane was blocked for 1 h with 5% dry milk in tris buffered saline with tween 20 (TBST), incubated with human recombinant Fab monoclonal anti-PHOSPHO1 primary antibody (1:500, AbD Serotec, Morphosys AG) for 1 h, followed by washing in TBST three times for 15 min and incubation with anti-mouse IgG HRP conjugated secondary antibody (1:2,000, cell signaling) for 1 h. The signal was detected using a chemiluminescent substrate (Thermo Scientific, USA).

Statistical Analysis

The width and the inter-prism space of enamel prisms was measured based on three control and three *Phospho1*$^{-/-}$ samples. Measurement of prism width and interprismatic distance were obtained from scanning electron micrographs of etched mouse molar enamel cross sections. For our analysis, only mid-sagittal cross sections were chosen, and all samples were etched at identical times and concentrations, and rinsed for the same amount of time. Representative micrographs at 750x magnification from the distal interproximal enamel of the first molar were chosen for further analysis based on optimal prism pattern identification. Ten prisms were randomly chosen from each micrograph, and their width and the inter-prism space were measured using the ImageJ software. To analyze the silver grain density in von Kossa stained sections, micrographs at 400x magnification were imported into the ImageJ software package, and three 100 × 100 μm areas within the *Phospho1*$^{-/-}$ and WT cuspal tip molar enamel region were randomly chosen and pixel density was analyzed. For EDS analysis, ten points were randomly chosen in the enamel region of three *Phospho1*$^{-/-}$ and WT molars, and the values of calcium and phosphorus at the selected points was compared between both groups. All experiments were done in triplicates, the data analysis was conducted using student's *T*-test, and the significance value was set at $p < 0.05$.

RESULTS

PHOSPHO1 Protein Localization in the Enamel Layer and the Walls of Secretory Vesicles

Immunohistochemical and Western blot analysis were performed to verify whether the PHOSPHO1 protein was localized in the enamel organ. Our analysis of paraffin sections

of 3 days old wildtype mice revealed PHOSPHO1 protein localization in the enamel layer, Tomes' processes, and in ameloblast secretory vesicles (**Figure 1**). Positive signals for PHOSPHO1 were obtained using both antibodies available to us (GTX119275 from Genetex in **Figures 1A,C** and AbD Serotec/Millán in **Figures 1B,D**) and independent from the type of fixative employed (Formalin in **Figures 1A,C,E,** and Bouin in **Figures 1B,D**). In general, PHOSPHO1 expression levels were stronger in the mineralized enamel layer and at the ameloblast secretory pole (**Figures 1A,C**), while there was no staining in the control section using the same technique without primary antibody (**Figure 1E**). High magnification images revealed positive staining for PHOSPHO1 at the periphery of circular organelles at the ameloblast secretory pole (**Figure 1C,D**). A Western blot using the AbD Serotec antibody and performed on guanidine or SDS extracts of enamel organs demonstrated a characteristic 32 KDa full-length PHOSPHO1 band and a 25 kDa cleavage product, confirming the presence of PHOSPHO1 in the enamel organ.

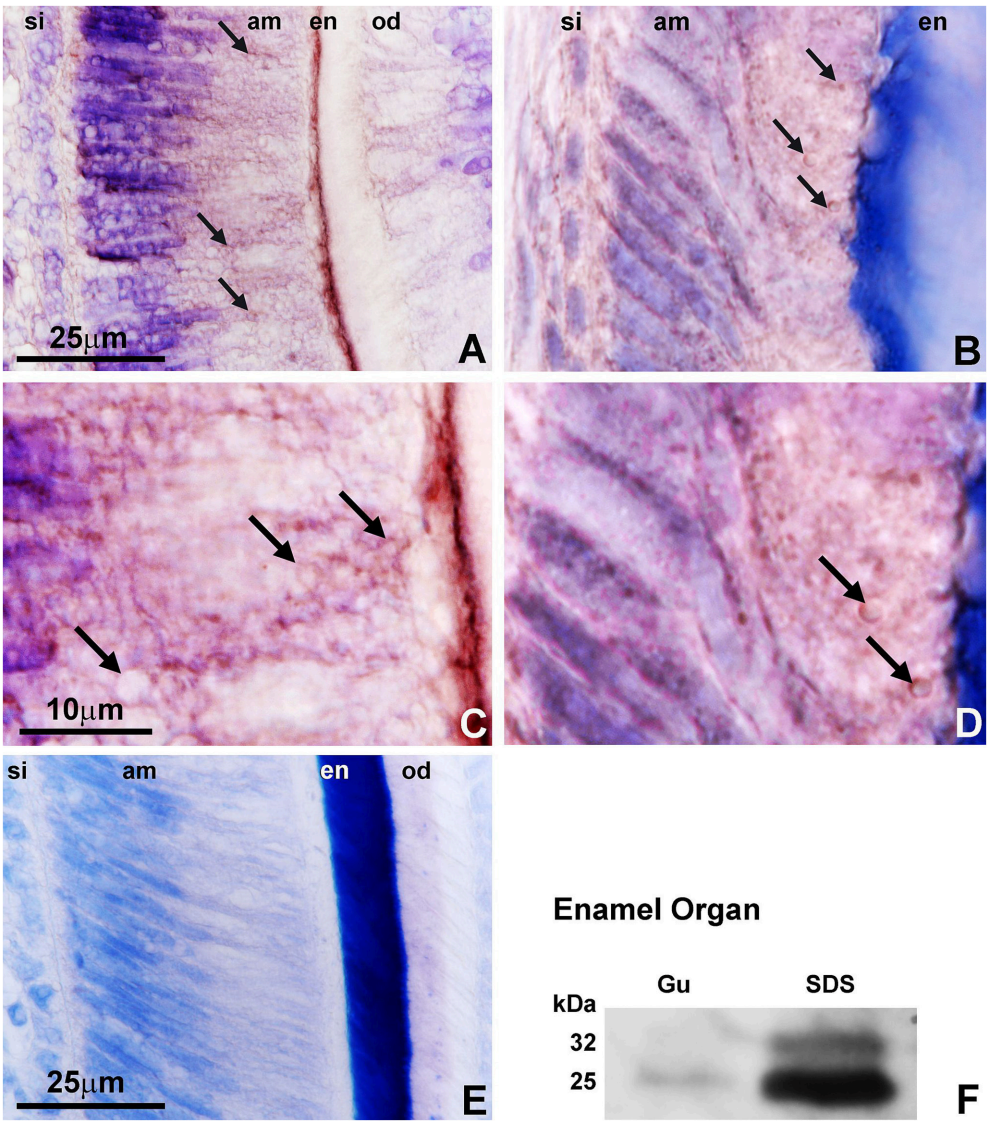

FIGURE 1 | PHOSPHO1 localization in the ameloblast secretory vesicle walls. The first set of immunoreactions **(A,C)** was generated using a commercial antibody (GTX119275) and the second set was based on the original antibody from the Millán lab (AbD Serotec) **(B,D)**. Immunohistochemical labeling **(A–D)** located PHOSPHO1 at the periphery of secretory vesicles (arrows) and in the enamel layer of 3 days postnatal (dpn) WT mouse molars (en). **(C,D)** are higher magnification images of **(A,B)** allowing for detailed assessment of Phospho1 localization in ameloblast secretory vesicle walls (arrows). **(E)** is a same stage mouse molar control in which the primary antibody was replaced with pre-immune serum. **(F)** is a Western blot demonstrating the characteristic 32 KDa full-length PHOSPHO1 band and a 25 kDa cleavage product using the AbD Serotec antibody on blotted enamel organ extracts. Gu were 4M guanidine extracts and SDS were SDS extracts of enamel organ tissues. The scale bar was 25 μm for **(A,B,E)**, and 10 μm for **(C,D)**.

Decreased Enamel Mineralization and Loss of Sharp Incisal Tips in *Phospho1*$^{-/-}$ Mice

To determine how loss of PHOSPHO1 affects enamel quality, a number of physicochemical parameters such as total enamel volume, calcium, and phosphate ratios, level of mineralization based on von Kossa sections, and sharpness of incisal tips were assessed and compared between *Phospho1*$^{-/-}$ and WT mice. Comparison of X-ray radiographs and alizarin red stained ground sections between 30 day old control and *Phospho1*$^{-/-}$ mouse teeth revealed a rounded incisal tip in the PHOSPHO1 null incisors compared to the sharp incisal tips of their wild-type counterparts (**Figures 2A–D**). There was a significant 2-fold reduction in silver grain density on von Kossa stained ground sections (1.44 ± 0.11 vs. 0.71 ± 0.04 pixel units) indicative of

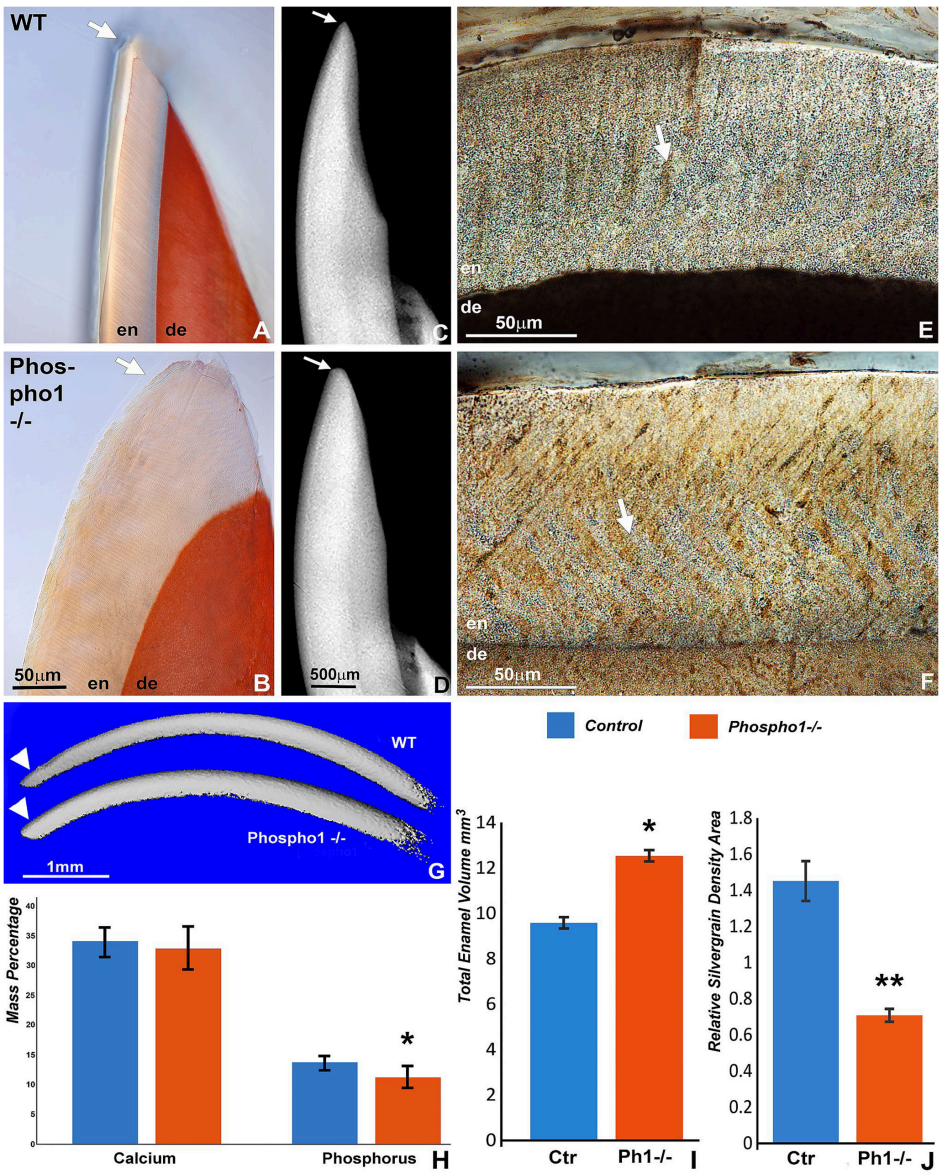

FIGURE 2 | Decreased mineralization in the enamel layer of 30 days old *Phospho1*$^{-/-}$ mice**.** Incisal tips of *Phospho1*$^{-/-}$ mice **(B,D)** were thicker and rounded (arrows) when compared to those of WT mice. The molar enamel layer of *Phospho1*$^{-/-}$ mice contained less von Kossa staining and more organic material in the prisms **(F)** than the WT mice **(E)**. Three-D micro-CT reconstructions of representative WT and *Phospho1*$^{-/-}$ mouse incisors confirm differences in incisal tip contours and in the overall enamel volume **(G)**. Elemental analysis revealed a significant difference in the amount of phosphorus in the *Phospho1*$^{-/-}$ mice when compared to the WT mice as demonstrated by EDS-SEM. The EDS-SEM data were calculated as average mass percent of calcium and phosphorus **(H)**. **(I)** Statistical analysis of the differences in enamel volume between WT and *Phospho1*$^{-/-}$ mice based on 3D reconstructed micro-CT images. **(J)** Comparative analysis of differences in mineralization between WT and *Phospho1*$^{-/-}$ mice as revealed by von Kossa stained ground sections using a grain counting algorithm. *$p < 0.05$, **$p < 0.001$. Control values are shown in blue columns and *Phospho1*$^{-/-}$ data are displayed in orange/red colored columns. The scale bar is 50 μm for **(A,B)**, 500 μm for **(C,D)**, and 50 μm for **(E,F)**.

reduced mineralization in the enamel layer of the *Phospho1*$^{-/-}$ mice when compared to the WT mice (**Figures 2E,F,J**). Von Kossa staining also demonstrated a substantial reduction in dentin mineralization in the *Phospho1*$^{-/-}$ mice vs. controls (**Figures 2E,F**). Total enamel volume as measured by micro-CT volumetric analysis was significantly higher in *Phospho1*$^{-/-}$ incisors compared to WT controls (**Figures 2G,I**). EDS elemental analysis demonstrated a significant decrease in the amount of phosphorus in the *Phospho1*$^{-/-}$ mice when compared to controls ($p < 0.05$), while calcium levels were only little affected by the loss of PHOSPHO1 (**Figure 2H**).

Disintegration and Loss of Enamel Prism Structure in *Phospho1*$^{-/-}$ Mouse Enamel

Scanning electron microscopy comparisons between 30 days old *Phospho1*$^{-/-}$ and control mice demonstrated a complete loss of the prominent enamel prism "picket fence" structure on surface etched *Phospho1*$^{-/-}$ mouse enamel preparations when compared to controls (**Figures 3A–D**). High magnification scanning electron micrographs at individual crystal resolution revealed a loss of individual prism boundaries as a result of a 45.3% reduction in the mineral-free inter-prism space between individual prisms (**Figure 3F**) in *Phospho1*$^{-/-}$ mice

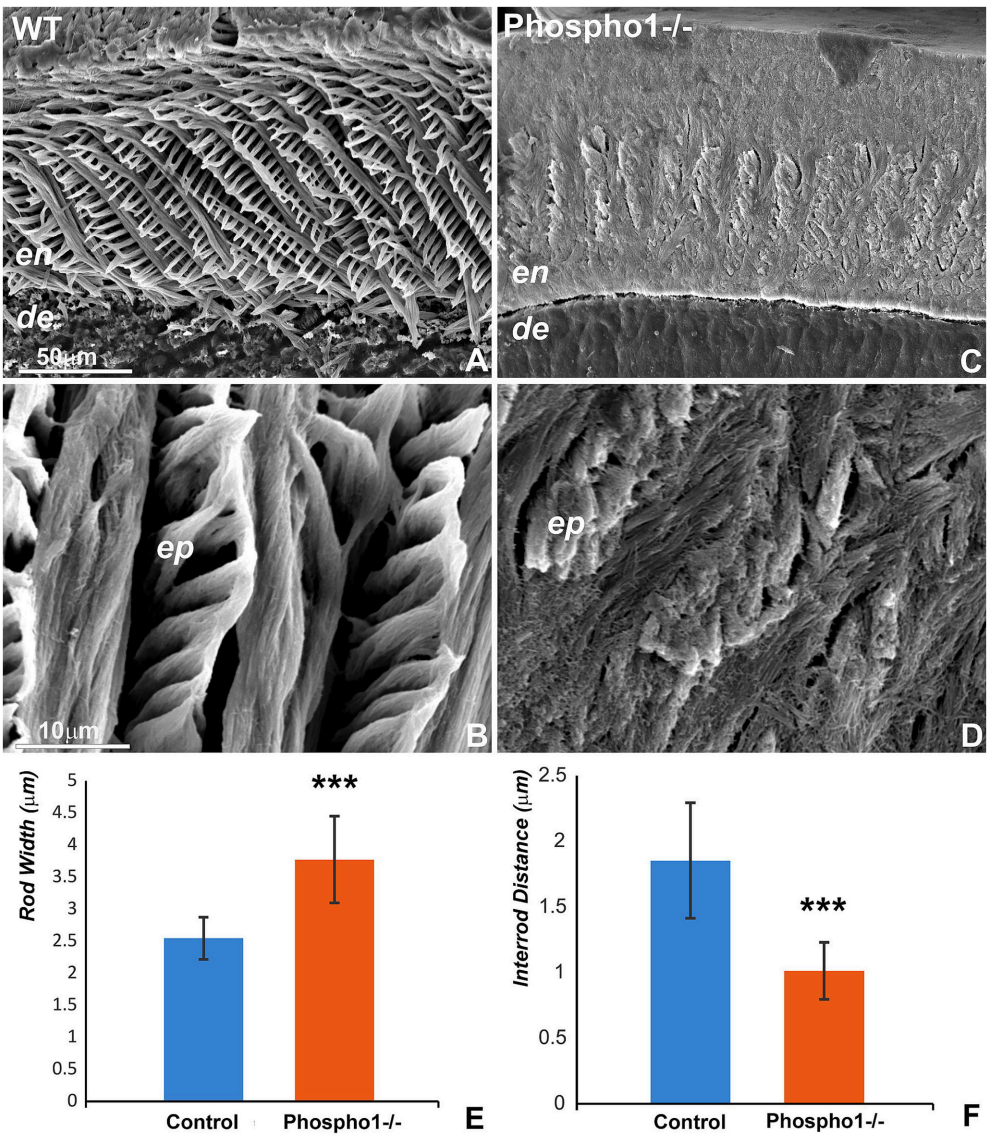

FIGURE 3 | Loss of enamel prism structure and crystal organization in *Phospho1*$^{-/-}$ mouse molars**.** Scanning electron micrographs of 30 days old mouse molars illustrate the arrangement of enamel prims at 750x and 5000x magnifications (**A,B**, respectively) in WT **(A,B)** and *Phospho1*$^{-/-}$ **(C,D)** mouse molars. There was a significant loss of enamel prism structure as well as a dramatic change in the organization of the enamel crystals in the PHOSPHO1 null mice. **(E,F)** Morphometric comparison of enamel prism width **(E)** and inter-rod distance **(F)** between WT and *Phospho1*$^{-/-}$ mice. ***$p < 0.0001$. The scale bar is 50 μm for **(A,C)** and 10 μm for **(B,D)**.

when compared to controls (**Figures 3C,D** vs. **Figures 3A,B**). These micrographs also documented a loss of parallel crystal organization within prisms (**Figure 3D**). Moreover, there was a 1.56-fold increase in enamel prism width (**Figure 3E**) in *Phospho1*$^{-/-}$ mutant mice ($p < 0.0001$).

Presence of Mineral Precipitates in Ameloblast Secretory Vesicles as Revealed by Transmission Electron Microscopy

Ameloblast secretory vesicles (sketch in **Figure 4A**) were long considered to be protein-rich intracellular entities within ameloblasts. Micrographs presented in this study illustrate that following 12 days of organ culture, these secretory vesicles also contained numerous mineral precipitates at the outside of and within the secretory vesicles (**Figure 4B**). Moreover, high magnification immunohistochemistry micrographs demonstrated the presence of half-moon shaped PHOSPHO1-positive signals in the walls of ameloblast secretory vesicles close to the developing enamel front (**Figure 4C**). Supportive of their involvement in secretory processes during amelogenesis, vesicles also stained positively for amelogenin and the vesicular marker protein HSP70 on paraffin sections of secretory ameloblasts (**Figures 4D,E**).

DISCUSSION

The purpose of the present study was to determine the function of the matrix vesicle phosphatase PHOSPHO1 during amelogenesis and on the structural integrity of the enamel layer. In this study we compared the enamel layers of wild-type and *Phospho1*$^{-/-}$ mice using light and electron microscopy as well as elemental mapping and von Kossa staining. Three different models have been used to verify PHOSPHO1 expression and function during amelogenesis: (i) the *Phospho1*$^{-/-}$ mouse molar model for phenotype analysis and immunohistochemistry, (ii) E16 mouse molar organ culture to visualize secretory vesicles using electron microscopy, (iii) and porcine enamel organ protein extracts to verify the presence of PHOSPHO1 in the enamel organ. In general, our study demonstrated reduced enamel mineralization and prism formation as a results of loss of PHOSPHO1. Using immunohistochemistry, PHOSPHO1 was localized to the walls of ameloblast secretory vesicles and in the enamel layer. Together, these findings demonstrate that PHOSPHO1 is essential for physiological enamel ion transport and for the structure of the enamel layer.

Our immunochemical analysis using two different antibodies against PHOSPHO1 and two different types of fixation procedures demonstrated that PHOSPHO1 was localized in the enamel layer and adjacent to the walls of ameloblast secretory vesicles. The presence of PHOSPHO1 in the walls of ameloblast secretory vesicles was a surprise finding as ameloblast vesicles are commonly distinguished from the matrix vesicles involved in the mineralization of bone, dentin, and cartilage (Nanci, 2008). The presence of PHOSPHO1 in ameloblast vesicles would suggest potential similarities between matrix vesicles and ameloblast secretory vesicles as PHOSPHO1 functions to facilitate initial mineralization inside of such vesicles. PHOSPHO1 presence in ameloblast vesicles was previously documented by McKee et al. (2013), and the substantial enamel defects in mice lacking the PHOSPHO1 enzyme reported here support the concept

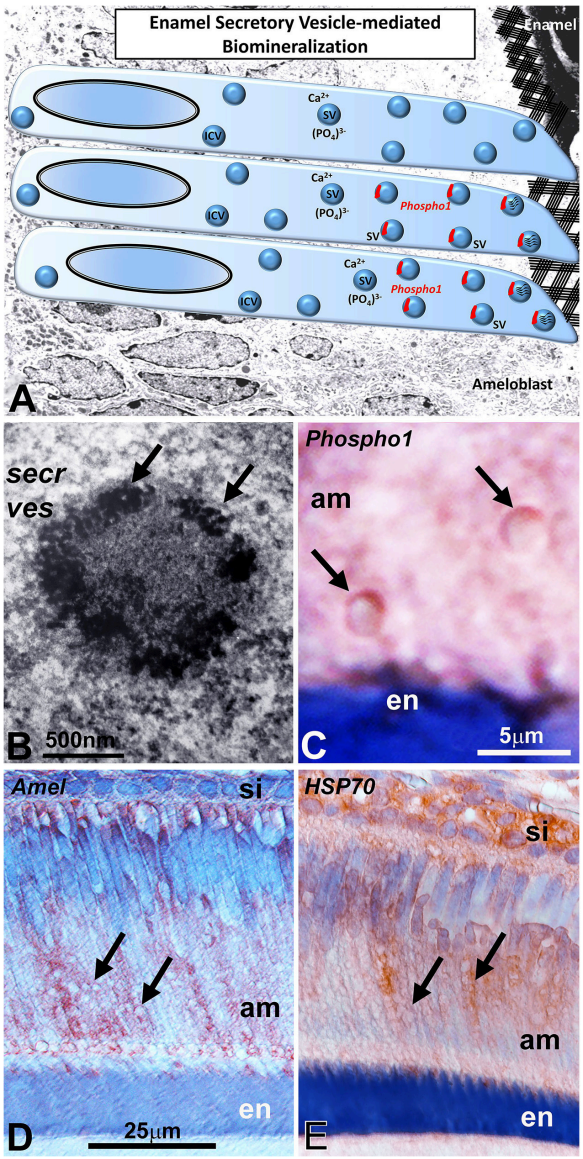

FIGURE 4 | PHOSPHO1 as an intravesicular apatite nucleation enzyme in ameloblast secretory vesicles **(A)**. The presence of PHOSPHO1 as a secretory vesicle (SV) component in ameloblast secretory vesicles suggests intravesicular mineral/matrix assembly prior to secretion into the ameloblast extracellular matrix. The transmission electron micrograph **(B)** of ameloblast intracellular secretory vesicles supports the concept of mineral nucleation sites (arrows) within such secretory vesicles (secr ves). This secretory vesicle was localized at the secretory face of the ameloblast. **(C)** is a high magnification micrograph demonstrating highly specific immunostaining for PHOSPHO1 in the walls of ameloblast secretory vesicles (arrows). **(D,E)** are immunoreactions using either anti-amelogenin **(D)** or anti-HSP70 antibodies **(E)**, demonstrating immunoreactivity associated with secretory vesicles (arrows). secr ves, secretory vesicles; am, ameloblasts; si, stratum intermedium; en, enamel. The scale bar is 500 nm **(B)**, 5 μm for **(A,C)** and 25 μm for **(D,E)**.

of a putative function of PHOSPHO1 during amelogenesis. Similar to matrix vesicles, ameloblast secretory vesicles are surrounded by a distinct membrane and contain a mixture of protein matrix and small mineral crystallites (Diekwisch, 1998; Brookes et al., 2014), even though they lack the double layer membrane commonly associated with matrix vesicles (Hsu and Anderson, 1978). There was also an obvious size difference between the ameloblast secretory vesicles described here (2–3 μm) and the average diameter of typical matrix vesicles of the bone extracellular matrix (100 nm, Anderson, 2003), and this size difference may be explained by the function of ameloblasts to transport and deposit substantial amounts of protein and mineral within a relatively short period of time. Nevertheless, further studies will be needed to establish the similarities and differences between the matrix vesicles of the mesenchymal bone extracellular matrix and the secretory vesicles of ameloblast epithelial cells beyond the differences in localization, content, and size. Especially, cryoimmuno-electron microscopic techniques to map individual matrix components within individual vesicle components would further advance our understanding of the secretory machinery common to epithelial and mesenchymal mineral forming cells. While the presence of PHOSPHO1 in ameloblast secretory vesicles alone may not suffice to draw parallels between matrix vesicles and ameloblast vesicles, PHOSPHO1 as a common apatite nucleation enzyme in both types of vesicles suggests similar mechanisms of mineral growth related to early intravesicular apatite nucleation between mineralized tissues of ectodermal and ectomesenchymal origin (**Figure 4A**).

Loss of *Phospho1* in our mouse model had a number of dramatic effects on enamel prism structure and mineralization, including reduced mineralization as indicated by von Kossa staining, rounded incisal tips, disrupted enamel prism pattern, and lack of individual crystal integrity within their prismatic subunit. Together, this phenotype indicates that enamel biomineralization in *Phospho1*$^{-/-}$ mice was severely impaired. Based on the present phenotype it is not entirely clear whether the dramatic phenotype in the mature enamel was due to a failure of mineralization initiation or due to a failure of PHOSPHO1 to continuously function during enamel maturation within the enamel layer. It is also not clear whether PHOSPHO1 plays only a direct role in early crystal nucleation and growth, and the lack of sufficiently hardened crystals impairs their assembly into enamel prisms, or whether PHOSPHO1 has additional functions during prism organization. Nevertheless, the remarkable enamel phenotype reported in the present study confirms that a phosphatase so far only known for its role during the early phase of bone and dentin crystal growth is essential for physiological enamel mineralization and prism patterning. Moreover, our electron micrographs of intravesicular mineral precipitation within ameloblast secretory vesicles support the concept of PHOSPHO1 function during initial mineralization.

In addition to the mineralization defects discussed above, there was also a significant increase in overall enamel volume and in the thickness of the enamel layer. This is a remarkable finding as the thickness of the enamel layer is usually highly consistent within a species. Yet, the reduced level of mineralization might have caused a delayed onset of enzymatic degradation of the enamel matrix via enamel-related proteases such as MMP20 and KLK4. Alternatively, the higher level of mineralization in the wild-type mice might have been associated with a greater degree of protein compaction and a resulting thinner enamel layer. The less mineralized enamel layer also explains the rounded incisal tips of *Phospho1*$^{-/-}$ mice, where a different mineral content results in an altered wear pattern. Finally, the reduced level of underlying dentin mineralization might have affected the mechanosensory control of the ameloblast secretory apparatus, resulting in an overcompensation through enhanced enamel secretion.

While our data revealed remarkable structural defects in the enamel layer of *Phospho1*$^{-/-}$ mice, our elemental analysis demonstrated that only phosphate incorporation into the enamel layer of *Phospho1*$^{-/-}$ mice was significantly reduced, and calcium levels were not significantly different between mutant and wild-type mice. Phosphate content is essential for normal bone health, and loss of phosphate is destined to set the physiological calcium/phosphate homeostasis out of balance (Penido and Alon, 2012). However, the role of PHOSPHO1 is predominantly associated with early intravesicular mineral nucleation, suggesting the phenotype observed here is less due to a reduction in phosphate transport but rather because of the failure of early intravesicular crystals to form as precursors and templates for mature enamel crystals and subsequently enamel prisms.

ETHICS STATEMENT

All animal studies were approved by and conducted in accordance with the guidelines of the Texas A&M University College of Dentistry Animal Care Committee.

AUTHOR CONTRIBUTIONS

MP and TD wrote the manuscript, TD, JM, and CF designed the experiments, and MP and LR conducted the experiments.

FUNDING

This study was supported by NIDCR grant DE018900 to TD.

REFERENCES

Anderson, H. C. (1984). Mineralization by matrix vesicles. *Scan Electron. Microsc.* 953–964.

Anderson, H. C. (2003). Matrix vesicles and calcification. *Curr. Rheumatol. Rep.* 5, 222–226. doi: 10.1007/s11926-003-0071-z

Bonucci, E. (1992). Comments on the ultrastructural morphology of the calcification process: an attempt to reconcile matrix vesicles, collagen fibrils, and crystal ghosts. *Bone Miner.* 17, 219–222. doi: 10.1016/0169-6009(92)90740-5

Brookes, S. J., Barron, M. J., Boot-Handford, R., Kirkham, J., and Dixon, M. J. (2014). Endoplasmic reticulum stress in amelogenesis imperfecta and

phenotypic rescue using 4-phenylbutyrate. *Hum. Mol. Genet.* 23, 2468–2480. doi: 10.1093/hmg/ddt642

Cui, L., Houston, D. A., Farquharson, C., and MacRae, V. E. (2016). Characterisation of matrix vesicles in skeletal and soft tissue mineralisation. *Bone* 87, 147–158. doi: 10.1016/j.bone.2016.04.007

Dean, D. D., Schwartz, Z., Muniz, O. E., Gomez, R., Swain, L. D., Howell, D. S., et al. (1992). Matrix vesicles are enriched in metalloproteinases that degrade proteoglycans. *Calcif. Tissue Int.* 50, 342–349. doi: 10.1007/BF00301632

Diekwisch, T., David, S., Bringas, P., Santos, V., and Slavkin, H. C. (1993). Antisense inhibition of AMEL translation demonstrates supramolecular controls for enamel HAP crystal growth during embryonic mouse molar development. *Development* 117, 471–482.

Diekwisch, T. G. (1998). Subunit compartments of secretory stage enamel matrix. *Connect. Tissue Res.* 38, 101–111; discussion: 139–145. doi: 10.3109/03008209809017026

Golub, E. E. (2009). Role of matrix vesicles in biomineralization. *Biochim. Biophys. Acta* 1790, 1592–1598. doi: 10.1016/j.bbagen.2009.09.006

Gopinathan, G., Jin, T., Liu, M., Li, S., Atsawasuwan, P., Galang, M. T., et al. (2014). The expanded amelogenin polyproline region preferentially binds to apatite versus carbonate and promotes apatite crystal elongation. *Front. Physiol.* 5:430. doi: 10.3389/fphys.2014.00430

Hatakeyama, J., Fukumoto, S., Nakamura, T., Haruyama, N., Suzuki, S., Hatakeyama, Y., et al. (2009). Synergistic roles of amelogenin and ameloblastin. *J. Dent. Res.* 88, 318–322. doi: 10.1177/0022034509334749

Houston, B., Stewart, A. J., and Farquharson, C. (2004). PHOSPHO1-A novel phosphatase specifically expressed at sites of mineralisation in bone and cartilage. *Bone* 34, 629–637. doi: 10.1016/j.bone.2003.12.023

Hsu, H. H., and Anderson, H. C. (1978). Calcification of isolated matrix vesicles and reconstituted vesicles from fetal bovine cartilage. *Proc. Natl. Acad. Sci. U.S.A.* 75, 3805–3808. doi: 10.1073/pnas.75.8.3805

Hu, Y., Smith, C. E., Richardson, A. S., Bartlett, J. D., Hu, J. C., and Simmer, J. P. (2016). MMP20, KLK4, and MMP20/KLK4 double null mice define roles for matrix proteases during dental enamel formation. *Mol. Genet. Genomic Med.* 4, 178–196. doi: 10.1002/mgg3.194

Liu, M., Reed, D. A., Cecchini, G. M., Lu, X., Ganjawalla, K., Gonzales, C. S., et al. (2016). Varanoid tooth eruption and implantation modes in a late cretaceous mosasaur. *Front. Physiol.* 7:145. doi: 10.3389/fphys.2016.00145

Lu, Y., Papagerakis, P., Yamakoshi, Y., Hu, J. C., Bartlett, J. D., and Simmer, J. P. (2008). Functions of KLK4 and MMP-20 in dental enamel formation. *Biol. Chem.* 389, 695–700. doi: 10.1515/BC.2008.080

Masuya, H., Shimizu, K., Sezutsu, H., Sakuraba, Y., Nagano, J., Shimizu, A., et al. (2005). Enamelin (Enam) is essential for amelogenesis: ENU-induced mouse mutants as models for different clinical subtypes of human amelogenesis imperfecta (AI). *Hum. Mol. Genet.* 14, 575–583. doi: 10.1093/hmg/ddi054

McKee, M. D., Yadav, M. C., Foster, B. L., Somerman, M. J., Farquharson, C., and Millán, J. L. (2013). Compounded PHOSPHO1/ALPL deficiencies reduce dentin mineralization. *J. Dent. Res.* 92, 721–727. doi: 10.1177/0022034513490958

Millán, J. L. (2013). The role of phosphatases in the initiation of skeletal mineralization. *Calcif. Tissue Int.* 93, 299–306. doi: 10.1007/s00223-012-9672-8

Nanci, A. (2008). *Ten Cate's Oral Histology: Development, Structure, and Function.* St Louis, MO: Elsevier Health Sciences.

Penido, M. G. M. G., and Alon, U. S. (2012). Phosphate homeostasis and its role in bone health. *Pediatr. Nephrol.* 27, 2039–2048. doi: 10.1007/s00467-012-2175-z

Roberts, S., Narisawa, S., Harmey, D., Millán, J. L., and Farquharson, C. (2007). Functional involvement of PHOSPHO1 in matrix vesicle-mediated skeletal mineralization. *J. Bone Miner. Res.* 22, 617–627. doi: 10.1359/jbmr.070108

Ryu, O., Hu, J. C., Yamakoshi, Y., Villemain, J. L., Cao, X., Zhang, C., et al. (2002). Porcine kallikrein-4 activation, glycosylation, activity, and expression in prokaryotic and eukaryotic hosts. *Eur. J. Oral Sci.* 110, 358–365. doi: 10.1034/j.1600-0722.2002.21349.x

Shin, M., Hu, Y., Tye, C. E., Guan, X., Deagle, C. C., Antone, J. V., et al. (2014). Matrix metalloproteinase-20 over-expression is detrimental to enamel development: a *Mus musculus* model. *PLoS ONE* 9:e86774. doi: 10.1371/journal.pone.0086774

Wuthier, R. E., Wu, L. N., Sauer, G. R., Genge, B. R., Yoshimori, T., and Ishikawa, Y. (1992). Mechanism of matrix vesicle calcification: characterization of ion channels and the nucleational core of growth plate vesicles. *Bone Miner.* 17, 290–295. doi: 10.1016/0169-6009(92)90753-Z

Yadav, M. C., de Oliveira, R. C., Foster, B. L., Fong, H., Cory, E., Narisawa, S., et al. (2012). Enzyme replacement prevents enamel defects in hypophosphatasia mice. *J. Bone Miner. Res.* 27, 1722–1734. doi: 10.1002/jbmr.1619

Yadav, M. C., Simão, A. M., Narisawa, S., Huesa, C., McKee, M. D., Farquharson, C., et al. (2011). Loss of skeletal mineralization by the simultaneous ablation of PHOSPHO1 and alkaline phosphatase function: a unified model of the mechanisms of initiation of skeletal calcification. *J. Bone Miner. Res.* 26, 286–297. doi: 10.1002/jbmr.195

Zweifler, L. E., Ao, M., Yadav, M., Kuss, P., Narisawa, S., Kolli, T. N., et al. (2016). Role of PHOSPHO1 in periodontal development and function. *J. Dent. Res.* 95, 742–751. doi: 10.1177/0022034516640246

Conflict of Interest Statement: The authors declare that the research was conducted in the absence of any commercial or financial relationships that could be construed as a potential conflict of interest.

Copyright © 2017 Pandya, Rosene, Farquharson, Millán and Diekwisch. This is an open-access article distributed under the terms of the Creative Commons Attribution License (CC BY). The use, distribution or reproduction in other forums is permitted, provided the original author(s) or licensor are credited and that the original publication in this journal is cited, in accordance with accepted academic practice. No use, distribution or reproduction is permitted which does not comply with these terms.

frontiers in Physiology

REVIEW
published: 31 July 2017
doi: 10.3389/fphys.2017.00529

Endocytosis and Enamel Formation

*Cong-Dat Pham[1], Charles E. Smith[2,3], Yuanyuan Hu[3], Jan C-C. Hu[3], James P. Simmer[3] and Yong-Hee P. Chun[1,4]**

[1] Department of Periodontics, School of Dentistry, University of Texas Health Science Center at San Antonio, San Antonio, TX, United States, [2] Department of Anatomy and Cell Biology, McGill University, Montreal, QC, Canada, [3] Department of Biologic and Materials Sciences, University of Michigan, Ann Arbor, MI, United States, [4] Department of Cell Systems & Anatomy, School of Medicine, University of Texas Health Science Center at San Antonio, San Antonio, TX, United States

Enamel formation requires consecutive stages of development to achieve its characteristic extreme mineral hardness. Mineralization depends on the initial presence then removal of degraded enamel proteins from the matrix via endocytosis. The ameloblast membrane resides at the interface between matrix and cell. Enamel formation is controlled by ameloblasts that produce enamel in stages to build the enamel layer (secretory stage) and to reach final mineralization (maturation stage). Each stage has specific functional requirements for the ameloblasts. Ameloblasts adopt different cell morphologies during each stage. Protein trafficking including the secretion and endocytosis of enamel proteins is a fundamental task in ameloblasts. The sites of internalization of enamel proteins on the ameloblast membrane are specific for every stage. In this review, an overview of endocytosis and trafficking of vesicles in ameloblasts is presented. The pathways for internalization and routing of vesicles are described. Endocytosis is proposed as a mechanism to remove debris of degraded enamel protein and to obtain feedback from the matrix on the status of the maturing enamel.

Keywords: endocytosis, amelogenesis, endocytic trafficking, Rab proteins, clathrin, pinocytosis

OPEN ACCESS

Edited by:
Ariane Berdal, UMRS 1138 INSERM University Paris-Diderot Team POM, France

Reviewed by:
Victor E. Arana-Chavez, University of São Paulo, Brazil
Olivier Cases, Centre National de la Recherche Scientifique (CNRS), France
Claudio Cantù, University of Zurich, Switzerland

****Correspondence:***
Yong-Hee P. Chun
chuny@uthscsa.edu

Specialty section:
This article was submitted to Craniofacial Biology and Dental Research, a section of the journal Frontiers in Physiology

Received: *30 April 2017*
Accepted: *10 July 2017*
Published: *31 July 2017*

Citation:
Pham C-D, Smith CE, Hu Y, Hu JC-C, Simmer JP and Chun Y-HP (2017) Endocytosis and Enamel Formation. Front. Physiol. 8:529. doi: 10.3389/fphys.2017.00529

ENDOCYTOSIS IN AMELOBLASTS

Enamel formation is a unique process that coordinates the movement of proteins and ions between ameloblasts and the developing extracellular matrix (Smith and Nanci, 1996; Lacruz et al., 2013b). The extracellular matrix represents a sealed compartment between ameloblasts and the mineralized dentin without direct access to the vascular system or the connective tissue compartment (Bronckers, 2016). The transport of proteins and ions between ameloblasts and matrix for crystal mineralization is controlled by ameloblasts. As the enamel organ develops, the inner epithelial cells differentiate into polarized ameloblasts. The two key protein transport functions of ameloblasts are the secretion and the resorption of enamel proteins. Ameloblasts secrete enamel proteins at the surface of forming enamel that assemble into a scaffold to initiate and lengthen the growing mineral crystals (Smith et al., 2016). As enamel proteins are selectively cleaved by proteinases, fragments and perhaps some almost intact proteins are removed from the matrix via endocytosis by ameloblasts, a process that speeds up over time as enamel formation continues (Reith and Cotty, 1967; Smith, 1979; Kallenbach, 1980a,b). The freed up space is then utilized to widen the individual enamel ribbons. The final product contains <5% of proteins and water (Schmitz et al., 2014). The failure of efficient removal of enamel proteins and deposition of mineral results in hypomineralized or hypomature enamel. The enamel proteins constitute the protein backbone of the enamel matrix and include amelogenin, ameloblastin, and enamelin. All of them are part of the cluster called secreted calcium-binding phosphoproteins

(Kawasaki et al., 2004). Structurally, all enamel proteins possess a poorly defined secondary structure, a feature characteristic for intrinsically disordered proteins (Wald et al., 2017). Regions of hydrophobic residues of amelogenin facilitate protein-protein interactions resulting in assemblies of nanospheres (Fincham et al., 1995). In the absence of amelogenin, enamel ribbons lose their self-sufficiency and fuse together in fan-like structures (Smith et al., 2016). Enamel proteins are sequentially processed into fragments that are then internalized by ameloblasts (Bartlett, 2013). Initially, matrix metalloproteinase 20 cleaves enamel proteins at highly selective internal sites during the secretory stage (Fukae et al., 1998). The remaining fragments are then further degraded into smaller peptides by kallikrein4 (kallikrein related peptidase 4) during the maturation stage (Nagano et al., 2009).

The uptake of degraded proteins takes place throughout all stages of enamel formation (Ozawa et al., 1983). The endocytic activities of preameloblasts and ameloblasts include the removal of basement membrane proteins and enamel proteins via vesicles and their transport to lysosomes (Katchburian and Holt, 1969; Kallenbach, 1980a; Takano and Ozawa, 1980; Ozawa et al., 1983; Salama et al., 1989, 1990a,b; Smith et al., 1989; Nanci et al., 1996). The localization of amelogenin with immune gold labeling techniques has established that enamel proteins are found in large quantities in organelles with functions in endocytosis in ameloblasts of both secretory and maturation stages (**Figure 1**, **Table 1**).

Endocytosis is linked to enamel mineralization to remove processed enamel proteins from the matrix and to deposit mineral (Smith, 1979, 1998; Nanci et al., 1987a; Smith et al., 1989). The site and configuration of plasma membrane from which enamel proteins are secreted and endocytosed differ in morphology depending on developmental stage. During the pre-secretory stage fragments of the degraded basal lamina are removed through finger-like cell processes penetrating into the pre-dentin (Reith, 1967; Kallenbach, 1976; Nanci et al., 1989). During secretory and maturation stages stippled material adjacent to ameloblasts is interpreted as degraded enamel proteins and their localization is indicative of resorptive activity (Kallenbach, 1980b; Ozawa et al., 1983; Nanci et al., 1987b).

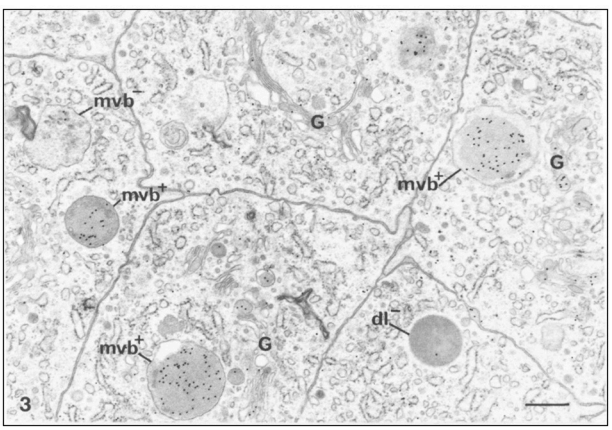

FIGURE 1 | Immunocytochemical preparation illustrating the distribution of gold labeled amelogenin over various compartments of ameloblasts from the secretion stage in mouse incisors. Lysosomes appear variably labeled. Multivesicular bodies are often intensely labeled (mvb+). An unlabeled multivesicular body (mvb−) and an unlabeled dark lysosome (dl−) are shown. The Golgi apparatus (G) shows some labeling by gold particles, × 24,875. Bar = 0.5 μm. Permission to reprint from: Application of High-Resolution Immunocytochemistry To the Study of the Secretory, Resorptive, and Degradative Functions of Ameloblasts by Nanci et al. (1987a).

With the formation of the Tomes' process on the apical membrane during secretory stage, proteins are secreted in large quantities from two growth sites, distal and proximal, to give rise to orientation of rod and interrod enamel (Nanci and Warshawsky, 1984). Both of these sites are characterized by deep membrane infoldings (Weinstock and Leblond, 1971; Kallenbach, 1973; Nanci and Warshawsky, 1984; Uchida and Warshawsky, 1992; Kim et al., 1994). Vesicles with granular content to be secreted are found in close proximity to infoldings suggesting that a membrane fusion event between vesicle and infolding results in the discharge of the luminal content of the vesicle into the channel of the infolding (Simmelink, 1982). The enamel proteins then could escape through the channels between the infoldings to the outer surface of the secretory face (**Figures 2**, **3**). Conversely, it is conceivable that endocytosis could occur in the reverse direction, inside the membrane infolding similar to a tubular network (Smith, 1979). The space inside an infolding ranges from small and narrow to bloated and filled with granular material (Kallenbach, 1974; Nanci et al., 1987b). This mechanism allows several vesicles to fuse in a limited area of the cell surface and to release and internalize material in large quantities. Enamel ribbons are bundled and closely related to the openings of the infoldings and extend in the direction of the opening (Nanci and Warshawsky, 1984). The ameloblast surface seems to be less infolded when there is loss of function of any one of the enamel matrix scaffold proteins (Smith et al., 2016). In the maturation stage, ameloblasts acquire a ruffle-ended membrane 80% of the time compared to smooth-ended borders. Ruffle-ended ameloblasts are more absorptive than smooth-ended ameloblasts (Nanci et al., 1987b). The ruffle-ended membrane forms a complex, infolded apical surface constantly changing its configuration.

In addition to endocytosis of enamel proteins from the apical membranes of secretory and maturation stage ameloblasts, some small amounts of enamel matrix proteins are secreted and endocytosed from the lateral extracellular spaces between the cells (Nanci and Smith, 1992). Granular material containing amelogenin has been found in accumulations between the tight junctions of secretory stage ameloblasts (Nanci and Warshawsky, 1984; Nanci et al., 1987a). These "patches" are associated with sites of the ameloblasts membrane that lack membrane infoldings and mineralization. It was suggested that the microenvironment of rod and interrod growth sites is unique for the initiation of mineralization (Nanci et al., 1987c). At the lateral surfaces pinocytosis is frequently observed (**Figure 3**).

The packing of vesicles for secretion and endocytosis is a membrane consuming process altering the surface area. Given the large quantity of secreted enamel proteins, the gain of membrane during fusion events could alter the shape of the

TABLE 1 | Density of gold labeling over enamel and organelles in ameloblasts following incubations with anti-amelogenin antibody[a].

Compartment	Density of labeling[b]		
	Early secretion (mouse)	Mid secretion (rat)	Early maturation (rat)
Enamel	129.9 ± 9.4	121.4 ± 9.6	80.0 ± 3.9
Rough endoplasmic reticulum	7.2 ± 0.4	8.4 ± 0.4	9.2 ± 0.4
Golgi saccules	17.7 ± 0.8	15.1 ± 1.0	9.8 ± 0.6
Secretory granules	154.7 ± 10.9	137.6 ± 8.3	137.0 ± 14.5
Dark lysosomes	16.1 ± 3.3	8.5 ± 0.7	5.9 ± 0.5
Pale lysosomes	14.8 ± 2.9	11.1 ± 0.9	9.8 ± 1.2
Multivesicular bodies	19.8 ± 3.8	37.0 ± 3.5	26.9 ± 1.3
Mitochondria[c]	3.9 ± 0.7	3.8 ± 0.6	4.1 ± 0.2

Amelogenin is found in compartments associated with protein synthesis and secretion (rough endoplasmatic reticulum, Golgi, and secretory granules) and endocytosis (dark and pale lysosomes, and multivesicular bodies) pathways.

[a]*Data modified from Nanci et al. (1985, 1987b).*

[b]*Number of particles / μm^2 ± SEM.*

[c]*Index of background labeling.*

Permission to reprint from: Application of High-Resolution Immunocytochemistry To the Study of the Secretory, Resorptive, and Degradative Functions of Ameloblasts by Nanci et al. (1987a).

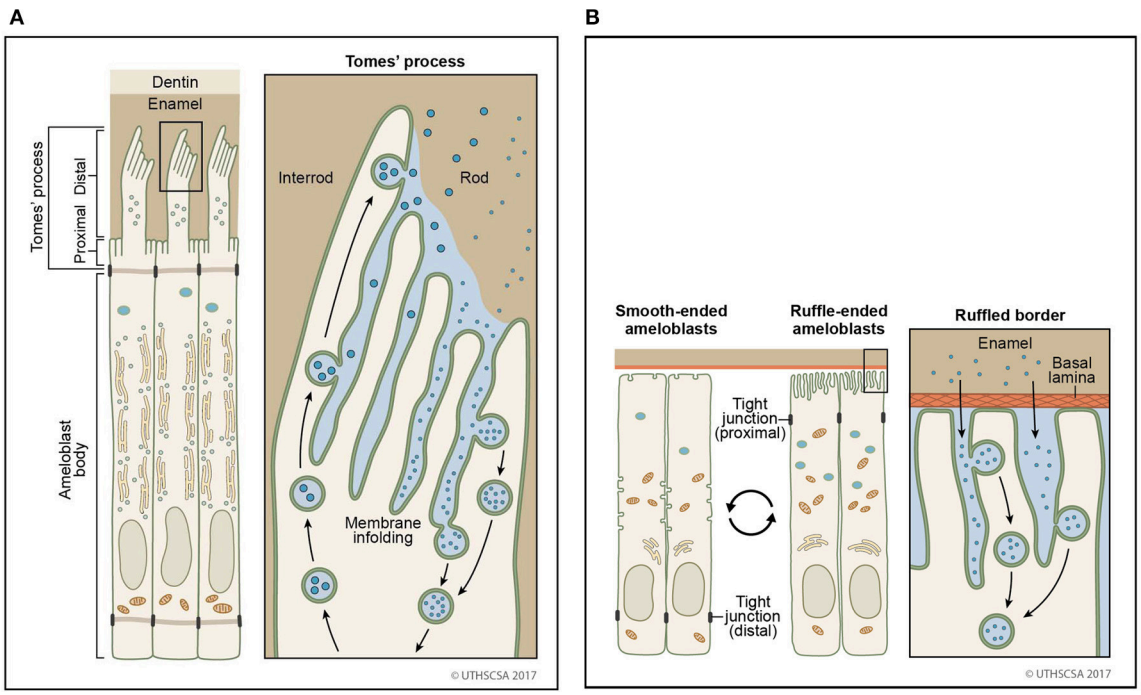

FIGURE 2 | Sites of secretion and endocytosis of the ameloblast membrane. **(A)** The secretory ameloblasts forms a Tomes' process from the apical membrane with a proximal portion and a distal portion. The proximal portion is associated with formation of interrod enamel, the distal portion with rod enamel formation. Vesicle fusion can be observed on the surface membrane adjacent to the rod growth site. Many vesicles fuse (secretion) or originate (endocytosis) from membrane infoldings found on the proximal portion and the distal portion. **(B)** In the maturation stage, degraded enamel proteins are internalized by ameloblasts. Ameloblasts modulate between smooth-ended and ruffle bordered membranes. In 80% of the maturation stage, ameloblasts are ruffle-ended with deep membrane invaginations. Degraded enamel proteins from the enamel matrix permeate the area between convoluted tubules and are resorbed via vesicles.

cell. However, for the Tomes' process maintaining the shape is critical to allow a defined mineralization front. By fusing with the membrane of infoldings or ruffles, membrane is recycled and the outer plasma membrane is not affected. As a result, infoldings and ruffles become longer and branched (Nanci and Smith, 1992).

ENDOCYTOSIS TYPES, MECHANISMS, PATHWAYS

Endocytosis is a form of active, energy-using transport of extracellular molecules internalized by a cell into vesicles. As

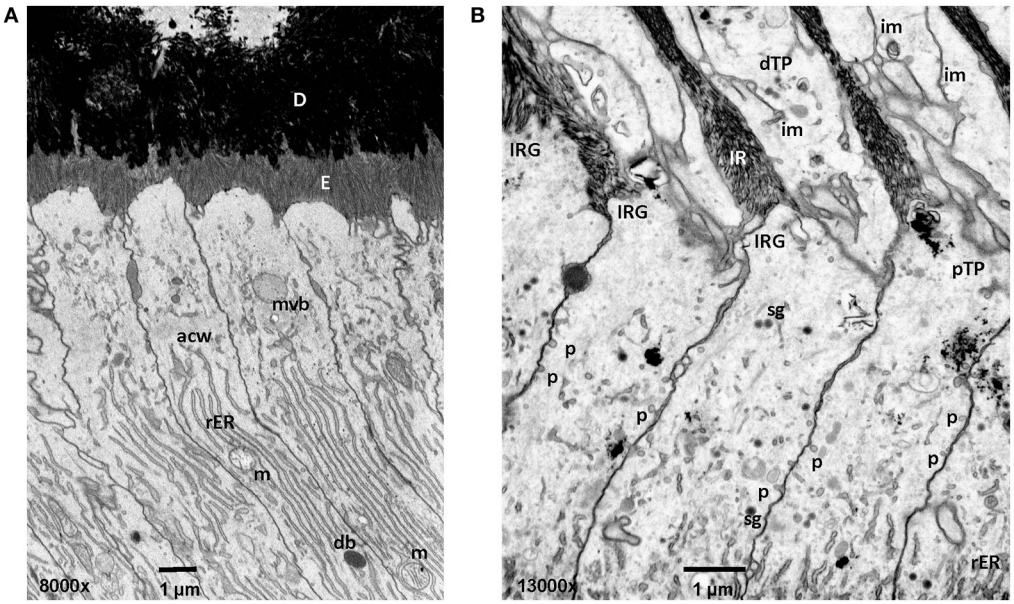

FIGURE 3 | Early and mid secretory stage ameloblasts in mandibular mouse incisors. All procedures involving animals were reviewed and approved by the IACUC committee at the University of Michigan and all relevant guidelines were followed. Handling of animals and tissues was followed according to protocols described earlier (Smith et al., 2016). **(A)** The Tomes' processes are not fully developed in early secretory stage ameloblasts. Enamel crystallite ribbons in the initial interrod layer are oriented perpendicular to dentin and the apical ameloblast membrane. **(B)** In mid secretory ameloblasts pinocytotic vesicles are observed along the non-secreting surface of the Tomes' process and laterally between adjacent ameloblasts below the level of the apical junctional complex. In the distal portion of the Tomes process membrane infoldings form a complex network and are in close relationship to vesicles. D, dentin; E, enamel; mvb, multivesicular body; acw, apical cell web; rER, rough endoplasmic reticulum; m, mitochondria; db, dense body (lysosome); im, membrane infolding; dTP, distal portion of Tomes' process; IRG, interrod growth site; pTP, proximal portion of Tomes' process; sg, secretory granule; p, pinocytotic vesicle.

a mechanism to communicate the status of the extracellular environment and the cells, endocytosis is a vehicle for executing cell homeostasis including uptake of nutrients, matrix- cell communication, changes in cell shape and polarity (Mills, 2007; Eaton and Martin-Belmonte, 2014; Villasenor et al., 2016). Beyond the homeostasis of a single cell, endocytosis is essential for the homeostasis of multicellular tissues, organs and communities (Mostov and Cardone, 1995; Mellman, 1996).

The prerequisite for the regulation of endocytosis is that cells are able to receive and respond to external signals (Pelkmans et al., 2005). The interaction can be modulated through different uptake mechanisms and through ligand-receptor binding, inducing specific cellular functions (Le Roy and Wrana, 2005). Identified uptake pathways include non-specific macropinocytosis and specific receptor-mediated/clathrin-mediated and caveolae/raft-mediated endocytosis (Racoosin and Swanson, 1992; Swanson and Watts, 1995; Mellman, 1996; Conner and Schmid, 2003). The interaction between receptor and ligand triggers a change in the conformation in the cytosolic tail that includes motifs for internalization (Dahlen et al., 2003; Pandey, 2009). These motifs are tyrosine or dileucine based and are critical for internalization efficiency and for routing the cargo to the intended designation (Collawn et al., 1993; Dahlen et al., 2003; Pandey, 2009).

Clathrin-Mediated Endocytosis

The most extensively described endocytosis pathway is clathrin-mediated endocytosis. The generation of coated vesicles was discovered in mosquito oocytes (Roth and Porter, 1964). Each clathrin subunit consists of three large (heavy) and three small (light) polypeptide chains resembling a triskelion, a three-legged structure (Pearse, 1975, 1976). Clathrin molecules self-assemble into a 3-dimensional lattice supported by the heavy chains in the shape of a basket. The assembly and disassembly of clathrin around the vesicle is controlled by the clathrin light chains (Pearse, 1976). Clathrin uses adapter proteins (AP) to bind to membranes or cargo (Pearse et al., 2000; Sorkin, 2004). Clathrin-mediated endocytosis regulates the internalization and recycling of receptors employed in cellular activities. Some examples are signal transduction, cell adhesion, cell proliferation, nutrient uptake and synaptic vesicle reformation (Polo and Di Fiore, 2006; Saheki and De Camilli, 2012; Antonescu et al., 2014).

Vesicles found in preameloblasts, Tomes' processes of secretory ameloblasts and maturation stage ameloblasts are either coated or non-coated (Smith, 1979; Ozawa et al., 1983; Sasaki, 1984a,b; Franklin et al., 1991; Uchida and Warshawsky, 1992). Compared to uncoated vesicles originating either from secretion or endocytosis, coated vesicles are inactive for the internalized vesicles via the clathrin-mediated pathway. Coated vesicles are described in electron micrographs of secretory stage ameloblasts with a size of 0.1–0.12 µm in diameter

(Reith and Cotty, 1967; Garant and Nalbandian, 1968). In presecretory ameloblasts, coated vesicles are found in the cytoplasmic protrusion that penetrate the basal lamina and facilitate its degradation (Katchburian and Burgess, 1983). In secretory stage ameloblasts, extracellular material is internalized by coated vesicles and tubulovesicular structures (Sasaki, 1984a). Coated vesicles have a tight relationship to tubules residing in the core of the Tomes' process (Uchida and Warshawsky, 1992). Tubules branch out from the core and are part of a network. In maturation stage ameloblasts, coated vesicles are found in ruffle-ended ameloblasts that are filled with fine granular material (Sasaki, 1984b). In contrast, smooth-ended ameloblasts contain only few coated vesicles (Kallenbach, 1980a; Sasaki, 1984b). The morphological difference in the apical membrane of maturation stage ameloblasts suggests that their function is dedicated to different processes with high resorptive activities associated with a ruffled border and low resorptive, but homeostasis activities with a smooth-ended border (**Figure 2**; Takano and Ozawa, 1980).

The endocytosis of amelogenin in enamel organ epithelium is proposed via clathrin dependent endocytosis involving the receptor proteins lysosome-associated membrane protein 1 (Lamp1) and cluster of differentiation 63 (CD63) (Shapiro et al., 2007; Lacruz et al., 2013a). Lamp1 and CD63 are transmembrane proteins routed between the membranes of the cell surface and lysosomes via endocytosis and via recycling pathways. Lamp1 and CD63 may interact with AP-2 clathrin AP for the uptake of clathrin-coated vesicles in ameloblasts (Lacruz et al., 2013a). The regulation of endocytosis may involve the microRNA miR-153 through interactions with Lamp1 and clathrin (Yin et al., 2017).

Pinocytosis

Fluid-phase endocytosis called pinocytosis can be distinguished by the size of the pinosomes as macropinocytosis and micropinocytosis. While macropinocytosis marks the uptake of fluid phase, micropinocytosis is associated with receptor-mediated and fluid-phase uptake.

Fluid phase endocytosis represents an uptake mechanism documented as occurring in ameloblasts. The process of fluid phase endocytosis trafficking of cargo can be demonstrated by supplying exogenously provided horseradish peroxidase (HRP) and observing the intracellular localization of HRP in cell organelles to which HRP is transported. For this technique, HRP is intravenously injected as a 5% solution and animals are sacrificed after 15–90 min (Sasaki, 1984c). During secretory stage, the apical terminal bars are not permeable for HRP (Kallenbach, 1980b). HRP accumulates at rod and interrod growth sites. The uptake of large quantities of HRP takes place at the Tomes' process and is subsequently trafficked to endosomes and lysosomes (Kallenbach, 1980b; Matsuo et al., 1986). In maturation stage ameloblasts, the apical and basal tight junctions open and close as ameloblasts modulate between ruffle-ended and smooth-ended forms and allow HRP to reach intercellular spaces between ameloblasts and close to the papillary layer (Sasaki et al., 1983a). HRP is rapidly internalized in large quantities and is carried forward in coated pits, vesicles, multivesicular bodies (MVB) and tubulovesicular structures (Sasaki and Higashi, 1983; Sasaki et al., 1983b; Sasaki, 1984a,c). Accumulated HRP is incorporated from the cell membrane into the cytoplasm through pinosomes and pinocytotic coated vesicles (Sasaki, 1984a). The pinosomes then fuse to form large endocytic vesicles. HRP is accumulated in the endocytic vacuoles and MVB which serve as a carrier for HRP (Sasaki, 1984c). High magnification focused ion beam micrographs reveal pinocytotic activity at the lateral membranes of the proximal portion of the Tomes' Process (**Figure 3**). HRP can be followed from internalization through the endocytic compartment to the lysosomes where it is digested by lysosomes (Kallenbach, 1980b).

Phagocytosis

Phagocytosis describes the uptake of a solid particle (>0.5 μm) by the cell to form an internal compartment known as a phagosome (Gordon, 2016). In unicellular eukaryotes, phagocytosis serves in the acquisition of nutrients. In mammalian cells, phagocytosis is a mechanism for immune cells, such as macrophages, neutrophils, and dendritic cells to remove pathogens, damaged cell organelles and dead cells. In contrast to pinocytosis endosomes, phagosomes can be as large as the phagocyte, depending on the size of the ingested particle. Phagocytosis is initiated by membrane protrusions (filopodia) in direction of the particle and through binding of the particle to cell surface receptors. Pathogen-associated molecular patterns, Fc regions of antibodies, complement molecules and apoptotic cells are recognized by cell surface receptors (Flannagan et al., 2012; Gordon, 2016). After ingestion of the particle the phagosome fuses with a lysosome where the particle is exposed to degradation and microbicidal action.

After completion of the secretory stage, ameloblasts go through a brief shift to enter the maturation stage. This shift is accompanied by notable changes in ameloblasts morphology from tall polarized cells with a Tomes' process to shorter polarized cells without an apical process. In rodent incisors, this change occurs within 19 hours (Smith and Warshawsky, 1977). About 25% of transitional stage ameloblasts perish into cellular debris of varying size found between and below ameloblasts (Moe and Jessen, 1972). Cellular debris is distinct from ameloblasts with their dense cytoplasm surrounded by wide intercellular spaces between ameloblasts. It can cross intercellular spaces to the adjacent cell layer (stratum intermedium). Cells of the stratum intermedium form cytoplasmic processes to engulf ameloblast debris (Moe and Jessen, 1972). During the transition and maturation stages, macrophages are present in the forming papillary layer that are involved in the removal of cellular debris (Jessen and Moe, 1972; Nishikawa and Sasaki, 1996).

ENDOCYTIC TRAFFICKING OF VESICLES

Vesicles that originated by phagocytosis or pinocytosis contain cargo in the form of bound ligands or extracellular liquid phase material. The movement of vesicles within the cell to their destination compartment or organelle is called endocytic trafficking. Newly formed vesicles are first transported into early endosomes to sort them based on their content and to direct

them to their destination. Endosomes can progress to lysosomes to degrade their content or fuse with the plasma membrane to return receptors and release the content to the environment. A group of proteins in the Ras superfamily of GTPases (Rab proteins) have been identified as the molecular machinery that regulates membrane trafficking pathways (Segev, 2001). They take part in vesicle formation, motility, docking, membrane remodeling and fusion (Segev, 2001).

Ras Superfamily of GTPases

Rab proteins constitute the largest branch of the Ras superfamily with over 70 members. They are small GTPases/GTP-binding proteins of 21–25 kDa and localize to the cytosolic periphery of the membrane. As the predominant regulators of trafficking of endocytic vesicles, they control the un-coating, tethering, and membrane fusion and are executed by different types of Rabs (Hutagalung and Novick, 2011; Jena, 2011). The directionality of the vesicles is determined by the type of Rab protein localizing with the membrane of the endocytic organelle (**Table 2**, **Figure 4**; Hutagalung and Novick, 2011). Rab genes are highly conserved from yeast to human (Colicelli, 2004). Rab GTPases interact with the cytosolic aspect of the intracellular compartment to regulate and direct vesicles along different pathways. Through their effectors, Rab GTPases control vesicle formation, vesicle movement mediated by microfilaments, and membrane fusion (Hammer and Wu, 2002; Short et al., 2002).

In the enamel organ, a limited number of Rab GTPases have been investigated. Rab10 and Rab24 were localized to ameloblasts of the maturation stages and papillary cells (Lacruz et al., 2013a). Rab10 assists in the trafficking of vesicles from the Golgi apparatus to the basolateral membrane (Schuck et al., 2007). Rab24 is found in the endoplasmatic reticulum, cis-Golgi and late endosomes related to autophagy (Munafo and Colombo, 2002). In presecretory to secretory ameloblasts Rab23 was localized possibly negatively regulating sonic hedgehog signaling (Miletich et al., 2005).

Endosomal Vesicles

Endosomes are membrane-bound compartments inside of eukaryotic cells containing material that was internalized from the exterior of the cell. Their function is to sort and transport vesicles containing internalized solutes, receptors, lipids or pathogenic agents. Through their cargo, they also carry information from the extracellular compartment into the cell critical for cell morphology, maintenance and response to signals (Villasenor et al., 2016). Efficient sorting routes the vesicles to their destinations within the cells, such as the Golgi apparatus, lysosomes and plasma membrane. The two major sorting stations are the early and late endosomes (Mellman, 1996; Russell et al., 2006). Among the early endosomes, late endosomes, and lysosomes exists a dynamic and adaptable continuum with transient hybrid forms. An endosome fused with a lysosome is called an endo-lysosome. The endocytosis pathway is versatile because the organelles undergo continuous maturation, transformation, fusion, and fission (Huotari and Helenius, 2011). The following paragraphs describe the endocytic pathways of

TABLE 2 | Intracellular proteins in endocytic, transcytic, and exocytic pathways.

Protein	Human genes	Intracellular localization	Function	References (cloning, localization, function)
RAB PROTEINS				
Rab1	*RAB1A, RAB1, YPT1*	ER–Golgi intermediate	Anterograde trafficking from ER to Golgi	Zahraoui et al., 1989; Tisdale et al., 1992; Zerial and McBride, 2001
Rab2	*RAB2A, LHX, RAB2*	ER–Golgi intermediate	Retrograde trafficking from Golgi to ER	Zahraoui et al., 1989; Chavrier et al., 1990; Tisdale et al., 1992
Rab4	*RAB4A*	EE and RE	Trafficking from EE and RE to plasma membrane	Zahraoui et al., 1989; van der Sluijs et al., 1992; Seachrist and Ferguson, 2003
Rab5	*RAB5A, RAB5*	Clathrin coated vesicles and EE	Endocytic internalization and EE fusion	Zahraoui et al., 1989; Chavrier et al., 1990; Somsel Rodman and Wandinger-Ness, 2000
Rab7a	*RAB7A, PRO2706*	LE	Trafficking from EE to LE and from LE to lysosomes	Chavrier et al., 1990; Harrison et al., 2003; Guerra and Bucci, 2016
Rab7b	*RAB7B, RAB7*	LE	Trafficking from LE to TGN	Surmacz et al., 2006; Progida et al., 2010
Rab8	*RAB8A, MEL, RAB8*	Median Golgi and TGN	Trafficking from median Golgi and TGN to basolateral membrane	Huber et al., 1993; Chen and Wandinger-Ness, 2001; Peranen, 2011
Rab9	*RAB9A, RAB9*	LE	Retrograde transport from LE to trans-Golgi	Lombardi et al., 1993; Soldati et al., 1995; Davies et al., 1997
Rab10	*RAB10*	Golgi	Trafficking and recycling from Golgi to basolateral membrane	Chen et al., 1993; Bao et al., 1998; Schuck et al., 2007
Rab14	*RAB14, FBP*	EE and Golgi	Transport from Golgi to EE	Elferink et al., 1992; Junutula et al., 2004; Proikas-Cezanne et al., 2006
Rab31 (alternate name Rab22b)	*RAB31*	EE and TGN	Anterograde transport from TGN to early endosomes	Rodriguez-Gabin et al., 2001; Ng et al., 2007

ER, endoplasmatic reticulum; EE, early endosome; RE, recycling endosome; LE, late endosome; TGN, trans-Golgi network.

vesicles following internalization from the extracellular matrix (**Figure 4**).

Early Endosomes

Early endosomes are the initial endocytic vesicle to accept incoming internalized molecules (Gruenberg et al., 1989). Their shapes vary from thin tubes (∼60 nm diameter) to large spheres (∼400 nm diameter). As membrane invaginations and scission events occur simultaneously on the endosome membrane, the shape of the endosomes underlies dynamic changes (Gruenberg, 2001). Proteins targeted for recycling may accumulate within tubular membranes. Early endosomes are a hub for sending vesicles off to late endosomes, recycling endosomes, vesicles from the Trans Golgi network or lysosomes. Internalized vesicles are assisted in their transport to and fusion with early endosomes by Rab5. Rab5 tethers to the membranes of cells and endosomes via a C-terminal hydrophobic isoprenoid moiety (Peter et al., 1992; Desnoyers et al., 1996; Shen and Seabra, 1996). In addition to controlling the origination of vesicles from the plasma membrane, vesicle Rab5 helps to recruit Rab7 as endosomes progress from early to late endosomes via fusion events (Gorvel et al., 1991; Huotari and Helenius, 2011). The fusion of endosomes is facilitated by effector proteins including early endosome antigen 1 (EEA1), rabenosyn5 and multiprotein complex C core vacuole/endosome tethering (CORVET) (Rubino et al., 2000; Balderhaar and Ungermann, 2013; Gautreau et al., 2014).

Trans-Golgi Network and Recycling Endosomes

The trans-Golgi network (TGN) is the site for sorting newly translated membrane and secretory proteins (Griffiths and Simons, 1986; Mellman and Warren, 2000). Several Rab proteins carry out the vesicle transport from the TGN to early endosomes or plasma membrane for release (**Figure 4**). Rab31 transports vesicles bidirectionally between the TGN and early endosomes (Rodriguez-Gabin et al., 2009). Vesicles with Rab1 and Rab2 are transported from the TGN to the endoplasmatic reticulum and vice versa, respectively (Plutner et al., 1991; Tisdale et al., 1992, 2004). Rab8 is recruited for the transport of vesicles destined to release proteins from the TGN to basolateral membranes (Huber et al., 1993). Vesicles arriving at the TGN from either the endoplasmatic reticulum or the late endosome are bound for secretion at the plasma membrane via Rab4 (van der Sluijs et al., 1992; Junutula et al., 2004).

Synthesis and secretion are major functions of ameloblasts during enamel formation. The morphology of ameloblasts changes greatly when they differentiate and begin appositional growth of the enamel layer thereby initiating the secretory stage. Secretory stage ameloblasts in rodent incisors, for example, have width to height dimensions of approximately 4–60 μm (1:15). The extreme extension of the ameloblasts facilitates the accommodation of a large number of pronounced cell organelles to synthesize and secrete enamel proteins and to support enamel mineralization. After transcription into mRNA in the nucleus and protein translation in the rough endoplasmatic reticulum, the synthesized enamel proteins progress through the centrally located and very large tubular-shaped Golgi apparatus for post-translational modification and packaging into secretory granules. The supranuclear cytoplasm between nucleus and the Tomes' process is filled with rough endoplasmatic reticulum, Golgi apparatus cisternae, and vesicles, forming an intricate network of membranes in constant exchange of membrane and cargo (Garant and Nalbandian, 1968; Warshawsky, 1968; Sasaki, 1983a; Sasaki and Higashi, 1983). The Golgi cisternae are oriented perpendicular to the nucleus, following the long axis of the cell body. They occupy much of the supranuclear compartment between the nucleus and the microfilaments of the apical cell web with the dimension of 25 × 1.5 μm, but do not penetrate into the Tomes' process (Kallenbach et al., 1963; Garant and Nalbandian, 1968). The saccular stacks of the Golgi apparatus adopt an open-ended, tubular structure and are polarized with shorter saccular stacks on the periphery and long flattened cisternae internally located (Garant and Nalbandian, 1968; Nanci et al., 1993). The

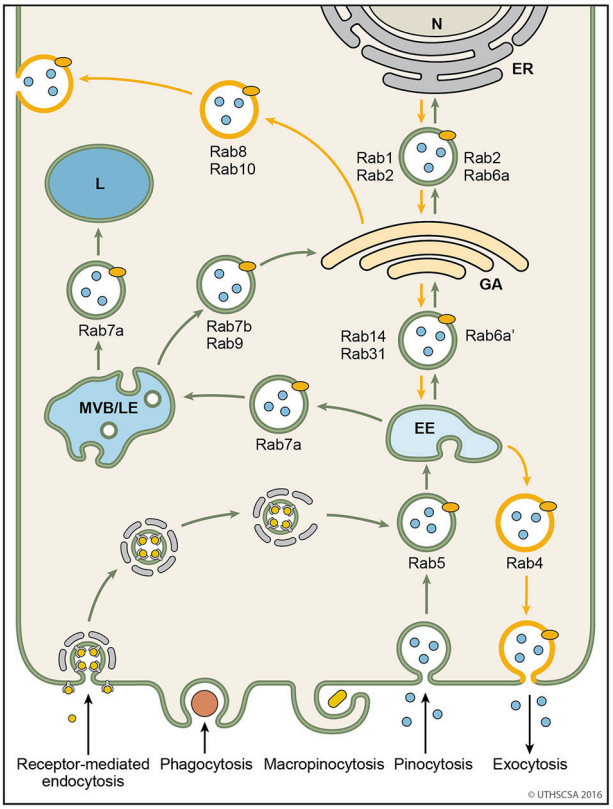

FIGURE 4 | Vesicular trafficking pathways during endocytosis. Schematic diagram showing the general pathways of internalized material. Molecules are taken up into vesicles via various types of endocytosis (receptor-mediated, phagocytosis, micropinocytosis, pinocytosis). Vesicles (coated and non-coated) fuse with EE, the first cellular sorting station, where the cargo is distributed to MVB/LE, GA or back to the plasma membrane (recycling pathway) via their respective Rab proteins. Cargo which is destined for degradation in lysosomes, is transported from EE to lysosomes via MVB/LE. At MVB/LE vesicles can still enter the recycling pathway via GA. Decreasing pH in the EE, MVB/LE, and lysosome are indicated by different shades of blue. EE, early endosome; ER, endoplasmatic reticulum; GA, Golgi apparatus; L, lysosome; MVB/LE, multivesicular body/late endosome; N, nucleus.

endoplasmatic reticulum surrounds the Golgi apparatus in the periphery.

The number of vesicles shuttling between the rough endoplasmatic reticulum, the Golgi apparatus and the plasma membrane is large (Garant and Nalbandian, 1968). They accumulate in the Tomes' process close to the secretory face (Reith, 1967; Garant and Nalbandian, 1968). Vesicles with a dense content are, in average, of 0.8–0.16 μm in diameter (Garant and Nalbandian, 1968; Warshawsky, 1968) and contain enamel proteins to be released at the plasma membrane (Uchida et al., 1991).

All secretory stage enamel proteins, amelogenin (Nanci et al., 1987a, 1989; Inage et al., 1989), enamelin (Uchida et al., 1991; Dohi et al., 1998), and ameloblastin (Lee et al., 1996; Murakami et al., 1997; Uchida et al., 1998) were found in the Golgi apparatus of ameloblasts. They have also been identified in secretory vesicles and at the secretory face of the Tomes' process (Nanci et al., 1989; Uchida et al., 1991). One of the commonalities of the enamel proteins as part of the secreted calcium-binding phosphoprotein cluster is that all members are phosphorylated on a conserved serine residue in a SXE motif of exon 3 (Kawasaki et al., 2004). The enzyme catalyzing the phosphorylation has been identified as Golgi-localized casein kinase, encoded by FAM20C (Tagliabracci et al., 2012), localized to the Golgi apparatus of ameloblasts (Wang et al., 2013). The phosphorylation of enamel proteins is essential as mutations lead to non-lethal Raine syndrome with hypoplastic amelogenesis imperfecta (Acevedo et al., 2015).

After the completion of the secretory stage, maturation stage ameloblasts reduced their height, and the Golgi apparatus reduces its dimensions (Nanci et al., 1993). Most of the enamel proteins synthesized during the secretory stage are greatly reduced in expression by maturation stage ameloblasts (Somogyi-Ganss et al., 2012). They start to produce and secrete the basement membrane proteins amelotin (Holcroft and Ganss, 2011) and ODAM (Iwasaki et al., 2005; Nishio et al., 2010; Dos Santos Neves et al., 2012), implicated in the mineralization of the enamel surface (Abbarin et al., 2015; Nakayama et al., 2015; Núñez et al., 2016).

Late Endosomes

Along the endocytic pathway, early endosomes mature into late endosomes (Huotari and Helenius, 2011). Late endosomes are a sorting center to direct cargo to the lysosome, Golgi apparatus or opposite plasma membrane (recycling, transcytosis). In the course of conversion from early to late endosomes, Rab5 is removed and replaced with Rab7 (Rink et al., 2005) which is controlled by the membrane protein complex SAND-1/Mon-1 and HOPS (homotypic fusion and protein sorting) (Rink et al., 2005; Peralta et al., 2010; Poteryaev et al., 2010; Plemel et al., 2011). The late endosome is recruited to the target lysosome and tethered onto the lysosomal membrane by HOPS accomplishing the fusion (Balderhaar and Ungermann, 2013). Late endosomes provide an intersection for arriving and leaving vesicles and have a size between 250 and 1,000 nm (Huotari and Helenius, 2011). Incoming vesicles bring information about the environmental conditions and nutrients for the cell. Outgoing vesicles can carry signals for protein synthesis, secretion, endocytosis, recycling, and autophagy. Fusion events with other endosomes and lysosomes are executed by Rab7. Once the endosome fuses with a lysosome, the vesicle content will be degraded and the endosomal pathway cannot be re-entered (Luzio et al., 2007). Endocytic vesicles contain acid hydrolases that operate in an acidic environment and are indicative for degradation (Yamashiro and Maxfield, 1987).

Molecular markers for late endosomes in ameloblasts have not been described. In electron microscopy images unique features of late endosomes can be identified in ameloblasts in secretory and maturation stages with intraluminal vesicles (Katchburian et al., 1967; Reith and Cotty, 1967; Garant and Nalbandian, 1968; Katchburian and Holt, 1969; Smith, 1979; Matsuo et al., 1986; Nanci et al., 1987a, 1993; Salama et al., 1989; Franklin et al., 1991; Uchida and Warshawsky, 1992). MVB originate from fusion with early endosomes and lysosomes and can release their content into the extracellular environment. They represent a type of late endosomes and are found during the entire life cycle of ameloblasts. MVB are first found in pre-secretory ameloblast associated with finger-like projections and the disruption of the basement membrane between odontoblasts and pre-ameloblasts (Reith, 1967; Nanci et al., 1989). In ameloblasts of the secretory stage, MVB reside in the supranuclear zone of the cell (Sasaki, 1983b). During the maturation stage, the resorptive activity at the ruffled border is intense. Large quantities of HRP labeled fluid-phase material are resorbed via pinosomes and delivered to MVB (Sasaki, 1984c). The number of MVB is greater in early maturation compared to late maturation stage (Salama et al., 1990a).

Multivesicular bodies (MVB) containing amelogenin protein have been found with immune gold labeling techniques in secretory-stage, smooth-ended, and ruffle-ended ameloblasts (Nanci et al., 1987a, 1993). However, immunolocalization studies do not answer the question whether the proteins had intracellular or extracellular origin.

Lysosomes

Lysosomes originate from late endosomes. The transition between these two organelles is continuous, often forming an endo-lysosome before it transforms into a secondary or dense lysosome (Luzio et al., 2007; Huotari and Helenius, 2011). Lysosomes are the cell's primary degradation center and the terminal station in the endocytic pathway. They contain the breakdown of proteins, polysaccharides, and lipids catalyzed by a wide array of lipases, proteases, and glycosidases in an acidic environment (Luzio et al., 2007; Huotari and Helenius, 2011; Xu and Ren, 2015). Lysosomes generate an acidic luminal pH to activate hydrolytic enzymes and degrade. Acidification is accomplished by proton transport into the lysosome lumen countered by chloride (Dell'Antone, 1979; Ohkuma et al., 1982; Nelson et al., 2000; Sun-Wada et al., 2004; Mindell, 2012). Among lysosomal hydrolases, cathepsins play a major role in peptide degradation. Cathepsins are classified into serine, aspartic and cysteine proteases referring to the amino acid residue in the catalytic center. Cathepsins A (also called human protective protein) and G contain a serine residue in their active site (Kawamura et al., 1980; Rudenko et al., 1995; Hof et al., 1996),

while cathepsins D and E have an aspartic acid residue in their active site (Shewale and Tang, 1984; Ostermann et al., 2004). Accordingly, cathepsins B, C (also known as dipeptidyl peptidase I), F, H, K, L, O, S, V, W, and X each feature a cysteine residue in the catalytic site (Turk et al., 2012). While cathepins B, H, L, C, X, F, O, and V are ubiquitously expressed (Turk et al., 2012), cathepsins K, W, and S are only found in specific tissues. Cathepsin K, for example is highly expressed in osteoclasts, and in many epithelial cells (Drake et al., 1996; Buhling et al., 1999; Salminen-Mankonen et al., 2007).

In enamel formation lysosomes are found in ameloblasts at presecretory, secretory and maturation stages (Katchburian and Burgess, 1983; Nanci et al., 1987a,b). Lysosomal activity for acid phosphatase has been demonstrated in preameloblasts, secretory and maturation stage ameloblasts located in granules within the center of the supranuclear region and in the Tomes' process (Katchburian et al., 1967). In preameloblasts, the target of the resorptive function is the basal lamina facing odontoblasts (Katchburian and Burgess, 1983; Uchida et al., 1989). During secretory and maturation stages, enamel proteins are removed from the matrix through resorption by ameloblasts (Reith and Cotty, 1967; Nanci et al., 1987a,b; Salama et al., 1990a). Large lysosomes can have smooth or rough surfaces in maturation stage ameloblasts (Nanci et al., 1993). The shape of lysosomes is described as spherical and elongated, tubular with sizes ranging from 80 to 140 nm in length (Salama et al., 1989).

Lysosomal enzymes present in ameloblasts include acid phosphatase, β-glucoronidase, and leucyl-naphthylamidase (Beynon, 1972). The distinction between pale and dark lysosomes was derived from the electron density of deposits observed with electron microscopy. Pale lysosomes stain inconsistently with inorganic trimetaphosphatase and acid phosphatase. In contrast, dark lysosomes are reliably positive for inorganic trimetaphosphatase (Nanci et al., 1987b). Dark lysosomes contain less protein than pale lysosomes as they are secondary lysosomes with ongoing protein degradation (Nanci et al., 1987a). Ruffle-ended ameloblasts show more endocytic activity than smooth-ended ameloblasts (Nanci et al., 1987b). Interestingly, the lysosomal activity of ameloblasts is higher during secretory stage compared to maturation stages (**Table 1**). Among the enamel proteins, amelogenin localizes to lysosomes (Nanci et al., 1987b; Inage et al., 1989). Whether enamelin localizes to lysosomes is not clear since the antibody was raised against a protein species of 50–70 kDa potentially containing enamelin and/or ameloblastin (Inage et al., 1989). Much of the degradative effort in lysosomes is associated with cathepsin B, D, F, H, K, L, O, S, and Z expressed by maturation stage ameloblasts (Tye et al., 2009).

PERSPECTIVES AND FUTURE DIRECTIONS

Enamel mineralizes and matures as a result of a balance between synthesis, deposition, degradation and internalization. The homeostasis between ameloblasts and matrix is critical for proper enamel formation. The intracellular transport of vesicles is important for polarization of epithelial cells, serving as a mechanism to regulate differentiation (Bryant and Mostov, 2008; Butler and Wallingford, 2017). Endocytosis is a fundamental cell function executed during all stages of the ameloblast life cycle to create the most mineralized hard tissue. Since the enamel matrix represents a secluded compartment surrounded by dentin and ameloblasts (Bronckers, 2016), ameloblasts are granted full control of enamel formation. No other cell type has direct access to the enamel matrix. As a result, ameloblasts closely monitor the transport of ions and proteins across the membrane, necessary to control crystal growth. Endocytosis may be a mechanism for communicating changes in the maturing enamel to the ameloblasts. Each of the various stages of amelogenesis has specific criteria that need to be fulfilled to allow cells to advance to the next stage. Disruption of the completion of a stage results in severe cell pathology as caused by absence of any of the enamel proteins (amelogenin, ameloblastin, enamelin), matrix metalloproteinase 20 or kallikrein4 (Fukumoto et al., 2004; Simmer et al., 2009; Bartlett et al., 2011; Hu et al., 2014, 2016). The inability to cleave the enamel proteins is associated with hypomineralized enamel and matrix-retained proteins (Simmer et al., 2009; Bartlett et al., 2011), allowing the conclusion that cleavage and degradation of enamel proteins are a prerequisite for effective endocytosis. Appropriate feedback to ameloblasts is required to maintain ameloblast function (Chun et al., 2010).

Aside from releasing and internalizing vesicle content, the vesicle membrane may supply or reduce the plasma membrane surface when vesicles fuse with the membrane or are pinched off from the membrane. Thereby, the shape and size of the cell may be modified. During the life cycle of an ameloblast, the cell undergoes significant changes in cell shape. During the development of the Tomes' process in preameloblasts, the membrane surface is enlarged which could be supplied by secretory vesicles. During this event, secretion may dominate over endocytosis. Once the Tomes process has been established in secretory stage ameloblasts, secretion and endocytosis may take place in equilibrium. Given the intense protein synthesis activity of secretory ameloblasts, a mechanism is needed to attain homeostasis of membrane surface and the overall cell shape. The three-dimensional shape of the Tomes' process coordinates enamel ribbons in the characteristic rod and interrod enamel. The forming interrod enamel completely surrounds the protruded distal portion of the Tomes' process like prongs. The interrod enamel originates from the proximal portions of the Tomes' process. If ameloblasts were separated from the forming enamel, a cavity in which the Tomes' process resides would become visible from a baso-apical direction. The interrod enamel would be elevated and form a rim surrounding a cavity in the shape of the Tomes' process. The interrod is partially mineralized, and therefore may restrict the size and shape the Tomes' process is able to adopt. When a secretory vesicle undergoes fusion with the surface membrane of a cell, the vesicle experiences a gain in membrane and increases the overall surface of the cell. For the Tomes' process, a gain in membrane from secretory vesicles would alter and enlarge the shape of the Tomes' process. However, being encased by rigid rod and interrod enamel, an enlarged Tomes' process would collide with

enamel ribbons. Endocytosis, on the other hand, removes plasma membrane from the cell surface when vesicles are pinched off and trim the contour of the Tomes' process. Invaginations of the plasma membrane of the Tomes' process present an elegant solution to offer surface membrane, but because it is shifted internally, variability in the shape due to membrane fusion from secretory or endocytic vesicles is bypassed. As a result, the surface membrane and the shape of the Tomes' process remain largely unaltered. When the ameloblast progresses from secretory stage to transition stage and maturation stages, the cell's dimensions are reduced and the Tomes' process is dismantled. A preference of endocytosis events would facilitate a reduction in cell surface membrane. Ruffle-ended maturation stage ameloblasts display high activity in endocytosis. Throughout amelogenesis, secretion and endocytosis are highly prominent operations in ameloblasts that may participate in the control of the cell membrane surface available to form and disassemble cell appendages and infoldings and invaginations.

During their life cycle, ameloblasts adopt many different morphologically distinct appearances as preameloblast, secretory ameloblast, transition stage ameloblast, ruffle-ended ameloblast, smooth-ended ameloblast, and reduced enamel epithelium. The sites of endocytosis on the ameloblast membrane are different in each stage. Small processes are protruded into the basal lamina in preameloblasts. The Tomes' process of the secretory ameloblast is a very large projection from the apical membrane. The infoldings of the membrane distal portion form inwards in the Tomes' process. The ruffled border of maturation stage ameloblasts is formed much differently from the secretory stage infoldings associated with rod and interrod growth sites. They sink into the supranuclear cytoplasmic mass. The stage-specific mechanisms and pathways of endocytosis in ameloblasts are not well defined. While strong evidence is available to document vesicles generated during endocytosis, so far, only clathrin-mediated endocytosis and pinocytosis have been identified in ameloblasts as internalization routes. Lipid rafts or caveolae-mediated endocytosis as a clathrin independent form of endocytosis has not been described in ameloblasts. Future directions in understanding endocytosis in ameloblasts should address the feedback mechanisms, differences in endocytosis types depending on the vesicle origin from the infolding of the Tomes' process vs. ruffled border vs. smooth-ended border vs. lateral membrane and the trafficking of endosomes.

AUTHOR CONTRIBUTIONS

CP and YC drafted the manuscript with help from CS. JH, JS, and CS planned experiments for **Figure 3**. YH and CS performed experiments for **Figure 3**. All authors contributed to the manuscript and approved it.

FUNDING

This work was supported by T32DE014318 (CP), K08DE022800 (YC), R21DE025758 (YC), R01DE026769 (YC), and R01DE015846 (JH) from the National Institute of Dental and Craniofacial Research and UL1TR001120 from the National Center for Advancing Translational Sciences. The authors are responsible for the content. It does not necessarily represent the official views of the National Institutes of Health.

ACKNOWLEDGMENTS

The authors thank Susan Simon, Medical Illustrator in Creative Media Services, University of Texas Health Science Center at San Antonio, for designing **Figures 2** and **4**.

REFERENCES

Abbarin, N., San Miguel, S., Holcroft, J., Iwasaki, K., and Ganss, B. (2015). The enamel protein amelotin is a promoter of hydroxyapatite mineralization. *J. Bone Miner. Res.* 30, 775–785. doi: 10.1002/jbmr.2411

Acevedo, A. C., Poulter, J. A., Alves, P. G., de Lima, C. L., Castro, L. C., Yamaguti, P. M., et al. (2015). Variability of systemic and oro-dental phenotype in two families with non-lethal Raine syndrome with FAM20C mutations. *BMC Med. Genet.* 16:8. doi: 10.1186/s12881-015-0154-5

Antonescu, C. N., McGraw, T. E., and Klip, A. (2014). Reciprocal regulation of endocytosis and metabolism. *Cold Spring Harb. Perspect. Biol.* 6:a016964. doi: 10.1101/cshperspect.a016964

Balderhaar, H. J., and Ungermann, C. (2013). CORVET and HOPS tethering complexes-coordinators of endosome and lysosome fusion. *J. Cell Sci.* 126(Pt 6), 1307–1316. doi: 10.1242/jcs.107805

Bao, S., Zhu, J., and Garvey, W. T. (1998). Cloning of Rab GTPases expressed in human skeletal muscle: studies in insulin-resistant subjects. *Horm. Metab. Res.* 30, 656–662. doi: 10.1055/s-2007-978953

Bartlett, J. D. (2013). Dental enamel development: proteinases and their enamel matrix substrates. *SRN Dent.* 2013:684607. doi: 10.1155/2013/684607

Bartlett, J. D., Skobe, Z., Nanci, A., and Smith, C. E. (2011). Matrix metalloproteinase 20 promotes a smooth enamel surface, a strong dentino-enamel junction, and a decussating enamel rod pattern. *Eur. J. Oral Sci.* 119, 199–205. doi: 10.1111/j.1600-0722.2011.00864.x

Beynon, A. D. (1972). Enzymes in enamel maturation. *Proc. R. Soc. Med.* 65, 911–912.

Bronckers, A. L. (2016). Ion transport by ameloblasts during amelogenesis. *J. Dent. Res.* 96, 243–253. doi: 10.1177/0022034516681768

Bryant, D. M., and Mostov, K. E. (2008). From cells to organs:building polarized tissue. *Nat. Rev. Mol. Cell Biol.* 9, 887–901. doi: 10.1038/nrm2523

Buhling, F., Gerber, A., Hackel, C., Kruger, S., Kohnlein, T., Bromme, D., et al. (1999). Expression of cathepsin K in lung epithelial cells. *Am. J. Respir. Cell Mol. Biol.* 20, 612–619. doi: 10.1165/ajrcmb.20.4.3405

Butler, M. T., and Wallingford, J. B. (2017). Planar cell polarity in development and disease. *Nat. Rev. Mol. Cell Biol.* 18, 375–388. doi: 10.1038/nrm.2017.11

Chavrier, P., Parton, R. G., Hauri, H. P., Simons, K., and Zerial, M. (1990). Localization of low molecular weight GTP binding proteins to exocytic and endocytic compartments. *Cell* 62, 317–329. doi: 10.1016/0092-8674(90)90369-P

Chen, W., and Wandinger-Ness, A. (2001). Expression and functional analyses of Rab8 and Rab11a in exocytic transport from trans-Golgi network. *Meth. Enzymol.* 329, 165–175. doi: 10.1016/S0076-6879(01)29077-6

Chen, Y. T., Holcomb, C., and Moore, H. P. (1993). Expression and localization of two low molecular weight GTP-binding proteins, Rab8 and Rab10, by epitope tag. *Proc. Natl. Acad. Sci. U.S.A.* 90, 6508–6512. doi: 10.1073/pnas.90.14.6508

Chun, Y.-H. P., Lu, Y., Hu, Y., Krebsbach, P. H., Yamada, Y., Hu, J. C.-C., Simmer, J. P. et al. (2010). Transgenic rescue of enamel phenotype in ambn null mice. *J. Dent. Res.* 89, 1414–1420. doi: 10.1177/0022034510379223

Colicelli, J. (2004). Human RAS superfamily proteins and related GTPases. *Sci. STKE* 250:RE13. doi: 10.1126/stke.2502004re13

Collawn, J. F., Lai, A., Domingo, D., Fitch, M., Hatton, S., and Trowbridge, I. S. (1993). YTRF is the conserved internalization signal of the transferrin receptor, and a second YTRF signal at position 31-34 enhances endocytosis. *J. Biol. Chem.* 268, 21686–21692.

Conner, S. D., and Schmid, S. L. (2003). Regulated portals of entry into the cell. *Nature* 422, 37–44. doi: 10.1038/nature01451

Dahlen, D. D., Broudy, V. C., and Drachman, J. G. (2003). Internalization of the thrombopoietin receptor is regulated by 2 cytoplasmic motifs. *Blood* 102, 102–108. doi: 10.1182/blood-2002-11-3468

Davies, J. P., Cotter, P. D., and Ioannou, Y. A. (1997). Cloning and mapping of human Rab7 and Rab9 cDNA sequences and identification of a Rab9 pseudogene. *Genomics* 41, 131–134. doi: 10.1006/geno.1997.4644

Dell'Antone, P. (1979). Evidence for an ATP-driven "proton pump" in rat liver lysosomes by basic dyes uptake. *Biochem. Biophys. Res. Commun.* 86, 180–189. doi: 10.1016/0006-291X(79)90398-X

Desnoyers, L., Anant, J. S., and Seabra, M. C. (1996). Geranylgeranylation of Rab proteins. *Biochem. Soc. Trans*. 24, 699–703. doi: 10.1042/bst0240699

Dohi, N., Murakami, C., Tanabe, T., Yamakoshi, Y., Fukae, M., Yamamoto, Y., et al. (1998). Immunocytochemical and immunochemical study of enamelins, using antibodies against porcine 89-kDa enamelin and its N-terminal synthetic peptide, in porcine tooth germs. *Cell Tissue Res.* 293, 313–325. doi: 10.1007/s004410051123

Dos Santos Neves, J., Wazen, R. M., Kuroda, S., Francis Zalzal, S., Moffatt, P., and Nanci, A. (2012). Odontogenic ameloblast-associated and amelotin are novel basal lamina components. *Histochem. Cell Biol.* 137, 329–338. doi: 10.1007/s00418-011-0901-4

Drake, F. H., Dodds, R. A., James, I. E., Connor, J. R., Debouck, C., Richardson, S., et al. (1996). but not cathepsins B, L, or S, is abundantly expressed in human osteoclasts. *J. Biol. Chem.* 271, 12511–12516. doi: 10.1074/jbc.271.21.12511

Eaton, S., and Martin-Belmonte, F. (2014). Cargo sorting in the endocytic pathway: a key regulator of cell polarity and tissue dynamics. *Cold Spring Harb. Perspect. Biol.* 6:a016899. doi: 10.1101/cshperspect.a016899

Elferink, L. A., Anzai, K., and Scheller, R. H. (1992). rab15, a novel low molecular weight GTP-binding protein specifically expressed in rat brain. *J. Biol. Chem.* 267, 5768–5775.

Fincham, A. G., Moradian-Oldak, J., Diekwisch, T. G., Lyaruu, D. M., Wright, J. T., Bringas, P. Jr., et al. (1995). Evidence for amelogenin "nanospheres" as functional components of secretory-stage enamel matrix. *J. Struct. Biol.* 115, 50–59. doi: 10.1006/jsbi.1995.1029

Flannagan, R. S., Jaumouille, V., and Grinstein, S. (2012). The cell biology of phagocytosis. *Annu. Rev. Pathol.* 7, 61–98. doi: 10.1146/annurev-pathol-011811-132445

Franklin, D. L., Severs, N. J., and Katchburian, E. (1991). Development of the distal end and Tomes' processes of ameloblasts observed by freeze-fracture and ultrathin section electron microscopy. *J. Anat.* 174, 103–114.

Fukae, M., Tanabe, T., Uchida, T., Lee, S. K., Ryu, O. H., Murakami, C., et al. (1998). Enamelysin (matrix metalloproteinase-20): localization in the developing tooth and effects of pH and calcium on amelogenin hydrolysis. *J. Dent. Res.* 77, 1580–1588. doi: 10.1177/00220345980770080501

Fukumoto, S., Kiba, T., Hall, B., Iehara, N., Nakamura, T., Longenecker, G., et al. (2004). Ameloblastin is a cell adhesion molecule required for maintaining the differentiation state of ameloblasts. *J. Cell Biol.* 167, 973–983. doi: 10.1083/jcb.200409077

Garant, P. R., and Nalbandian, J. (1968). Observations on the ultrastructure of ameloblasts with special reference to the golgi complex and related components. *J. Ultrastruct. Res.* 23, 427–443. doi: 10.1016/S0022-5320(68)80108-X

Gautreau, A., Oguievetskaia, K., and Ungermann, C. (2014). Function and regulation of the endosomal fusion and fission machineries. *Cold Spring Harb Perspect Biol.* 6:a016832. doi: 10.1101/cshperspect.a016832

Gordon, S. (2016). Phagocytosis: a immunobiologic process. *Cell* 44, 463–475. doi: 10.1016/j.immuni.2016.02.026

Gorvel, J. P., Chavrier, P., Zerial, M., and Gruenberg, J. (1991). rab5 controls early endosome fusion *in vitro*. *Cell* 64, 915–925. doi: 10.1016/0092-8674(91)90316-Q

Griffiths, G., and Simons, K. (1986). The trans Golgi network: sorting at the exit site of the Golgi complex. *Science* 234, 438–443. doi: 10.1126/science.2945253

Gruenberg, J. (2001). The endocytic pathway: a mosaic of domains. *Nat. Rev. Mol. Cell Biol.* 2, 721–730. doi: 10.1038/35096054

Gruenberg, J., Griffiths, G., and Howell, K. E. (1989). Characterization of the early endosome and putative endocytic carrier vesicles *in vivo* and with an assay of vesicle fusion *in vitro*. *J. Cell Biol.* 108, 1301–1316. doi: 10.1083/jcb.108.4.1301

Guerra, F., and Bucci, C. (2016). Multiple roles of the small GTPase Rab7. *Cells* 5:E34. doi: 10.3390/cells5030034

Hammer, J. A. III, and Wu, X. S. (2002). Rabs grab motors: defining the connections between Rab GTPases and motor proteins. *Curr. Opin. Cell Biol.* 14, 69–75. doi: 10.1016/S0955-0674(01)00296-4

Harrison, R. E., Bucci, C., Vieira, O. V., Schroer, T. A., and Grinstein, S. (2003). Phagosomes fuse with late endosomes and/or lysosomes by extension of membrane protrusions along microtubules: role of Rab7 and RILP. *Mol. Cell. Biol.* 23, 6494–6506. doi: 10.1128/MCB.23.18.6494-6506.2003

Hof, P., Mayr, I., Huber, R., Korzus, E., Potempa, J., Travis, J., et al. (1996). The 1.8 A crystal structure of human cathepsin G in complex with Suc-Val-Pro-PheP-(OPh)2: a Janus-faced proteinase with two opposite specificities. *EMBO J.* 15, 5481–5491.

Holcroft, J., and Ganss, B. (2011). Identification of amelotin- and ODAM-interacting enamel matrix proteins using the yeast two-hybrid system. *Eur. J. Oral Sci.* 119(Suppl. 1), 301–306. doi: 10.1111/j.1600-0722.2011.00870.x

Hu, J. C., Hu, Y., Lu, Y., Smith, C. E., Lertlam, R., Wright, J. T., et al. (2014). Enamelin is critical for ameloblast intergity and enamel ultrastructure formation. *PLoS ONE* 9:e89303. doi: 10.1371/journal.pone.0089303

Huber, L. A., Pimplikar, S., Parton, R. G., Virta, H., Zerial, M., and Simons, K. (1993). Rab8, a small GTPase involved in vesicular traffic between the TGN and the basolateral plasma membrane. *J. Cell Biol.* 123, 35–45. doi: 10.1083/jcb.123.1.35

Huotari, J., and Helenius, A. (2011). Endosome maturation. *EMBO J.* 30, 3481–3500. doi: 10.1038/emboj.2011.286

Hutagalung, A. H., and Novick, P. J. (2011). Role of Rab GTPases in membrane traffic and cell physiology. *Physiol. Rev.* 91, 119–149. doi: 10.1152/physrev.00059.2009

Hu, Y., Smith, C. E., Cai, Z., Donnelly, L. A., Yang, J., Hu, J. C., et al. (2016). Enamel ribbons, surface nodules, and octacalcium phosphate in C57BL/6 Amelx$^{-/-}$ mice and Amelx$^{+/-}$ lyonization. *Mol. Genet. Genomic Med.* 4, 641–661. doi: 10.1002/mgg3.252

Inage, T., Shimokawa, H., Teranishi, Y., Iwase, T., Toda, Y., and Moro, I. (1989). Immunocytochemical demonstration of amelogenins and enamelins secreted by ameloblasts during the secretory and maturation stages. *Arch. Histol. Cytol.* 52, 213–229. doi: 10.1679/aohc.52.213

Iwasaki, K., Bajenova, E., Somogyi-Ganss, E., Miller, M., Nguyen, V., Nourkeyhani, H., et al. (2005). Amelotin–a novel secreted, ameloblast-specific protein. *J. Dent. Res.* 84, 1127–1132. doi: 10.1177/154405910508401207

Jena, B. P. (2011). Role of SNAREs in membrane fusion. *Adv. Exp. Med. Biol.* 713, 13–32. doi: 10.1007/978-94-007-0763-4_3

Jessen, H., and Moe, H. (1972). The fine structure of macrophages in the enamel organ, with special reference to the microtubular system. *Z. Zellforsch. Microsk. Anat.* 126, 466–482. doi: 10.1007/BF00306907

Junutula, J. R., De Maziere, A. M., Peden, A. A., Ervin, K. E., Advani, R. J., van Dijk, S. M., et al. (2004). Rab14 is involved in membrane trafficking between the Golgi complex and endosomes. *Mol. Biol. Cell* 15, 2218–2229. doi: 10.1091/mbc.E03-10-0777

Kallenbach, E. (1973). The fine structure of Tomes' process of rat incisor ameloblasts and its relationship to the elaboration of enamel. *Tissue Cell* 5, 501–524. doi: 10.1016/S0040-8166(73)80041-2

Kallenbach, E. (1974). Fine structure of rat incisor ameloblasts in transition between enamel secretion and maturation stages. *Tissue Cell* 6, 173–190. doi: 10.1016/0040-8166(74)90030-5

Kallenbach, E. (1976). Fine structure of differentiating ameloblasts in the kitten. *Am. J. Anat.* 145, 283–318. doi: 10.1002/aja.1001450302

Kallenbach, E. (1980a). Access of horseradish peroxidase (HRP) to the extracellular spaces of the maturation zone of the rat incisor enamel organ. *Tissue Cell* 12, 165–174. doi: 10.1016/0040-8166(80)90059-2

Kallenbach, E. (1980b). Fate of horseradish peroxidase in the secretion zone of the rat incisor enamel organ. *Tissue Cell* 12, 491–501. doi: 10.1016/0040-8166(80)90038-5

Kallenbach, E., Sandborn, E., and Warshawsky, H. (1963). The Golgi apparatus of the ameloblast of the rat at the stage of enamel matrix formation. *J. Cell Biol.* 16, 629–632. doi: 10.1083/jcb.16.3.629

Katchburian, E., and Burgess, A. M. (1983). Lysosomes and removal of the basal lamina of ameloblasts in early stages of odontogenesis. *Cell Biol. Int. Rep.* 7, 407–415. doi: 10.1016/0309-1651(83)90129-7

Katchburian, E., and Holt, S. J. (1969). Role of lysosomes in amelogenesis. *Nature* 223, 1367–1368. doi: 10.1038/2231367a0

Katchburian, E., Katchburian, A. V., and Pearse, A. G. E. (1967). Histochemistry of lysosomal enzymes in developing teeth of albino rats. *J. Anat.* 101, 783–792.

Kawamura, Y., Matoba, T., and Doi, E. (1980). Subunit structure of pig kidney cathepsin. *J. Biochem. A.* 88, 1559–1561.

Kawasaki, K., Suzuki, T., and Weiss, K. M. (2004). Genetic basis for the evolution of vertebrate mineralized tissue. *Proc. Natl. Acad. Sci. U.S.A.* 101, 11356–11361. doi: 10.1073/pnas.0404279101

Kim, S., Inoue, S., and Akisaka, T. (1994). Ultrastructure of quick-frozen secertory ameloblasts of the rat milar tooth. *Tissue Cell* 26, 29–41. doi: 10.1016/0040-8166(94)90081-7

Lacruz, R. S., Brookes, S. J., Wen, X., Jimenez, J. M., Vikman, S., Hu, P., et al. (2013a). Adaptor protein complex 2-mediated, clathrin-dependent endocytosis, and related gene activities, are a prominent feature during maturation stage amelogenesis. *J. Bone Miner. Res.* 28, 672–687. doi: 10.1002/jbmr.1779

Lacruz, R. S., Smith, C. E., Kurtz, I., Hubbard, M. J., and Paine, M. L. (2013b). New paradigms on the transport functions of maturation-stage ameloblasts. *J. Dent. Res.* 92, 122–129. doi: 10.1177/0022034512470954

Lee, S. K., Krebsbach, P. H., Matsuki, Y., Nanci, A., Yamada, K. M., and Yamada, Y. (1996). Ameloblastin expression in rat incisors and human tooth germs. *Int. J. Dev. Biol.* 40, 1141–1150.

Le Roy, C., and Wrana, J. L. (2005). Clathrin- and non-clathrin-mediated endocytic regulation of cell signalling. *Nat. Rev. Mol. Cell Biol.* 6, 112–126. doi: 10.1038/nrm1571

Lombardi, D., Soldati, T., Riederer, M. A., Goda, Y., Zerial, M., and Pfeffer, S. R. (1993). Rab9 functions in transport between late endosomes and the trans Golgi network. *EMBO J.* 12, 677–682.

Luzio, J. P., Pryor, P. R., and Bright, N. A. (2007). Lysosomes: fusion and function. *Nat. Rev. Mol. Cell Biol.* 8, 622–632. doi: 10.1038/nrm2217

Matsuo, S., Yamamoto, K., Nishikawa, S., Ichikawa, H., Wakisaka, S., Takano, Y., et al. (1986). Influence of colchicine on the distribution of horseradish peroxidase in the secretory ameloblast layer *in vitro*. *Anat. Rec.* 216, 10–18. doi: 10.1002/ar.1092160103

Mellman, I. (1996). Endocytosis and molecular sorting. *Annu. Rev. Cell Dev. Biol.* 12, 575–625. doi: 10.1146/annurev.cellbio.12.1.575

Mellman, I., and Warren, G. (2000). The road taken: past and future foundations of membrane traffic. *Cell* 100, 99–112. doi: 10.1016/S0092-8674(00)81687-6

Miletich, I., Cobourne, M. T., Abdeen, M., and Sharpe, P. T. (2005). Expression of the Hedgehog antagonists Rab23 and Slimb/beta TrCP during mouse tooth development. *Arch. Oral Biol.* 50, 147–151. doi: 10.1016/j.archoralbio.2004.09.006

Mills, I. G. (2007). The interplay between clathrin-coated vesicles and cell signalling. *Semin. Cell Dev. Biol.* 18, 459–470. doi: 10.1016/j.semcdb.2007.07.001

Mindell, J. A. (2012). Lysosomal acidification mechanisms. *Annu. Rev. Physiol.* 74, 69–86. doi: 10.1146/annurev-physiol-012110-142317

Moe, H., and Jessen, H. (1972). Phagocytosis and elimination of amelocyte debris by stratum intermedium cells in the trasitional zone of the enamel organ of the rat incisor. *Z. Zellforsch. Mikrosk. Anat.* 131, 63–75. doi: 10.1007/BF00307201

Mostov, K. E., and Cardone, M. H. (1995). Regulation of protein traffic in polarized cells. *Bioessays* 17, 129–138. doi: 10.1002/bies.950170208

Munafo, D. B., and Colombo, M. I. (2002). Induction of autophagy causes dramatic changes in the subcellular distribution of GFP-Rab24. *Traffic* 3, 472–482. doi: 10.1034/j.1600-0854.2002.30704.x

Murakami, C., Dohi, N., Fukae, M., Tanabe, T., Yamakoshi, Y., Wakida, K., et al. (1997). Immunochemical and immunohistochemical study of the 27- and 29-kDa calcium-binding proteins and related proteins in the porcine tooth germ. *Histochem. Cell Biol.* 107, 485–494. doi: 10.1007/s004180050136

Nagano, T., Kakegawa, A., Yamakoshi, Y., Tsuchiya, S., Hu, J. C., Gomi, K., et al. (2009). Mmp-20 and Klk4 cleavage site preferences for amelogenin sequences. *J. Dent. Res.* 88, 823–828. doi: 10.1177/0022034509342694

Nakayama, Y., Holcroft, J., and Ganss, B. (2015). Enamel hypomineralization and structural defects in amelotin-deficient mice. *J. Dent. Res.* 94, 697–705. doi: 10.1177/0022034514566214

Nanci, A., Ahluwalia, J. P., Pompura, J. R., and Smith, C. E. (1989). Biosynthesis and secretion of enamel proteins in the rat incisor. *Anat. Rec.* 224, 277–291. doi: 10.1002/ar.1092240218

Nanci, A., Bendayan, M., and Slavkin, H. C. (1985). Enamel protein biosynthesis and secretion in mouse incisor secretory ameloblasts as revealed by high-resolution immunocytochemistry. *J. Histochem. Cytochem.* 33, 1153–1160. doi: 10.1177/33.11.4056379

Nanci, A., Fortin, M., and Ghitescu, L. (1996). Endocytotic functions of ameloblasts and odontoblasts: immunocytochemical and tracer studies on the uptake of plasma proteins. *Anat. Rec.* 245, 219–234. doi: 10.1002/(SICI)1097-0185(199606)245:2<219::AID-AR9>3.0.CO;2-R

Nanci, A., Slavkin, H. C., and Smith, C. E. (1987a). Application of high resolution immunocytochemistry to the study of the secretory, resorptive and degradative functions of ameloblasts. *Adv. Dent. Res.* 1, 148–161. doi: 10.1177/08959374870010020301

Nanci, A., Slavkin, H. C., and Smith, C. E. (1987b). Immunocytochemical and radioautographic evidence for secretion and intracellular degradation of enamel proteins by ameloblasts during the maturation stage of amelogenesis in rat incisors. *Anat. Rec.* 217, 107–123. doi: 10.1002/ar.1092170202

Nanci, A., Uchida, T., and Warshawsky, H. (1987c). The effects of vinblastine on the secretory ameloblasts: an ultrastructural, cytochemical, and immunocytochemical study in the rat incisor. *Anat. Rec.* 219, 113–126. doi: 10.1002/ar.1092190203

Nanci, A., and Smith, C. E. (1992). "Development and calcification of enamel," in *Calcification in Biological Systems*, ed E. Bonucci (Boca Raton, FL: CRC Press), 313–343.

Nanci, A., and Warshawsky, H. (1984). Characterization of putative secretory sites on ameloblasts of the rat incisor. *Am. J. Anat.* 171, 163–189. doi: 10.1002/aja.1001710204

Nanci, A., Zalzal, S., and Kan, F. W. (1993). High-resolution scanning electron microscopy of rat incisor ameloblasts. *Scanning Microsc.* 7, 165–174; discussion 174–175.

Nelson, N., Perzov, N., Cohen, A., Hagai, K., Padler, V., and Nelson, H. (2000). The cellular biology of proton-motive force generation by V-ATPases. *J. Exp. Biol.* 203(Pt 1), 89–95.

Ng, E. L., Wang, Y., and Tang, B. L. (2007). Rab22B's role in trans-Golgi network membrane dynamics. *Biochem. Biophys. Res. Commun.* 361, 751–757. doi: 10.1016/j.bbrc.2007.07.076

Nishikawa, S., and Sasaki, F. (1996). Phagocytotic processing of apoptotic bodies of transitional ameloblasts by MHC Class II-expressing macrophages in rat incisor. *J. Histochem. Cytochem.* 44, 1459–1467. doi: 10.1177/44.12.8985138

Nishio, C., Wazen, R., Kuroda, S., Moffatt, P., and Nanci, A. (2010). Expression pattern of odontogenic ameloblast-associated and amelotin during formation and regeneration of the junctional epithelium. *Eur. Cell. Mater.* 20, 393–402. doi: 10.22203/eCM.v020a32

Núñez, S. M., Chun Y. H., Ganss, B., Hu, Y., Richardson, A. S., Schmitz, J. E., Simmer, J. P. et al. (2016). Maturation stage enamel malformations in Amtn and Klk4 null mice. *Matrix Biol.* 52–54, 219–233. doi: 10.1016/j.matbio.2015.11.007

Ohkuma, S., Moriyama, Y., and Takano, T. (1982). Identification and characterization of a proton pump on lysosomes by fluorescein-isothiocyanate-dextran fluorescence. *Proc. Natl. Acad. Sci. U.S.A.* 79, 2758–2762. doi: 10.1073/pnas.79.9.2758

Ostermann, N., Gerhartz, B., Worpenberg, S., Trappe, J., and Eder, J. (2004). Crystal structure of an activation intermediate of cathepsin E. *J. Mol. Biol.* 342, 889–899. doi: 10.1016/j.jmb.2004.07.073

Ozawa, H., Yamada, M., Uchida, T., Yamamoto, T., and Takano, Y. (1983). "Fine structural and cytochemical studies of the Golgi-SER system of ameloblasts with special reference to its resorptive function," in *Mechanisms of Tooth Enamel Formation*, ed S. Suga (Tokyo: Quintessence), 17–48.

Pandey, K. N. (2009). Functional roles of short sequence motifs in the endocytosis of membrane receptors. *Front. Biosci.* 14, 5339–5360. doi: 10.2741/3599

Pearse, B. M. (1975). Coated vesicles from pig brain: purification and biochemical characterization. *J. Mol. Biol.* 97, 93–98. doi: 10.1016/S0022-2836(75)80024-6

Pearse, B. M. (1976). Clathrin: a unique protein associated with intracellular transfer of membrane by coated vesicles. *Proc. Natl. Acad. Sci. U.S.A.* 73, 1255–1259. doi: 10.1073/pnas.73.4.1255

Pearse, B. M., Smith, C. J., and Owen, D. J. (2000). Clathrin coat construction in endocytosis. *Curr. Opin. Struct. Biol.* 10, 220–228. doi: 10.1016/S0959-440X(00)00071-3

Pelkmans, L., Fava, E., Grabner, H., Hannus, M., Habermann, B., Krausz, E., et al. (2005). Genome-wide analysis of human kinases in clathrin- and caveolae/raft-mediated endocytosis. *Nature* 436, 78–86. doi: 10.1038/nature03571

Peralta, E. R., Martin, B. C., and Edinger, A. L. (2010). Differential effects of TBC1D15 and mammalian Vps39 on Rab7 activation state, lysosomal morphology, and growth factor dependence. *J. Biol. Chem.* 285, 16814–16821. doi: 10.1074/jbc.M110.111633

Peranen, J. (2011). Rab8 GTPase as a regulator of cell shape. *Cytoskeleton* 68, 527–539. doi: 10.1002/cm.20529

Peter, M., Chavrier, P., Nigg, E. A., and Zerial, M. (1992). Isoprenylation of rab proteins on structurally distinct cysteine motifs. *J. Cell Sci.* 102(Pt 4), 857–865.

Plemel, R. L., Lobingier, B. T., Brett, C. L., Angers, C. G., Nickerson, D. P., Paulsel, A., et al. (2011). Subunit organization and Rab interactions of Vps-C protein complexes that control endolysosomal membrane traffic. *Mol. Biol. Cell* 22, 1353–1363. doi: 10.1091/mbc.E10-03-0260

Plutner, H., Cox, A. D., Pind, S., Khosravi-Far, R., Bourne, J. R., Schwaninger, R., et al. (1991). Rab1b regulates vesicular transport between the endoplasmatic reticulum and successive Golgi compartments. *J. Cell Biol.* 115, 31–43. doi: 10.1083/jcb.115.1.31

Polo, S., and Di Fiore, P. P. (2006). Endocytosis conducts the cell signaling orchestra. *Cell* 124, 897–900. doi: 10.1016/j.cell.2006.02.025

Poteryaev, D., Datta, S., Ackema, K., Zerial, M., and Spang, A. (2010). Identification of the switch in early-to-late endosome transition. *Cell* 141, 497–508. doi: 10.1016/j.cell.2010.03.011

Progida, C., Cogli, L., Piro, F., De Luca, A., Bakke, O., and Bucci, C. (2010). Rab7b controls trafficking from endosomes to the TGN. *J. Cell Sci.* 123(Pt 9), 1480–1491. doi: 10.1242/jcs.051474

Proikas-Cezanne, T., Gaugel, A., Frickey, T., and Nordheim, A. (2006). Rab14 is part of the early endosomal clathrin-coated TGN microdomain. *FEBS Lett.* 580, 5241–5246. doi: 10.1016/j.febslet.2006.08.053

Racoosin, E. L., and Swanson, J. A. (1992). M-CSF-induced macropinocytosis increases solute endocytosis but not receptor-mediated endocytosis in mouse macrophages. *J. Cell Sci.* 102(Pt 4), 867–880.

Reith, E. J. (1967). The early stage of amelogenesis as observed in molar teeth of young rats. *J. Ultrastruct. Res.* 17, 503–526. doi: 10.1016/S0022-5320(67)80138-2

Reith, E. J., and Cotty, V. F. (1967). The absorptive activity of ameloblasts during the maturation of enamel. *Anat. Rec.* 157, 577–588. doi: 10.1002/ar.1091570404

Rink, J., Ghigo, E., Kalaidzidis, Y., and Zerial, M. (2005). Rab conversion as a mechanism of progression from early to late endosomes. *Cell* 122, 735–749. doi: 10.1016/j.cell.2005.06.043

Rodriguez-Gabin, A. G., Cammer, M., Almazan, G., Charron, M., and Larocca, J. N. (2001). Role of rRAB22b, an oligodendrocyte protein, in regulation of transport of vesicles from trans Golgi to endocytic compartments. *J. Neurosci. Res.* 66, 1149–1160. doi: 10.1002/jnr.1253

Rodriguez-Gabin, A. G., Yin, X., Si, Q., and Larocca, J. N. (2009). Transport of mannose-6-phosphate receptors from the trans-Golgi network to endosomes requires Rab31. *Exp. Cell Res.* 315, 2215–2230. doi: 10.1016/j.yexcr.2009.03.020

Roth, T. F., and Porter, K. R. (1964). Yolk protein uptake in the oocyte of the mosquito *Aedes aegypti* L. *J. Cell Biol.* 20, 313–332. doi: 10.1083/jcb.20.2.313

Rubino, M., Miaczynska, M., Lippe, R., and Zerial, M. (2000). Selective membrane recruitment of EEA1 suggests a role in directional transport of clathrin-coated vesicles to early endosomes. *J. Biol. Chem.* 275, 3745–3748. doi: 10.1074/jbc.275.6.3745

Rudenko, G., Bonten, E., d'Azzo, A., and Hol, W. G. (1995). Three-dimensional structure of the human 'protective protein': structure of the precursor form suggests a complex activation mechanism. *Structure* 3, 1249–1259. doi: 10.1016/S0969-2126(01)00260-X

Russell, M. R., Nickerson, D. P., and Odorizzi, G. (2006). Molecular mechanisms of late endosome morphology, identity and sorting. *Curr. Opin. Cell Biol.* 18, 422–428. doi: 10.1016/j.ceb.2006.06.002

Saheki, Y., and De Camilli, P. (2012). Synaptic vesicle endocytosis. *Cold Spring Harb. Perspect. Biol.* 4:a005645. doi: 10.1101/cshperspect.a005645

Salama, A. H., Bailey, R. L., Eisenmann, D. R., and Zaki, A. E. (1990a). Quantitative cytochemistry of lysosomal structures in rat incisor maturation enamel organ. *Arch. Oral Biol.* 35, 535–539. doi: 10.1016/0003-9969(90)90084-N

Salama, A. H., Zaki, A. E., and Eisenmann, D. R. (1989). Tubular lysosomes in ruffle-ended ameloblasts associated with enamel maturation in rat incisor. *J. Histochem. Cytochem.* 37, 801–811. doi: 10.1177/37.6.2542393

Salama, A. H., Zaki, A. E., and Eisenmann, D. R. (1990b). Tubular lysosomes in papillary cells during maturation of enamel in the rat. *Arch. Oral Biol.* 35, 119–126. doi: 10.1016/0003-9969(90)90173-8

Salminen-Mankonen, H. J., Morko, J., and Vuorio, E. (2007). Role of cathepsin K in normal joints and in the development of arthritis. *Curr. Drug Targets* 8, 315–323. doi: 10.2174/138945007779940188

Sasaki, T. (1983a). Ultrastructure and cytochemistry of the Golgi apparatus and related organelles of the secretory ameloblasts of the rat incisor. *Arch. Oral Biol.* 28, 895–905. doi: 10.1016/0003-9969(83)90084-5

Sasaki, T. (1983b). Ultrastructure and cytochemical studies of resorptive and digestive functions of secretory ameloblasts in kitten tooth germs. *Acta Anat.* 115, 361–375. doi: 10.1159/000145713

Sasaki, T. (1984a). Tracer, cytochemical, and freeze-fracture study on the mechanisms whereby secretory ameloblasts absorb exogenous proteins. *Acta Anat.* 118, 23–33. doi: 10.1159/000145817

Sasaki, T. (1984b). Morphology and function of maturation ameloblasts in kitten tooth germs. *J. Anat.* 138, 333–342.

Sasaki, T. (1984c). Endocytotic pathways at the ruffled borders of rat maturation ameloblasts. *Histochemistry* 80, 263–268. doi: 10.1007/BF00495775

Sasaki, T., and Higashi, S. (1983). A morphological, tracer and cytochemical study of the role of the papillary layer of the rat-incisor enamel organ during enamel maturation. *Arch. Oral Biol.* 28, 201–210. doi: 10.1016/0003-9969(83)90148-6

Sasaki, T., Higashi, S., Tachikawa, T., and Yoshiki, S. (1983a). Morphology and permeability of junctional complexes in maturing ameloblasts of rat incisors. *Acta Anat.* 116, 74–83. doi: 10.1159/000145728

Sasaki, T., Higashi, S., Tachikawa, T., and Yoshiki, S. (1983b). Thin-section, tracer, and freeze-fracture study of the smooth-ended maturation ameloblasts in rat incisors. *Acta Anat.* 117, 303–313. doi: 10.1159/000145802

Schmitz, J. E., Teepe, J. D., Hu, Y., Smith, C. E., Fajardo, R. J., and Chun, Y. H. P. (2014). Estimating mineral changes in enamel formation by ashing/BSE and microCT. *J. Dent. Res.* 93, 256–262. doi: 10.1177/0022034513520548

Schuck, S., Gerl, M. J., Ang, A., Manninen, A., Keller, P., Mellman, I., et al. (2007). Rab10 is involved in basolateral transport in polarized Madin-Darby canine kidney cells. *Traffic* 8, 47–60. doi: 10.1111/j.1600-0854.2006.00506.x

Seachrist, J. L., and Ferguson, S. S. (2003). Regulation of G protein-coupled receptor endocytosis and trafficking by Rab GTPases. *Life Sci.* 74, 225–235. doi: 10.1016/j.lfs.2003.09.009

Segev, N. (2001). Ypt/rab gtpases: regulators of protein trafficking. *Sci. STKE* 2001:re11. doi: 10.1126/stke.2001.100.re11

Shapiro, J. L., Wen, X., Okamoto, C. T., Wang, H. J., Lyngstadaas, S. P., Goldberg, M., et al. (2007). Cellular uptake of amelogenin, and its localization to CD63, and Lamp1-positive vesicles. *Cell. Mol. Life Sci.* 64, 244–256. doi: 10.1007/s00018-006-6429-4

Shen, F., and Seabra, M. C. (1996). Mechanism of digeranylgeranylation of Rab proteins. Formation of a complex between monogeranylgeranyl-Rab and Rab escort protein. *J. Biol. Chem.* 271, 3692–3698. doi: 10.1074/jbc.271.7.3692

Shewale, J. G., and Tang, J. (1984). Amino acid sequence of porcine spleen cathepsin D. *Proc. Natl. Acad. Sci. U.S.A.* 81, 3703–3707. doi: 10.1073/pnas.81.12.3703

Short, B., Preisinger, C., Schaletzky, J., Kopajtich, R., and Barr, F. A. (2002). The Rab6 GTPase regulates recruitment of the dynactin complex to Golgi membranes. *Curr. Biol.* 12, 1792–1795. doi: 10.1016/S0960-9822(02)01221-6

Simmelink, J. W. (1982). Mode of enamel matrix secretion. *J. Dent. Res.* 61, 1483–1488.

Simmer, J. P., Hu, Y., Lertlam, R., Yamakoshi, Y., and Hu, J. C. (2009). Hypomaturation enamel defects in Klk4 knockout/LacZ knockin mice. *J. Biol. Chem.* 284, 19110–19121. doi: 10.1074/jbc.M109.013623

Smith, C. E. (1979). Ameloblasts: secretory and resorptive functions. *J. Dent. Res.* 58, 695–707. doi: 10.1177/00220345790580022101 1

Smith, C. E. (1998). Cellular and chemical eventsduring enamel maturation. *Crit. Rev. Oral Biol. Med*. 9, 128–161. doi: 10.1177/10454411980090020101

Smith, C. E., Hu, Y., Hu, J. C., and Simmer, J. P. (2016). Ultrastructure of early amelogenesis in wild-type, Amelx$^{-/-}$, and Enam$^{-/-}$ mice: enamel ribbon initiation on dentin mineral and ribbon orientation by ameloblasts. *Mol. Genet. Genomic Med*. 4, 662–683. doi: 10.1002/mgg3.253

Smith, C. E., and Nanci, A. (1996). Protein dynamics of amelogenesis. *Anat. Rec.* 245, 186–207. doi: 10.1002/(SICI)1097-0185(199606)245:2<186::AID-AR7>3.0.CO;2-V

Smith, C. E., Pompura, J. R., Borenstein, S., Fazel, A., and Nanci, A. (1989). Degradation and loss of matrix proteins from developing enamel. *Anat. Rec.* 224, 292–316. doi: 10.1002/ar.1092240219

Smith, C. E., and Warshawsky, H. (1977). Quantitative analysis of cell tunrover in the enamel organ of the rat incisor. Evidence for ameloblast death immediately after enamel matrix secretion. *Anat Rec*. 187, 63–98. doi: 10.1002/ar.1091870106

Soldati, T., Rancano, C., Geissler, H., and Pfeffer, S. R. (1995). Rab7 and Rab9 are recruited onto late endosomes by biochemically distinguishable processes. *J. Biol. Chem.* 270, 25541–25548. doi: 10.1074/jbc.270.43.25541

Somogyi-Ganss, E., Nakayama, Y., Iwasaki, K., Nakano, Y., Stolf, D., McKee, M. D., et al. (2012). Comparative temporospatial expression profiling of murine amelotin protein during amelogenesis. *Cells Tissues Organs* 195, 535–549. doi: 10.1159/000329255

Somsel Rodman, J., and Wandinger-Ness, A. (2000). Rab GTPases coordinate endocytosis. *J. Cell Sci.* 113(Pt 2), 183–92.

Sorkin, A. (2004). Cargo recognition during clathrin-mediated endocytosis: a team effort. *Curr. Opin. Cell Biol.* 16, 392–399. doi: 10.1016/j.ceb.2004.06.001

Sun-Wada, G. H., Wada, Y., and Futai, M. (2004). Diverse and essential roles of mammalian vacuolar-type proton pump ATPase: toward the physiological understanding of inside acidic compartments. *Biochim. Biophys. Acta*. 1658, 106–114. doi: 10.1016/j.bbabio.2004.04.013

Surmacz, L., Wiejak, J., and Wyroba, E. (2006). Cloning of two genes encoding Rab7 in Paramecium. *Acta Biochim. Pol*. 53, 149–156.

Swanson, J. A., and Watts, C. (1995). Macropinocytosis. *Trends Cell Biol*. 5, 424–428. doi: 10.1016/S0962-8924(00)89101-1

Tagliabracci, V. S., Engel, J. L., Wen, J., Wiley, S. E., Worby, C. A., Kinch, L. N., et al. (2012). Secreted kinase phosphorylates extracellular proteins that regulate biomineralization. *Science* 336, 1150–1153. doi: 10.1126/science.1217817

Takano, Y., and Ozawa, H. (1980). Ultrastructural and cytochemical observations on the alternating morphologic changes of the ameloblasts at the stage of enamel maturation. *Arch. Histol. Jpn.* 43, 385–399. doi: 10.1679/aohc1950.43.385

Tisdale, E. J., Bourne, J. R., Khosravi-Far, R., Der, C. J., and Balch, W. E. (1992). GTP-binding mutants of rab1 and rab2 are potent inhibitors of vesicular transport from the endoplasmic reticulum to the Golgi complex. *J. Cell Biol.* 119, 749–761. doi: 10.1083/jcb.119.4.749

Tisdale, E. J., Kelly, C., and Artalejo, C. R. (2004). Glyceraldehyde-3-phosphate dehydrogenase interacts with Rab2 and plays an essential role in endoplasmic reticulum to Golgi transport exclusive of its glycolytic activity. *J. Biol. Chem.* 279, 54046–54052. doi: 10.1074/jbc.M409472200

Turk, V., Stoka, V., Vasiljeva, O., Renko, M., Sun, T., Turk, B., et al. (2012). Cysteine cathepsins: from structure, function and regulation to new frontiers. *Biochim. Biophys. Acta* 1824, 68–88. doi: 10.1016/j.bbapap.2011.10.002

Tye, C. E., Lorenz, R. L., and Bartlett, J. D. (2009). Lysosomal protease expression in mature enamel. *Cells Tissues Organs* 189, 111–114. doi: 10.1159/000151431

Uchida, T., Murakami, C., Wakida, K., Dohi, N., Iwai, Y., Simmer, J. P., et al. (1998). Sheath proteins: synthesis, secretion, degradation and fate in forming enamel. *Eur. J. Oral Sci*. 106(Suppl. 1), 308–314. doi: 10.1111/j.1600-0722.1998.tb02191.x

Uchida, T., Tanabe, T., and Fukae, M. (1989). Immunocytochemical localization of amelogenins in the deciduous tooth germs of the human fetus. *Arch. Histol. Cytol.* 52, 543–552. doi: 10.1679/aohc.52.543

Uchida, T., Tanabe, T., Fukae, M., and Shimizu, M. (1991). Immunocytochemical and immunochemical detection of a 32 kDa nonamelogenin and related proteins in porcine tooth germs. *Arch. Histol. Cytol.* 54, 527–538. doi: 10.1679/aohc.54.527

Uchida, T., and Warshawsky, H. (1992). Zinc iodine-osmium tetroxide impregnation of the "tubulo-vesicular system" in Tomes' Process of the rat incisor ameloblast. *Anat. Rec.* 232, 325–339. doi: 10.1002/ar.1092320302

van der Sluijs, P., Hull, M., Webster, P., Male, P., Goud, B., and Mellman, I. (1992). The small GTP-binding protein rab4 controls an early sorting event on the endocytic pathway. *Cell* 70, 729–740. doi: 10.1016/0092-8674(92)90307-X

Villasenor, R., Kalaidzidis, Y., and Zerial, M. (2016). Signal processing by the endosomal system. *Curr. Opin. Cell Biol.* 39, 53–60. doi: 10.1016/j.ceb.2016.02.002

Wald, T., Spoutil, F., Osickova, A., Prochazkova, M., Benada, O., Kasparek, P., et al. (2017). Intrinsically disordered proteins drive enamel formation via an evolutionarily conserved self-assembly motif. *Proc. Natl. Acad. Sci. U.S.A.* 114, E1641–E1650. doi: 10.1073/pnas.1615334114

Wang, S. K., Samann, A. C., Hu, J. C., and Simmer, J. P. (2013). FAM20C functions intracellularly within both ameloblasts and odontoblasts *in vivo*. *J. Bone Miner. Res.* 28, 2508–2511. doi: 10.1002/jbmr.1990

Warshawsky, H. (1968). The fine structure of secretory ameloblasts in rat incisors. *Anat. Rec.* 161, 211–229. doi: 10.1002/ar.1091610207

Weinstock, A., and Leblond, C. P. (1971). Elaboration of the matrix glycoproteins of enamel by the secretory ameloblasts of the rat incisor as revealed by radioautography after galactose-H3 injection. *J. Cell Biol.* 51, 26–51. doi: 10.1083/jcb.51.1.26

Xu, H., and Ren, D. (2015). Lysosomal physiology. *Annu. Rev. Physiol*. 77, 57–80. doi: 10.1146/annurev-physiol-021014-071649

Yamashiro, D. J., and Maxfield, F. R. (1987). Acidification of morphologically distinct endosomes in mutant and wild-type Chinese hamster ovary cells. *J. Cell Biol.* 105(6 Pt 1), 2723–2733. doi: 10.1083/jcb.105.6.2723

Yin, K., Lin, W., Guo, J., Sugiyama, T., Snead, M. L., Hacia, J. G., et al. (2017). MiR-153 regulates amelogenesis by targeting endocytotic and endosomal/lososomal pathway-novel insight into the origins of enamel pathologies. *Sci. Rep*. 7:44118. doi: 10.1038/srep44118

Zahraoui, A., Touchot, N., Chardin, P., and Tavitian, A. (1989). The human Rab genes encode a family of GTP-binding proteins related to yeast YPT1 and SEC4 products involved in secretion. *J. Biol. Chem*. 264, 12394–12401.

Zerial, M., and McBride, H. (2001). Rab proteins as membrane organizers. *Nat. Rev. Mol. Cell Biol*. 2, 107–117. doi: 10.1038/35052055

Conflict of Interest Statement: The authors declare that the research was conducted in the absence of any commercial or financial relationships that could be construed as a potential conflict of interest.

Copyright © 2017 Pham, Smith, Hu, Hu, Simmer and Chun. This is an open-access article distributed under the terms of the Creative Commons Attribution License (CC BY). The use, distribution or reproduction in other forums is permitted, provided the original author(s) or licensor are credited and that the original publication in this journal is cited, in accordance with accepted academic practice. No use, distribution or reproduction is permitted which does not comply with these terms.

frontiers in Physiology

PERSPECTIVE
published: 24 May 2017
doi: 10.3389/fphys.2017.00326

Claudin Loss-of-Function Disrupts Tight Junctions and Impairs Amelogenesis

Claire Bardet[1], Sandy Ribes[1], Yong Wu[1,2], Mamadou Tidiane Diallo[1], Benjamin Salmon[1,3], Tilman Breiderhoff[4], Pascal Houillier[5], Dominik Müller[4] and Catherine Chaussain[1,3]*

[1] Laboratory Orofacial Pathologies, Imaging and Biotherapies, Dental School, Paris Descartes University, Sorbonne Paris Cité, Paris, France, [2] Shanghai Key Laboratory of Stomatology, Department of Oral and Cranio-maxillofacial Science, Ninth People's Hospital, Shanghai Jiao Tong University School of Medicine, Shanghai, China, [3] Department of Odontology, AP-HP, and Reference Center for Rare Dieases of the Metabolism of Calcium and Phosphorus, Nord Val de Seine Hospital (Bretonneau), Paris, France, [4] Department of Pediatric Nephrology, Charité University School of Medicine, Berlin, Germany, [5] Cordeliers Research Center, Centre National de la Recherche Scientifique, Institut National de la Santé et de la Recherche Médicale UMRS 1138, Paris-Diderot, Pierre et Marie Curie and Paris Descartes Universities, ERL, Paris, France

Claudins are a family of proteins that forms paracellular barriers and pores determining tight junctions (TJ) permeability. Claudin-16 and -19 are pore forming TJ proteins allowing calcium and magnesium reabsorption in the thick ascending limb of Henle's loop (TAL). Loss-of-function mutations in the encoding genes, initially identified to cause Familial Hypomagnesemia with Hypercalciuria and Nephrocalcinosis (FHHNC), were recently shown to be also involved in *Amelogenesis Imperfecta* (AI). In addition, both claudins were expressed in the murine tooth germ and *Claudin-16* knockout (KO) mice displayed abnormal enamel formation. Claudin-3, an ubiquitous claudin expressed in epithelia including kidney, acts as a barrier-forming tight junction protein. We determined that, similarly to claudin-16 and claudin-19, claudin-3 was expressed in the tooth germ, more precisely in the TJ located at the apical end of secretory ameloblasts. The observation of *Claudin-3* KO teeth revealed enamel defects associated to impaired TJ structure at the secretory ends of ameloblasts and accumulation of matrix proteins in the forming enamel. Thus, claudin-3 protein loss-of-function disturbs amelogenesis similarly to claudin-16 loss-of-function, highlighting the importance of claudin proteins for the TJ structure. These findings unravel that loss-of-function of either pore or barrier-forming TJ proteins leads to enamel defects. Hence, the major structural function of claudin proteins appears essential for amelogenesis.

Keywords: *Amelogenesis Imperfecta*, enamel, barrier-forming tight junction protein, pore-forming tight junction protein, claudins

OPEN ACCESS

Edited by:
Alexandre Rezende Vieira, University of Pittsburgh, United States

Reviewed by:
Yuqiao Zhou, University of Pittsburgh, United States
Claudio Cantù, University of Zurich, Switzerland
Jan Hu, University of Michigan, United States

****Correspondence:***
Claire Bardet
claire.bardet@parisdescartes.fr

Specialty section:
This article was submitted to Craniofacial Biology and Dental Research, a section of the journal Frontiers in Physiology

Received: *27 March 2017*
Accepted: *05 May 2017*
Published: *24 May 2017*

Citation:
Bardet C, Ribes S, Wu Y, Diallo MT, Salmon B, Breiderhoff T, Houillier P, Müller D and Chaussain C (2017) Claudin Loss-of-Function Disrupts Tight Junctions and Impairs Amelogenesis. Front. Physiol. 8:326. doi: 10.3389/fphys.2017.00326

Epithelial cells are attached to each other at their lateral membranes by a complex of intercellular junctions (Farquhar and Palade, 1963). The most apical complex of the intercellular junctions is the *zona occludens* also named tight junctions (TJ). TJ represent the principal component of the paracellular diffusion barrier by determining epithelial permeability of small molecules and water, and participate in the control of the diffusion of membrane components between the basolateral and apical regions. Abrogation of such a barrier function in epithelia that interfaces with the environment is associated with a variety of gastrointestinal (Barmeyer et al., 2017), renal (Hou, 2014), and cutaneous disorders (Basler and Brandner, 2017). TJ are composed of several

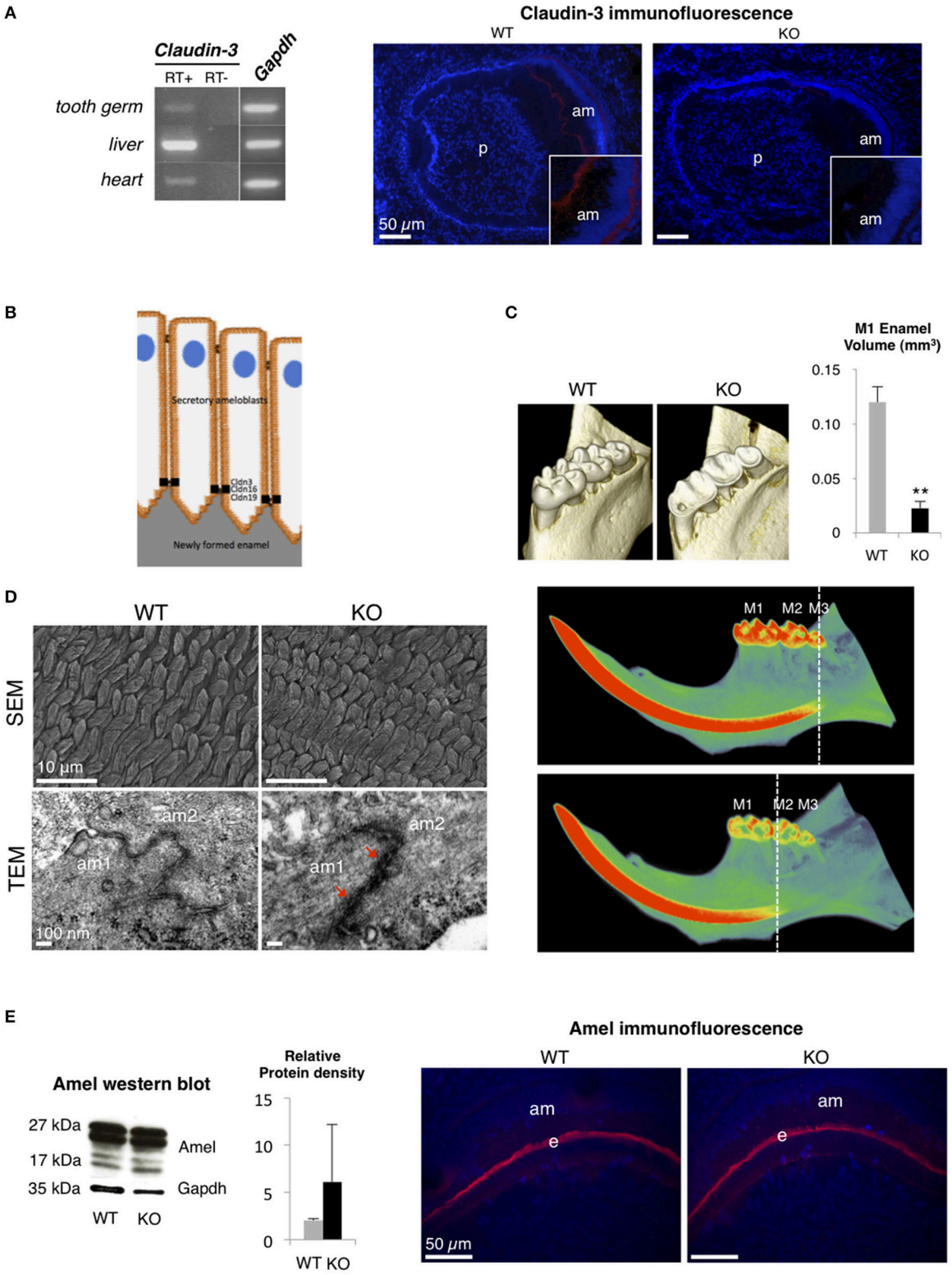

FIGURE 1 | Dental phenotype of *Claudin-3* KO mice. (A) *Claudin-3* mRNA expression was analyzed in mouse tissues by RT-PCR using forward primer 5′-ATG TGG CGC GTT TCG-3′ and reverse primer 5′-GCG AGT CGT ACA TTT TGC-3′ for *Claudin-3* (124 bp), and forward primer 5′-TGT GTC CGT CGT GGA TCT GA-3′ and reverse primer 5′-TTG CTG TTG AAG TCG CAG GAG-3′ for *Gapdh* (150 bp). A representative gel image of the selected tissues showed *Claudin-3* expression in

(Continued)

FIGURE 1 | Continued
mouse in post-natal day 3 tooth germ, liver and heart. Identification of claudin-3 in the continuously growing incisor was performed by immunofluorescence using claudin-3 antibody (#34-1700, Invitrogen) at 1/100 dilution and a Goat anti-Rabbit antibody (#R-6394, Invitrogen). Claudin-3 was localized at the distal end of secretory ameloblasts (am). Protein expression was also observed at the basal end of the cells ($n = 3$ per group). (p) pulp. **(B)** Recapitulative schema of claudin TJ proteins expression at the apical end of secretory ameloblasts. Claudin-3, -16, and -19 were shown to be expressed at TJ level of ameloblast secretory ends during enamel formation in the mouse. **(C)** 3D volume rendering from Micro-CT data showed severe enamel loss on lingual molar cusps in *Claudin-3* KO mice. Quantitative analysis confirmed a significant lower enamel volume in *Claudin-3* KO mice when compared to WT (0.022 vs. 0.120 mm^3 respectively) ($n = 8$ per group). In WT mice, incisor mineralization is observed under the third molar (M3) whereas in *Claudin-3* KO mice it is detected under the second molar (M2). $^{**}P < 0.00001$ (M1) first molar. **(D)** Scanning electron microscopy (SEM) analysis showed enamel prisms normally constituted in *Claudin-3* KO incisor when compared to WT ($n = 3$ per group). Transmission electron microscopy (TEM) analysis of WT tooth germs showed TJ as adjoining ameloblast membranes converging to form a thin intermediate line at the distal end of the cells. In contrast, the TJ structure was altered in *Claudin-3* KO tooth germs, with thicker and packed structures (red arrows). (am) ameloblast. **(E)** Enamel matrix protein expression by secretory ameloblasts of *Claudin-3* KO mice ($n = 3$ per group). Western blot analysis of the protein extracts of the soft part of the growing incisor showed slightly higher levels of amelogenin (amel). No difference was observed by immunostaining regarding amelogenin expression in the forming enamel matrix (e) between *Claudin-3* KO and WT incisors.

transmembrane and membrane-associated proteins including the claudin proteins. Claudins form either paracellular barrier or pores that determine TJ properties. They interact with each other and with additional membrane and non-membrane proteins, such as the intracellular *zonula occludens* ZO-1 and ZO-2 and other PDZ domain-containing proteins. Claudins are considered as core components of TJ strands and determine epithelial permeability of small molecules and water (Gunzel and Yu, 2013). Only few claudins are unequivocally qualified as pore-forming proteins, including claudin-2, -10b, and -15 as cation pores and claudin-10a and -17 as anion pores. Other claudins have been reported to form pores only when specifically interacting with another claudin (Gunzel and Yu, 2013). Such is the case of claudin-16 and claudin-19, which form a cation-selective TJ complex in the thick ascending limb of Henle's loop (Hou et al., 2008).

Mineral transport involves the epithelial permeability which is tightly related to the type and properties of TJ. During amelogenesis, secretory ameloblast TJ are responsible for restricted paracellular access to the enamel compartment. The paracellular permeability (tightness) of the ameloblast layer depends on the composition of TJ relying on claudin proteins. Hence, a combination of different claudins may either allow some paracellular ion passage or restrict this passage (Denker and Sabath, 2011; Bronckers, 2017). To date, 11 claudins have been identified in the tooth germ at various developmental stages (Ohazama and Sharpe, 2007; Bardet et al., 2016; Yamaguti et al., 2017). We recently associated the abrogation of a pore function and a dental disorder. Indeed, we demonstrated that loss-of-function mutations in *Claudin-16 and -19* (*CLDN16* and *19*) genes, initially identified to cause Familial Hypomagnesemia with Hypercalciuria and Nephrocalcinosis (FHHNC), also resulted in *Amelogenesis Imperfecta (AI)* (Bardet et al., 2016; Yamaguti et al., 2017). At the time of this discovery, it was acknowledged that claudin-16 and -19 were mainly expressed in the thick ascending limb of Henle loop in the kidney, suggesting that the *AI* diagnosed in patients with FHHNC was a consequence of the disturbed mineral homeostasis. However, we were able to show that claudin-16 and claudin-19 were also expressed in the ameloblast TJ, indicating that the *AI* diagnosed in patients with FHHNC was an intrinsic consequence of the *Claudin* mutation. Furthermore, studying *Claudin-16* Knockout (KO) mice, we showed that the structure of ameloblast TJ was altered.

Claudin-3, which is expressed in epithelia of a wide variety of organs such as intestine, kidney, liver, skin, and lung, acts as a barrier-forming TJ protein (Milatz et al., 2010; Gunzel and Yu, 2013). To analyze the substantial role of a barrier-forming TJ protein in amelogenesis, we explored the dental phenotype of *Claudin-3* KO mice using the methods previously described in Bardet et al. (2016) (ethical agreement D92-049-01). We first determined that, similar to claudin-16 and claudin-19 (Bardet et al., 2016; Yamaguti et al., 2017), claudin-3 was expressed in the tooth germ and located in the TJ at the apical end of secretory ameloblasts (**Figures 1A,B**). Dental examination of adult *Claudin-3* KO mice revealed a lower enamel volume in molars when compared to WT mice and a mineralization delay in the continuously growing incisor (**Figure 1C**). At the structural level, when examining the forming enamel in the intrabony part of the incisor, we observed normally formed prisms by scanning electron microscopy in *Claudin-3* KO mice (**Figure 1D**). However, transmission electron microscopy (TEM) analysis of tooth germs showed altered TJ structure in *Claudin-3* KO ameloblasts displaying thicker and packed structures compared to the thin intermediate line observed in the WT mice (**Figure 1D**). At the molecular level, enamel matrix formation was disturbed by claudin-3 deficiency, manifesting by an accumulation of enamel proteins further confirmed by Western blot analysis of the protein extracts of the soft part of the growing incisor (**Figure 1E**). Thus, claudin-3 protein loss-of-function disturbs amelogenesis similar to claudin-16 loss-of-function, where accumulation of enamel matrix protein led to *Amelogenesis Imperfecta* (Bardet et al., 2016).

During amelogenesis, TJ are composed of pore- and barrier-forming claudin proteins. Deficiency of both types of claudin proteins in murine models as well as in human disorders such as FHHNC led to enamel defects. To date, no human disease was associated with *CLDN3* mutation. Interestingly, the hemizygous contiguous gene microdeletion at 7q11.23 in Williams-Beuren syndrome (WBS; OMIM 194050) includes the *CLDN3* gene (Dutra et al., 2011) and several dental manifestations have been reported in patients with WBS, including hypodontia, abnormal tooth shape (microdontia), but also hypoplastic enamel defects and higher caries susceptibility (Hertzberg et al., 1994; Axelsson et al., 2003).

Our observations highlight the importance of claudin proteins for TJ structure. Indeed, either barrier or a pore forming claudins

link to adaptor proteins such as ZO proteins and other PDZ protein family of the cytosolic TJ plaque. This interaction allows direct or indirect bonding to actin, anchoring the TJ within the underlying cytoskeleton. This scaffold facilitates the assembly of highly ordered structures, such as junctional complexes, regulating epithelial cell polarity, proliferation and differentiation (Sluysmans et al., 2017). This is consistent with our data showing a disturbed actin filament network at apical end of ameloblasts and a more diffused ZO-1 labeling in *Claudin-16* KO mice (Bardet et al., 2016). Claudins are necessary for the TJ assembly process and their loss impairs TJ organization in ameloblasts and consequently disturbs enamel formation.

Overall, although TJ insure suitable microenvironments for enamel deposition and concomitant early maturation by determining the paracellular permeability and selectivity of solutes, the ion transport is tightly regulated during amelogenesis, involving barrier or channel properties of a certain claudin. Impaired TJ structure resulting from claudin loss-of function disturbs enamel formation. Hence, the major structural function of claudin proteins appears essential for amelogenesis.

AUTHOR CONTRIBUTIONS

CB and CC wrote the manuscript with contributions from all authors. CB, SR, YW, and CC contributed to the design of the experiments. CB, SR, YW, MD, BS, TB, PH, DM, and CC performed and analyzed experiments. CB and CC supervised the project. All authors reviewed and approved the final version of the manuscript.

FUNDING

This work was supported by grants from Paris Descartes University, from Foundation pour la Recherche Médicale for EA2496 and Plateforme d'Imagerie du Vivant Paris Descartes (FRM DGE20111123012). DM was supported by a CRG grant of the Berlin Institute of Health. YW (post-doctoral position) was supported by the French Chinese Foundation for Science and Applications (FFSCA), Académie des Sciences, and the China Scholars Council (CSC).

ACKNOWLEDGMENTS

Authors thank Stephane Le Goff (EA 4462, Paris Descartes University, France) for his help producing SEM data, and Jean-Marc Massé and Alain Schmitt (Cochin Institute, INSERM U1016, CNRS UMR8104, Paris Descartes University, France) for their help producing TEM data.

REFERENCES

Axelsson, S., Bjornland, T., Kjaer, I., Heiberg, A., and Storhaug, K. (2003). Dental characteristics in Williams syndrome: a clinical and radiographic evaluation. *Acta Odontol. Scand.* 61, 129–136. doi: 10.1080/00016350310001451

Bardet, C., Courson, F., Wu, Y., Khaddam, M., Salmon, B., Ribes, S., et al. (2016). Claudin-16 deficiency impairs tight junction function in ameloblasts, leading to abnormal enamel formation. *J. Bone Miner. Res.* 31, 498–513. doi: 10.1002/jbmr.2726

Barmeyer, C., Fromm, M., and Schulzke, J. D. (2017). Active and passive involvement of claudins in the pathophysiology of intestinal inflammatory diseases. *Pflugers Arch.* 469, 15–26. doi: 10.1007/s00424-016-1914-6

Basler, K., and Brandner, J. M. (2017). Tight junctions in skin inflammation. *Pflugers Arch.* 469, 3–14. doi: 10.1007/s00424-016-1903-9

Bronckers, A. L. (2017). Ion transport by Ameloblasts during Amelogenesis. *J. Dent. Res.* 96, 243–253. doi: 10.1177/0022034516681768

Denker, B. M., and Sabath, E. (2011). The biology of epithelial cell tight junctions in the kidney. *J. Am. Soc. Nephrol.* 22, 622–625. doi: 10.1681/ASN.2010090922

Dutra, R. L., Pieri Pde, C., Teixeira, A. C., Honjo, R. S., Bertola, D. R., and Kim, C. A. (2011). Detection of deletions at 7q11.23 in Williams-Beuren syndrome by polymorphic markers. *Clinics* 66, 959–964. doi: 10.1590/S1807-59322011000600007

Farquhar, M. G., and Palade, G. E. (1963). Junctional complexes in various epithelia. *J. Cell Biol.* 17, 375–412. doi: 10.1083/jcb.17.2.375

Gunzel, D., and Yu, A. S. (2013). Claudins and the modulation of tight junction permeability. *Physiol. Rev.* 93, 525–569. doi: 10.1152/physrev.00019.2012

Hertzberg, J., Nakisbendi, L., Needleman, H. L., and Pober, B. (1994). Williams syndrome–oral presentation of 45 cases. *Pediatr. Dent.* 16, 262–267.

Hou, J. (2014). The kidney tight junction (Review). *Int. J. Mol. Med.* 34, 1451–1457. doi: 10.3892/ijmm.2014.1955

Hou, J., Renigunta, A., Konrad, M., Gomes, A. S., Schneeberger, E. E., Paul, D. L., et al. (2008). Claudin-16 and claudin-19 interact and form a cation-selective tight junction complex. *J. Clin. Invest.* 118, 619–628. doi: 10.1172/jci33970

Milatz, S., Krug, S. M., Rosenthal, R., Gunzel, D., Muller, D., Schulzke, J. D., et al. (2010). Claudin-3 acts as a sealing component of the tight junction for ions of either charge and uncharged solutes. *Biochim. Biophys. Acta* 1798, 2048–2057. doi: 10.1016/j.bbamem.2010.07.014

Ohazama, A., and Sharpe, P. T. (2007). Expression of claudins in murine tooth development. *Dev. Dyn.* 236, 290–294. doi: 10.1002/dvdy.21001

Sluysmans, S., Vasileva, E., Spadaro, D., Shah, J., Rouaud, F., and Citi, S. (2017). The role of apical cell-cell junctions and associated cytoskeleton in mechanotransduction. *Biol. Cell.* 109, 139–161. doi: 10.1111/boc.201600075

Yamaguti, P. M., Neves, F. A., Hotton, D., Bardet, C., De La Dure-Molla, M., Castro, L. C., et al. (2017). Amelogenesis imperfecta in familial hypomagnesaemia and hypercalciuria with nephrocalcinosis caused by CLDN19 gene mutations. *J. Med. Genet.* 54, 26–37. doi: 10.1136/jmedgenet-2016-103956

Conflict of Interest Statement: The authors declare that the research was conducted in the absence of any commercial or financial relationships that could be construed as a potential conflict of interest.

The reviewer YZ and handling Editor declared their shared affiliation, and the handling Editor states that the process nevertheless met the standards of a fair and objective review.

Copyright © 2017 Bardet, Ribes, Wu, Diallo, Salmon, Breiderhoff, Houillier, Müller and Chaussain. This is an open-access article distributed under the terms of the Creative Commons Attribution License (CC BY). The use, distribution or reproduction in other forums is permitted, provided the original author(s) or licensor are credited and that the original publication in this journal is cited, in accordance with accepted academic practice. No use, distribution or reproduction is permitted which does not comply with these terms.

frontiers in Physiology

ORIGINAL RESEARCH
published: 23 May 2017
doi: 10.3389/fphys.2017.00336

Multiple Calcium Export Exchangers and Pumps Are a Prominent Feature of Enamel Organ Cells

*Sarah Y. T. Robertson[1], Xin Wen[1], Kaifeng Yin[1], Junjun Chen[1,2,3], Charles E. Smith[4] and Michael L. Paine[1]**

[1] Center for Craniofacial Molecular Biology, Herman Ostrow School of Dentistry, University of Southern California, Los Angeles, CA, United States, [2] Department of Oral Medicine, Shanghai Ninth People's Hospital, Shanghai Jiao Tong University School of Medicine, Shanghai, China, [3] Shanghai Key Laboratory of Tumor Microenvironment and Inflammation, Department of Biochemistry and Molecular Cell Biology, Shanghai Jiao Tong University School of Medicine, Shanghai, China, [4] Department of Anatomy and Cell Biology, Faculty of Medicine, McGill University, Montreal, QC, Canada

OPEN ACCESS

Edited by:
Steven Joseph Brookes, Leeds Dental Institute, United Kingdom

Reviewed by:
Petros Papagerakis, University of Michigan, United States
Felicitas B. Bidlack, Forsyth Institute, United States
Javier Catón, CEU San Pablo University, Spain

***Correspondence:**
Michael L. Paine
paine@usc.edu

Specialty section:
This article was submitted to Craniofacial Biology and Dental Research, a section of the journal Frontiers in Physiology

Received: *13 March 2017*
Accepted: *08 May 2017*
Published: *23 May 2017*

Citation:
Robertson SYT, Wen X, Yin K, Chen J, Smith CE and Paine ML (2017) Multiple Calcium Export Exchangers and Pumps Are a Prominent Feature of Enamel Organ Cells. Front. Physiol. 8:336. doi: 10.3389/fphys.2017.00336

Calcium export is a key function for the enamel organ during all stages of amelogenesis. Expression of a number of ATPase calcium transporting, plasma membrane genes (ATP2B1-4/PMCA1-4), solute carrier SLC8A genes (sodium/calcium exchanger or NCX1-3), and SLC24A gene family members (sodium/potassium/calcium exchanger or NCKX1-6) have been investigated in the developing enamel organ in earlier studies. This paper reviews the calcium export pathways that have been described and adds novel insights to the spatiotemporal expression patterns of PMCA1, PMCA4, and NCKX3 during amelogenesis. New data are presented to show the mRNA expression profiles for the four Atp2b1-4 gene family members (PMCA1-4) in secretory-stage and maturation-stage rat enamel organs. These data are compared to expression profiles for all Slc8a and Slc24a gene family members. PMCA1, PMCA4, and NCKX3 immunolocalization data is also presented. Gene expression profiles quantitated by real time PCR show that: (1) PMCA1, 3, and 4, and NCKX3 are most highly expressed during secretory-stage amelogenesis; (2) NCX1 and 3, and NCKX6 are expressed during secretory and maturation stages; (3) NCKX4 is most highly expressed during maturation-stage amelogenesis; and (4) expression levels of PMCA2, NCX2, NCKX1, NCKX2, and NCKX5 are negligible throughout amelogenesis. In the enamel organ PMCA1 localizes to the basolateral membrane of both secretory and maturation ameloblasts; PMCA4 expression is seen in the basolateral membrane of secretory and maturation ameloblasts, and also cells of the stratum intermedium and papillary layer; while NCKX3 expression is limited to Tomes' processes, and the apical membrane of maturation-stage ameloblasts. These new findings are discussed in the perspective of data already present in the literature, and highlight the multiplicity of calcium export systems in the enamel organ needed to regulate biomineralization.

Keywords: amelogenesis, biomineralization, calcium channels, calcium exchangers, calcium pumps

INTRODUCTION

Enamel is the hardest and most calcified tissue in mammals, and understanding enamel formation is crucial for developing strategies to repair or regenerate it (Smith, 1998; Hubbard, 2000; Lacruz et al., 2013). Amelogenesis, the process of enamel development, can be divided into the secretory and maturation stages with a brief pre-secretory stage before the secretory stage and a transition stage between the secretory and maturation stages. Epithelial-derived enamel-forming cells (ameloblasts) differentiate from the inner enamel epithelium (IEE) during the pre-secretory stage (Orrenius et al., 2015). These amelobasts are highly polarized with an apical end that faces the enamel area and a basal end that faces the blood circulation. During the secretory stage, ameloblasts migrate away from the dentin while synthesizing and secreting enamel matrix proteins (EMPs) such as amelogenin, ameloblastin, and enamelin into the enamel area from Tomes' processes at their apical ends. These EMPs serve as a scaffold for the orientation and elongation of enamel hydroxyapatite (Hap) crystals (Smith, 1998). Each enamel rod follows a single ameloblast's Tomes' process with the interrod following the border of the cell, giving enamel its characteristic rod-interrod pattern (Skobe, 2006; Hu et al., 2007). There is a massive shift in gene expression during the transition stage, when approximately 25% of ameloblasts undergo apoptosis, after which another 25% undergo apoptosis throughout the following stages of amelogenesis (Tsuchiya et al., 2009). During the maturation stage, the ameloblasts undergo cyclical changes between ruffle-ended (RA) and smooth-ended (SA) morphology (Smith, 1998; Lacruz et al., 2013). Maturation-stage ameloblasts become specialized for ion transport and resorptive activities, which includes the secretion of the protease KLK4 to aid in the degradation of EMPs that are subsequently removed through endocytosis (Smith, 1998; Lacruz et al., 2012a, 2013). The continuously growing incisor of mice makes it a good model for studying the chronological progression of amelogenesis. While general concepts of ion transport throughout amelogenesis have been well-studied and discussed elsewhere (Arquitt et al., 2002; Paine et al., 2007; Lyaruu et al., 2008; Bronckers et al., 2010, 2015; Josephsen et al., 2010; Yin et al., 2015), and in particular the transcellular calcium ion (Ca^{2+}) transport (reviewed in Nurbaeva et al., 2015b), in this paper we focus primarily on Ca^{2+} export.

Overview—Calcium Transport

In general high intracellular concentrations of calcium (Ca^{2+}) catalyze cell death signaling cascades, so cells maintain a gradient of $\sim 10^{-3}$ M Ca^{2+} concentration outside the cell, in the mitochondria, and in the endoplasmic reticulum (ER) where Ca^{2+} is stored; while in the cytoplasm, the concentration is $\sim 10^{-7}$ M (Brini and Carafoli, 2011). The plasma membrane contains a variety of Ca^{2+} channels that transiently open to allow Ca^{2+} influx in response to plasma membrane voltage changes, ligand-receptor interaction, or emptying Ca^{2+} stores of the ER and mitochondria (Brini and Carafoli, 2011). Calcium is removed from the cytoplasm through a number of mechanisms including the SERCA pump that replenishes ER stores, the mitochondrial Ca^{2+} uniporter, that replenishes mitochondrial stores, the plasma membrane low-affinity high capacity Na^+/Ca^{2+} exchanger proteins (NCX), the Na^+/Ca^{2+} K^+ exchanger proteins (NCKX), and the high-affinity low-capacity plasma membrane Ca^{2+}-ATPase (PMCA) pump proteins (Berridge et al., 2003; Brini and Carafoli, 2011; Hu et al., 2012; Bronckers et al., 2015).

Calcium (Ca^{2+}) transport is crucial to understand the process of amelogenesis because not only is unbound Ca^{2+} a major component of hydroxyapatite (Hap), Ca^{2+} can also act as a major signaling molecule capable of regulating cell processes in eukaryotic cells such as cell division, cell attachment, motility, survival, differentiation as well as gene expression (Hubbard, 1996; Blair et al., 2011).

Calcium Extrusion

The SLC8A (sodium/calcium exchangers or NCX), SLC24A (potassium-dependent sodium/calcium exchangers or NCKX), and ATP2B (ATPase plasma membrane Ca^{2+} transporting pumps or PMCA pumps) gene families of Ca^{2+} transporters mediate Ca^{2+} extrusion in most cell types (Brini and Carafoli, 2011), and proteins from all three of these families have been reported in enamel organ cells (Sasaki and Garant, 1986c; Borke et al., 1995; Zaki et al., 1996; Okumura et al., 2010; Hu et al., 2012; Wang et al., 2014). The SLC8A gene family has 3 members (NCX1-3) and all have a generally accepted stoichiometry of the extrusion of 1 Ca^{2+} in exchange for the intrusion of 3 Na^+ (Brini and Carafoli, 2011), while the SLC24A gene family has 5 members (NCKX1-5) and extrudes 1 Ca^{2+} and 1 K^+ in exchange for 4 Na^+, typically against the Ca^{2+} gradient; however, the directionality both NCX and NCKX exchangers can be reversed depending on the Na^+ and Ca^{2+} gradients (Jalloul et al., 2016b; Zhekova et al., 2016). SLC8A and SLC24A gene families are electrogenic because there is a translocation of net charge across the plasma membrane, have a low Ca^{2+} affinity, and are capable of transporting Ca^{2+} in bulk rapidly across the plasma membrane (Brini, 2009). They are reversible but in ameloblasts they likely operate in extruding Ca^{2+} from the cytoplasm facilitated by transport of Na^+ and K^+ down their gradients (Brini and Carafoli, 2011; Hu et al., 2012). PMCA pumps/proteins have 4 members (PMCA1-4, coded by genes ATP2B1-4) and are part of a larger family of genes, called P-type primary ion transport ATPases, that catalyze the auto-phosphorylation of a conserved aspartyl residue within the pump from ATP (Palmgren and Nissen, 2011).

Calcium Extrusion—SLC8A and SLC24A Gene Products

The SLC8A and SLC24A families are primarily expressed in excitable tissues such as muscle and heart, as their rapid bulk transport of Ca^{2+} is important in, for example, muscle and heart contraction (Brini and Carafoli, 2011). The SLC8A/NCX and SLC24A/NCKX transporters are Na^+/Ca^+ exchangers and can be either K^+-dependent (NCKX) or K^+-independent (NCX) (Shumilina et al., 2010).

NCX1 is expressed in heart, brain, bladder, kidney, and cells of the enamel organ; NCX2 is expressed in brain and skeletal muscle; and NCX3 is expressed in brain, skeletal muscle and

cells of the enamel organ (Lytton, 2007; Okumura et al., 2010; Lacruz et al., 2012b; Sharma and O'halloran, 2014). Okumura et al. demonstrated NCX1 and NCX3 expression at the apical pole of both secretory and maturation ameloblasts, and expression of NCX1 was also observed in cells of the stratum intermedium and papillary layer (Okumura et al., 2010). In addition, protein levels of NCX1 and NCX3 throughout amelogenesis remained relatively unchanged (Okumura et al., 2010). Using real-time PCR, Lacruz et al. confirmed that the mRNA levels of both NCX1 and NCX3 did not significantly change from secretory- to maturation-stage enamel organ cells (Lacruz et al., 2012b).

NCKX1 is expressed primarily in retinal rod photoreceptors and platelets (Schnetkamp, 2004; Lytton, 2007). NCKX2 is expressed in cone photoreceptors and is involved in mouse motor learning and memory (Schnetkamp, 2004; Lee et al., 2009, 2013), and NCKX3 is expressed in the brain and the kidneys (Schnetkamp, 2004; Lee et al., 2009) though it is expressed in the kidneys at higher levels in female mice than in male mice (Lee et al., 2009). NCKX3 is also highly expressed in the human endometrium during the menstrual cycle, where its expression is partially regulated by the steroid hormone 17β-estradiol (Yang et al., 2011). NCKX4 is expressed in olfactory neurons (Stephan et al., 2011), and also in the maturation-stage ameloblasts (Hu et al., 2012). NCKX5 is expressed in skin melanocytes, retinal epithelium, and brain (Schnetkamp, 2004; Lytton, 2007; Sharma and O'halloran, 2014; Jalloul et al., 2016a,b). NCKX6/NCLX was originally considered a member of the NCKX family but is now considered part of the Ca^{2+} cation (CCX) exchanger branch (Cai and Lytton, 2004; Sharma and O'halloran, 2014) as a mitochondrial membrane Ca^{2+}, Li^{+}/Na^{+} exchanger with a wide tissue distribution (Schnetkamp, 2004; Lytton, 2007; Sharma and O'halloran, 2014).

Calcium Extrusion—ATP2B Gene Products

The ATPase plasma membrane Ca^{2+} transporting (or PMCA) gene family is postulated to be involved in Ca^{2+} homeostasis, as it has a high affinity for Ca^{2+} but cannot transport Ca^{2+} as rapidly as either the NCX or NCKX transporters (Brini and Carafoli, 2011). The PMCA family is part of the superfamily of P-type ATPase pumps that form a stable phosphorylated intermediate as it hydrolyzes one molecule of ATP for each Ca^{2+} transported (Strehler and Zacharias, 2001; Cai and Lytton, 2004). The phosphorylated enzyme intermediate of the P-type ATPases, which include the SERCA family of transporters in the ER membrane (Giacomello et al., 2013), occurs between γ-phosphate of a hydrolyzed ATP with a D-residue in a highly conserved region of the ATPase pump (Brini and Carafoli, 2011).

PMCA1 is expressed in most tissues throughout development. Its expression is highest in the nervous system, heart, skeletal muscle, and intestine (Zacharias and Kappen, 1999), and regulated by growth factors such as glucocorticoids and Vitamin D (Zacharias and Kappen, 1999; Giacomello et al., 2013). PMCA2 is expressed mainly in the brain, heart, mammary glands and ear, and decreased expression of PMCA2 causes increased apoptosis in breast cancer cells (Curry et al., 2012; Giacomello et al., 2013). PMCA3 has the highest calmodulin affinity and is detected primarily in the brain and skeletal muscles (Krebs, 2009; Giacomello et al., 2013). PMCA4 is involved in the fertilization process and cardiac function, and has been found to associate with lipid rafts, which often function to aggregate protein complexes important in signaling pathways (Giacomello et al., 2013). It has been suggested that PMCA4 is more involved in cell-specific Ca^{2+} signaling than as a pump for bulk Ca^{2+} export (Strehler, 2013; Brini et al., 2017). PMCA4 interacts with nitric oxide synthase and with calcineurin, which regulates NFAT signaling (Brini, 2009; Kim et al., 2012; Strehler, 2013).

PMCA1 and PMCA4 are important in osteoclast differentiation, maturity, and survival, and *Atp2b1*$^{+/-}$ and *Atp2b4*$^{-/-}$ mice have decreased bone density due to an increased number of mature osteoclasts and increased osteoclast apoptosis (Kim et al., 2012). The PMCA family members can also influence IP_3-mediated calcium signaling by binding to phosphatidylinositol-4,5-bisphosphate (PIP_2) on the plasma membrane as well as removing Ca^{2+} necessary for phospholipase C (PLC) activity, which prevents cleaving by PLC and thereby prevents Ca^{2+} release from the ER (Penniston et al., 2014). Altered PMCA expression is a characteristic of many cancers (Curry et al., 2011) and many other human diseases (Brini et al., 2013), but the diversity in isoforms and splicing and lack of specificity of small molecules to target PMCAs present challenges in therapeutic agent development (Strehler, 2013).

Summary—Calcium Export Exchangers and Pumps in Amelogenesis

There now are a number of reports that show expression and localization data for NCX1 and NCX3 (Okumura et al., 2010; Lacruz et al., 2012b), and NCKX4 (Hu et al., 2012; Wang et al., 2014) in the enamel organ. Reports on PMCA expression and activities throughout amelogenesis are scant (Sasaki and Garant, 1986c; Borke et al., 1995; Zaki et al., 1996), and to the authors' knowledge, the only investigations into the role of PMCA proteins in amelogenesis date back decades. Data presented here better defines the mRNA profiles of all SLC8A, SLC24A, and ATP2B gene family members, and adds additional insight into the protein and spatiotemporal expression profiles of NCKX3, PMCA1, and PMCA4.

Calcium Export Exchangers and Pumps and Disease

A number of the ATP2B, SLC8A, and SLC24A gene family members are linked to mammalian disease, but notably mutations to *SLC24A4* are associated with non-syndromic amelogenesis imperfecta (AI) (Parry et al., 2013; Seymen et al., 2014; Wang et al., 2014; Herzog et al., 2015). A comprehensive list of the PMCA, NCX, and NCKX pumps and exchangers, their links to human pathologies, and mouse models of each gene is found in **Table 1**.

MATERIALS AND METHODS

Animals

All vertebrate animal manipulation was carried out in accordance with Institutional and Federal guidelines. The animal protocols were approved by the Institutional Animal Care and Use

TABLE 1 | Pathologies associated with genes ATP2B1-4, SLC8A1-3 and SLC24A1-6.

Gene symbol	Protein name	Predominant substrates	Link to human disease	Animal models	References
ATP2B1	PMCA1	Ca^{2+}		Embryonic lethal	Okunade et al., 2004
ATP2B2	PMCA2	Ca^{2+}		Vestibular/motor imbalance, Deafness	Street et al., 1998; Bortolozzi et al., 2010
ATP2B3	PMCA3	Ca^{2+}	Spinocerebellar ataxia		Bertini et al., 2000; Zanni et al., 2012
ATP2B4	PMCA4	Ca^{2+}	Familial spastic paraplegia	No overt phenotype in Atp2b4 null mice, Male mice are infertile	Okunade et al., 2004; Ho et al., 2015
SLC8A1	NCX1	Na^{+}, Ca^{2+}		Embryonic lethal	Wakimoto et al., 2000
SLC8A2	NCX2	Na^{+}, $Ca2^{+}$			
SLC8A3	NCX3	Na^{+}, Ca^{2+}		Skeletal muscle fiber necrosis, Defective neuromuscular transmission	Sokolow et al., 2004
SLC8B1*	NCLX	Na^{+}, Li^{+}, Ca^{2+}			Khananshvili, 2013
SLC24A1	NCKX1	Na^{+}, Ca^{2+}, K^{+}	Congenital stationary night blindness	Night blindness	Riazuddin et al., 2010; Vinberg et al., 2015
SLC24A2	NCKX2	Na^{+}, Ca^{2+}, K^{+}			
SLC24A3	NCKX3	Na^{+}, Ca^{2+}, K^{+}			
SLC24A4	NCKX4	Na^{+}, Ca^{2+}, K^{+}	Amelogenesis imperfecta	Amelogenesis imperfecta	Parry et al., 2013; Seymen et al., 2014; Wang et al., 2014; Herzog et al., 2015
SLC24A5	NCKX5	Na^{+}, Ca^{2+}, K^{+}	Hypopigmentation, Oculocutaneous albinism		Mondal et al., 2012; Wei et al., 2013
SLC24A6	NCKX6	Na^{+}, Ca^{2+}, K^{+}			

Note that SLC8B1 is found in the mitochrodria of mammalian skeletal and heart muscle, neurons and a few other cell types.

Committee at the University of Southern California (Protocol #20461).

Quantitative PCR Analysis

Secretory-stage and maturation-stage enamel organ cells from mandibular incisors of 4-week old Wistar Hanover rats were collected as previously described (Lacruz et al., 2012b; Wen et al., 2014), and RNA extraction was performed using a QIAshredder, an RNeasy Protect Mini Kit, and DNase I solution from Qiagen (Valencia, CA, USA). Reverse transcription and real-time PCR were performed using the iScript cDNA Synthesis kit and SYBR Green Supermix from BioRad, respectively. Real-time PCR was performed on the CFX96 system (BioRad Laboratories, Hercules, CA, USA) in 10 μl volumes with a final primer concentration of 100 nm, for 40 cycles at 95°C for 10 s and 58°C for 45 s. Six independent real-time PCR analyses were conducted using samples from a total of 6 rats, 3 males, and 3 females, for each gene of interest (primers are listed in **Table 2**), and for both stages of amelogenesis. The male and female data were analyzed separately and no significant differences were noted between the sexes, so the data presented in the graph were generated from all 6 animals ($n = 6$). Rat enamel organ is preferred to mouse enamel organ for real-time PCR and western blot studies because separating secretory and maturation stage from adult mouse incisors is technically difficult and yields less RNA and protein per animal.

Western Blot Analysis

Secretory (S) and maturation (M) enamel organ cells from mandibular incisors of 4-week old Wistar Hanover rats were collected. Brain (B) and heart (H) tissues were also collected as control tissues. Total protein extraction was performed with RIPA buffer (1% Nonidet P-40, 0.1% SDS, 0.5% deoxycholic acid, 150 mm NaCl, 50 mm Tris, pH 8.0) and protease inhibitor cocktail, complete mini (Roche Applied Sciences, Indianapolis, IN, USA). Samples were homogenized manually with a pestle six times, then sonicated with a BRANSON digital sonifier Model 450 (All-Spec Industries, Wilmington, NC, USA; 10% intensity, 10 s on and 10 s off). Samples were then cleared by centrifugation (15,000 g, 15 min, 4°C). Proteins were quantified using the bicinchoninic acid (BCA) assay (Pierce, Rockford, IL, USA) and equal quantities were loaded (15 μg per lane) onto 4–12% SDS–PAGE resolving gels. Protein was transferred to a PVDF membrane, then blocked with 5% milk in TBST. Antibodies against PMCA1 (AbCam, Cambridge, MA, USA; catalog #ab190355), PMCA2 (ab3529), PMCA3 (ab3530), PMCA4 (ab2783), NCKX3 (St. John's Laboratory, London, UK, catalog #STJ94358), GAPDH (Santa Cruz Biotechnology, Santa Cruz, CA, USA, catalog #sc-32233), amelogenin (ThermoFisher Scientific, catalog #PA5-31286), and cardiac muscle actin (ACTC1) (GeneTex Inc., Irvine, CA, catalog #GTX101876) were used at dilutions of 1:500, 1:2,000, 1:300, 1:5,000, 1:500, 1:500, 1:3,000, and 1:500, respectively in 5% milk in TBST. Secondary antibody for PMCA1-4 from Cell Signaling (Danvers, MA, USA; catalog #7074 and #7076) was applied at a dilution of 1:10,000. Secondary antibodies for NCKX3, amelogenin, and ACTC1 from Santa Cruz Biotechnology (Santa Cruz, CA, USA; catalog #sc-2004 and sc-2418) were applied at a dilution of 1:7500. Pierce ECL Plus Western Blotting Substrate (Thermo Scientific, Rockford, IL, USA; catalog #32132) was used as the detection system for all antibodies. TBST (tris-buffered saline with.1% Tween-20) was used as a wash buffer.

Immunofluorescence

Mandibular incisors were dissected from 9-day-old wild type mice and placed in 4% paraformaldehyde in PBS overnight. Mouse incisors were preferred to rat incisors in the immunofluorescence studies because mouse incisors decalcify more rapidly and all stages of amelogenesis are visible in one sagittal section. The incisors were then washed in PBS and decalcified in 10% EDTA in PBS pH 7.4 for 4 weeks at 4°C. The sample was embedded in paraffin and 4 μm sections were cut with a microtome. The sections were deparaffinized and rehydrated. The primary antibodies for PMCA1 and PMCA4 (AbCam, Cambridge, MA, USA; catalog #ab3528 and #ab2783, respectively) were used at dilutions of 1:40 and 1:200 in 1% BSA in PBS, respectively. The primary antibody for NCKX3 (Santa Cruz Biotechnology, Santa Cruz, CA, USA; catalog #sc-50129) was used at a dilution of 1:50. The secondary antibodies (Vector Laboratories, Burlingame, CA, catalog #DI-1088, DI-2488, DI-2594, DI-3094) were used at a dilution of 1:300 in 1% BSA in PBST. Sections were mounted with mounting medium with DAPI (Vector Laboratories, Burlingame, CA, catalog #H-1200) and imaged on a Leica TCS SP8 confocal microscope (Leica Biosystems). PBST (0.1% Tween-20) was used as a wash buffer for the experiments. Negative control sections, using secondary antibody only, under identical conditions, were included and showed negligible auto fluorescence—see Supplemental Figure 1.

RESULTS

Messenger RNA Expression Profiles

Quantitative PCR (qPCR) comparing mRNA expression levels in secretory and maturation enamel organ cells for all PMCA (Atp2b), NCX (Slc8) and NCKX (Slc24) gene family members indicate that: (1) PMCA1 (*Atp2b1*), 3 (*Atp2b3*), and 4 (*Atp2b4*), and NCKX3 (*Slc24a3*) expression is highest during secretory-stage amelogenesis; (2) NCX1 (*Slc8a1*) and 3 (*Slc8a3*), and NCKX6 (*Slc24a6*) were expressed during secretory and maturation stages; and (3) NCKX4 (*Slc24a4*) is most highly expressed during maturation-stage amelogenesis (**Figure 1**). The expression levels of PMCA2 (*Atp2b2*), NCX2 (*Slc8a2*), NCKX1

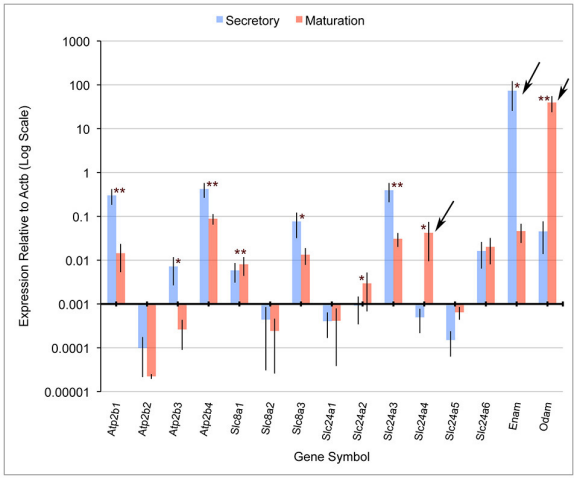

FIGURE 1 | Real-time PCR for rat Atp2b, Slc8a, and Slc24a gene family members. Atp2b1, Atp2b3, Atp2b4, Slc8a3, and Slc24a3 have significantly higher expression in secretory stage than maturation stage, while Slc8a1, Slc24a2, and Slc24a4 were significantly more highly expressed in maturation stage compared to secretory stage. β-actin (Actb) served as a normalizing control, and enamelin (Enam) and Odam as control transcripts that were significantly down-regulated and up-regulated, respectively (as expected), during maturation-stage amelogenesis. Slc24a4, Enam and Odam (arrows) have all been linked to non-syndromic cases or amelogenesis imperfecta. The x-axis is placed at the 0.001 expression level relative to Actb, and below this "cut-off" figure is arbitrarily considered non-significant. The Student's *t*-test (paired two-tail) was used to compare the expression of each gene between the secretory and maturation stages (*$p < 0.05$, and **$p < 0.01$). Standard deviations are also included.

TABLE 2 | Primers used for real-time PCR.

Symbol	Accession	Size	Region	Forward	Reverse	Temp
Atp2b1	NM_053311	219	1,387–1,605	AAAGCAGGTCTGCTGATGTC	GACGGAGTAAGCCAGTGAGA	58
Atp2b2	NM_012508	168	4,129–4,296	GAGACGTCGCTTTAGCTGAG	AAAGGGTCTGTGTGTGGAAA	58
Atp2b3	NM_133288	207	4,073–4,279	GCTCCATGACGTAACCAATC	GCGGAATATTGTGGGTGTAG	58
Atp2b4	NM_001005871	184	3,698–3,881	AATCCAAGAACCAGGTCTCC	ACGGCATTGTTATTCGTGTT	58
Slc8a1	NM_019268	150	2,430–2,579	CCTGCTTCATTGTCTCCATC	CAAATGTGTCTGGCACTGAG	58
Slc8a2	NM_078619	166	377–542	AAACGGTGTCCAACCTTACA	ACACACACAGCAATGACCAC	58
Slc8a3	NM_078620	206	4,310–4,515	TGGTGGAAGCCATTCTATGT	AATATGGCCCACTCCCTTAG	58
Slc24a1	NM_004727	155	3,238–3,392	TTCCTGACCTCATCACCAGT	TGGAACTGGCTGTAATCCAT	58
Slc24a2	NM_031743	214	1,280–1,493	GGGAGGTTCAGAGAAAAAGC	CGATGCTGTGAGAGAGGTTT	58
Slc24a3	NM_053505	150	2,941–3,090	TGACATGTGCTCTTGTTGCT	AATTGGGACTTCATTGACGA	58
Slc24a4	NM_001108051	235	401–635	AAAGTTGATGGCACCGATAA	AGGGATGGGACAAAGAAGTC	58
Slc24a5	NM_001107769	161	371–531	AACATGGTTTCAACGCTCTC	CACAGCAGCAGGACATACAG	58
Slc24a6	NM_001017488	160	613–772	TTCTCAGACCCTCGTACTGC	ACACGGCCACCATATAGAAA	58
Enam	NM_001106001	169	1,139–1,307	ATGCTGGGAACAATCCTACA	GTGGTTTGCCATTGTCTTTC	58
Odam	NM_001044274	206	658–863	TTGACAGCTTTGTAGGCACA	GACCTTCTGTTCTGGAAGCAG	58
Actb	NM_031144	272	559–830	CACACTGTGCCCATCTATGA	CCGATAGTGATGACCTGACC	58

(*Slc24a1*), NCKX2 (*Slc24a2*), and NCKX5 (*Slc24a5*) are negligible throughout amelogenesis (**Figure 1**). These data for NCX (Slc8) and NCKX (Slc24) gene family members are consistant with previously published gene expression data (Okumura et al., 2010; Hu et al., 2012), and add novel information suggesting that PMCA1, PMCA4, and to a lesser extent PMCA3 (which is expressed in secretory enamel organ cells at a level an order of magnitude lower than seen for PMCA1 and PMCA4), play an important role in secretory-stage amelogenesis.

Western Blot Analysis Confirms Expression of PMCA Proteins in Enamel Organ Cells

Western blot data indicate that PMCA1 and PMCA4 are more highly expressed in secretory stage than in maturation stage, and PMCA2 is not expressed at any appreciable level in amelogenesis, consistent with the qPCR data (**Figures 2Ai,Aiv,Aii** respectively). Contrary to the qPCR data, PMCA3 and NCKX3 appear to be expressed at similar levels during both secretory stage and maturation stage (**Figures 2Aiii,B** respectively). Rat brain and heart protein samples were used as control tissues and analyzed with the secretory- and maturation-stage protein samples. The expected molecular weights for PMCA1-4 are ∼130, 133, 123, and 129 kDa respectively, and relate to the single bands seen at approximately the 150 kDa molecular weight mark (as indicated by an arrow, **Figure 2A**). The expected molecular weight of NCKX3 is ∼60 kDa (**Figure 2B**). Gapdh has been included as a loading control for all samples, and additional controls include Western analysis for both amelogenin (Amelx) and cardiac muscle alpha actin (Actc) (**Figure 2B**).

PMCA1 and PMCA4 Localization by Immunofluorescence

In the enamel organ, PMCA1 expression is seen primarily on the basolateral membrane of both secretory- and maturation-stage ameloblasts, with stronger signals seen in secretory ameloblasts (green; **Figures 3A–C**). These data complement both the qPCR (**Figure 1**) and Western blot data (**Figure 2**) on the spatiotemporal expression of PMCA1 in enamel organ cells. When compared to ameloblasts, a weaker signal of PMCA1 is seen in the stratum intermedium (**Figure 3A**) and papillary layer cells of the enamel organ (**Figure 3B**); as reflected by the orange color observed in the merged images (**Figures 3G–I**). In the enamel organ, PMCA4 expression is also seen on the basolateral membrane of secretory- and maturation-stage ameloblasts, and also cells of the stratum intermedium and papillary layer cells (red; **Figures 3D–F**). Similar to the PMCA1 data, these PMCA4 immunolocalization data complement the qPCR and Western blot data (**Figures 1**, **2**). The co-localization of both PMCA1 and PMCA4 in polarized ameloblasts can be appreciated in the merged image (yellow; **Figures 3G–I**), while PMCA4 (but not PMCA1) is also expressed in the stratum intermedium and papillary layer cells of the enamel organ (red; **Figures 3G–I**).

NCKX3 Localization by Immunofluorescence

NCKX3 expression is highest in the Tomes' processes (**Figure 3M**) and the apical membrane of transition- and maturation-stage ameloblasts (**Figures 3N,O**), while some minor ameloblast-specific intracellular granular immune-reaction is also apparent (**Figures 3M–O**). We compared the expression

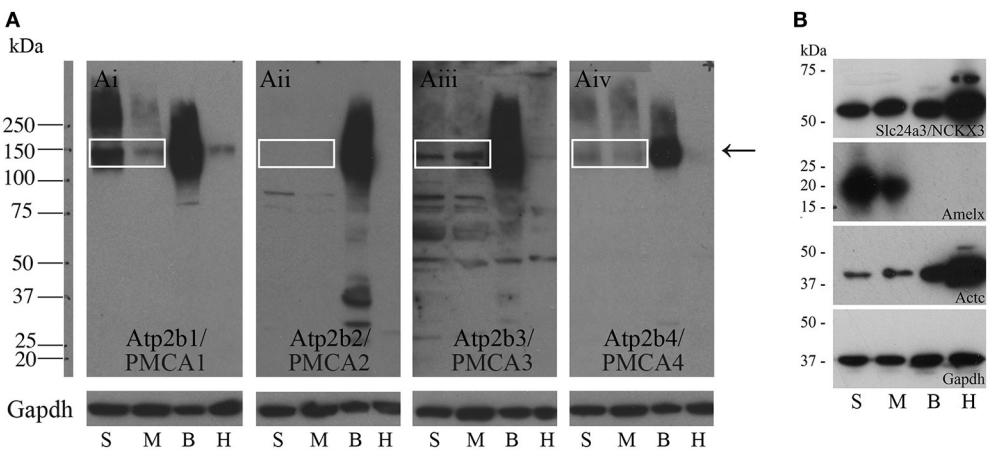

FIGURE 2 | Western blot analyses of PMCA1-4, and NCKX3 in secretory-stage and maturation-stage rat enamel organs. (A) Western blot analysis for PMCA1 **(Ai)**, PMCA2 **(Aii)**, PMCA3 **(Aiii)** and PMCA4 **(Aiv)**. Samples are secretory-stage enamel organ cells (S), maturation-stage enamel organ cells (M), brain tissue (B) and heart tissue (H). Brain and heart samples are shown for comparison, as all PMCAs are highly expressed in brain and at lower levels in the heart (Brini and Carafoli, 2011; Brini et al., 2017). Molecular weight markers are indicated at left. The expected molecular weights for PMCA1, PMCA2, PMCA3, and PMCA4 are ∼130, 133, 123, and 129 kDa, respectively. The bands are seen for PMCA1, PMCA3, and PMCA4 (boxed and arrow). No expression of PMCA2 is evident. GAPDH is used here as a loading control. **(B)** Western blot analysis of NCKX3. The expected molecular weight for NCKX3 is ∼60 kDa. NCKX3 is expressed in all 4 tissue samples tested, with similar expression noted in both secretory-stage and maturation-stage enamel organ cells, and brain tissue. Relatively higher levels of NCKX3 expression can be appreciated in heart tissue. Amelx and Actc are used as controls as expression is highest in secretory-stage ameloblasts (Lacruz et al., 2012a,b) and heart tissue (Hamada et al., 1982) respectively. GAPDH is used here as a loading control.

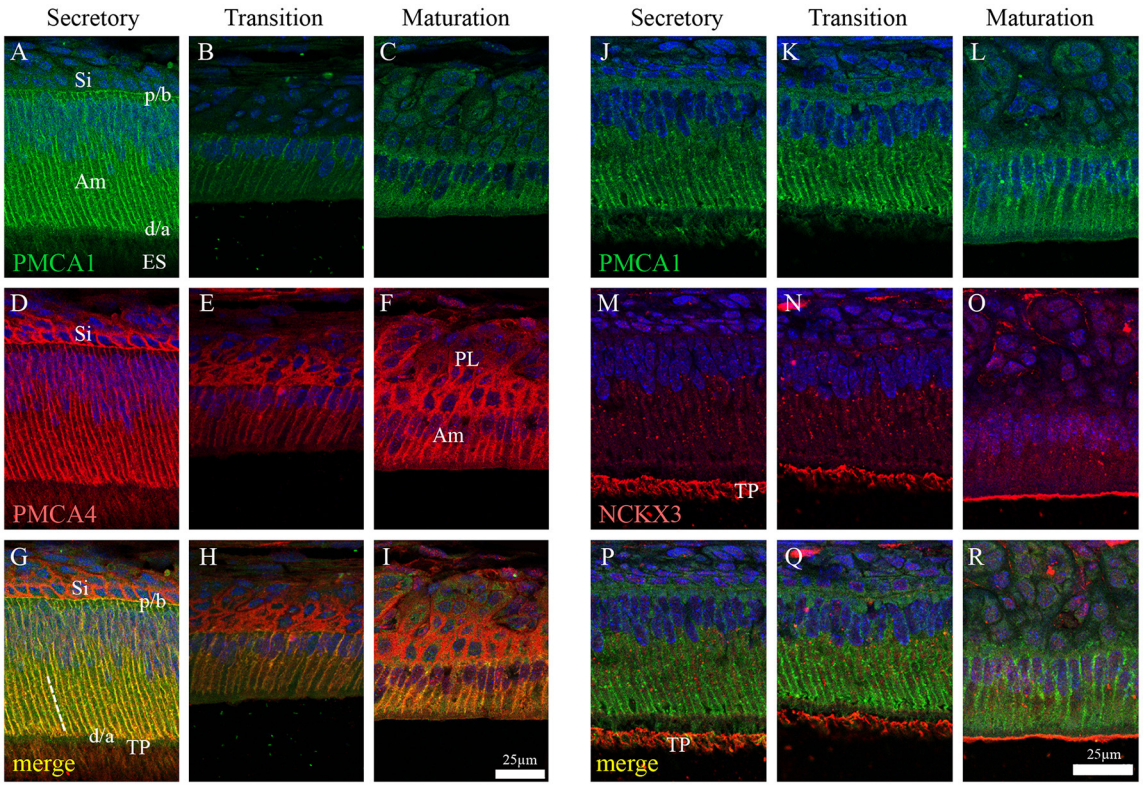

FIGURE 3 | Immunofluorescence analysis of PMCA1, PMCA4, and NCKX3 in 9-day-old mouse mandibular incisors. Columns from left to right show secretory-stage **(A,D,G,J,M,P)**, transition-stage **(B,E,H,K,N,Q)** and maturation-stage **(C,F,I,L,O,R)** ameloblasts; while rows show immunoreactivity for PMCA1 (green; **A–C** and **J–L**), PMCA4 (red; **D–F**) and NCKX3 (red; **M–O**). Merged images are also shown for each column (**A,D** merged to **G**; **B,E** merged to **H**; **C,F** merged to **I**; **J,M** merged to **P**; **K,N** merged to **Q**; and **L** and **O** merged to **R**). Am, Ameloblasts; ES, enamel space; Si, stratum intermediu (TP; secretory ameloblasts only), Tomes' processes and (PL, maturation ameloblasts only), papillary layer. The proximal/basal poles (p/b) and distal/apical poles (d/a) of ameloblast cells are identified, as are the lateral membranes of ameloblasts (broken while line in **G**). Scale for **(A–I)** shown in **(I)**; and scale for **(J–R)** shown in **R**.

profile for NCKX3 (red; **Figures 3M–O**) to the expression profile of the control PMCA1 (green; **Figures 3J–L**). As can be appreciated from the images (**Figures 3M–R**), the expression profile for NCKX3 in the enamel organ is highest at the distal/apical pole, and this is distinct from the expression profiles seen for PMCA1 and PMCA4 where expression is seen on the lateral membranes of polarized ameloblasts (for both PMCA1 and PMCA4) and stratum intermedium and papillary layer cells (only PMCA4) (**Figures 3A–L**).

DISCUSSION

From data presented here and prior studies, it is possible to make the following generalizations. First, of the four unique genes coding the PMCAs, PMCA1, and PMCA4 are highly expressed on the basolateral membranes of polarized ameloblasts; and both are expressed during secretory- and maturation-stage amelogenesis. These data somewhat contradicts previously published data suggesting PMCA1 and PMCA4 are localized primarily to Tomes' processes of secretory ameloblasts (Sasaki and Garant, 1986c; Borke et al., 1995). These differences likely result from the different specificities of antibodies used to carry out these studies, and as noted previously, protein localization differences may also result from the different chemical and processing techniques used by the various laboratories (Takano, 1995). While expression of PMCA1 is primarily in the basolateral membrane of ameloblasts, there are also lower expression levels noted in the cells of stratum intermedium and papillary layer. Similarly, while expression of PMCA4 is seen in the basolateral membrane of ameloblasts, expression of PMCA4 is also recognized as a feature of the cells of the stratum intermedium and papillary layer cells. Of the three unique genes coding for the NCXs, NCX1, and NCX3 are highly expressed at the apical pole of both secretory- and maturation-stage ameloblasts (Okumura et al., 2010). Finally, of the six unique genes coding for NCKXs, NCKX3 (data reported here; **Figures 1–3**) and NCKX4 (Hu et al., 2012; Wang et al., 2014) are both highly expressed at the apical pole of polarized ameloblasts. A similar level of expression of NCKX3 is noted in both secretory- and maturation-stage ameloblasts (**Figures 2**, **3**). While expression of NCKX4 is negligible in secretory-stage ameloblasts, it is highly expressed in maturation-stage ameloblasts (Hu et al., 2012; Wang et al., 2014). All six proteins expressed in ameloblasts (PMCA1, PMCA4, NCX1, NCX3, NCKX3, and NCKX4) export Ca^{2+} from the

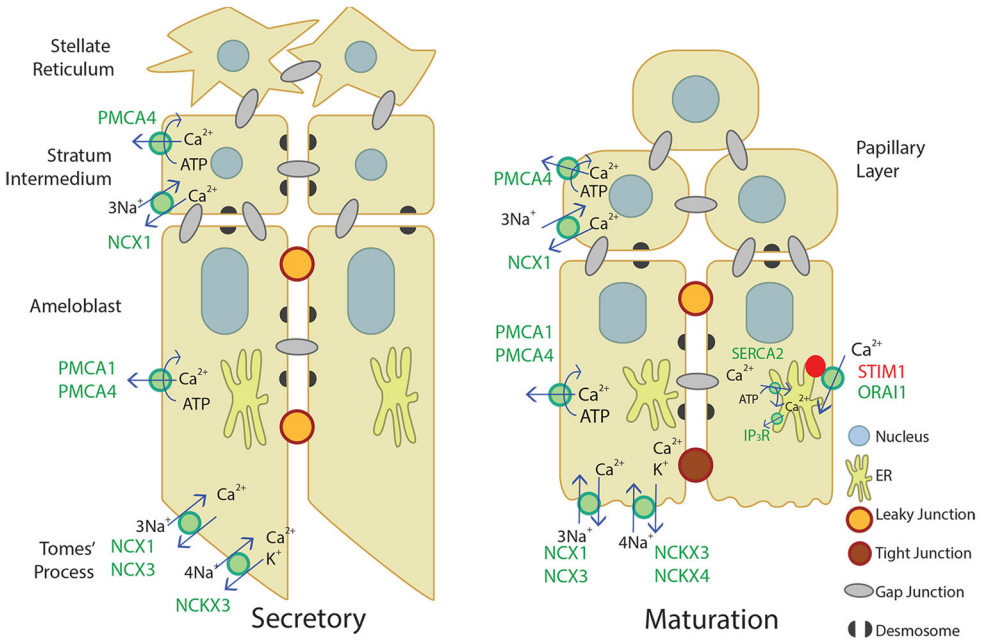

FIGURE 4 | Schematic of what is currently proposed for secretory- and maturation-stage transcellular calcium transport in amelogenesis. During the secretory-stage (left image), active Ca^{2+} transport on the lateral membrane is primarily mediated by PMCA1 and PMCA4 and ATP is hydrolyzed in the process. NCX1, NCX3, and NCKX3 mediate Ca^{2+} export in the Tomes' process. More calcium transporters are expressed during the maturation stage (right image). The CRAC channel, composed of the channel ORAI1 and the ER membrane calcium sensor STIM1, mediates the bulk of calcium entry and is active in response to ER calcium store depletion through IP_3R. The cell then removes calcium from the cytoplasm through the SERCA2 pump that replenishes ER stores, and the NCKX and NCX proteins on the apical border plasma membrane that export calcium into the enamel area and facilitate mineralization (Nurbaeva et al., 2015a,b, 2017). NCX1 and PMCA4 export Ca^{2+} from the stratum intermedium (secretory-stage enamel organ) and papillary layer (maturation-stage enamel organ). Desmosomes (Sasaki et al., 1984; Fausser et al., 1998; Jheon et al., 2011) and gap junctions (Sasaki and Garant, 1986a,b,d; Pinero et al., 1994; Inai et al., 1997) have also been identified bridging or uniting adjacent epithelial cells in the enamel organ, and are also illustrated.

cytoplasm to the extracellular space, thus ameloblasts may be one of the more complicated epithelial cell types when it comes to understanding ion movements related to Ca^{2+} transport as they relate to a mineralizing dental enamel.

The data suggest that there are likely redundancies amongst similarly functioning proteins from these gene families. For example, from this list of six Ca^{2+} export proteins expressed in ameloblasts, only mutations to SLC24A4/NCKX4 have been linked to enamel pathologies (Parry et al., 2013; Seymen et al., 2014; Wang et al., 2014; Herzog et al., 2015). NCKX4 exports Ca^{2+} from the apical pole of maturation-stage ameloblasts at the developmental stage where enamel mineralization is at its greatest; thus, NCKX4 may play a greater role in enamel formation than either NCX1 or NCX3, which have expression localized to the apical pole throughout the entire process of amelogenesis. It is conceivable that if the function of either NCX1 or NCX3 is less than optimal, the other may compensate such that no overt enamel phenotype results. Future studies may be able to address whether NCX1 and NCX3 are equivalent in enamel formation.

Similar to NCX1 and NCX3 in ameloblasts, PMCA1 and PMCA4 or other calcium handling proteins may be able to overcome the effects of *Atp2b1* or *Atp2b4* mutations, or gene silencing. No human pathologies have yet been linked to *ATP2B1* mutations (as noted in the Online Mendelian Inheritance in Man; http://omim.org/entry/108731), however *Atp2b1*-null mice are embryonic lethal (Okunade et al., 2004). Only recently a case of familial spastic paraplegia has been linked to an *ATP2B4* mutation (Ho et al., 2015; http://omim.org/entry/108732), and while *Atp2b4*-null mice have no overt phenotype, the male mice are infertile due to reduced sperm motility (Okunade et al., 2004; Schuh et al., 2004; Kim et al., 2012). The similar expression profiles of PMCA1 and PMCA4 in ameloblasts (that being to the basolateral membrane) may suggest that loss of PMCA4 function in ameloblasts may be compensated by PMCA1, while the loss of PMCA1 function remains embryonic lethal. If this is correct, studying PMCA1 activities in *in vivo* enamel formation would, in the future, be limited to conditional knockout or heterozygote animal models. The localization of PMCA1 and PMCA4 on the ameloblast basolateral membrane may suggest that these Ca^{2+} pumps are unlikely to have a critical role in enamel mineralization; i.e., Ca^{2+} removed by the PMCA pumps may not directly be incorporated into the Hap mineral phase. Instead, the PMCA pumps may be indirectly involved in amelogenesis by maintaining ameloblast Ca^{2+} homeostasis; or being a part of ameloblast cell signaling pathways. As calcium is transported through the stratum intermedium and papillary layer to the ameloblasts and the enamel organ, the PMCA

TABLE 3 | Major and most highly expressed calcium export pumps and exchangers in enamel organ cells.

Gene/protein	Secretory ameloblasts	Stratum intermedium	Stellate reticulum	Maturation ameloblasts	Papillary layer cells	References
Atp2b1/PMCA1	Basolateral	✔ (weak)	✗	Basolateral	✔ (Weak)	
Atp2b4/PMCA4	Basolateral	✔	✗	Basolateral	✔	
Slc8a1/NCX1	Apical	✔	✗	Apical	✔	Okumura et al., 2010
Slc8a3/NCX3	Apical	✗	✗	Apical	✗	Okumura et al., 2010
Slc24a3/NCKX3	Apical	✗	✗	Apical	✗	
Slc24a4/NCKX4	✗	✗	✗	Apical	✗	Hu et al., 2012; Wang et al., 2014

family may additionally be valuable in shuttling the calcium from circulation to the ameloblasts. The PMCA family can be involved in IP_3-mediated calcium signaling (Penniston et al., 2014), and PMCA1 and PMCA4 are involved in RANKL signaling and regulate osteoclast differentiation (Kim et al., 2012). In cultured osteoclasts, the knockdown and/or silencing of both PMCA1 and PMCA4 increased protein expression of SERCA2 and TRPV5 (Kim et al., 2012). Indeed, the PMCA transporters may have evolved to fine-tune intracellular calcium concentration as they have higher calcium affinity and lower capability for bulk Ca^{2+} transport than the NCX/NCKX exchangers (Brini and Carafoli, 2011), and are therefore more likely to play a housekeeping role by removal of intracelullar Ca^{2+} during maturation stage enamel mineralization which may also prevent calcium overload and possibly ameloblasts apoptosis. The PMCA transporters have multiple known expressed isoforms in other tissues but this has not yet been studied in the enamel organ.

Our novel data adds to the current understanding of Ca^{2+} transport in secretory and maturation stage enamel organ, described in **Figure 4**. Ca^{2+} import by the CRAC channel, ER Ca^{2+} export by IP_3R, and ER Ca^{2+} import by the SERCA2 pump have been well-described elsewhere (Nurbaeva et al., 2015a,b, 2017). In summary, when Ca^{2+} is released from the ER through IP_3R, STIM1 associates with ORAI1 and forms the CRAC channel that allows Ca^{2+} to flow into the cell. Ca^{2+} is then removed from the cytoplasm through PMCA1 and PMCA4 on the basal and lateral membranes, NCX1, NCX3, NCKX3, and NCKX4 on the apical membrane, and SERCA2 on the ER membrane. NCX1 and PMCA4 are also involved in Ca^{2+} export in the stratum intermedium and papillary layer. This process of Ca^{2+} cycling occurs more during the maturation stage, when large amounts of Ca^{2+} are necessary for enamel mineralization. During the secretory stage, PMCA1, PMCA4, NCX1, NCX3, and NCKX3 are the known Ca^{2+} exporters expressed, but further studies are necessary to understand Ca^{2+} import and other mechanisms of Ca^{2+} export during enamel secretion.

CONCLUSION

Based on the available data, we have reviewed and summarized the expression profiles of the major Ca^{2+} export pumps and exchangers in enamel organ cells (**Table 3**; Okumura et al., 2010; Hu et al., 2012; Wang et al., 2014), and illustrated these Ca^{2+} export proteins along with the current model for Ca^{2+} import in enamel organ cells as proposed by Nurbaeva et al. (2015a,b, 2017) (**Figure 4**). As future studies continue to better define Ca^{2+} export (and also Ca^{2+} import—see Nurbaeva et al., 2015a,b, 2017) during amelogenesis, the information in **Table 3** will undoubtedly expand and become more precisely defined. Ultimately, elucidating the multitude of mechanisms involved in transcellular Ca^{2+} movements in the enamel-forming cells will result in a better understanding of the physiology and formation of enamel, the hardest and most calcified tissue in mammals.

AUTHOR CONTRIBUTIONS

SR, XW, CS, and MP designed the experiments and wrote the manuscript; SR and XW performed the experiments; SR, XW, KY, JC, CS, and MP analyzed the data; SR, XW, and MP prepared the figures and tables; All listed authors critically read, edited, and approved the final manuscript. MP accepts full responsibility for the integrity of the data analysis.

ACKNOWLEDGMENTS

The authors would like to thank Bridget Samuels for her help in the preparation of this manuscript, and Dr. Rodrigo S. Lacruz for his helpful comments and edits of the final version. This work was supported by grants DE019629 (MP), DE021982 (SR), and DE022528 (KY) from the National Institute of Dental and Craniofacial Research/National Institutes of Health. The authors declare no potential conflicts of interest with respect to the authorship and/or publication of this article.

SUPPLEMENTARY MATERIAL

The Supplementary Material for this article can be found online at: http://journal.frontiersin.org/article/10.3389/fphys.2017.00336/full#supplementary-material

REFERENCES

Arquitt, C. K., Boyd, C., and Wright, J. T. (2002). Cystic fibrosis transmembrane regulator gene (CFTR) is associated with abnormal enamel formation. *J. Dent. Res.* 81, 492–496. doi: 10.1177/154405910208100712

Berridge, M. J., Bootman, M. D., and Roderick, H. L. (2003). Calcium signalling: dynamics, homeostasis and remodelling. *Nat. Rev. Mol. Cell Biol.* 4, 517–529. doi: 10.1038/nrm1155

Bertini, E., Des Portes, V., Zanni, G., Santorelli, F., Dionisi-Vici, C., Vicari, S., et al. (2000). X-linked congenital ataxia: a clinical and genetic study. *Am. J. Med. Genet.* 92, 53–56. doi: 10.1002/(SICI)1096-8628(20000501)92:1<53::AID-AJMG9>3.0.CO;2-F

Blair, H. C., Robinson, L. J., Huang, C. L., Sun, L., Friedman, P. A., Schlesinger, P. H., et al. (2011). Calcium and bone disease. *Biofactors* 37, 159–167. doi: 10.1002/biof.143

Borke, J. L., Zaki, A. E.-M., Eisenmann, D. R., and Mednieks, M. I. (1995). Localization of plasma membrane Ca^{2+} pump mRNA and protein in human ameloblasts by *in situ* hybridization and immunohistochemistry. *Connect. Tissue Res.* 33, 139–144. doi: 10.3109/03008209509016993

Bortolozzi, M., Brini, M., Parkinson, N., Crispino, G., Scimemi, P., De Siati, R. D., et al. (2010). The novel PMCA2 pump mutation Tommy impairs cytosolic calcium clearance in hair cells and links to deafness in mice. *J. Biol. Chem.* 285, 37693–37703. doi: 10.1074/jbc.M110.170092

Brini, M. (2009). Plasma membrane Ca^{2+}-ATPase: from a housekeeping function to a versatile signaling role. *Pflugers Arch.* 257, 657–664. doi: 10.1007/s00424-008-0505-6

Brini, M., Cali, T., Ottolini, D., and Carafoli, E. (2013). The plasma membrane calcium pump in health and disease. *FEBS J.* 280, 5385–5397. doi: 10.1111/febs.12193

Brini, M., and Carafoli, E. (2011). The plasma membrane Ca^{2+} ATPase and the plasma membrane sodium calcium exchanger cooperate in the regulation of cell calcium. *Cold Spring Harb. Perspect. Biol.* 3:a004168. doi: 10.1101/cshperspect.a004168

Brini, M., Carafoli, E., and Cali, T. (2017). The plasma membrane calcium pumps: focus on the role in (neuro)pathology. *Biochem. Biophys. Res. Commun.* 483, 1116–1124. doi: 10.1016/j.bbrc.2016.07.117

Bronckers, A., Kalogeraki, L., Jorna, H. J., Wilke, M., Bervoets, T. J., Lyaruu, D. M., et al. (2010). The cystic fibrosis transmembrane conductance regulator (CFTR) is expressed in maturation stage ameloblasts, odontoblasts and bone cells. *Bone* 46, 1188–1196. doi: 10.1016/j.bone.2009.12.002

Bronckers, A. L., Lyaruu, D., Jalali, R., Medina, J. F., Zandieh-Doulabi, B., and Denbesten, P. K. (2015). Ameloblast modulation and transport of Cl^-, Na^+, and K^+ during Amelogenesis. *J. Dent. Res.* 94, 1740–1747. doi: 10.1177/0022034515606900

Cai, X., and Lytton, J. (2004). Molecular cloning of a sixth member of the K^+-dependent Na^+/Ca^{2+} exchanger gene family, NCKX6. *J. Biol. Chem.* 279, 5867–5876. doi: 10.1074/jbc.M310908200

Curry, M. C., Luk, N. A., Kenny, P. A., Roberts-Thomson, S. J., and Monteith, G. R. (2012). Distinct regulation of cytoplasmic calcium signals and cell death pathways by different plasma membrane calcium ATPase isoforms in MDA-MB-231 breast cancer cells. *J. Biol. Chem.* 287, 28598–28608. doi: 10.1074/jbc.M112.364737

Curry, M. C., Roberts-Thomson, S. J., and Monteith, G. R. (2011). Plasma membrane calcium ATPases and cancer. *Biofactors* 37, 132–138. doi: 10.1002/biof.146

Fausser, J. L., Schlepp, O., Aberdam, D., Meneguzzi, G., Ruch, J. V., and Lesot, H. (1998). Localization of antigens associated with adherens junctions, desmosomes, and hemidesmosomes during murine molar morphogenesis. *Differentiation* 63, 1–11. doi: 10.1046/j.1432-0436.1998.6310001.x

Giacomello, M., De Mario, A., Scarlatti, C., Primerano, S., and Carafoli, E. (2013). Plasma membrane calcium ATPases and related disorders. *Int. J. Biochem. Cell Biol.* 45, 753–762. doi: 10.1016/j.biocel.2012.09.016

Hamada, H., Petrino, M. G., and Kakunaga, T. (1982). Molecular structure and evolutionary origin of human cardiac muscle actin gene. *Proc. Natl. Acad. Sci. U.S.A.* 79, 5901–5905. doi: 10.1073/pnas.79.19.5901

Herzog, C. R., Reid, B. M., Seymen, F., Koruyucu, M., Tuna, E. B., Simmer, J. P., et al. (2015). Hypomaturation amelogenesis imperfecta caused by a novel SLC24A4 mutation. *Oral Surg. Oral Med. Oral Pathol. Oral Radiol.* 119, e77–e81. doi: 10.1016/j.oooo.2014.09.003

Ho, P. W., Pang, S. Y., Li, M., Tse, Z. H., Kung, M. H., Sham, P. C., et al. (2015). PMCA4 (ATP2B4) mutation in familial spastic paraplegia causes delay in intracellular calcium extrusion. *Brain Behav.* 5:e00321. doi: 10.1002/brb3.321

Hu, J. C., Chun, Y. H., Al Hazzazzi, T., and Simmer, J. P. (2007). Enamel formation and amelogenesis imperfecta. *Cells Tissues Organs* 186, 78–85. doi: 10.1159/000102683

Hu, P., Lacruz, R. S., Smith, C. E., Smith, S. M., Kurtz, I., and Paine, M. L. (2012). Expression of the sodium/calcium/potassium exchanger, NCKX4, in ameloblasts. *Cells Tissues Organs* 196, 501–509. doi: 10.1159/000337493

Hubbard, M. J. (1996). Articular debridement versus washout for degeneration of the medial femoral condyle. A five-year study. *J. Bone Joint Surg. Br.* 78, 217–219.

Hubbard, M. J. (2000). Calcium transport across the dental enamel epithelium. *Crit. Rev. Oral Biol. Med.* 11, 437–466. doi: 10.1177/10454411000110040401

Inai, T., Nakamura, K., Kurisu, K., and Shibata, Y. (1997). Immunohistochemical localization of connexin43 in the enamel organ of the rat upper incisor during ameloblast development. *Arch. Histol. Cytol.* 60, 297–306. doi: 10.1679/aohc.60.297

Jalloul, A. H., Rogasevskaia, T. P., Szerencsei, R. T., and Schnetkamp, P. P. (2016a). A functional study of mutations in K^+-dependent Na^+-Ca^{2+} exchangers associated with amelogenesis imperfecta and non-syndromic Oculocutaneous Albinism. *J. Biol. Chem.* 291, 13113–13123. doi: 10.1074/jbc.M116.728824

Jalloul, A. H., Szerencsei, R. T., and Schnetkamp, P. P. (2016b). Cation dependencies and turnover rates of the human K^+-dependent Na^+-Ca^2 exchangers NCKX1, NCKX2, NCKX3 and NCKX4. *Cell Calcium* 59, 1–11. doi: 10.1016/j.ceca.2015.11.001

Jheon, A. H., Mostowfi, P., Snead, M. L., Ihrie, R. A., Sone, E., Pramparo, T., et al. (2011). PERP regulates enamel formation via effects on cell-cell adhesion and gene expression. *J. Cell Sci.* 124, 745–754. doi: 10.1242/jcs.078071

Josephsen, K., Takano, Y., Frische, S., Praetorius, J., Nielsen, S., Aoba, T., et al. (2010). Ion transporters in secretory and cyclically modulating ameloblasts: a new hypothesis for cellular control of preeruptive enamel maturation. *Am. J. Physiol. Cell Physiol.* 299, C1299–C1307. doi: 10.1152/ajpcell.00218.2010

Khananshvili, D. (2013). The SLC8 gene family of sodium-calcium exchangers (NCX) - structure, function, and regulation in health and disease. *Mol. Aspects Med.* 34, 220–235. doi: 10.1016/j.mam.2012.07.003

Kim, H. J., Prasad, V., Hyung, S. W., Lee, Z. H., Lee, S. W., Bhargava, A., et al. (2012). Plasma membrane calcium ATPase regulates bone mass by fine-tuning osteoclast differentiation and survival. *J. Cell Biol.* 199, 1145–1158. doi: 10.1083/jcb.201204067

Krebs, J. (2009). The influence of calcium signaling on the regulation of alternative splicing. *Biochim. Biophys. Acta* 1793, 979–984. doi: 10.1016/j.bbamcr.2008.12.006

Lacruz, R. S., Smith, C. E., Bringasjr, P., Chen, Y. B., Smith, S. M., Snead, M. L., et al. (2012a). Identification of novel candidate genes involved in mineralization of dental enamel by genome-wide transcript profiling. *J. Cell. Physiol.* 227, 2264–2275. doi: 10.1002/jcp.22965

Lacruz, R. S., Smith, C. E., Kurtz, I., Hubbard, M. J., and Paine, M. L. (2013). New paradigms on the transport functions of maturation-stage ameloblasts. *J. Dent. Res.* 92, 122–129. doi: 10.1177/0022034512470954

Lacruz, R. S., Smith, C. E., Moffatt, P., Chang, E. H., Bromage, T. G., Bringas, P. Jr., et al. (2012b). Requirements for ion and solute transport, and pH regulation during enamel maturation. *J. Cell. Physiol.* 227, 1776–1785. doi: 10.1002/jcp.22911

Lee, G. S., Choi, K. C., and Jeung, E. B. (2009). K^+-dependent Na^+/Ca^{2+} exchanger 3 is involved in renal active calcium transport and is differentially expressed in the mouse kidney. *Am. J. Physiol. Renal Physiol.* 297, F371–F379. doi: 10.1152/ajprenal.90615.2008

Lee, K. H., Ho, W. K., and Lee, S. H. (2013). Endocytosis of somatodendritic NCKX2 is regulated by Src family kinase-dependent tyrosine phosphorylation. *Front. Cell. Neurosci.* 7:14. doi: 10.3389/fncel.2013.00014

Lyaruu, D. M., Bronckers, A. L., Mulder, L., Mardones, P., Medina, J. F., Kellokumpu, S., et al. (2008). The anion exchanger Ae2 is required for enamel maturation in mouse teeth. *Matrix Biol.* 27, 119–127. doi: 10.1016/j.matbio.2007.09.006

Lytton, J. (2007). Na^+/Ca^{2+} exchangers: three mammalian gene families control Ca^{2+} transport. *Biochem. J.* 406, 365–382. doi: 10.1042/BJ20070619

Mondal, M., Sengupta, M., Samanta, S., Sil, A., and Ray, K. (2012). Molecular basis of albinism in India: evaluation of seven potential candidate genes and some new findings. *Gene* 511, 470–474. doi: 10.1016/j.gene.2012.09.012

Nurbaeva, M. K., Eckstein, M., Concepcion, A. R., Smith, C. E., Srikanth, S., Paine, M. L., et al. (2015a). Dental enamel cells express functional SOCE channels. *Sci. Rep.* 5:15803. doi: 10.1038/srep15803

Nurbaeva, M. K., Eckstein, M., Feske, S., and Lacruz, R. S. (2017). Ca^{2+} transport and signalling in enamel cells. *J. Physiol.* 595, 3015–3039. doi: 10.1113/JP272775

Nurbaeva, M. K., Eckstein, M., Snead, M. L., Feske, S., and Lacruz, R. S. (2015b). Store-operated Ca^{2+} entry modulates the expression of enamel genes. *J. Dent. Res.* 94, 1471–1477. doi: 10.1177/0022034515598144

Okumura, R., Shibukawa, Y., Muramatsu, T., Hashimoto, S., Nakagawa, K., Tazaki, M., et al. (2010). Sodium-calcium exchangers in rat ameloblasts. *J. Pharmacol. Sci.* 112, 223–230. doi: 10.1254/jphs.09267FP

Okunade, G. W., Miller, M. L., Pyne, G. J., Sutliff, R. L., O'connor, K. T., Neumann, J. C., et al. (2004). Targeted ablation of plasma membrane Ca^{2+}-ATPase (PMCA) 1 and 4 indicates a major housekeeping function for PMCA1 and a critical role in hyperactivated sperm motility and male fertility for PMCA4. *J. Biol. Chem.* 279, 33742–33750. doi: 10.1074/jbc.M404628200

Orrenius, S., Gogvadze, V., and Zhivotovsky, B. (2015). Calcium and mitochondria in the regulation of cell death. *Biochem. Biophys. Res. Commun.* 460, 72–81. doi: 10.1016/j.bbrc.2015.01.137

Paine, M. L., Wang, H. J., Abuladze, N., Liu, W., Wall, S., Kim, Y. H., et al. (2007). "Expression of AE2 and NBC1 in secretory ameloblasts," in *Experimental Biology Annual Meeting* (Washington, DC).

Palmgren, M. G., and Nissen, P. (2011). P-type ATPases. *Annu. Rev. Biophys.* 40, 243–266. doi: 10.1146/annurev.biophys.093008.131331

Parry, D. A., Poulter, J. A., Logan, C. V., Brookes, S. J., Jafri, H., Ferguson, C. H., et al. (2013). Identification of mutations in SLC24A4, encoding a potassium-dependent sodium/calcium exchanger, as a cause of amelogenesis imperfecta. *Am. J. Hum. Genet.* 92, 307–312. doi: 10.1016/j.ajhg.2013.01.003

Penniston, J. T., Padanyi, R., Paszty, K., Varga, K., Hegedus, L., and Enyedi, A. (2014). Apart from its known function, the plasma membrane Ca^{2+} ATPase can regulate Ca^{2+} signaling by controlling phosphatidylinositol 4,5-bisphosphate levels. *J. Cell Sci.* 127, 72–84. doi: 10.1242/jcs.132548

Pinero, G. J., Parker, S., Rundus, V., Hertzberg, E. L., and Minkoff, R. (1994). Immunolocalization of connexin 43 in the tooth germ of the neonatal rat. *Histochem. J.* 26, 765–770. doi: 10.1007/BF02388633

Riazuddin, S. A., Shahzadi, A., Zeitz, C., Ahmed, Z. M., Ayyagari, R., Chavali, V. R., et al. (2010). A mutation in SLC24A1 implicated in autosomal-recessive congenital stationary night blindness. *Am. J. Hum. Genet.* 87, 523–531. doi: 10.1016/j.ajhg.2010.08.013

Sasaki, T., and Garant, P. R. (1986a). Fate of annular gap junctions in the papillary cells of the enamel organ in the rat incisor. *Cell Tissue Res.* 246, 523–530. doi: 10.1007/BF00215192

Sasaki, T., and Garant, P. R. (1986b). A study of post-secretory maturation ameloblasts in the cat by transmission and freeze-fracture electron-microscopy. *Arch. Oral Biol.* 31, 587–596. doi: 10.1016/0003-9969(86)90082-8

Sasaki, T., and Garant, P. R. (1986c). Ultracytochemical demonstration of ATP-dependent calcium pump in ameloblasts of rat incisor enamel organ. *Calcif. Tissue Int.* 39, 86–96. doi: 10.1007/BF02553296

Sasaki, T., and Garant, P. R. (1986d). An ultrastructural study of the papillary layer and its vascular bed in the kitten enamel organ. *Anat. Rec.* 214, 353–364. doi: 10.1002/ar.1092140404

Sasaki, T., Segawa, K., Takiguchi, R., and Higashi, S. (1984). Intercellular junctions in the cells of the human enamel organ as revealed by freeze-fracture. *Arch. Oral Biol.* 29, 275–286. doi: 10.1016/0003-9969(84)90101-8

Schnetkamp, P. P. (2004). The SLC24 Na^+/Ca^{2+}-K^+ exchanger family: vision and beyond. *Pflugers Arch.* 447, 683–688. doi: 10.1007/s00424-003-1069-0

Schuh, K., Cartwright, E. J., Jankevics, E., Bundschu, K., Liebermann, J., Williams, J. C., et al. (2004). Plasma membrane Ca^{2+} ATPase 4 is required for sperm motility and male fertility. *J. Biol. Chem.* 279, 28220–28226. doi: 10.1074/jbc.M312599200

Seymen, F., Lee, K. E., Tran Le, C. G., Yildirim, M., Gencay, K., Lee, Z. H., et al. (2014). Exonal deletion of SLC24A4 causes hypomaturation amelogenesis imperfecta. *J. Dent. Res.* 93, 366–370. doi: 10.1177/0022034514523786

Sharma, V., and O'halloran, D. M. (2014). Recent structural and functional insights into the family of sodium calcium exchangers. *Genesis* 52, 93–109. doi: 10.1002/dvg.22735

Shumilina, E., Xuan, N. T., Matzner, N., Bhandaru, M., Zemtsova, I. M., and Lang, F. (2010). Regulation of calcium signaling in dendritic cells by 1,25-dihydroxyvitamin D3. *FASEB J.* 24, 1989–1996. doi: 10.1096/fj.09-142265

Skobe, Z. (2006). SEM evidence that one ameloblast secretes one keyhole-shaped enamel rod in monkey teeth. *Eur. J. Oral Sci.* 114, 338–342. doi: 10.1111/j.1600-0722.2006.00305.x

Smith, C. E. (1998). Cellular and chemical events during enamel maturation. *Crit. Rev. Oral Biol. Med.* 9, 128–161. doi: 10.1177/10454411980090020101

Sokolow, S., Manto, M., Gailly, P., Molgo, J., Vandebrouck, C., Vanderwinden, J. M., et al. (2004). Impaired neuromuscular transmission and skeletal muscle fiber necrosis in mice lacking Na/Ca exchanger 3. *J. Clin. Invest.* 113, 265–273. doi: 10.1172/JCI18688

Stephan, A. B., Tobochnik, S., Dibattista, M., Wall, C. M., Reisert, J., and Zhao, H. (2011). The Na^+/Ca^{2+} exchanger NCKX4 governs termination and adaptation of the mammalian olfactory response. *Nat. Neurosci.* 15, 131–137. doi: 10.1038/nn.2943

Street, V. A., Mckee-Johnson, J. W., Fonseca, R. C., Tempel, B. L., and Noben-Trauth, K. (1998). Mutations in a plasma membrane Ca^{2+}-ATPase gene cause deafness in deafwaddler mice. *Nat. Genet.* 19, 390–394. doi: 10.1038/1284

Strehler, E. E. (2013). Plasma membrane calcium ATPases as novel candidates for therapeutic agent development. *J. Pharm. Pharm. Sci.* 16, 190–206. doi: 10.18433/J3Z011

Strehler, E. E., and Zacharias, D. A. (2001). Role of alternative splicing in generating isoform diversity among plasma membrane calcium pumps. *Physiol. Rev.* 81, 21–50.

Takano, Y. (1995). Enamel mineralization and the role of ameloblasts in calcium transport. *Connect. Tissue Res.* 33, 127–137. doi: 10.3109/03008209509016992

Tsuchiya, M., Sharma, R., Tye, C. E., Sugiyama, T., and Bartlett, J. D. (2009). Transforming growth factor-beta1 expression is up-regulated in maturation-stage enamel organ and may induce ameloblast apoptosis. *Eur. J. Oral Sci.* 117, 105–112. doi: 10.1111/j.1600-0722.2009.00612.x

Vinberg, F., Wang, T., Molday, R. S., Chen, J., and Kefalov, V. J. (2015). A new mouse model for stationary night blindness with mutant Slc24a1 explains the pathophysiology of the associated human disease. *Hum. Mol. Genet.* 24, 5915–5929. doi: 10.1093/hmg/ddv319

Wakimoto, K., Kobayashi, K., Kuro, O. M., Yao, A., Iwamoto, T., Yanaka, N., et al. (2000). Targeted disruption of Na^+/Ca^{2+} exchanger gene leads to cardiomyocyte apoptosis and defects in heartbeat. *J. Biol. Chem.* 275, 36991–36998. doi: 10.1074/jbc.M004035200

Wang, S., Choi, M., Richardson, A. S., Reid, B. M., Seymen, F., Yildirim, M., et al. (2014). STIM1 and SLC24A4 are critical for enamel maturation. *J. Dent. Res.* 93, 94S–100S. doi: 10.1177/0022034514527971

Wei, A. H., Zang, D. J., Zhang, Z., Liu, X. Z., He, X., Yang, L., et al. (2013). Exome sequencing identifies SLC24A5 as a candidate gene for nonsyndromic oculocutaneous albinism. *J. Invest. Dermatol.* 133, 1834–1840. doi: 10.1038/jid.2013.49

Wen, X., Lacruz, R. S., Smith, C. E., and Paine, M. L. (2014). Gene-expression profile and localization of Na^+/K^+-ATPase in rat enamel organ cells. *Eur. J. Oral Sci.* 122, 21–26. doi: 10.1111/eos.12106

Yang, H., Kim, T. H., Lee, H. H., Choi, K. C., and Jeung, E. B. (2011). Distinct expression of the calcium exchangers, NCKX3 and NCX1, and their regulation by steroid in the human endometrium during the menstrual cycle. *Reprod. Sci.* 18, 577–585. doi: 10.1177/1933719110396229

Yin, K., Lei, Y., Wen, X., Lacruz, R. S., Soleimani, M., Kurtz, I., et al. (2015). SLC26A gene family participate in ph regulation during enamel maturation. *PLoS ONE* 10:e0144703. doi: 10.1371/journal.pone.0144703

Zacharias, D. A., and Kappen, C. (1999). Developmental expression of the four plasma membrane calcium ATPase (Pmca) genes in the mouse. *Biochim. Biophys. Acta* 1428, 397–405. doi: 10.1016/S0304-4165(99)00058-6

Zaki, A. E., Hand, A. R., Mednieks, M. I., Eisenmann, D. R., and Borke, J. L. (1996). Quantitative immunocytochemistry of Ca^{2+}-Mg^{2+} ATPase in ameloblasts associated with enamel secretion and maturation in the rat incisor. *Adv. Dent. Res.* 10, 245–251. doi: 10.1177/08959374960100022101

Zanni, G., Cali, T., Kalscheuer, V. M., Ottolini, D., Barresi, S., Lebrun, N., et al. (2012). Mutation of plasma membrane Ca^{2+} ATPase isoform 3 in a family with X-linked congenital cerebellar ataxia impairs Ca^{2+} homeostasis. *Proc. Natl. Acad. Sci. U.S.A.* 109, 14514–14519. doi: 10.1073/pnas.1207488109

Zhekova, H., Zhao, C., Schnetkamp, P. P., and Noskov, S. Y. (2016). Characterization of the cation binding sites in the NCKX2 Na^{+}/Ca^{2+}-K^{+} exchanger. *Biochemistry* 55, 6445–6455. doi: 10.1021/acs.biochem.6b00591

Conflict of Interest Statement: The authors declare that the research was conducted in the absence of any commercial or financial relationships that could be construed as a potential conflict of interest.

Copyright © 2017 Robertson, Wen, Yin, Chen, Smith and Paine. This is an open-access article distributed under the terms of the Creative Commons Attribution License (CC BY). The use, distribution or reproduction in other forums is permitted, provided the original author(s) or licensor are credited and that the original publication in this journal is cited, in accordance with accepted academic practice. No use, distribution or reproduction is permitted which does not comply with these terms.

frontiers in Physiology

ORIGINAL RESEARCH
published: 16 May 2017
doi: 10.3389/fphys.2017.00307

Deletion of *Slc26a1* and *Slc26a7* Delays Enamel Mineralization in Mice

*Kaifeng Yin[1,2], Jing Guo[3], Wenting Lin[1], Sarah Y. T. Robertson[1], Manoocher Soleimani[4] and Michael L. Paine[1]**

[1] Center for Craniofacial Molecular Biology, Herman Ostrow School of Dentistry of University of Southern California, Los Angeles, CA, USA, [2] Department of Orthodontics, Herman Ostrow School of Dentistry of University of Southern California, Los Angeles, CA, USA, [3] Department of Endodontics, Herman Ostrow School of Dentistry of University of Southern California, Los Angeles, CA, USA, [4] Department of Medicine, University of Cincinnati, Research Services, Veterans Affairs Medical Center, Cincinnati, OH, USA

Amelogenesis features two major developmental stages—secretory and maturation. During maturation stage, hydroxyapatite deposition and matrix turnover require delicate pH regulatory mechanisms mediated by multiple ion transporters. Several members of the Slc26 gene family (*Slc26a1, Slc26a3, Slc26a4, Slc26a6, and Slc26a7)*, which exhibit bicarbonate transport activities, have been suggested by previous studies to be involved in maturation-stage amelogenesis, especially the key process of pH regulation. However, details regarding the functional role of these genes in enamel formation are yet to be clarified, as none of the separate mutant animal lines demonstrates any discernible enamel defects. Continuing with our previous investigation of *Slc26a1*$^{-/-}$ and *Slc26a7*$^{-/-}$ animal models, we generated a double-mutant animal line with the absence of both *Slc26a1* and *Slc26a7*. We showed in the present study that the double-mutant enamel density was significantly lower in the regions that represent late maturation-, maturation- and secretory-stage enamel development in wild-type mandibular incisors. However, the "maturation" and "secretory" enamel microstructures in double-mutant animals resembled those observed in wild-type secretory and/or pre-secretory stages. Elemental composition analysis revealed a lack of mineral deposition and an accumulation of carbon and chloride in double-mutant enamel. Deletion of *Slc26a1* and *Slc26a7* did not affect the stage-specific morphology of the enamel organ. Finally, compensatory expression of pH regulator genes and ion transporters was detected in maturation-stage enamel organs of double-mutant animals when compared to wild-type. Combined with the findings from our previous study, these data indicate the involvement of SLC26A1and SLC26A7 as key ion transporters in the pH regulatory network during enamel maturation.

Keywords: amelogenesis, enamel maturation, pH regulation, bicarbonate transport, SLC26a1, SLC26A7

OPEN ACCESS

Edited by:
Steven Joseph Brookes, Leeds Dental Institute, UK

Reviewed by:
Eric Everett, University of North Carolina at Chapel Hill, USA
Pamela DenBesten, University of California, San Francisco, USA

***Correspondence:**
Michael L. Paine
paine@usc.edu

Specialty section:
This article was submitted to Craniofacial Biology and Dental Research, a section of the journal Frontiers in Physiology

Received: *16 March 2017*
Accepted: *28 April 2017*
Published: *16 May 2017*

Citation:
Yin K, Guo J, Lin W, Robertson SYT, Soleimani M and Paine ML (2017) Deletion of Slc26a1 and Slc26a7 Delays Enamel Mineralization in Mice. Front. Physiol. 8:307. doi: 10.3389/fphys.2017.00307

INTRODUCTION

Acid-base balance is one of the major essential processes during amelogenesis (Simmer and Fincham, 1995; Smith et al., 1996; Smith and Nanci, 1996; Lacruz et al., 2010a, 2012b), and it has been suggested that fluctuations in extracellular pH level during maturation-stage enamel development are essential for mineral growth (Simmer and Fincham, 1995). Digestion of enamel

matrix proteins (EMPs) through the endosome/lysosome pathway, following trafficking from the enamel space, relies highly on the acidic intracellular luminal environment (Lloyd, 1996). Previous studies have identified the functional role of several groups of genes, including carbonic anhydrases (Lezot et al., 2008), cystic fibrosis transmembrane conductance regulator (CFTR), chloride channels (CLCNs), solute carrier gene family 4 (SLC4s) and solute carrier gene family 9 (SLC9s), in maintaining the ameloblast-mediated pH homeostasis within both extracellular space and intracellular lumens (Dogterom and Bronckers, 1983; Lin et al., 1994; Wright et al., 1996a,b; Arquitt et al., 2002; Lyaruu et al., 2008; Paine et al., 2008; Bronckers et al., 2009, 2010; Josephsen et al., 2010; Wang et al., 2010; Lacruz et al., 2010a,b, 2012c, 2013a; Chang et al., 2011; Duan et al., 2011; Duan, 2014; Jalali et al., 2014; Reibring et al., 2014; Wen et al., 2014).

The solute carrier (SLC) 26A gene family encodes multiple anion transporters with chloride/bicarbonate exchanger activities (Xie et al., 2002; Petrovic et al., 2003a,b, 2004; Alper and Sharma, 2013). Animal models with mutations of *Slc26a1*, *Slc26a6,* and *Slc26a7* exhibit disorders featuring disruption of ion homeostasis, such as urolithiasis, hepatotoxicity, renal tubular acidosis and impaired gastric secretion (Freel et al., 2006; Jiang et al., 2006; Xu et al., 2009; Dawson et al., 2010). Based on our previous study and those of Bronckers et al., Slc26a1/Sat1, Slc26a3/Dra, Slc26a4/pendrin, Slc26a6/Pat1 and Slc26a7/Sut1 are immunolocalized in secretory- and maturation-stage ameloblasts (Bronckers et al., 2011; Jalali et al., 2015; Yin et al., 2015). In particular, these genes mainly localize to the apical membrane/subapical vesicles of maturation ameloblast. In addition, the expression of Slc26a1, Slc26a6, and Slc26a7 is significantly upregulated at both RNA and protein levels during maturation stage compared to secretory stage (Yin et al., 2014, 2015). These are strong indications of the functional involvement of the Slc26 gene family in pH regulation during amelogenesis. However, the deletion of these genes individually fails to induce any abnormal enamel phenotypes, likely due to the compensatory expression of other pH regulatory genes and Slc26a isoforms, suggesting a yet-to-be-identified master pH response regulatory mechanism in amelogenesis (Bronckers et al., 2011; Jalali et al., 2015; Yin et al., 2015).

In this study, we generated an animal model with the absence of both *Slc26a1* and *Slc26a7* by breeding homozygous parents ($Slc26a1^{-/-}$ and $Slc26a7^{-/-}$). We showed that the double-null enamel density was significantly lower in the regions that represent late maturation-, maturation-, and secretory-stage enamel development in wild-type mandibular incisors. However, the "maturation" and "secretory" enamel microstructures in double-mutant animals resembled those observed in wild-type secretory and/or pre-secretory stages. Elemental composition analysis revealed a lack of mineral deposition and an accumulation of carbon and chloride in double-mutant enamel, although absence of *Slc26a1* and *Slc26a7* did not affect the stage-specific morphology of the enamel organ including ameloblasts. Finally, compensatory expression of pH regulators and ion transporters at RNA level was detected in maturation-stage enamel organs of double-mutant animals. Taken together, the data obtained from double mutant animals ($Slc26a1^{-/-}$ and $Slc26a7^{-/-}$) provide new evidence from a functional perspective to support the hypothesis that SLC26A1/SAT1 and SLC26A7/SUT1 are actively involved in ameloblast-mediated pH regulation during maturation-stage amelogenesis.

MATERIALS AND METHODS

Animals

All vertebrate animal manipulation was carried out in accordance with Institutional and Federal guidelines. The animal protocols were approved by the Institutional Animal Care and Use Committee at the University of Southern California (Protocol # 11736). For immunofluorescence analysis, we dissected mandibles and kidneys from rats (Wistar Hannover, 4-week, 100–110 g). $Slc26a1^{+/-}$ mice were purchased from the Jackson Laboratory (stock # 012892) and $Slc26a7^{+/-}$ mice were a kind gift from Dr. Manoocher Soleimani (Xu et al., 2009; Dawson et al., 2010). $Slc26a1^{-/-}$ and $Slc26a7^{-/-}$ mice were generated by breeding heterozygous ($Slc26a1^{+/-}$ or $Slc26a7^{+/-}$) parents. To generate double-mutant animals with the absence of *Slc26a1* and *Slc26a7*, we crossed $Slc26a1^{-/-}$ and $Slc26a7^{-/-}$ mice. The double-mutant lines were genotyped by PCR using primers designed in earlier studies (Xu et al., 2009; Dawson et al., 2010).

Immunofluorescence

The expression patterns of Slc26a1 and Slc26a7 in maturation-stage ameloblasts were shown by co-localization using immunofluorescence (IF). Hemi-mandibles and kidneys obtained from Wistar Hannover rats (100–110 g body weight, 4 weeks old) were fixed in 4% paraformaldehyde (PFA) at 4°C overnight. The hemi-mandibles were then decalcified in 10% EDTA (pH 7.4) for 2 months. Sagittal sections were prepared from paraffin-embedded tissue blocks with a thickness of 7 μm. After being dewaxed, rehydrated and blocked by 1% bovine serum albumin (BSA) in PBST (1X, pH 7.4), the tissue sections were incubated with primary antibodies against Slc26a1 (Santa Cruz Biotechnology, Catalog # sc-132090, dilution 1:400) and Slc26a7 (Abcam, Catalog # ab65367, dilution 1:300). All tissue sections were stained with DAPI (Vector Laboratories; Catalog # H-1200) before cover slides were applied.

μCT Analysis

Mandibles were dissected from 4-week-old double-mutant animals and their age-matched wild-type controls. Samples from 12 animals in each group were prepared for μCT analysis ($n = 12$, SkyScan 1174) with the scanner setting to 50 kVp, 800 μA, and 6.7 μm resolution. The reconstruction and calculation of the enamel density of mandibular incisors and first molars were performed with Amira 3D Visualization and Analysis Software 5.4.3 (FEI Visualization Science Group, Burlington, MA, USA) (Wen et al., 2015). The potential statistical differences in the relative enamel density between double-mutant and wild-type groups were evaluated by a two-tailed Student's *t*-test using IBM SPSS Statistics 22.0 (significance level defined as $P < 0.05$).

Scanning Electron Microscopy and Energy-dispersive X-ray Spectroscopy (EDS)

The hemi-mandibles prepared for μCT analysis ($n = 12$) were used for the subsequent SEM and EDS analyses. The samples were scanned and imaged by SEM and EDS according to previously published protocols (Lacruz et al., 2010b; Wen et al., 2014; Yin et al., 2015).

Hematoxylin and Eosin (H & E) Staining

Mandibles were dissected from 4-week-old double-mutant animals and wild-type controls for H & E staining. The protocols followed those described in a previous study (Lacruz et al., 2012a).

Realtime PCR Analysis

RNA samples of maturation-stage enamel organs were extracted from mandibles of double-mutant and wild-type animals ($n = 6$) using a method described previously (Yin et al., 2015). cDNA used for real-time PCR analysis was prepared using the miScript II RT Kit with miScript HiFlex Buffer (Qiagen). To detect the expression changes in the genes that have been identified to be involved in maturation-stage pH regulation (Dogterom and Bronckers, 1983; Wright et al., 1996a,b; Andrejewski et al., 1999; Arquitt et al., 2002; Lyaruu et al., 2008; Paine et al., 2008; Bertrand et al., 2009; Bronckers et al., 2009, 2010, 2011; Josephsen et al., 2010; Wang et al., 2010; Lacruz et al., 2010a,b, 2011, 2012b,c, 2013b; Chang et al., 2011; Duan, 2014; Jalali et al., 2014; Yin et al., 2014, 2015), real-time PCR reactions were performed on a CFX96 TouchTM Real-Time PCR Detection System (Bio-rad Life Sciences) with iQ SYBR® Green supermix (Bio-rad Life Science) and mouse-specific primers (**Table 1**). The Ct values were normalized to those of *Actb* (*Beta-actin*). The ΔΔCt method was used to calculate the fold changes in gene expression (double-mutant relative to wild-type; Livak and Schmittgen, 2001; Schmittgen and Livak, 2008). Two-tailed Student's *t*-tests were used to detect the potential differences in the expression levels of gene transcripts between double-mutant and wild-type groups (significance level defined as $P < 0.05$). Data were analyzed using IBM SPSS Statistics 22.0 software.

RESULTS

SLC26A1 and SLC26A7 Do Not Colocalize in Maturation-Stage Ameloblasts

We revisited the expression patterns of SLC26A1 and SLC26A7 in rodent maturation-stage ameloblasts by conducting colocalization analysis using immunofluorescence. The expression of Slc26a1 was mainly immunolocalized to the apical membrane of maturation ameloblast (**Figure 1A**). In contrast, SLC26A7 showed more expression in the cytoplasmic area in addition to an apical/subapical distribution (**Figure 1A**). No apparent overlaps in fluorescence signals from SLC26A1 and SLC26A7 were observed (**Figure 1A**). Tissue sections prepared from rat kidneys were stained with the same antibodies as a reference (**Figure 1B**).

Double-Mutant Mandibular Incisors Demonstrate Decreased Enamel Density

We dissected hemi-mandibles from 4-week-old double-mutant animals and their age-matched wild-type controls for μCT analysis. After 3D reconstruction from raw dicom files, we selected three regions to analyze the enamel density of incisors, which were indicated by the three reference planes along the long axis of the mandibular incisors (**Figure 2**). The first reference plane was placed at the region where bony support ends (**Figures 2A3,B3**). The second and the third reference planes sectioned though the first and the third mandibular

TABLE 1 | Mouse-specific primers for qPCR.

Symbol	Accession	Region	Forward (5′–3′)	Reverse (5′–3′)
Car2	NM_009801	4–173	TCCCACCACTGGGGATACAG	CTCTTGGACGCAGCTTTATCATA
Car6	NM_009802	61–160	TGGAGCTATTCAGGGGATGATG	CCGTCTTCACGTCGATGGG
Cftr	NM_021050	957–1,132	GCATATTGTTGGGAATCAGC	ACGATTCCGTTGATGACTGT
Ae2	NM_009207	3,282–3,523	CATGGAGACACAGATCACCA	GCTGTTCCTTGACTTCCTGA
Ae4	NM_172830	10-127	CCAGGGCAGGGGGATTTTG	CCCCAATGTCTATGCCTGAGG
NBCe1	NM_018760	246–489	CTCCGAGAACTACTCCGACA	ACCCTGCTCCACTTTCTCTT
Slc26a6	NM_134420	2,023–2,184	TTGCTGGAGCTGTATCTTCC	TGTTTGCCTTCCAAAGAGAG
Lamp1	NM_010684	930–1,076	TCTATGGCACTGCAACTGAA	GGCTCTGTTCTTGTTCTCCA
Lamp2	NM_001017959	785–916	AACTTCAACACCCACTCCAA	AAAGGCACCTTCTCCTCAGT
Lamp3	NM_007653	598–809	CACAGACTGGGAAAACATCC	TAATTCCCAAGACCTCCACA
Lamp4	NM_009853	630–811	ACATCAGAGCCCGAGTACAG	GGTGAACAGCTGGAGAAAGA
Clcn7	NM_011930	316–477	CCAAGGAGATTCCACACAAC	CAATGAGGGCACAGATAACC
Rab21	NM_024454	723–963	TCCGCTAAACAGAACAAAGG	GGCAATGATCCACAGTTCTC
Alpl	NM_007431	2,228–2,472	TCTGCTCAGGATGAGACTCC	TCCCTTTTAACCAACACCAA
Nhe1	NM_016981.2	780–972	CATCCTTGTCTTCGGGGAGTC	GGAGGTGAAAGCTGCGATTAC
Actb	NM_007393	792–951	AAGAGCTATGAGCTGCCTGA	TACGGATGTCAACGTCACAC

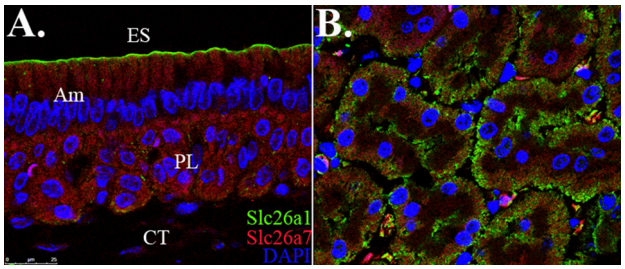

FIGURE 1 | *Colocalization analysis of Slc26a1 with Slc26a7.* ES, Enamel space; Am, Ameloblast; PL, Papillary layer; CT, Connective tissue. **(A)** Colocalization of SLC26A1and SLC26A7 in maturation-stage ameloblasts by confocal microscopy at 63x magnification. SLC26A1 immunolocalized to the apical membrane of maturation-stage ameloblasts. SLC26A7 showed more expression in the cytoplasmic area in addition to an apical/subapical distribution. Apparent overlaps in fluorescence from SLC26A1 and SLC26A7 were not observed. **(B)** Tissue sections prepared from rat kidneys were stained with the same antibodies as a reference. All sections were counterstained with DAPI to highlight the nuclei (blue).

molars (**Figures 2A5,A7,B5,B7**). The three reference planes from anterior to posterior represent late-maturation, maturation and secretory stages, respectively (Nanci, 2008; Lacruz et al., 2011, 2012b; Yin et al., 2014, 2015). In a 4-week-old wild-type mouse, the enamel of the mandibular incisor is fully mature (maturation-stage) between the first and the second reference planes (**Figures 2A2–A6**) (Yin et al., 2015). In contrast, the double-mutant enamel at the first and second reference planes showed statistically significant decreases in relative density (**Figures 2B2–B6**, **3A,B**, $P < 0.05$). The double-mutant enamel density was approximately 14.3% lower than wild-type enamel density at the first reference plane (**Figure 3A**). At the second reference plane, the density gap between double-mutant and wild-type enamel was even higher—35.7% (**Figure 3B**). The enamel on mandibular incisors at the third reference plane is in secretory stage in wild-type animals (Yin et al., 2015), and the difference in relative enamel density of incisors was not statistically significant between wild-type and double-mutant groups (**Figures 2A8,B8**, **3C**).

Based on μCT analysis, we also quantified the relative density of mandibular first molars. For calculating the enamel density of each molar, we averaged the measurements obtained from mesial, middle and distal cusps (**Figure 4**). Although the double-mutant molars demonstrated lower enamel density than wild-type molars, the differences were not statistically significant (**Figure 4C**, $P = 0.35$).

Absence of *Slc26a1* and *Slc26a7* Disrupts Development of Enamel Microstructure

For SEM analysis, we used the same reference planes as in the μCT analysis (**Figures 2**, **5**). We exposed the surface of interest by fracturing the mandibular incisors in the coronal direction, which was consistent with the orientation of the reference planes. At the first and the second reference planes, wild-type enamel showed typical microstructure of maturation-stage enamel with rods and interrods laid out in a decussating and orderly pattern (**Figures 5A1,A1',B1,B1'**). In wild-type enamel at secretory stage, which was marked by the third reference plane, enamel rods did not reach full thickness and the boundary between rod and interrod structure was not yet well defined (**Figures 5C1,C1**). In comparison, the structure of double-mutant enamel at the first and the second reference planes was similar to that observed at the second and the third reference planes in wild-type group, respectively (**Figures 5A2,A2',B2,B2'**), suggesting the double knockout animals showed a delay in maturation. Furthermore, there was a complete lack of decussating pattern in double-mutant enamel in the region labeled by the third reference plane, and aprismatic enamel/enamel-like structure dominated the whole vision field (**Figures 5C2,C2′**).

Double Mutations Impact Mineral Deposition

Following SEM, we analyzed the elemental compositions using EDS on the same regions of mandibular incisor enamel marked by the three previously mentioned reference planes (**Figures 2**, **5**). At the first reference plane, there were no statistically significant differences between wild-type and double-mutant enamel in the atomic percentages (At%) of all the elements analyzed—Ca, P, O, C, Cl, Na, and Mg (**Figures 6A1–A3**). At the second reference plane, statistically significant changes were detected in the At% of Ca, P, C, and Cl (**Figures 6B1–B3**). The At% of Ca and P in double-mutant enamel decreased by ∼26.7 and ∼35.1%, respectively, compared to those in wild-type enamel (**Figures 6B1–B3**), while there were increases in the At% of C and Cl— ∼268.4 and ∼18.6%, respectively (double-mutant/wild-type, **Figures 6B1–B3**). Changes in the elemental compositions at the third reference plane showed similar trends to those detected at the second reference plane—double-mutant enamel showed significantly lower At% of Ca, P, O, Mg (∼92.8, ∼69.2, ∼29.6, and ∼57.9%, **Figures 6B1–C3**), and higher At% of C and Cl (∼20.0 and ∼35.6%, **Figures 6B1–C3**).

Deletion of *Slc26a1* and *Slc26a7* Does Not Affect Morphology of Ameloblasts

We prepared tissue sections from 4-week-old mouse mandibles (wild-type and double-mutant) for H & E staining. At the regions marked by the three reference planes, wild-type enamel organs demonstrated typical morphology of ameloblasts in late-maturation, maturation, and secretory stages (**Figures 7A1–A3**). Compared with the findings in the wild-type group, cell morphology in double-mutant enamel organs in the same regions was not significantly different (**Figures 7B1–B3**).

pH Regulators Show Compensatory Expression in Double-Mutant Animals

The expression levels of 16 genes involved in pH regulation and ion transport during maturation-stage amelogenesis were quantified by realtime PCR using RNA samples isolated from wild-type and double-mutant maturation-stage enamel organs. Significant upregulation was detected for all the genes quantified (double-mutant/wild-type, **Figure 8**). Note that *Ae4* and *Slc26a9* showed the most striking fold changes—∼70.5 and ∼83.0%,

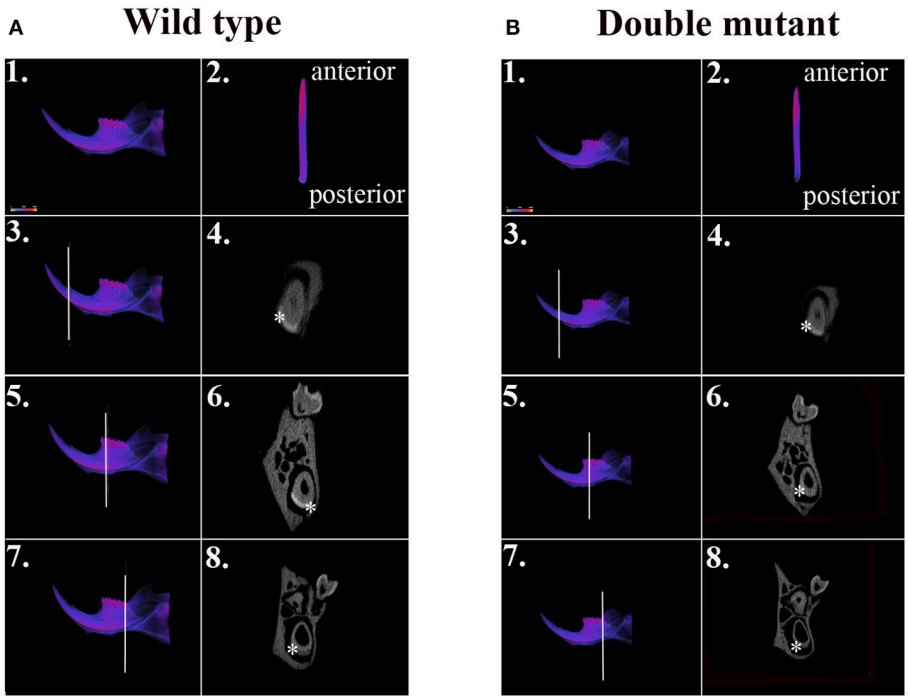

FIGURE 2 | μCT analysis of wild-type and double-mutant mandibular incisors. (A1) Wild-type semi-mandible. **(A2)** Wild-type incisor viewed from the labial surface. **(B1)** Double-mutant semi-mandible. **(B2)** Double-mutant incisor viewed from the labial surface. We selected three regions to analyze the enamel density of incisors, which are indicated by the three reference planes along the long axis of mandibular incisors. The first reference plane was placed at the region where bony support begins **(A3,B3)**. The second and the third reference planes sectioned though the first **(A5,B5)** and the third mandibular molars **(A7,B7)**. In the wild-type sample, the three reference planes from anterior to posterior represent late maturation, maturation and secretory stages, respectively. **(A4,A6,A8,B4,B6,B8)** Are cross-sectional views of the regions of the three reference planes. Colors varying from blue to red in **(A1–A3,A5,A7,B1–B3,B5,B7)** indicate an increase in density. The area of mandibular incisor enamel is labeled by * in **(A4,A6,A8,B4,B6,B8)**.

respectively (**Figure 8B**), and the fold changes for the remaining genes were all above 2, except for *Lamp3*, *Rab21,* and *Nhe1* (**Figure 8B**).

DISCUSSION

Enamel formation during maturation-stage amelogenesis involves mineral deposition, crystal growth, protease activities and the degradation of the internalized organic matrix, all of which are highly pH-dependent (Simmer and Fincham, 1995; Smith et al., 1996; Smith and Nanci, 1996; Lacruz et al., 2010a, 2012b). Acid-base balance in the extracellular matrix and intracellular lumens is maintained by a complex regulatory network involving multiple ion transporters and carbonic anhydrases (Dogterom and Bronckers, 1983; Lin et al., 1994; Wright et al., 1996a,b; Arquitt et al., 2002; Lyaruu et al., 2008; Paine et al., 2008; Bronckers et al., 2009, 2010; Josephsen et al., 2010; Wang et al., 2010; Lacruz et al., 2010a,b, 2012c, 2013a; Chang et al., 2011; Duan et al., 2011; Duan, 2014; Jalali et al., 2014; Reibring et al., 2014; Wen et al., 2014). Although details regarding the mechanism of pH control are yet to be clarified, the critical roles of many genes in maturation-stage pH regulation have been implicated by previous studies on transgenic animal models. For example, NBCe1 is a sodium-bicarbonate cotransporter expressed mainly on the basolateral membrane of maturation-stage ameloblasts (Lacruz et al., 2010b; Jalali et al., 2014). *NBCe1*$^{-/-}$ animals demonstrated hypomineralized and weak enamel with an abnormal prismatic architecture. Severe enamel phenotypes have also been documented from *Cftr*$^{-/-}$ and *Ae2*$^{-/-}$ animals (Arquitt et al., 2002; Lyaruu et al., 2008; Bronckers et al., 2010; Chang et al., 2011). Bronckers et al. started to investigate the role of Slc26 family genes in tooth enamel formation in 2011 (Bronckers et al., 2011). Since then, all the animal studies on Slc26 mutations have reach similar conclusions: mutation or silencing of individual Slc26 gene members (*Slc26a1, Slc26a3, Slc26a4, Slc26a6,* and *Slc26a7*) is not sufficient to generate abnormal enamel phenotypes, yet the deletion of a single *Slc26* gene can induce strong compensatory expression of other pH regulatory genes and SLC26 family members (Bronckers et al., 2011; Jalali et al., 2015; Yin et al., 2015).

In the present study, we continued with our previous investigation of *Slc26a1*$^{-/-}$ and *Slc26a7*$^{-/-}$ animal models. We generated a double-null animal line with the absence of both *Slc26a1* and *Slc26a7* (*Slc26a1*$^{-/-}$/*Slc26a7*$^{-/-}$). The enamel density of double-null animals was significantly lower in the regions that represent late maturation-, maturation- and

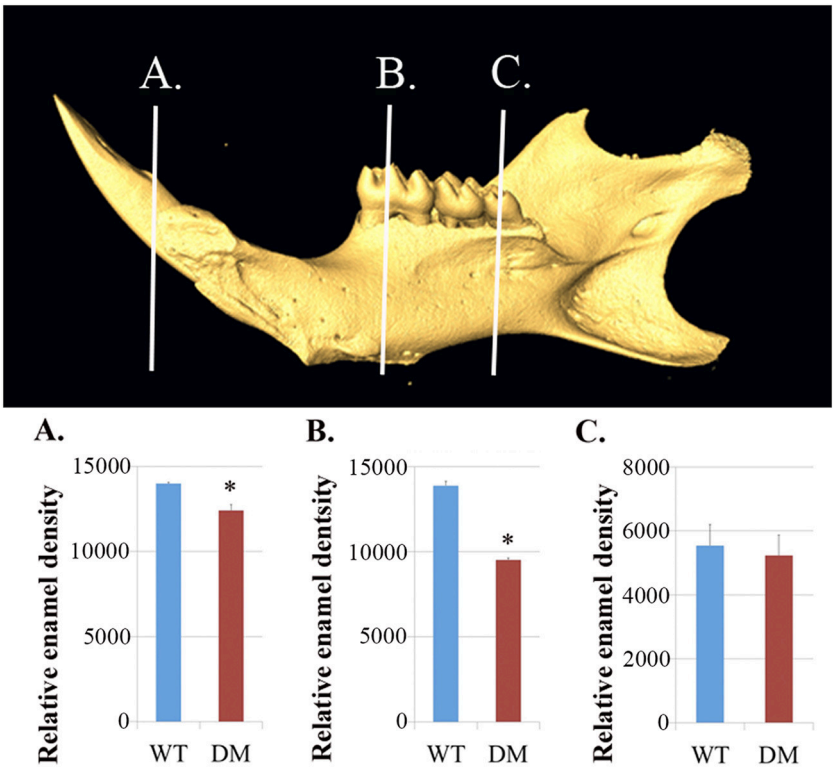

FIGURE 3 | Quantification of enamel density in wild-type and double-mutant mandibular incisors. WT, Wild-type; DM, Double-mutant. **(A)** At the first reference plane, the double-mutant enamel density was approximately 14.3% lower than that of wild-type enamel ($P = 0.015$). **(B)** At the second reference plane, the density gap between double-mutant and wild-type enamel was even higher—35.7% ($P = 0.010$). **(C)** The difference in relative enamel density of mandibular incisors was not significant between the wild-type and double-mutant groups ($P = 0.56$). *$P < 0.05$.

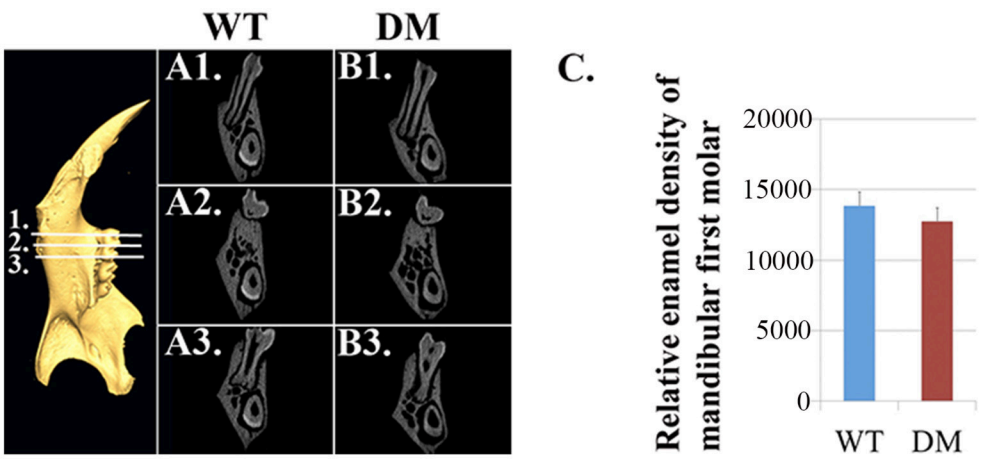

FIGURE 4 | Quantification of enamel density in wild-type and double-mutant mandibular first molars. WT, Wild-type; DM, Double-mutant. **(A1–A3)** Cross-sectional views of wild-type hemi-mandible at reference planes 1, 2 and 3. **(B1–B3)** Cross-sectional views of double-mutant hemi-mandible at reference planes 1, 2, and 3. **(C)** We averaged the measurements obtained from mesial, middle and distal cusps (reference planes 1, 2, and 3). The double-mutant molars demonstrated lower enamel density than wild-type molars, but the difference was not statistically significant ($P = 0.35$).

secretory-stage enamel development in age-matched wild-type siblings (**Figures 2**, **3**). However, the difference in enamel density between double-mutant and wild-type mandibular first molars was not statistically significant, which suggests that incisor and molar maturation events differ to some extent (**Figure 4**). In addition, the "maturation" and "secretory"

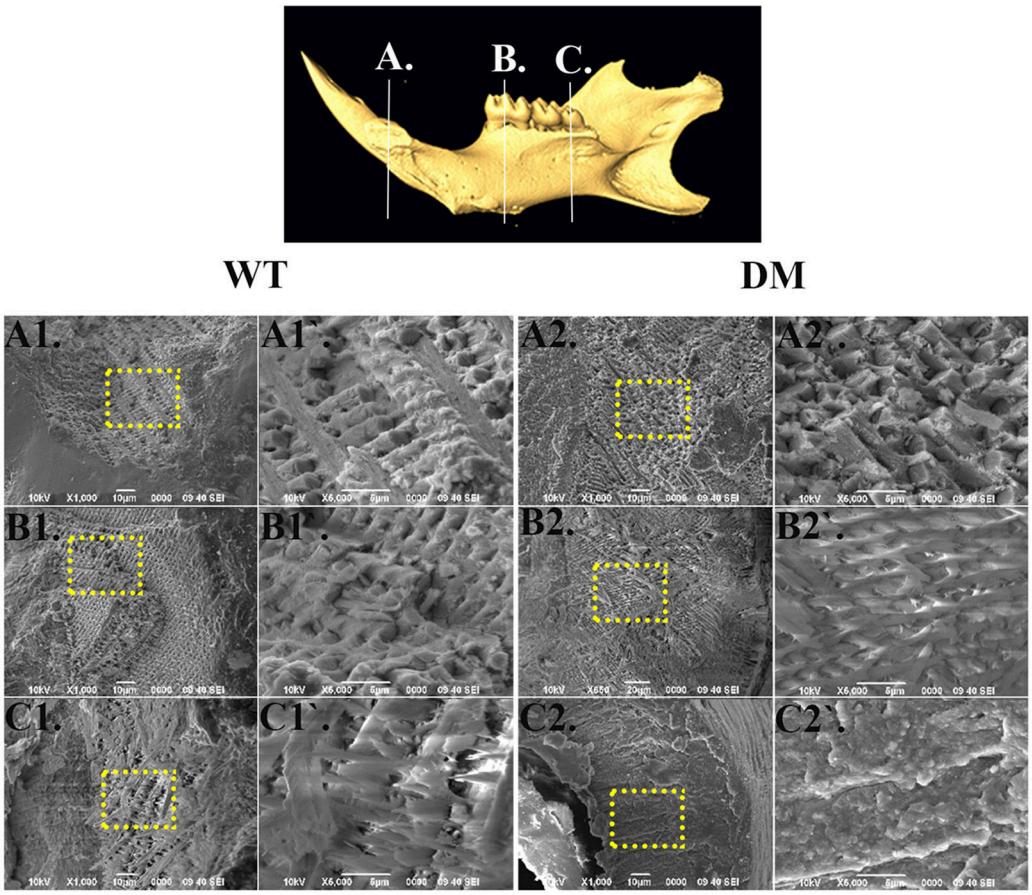

FIGURE 5 | SEM analysis of enamel microstructures in wild-type and double-mutant mandibular incisors. WT, Wild-type; DT, Double-mutant. **(A1–C1)** Wild-type enamel at reference planes A, B, and C under 1000x magnification. **(A1'–C1')** The areas in **(A1–B1)** labeled with dotted frames under 5000x magnification. (**A2–C2)** Double-mutant enamel at the reference planes A, B, and C under 1000x magnification. **(A2'–C2')** The areas in **(A2–B2)** labeled with dotted frames under 5000x magnification. At the first and the second reference planes, wild-type enamel showed typical microstructure of maturation-stage enamel with rods and interrods laid out in a decussating and orderly pattern **(A1,A1',B1,B1)**. In wild-type enamel at secretory stage, marked by the third reference plane, enamel rods did not reach full thickness and the boundary between rod and interrod structure was not yet well defined **(C1,C1)**. In comparison, the structure of double-mutant enamel at the first and the second reference planes was similar to that observed at the second and the third reference planes, respectively, in the wild-type group **(A2,A2,B2,B2)**. There was a complete lack of decussating pattern in double-mutant enamel in the region labeled by the third reference plane, and aprismatic enamel/enamel-like structure dominated the whole vision field **(C2,C2)**.

enamel microstructures in double-mutant animals resembled those observed in wild-type secretory and/or pre-secretory stages (**Figure 5**). This indicates that deletion of *Slc26a1* and *Slc26a7* delayed enamel development in mandibular incisors, although such an impact was not observed after full eruption of the mandibular first molars in double-mutant animals (only data from 4-week-old animals are shown in **Figure 4**). Subsequent elemental composition analysis of double-mutant incisors revealed that decreased enamel density could be attributed to a lack of mineral deposition (Ca^{2+} and HPO_3, **Figure 6**). The accumulation of Cl^- in double-mutant enamel was consistent with our previous findings in *Slc26a1*$^{-/-}$ and *Slc26a7*$^{-/-}$ animals (Yin et al., 2015), while the increase of carbon in double-mutant enamel is a possible manifestation of disrupted EMP retrieval and hydrolysis (**Figure 6**). These findings indicate functional redundancy within the SLC26 gene family, and also in the scope of the pH regulatory network during enamel maturation (Yin et al., 2015). Such a redundancy is not uncommon in developmental processes and pathogenesis of diseases, e.g., matrix metalloproteinases (MMPs) in embryonic development and amyloid precursor protein (APP) genes in Alzheimer's disease (Heber et al., 2000; Page-McCaw et al., 2007).

Amelogenesis imperfecta (AI) is the most severe inherited disorder among all enamel pathologies. The genes responsible for AI in human patients include *AMELX, AMBN, ENAM, MMP20, KLK4, WDR72, FAM83H, LAMB3, ITGB6, and SLC24A4*, and current evidence tends to support a single-gene origin for many AI cases (Aldred et al., 1992; Lench et al., 1994; Lagerstrom-Fermer and Landegren, 1995; Lagerstrom-Fermer et al., 1995; Collier et al., 1997; MacDougall et al., 1997; Hart et al., 2000,

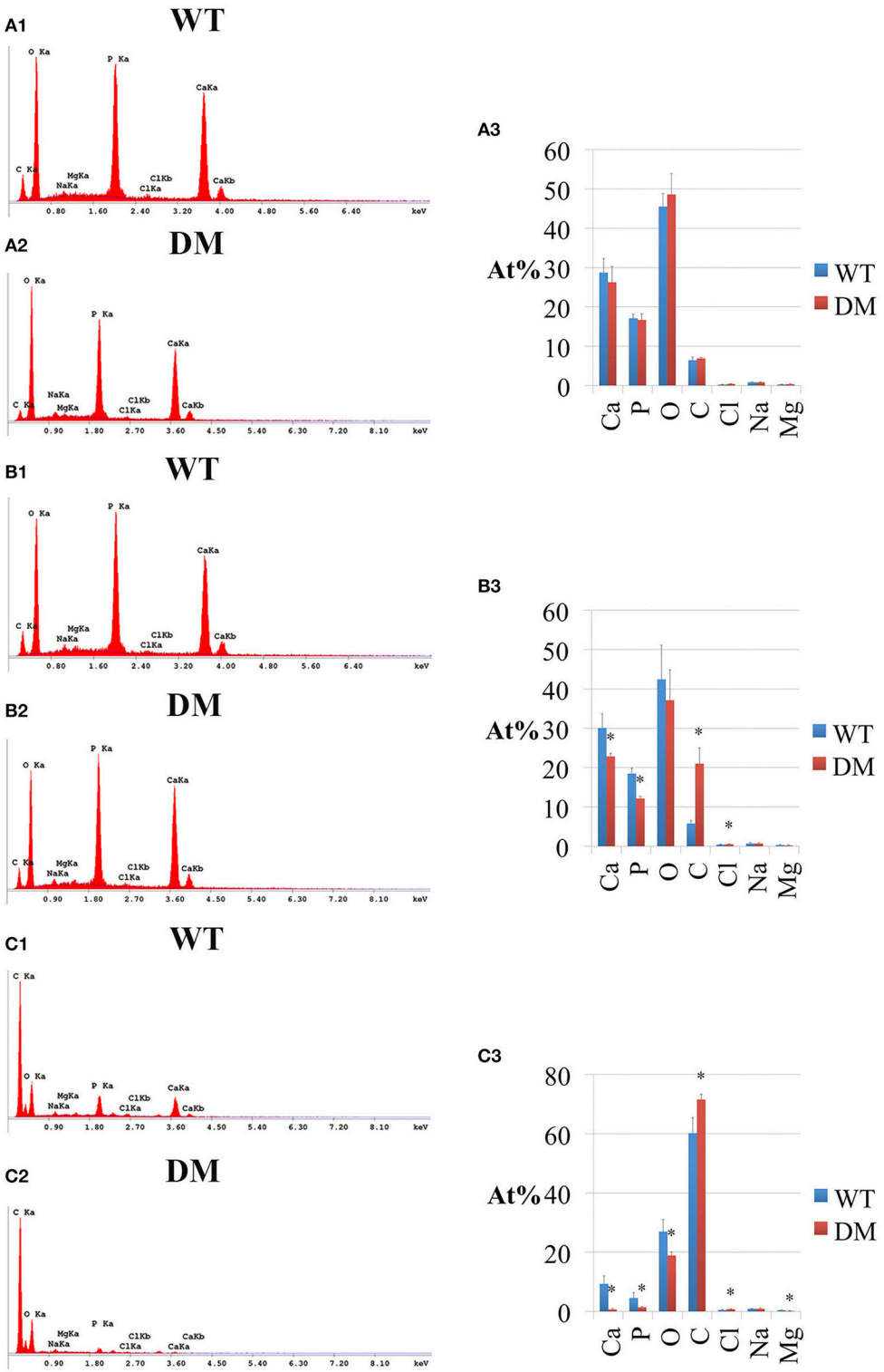

FIGURE 6 | EDS analysis of enamel in wild-type and double-mutant mandibular incisors. WT, Wild-type; DM, Double-mutant; At%, Atomic percentage. **(A1,A2)** EDS spectrum of enamel at the first reference plane. **(A3)** Between wild-type and double-mutant enamel at the first reference plane, there were no statistically significant differences in the atomic percentages (At%) of all the elements analyzed—Ca, P, O, C, Cl, Na, and Mg. **(B1,B2)** EDS spectrum of enamel at the second reference plane. **(B3)** Statistically significant changes were detected in the At% of Ca, P, C, and Cl. The At% of Ca and P in double-mutant enamel decreased by ∼26.7 and ∼35.1%, respectively, compared to those in wild-type enamel. There were increases in the At% of C and Cl— ∼268.4 and ∼18.6%, respectively (double-mutant/wild-type). **(C1,C2)** EDS spectrum of enamel at the third reference plane. **(C3)** Double-mutant enamel showed significantly lower At% of Ca, P, O, Mg (∼92.8, ∼69.2, ∼29.6, and ∼57.9%), and higher At% of C and Cl (∼20.0 and ∼35.6%).

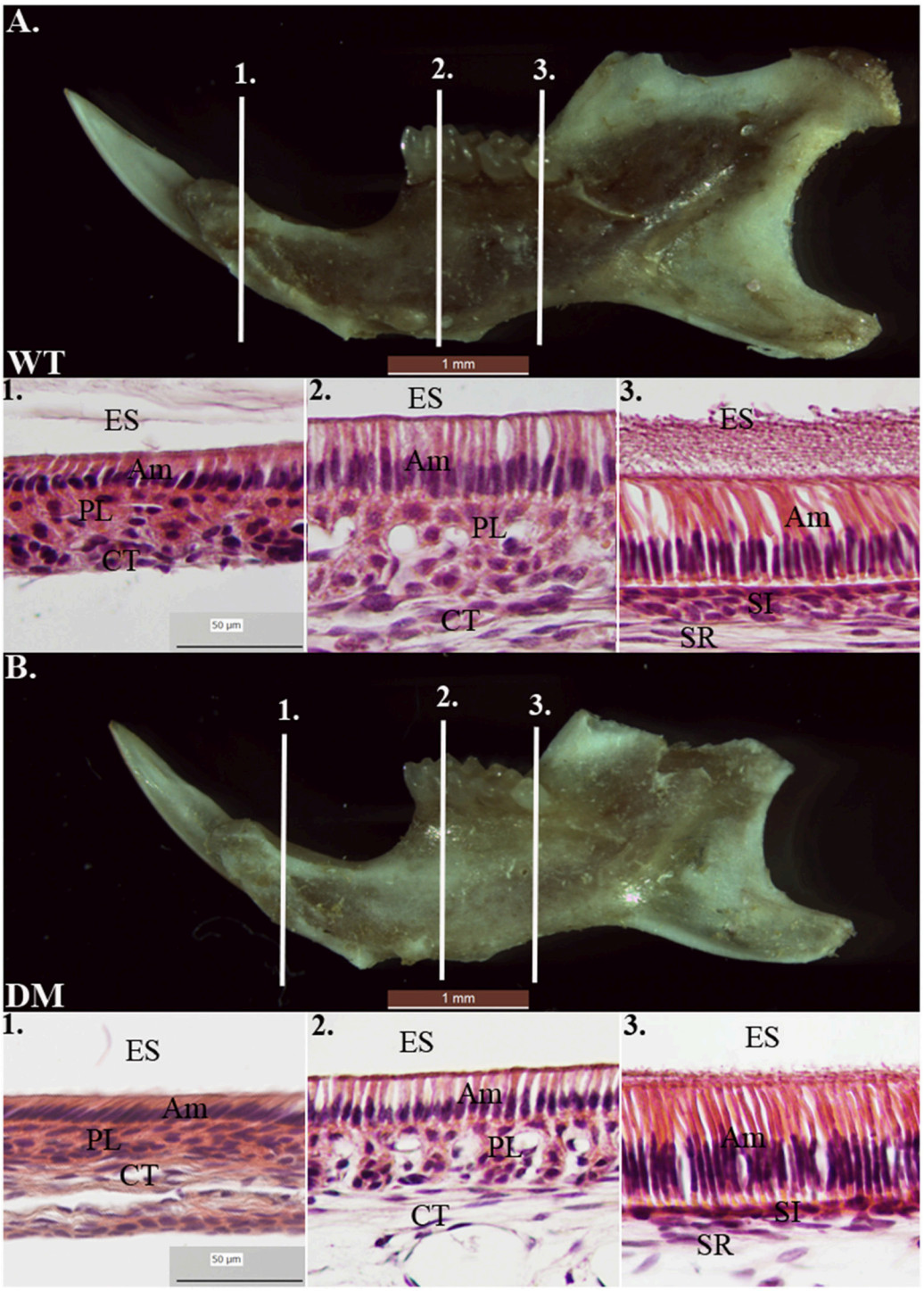

FIGURE 7 | Histological analysis of wild-type and double-mutant enamel organs by H& E staining. WT, Wild-type; DM, Double-mutant; ES, Enamel space; Am, Ameloblast; PL, Papillary layer; CT, Connective tissue; SI, Stratum intermedium; SR, Stellate reticulum. **(A1–A3)** Wild-type enamel organ in late-maturation, maturation and secretory stages (labeled by three reference planes 1, 2, and 3). **(B1–B3)** Double-mutant enamel organ at the three reference planes. Magnification 40x. Compared to the wild-type group, cell morphology in double-mutant enamel organs in the same regions was not significantly different.

2003, 2004, 2009; Kindelan et al., 2000; Mardh et al., 2002; Kim et al., 2004, 2005, 2008, 2013; El-Sayed et al., 2009; Wright et al., 2009; Poulter et al., 2014a,b,c; Wang S. et al., 2014; Wang S. K. et al., 2014; Herzog et al., 2015). Our data from the double-mutant animals (*Slc26a1*$^{-/-}$/*Slc26a7*$^{-/-}$) suggest that polygenic etiologic factors might also be involved

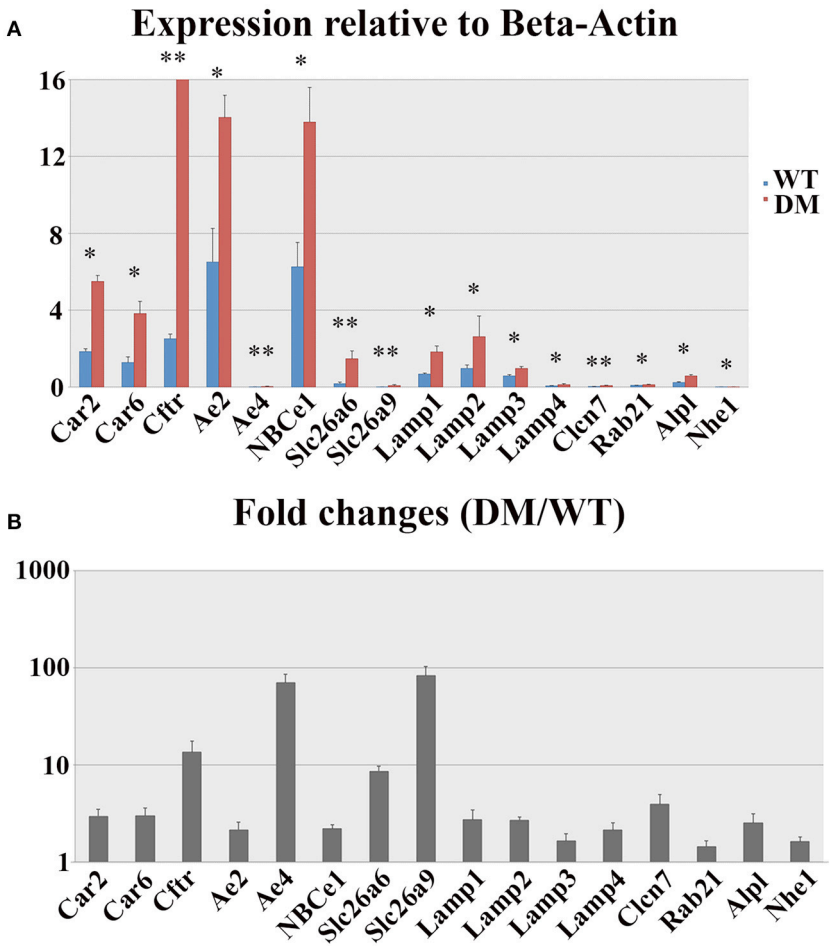

FIGURE 8 | Realtime PCR analysis of gene expression in wild-type and double-mutant maturation enamel organs. WT, Wild-type; DM, Double-mutant. **(A)** Relative expression values normalized to that of *Beta-Actin*. **(B)** Fold changes. Significant upregulation was detected for all the genes quantified (DM/WT). *Ae4* and *Slc26a9* showed most striking fold changes— ∼70.5 and ∼83.0%, respectively. The fold changes for the remaining genes were all above 2, except for *Lamp3*, *Rab21,* and *Nhe1*. *$P < 0.05$; **$P < 0.01$.

in the pathogenesis of AI/AI-like symptoms, which increases the complexity of genetic diagnosis for enamel disorders. The statement is further corroborated by the findings from a recent study on BMPs, in which double deletion of *Bmp2* and *Bmp4* in the epithelium led to hypoplastic enamel in mice (Xie et al., 2016).

We proposed in our previous study that pH regulation during enamel maturation might be achieved by the coordination of functional protein complexes (Yin et al., 2015). This is based on our findings that physical protein-protein interactions exist between Cftr and Slc26 gene family members *Slc26a1, Slc26a6,* and *Slc26a7* in maturation-stage ameloblasts, as supported by colocalization analyses, including co-immunofluorescence and co-immunoprecipitation studies. Here we examined the co-distribution pattern of SLC26A1 and SLC26A7 in maturation-stage ameloblasts by conducting immunostaining. We did not observe any overlaps in fluorescence of SLC26A1 and SLC26A7, which indicates a possible lack of colocalization of these two anion exchangers on the apical membrane of ameloblasts (**Figure 1A**). Nevertheless, the interactions between other different pH regulators in enamel maturation still warrants further investigation.

In conclusion, the data obtained from *Slc26a1*$^{-/-}$/*Slc26a7*$^{-/-}$ mutant mice provide new evidence in support of the hypothesis that SLC26A1 and SLC26A7 are actively involved in the ameloblast-mediated pH regulation process during maturation-stage amelogenesis.

AUTHOR CONTRIBUTIONS

KY, JG, MS and MP designed the experiments; KY and WL performed the experiments; MS developed the mutant animal model; KY, JG, SR and MP analyzed the data; KY and JG prepared the Figures and tables; and KY and MP wrote the manuscript. All listed authors critically read, edited, and approved the final manuscript. MP accepts full responsibility for the integrity of the data analysis.

FUNDING

This work was supported by NIH/NIDCR [grants # R01 DE019629 and R21 DE024704 (MP), R90 DE021982 (KY), and from the Department of Veterans Affairs [grant - Merit Review 5 I01 BX001000-06 award (MS)].

ACKNOWLEDGMENTS

We sincerely thank Thach-Vu Ho and Dr. Jingtan Su (University of Southern California) for their assistance in μCT scanning and EDS analysis. We also thank Bridget Samuels for her critical reading and editing of the manuscript.

REFERENCES

Aldred, M. J., Crawford, P. J., Roberts, E., Gillespie, C. M., Thomas, N. S., Fenton, I., et al. (1992). Genetic heterogeneity in X-linked amelogenesis imperfecta. *Genomics* 14, 567–573.

Alper, S. L., and Sharma, A. K. (2013). The SLC26 gene family of anion transporters and channels. *Mol. Aspects Med.* 34, 494–515. doi: 10.1016/j.mam.2012.07.009

Andrejewski, N., Punnonen, E. L., Guhde, G., Tanaka, Y., Lullmann-Rauch, R., Hartmann, D., et al. (1999). Normal lysosomal morphology and function in LAMP-1-deficient mice. *J. Biol. Chem.* 274, 12692–12701.

Arquitt, C. K., Boyd, C., and Wright, J. T. (2002). Cystic fibrosis transmembrane regulator gene (CFTR) is associated with abnormal enamel formation. *J. Dent. Res.* 81, 492–496. doi: 10.1177/154405910208100712

Bertrand, C. A., Zhang, R., Pilewski, J. M., and Frizzell, R. A. (2009). SLC26A9 is a constitutively active, CFTR-regulated anion conductance in human bronchial epithelia. *J. Gen. Physiol.* 133, 421–438. doi: 10.1085/jgp.200810097

Bronckers, A., Kalogeraki, L., Jorna, H. J., Wilke, M., Bervoets, T. J., Lyaruu, D. M., et al. (2010). The cystic fibrosis transmembrane conductance regulator (CFTR) is expressed in maturation stage ameloblasts, odontoblasts and bone cells. *Bone* 46, 1188–1196. doi: 10.1016/j.bone.2009.12.002

Bronckers, A. L., Guo, J., Zandieh-Doulabi, B., Bervoets, T. J., Lyaruu, D. M., Li, X., et al. (2011). Developmental expression of solute carrier family 26A member 4 (SLC26A4/pendrin) during amelogenesis in developing rodent teeth. *Eur. J. Oral. Sci.* 119 (Suppl. 1), 185–192. doi: 10.1111/j.1600-0722.2011.00901.x

Bronckers, A. L., Lyaruu, D. M., Jansen, I. D., Medina, J. F., Kellokumpu, S., Hoeben, K. A., et al. (2009). Localization and function of the anion exchanger Ae2 in developing teeth and orofacial bone in rodents. *J. Exp. Zool. B Mol. Dev. Evol.* 312B, 375–387. doi: 10.1002/jez.b.21267

Chang, E. H., Lacruz, R. S., Bromage, T. G., Bringas, P. Jr., Welsh, M. J., Zabner, J., et al. (2011). Enamel pathology resulting from loss of function in the cystic fibrosis transmembrane conductance regulator in a porcine animal model. *Cells Tiss. Organs.* 194, 249–254. doi: 10.1159/000324248

Collier, P. M., Sauk, J. J., Rosenbloom, S. J., Yuan, Z. A., and Gibson, C. W. (1997). An amelogenin gene defect associated with human X-linked amelogenesis imperfecta. *Arch. Oral Biol.* 42, 235–242.

Dawson, P. A., Russell, C. S., Lee, S., McLeay, S. C., van Dongen, J. M., Cowley, D. M., et al. (2010). Urolithiasis and hepatotoxicity are linked to the anion transporter Sat1 in mice. *J. Clin. Invest.* 120, 706–712. doi: 10.1172/JCI31474

Dogterom, A. A., and Bronckers, A. L. (1983). Carbonic anhydrase in developing hamster molars. *J. Dent. Res.* 62, 789–791.

Duan, X. (2014). Ion channels, channelopathies, and tooth formation. *J. Dent. Res.* 93, 117–125. doi: 10.1177/0022034513507066

Duan, X., Mao, Y., Wen, X., Yang, T., and Xue, Y. (2011). Excess fluoride interferes with chloride-channel-dependent endocytosis in ameloblasts. *J. Dent. Res.* 90, 175–180. doi: 10.1177/0022034510385687

El-Sayed, W., Parry, D. A., Shore, R. C., Ahmed, M., Jafri, H., Rashid, Y., et al. (2009). Mutations in the beta propeller WDR72 cause autosomal-recessive hypomaturation amelogenesis imperfecta. *Am. J. Hum. Genet.* 85, 699–705. doi: 10.1016/j.ajhg.2009.09.014

Freel, R. W., Hatch, M., Green, M., and Soleimani, M. (2006). Ileal oxalate absorption and urinary oxalate excretion are enhanced in Slc26a6 null mice. *Am. J. Physiol. Gastrointest. Liver Physiol.* 290, G719–728. doi: 10.1152/ajpgi.00481.2005

Hart, P. S., Becerik, S., Cogulu, D., Emingil, G., Ozdemir-Ozenen, D., Han, S. T., et al. (2009). Novel FAM83H mutations in Turkish families with autosomal dominant hypocalcified amelogenesis imperfecta. *Clin. Genet.* 75, 401–404. doi: 10.1111/j.1399-0004.2008.01112.x

Hart, P. S., Hart, T. C., Michalec, M. D., Ryu, O. H., Simmons, D., Hong, S., et al. (2004). Mutation in kallikrein 4 causes autosomal recessive hypomaturation amelogenesis imperfecta. *J. Med. Genet.* 41, 545–549. doi: 10.1136/jmg.2003.017657

Hart, S., Hart, T., Gibson, C., and Wright, J. T. (2000). Mutational analysis of X-linked amelogenesis imperfecta in multiple families. *Arch. Oral Biol.* 45, 79–86. doi: 10.1016/S0003-9969(99)00106-5

Hart, T. C., Hart, P. S., Gorry, M. C., Michalec, M. D., Ryu, O. H., Uygur, C., et al. (2003). Novel ENAM mutation responsible for autosomal recessive amelogenesis imperfecta and localised enamel defects. *J. Med. Genet.* 40, 900–906. doi: 10.1136/jmg.40.12.900

Heber, S., Herms, J., Gajic, V., Hainfellner, J., Aguzzi, A., Rulicke, T., et al. (2000). Mice with combined gene knock-outs reveal essential and partially redundant functions of amyloid precursor protein family members. *J. Neurosci.* 20, 7951–7963.

Herzog, C. R., Reid, B. M., Seymen, F., Koruyucu, M., Tuna, E. B., Simmer, J. P., et al. (2015). Hypomaturation amelogenesis imperfecta caused by a novel SLC24A4 mutation. *Oral Surg. Oral Med. Oral Pathol. Oral Radiol.* 119, e77–e81. doi: 10.1016/j.oooo.2014.09.003

Jalali, R., Guo, J., Zandieh-Doulabi, B., Bervoets, T. J., Paine, M. L., Boron, W. F., et al. (2014). NBCe1 (SLC4A4) a potential pH regulator in enamel organ cells during enamel development in the mouse. *Cell Tissue Res.* 358, 433–442. doi: 10.1007/s00441-014-1935-4

Jalali, R., Zandieh-Doulabi, B., DenBesten, P. K., Seidler, U., Riederer, B., Wedenoja, S., et al. (2015). Slc26a3/Dra and Slc26a6 in Murine Ameloblasts. *J. Dent. Res.* 94, 1732–1739. doi: 10.1177/0022034515606873

Jiang, Z., Asplin, J. R., Evan, A. P., Rajendran, V. M., Velazquez, H., Nottoli, T. P., et al. (2006). Calcium oxalate urolithiasis in mice lacking anion transporter Slc26a6. *Nat. Genet.* 38, 474–478. doi: 10.1038/ng1762

Josephsen, K., Takano, Y., Frische, S., Praetorius, J., Nielsen, S., Aoba, T., et al. (2010). Ion transporters in secretory and cyclically modulating ameloblasts: a new hypothesis for cellular control of preeruptive enamel maturation. *Am. J. Physiol., Cell Physiol.* 299, C1299–1307. doi: 10.1152/ajpcell.00218.2010

Kim, J. W., Lee, S. K., Lee, Z. H., Park, J. C., Lee, K. E., Lee, M. H., et al. (2008). FAM83H mutations in families with autosomal-dominant hypocalcified amelogenesis imperfecta. *Am. J. Hum. Genet.* 82, 489–494. doi: 10.1016/j.ajhg.2007.09.020

Kim, J. W., Seymen, F., Lee, K. E., Ko, J., Yildirim, M., Tuna, E. B., et al. (2013). LAMB3 mutations causing autosomal-dominant amelogenesis imperfecta. *J. Dent. Res.* 92, 899–904. doi: 10.1177/0022034513502054

Kim, J. W., Simmer, J. P., Hart, T. C., Hart, P. S., Ramaswami, M. D., Bartlett, J. D., et al. (2005). MMP-20 mutation in autosomal recessive pigmented hypomaturation amelogenesis imperfecta. *J. Med. Genet.* 42, 271–275. doi: 10.1136/jmg.2004.024505

Kim, J. W., Simmer, J. P., Hu, Y. Y., Lin, B. P., Boyd, C., Wright, J. T., et al. (2004). Amelogenin p.M1T and p.W4S mutations underlying hypoplastic X-linked amelogenesis imperfecta. *J. Dent. Res.* 83, 378–383. doi: 10.1177/154405910408300505

Kindelan, S. A., Brook, A. H., Gangemi, L., Lench, N., Wong, F. S., Fearne, J., et al. (2000). Detection of a novel mutation in X-linked amelogenesis imperfecta. *J. Dent. Res.* 79, 1978–1982. doi: 10.1177/00220345000790120901

Lacruz, R. S., Brookes, S. J., Wen, X., Jimenez, J. M., Vikman, S., Hu, P., et al. (2013a). Adaptor protein complex 2-mediated, clathrin-dependent endocytosis, and related gene activities, are a prominent feature during maturation stage amelogenesis. *J. Bone Miner. Res.* 28, 672–687. doi: 10.1002/jbmr.1779

Lacruz, R. S., Nakayama, Y., Holcroft, J., Nguyen, V., Somogyi-Ganss, E., Snead, M. L., et al. (2012a). Targeted overexpression of amelotin disrupts the microstructure of dental enamel. *PLoS ONE* 7:e35200. doi: 10.1371/journal.pone.0035200

Lacruz, R. S., Nanci, A., Kurtz, I., Wright, J. T., and Paine, M. L. (2010a). Regulation of pH During Amelogenesis. *Calcif. Tiss. Int.* 86, 91–103. doi: 10.1007/s00223-009-9326-7

Lacruz, R. S., Nanci, A., White, S. N., Wen, X., Wang, H., Zalzal, S. F., et al. (2010b). The sodium bicarbonate cotransporter (NBCe1) is essential for normal development of mouse dentition. *J. Biol. Chem.* 285, 24432–24438. doi: 10.1074/jbc.M110.115188

Lacruz, R. S., Smith, C. E., Bringas, P. Jr., Chen, Y. B., Smith, S. M., Snead, M. L., et al. (2012b). Identification of novel candidate genes involved in mineralization of dental enamel by genome-wide transcript profiling. *J. Cell. Physiol.* 227, 2264–2275. doi: 10.1002/jcp.22965

Lacruz, R. S., Smith, C. E., Chen, Y. B., Hubbard, M. J., Hacia, J. G., and Paine, M. L. (2011). Gene-expression analysis of early- and late-maturation-stage rat enamel organ. *Eur. J. Oral. Sci.* 119 (Suppl. 1), 149–157. doi: 10.1111/j.1600-0722.2011.00881.x

Lacruz, R. S., Smith, C. E., Kurtz, I., Hubbard, M. J., and Paine, M. L. (2013b). New paradigms on the transport functions of maturation-stage ameloblasts. *J. Dent. Res.* 92, 122–129. doi: 10.1177/0022034512470954

Lacruz, R. S., Smith, C. E., Moffatt, P., Chang, E. H., Bromage, T. G., Bringas, P. Jr., et al. (2012c). Requirements for ion and solute transport, and pH regulation during enamel maturation. *J. Cell. Physiol.* 227, 1776–1785. doi: 10.1002/jcp.22911

Lagerstrom-Fermer, M., and Landegren, U. (1995). Understanding enamel formation from mutations causing X-linked amelogenesis imperfecta. *Connect. Tissue Res.* 32, 241–246.

Lagerstrom-Fermer, M., Nilsson, M., Backman, B., Salido, E., Shapiro, L., Pettersson, U., et al. (1995). Amelogenin signal peptide mutation: correlation between mutations in the amelogenin gene (AMGX) and manifestations of X-linked amelogenesis imperfecta. *Genomics* 26, 159–162.

Lench, N. J., Brook, A. H., and Winter, G. B. (1994). SSCP detection of a nonsense mutation in exon 5 of the amelogenin gene (AMGX) causing X-linked amelogenesis imperfecta (AIH1). *Hum. Mol. Genet.* 3, 827–828.

Lezot, F., Thomas, B., Greene, S. R., Hotton, D., Yuan, Z. A., Castaneda, B., et al. (2008). Physiological implications of DLX homeoproteins in enamel formation. *J. Cell. Physiol.* 216, 688–697. doi: 10.1002/jcp.21448

Lin, H. M., Nakamura, H., Noda, T., and Ozawa, H. (1994). Localization of H(+)-ATPase and carbonic anhydrase II in ameloblasts at maturation. *Calcif. Tissue Int.* 55, 38–45.

Livak, K. J., and Schmittgen, T. D. (2001). Analysis of relative gene expression data using real-time quantitative PCR and the 2(-Delta Delta C(T)) Method. *Methods* 25, 402–408. doi: 10.1006/meth.2001.1262

Lloyd, J. B. (1996). Metabolite efflux and influx across the lysosome membrane. *Subcell. Biochem.* 27, 361–386.

Lyaruu, D. M., Bronckers, A. L., Mulder, L., Mardones, P., Medina, J. F., Kellokumpu, S., et al. (2008). The anion exchanger Ae2 is required for enamel maturation in mouse teeth. *Matrix Biol.* 27, 119–127. doi: 10.1016/j.matbio.2007.09.006

MacDougall, M., DuPont, B. R., Simmons, D., Reus, B., Krebsbach, P., Karrman, C., et al. (1997). Ameloblastin gene (AMBN) maps within the critical region for autosomal dominant amelogenesis imperfecta at chromosome 4q21. *Genomics* 41, 115–118. doi: 10.1006/geno.1997.4643

Mardh, C. K., Backman, B., Holmgren, G., Hu, J. C., Simmer, J. P., and Forsman-Semb, K. (2002). A nonsense mutation in the enamelin gene causes local hypoplastic autosomal dominant amelogenesis imperfecta (AIH2). *Hum. Mol. Genet.* 11, 1069–1074. doi: 10.1093/hmg/11.9.1069

Nanci, A. (2008). *Ten* Cate's oral *Histology Development*, *Structure* and *Function*. St Louis, MO: Mosby Elsevier.

Page-McCaw, A., Ewald, A. J., and Werb, Z. (2007). Matrix metalloproteinases and the regulation of tissue remodelling. *Nat. Rev. Mol. Cell Biol.* 8, 221–233. doi: 10.1038/nrm2125

Paine, M. L., Snead, M. L., Wang, H. J., Abuladze, N., Pushkin, A., Liu, W., et al. (2008). Role of NBCe1 and AE2 in secretory ameloblasts. *J. Dent. Res.* 87, 391–395. doi: 10.1177/154405910808700415

Petrovic, S., Barone, S., Xu, J., Conforti, L., Ma, L., Kujala, M., et al. (2004). SLC26A7: a basolateral Cl-/HCO3- exchanger specific to intercalated cells of the outer medullary collecting duct. *Am. J. Physiol. Renal Physiol.* 286, F161–169. doi: 10.1152/ajprenal.00219.2003

Petrovic, S., Ju, X., Barone, S., Seidler, U., Alper, S. L., Lohi, H., et al. (2003a). Identification of a basolateral Cl-/HCO3- exchanger specific to gastric parietal cells. *Am. J. Physiol. Gastrointest. Liver Physiol.* 284, G1093–1103. doi: 10.1152/ajpgi.00454.2002

Petrovic, S., Ma, L., Wang, Z., and Soleimani, M. (2003b). Identification of an apical Cl-/HCO-3 exchanger in rat kidney proximal tubule. *Am. J. Physiol. Cell Physiol.* 285, C608–617. doi: 10.1152/ajpcell.00084.2003

Poulter, J. A., Brookes, S. J., Shore, R. C., Smith, C. E., Abi Farraj, L., Kirkham, J., et al. (2014a). A missense mutation in ITGB6 causes pitted hypomineralized amelogenesis imperfecta. *Hum. Mol. Genet.* 23, 2189–2197. doi: 10.1093/hmg/ddt616

Poulter, J. A., El-Sayed, W., Shore, R. C., Kirkham, J., Inglehearn, C. F., and Mighell, A. J. (2014b). Whole-exome sequencing, without prior linkage, identifies a mutation in LAMB3 as a cause of dominant hypoplastic amelogenesis imperfecta. *Eur. J. Hum. Genet.* 22, 132–135. doi: 10.1038/ejhg.2013.76

Poulter, J. A., Murillo, G., Brookes, S. J., Smith, C. E., Parry, D. A., Silva, S., et al. (2014c). Deletion of ameloblastin exon 6 is associated with amelogenesis imperfecta. *Hum. Mol. Genet.* 23, 5317–5324. doi: 10.1093/hmg/ddu247

Reibring, C. G., El Shahawy, M., Hallberg, K., Kannius-Janson, M., Nilsson, J., Parkkila, S., et al. (2014). Expression patterns and subcellular localization of carbonic anhydrases are developmentally regulated during tooth formation. *PLoS ONE* 9:e96007. doi: 10.1371/journal.pone.0096007

Schmittgen, T. D., and Livak, K. J. (2008). Analyzing real-time PCR data by the comparative C(T) method. *Nat. Protoc.* 3, 1101–1108. doi: 10.1038/nprot.2008.73

Simmer, J. P., and Fincham, A. G. (1995). Molecular mechanisms of dental enamel formation. *Crit. Rev. Oral Biol. Med.* 6, 84–108.

Smith, C. E., Issid, M., Margolis, H. C., and Moreno, E. C. (1996). Developmental changes in the pH of enamel fluid and its effects on matrix-resident proteinases. *Adv. Dent. Res.* 10, 159–169.

Smith, C. E., and Nanci, A. (1996). Protein dynamics of amelogenesis. *Anat. Rec.* 245, 186–207. doi: 10.1002/(SICI)1097-0185(199606)245:2<186::AID-AR7>3.0.CO;2-V

Wang, S., Choi, M., Richardson, A. S., Reid, B. M., Seymen, F., Yildirim, M., et al. (2014). STIM1 and SLC24A4 are critical for enamel maturation. *J. Dent. Res.* 93(7 Suppl.), 94S–100S. doi: 10.1177/0022034514527971

Wang, S. K., Choi, M., Richardson, A. S., Reid, B. M., Lin, B. P., Wang, S. J., et al. (2014). ITGB6 loss-of-function mutations cause autosomal recessive amelogenesis imperfecta. *Hum. Mol. Genet.* 23, 2157–2163. doi: 10.1093/hmg/ddt611

Wang, X., Suzawa, T., Ohtsuka, H., Zhao, B., Miyamoto, Y., Miyauchi, T., et al. (2010). Carbonic anhydrase II regulates differentiation of ameloblasts via intracellular pH-dependent JNK signaling pathway. *J. Cell. Physiol.* 225, 709–719. doi: 10.1002/jcp.22267

Wen, X., Kurtz, I., and Paine, M. L. (2014). Prevention of the disrupted enamel phenotype in Slc4a4-null mice using explant organ culture maintained in a living host kidney capsule. *PLoS ONE* 9:e97318. doi: 10.1371/journal.pone.0097318

Wen, X., Lacruz, R. S., and Paine, M. L. (2015). Dental and Cranial Pathologies in Mice Lacking the Cl^- /H^+ -Exchanger ClC-7. *Anat. Rec. (Hoboken).* 298, 1502–1508. doi: 10.1002/ar.23118

Wright, J. T., Frazier-Bowers, S., Simmons, D., Alexander, K., Crawford, P., Han, S. T., et al. (2009). Phenotypic variation in FAM83H-associated amelogenesis imperfecta. *J. Dent. Res.* 88, 356–360. doi: 10.1177/0022034509333822

Wright, J. T., Hall, K. I., and Grubb, B. R. (1996a). Enamel mineral composition of normal and cystic fibrosis transgenic mice. *Adv. Dent. Res.* 10, 270–274; discussion 275.

Wright, J. T., Kiefer, C. L., Hall, K. I., and Grubb, B. R. (1996b). Abnormal enamel development in a cystic fibrosis transgenic mouse model. *J. Dent. Res.* 75, 966–973.

Xie, Q., Welch, R., Mercado, A., Romero, M. F., and Mount, D. B. (2002). Molecular characterization of the murine Slc26a6 anion exchanger: functional comparison with Slc26a1. *Am. J. Physiol. Renal Physiol.* 283, F826–F838. doi: 10.1152/ajprenal.00079.2002

Xie, X., Liu, C., Zhang, H., Jani, P. H., Lu, Y., Wang, X., et al. (2016). Abrogation of epithelial BMP2 and BMP4 causes Amelogenesis Imperfecta by reducing MMP20 and KLK4 expression. *Sci. Rep.* 6:25364. doi: 10.1038/srep 25364

Xu, J., Song, P., Nakamura, S., Miller, M., Barone, S., Alper, S. L., et al. (2009). Deletion of the chloride transporter slc26a7 causes distal renal tubular acidosis and impairs gastric acid secretion. *J. Biol. Chem.* 284, 29470–29479. doi: 10.1074/jbc.M109.044396

Yin, K., Hacia, J. G., Zhong, Z., and Paine, M. L. (2014). Genome-wide analysis of miRNA and mRNA transcriptomes during amelogenesis. *BMC Genomics* 15:998. doi: 10.1186/1471-2164-15-998

Yin, K., Lei, Y., Wen, X., Lacruz, R. S., Soleimani, M., Kurtz, I., et al. (2015). SLC26A Gene family participate in pH regulation during enamel maturation. *PLoS ONE* 10:e0144703. doi: 10.1371/journal.pone.0144703

Conflict of Interest Statement: The authors declare that the research was conducted in the absence of any commercial or financial relationships that could be construed as a potential conflict of interest.

Copyright © 2017 Yin, Guo, Lin, Robertson, Soleimani and Paine. This is an open-access article distributed under the terms of the Creative Commons Attribution License (CC BY). The use, distribution or reproduction in other forums is permitted, provided the original author(s) or licensor are credited and that the original publication in this journal is cited, in accordance with accepted academic practice. No use, distribution or reproduction is permitted which does not comply with these terms.

frontiers in Physiology

ORIGINAL RESEARCH
published: 16 November 2017
doi: 10.3389/fphys.2017.00932

Dose-Dependent Rescue of KO Amelogenin Enamel by Transgenes *in Vivo*

Felicitas B. Bidlack[1,2], *Yan Xia*[1] *and Megan K. Pugach*[1,2]*

[1] Forsyth Institute, Cambridge, MA, United States, [2] Department of Developmental Biology, Harvard School of Dental Medicine, Boston, MA, United States

Mice lacking amelogenin (KO) have hypoplastic enamel. Overexpression of the most abundant amelogenin splice variant M180 and LRAP transgenes can substantially improve KO enamel, but only ∼40% of the incisor thickness is recovered and the prisms are not as tightly woven as in WT enamel. This implies that the compositional complexity of the enamel matrix is required for different aspects of enamel formation, such as organizational structure and thickness. The question arises, therefore, how important the ratio of different matrix components, and in particular amelogenin splice products, is in enamel formation. Can optimal expression levels of amelogenin transgenes representing both the most abundant splice variants and cleavage product at protein levels similar to that of WT improve the enamel phenotype of KO mice? Addressing this question, our objective was here to understand dosage effects of amelogenin transgenes (*Tg*) representing the major splice variants M180 and LRAP and cleavage product CTRNC on enamel properties. Amelogenin KO mice were mated with M180*Tg*, CTRNC*Tg* and LRAP*Tg* mice to generate M180*Tg* and CTRNC*Tg* double transgene and M180*Tg*, CTRNC*Tg*, LRAP*Tg* triple transgene mice with transgene hemizygosity (on one allelle) or homozygosity (on both alleles). Transgene homo- vs. hemizygosity was determined by qPCR and relative transgene expression confirmed by Western blot. Enamel volume and mineral density were analyzed by microCT, thickness and structure by SEM, and mechanical properties by Vickers microhardness testing. There were no differences in incisor enamel thickness between amelogenin KO mice with three or two different transgenes, but mice homozygous for a given transgene had significantly thinner enamel than mice hemizygous for the transgene ($p < 0.05$). The presence of the LRAP*Tg* did not improve the phenotype of M180*Tg*/CTRNC*Tg*/KO enamel. In the absence of endogenous amelogenin, the addition of amelogenin transgenes representing the most abundant splice variants and cleavage product can rescue abnormal enamel properties and structure, but only up to a maximum of ∼80% that of molar and ∼40% that of incisor wild-type enamel.

Keywords: enamel development, transgenic, knockout, amelogenin, mineralization

OPEN ACCESS

Edited by:
Alexandre Rezende Vieira, University of Pittsburgh, United States

Reviewed by:
Pierfrancesco Pagella, University of Zurich, Switzerland
Yuqiao Zhou, University of Pittsburgh, United States
Lucia Jimenez-Rojo, University of Zurich, Switzerland

***Correspondence:**
Megan K. Pugach
mpugach@forsyth.org

Specialty section:
This article was submitted to Craniofacial Biology and Dental Research, a section of the journal Frontiers in Physiology

Received: *22 June 2017*
Accepted: *02 November 2017*
Published: *16 November 2017*

Citation:
Bidlack FB, Xia Y and Pugach MK (2017) Dose-Dependent Rescue of KO Amelogenin Enamel by Transgenes in Vivo. Front. Physiol. 8:932. doi: 10.3389/fphys.2017.00932

INTRODUCTION

Tooth enamel forms through appositional growth in an organic matrix that is secreted in daily increments until the full thickness of the crown is reached. During this first, secretory, stage of enamel formation, enamel crystallites grow primarily in length. Once the final enamel thickness is attained, the mineral content increases as crystallites grow

in thickness, while the organic phase is removed in a highly controlled way. The enamel matrix facilitates mineralization and organization, and is transient in abundance as well as composition. Starting out with a ratio of 70 wt% organic matter and water, and 30 wt% mineral (Smith, 1998) the ratio of organic matrix to mineral changes over the course of enamel development and reaches 95% mineral content, with about 1–2% organic matter retained in completed enamel. During the secretory stage, the full-length enamel matrix molecules amelogenin, ameloblastin, and enamelin are cleaved upon their secretion by matrix metalloproteinase 20 (MMP20). After the secretory stage, a second enzyme, kallikrein 4 (KLK-4) is active to further cleave the matrix proteins and allow for the removal of matrix until only a very small amount remains, which is important for the mechanical properties through the control of crack propagation. The three structural enamel matrix proteins and the alternative splice product of amelogenin, leucine rich amelogenin protein (LRAP) have been described (Smith, 1998; Bartlett, 2013; Tarasevich et al., 2015; Lacruz et al., 2017). Yet, is not resolved what the *in vivo* function of these matrix components is, what role the full-length molecules, their alternative splice products as well as their cleavage products play for the control of mineral phase, crystallite shape and orientation, pH regulation, and potentially feed-back to ameloblasts (Lacruz et al., 2017).

The organic enamel matrix comprises the three structural matrix proteins amelogenin, enamelin, and ameloblastin, with amelogenin accounting for 90 wt% of the composition. However, the amelogenin primary RNA transcript is extensively alternatively spliced to produce 16 amelogenin isoforms reported (Bartlett et al., 2006). It is not clear, whether these isoforms are critical for enamel formation, or what their roles are in amelogenesis. The most abundant of these isoforms are the full-length molecule of 180 amino acids and the 59-amino acid long LRAP, leucine-rich amelogenin protein, which consist of the 33 N-terminal and 26 C-terminal amino acids, but lacks the hydrophobic core of the full-length molecule.

Ameloblasts secrete the full-length 180 amino acid sized amelogenin, which shortly thereafter is cleaved by the metalloproteinase MMP20, beginning from the C-terminus. The most abundant cleavage product is 167 amino acids long, and referred here to as CTRNC. All three structural matrix proteins are required for proper enamel formation and the AmelxKO enamel is hypoplastic, with no prismatic architecture. In order to determine the roles of the most abundant amelogenin isoforms, transgenic mice have been developed that overexpress (a) the full-length amelogenin M180, (b) the major amelogenin cleavage product CTRNC, and (c) LRAP in both C57BL6/J wild-type and *Amelx*KO genetic backgrounds (see **Table 1** for abbreviations).

Addition of LRAP*Tg* to M180*Tg* in the amelogenin KO model improves the thickness and structure of enamel, suggesting that transgenes have a complementary function (Gibson et al., 2011). Among amelogenin isoforms, M180 by itself is sufficient for the formation of normal mechanical properties and prism patterns in enamel. Yet, additional amelogenin splice products are required to restore enamel thickness (Gibson et al., 2011; Snead et al., 2011; Pugach et al., 2013). The overexpression of CTRNC*Tg* and LRAP*Tg* together improved significantly the enamel phenotype of LRAP*Tg*/KO and CTRNC*Tg*/KO mouse enamel, however enamel microhardness was recovered only when M180*Tg* was expressed, alone or with LRAP*Tg*. Expression of LRAP and CTRNC together provides all three regions of the amelogenin protein N-terminus, C-terminus and hydrophobic core further improved the phenotype to reach normal WT enamel thickness and prism organization in the reported mouse model (Chen et al., 2003; Pugach et al., 2010; Xia et al., 2016). Enamel phenotypes in M180*Tg*/KO, CTRNC*Tg*/KO, LRAP*Tg*/KO, and double transgenic mice have been heterogeneous. This is due to varying transgene dosages and suggests a cumulative effect on improving the *Amelx*KO enamel phenotype (Xia et al., 2016).

The importance of the ratio between cleaved and uncleaved amelogenin has been previously reported (Shin et al., 2014). In order to determine the optimal ratio of amelogenin major cleavage products and splice variants required for normal enamel structure, thickness, and mechanical properties, we generated double and triple transgenic mice with two different transgene dosages in KO backgrounds.

MATERIALS AND METHODS

Generation of Transgenic Mice and Genotyping

To generate M180*Tg*/CTRNC*Tg*/LRAP*Tg*/KO and M180*Tg*/CTRNC*Tg*/KO mice, animals overexpressing M180, CTRNC, and LRAP transgenes from the bovine amelogenin promoter were mated with male Amelx–/0 mice. After two generations of mating, both male and female mice were genotyped using PCR primers to detect transgenes as well as amelogenin WT and Amelx−/− (KO) DNA (Gibson et al., 2001, 2007; Chen et al., 2003; Pugach et al., 2010). Four different genotypes were generated with either 2 (M180*Tg* and CTRNC*Tg*) or 3 (M180*Tg*, CTRNC*Tg,* and LRAP*Tg*) transgenes, and either homozygous (++) or hemizygous (+/−) for the transgenes (N = 3–5 mice per genotype). PCR primers for M180*Tg*, CTRNC*Tg*, LRAP*Tg,* and KO mice have been previously published (Gibson et al., 2001; Chen et al., 2003; Li et al., 2008; Pugach et al., 2010). Relative copy number determined transgene homo- (++ = on both alleles) vs. hemizygosity (+ = on one allelle), and was determined by qPCR analysis using M180, CTRNC, and LRAP *Tg*-specific probes designed by Transnetyx (Cordova, TN) (**Table 2**). WT, KO, and hemizygous (+/−) M180*Tg*/LRAP*Tg*/KO mice, which have been previously reported were used as controls (Gibson et al., 2001, 2011).

Western Blot Analysis

To analyze expression of endogenous and transgenic amelogenin in M180*Tg*/CTRNC*Tg*/LRAP*Tg*/KO and M180*Tg*/CTRNC*Tg*/KO male and female mice and controls, first molars were harvested from 5-day-old mouse pups (with ameloblasts in the secretory stage) and protein was extracted. Equal amounts of protein were loaded in each lane and run on a 4–20% SDS-PAGE gel (BioRad). Membranes were immunoblotted with an antibody against full-length *Amelx* (FL-191, Santa Cruz Biotechnology, Santa Cruz, CA) and against

TABLE 1 | Abbreviations for amelogenin protein, transgenes, and mouse models.

M180—M180*Tg*—M180*Tg*/KO	Full-length amelogenin isoform of 180 amino acids—M180 transgene—mouse model with M180 transgene in amelogenin null background
CTRNC—CTRNC*Tg*—CTRNC*Tg*/KO	Cleaved (M180) amelogenin of 167 amino acids—CTRNC transgene—mouse model with CTRNC transgene in amelogenin null background
LRAP—LRAP*Tg*—LRAP*Tg*/KO	Amelogenin isoform of 59 amino acids—LRAP transgene—mouse model with LRAP transgene in amelogenin null background

TABLE 2 | Mouse genotypes (KO and transgenic status) as determined by PCR for genotyping for endogenous amelogenin and qPCR for measuring relative copy number of the three transgenes, using transgene-specific probes against M180*Tg*, CTRNC*Tg*, and LRAP*Tg*.

Genotypes	*Amelx*KO	M180*Tg* (180aa)	CTRNC*Tg* (167aa, no C-terminus)	LRAP*Tg* (59aa, C- and N-only)
1: M180*Tg*/CTRNC*Tg*/LRAP*Tg*/KO++	−/o or −/−	++	++	++
2: M180*Tg*/CTRNC*Tg*/LRAP*Tg*/KO+	−/o or −/−	+	+	+
3: M180*Tg*/CTRNC*Tg*/KO++	−/o or −/−	++	++	−
4: M180*Tg*/CTRNC*Tg*/KO+	−/o or −/−	+	+	−
Control: M180*Tg*/LRAP*Tg*/KO+	−/o or −/−	+	−	+
Control: *Amelx*KO	−/o or −/−	−	−	−
Control: WT	+/o or +/+	−	−	−

β-actin (A2103, Sigma-Aldrich, St. Louis, MO), with a goat anti-rabbit secondary antibody (Santa Cruz Biotechnology). Relative transgene expression was confirmed by Western blot, and mice with the same genotypes but *Mmp20*KO background were used as controls (**Figure 1**). β-actin was used as the loading control to quantify relative transgene expression levels.

Tooth Sample Preparation and Analyses of Enamel

Six 6-week-old male and female adult hemi-mandibles were dissected and fixed in Zinc-formalin for 24 h, then rinsed and transferred to 50% ethanol. Samples were first analyzed by μCT, then dehydrated in a graded ethanol series and embedded in LR-White (Electron Microscopy Sciences, Hatfield, PA, USA) for micro-hardness testing, and lastly SEM analyses.

Enamel Mineral Density

Enamel mineral density was determined by μCT and compared between standardized regions of interest in incisor and molar enamel in mutant and control mice as described previously (Pugach et al., 2013). Hemimandibles with soft tissues removed were scanned in a μCT-40 (Scanco, Brüttisellen, Switzerland) at 70 kV, 114 mA, and 6 μm resolution. Images were processed with μCT-40 evaluation software and FIJI (https://fiji.sc/) was used to orient the mandibles in a standardized way based on anatomical landmarks to clearly observe and compare enamel mineralization in two locations: (1) In the first molar, in a coronal plane through the distal root and, extending this plane, in the early maturation stage of the developing incisor and, (2) in the maturation stage incisor, in coronal plane through the mandible proximal to the point of tooth eruption, that is where the incisor is still completely enclosed by bone.

Enamel Hardness

Enamel hardness was determined from first molars on LR White embedded samples that were polished on M3 polishing film (Precision Surfaces International, Houston Texas, USA) to 0.3 μm grit size in parasagittal plane. The polished samples were tested for enamel microhardness on an M400 HI testing machine (Leco, St. Joseph, MI) with a load of 10 g for 5 s with a Vickers tip, applying 20 indentations per sample on at least four teeth per group, with data averaged per group.

Enamel Thickness Analyses

Enamel thickness analyses were performed on samples subsequently to micro-hardness testing. The sample surface was etched with 0.1 M phosphoric acid for 15 s, gold coated, and imaged with a Zeiss Evo LS 10 SEM at 15 kV, 6–8 mm WD, and 120 pA probe current. Enamel thickness was measured in first molars and incisors on images taken at 1000X at the mesial side of the first molar using lateral enamel and in incisors in the area underneath the mesial first molar root tip, respectively, in at least six samples per genotype.

Enamel Microstructure

Enamel microstructure was analyzed on both para-sagittal sections prepared for enamel thickness measurements as well as coronal sections through the mesial root of the first molar and visualized at 2000X and higher magnification.

Toluidine Blue Staining

Toluidine Blue staining was applied to visualize organic matter in enamel. The same samples analyzed for microstructure by SEM were used for toluidine blue staining. The gold coating was polished off, the sample mounted on a glass slide, and a thin section prepared through polishing to a final thickness of

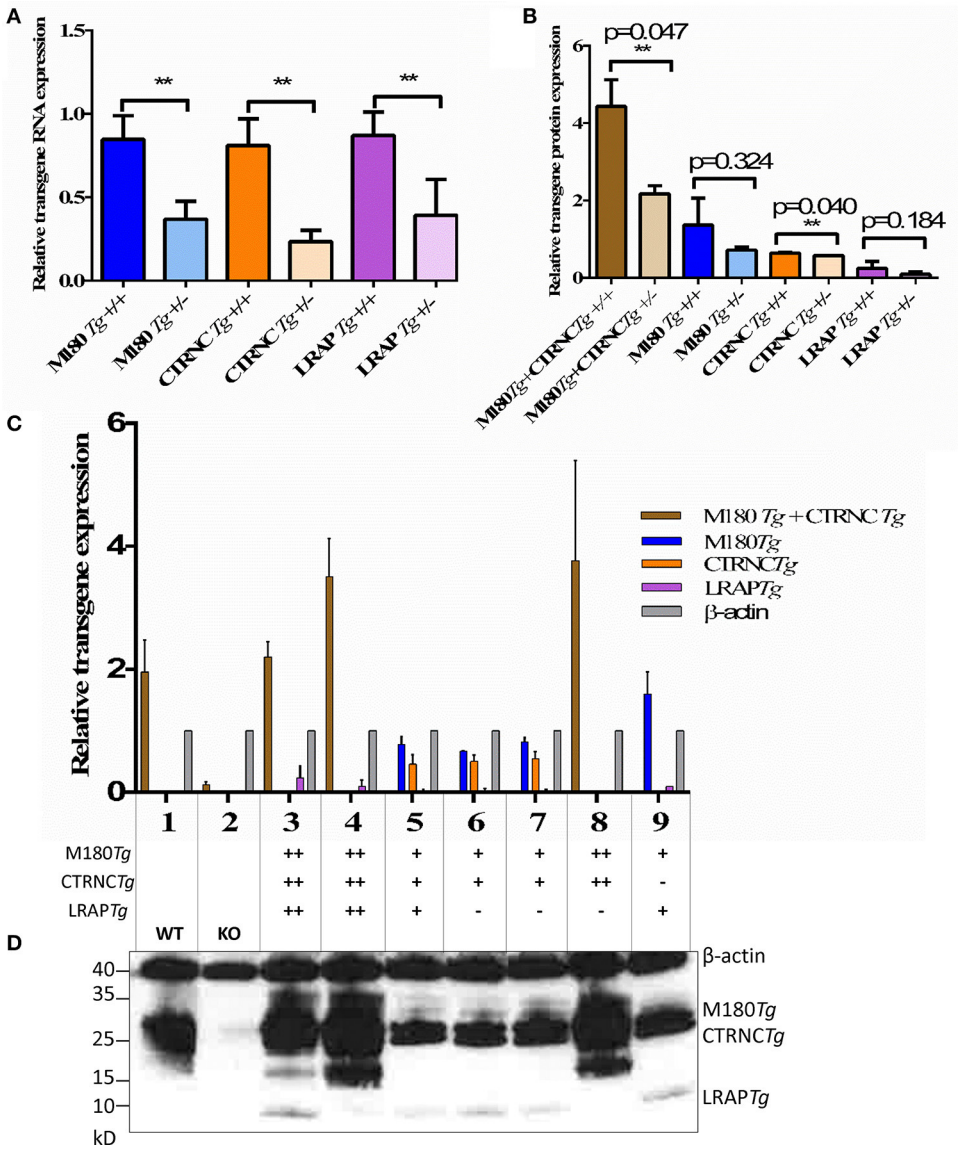

FIGURE 1 | Relative amelogenin transgene DNA and protein expression in double and triple transgenic/*Amelx*KO mice. **(A)** Relative transgene copy number of homozygous vs. hemizygous M180*Tg*, CTRNC*Tg*, and LRAP*Tg* as determined by qPCR analyses with transgene-specific probes designed and tested by Transnetyx (Cordova, TN) (**indicates significant difference, $p < 0.0001$). **(B–D)** Western blot of *Amelx* protein expression using anti-Amelogenin FL-191 (Santa Cruz), with β-actin control (Sigma) in transgenic 5 day-old developing molars. **(B)** Relative transgene protein expression of homozygous vs. hemizygous M180*Tg*, CTRNC*Tg*, and LRAP*Tg* as determined by Western blot analyses as measured by ImageJ using β-actin to normalize. Since we could not differentiate between M180*Tg* and CTRNC*Tg* in lanes 1, 3, 4, and 8, M180*Tg* and CTRNC*Tg* expression intensities were pooled when quantifying. Due to the lack of Mmp20 in lanes 5, 6, and 7, we were able to differentiate between M180Tg and CTRNC*Tg*. ($n = 3$ blots, **indicates significant difference, $p < 0.005$). **(C)** Relative transgene protein expression for different genotypes as determined by Western blot analyses as measured by ImageJ using β-actin to normalize. Lane 1, WT; Lane 2, *Amelx*KO; Lane 3, M180*Tg*/CTRNC*Tg*/LRAP*Tg*/KO++; Lane 4, M180*Tg*/CTRNC*Tg*/KO++; Lane 5, M180*Tg*/CTRNC*Tg*/KO+ (*Mmp20*KO background control); Lane 6, M180*Tg*/CTRNC*Tg*/LRAP*Tg*/KO++ (*Mmp20*KO background control); Lane 7, M180*Tg*/CTRNC*Tg*/LRAP*Tg*/KO+ (*Mmp20*KO background control); Lane 8, M180*Tg*/CTRNC*Tg*/KO++; Lane 9, M180*Tg*/LRAP*Tg*/KO+. **(D)** Western blot with primary antibodies anti-Amelogenin and anti-β-actin, with lane numbers corresponding to genotypes in **(C)**. In lane 1, molars had a smear of amelogenin protein between 17 and 20 kD representing most of the WT splice variants and cleavage products expressed during the secretory stage, which are absent in the *Amelx*KO lane 2. The M180*Tg* band is visible at ∼25 kD in all lanes except lane 2. The CTRNC*Tg* is visible ∼22 kD in lanes 5, 6, and 7, since the absence of *Mmp20* prevented its proteolytic degradation. The LRAP*Tg* band is visible ∼7 kD in lanes 3, 6 7, and 9, but below the detection level in lane 1. The β-actin loading control bands is visible in all lanes ∼40 kD.

∼100 μm. A 1% toluidine blue solution was used for 3 min, rinsed off and samples air-dried before viewing in a Leica upright microscope.

Statistical Methods

We used ANOVA with the Tukey *post-hoc* test to detect differences ($p < 0.05$) in RNA expression, protein expression,

enamel thickness, and microhardness between groups of teeth analyzed for enamel thickness and Vickers microhardness (GraphPad Software, San Diego, CA, USA).

RESULTS

Relative Amelogenin Transgene Protein Expression

qPCR and Western blot analyses confirmed that we generated four different genotypes with either two transgenes (M180 & CTRNC) or three transgenes (M180, CTRNC, LRAP) and homozygous (++) or hemizygous (+) expression in KO mice (**Table 2**). As expected, qPCR data confirm that the transgene copy numbers are higher in the homozygous than in hemizygous transgenic mice. However, the double transgene expression level of M180 with only CTRNC, without LRAP, is decreased in the homozygous transgenic compared to the triple homozygous transgenic containing LRAP (**Figure 1A**). Western Blot analyses show that in developing day-5 molars, that in the triple transgene on *Amelx*KO background most of the splice variants and cleavage products are expressed during the secretory stage and visible as bands between 17 and 20 kD for M180 and CTRNC, and the LRAP band around 7 kD (**Figure 1B**). The LRAP*Tg* expression in triple transgenic/*Amelx*−/− mice is higher in the homozygous mouse compared to hemizygous, as expected, but also higher than that in WT molars.

Relative Enamel Mineral Density

Results from μCT analyses of incisor and molar enamel show differences between the five different genotypes and compared to WT and *Amelx*KO (**Figure 2**). In no transgene combination was the enamel thickness of WT enamel achieved. In addition, mineral density was decreased in both molar and incisor enamel with homozygous (++) transgene expression (**Figures 2A–C, G–H**), compared to hemizygous (+) transgene expression (**Figures 2D–F, J–O**). The enamel layer seen in the homozygous triple transgene M180*Tg*/CTRNC*Tg*/LRAP*Tg*/KO++ (**Figures 2A–C**) is also thinner than in the hemizygous double transgene M180*Tg*/CTRNC*Tg*/KO+ (**Figures 2J–L**) and M180*Tg*/LRAP*Tg*/KO+ (**Figures 2M–O**) on both molar and incisor. We observed ectopic depositions in mice with excess CTRNC*Tg* (++) without LRAP*Tg* (**Figures 2A–C, G–I**).

Enamel Thickness Analyses

Based on SEM data (**Table 3**), incisor enamel of triple transgenic homozygous (++) mice was statistically ($p < 0.05$) thicker than triple transgenic enamel with less transgene expression (+), indicating a dosage effect. This effect is not seen in the molars. However, a difference between double and triple homozygous transgenic mice was clear in molar enamel, which was thicker in the triple transgene ($p = 0.038$), relating molar enamel thickness to the presence of LRAP in the matrix (**Table 3**). Interestingly, enamel thickness is highest in hemizygous double transgenic mice, which is when the matrix lacks LRAP but does contain M180 and CTRNC.

Enamel Microhardness

Vickers microhardness data of the four different genotypes are shown in **Table 3**. The enamel phenotypes are highly variable due to a mosaic appearance of properties including ectopic depositions and resulted in such high standard deviations of microhardness data that differences in hardness were not statistically significant between groups. However, molar double transgenic hemizygous enamel was harder than homozygous double transgenic molar enamel ($p < 0.05$).

Enamel Structure Analyses by SEM and Organic Matter Content

The incisors of all transgene combinations analyzed here differ from WT enamel in both an excess of retained organic matter and a distinctly layered structural organization of inner and outer enamel. This layering is clearly seen in the homozygous triple transgene M180Tg/CTRNC*Tg*/LRAP*Tg*/KO ++ incisor and molar, with layers distinguished by the pattern and clarity of prism decussation and amount of organic matrix (**Figures 3A–C**, **4B**). In comparison, the hemizygous triple transgene expression appeared to result in fewer layers in the incisor (**Figure 3D**) and less organic matrix retention in molars (**Figures 3E,F**), while maintaining prism organization (**Figures 3D–F**). Toluidine blue staining shows more homogeneity within the molar compared to the incisor where we see organic matter close to the DEJ and near the enamel surface (**Figures 4C,D**). In contrast, homozygous double transgenic enamel had extensive disruption of structural organization, appeared to contain more organic matrix and showed only rudimentary prismatic organization (**Figures 3G–I**, **4E,F**). Ectopic depositions were observed in mice with homozygous expression of the CTRNC transgene (**Figure 3G**).

Retained organic matrix was observed in incisor and molar enamel from all four genotypes, especially those with homozygous transgene expression of CTRNC*Tg* (**Figures 3B,C,G,H**, **4A–H**). The inclusion of the LRAP*Tg* did not improve the structure of M180Tg/CTRNC*Tg* enamel in homozygous nor hemizygous transgenes. Consistent with μCT and SEM derived thickness data, the enamel of hemizygous double transgenic mouse molars M180*Tg*/CTRNC*Tg*/KO+ and M180*Tg*/LRAP*Tg*/KO+ are most similar to WT (**Figures 3K,L,N,O,T,U**). In a given animal the incisor enamel contains more retained organic matrix in the inner enamel, compared to the molars and WT as seen in SEM (**Figures 3J,M,S**), and toluidine blue stained samples (**Figures 4G,K**).

DISCUSSION

It has been shown previously that enamel prism decussation and 83% of thickness is recovered in the double hemizygous transgenic mouse M180*Tg*/LRAP*Tg*/KO model (Gibson et al., 2011). To better understand the *in vivo* role of full-length amelogenin vs. cleavage and alternative splice products, we generated four genotypes that differ from each other in their relative abundance of M180, its most abundant cleavage product

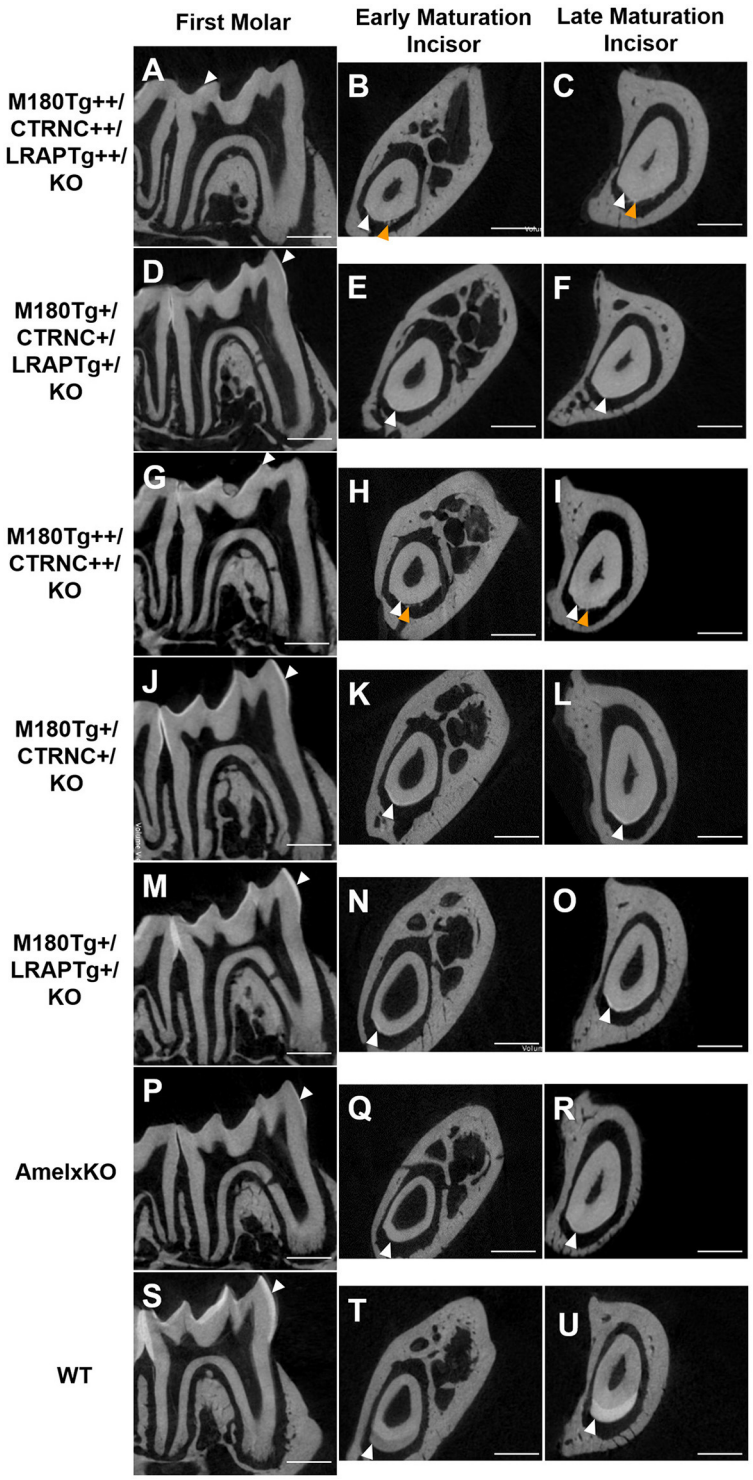

FIGURE 2 | MicroCT analyses of adult molar and incisor enamel. First column: first molars in mid sagittal plane. Middle column: Incisor enamel in coronal plane through the distal root of the first molar, representing early maturation stage. Last column: Incisor enamel in coronal plane adjacent and mesial to the first molar, representing maturation stage enamel. White arrowheads point to mineralized enamel layers visible in molars and incisors. WT seen in last row **(S–U)**; **(P–R)** *Amelx*KO with little enamel on molars and no enamel in the incisor enamel. **(A–C)** homozygous triple transgene M180*Tg*/CTRNC*Tg*/LRAP*Tg*/KO++, showing the thinnest enamel layer compared to all samples shown on both molars and incisors. **(D–F)** Hemizygous triple transgene M180*Tg*/CTRNC*Tg*/LRAP*Tg*/KO+ and **(M–O)** hemizygous double transgene M180*Tg*/LRAP*Tg*/KO+ with thicker enamel than all other transgene phenotypes shown, but thinner than WT. **(G–I)** double transgene M180*Tg*/CTRNC*Tg*/KO++ with a thin layer of enamel as is also seen in **(J–L)** M180*Tg*/CTRNC*Tg*/KO+. Ectopic depositions (orange arrowheads) were visible in incisors of homozygous transgenes M180*Tg*/CTRNC*Tg*/LRAP*Tg*/KO++ and M180*Tg*/CTRNC*Tg*/KO++ **(A–C, G–I)**. Scale bars, 500 μm.

TABLE 3 | Enamel thickness and hardness of adult mandibular molars and incisors.

Genotype	*N*	Incisor enamel thickness (μm)	Molar enamel thickness (μm)	Molar enamel hardness (GPa)
Wild-type (C57BL/6J)	12	119.7 (4.3)^{x}	61.6 (3.8)^{x}	257.4 (64.6)
Amelogenin KO	12	19.1 (5.2)^{w}	11.5 (1.2)^{w}	217.2 (60.0)
M180*Tg*/CTRNC*Tg*/LRAP*Tg*/KO (++)	4	33.7 (10.9)$^{w\ x}$	33.4 (17.2)$^{w\ x}$	238 (87.4)
M180*Tg*/CTRNC*Tg*/LRAP*Tg*/KO (+)	4	28.1 (4.5)^{w}	33.4 (10.9)$^{w\ x}$	200.4 (61.6)
M180*Tg*/CTRNC*Tg*/KO (++)	4	33.7 (11.4)$^{w\ x}$	23.7 (4.1)$^{w\ x\ 3o}$	150 (52.3)
M180*Tg*/CTRNC*Tg*/KO (+)	4	41.6 (10.1)$^{w\ x\ 3t}$	36.0 (7.2)$^{w\ x\ 2o}$	294 (108.6)^{x}
M180*Tg*/LRAP*Tg*/KO (+)[a]	6	45.3 (4.5)$^{w\ x\ 3o\ 3t\ 2o}$	51.4 (7.6)$^{w\ x\ 3o\ 3t\ 2o\ 2t}$	265.0 (59.9)
CTRNC*Tg*/LRAP*Tg*/KO (+)[b]	6	53.1 (14.7)$^{w\ x\ 3o\ 3t\ 2o\ 2t}$	41.4 (13.0)$^{w\ x\ 3o\ 3t\ 2o}$	190.2 (65.3)$^{w\ 2t}$
M180*Tg*/KO (+)[c,d]	6	26.8 (9.6)$^{w\ 2t}$	43.0 (7.5)$^{w\ x\ 3o\ 3t\ 2o}$	291.2 (39.8)$^{x\ 3t}$
CTRNC*Tg*/KO (+)[e]	6	28.1 (11.7)$^{w\ x\ 2t}$	19.6 (3.9)$^{w\ x\ 3o\ 3t\ 2t}$	208.0 (75.0)$^{w\ 2t}$
LRAP*Tg*/KO (+)[f,g]	6	24.1 (7.3)$^{w3o\ 2o\ 2t}$	19.0 (2.2)$^{w\ x\ 3o\ 3t\ 2t}$	193.3 (66.5)^{2t}

Significant differences ($p < 0.05$) are indicated as follows: ^{w}from WT; ^{x}from Amelogenin KO; ^{3o}from M180Tg/CTRNCTg/LRAPTg/KO (++); ^{3t}from M180Tg/CTRNCTg/LRAPTg/KO (+); ^{2o}from M180Tg/CTRNCTg/KO (++); ^{2t}from M180Tg/CTRNCTg/KO (+).

[a]Gibson et al. (2011); [b]Xia et al. (2016), [c]Li et al. (2008), [d]Pugach et al. (2013), [e]Pugach et al. (2010), [f]Chen et al. (2003), [g]Gibson et al. (2009).

CTRNC that lacks the C-terminus, and the most abundant alternative splice product LRAP, which contains only the N- and C-terminus of the full-length molecule, but not the hydrophobic core region. However, in the present study, enamel thickness did not rescue by more than 58%, and prism organization was not fully achieved in incisors (**Figure 3**; **Table 3**).

In normal enamel development, M180 is cleaved shortly after secretion. Mutations in either the C-terminus or N-terminus compromise enamel formation. There are five reported mutations in the *AMELX* C-terminal region, and six mutations in the N-terminal region, leading to thin, discolored, and hypoplastic enamel (Lagerström et al., 1991; Lagerström-Fermer et al., 1995; Lench and Winter, 1995; Kindelan et al., 2000; Sekiguchi et al., 2001; Greene et al., 2002; Hart et al., 2002; Kim et al., 2004; Cho et al., 2014). Mutations in the N-terminus cause self-assembly defects *in vitro* (Buchko et al., 2013). Amelogenin lacking the N-terminus does not form nanospheres *in vitro,* and *in vivo*, the enamel is thin with short crystallites and irregular enamel prisms, indicating the key role of the N-terminus in amelogenin self-assembly and crystallite elongation (Zhu et al., 2006).

Both recent *in vitro* and *in vivo* evidence suggest that CTRNC plays an important role in enamel mineralization (Kwak et al., 2009, 2011; Martinez-Avila et al., 2011; Xia et al., 2016). *In vitro* studies have suggested a role of full-length amelogenin in the control of mineral phase, specifically the stabilization of amorphous mineral phases such as amorphous calcium phosphate (ACP), and alignment of forming crystallites (Kwak et al., 2011). With cleavage of the full-length molecule, one would expect the transformation of ACP to hydroxyapatite to proceed. *In vivo*, amelogenin transcription and MMP20 activity regulate the ratio of M180 to its cleavage product. The choreographed interplay between amelogenin secretion, MMP20 activity, and the resulting abundance and ratio of M180 to CTRNC can provide a mechanism to regulate mineralization rate.

Our data show that the dose of transgene expression has a major effect on enamel formation as is seen in the comparison between homozygous double transgene of M180*Tg*++/CTRNC*Tg*++/KO and hemizygous transgene of M180 and CTRNC. This hemizygous transgene best rescues the structural organization and prism decussation of enamel. However, the produced enamel is softer than in any other transgene model used in this study. In contrast, the homozygous transgene provides excess protein that disrupts the process of both mineral phase regulation and crystallite alignment, as seen in the small platelets compared to the elongated crystals (**Figure 3I**) in the hemizygous enamel. The excess organic matrix in the homozygous M180*Tg*++/CTRNC*Tg*++/KO transgene remains in the extracellular space, covers enamel prisms and seems to prevent proper decussation resulting in diminished hardness (**Figures 3G,H**; **Table 3**). In addition, matrix secretion is disrupted in the homozygous transgene, resulting in ectopic depositions (**Figures 2H,I**, **3G**) and decreased enamel thickness. This finding highlights the importance of sheer abundance of matrix components at a given time, and in relation to MMP20 activity, and is paralleled in the results for the homozygous transgene M180*Tg*++/CTRNC*Tg*++/LRAP*Tg*++, where also ectopic depositions are observed, excess organic material covering prisms and diminished enamel thickness (**Figures 2**, **3**). The rate of enamel apposition and crown extension is higher in incisors compared to molars, which could contribute to the observed differences in structural organization, matrix deposition, and matrix removal between molars and incisors (Smith and Warshawsky, 1977).

Interestingly, enamel organization and prism decussation, as well as hardness is better rescued than in the homozygous transgene without LRAP, M180Tg++/CTRNCTg++. The capacity of LRAP to regulate mineral phase *in vitro*, specifically stabilize ACP, has been shown by Le Norcy et al. (2011). In contrast to the homozygous transgene model, a comparison between the hemizygous transgenic mice M180*Tg*+/CTRNC*Tg*+/LRAP*Tg*+ and M180*Tg*+/CTRNC*Tg*+ shows that the structural organization is much better without LRAP than when it is expressed uniformly with M180 and CTRNC. Our data further suggest that LRAP*Tg* overexpressed with M180*Tg* and CTRNC*Tg* does not affect enamel thickness

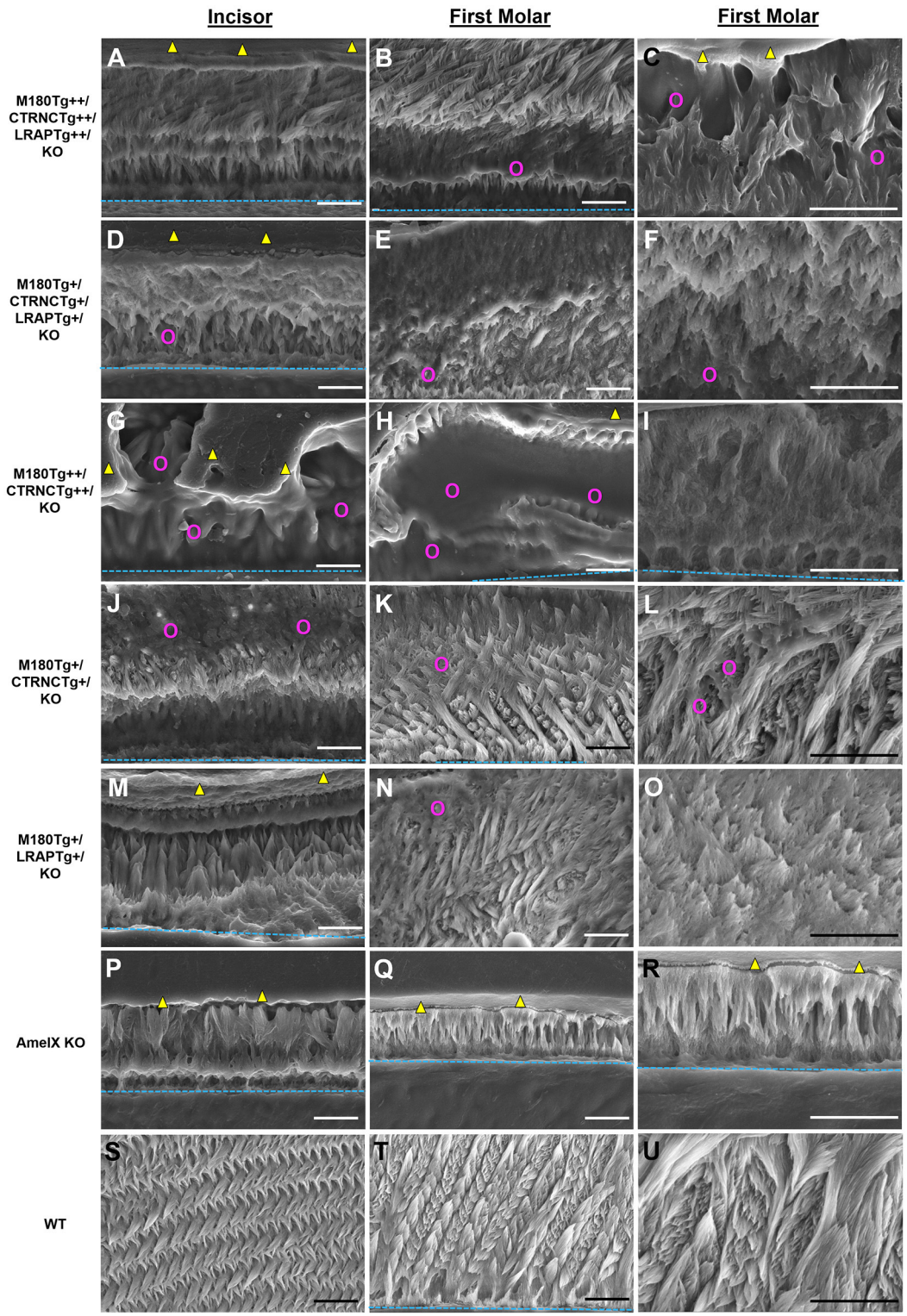

FIGURE 3 | SEM analysis of double and triple transgenic/KO incisor and molar enamel**.** Polished and etched sections through mandibular incisor enamel and first molars imaged by scanning electron microscopy with secondary electron detection. **(A–C)** Homozygous triple transgenic M180*Tg*/CTRNC*Tg*/LRAP*Tg*/KO++, **(D–F)** hemizygous triple transgenic M180*Tg*/CTRNC*Tg*/LRAP*Tg*/KO+, **(G–I)** homozygous double transgenic M180*Tg*/CTRNC*Tg*/KO++, **(J–L)** hemizygous double transgenic M180*Tg*/CTRNC*Tg*/KO+ enamel, and **(M–O)** hemizygous double transgenic M180*Tg*/LRAP*Tg*/KO+, **(P–R)** AmelX null, **(S–U)** WT enamel. First column: Incisors, scale bars 10 μm. Second column: Molars, scale bars 10 μm. Third column: Molars, scale bars 10 μm. Yellow triangles: LR White resin; turquoise dashed lines: DEJ; magenta colored circles: organic matrix in forming enamel.

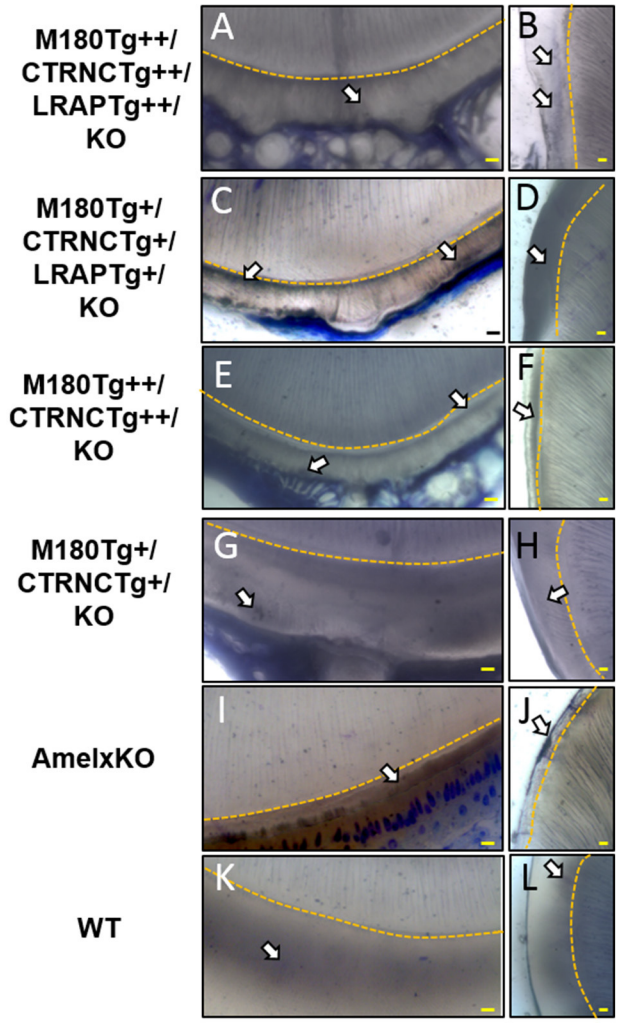

FIGURE 4 | Toluidine Blue staining of LR White embedded samples processed further after SEM analyses. **(A,B)** Homozygous triple transgenic enamel M180Tg/CTRNCTg/LRAPTg/KO++, **(C,D)** hemizygous triple transgenic M180Tg/CTRNCTg/LRAPTg/KO+, **(E,F)** homozygous double transgenic M180Tg/CTRNCTg/KO++, **(G,H)** hemizygous double transgenic M180Tg/CTRNCTg/KO+ enamel, **(I,J)** AmelX null, **(K,L)** WT enamel. Coronal sections through incisors (first column) and molars (second column). Nuclei and organic matter stained blue and marked by arrows, DEJ highlighted in yellow. Scale bars, 10 μm. Magnification 400X.

(**Table 3**). These findings underscore the importance of other factors besides absolute abundance of matrix molecules, namely, the timing of transgene expression and the relative abundance of cleavage product and alternative splice products. While LRAP uses the same promoter *in vivo* as M180, it is not known how LRAP expression varies between stages of enamel development. In addition, the pH buffering effect of matrix components is relevant for mineralization rate and produced mineral phase.

A possible role of the central core domain of amelogenin is the buffering of pH during enamel mineralization and it has been suggested previously that amelogenins may act as a buffer to neutralize protons generated during enamel crystal formation in the secretory stage (Smith, 1998; Smith et al., 2005). Although the role of the central hydrophobic core remains elusive, seven amelogenesis imperfecta-causing mutations in this region are published to date (Aldred et al., 1992; Lench et al., 1994; Lench and Winter, 1995; Collier et al., 1997; Hart et al., 2000, 2002; Ravassipour et al., 2000; Sekiguchi et al., 2001; Greene et al., 2002). In all the transgene models presented here, enamel thickness is decreased, indicating abridged matrix secretion compared to normal enamel development in the WT, where the ending of amelogenin secretion coincides with both the attainment of the full enamel thickness and the enamel matrix becoming acidic (Smith, 1998). Amelogenins including the central hydrophobic core contain 14 histidine residues, which can bind protons such that a single amelogenin molecule can bind up to 15 protons *in vitro* (Ryu et al., 1998). Further support for a suggested role of amelogenin in pH regulation comes from data comparing ion channel expression in ameloblasts during secretory and maturation stage between WT and *Amelx*KO mice. In WT, secretory ameloblasts do not express the anion exchanger Ae2 basolaterally (Lyaruu et al., 2008; Bronckers et al., 2009). However, the expression of Ae2 in secretory ameloblasts of amelogenin KO mice indicate a mechanism to compensate for the lack of buffering in the absence of amelogenin through upregulation of Ae2 expression to secrete bicarbonate (Guo et al., 2015).

Taken together, our data suggest that all three domains of amelogenin play key roles in enamel formation and that the relative abundance over time is critical. The N- and C-termini of amelogenin, which are present in both the most abundant amelogenin (M180) and LRAP, are highly conserved and believed to have different but critical roles in enamel formation (Delgado et al., 2007). Our results support the hypothesis that the core domain affects enamel formation, in particular the aspects of enamel thickness *in vivo* through crystal elongation. This study highlights the need to appreciate the relative abundance of enamel matrix molecules and their role for pH regulation as a key factor of enamel formation. In conclusion, we have shown that excess amelogenin transgenes disrupted the process of enamel formation, likely through the disproportionate presence of amelogenin splice products and disruption of matrix removal. The presence of excess retained organic matrix, layering within enamel, and ectopic depositions in the mouse models studied, suggest that an optimal ratio between M180, CTRNC, and LRAP is critical for normal enamel structure, thickness, and hardness.

ETHICS STATEMENT

This study was carried out in accordance with the recommendations of Institute, Federal and Institutional Animal Care and Use Committee (IACUC) guidelines. The protocol was approved by the IACUC at Forsyth.

AUTHOR CONTRIBUTIONS

MP and FB wrote the manuscript with contributions from all authors. MP, FB, and YX contributed to the design of

the experiments. MP, FB, and YX performed and analyzed experiments. MP and FB supervised the project. All authors reviewed and approved the final version of the manuscript.

FUNDING

Research reported in this publication was supported by the National Institute of Dental and Craniofacial Research of the National Institutes of Health grant R00DE022624 (MP) and R01DE025865 (FB).

ACKNOWLEDGMENTS

We gratefully acknowledge Bhumi Patel for assistance with Western blot experiments, Carolyn Gibson and Ashok Kulkarni for developing the *Amelx*KO mouse model, and John Bartlett for contributing the *Mmp20*KO mice used as the Western blot control lanes.

REFERENCES

Aldred, M. J., Crawford, P. J., Roberts, E., and Thomas, N. S. (1992). Identification of a nonsense mutation in the amelogenin gene (AMELX) in a family with X-linked amelogenesis imperfecta (AIH1). *Hum. Genet.* 90, 413–416.

Bartlett, J. D. (2013). Dental enamel development: proteinases and their enamel matrix substrates. *ISRN Dent.* 2013:684607. doi: 10.1155/2013/684607

Bartlett, J. D., Ball, R. L., Kawai, T., Tye, C. E., Tsuchiya, M., and Simmer, J. P. (2006). Origin, splicing, and expression of rodent amelogenin exon 8. *J. Dent. Res.* 85, 894–899. doi: 10.1177/154405910608501004

Bronckers, A. L., Lyaruu, D. M., Jansen, I. D., Medina, J. F., Kellokumpu, S., Hoeben, K. A., et al. (2009). Localization and function of the anion exchanger Ae2 in developing teeth and orofacial bone in rodents. *J. Exp. Zool. B Mol. Dev. Evol.* 312B, 375–387. doi: 10.1002/jez.b.21267

Buchko, G. W., Lin, G., Tarasevich, B. J., and Shaw, W. J. (2013). A solution NMR investigation into the impaired self-assembly properties of two murine amelogenins containing the point mutations T21–>I or P41–>T. *Arch. Biochem. Biophys.* 537, 217–224. doi: 10.1016/j.abb.2013.07.015

Chen, E., Yuan, Z. A., Wright, J. T., Hong, S. P., Li, Y., Collier, P. M., et al. (2003). The small bovine amelogenin LRAP fails to rescue the amelogenin null phenotype. *Calcif. Tissue Int.* 73, 487–495. doi: 10.1007/s00223-002-0036-7

Cho, E. S., Kim, K. J., Lee, K. E., Lee, E. J., Yun, C. Y., Lee, M. J., et al. (2014). Alteration of conserved alternative splicing in AMELX causes enamel defects. *J. Dent. Res.* 93, 980–987. doi: 10.1177/0022034514547272

Collier, P. M., Sauk, J. J., Rosenbloom, S. J., Yuan, Z. A., and Gibson, C. W. (1997). An amelogenin gene defect associated with human X-linked amelogenesis imperfecta. *Arch. Oral Biol.* 42, 235–242.

Delgado, S., Ishiyama, M., and Sire, J. Y. (2007). Validation of amelogenesis imperfecta inferred from amelogenin evolution. *J. Dent. Res.* 86, 326–330. doi: 10.1177/154405910708600405

Gibson, C. W., Li, Y., Daly, B., Suggs, C., Yuan, Z. A., Fong, H., et al. (2009). The leucine-rich amelogenin peptide alters the amelogenin null enamel phenotype. *Cells Tissues Organs* 189, 169–174. doi: 10.1159/000151384

Gibson, C. W., Li, Y., Suggs, C., Kuehl, M. A., Pugach, M. K., Kulkarni, A. B., et al. (2011). Rescue of the murine amelogenin null phenotype with two amelogenin transgenes. *Eur. J. Oral Sci.* 119(Suppl. 1), 70–74. doi: 10.1111/j.1600-0722.2011.00882.x

Gibson, C. W., Yuan, Z. A., Hall, B., Longenecker, G., Chen, E., Thyagarajan, T., et al. (2001). Amelogenin-deficient mice display an amelogenesis imperfecta phenotype. *J. Biol. Chem.* 276, 31871–31875. doi: 10.1074/jbc.M104624200

Gibson, C. W., Yuan, Z. A., Li, Y., Daly, B., Suggs, C., Aragon, M. A., et al. (2007). Transgenic mice that express normal and mutated amelogenins. *J. Dent. Res.* 86, 331–335. doi: 10.1177/154405910708600406

Greene, S. R., Yuan, Z. A., Wright, J. T., Amjad, H., Abrams, W. R., Buchanan, J. A., et al. (2002). A new frameshift mutation encoding a truncated amelogenin leads to X-linked amelogenesis imperfecta. *Arch. Oral Biol.* 47, 211–217.

Guo, J., Lyaruu, D. M., Takano, Y., Gibson, C. W., Denbesten, P. K., and Bronckers, A. L. (2015). Amelogenins as potential buffers during secretory-stage amelogenesis. *J. Dent. Res.* 94, 412–420. doi: 10.1177/0022034514564186

Hart, P. S., Aldred, M. J., Crawford, P. J., Wright, N. J., Hart, T. C., and Wright, J. T. (2002). Amelogenesis imperfecta phenotype-genotype correlations with two amelogenin gene mutations. *Arch. Oral Biol.* 47, 261–265. doi: 10.1016/S0003-9969(02)00003-1

Hart, S., Hart, T., Gibson, C., and Wright, J. T. (2000). Mutational analysis of X-linked amelogenesis imperfecta in multiple families. *Arch. Oral Biol.* 45, 79–86. doi: 10.1016/S0003-9969(99)00106-5

Kim, J. W., Simmer, J. P., Hu, Y. Y., Lin, B. P., Boyd, C., Wright, J. T., et al. (2004). Amelogenin p.M1T and p.W4S mutations underlying hypoplastic X-linked amelogenesis imperfecta. *J. Dent. Res.* 83, 378–383. doi: 10.1177/154405910408300505

Kindelan, S. A., Brook, A. H., Gangemi, L., Lench, N., Wong, F. S., Fearne, J., et al. (2000). Detection of a novel mutation in X-linked amelogenesis imperfecta. *J. Dent. Res.* 79, 1978–1982. doi: 10.1177/00220345000790120901

Kwak, S. Y., Green, S., Wiedemann-Bidlack, F. B., Beniash, E., Yamakoshi, Y., Simmer, J. P., et al. (2011). Regulation of calcium phosphate formation by amelogenins under physiological conditions. *Eur. J. Oral Sci.* 119(Suppl. 1), 103–111. doi: 10.1111/j.1600-0722.2011.00911.x

Kwak, S. Y., Wiedemann-Bidlack, F. B., Beniash, E., Yamakoshi, Y., Simmer, J. P., Litman, A., et al. (2009). Role of 20-kDa amelogenin (P148) phosphorylation in calcium phosphate formation *in vitro*. *J. Biol. Chem.* 284, 18972–18979. doi: 10.1074/jbc.M109.020370

Lacruz, R. S., Habelitz, S., Wright, J. T., and Paine, M. L. (2017). Dental Enamel Formation and Implications for Oral Health and Disease. *Physiol. Rev.* 97, 939–993. doi: 10.1152/physrev.00030.2016

Lagerström, M., Dahl, N., Nakahori, Y., Nakagome, Y., Bäckman, B., Landegren, U., et al. (1991). A deletion in the amelogenin gene (AMG) causes X-linked amelogenesis imperfecta (AIH1). *Genomics* 10, 971–975.

Lagerström-Fermer, M., Nilsson, M., Bäckman, B., Salido, E., Shapiro, L., Pettersson, U., et al. (1995). Amelogenin signal peptide mutation: correlation between mutations in the amelogenin gene (AMGX) and manifestations of X-linked amelogenesis imperfecta. *Genomics* 26, 159–162.

Lench, N. J., Brook, A. H., and Winter, G. B. (1994). SSCP detection of a nonsense mutation in exon 5 of the amelogenin gene (AMGX) causing X-linked amelogenesis imperfecta (AIH1). *Hum. Mol. Genet.* 3, 827–828.

Lench, N. J., and Winter, G. B. (1995). Characterisation of molecular defects in X-linked amelogenesis imperfecta (AIH1). *Hum. Mutat.* 5, 251–259. doi: 10.1002/humu.1380050310

Le Norcy, E., Kwak, S. Y., Allaire, M., Fratzl, P., Yamakoshi, Y., Simmer, J. P., et al. (2011). Effect of phosphorylation on the interaction of calcium with leucine-rich amelogenin peptide. *Eur. J. Oral Sci.* 119(Suppl. 1), 97–102. doi: 10.1111/j.1600-0722.2011.00900.x

Li, Y., Suggs, C., Wright, J. T., Yuan, Z. A., Aragon, M., Fong, H., et al. (2008). Partial rescue of the amelogenin null dental enamel phenotype. *J. Biol. Chem.* 283, 15056–15062. doi: 10.1074/jbc.M707992200

Lyaruu, D. M., Bronckers, A. L., Mulder, L., Mardones, P., Medina, J. F., Kellokumpu, S., et al. (2008). The anion exchanger Ae2 is required for enamel maturation in mouse teeth. *Matrix Biol.* 27, 119–127. doi: 10.1016/j.matbio.2007.09.006

Martinez-Avila, O. M., Wu, S., Cheng, Y., Lee, R., Khan, F., and Habelitz, S. (2011). Self-assembly of amelogenin proteins at the water-oil interface. *Eur. J. Oral Sci.* 119(Suppl. 1), 75–82. doi: 10.1111/j.1600-0722.2011.00907.x

Pugach, M. K., Li, Y., Suggs, C., Wright, J. T., Aragon, M. A., Yuan, Z. A., et al. (2010). The amelogenin C-terminus is required for enamel development. *J. Dent. Res.* 89, 165–169. doi: 10.1177/0022034509358392

Pugach, M. K., Suggs, C., Li, Y., Wright, J. T., Kulkarni, A. B., Bartlett, J. D., et al. (2013). M180 amelogenin processed by MMP20 is sufficient for decussating murine enamel. *J. Dent. Res.* 92, 1118–1122. doi: 10.1177/0022034513506444

Ravassipour, D. B., Hart, P. S., Hart, T. C., Ritter, A. V., Yamauchi, M., Gibson, C., et al. (2000). Unique enamel phenotype associated with amelogenin gene (AMELX) codon 41 point mutation. *J. Dent. Res.* 79, 1476–1481. doi: 10.1177/00220345000790070801

Ryu, O. H., Hu, C. C., and Simmer, J. P. (1998). Biochemical characterization of recombinant mouse amelogenins: protein quantitation, proton absorption, and relative affinity for enamel crystals. *Connect Tissue Res.* 38, 207–214; discussion 241–206.

Sekiguchi, H., Tanakamaru, H., Minaguchi, K., Machida, Y., and Yakushiji, M. (2001). A case of amelogenesis imperfecta of deciduous and all permanent teeth. *Bull. Tokyo Dent. Coll.* 42, 45–50. doi: 10.2209/tdcpublication.42.45

Shin, M., Hu, Y., Tye, C. E., Guan, X., Deagle, C. C., Antone, J. V., et al. (2014). Matrix metalloproteinase-20 over-expression is detrimental to enamel development: a Mus musculus model. *PLoS ONE* 9:e86774. doi: 10.1371/journal.pone.0086774

Smith, C. E. (1998). Cellular and chemical events during enamel maturation. *Crit. Rev. Oral Biol. Med.* 9, 128–161.

Smith, C. E., and Warshawsky, H. (1977). Quantitative analysis of cell turnover in the enamel organ of the rat incisor. Evidence for ameloblast death immediately after enamel matrix secretion. *Anat. Rec.* 187, 63–98. doi: 10.1002/ar.1091870106

Smith, C. E., Chong, D. L., Bartlett, J. D., and Margolis, H. C. (2005). Mineral acquisition rates in developing enamel on maxillary and mandibular incisors of rats and mice: implications to extracellular acid loading as apatite crystals mature. *J. Bone Miner. Res.* 20, 240–249. doi: 10.1359/JBMR.041002

Snead, M. L., Zhu, D. H., Lei, Y., Luo, W., Bringas, P. O. Jr., Sucov, H. M., et al. (2011). A simplified genetic design for mammalian enamel. *Biomaterials* 32, 3151–3157. doi: 10.1016/j.biomaterials.2011.01.024

Tarasevich, B. J., Philo, J. S., Maluf, N. K., Krueger, S., Buchko, G. W., Lin, G., et al. (2015). The leucine-rich amelogenin protein (LRAP) is primarily monomeric and unstructured in physiological solution. *J. Struct. Biol.* 190, 81–91. doi: 10.1016/j.jsb.2014.10.007

Xia, Y., Ren, A., and Pugach, M. K. (2016). Truncated amelogenin and LRAP transgenes improve Amelx null mouse enamel. *Matrix Biol.* 52–54, 198–206. doi: 10.1016/j.matbio.2015.11.005

Zhu, D., Paine, M. L., Luo, W., Bringas, P. Jr., and Snead, M. L. (2006). Altering biomineralization by protein design. *J. Biol. Chem.* 281, 21173–21182. doi: 10.1074/jbc.M510757200

Conflict of Interest Statement: The authors declare that the research was conducted in the absence of any commercial or financial relationships that could be construed as a potential conflict of interest.

The reviewer YZ and handling Editor declared their shared affiliation.

Copyright © 2017 Bidlack, Xia and Pugach. This is an open-access article distributed under the terms of the Creative Commons Attribution License (CC BY). The use, distribution or reproduction in other forums is permitted, provided the original author(s) or licensor are credited and that the original publication in this journal is cited, in accordance with accepted academic practice. No use, distribution or reproduction is permitted which does not comply with these terms.

frontiers in Physiology

ORIGINAL RESEARCH
published: 17 October 2017
doi: 10.3389/fphys.2017.00790

Posttranslational Amelogenin Processing and Changes in Matrix Assembly during Enamel Development

Mirali Pandya[1], *Tiffani Lin*[2,3], *Leo Li*[3,4], *Michael J. Allen*[5], *Tianquan Jin*[3,6], *Xianghong Luan*[3] *and Thomas G. H. Diekwisch*[1,3]*

[1] Texas A&M Center for Craniofacial Research and Diagnosis, Dallas, TX, United States, [2] UCLA School of Dentistry, Los Angeles, CA, United States, [3] Brodie Laboratory for Craniofacial Genetics, University of Illinois at Chicago, Chicago, IL, United States, [4] University of Michigan Medical School, Ann Arbor, MI, United States, [5] Biometrology Inc., Chicago, IL, United States, [6] Biocytogen, Worcester, MA, United States

OPEN ACCESS

Edited by:
Steven Joseph Brookes,
Leeds Dental Institute,
United Kingdom

Reviewed by:
Harald Osmundsen,
University of Oslo, Norway
Michel Goldberg,
Institut National de la Santé et de la Recherche Médicale, France
Claudio Cantù,
University of Zurich, Switzerland

***Correspondence:**
Thomas G. H. Diekwisch
diekwisch@tamhsc.edu

Specialty section:
This article was submitted to Craniofacial Biology and Dental Research, a section of the journal Frontiers in Physiology

Received: 22 June 2017
Accepted: 26 September 2017
Published: 17 October 2017

Citation:
Pandya M, Lin T, Li L, Allen MJ, Jin T, Luan X and Diekwisch TGH (2017) Posttranslational Amelogenin Processing and Changes in Matrix Assembly during Enamel Development. Front. Physiol. 8:790. doi: 10.3389/fphys.2017.00790

The extracellular tooth enamel matrix is a unique, protein-rich environment that provides the structural basis for the growth of long and parallel oriented enamel crystals. Here we have conducted a series of *in vivo* and *in vitro* studies to characterize the changes in matrix shape and organization that take place during the transition from ameloblast intravesicular matrices to extracellular subunit compartments and pericrystalline sheath proteins, and correlated these changes with stages of amelogenin matrix protein posttranslational processing. Our transmission electron microscopic studies revealed a 2.5-fold difference in matrix subunit compartment dimensions between secretory vesicle and extracellular enamel protein matrix as well as conformational changes in matrix structure between vesicles, stippled materials, and pericrystalline matrix. Enamel crystal growth in organ culture demonstrated granular mineral deposits associated with the enamel matrix framework, dot-like mineral deposits along elongating initial enamel crystallites, and dramatic changes in enamel matrix configuration following the onset of enamel crystal formation. Atomic force micrographs provided evidence for the presence of both linear and hexagonal/ring-shaped full-length recombinant amelogenin protein assemblies on mica surfaces, while nickel-staining of the N-terminal amelogenin N92 His-tag revealed 20 nm diameter oval and globular amelogenin assemblies in N92 amelogenin matrices. Western blot analysis comparing loosely bound and mineral-associated protein fractions of developing porcine enamel organs, superficial and deep enamel layers demonstrated (i) a single, full-length amelogenin band in the enamel organ followed by 3 kDa cleavage upon entry into the enamel layer, (ii) a close association of 8–16 kDa C-terminal amelogenin cleavage products with the growing enamel apatite crystal surface, and (iii) a remaining pool of N-terminal amelogenin fragments loosely retained between the crystalline phases of the deep enamel layer. Together, our data establish a temporo-spatial correlation between amelogenin protein processing and the changes in enamel matrix configuration that take place during the transition from intracellular vesicle

compartments to extracellular matrix assemblies and the formation of protein coats along elongating apatite crystal surfaces. In conclusion, our study suggests that enzymatic cleavage of the amelogenin enamel matrix protein plays a key role in the patterning of the organic matrix framework as it affects enamel apatite crystal growth and habit.

Keywords: amelogenin, extracellular matrix, self-assembly, stippled materials, apatite crystal growth

INTRODUCTION

Tooth enamel is a remarkable bioceramic characterized by extraordinary hardness, resilience and fracture resistance. The formation of this extremely hard biomineral within the soft and gel-like extracellular enamel matrix remains an enigma in biomedical research to this day. In-depth understanding and visualization of the biological processes and mechanisms involved in amelogenesis are hampered by the limitations of conventional imaging techniques and artifacts introduced because of sample preparation. Specifically, optical *in vitro* and *in vivo* imaging are limited by the resolution of conventional light microscopy; scanning and transmission electron microscopy are limited by sample preparation for near-vacuum electron beam imaging conditions, contrasting procedures for organic matrix visualization, and beam damage to the mineral phase; atomic force microscopy provides high resolution but is restricted to surface topographies; and nuclear magnetic resonance spectroscopy lacks the topographical information provided by electro-optical imaging techniques. Yet, disregarding the weaknesses of individual strategies, the combination of information derived from complimentary approaches has yielded much progress toward a comprehensive understanding of the many aspects contributing to early enamel biomineralization. The combination of imaging and analytical techniques together with a plethora of individual approaches has resulted in a number of model systems that explain various aspects of enamel biomineralization.

Early enamel researchers thought of the enamel matrix as a "concentrated amorphous gel structure, rather than a more highly oriented assembly of fibers"(Fearnhead, 1963)and believed that the concept of the enamel matrix as a thixotropic gel would explain its "potential mobility as the protein would flow from regions where rapid growth of apatite crystallites caused a local increase in pressure to adjacent, relatively unmineralized regions, where it could initiate further crystals" (Eastoe, 1963). John E. Eastoe fathomed that the enamel proteins should be considered "as the true matrix of enamel in which the apatite crystallites are laid down, by a process which is not yet explored by which may be analogous to the epitactic mechanism believed to occur in collagenous mineralized tissues"(Glimcher, 1959; Eastoe, 1963). Thus, Eastoe imagined the enamel matrix as a homogeneous gel in which the enamel proteins freely float between further crystallized regions close to the dentin-enamel junction to the sites of early apatite crystallization at the ameloblast cell membrane, readily aiding each crystal to be initiated and grown "until they come into contact with their neighbors" (Eastoe, 1963). Notwithstanding this insightful speculation related to the function of the enamel matrix, Eastoe deserves much credit for the discovery of amelogenins as tissue-specific enamel proteins rich in proline, glutamic acid, and histidine (Eastoe, 1960).

Eastoe's contemporaries, the electron microscopists Dorothy F. Travis and Marie U. Nylen, pioneered an ultrastructural perspective of the developing enamel matrix by recognizing the stippled or finely granular materials located at the mineralization front as morphological building blocks of the enamel matrix (Frank et al., 1964; Travis and Glimcher, 1964; Reith, 1967; Nylen, 1979). They and others reported the presence of 5–7 nm granules in sectioned material and in suspensions of developing enamel (Fearnhead, 1965; Nylen, 1979). The existence of stippled materials was briefly called into question when the effect of fixative temperature on matrix structure was discovered (Lyaruu et al., 1982, 1984). Changes in enamel suprastructure at 4°C temperature had been described earlier and attributed to the high proline content of the enamel matrix (Nikiforuk and Simmons, 1965). Needless to say, faithful ultrastructural examination of the enamel matrix requires fixation at 37°C or room temperature as the mammalian body temperature does not drop to 4°C (Diekwisch et al., 1993, 1995). The functional significance of the enamel matrix stippled materials as supramolecular subunit compartments responsible for the control of enamel crystal growth became evident in study in which the translation of the key enamel matrix protein amelogenin was inhibited using an antisense strategy (Diekwisch et al., 1993). The concept of enamel matrix supramolecular assemblies as the basis for enamel crystal spacing and growth was thereafter confirmed using organ culture data (Diekwisch et al., 1995) and atomic force microcroscopy of unfixed freshly prepared enamel matrix (Diekwisch et al., 1993, 1995; Diekwisch, 1998).

Inversely interpreted transmission electron micrographs together with atomic force microscopy images and dynamic light scattering data helped to advance the nanosphere theory of enamel crystal growth (Fincham et al., 1994, 1995; Paine et al., 2001). A simplified sketch (Fincham et al., 1999) illustrates beaded rows of amelogenin nanospheres surrounding growing enamel crystals, and begs for the question as to how the needle-shaped thin enamel crystals would possibly grow while surrounded by densely packed globular structures. Indeed, the task of reconciling the rounded globes of amelogenin nanospheres with the sharp-edged hexagonal cross-sections of enamel apatite crystals resembles the fitting of a square peg in a round hole. Today, none of the three pillars of the nanosphere theory clearly provides evidence for the presence of spherical subunits in the enamel matrix: (i) light scattering data simply reference radii and not necessarily imply the presence of spherical assemblies, (ii) atomic force micrographs visualize the surface topographies of enamel proteins assembled on mica sheets and not in three dimensions, and (iii) the electron micrographs

initially recruited to support the nanosphere theory incorrectly refer to the circular spaces in between nanospheres as protein assemblies instead of the electron dense protein coats associated with the growing enamel crystals (Diekwisch, 1998), a reversal of stained and unstained matrix compartments analogous to Edgar Rubin's young girl/old woman optical illusion. Moreover, the concept of self-assembly of amelogenins into spherical subunits is not universally accepted, as some investigators have argued that the organic enamel matrix organizes into fibrillar (Frank et al., 1960), lamellar (Ronnholm, 1962), or helical structures (Smales, 1975), or filaments and ribbons (Martinez-Avila et al., 2012; Carneiro et al., 2016). Recent small angle X-ray scattering (SAXS) studies propose that amelogenins self-assemble as nano-oblates with a 1:2 aspect ratio (Aichmayer et al., 2005; Margolis et al., 2006). Nevertheless, the nanosphere theory has established a model for the role of globular enamel protein assemblies as structural entities involved in enamel hydroxyapatite crystal growth.

The ubiquitous presence of the amelogenin-rich extracellular enamel matrix throughout all stages of enamel crystal formation infers an involvement in multiple aspects of matrix-mediated enamel crystal growth, including (i) matrix assembly, (ii) enamel crystal nucleation, (iii) initial crystal fusion of apatite precursors into apatite ribbons, and (iv) eventual crystal elongation and growth of true apatite crystals. Three models have been established to explain amelogenin nanosphere assembly and interaction among nanospheres. A first model based on SAXS data postulates that amelogenin nanospheres assemble into nanospheres with a dense hydrophobic core and a shell of hydrophilic and negatively charged chain segments (Aichmayer et al., 2005; Margolis et al., 2006). A second model, the amelogenin micelle model, focuses on the distribution of hydrophilic and hydrophobic regions within the amelogenin molecule and hypothesize that amelogenins aggregate into micelles through the ionic interactions between positively and negatively charged mini-domains and the complementary domain of another amelogenin molecule in reverse orientation (Fukae et al., 2007). A third model based on heteronuclear single quantum coherence nuclear magnetic resonance (HSQC NMR) spectra and analytical ultracentrifugation proposes that amelogenins self-assemble as donut-shaped entities through ipsilateral interactions at the α-helical N-terminus of the molecule, while the hydrophilic C-termini point toward the outside of the assembly (Zhang et al., 2011). Together, these studies provide a good understanding of the *in vitro* self-assembly capacity of amelogenin into nanoscale subunits. However, a universally accepted model explaining the *in vivo* structural entities of protein-mediated enamel crystal growth and their transformation throughout development is still lacking and in need of further investigation (Ruan and Moradian-Oldak, 2015).

Three recent *in vitro* studies have shed light on the possible protein/mineral interactions that take place during the onset of enamel crystal growth. The first of these three studies took advantage of a constant composition crystallization system, allowing for the control of ion concentration changes at the nanomolar level (Tomson and Nancollas, 1978). When used in combination with recombinant porcine amelogenin, this constant composition crystallization approach yielded hierarchically organized amelogenin and amorphous calcium phosphate (ACP) nanorod microstructures involving the coassembly of amelogenin-ACP particles (Yang et al., 2010). Second, a cryoelectron microscopy-based study has further confirmed that amelogenin undergoes stepwise hierarchical self-assembly, and that these assemblies are involved in the stabilization of mineral prenucleation clusters and their arrangement into linear chains (Fang et al., 2011). This study also demonstrated that the prenucleation clusters subsequently fused to form needle-shaped mineral particles and subsequently apatite crystallites (Fang et al., 2011). Finally, a combined circular dichroism/nuclear magnetic resonance (CD/NMR), dynamic light scattering, and fluorescence spectroscopy study resulted in a model for nanosphere formation via oligomers, suggesting that nanospheres disassemble to form oligomers in mildly acidic environment via histidine protonation (Bromley et al., 2011). In their model, amelogenins undergo stepwise self-assembly from monomers at pH3.5 to oligomers at pH5.5 and to nanospheres at pH8, while subsequent nanosphere breakdown would increase the amelogenin binding surface area to interact with the apatite crystal surface (Bromley et al., 2011). All three of these models postulate a very close interaction between the mineral and the protein phase at the site of initial calcium phosphate crystal growth. Such an intimate relationship between the organic protein matrix and the growing crystal phase goes back to earlier concepts proposed as part of Ermanno Bonucci's crystal ghost theory (Bonucci et al., 1988; Bonucci, 2014).

A number of morphological findings have helped to further expand our understanding of enamel crystal growth beyond the nanosphere stage, including the visualization of rows of globular assemblies on the surface of developing enamel hydroxyapatite crystal planes via freeze fracture electron microscopy (Moradian-Oldak and Goldberg, 2005), reports of nanosphere disassembly and "shedding" of amelogenins onto apatite surfaces and associated changes in amelogenin secondary structure (Tarasevich et al., 2009a,b, 2010; Lu et al., 2013), and the binding of globular matrix protein assemblies to developing enamel crystals *in vitro* (Robinson et al., 1981; Wallwork et al., 2001). Together, these findings lend support for a classic model of matrix mediated enamel crystal growth, henceforth dubbed the beehive model, which is comprised of strings of mineral/matrix nuclei that form a mantle of hexagonally arranged enamel mineral precursor deposits on the surface of growing enamel apatite crystals (Robinson et al., 1990).

Most recent reports about filamentous amelogenin nanoribbon self-assembly and their potential impact on enamel crystal formation add a unique dimension to the many shapes and forms resulting from amelogenin intermolecular associations (Martinez-Avila et al., 2011, 2012; Carneiro et al., 2016). Originally, these filamentous amelogenin nanoribbons were detected at water-oil interfaces (Martinez-Avila et al., 2011) or in the presence of calcium and phosphate ions (Martinez-Avila et al., 2011). Similarities between amelogenin nanoribbons and the amyloid polyglutamine fibrillar aggregates as they occur in neurodegenerative diseases (Chen et al., 2002; Tanaka et al., 2002;

Schneider et al., 2011; Lyubchenko et al., 2012; Buchanan et al., 2014) have been invoked to explain the concept of nanoribbons templating apatite growth in human enamel (Carneiro et al., 2016). However, elongated enamel protein matrix ribbons without a close association to the adjacent mineral do not occur during enamel development *in vivo* (Diekwisch et al., 1995, 2002), and the protein assemblies generated in the filamentous nanoribbon studies are rather evidence of the unique propensity of amelogenins to form elongated assemblies *in vitro* than a physiological occurrence during mammalian amelogenesis. Nevertheless, this propensity of amelogenins to form elongated protein/mineral assemblies is likely a major force contributing to c-axis enamel crystal growth.

The present contribution seeks to introduce a developmental approach toward the relationship between enamel ions and proteins during enamel crystal formation and growth. Here we hypothesize that enamel ions and proteins are intimately associated with each other throughout the course of amelogenesis, starting from ion transport until advanced crystal growth, and that changes in mineral habit and protein conformation are caused by amelogenin enamel protein fragmentation. To verify our dynamic three-phase model of enamel matrix transformation and crystal growth (**Figure 4**) we have interrogated electron micrographs of developing mouse molar enamel *in vivo* and *in vitro* and analyzed amelogenin self-assemblies using atomic force microscopy, fluorescence microscopy, and nickel-labeling of the amelogenin N-terminus. To ask whether stage-specific changes in enamel matrix configuration were related to the presentation of amelogenin cleavage products within the matrix and adjacent to the crystal surface, we have separated porcine tooth molars into enamel organ, superficial and deep enamel preparations and performed a two-step protein extraction procedure separating loosely bound and mineral bound enamel proteins and probed protein extracts using N- and C-terminal amelogenin antibodies on Western blots. Together, these data provide new insights into the conformational changes of enamel matrix structure and related effects of amelogenin processing that take place during enamel matrix assembly, enamel crystal nucleation, and enamel crystal growth.

MATERIALS AND METHODS

Animal Experiments and Organ Culture

For the preparation of 2 days postnatal mouse molars, mice were sacrificed according to UIC animal care regulation, molars were dissected from mandibles and immersed into Karnovsky's fixative as previously described (Diekwisch et al., 1995). For tooth organ culture studies, E16 timed-pregnant Swiss-Webster mice were sacrificed and mandibular first molars were dissected.

El6 cap stage tooth organs were cultured for 12 days in BGJb+ medium (Fitton-Jackson's modified BGJ medium) supplemented with 100 g/ml L-ascorbic acid and 100 U/ml penicillin/streptomycin as previously described (Diekwisch et al., 1995). Explanted molars were cultured at 37°C with 95% air and 5% CO_2. Initial pH was adjusted to 7.4 and the medium was changed every other day.

Transmission Electron Microscopy

Three days postnatal mouse molar tooth organs as well as E16 tooth organs cultured for 12 days were fixed in Karnovsky's fixative as previously described (Diekwisch, 1998), dehydrated and embedded in Eponate 12 (Ted Pella, Redding, CA). Sections were cut on a Leica Ultracut UCT ultramicrotome. After drying, sections were contrasted in 1% uranyl acetate followed by Reynold's lead citrate for 15 min each. Observations were made on a JEOL 1220EX transmission electron microscope at the UIC Research Resources Center (Chicago, IL).

Proteins

The full length mouse amelogenin (M179), the N-terminal amelogenin N92 coding sequence, and the C-terminal amelogenin C86 were cloned into pASK-43(+) with EcoR I and XhoI restriction sites at the 5' and 3' end respectively as previously described(Jin et al., 2009; Zhang et al., 2011). M179 is the full-length mouse amelogenin protein lacking the N-terminal methionine (Simmer et al., 1994), while the terms N92 and C86 denote recombinant proteins based on the N-terminal amelogenin 92 amino acid fragment or the C-terminal amelogenin 86 amino acid fragment (Zhang et al., 2011). For nickel staining of the N-terminal polyhistidine tag, an N-terminal MRGSHHHHHHGAGDRGPE HIS-tag was inserted at N-terminus of the protein. BL21-DM* host bacteria were cultured at 37°C until the OD_{600} reached 0.8 and then were induced at 32°C for 4 h. The expressed proteins were absorbed onto a Ni-NTA agarose column and washed with 10 column volumes of PBS and 3 column volumes of 40 mM imidazole in PBS, followed by protein elution with a pH 5.0 gradient (from 50 to 500 mM) imidazole PBS solution and dialysis against H_2O. Subsequently, the purified proteins were concentrated to about 10 mg/ml using a Centriprep YM-3 column. Finally, the polyproline repeat amelogenin PXX33 peptide (>99% purity, sequence PMQPQPPVHPMQPLPPQPPLPPMFPMQPLPPML) was synthesized by Genescript (Piscataway, NJ).

Atomic Force Microscopy

The atomic force microscope (AFM) measurements were carried out using an extended MultiMode AFM (MMAFM) integrated with a NanoScope IIIa controller (Veeco Instruments, Santa Barbara, CA) and a Q-Control Module (nanoAnalytics, Muenster, Germany) as previously described (Jin et al., 2009). The MMAFM was equipped with a calibrated E-type piezoelectric scanner and a glass cell for fluid TappingMode AFM (both from Veeco). The silicon AFM cantilever/probe used in this study was rectangular in shape, 130 μm in length and 35 μm in width (NSC36, MikroMasch). The advertised typical force constant and resonant frequency of this cantilever/probe is 0.6 N/m and 75 kHz respectively. Nominal sharpness of the probe-tip end radius is ≤10 nm. The cantilever/probes were oscillated near 30 kHz at low amplitude for fluid tapping mode AFM. Fluid damping reduces the resonant frequency of rectangular AFM cantilevers in air by approximately 50%. The AFM substrate used for protein adsorption was Grade V5, Pelco mica (10 × 40 mm) purchased from Ted Pella (Redding, CA). The mica was freshly cleaved using adhesive tape prior to use. Stock solutions

of 10–20 mg/ml protein (either amelogenin M179 or C86) in 40 mM Tris (pH 8.0) were mixed and stored at 4°C and analyzed by AFM. Stock solutions were diluted typically at 1:100 into the blank AFM imaging buffer (40 mM Tris, pH 8.0) during scanning and adsorption to mica was monitored. Typical AFM scan rates were 1.0–1.25 Hz for 512 data points × 256 lines. The AFM images were planefit to correct for background sloping errors.

Fluorescent Images of Aqueous Protein Assemblies

Lyophilized recombinant M179 full-length mouse amelogenin and synthesized PXX polyproline repeat peptide were immersed in DDW (pH 7.4) overnight and allowed to self-assemble on a glass slide kept within a humid chamber. Same amounts of each protein were used in this study. After 24 h, 1% fluorescein was added to the aqueous solution for 1 h. Subsequently protein solutions on glass slides were examined under a cover slip using a Leica fluorescent microscope with a 100x oil immersion lens.

Polyhistidine Tag Labeling and Electron Microscopy

Droplets containing 100 μl of diluted (1 mg/ml) pH7.5–8.0 His-tagged recombinant N92 amelogenin were placed on carbon coated copper TEM grids (Ted Pella, Redding, CA) and incubated in a moisturized container at 37°C for 2 h. Thereafter, TEM grids were quickly rinsed with DDW, immersed into 100 μl of freshly prepared 1% $NiSO_4$ (Sigma, St. Louis, MO) solution for 30 min, quickly rinsed with DDW again, air dried, and analyzed using a JEOL 1220EX transmission electron microscope at the UIC Research Resources Center (Chicago, IL).

Western Blot

Three months old porcine mandibles were obtained from a local animal farm, and enamel organ epithelium and enamel matrix proteins were collected immediately after slaughter from unerupted mandibular molars. As a first step, the epithelial enamel organ (EO) was collected separately from the matrix and subjected to protein extraction. As a second step, two successive layers of the protein rich enamel matrix were scraped off the tooth surface: (i) a superficial enamel matrix layer that was soft in consistency and easily removable without application of force (SEL), and (ii) a deeper enamel matrix layer that was already hardened and required mechanical force to be separated from the underlying and already mineralized dentin surface (DEL). Tissue and matrix from all three groups were then subjected to protein extraction for 5 days with SDS lysis buffer containing 0.5% sodium dodecyl sulfate, 0.05 M TRIS-Cl, 1 mMol dithiothreitol (DTT) with a pH of 8.0. After lysis, samples were dialyzed for 1 week at 4°C against DDH_2O, and centrifuged for 15 min at 2,400 g and 4°C. As a first step, the SDS soluble supernatant from all three groups was collected for Western blot. After removal of the supernatant, the pellet of all three extracts was subject to a second round of extraction with 4 M guanidine HCl. After 5 days of extraction in 4 M guanidine HCL, the extraction solution was once more centrifuged, and the supernatant of the 4 M guanidine group of each group was collected and dialyzed for 1 week at 4°C. Thereafter, proteins were concentrated using Amicon spin columns (3 kDa cut-off, Millipore, Billerica, MA), and re-suspended in RIPA buffer for Western blot detection.

For Western blot analysis, equal amounts of protein were loaded onto a 10% SDS polyacrylamide gel, subjected to SDS gel electrophoresis and then transferred onto a polyvinylidine difluoride (PVDF) membrane using a semi dry transfer system. The membrane was blocked with 5% dry milk in TBST, probed either with primary antibody against the C-terminal amelogenin fragment or against the N-terminal amelogenin fragment (1:1,000), followed by anti-rabbit IgG HRP conjugated secondary antibody (1:2,000; cell signaling) incubation. Primary antibodies were based on the following amelogenin-derived peptides: LPPHP GSPGY INLSY EVLTP LKWYQ SMIRQ P (N-terminal antibody) and PLSPI LPELP LEAWP ATDKT KREEV D (C-terminal antibody) and generated in collaboration with Zymed (South San Francisco, CA). A chemiluminescent substrate (Thermo Scientific) was used to reveal the HRP signal.

Statistical Analysis

For this analysis, 15 subunit compartments located either in secretory vesicles or within the enamel matrix were selected using a random generator and average subunit size and standard deviations were calculated and reported for both groups. Student's *t*-test was used to determine statistically significant differences between the two groups and the significance level was set at $\alpha \leq 0.05$.

RESULTS

Changes in Matrix Subunit Compartment Dimensions between Secretory Vesicle Matrix, Extracellular Enamel Protein Matrix ("Nanospheres"), and Pericrystalline Protein Matrix ("Crystal Ghosts")

Transmission electron micrographs of developing mouse molar enamel revealed three stages involved in matrix mediated enamel crystal growth (**Figure 1A**): (i) initial matrix assembly in ameloblast secretory vesicles, (ii) deposition of an extracellular enamel matrix consisting of stippled materials, and (iii) formation of initial enamel crystallites within this extracellular matrix. Comparison between **Figures 1B,C** illustrates the remarkable subunit size differences between the enamel matrix of the stippled materials (**Figure 1C**) and the matrix within the secretory vesicles (**Figure 1B**). Subunit dimensions were 7.07 nm ± 1.61 nm for the secretory vesicle matrix and 17.47 nm ± 3.44 nm in the extracellular enamel matrix of the stippled materials (**Figure 1B** vs. **Figure 1C**). The 2.5-fold difference in subunit size was statistically highly significant ($p < 0.0001$). Transmission electron micrographs also demonstrated the less than parallel alignment of the earliest enamel crystallites (**Figure 1D**) in comparison to the fairly parallel aligned crystal needles at a further advanced state of crystal growth (**Figure 1E**). In terms of matrix assembly, these images revealed electron dense globular organic enamel matrix

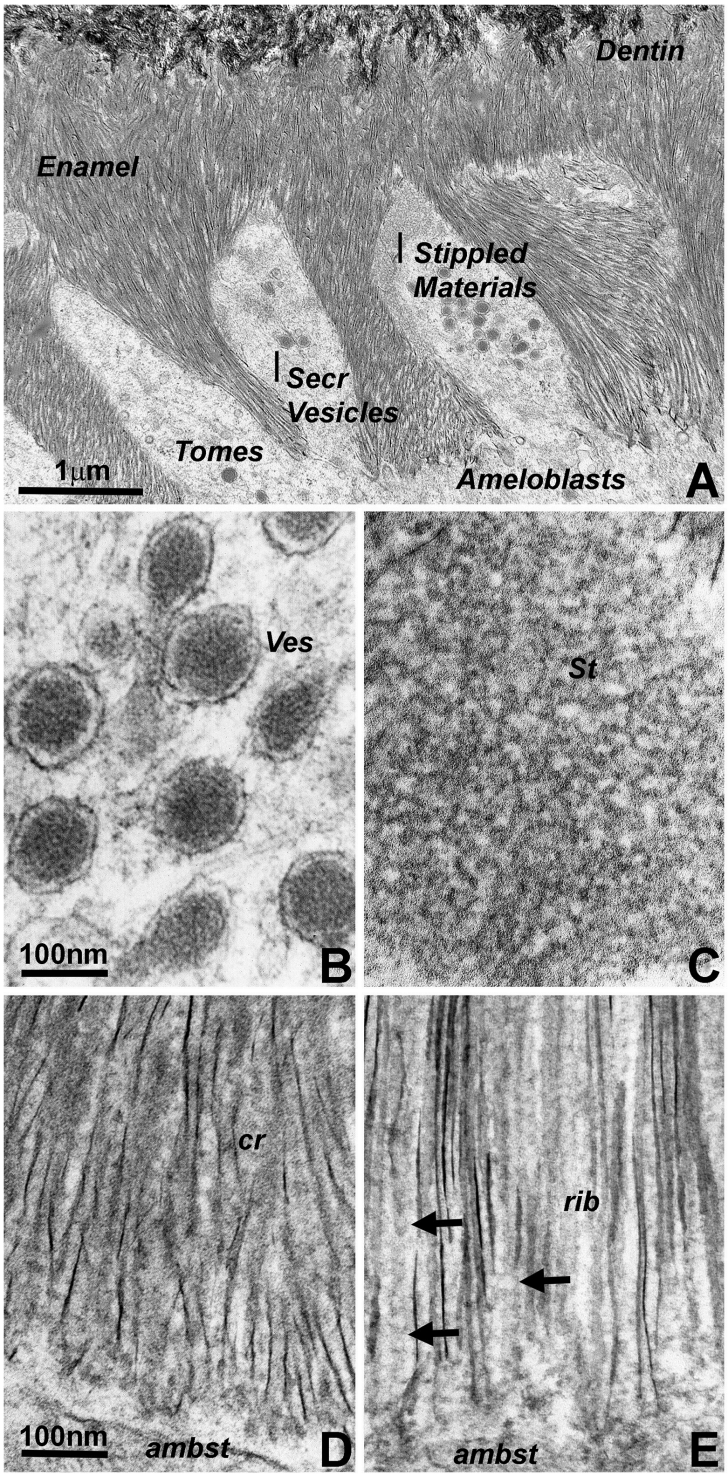

FIGURE 1 | Electron micrographs illustrating subunit assembly and structural transformation during initial enamel crystal formation *in vivo*. **(A)** Interface between Tomes' processes and early enamel prisms. Note the presence of enamel matrix carrying secretory vesicles (Secr Vesicles) within the Tomes' process (Tomes) at the apical ameloblast pole. Bulk deposits of an extracellular matrix containing stippled materials were recognized between the ameloblast cell membrane and the newly formed enamel crystal layer. The border between enamel (Enamel) and dentin (Dentin) was delineated by differences in crystal structure and organization). **(B)** High resolution ultrastructure of an ameloblast secretory vesicle (ves). **(C)** Ultrastructure and subunit organization of the non-mineralized enamel extracellular matrix commonly identified as stippled materials (St). **(D,E)** Ultramicrographs of early enamel crystals. **(D)** illustrates the somewhat disorganized arrangement of initial enamel crystals (cr), and **(E)** reveals ribbon-shaped assemblies (rib, arrows) of organic matter in between highly parallel rows of enamel crystals. Scale bar **(A)** = 1 μm; **(B,C)** = 100 nm; **(D,E)** = 100 nm. The same scale bar applies for **(B–E)**.

subunits closely associated with growing enamel crystallites (**Figure 1D**) and beaded or helical arrangement of organic nanoribbons in close proximity to the elongating apatite crystals (**Figure 1E**). Exposure of isolated and free-standing enamel protein nanoribbons (arrows) was likely due to the thin plane of section on these 400Å diameter ultrathin sections (**Figure 1**).

Key Features of Enamel Crystal Growth in Organ Culture: (i) Granular Mineral Deposits Associated with the Enamel Matrix Framework, (ii) Dot-Like Mineral Deposits along Elongating Initial Enamel Crystallites, and (iii) "Crystal Ghost" Organic Matrix Adjacent to Forming Enamel Crystals

Organ culture models are unique experimental systems in which the loss of circulation and the reduced access to nutrients allows for enhanced morphological insights into key events of mineralized tissue formation (Diekwisch et al., 1993, 1995; Diekwisch, 1998). Here, our tooth organ culture study revealed granular electron dense mineral deposits onto the organic matrix framework of the enamel matrix stippled materials (**Figure 2C**), suggestive of a high mineral content in the pre-crystalline enamel extracellular matrix. Initial crystallites were surrounded by a fairly electron dense organic matrix (**Figure 2D**). These initial mineral protein/mineral assemblies were separated from each other by electron-lucent zones in between discrete mineral assembly deposits (**Figure 2D**). Elongated crystals were surrounded by an electron dense coat of mineral granules in immediate proximity to the crystal surface, indicative of epitaxial crystal growth (**Figure 2E**). Finally, transmission electron micrographs of the enamel matrix/initial crystallization interface demonstrated an almost linear separation between the subunit compartments of the non-mineralized matrix and the crystal-associated matrix of the early crystalline phase, suggestive of an *en block* conversion of matrix assemblies from crystal-free to crystal-rich matrix (**Figure 2F**).

Linear and 20 nm Hexagonal/Ring-Shaped Amelogenin Protein Assemblies on Mica Surfaces and 20 nm Globular Amelogenin Assemblies of Nickel-Stained N92 Amelogenins on Carbon Coated Grids As Revealed via AFM and TEM

Three different types of experiments were conducted to visualize modes of amelogenin self-assembly and address the question as to which amelogenin motifs were involved in self-assembly and protein elongation. In a first set of experiments, recombinant full-length mouse amelogenin (M179) and C-terminal C86 amelogenin were placed on freshly cleaved mica and allowed to self-assemble (**Figures 3A,B**). Tapping mode AFM images revealed parallel rows of globular amelogenin protein as well as circular/hexagonal inter-row assemblies (**Figure 3A**) indicative of a propensity of full-length amelogenins to self-assemble either in linear rows or as hexagonal patterned subunit compartments when exposed to flat mica surfaces at pH 7.4 without the addition of additional proteins or ions. The C-terminal amelogenin alone without the helical N-terminus did not form any detectable surface patterns (**Figure 3B**). To ask whether the amelogenin N-terminus was involved in self-assemblies, our previously generated N-terminally His-tagged N92 amelogenin (Zhang et al., 2011) was incubated on carbon-coated mesh wire grids and subjected to nickel staining. Transmission electron micrographs of stained N92 matrices revealed oval or donut-shaped electron-dense assemblies measuring approximately 20 nm in diameter (**Figure 3C**). Fluorescent labeling of overnight incubated amelogenins in aqueous solution at pH 7.4 resulted in complex large scale assemblies measuring several micrometers in length (**Figure 3D**). In contrast, self-assemblies of PXX33 polyproline-rich amelogenin peptides incubated under the same conditions were substantially thinner and smaller (**Figure 3E**).

Western Blot Analysis Reveals Parallels between Amelogenin Fragmentation and Changes in Matrix Organization during Enamel Protein Transport, "Nanosphere" Assembly, and Crystal Growth

Here we asked whether changes in enamel matrix configuration as they occur during amelogenesis coincide with the gradual processing of the full-length amelogenin into enzymatically cleaved fragments. In addition, we employed two successive stages of protein extraction to separate loosely-bound and crystal-associated matrix proteins. First, loosely bound intercrystalline proteins were harvested using a sodium dodecyl sulfate (SDS)-based extraction procedure that functions similar to a detergent. Thereafter, crystal-bound enamel matrix proteins were extracted via 4 M guanidine (modified after Termine et al., 1980). Individual SDS-based or guanidine (Gu)-based extracts from enamel organ, superficial or deep enamel matrix were then subjected to gel electrophoresis and Western blot (**Figure 4A**). We postulated that our layer- and binding-level based analysis would provide new insights into relationship between amelogenin processing, matrix assembly, and protein-mediated crystal growth.

Our C-terminal amelogenin antibody recognized a distinct 28 kDa band indicative of the full-length amelogenin on the SDS-based enamel organ extract (**Figure 4C**, lane 1). This antibody identified two strong bands at 28 and 25 kDa and a less intense band at 15 kDa on the SDS-based extract of the superficial enamel matrix, while there was a single 26 kDa band on the SDS-based extract of the deep enamel matrix (**Figure 4C**, lanes 2 and 3). There was a 23 kDa amelogenin positive band on the Gu-based extract of the enamel organ and a series of three amelogenin positive bands ranging from 8 to 16 kDa on the Gu-based extract of the deep enamel matrix (**Figure 4C**, lanes 4 and 6). In opposite to the strong amelogenin signal in the SDS extract of the superficial enamel layer, the amelogenin signal in the Gu extract of the

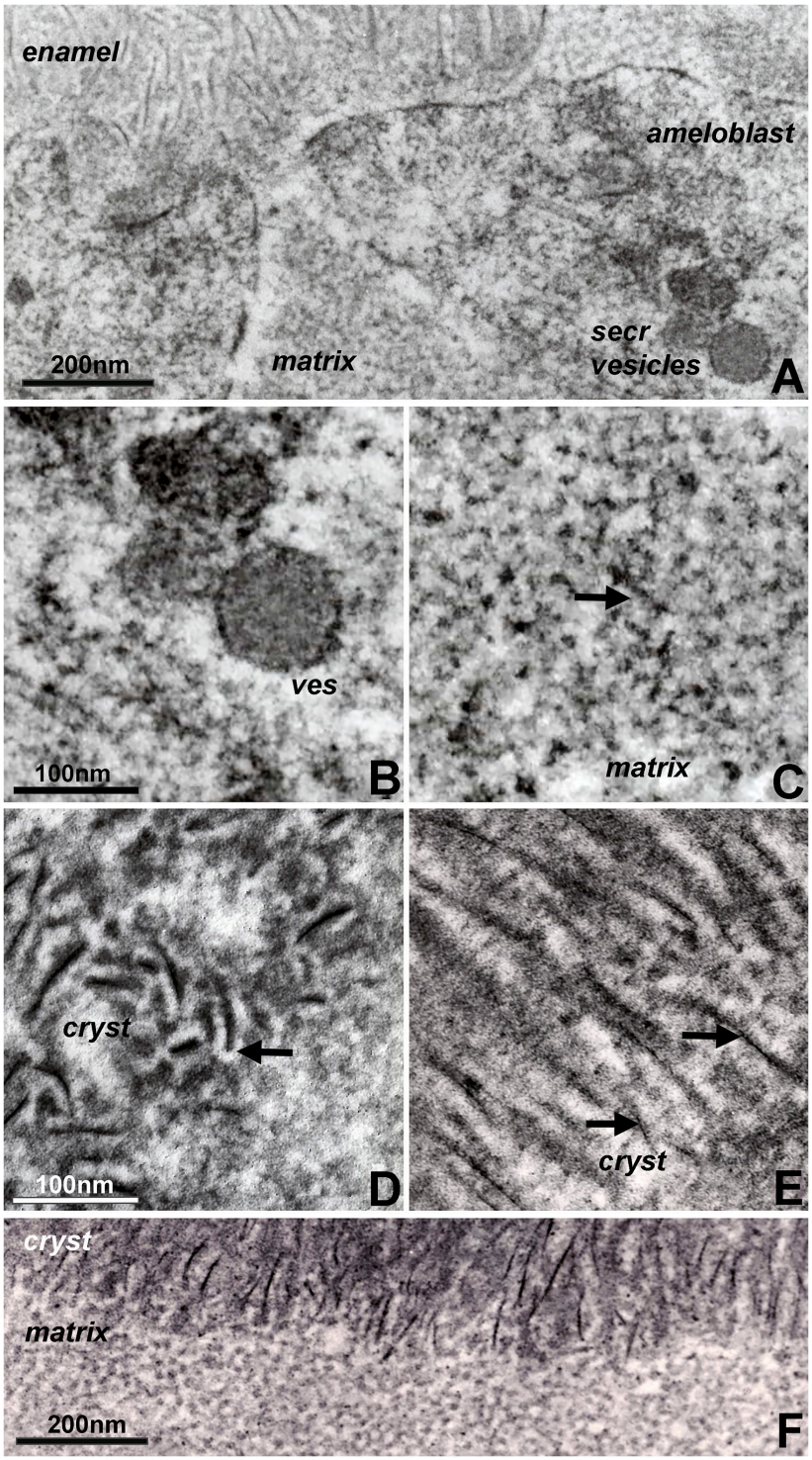

FIGURE 2 | Constituents of first mandibular mouse molar enamel formation in organ culture as revealed by electron microscopy**.** Note the differences between **Figure 1** (*in vivo*) and this figure (*in vitro*). **(A)** Interface between apical ameloblast cell membrane (ameloblast), organic extracellular enamel matrix (matrix), and initial enamel crystal deposits (enamel). Note the secretory vesicles (secr vesicles) at the apical ameloblast pole. **(B,C)** High magnification ultrastructural comparison between enamel matrix structure within secretory vesicles **(B)** and extracellular matrix **(C)**. The arrow in **(C)** points to electron dense mineral deposits as part of the supramolecular matrix framework. **(D,E)** Initial stages of enamel crystal (cryst) formation in organ culture. Note the electron opaque coat (arrow) surrounding initial crystal precipitates **(D)** and the electron dense particles (arrow) in immediate proximity of the elongated crystals **(E)**. **(F)** Sharply delineated interface between non-crystallized organic matrix (matrix) and the initial crystallized enamel layer (cryst). Scale bar **(A)** = 200 nm; **(B,C)** = 100 nm; **(D,E)** = 100 nm; **(F)** = 200 nm. The same scale bar applies for **(B–E)**.

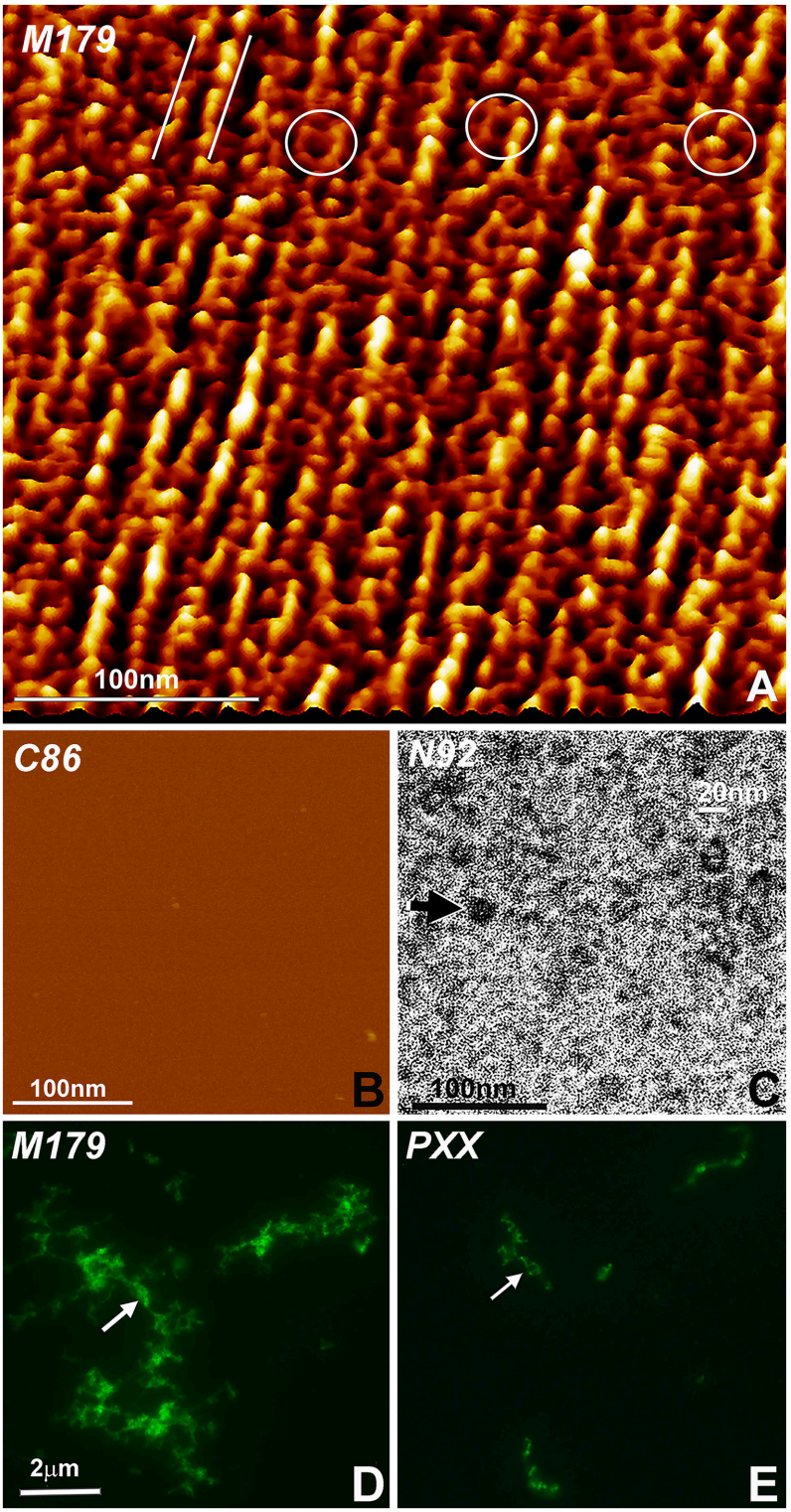

FIGURE 3 | Amelogenin protein self-assembly *in vitro*. **(A)** AFM image of M179 amelogenin on freshly cut mica. Note the parallel rows of self-assembled amelogenin spheres (parallel white lines) next to hexagon-shaped, ring-like assemblies (white circles). **(B)** In contrast, C86 amelogenin on freshly cut mica did not reveal any prominent structural entities. **(C)** Oval shaped, N-terminal His-tagged amelogenin N92 assemblies (arrow) as revealed by nickel-stain. **(D)** Fluorescently labeled, self-assembled full-length amelogenins in aqueous solution. **(E)** Fluorescently labeled, self-assembled amelogenin PXX33 polyproline repeat peptides in aqueous solution. The arrow points to elongated amelogenin structures **(D,E)**. The same scale bar applies for **(D,E)**.

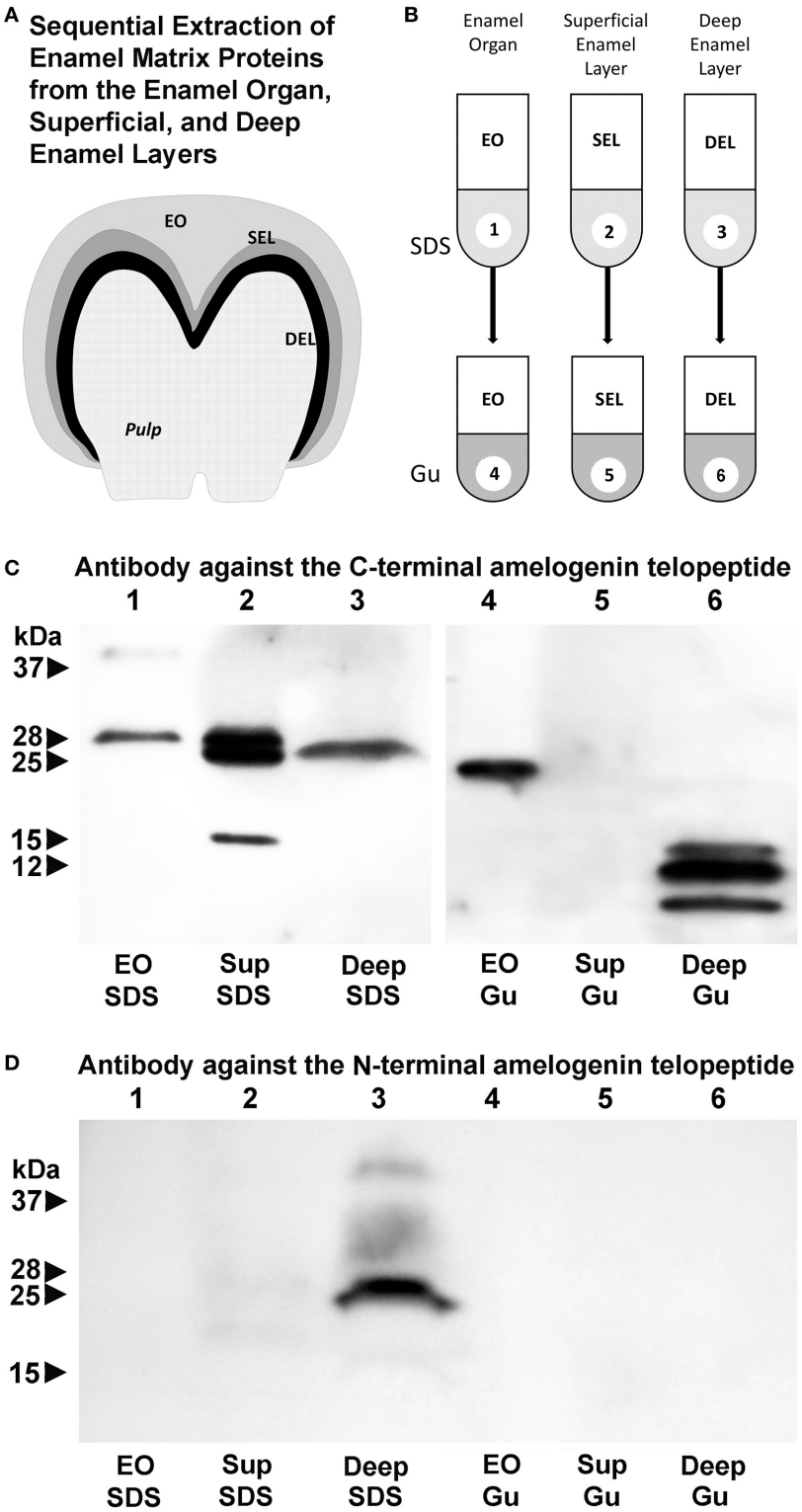

FIGURE 4 | Localization of amelogenin fragments in enamel organ, superficial, and deep enamel layers based on fractionated protein extraction and antibody recognition site. **(A)** Porcine enamel organ dissection and preparation scheme. Enamel organ (EO), superficial enamel layer (SEL), and deep enamel layer (DEL) were separately collected for further analysis. **(B)** Fractionated enamel protein extraction procedure using sodium dodecylsulfate (SDS) as a first step and 4 M guanidine HCl for subsequent extraction of the SDS-insoluble residue as a second step. **(C)** C-terminal amelogenin peptide antibody based Western blots of SDS extracts (SDS) or SDS residue guanidine extracts (Gu) of EO, SEL, and DEL enamel organ/enamel layer protein preparations. **(D)** N-terminal amelogenin peptide antibody based Western blot of SDS extracts (SDS) or SDS residue guanidine extracts (Gu) of EO, SEL, and DEL enamel organ/enamel layer protein preparations.

superficial enamel was below detection threshold (**Figure 4C**, lane 5). In contrast, our N-terminal amelogenin antibody only reacted with the SDS-based extract of the deep enamel layer (**Figure 4D**), indicating that the N-terminal amelogenin fragment is not immediately associated with the growing crystal surface.

DISCUSSION

For the present contribution we have queried the developing enamel matrix using *in vivo* and *in vitro* models as well as amelogenin self-assembly patterns to reconcile seemingly divergent models and proposed mechanisms of mammalian matrix mediated tooth enamel formation. We have revisited electron micrographs of mouse enamel development, carefully analyzed lesser known aspects of enamel matrix reconfiguration and initial crystal growth in organ culture, and characterized amelogenin *in vitro* self-assembly patterns using atomic force microscopy, fluorescence microscopy, and nickel-labeling of the N-terminal polyhistidine tags at the N-terminus of amelogenin N92 fragments. We have also performed Western blot analyses to determine whether stage-specific changes in enamel matrix configuration were related to the amelogenin posttranslational processing along stages and layers of enamel development using N- and C-terminal amelogenin antibodies. Together, these studies establish the enamel matrix as a dynamic and multifunctional protein assembly involved in all aspects of enamel formation, including vesicular transport, matrix assembly, spacing of crystal nucleation sites, and protein mediated crystal elongation.

Our micrographs indicate substantial differences in matrix subunit dimensions and shapes between secretory vesicles, pre-crystallization enamel protein matrix, and intercrystalline protein matrix during the crystal elongation phase. Specifically, there was a significant difference in matrix subunit compartment size between secretory vesicle assemblies measuring approximately 7 nm in diameter and the extracellular enamel protein matrix subunit compartments with an average diameter of 17.5 nm. Similar changes in subunit dimensions have been reported in earlier molecular cross-linking studies (Brookes et al., 2006). A detailed analysis of matrix dimensions in an earlier transmission electron microscopic study reported 5 nm diameters in secretory vesicles and 20 nm diameters in stippled materials and in the protein coat covering initial enamel crystal deposits (Diekwisch et al., 1995). Estimates of protein assembly dimensions based on transmission electron micrographs are likely to underestimate actual dimensions by a small percentage because of the dehydration involved in sample preparation, suggesting that actual subunit dimensions may be closer to 10 nm in secretory vesicles and 25 nm in the extracellular matrix. Together, these findings indicate that the enamel matrix is reconfigured when the enamel mineral/protein cargo leaves the secretory vesicles and enters the extracellular matrix milieu. Our data are also suggestive of a second change in matrix configuration after initial crystal precipitation. In fact, the structures presented in our transmission electron micrographs somewhat resemble helical structures (Smales, 1975), but more likely consist of ribbon-like assemblies of donut-shaped protein nanospheres (Zhang et al., 2011; Carneiro et al., 2016) in immediate proximity to the elongating crystal needles. Such protein nanoribbons not always display the corresponding crystal needle in the same section because of the ultrathin sectioning technique involved in sample preparation. However, electron micrographs of earlier and later stages illustrate the intimate relationship between each individual electrondense enamel crystal needle and its slightly less electrondense pericrystalline protein coat. Similar images of pre-fusion initial enamel crystals and consecutive stages of apatite fusion into mature enamel crystals have been published earlier (Robinson, 2007; Beniash et al., 2009; Fang et al., 2011).

Organ culture studies revealed four key findings related to our understanding of potential mechanisms involved in enamel crystal growth: (i) granular mineral deposits associated with the enamel matrix framework, (ii) dot-like mineral deposits along elongating initial enamel crystallites, (iii) a mineral free-zone surrounding initial enamel crystal precipitates, and (iv) dramatic changes in enamel matrix configuration following the onset of enamel crystal formation. Organ cultures are unique experimental environments that faithfully mimic the timely progression of physiologic events during embryonic organogenesis (Trowell, 1954; Yamada et al., 1980; Saxen et al., 1983; Evans et al., 1988). However, because of a limited supply in nutrients, limited ion and protein diffusion, isolation from surrounding tissues, and physical separation from long-range signaling events, amelogenesis in organ culture is effectively a time-lapse process that progresses at approximately twice the speed of *in vivo* amelogenesis. The time-lapse progression of events and the slight augmentation of key morphological features due to an accumulation of matrix and mineral allows for the visualization of events and structures that would otherwise remain below the threshold of detection (Diekwisch et al., 1993, 1995; Diekwisch, 1998).

Among the unique findings presented here is the evidence for granular mineral deposits along the stippled materials framework of matrix subunit compartments, suggesting that the stippled materials structure previously thought of as a mineral-free protein zone in fact contains a mixture of mineral ions and proteins. This finding and the detection of dot-like, granular mineral deposits along the elongating apatite crystal surface not only confirm earlier reports of linearly arranged, electron-dense dots and globular subunits (Frank and Nalbandian, 1963; Hohling et al., 1966; Robinson et al., 1981, 1983), but also lends support to more recent concepts involving co-assembled amelogenin protein/calcium phosphate mineral nanoclusters as the basis for enamel mineral growth (Beniash et al., 2005, 2009; Yang et al., 2010; Bromley et al., 2011; Ruan and Moradian-Oldak, 2015). In fact, the presence of an electron lucent zone surrounding initial crystal precipitates with adjacent matrix deposits in organ culture may indicate that protein/mineral nanoclusters had disassembled ("shed") from nanospherical matrix subunits onto the crystal surface and were no longer present at the interface between crystals. One of the most remarkable sights in our electron

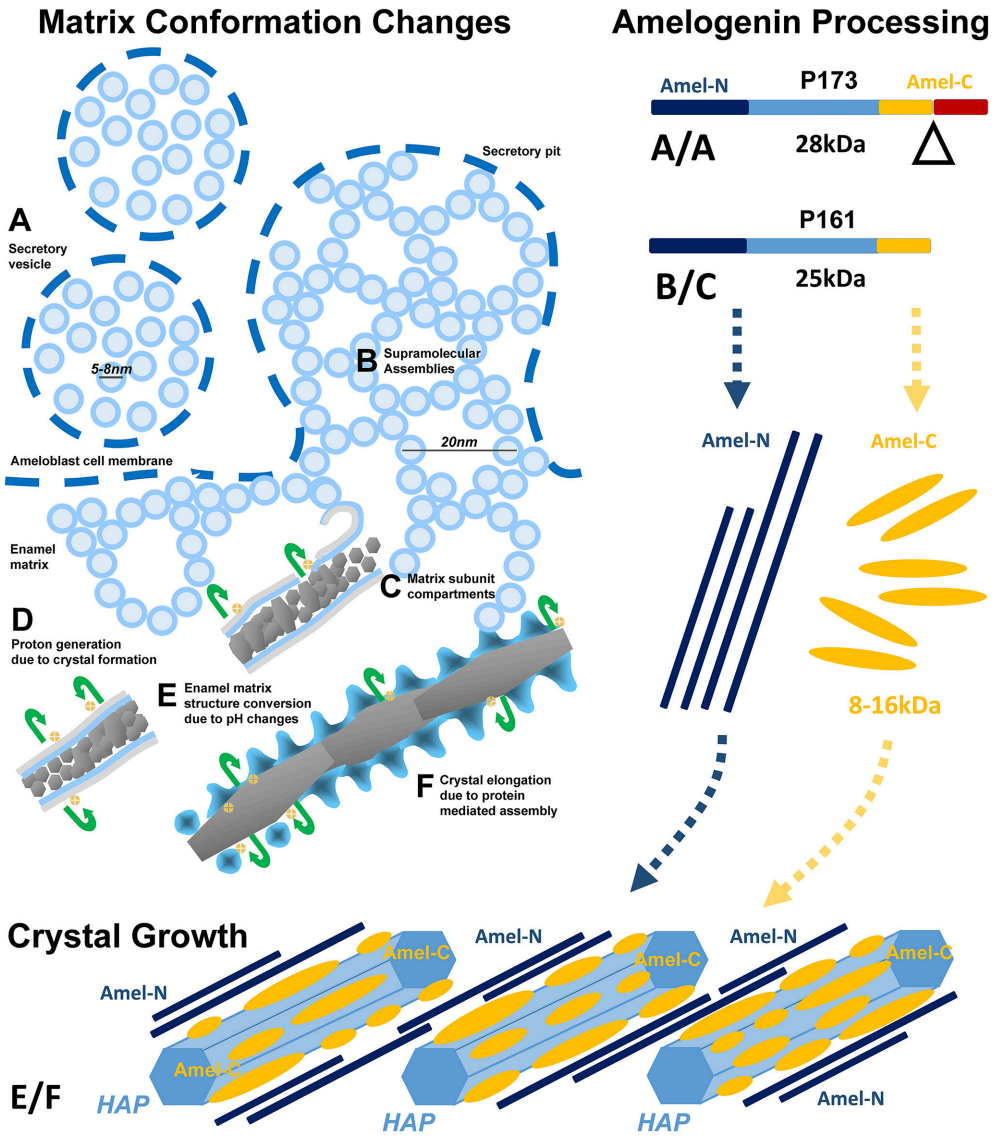

FIGURE 5 | Model explaining enamel crystal formation through matrix assembly and processing. **(A–F)** Changes in matrix conformation. Enamel matrix assembly begins as 5–7 nm subunits within ameloblast secretory vesicles **(A)**. Once secreted into the extracellular space, mineral-rich enamel proteins self-assemble as 20 nm diameter subunit compartments that provide the structural basis for orderly spaced enamel crystal nucleation **(B,C)**. Proton generation during initial crystallization results in a dissociation of the stippled materials matrix and a "shedding" of enamel protein assemblies onto the surfaces of growing enamel hydroxyapatite crystals **(E,F)**. **(A/A–B/C)** Temporo-spatial amelogenin processing during enamel maturation. (A/A) Full-length P173 amelogenins are exclusive to the enamel organ (**Figure 4C** lane 1), where they are packaged into 5–8 nm subunits within secretory vesicles (**Figures 1A,B**, **2A,B**). Upon entry into the enamel extracellular matrix, cleavage of the hydrophilic C-terminus generates P161 amelogenins (**Figure 4C** lanes 2,3), and resulting hydrophobic interactions between P161 amelogenins trigger the formation of 20 nm sized subunit compartments ("nanospheres," **Figures 1C**, **2C**) for the spacing of enamel crystal nucleation sites. (E/F) N- and C-terminal amelogenins during enamel crystal formation and elongation. Further processed amelogenin C-terminal fragments (**Figure 4C** lane 6, 8–16 kDa) are tightly associated with the elongating crystal surface (**Figures 1E**, **2D,E**) as revealed by guanidine extracts. In contrast, N-terminal amelogenins likely float in between elongating apatite crystals as they were only detected in SDS detergent extracts and not in the guanidine fraction (**Figure 4D**).

micrographs of initial enamel mineralization *in vitro* and *in vivo* was the drastic conversion of matrix structure from the stippled materials matrix to the elongated protein and mineral assemblies of initial crystal growth. Such a conversion of matrix organization may be due to the deprotonation of amelogenin histidine residues and simultaneous protonation of crystal surfaces, resulting in the disassembly and shedding of nanosphere substructures (Tarasevich et al., 2009a,b; Bromley et al., 2011; Robinson, 2014; Ruan and Moradian-Oldak, 2015), and the initiation of a cascade of events related to crystal formation, epitaxial crystal growth, and crystal elongation.

Our atomic force micrographs of full-length amelogenin *in vitro* self-assemblies on freshly cleaved mica not only demonstrate that amelogenins have the capacity to form linear protein assemblies but also self-organize into hexagonal rings resembling the subunit compartment organization of the stippled enamel extracellular matrix. As striking as those linear protein assemblies might be, careful examination of these images reveals the large number of hexagonal ring subunits in between rows of globular protein structures. As mentioned earlier, the linear arrangement of protein subunits may be evidence of the unique propensity of amelogenins to form elongated assemblies, which in turn might facilitate longitudinal enamel crystal growth along the crystal c-axis. As to the involvement of individual amelogenin motifs in amelogenin self-assembly, our nickel labeling of the N92 amelogenin polyhistidine tag confirms the essential role of the amelogenin N-terminus in the self-assembly of 20 nm diameter aggregates (Zhang et al., 2011). In contrast, our fluorescein labeling studies indicate that the polyproline domain alone results in very limited protein self-assembly and might rather contribute to nanosphere compaction and enamel prism formation (Jin et al., 2009), while the C-terminus has been shown to preferentially bind to the (100) face of apatite crystals when compared to the (001) phase and contribute to c-axis crystal growth (Moradian-Oldak et al., 2002; Pugach et al., 2010; Friddle et al., 2011; Gopinathan et al., 2014).

Our Western blot analysis of sequentially extracted enamel matrix proteins from the enamel organ, superficial and deep enamel matrix layers revealed a 3 kDa cleavage of the full-length amelogenin when the protein leaves the enamel epithelium, enters the enamel matrix, and then associates with the crystal surfaces. This finding indicates that the amelogenins of the enamel organ epithelium are of higher molecular weight than the amelogenins in the enamel matrix. Such higher molecular weight (28 kDa) amelogenins likely provide the structural framework for the 5–8 nm subunit assemblies within the ameloblast secretory vesicles. Once expelled from the ameloblast cell body and upon entry into the enamel matrix, the transition from ameloblast secretory vesicle subunit compartments into 20 nm enamel matrix "nanosphere" assemblies is likely accomplished by C-terminal amelogenin cleavage via the matrix metalloproteinase MMP20 (Zhu et al., 2014) into slightly lower molecular weight (25 kDa) amelogenins. MMP20 is abundant at the ameloblast/enamel matrix interface and activated in the proton-rich environment of initial apatite crystal formation (Khan et al., 2012). The C-terminal cleavage then results in a reassembly of the enamel protein matrix structure from the 5–8 nm subunit assemblies into the 20 nm matrix subunit compartments.

The second key finding of our Western blot analysis focuses on the transition from the loosely bound and SDS extractable 25/28 kDa amelogenins of the superficial enamel matrix to the crystal associated 8–16 kDa C-terminal amelogenin fragments that were only resolved after subsequent guanidine extraction. In our laboratory, 4 M guanidine alone is commonly employed to cause a profound dissolution of the mineral phase, even though addition of EDTA would result in further removal of the enamel mineral. Changes in amelogenin molecular weight from the full-length molecule in the superficial enamel layer to shorter fragments in the crystal-bound phase explains the dramatic change in enamel matrix configuration from "nanosphere"-type supramolecular matrix assemblies to the "crystal ghost"-type organic crystal coverings on the surface of elongating apatite crystals as a result of further enzymatic processing. This finding confirms previous studies on the close proximity of the amelogenin C-terminus to the apatite surface (Tarasevich et al., 2009a,b, 2010; Lu et al., 2013). In contrast to the apatite-associated amelogenin C-terminus, the amelogenin N-terminus was accessible to our SDS solvent based extraction procedure, suggesting that the N-terminal amelogenin resided loosely bound in the intercrystalline space of the deep enamel layer.

In conclusion, our *in vivo*, organ culture, and amelogenin *in vitro* assembly studies have resulted in a dynamic three-phase model of enamel matrix transformation and crystal growth (**Figure 5**). Based on our data and other findings presented in this contribution, enamel matrix assembly begins as 5–10 nm subunits formed by full-length amelogenins within ameloblast secretory vesicles (A). Once secreted into the extracellular space, mineral-enriched enamel protein self-assemblies consisting of C-terminally cleaved amelogenins organize into 20–25 nm diameter subunit compartments that provide the structural basis for orderly spaced enamel crystal nucleation (B,C). Proton generation during initial crystallization results in further matrix reorganization and amelogenin processing, a dissociation of the stippled materials matrix and a "shedding" of C-terminal amelogenin/mineral nanoclusters onto the surfaces of growing enamel hydroxyapatite crystals (E,F).

ETHICS STATEMENT

All animals studies were approved by the Institutional Animal Care Committee of the University of Illinois at Chicago.

AUTHOR CONTRIBUTIONS

MP and TD wrote the article, TD designed the experiments, TL, LL, MA, TJ, and XL conducted experiments.

FUNDING

Research reported in this publication was supported by the National Institute of Dental and Craniofacial Research of the National Institutes of Health under award number R01 DE018900. The content is solely the responsibility of the authors and does not necessarily represent the official views of the National Institutes of Health.

REFERENCES

Aichmayer, B., Margolis, H. C., Sigel, R., Yamakoshi, Y., Simmer, J. P., and Fratzl, P. (2005). The onset of amelogenin nanosphere aggregation studied by small-angle X-ray scattering and dynamic light scattering. *J. Struct. Biol.* 151, 239–249. doi: 10.1016/j.jsb.2005.06.007

Beniash, E., Metzler, R. A., Lam, R. S., and Gilbert, P. U. (2009). Transient amorphous calcium phosphate in forming enamel. *J. Struct. Biol.* 166, 133–143. doi: 10.1016/j.jsb.2009.02.001

Beniash, E., Simmer, J. P., and Margolis, H. C. (2005). The effect of recombinant mouse amelogenins on the formation and organization of hydroxyapatite crystals *in vitro*. *J. Struct. Biol.* 149, 182–190. doi: 10.1016/j.jsb.2004.11.001

Bonucci, E. (2014). Understanding nanocalcification: a role suggested for crystal ghosts. *Mar. Drugs* 12, 4231–4246. doi: 10.3390/md12074231

Bonucci, E., Silvestrini, G., and Di Grezia, R. (1988). The infrastructure of the organic phase associated with the inorganic substance in Calcified tissues. *Clin. Orthop. Relat. Res.* 233, 243–261.

Bromley, K. M., Kiss, A. S., Lokappa, S. B., Lakshminarayanan, R., Fan, D., Ndao, M., et al. (2011). Dissecting amelogenin protein nanospheres characterization of metastable oligomers. *J. Biol. Chem.* 286, 34643–34653. doi: 10.1074/jbc.M111.250928

Brookes, S. J., Lyngstadaas, S. P., Robinson, C., Shore, R. C., and Kirkham, J. (2006). Intracellular nanosphere subunit assembly as revealed by amelogenin molecular cross-linking studies. *Eur. J. Oral Sci.* 114(Suppl. 1), 280–284. discussion: 285–286, 382. doi: 10.1111/j.1600-0722.2006.00311.x

Buchanan, L. E., Carr, J. K., Fluitt, A. M., Hoganson, A. J., Moran, S. D., de Pablo, J. J., et al. (2014). Structural motif of polyglutamine amyloid fibrils discerned with mixed-isotope infrared spectroscopy. *Proc. Natl. Acad. Sci. U.S.A.* 111, 5796–5801. doi: 10.1073/pnas.1401587111

Carneiro, K. M., Zhai, H., Zhu, L., Horst, J. A., Sitlin, M., Nguyen, M., et al. (2016). Amyloid-like ribbons of amelogenins in enamel mineralization. *Sci. Rep.* 6:23105. doi: 10.1038/srep23105

Chen, S., Berthelier, V., Hamilton, J. B., O'nuallai, B., and Wetzel, R. (2002). Amyloid-like features of polyglutamine aggregates and their assembly kinetics. *Biochemistry* 41, 7391–7399. doi: 10.1021/bi011772q

Diekwisch, T. G. (1998). Subunit compartments of secretory stage enamel matrix. *Connect. Tissue Res.* 38, 101–111. doi: 10.3109/03008209809017026

Diekwisch, T. G., Berman, B. J., Anderton, X., Gurinsky, B., Ortega, A. J., Satchell, P. G., et al. (2002). Membranes, minerals, and proteins of developing vertebrate enamel. *Microsc. Res. Tech.* 59, 373–395. doi: 10.1002/jemt.10218

Diekwisch, T. G., Berman, B. J., Gentner, S., and Slavkin, H. C. (1995). Initial enamel crystals are not spatially associated with mineralized dentine. *Cell Tissue Res.* 279, 149–167. doi: 10.1007/BF00300701

Diekwisch, T., David, S., Bringas, P., Santos, V., and Slavkin, H. C. (1993). Antisense inhibition of AMEL translation demonstrates supramolecular controls for enamel HAP crystal growth during embryonic mouse molar development. *Development* 117, 471–482.

Eastoe, J. E. (1960). Organic matrix of tooth enamel. *Nature* 187, 411–412. doi: 10.1038/187411b0

Eastoe, J. E. (1963). The amino acid composition of proteins from the oral tissues II: the matrix proteins in dentine and enamel from developing human deciduous teeth. *Arch. Oral Biol.* 8, 633–652. doi: 10.1016/0003-9969(63)90078-5

Evans, J., Bringas, P. Jr., Nakamura, M., Nakamura, E., Santos, V., and Slavkin, H. C. (1988). Metabolic expression of intrinsic developmental programs for dentine and enamel biomineralization in serumless, chemically-defined, organotypic culture. *Calcif. Tissue Int.* 42, 220–230. doi: 10.1007/BF02553747

Fang, P. A., Conway, J. F., Margolis, H. C., Simmer, J. P., and Beniash, E. (2011). Hierarchical self-assembly of amelogenin and the regulation of biomineralization at the nanoscale. *Proc. Natl. Acad. Sci. U.S.A.* 108, 14097–14102. doi: 10.1073/pnas.1106228108

Fearnhead, R. (1963). Organic components of human dental enamel. *J. Dent. Res.: Am. Assoc. Dent. Res.* 42:1111.

Fearnhead, R. (1965). The insoluble organic component of human enamel. *Tooth Enamel* I, 127–131.

Fincham, A., Moradian-Oldak, J., and Simmer, J. (1999). The structural biology of the developing dental enamel matrix. *J. Struct. Biol.* 126, 270–299. doi: 10.1006/jsbi.1999.4130

Fincham, A. G., Moradian-Oldak, J., Diekwisch, T. G., Lyaruu, D. M., Wright, J. T., Bringas, P., et al. (1995). Evidence for amelogenin"nanospheres" as functional components of secretory-stage enamel matrix. *J. Struct. Biol.* 115, 50–59. doi: 10.1006/jsbi.1995.1029

Fincham, A. G., Moradian-Oldak, J., Simmer, J. P., Sarte, P., Lau, E. C., Diekwisch, T., et al. (1994). Self-assembly of a recombinant amelogenin protein generates supramolecular structures. *J. Struct. Biol.* 112, 103–109. doi: 10.1006/jsbi.1994.1011

Frank, R. M., and Nalbandian, J. (1963). Electron microscopy of the mode of secretion of the ameloblast bodies during amelogenesis. *C. R. Seances Soc. Biol. Fil.* 157, 2297–2298.

Frank, R. M., Sognnaes, R. F., and Kern, R. (1960). Calcification of dental tissues with special reference to enamel ultrastructure. *Calcif. Biol. Syst*. 64, 163–202.

Frank, R. M., Wolff, F., and Gutmann, B. (1964). The organic structure of human fetal enamel in the electron microscope. *Arch. Oral Biol.* 9, 105–110. doi: 10.1016/0003-9969(64)90053-6

Friddle, R. W., Battle, K., Trubetskoy, V., Tao, J., Salter, E. A., Moradian-Oldak, J., et al. (2011). Single-molecule determination of the face-specific adsorption of Amelogenin's C-terminus on hydroxyapatite. *Angewandte Chemie Int. Ed.* 50, 7541–7545. doi: 10.1002/anie.201100181

Fukae, M., Yamamoto, R., Karakida, T., Shimoda, S., and Tanabe, T. (2007). Micelle structure of amelogenin in porcine secretory enamel. *J. Dent. Res.* 86, 758–763. doi: 10.1177/154405910708600814

Glimcher, M. J. (1959). Molecular biology of mineralized tissues with particular reference to bone. *Rev. Mod. Phys.* 31:359. doi: 10.1103/RevModPhys.31.359

Gopinathan, G., Jin, T., Liu, M., Li, S., Atsawasuwan, P., Galang, M.-T., et al. (2014). The expanded amelogenin polyproline region preferentially binds to apatite versus carbonate and promotes apatite crystal elongation. *Front. Physiol.* 5:430. doi: 10.3389/fphys.2014.00430

Hohling, H. J., Hake, T., and Katterbach, R. (1966). Collegen and apatite in healthy and carious dentin. *Adv. Fluorine Res.* 4, 201–212.

Jin, T., Ito, Y., Luan, X., Dangaria, S., Walker, C., Allen, M., et al. (2009). Elongated polyproline motifs facilitate enamel evolution through matrix subunit compaction. *PLoS Biol.* 7:e1000262. doi: 10.1371/journal.pbio.1000262

Khan, F., Li, W., and Habelitz, S. (2012). Biophysical characterization of synthetic amelogenin C-terminal peptides. *Eur. J. Oral Sci.* 120, 113–122. doi: 10.1111/j.1600-0722.2012.00941.x

Lu, J. X., Xu, Y. S., Buchko, G.W., and Shaw, W. J. (2013). Mineral association changes the secondary structure and dynamics of murine amelogenin. *J. Dent. Res.* 92, 1000–1004. doi: 10.1177/0022034513504929

Lyaruu, D. M., Belcourt, A., Fincham, A. G., and Termine, J. D. (1982). Neonatal hamster molar tooth development: extraction and characterization of amelogenins, enamelins, and soluble dentin proteins. *Calcif. Tissue Int.* 34, 86–96. doi: 10.1007/BF02411214

Lyaruu, D., Bronckers, A., and Wöltgens, J. (1984). "The Tomes' process: is stippled material a reality? The effect of fixative temperature on the structure of stippled material in enamel," in *Proceedings of the Second International Conference on Tooth Morphogenesis and Differentiation* (Paris: Les Colloques de *l'INSERM*), 25, 257–272.

Lyubchenko, Y. L., Krasnoslobodtsev, A. V., and Luca, S. (2012). Fibrillogenesis of huntingtin and other glutamine containing proteins. *Subcell Biochem.* 65, 225–251. doi: 10.1007/978-94-007-5416-4_10

Margolis, H. C., Beniash, E., and Fowler, C. (2006). Role of macromolecular assembly of enamel matrix proteins in enamel formation. *J. Dent. Res.* 85, 775–793. doi: 10.1177/154405910608500902

Martinez-Avila, O. M., Wu, S., Cheng, Y., Lee, R., Khan, F., and Habelitz, S. (2011). Self-assembly of amelogenin proteins at the water–oil interface. *Eur. J. Oral Sci.* 119, 75–82. doi: 10.1111/j.1600-0722.2011.00907.x

Martinez-Avila, O., Wu, S., Kim, S. J., Cheng, Y., Khan, F., Samudrala, R., et al. (2012). Self-assembly of filamentous amelogenin requires calcium and phosphate: from dimers via nanoribbons to fibrils. *Biomacromolecules* 13, 3494–3502. doi: 10.1021/bm300942c

Moradian-Oldak, J., and Goldberg, M. (2005). Amelogenin supra-molecular assembly *in vitro* compared with the architecture of the forming enamel matrix. *Cells Tissues Organs.* 181, 202–218. doi: 10.1159/000091382

Moradian-Oldak, J., Bouropoulos, N., Wang, L., and Gharakhanian, N. (2002). Analysis of self-assembly and apatite binding properties of amelogenin

proteins lacking the hydrophilic C-terminal. *Matrix Biol.* 21, 197–205. doi: 10.1016/S0945-053X(01)00190-1

Nikiforuk, G., and Simmons, N. (1965). Purification and properties of protein from embryonic bovine enamel. *J. Dent. Res.* 44, 1119–1122. doi: 10.1177/00220345650440061101

Nylen, M. (1979). Matrix-Mineral Relationships-A. morphologist's viewpoint. *J. Dent. Res.* 58, 922–929. doi: 10.1177/00220345790580024601

Paine, M. L., White, S. N., Luo, W., Fong, H., Sarikaya, M., and Snead, M. L. (2001). Regulated gene expression dictates enamel structure and tooth function. *Matrix Biol.* 20, 273–292. doi: 10.1016/S0945-053X(01)00153-6

Pugach, M. K., Li, Y., Suggs, C., Wright, J. T., Aragon, M. A., Yuan, Z. A., et al. (2010). The amelogenin C-terminus is required for enamel development. *J. Dent. Res.* 89, 165–169. doi: 10.1177/0022034509358392

Reith, E. J. (1967). The early stage of amelogenesis as observed in molar teeth of young rats. *J. Ultrastruct. Res.* 17, 503–526. doi: 10.1016/S0022-5320(67)80138-2

Robinson, C. (2007). Self-oriented assembly of nano-apatite particles: a subunit mechanism for building biological mineral crystals. *J. Dent. Res.* 86, 677–679. doi: 10.1177/154405910708600801

Robinson, C. (2014). Enamel maturation: a brief background with implications for some enamel dysplasias. *Front. Physiol.* 5:388. doi: 10.3389/fphys.2014.00388

Robinson, C., Briggs, H. D., Kirkham, J., and Atkinson, P. J. (1983). Changes in the protein components of rat incisor enamel during tooth development. *Arch. Oral Biol.* 28, 993–1000. doi: 10.1016/0003-9969(83)90053-5

Robinson, C., Briggs, H., and Atkinson, P. (1981). Histology of enamel organ and chemical composition of adjacent enamel in rat incisors. *Calcif. Tissue Int.* 33, 513–520. doi: 10.1007/BF02409483

Robinson, C., Shore, R. C., Kirkham, J., and Stonehouse, N. (1990). Extracellular processing of enamel matrix proteins and the control of crystal growth. *J. Biol. Buccale* 18, 355–361.

Ronnholm, E. (1962). III. The structure of the organic stroma of human enamel during amelogenesis. *J. Ultrastruct. Res.* 6, 368–389. doi: 10.1016/S0022-5320(62)80041-0

Ruan, Q., and Moradian-Oldak, J. (2015). Amelogenin and enamel biomimetics. *J. Mat. Chem. B* 3, 3112–3129. doi: 10.1039/C5TB00163C

Saxen, L., Salonen, J., Ekblom, P., and Nordling, S. (1983). DNA synthesis and cell generation cycle during determination and differentiation of the metanephric mesenchyme. *Dev. Biol.* 98, 130–138. doi: 10.1016/0012-1606(83)90341-X

Schneider, R., Schumacher, M. C., Mueller, H., Nand, D., Klaukien, V., Heise, H., et al. (2011). Structural characterization of polyglutamine fibrils by solid-state NMR spectroscopy. *J. Mol. Biol.* 412, 121–136. doi: 10.1016/j.jmb.2011.06.045

Simmer, J. P., Lau, E. C., Hu, C. C., Aoba, T., Lacey, M., Nelson, D., et al. (1994). Isolation and characterization of a mouse amelogenin expressed in *Escherichia coli*. *Calcif. Tissue Int.* 54, 312–319.

Smales, F. (1975). Structural subunit in prisms of immature rat enamel. *Nature* 258, 772–774. doi: 10.1038/258772a0

Tanaka, M., Machida, Y., Nishikawa, Y., Akagi, T., Morishima, I., Hashikawa, T., et al. (2002). The effects of aggregation-inducing motifs on amyloid formation of model proteins related to neurodegenerative diseases. *Biochemistry* 41, 10277–10286. doi: 10.1021/bi0258905

Tarasevich, B. J., Lea, S., and Shaw, W. J. (2010). The leucine rich amelogenin protein (LRAP) adsorbs as monomers or dimers onto surfaces. *J. Struct. Biol.* 169, 266–276. doi: 10.1016/j.jsb.2009.10.007

Tarasevich, B. J., Lea, S., Bernt, W., Engelhard, M., and Shaw, W. J. (2009a). Adsorption of amelogenin onto self-assembled and fluoroapatite surfaces. *J. Phys. Chem. B* 113, 1833–1842. doi: 10.1021/jp804548x

Tarasevich, B. J., Lea, S., Bernt, W., Engelhard, M. H., and Shaw, W. J. (2009b). Changes in the quaternary structure of amelogenin when adsorbed onto surfaces. *Biopolymers* 91, 103–107. doi: 10.1002/bip.21095

Termine, J. D., Belcourt, A. B., Christner, P. J., Conn, K. M., and Nylen, M. U. (1980). Properties of dissociatively extracted fetal tooth matrix proteins. I. principal molecular species in developing bovine enamel. *J. Biol. Chem.* 255, 9760–9768.

Tomson, M. B., and Nancollas, G.H. (1978). Mineralization kinetics: a constant composition approach. *Science* 200, 1059–1060. doi: 10.1126/science.200.4345.1059

Travis, D. F., and Glimcher, M. J. (1964). The structure and organization of, and the relationship between the organic matrix and the inorganic crystals of embryonic bovine enamel. *J. Cell Biol.* 23:447. doi: 10.1083/jcb.23.3.447

Trowell, O. A. (1954). A modified technique for organ culture *in vitro*. *Exp. Cell Res.* 6, 246–248. doi: 10.1016/0014-4827(54)90169-X

Wallwork, M. L., Kirkham, J., Zhang, J., Smith, D. A., Brookes, S. J., Shore, R. C., et al. (2001). Binding of matrix proteins to developing enamel crystals: an atomic force microscopy study. *Langmuir* 17, 2508–2513. doi: 10.1021/la001281r

Yamada, M., Bringas, P. Jr., Grodin, M., Macdougall, M., Cummings, E., Grimmett, J., et al. (1980). Chemically-defined organ culture of embryonic mouse tooth organs: morphogenesis, dentinogenesis and amelogenesis. *J. Biol. Buccale* 8, 127–139.

Yang, X., Wang, L., Qin, Y., Sun, Z., Henneman, Z. J., Moradian-Oldak, J., et al. (2010). How amelogenin orchestrates the organization of hierarchical elongated microstructures of apatite. *J. Phys. Chem. B* 114, 2293–2300. doi: 10.1021/jp910219s

Zhang, X., Ramirez, B. E., Liao, X., and Diekwisch, T. G. (2011). Amelogenin supramolecular assembly in nanospheres defined by a complex helix-coil-PPII helix 3D-structure. *PLoS ONE* 6:e24952. doi: 10.1371/journal.pone.0024952

Zhu, L., Liu, H., Witkowska, H. E., Huang, Y., Tanimoto, K., and Li, W. (2014). Preferential and selective degradation and removal of amelogenin adsorbed on hydroxyapatites by MMP20 and KLK4 *in vitro*. *Front. Physiol.* 5:268. doi: 10.3389/fphys.2014.00268

Conflict of Interest Statement: The authors declare that the research was conducted in the absence of any commercial or financial relationships that could be construed as a potential conflict of interest.

Copyright © 2017 Pandya, Lin, Li, Allen, Jin, Luan and Diekwisch. This is an open-access article distributed under the terms of the Creative Commons Attribution License (CC BY). The use, distribution or reproduction in other forums is permitted, provided the original author(s) or licensor are credited and that the original publication in this journal is cited, in accordance with accepted academic practice. No use, distribution or reproduction is permitted which does not comply with these terms.

frontiers in Physiology

ORIGINAL RESEARCH
published: 27 July 2017
doi: 10.3389/fphys.2017.00531

Phosphorylation Modulates Ameloblastin Self-assembly and Ca^{2+} Binding

*Øystein Stakkestad[1], Ståle P. Lyngstadaas[1], Bernd Thiede[2], Jiri Vondrasek[3], Bjørn S. Skålhegg[4] and Janne E. Reseland[1]**

[1] Department of Biomaterials, Institute of Clinical Dentistry, University of Oslo, Oslo, Norway, [2] Section for Biochemistry and Molecular Biology, Department of Biosciences, University of Oslo, Oslo, Norway, [3] Department of Bioinformatics, Institute of Organic Chemistry and Biochemistry, Czech Academy of Sciences, Prague, Czechia, [4] Division of Molecular Nutrition, Department of Nutrition, University of Oslo, Oslo, Norway

Ameloblastin (AMBN), an important component of the self-assembled enamel extra cellular matrix, contains several *in silico* predicted phosphorylation sites. However, to what extent these sites actually are phosphorylated and the possible effects of such post-translational modifications are still largely unknown. Here we report on *in vitro* experiments aimed at investigating what sites in AMBN are phosphorylated by casein kinase 2 (CK2) and protein kinase A (PKA) and the impact such phosphorylation has on self-assembly and calcium binding. All predicted sites in AMBN can be phosphorylated by CK2 and/or PKA. The experiments show that phosphorylation, especially in the exon 5 derived part of the molecule, is inversely correlated with AMBN self-assembly. These results support earlier findings suggesting that AMBN self-assembly is mostly dependent on the exon 5 encoded region of the AMBN gene. Phosphorylation was significantly more efficient when the AMBN molecules were in solution and not present as supramolecular assemblies, suggesting that post-translational modification of AMBN must take place before the enamel matrix molecules self-assemble inside the ameloblast cell. Moreover, phosphorylation of exon 5, and the consequent reduction in self-assembly, seem to reduce the calcium binding capacity of AMBN suggesting that post-translational modification of AMBN also can be involved in control of free Ca^{2+} during enamel extra cellular matrix biomineralization. Finally, it is speculated that phosphorylation can provide a functional crossroad for AMBN either to be phosphorylated and act as monomeric signal molecule during early odontogenesis and bone formation, or escape phosphorylation to be subsequently secreted as supramolecular assemblies that partake in enamel matrix structure and mineralization.

Keywords: ameloblastin, phosphorylation, self-assembly, Ca^{2+}- binding, enamel, intrinsically disordered proteins, casein kinase 2, protein kinase A

OPEN ACCESS

Edited by:
Ariane Berdal,
UMRS 1138 INSERM University Paris-Diderot Team POM, France

Reviewed by:
Claudio Cantù,
University of Zurich, Switzerland
Michel Goldberg,
Institut National de la Santé et de la Recherche Médicale, France
Pamela DenBesten,
University of California, San Francisco, United States

****Correspondence:***
Janne E. Reseland
j.e.reseland@odont.uio.no

Specialty section:
This article was submitted to Craniofacial Biology and Dental Research, a section of the journal Frontiers in Physiology

Received: *27 April 2017*
Accepted: *10 July 2017*
Published: *27 July 2017*

Citation:
Stakkestad Ø, Lyngstadaas SP, Thiede B, Vondrasek J, Skålhegg BS and Reseland JE (2017) Phosphorylation Modulates Ameloblastin Self-assembly and Ca^{2+} Binding. Front. Physiol. 8:531. doi: 10.3389/fphys.2017.00531

INTRODUCTION

Ameloblastin (AMBN) is an enamel extracellular matrix protein (Paine and Snead, 1997; Bartlett et al., 2006; Chun et al., 2010a; Geng et al., 2015) with multiple roles during odontogenesis, including mesenchymal and ectodermal cell differentiation (Fukumoto et al., 2004, 2005; Iizuka et al., 2011; Kitagawa et al., 2011) and enamel and dentin biomineralization (Nanci et al., 1998; Nakamura et al., 2006). Formation of enamel has been shown to be dependent on self-assembly of

enamel matrix proteins such as AMBN (Wazen et al., 2009; Poulter et al., 2014; Lu et al., 2016a,b; Wald et al., 2017), and amelogenin (AMEL; Fincham et al., 1994; Paine et al., 2000; Moradian-Oldak et al., 2002). Self-assembly of AMBN depends mostly on the exon 5 derived region located in the N-terminal half of the molecule (Wald et al., 2013). The N-terminus is itself processed from complete AMBN and it is found within self-assembled fibrillary structures in the sheath space (Geng et al., 2015), that define the boundaries of the enamel prisms. AMBN and AMEL are both elongated intrinsically disordered proteins that are hydrophobic and may also function to concentrate calcium phosphate minerals for hydroxy apatite (HAp) crystal nucleation and growth in enamel. AMBN spontaneously self-assemble (Wald et al., 2013), yet the control of self-assembly remain obscure. AMBN is potentially phosphorylated by protein kinase A (PKA) and casein kinase 2 (CK2) in predicted sites that cover both the N-terminus and C-terminus, including sites in exon 5 and exon 6 (Toyosawa et al., 2000; Lee et al., 2003; Perdigao et al., 2004, 2009).

The enamel sheath is laid down as one unit and embeds the prisms in their entire length from the ameloblast cells to the dentin surface. Full length AMBN self-assembles (Wald et al., 2013) and may initially only populate the enamel sheath. While still a part of unprocessed AMBN, the C-terminus is suggested to be involved in docking the sheath to the ameloblast cell surface through heparin binding domains (Sonoda et al., 2009). Complete AMBN is however not found *in vivo* other than as trace elements (Murakami et al., 1997; Uchida et al., 1998). One may envision that the C-terminus must be processed from the full length AMBN protein to allow for continuous growth of the sheath in the growth direction of the enamel prisms. *In silico* modeling of the full-length folded protein also suggest Ca^{2+} binding in the C-terminus region (Vymetal et al., 2008). The C-terminus processing products are quickly removed from the ECM and are only found in the sheath space in close proximity to the ameloblast cell surface (Uchida et al., 1997; Geng et al., 2015). The specific mechanism(s) for how AMBN C-terminus and its processing products contribute to enamel organization and mineralization and especially sheath formation is still poorly understood.

Transgenic mice that express a version of AMBN C-terminus (Ma et al., 2016) that is phosphorylated in a site close to several predicted Ca^{2+} binding sites (Zhang et al., 2011), show disturbance in enamel mineralization. Binding of Ca^{2+} may regulate crystal nucleation, mineralization and cellular attachment (Zhang et al., 2011). It is therefore important to see if more of the *in silico* predicted phosphorylation sites actually are phosphorylated and thus can partake in the regulation of AMBN function(s). It is also interesting to see if specific phosphorylation sites directly influence self-assembly and/or calcium binding in the full-length molecule and the major processing products. Finally, to better understand the relation between phosphorylation, Ca^{2+} binding and molecular organization, it is necessary to analyze whether Ca^{2+} binding itself has effect on the structural order in self-assembled and non-assembled AMBN.

MATERIALS AND METHODS

Radioactively Labeled Kinase Assay

Purified AMBN DelEx5 was incubated with 1,000 units of recombinant PKA Cα1 (New England Biolabs, Ipswich, MA) in PKA reaction buffer, or 5,000 units CK2 (New England Biolabs) in CK2 reaction buffer supplied with 0.1 μl γ-[32P] ATP (∼6,000 Ci/mmol, PerkinElmer, Waltham, MA, USA) in a total volume of 20 μl for 30 min at 30°C. The reactions were terminated by addition of 4 μl SDS loading buffer and boiled for 10 min. Subsequently the samples were separated by SDS-PAGE in 12% Tris-HCl (BioRad, Hercules, CA, USA), and the bands were exposed by Coomassie stain and the radioactivity was detected by exposure to CL-Xposure film (ThermoFischer Scientific, Waltham, MA, USA).

Kinase Assay

His-tagged (1 μg) PKA Cα1 (Millipore, Billerica, MA, USA,) or his-tagged (1 μg) CK2 (ATGen Ltd, Bundang-gu, Seongnam-si, Gyeonggi-do, South Korea,) was incubated with purified AMBN-WT (100 pmol), C-terminus (314 pmol), N-terminus (100 pmol), or DelEx5 (100 pmol) in CK2 or PKA reaction buffer supplied with 1 mM ATP in a total volume of 20 μl at 30°C for 24 h. Ten picomoles from each of the samples were submitted to LC-ESI-MS analyses. The remaining of the samples were boiled in Laemmli buffer, loaded on a 12% Ready Gel Tris-HCL (BioRad), and separated by electrophoresis, and the gel stained for phospho-proteins with Pro-Q® Diamond Phosphoprotein Gel Stain and destained with Pro-Q® Diamond Phosphoprotein Gel Destaining Solution (ThermoFisher Scientific, Waltham, MA, USA) according to manufacturer's protocol. The phosphor luminiscent gel bands were then scanned at in ChemiDoc XRS+ imaging system (BioRad) at 510 nm.

Liquid Chromatography Electrospray Ionization-Mass Spectrometry (LC-ESI-MS)

To detect phosphorylation sites of AMBN, 10 pmol of protein was digested by adding 0.2 μg trypsin in 20 μl 25 mM ammonium bicarbonate and incubation for 16 h at 37°C. The digestion was stopped by adding 2 μl 5% formic acid. The generated peptides were purified using an OMIX C18 (Agilent, Santa Clara, CA, USA), and dried using a Speed Vac concentrator (Concentrator Plus, Eppendorf, Hamburg, Germany).

The tryptic peptides were dissolved in 10 μl 0.1% formic acid/2% acetonitrile and 5 μl analyzed using an Ultimate 3000 RSLCnano-UHPLC system connected to a Q Exactive mass spectrometer (ThermoFisher Scientific) equipped with a nano electrospray ion source. For liquid chromatography separation, an Acclaim PepMap 100 column (C18, 2 μm beads, 100 Å, 75 μm inner diameter, 50 cm length) (Dionex, Sunnyvale CA, USA) was used. A flow rate of 300 nL/min was employed with a solvent gradient of 4–35% B in 47 min, to 50% B in 10 min and then to 80% B in 3 min. Solvent A was 0.1% formic acid and solvent B was 0.1% formic acid/90% acetonitrile. The mass spectrometer was operated in the data-dependent mode to automatically switch between MS and MS/MS acquisition. Survey full scan MS spectra (from m/z 300 to 2,000) were acquired with the resolution

R = 70,000 at m/z 200, after accumulation to a target of 1e6. The maximum allowed ion accumulation times were 60 ms. The method used allowed sequential isolation of up to the 10 most intense ions, depending on signal intensity (intensity threshold 1.7e4), for fragmentation using higher-energy collisional induced dissociation (HCD) at a target value of 10,000 charges and a resolution R = 17,500 Target ions already selected for MS/MS were dynamically excluded for 60 s. The isolation window was m/z = 2 without offset. For accurate mass measurements, the lock mass option was enabled in MS mode.

Data were acquired using Xcalibur v2.5.5 and raw files were processed to generate peak list in Mascot generic format (*.mgf) using ProteoWizard release version 3.0.331. Database searches were performed using Mascot in-house version 2.4.0 to search the SwissProt database (Human, 20.279 proteins), assuming the digestion enzyme trypsin at maximum one cleavage site, fragment ion mass tolerance of 0.05 Da, parent ion tolerance of 10 ppm, and oxidation of methionines, and acetylation of the protein N-terminus as variable modifications. Scaffold (version Scaffold_4.4.8, Proteome Software Inc., Portland, OR) was used to validate MS/MS based peptide and protein identifications. Peptide identifications were accepted if they could be established at >95.0% probability by the Scaffold Local FDR algorithm.

Dynamic Light Scattering (DLS)

In dynamic light scattering (DLS), a particle in solution is illuminated by laser and scatter light that fluctuate with the random movement (Brownian motion) of the particles. As movement of a particle is inversely correlated with its mass, the light scattering fluctuations may be used to estimate particle size. DLS was measured in a Zetasizer Nano ZS (Malvern Instruments Ltd, Worcestershire, UK) in DTS1070 disposable foldable capillary cells (Malvern Instruments Ltd) at 12°C, using a backscatter angle of 173°, an equilibration time of 5 min and three replications per sample. Analysis was done in the Zetasizer Software v7.11 (Malvern Instruments Ltd). The dispersant was chosen in the software as water with a refractive index of 1.330 and viscosity 0.8872 cP, the particle protein with refractive index 1.450 and absorption 0.001. The distribution analysis was done using the protein analysis option in the software which is a non-negative least squares analysis with an automatically determined regularizer and L-curve analysis.

Small Angle X-Ray Scattering (SAXS)

Small angle X-ray scattering is used to gather information about the structure of proteins in solution. This information is obtained by analyzing the intensity of photons (I) scattered in terms of the scattering vectors (s). To analyze the degree of folding of macromolecules, $I(s)\cdot(s)^2$ against (s nm^{-1}) is plotted in a Kratky plot (Putnam et al., 2007). Folded macromolecules have a high I at lower values of (s), illustrated as a peak in the plot. For a disordered and elongated protein, the function of I is linear and reaches a plateau at higher (s) values. SAXS was performed at the European Synchrotron Radiation Facility (ESRF) in Grenoble at the BioSAXS beamline BM29 using the automated sample changer in flow mode at 20°C, with 10 frames measured, of 1 second duration, per injected sample and an injected volume of 50 µl. The quartz capillary sample cell diameter was 1.8 mm, detector distance 2.867 m, with wavelength λ = 1.008 Å. A buffer baseline was measured before and after each measurement using 50 µl buffer. Before each measurement the protein was diluted into concentrations ranging from 0.2 to 1.8 mg/ml. The size of the particles that is analyzed is limited by the resolution of the instrument. As is the case for the beamline intended for biological SAXS at ESRF, the largest object that can be resolved is 50 nm in size (D_{max}); thus all particles larger than that will be presented with a size similar to D_{max} of 50 nm. The average size of the particle is presented as radius of gyration (R_g). Molecular weight of the protein in solution is calculated based the known concentration of protein and the volume calculated. A detailed description of the calculation method can be found at: http://www.esrf.eu/home/UsersAndScience/Experiments/MX/About_our_beamlines/bm29/computing-environment.html.

Experimental Design

An outline of the experimental design is presented in **Figure 1**, indicating the various recombinant AMBN proteins and peptides and test methods used in this study.

The procedure for cloning, expression and purification has previously been described by Wald et al. (2013). The various constructs were wild type, full-length AMBN (AMBN-WT), a variant deleted for exon 5 (DelEx5), a C terminal fragment representing amino acids 223–447 (C-terminus), a N-terminal fragment representing amino acid 27–222 (N-terminus). In addition, peptide representing exon 2–4 (Ex2–4 34 AA, VPFFPQQSGTPGMASLSLETMRQLGSLQRLNTLS), 37 amino acids of exon 5 (Ex5 37 AA, YSRYGFGKSFNSLWMHGLLPPHSSLPWMRPREHETQQ) and Ex5 including the splice variant of exon 6 designated Ex5|Q9NP70 (52 AA, YSRYGFGKSFNSLWMHGLLPPHSSLP-WMRPREHETQQYEYSLPVHPPPLPSQ) were included for *in vitro* phosphorylation in addition to AMBN-WT, DelEx5, N-terminus and C-terminus. All the peptides were in a buffer containing 20 mM Tris-HCl, and 50 mM NaCl. The concentration of the various AMBN proteins and peptides were

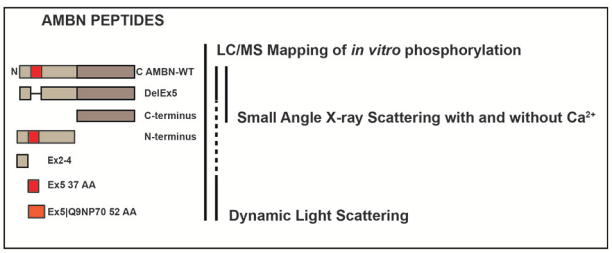

FIGURE 1 | The experimental design indicating the various recombinant AMBN proteins and peptides and test methods used in this study. Recombinant human AMBN-WT, N-terminus, C-terminus, DelEx5, Ex2-4, Ex5 proteins, and peptides were tested with LC-ESI-MS mapping of all peptides phosphorylated *in vitro*, dynamic light scattering (DLS) of Ex5, Ex5|Q9NP70, AMBN-WT, and DelEx5 and small angle x-ray scattering (SAXS) of AMBN-WT, DelEx5, and C-terminus with and without Ca^{2+}.

quantitated using the standard colorimetric Bradford protein assay (Bradford, 1976).

For the DLS experiments the peptide Ex5 37 AA, Ex5|Q9NP70 52 AA and full-length AMBN (AMBN-WT) were employed. Finally, the SAXS experiments were conducted on AMBN-WT, DelEx5, C-terminus. The latter experiments were performed in the presence and absence of Ca^{2+} (0.01 mM).

RESULTS

Both PKA and CK2 phosphorylated AMBN DelEx5 in a dose–dependent fashion (**Figure 2A**). It should be noted that phosphorylation appeared more pronounced for PKA compared to CK2 as the exposure time was 2 h for PKA and 24 h for CK2 using 5 μg recombinant AMBN DelEx5. Glycerol, which is known to dissociate the tight structure between proteins (Contaxis and Reithel, 1971) were added in the range 5–30% to AMBN protein solutions to assess its effect on the size distribution of AMBN complexes. Under the present conditions, a concentration of 5% glycerol caused the AMBN complexes to dissolve into monomers (**Figure 2B**). Consequently, 5% glycerol was included in the reaction solutions to ensure that molecules did not self-assemble during the kinase assays.

Differential Phosphorylation of AMBN by PKA and CK2

CK2 phosphorylated AMBN-WT and the C-terminus fragment effectively because dominant bands were observed by SDS-PAGE and phosphoprotein staining. However, neither the AMBN molecule without exon 5 (DelEx5) nor the N-terminus peptide could be effectively phosphorylated with CK2 (**Figure 3**). PKA phosphorylated both the N-terminus and the C-terminus fragments effectively. On the other hand, PKA was less effective in phosphorylating AMBN-WT and the DelEx5 fragment as visible by the presence of additional significant bands with different molecular weights (**Figure 3**).

Differential Phosphorylation of Regions in Self-assembled AMBN and Peptides Encoded by the Exons 2–6

LC–ESI-MS analysis of aliquots from the experiments conducted in **Figure 3**, revealed a higher incidence of phosphorylation in the C-terminus region of AMBN-WT than in the self-assembled N-terminus and the N-terminus region in AMBN-WT. Moreover, the C-terminus was phosphorylated in additional sites as a region in the self-assembled AMBN-WT than in the C-terminus monomeric peptide (**Figure 4** and **Table 1**).

DLS analyses of peptides Ex5 and Ex5|Q9NP70 indicated no sign of self-assembly (results not shown) confirming the findings reported by Wald et al. (2013). Kinase assays with CK2 and PKA performed on peptides Ex2–4, Ex5, and Ex5|Q9NP70 were analyzed in LC-ESI-MS indicating efficient phosphorylation by PKA. The exons 2–5 encode most of the N-terminal part of AMBN. Yet, the N-terminus fragment was only partly phosphorylated by PKA; both as a self-assembled fragment, and as a region in the full length AMBN-WT. In overall PKA phosphorylated sites in both the N-terminus and the C-terminus part of both the DelEx5 and the full-length AMBN proteins but with un-equal efficacy. This is in accordance with several molecular weights of phosphorylated proteins separated as multiple bands shown in **Figure 3** (lanes 3 and 11, respectively). For a detailed overview of phosphorylation sites and incidence in all peptides see **Figure 4** and **Table 1**.

The Effect of Self-assembled AMBN on Structure and Ca^{2+} Binding

Only AMBN-WT displayed a peak that is typical for folded macromolecules. This feature of AMBN-WT was altered in the presence of Ca^{2+} in all concentrations (**Figure 5**). DelEx5 had a disordered profile comparable to the C-terminus. The disorder in DelEx5 and C-terminus seemed un-affected by exposure to Ca^{2+} (**Figure 5**).

SAXS analyzes of AMBN-WT indicated structures above 50 nm in size (D_{max}) while radius of gyration (R_g) was calculated to 14.5 nm that was that increased upon exposure to Ca^{2+} in all the measured concentrations of AMBN (**Table 2**). For the self-assembled AMBN with a size larger than the D_{max} resolution, Rg may here be viewed as the dimensions of AMBN in terms of the width of its fibrils. For DelEx5 and C-terminus within the D_{max} range, both Rg and D_{max} may be viewed as dimension of the individual proteins. For DelEx5 and the C-terminus, the Rg was smaller and less affected by Ca^{2+} compared to AMBN-WT. The default settings were employed in calculating Rg for comparison of disordered proteins with fibrillary AMBN proteins (AMBN-WT).

The molecular weight calculated was higher than expected for DelEx5 ranging between 70 and 90 kDa while the C-terminus had close to expected MW ranging between 27 and 43 kDa (**Table 2**). AMBN-WT was calculated a very high molecular weight, indicative of some sort of supramolecular assembly but these data are restricted by the resolution limit of the instrument at 50 nm (D_{max}).

DISCUSSION AND CONCLUSION

AMBN is a calcium-binding phosphoprotein found within the self-assembled enamel extracellular matrix. The results presented suggest that the phosphorous acceptor sites identified here are hidden in self-assembled AMBN and could point at a mechanism for regulation of self-assembly through the cAMP-PKA pathway. During formation of enamel, G-protein coupled receptors that may influence cAMP levels are expressed in differentiated and differentiating ameloblast cells (Bawden et al., 1996). Furthermore, Enamel extracellular Matrix Derivative (EMD) enhance cAMP levels in human epithelial and periodontal ligament cells (PDL; Lyngstadaas et al., 2001). This suggests the cAMP-PKA signaling pathway is likely to coincide with AMBN expression.

Located in the N-terminus, the regions encoded by exon 5 and exon 6 are both found to be important for biomineralization of enamel (Wazen et al., 2009) and bone (Lu et al., 2016a,b). We recently showed that self-assembled AMBN and monomeric

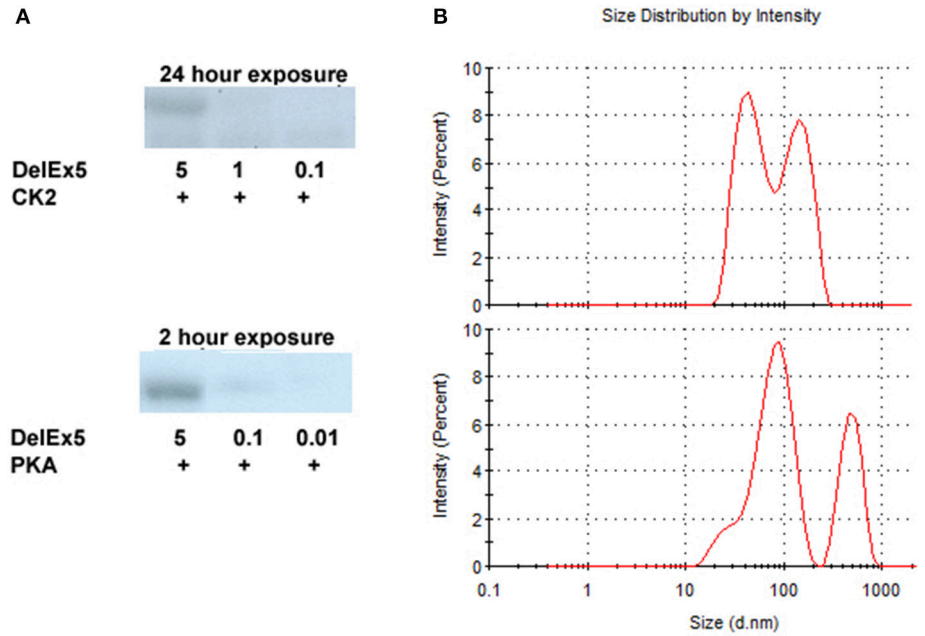

FIGURE 2 | Autoradiography of DelEx5 (0.01–5 μg) phosphorylated with CK2 and PKA **(A)**. Dynamic light scattering of AMBN-WT (upper panel) and AMBN-WT incubated with 5% glycerol (lower panel) **(B)**. In these experiments the phosphorylation of DelEx5 by CK2 required an exposure time of 24 h to match a 2 h exposure of DelEx5 phosphorylated by PKA.

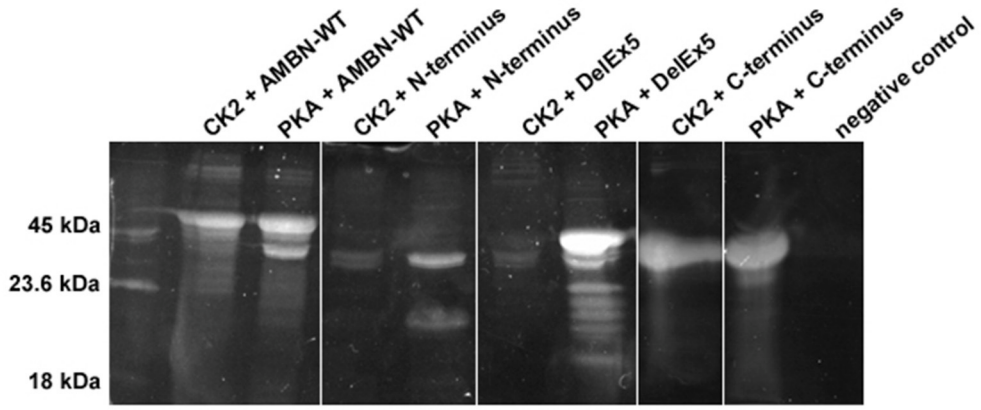

FIGURE 3 | Composite image representative of phosphorylated AMBN proteins and peptide by casein kinase2 (CK2) and protein kinase A (PKA). C-terminus, and AMBN-WT, N-terminus, and DelEx5 was phosphorylated by CK2 or PKA for 24 h, separated in 12% SDS-PAGE, and stained by ProQ diamond phosphorous stain. The intensity of bands between lanes can be interpreted as a semi-quantitative measurement of phosphorylation.

peptides encoded by exon 5 influence differentiation of human mesenchymal stem cells (hMSC; Stakkestad et al., 2017). Tamburstuen et al. also showed that AMBN is expressed in hMSC, stromal stem cells, and bone cells (Tamburstuen et al., 2011a), and that upstream regulatory elements essential for osteogenesis, adipogenesis, and chondrogenesis are present directly upstream of the human *AMBN* gene (Tamburstuen et al., 2011b). AMBN is functional, and is also expressed in adult bone repair (Nakamura et al., 2006; Spahr et al., 2006; Tamburstuen et al., 2010). During tooth development AMBN is induced by epithelial-mesenchymal interactions and expressed in MSC and epithelial cells (Fong et al., 1998; Takahashi et al., 2012) and in the pre-secretory and secretory stages of ameloblasts development (Nanci et al., 1998). Exon 5 and exon 6 knock down experiments in mice did however, not have any observable effects on the pre-secretory stages of ameloblasts development (Wazen et al., 2009). As this abrogation of AMBN self-assembly did not cause developmental effects, one may argue that AMBN self-assembly

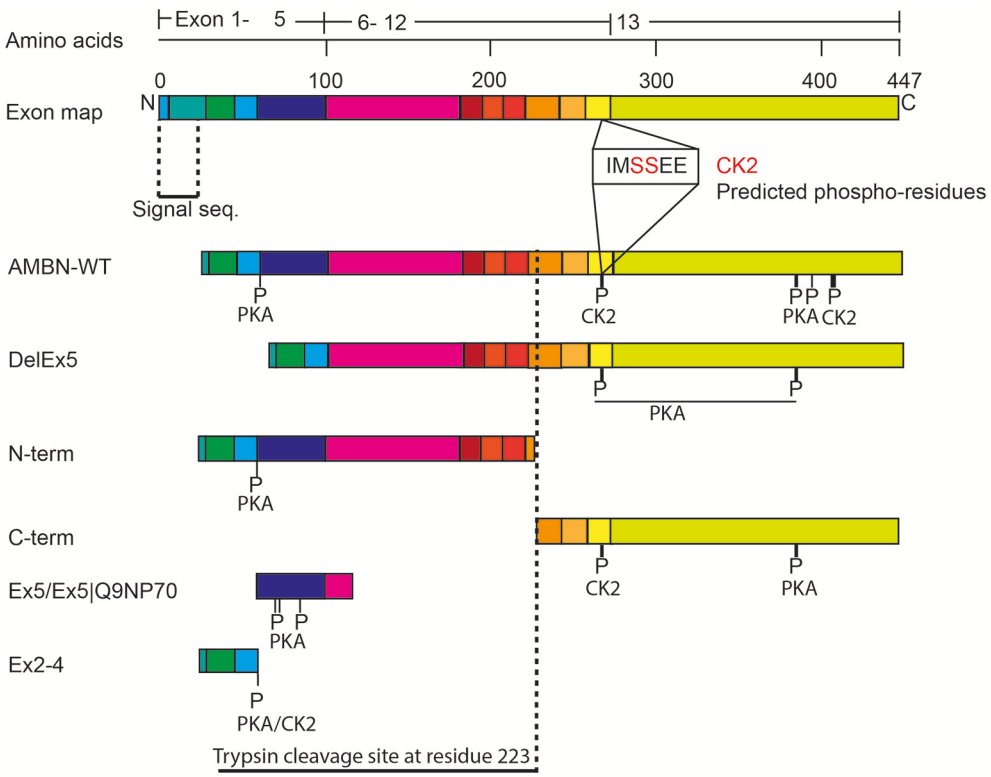

FIGURE 4 | Schematic overview of the phosphorylated sites in AMBN. The exon organization in relation to the various recombinant proteins and peptides are illustrated. P-indicate position of phosphorylated residues. The vertical dotted line indicates the known trypsin cleavage site between A222 and L223 (Iwata et al., 2007).

and interaction with AMEL is important only in enamel matrix secretion and mineralization.

From our SAXS results we can infer that AMBN self-assembly mostly rely on the exon 5 derived region as variants lacking this region (DelEx5) were all disordered. Moreover, self-assembly of AMBN seems directly related to biomineralization since only intact, self-assembled AMBN-WT is structurally influenced by Ca^{2+}. The here reported findings support previous results (Wazen et al., 2009; Lu et al., 2011, 2016a; Wald et al., 2017) suggesting that the exon 5 deletion variant (DelEx5) cannot bind Ca^{2+}efficiently and compromises biomineralization when present in the enamel matrix. This also corresponds well with previous *in silico* analysis of AMBN that suggested the calcium-binding site located to the C-terminus part of the protein (Vymetal et al., 2008; Zhang et al., 2011) and Ca^{2+} binding in the isolated 27 and 29 kDa C-terminal processing products (Yamakoshi et al., 2001). Interestingly the C-terminus protein in solution (monomeric) was inefficient in binding Ca^{2+}, confirming the previous observation by (Wald et al., 2011).

We here suggest that AMBN function depends on whether the molecules are self-assembled as a matrix component or exist as a mono-disperse soluble molecule. The observed phosphorylation of the exon 5 encoded region probably modulate the ability for self-assembly. In the phosphorylated, soluble form AMBN probably have functions that are not yet fully elucidated, possibly including roles in cell signaling and stem cell recruitment and differentiation. AMBN was initially predicted to function as a signaling molecule (Cerny et al., 1996; Fukae et al., 2006) during early tooth formation, but also assigned to be involved in generating the prismatic structure of mature enamel (Robinson et al., 1998). This ambiguity of the AMBN molecule may rest on the phosphorylation status of the molecule, providing a "one-molecule-to-many-functions" system that is observed also in other intrinsically disordered proteins in the Osteonectin (aka SPARC) family (Kawasaki et al., 2007). In this way AMBN can both be involved in the self-assembled, insoluble, fibrillary structures in the sheath space (Geng et al., 2015) interacting with the major enamel protein AMEL through the exon 5 derived region (Su et al., 2016), and act in cell-matrix attachment (Zhang et al., 2011), and as a signaling molecule involved in cell signaling and extracellular matrix feedback.

We also suggest that processing of AMBN is involved in transport and release of Ca^{2+} to the enamel extracellular compartment: Ca^{2+} are then brought out of the cell bound to and supported by the self-assembled chelating AMBN complex, thus allowing easy transport against the high osmotic gradient present in the supersaturated enamel extracellular milieu. Despite the numerous predicted phosphor acceptor sites in AMBN (Toyosawa et al., 2000; Lee et al., 2003), few residues of AMBN

TABLE 1 | Ratio of phosphorylated residues of AMBN.

		exon 2–4	exon 5–6		exon 12	exon 13	
Fragments	**Enzyme**	**T-58**	**S-70,-73,-85**		**S-261/2**	**S-377**	**S-397/8**
AMBN-WT	CK2	0% (0/8)	NF	NF	50% (5/5)	5% (1/21)	75%(3/1)
	PKA	8% (1/11)	0% (0/2)	(0/2)	0% (0/9)	32% (11/23)	0% (0/5)
DelEx5	CK2	N/F		N/F	0% (0/29)	0% (0/46)	N/F
	PKA	N/F		N/F	5% (2/39)	28% (10/26)	N/F
N-terminus	CK2	N/F	NF	N/F			
	PKA	8% (1/11)	0% (0/1)	N/F			
C-terminus	CK2				59% (23/16)	0% (0/3)	N/F
	PKA				0% (0/29)	42% (25/34)	N/F
Ex2–4	CK2	11% (1/8)					
	PKA	71% (10/4)					
Ex5	CK2		N/F				
	PKA		84% (5+9+7/4)				
Ex5|Q9NP70	CK2		0% (0/12)				
	PKA		80% (1+7+4/3)				

The amino acids phosphorylated are indicated in the upper row (T, threonine; S, serine). The percentage of phosphorylated sites found by LC-ESI-MS column is calculated from the ratio of phosphorylated fragments to number of total identified fragments. The number of phosphorylated and non-phosphorylated residues is given in brackets. N/F, sequence not found.

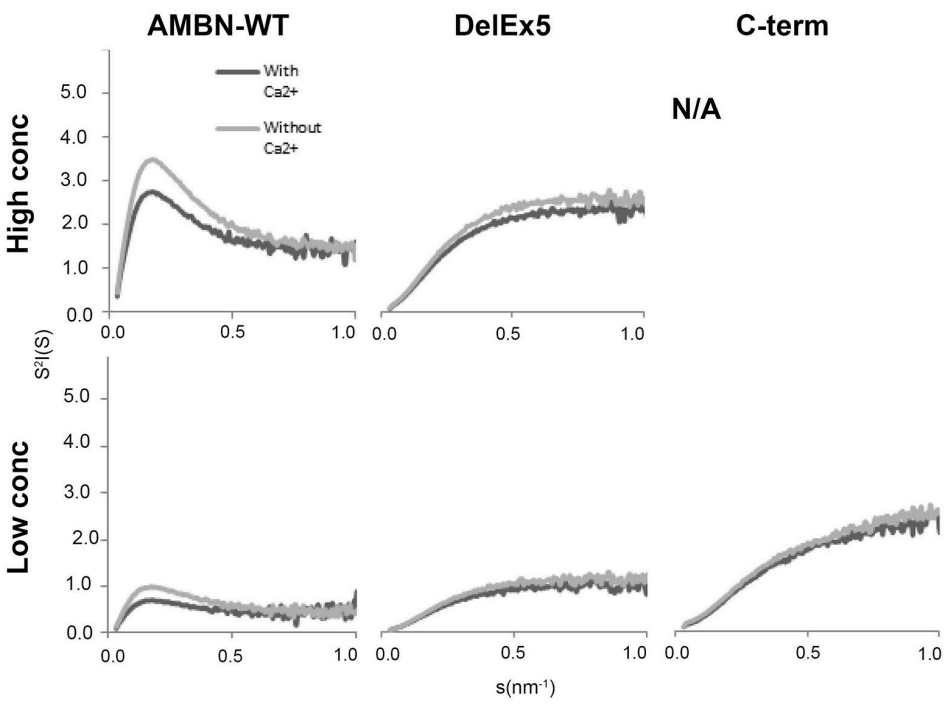

FIGURE 5 | Short Angle X-ray Scattering (SAXS) Kratky plots of AMBN-WT, DelEx5, and C-terminus with or without Ca^{2+}. High concentration corresponds to 0.7, 0.88 mg/ml, and N/A, respectively, whereas low concentration corresponds to 0.4, 0.44, and 0.44 mg/ml, respectively. N/A means not analyzed due to lack of material.

TABLE 2 | Results from small angle X-ray scattering (SAXS) of AMBN, DelEx5 and C-terminus.

Sample	R_g (Gu) nm	R_g (Gn) nm	MMVol. kDa	D_{max}	Qual. (%)
WT 1 mg/ml	14.6	15.1	3,027–4,037	51.1	90.4
WT 0.7 mg/ml	14.6	15.1	2,948–3,931	51.0	90.1
WT 0.4 mg/ml	14.2	14.8	2,908–3,878	49.7	90.8
WT 0.2 mg/ml	14.2	14.9	2,923–3,897	49.7	89.7
WT 0.7 mg/ml + Ca^{2+}	14.9	15.3	3,067–4,889	52.0	92.5
WT 0.4 mg/ml + Ca^{2+}	14.8	15.2	3,017–4,022	51.7	91.1
WT 0.2 mg/ml + Ca^{2+}	14.9	15.5	3,159–4,212	52.2	83.3
Del Ex 5 1.8 mg/ml	5.7	5.9	74–98	19.9	65.6
Del Ex 5 0.9 mg/ml	5.9	6.0	76–102	20.3	65.7
Del Ex 5 0.4 mg/ml	5.7	5.9	72–96	20.0	65.5
Del Ex 5 0.3 mg/ml	5.8	6.0	75–100	20.4	59.3
Del Ex 5 0.9 mg/ml + Ca^{2+}	5.7	5.8	71–95	19.1	65.4
Del Ex 5 0.4 mg/ml + Ca^{2+}	5.8	5.8	72–96	19.3	59.8
C-terminus 0.4 mg/ml	4.6	4.6	31–42	14.9	64.7
C-terminus 0.3 mg/ml	4.4	4.3	27–36	13.5	64.9
C-terminus 0.4 mg/ml + Ca^{2+}	4.8	4.7	32–43	16.2	69.6
C-terminus 0.2 mg/ml + Ca^{2+}	4.6	4.8	33–43	15.1	58.1

The distribution of AMBN in space around its axis is given as gunier (Gu) and Gnome (Gn) radius of gyration, molecular mass is given in kilo Daltons (MMVol. kDa) and the maximum size of particle is given as D_{max}, and the quality (Qual) of the data is given in % refers to the autoRg calculation of Rg (Gu). For detail, see http://www.esrf.eu/home/UsersAndScience/Experiments/MX/About_our_beamlines/bm29/computing-environment.html.

have been found to be phosphorylated (reviewed in Delsuc et al., 2015). It is possible that phosphorylation of AMBN is more efficient *in vivo,* but is effectively removed by alkaline phosphatases before it can be detected. Especially the CK2 predicted sites in the C-terminus (Toyosawa et al., 2000; Lee et al., 2003), that does not partake in self-assembly, are suggested to be functional during biomineralization (Ma et al., 2016). The C-terminus of AMBN is processed from the self-assembled AMBN full length protein by metalloproteases (Iwata et al., 2007; Chun et al., 2010b) and the 20S proteasome subunit (Geng et al., 2015), and may subsequently release phosphate and Ca^{2+} into the enamel fluid for HAp crystal nucleation and/or growth.

In conclusion, phosphorylation seems to regulate molecular organization and Ca^{2+} binding in AMBN. In a phosphorylated state, the molecules do not organize into supramolecular assemblies and Ca^{2+} binding is probably insignificant. However, when phosphorylation is lacking, the molecules self-assemble into organized structures that can bind Ca^{2+}. Calcium is probably secondary in modulation of AMBN organization as un-phosphorylated molecules also form assemblies without it. Thus, calcium alone has only minor effect on the structural order of AMBN. Based on our findings, we speculate that phosphorylation provide a switch for the function of the molecule, either to act as an un-phosphorylated and insoluble, Ca^{2+} binding complex in mineralizing extracellular matrices, or as a phosphorylated and soluble signal molecule in tissue development and repair. Further work needs to be done with respect to the kinetics and quantitation of the extent and effect(s) on phosphorylation, and findings need to be confirmed in *in vivo* models before the complete picture of AMBN functions in hard tissue development, mineralization and repair is revealed.

AUTHOR CONTRIBUTION

ØS: Designed the setup of experiments, performed experiments, and drafted the manuscript. SL: Participated in experimental design and in drafting the manuscript, BT: Performed experiments, participated in experimental design, and drafting the manuscript, JV: Provided material, participated in experimental design, and drafting the manuscript, BS: Participated in experimental design, and drafting the manuscript, JR: Participated in experimental design, and drafting the manuscript.

ACKNOWLEDGMENTS

This work was supported by grants from EU (QLK3-CT-2001-00090) and the Research Council of Norway (231530). The authors are grateful for the skillful technical assistance of Rune Hartvig, Department of Biomaterials. We are thankful for help provided by the staff at the European Synchotron Radiation Facility (Grenoble, France). The authors declare no conflict of interest.

REFERENCES

Bartlett, J. D., Ganss, B., Goldberg, M., Moradian-Oldak, J., Paine, M. L., Snead, M. L., et al. (2006). 3. Protein-protein interactions of the developing enamel matrix. *Curr. Top. Dev. Biol.* 74, 57–115. doi: 10.1016/S0070-2153(06)74003-0

Bawden, J. W., Moran, R. A., Deaton, T. G., and Saour, C. M. (1996). Immunohistochemical localization of signal transduction pathways during amelogenesis: an initial exploration. *Adv. Dent. Res.* 10, 105–110. doi: 10.1177/08959374960100020101

Bradford, M. M. (1976). A rapid and sensitive method for the quantitation of microgram quantities of protein utilizing the principle of protein-dye binding. *Anal. Biochem.* 72, 248–254. doi: 10.1016/0003-2697(76)90527-3

Cerny, R., Slaby, I., Hammarstrom, L., and Wurtz, T. (1996). A novel gene expressed in rat ameloblasts codes for proteins with cell binding domains. *J. Bone Miner. Res.* 11, 883–891. doi: 10.1002/jbmr.5650110703

Chun, Y. H., Lu, Y., Hu, Y., Krebsbach, P. H., Yamada, Y., Hu, J. C., et al. (2010a). Transgenic rescue of enamel phenotype in Ambn null mice. *J. Dent. Res.* 89, 1414–1420. doi: 10.1177/0022034510379223

Chun, Y. H., Yamakoshi, Y., Yamakoshi, F., Fukae, M., Hu, J. C., Bartlett, J. D., et al. (2010b). Cleavage site specificity of MMP-20 for secretory-stage ameloblastin. *J. Dent. Res.* 89, 785–790. doi: 10.1177/0022034510366903

Contaxis, C. C., and Reithel, F. J. (1971). Studies on Protein Multimers. II study of mechanism of urease dissociation in 1,2-propanediol - comparative studies with ethylene glycol and glycerol. *J. Biol. Chem.* 246, 677–685.

Delsuc, F., Gasse, B., and Sire, J.-Y. (2015). Evolutionary analysis of selective constraints identifies ameloblastin (AMBN) as a potential candidate for amelogenesis imperfecta. *BMC Evol. Biol.* 15:148. doi: 10.1186/s12862-015-0431-0

Fincham, A. G., Moradianoldak, J., Simmer, J. P., Sarte, P., Lau, E. C., Diekwisch, T., et al. (1994). Self-assembly of a recombinant amelogenin protein generates supramolecular structures. *J. Struct. Biol.* 112, 103–109. doi: 10.1006/jsbi.1994.1011

Fong, C. D., Cerny, R., Hammarstrom, L., and Slaby, I. (1998). Sequential expression of an amelin gene in mesenchymal and epithelial cells during odontogenesis in rats. *Eur. J. Oral Sci.* 106(Suppl. 1), 324–330. doi: 10.1111/j.1600-0722.1998.tb02193.x

Fukae, M., Kanazashi, M., Nagano, T., Tanabe, T., Oida, S., and Gomi, K. (2006). Porcine sheath proteins show periodontal ligament regeneration activity. *Eur. J. Oral Sci.* 114(Suppl 1), 212–218; discussion: 254–216, 381–212. doi: 10.1111/j.1600-0722.2006.00309.x

Fukumoto, S., Kiba, T., Hall, B., Iehara, N., Nakamura, T., Longenecker, G., et al. (2004). Ameloblastin is a cell adhesion molecule required for maintaining the differentiation state of ameloblasts. *J. Cell Biol.* 167, 973–983. doi: 10.1083/jcb.200409077

Fukumoto, S., Yamada, A., Nonaka, K., and Yamada, Y. (2005). Essential roles of ameloblastin in maintaining ameloblast differentiation and enamel formation. *Cells Tissues Organs* 181, 189–195. doi: 10.1159/000091380

Geng, S., White, S. N., Paine, M. L., and Snead, M. L. (2015). Protein interaction between ameloblastin and proteasome subunit alpha type 3 can facilitate redistribution of ameloblastin domains within forming enamel. *J. Biol. Chem.* 290, 20661–20673. doi: 10.1074/jbc.M115.640185

Iizuka, S., Kudo, Y., Yoshida, M., Tsunematsu, T., Yoshiko, Y., Uchida, T., et al. (2011). Ameloblastin regulates osteogenic differentiation by inhibiting Src kinase via cross talk between integrin beta1 and CD63. *Mol. Cell. Biol.* 31, 783–792. doi: 10.1128/MCB.00912-10

Iwata, T., Yamakoshi, Y., Hu, J. C., Ishikawa, I., Bartlett, J. D., Krebsbach, P. H., et al. (2007). Processing of ameloblastin by MMP-20. *J. Dent. Res.* 86, 153–157. doi: 10.1177/154405910708600209

Kawasaki, K., Buchanan, A. V., and Weiss, K. M. (2007). Gene duplication and the evolution of vertebrate skeletal mineralization. *Cells Tissues Organs* 186, 7–24. doi: 10.1159/000102678

Kitagawa, M., Kitagawa, S., Nagasaki, A., Miyauchi, M., Uchida, T., and Takata, T. (2011). Synthetic ameloblastin peptide stimulates differentiation of human periodontal ligament cells. *Arch. Oral Biol.* 56, 374–379. doi: 10.1016/j.archoralbio.2010.10.012

Lee, S. K., Kim, S. M., Lee, Y. J., Yamada, K. M., Yamada, Y., and Chi, J. G. (2003). The structure of the rat ameloblastin gene and its expression in amelogenesis. *Mol. Cells* 15, 216–225.

Lu, X., Fukumoto, S., Yamada, Y., Evans, C. A., Diekwisch, T. G., and Luan, X. (2016a). Ameloblastin, an extracellular matrix protein, affects long bone growth and mineralization. *J. Bone Miner. Res.* 31, 1235–1246. doi: 10.1002/jbmr.2788

Lu, X., Ito, Y., Kulkarni, A., Gibson, C., Luan, X., and Diekwisch, T. G. (2011). Ameloblastin-rich enamel matrix favors short and randomly oriented apatite crystals. *Eur. J. Oral Sci.* 119(Suppl. 1), 254–260. doi: 10.1111/j.1600-0722.2011.00905.x

Lu, X., Li, W., Fukumoto, S., Yamada, Y., Evans, C. A., Diekwisch, T., et al. (2016b). The ameloblastin extracellular matrix molecule enhances bone fracture resistance and promotes rapid bone fracture healing. *Matrix Biol.* 52–54, 113–126. doi: 10.1016/j.matbio.2016.02.007

Lyngstadaas, S. P., Lundberg, E., Ekdahl, H., Andersson, C., and Gestrelius, S. (2001). Autocrine growth factors in human periodontal ligament cells cultured on enamel matrix derivative. *J. Clin. Periodontol.* 28, 181–188. doi: 10.1034/j.1600-051x.2001.028002181.x

Ma, P., Yan, W., Tian, Y., He, J., Brookes, S. J., and Wang, X. (2016). The importance of serine phosphorylation of ameloblastin on enamel formation. *J. Dent. Res.* 95, 1408–1414. doi: 10.1177/0022034516661513

Moradian-Oldak, J., Bouropoulos, N., Wang, L., and Gharakhanian, N. (2002). Analysis of self-assembly and apatite binding properties of amelogenin proteins lacking the hydrophilic C-terminal. *Matrix Biol.* 21, 197–205. doi: 10.1016/S0945-053X(01)00190-1

Murakami, C., Dohi, N., Fukae, M., Tanabe, T., Yamakoshi, Y., Wakida, K., et al. (1997). Immunochemical and immunohistochemical study of the 27- and 29-kDa calcium-binding proteins and related proteins in the porcine tooth germ. *Histochem. Cell Biol.* 107, 485–494. doi: 10.1007/s004180050136

Nakamura, Y., Slaby, I., Spahr, A., Pezeshki, G., Matsumoto, K., and Lyngstadaas, S. P. (2006). Ameloblastin fusion protein enhances pulpal healing and dentin formation in porcine teeth. *Calcif. Tissue Int.* 78, 278–284. doi: 10.1007/s00223-005-0144-2

Nanci, A., Zalzal, S., Lavoie, P., Kunikata, M., Chen, W., Krebsbach, P. H., et al. (1998). Comparative immunochemical analyses of the developmental expression and distribution of ameloblastin and amelogenin in rat incisors. *J. Histochem. Cytochem.* 46, 911–934. doi: 10.1177/002215549804600806

Paine, M. L., and Snead, M. L. (1997). Protein interactions during assembly of the enamel organic extracellular matrix. *J. Bone Miner. Res.* 12, 221–227. doi: 10.1359/jbmr.1997.12.2.221

Paine, M. L., Zhu, D.-H., Luo, W., Bringas, P., Goldberg, M., White, S. N., et al. (2000). Enamel biomineralization defects result from alterations to amelogenin self-assembly. *J. Struct. Biol.* 132, 191–200. doi: 10.1006/jsbi.2000.4324

Perdigao, P. F., Carvalho, V. M., De Marco L., and Gomez, R. S. (2009). Mutation of ameloblastin gene in calcifying epithelial odontogenic tumor. *Anticancer Res.* 29, 3065–3067.

Perdigao, P. F., Gomez, R. S., Pimenta, F. J., and De Marco, L. (2004). Ameloblastin gene (AMBN) mutations associated with epithelial odontogenic tumors. *Oral Oncol.* 40, 841–846. doi: 10.1016/j.oraloncology.2004.03.004

Poulter, J. A., Murillo, G., Brookes, S. J., Smith, C. E., Parry, D. A., Silva, S., et al. (2014). Deletion of ameloblastin exon 6 is associated with amelogenesis imperfecta. *Hum. Mol. Genet.* 23, 5317–5324. doi: 10.1093/hmg/ddu247

Putnam, C. D., Hammel, M., Hura, G. L., and Tainer, J. A. (2007). X-ray solution scattering (SAXS) combined with crystallography and computation: defining accurate macromolecular structures, conformations and assemblies in solution. *Q. Rev. Biophys.* 40, 191–285. doi: 10.1017/S0033583507004635

Robinson, C., Brookes, S. J., Shore, R. C., and Kirkham, J. (1998). The developing enamel matrix: nature and function. *Eur. J. Oral Sci.* 106(Suppl. 1), 282–291. doi: 10.1111/j.1600-0722.1998.tb02188.x

Sonoda, A., Iwamoto, T., Nakamura, T., Fukumoto, E., Yoshizaki, K., Yamada, A., et al. (2009). Critical role of heparin binding domains of ameloblastin for dental epithelium cell adhesion and ameloblastoma proliferation. *J. Biol. Chem.* 284, 27176–27184. doi: 10.1074/jbc.M109.033464

Spahr, A., Lyngstadaas, S. P., Slaby, I., and Pezeshki, G. (2006). Ameloblastin expression during craniofacial bone formation in rats. *Eur. J. Oral Sci.* 114, 504–511. doi: 10.1111/j.1600-0722.2006.00403.x

Stakkestad, Ø., Lyngstadaas, S. P., Vondrasek, J., Gordeladze, J. O., and Reseland, J. E. (2017). Ameloblastin peptides modulates the osteogenic capacity of human mesenchymal stem cells. *Front. Physiol.* 8:58. doi: 10.3389/fphys.2017.00058

Su, J., Chandrababu, K. B., and Moradian-Oldak, J. (2016). Ameloblastin peptide encoded by exon 5 interacts with amelogenin N-terminus. *Biochem. Biophys. Rep.* 7, 26–32. doi: 10.1016/j.bbrep.2016.05.007

Takahashi, K., Shimonishi, M., Wang, R., Watanabe, H., and Kikuchi, M. (2012). Epithelial-mesenchymal interactions induce enamel matrix proteins and proteases in the epithelial cells of the rests of Malassez *in vitro*. *Eur. J. Oral Sci.* 120, 475–483. doi: 10.1111/j.1600-0722.2012.01002.x

Tamburstuen, M. V., Reppe, S., Spahr, A., Sabetrasekh, R., Kvalheim, G., Slaby, I., et al. (2010). Ameloblastin promotes bone growth by enhancing proliferation of progenitor cells and by stimulating immunoregulators. *Eur. J. Oral Sci.* 118, 451–459. doi: 10.1111/j.1600-0722.2010.00760.x

Tamburstuen, M. V., Reseland, J. E., Spahr, A., Brookes, S. J., Kvalheim, G., Slaby, I., et al. (2011a). Ameloblastin expression and putative autoregulation in mesenchymal cells suggest a role in early bone formation and repair. *Bone* 48, 406–413. doi: 10.1016/j.bone.2010.09.007

Tamburstuen, M. V., Snead, M. L., Reseland, J. E., Paine, M. L., and Lyngstadaas, S. P. (2011b). Ameloblastin upstream region contains structural elements regulating transcriptional activity in a stromal cell line derived from bone marrow. *Eur. J. Oral Sci.* 119(Suppl. 1), 286–292. doi: 10.1111/j.1600-0722.2011.00910.x

Toyosawa, S., Fujiwara, T., Ooshima, T., Shintani, S., Sato, A., Ogawa, Y., et al. (2000). Cloning and characterization of the human ameloblastin gene. *Gene* 256, 1–11. doi: 10.1016/s0378-1119(00)00379-6

Uchida, T., Murakami, C., Dohi, N., Wakida, K., Satoda, T., and Takahashi, O. (1997). Synthesis, secretion, degradation, and fate of ameloblastin during the matrix formation stage of the rat incisor as shown by immunocytochemistry and immunochemistry using region-specific antibodies. *J. Histochem. Cytochem.* 45, 1329–1340. doi: 10.1177/002215549704501002

Uchida, T., Murakami, C., Wakida, K., Dohi, N., Iwai, Y., Simmer, J. P., et al. (1998). Sheath proteins: synthesis, secretion, degradation and fate in forming enamel. *Eur. J. Oral Sci.* 106(Suppl. 1), 308–314. doi: 10.1111/j.1600-0722.1998.tb02191.x

Vymetal, J., Slaby, I., Spahr, A., Vondrasek, J., and Lyngstadaas, S. P. (2008). Bioinformatic analysis and molecular modelling of human ameloblastin suggest a two-domain intrinsically unstructured calcium-binding protein. *Eur. J. Oral Sci.* 116, 124–134. doi: 10.1111/j.1600-0722.2008.00526.x

Wald, T., Bednarova, L., Osicka, R., Pachl, P., Sulc, M., Lyngstadaas, S. P., et al. (2011). Biophysical characterization of recombinant human ameloblastin. *Eur. J. Oral Sci.* 119(Suppl. 1), 261–269. doi: 10.1111/j.1600-0722.2011.00913.x

Wald, T., Osickova, A., Sulc, M., Benada, O., Semeradtova, A., Rezabkova, L., et al. (2013). Intrinsically disordered enamel matrix protein ameloblastin forms ribbon-like supramolecular structures via an N-terminal segment encoded by exon 5. *J. Biol. Chem.* 288, 22333–22345. doi: 10.1074/jbc.M113.456012

Wald, T., Spoutil, F., Osickova, A., Prochazkova, M., Benada, O., Kasparek, P., et al. (2017). Intrinsically disordered proteins drive enamel formation via an evolutionarily conserved self-assembly motif. *Proc. Natl. Acad. Sci. U.S.A.* 114, E1641–E1650. doi: 10.1073/pnas.1615334114

Wazen, R. M., Moffatt, P., Zalzal, S. F., Yamada, Y., and Nanci, A. (2009). A mouse model expressing a truncated form of ameloblastin exhibits dental and junctional epithelium defects. *Matrix Biol.* 28, 292–303. doi: 10.1016/j.matbio.2009.04.004

Yamakoshi, Y., Tanabe, T., Oida, S., Hu, C. C., Simmer, J. P., and Fukae, M. (2001). Calcium binding of enamel proteins and their derivatives with emphasis on the calcium-binding domain of porcine sheathlin. *Arch. Oral Biol.* 46, 1005–1014. doi: 10.1016/S0003-9969(01)00070-X

Zhang, X., Diekwisch, T. G. H., and Luan, X. H. (2011). Structure and function of ameloblastin as an extracellular matrix protein: adhesion, calcium binding, and CD63 interaction in human and mouse. *Eur. J. Oral Sci.* 119, 270–279. doi: 10.1111/j.1600-0722.2011.00889.x

Conflict of Interest Statement: The authors declare that the research was conducted in the absence of any commercial or financial relationships that could be construed as a potential conflict of interest.

The reviewer MG and handling Editor declared their shared affiliation, and the handling Editor states that the process met the standards of a fair and objective review.

Copyright © 2017 Stakkestad, Lyngstadaas, Thiede, Vondrasek, Skålhegg and Reseland. This is an open-access article distributed under the terms of the Creative Commons Attribution License (CC BY). The use, distribution or reproduction in other forums is permitted, provided the original author(s) or licensor are credited and that the original publication in this journal is cited, in accordance with accepted academic practice. No use, distribution or reproduction is permitted which does not comply with these terms.

frontiers in Physiology

ORIGINAL RESEARCH
published: 29 June 2017
doi: 10.3389/fphys.2017.00450

Protein Phosphorylation and Mineral Binding Affect the Secondary Structure of the Leucine-Rich Amelogenin Peptide

Hajime Yamazaki[1,2], *Elia Beniash*[3], *Yasuo Yamakoshi*[4], *James P. Simmer*[5] and *Henry C. Margolis*[1,2]*

[1] Center for Biomineralization, The Forsyth Institute, Cambridge, MA, United States, [2] Department of Developmental Biology, Harvard School of Dental Medicine, Boston, MA, United States, [3] Department of Oral Biology, Center for Craniofacial Regeneration, McGowan Institute for Regenerative Medicine, University of Pittsburgh, Pittsburgh, PA, United States, [4] Department of Biochemistry and Molecular Biology, School of Dental Medicine, Tsurumi University, Yokohama, Japan, [5] Department of Biologic and Materials Sciences, University of Michigan School of Dentistry, Ann Arbor, MI, United States

OPEN ACCESS

Edited by:
Steven Joseph Brookes,
Leeds Dental Institute,
United Kingdom

Reviewed by:
Thomas G. H. Diekwisch,
Texas A&M University Baylor College of Dentistry, United States
Tomas Wald,
University of California, San Francisco, United States

***Correspondence:**
Henry C. Margolis
hmargolis@forsyth.org

Specialty section:
This article was submitted to Craniofacial Biology and Dental Research, a section of the journal Frontiers in Physiology

Received: 14 April 2017
Accepted: 14 June 2017
Published: 29 June 2017

Citation:
Yamazaki H, Beniash E, Yamakoshi Y, Simmer JP and Margolis HC (2017) Protein Phosphorylation and Mineral Binding Affect the Secondary Structure of the Leucine-Rich Amelogenin Peptide. Front. Physiol. 8:450. doi: 10.3389/fphys.2017.00450

Previously, we have shown that serine-16 phosphorylation in native full-length porcine amelogenin (P173) and the Leucine-Rich Amelogenin Peptide (LRAP(+P)), an alternative amelogenin splice product, affects protein assembly and mineralization *in vitro*. Notably, P173 and LRAP(+P) stabilize amorphous calcium phosphate (ACP) and inhibit hydroxyapatite (HA) formation, while non-phosphorylated counterparts (rP172, LRAP(−P)) guide the growth of ordered bundles of HA crystals. Based on these findings, we hypothesize that the phosphorylation of full-length amelogenin and LRAP induces conformational changes that critically affect its capacity to interact with forming calcium phosphate mineral phases. To test this hypothesis, we have utilized Fourier transform infrared spectroscopy (FTIR) to determine the secondary structure of LRAP(−P) and LRAP(+P) in the absence/presence of calcium and selected mineral phases relevant to amelogenesis; i.e., hydroxyapatite (HA: an enamel crystal prototype) and (ACP: an enamel crystal precursor phase). Aqueous solutions of LRAP(−P) or LRAP(+P) were prepared with or without 7.5 mM of $CaCl_2$ at pH 7.4. FTIR spectra of each solution were obtained using attenuated total reflectance, and amide-I peaks were analyzed to provide secondary structure information. Secondary structures of LRAP(+P) and LRAP(−P) were similarly assessed following incubation with suspensions of HA and pyrophosphate-stabilized ACP. Amide I spectra of LRAP(−P) and LRAP(+P) were found to be distinct from each other in all cases. Spectra analyses showed that LRAP(−P) is comprised mostly of random coil and β-sheet, while LRAP(+P) exhibits more β-sheet and α-helix with little random coil. With added Ca, the random coil content increased in LRAP(−P), while LRAP(+P) exhibited a decrease in α-helix components. Incubation of LRAP(−P) with HA or ACP resulted in comparable increases in β-sheet structure. Notably, however, LRAP(+P) secondary structure was more affected by ACP, primarily showing an increase in β-sheet structure, compared to that observed with added HA. These

collective findings indicate that phosphorylation induces unique secondary structural changes that may enhance the functional capacity of native phosphorylated amelogenins like LRAP to stabilize an ACP precursor phase during early stages of enamel mineral formation.

Keywords: amelogenesis, amelogenin, leucine-rich amelogenin peptide, secondary structure, FTIR, tooth enamel

INTRODUCTION

Tooth enamel, the most highly mineralized tissue in the human body (>95 wt% mineral content), is comprised of intricate interwoven patterns of extremely long and narrow crystals of carbonated hydroxyapatite, which contribute to its exceptional functional capabilities. This extremely well-organized structure is established through highly-regulated extracellular processes during the secretory stage of amelogenesis (Nanci, 2013). During this stage where initial enamel mineralization takes place, amelogenin, the predominant protein component of the enamel matrix (>90%), is believed to play a major role in regulating the nucleation, growth, morphology, and organization of forming enamel crystals (Margolis et al., 2014). Full-length amelogenin (with 173 amino acids in porcine enamel) is comprised of a tyrosine-rich N-terminal domain that includes its only post-translational modification (phosphorylation) site at serine-16 (Ser-16), a large hydrophobic central domain, and a highly conserved hydrophilic C-terminal domain. Amelogenin has been shown to assemble into nano particles (nanospheres) or higher order chain-like structures under specific (including physiological) conditions (for reviews, see Fincham et al., 1999; Margolis et al., 2006). Previous studies also suggest this higher-order structure helps regulate calcium phosphate mineralization *in vitro* through cooperative interactions with forming mineral (Beniash et al., 2005), leading to the formation of crystalline arrays of mineral particles, similar to those found in developing enamel (Beniash et al., 2005; Kwak et al., 2009; Deshpande et al., 2010; Yang et al., 2010; Wiedemann-Bidlack et al., 2011). Importantly, recombinant non-phosphorylated amelogenins have been shown to transiently stabilize amorphous calcium phosphate (ACP) precursor phases *in vitro,* prior to their spontaneous transformation to crystalline hydroxyapatite (HA) (Kwak et al., 2009, 2011, 2014, 2016; Yang et al., 2010; Wiedemann-Bidlack et al., 2011). A similar transformation of ACP to crystalline mineral has also been observed in developing enamel (Diekwisch, 1998; Beniash et al., 2009). Most notably, the single-site phosphorylation of amelogenin (porcine) has been shown to have a marked effect on calcium phosphate mineralization *in vitro*; that is, both full-length and truncated phosphorylated amelogenins have an enhanced capacity to stabilize ACP and prevent HA formation (Kwak et al., 2009, 2011, 2014; Wiedemann-Bidlack et al., 2011) in a concentration-dependent fashion (Kwak et al., 2009, 2014; Fang et al., 2013).

The leucine rich amelogenin peptide (LRAP) is an alternative-splicing product of the amelogenin gene expressed throughout enamel development (Yuan et al., 1996). For example, the 56 amino acid porcine LRAP is comprised of the first 33 N-terminal amino acids (including the phosphorylation site) and the last 23 C-terminal amino-acids (including the hydrophilic domain) of the full-length porcine amelogenin. Numerous attempts have been made to elucidate the physiological function of LRAP in enamel formation. It has been proposed to have roles as a cell signaling molecule (Veis et al., 2000; Boabaid et al., 2004; Warotayanont et al., 2008, 2009; Wen et al., 2011) or to be involved in the regulation of the kinetics of calcium phosphate mineralization and the morphology of formed crystals (Le Norcy et al., 2011a; Xia et al., 2016). However, a consensus regarding the roles of LRAP in amelogenesis has not been reached and still many questions remain unanswered. Nevertheless, previous studies have shown that LRAP shares many common properties with the full-length amelogenin with respect to its capacity to regulate mineral formation *in vitro*. Like full-length amelogenin, LRAP forms nanospheres (Habelitz et al., 2006; Tarasevich et al., 2010; Le Norcy et al., 2011a), and appears to interact with hydroxyapatite (Shaw et al., 2004, 2008). Furthermore, it has been shown that non-phosphorylated recombinant human LRAP and recombinant full-length human amelogenin (rH174) have the same capacity to bind calcium (i.e., four to six calcium ions per molecule), although the calcium affinity constant for the LRAP was greater than that for the full-length amelogenin (Le et al., 2006). We have also demonstrated that non-phosphorylated porcine LRAP (LRAP(−P)) can similarly guide the formation of aligned bundles of HA crystals, as does the recombinant non-phosphorylated amelogenin (Le Norcy et al., 2011a), while, like native phosphorylated versions of amelogenin, phosphorylated porcine LRAP (LRAP(+P)) similarly stabilizes ACP and prevents HA formation *in vitro*. Based on similarities of amino acid sequences and behaviors, LRAP has also allowed us to investigate the potential role of specific amino-acid domains of amelogenin and phosphorylation in protein self-assembly. Our previous study using dynamic light scattering (DLS) and transmission electron microscopy (TEM) illustrates that there are potentially important differences in the self-assembly and conformational behavior between phosphorylated LRAP(+P) and its non-phosphorylated counterpart, LRAP(−P) (Le Norcy et al., 2011a). Also, previous studies from our laboratory using small angle X-ray scattering (SAXS) techniques showed dramatic structural differences between LRAP(+P) and LRAP(−P) that are further affected by the presence of calcium ions (Le Norcy et al., 2011b). We are specifically interested in the role the single phosphate group in amelogenin plays in enamel mineral formation and have hypothesized that phosphorylation of amelogenin induces conformational changes that critically affect its capacity to interact with forming calcium phosphate mineral phases. To test this hypothesis, we have utilized Fourier transform infrared spectroscopy (FTIR) in the present study to ascertain the effect of phosphorylation on the secondary structures of LRAP(−P) and LRAP(+P) in the presence and absence of calcium in solution and upon interacting with relevant mineral phases (i.e., HA

and ACP). FTIR spectroscopy is extremely sensitive to global conformational changes in proteins (Surewicz et al., 1993; Wang et al., 2010) and uniquely suited to study structural changes in proteins upon self-assembly (Bouchard et al., 2000; Wang et al., 2010) and adsorption to solid surfaces (Roach et al., 2005; Elangovan et al., 2007).

MATERIALS AND METHODS

Preparation of LRAP Solutions

Porcine LRAP with or without a phosphate group on Ser-16 [i.e., LRAP(+P) and LRAP(−P), respectively] were synthesized commercially (RS Synthesis, Louisville, KY, USA) and re-purified by high-pressure liquid chromatography (HPLC), as previously described (Nagano et al., 2009). Lyophilized LRAP(+P) and LRAP(−P) were weighed and dissolved in distilled deionized water at room temperature to yield stock solutions of 17.5 mg/mL (pH 2.5 ∼ 3) solutions. The stock solutions were left for 12–24 h at 4°C to aid complete protein dissolution. Stock solutions were then stored at −20°C. Just prior to use, aliquots of the LRAP stock solutions were centrifuged (12,500 × g, 4°C, 20 min) and the supernatants were diluted to 15 mg/mL with either distilled deionized water or calcium chloride solution to yield 7.5 mM calcium. The pH of each solution was adjusted to pH 7.4 at room temperature using potassium hydroxide aqueous solution. Each experimental solution type [i.e., LRAP(−P) and LRAP(+P), with and without added calcium] was prepared in the same fashion in triplicate ($n = 3$).

Dynamic Light-Scattering (DLS) Measurements of LRAP Solutions

To acquire information on the aggregation of LRAP, each solution type was subjected to dynamic light-scattering (DLS) analysis, as previously described (Wiedemann-Bidlack et al., 2007). Each DLS measurement (DynaPro MSXTC/12) was comprised of 5 measurements of 20 acquisitions (5 sec each) at 5-min intervals at 25°C and the sizes (hydrodynamic radius, R_H) of protein particles were determined. Unpaired *t*-tests were used to compare differences in protein particle sizes.

Incubation of LRAP(+P) and LRAP(−P) with Selected Mineral Phases

Standard HA was purchased from National Institute of Standards and Technology (2910 Calcium Hydroxyapatite, Gaithersburg, MD, USA). Stabilized ACP was prepared by mixing $CaCl_2$ and NaH_2PO_4 in distilled water to final concentrations of 5 and 3 mM, respectively, at ambient conditions with stirring in the presence of 150 μM of $Na_4P_2O_7$. After 60 min, the reaction suspension was centrifuged at 12,000 × g at 4°C for 20 min. The pellets were washed with distilled water twice, lyophilized, and stored at −20°C. The composition and structure of the standards were confirmed using FTIR prior to use. The stability of the ACP phase in water was also confirmed by FTIR after incubation in water for 4 h at 37°C, following the experimental protocol described in the next paragraph. These latter selected measurements were carried out at Emmanuel College in Boston, MA (see Acknowledgments).

HA or ACP (0.3 mg) were incubated in 40 μL of 5, 10, and15 mg/mL LRAP(+P) and LRAP(−P) solutions with rocking for 4 h at 37°C. After equilibration, the mineral-protein mixtures were centrifuged at 12,000 × g for 10 min at 4°C. After centrifugation, the supernatants were removed, and the pellets were washed twice (10 min each) with 20 μL of distilled deionized water (pH adjusted to 7.4). The washed samples with bound protein were then re-suspended in 10 μL of the pH-adjusted distilled deionized water, and the suspensions were used for FTIR measurements. In this fashion, the effect of the binding of LRAP(+P) and LRAP(−P) to HA and ACP on protein secondary structure were assessed, as was done similarly for full-length amelogenin (Beniash et al., 2012).

FTIR Spectroscopic Measurement of LRAPs in the Absence and Presence of Calcium and Following Equilibration with Mineral Particles

FTIR spectroscopic measurements were conducted at room temperature, as previously described (Elangovan et al., 2007; Beniash et al., 2012), using the attenuated total reflection (ATR) mode. Fifteen microliters of protein solution or washed mineral suspension were placed within a small rubber O-ring (i.d., 3 mm) on the ATR crystal. The sample was then covered with a glass slide that was pressed down with the ATR accessory press against the O-ring to minimize evaporation. Sample and background (distilled deionized water) spectra were taken at a resolution of 4 cm^{-1}, and 128 scans were collected *per* spectrum.

FTIR Spectra Analyses

Analyses were performed using the Origin 9.0 software package (OriginLab Corporation, Northampton, MA), as previously described (Elangovan et al., 2007; Beniash et al., 2012). For LRAP(−P) and LRAP(+P) in the presence and absence of calcium ions, FTIR spectra were measured three times for each solution, and the averaged spectra of the triplicate measurements were used for the further analyses. For suspensions of LRAP(−P) or LRAP(+P) with the mineral particles (HA or ACP), however, only data from the experiment with 15 mg/mL LRAP were used, since the spectra obtained with the 5 and 10 mg/mL solutions were too noisy for reliable deconvolution analyses (described in the following paragraph). However, the observed tendency in differences of spectra from LRAP(+P) and LRAP(−P) at lower concentrations were the same as those seen in the experiments carried out with the highest concentration of each LRAP.

The amide I and amide II region (between 1,475 and 1,725 cm^{-1}) of the spectra were smoothed (5-point FFT smoothing), baseline corrected (straight line subtraction from the start to end points). Second derivative analyses were then performed to obtain peak minima that were used to identify the initial center of the identified individual peaks. Peak-fitting was performed using a Gaussian model. Identified peak positions were initially fixed, and several rounds of peak-fitting were performed until χ^2 values between the experimental and calculated spectra were reduced to a value below 1×10^{-6}. The same procedure was then repeated with the peak center released with the restriction of movement of ± 2 cm^{-1} until χ^2 values between the experimental

and calculated spectra were reduced to a value below 1×10^{-6}. The percentage of the each deconvoluted peak area within the peak area of the amide I region (between 1,600 and 1,700 cm^{-1}) was then calculated for each spectrum. Identified peaks within the amide I region were then attributed to specific secondary structural elements, as described in the next paragraph.

FTIR Peak Assignments

FTIR peak identifications were based on the following literature reports. Peaks observed at 1,620–1,630 cm^{-1} were identified as hydrated PPII helix (Johnston and Krimm, 1971; Wellner et al., 1996; Elangovan et al., 2007). Earlier reports indicate that the full length amelogenins contain a significant PPII fraction (Renugopalakrishnan et al., 1986; Goto et al., 1993; Sogah et al., 1994; Lakshminarayanan et al., 2007, 2009). In an overlapped region to this, peaks observed between 1,610 and 1,640 cm^{-1} were attributed to β-sheet (Susi and Byler, 1983; Jackson and Mantsch, 1995). Random coil conformation was attributed to peaks between 1,640 and 1,650 cm^{-1} (Krimm and Bandekar, 1986; Barth and Zscherp, 2002; Elangovan et al., 2007), which have also been reported in amelogenin (Renugopalakrishnan et al., 1986; Goto et al., 1993; Matsushima et al., 1998; Elangovan et al., 2007; Yang et al., 2010). Also, peaks observed between 1,650 and 1,655 cm^{-1} were attributed to α-helix conformation (Susi and Byler, 1983; Surewicz et al., 1993; Roach et al., 2005). Finally, peaks observed between 1,659 and 1,670 cm^{-1} were assigned to β-turn (Susi and Byler, 1983; Surewicz et al., 1993; Jackson and Mantsch, 1995; Vass et al., 2003). A later peak with a maximum around 1,680 and 1,690 cm^{-1} can also be attributed to β-turn or high-frequency split of the anti-parallel β-sheet (Krimm and Bandekar, 1986; Kubelka and Keiderling, 2001; Elangovan et al., 2007).

RESULTS

DLS Measurements of LRAP in Solution

Mean protein particle sizes from DLS measurements (S.D.) in the absence [LRAP(−P): 5.55 (0.18) nm; LRAP(+P): 3.87 (0.61) nm] and presence [LRAP(−P): 5.07 (0.57) nm; LRAP(+P): 5.51 (0.59) nm] of 7.5 mM calcium at pH 7.4 confirmed that both non-phosphorylated and phosphorylated LRAP undergo self-assembly to form small nanoparticles under near-neutral pH conditions, as we have previously reported (Le Norcy et al., 2011a). LRAP(+P) exhibits a smaller particle size ($p < 0.0005$) in comparison to LRAP(−P). In addition, the LRAP(+P) particle size increases significantly ($p < 0.00005$) in the presence of added calcium, while the particle size of LRAP(−P) changed only slightly ($p < 0.05$). These latter results on the effect of calcium on LRAP particle size are consistent with our earlier findings (Le Norcy et al., 2011a).

FTIR Analyses of the Secondary Structure of LRAP(−P) and LRAP(+P) in the Presence/Absence of Calcium Ions

Figures 1A–D show amide I and amide II regions of the FTIR spectra (1,475–1,725 cm^{-1}) and individual deconvoluted peaks obtained after peak analyses for LRAP(−P), LRAP(−P) with calcium ions, LRAP(+P), and LRAP(+P) with calcium ions, respectively. **Figures 1E,F** show the 4 mean spectra superimposed in the same plot for comparative purposes. Also, the results of the peak analysis are summarized in **Table 1**, as a list of peak positions (represented as wavenumbers of the individual peak centers) and the area percentage of the individual peaks identified within the amide I region, obtained from each deconvoluted peak. As shown in **Figure 1A** and **Table 1**, non-phosphorylated LRAP(−P) is mostly comprised of a 1,643 cm^{-1} peak (40%) that is attributed to random coil and a peak at 1,620 cm^{-1} (28%) that is attributed to PPII helix or β-sheet structure. In the presence of calcium ions with LRAP(−P), this β-sheet/PPII helix component at 1,620 cm^{-1} is significantly reduced (to 8.8%), and the overlapping major peak associated with random coil structure at 1,642 cm^{-1} increases in total area (*to* 74.3%), as shown in **Figure 1B** and **Table 1**. However, the overall change of the LRAP(−P) spectra upon addition of calcium is relatively subtle and the overall shape of the amide I peak of LRAP(−P) remains fairly similar (see **Figure 1F**) with the highest absorbance remaining at ∼1,620 cm^{-1}. As shown in **Figure 1C** and **Table 1**, however, phosphorylated LRAP(+P) exhibited evidence for three different β-sheet structures (total 42%) as multiple peaks (1,617, 1,629, and 1,639 cm^{-1}), although the possibility of PPII helix components cannot be ruled out (i.e., 1629 cm^{-1}). In contrast to the non-phosphorylated LRAP(−P) in the absence or presence of calcium, however, LRAP(+P) lacked random coil structure and exhibited a significant amount of α-helix (1,653 cm^{-1}, 31.4%) as a major secondary structure component. In the presence of calcium ions, the amide I peak of LRAP(+P) exhibited a decrease in α-helix conformation (from 31.4% to 21.2% at 1,652 cm^{-1}), along with notable increases in β-turn (1,666 cm^{-1}), β-sheet (1,637 cm^{-1}), and formed β-sheet/PPII helix components shown (1,620 cm^{-1}) (see **Figure 1D** and **Table 1**). As shown in **Figures 1E,F**, with the addition of calcium ions, the overall shape of the LRAP(+P) amide I peak changes dramatically, shifting its peak absorption frequency from 1,650 cm^{-1} toward 1,620 cm^{-1}, consistent with more significant changes in LRAP(+P) secondary structure, in comparison to that seen with the non-phosphorylated LRAP(−P).

FTIR Spectroscopic Analyses of the Secondary Structure of LRAP(−P) and LRAP(+P) in the Presence of HA or ACP

Amide I and amide II areas of FTIR spectra (1,475–1,725 cm^{-1}) of LRAPs, without mineral particles, with HA, and with ACP are shown in **Figure 2A** (LRAP(−P)) and **Figure 2B** (LRAP(+P)). Corresponding results of peak identification and analyses within the amide I region are summarized in **Table 2**, in the same manner as described above. As shown in **Figure 2A**, in comparison to the amide I peak of LRAP(−P) without minerals (dotted line), both the addition of HA and ACP mineral particles induced a significant relative increase in β-sheet/PPII helix structure at around 1,620 cm^{-1}, along with a notable decrease in random coil structure at 1,643 cm^{-1} in comparison to that seen at higher wavenumbers. The amide I peak of LRAP(−P) incubated with HA also showed the formation of an α-helix

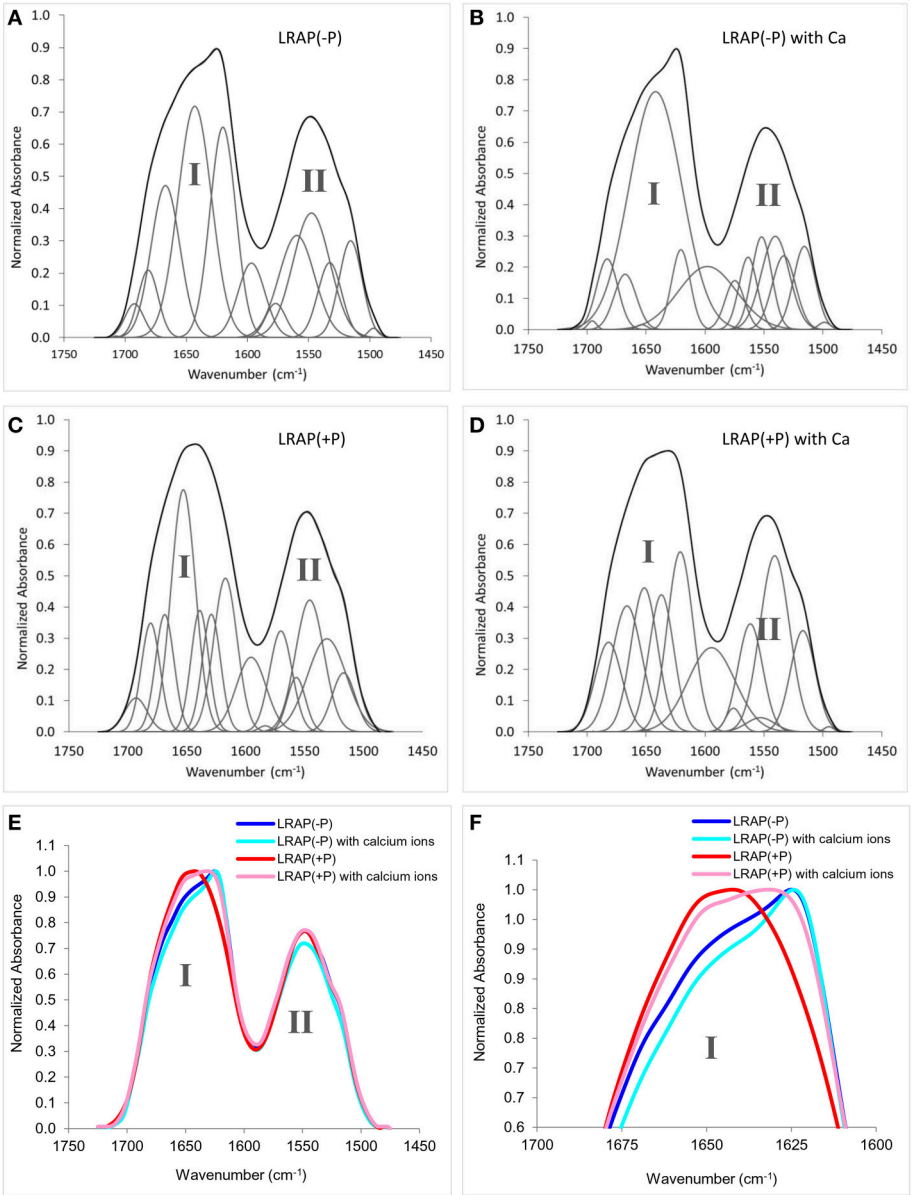

FIGURE 1 | Amide I and amide II regions of FTIR spectra and individual fittings, showing deconvoluted peaks of LRAPs in the presence or absence of calcium ions., Amide I (1,700–1,600 cm−1) and amide II regions (1,575–1,480 cm−1) are labeled "I" and "II", respectively. **(A)** LRAP(−P), **(B)** LRAP(−P) in the presence of calcium ions, **(C)** LRAP(+P), **(D)** LRAP(+P) in the presence of calcium ions. **(E)** Superimposed plotting of all 4 aforementioned spectra in **(A–D)**. **(F)** Expanded view of the upper portions of amide I peaks shown in **(E)**.

component (1,650 cm^{-1}), whereas amide I peak of LRAP(−P) incubated with ACP did not. In contrast to LRAP(−P), as shown in **Figure 2B**, observed changes in the secondary structure of LRAP(+P) showed a completely different pattern that also depended on the mineral phase in question, as can be clearly seen in **Figure 2B**. As summarized in **Table 2**, the amide I peak of LRAP(+P) incubated with HA showed a decrease in the α-helix component and an increase in random coil structure (1,641 cm^{-1}), resulting in an amide I peak with a maximum absorption around 1,650 cm^{-1}. On the other hand, the amide I peak of LRAP(+P) incubated with ACP showed a marked increase in β-sheet/PPII helix structure component at 1,619 cm^{-1}, along with a slight decrease (31–26%) in the α-helix component at 1,653 cm^{-1}. These collective changes resulted in the maximum absorption in the amide I band shifting to ∼1,620 cm^{-1} as was shown in the case of LRAP(−P) incubation with either mineral phase.

DISCUSSION

Prior studies to investigate the secondary structure of amelogenin (summarized in **Table 3**) have led to a general consensus that

TABLE 1 | Positions and relative areas of individual deconvoluted peaks within amide I region of FTIR spectra of LRAP(−P) and LRAP(+P) in the presence or absence of calcium ions.

	LRAP(–P)		LRAP(–P) with Ca		LRAP(+P)		LRAP(+P) with Ca	
	Center (cm^{-1})	Area%	Center (cm^{-1})	Area%	Center (cm^{-1})	Area%	Center (cm^{-1})	Area%
Anti-parallel β-sheet					1,617	19.3		
β-sheet or polyproline II helix	1,620	27.8	1,620	8.8			1,621	25.6
β-sheet or polyproline II helix					1,629	11.5		
β-sheet								
β-sheet					1,639	11.5	1,637	18.8
Random coil	1,643	39.7	1,642	74.3				
α-helix	1,652	0.0	1,654	0.2	1,653	31.4	1,652	21.2
β-turn or 3(10) helix								
β-turn or 3(10) helix	1,667	22.2	1,668	7.4	1,669	11.5	1,666	21.0
β-turn or β-sheet								
β-turn or β-sheet	1,681	6.9	1,683	9.0	1,680	10.8	1,682	13.4
β-turn or β-sheet	1,692	3.4	1,696	0.4	1,693	4.1	1,695	0.0

amelogenin is an intrinsically disordered molecule, having a secondary structure that is mostly composed of random coil. Some reports also suggest that the N-terminus of amelogenin contains β-sheets, β-strand, β-turns, and α-helix components and that poly-proline type II (PPII) helical structure is found in the mid-region of amelogenin, while random coil conformation comprise the main part of the C-terminal domain. The secondary structure of LRAP has also been extensively studied (see **Table 4** for summary and additional discussion). Some of these findings are discussed below. However, the general consensus is that LRAP is also an unstructured protein like full-length amelogenin, being comprised mostly of random coil, β-turn, and small amounts of helix structures, although LRAP is somewhat less structured in comparison to that proposed for the N- and C-terminal domains of full-length amelogenin (Delak et al., 2009; Zhang et al., 2011).

The focus of the present study was to investigate the influence of Ser-16 phosphorylation on the LRAP secondary structure using FTIR, because of the marked influence amelogenin phosphorylation has on mineralization *in vitro* (e.g., Kwak et al., 2009; Le Norcy et al., 2011a; Wiedemann-Bidlack et al., 2011) and the potential importance of this finding in the enamel formation process (Margolis et al., 2014). The results of comparative FTIR analyses of LRAP(+P) and LRAP(−P) in solution at pH 7.4 indicate that single-site phosphorylation of LRAP induces clear changes in the secondary structure of the LRAP molecule. The most marked difference is that LRAP(−P) has random coil as the main structure element, whereas LRAP(+P) exhibits more rigid α-helix and β-sheet structures. Our findings also indicate that the presence of calcium ions induces more drastic changes in the secondary structure of LRAP(+P), in comparison to that of LRAP(−P). These general findings mirror our previous TEM and SAXS findings that showed that added calcium had a greater influence on the quaternary and tertiary structures of LRAP(+P), respectively, in comparison to LRAP(−P) (Le Norcy et al., 2011a,b). Furthermore, comparing the changes in the secondary structure of LRAP induced by incubation with ACP or HA, LRAP(+P) showed a completely different pattern of the secondary structures induced by its incubation with ACP from that seen with HA, while LRAP(−P) showed relatively small differences in secondary structure changes following incubation with either HA or ACP.

As shown in **Table 1**, analyses of the amide I peak reveal that the main structural components of LRAP(−P) are random coil (39.7%) and β-sheets/PPII helix (27.8%). These results are similar to those previously obtained for rP172, which possess the same N- and C-terminal domains of LRAP(−P), along with a large (116 amino acid long) hydrophobic central domain (Lakshminarayanan et al., 2007; Beniash et al., 2012). In sharp contrast to these findings, the main components of LRAP(+P) were found to be α-helix (31.4%) and β-sheets/PPII helix (42.3%), with no evidence of a random coil component. On this basis alone, LRAP(+P) appears to adopt a more ordered secondary structure conformation in solution, in comparison with that found for the non-phosphorylated LRAP(−P).

Differences in amide I spectra (**Figure 1F**) and FTIR peak analyses (**Table 1**) also indicate that LRAP(−P) and LRAP(+P) are affected differently by the presence of calcium, as a result of Ser-16 phosphorylation. In the presence of calcium, the random coil component of LRAP(−P) increases substantially (by ∼90%) to 74.3%, while more structured elements of β-sheets/PPII helix and β-turn/3(10) helix decrease (by 20%) to yield an overall less rigid structure. This shift in the LRAP(−P) secondary structure in the presence of calcium to a less structured conformation indicates that there are interactions between calcium ions and the non-phosphorylated LRAP(−P). Our previous studies using SAXS, DLS, and TEM showed that addition of calcium to solutions of LRAP(−P) did not change LRAP's tendency to aggregate and form nanospheres in terms of their particle size (Le Norcy et al., 2011a), and had little effect on its globular protein structure observed using SAXS (Le Norcy et al., 2011b). Hence, the observed shift from β-sheet to a less rigid random coil conformation by addition of calcium ions does not appear to affect the tertiary structure of LRAP(−P) or

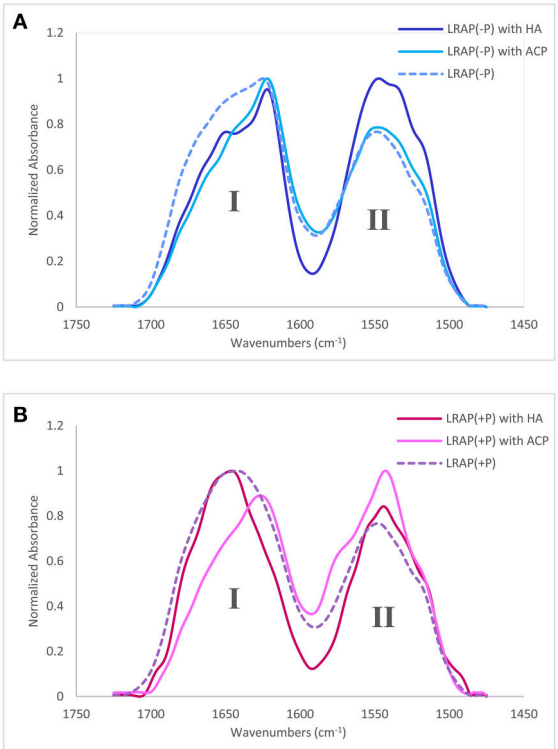

FIGURE 2 | Amide I and amide II regions of FTIR spectra and individual fittings, showing deconvoluted peaks of LRAPs in the presence or absence of mineral particles. Amide I (1,700–1,600 cm−1) and amide II regions (1,575–1,480 cm−1) are labeled "I" and "II", respectively. **(A)** Superimposed plots from three different experiments, LRAP(−P) (dotted line), LRAP(−P) in the presence of HA (dark blue), and LRAP(−P) in the presence of ACP (light blue). **(B)** Superimposed plot of three different experiments, LRAP(+P) (dotted line), LRAP(+P) in the presence of HA (dark red), and (LRAP(+P) in the presence of ACP (light pink).

its aggregation and tendency to form nanospheres. This result is in reasonable agreement with a previous study (Le et al., 2006) using circular dichroism (CD), in which it is concluded that non-phosphorylated recombinant human LRAP (58 amino acid residues) had mostly a random coil structure (see **Table 4**, footnote a).

Interestingly, LRAP(+P) in the presence of calcium ions induces more prominent conformational changes in comparison to the results for LRAP(−P) solutions, as is indicated by the relative magnitude of changes in the overall amide I peak shape (see **Figure 1F**). As shown in **Table 1**, LRAP(+P) once again yields a less rigid structure in the presence of calcium, indicated by a reduction in α-helix (from 31.4 to 21.2%) that is offset by an increase in β-turn/3(10) helix (from 11.5 to 21.0%), with essentially no change in the level of β-sheets/PPII helix components (42.3–44.4%). Our FTIR peak analyses also showed that LRAP(+P) in the presence of calcium ions, as in the absence of calcium, exhibits a lack of random coil conformation, unlike that seen with LRAP(−P). Although a slight decrease in the amount of α-helix component was observed, this finding may appear to be inconsistent with earlier CD findings suggesting that

TABLE 2 | Positions and relative areas of individual deconvoluted peaks within amide I region of FTIR spectra of LRAP(−P) and LRAP(+P) in the presence or absence of mineral particles (HA or ACP).

	LRAP(−P)		LRAP(−P) with HA		LRAP(−P) with ACP		LRAP(+P)		LRAP(+P) with HA		LRAP(+P) with ACP	
	Center (cm^{-1})	Area%	Center (cm^{-1})	Area%	Center (cm^{-1})	Area%	Center (cm^{-1})	Area%	Center (cm^{-1})	Area%	Center (cm^{-1})	Area%
Side chain									1,601	3.2		
Anti-parallel β-sheet							1,617	19.3	1,617	13.3		
β-sheet or polyproline II helix	1,620	27.8	1,622	42.6	1,621	53.7					1,619	47.8
β-sheet or polyproline II helix β-sheet							1,629	11.5	1,628	7.3	1,632	13.6
β-sheet			1,638	9.4			1,639	11.5				
Random coil	1,643	39.7			1,644	14.7			1,641	23.3		
α-helix	1,652	0.0	1,650	18.7			1,653	31.4			1,653	25.8
β-turn or 3(10) helix					1,661	21.7			1,659	28.5		
β-turn or 3(10) helix	1,667	22.2	1,664	15.4			1,669	11.5	1,669	10.3	1,667	5.5
β-turn or β-sheet												
β-turn or β-sheet	1,681	6.9	1,680	13.9	1,682	10.0	1,680	10.8	1,678	13.1	1,680	7.3
β-turn or β-sheet	1,692	3.4	1,694	0.0	1,695	0.0	1,693	4.1	1,695	1.1	1,695	0.0

TABLE 3 | Brief summary of previous reports on the secondary structure of amelogenin*.

Authors	Type of amelogenin	Ser16 phosphorylation	species	Experimental techniques	Experimental conditions	Information obtained
Renugopalakrishnan et al., 1986	Full-length	Native	Bovine	CD, FTIR (liquid and solid)	Various buffers at different pH values	Secondary structure
Goto et al., 1993	Full-length and cleaved (25, 20, and 13 kD)	Native	Porcine	CD	pH ∼5, ∼5 mM acetate	Secondary structure
Matsushima et al., 1998	Full-length and cleaved (20, and 13 kD)	Native	Porcine	SAXS, Computer modeling	2% acetic acid buffer	Secondary and tertiary structures
Lakshminarayanan et al., 2007	Full-length (rP172) and cleaved (rP148)	(−P)	Porcine (recombinant)	FTIR, CD, ITC, DLS	Tris buffer at pH 5.8	Secondary and quaternary structures, role of C-terminus
Delak et al., 2009	Full-length (rP172)	(−P)	Porcine (recombinant)	DLS, CD, NMR, computer simulation		Secondary structure
Lakshminarayanan et al., 2009	Full-length (rP172)	(−P)	Porcine (recombinant)	ITC, CD	Tris buffer, 5 mM Ca, pH 7.4, different temperatures	Secondary and quaternary structures
Lakshminarayanan et al., 2010	Full-length (rM180 with His-tag*, point mutation)	(−P)	Murine (recombinant)	DLS, CD, fluorescence spectrometry	acetate buffer, pH 5.8,	Secondary and quaternary structures—effects of selected point mutations
Zhang et al., 2011	Full-length (fragmented) with His-tag*		Murine (recombinant)	SS-NMR (REDOR), SV	Phosphate and acetate buffers	Secondary and quaternary structures
Beniash et al., 2012	Full-length (rP172)	(−P)	Porcine (recombinant)	FTIR	PBS, Ca	Secondary structure—effects of pH and added calcium

CD, Circular Dichroism; DLS, Dynamic Light Scattering; FTIR, Fourier Transform Infrared Spectroscopy; His-tag, 12 amino acid peptide tag (MRGSHHHHHHGS-); ITC, Isothermal Titration Calorimetry; NMR, Nuclear Magnetic Resonance; REDOR, Rotational Echo DOuble Resonance; SAXS, Small Angle X-ray Scattering; SS-NMR, Solid State Nuclear Magnetic resonance; SV, Sedimentation Velocity.

TABLE 4 | Brief summary of previous reports on the secondary structure of LRAP*.

Authors	Type of amelogenin	Ser16 Phosphorylation	species	Experimental techniques	Experimental conditions	Information obtained
Shaw et al., 2004	LRAP	(+P) and (−P)	Recombinant	SS-NMR (REDOR)	Phosphate buffer, 0.15 M NaCl, saturated CaP soln., pH 7.4, HA	Role of C-terminus in HA adsorption
Le et al., 2006[a]	LRAP and full-length amelogenin (rH174)		Human (recombinant)	ITC, NMR, CD	10 mM HEPES buffer, pH 7.5, pH 4.0 with 10 mM acetate buffer for NMR and CD	Secondary structure, interaction with Ca
Shaw et al., 2008	LRAP		Murine (recombinant)	SS-NMR (REDOR)	NaCl, saturated CaP soln., HA	Secondary structure, dynamics of LRAP interaction with HA
Shaw and Ferris, 2008	LRAP	(+P) and (−P)	Murine (recombinant)	SS-NMR (REDOR)	NaCl, saturated CaP soln., HA	Interaction with HA
Buchko et al., 2010	LRAP and full-length (M180 with His-tag*)		Murine (recombinant)	DLS, NMR	pH 3.0, 2% acetic acid, various ionic strength	Quaternary structure, effect of ionic strength
Tarasevich et al., 2010	LRAP	(+P)	Murine (recombinant)	DLS, SWE, AFM	NaCl, saturated CaP soln., or PBS	Quaternary structure, adsorption mechanism on HA
Masica et al., 2011[c]	LRAP	(+P) and (−P)	Murine (recombinant)	SS-NMR (REDOR)	Phosphate buffer, 0.15 M NaCl, saturated CaP soln., pH 7.4, HA	Secondary structure and adsorption mechanism on HA (effect of phosphorylation)
Lu et al., 2013	LRAP	(+P) and (−P)	Murine (recombinant)	SS-NMR (REDOR)	Phosphate buffer, NaCl, saturated CaP soln., HA	Secondary structure and adsorption mechanism on HA (role of phosphorylation, pH, ionic strength)
Tarasevich et al., 2013[c]	LRAP	(+P)	Bovine (recombinant)	SS-NMR (REDOR), SV, NR	Phosphate buffer, NaCl, saturated CaP soln., pH 7.4, HA	Secondary and quaternary structures, adsorption mechanism on HA
Lu et al., 2014	LRAP	(+P)	Murine (recombinant)	SS-NMR (REDOR)	Phosphate buffer, NaCl, saturated CaP soln, pH 7.4, HA and C-HA	Secondary structure and adsorption mechanism on HA or C-HA* (especially in K24-S28 region)
Tarasevich et al., 2015[b]	LRAP	(+P) and (−P)	Murine (recombinant)	SV, SANS, NMR, CD	Phosphate buffer, NaCl, saturated CaP soln	Secondary, tertiary, and quaternary structures

CaP, Calcium Phosphate; CD, Circular Dichroism; C-HA, carbonated Hydroxyapatite; DLS, Dynamic Light Scattering; FTIR, Fourier Transform Infrared Spectroscopy; HA, Hydroxyapatite; His-tag, 12 amino acid peptide tag (MRGSHHHHHHGS-); ITC, Isothermal Titration Calorimetry; NMR, Nuclear Magnetic Resonance; NR, Neutron Reflectivity; REDOR, Rotational Echo DOuble Resonance; SAXS, Small Angle X-ray Scattering; SANS, Small Angle Neutron Scattering; SS-NMR, Solid State Nuclear Magnetic resonance; SV, Sedimentation Velocity; SWE, Single wavelength ellipsometry.

[a] *This study concluded that non-phosphorylated recombinant human LRAP (58 amino acid residues) had mostly a random coil structure, as we have found in the present study using porcine LRAP. However, the addition of calcium ions did not induce a detectable change in the secondary structure of the human isoform. Although this latter finding may appear to be inconsistent with our present FTIR finding that the addition of calcium induces an increase in random coil structure, it should be noted that even in the absence of calcium we found that the major component (~40%) of the secondary structure of LRAP(−P) is random coil. That is, like Le et al. (2006), our findings similarly indicate that LRAP(−P) predominately exhibits a random coil structure in the absence and presence of calcium.*

[b] *The findings of this previous study suggest that addition of calcium ion did not affect the amount of α-helix or β-sheet components of LRAP(+P), which appear to be inconsistent with our present study, where a slight decrease in the amount of α-helix component was observed. In this reported study, experiments were carried out in high ionic strength solutions containing 150 mM NaCl, whereas no added background electrolyte was used in the present study. Ionic strength was clearly shown by these authors to affect the zeta potential of LRAP(+P), with a less negative surface charge seen (at neutral pH) at higher ionic strength. Hence, the reduced negative charge on LRAP(+P) may help explain why added calcium did not affect the LRAP(+P) α-helix structure under high ionic strength conditions.*

[c] *The observed change in LRAP(+P) structure upon HA binding in the present study is consistent with noted previous reports, in which results suggested that amino acid residues K24-K28 of LRAP(+P) molecule had a close to perfect helix structure without HA, but became unfolded to yield a more random structure when adsorbed onto HA.*

addition of calcium ion did not affect the amount of α-helix or β-sheet components of LRAP(+P) (Tarasevich et al., 2015) due to the fact that the latter study was carried out under different experimental conditions (see **Table 4**, footnote b). Once again, our present findings that the secondary structure of LRAP(+P) is affected substantially more by the addition of calcium ions in comparison to LRAP(−P) parallels our previous results using TEM and SAXS, which show that the assembly/aggregation (Le Norcy et al., 2011a) and the folding (Le Norcy et al., 2011b) of LRAP(+P), respectfully, are similarly more affected by the addition of calcium ions in comparison to LRAP(−P).

Our collective findings, which demonstrate that the presence of a single phosphate group at Ser-16 significantly affects the secondary structure of LRAP in solution and upon subsequent interactions with calcium ions, support the basis of our hypothesis that phosphorylation of this highly-conserved amino acid in an equally conserved context for phosphorylation by Golgi casein kinase induces conformational changes that could critically affect amelogenin's capacity to interact with forming calcium phosphate mineral phases. To explore this idea further, we examined the effect of the interaction of LRAP with HA and ACP. When the non-phosphorylated LRAP(−P) was incubated with either HA or ACP, the proportion of β-sheet structures increased from ∼28 to 43% and 54%, respectively (**Table 2**), along with a marked reduction in the random coil components (from ∼40 to 0% and 15%, respectively). As a result of these similar conformational shifts to more rigid structures, following incubation with both mineral phases, amide I peaks for LRAP(−P) in the presence of HA and ACP were also found to be similar (**Figure 2A**), with the same relatively sharp peak maxima at ∼1,620 cm^{-1}. The shape of the spectra, however, were found to differ slightly at ∼1,650 cm^{-1}, most likely due to different amounts of the α-helix component (1,650 cm^{-1}) of LRAP(−P) observed following incubation with HA (∼19%) in comparison to that observed with ACP (0%) (**Table 2**).

In contrast to that observed with LRAP(−P), the phosphorylated LRAP(+P) incubated with mineral particles showed more substantial differences in amide I peak shapes that further depended on the *nature* of the calcium phosphate phase present, i.e., HA or ACP (**Table 2**). When LRAP(+P) was incubated with HA, its secondary structure was found to yield a less rigid conformation, as indicated by a *loss* of α-helix components (from 31% in the absence of HA) and a reduction (from 42 to 20%) in β-sheet structure components, along with an appearance of unstructured random coil (from 0 to 23%), and an increase in 3(10) helix/β-turn components (from 0 to 29%). The observed change in LRAP(+P) structure upon HA incubation is consistent with previous reports (Masica et al., 2011; Tarasevich et al., 2013; see **Table 4**, footnote c). However, in contrast to that seen in the presence of HA, when LRAP(+P) was incubated with ACP, the overall structure became more rigid with a much greater level of β-sheet (from 42 to 61%), while α-helix components remained at a relatively high level (26%), along with an absence of random coil, similar to that found in the absence of added mineral.

It is interesting that LRAP(+P) showed a quite different pattern of interaction with ACP from that seen with HA, while LRAP(−P) showed relatively small differences in secondary structure changes induced by incubation with either HA or ACP. These findings are again consistent with our previous results (Le Norcy et al., 2011a), in which LRAP(−P) and LRAP(+P) were found to exhibit a marked difference in their ability to stabilize forming ACP under conditions that support spontaneous calcium phosphate precipitation. In this previous report, LRAP(−P) did not stabilize ACP but rather guided the formation of aligned bundles of HA crystals, suggesting a weaker interaction between LRAP(−P) and ACP, whereas LRAP(+P) was found to stabilize ACP and prevent its transformation to HA, suggesting a much stronger interaction between LRAP(+P) and ACP. Hence, the observed difference in the reactivity toward ACP between LRAP(−P) and LRAP(+P) appears to be reflected in observed differences in the secondary structure of LRAP caused by the single phosphorylation site.

Based upon our findings on the effect of phosphorylation on the secondary structure of LRAP(−P) and LRAP(+P) in the absence and presence of calcium in solution and upon binding with selected mineral phases, we conclude, as hypothesized, that Ser-16 phosphorylation induces unique secondary structural changes that may enhance the functional capacity of native phosphorylated amelogenin to effectively stabilize the enamel mineral precursor phase, ACP. The biological relevance of our findings is reflected in a recent study (Beniash et al., 2009) that convincingly demonstrates that the initial forming enamel mineral phase in the early secretory stage of amelogenesis to be ACP that subsequently transforms to HA-like enamel mineral crystals. Our present findings provide insight into how phosphorylation can affect the capacity of native (phosphorylated) amelogenins to stabilize this biologically important ACP enamel mineral precursor phase.

AUTHOR CONTRIBUTIONS

HY contributed data acquisition, analysis, interpretation, and drafting of the manuscript. HCM contributed to conception and design, data analysis and interpretation, and the drafting of the manuscript. EB contributed to consultation of the methodology and data analysis, interpretation, and critically revising the manuscript. YY and JS contributed to purifying, and providing LRAP, and also critically revising the manuscript. All authors gave final approval and agree to be accountable for all aspects of the work.

FUNDING

The authors are grateful to NIH and NIDCR for their support of this work through grant R01-DE023091 (HCM).

ACKNOWLEDGMENTS

The authors would like to thank Dr. Aren E. Gerdon for allowing us to carry out selected FTIR measurements at Emmanuel College (Boston, MA) and for his assistance with these analyses.

REFERENCES

Barth, A., and Zscherp, C. (2002). What vibrations tell us about proteins. *Q. Rev. Biophys.* 35, 369–430. doi: 10.1017/S0033583502003815

Beniash, E., Metzler, R. A., Lam, R. S. K., and Gilbert, P. U. P. A. (2009). Transient amorphous calcium phosphate in forming enamel. *J. Struct. Biol.* 166, 133–143. doi: 10.1016/j.jsb.2009.02.001

Beniash, E., Simmer, J. P., and Margolis, H. C. (2005). The effect of recombinant mouse amelogenins on the formation and organization of hydroxyapatite crystals *in vitro*. *J. Struct. Biol.* 149, 182–190. doi: 10.1016/j.jsb.2004.11.001

Beniash, E., Simmer, J. P., and Margolis, H. C. (2012). Structural changes in amelogenin upon self-assembly and mineral interactions. *J. Dent. Res.* 91, 967–972. doi: 10.1177/0022034512457371

Boabaid, F., Gibson, C. W., Kuehl, M. A., Berry, J. E., Snead, M. L., Nociti, F. H. J., et al. (2004). Leucine-rich amelogenin peptide: a candidate signaling molecule during cementogenesis. *J. Periodontol.* 75, 1126–1136. doi: 10.1902/jop.2004.75.8.1126

Bouchard, M., Zurdo, J., Nettleton, E. J., Dobson, C. M., and Robinson, C. V. (2000). Formation of insulin amyloid fibrils followed by FTIR simultaneously with CD and electron microscopy. *Protein Sci.* 9, 1960–1967. doi: 10.1110/ps.9.10.1960

Buchko, G. W., Tarasevich, B. J., Roberts, J., Snead, M. L., and Shaw, W. J. (2010). A solution NMR investigation into the murine amelogenin splice-variant LRAP (leucine-rich amelogenin protein). *Biochim. Biophys. Acta* 1804, 1768–1774. doi: 10.1016/j.bbapap.2010.03.006

Delak, K., Harcup, C., Lakshminarayanan, R., Sun, Z., Fan, Y., Moradian-Oldak, J., et al. (2009). The tooth enamel protein, porcine amelogenin, is an intrinsically disordered protein with an extended molecular configuration in the monomeric form. *Biochemistry* 48, 2272–2281. doi: 10.1021/bi802175a

Deshpande, A. S., Fang, P. A., Simmer, J. P., Margolis, H. C., and Beniash, E. (2010). Amelogenin-collagen interactions regulate calcium phosphate mineralization *in vitro*. *J. Biol. Chem.* 285, 19277–19287. doi: 10.1074/jbc.M109.079939

Diekwisch, T. G. H. (1998). Subunit compartments of secretory stage enamel matrix. *Connect. Tissue Res.* 39, 101–106.

Elangovan, S., Margolis, H. C., Oppenheim, F. G., and Beniash, E. (2007). Conformational changes in salivary proline-rich protein 1 upon adsorption to calcium phosphate crystals. *Langmuir* 23, 11200–11205. doi: 10.1021/la7013978

Fang, P. A., Margolis, H. C., Conway, J. F., Simmer, J. P., and Beniash, E. (2013). CryoTEM study of effects of phosphorylation on the hierarchical assembly of porcine amelogenin and its regulation of mineralization *in vitro*. *J. Struct. Biol.* 183, 250–257. doi: 10.1016/j.jsb.2013.05.011

Fincham, A. G., Moradian-Oldak, J., and Simmer, J. P. (1999). The structural biology of the developing dental enamel matrix. *J. Struct. Biol.* 126, 270–299.

Goto, Y., Kogure, E., Takagi, T., Aimoto, S., and Aoba, T. (1993). Molecular conformation of porcine amelogenin in solution: three folding units at the N-terminal, central, and C-terminal regions. *J. Biochem.* 113, 55–60.

Habelitz, S., Denbesten, P. K., Marshall, S. J., Marshall, G. W., and Li, W. (2006). Self-assembly and effect on crystal growth of the leucine-rich amelogenin peptide. *Eur. J. Oral Sci.* 114, 315–319. doi: 10.1111/j.1600-0722.2006.00312.x

Jackson, M., and Mantsch, H. H. (1995). The use and misuse of FTIR spectroscopy in the determination of protein structure. *Crit. Rev. Biochem. Mol. Biol.* 30, 95–120.

Johnston, N., and Krimm, S. (1971). An infrared study of unordered poly-L-proline in $CaCl_2$ solutions. *Biopolymers* 10, 2597–2605.

Krimm, S., and Bandekar, J. (1986). Vibrational spectroscopy and conformation of peptides, polypeptides, and proteins. *J. Adv. Protein Chem.* 38, 181–364.

Kubelka, J., and Keiderling, T. A. (2001). Differentiation of β-sheet-forming structures: Ab initio-based simulations of IR absorption and vibrational CD for model peptide and protein β-sheets. *J. Am. Chem. Soc.* 123, 12048–12058. doi: 10.1021/ja0116627

Kwak, S.-Y., Green, S., Wiedemann-Bidlack, F. B., Beniash, E., Yamakoshi, Y., Simmer, J. P., et al. (2011). Regulation of calcium phosphate formation by amelogenins under physiological conditions. *Eur. J. Oral Sci.* 119, 103–111. doi: 10.1111/j.1600-0722.2011.00911.x

Kwak, S.-Y., Kim, S., Yamakoshi, Y., Simmer, J. P., Beniash, E., and Margolis, H. C. (2014). Regulation of calcium phosphate formation by native amelogenins *in vitro*. *Connect. Tissue Res.* 55, 21–24. doi: 10.3109/03008207.2014.923853

Kwak, S.-Y., Wiedemann-Bidlack, F. B., Beniash, E., Yamakoshi, Y., Simmer, J. P., Litman, A., et al. (2009). Role of 20-kDa amelogenin (P148) phosphorylation in calcium phosphate formation *in vitro*. *J. Biol. Chem.* 284, 18972–18979. doi: 10.1074/jbc.M109.020370

Kwak, S.-Y., Yamakoshi, Y., Simmer, J. P., and Margolis, H. C. (2016). MMP20 proteolysis of native amelogenin regulates mineralization *in vitro*. *J. Dent. Res.* 95, 1511–1517. doi: 10.1177/0022034516662814

Lakshminarayanan, R., Bromley, K. M., Lei, Y. P., Snead, M. L., and Moradian-Oldak, J. (2010). Perturbed amelogenin secondary structure leads to uncontrolled aggregation in amelogenesis imperfecta mutant proteins. *J. Biol. Chem.* 285, 40593–40603. doi: 10.1074/jbc.M110.131136

Lakshminarayanan, R., Fan, D., Du, C., and Moradian-Oldak, J. (2007). The role of secondary structure in the entropically driven amelogenin self-assembly. *Biophys. J.* 93, 3664–3674. doi: 10.1529/biophysj.107.113936

Lakshminarayanan, R., Yoon, I., Hegde, B. G., Fan, D., Du, C., and Moradian-Oldak, J. (2009). Analysis of secondary structure and self-assembly of amelogenin by variable temperature circular dichroism and isothermal titration calorimetry. *Proteins* 76, 560–569. doi: 10.1002/prot.22369

Le Norcy, E., Kwak, S. Y., Allaire, M., Fratzl, P., Yamakoshi, Y., Simmer, J. P., et al. (2011b). Effect of phosphorylation on the interaction of calcium with leucine-rich amelogenin peptide. *Eur. J. Oral Sci.* 119, 97–102. doi: 10.1111/j.1600-0722.2011.00900.x

Le Norcy, E., Wiedemann-Bidlack, F. B., Beniash, E., Yamakoshi, Y., Simmer, J. P., and Margolis, H. C. (2011a). Leucine-rich amelogenin peptides regulate mineralization *in vitro*. *J. Dent. Res.* 90, 1091–1097. doi: 10.1177/0022034511411301

Le, T. Q., Gochin, M., Featherstone, J. D. B., Li, W., and Denbesten, P. K. (2006). Comparative calcium binding of leucine-rich amelogenin peptide and full-length amelogenin. *Eur. J. Oral Sci.* 114, 320–326. doi: 10.1111/j.1600-0722.2006.00313.x

Lu, J.-X., Burton, S. D., Xu, Y. S., Buchko, G. W., and Shaw, W. J. (2014). The flexible structure of the K24S28 region of Leucine-Rich Amelogenin Protein (LRAP) bound to apatites as a function of surface type, calcium, mutation, and ionic strength. *Front. Physiol.* 5:254. doi: 10.3389/fphys.2014.00254

Lu, J.-X., Xu, Y. S., and Shaw, W. J. (2013). Phosphorylation and ionic strength alter the LRAP − HAP interface in the N-terminus. *Biochemistry* 52, 2196–2205. doi: 10.1021/bi400071a

Margolis, H. C., Beniash, E., and Fowler, C. E. (2006). Role of macromolecular assembly of enamel matrix proteins in enamel formation. *J. Dent. Res.* 85, 775–793. doi: 10.1177/154405910608500902

Margolis, H. C., Kwak, S.-Y., and Yamazaki, H. (2014). Role of mineralization inhibitors in the regulation of hard tissue biomineralization: relevance to initial enamel formation and maturation. *Front. Physiol.* 5:339. doi: 10.3389/fphys.2014.00339

Masica, D. L., Gray, J. J., and Shaw, W. J. (2011). Partial high-resolution structure of phosphorylated and non-phosphorylated leucine-rich amelogenin protein adsorbed to hydroxyapatite. *J. Phys. Chem. C Nanomater. Interfaces* 115, 13775–13785. doi: 10.1021/jp202965h

Matsushima, N., Izumi, Y., and Aoba, T. (1998). Small-angle X-ray scattering and computer-aided molecular modeling studies of 20 kDa fragment of porcine amelogenin: does amelogenin adopt an elongated bundle structure? *J. Biochem.* 123, 150–156. doi: 10.1093/oxfordjournals.jbchem.a021902

Nagano, T., Kakegawa, A., Yamakoshi, Y., Tsuchiya, S., Hu, J. C.-C., Gomi, K., et al. (2009). Mmp-20 and Klk4 cleavage site preferences for amelogenin sequences. *J. Dent. Res.* 88, 823–828. doi: 10.1177/0022034509342694

Nanci, A. (2013). "Enamel: composition, formation, and structure," in Ten *Cate's Oral Histology: Development, Structure, and Function, 8th Edn*, (St. Louis, MI: Elsevier Mosby), 122–164.

Renugopalakrishnan, V., Strawich, E. S., Horowitz, P. M., and Glimcher, M. J. (1986). Studies of the secondary structures of amelogenin from bovine tooth enamel. *Biochemistry* 25, 4879–4887. doi: 10.1021/bi00365a023

Roach, P., Farrar, D., and Perry, C. C. (2005). Interpretation of protein adsorption: surface-induced conformational changes. *J. Am. Chem. Soc.* 127, 8168–8173. doi: 10.1021/ja042898o

Shaw, W. J., and Ferris, K. (2008). Structure, orientation, and dynamics of the C-terminal hexapeptide of LRAP determined using solid-state NMR. *J. Phys. Chem. B* 112, 16975–16981. doi: 10.1021/jp808012g

Shaw, W. J., Campbell, A. A., Paine, M. L., and Snead, M. L. (2004). The COOH terminus of the amelogenin, LRAP, is oriented next to the hydroxyapatite surface. *J. Biol. Chem.* 279, 40263–40266. doi: 10.1074/jbc.C400322200

Shaw, W. J., Ferris, K., Tarasevich, B., and Larson, J. L. (2008). The structure and orientation of the C-terminus of LRAP. *Biophys. J.* 94, 3247–3257. doi: 10.1529/biophysj.107.119636

Sogah, D. Y., Perle-Treves, D., Voyer, N., and DeGrado, W. F. (1994). Design and synthesis of polytripeptide (LeuGlnPro)n base on upon the matrix protein amelogenin. *Macromol. Symp.* 88, 149–163.

Surewicz, W. K., Mantsch, H. H., and Chapman, D. (1993). Determination of protein secondary structure by Fourier transform infrared spectroscopy: a critical assessment. *Biochemistry* 32, 389–394.

Susi, H., and Byler, D. M. (1983). Protein structure by fourier transform infrared spectroscopy: second derivative spectra. *Biochem. Biophys. Res. Commun.* 115, 391–397.

Tarasevich, B. J., Lea, S., and Shaw, W. J. (2010). The Leucine Rich Amelogenin Protein (LRAP) adsorbs as monomers or dimers onto surfaces. *J. Struct. Biol.* 169, 266–276. doi: 10.1016/j.jsb.2009.10.007

Tarasevich, B. J., Perez-Salas, U., Masica, D. L., Philo, J., Kienzle, P., Krueger, S., et al. (2013). Neutron reflectometry studies of the adsorbed structure of the amelogenin, LRAP. *J. Phys. Chem. B* 117, 3098−3109. doi: 10.1021/jp311936j

Tarasevich, B. J., Philo, J. S., Karl, N., Krueger, S., Buchko, G. W., Lin, G., et al. (2015). The Leucine-Rich Amelogenin Protein (LRAP) is primarily monomeric and unstructured in physiological solution. *J. Struct. Biol.* 190, 81–91. doi: 10.1016/j.jsb.2014.10.007

Vass, E., Hollosi, M., Besson, F., and Buchet, R. (2003). Vibrational spectroscopic detection of beta-and gamma-turns in synthetic and natural peptides and proteins. *Chem. Rev.* 103, 1917–1954. doi: 10.1021/cr000100n

Veis, A., Tompkins, K., Alvares, K., Wei, K., Wang, L., Wang, X. S., et al. (2000). Specific amelogenin gene splice products have signaling effects on cells in culture and in implants *in vivo*. *J. Biol. Chem.* 275, 41263–41272. doi: 10.1074/jbc.M002308200

Wang, Y., Petty, S., Trojanowski, A., Knee, K., Goulet, D., Mukerji, I., et al. (2010). Formation of amyloid fibrils *in vitro* from partially unfolded intermediates of human {gamma}C-crystallin. *Invest. Ophthalmol. Vis. Sci.* 51, 672–678. doi: 10.1167/iovs.09-3987

Warotayanont, R., Frenkel, B., Snead, M. L., and Zhou, Y. (2009). Leucine-rich amelogenin peptide induces osteogenesis by activation of the Wnt pathway. *Biochem. Biophys. Res. Commun.* 387, 558–563. doi: 10.1016/j.bbrc.2009.07.058

Warotayanont, R., Zhu, D., Snead, M. L., and Zhou, Y. (2008). Leucine-rich amelogenin peptide induces osteogenesis in mouse embryonic stem cells. *Biochem. Biophys. Res. Commun.* 367, 1–6. doi: 10.1016/j.bbrc.2007.12.048

Wellner, N., Belton, P. S., and Tatham, S. (1996). Fourier transform IR spectroscopic study of hydration-induced structure changes in the solid state of ω-gliadins. *Biochem. J.* 319, 741–747.

Wen, X., Cawthorn, W. P., MacDougald, O. A., Stupp, S. I., Snead, M. L., and Zhou, Y. (2011). The influence of leucine-rich amelogenin peptide on MSC fate by inducing Wnt10b expression. *Biomaterials* 32, 6478–6486. doi: 10.1016/j.biomaterials.2011.05.045

Wiedemann-Bidlack, F. B., Beniash, E., Yamakoshi, Y., Simmer, J. P., and Margolis, H. C. (2007). pH triggered self-assembly of native and recombinant amelogenins under physiological pH and temperature *in vitro*. *J. Struct. Biol.* 160, 57–69. doi: 10.1016/j.jsb.2007.06.007

Wiedemann-Bidlack, F. B., Kwak, S.-Y., Beniash, E., Yamakoshi, Y., Simmer, J. P., and Margolis, H. C. (2011). Effects of phosphorylation on the self-assembly of native full-length porcine amelogenin and its regulation of calcium phosphate formation *in vitro*. *J. Struct. Biol.* 173, 250–260. doi: 10.1016/j.jsb.2010.11.006

Xia, Y., Ren, A., and Pugach, M. K. (2016). Truncated amelogenin and LRAP transgenes improve Amelx null mouse enamel. *Matrix Biol.* 52–54, 198–206. doi: 10.1016/j.matbio.2015.11.005

Yang, X., Wang, L., Qin, Y., Sun, Z., Henneman, Z. J., Moradian-Oldak, J., et al. (2010). How amelogenin orchestrates the organization of hierarchical elongated microstructures of apatite. *J. Phys. Chem. B* 114, 2293–2300. doi: 10.1021/jp910219s

Yuan, Z. A., Collier, P. M., Rosenbloom, J., and Gibson, C. W. (1996). Analysis of amelogenin mRNA during bovine tooth development. *Arch. Oral Biol.* 41, 205–213.

Zhang, X., Ramirez, B. E., Liao, X., and Diekwisch, T. G. H. (2011). Amelogenin supramolecular assembly in nanospheres defined by a complex helix-coil-PPII helix 3D-structure. *PLoS ONE* 6:e24952. doi: 10.1371/journal.pone.0024952

Conflict of Interest Statement: The authors declare that the research was conducted in the absence of any commercial or financial relationships that could be construed as a potential conflict of interest.

Copyright © 2017 Yamazaki, Beniash, Yamakoshi, Simmer and Margolis. This is an open-access article distributed under the terms of the Creative Commons Attribution License (CC BY). The use, distribution or reproduction in other forums is permitted, provided the original author(s) or licensor are credited and that the original publication in this journal is cited, in accordance with accepted academic practice. No use, distribution or reproduction is permitted which does not comply with these terms.

frontiers in Physiology

METHODS
published: 16 June 2017
doi: 10.3389/fphys.2017.00424

Preparative SDS PAGE as an Alternative to His-Tag Purification of Recombinant Amelogenin

Claire M. Gabe, Steven J. Brookes and Jennifer Kirkham*

Division of Oral Biology, School of Dentistry, University of Leeds, Leeds, United Kingdom

Recombinant protein technology provides an invaluable source of proteins for use in structure-function studies, as immunogens, and in the development of therapeutics. Recombinant proteins are typically engineered with "tags" that allow the protein to be purified from crude host cell extracts using affinity based chromatography techniques. Amelogenin is the principal component of the developing enamel matrix and a frequent focus for biomineralization researchers. Several groups have reported the successful production of recombinant amelogenins but the production of recombinant amelogenin free of any tags, and at single band purity on silver stained SDS PAGE is technically challenging. This is important, as rigorous structure-function research frequently demands a high degree of protein purity and fidelity of protein sequence. Our aim was to generate His-tagged recombinant amelogenin at single band purity on silver stained SDS PAGE for use in functionality studies after His-tag cleavage. An acetic acid extraction technique (previously reported to produce recombinant amelogenin at 95% purity directly from *E. coli*) followed by repeated rounds of nickel column affinity chromatography, failed to generate recombinant amelogenin at single band purity. This was because following an initial round of nickel column affinity chromatography, subsequent cleavage of the His-tag was not 100% efficient. A second round of nickel column affinity chromatography, used in attempts to separate the cleaved His-tag free recombinant from uncleaved His-tagged contaminants, was still unsatisfactory as cleaved recombinant amelogenin exhibited significant affinity for the nickel column. To solve this problem, we used preparative SDS PAGE to successfully purify cleaved recombinant amelogenins to single band purity on silver stained SDS PAGE. The resolving power of preparative SDS PAGE was such that His-tag based purification of recombinant amelogenin becomes redundant. We suggest that acetic acid extraction of recombinant amelogenin and subsequent purification using preparative SDS PAGE provides a simple route to highly purified His-tag free amelogenin for use in structure-function experiments and beyond.

Keywords: recombinant amelogenin, His-tag, nickel column chromatography, protein purification, preparative SDS PAGE

OPEN ACCESS

Edited by:
Petros Papagerakis, University of Michigan, United States

Reviewed by:
Yiping Chen, Tulane University, United States
Thomas G. H. Diekwisch, Texas A&M University Baylor College of Dentistry, United States
Bernhard Ganss, University of Toronto, Canada

****Correspondence:***
Steven J. Brookes
s.j.brookes@leeds.ac.uk

Specialty section:
This article was submitted to Craniofacial Biology and Dental Research, a section of the journal Frontiers in Physiology

Received: *07 April 2017*
Accepted: *01 June 2017*
Published: *16 June 2017*

Citation:
Gabe CM, Brookes SJ and Kirkham J (2017) Preparative SDS PAGE as an Alternative to His-Tag Purification of Recombinant Amelogenin. Front. Physiol. 8:424. doi: 10.3389/fphys.2017.00424

INTRODUCTION

Amelogenesis involves the incremental secretion of an extracellular protein matrix by ameloblasts. Amelogenin, present as a range of related molecules generated through extracellular proteolysis of several alternatively spliced gene products, comprises ∼90% of the total extracellular protein matrix and is essential for normal enamel biomineralisation. Amelogenin mutations can lead to amelogenesis imperfecta (AI) in humans (Lagerstrom et al., 1991; Aldred et al., 1992; Lench and Winter, 1995; Collier et al., 1997; Kindelan et al., 2000; Hart et al., 2002; Kim et al., 2004; Wright et al., 2009) and mouse models (Barron et al., 2010) and amelogenin null mice fail to produce enamel (Gibson et al., 2001; Wright et al., 2009; Smith et al., 2016). However, the exact function of amelogenin remains unclear and studies are ongoing to elucidate amelogenin function and the etiologies that underpin AI when the amelogenin gene is mutated.

Our own interest is with the effect of a mouse amelogenin mutation (p.Y64H) on amelogenin aggregation/assembly and ameloblast secretory trafficking. Wild-type (WT) amelogenin begins to self-assemble during transit through the ameloblast secretory pathway (Brookes et al., 2006). On secretion, it forms "nanospheres" of ∼25–50 nm in diameter in the developing enamel (Fincham et al., 1995). Ameloblasts are secretory cells that are adapted to handle the large amount of amelogenin transiting through the rough endoplasmic reticulum (ER) and Golgi apparatus (Warshawsky, 1968). This is achieved by utilizing elements of the unfolded protein response (UPR) (Tsuchiya et al., 2008) to maintain ameloblast ER proteostasis; as commonly seen in other secretory cells (Moore and Hollien, 2012). The UPR aids cells to cope with a large secretory load by increasing ER volume and protein folding capacity and increasing the cell's ability to identify and handle misfolded proteins via ER associated protein degradation (Travers et al., 2000). This is important, as up to 30% of proteins destined for secretion can mis-fold spontaneously (Schubert et al., 2000) leading to pathological intracellular protein retention and severe ER stress (Ozcan and Tabas, 2012). Under circumstances when ER stress is abnormally high and prolonged, the UPR switches from a pro-survival mode to a pro-apoptotic mode which leads to cell death (Rutkowski and Kaufman, 2007). Our previous work has shown that the $Amelx^{p.(Y64H)}$ mutation promotes intracellular amelogenin retention, stalls the secretory pathway, and triggers the UPR to switch into pro-apoptotic mode resulting in ameloblast death, thus classifying this case of AI as a conformational disease (Brookes et al., 2014). Our current work seeks to investigate the effect of the p.Y64H mutation on amelogenin-amelogenin interactions. The availability of highly purified WT and p.Y64H amelogenin is therefore essential for use in structure-function studies.

It is possible to purify amelogenin from developing enamel itself but this requires a ready and plentiful supply of secretory stage enamel and expertise in protein purification to isolate a single amelogenin species from the plethora of discrete but related amelogenin molecules present in the tissue that are derived by extracellular processing of several alternatively spliced isoforms (Brookes et al., 1995). This is challenging but the advantage of purifying native amelogenin from tissue over producing recombinant protein in *E. coli* is that the protein will be phosphorylated at serine 16 via translational modification *in vivo* (Takagi et al., 1984; Fincham and Moradian-Oldak, 1993; Fincham et al., 1994) and this is believed to be important to its function (Kwak et al., 2009; Wiedemann-Bidlack et al., 2011). Typically, native enamel proteins are purified from porcine developing enamel as porcine developing teeth can be obtained as a by-product of the meat industry (Aoba et al., 1987; Limeback, 1987). Compared to rodent incisors, each porcine tooth provides a relatively large amount of starting material as the enamel thickness can be up to ten times that of rodent developing tissue. However, pigs must be obtained at a specific age to ensure that developing teeth are in the secretory phase and not all teeth will be undergoing amelogenesis at the same time. The main models for studying amelogenesis, the roles of specific proteins components and any effects of specific mutations are the mouse and rat. Rodents have the advantage that their incisors are continually erupting and the required secretory stage enamel is present in weaned animals of any age. However, the yield of secretory stage enamel per animal is so small that very few published studies have used purified rodent amelogenins.

The need to understand AI pathobiology associated with specific mutations effectively precludes the use of porcine teeth. In addition, as we reported previously in the case of our p.Y64H amelogenin mouse model, there are cases where the mutation results in failure to secrete the affected protein and this in turn prevents our purifying the protein from the enamel itself. The challenge of purifying amelogenin from whole cell extracts would be significant and the only viable source of mutated amelogenin (or for that matter WT rodent amelogenin) is via recombinant technology.

Recombinant proteins are widely used as therapeutic agents and as tools to study structure-function relationships, protein interactions with other molecules and as antigens for antibody production. *E. coli* based expression systems are the most widely used methodology for producing recombinant amelogenin even though post translational phosphorylation of serine 16 will be absent. Baculo virus (Taylor et al., 2006; Xu et al., 2006) and *Leishmania* (Yadegari et al., 2015) expression systems, having the potential to carry out post translational phosphorylation have been used to produce recombinant amelogenin, but as yet do not appear to have been widely adopted perhaps due to uncertainty as to whether the amelogenin was phosphorylated. In contrast, a yeast based expression system has been reported to generate correctly phosphorylated recombinant amelogenin (Cheng et al., 2012) but again has not been widely used. Regardless of the expression system used, the recombinant amelogenin will need to be purified and freed from host cell proteins, amelogenin degradation products, and other contaminants arising from the growth medium. Early reports describing the preparation of recombinant amelogenin used ammonium sulfate precipitation followed by repeated rounds of reverse phase chromatography (Simmer et al., 1994) or ammonium sulfate precipitation followed by cation exchange chromatography and reverse phase chromatography (Ryu et al., 1999) to effectively purify the final

product. However, it is now generally more common to purify recombinant proteins by engineering the inclusion of either an N or C-terminal tag comprising of a poly histidine sequence ("His-tag") or fused to glutathione S-transferase (GST) (Hochuli et al., 1988; Smith and Johnson, 1988). His-tags and GST have a high affinity for immobilized nickel ions and glutathione respectively which allows the recombinant proteins to be purified using affinity column chromatography. Tags typically include a proteolytic cleavage site which allows them to be removed following elution from the column.

In our hands, both His-tagged WT and p.Y64H amelogenins are expressed at acceptable levels in *E. coli* but after nickel column affinity purification they also invariably contain background contaminants especially on silver stained SDS PAGE; an issue also noted by others (Xu et al., 2006). In agreement with Taylor et al. (2006) we also find that the His-tag cleavage is not 100% efficient and our final cleaved product is a mixture of tagged and untagged recombinant proteins. Removal of the His-tag is desirable for functional studies; especially those focusing on intermolecular interactions occurring during amelogenesis in the enamel matrix. That said, the presence of a His-tag did not greatly alter the biological activity of recombinant amelogenin on gene expression in osteoblasts and periodontal ligament fibroblasts compared to extracts of native amelogenin from developing enamel (Svensson et al., 2006; Cheng et al., 2012). Certainly, for our intended applications, the removal of the His-tag is essential to generate unambiguous data in protein-protein interaction studies. Typically, contaminating uncleaved His-tagged protein is removed by a second round of nickel column chromatography. However, due to the histidine content of amelogenin (including a tri-histidine motif; Snead et al., 1985), even untagged amelogenin has a relatively high affinity for nickel, confounding nickel column separation of His-tagged from non-tagged amelogenins.

The aim of the present work was to develop an adjunctive purification step to remove background contaminants from recombinant amelogenins, including uncleaved His-tagged amelogenin, generating amelogenins with a high degree of purity. The results of this work lead us to conclude that we can purify recombinant amelogenin to a high level of purity from *E. coli* without the need for a His-tag using a previously reported acetic acid extraction technique and a single round of preparative SDS PAGE. This provides a faster means of obtaining purified recombinant amelogenin free of any residual His-tag remnants for use in structure-function studies and beyond.

MATERIALS AND METHODS

Expression and Extraction of Recombinant Amelogenin

Wild-type amelogenin was expressed using a pET28 expression vector (Novagen, Merck Chemicals Ltd.) modified with a HRV 3C protease site in Rosetta DE3 *E. coli* cells (Novagen). Once the cells reached an optical density of 0.6–1.2 recombinant protein expression was induced by adding isopropyl β-D-1-thiogalactopyranoside (IPTG). Induction of expression was confirmed by analytical SDS PAGE. After shaking overnight incubation at 37°C, the cells were harvested by centrifugation and amelogenin-enriched fractions obtained by extraction in acetic acid as previously reported (Svensson Bonde and Bulow, 2012). In brief, 1 g of pelleted cells were washed by resuspending in 30 mL of 150 mM NaCl. After centrifugation the pellet was resuspended in 30 mL 3% acetic acid, sonicated and heated at 75°C for 20 min. Insoluble material was pelleted by centrifugation and the acetic acid extracts were lyophilized. Lyophilized extracts were dissolved in a minimum volume of 125 mM formic acid and desalted against 125 mM formic acid using size exclusion chromatography (HiPrep 26/10 column, GE Healthcare). The volatile formic acid was then removed by lyophilization.

Affinity Nickel Column Purification of His-Tagged Recombinant Amelogenins Extracted Using Acetic Acid

Lyophilized crude extracts of recombinant amelogenin were dissolved in a minimum volume of nickel column binding buffer (20 mM imidazole, 4 M urea, 50 mM Tris, 400 mM NaCl, pH = 7.6), loaded on to a nickel affinity chromatography column (5 mL HisTrap FF, GE Health Care) up to a maximum protein load of 40 mg and eluted at a flow rate of 4 mL/min. Unbound proteins (column flow through) were collected. Bound recombinant amelogenin was eluted by increasing the imidazole concentration to 200 mM. The recombinant amelogenin was then buffer exchanged into 125 mM formic acid using size exclusion chromatography (HiPrep 26/10 column, GE Healthcare) and the fractions containing recombinant amelogenin collected and lyophilized. Fractions were analyzed by analytical SDS PAGE and anti-amelogenin Western blotting using rabbit IgGs raised against a peptide corresponding to the amelogenin hydrophilic C-terminal (Brookes et al., 2011) as described in the Section entitled Analytical SDS PAGE and Western Blotting.

His-Tag Cleavage

The lyophilized recombinant amelogenin, prepared as described above, was dissolved at 2 mg/mL in either 50 mM Tris-HCl, pH = 8 or 0.1 M Na_2CO_3, pH = 9 (the Na_2CO_3 buffer system was trialed in an attempt to improve cleavage efficiency but also allowed the cleavage products to be directly labeled with fluorescein at this point if required). The His-tag was removed enzymatically by adding recombinant restriction grade protease (HRV3C, Merck) at a concentration of 3 μL enzyme solution per mg recombinant protein. Cleavage was carried out over 20 h at 4°C. The resulting cleavage reaction mixture comprising cleaved recombinant, any uncleaved recombinant, free His-tag and other contaminants was finally buffer-exchanged into nickel column binding buffer by size exclusion chromatography ready for a second round of nickel affinity column chromatography.

Second Round Nickel Column Purification to Remove Uncleaved Recombinants, Free His-Tag, and Cleavage Enzyme

A second round of His-tag cleavage was employed to remove cleaved His-tag and other contaminants present in the cleavage reaction mixture including any uncleaved recombinant. Cleavage

products in binding buffer were loaded on to the nickel affinity column as described in the Section entitled Affinity Nickel Column Purification of His-Tagged Recombinant Amelogenins Extracted Using Acetic Acid. Unbound proteins (expected to contain the cleaved recombinant amelogenin) were collected in the column flow through. Bound proteins (expected to contain any uncleaved recombinant amelogenin, His-tag, and His-tagged HRV3C) were eluted using a stepped imidazole gradient (50, 60, 70, 90, 205, and 400 mM) in order to optimize the separation. Fractions were analyzed by analytical SDS PAGE as described in the Section entitled Analytical SDS PAGE and Western Blotting.

Analytical SDS PAGE and Western Blotting

Analytical SDS PAGE was carried out based upon the method of Laemmli (1970) except 20% v/v glycerol was included in the resolving gel. Proteins were separated using a 12% resolving gel at pH 8.8 and a 4% stacking gel at pH 6.8 using Mini-PROTEAN III or Criterion Cell electrophoresis systems (Bio-Rad laboratories Ltd., Hertfordshire, UK). Samples were dissolved in non-reducing SDS PAGE loading buffer (26 mM Tris-HCl pH 6.8, 10% v/v glycerol, 0.35% w/v SDS, and 0.01% w/v bromophenol blue). Prior to SDS PAGE samples were heated at 90°C for 1.5 min and run at a constant 200 V until the bromophenol blue reached the bottom of the gel. Loading for each gel was optimized in each case by running trial gels.

Following electrophoresis, proteins were detected using Coomassie Blue (Expedeon Ltd., Cambridgeshire, UK) or silver staining (ThermoFischer Scientific, Leicestershire, UK) or were transferred to nitrocellulose membranes (Bio-Rad, Ltd., Hertfordshire, UK) for Western blot analysis. After blocking and washing, the membrane was incubated with primary antibody (rabbit anti-amelogenin teleopeptide; Brookes et al., 2006, diluted 1:2,000 in blocking buffer) for 95 min, washed and then incubated for 90 min with secondary antibody (goat anti-rabbit conjugated to horse-radish peroxidase diluted 1:3,000 in blocking buffer). Immunoreactive protein was visualized using DAB with metal enhancer, (Sigma-Aldrich, Dorsetshire, UK) according to the manufacturer's instructions.

Alternative Purification Methodology Using Preparative SDS PAGE

The cleaved recombinant amelogenin fractions produced by the second round nickel column purification described above still contained traces of uncleaved protein and other minor contaminants when examined using analytical SDS PAGE. To eliminate this problem both rounds of affinity column purification were replaced by preparative SDS PAGE. Desalted and lyophilized cleaved recombinant amelogenin was dissolved in non-reducing SDS PAGE loading buffer (as described in the Section entitled Analytical SDS PAGE and Western Blotting) at a concentration of 5–7mg/1.5 mL. Preparative electrophoresis was carried out using a Model 491 Prep Cell (Bio-Rad Ltd., Hertfordshire, UK). A 12% resolving gel was cast in the 28 mm internal diameter gel tube to a height of 9.5 cm with a 2 cm 4% stacking gel. The gel was run at a constant 12 W power at room temperature using the circulating cooling pump as recommended by the manufacturer. Once the tracker dye reached the bottom of the gel, 2.5 mL fractions were collected at a flow rate of 0.8 mL/min. Fractions of interest were identified by subjecting every third fraction to analytical SDS PAGE. All fractions of interest were then subjected to analytical SDS PAGE to accurately determine any fractions containing cleaved recombinant amelogenin at single band purity on silver staining.

The methodologies described above are summarized in **Figure 1**.

RESULTS

Expression and Extraction of Recombinant Amelogenin

Total protein was extracted from *E. coli* both immediately after the addition of IPTG and 1 h post induction to determine the presence of any induced recombinant protein expression using analytical SDS PAGE and Coomassie Blue staining (**Figure 2**). One hour after IPTG induction, the results clearly demonstrated an additional protein band at 27 kDa, corresponding to the molecular weight of recombinant amelogenin against a

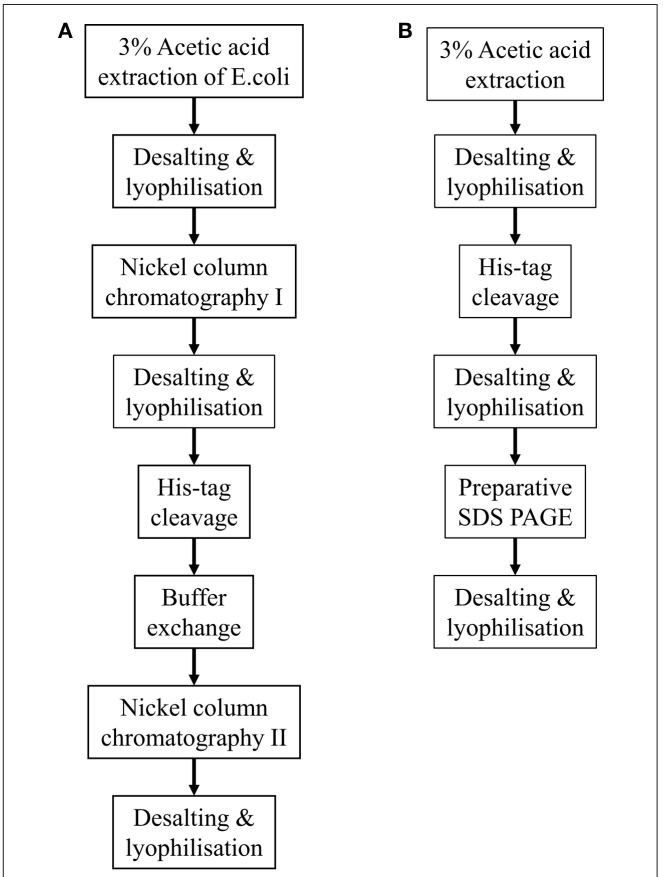

FIGURE 1 | Flow diagrams summarizing the two methodologies described for purifying His-tagged recombinant amelogenin. **(A)** Purification of recombinant His-tagged amelogenin using conventional His-tag column purification. **(B)** Alternative methodology described here using preparative SDS PAGE in place of His-tag column chromatography to purify recombinant His-tagged amelogenin.

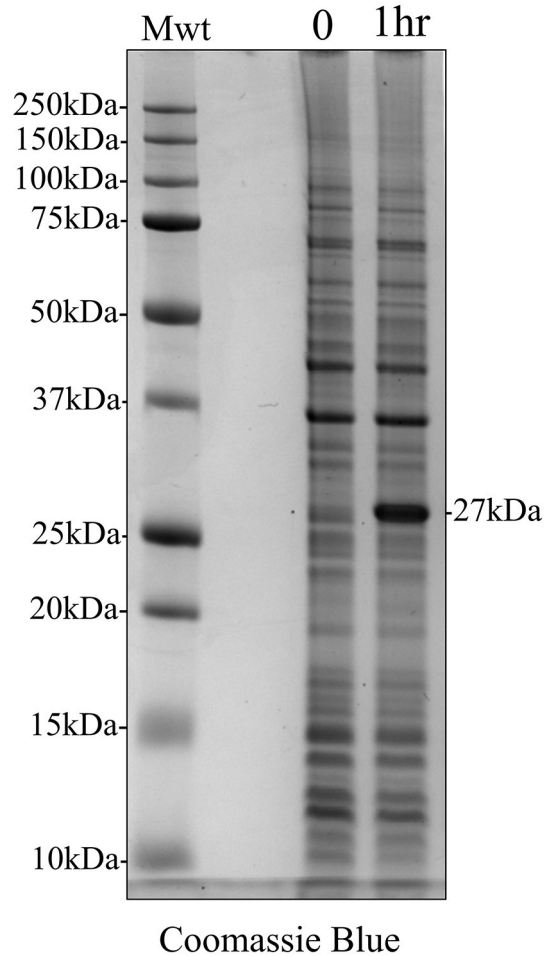

FIGURE 2 | Coomassie Blue stained analytical SDS PAGE showing IPTG induction of recombinant amelogenin expression in *E. coli*. *E. coli* were extracted at the time of induction (0) and 1 h post-induction (1 h). IPTG induced the expression of a 27 kDa protein corresponding to the expected molecular weight of recombinant amelogenin.

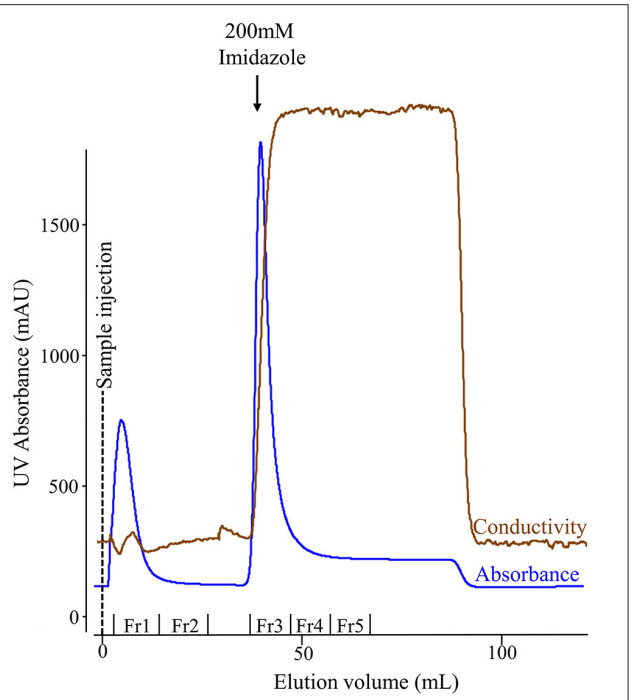

FIGURE 3 | Nickel column chromatography of the soluble protein extracted from *E. coli* using 3% acetic acid. The chromatogram shows fractions comprising proteins that failed to bind the column in 20 mM imidazole (flow-through: fractions 1–2) and bound proteins eluted when the imidazole concentration was increased from 20 to 200 mM (fractions 3–5). The conductivity trace indicates the increase in imidazole concentration in the buffer flowing through the column.

background of multiple components derived from the expression system.

Acetic Acid Extraction of His-Tagged Recombinant Amelogenin and Affinity Nickel Column Purification

We used affinity chromatography to purify His-tagged recombinant amelogenin following acetic acid extraction of the crude bacterial extracts (**Figure 3**). Fractions 1–2 (**Figure 3**, Fr1, Fr2) contained the column flow-through i.e., material that did not bind to the nickel column in 20 mM imidazole loading buffer. Fractions 3–5 (**Figure 3**, Fr3–Fr5) contained the column bound material eluted by 200 mM imidazole, with the bulk of the material eluting in fraction 3. The fractions were then characterized by analytical SDS PAGE (**Figure 4A**) and Western blotting using anti-amelogenin antibodies (**Figure 4B**). Analytical SDS PAGE showed that the original crude bacterial acetic acid extract was clearly enriched with the putative recombinant amelogenin migrating with a relative molecular weight of ∼27 kDa but also contained a number of contaminating proteins migrating between 10 and 75 kDa. The majority of these contaminants were not bound by the nickel column and eluted in the flow through (**Figure 4A**, fractions 1–2). Fractions 3–5, eluted from the column in 200 mM imidazole, contained the putative recombinant amelogenin. The level of contaminants in the putative recombinant amelogenin fraction was reduced after nickel affinity chromatography but some contamination was still evident at this loading. The corresponding anti-amelogenin Western blot confirmed the identity of the 27 kDa protein to be recombinant amelogenin. Anti-amelogenin-immunoreactive protein was also evident at above 27 kDa, as a smear centered on ∼53 kDa. This corresponds to the formation and re-equilibration of amelogenin complexes (predominantly dimers) that can exist during SDS PAGE of amelogenin (Limeback and Simic, 1990).

His-Tag Cleavage and Repeated Nickel Column Purification to Remove Uncleaved Recombinants, Freed His-Tag, and Cleavage Enzyme

We attempted to remove the His-tag from recombinant amelogenin via proteolytic cleavage and then carried out a second round of affinity chromatography to remove any uncleaved

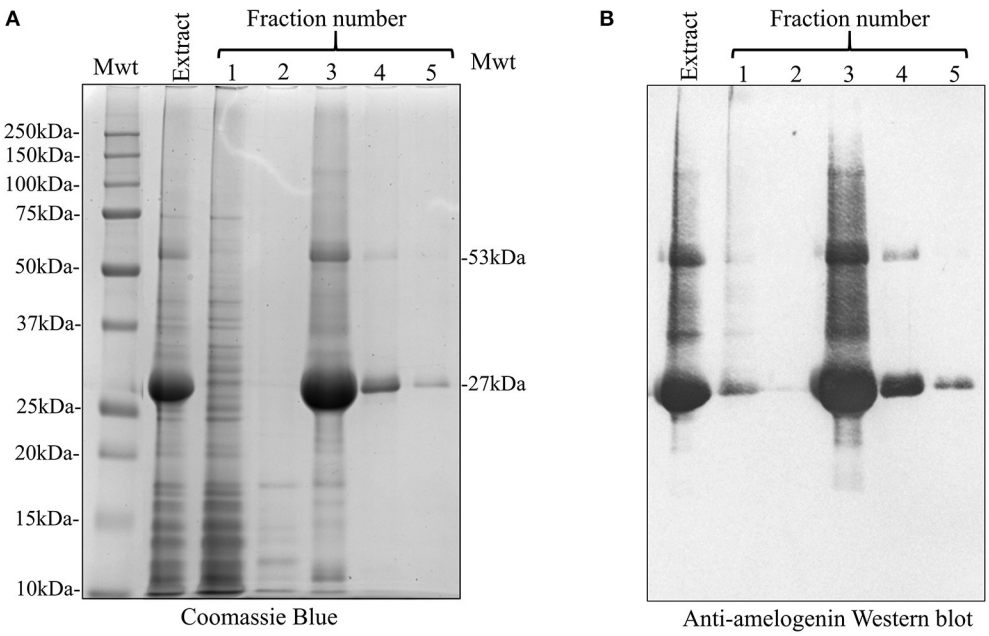

FIGURE 4 | SDS PAGE and anti-amelogenin Western blot analysis of the crude 3% acetic acid *E. coli* extract and nickel column fractions 1–5. **(A)** Extraction with 3% acetic acid (Extract) generated an enriched recombinant amelogenin fraction. In particular, bacterial contaminants migrating above 27 kDa were selectively removed (compare with **Figure 2**). Fractions 1–2, corresponding to the column flow-through, contained many of the bacterial proteins contaminating the crude acetic acid extract. Fractions 3–4 contain proteins eluted by 200 mM imidazole. The 27 kDa recombinant protein is further enriched but still contains contaminating proteins. **(B)** Corresponding anti-amelogenin Western blot confirms the identity of the 27 kDa recombinant protein as amelogenin. The smear centered on the 53 kDa band correspond to re-equilibrating amelogenin aggregates stable in SDS (dimers at 53 kDa being the predominant species present).

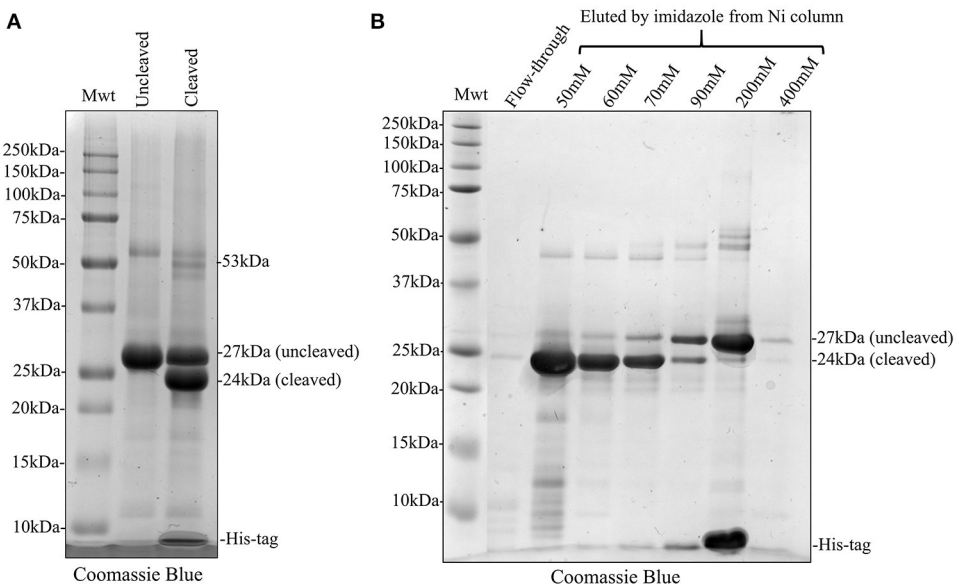

FIGURE 5 | Coomassie Blue stained SDS PAGE showing His-tag cleavage of recombinant amelogenin and second round of nickel column purification using stepped elution gradient to optimize purification of cleaved amelogenin from the cleavage reaction mixture. **(A)** Cleavage of His-tagged 27 kDa recombinant (Uncleaved) with HRV3C protease was not 100% efficient. The cleaved reaction mixture (Cleaved) contained 24 kDa cleaved and 27 kDa uncleaved recombinant. **(B)** The cleaved recombinant was retained on the nickel column despite lacking a His-tag and did not appear in the column flow-through (Flow-through). Subsequent elution with an increasing stepped imidazole gradient eluted the cleaved recombinant at imidazole concentrations of 50 mM and above but some uncleaved recombinant amelogenin and lower molecular weight contaminants were co-eluted. The bulk of uncleaved recombinant amelogenin and free His-tags were eluted by 200 mM imidazole. Elution using 60 mM imidazole was selected since compared to 50 mM this would increase the yield of cleaved recombinant without overly increasing the elution of uncleaved recombinant as a contaminant.

amelogenin (still carrying the His-tag), free His-tag and the cleavage enzyme itself. Following analytical SDS PAGE, it was clear that that cleavage was only around 50% efficient at either pH 8 or 9 (**Figure 5A** and Supplementary Figure 1). In an attempt to purify cleaved from uncleaved His-tagged recombinant amelogenin, the sample was applied to the nickel column in 20 mM imidazole buffer after the cleavage step. Both cleaved and uncleaved recombinant amelogenins (without and with the His-tag, respectively) were retained on the column with very little cleaved recombinant appearing in the column flow through (**Figure 5B**). Increasing concentrations of imidazole buffer were then used in further attempts to optimize separation of cleaved from uncleaved His-tagged recombinant amelogenin via a 50–400 mM imidazole stepped gradient. However, low molecular weight contaminants and a trace of uncleaved recombinant amelogenin co-eluted with the cleaved recombinant amelogenin even at the lowest imidazole concentration employed (**Figure 5B**). Uncleaved recombinant and free His-tag were eluted using >200 mM imidazole. The cleavage enzyme, which is also His-tagged, has a molecular weight of 22 kDa and theoretically elutes at high imidazole concentration though it was not present in high enough concentrations to be detected here. Based on these data, we chose 60 mM imidazole as the optimum concentration to use for elution in subsequent experiments (**Figure 6**) as it would be expected to give a better yield than 50 mM imidazole without eluting appreciably more uncleaved contaminant.

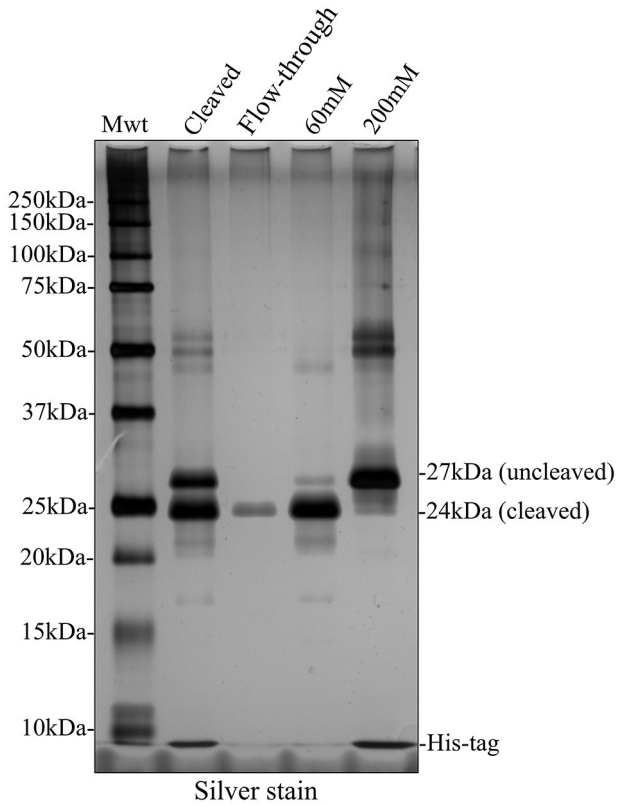

FIGURE 6 | Silver stained SDS PAGE showing second round of nickel column purification to separate cleaved and uncleaved recombinant amelogenin. The bulk of cleaved recombinant amelogenin was eluted by 60 mM imidazole together with lower molecular weight contaminants and some uncleaved recombinant. The uncleaved amelogenin was eluted after increasing the imidazole concentration to 200 mM.

Alternative Strategy Avoiding a Second Round of Nickel Column Purification: Preparative SDS PAGE

Given that a second round of nickel column purification failed to provide cleaved recombinant amelogenin at single band purity, we pursued an alternative strategy using preparative SDS PAGE. Fractions collected from preparative SDS PAGE were characterized using analytical SDS PAGE and silver staining (**Figure 7**). Using this method, cleaved recombinant amelogenin (without His-tag), migrating at 24 kDa, was completely separated from the uncleaved recombinant migrating at 27 kDa and any lower molecular weight contaminants. These were collected in earlier fractions (data not shown).

DISCUSSION

The production of recombinant proteins is essential to the study of protein function and particularly in the case of amelogenins, which are difficult to purify from native tissue due to their aggregative behavior, multiplicity of isoforms and their degradation products and scarcity of material in the most commonly used animal models. In addition, without recourse to recombinant expression, it would be almost impossible to study the effects of specific mutations on amelogenin behavior.

Despite much effort to obtain highly purified recombinant amelogenin using His-tag affinity chromatography we were unable to produce recombinant amelogenin of single band purity when analyzed by silver stained SDS PAGE. Apparent single band purity on SDS PAGE can be achieved by reducing sample load or by employing less sensitive gel staining techniques such as Coomassie Blue but this merely places any contaminants below the limit of stain detection. SDS PAGE is a standard technique for assessing degrees of protein heterogeneity in sample mixtures but additional analyses such as isoelectric focusing or mass spectroscopy would be needed to confirm absolute purity. With that caveat in mind, our goal was to produce recombinant amelogenin exhibiting single band purity on silver stained SDS PAGE gels. The challenges were twofold: (i) removing contaminating bacterial proteins and (ii) separating contaminating His-tagged recombinant amelogenin from His-tag-free recombinant amelogenin following His-tag cleavage, which is <100% efficient.

In an attempt to reduce contamination with bacterial proteins, we employed a previously described acetic acid extraction technique that reportedly produces recombinant amelogenin from *E. coli* at >95% purity in a single purification step (Svensson Bonde and Bulow, 2012). This technique is based on the simple premise that *E. coli* proteins are insoluble in 3% acetic acid at 80°C whereas amelogenin is soluble under these conditions. In our hands, the technique certainly provided a fraction

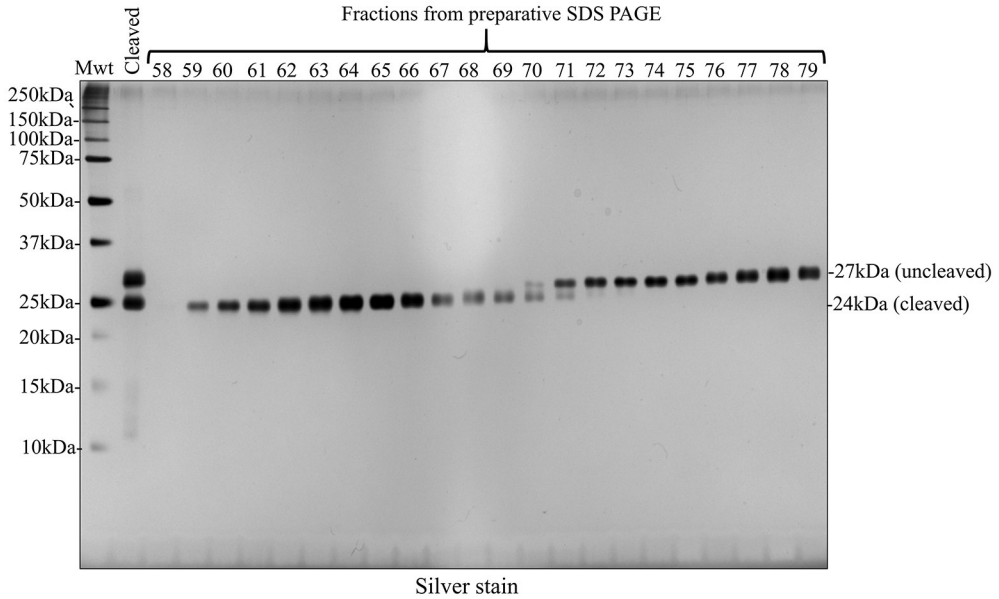

FIGURE 7 | Preparative SDS PAGE purified cleaved recombinant amelogenin to single band purity on silver stained SDS PAGE analytical gels. Fractions 58–79 collected during preparative SDS PAGE of the HRV3C cleavage reaction mixture contained the 24 kDa cleaved and 27 kDa uncleaved recombinant amelogenins. Enhanced resolution of cleaved recombinant amelogenin was achieved compared with nickel column chromatography shown in **Figures 5B**, **6**.

highly enriched with recombinant amelogenin but this still contained contaminants easily detectable on silver stained SDS PAGE. Nevertheless, this initial acetic acid extraction provided a greatly enriched and "cleaner" sample for subsequent affinity chromatography on nickel columns. This is important as *E. coli* express a number of proteins (e.g., Fur, Crp, ArgE, SlyD, GlmS, GlgA, ODO1, ODO2, YadF, and YfbG) that are commonly co-purified when using immobilized metal affinity chromatography due to their metal chelating properties or clusters of exposed histidine residues (Bolanos-Garcia and Davies, 2006). Analytical SDS PAGE followed by silver staining showed that nickel column chromatography removed some of the residual contaminating protein from the initial acetic acid extract. Silver staining is highly sensitive but is non-quantitative so attempts were not made to quantify the efficiency of this purification step using gel densitometry.

Our data showed that His-tag cleavage of recombinant amelogenin by HRV3C protease was far from 100% efficient. This is in agreement with a previous report using rTEV protease to remove His-tags from recombinant amelogenin (Taylor et al., 2006). In some cases, cleavage efficiency was as low as 50% which significantly impacted on final yield. Poor cleavage efficiency may be due to steric hindrance blocking access of the enzyme to the cleavage site (Waugh, 2011). Amelogenin shows a great propensity to aggregate at physiological pH and temperatures (Moradian-Oldak et al., 1994, 1995, 1998; Simmer et al., 1994; Tan et al., 1998; Wiedemann-Bidlack et al., 2007; Aichmayer et al., 2010) and self assembles via N-terminal and/or C-terminal interactions to form higher order structures (Paine and Snead, 1997; Moradian-Oldak et al., 2000; Paine et al., 2000, 2003; Fang et al., 2011; Wald et al., 2017). We therefore hypothesized that amelogenin-amelogenin interactions may hinder HRV3C accessing the His-tag cleavage site. However, carrying out cleavage at 4°C (data not shown) and increasing the pH to 9.0, (both expected to favor amelogenin monomerization) had no effect (Supplementary Figure 1). Finally, we increased the cleavage time to 48 h but again this did not improve cleavage efficiency (data not shown).

Accepting the fact that His-tag cleavage was not 100% efficient, we subjected the cleaved sample (containing recombinant amelogenin with and without His-tags, free His-tag, cleavage enzyme, and any other residual contaminant) to a second round of nickel column affinity chromatography. In theory, the cleaved recombinant amelogenin should have little affinity for the column after removal of the His-tag ligand and would be easily collected in the flow through or at low imidazole concentration while the uncleaved recombinant amelogenin, free His-tag and HRV3C cleavage enzyme (which is itself His-tagged) would remain bound to the nickel column. However, cleaved recombinant amelogenin still exhibited significant affinity for the nickel column. This may be due to the high histidine content of amelogenin which includes a tri-histidine domain (Snead et al., 1985) which can cause non-specific binding confounding His-tag purification (Schmitt et al., 1993; Bornhorst and Falke, 2000). The cleaved recombinant amelogenin could be partially eluted with 50 mM imidazole but stepwise increases in the imidazole concentration resulted in the elution of more uncleaved recombinant amelogenin (**Figure 5B**). This suggested that several conformational isoforms of the cleaved recombinant amelogenin were present, each

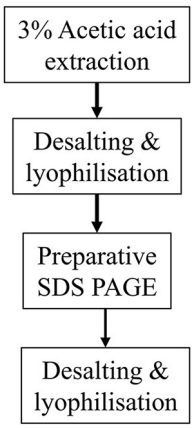

FIGURE 8 | Proposed methodology using preparative SDS PAGE purification of His-tag free recombinant amelogenin.

having a different affinity for the nickel column. The real problem however was that uncleaved recombinant amelogenin began to elute as the imidazole concentration approached 60 mM. This meant that eluting the cleaved recombinant amelogenin with 60 mM imidazole to maximize yield would result in the co-elution of contaminating uncleaved recombinant amelogenin. Even elution at 50 mM imidazole resulted in the co-elution of readily detectable uncleaved recombinant amelogenin.

To solve this problem we decided to employ preparative SDS PAGE rather than using nickel column affinity chromatography. This method was able to separate cleaved recombinant amelogenin from all contaminants to single band purity on analytical silver stained SDS PAGE. Substituting nickel column affinity purification with preparative SDS PAGE reduces the number of steps and leads to a much purer end product. Indeed, the excellent resolving power of preparative SDS PAGE, coupled with the acetic acid extraction technique makes the need for nickel column purification of His-tagged recombinant amelogenin redundant. We suggest that recombinant amelogenin without any His-tag could be purified to single band purity using preparative SDS PAGE (**Figure 8**). In comparison to other more costly and labor intensive methods, using the acetic acid extraction procedure in combination with preparative SDS PAGE provides an economical and speedy method for generating recombinant amelogenin. The lack of an N-terminal His-tag also eliminates any unwanted amino acids at the N-terminal remaining after His-tag cleavage. We are currently re-engineering our recombinant amelogenin vectors to remove the His-tag to take full advantage of the methodology described.

The preparative electrophoretic equipment employed here is not restricted to purifying proteins using SDS PAGE which separates proteins based on their molecular size. Separations can also be achieved using native PAGE buffer systems where proteins, in the absence of SDS, are separated based on their net charge which in turns depends on pH. The manufacturer's instructions provide a range of buffer formulations covering the pH range 3.8–10.2 which can be further adapted by the addition of chaotropic agents and uncharged detergents to aid protein solubility. Although, this additional flexibility is not required in the application reported here, it may prove useful if using preparative electrophoresis for other application such as purifying native enamel proteins extracted from developing enamel.

AUTHOR CONTRIBUTIONS

SB, JK and CG made substantial contributions to the conception and analysis of data; drafted the paper and/or revised it critically for intellectual content; provided final approval of the version to be published; agree to be accountable for all aspects of the work in ensuring that questions related to the accuracy or integrity of any part of the work are appropriately investigated and resolved. CG acquired the data.

FUNDING

CG was supported by a University of Leeds Anniversary Ph.D. Scholarship. We also acknowledge the support of the Wellcome Trust (Grant no. 075945).

ACKNOWLEDGMENTS

We thank Dr. Sarah Myers for her excellent technical support.

SUPPLEMENTARY MATERIAL

The Supplementary Material for this article can be found online at: http://journal.frontiersin.org/article/10.3389/fphys.2017.00424/full#supplementary-material

REFERENCES

Aichmayer, B., Wiedemann-Bidlack, F. B., Gilow, C., Simmer, J. P., Yamakoshi, Y., Emmerling, F., et al. (2010). Amelogenin nanoparticles in suspension: deviations from spherical shape and pH-dependent aggregation. *Biomacromolecules* 11, 369–376. doi: 10.1021/bm900983b

Aldred, M. J., Crawford, P. J., Roberts, E., and Thomas, N. S. (1992). Identification of a nonsense mutation in the amelogenin gene (AMELX) in a family with X-linked amelogenesis imperfecta (AIH1). *Hum. Genet.* 90, 413–416. doi: 10.1007/BF00220469

Aoba, T., Fukae, M., Tanabe, T., Shimizu, M., and Moreno, E. (1987). Selective adsorption of porcine-amelogenins onto hydroxyapatite and their inhibitory activity on hydroxyapatite growth in supersaturated solutions. *Calcif. Tissue Int.* 41, 281–289. doi: 10.1007/BF02555230

Barron, M. J., Brookes, S. J., Kirkham, J., Shore, R. C., Hunt, C., Mironov, A., et al. (2010). A mutation in the mouse Amelx tri-tyrosyl domain results in impaired secretion of amelogenin and phenocopies human X-linked amelogenesis imperfecta. *Hum. Mol. Genet.* 19, 1230–1247. doi: 10.1093/hmg/ddq001

Bolanos-Garcia, V. M., and Davies, O. R. (2006). Structural analysis and classification of native proteins from *E. coli* commonly co-purified by

immobilised metal affinity chromatography. *Biochim. Biophys. Acta* 1760, 1304–1313. doi: 10.1016/j.bbagen.2006.03.027

Bornhorst, J. A., and Falke, J. J. (2000). [16] Purification of proteins using polyhistidine affinity tags. *Methods Enzymol.* 326, 245–254. doi: 10.1016/S0076-6879(00)26058-8

Brookes, S. J., Barron, M. J., Boot-Handford, R., Kirkham, J., and Dixon, M. J. (2014). Endoplasmic reticulum stress in amelogenesis imperfecta and phenotypic rescue using 4-phenylbutyrate. *Hum. Mol. Genet.* 23, 2468–2480. doi: 10.1093/hmg/ddt642

Brookes, S. J., Kingswell, N. J., Barron, M. J., Dixon, M. J., and Kirkham, J. (2011). Is the 32-kDa fragment the functional enamelin unit in all species? *Eur. J. Oral Sci.* 119(Suppl. 1), 345–350. doi: 10.1111/j.1600-0722.2011.00869.x

Brookes, S. J., Lyngstadaas, S. P., Robinson, C., Shore, R. C., and Kirkham, J. (2006). Intracellular nanosphere subunit assembly as revealed by amelogenin molecular cross-linking studies. *Eur. J. Oral Sci.* 114(Suppl. 1), 280–284; discussion 285–286, 382. doi: 10.1111/j.1600-0722.2006.00311.x

Brookes, S. J., Robinson, C., Kirkham, J., and Bonass, W. A. (1995). Biochemistry and molecular biology of amelogenin proteins of developing dental enamel. *Arch. Oral Biol.* 40, 1–14. doi: 10.1016/0003-9969(94)00135-X

Cheng, L., Lin, Z. K., Shu, R., Liu, D. L., Zhang, X. L., Liu, B., et al. (2012). Analogous effects of recombinant human full-length amelogenin expressed by *Pichia pastoris* yeast and enamel matrix derivative *in vitro*. *Cell Prolif.* 45, 456–465. doi: 10.1111/j.1365-2184.2012.00834.x

Collier, P. M., Sauk, J. J., Rosenbloom, S. J., Yuan, Z. A., and Gibson, C. W. (1997). An amelogenin gene defect associated with human X-linked amelogenesis imperfecta. *Arch. Oral Biol.* 42, 235–242. doi: 10.1016/S0003-9969(96)00099-4

Fang, P. A., Conway, J. F., Margolis, H. C., Simmer, J. P., and Beniash, E. (2011). Hierarchical self-assembly of amelogenin and the regulation of biomineralization at the nanoscale. *Proc. Natl. Acad. Sci. U.S.A.* 108, 14097–14102. doi: 10.1073/pnas.1106228108

Fincham, A. G., and Moradian-Oldak, J. (1993). Amelogenin post-translational modifications: carboxy-terminal processing and the phosphorylation of bovine and porcine "TRAP" and "LRAP" amelogenins. *Biochem. Biophys. Res. Commun.* 197, 248–255. doi: 10.1006/bbrc.1993.2468

Fincham, A. G., Moradian-Oldak, J., Diekwisch, T. G., Lyaruu, D. M., Wright, J. T., Bringas, P. Jr., et al. (1995). Evidence for amelogenin "nanospheres" as functional components of secretory-stage enamel matrix. *J. Struct. Biol.* 115, 50–59. doi: 10.1006/jsbi.1995.1029

Fincham, A., Moradian-Oldak, J., and Sarte, P. (1994). Mass-spectrographic analysis of a porcine amelogenin identifies a single phosphorylated locus. *Calcif. Tissue. Int.* 55, 398–400. doi: 10.1007/BF00299322

Gibson, C. W., Yuan, Z.-A., Hall, B., Longenecker, G., Chen, E., Thyagarajan, T., et al. (2001). Amelogenin-deficient mice display an amelogenesis imperfecta phenotype. *J. Biol. Chem.* 276, 31871–31875. doi: 10.1074/jbc.M104624200

Hart, P. S., Aldred, M. J., Crawford, P. J., Wright, N. J., Hart, T. C., and Wright, J. T. (2002). Amelogenesis imperfecta phenotype-genotype correlations with two amelogenin gene mutations. *Arch. Oral. Biol.* 47, 261–265. doi: 10.1016/S0003-9969(02)00003-1

Hochuli, E., Bannwarth, W., Döbeli, H., Gentz, R., and Stüber, D. (1988). Genetic approach to facilitate purification of recombinant proteins with a novel metal chelate adsorbent. *Nat. Biotechnol.* 6, 1321–1325. doi: 10.1038/nbt1188-1321

Kim, J. W., Simmer, J. P., Hu, Y. Y., Lin, B. P., Boyd, C., Wright, J. T., et al. (2004). Amelogenin p.M1T and p.W4S mutations underlying hypoplastic X-linked amelogenesis imperfecta. *J Dent. Res.* 83, 378–383. doi: 10.1177/154405910408300505

Kindelan, S. A., Brook, A. H., Gangemi, L., Lench, N., Wong, F. S., Fearne, J., et al. (2000). Detection of a novel mutation in X-linked amelogenesis imperfecta. *J. Dent. Res.* 79, 1978–1982. doi: 10.1177/00220345000790120901

Kwak, S.-Y., Wiedemann-Bidlack, F. B., Beniash, E., Yamakoshi, Y., Simmer, J. P., Litman, A., et al. (2009). Role of 20-kDa amelogenin (P148) phosphorylation in calcium phosphate formation *in vitro*. *J. Biol. Chem.* 284, 18972–18979. doi: 10.1074/jbc.M109.020370

Laemmli, U. K. (1970). Cleavage of structural proteins during the assembly of the head of bacteriophage T4. *Nature* 227, 680–685. doi: 10.1038/227680a0

Lagerstrom, M., Dahl, N., Nakahori, Y., Nakagome, Y., Backman, B., Landegren, U., et al. (1991). A deletion in the amelogenin gene (AMG) causes X-linked amelogenesis imperfecta (AIH1). *Genomics* 10, 971–975. doi: 10.1016/0888-7543(91)90187-J

Lench, N. J., and Winter, G. B. (1995). Characterisation of molecular defects in X-linked amelogenesis imperfecta (AIH1). *Hum. Mutat.* 5, 251–259. doi: 10.1002/humu.1380050310

Limeback, H. (1987). Isolation and characterization of pig enamelins. *Biochem. J.* 243, 385–390. doi: 10.1042/bj2430385

Limeback, H., and Simic, A. (1990). Biochemical characterization of stable high molecular-weight aggregates of amelogenins formed during porcine enamel development. *Arch. Oral. Biol.* 35, 459–468. doi: 10.1016/0003-9969(90)90209-S

Moore, K. A., and Hollien, J. (2012). The unfolded protein response in secretory cell function. *Annu. Rev. Genet.* 46, 165–183. doi: 10.1146/annurev-genet-110711-155644

Moradian-Oldak, J., Leung, W., and Fincham, A. (1998). Temperature and pH-dependent supramolecular self-assembly of amelogenin molecules: a dynamic light-scattering analysis. *J. Struct. Biol.* 122, 320–327. doi: 10.1006/jsbi.1998.4008

Moradian-Oldak, J., Paine, M. L., Lei, Y. P., Fincham, A. G., and Snead, M. L. (2000). Self-assembly properties of recombinant engineered amelogenin proteins analyzed by dynamic light scattering and atomic force microscopy. *J. Struct. Biol.* 131, 27–37. doi: 10.1006/jsbi.2000.4237

Moradian-Oldak, J., Simmer, J., Lau, E., Sarte, P., Slavkin, H., and Fincham, A. (1994). Detection of monodisperse aggregates of a recombinant amelogenin by dynamic light scattering. *Biopolymers* 34, 1339–1347. doi: 10.1002/bip.360341006

Moradian-Oldak, J., Simmer, J. P., Lau, E. C., Diekwisch, T., Slavkin, H. C., and Fincham, A. G. (1995). A review of the aggregation properties of a recombinant amelogenin. *Connect. Tissue Res.* 32, 125–130. doi: 10.3109/03008209509013714

Ozcan, L., and Tabas, I. (2012). Role of endoplasmic reticulum stress in metabolic disease and other disorders. *Annu. Rev. Med.* 63, 317–328. doi: 10.1146/annurev-med-043010-144749

Paine, M. L., Luo, W., Zhu, D. H., Bringas, P., and Snead, M. L. (2003). Functional domains for amelogenin revealed by compound genetic defects. *J. Bone Miner. Res.* 18, 466–472. doi: 10.1359/jbmr.2003.18.3.466

Paine, M. L., and Snead, M. L. (1997). Protein interactions during assembly of the enamel organic extracellular matrix. *J. Bone Miner. Res.* 12, 221–227. doi: 10.1359/jbmr.1997.12.2.221

Paine, M. L., Zhu, D. H., Luo, W., Bringas, P. Jr., Goldberg, M., White, S. N., et al. (2000). Enamel biomineralization defects result from alterations to amelogenin self-assembly. *J. Struct. Biol.* 132, 191–200. doi: 10.1006/jsbi.2000.4324

Rutkowski, D. T., and Kaufman, R. J. (2007). That which does not kill me makes me stronger: adapting to chronic ER stress. *Trends Biochem. Sci.* 32, 469–476. doi: 10.1016/j.tibs.2007.09.003

Ryu, O. H., Fincham, A. G., Hu, C. C., Zhang, C., Qian, Q., Bartlett, J. D., et al. (1999). Characterization of recombinant pig enamelysin activity and cleavage of recombinant pig and mouse amelogenins. *J. Dent. Res.* 78, 743–750. doi: 10.1177/00220345990780030601

Schmitt, J., Hess, H., and Stunnenberg, H. G. (1993). Affinity purification of histidine-tagged proteins. *Mol. Biol. Rep.* 18, 223–230. doi: 10.1007/BF01674434

Schubert, U., Antón, L. C., Gibbs, J., Norbury, C. C., Yewdell, J. W., and Bennink, J. R. (2000). Rapid degradation of a large fraction of newly synthesized proteins by proteasomes. *Nature* 404, 770–774. doi: 10.1038/35008096

Simmer, J., Lau, E., Hu, C., Aoba, T., Lacey, M., Nelson, D., et al. (1994). Isolation and characterization of a mouse amelogenin expressed in Escherichia coli. *Calcif. Tissue Int.* 54, 312–319. doi: 10.1007/BF00295956

Smith, C. E., Hu, Y., Hu, J. C. C., and Simmer, J. P. (2016). Ultrastructure of early amelogenesis in wild-type, Amelx-/-, and Enam-/- mice: enamel ribbon initiation on dentin mineral and ribbon orientation by ameloblasts. *Mol. Genet. Genomic Med.* 4, 662–683. doi: 10.1002/mgg3.253

Smith, D. B., and Johnson, K. S. (1988). Single-step purification of polypeptides expressed in Escherichia coli as fusions with glutathione S-transferase. *Gene* 67, 31–40. doi: 10.1016/0378-1119(88)90005-4

Snead, M. L., Lau, E. C., Zeichner-David, M., Fincham, A. G., Woo, S. L., and Slavkin, H. C. (1985). DNA sequence for cloned cDNA for murine amelogenin reveal the amino acid sequence for enamel-specific protein. *Biochem. Biophys. Res. Commun.* 129, 812–818. doi: 10.1016/0006-291X(85)91964-3

Svensson, J., Andersson, C., Reseland, J. E., Lyngstadaas, P., and Bülow, L. (2006). Histidine tag fusion increases expression levels of active recombinant amelogenin in *Escherichia coli*. *Protein Exp. Purif.* 48, 134–141. doi: 10.1016/j.pep.2006.01.005

Svensson Bonde, J., and Bulow, L. (2012). One-step purification of recombinant human amelogenin and use of amelogenin as a fusion partner. *PLoS ONE* 7:e33269. doi: 10.1371/journal.pone.0033269

Takagi, T., Suzuki, M., Baba, T., Minegishi, K., and Sasaki, S. (1984). Complete amino acid sequence of amelogenin in developing bovine enamel. *Biochem. Biophys. Res. Commun.* 121, 592–597. doi: 10.1016/0006-291X(84)90223-7

Tan, J., Leung, W., Moradian-Oldak, J., Zeichner-David, M., and Fincham, A. (1998). The pH dependent amelogenin solubility and its biological significance. *Connect. Tissue Res.* 38, 215–221. doi: 10.3109/03008209809017039

Taylor, A. L., Haze-Filderman, A., Blumenfeld, A., Shay, B., Dafni, L., Rosenfeld, E., et al. (2006). High yield of biologically active recombinant human amelogenin using the baculovirus expression system. *Protein Exp. Purif.* 45, 43–53. doi: 10.1016/j.pep.2005.05.010

Travers, K. J., Patil, C. K., Wodicka, L., Lockhart, D. J., Weissman, J. S., and Walter, P. (2000). Functional and genomic analyses reveal an essential coordination between the unfolded protein response and ER-associated degradation. *Cell* 101, 249–258. doi: 10.1016/S0092-8674(00)80835-1

Tsuchiya, M., Tye, C. E., Sharma, R., Smith, C. E., and Bartlett, J. D. (2008). XBP1 may determine the size of the ameloblast endoplasmic reticulum. *J. Dent. Res.* 87, 1058–1062. doi: 10.1177/154405910808701115

Wald, T., Spoutil, F., Osickova, A., Prochazkova, M., Benada, O., Kasparek, P., et al. (2017). Intrinsically disordered proteins drive enamel formation via an evolutionarily conserved self-assembly motif. *Proc. Natl. Acad. Sci. U.S.A.* 114, E1641–E1650. doi: 10.1073/pnas.1615334114

Warshawsky, H. (1968). The fine structure of secretory ameloblasts in rat incisors. *Anat. Rec.* 161, 211–229. doi: 10.1002/ar.1091610207

Waugh, D. S. (2011). An overview of enzymatic reagents for the removal of affinity tags. *Protein Exp. Purif.* 80, 283–293. doi: 10.1016/j.pep.2011.08.005

Wiedemann-Bidlack, F. B., Beniash, E., Yamakoshi, Y., Simmer, J. P., and Margolis, H. C. (2007). pH triggered self-assembly of native and recombinant amelogenins under physiological pH and temperature *in vitro*. *J. Struct. Biol.* 160, 57–69. doi: 10.1016/j.jsb.2007.06.007

Wiedemann-Bidlack, F. B., Kwak, S.-Y., Beniash, E., Yamakoshi, Y., Simmer, J. P., and Margolis, H. C. (2011). Effects of phosphorylation on the self-assembly of native full-length porcine amelogenin and its regulation of calcium phosphate formation *in vitro*. *J. Biol. Chem.* 173, 250–260. doi: 10.1016/j.jsb.2010.11.006

Wright, J. T., Hart, T. C., Hart, P. S., Simmons, D., Suggs, C., Daley, B., et al. (2009). Human and mouse enamel phenotypes resulting from mutation or altered expression of AMEL, ENAM, MMP20 and KLK4. *Cells Tissues Organs* 189, 224–229. doi: 10.1159/000151378

Xu, L., Harada, H., Yokohama-Tamaki, T., Matsumoto, S., Tanaka, J., and Taniguchi, A. (2006). Reuptake of extracellular amelogenin by dental epithelial cells results in increased levels of amelogenin mRNA through enhanced mRNA stabilization. *J. Biol. Chem.* 281, 2257–2262. doi: 10.1074/jbc.M507695200

Yadegari, Z., Bandehpour, M., Kazemi, B., and Sharifi-Sarasiabi, K. (2015). Expression of recombinant human amelogenin in iranian lizard leishmania and its biological function assay. *Iran. J. Public Health* 44, 987–996.

Conflict of Interest Statement: The authors declare that the research was conducted in the absence of any commercial or financial relationships that could be construed as a potential conflict of interest.

Copyright © 2017 Gabe, Brookes and Kirkham. This is an open-access article distributed under the terms of the Creative Commons Attribution License (CC BY). The use, distribution or reproduction in other forums is permitted, provided the original author(s) or licensor are credited and that the original publication in this journal is cited, in accordance with accepted academic practice. No use, distribution or reproduction is permitted which does not comply with these terms.

frontiers in Physiology

METHODS
published: 25 April 2017
doi: 10.3389/fphys.2017.00239

Optimizing Immunostaining of Enamel Matrix: Application of Sudan Black B and Minimization of False Positives from Normal Sera and IgGs

Xu Yang[1], *Alexander J. Vidunas*[1] *and Elia Beniash*[1,2]*

[1] Department of Oral Biology, School of Dental Medicine, University of Pittsburgh, Pittsburgh, PA, USA, [2] Department of Bioengineering, Center for Craniofacial Regeneration, Swanson School of Engineering, McGowan Institute for Regenerative Medicine, University of Pittsburgh, Pittsburgh, PA, USA

Non-specific fluorescence from demineralized enamel matrix can significantly compromise the immunofluorescence studies and lead to false positives. Our goal was to assess degrees of non-specific binding under different conditions and try to optimize procedures for immunofluorescence studies of forming enamel. Firstly, we compared two methods for background fluorescence elimination, i.e., sodium borohydride and Sudan Black B treatments. The results demonstrated that Sudan Black B is far superior to sodium borohydride in reducing the background fluorescence in dental tissues. We also studied the extent of non-specific binding of normal sera and purified polyclonal immunoglobulins (IgG) from five mammalian species, guinea pig, rat, rabbit, goat, and sheep, over a broad range of dilutions. For all sera tested fluorescence signals increased exponentially from 1:1000 to 1:100. Interestingly, the non-specific binding of sera from rodent species was below that of positive control in the whole range of dilutions. In contrast, incubation with sera from 3 non-rodent species produced much higher signals which surpassed the positive control signal at 1:250∼1:500 dilution range. Most of the IgGs didn't show significant non-specific binding within 0.25–5 μg/ml range, except rabbit IgG which demonstrated extremely high affinity to the enamel matrix even at concentrations as low as 1 μg/ml. Further, studies confirmed that Fab fragments of purified normal rabbit IgG, not conserved Fc fragments, were involved in the interactions. Our observations suggest this high affinity is associated with the antigen binding sites of rabbit IgG. We anticipate that our results will help enamel researchers to optimize and standardize their immunochemical procedures.

Keywords: amelogenesis, enamel, immunofluorescence microscopy, false positive, Sudan Black B

OPEN ACCESS

Edited by:
Ariane Berdal,
UMRS 1138 INSERM University Paris-Diderot Team POM, France

Reviewed by:
Victor E. Arana-Chavez,
University of São Paulo, Brazil
Javier Catón,
CEU San Pablo University, Spain
Bernhard Ganss,
University of Toronto, Canada

***Correspondence:**
Elia Beniash
ebeniash@pitt.edu

Specialty section:
This article was submitted to Craniofacial Biology and Dental Research, a section of the journal Frontiers in Physiology

Received: *16 February 2017*
Accepted: *05 April 2017*
Published: *25 April 2017*

Citation:
Yang X, Vidunas AJ and Beniash E (2017) Optimizing Immunostaining of Enamel Matrix: Application of Sudan Black B and Minimization of False Positives from Normal Sera and IgGs. Front. Physiol. 8:239. doi: 10.3389/fphys.2017.00239

INTRODUCTION

Although mature enamel is the hardest tissue of the human body which primarily comprises carbonated apatite with <1% w/w organics, it starts as a tissue with ∼30% organic matrix by weight (Margolis et al., 2006). Unlike other mineralized tissues, such as bone and dentin, which contain roughly 30% of collagenous matrix, most of the enamel organic matrix is degraded during the maturation stage (Simmer and Hu, 2002). Studies of enamel secretion and maturation are

key for our understanding of enamel mineralization strategies. These studies can provide valuable information about enamel formation in norm and disease and an inspiration for design of novel nanostructured hierarchical materials.

Immunofluorescence is a powerful tool, which can provide wealth of information regarding structural and functional properties of biological samples. One of the perennial problems researchers face when using this technique are false positives due to autofluorescence or non-specific antibody binding which, if not taken into account can lead to wrong conclusions (Baschong et al., 2001; True, 2008; Tan et al., 2012). Although no systematic studies of autofluorescence or non-specific staining of enamel were published, enamel researchers are generally aware of these issues and interpret immunofluorescence studies of amelogenesis with caution.

Sudan Black B (SBB) is widely used to eliminate autofluorescence in histology studies, although exact mechanisms of its action are unknown. It was shown to dramatically reduce background signals not only in biological tissues (Romijn et al., 1999; Viegas et al., 2007; Oliveira et al., 2010; Nakata et al., 2011; Sun et al., 2011; Yang and Honaramooz, 2012; Neo et al., 2015; Erben et al., 2016; Kajimura et al., 2016), such as lymph node, thymus, liver, kidney, pancreas, testis, brain, and silk, but also in synthesized polymers (Jaafar et al., 2011). Another chemical which is widely used to reduce autofluorescence from aldehyde fixed samples is $NaBH_4$ (Clancy and Cauller, 1998; Davis et al., 2014). In this study we compared two methods of reducing non-specific staining in decalcified mouse enamel matrix. We also investigated interactions between the enamel matrix and normal sera or polyclonal immunoglobulins (IgGs) from a number of mammalian species. These studies were conducted over a broad range of dilutions typically used in the immunochemistry studies. We hope that the information presented in this paper will help other researchers to better design and interpret the immunofluorescence studies of dental tissues.

MATERIALS AND METHODS

Sample Preparation

Four weeks old wild type C56BL/6J mice were sacrificed according to an approved protocol. Mandibles were dissected out immediately and fixed with 4% paraformaldehyde in PBS for 24 h at 4°C. Fixed mandibles were kept in 8% EDTA solution for 1 week, and the solution was changed every other day. De-mineralized mandibles were then embedded in paraffin blocks and 8 μm sections were prepared using a Leica RM2245 (Leica Biosystems, Nussloch, Germany). The sectioning was conducted in the coronal plane at the location of the first molar. Serial sections from three different animals were used. For fluorescence blocking study, additional sectioning was conducted in the sagittal plane.

Antigen Retrieval and Blocking Procedures

Sections were de-paraffinized and treated with trypsin-EDTA (Sigma, T4049) for 10 min at 37°C for antigen retrieval, then blocked with 10% Donkey serum, 2.5% BSA (Jackson Immunoresearch, 001-000-161), 0.1% Triton X-100 (Sigma, T9284), 0.15% glycine (Sigma, 410225), 0.25% casein (Fisher, BP-337) and 0.1% gelatin (Sigma, G7765) in Tris-buffer solution plus 0.05%Tween-20 (TBST) for 1 h.

Non-specific Fluorescence Blocking

In the experiment aimed at comparing the effects of different non-specific fluorescence blockers serial sections were grouped by three treatments. One group was treated with 1 mg/ml of freshly made sodium borohydride ($NaBH_4$) solution before the blocking step. Sections were incubated 10 min X 3 with $NaBH_4$ and washed three times with TBST. The sections were incubated with or without secondary antibodies (1:500, see **Table 1**) for an hour at room temperature, followed by TBST washing and DAPI staining. Another group was treated with 1.5% Sudan Black B (SBB) in 70% ethanol (SBB, filtered before use) after secondary antibody (1:500) incubation or in ½ blocking buffer only for 1 h. The sections were washed with TBST four times, then incubated with SBB for 20 min, washed with TBST and stained with DAPI. Untreated sections with or without secondary antibodies incubation were used as controls.

Non-specific Binding Studies

In the study of non-specific interactions of sera and IgGs with dental tissues, sections incubated overnight in the 2 times diluted blocking buffer at 4°C (see the Antigen retrieval and blocking procedures section for the blocking buffer composition). Some of these sections were used as negative control. For positive controls, after blocking sections were incubated with affinity purified ameloblastin (Santa Cruz, sc-50534) or enamelin (Santa Cruz, sc-33107) antibodies at concentration of 1 μg/ml overnight at 4°C. Serial sections from 2 incisors were incubated overnight at 4°C with sera from different species (see **Table 1**) at 1:1000, 1:500, 1:250 and 1:100 series of dilutions. Other serial sections were incubated overnight at 4°C with IgGs obtained from different species at concentrations of 0.25, 1, 2.5, and 5 μg/ml (**Table 1**). In an additional set of experiments we tested normal rabbit IgGs from 4 different manufacturers (see **Table 1**), Fab fragment and Fc fragment and rabbit anti-calreticulin peptide 1 (CP1) monoclonal IgG (Developmental Studies Hybridoma Bank, CPTC-CALR-1-s). In this set of experiment a concentration of 2 μg/ml was used. The sections were washed with TBST 5 min for six times and incubated with secondary antibodies (see **Table 1**) at 1:500 dilution in ½ blocking buffer for an hour. SBB was used to eliminate the background and DAPI (0.2 μg/ml for 5 min) was used as counter stain. Importantly, for all fluorescence studies adjacent serial sections were used to minimize intra and intergroup variability.

All sections were scanned using Nikon A1 confocal microscope (Nikon Instruments, Melville, NY) at Center for Biologic Imaging (CBI) of University of Pittsburgh. Sections from same block were scanned under the same imaging conditions. The images were captured in 16 bit RGB mode and stored in the native nd2 or tiff file format.

TABLE 1 | The product information for antibodies used in the study.

	Donkey	Goat	Guinea pig	Rabbit	Rat	Sheep
Sera	017-000-121*	005-000-121*	006-000-001*	011-000-001*	012-000-001*	013-000-001*
IgG		sc-2028#	sc-2711#	sc-2027#	sc-2026#	sc-2717#
2nd Ab		705-165-147*	706-165-148*	711-165-152* 711-545-152*	712-165-150*	713-165-147*
	Thermo fisher	**Millipore**	**Jackson immuno**	**DSHB**	**Fab**	**Fc**
Other Rb IgG	026102	NI01	011-000-003	CPTC-CALR-1-s	011-000-007	011-000-008

Sera were purchased Jackson Immunoreasearch Inc. from PA, USA.
#IgGs were purchased from Santa Cruz Biotechnology, Inc. from CA, USA.

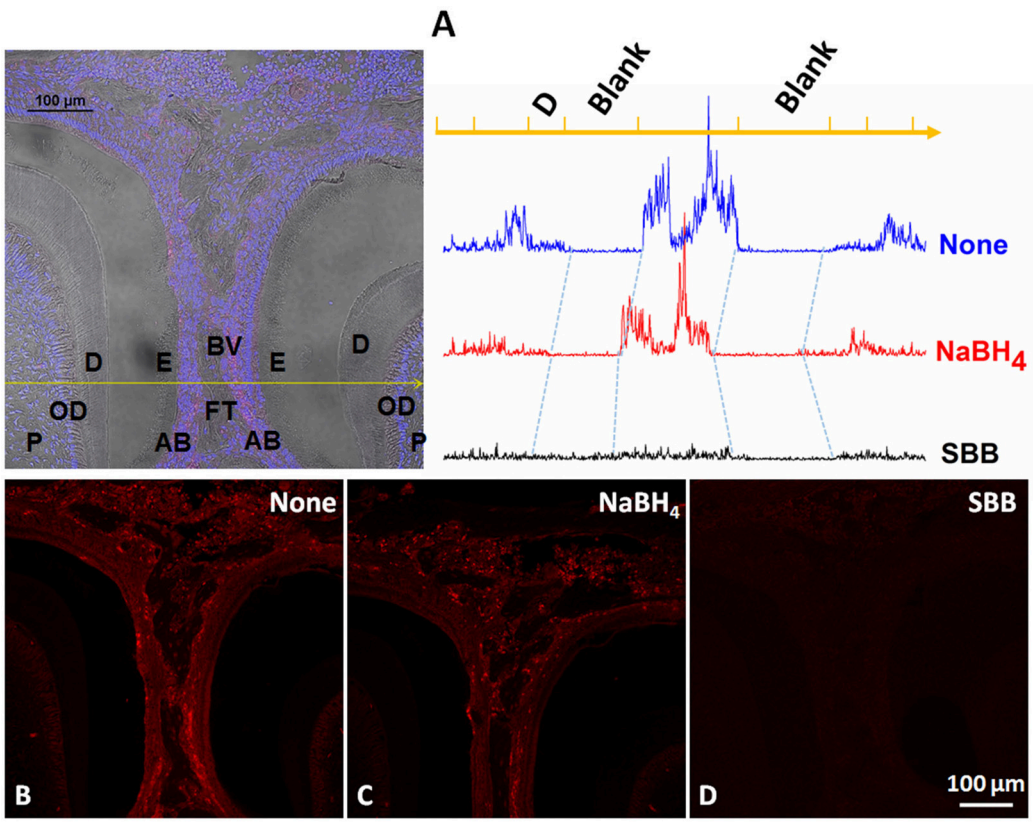

FIGURE 1 | Comparison of the autofluorescence blocking by $NaBH_4$ and SBB in sections of mouse mandibles. (A) Left. Multi-channel image, containing bright field, DAPI and TRITC channels, of a section including parts of 1st and 2nd molar. Yellow line identifies the location at which the fluorescence profiles on the right were obtained in the adjacent sections shown in **(B,C)** and Right, **(D)**, fluorescence profile on the top is from th non-treated section **(B)**; middle profile is from the $NaBH_4$ treated section **(C)** and the bottom profile is from the SBB treated section **(D)**. P, pulp; OD, odontoblast; D, dentin; E, enamel; AB, ameloblast; BV, blood vessel; FT, fibrous tissue.

Data Analysis

All images were analyzed in NIS-Elements AR software (Nikon Instruments, Melville, NY) or in imageJ image analysis package (Bethesda, MD). In general, similar areas of interest (at least 1,000 μm^2) were selected and average signal intensity values were measured. The data was plotted using Origin 2016 graphing software (Origin Labs, Waltham, MA).

RESULTS

Comparison of the $NABH_4$ and SBB for Reduction of Auto-Fluorescence

Strong non-specific signal was observed in the control group (**Figures 1A,B**). It was strongest in fibrous tissue and blood vessels while lower in odontoblasts, ameloblasts, enamel and

dentin. Treatment with $NaBH_4$ lead to a minimal decrease in fluorescence signal compared to the control (**Figures 1A,C**), while incubation in SBB greatly reduced staining of all tissues in the sections (**Figures 1A,D**). No obvious differences were found after incubation with secondary antibody in each group.

Reactivity of Sera from Different Species with the Enamel Matrix

Fluorescence at the 1:1000 dilution of all sera was at the level of the background signal (**Figures 2A,C**). The fluorescence increased exponentially with the increase of sera concentrations. Plotting the data on a natural logarithm (Ln) scale lead to linearization of the curve, which confirmed the exponential relationships between the sera dilution and the fluorescence intensity (**Figures 2B,D**). Interestingly, the fluorescence signals in experiments with sera from rodent species, rat and guinea pig, increased ~10 times from 0 to 1/100 dilution, while fluorescence from the samples treated with sera from other mammalian orders, i.e., rabbit, goat, and sheep increased up to 100 times over the same range of dilutions (**Figure 3**). Importantly, the non-specific signal from the samples treated with rodent sera reached the signal intensity level of the positive control at 1/100 dilution, while for the non-rodent sera this level of intensity was reached at around 1/500. Adjacent periodontal ligament (PDL) tissue showed non-specific fluorescence levels similar to forming enamel while signal from dentin tissue was always at the background level (**Figures 2E,F**).

Reactivity of IgGs from Different Species with Enamel Matrix

In contrast to sera, most of the IgGs exhibited low level of fluorescence over the range from 0 to 5 μg/ml (**Figures 4A,B**), well below the intensity levels of positive controls, with the exception of rabbit IgG which strongly reacted with enamel matrix (**Figures 4A,B** blue line, **Figures 5E–H**). The fluorescence intensity of the rabbit IgG grew linearly with the increase in concentration. It reached the fluorescence levels of the positive control around 1 μg/mL and was 50–100 times higher than the baseline fluorescence at the maximum concentration of 5 μg/ml. Adjacent tissues such as PDL and dentin didn't show an affinity to rabbit IgG and their fluorescence remained low in the range of the concentrations tested (**Figures 4C,D**, **5**). There were no major differences between rabbit IgGs from different manufacturers tested in the study (**Figures 6A–D**). The same phenomenon was also observed in routine immunohistochemistry staining (**Figures 6I,J**).

Reactivity of Rabbit Monoclonal Antibodies and IgG Fragments with Enamel Matrix

Rabbit monoclonal antibody against CP1, a ER marker, did not interact with the enamel matrix, while adjacent cells

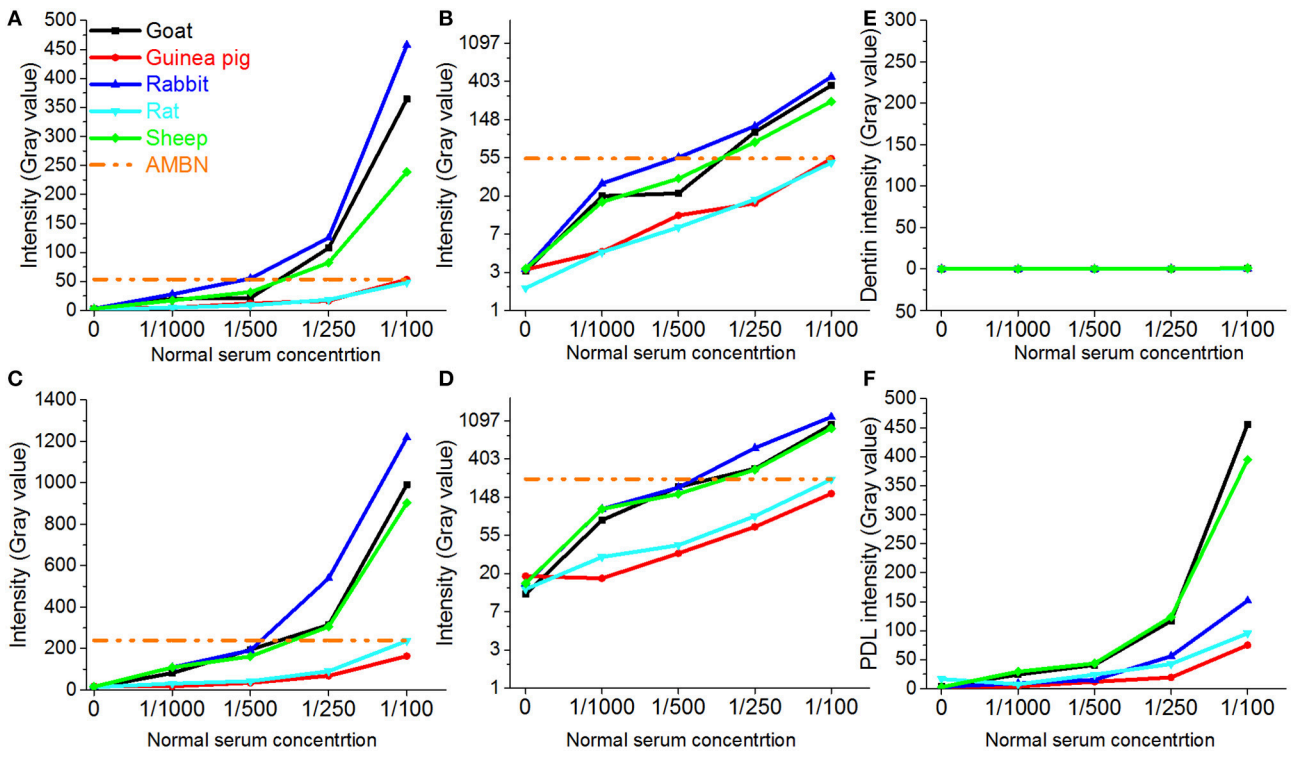

FIGURE 2 | Changes in fluorescence intensities of different dental tissues incubated with sera from different species. (A) Fluorescence intensity profiles of enamel matrix from incisor 1; **(B)** data in **A** presented on the natural logarithmic scale; **(C)** Fluorescence intensity profiles of enamel matrix from incisor 2; **(D)** data in **(C)** presented on the natural logarithmic scale; **(E)** Fluorescence intensity profiles of dentin matrix from incisor 1; **(F)** Fluorescence intensity profiles of periodontium from incisor 1.

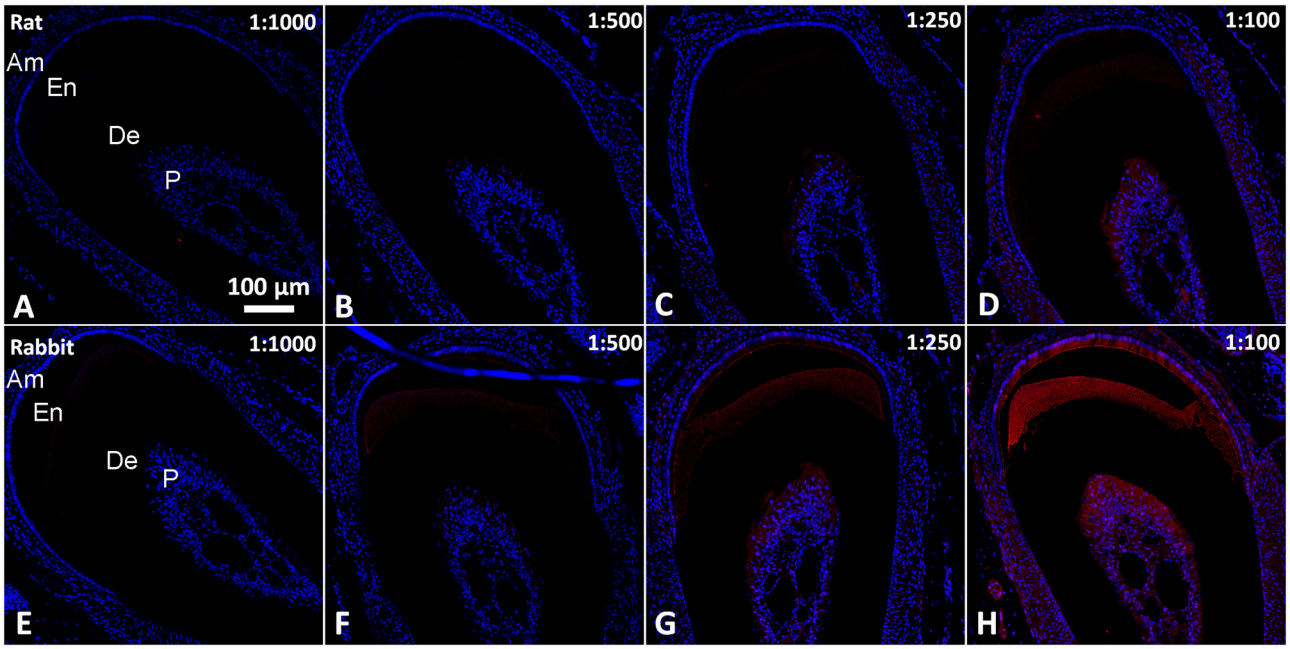

FIGURE 3 | Epifluorescence micrographs from serial coronal sections of mouse incisor incubated with normal sera in in the 1/1000–1/100 range of dilutions. (A–D) Rat serum. **(E–H)** Rabbit serum. All images were taken under the same magnification. Am, ameloblasts and stratum intrermedium; De, dentin; En, enamel; P, Pulp.

demonstrated a strong signal (**Figure 6G**). At the same time rabbit Fab fragments showed similar binding to enamel matrix as rabbit IgG whole molecule (**Figure 6E**). When the sections were incubated with Fc fragment only, no signal was detected (**Figure 6F**). No signal was detected in the negative control (**Figure 6H**).

DISCUSSION

Our results clearly demonstrate an excellent ability of SBB to block the non-specific signal from the enamel matrix and other tissues. This was in a good agreement with the results of autofluorescence quenching by SBB in other tissues (Viegas et al., 2007; Davis et al., 2014; Erben et al., 2016). In fact, fluorescence of almost all the tissues in SBB treated sections were reduced to a level close to the background signal. At the same time $NaBH_4$ had little or no effect on the non-specific fluorescence, suggesting that this method is not appropriate for dental tissues. A potential explanation of the low effectiveness of $NaBH_4$ might lie in the fact that after fixation the samples in our study underwent a decalcification step which involves prolonged incubation in EDTA, which might reduce the levels of aldehyde crosslinks, resulting in reduced aldehyde-related autofluorescence.

In the course of our immunochemical studies we noticed repeatedly a very high background signal in enamel matrix treated with normal rabbit IgG as an isotype control. To systematically investigate this phenomenon, we tested the levels of non-specific binding to enamel matrix of normal sera and IgGs from several commonly used mammalian species. Our results demonstrate high levels of fluorescence in the mouse enamel matrix treated with sera from the non-rodent species. The fluorescence intensity for sera from 3 non-rodent species was at the level of the positive control at the dilutions of 1/500 or less. Remarkably, sera from two rodent species showed much lower degree of non-specific binding, perhaps due to the evolutionary proximity between the host and target species. Our results indicate that caution should be taken when using goat, sheep and rabbit sera at the dilutions around 1:500 or less, while for rat and guinea pig sera using dilutions lower than 1:100 is not recommended (**Figures 2A,C**). It is important to note that dentin tissue has a very low level of non-specific binding for all sera, suggesting that it cannot be used as an internal control in immunofluorescence studies of forming enamel.

In contrast to the results of the experiments using whole sera, most affinity purified IgGs showed low affinity to the mouse enamel matrix across concentrations ranging from 0.25 to 5 µg/ml, and the fluorescence levels of the IgG treated samples were close to the background levels over this range. The only exception was rabbit IgG which showed very high affinity to the enamel matrix. To exclude the possibility that this strong binding was limited to IgGs form Santa Cruz, rabbit IgGs from three other manufacturers were also tested, and all of them showed high levels of binding. In order to understand which portion of the IgG interacts with enamel matrix, we also examined Fc (conserved) and Fab (variable) fragments from IgG purified from normal rabbit serum. Our results clearly demonstrated that the variable Fab fragment strongly interacts with enamel matrix, while the

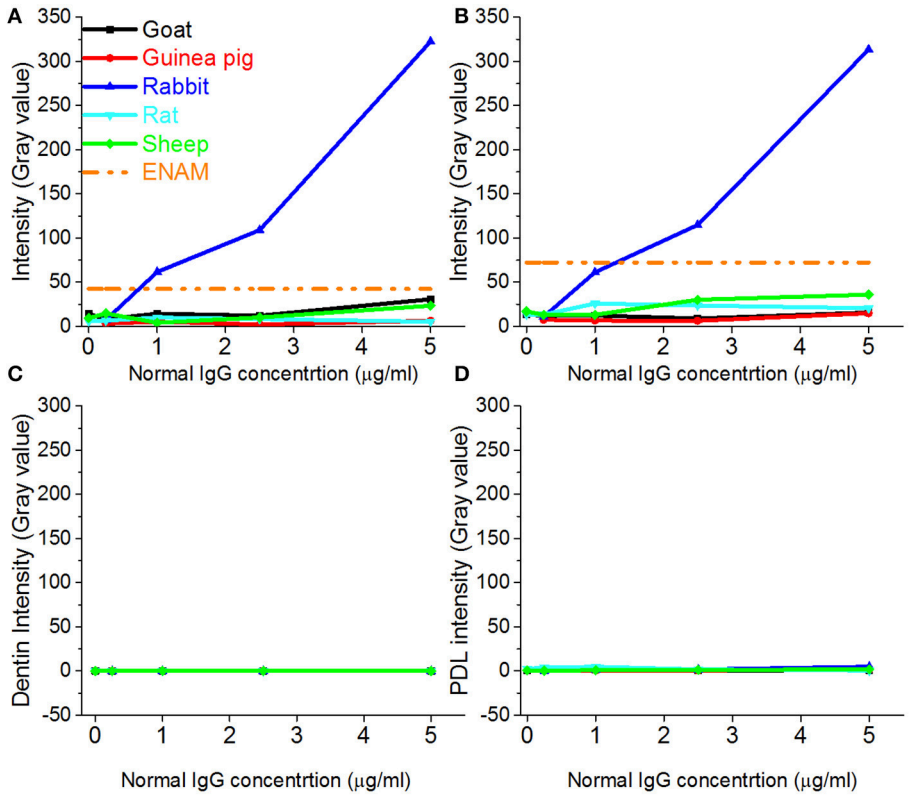

FIGURE 4 | Changes in fluorescence intensities of different dental tissues incubated with IgGs from different species. Fluorescence intensity profiles of enamel matrix from incisor 1 **(A)**, incisor 2 **(B)**, dentin from incisor 1 **(C)** and periodontium from incisor 1 **(D)**.

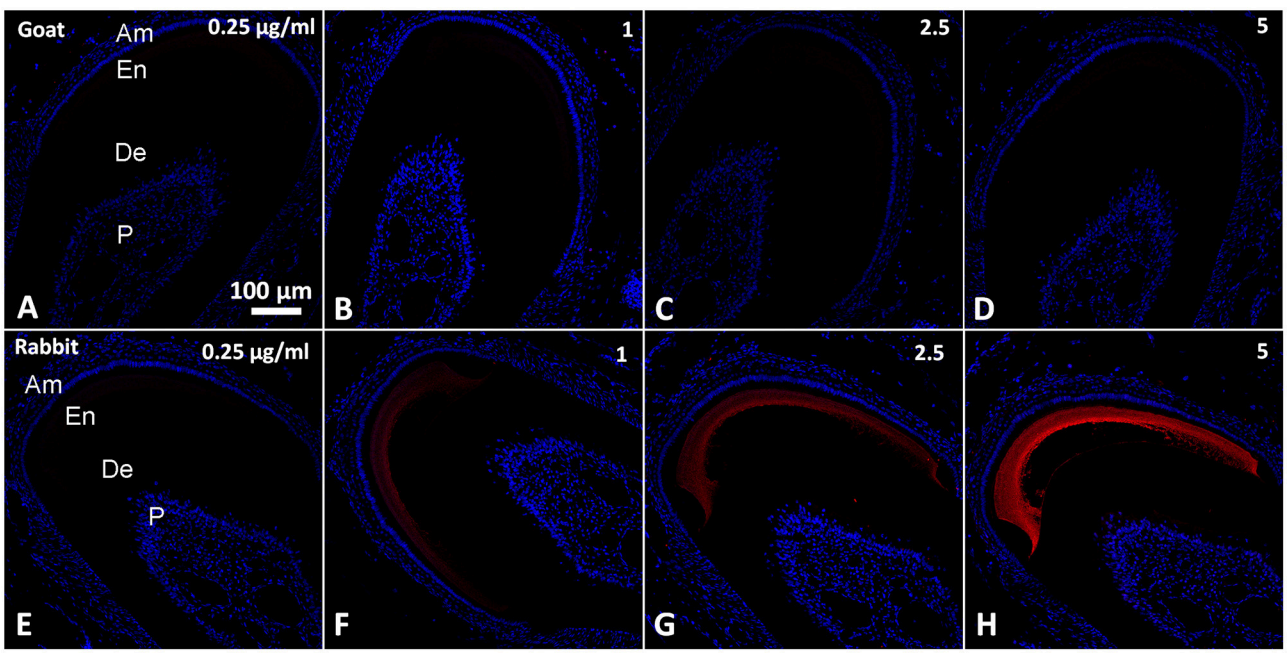

FIGURE 5 | Epifluorescence micrographs from serial coronal sections of mouse incisors incubated with normal IgGs in a range of concentrations from 1 to 5 μg/mL. (A–D) Goat IgG; **(E–H)** Rabbit IgG. All images were taken under the same magnification. Am, ameloblasts and stratum intrermedium; De, dentin; En, enamel; P, Pulp.

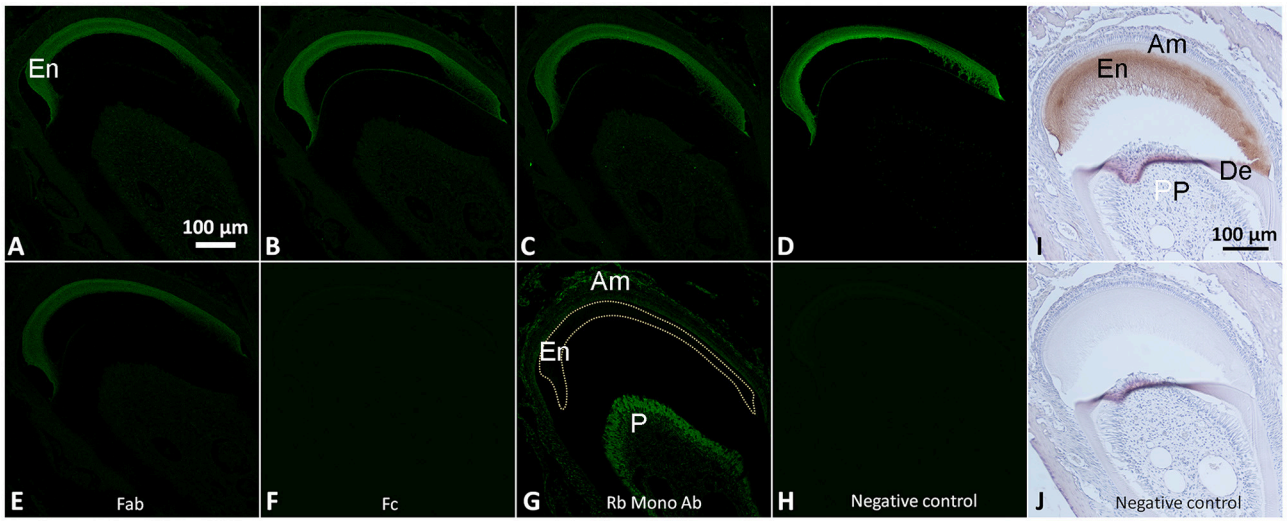

FIGURE 6 | Immunofluorescence images of serial coronal sections of mouse incisors incubated with normal IgGs from Thermo Fisher (A), Jackson Immunoresearch **(B)**, Millipore **(C)** and Santa Cruz **(D)**, Fab **(E)** and Fc **(F)** fragments and the monoclonal rabbit antibody against CP1 **(H)**. Note that in **(H)** the staining is only associated with cells, not the enamel matrix. **(I,J)** show bright field micrographs of the immunohistochemistry staining with normal rabbit IgGs and the negative control, respectively. Note that the fluorescence signal is present in enamel matrix (En) after incubation with rabbit IgGs and the Fab fragment while no obvious signals are present after Fc incubation and in the negative control. **(A–H)** were acquired under the same magnification; **(I,J)** were acquired under the same magnification. All incubations were conducted at 2 μg/mL concentrations of antibodies. Abbreviations are the same as in **Figure 1**. Am, ameloblasts and stratum intrermedium; De, dentin; En, enamel; P, Pulp.

conserved Fc portion did not bind to the enamel matrix. At the same time, monoclonal anti-CP1 rabbit IgG didn't show any affinity to the enamel matrix. Together these data suggest that the high affinity of purified IgGs and Fab fragments to the enamel matrix is not an intrinsic property of any rabbit immunoglobulin but is specific to the certain antigen binding site. This observation was quite unexpected and very intriguing. Our recent study showed the existence of keratins in enamel matrix (Duverger et al., 2014), and based on the personal communication by Dr. Maria Morasso (NIH, Bethesda, MD), even normal rabbit serum might react with keratins because rabbits often get wounded while scratching which presents an opportunity for skin and hair keratins to end up in the blood stream. However, at this time we can only surmise what are the reasons for such high affinity of rabbit IgG to the enamel matrix. More studies will be necessary to understand the mechanisms behind the phenomenon.

CONCLUSION

We conducted a number of experiments aimed at optimization of the immunofluorescence procedure for the extracellular matrix of forming enamel. Specifically, we showed that treatment of sections with SBB leads to significant reduction in autofluorescence of all dental tissues. We also determined the ranges of sera dilution and concentrations of IgG which can be used to minimize false positives, suggesting that proper isotype controls will be necessary when working beyond this range. Our observations indicate that rabbit sera and IgG have a very high affinity to the enamel matrix, and this high affinity is associated with the antigen binding sites.

ETHICS STATEMENT

This study was carried out in accordance with the recommendations of IACUC of the University of Pittsburgh. The protocol was approved by the IACUC of the University of Pittsburgh.

AUTHOR CONTRIBUTIONS

XY and EB participated in the study design, data analysis and manuscript writing. XY and AV conducted the experiments.

ACKNOWLEDGMENTS

We are grateful to the faculty and staff at the Center for Biological Imaging, University of Pittsburgh (Pittsburgh, PA) for their support and advice. We also thank Samer Zaky for his suggestion to use SBB as blocking agent.

REFERENCES

Baschong, W., Suetterlin, R., and Laeng, R. H. (2001). Control of autofluorescence of archival formaldehyde-fixed, paraffin-embedded tissue in confocal laser scanning microscopy (CLSM). *J. Histochem. Cytochem.* 49, 1565–1571. doi: 10.1177/002215540104901210

Clancy, B., and Cauller, L. J. (1998). Reduction of background autofluorescence in brain sections following immersion in sodium borohydride.

J. Neurosci. Methods 83, 97–102. doi: 10.1016/S0165-0270(98)00066-1

Davis, A. S., Richter, A., Becker, S., Moyer, J. E., Sandouk, A., Skinner, J., et al. (2014). Characterizing and diminishing autofluorescence in formalin-fixed paraffin-embedded human respiratory tissue. *J. Histochem. Cytochem.* 62, 405–423. doi: 10.1369/0022155414531549

Duverger, O., Ohara, T., Shaffer, J. R., Donahue, D., Zerfas, P., Dullnig, A., et al. (2014). Hair keratin mutations in tooth enamel increase dental decay risk. *J. Clin. Invest.* 124, 5219–5224. doi: 10.1172/JCI78272

Erben, T., Ossig, R., Naim, H. Y., and Schnekenburger, J. (2016). What to do with high autofluorescence background in pancreatic tissues - an efficient Sudan black B quenching method for specific immunofluorescence labelling. *Histopathology* 69, 406–422. doi: 10.1111/his.12935

Jaafar, I. H., LeBlon, C. E., Wei, M. T., Ou-Yang, D., Coulter, J. P., and Jedlicka, S. S. (2011). Improving fluorescence imaging of biological cells on biomedical polymers. *Acta Biomater* 7, 1588–1598. doi: 10.1016/j.actbio.2010.12.007

Kajimura, J., Ito, R., Manley, N. R., and Hale, L. P. (2016). Optimization of single- and dual-color immunofluorescence protocols for formalin-fixed, paraffin-embedded archival tissues. *J. Histochem. Cytochem.* 64, 112–124. doi: 10.1369/0022155415610792

Margolis, H. C., Beniash, E., and Fowler, C. E. (2006). Role of macromolecular assembly of enamel matrix proteins in enamel formation. *J. Dent. Res.* 85, 775–793. doi: 10.1177/154405910608500902

Nakata, T., Takayama, E., Magari, H., Kato, J., Kondo, N., and Masao, I. (2011). Simultaneous detection of T lymphocyte-related antigens (CD4/CD8, CD57, TCRβ) with nuclei by fluorescence-based immunohistochemistry in paraffin-embedded human lymph node, liver cancer and stomach cancer, *Acta Cytol.* 55, 357–363. doi: 10.1159/000329487

Neo, P. Y., Tan, D. J., Shi, P., Toh, S. L., and Goh, J. C. (2015). Enhancing analysis of cells and proteins by fluorescence imaging on silk-based biomaterials: modulating the autofluorescence of silk. *Tissue Eng. C Methods* 21, 218–228. doi: 10.1089/ten.tec.2014.0209

Oliveira, V. C., Carrara, R. C., Simoes, D. L., Saggioro, F. P., Carlotti, C. G. Jr., Covas, D. T., et al. (2010). Sudan Black B treatment reduces autofluorescence and improves resolution of *in situ* hybridization specific fluorescent signals of brain sections. *Histol. Histopathol.* 25, 1017–1024. doi: 10.14670/HH-25.1017

Romijn, H. J., van Uum, J. F., Breedijk, I., Emmering, J., Radu, I., and Pool, C. W. (1999). Double immunolabeling of neuropeptides in the human hypothalamus as analyzed by confocal laser scanning fluorescence microscopy. *J. Histochem. Cytochem.* 47, 229–236. doi: 10.1177/002215549904700211

Simmer, J. P., and Hu, J. C. C. (2002). Expression, structure, and function of enamel proteinases. *Connect. Tissue Res.* 43, 441–449. doi: 10.1080/03008200290001159

Sun, Y., Yu, H., Zheng, D., Cao, Q., Wang, Y., Harris, D., et al. (2011). Sudan black B reduces autofluorescence in murine renal tissue. *Arch. Pathol. Lab Med.* 135, 1335–1342. doi: 10.5858/arpa.2010-0549-OA

Tan, N. C., Tran, H., Roscioli, E., Wormald, P. J., and Vreugde, S. (2012). Prevention of false positive binding during immunofluorescence of *Staphylococcus aureus* infected tissue biopsies. *J. Immunol. Methods* 384, 111–117. doi: 10.1016/j.jim.2012.07.015

True, L. D. (2008). Quality control in molecular immunohistochemistry. *Histochem. Cell Biol.* 130, 473–480. doi: 10.1007/s00418-008-0481-0

Viegas, M. S., Martins, T. C., Seco, F., and do Carmo, A. (2007). An improved and cost-effective methodology for the reduction of autofluorescence in direct immunofluorescence studies on formalin-fixed paraffin-embedded tissues. *Eur. J. Histochem.* 51, 59–66. doi: 10.4081/1013

Yang, Y., and Honaramooz, A. (2012). Characterization and quenching of autofluorescence in piglet testis tissue and cells. *Anat. Res. Int.* 2012:820120. doi: 10.1155/2012/820120

Conflict of Interest Statement: The authors declare that the research was conducted in the absence of any commercial or financial relationships that could be construed as a potential conflict of interest.

Copyright © 2017 Yang, Vidunas and Beniash. This is an open-access article distributed under the terms of the Creative Commons Attribution License (CC BY). The use, distribution or reproduction in other forums is permitted, provided the original author(s) or licensor are credited and that the original publication in this journal is cited, in accordance with accepted academic practice. No use, distribution or reproduction is permitted which does not comply with these terms.

frontiers in Physiology

ORIGINAL RESEARCH
published: 24 October 2017
doi: 10.3389/fphys.2017.00793

Integrative Temporo-Spatial, Mineralogic, Spectroscopic, and Proteomic Analysis of Postnatal Enamel Development in Teeth with Limited Growth

*Mirali Pandya[1], Hui Liu[2], Smit J. Dangaria[2], Weiying Zhu[3], Leo L. Li[4], Shuang Pan[2], Moufida Abufarwa[1], Roderick G. Davis[5], Stephen Guggenheim[6], Timothy Keiderling[4], Xianghong Luan[2] and Thomas G. H. Diekwisch[1]**

[1] Texas A&M Center for Craniofacial Research and Diagnosis, Dallas, TX, United States, [2] Brodie Laboratory for Craniofacial Genetics, University of Illinois at Chicago, Chicago, IL, United States, [3] Department of Chemistry, University of Illinois at Chicago, Chicago, IL, United States, [4] Medicine, University of Michigan, Ann Arbor, MI, United States, [5] Proteomics Center of Excellence, Northwestern University, Evanston, IL, United States, [6] Department of Earth and Environmental Sciences, University of Illinois at Chicago, Chicago, IL, United States

OPEN ACCESS

Edited by:
Steven Joseph Brookes,
Leeds Dental Institute,
United Kingdom

Reviewed by:
Claudio Cantù,
University of Zurich, Switzerland
Zhi Chen,
Wuhan University, China
Brad A. Amendt,
University of Iowa, United States

***Correspondence:**
Thomas G. H. Diekwisch
diekwisch@tamhsc.edu

Specialty section:
This article was submitted to Craniofacial Biology and Dental Research, a section of the journal Frontiers in Physiology

Received: 22 June 2017
Accepted: 27 September 2017
Published: 24 October 2017

Citation:
Pandya M, Liu H, Dangaria SJ, Zhu W, Li LL, Pan S, Abufarwa M, Davis RG, Guggenheim S, Keiderling T, Luan X and Diekwisch TGH (2017) Integrative Temporo-Spatial, Mineralogic, Spectroscopic, and Proteomic Analysis of Postnatal Enamel Development in Teeth with Limited Growth. Front. Physiol. 8:793. doi: 10.3389/fphys.2017.00793

Tooth amelogenesis is a complex process beginning with enamel organ cell differentiation and enamel matrix secretion, transitioning through changes in ameloblast polarity, cytoskeletal, and matrix organization, that affects crucial biomineralization events such as mineral nucleation, enamel crystal growth, and enamel prism organization. Here we have harvested the enamel organ including the pliable enamel matrix of postnatal first mandibular mouse molars during the first 8 days of tooth enamel development to conduct a step-wise cross-sectional analysis of the changes in the mineral and protein phase. Mineral phase diffraction pattern analysis using single-crystal, powder sample X-ray diffraction analysis indicated conversion of calcium phosphate precursors to partially fluoride substituted hydroxyapatite from postnatal day 4 (4 dpn) onwards. Attenuated total reflectance spectra (ATR) revealed a substantial elevation in phosphate and carbonate incorporation as well as structural reconfiguration between postnatal days 6 and 8. Nanoscale liquid chromatography coupled with tandem mass spectrometry (nanoLC-MS/MS) demonstrated highest protein counts for ECM/cell surface proteins, stress/heat shock proteins, and alkaline phosphatase on postnatal day 2, high counts for ameloblast cytoskeletal proteins such as tubulin β5, tropomyosin, β-actin, and vimentin on postnatal day 4, and elevated levels of cofilin-1, calmodulin, and peptidyl-prolyl cis-trans isomerase on day 6. Western blot analysis of hydrophobic enamel proteins illustrated continuously increasing amelogenin levels from 1 dpn until 8 dpn, while enamelin peaked on days 1 and 2 dpn, and ameloblastin on days 1–5 dpn. In summary, these data document the substantial changes in the enamel matrix protein and mineral phase that take place during postnatal mouse molar amelogenesis from a systems biological perspective, including (i) relatively high levels of matrix protein expression during the early secretory stage on postnatal day 2, (ii) conversion of calcium phosphates to apatite, peak protein folding and stress protein counts, and increased cytoskeletal

protein levels such as actin and tubulin on day 4, as well as (iii) secondary structure changes, isomerase activity, highest amelogenin levels, and peak phosphate/carbonate incorporation between postnatal days 6 and 8. Together, this study provides a baseline for a comprehensive understanding of the mineralogic and proteomic events that contribute to the complexity of mammalian tooth enamel development.

Keywords: enamel, hydroxyapatite, X-ray powder diffraction, proteomics, amelogenin

INTRODUCTION

Enamel development is an integral process of symphonic dimensions that is characterized by a continuous interplay between cells, matrices, minerals, proteins, and signals over the entire period of amelogenesis. Allegorically speaking, the key players in this symphony have been known for decades, including a mineral section that undergoes a transition from amorphous calcium phosphate and a protein section made up by classic enamel proteins such as amelogenins, ameloblastin, and enamelin, as they are further processed by enamel-related enzymes, including MMP20 and KLK4. As amelogenesis progresses, the volume percentage of proteins and water decreases, while the mineral content increases, resulting in a 96% mineral content in the mature enamel layer of adult mammals (Deakins, 1942; Stack, 1960; Robinson et al., 1978, 1979, 1988). Changes in the metastable enamel matrix that result from the loss of water and proteins have even been described as a "kind of crisis" (Eastoe, 1979), referring to the multiple effects of water and protein resorption on the interface between remaining proteins and maturing enamel crystals.

For decades, the effect of individual enamel proteins such as amelogenin on enamel crystal growth have been a most intriguing and rewarding subject of study (Lagerström et al., 1991; Diekwisch et al., 1993; Gibson et al., 2001; Iijima and Moradian–Oldak, 2004; Jin et al., 2009; Gopinathan et al., 2014). In addition to deciphering individual aspects of amelogenin function, much progress has been made elucidating the role of the less prominent enamel-related proteins ameloblastin and enamelin on enamel crystal growth and habit (Masuya et al., 2005; Lu et al., 2011; Hu et al., 2014). Moreover, it has been demonstrated that enamel proteins undergo posttranslational processing by the enamel proteinases MMP20 and KLK4 (Bartlett and Simmer, 1999; Simmer and Hu, 2002; Bartlett, 2013).

While much is known about the major proteins and minerals involved in tooth enamel formation, it has become increasingly obvious that amelogenesis is more complex than a mixture of an aqueous enamel protein solution with a combination of calcium and phosphate ions, subjected to enzymatic protein digestion and gradual removal of water over time. Recent studies have illustrated the importance of ion transport mechanisms for mineral transport (Hubbard, 2000; Paine et al., 2001; Lacruz, 2017), the effect of pH modulation through regulatory molecules (Takagi et al., 1998; Lacruz et al., 2010; Moradian-Oldak, 2012; Robinson, 2014) and the role of junctional proteins such as cadherins for ameloblast movement (Bartlett and Smith, 2013; Guan et al., 2014). These molecules and events are only one part of a process that ensures a gradual deposition of minerals at the dentin-enamel junction throughout amelogenesis and their step-wise conversion into hydroxyapatite crystals and alignment into enamel prisms into one of the most fascinating biomaterials found in nature.

Development of a synthetic or mimetic model of amelogenesis would greatly benefit from a temporo-spatial integration of the multitude of processes involved in mammalian amelogenesis. Such multi-level and multi-scale data mining commonly requires a systems biology approach. Systems biology of development seeks to integrate bioinformatic data analysis with other molecular, cellular, and tissue-related information to reach a higher-level, multifaceted, and integrative understanding of developmental processes (Bard, 2007; Edelman et al., 2009). Integrative approaches toward biological problems have become possible as a result of recent advances in bioinformatics and omics technologies, including proteomics, transcriptomics, and metabolomics (Mochida and Shinozaki, 2011). In mineralized tissue biology, systems biology would need to integrate genetic and proteomic data with mineralogic, structural, and spectroscopic data to develop a multi-dimensional understanding of a complex process such as amelogenesis.

In the present study we have employed first mandibular mouse molar amelogenesis as a model system to systematically map proteomic, spectroscopic, temporo-spatial, and mineralogic events during the first 8 days of postnatal enamel development. The benefit of a model based on teeth with limited growth is the synchronicity of developmental events leading up to maturation of the entire tooth surface by the time of tooth eruption and providing a homogeneous enamel matrix at each stage ideally suited for proteomic and spectroscopic analysis. During the course of this study we have generated sets of spectroscopic, proteomic, and mineralogic data and integrated related events through their common timescale of development. Our analysis provides timing of events, novel proteomic and spectroscopic data, and identification of novel non-hydrophobic groups of proteins and individual proteins that may contribute toward amelogenesis. Future studies will enhance our understanding of the interconnectedness between these processes during the progression of amelogenesis as they contribute to the formation of highly organized tooth enamel.

MATERIALS AND METHODS

Vertebrate Animals and Tissue Preparation

First mandibular molars of 1, 2, 3, 4, 5, 6, 7, and 8 day postnatal mice (**Figures 1A–H**) were dissected from alveolar bone crypts (**Figure 2E**) to characterize the developing enamel

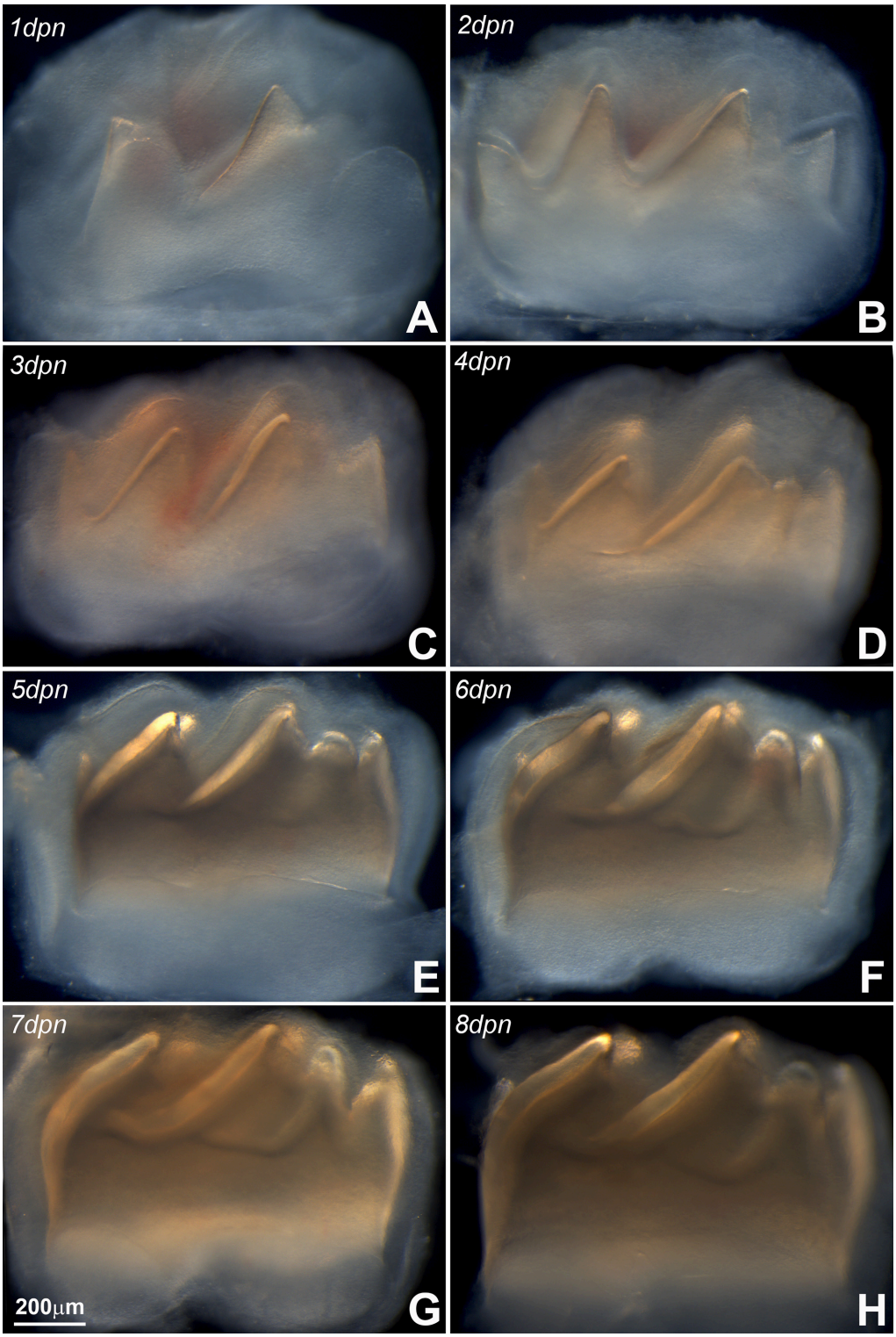

FIGURE 1 | Panel **(A)** represents the mandibular molar at postnatal day (pnd) 1, **(B)** is pnd 2, **(C)** is pnd 3, **(D)** is pnd 4, **(E)** is pnd 5, **(F)** is pnd 6, **(G)** is pnd 7, and **(H)** is pnd 8. During the first 8 days of postnatal mouse molar development, the mineralized portion of the crown dentin continuously increased in height, while the length of the crown remained fairly unchanged. Note the gradual increase in the thickness of the enamel layer (identified in **Figure 2F**).

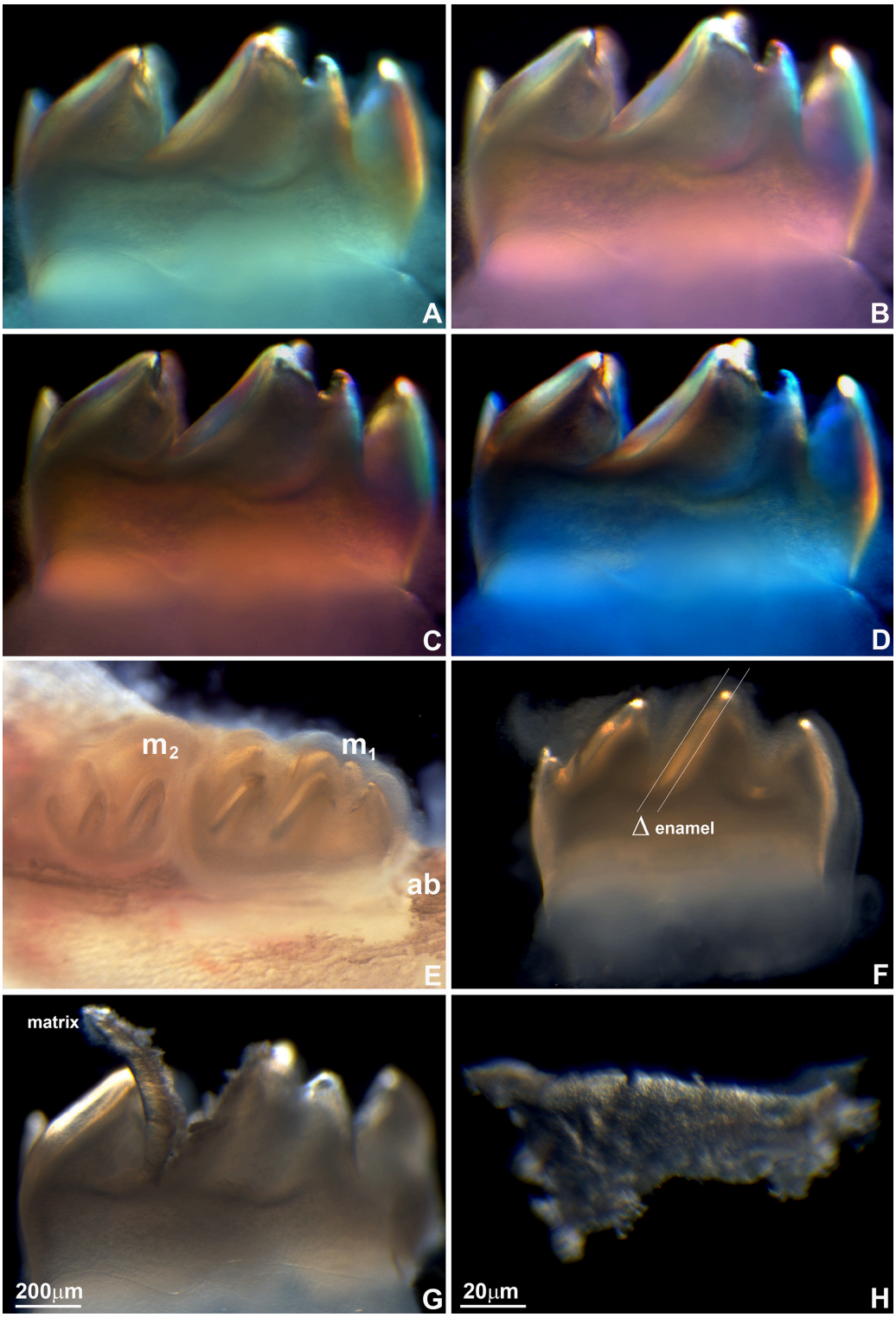

FIGURE 2 | Mouse molar enamel birefringence **(A–D)** and enamel matrix layer dissection for mineral and protein analysis **(E–H). (A–D)** Mouse molars were dissected from mouse jaws and placed between crossed polarizers. Polarizers were oriented at the following angles: 0 degrees **(A),** 90° **(B),** 180° **(C),** and 270° **(D)**. **(E)** Position of the first (m_1) and the second (m_2) mouse mandibular molar relative to the jaw bone and the alveolar bone (ab). **(F)** Enamel layer on the distal slope of the middle cusp of the first mandibular mouse molar used for the present analysis. Δ marks the thickness of the enamel layer between two parallel lines. **(G)** Preparation of the matrix layer from the distal slope of the middle cusp of the first mandibular mouse molar. **(H)** High magnification light micrograph of the dissected enamel layer.

matrix. Postnatal days 1–8 were used for Western blot. Days 2, 4, and 6 were selected for proteomics analysis. Days 1, 2, 4, 6, and 8 were used for X-ray powder diffraction, tissue dissection, and polarized microscopy. All animal experiments were approved by the IACUC committees at the University of Illinois, Chicago and Texas A&M College of Dentistry.

Enamel Thickness Measurements and Polarized Light Microscopy

Enamel thickness was measured on enlarged micrographs generated by a Leica stereo microscope. Enamel thickness was determined by calibration against a metric scale bar imaged at the same magnification. Birefringence of the enamel matrix was assessed by placing the enamel organs between crossed polarizers. The first polarizer was placed between the light source and the tooth organ and the second polarizer was placed between the tooth organ and the camera. The second polarizer was rotated in 45° intervals, and birefringence was identified based on the color changes within the enamel matrix.

X-Ray Powder Diffraction

For this study, the tooth enamel matrices of molars from days 1 to 8 postnatal mice were analyzed using X-ray powder diffraction in 1-day intervals (excluding samples from 3 day postnatal mice). For each day of analysis, the enamel matrix of four different mouse molars was harvested in distilled water, and samples from all four teeth at each developmental stage were pooled for further analysis. Samples were stored for about 24 h at $< 0°$C until analyzed at room temperature. Debye-Scherrer data simulations were obtained using a Bruker three-circle (transmission-mode) diffractometer using Mo radiation (0.7107 Å, APEX CCD detector, graphite monochromator, 0.3 mm Monocap capillary collimator, at operating conditions of 45 kV, 25 mA). Analyzed samples were$\sim$0.1 mm^3 in volume, with each sample mounted on the end of a glass fiber, placed in the X-ray beam and rotated 360° about the glass-fiber axis. Detector positions were at two theta = 0, 20, and 35° using a frame resolution of 1,024 × 1,024 pixels, sample-to-detector distance of 120 mm, and each exposure was for 1,200 s. Data collection using the SMART collection software (Braintree, MA) and initial data processing using the Bruker GADDS software package (Bruker, Billerica, MA). Integration along the Debye rings was performed after data collection with a step (bin) size of 0.02, followed by construction of intensity vs. two-theta plots for each of the three detector positions, followed by a merger of the three plots based on the overlap of adjacent exposures to produce a traditional powder diffraction pattern. Additional pattern processing and phase identification using the Internal Center for Diffraction Data (ICDD, Newtown Square, PA, 2010) powder diffraction file was applied using the JADE software (Materials Data, Inc., Livermore, CA, 2009). Details of the Debye-Scherrer technique have been published in Klug and Alexander (1954) and the use of the Bruker three-circle diffractometer to simulate the Debye-Scherrer technique have been previously reported (Guggenheim, 2005).

Attenuated Total Reflectance Fourier Transform Infrared (ATR-FTIR) Spectra

For FTIR analysis, mice molar enamel matrix samples were transferred to an ATR crystal (PIKE MIRacle single reflection diamond ATR) accessory placed in an FTIR (Bruker Vertex 80) sample compartment. Samples were pressed against the crystal surface with a pressure clamp to form a better contact covering most of the crystal surface. Sample absorbance spectra over the range 4,500–600 cm^{-1} were collected as an average of 2,048 scans (10 kHz scan speed with a DTGS detector) and processed with 3-term Blackman-Harris apodization and zero filling of 2. Background spectra, collected with same measurement parameters but without sample on the ATR crystal surface, were subtracted as a baseline correction.

Proteomics Sample Preparation

Distal slope enamel matrices of 50 first mouse mandibular molars were prepared from 2, 4, and 6 dpn mice, and four sets of samples per time point were chosen. Enamel matrices from mice earlier than 2 dpn were not harvested due to a lack of overall quantity and enamel matrices from mice later than 6 dpn were omitted due to the advanced mineralization of those samples. Following cold acetone/trichloric acid precipitation, samples were redissolved in fifty microliters of 8 M urea. Reduction and alkylation of cysteines was accomplished by adding 1/10 volume of 45 mM DTT to the sample, followed by 45 min incubation at 37°C. After samples were cooled to room temperature, 1/10 volume of 100 mM iodoacetamide were added to the solution and samples were placed in dark at room temperature for 30 min. To equilibrate the sample for trypsin digestion, sufficient water was added to dilute the original 8 M urea/0.4 M ammonium bicarbonate solution 4-fold. A total of 1 μg trypsin was added and the sample was incubated at 37°C for 18–24 h. The trypsin digest was stopped by freezing until nanoLC-MS/MS analysis.

Nano-Scale Liquid Chromatography

Nano-scale liquid chromatography was performed using a Dionex Ultimate 3000 system. Mobile phase A was water/acetonitrile (95:5) with 0.1% formic acid. Mobile phase B was water: acetonitrile (5:95) with 0.1% formic acid. Digested sample was loaded offline onto a Thermo Scientific C18 PepMap100 peptide trap (300 μm ID × 5 mm, 5 μm, 100 A) with 100% mobile phase A flowing at 50 μL per minute. After allowing the peptides to concentrate and desalt for 10 min., the trap was switched inline with an Agilent Zorbax 300SB C18 nanoLC column (3.5 μm, 150 mm × 75 μm ID). The peptides were then resolved using a linear gradient from 5% B to 35% B over 60 min. The flow rate through the column was 250 nL per minute.

Mass Spectrometry

The instrument used for mass spectrometry was an LTQ Orbitrap Velos Pro (Thermo Fisher) equipped with a Thermo LTQ nanospray source, which was operated at an ion spray voltage of 1.8 kV and a heated capillary temperature of 275°C. Full scan mass data were obtained between 400–1,800 Da and the Orbitrap resolution was 30,000. The Orbitrap was operated in

data dependent acquisition mode with dynamic exclusion (120 s). Twenty most intense ions above the minimum signal threshold with charge states greater than or equal to 2 were selected for low-energy CID in the ion trap. Other operating parameters included a minimum signal threshold of 25,000 and an activation time of 30.0 ms.

Proteomics Data Analysis

Raw data files were processed using the Mass Matrix Conversion tool to generate Mascot generic files (MGFs) for the protein database search. Mascot 2.2 was used as a search engine and NCBI Mascot search results were imported into Scaffold.

Western Blot

Cheesy enamel matrix from 1 to 8 days postnatal mouse molars was scraped off and the proteins were homogenized and extracted using sodium dodecyl sulfate-polyacrylamide gel electrophoresis (SDS-PAGE) sample buffer. Equal amounts of the extracted proteins were loaded and separated on a 10% SDS-PAGE gel. From the gel, proteins were transferred to a polyvinylidene difluoride (PVDF) membrane in a semi-dry blotting apparatus at 18 V for 40 min. The membrane was blocked for 1 h with 5% milk powder after which it was incubated with anti-AMEL (1:200, custom made full-length), anti-AMBN (ab72776 1:200, Abcam), anti-ENAM (sc-33107, 1:100, Santa Cruz), anti-MMP20 (ab84737, 1:50, Abcam), and anti-carbonic anhydrase 2 (ab191343, 1:100, Abcam) primary antibodies for 1 h. Following primary antibody incubation, the membrane was washed three times with washing buffer (TBS-T) for 15 min each and then incubated with HRP conjugated secondary anti-chicken, anti-mouse, or anti-rabbit antibodies. To detect HRP, a chemiluminescent substrate (Thermo Scientific) was used. Positive bands were quantitatively assessed using densitometry analysis using the Image J software.

Statistical Analysis

For X-ray diffraction and ATR-FTIR studies, enamel matrix from four different mice of the same position and developmental stage was pooled, and pooled enamel matrix was used for further analysis. Mass-spectroscopy data and proteomics analysis were based on separately collected biological quadruplicates. All other data (thickness measurements and Western blot analyses) were based on triplicates. Data analysis was performed using SPSS software. Statistical significance was assessed using the non-parametric Mann-Whitney *U*-test, and the significance level was set at $p < 0.05$.

RESULTS

Increasing Thickness and Birefringence of the Developing Enamel Matrix

First mandibular molars of 1, 2, 3, 4, 5, 6, 7, and 8 day postnatal mice (**Figures 1A–H**) were dissected from alveolar bone crypts (**Figure 2E**) to characterize the developing enamel matrix. Stereo micrographs documented a continuous increase in enamel matrix thickness from 1–2 μm (1 day postnatal) to 75 μm (6–8 days postnatal) based on measurements of the enamel matrix thickness of the distal slope of the central major cusp, while the overall length of the tooth did not increase (**Figures 1A–H**, **2F**). Analysis of 8 days postnatal molars between crossed polarizers revealed changes in matrix color pattern when analyzers were rotated in 90 degree intervals indicative of birefringence (**Figures 2A–D**). The soft and pliable consistency of the enamel matrix allowed for mechanical separation from the underlying dentin layer using a scalpel (**Figures 2G,H**).

Single-Crystal Powder Sample X-ray Diffraction Analysis of the Postnatal Enamel Matrix Yields Calcium Phosphate Diffraction Patterns on Postnatal Days 1 and 2, and Apatite Diffraction Patterns from Postnatal Day 4 Onward

Previous studies have indicated that the mineral phase of mouse molar enamel transitions from calcium carbonate, tri- and octacalcium phosphate precursors to partially fluoride substituted hydroxyapatite (Diekwisch et al., 1995; Diekwisch, 1998; Gopinathan et al., 2014). To determine at what stage the mineral phase of the entire postnatal mouse molar enamel matrix converts from calcium phosphate precursor stages to apatite (**Figure 3A**), dried enamel matrix preparations from developing mouse molars were subjected to single-crystal, powder sample X-ray diffraction analysis. Mineral phase analysis on days 1 and 2 revealed well-defined, weak-intensity peaks that only partially matched those of the apatite standard pattern and were indicative of a calcium phosphate precursor (**Figure 3B**). In contrast, samples from postnatal days 4–8 yielded partially fluoride substituted hydroxyapatite diffraction patterns based on powder diffraction standards (Hughes et al., 1991)(PDF# 73-9797) (**Figure 3B**). Four peaks labeled as X could not be matched to any ICDD data base pattern (**Figure 3B**).

Attenuated Total Reflectance Spectra (ATR) Demonstrated Enhanced Secondary Structure and Increased Phosphate and Carbonate Incorporation into the Enamel Matrix from Postnatal Day 2 to Day 8

The ATR spectra were measured for teeth obtained at four stages of development (2, 4, 6, and 8 days postnatal, labeled as 2, 4, 6, and 8 dpn) of which 2, 6, and 8 dpn are shown in **Figure 3C**. The 4 dpn spectrum exhibited spectral characteristics similar to the 2 and 6 dpn spectra. The large band at ∼1,650 cm^{-1} and the following one at ∼1,540 cm^{-1} represent the amide I and II bands of enamel matrix proteins. The peak at ∼1,237 cm^{-1} included the amide III band and likely other sources such as PO_2 type modes due to its intensity. The strong peaks at 1,018 cm^{-1} with a shoulder at 1,105 and 958 cm^{-1} that emerged after 6 days was assigned to characteristic phosphate peaks (ν_3 PO_4 mode and ν_1 PO_4 stretching IR mode) (Antonakos et al., 2007; Leventouri et al., 2009). The peak at 872 cm^{-1} was representative of the ν_2 CO_3 band. Based on previous studies, we have assigned the weak shoulders at 1,520 and 880 cm^{-1} that appear after 6 days of development to A-type carbonate substitution (Elliot, 1994) and

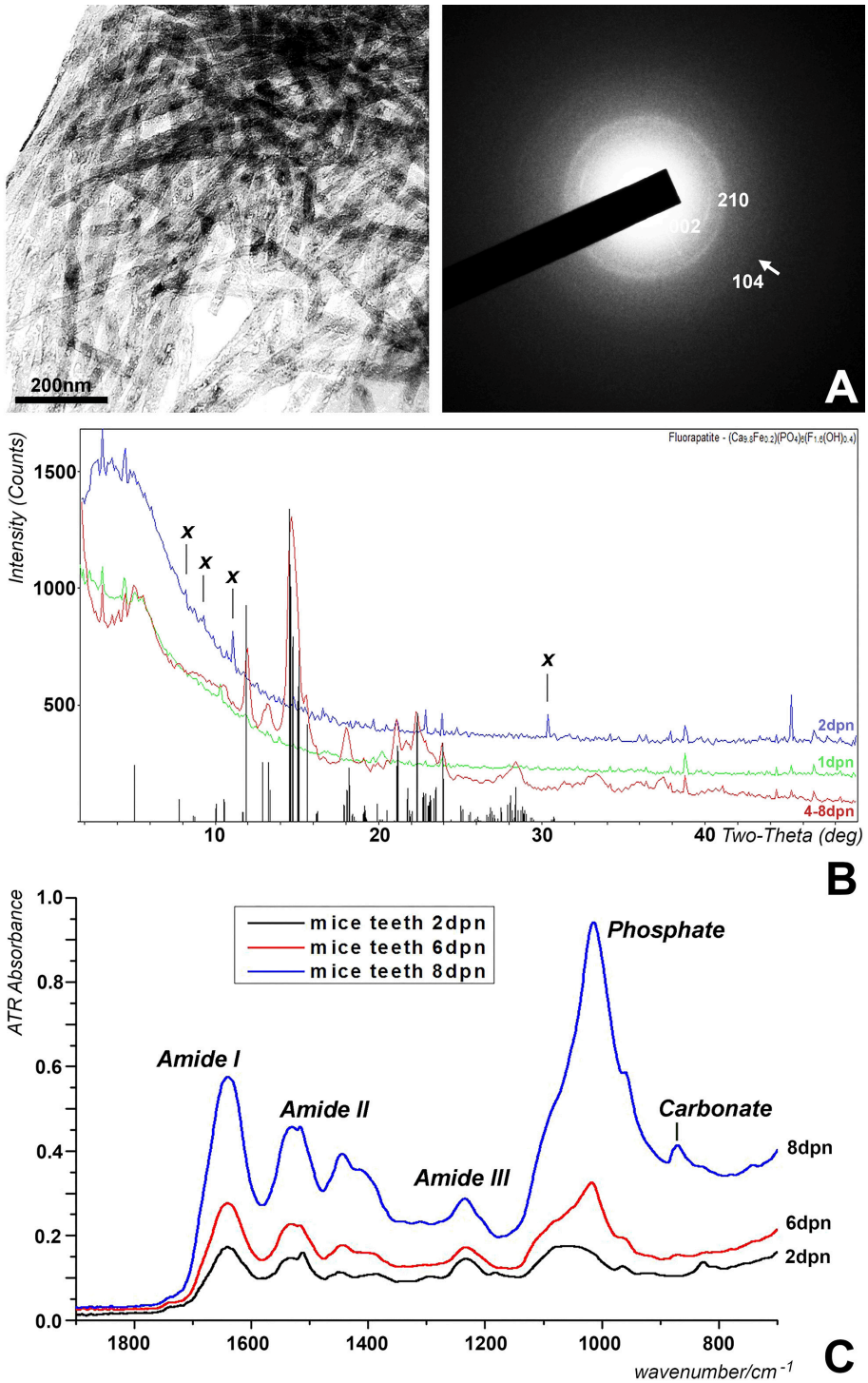

FIGURE 3 | Analysis of the postnatal mouse molar enamel mineral layer. **(A)** Transmission electron microscopy of 4 days postnatal mouse molar enamel matrix revealed bundles of thick apatite crystals with diffraction rings in the 002 and 210 planes, and a faint diffraction ring in the 104 plane, indicative of hydroxyapatite. **(B)** X-ray powder diffraction analysis of enamel matrix preparations from the distal slopes of 1 day postnatal (1 dpn), 2days postnatal (2 dpn), 4, 6, and 8 days postnatal (4–8 dpn) mouse mandibular molars. The vertical bars at the base of the figure illustrate the partially fluoride substituted hydroxyapatite powder diffraction pattern with the height of the bars representing relative peak intensities. Unique unmatched peaks in the spectrum of 2 days postnatal samples were marked by an X. Only the 4–8 dpn samples matched hydroxyapatite powder diffraction standards. **(C)** Fourier-transform infrared spectra of developing enamel matrix preparations from the distal slopes of 2 days postnatal (2 dpn), 6 days postnatal (6 dpn), and 8 days postnatal (8 dpn) mouse mandibular molars. Peaks corresponding to vibrations for phosphate, carbonate, proteoglycan, and amide I–III are labeled individually.

the increased peaks at 1,405 and 1,445 cm^{-1} to B-type carbonate substitution (ν_3 CO_3 mode) (Vignoles-Montrejaud, 1984). The major developmental changes in the spectrum when comparing 2, 4, 6, and 8 dpn enamel included the substantial elevation of the phosphate and carbonate bands (800–1,100 cm^{-1} and 1,400–1,480 cm^{-1}) and the increased peak height of the amide I and II bands (1,650 and 1,540 cm^{-1}, respectively), between postnatal day 6 and day 8.

Proteomics Demonstrated Unique Changes in the Enamel Organ/Enamel Matrix Protein Complex between Postnatal Days 2, 4, and 6

Enamel organ proteomics analysis by nanoLC-MS/MS resulted in discrete peptide identification patterns distinguished between enamel organ/enamel matrix protein complex samples from postnatal days 2, 4, and 6. In these samples, individual proteins were identified using the Mascot search software and ranked based on quantitative Orbitrap counts. Mascot data analysis yielded five protein groups with high spectral counts (**Figure 4**), including (i) mineralization proteins, (ii) cytoskeletal proteins, (iii) extracellular matrix/cell surface proteins, (iv) stress proteins, and (v) isomerases. Within each group, individual proteins were ranked based on spectral count, and individual counts per day for each postnatal day (postnatal days 2, 4, and 6) were subjected to statistical analysis and displayed in **Figure 4**.

Among the biomineralization proteins, alkaline phosphatase 2 peaked on day 2 and significantly decreased by 0.9-fold ($p < 0.05$) from day 2 to day 4 while there was no alkaline phosphatase detected on day 6. Calmodulin was detected on day 2, decreased below the detection threshold on day 4, but once more rose to a significant peak on day 6. There was a 36-fold increase of reticulocalbin 3 levels from day 2 to day 4 ($p < 0.05$) but thereafter the reticulocalbin counts decreased significantly ($p < 0.05$) from day 4 to day 6. Calnexin levels decreased continuously from day 2 through day 6, including a significant decrease ($p < 0.05$) between days 4 and day 6. No expression for cathepsin B was observed at day 2, however the expression significantly peaked at day 4 ($p < 0.05$) and decreased again at day 6. In addition to the proteins displayed in **Figure 4**, peaks for the major enamel protein amelogenin continuously increased from day 2 to day 4 and day 6 ($p < 0.05$).

Four cytoskeleton related proteins displayed an increase in expression levels between days 2 and 4 and then decreased on day 6. Tubulin β5, β-actin and vimentin were detected at high levels on day 4 with a significant 10-fold ($p < 0.05$), 22-fold ($p < 0.05$), and 17-fold ($p < 0.05$) increase from day 2 to day 4, respectively, and a subsequent decrease between days 4 and 6 by 0.9-fold ($p < 0.05$). Cytoskeleton associated protein 4 on the other hand peaked on day 2, followed by a 0.9-fold ($p < 0.05$) decrease from day 2 to day 4, while cofilin-1 increased significantly from day 4 to day 6 ($p < 0.05$). Tropomyosin was not detected on days 2 and 6 but rose to significant levels on day 4 ($p < 0.05$).

All of the proteins related to extracellular matrix/cell surface displayed an identical trend of high levels on day 2, followed by a steep decrease through day 6. Catenin α1, vinculin, integrin β1, laminin B1, cadherin 1, and cadherin 2 all exhibited a significant decrease from day 2 to day 4 by 0.9-fold ($p < 0.05$), 0.9-fold ($p < 0.05$), 1-fold ($p < 0.05$), and 1-fold ($p < 0.05$), respectively. Vinculin and integrin β1 significantly decreased from day 4 to day 6 ($p < 0.05$). Laminin B1, cadherin 1, and cadherin 2 were only counted on day 2 and were not detected on days 4 and 6.

High levels of stress proteins 60 kDa heat shock protein and 78 kDa glucose regulated protein were detected on day 2, and then gradually decreased through day 6 with a 0.8-fold ($p < 0.05$) and 1-fold ($p < 0.05$) decrease, respectively, from day 2 to day 4 and a 1-fold ($p < 0.05$) decrease from day 4 to day 6 for both proteins. Chaperone stress 70 protein was present at high levels on day 2 but its expression level dropped significantly as it was not expressed either on day 4 ($p < 0.05$) or day 6. Protein disulfide isomerase A6 displayed a significant 7-fold ($p < 0.05$) increase from 2 to 4 dpn and a 1 fold decrease between days 4 and 6 ($p < 0.05$), while protein disulfide isomerase A3 peaked on day 4 and significantly decreased 1-fold ($p < 0.05$) on day 6. There was a remarkable 61-fold increase of peptidyl-propyl cis-trans isomerase between days 4 and 6 ($p < 0.05$).

Western Blot Analysis of Hydrophobic Enamel Proteins Illustrated Continuously Increasing Amelogenin Levels from 1 dpn Until 8 dpn, While Enamelin Peaked on Days 1 and 2 dpn, and Ameloblastin on Days 1–5 dpn

As an alternative strategy and because of the hydrophilic bias of our proteomics technology, known enamel organ/enamel matrix protein complex samples were assayed using classic Western blot methodology (**Figures 5A,B**). There was a continuous increase in the 26 kDa amelogenin band in our enamel organ extracts from postnatal days 1 to 8. Ameloblastin levels were high and unchanged between postnatal days 1 to 5, featuring both 50 and 55 kDa bands. Beginning with day 6, overall ameloblastin levels were reduced, only the upper 55 kDa band was present, and several bands of lesser molecular weight than the 50 kDa band were detected in addition to the 55 kDa band. Enamelin levels (130 kDa band) were relatively high on postnatal days 1 and 2, and gradually diminished thereafter. The 46 kDa band specific for the enamel protease MMP20 was present at relatively high levels from days 1 to 3 postnatal, and intensity decreased from 4 days postnatal onward. The pH regulator carbonic anhydrase II peaked between postnatal days 2 and 4, reaching a maximum on postnatal day 3 on our Western blot, while it was present at lesser quantities on postnatal days 1 and 5–8 (all Western blot data illustrated in **Figures 5A,B**).

DISCUSSION

Here we have used the developing mouse mandibular molar as a model system to track changes in protein and mineral composition during postnatal amelogenesis and to correlate findings from individual protein and mineral analyses to synthesize an integrated systems perspective of enamel formation in the mouse molar. The key benefit of the postnatal mouse

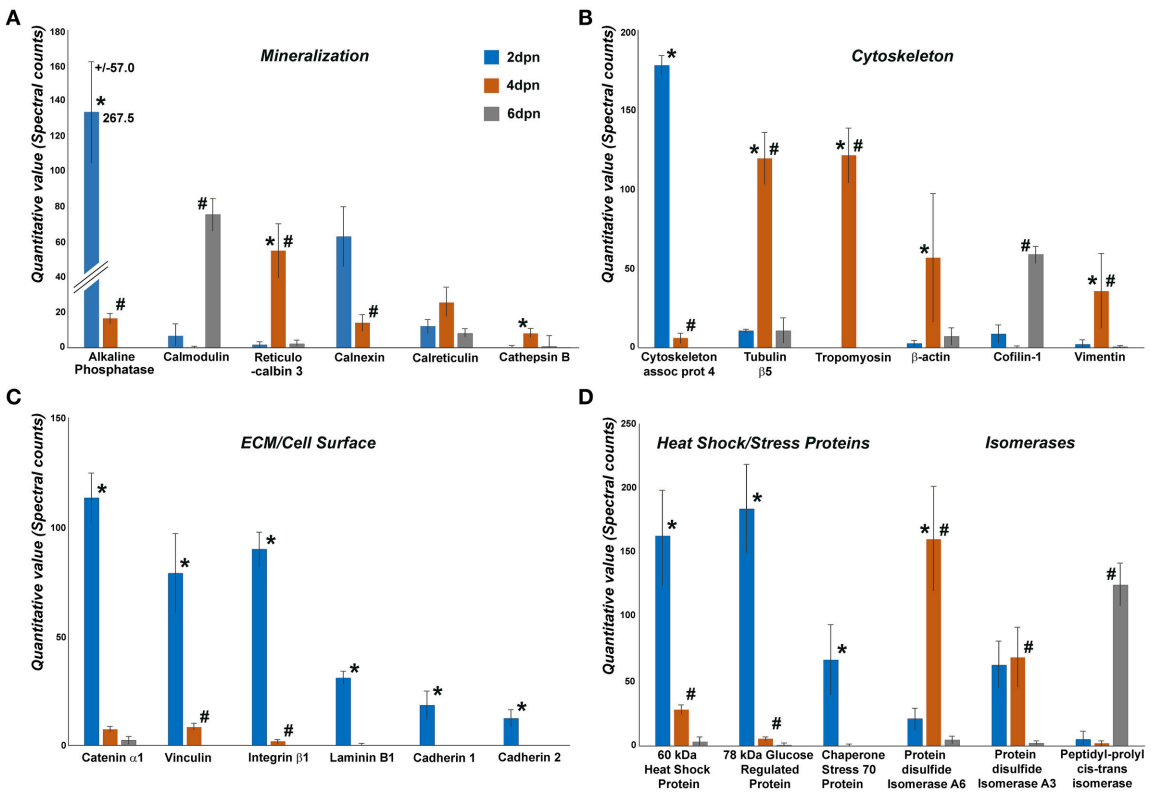

FIGURE 4 | Comparison between spectral counts of individual proteins identified during postnatal mouse molar enamel development (days 2, 4, and 6 dpn)(99% probability, 2 peptide minimum). Proteins were grouped into four categories: **(A)** mineralization, **(B)** cytoskeleton, **(C)** extracellular matrix/cell surface, and **(D)** other. Six proteins with highest quantitative values in each group were chosen for display and further analysis. Orbitrap mass spectrometry is inherently biased to exclude hydrophobic proteins (Carroll et al., 2007; Griffin and Schnitzer, 2011), promoting a methodological focus on hydrophilic proteins at the expense of the hydrophobic proteins that occupy the majority of the developing enamel matrix. Spectral counts of 2 dpn (blue), 4 dpn (yellow), and 6 dpn (gray) enamel matrix were distinguished by color coding, and levels of significance were marked as $^{*}p < 0.05$, for comparisons between 2 and 4 dpn data, and $^{\#}p < 0.05$, for comparisons between 4 and 6 dpn data.

molar model was the suitability of the distal slopes of first molar cusps to harvest sufficient quantities of fresh enamel matrix for proteomic and mineral composition analysis in daily increments. Moreover, the mouse mandibular molar has a long history as a model for morphogenesis, cytodifferentiation, and tissue specific biomineralization (Gaunt, 1955; Slavkin et al., 1976, 1988), allowing for cross-referencing between classic developmental biology data, mouse genetics models of amelogenesis, proteomics analysis databases, and the present systems biological study. The mouse molar model owes its popularity to its resemblance to the human molar in terms of completion of enamel formation following eruption and to the ubiquitous availability of mice and mouse genetic tools for experimental studies. In general, the mouse incisor would be equally attractive for studies of mammalian amelogenesis. However, for historical reasons and because of its larger size, the continuously erupting rat incisor has provided an alternative model for the study of enamel matrix and mineral composition during development (Schour and Massler, 1949; Robinson et al., 1979, 1981; Smith and Nanci, 1989). The rat incisor model relies on the preparation of sequential segments along the rat incisor labial surface representative of the entire sequence of amelogenesis from the youngest enamel at the root apex to the oldest enamel at the incisal edge (Robinson et al., 1997). We expect that amelogenesis in the continuously erupting rat incisor and in mouse molars of limited growth are highly similar because of the known similarities in the rat and mouse genomes, overall developmental patterns, and enamel mineral composition. In the present study, the mouse molar amelogenesis model was chosen because of the availability of mouse proteomics analysis tools and the feasibility of fresh enamel matrix preparation on successive days of postnatal amelogenesis.

We began our study by documenting the daily incremental increase in the thickness of enamel covering the distal slopes of the molar cusps between 1 dpn until 8 dpn. During this time, the semi-transparent enamel layer increased in thickness from 1 μm covering to 75 μm. Throughout those 8 days, the matrix was pliable and ideally suited for further biochemical analysis as it allowed for harvesting of the matrix and the attached enamel organ in bulk and in daily increments. The pliable nature of the developing enamel matrix has impressed naturalists and early biochemists since John Hunter's time (Hunter, 1778; Eastoe,

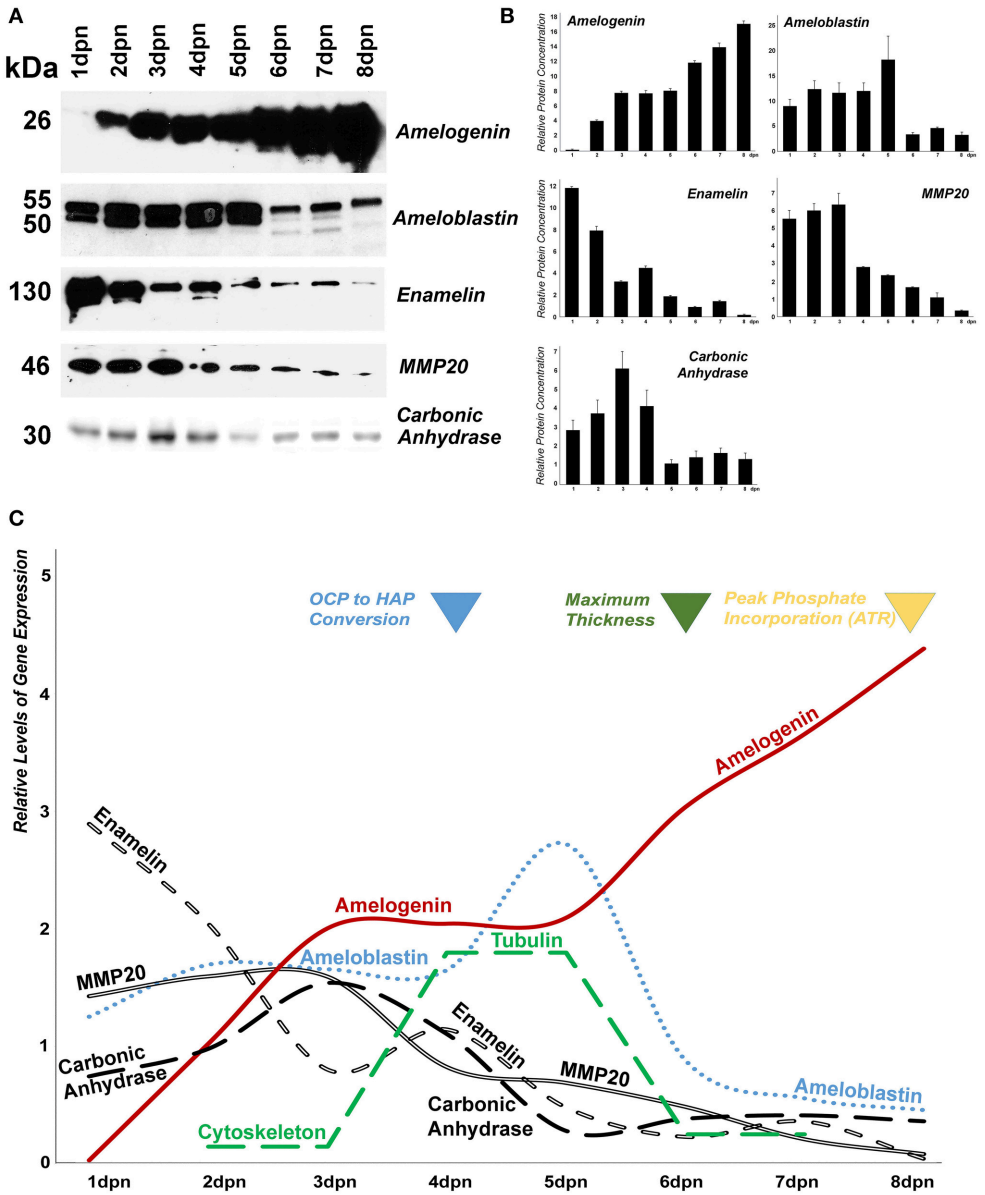

FIGURE 5 | Changes in mouse molar enamel matrix protein levels from postnatal day 1–8. **(A)** Changes in amelogenin, ameloblastin, enamelin, MMP20, and carbonic anhydrase II, protein levels in enamel matrix preparations as revealed by Western blot. **(B)** Densitometric evaluation of protein levels in the Western blot shown in **(A)**. **(C)** Sketch correlating changes in protein levels with changes in the enamel mineral phase.

1979; Termine et al., 1980), and as a result has been termed cheesy or cheese-like by the early enamel biochemists (Alan Fincham, personal communication). The mouse molar enamel matrix retained its opaque, soft, and cheese-like consistency throughout postnatal development, with the exception of postnatal day 8, when the hardening of the matrix began. At that stage, matrix birefringence was at its peak, causing the enamel matrix to appear in alternating polarization colors depending on the angle between polarizing and analyzing filters. Earlier studies have focused on the anisotropy of the enamel matrix during the secretory stage (Keil, 1935; Schmidt, 1959; Spears et al., 1993; Do Espirito Santo et al., 2006). The highly polarized structure of the enamel matrix is evidence of the highly ordered enamel matrix structure as it provides a template for the highly ordered enamel mineral layer as a biomechanical buffer to occlusal loads and stresses.

X-ray diffraction analysis unambiguously identified enamel matrix diffraction patterns from day 4 to day 8 postnatal as partially fluoride substituted hydroxyapatite, and apatite electron diffraction patterns of 6 and 7 dpn mouse molar enamel were confirmed in the present study and in earlier electron

diffraction studies (Diekwisch et al., 1995; Diekwisch, 1998). In contrast, X-ray diffraction patters from 1 to 2 dpn samples contained less prominent peaks that nevertheless matched the same overall partially fluoride substituted hydroxyapatite pattern of the samples from older enamel, and similarly, our earlier electron diffractions studies revealed fewer and less pronounced diffraction rings, suggesting that these earlier stages of enamel matrix maturation contain precursor phases of apatite maturation, such as octacalcium phosphate or tricalcium phosphate (Diekwisch et al., 1995; Aoba et al., 1998; Diekwisch, 1998). There were several non-identified peaks present in the 2 dpn sample, which were neither found in the 1 dpn sample nor in the 4–8 dpn samples, suggesting the presence of unusual intermediate phases during the transition from apatite precursors to fully mature hydroxyapatite. Together, these data demonstrate that the bulk of the distal slope first mandibular mouse molar enamel matrix converts from a lesser order of crystallinity into crystalline partially fluoride substituted hydroxyapatite between 2 and 4 dpn.

Our ATR data were interpreted according to previously published band assignments (Vignoles-Montrejaud, 1984; Elliot, 1994; Gadaleta et al., 1996; Boskey et al., 2006; Antonakos et al., 2007; Leventouri et al., 2009) and provide spectroscopic evidence for the structural conversion of the mouse molar enamel matrix from a mixed amorphous calcium phosphate/protein layer at 2 dpn to a crystalline hydroxyapatite structure featuring highly elongated crystals at 8 dpn. On a protein level, this change was accompanied by increased peak heights of the amide I and II bands, especially from postnatal day 6 to day 8, indicative of changes in protein secondary structure and increased rigidity of the peptide bonds between the carboxyl and the amino groups of two adjacent amino acids through an increase in the double bond character of the peptide bond, resulting in increased structural rigidity of the enamel protein matrix.

Our ATR data revealed dramatic changes in the phosphate region (800–1,100 cm^{-1}) in the postnatal mouse molar develop enamel matrix. Specifically, our data demonstrated a transition from a contoured plateau (1,000–1,100 cm^{-1}) indicative of amorphous calcium phosphate at 2 dpn to a single sharp and highly elevated peak (1,015 cm^{-1}) with shoulders at 1,105 and 958 cm^{-1} at 8 dpn representative of high crystalline hydroxyapatite with crystals featuring long c-axis dimensions (Gadaleta et al., 1996). These findings are in congruence with our previous studies suggestive of a gradual transition from amorphous calcium phosphate to highly ordered and elongated apatite crystals during amelogenesis through a process called Ostwald ripening (Diekwisch et al., 1995; Aoba et al., 1998; Diekwisch, 1998).

Moreover, there was strong evidence for carbonate substitution in the enamel matrix between postnatal days 6 and 8, as the peaks at 880 cm^{-1} (A-type carbonate) and 1,405 and 1,445 cm^{-1} (B-type carbonate) indicated. Carbonate is known to replace phosphate in biological apatites (Zapanta-Legeros, 1965; Wopenka and Pasteris, 2005), affects its physical properties, including decreased crystallinity and increased c-axis length (Fleet et al., 2004; Wopenka and Pasteris, 2005; Boskey et al., 2006) and mechanical properties, such as decreased hardness and Young's modulus (Morgan et al., 1997; Xu et al., 2012).

Our proteomic analysis provided only low counts for classic enamel proteins, which are known to be of hydrophobic nature (Eastoe, 1965), even though its most prominent member, amelogenin, comprises 80–90% of the developing enamel matrix protein composition (Fincham et al., 1999). This result is characteristic for unmodified proteomic studies, which have a systematic bias against hydrophobic proteins and membrane proteins and favor hydrophilic components instead (Santoni et al., 2000; Chandramouli and Qian, 2009; Josic, 2014). To address the systematic scarcity of hydrophobic proteins in proteomic datasets, classic Western blot studies of enamel protein expression from days 1 to 8 postnatal were performed. These studies demonstrated a continuous increase in amelogenin from day 1 to 8, relatively high levels of ameloblastin from days 1 to 5, peak enamelin protein level peaks on day 1 and 2, relatively high levels of MMP20 from days 1 to 3, and relatively high levels of carbonic anhydrase between postnatal days 2 and 4. These data underscore the continuous presence of amelogenin during the secretory stages of amelogenesis (Termine et al., 1980), while ameloblastin, enamelin, and MMP20 are only prominent during early secretory stage enamel development, possibly establishing a patterning template for enamel crystal and prism growth (Bartlett, 2013; Pugach et al., 2013; Zhu et al., 2014; Prajapati et al., 2016). Our Western blot data provided evidence for relatively high levels of carbonic anhydrase during early enamel development (days 1–4), indicative of a role for pH adjustment during initial crystal nucleation, while other regulators may be involved in the pH regulation during the massive elevation of phosphate and carbonate during late-stage crystal growth. In addition, the continuous increase in amelogenin during postnatal enamel development was also verified by our proteomics study, albeit at a lower level of counts due to its hydrophobicity. Three of the proteins analyzed in **Figure 4** (Calmodulin, Cofilin-1, and Peptidyl-prolyl cis-trans isomerase) featured higher levels of expression on days 2 and 6, and a substantial decline in protein counts on day 4. We interpret these data to indicate that such proteins may have dual functions during enamel ion transport and enamel crystal growth.

Disregarding the moderate counts for classic enamel proteins such as amelogenin, ameloblastin, and enamelin, our proteomics analysis detected a number of other proteins relevant for enamel mineralization during our 2–6 days postnatal mouse molar enamel matrix sampling window. Among these was the protein with the highest number of counts in our analysis, alkaline phosphatase, which peaked at day 2 during the early secretory stage. At the onset of amelogenesis, alkaline phosphatase may be involved in transporting phosphate from blood vessels near the stratum intermedium into the enamel organ by increasing local phosphate concentrations in the stratum intermedium via hydrolysis of phosphorylated substrates. Phosphatase mediated hydrolysis of pyrophosphate may also be involved in the generation of other phosphorylated macromolecules (Woltgens et al., 1995; Liu et al., 2016). The other mineralization-related protein with an early peak at 2 days postnatal was the protein

folding chaperone calnexin, which may play a role in the prevention of endoplasmic reticulum stress due to misfolded enamel proteins or in calcium transport (Wang et al., 2005; Brookes et al., 2014). Calreticulin, which peaked at postnatal day 4, is another enamel protein with a dual function misfolded protein processing and calcium transport (Somogyi et al., 2003) that was detected in our proteomics analysis. Two other calcium transport proteins, calmodulin and reticulocalbin-3, peaked on day 6 (maturation stage, calmodulin) or on day 4 (late secretory stage, reticulocalbin-3). Calmodulin and reticulocalbin are capable of binding calcium using an EF-hand motif, and this function may be related to the protein-mediated transport of calcium ions through the ameloblast cell layer. The most prominent enzyme in our proteomics analysis of mouse molar enamel organs was the lysosomal cysteine protease cathepsin B, which peaked on day 4 postnatal. Cathepsin B is an important lysosomal enzyme of the enamel matrix (Al Kawas et al., 1996; Tye et al., 2009) that has been shown to enhance the activity of other proteases such as metalloproteinases and cathepsin D (Hammarström et al., 1971; Blair et al., 1989). As such, cathepsin B may promote the proteolytic degradation of the enamel matrix by enhancing the activity of MMP20 and cathepsin D.

Four of the six high-scoring cytoskeletal proteins in the enamel organ, including actin, tubulin, tropomyosin, and vimentin isoforms, peaked at postnatal day 4 during the late secretory stage. Increased presence of cytoskeletal proteins during the late secretory stage is likely indicative of their role in cell polarization and vesicular secretion (Manneville et al., 2003; Neco et al., 2003; De Lisle, 2015). Highly specific actin and tubulin immunoreactivity in secretory ameloblasts has been reported earlier (Diekwisch, 1988; Kero et al., 2014). Cytoskeleton associated protein 4 (CLIMP63) is actually a transmembrane protein that is instrumental in anchoring the endoplasmic reticulum to microtubules (Vedrenne et al., 2005), and its early secretory stage expression matches that of other transmembrane proteins reported here (cadherin, catenin). In contrast, Cofilin-1 levels only became elevated during the resorptive maturation stage (6 dpn), which may be explained by its role in actin depolymerization (Maciver and Hussey, 2002; Morita et al., 2016). Vimentin has long been hailed as an intermediate filament protein marker of mesenchymal tissues (Kidd et al., 2014). However, our present study reports strong evidence for vimentin signals in the enamel organ, lending support to earlier studies about transitory vimentin expression in the stellate reticulum (Kasper et al., 1989; Kero et al., 2014). Together, our proteomic data provide strong evidence for high levels of cytoskeletal proteins at the late secretory stage, likely related to their role in ameloblast polarization and enamel matrix secretion.

Our proteomics data indicated that six high-scoring extracellular matrix/cell surface molecules identified in the present study all peaked on day 2 postnatal at the onset of the secretory stage. This group included the classic extracellular matrix molecule laminin, the integrin β1 cell surface receptor, the β-integrin binding extracellular matrix adhesion molecule vinculin, and three cell adhesion molecules of the catenin/cadherin complex. The presence of laminin as part of the ameloblast basal lamina at the dentin-enamel junction has been demonstrated to play a role in terminal odontoblast differentiation (Lesot et al., 1981), and this basal lamina is removed during further ameloblast differentiation, presumably facilitating enamel deposition in sarcopterygian vertebrates (Diekwisch et al., 2002). Based on previous studies, we speculate that both the adherens junction protein vinculin and its binding partner β-integrin function to establish the sliding interface between secretory ameloblasts that allows for ameloblast cell movements during prism formation (Kubler et al., 1988; Nishikawa et al., 1988, 1990; Xu et al., 1998; Saito et al., 2015). Three of the six significantly upregulated proteins belonged to the cadherin-based adherens junction complex, namely catenin α1 and cadherins 1 and 2. Catenins are known to interact with cadherins (Rangarajan and Izard, 2013) and provide a link between adherens junctions and the actin cytoskeleton (McCrea and Gu, 2010). In ameloblasts, E-cadherin appears to be involved in ameloblast polarization (Terling et al., 1998) and β-catenin is essential for ameloblast movement (Guan et al., 2016). A switch between E-cadherin and N-cadherin has been documented in ameloblasts that slide by each other to form decussating enamel rod patterns (Guan et al., 2014). Together, the high levels of adherens junction and matrix proteins in the early enamel organ are indicative of the involvements of these proteins at the early secretory stage of amelogenins.

Three heat shock/stress proteins also were among the high-scoring proteins that peaked at the onset of the secretory stage. These proteins included the 60 kDa heat shock protein (Hspd1), the 78 kDa glucose regulated protein (Grp-78), and the chaperone stress 70 protein (Hsp70). All three of these proteins are involved in macromolecular assembly, the prevention of misfolding, as well as the prevention of aggregation. One of the major challenges of amelogenesis is the transport of amelogenin, a protein prone to self-assembly (Zhang et al., 2011), through the ameloblast cells. It is likely that both Grp-78 and Hsp70 may be involved in the prevention of amelogenin self-assembly inside of the ameloblast cell body, as both proteins are known to prevent protein aggregation (Wegele et al., 2004; Mayer and Bukau, 2005), while Hspd1 might rather function to prevent amelogenin misfolding (Xu et al., 2006).

Three isomerases joined the list of high-scoring enamel proteins, including the protein disulfide isomerases A3 and A6, and the peptidyl-prolyl cis-trans isomerase. Disulfide isomerases (PDIs) catalyze protein folding by facilitating disulfide bond formation and arrangement (Kersteen and Raines, 2003), a process that apparently takes place during the entire secretory stage, as PDI peaks in our proteomics data indicate. In contrast, peptidyl-prolyl cis-trans isomerase interconverts the trans-isomers of newly synthesized peptide bonds into cis-isomers of higher biological activity (Herzberg and Moult, 1991; Pal and Chakrabarti, 1999; Balbach and Schmid, 2000; Shaw, 2002). Peptidyl-prolyl cis-trans isomerase function may play a role in the conformational modification of amelogenin and enable its role as a molecular hinge in the promotion of crystal growth (Delak et al., 2009).

In conclusion, this integrative proteomic/cell biological analysis of postnatal mouse molar enamel development identifies many of the substantial changes in the enamel matrix protein and mineral phase that take place during postnatal mouse molar amelogenesis, including (i) relatively high levels of matrix protein secretion during the early secretory stage on postnatal day 2, (ii) conversion of calcium phosphates to apatite, peak protein folding and stress protein counts, and increased cytoskeletal protein levels such as actin and tubulin on day 4, as well as (iii) secondary structure changes, isomerase activity, highest amelogenin levels, and peak phosphate/carbonate incorporation between postnatal days 6 and 8 (**Figure 5C**).

ETHICS STATEMENT

All animal experiments were approved by the IACUC committees at the University of Illinois, Chicago and Texas A&M College of Dentistry.

AUTHOR CONTRIBUTIONS

MP, WZ, and TD wrote the manuscript. SG, TK, XL and TD designed the experiments. MP, HL, SD, LL,WZ, SP, and RD performed the experiments. MA designed and performed the statistical analysis.

FUNDING

This study was supported by NIDCR grant DE018900 to TD.

ACKNOWLEDGMENTS

We thank Ms. C. Beck and Ms. K. Kuc for help with the X-ray analysis. Proteomics and informatics services were performed at the CBC-UIC Research Resources Center Mass Spectrometry, Metabolomics, and Proteomics Facility established in part by a grant from Searle Funds at the Chicago Community trust to the Chicago Biomedical Consortium.

REFERENCES

Al Kawas, S., Amizuka, N., Bergeron, J. J., and Warshawsky, H. (1996). Immunolocalization of the cation-independent mannose 6-phosphate receptor and cathepsin B in the enamel organ and alveolar bone of the rat incisor. *Calcif. Tissue Int.* 59, 192–199. doi: 10.1007/s002239900108

Antonakos, A., Liarokapis, E., and Leventouri, T. (2007). Micro-Raman and FTIR studies of synthetic and natural apatites. *Biomaterials* 28, 3043–3054. doi: 10.1016/j.biomaterials.2007.02.028

Aoba, T., Komatsu, H., Shimazu, Y., Yagishita, H., and Taya, Y. (1998). Enamel mineralization and an initial crystalline phase. *Connect. Tissue Res.* 38, 129–137. doi: 10.3109/03008209809017029

Balbach, J., and Schmid, F. X. (2000). Proline isomerization and its catalysis in protein folding. *Mech. Protein Fold.* 2, 212–249.

Bard, J. (2007). Systems developmental biology: the use of ontologies in annotating models and in identifying gene function within and across species. *Mamm. Genome* 18, 402–411. doi: 10.1007/s00335-007-9027-3

Bartlett, J. D. (2013). Dental enamel development: proteinases and their enamel matrix substrates. *ISRN Dent.* 2013:684607. doi: 10.1155/2013/684607

Bartlett, J. D., and Simmer, J. P. (1999). Proteinases in developing dental enamel. *Crit. Rev. Oral Biol. Med.* 10, 425–441. doi: 10.1177/10454411990100040101

Bartlett, J. D., and Smith, C. E. (2013). Modulation of cell-cell junctional complexes by matrix metalloproteinases. *J. Dent. Res.* 92, 10–17. doi: 10.1177/0022034512463397

Blair, H. C., Teitelbaum, S. L., Ghiselli, R., and Gluck, S. (1989). Osteoclastic bone resorption by a polarized vacuolar proton pump. *Science* 245, 855–858. doi: 10.1126/science.2528207

Boskey, A. L., Goldberg, M., Kulkarni, A., and Gomez, S. (2006). Infrared imaging microscopy of bone: illustrations from a mouse model of Fabry disease. *Biochim. Biophys. Acta* 1758, 942–947. doi: 10.1016/j.bbamem.2006.02.019

Brookes, S. J., Barron, M. J., Boot-Handford, R., Kirkham, J., and Dixon, M. J. (2014). Endoplasmic reticulum stress in amelogenesis imperfecta and phenotypic rescue using 4-phenylbutyrate. *Hum. Mol. Genet.* 23, 2468–2480. doi: 10.1093/hmg/ddt642

Carroll, J., Altman, M. C., Fearnley, I. M., and Walker, J. E. (2007). Identification of membrane proteins by tandem mass spectrometry of protein ions. *Proc. Natl. Acad. Sci. U.S.A.* 104, 14330–14335. doi: 10.1073/pnas.0706817104

Chandramouli, K., and Qian, P.-Y. (2009). Proteomics: challenges, techniques and possibilities to overcome biological sample complexity. *Hum. Genomics Proteomics* 2009:239204. doi: 10.4061/2009/239204

De Lisle, R. C. (2015). "Role of the actin cytoskeleton in acinar cell protein secretion," in *Pancreapedia: Exocrine Pancreas Knowledge Base.* doi: 10.3998/panc.2015.22

Deakins, M. (1942). Changes in the ash, water, and organic content of pig enamel during calcification. *J. Dent. Res.* 21, 429–435. doi: 10.1177/00220345420210050201

Delak, K., Harcup, C., Lakshminarayanan, R., Sun, Z., Fan, Y., Moradian-Oldak, J., et al. (2009). The tooth enamel protein, porcine amelogenin, is an intrinsically disordered protein with an extended molecular configuration in the monomeric form. *Biochemistry* 48, 2272–2281. doi: 10.1021/bi802175a

Diekwisch, T. (1988). Localization of microfilaments and microtubules during dental development in the rat. *Acta Histochem. Suppl.* 37, 209–212.

Diekwisch, T., David, S., Bringas, P., Santos, V., and Slavkin, H. C. (1993). Antisense inhibition of AMEL translation demonstrates supramolecular controls for enamel HAP crystal growth during embryonic mouse molar development. *Development* 117, 471–482.

Diekwisch, T. G. (1998). Subunit compartments of secretory stage enamel matrix. *Connect. Tissue Res.* 38, 101–111. doi: 10.3109/03008209809017026

Diekwisch, T. G., Berman, B. J., Anderton, X., Gurinsky, B., Ortega, A. J., Satchell, P. G., et al. (2002). Membranes, minerals, and proteins of developing vertebrate enamel. *Microsc. Res. Tech.* 59, 373–395. doi: 10.1002/jemt.10218

Diekwisch, T. G., Berman, B. J., Gentner, S., and Slavkin, H. C. (1995). Initial enamel crystals are not spatially associated with mineralized dentine. *Cell Tissue Res.* 279, 149–167. doi: 10.1007/BF00300701

Do Espirito Santo, A. R., Novaes, P. D., and Line, S. R. (2006). Anisotropic properties of the enamel organic extracellular matrix. *Eur. J. Oral Sci.* 114, 333–337. doi: 10.1111/j.1600-0722.2006.00326.x

Eastoe, J. (1979). Enamel protein chemistry-past, present and future. *J. Dent. Res.* 58, 753–764. doi: 10.1177/00220345790580022701

Eastoe, J. E. (1965). The chemical composition of bone and teeth. *Adv. Fluorine Res. Dent. Caries Prevent.* 3, 5–17.

Edelman, L. B., Chandrasekaran, S., and Price, N. D. (2009). Systems biology of embryogenesis. *Reprod. Fertil. Dev.* 22, 98–105. doi: 10.1071/RD09215

Elliot, J. C. (ed.). (1994). "Mineral, synthetic and biological carbonate apatites," in *Structure and Chemistry of Apatites and Other Calcium Orthophosphates* (Amsterdam: Elsevier), 191–304.

Fincham, A., Moradian-Oldak, J. P., and Simmer, J. (1999). The structural biology of the developing dental enamel matrix. *J. Struct. Biol.* 126, 270–299. doi: 10.1006/jsbi.1999.4130

Fleet, M. E., Liu, X., and King, P. L. (2004). Accommodation of the carbonate ion in apatite: An FTIR and X-ray structure study of crystals synthesized at 2–4 GPa. *Am. Mineral.* 89, 1422–1432. doi: 10.2138/am-2004-1009

Gadaleta, S. J., Paschalis, E. P., Betts, F., Mendelsohn, R., and Boskey, A. L. (1996). Fourier transform infrared spectroscopy of the solution-mediated conversion of amorphous calcium phosphate to hydroxyapatite: new correlations between X-ray diffraction and infrared data. *Calcif. Tissue Int.* 58, 9–16. doi: 10.1007/BF02509540

Gaunt, W. A. (1955). The development of the molar pattern of the mouse (*Mus musculus*). *Cells Tissues Organs* 24, 249–268. doi: 10.1159/000141046

Gibson, C. W., Yuan, Z.-A., Hall, B., Longenecker, G., Chen, E., Thyagarajan, T., et al. (2001). Amelogenin-deficient mice display an amelogenesis imperfecta phenotype. *J. Biol. Chem.* 276, 31871–31875. doi: 10.1074/jbc.M104624200

Gopinathan, G., Jin, T., Liu, M., Li, S., Atsawasuwan, P., Galang, M.-T., et al. (2014). The expanded amelogenin polyproline region preferentially binds to apatite versus carbonate and promotes apatite crystal elongation. *Front. Physiol.* 5:430. doi: 10.3389/fphys.2014.00430

Griffin, N. M., and Schnitzer, J. E. (2011). Overcoming key technological challenges in using mass spectrometry for mapping cell surfaces in tissues. *Mol. Cell. Proteomics* 10:R110. 000935. doi: 10.1074/mcp.R110.000935

Guan, X., Bidlack, F. B., Stokes, N., and Bartlett, J. D. (2014). E-Cadherin can replace N-cadherin during secretory-stage enamel development. *PLoS ONE* 9:e102153. doi: 10.1371/journal.pone.0102153

Guan, X., Xu, M., Millar, S. E., and Bartlett, J. D. (2016). Beta-catenin is essential for ameloblast movement during enamel development. *Eur. J. Oral Sci.* 124, 221–227. doi: 10.1111/eos.12261

Guggenheim, S. (2005). *Simulations of Debye-Scherrer and Gandolfi Patterns Using a Bruker SMART/APEX Diffractometer System*. Bruker-AXS Application Notes Series 373, 1–8.

Hammarström, L. E., Hanker, J. S., Toverud, S. U. (1971). Cellular differences in acid phosphatase isoenzymes in bone and teeth. *Clin. Orthop. Relat. Res.* 78, 151–167. doi: 10.1097/00003086-197107000-00012

Herzberg, O., and Moult, J. (1991). Analysis of the steric strain in the polypeptide backbone of protein molecules. *Proteins* 11, 223–229. doi: 10.1002/prot.340110307

Hu, J. C., Hu, Y., Lu, Y., Smith, C. E., Lertlam, R., Wright, J. T., et al. (2014). Enamelin is critical for ameloblast integrity and enamel ultrastructure formation. *PLoS ONE* 9:e89303. doi: 10.1371/journal.pone.0089303

Hubbard, M. J. (2000). Calcium transport across the dental enamel epithelium. *Crit. Rev. Oral Biol. Med.* 11, 437–466. doi: 10.1177/10454411000110040401

Hughes, J. M., Cameron, M., and Mariano, A. N. (1991). Rare-earth-element ordering and structural variations in natural rare-earth-bearing apatites. *Am. Mineral.* 76, 1165–1173.

Hunter, J. (1778). *The Natural History of the Human Teeth: Explaining their Structure, Use, Formation, Growth, and Diseases. Illustrated with Copper-Plates.* London: J. Johnson.

Iijima, M., and Moradian–Oldak, J. (2004). Interactions of amelogenins with octacalcium phosphate crystal faces are dose dependent. *Calcif. Tissue Int.* 74, 522–531. doi: 10.1007/s00223-002-0011-3

Jin, T., Ito, Y., Luan, X., Dangaria, S., Walker, C., Allen, M., et al. (2009). Elongated polyproline motifs facilitate enamel evolution through matrix subunit compaction. *PLoS Biol.* 7:e1000262. doi: 10.1371/journal.pbio.1000262

Josic, D. (2014). Strategies for complete proteomic analysis of hydrophobic proteins in complex biological samples-hyde-and seek. *J. Data Mining Genomics Proteomics* 5:1. doi: 10.4172/2153-0602.1000e111

Kasper, M., Karsten, U., Stoslek, P., and Moll, R. (1989). Distribution of intermediate-filament proteins in the human enamel organ: unusually complex pattern of coexpression of cytokeratin polypeptides and vimentin. *Differentiation* 40, 207–214. doi: 10.1111/j.1432-0436.1989.tb00600.x

Keil, A. (1935). Über den wandel der doppelbrechung des zahnschmelzes bei entkalkung, wärmeeinwirkung und karies. *Cell Tissue Res.* 22, 633–649.

Kero, D., Govorko, D., Vukojevic, K., Cubela, M., Soljic, V., and Saraga-Babic, M. (2014). Expression of cytokeratin 8, vimentin, syndecan-1 and Ki-67 during human tooth development. *J. Mol. Histol.* 45, 627–640. doi: 10.1007/s10735-014-9592-1

Kersteen, E. A., and Raines, R. T. (2003). Catalysis of protein folding by protein disulfide isomerase and small-molecule mimics. *Antioxid. Redox Signal.* 5, 413–424. doi: 10.1089/152308603768295159

Kidd, M. E., Shumaker, D. K., and Ridge, K. M. (2014). The role of vimentin intermediate filaments in the progression of lung cancer. *Am. J. Respir. Cell Mol. Biol.* 50, 1–6. doi: 10.1165/rcmb.2013-0314TR

Klug, H. P., and Alexander, L. E. (1954). *X-Ray Diffraction Procedures.* New York, NY: Wiley-Interscience.

Kubler, M.-D., Lesot, H., and Ruch, J. V. (1988). Temporo-spatial distribution of matrix and microfilament components during odontoblast and ameloblast differentiation. *Dev. Genes Evol.* 197, 212–220. doi: 10.1007/BF02439428

Lacruz, R. S. (2017). Enamel: molecular identity of its transepithelial ion transport system. *Cell Calcium*. 65, 1–7. doi: 10.1016/j.ceca.2017.03.006

Lacruz, R. S., Nanci, A., Kurtz, I., Wright, J. T., and Paine, M. L. (2010). Regulation of pH during amelogenesis. *Calcif. Tissue Int.* 86, 91–103. doi: 10.1007/s00223-009-9326-7

Lagerström, M., Dahl, N., Nakahori, Y., Nakagome, Y., Bäckman, B., Landegren, U., et al. (1991). A deletion in the amelogenin gene (AMG) causes X-linked amelogenesis imperfecta (AIH1). *Genomics* 10, 971–975. doi: 10.1016/0888-7543(91)90187-J

Lesot, H., Osman, M., and Ruch, J. V. (1981). Immunofluorescent localization of collagens, fibronectin, and laminin during terminal differentiation of odontoblasts. *Dev. Biol.* 82, 371–381. doi: 10.1016/0012-1606(81)90460-7

Leventouri, T., Antonakos, A., Kyriacou, A., Venturelli, R., Liarokapis, E., and Perdikatsis, V. (2009). Crystal structure studies of human dental apatite as a function of age. *Int. J. Biomater.* 2009:698547. doi: 10.1155/2009/698547

Liu, H., Yan, X., Pandya, M., Luan, X., and Diekwisch, T. G. (2016). Daughters of the enamel organ: development, fate, and function of the stratum intermedium, stellate reticulum, and outer enamel epithelium. *Stem Cells Dev.* 25, 1580–1590. doi: 10.1089/scd.2016.0267

Lu, X., Ito, Y., Kulkarni, A., Gibson, C., Luan, X., and Diekwisch, T. G. (2011). Ameloblastin-rich enamel matrix favors short and randomly oriented apatite crystals. *Eur. J. Oral Sci.* 119, 254–260. doi: 10.1111/j.1600-0722.2011.00905.x

Maciver, S. K., and Hussey, P. J. (2002). The ADF/cofilin family: actin-remodeling proteins. *Genome Biol.* 3:reviews3007.1. doi: 10.1186/gb-2002-3-5-reviews3007

Manneville, J.-B., Etienne-Manneville, S., Skehel, P., Carter, T., Ogden, D., and Ferenczi, M. (2003). Interaction of the actin cytoskeleton with microtubules regulates secretory organelle movement near the plasma membrane in human endothelial cells. *J. Cell Sci.* 116, 3927–3938. doi: 10.1242/jcs.00672

Masuya, H., Shimizu, K., Sezutsu, H., Sakuraba, Y., Nagano, J., Shimizu, A., et al. (2005). Enamelin (Enam) is essential for amelogenesis: ENU-induced mouse mutants as models for different clinical subtypes of human amelogenesis imperfecta (AI). *Hum. Mol. Genet.* 14, 575–583. doi: 10.1093/hmg/ddi054

Mayer, M. P., and Bukau, B. (2005). Hsp70 chaperones: cellular functions and molecular mechanism. *Cel. Mol. Life Sci.* 62:670. doi: 10.1007/s00018-004-4464-6

McCrea, P. D., and Gu, D. (2010). The catenin family at a glance. *J. Cell Sci.* 123, 637–642. doi: 10.1242/jcs.039842

Mochida, K., and Shinozaki, K. (2011). Advances in omics and bioinformatics tools for systems analyses of plant functions. *Plant Cell Physiol.* 52, 2017–2038. doi: 10.1093/pcp/pcr153

Moradian-Oldak, J. (2012). Protein-mediated enamel mineralization. *Front. Biosci.* 17:1996. doi: 10.2741/4034

Morgan, E. F., Yetkinler, D. N., Constantz, B. R., and Dauskardt, R. H. (1997). Mechanical properties of carbonated apatite bone mineral substitute: strength, fracture and fatigue behaviour. *J. Mat. Sci.* 8, 559–570.

Morita, R., Kihira, M., Nakatsu, Y., Nomoto, Y., Ogawa, M., Ohashi, K., et al. (2016). Coordination of cellular dynamics contributes to tooth epithelium deformations. *PLoS ONE* 11:e0161336. doi: 10.1371/journal.pone.0161336

Neco, P., Giner, D., del Mar Frances, M., Viniegra, S., Gutiérrez, L. M. (2003). Differential participation of actin-and tubulin-based vesicle transport systems during secretion in bovine chromaffin cells. *Eur. J. Neurosci.* 18, 733–742. doi: 10.1046/j.1460-9568.2003.02801.x

Nishikawa, S., Fujiwara, K., and Kitamura, H. (1988). Formation of the tooth enamel rod pattern and the cytoskeletal organization in secretory ameloblasts of the rat incisor. *Eur. J. Cell Biol.* 47, 222–232.

Nishikawa, S., Tsukita, S., Tsukita, S., and Sasa, S. (1990). Localization of adherens junction proteins along the possible sliding interface between secretory ameloblasts of the rat incisor. *Cell Struct. Funct.* 15, 245–249. doi: 10.1247/csf.15.245

Paine, M. L., White, S. N., Luo, W., Fong, H., Sarikaya, M., and Snead, M. L. (2001). Regulated gene expression dictates enamel structure and tooth function. *Matrix Biol.* 20, 273–292. doi: 10.1016/S0945-053X(01)00153-6

Pal, D., and Chakrabarti, P. (1999). Cis peptide bonds in proteins: residues involved, their conformations, interactions and locations. *J. Mol. Biol.* 294, 271–288. doi: 10.1006/jmbi.1999.3217

Prajapati, S., Tao, J., Ruan, Q., De Yoreo, J. J., and Moradian-Oldak, J. (2016). Matrix metalloproteinase-20 mediates dental enamel biomineralization by preventing protein occlusion inside apatite crystals. *Biomaterials* 75, 260–270. doi: 10.1016/j.biomaterials.2015.10.031

Pugach, M. K., Suggs, C., Li, Y., Wright, J. T., Kulkarni, A. B., Bartlett, J. D., et al. (2013). M180 amelogenin processed by MMP20 is sufficient for decussating murine enamel. *J. Dent. Res.* 92, 1118–1122. doi: 10.1177/0022034513506444

Rangarajan, E. S., and Izard, T. (2013). Dimer asymmetry defines α-catenin interactions. *Nat. Struct. Mol. Biol.* 20, 188–193. doi: 10.1038/nsmb.2479

Robinson, C. (2014). Enamel maturation: a brief background with implications for some enamel dysplasias. *Front. Physiol.* 5:388. doi: 10.3389/fphys.2014.00388

Robinson, C., Briggs, H. D., Atkinson, P. J., and Weatherell, J. A. (1979). Matrix and mineral changes in developing enamel. *J. Dent. Res.* 58, 871–882. doi: 10.1177/00220345790580024101

Robinson, C., Brookes, S. J., Bonass, W. A., Shore, R. C., and Kirkham, J. (1997). Enamel maturation. *Ciba Found. Symp.* 205, 156–170; discussion: 170–174.

Robinson, C., Fuchs, P., and Weatherell, J. (1981). The appearance of developing rat incisor enamel using a freeze fracturing technique. *J. Cryst. Growth* 53, 160–165. doi: 10.1016/0022-0248(81)90062-2

Robinson, C., Fuchs, P., Deutsch, D., and Weatherell, J. (1978). Four chemically distinct stages in developing enamel from bovine incisor teeth. *Caries Res.* 12, 1–11. doi: 10.1159/000260309

Robinson, C., Kirkham, J., and Hallsworth, A. (1988). Volume distribution and concentration of protein, mineral and water in developing bovine enamel. *Arch. Oral Biol.* 33, 159–162. doi: 10.1016/0003-9969(88)90040-4

Saito, K., Fukumoto, E., Yamada, A., Yuasa, K., Yoshizaki, K., Iwamoto, T., et al. (2015). Interaction between fibronectin and β1 integrin is essential for tooth development. *PLoS ONE* 10:e0121667. doi: 10.1371/journal.pone.0121667

Santoni, V., Molloy, M., and Rabilloud, T. (2000). Membrane proteins and proteomics: un amour impossible? *Electrophoresis* 21, 1054–1070. doi: 10.1002/(SICI)1522-2683(20000401)21:6<1054::AID-ELPS1054>3.0.CO;2-8

Schmidt, W. (1959). Texturdoppelbrechung der organischen Matrix fertigen menschlichen schmelzes nebst bemerkungen zur optik entkalkten dentins. *Cell Tissue Res.* 49, 319–329. doi: 10.1007/BF00334730

Schour, I., and Massler, M. (1949). "The teeth," in *The Rat in Laboratory Investigation*, eds E. J. Farras and J. Q. Griffith (New York, NY: Hafner Publishing), 104–165.

Shaw, P. E. (2002). Peptidyl-prolyl isomerases: a new twist to transcription. *EMBO Rep.* 3, 521–526. doi: 10.1093/embo-reports/kvf118

Simmer, J. P., and Hu, J. C. (2002). Expression, structure, and function of enamel proteinases. *Connect. Tissue Res.* 43, 441–449. doi: 10.1080/03008200290001159

Slavkin, H. C., Bessem, C., Bringas, P., Zeichner-David, M., Nanci, A., and Snead, M. L. (1988). Sequential expression and differential function of multiple enamel proteins during fetal, neonatal, and early postnatal stages of mouse molar organogenesis. *Differentiation* 37, 26–39. doi: 10.1111/j.1432-0436.1988.tb00793.x

Slavkin, H. C., Mino, W., and Bringas, P. (1976). The biosynthesis and secretion of precursor enamel protein by ameloblasts as visualized by autoradiography after tryptophan administration. *Anat. Rec.* 185, 289–312. doi: 10.1002/ar.1091850304

Smith, C. E., and Nanci, A. (1989). A method for sampling the stages of amelogenesis on mandibular rat incisors using the molars as a reference for dissection. *Anat. Rec.* 225, 257–266. doi: 10.1002/ar.1092250312

Somogyi, E., Petersson, U., Hultenby, K., and Wendel, M. (2003). Calreticulin—an endoplasmic reticulum protein with calcium-binding activity is also found in the extracellular matrix. *Matrix Biol.* 22, 179–191. doi: 10.1016/S0945-053X(02)00117-8

Spears, I. R., Van Noort, R., Crompton, R. H., Cardew, G. E., and Howard, I. C. (1993). The effects of enamel anisotropy on the distribution of stress in a tooth. *J. Dent. Res.* 72, 1526–1531. doi: 10.1177/00220345930720111101

Stack, M. (1960). Changes in the organic matrix of enamel during growth. *J. Bone Jt. Surg. B* 42B, 853.

Takagi, Y., Fujita, H., Katano, H., Shimokawa, H., and Kuroda, T. (1998). Immunochemical and biochemical characteristics of enamel proteins in hypocalcified amelogenesis imperfecta. *Oral Surg. Oral Med. Oral Pathol. Oral Radiol. Endodontol.* 85, 424–430. doi: 10.1016/S1079-2104(98)90068-3

Terling, C., Heymann, R., Rozell, B., Öbrink, B., and Wroblewski, J. (1998). Dynamic expression of E-cadherin in ameloblasts and cementoblasts in mice. *Eur. J. Oral Sci.* 106, 137–142. doi: 10.1111/j.1600-0722.1998.tb02166.x

Termine, J. D., Belcourt, A. B., Christner, P. J., Conn, K. M., and Nylen, M. U. (1980). Properties of dissociatively extracted fetal tooth matrix proteins. I. Principal molecular species in developing bovine enamel. *J. Biol. Chem.* 255, 9760–9768.

Tye, C. E., Lorenz, R. L., and Bartlett, J. D. (2009). Lysosomal protease expression in mature enamel. *Cells Tissues Organs* 189, 111–114. doi: 10.1159/000151431

Vedrenne, C., Klopfenstein, D. R., and Hauri, H.-P. (2005). Phosphorylation controls CLIMP-63–mediated anchoring of the endoplasmic reticulum to microtubules. *Mol. Biol. Cell* 16, 1928–1937. doi: 10.1091/mbc.E04-07-0554

Vignoles-Montrejaud, M. (1984). *Contibution a l'Etude des Apatites Carbonate es de Type B.* These d'Etat, Institut National Polytechnique de Toulouse.

Wang, H., Tannukit, S., Zhu, D., Snead, M. L., and Paine, M. L. (2005). Enamel matrix protein interactions. *J. Bone Miner. Res.* 20, 1032–1040. doi: 10.1359/JBMR.050111

Wegele, H., Müller, L., and Buchner, J. (2004). Hsp70 and Hsp90—a relay team for protein folding. *Rev. Physiol. Biochem. Pharmacol.* 151, 1–44. doi: 10.1007/s10254-003-0021-1

Woltgens, J. H., Lyaruu, D. M., Bronckers, A. L., Bervoets, T. J., and Van Duin, M. (1995). Biomineralization during early stages of the developing tooth *in vitro* with special reference to secretory stage of amelogenesis. *Int. J. Dev. Biol.* 39, 203–212.

Wopenka, B., and Pasteris, J. D. (2005). A mineralogical perspective on the apatite in bone. *Mater. Sci. Eng. C* 25, 131–143. doi: 10.1016/j.msec.2005.01.008

Xu, C., Reed, R., Gorski, J. P., Wang, Y., and Walker, M. P. (2012). The distribution of carbonate in enamel and its correlation with structure and mechanical properties. *J. Mater. Sci.* 47, 8035–8043. doi: 10.1007/s10853-012-6693-7

Xu, W., Coll, J.-L., and Adamson, E. D. (1998). Rescue of the mutant phenotype by reexpression of full-length vinculin in null F9 cells; effects on cell locomotion by domain deleted vinculin. *J. Cell Sci.* 111, 1535–1544.

Xu, X.-H., Zhang, H.-L., Han, R., Gu, Z.-L., and Qin, Z.-H. (2006). Enhancement of neuroprotection and heat shock protein induction by combined prostaglandin A 1 and lithium in rodent models of focal ischemia. *Brain Res.* 1102, 154–162. doi: 10.1016/j.brainres.2006.04.111

Zapanta-Legeros, R. (1965). Effect of carbonate on the lattice parameters of apatite. *Nature* 206, 403–404. doi: 10.1038/206403a0

Zhang, X., Ramirez, B. E., Liao, X., and Diekwisch, T. G. (2011). Amelogenin supramolecular assembly in nanospheres defined by a complex helix-coil-PPII helix 3D-structure. *PLoS ONE* 6:e24952. doi: 10.1371/journal.pone.0024952

Zhu, L., Liu, H., Witkowska, H. E., Huang, Y., Tanimoto, K., and Li, W. (2014). Preferential and selective degradation and removal of amelogenin adsorbed on hydroxyapatites by MMP20 and KLK4 *in vitro*. *Front. Physiol.* 5:268. doi: 10.3389/fphys.2014.00268

Conflict of Interest Statement: The authors declare that the research was conducted in the absence of any commercial or financial relationships that could be construed as a potential conflict of interest.

Copyright © 2017 Pandya, Liu, Dangaria, Zhu, Li, Pan, Abufarwa, Davis, Guggenheim, Keiderling, Luan and Diekwisch. This is an open-access article distributed under the terms of the Creative Commons Attribution License (CC BY). The use, distribution or reproduction in other forums is permitted, provided the original author(s) or licensor are credited and that the original publication in this journal is cited, in accordance with accepted academic practice. No use, distribution or reproduction is permitted which does not comply with these terms.

frontiers in Physiology

ORIGINAL RESEARCH
published: 21 July 2017
doi: 10.3389/fphys.2017.00524

Beyond the Map: Enamel Distribution Characterized from 3D Dental Topography

Ghislain Thiery[1,2]*, *Vincent Lazzari*[1], *Anusha Ramdarshan*[1] and *Franck Guy*[1]

[1] iPHEP UMR Centre National de la Recherche Scientifique 7262 INEE, Université de Poitiers, Poitiers, France, [2] School of Sociology and Anthropology, Sun Yat-Sen University, Guangzhou, China

Enamel thickness is highly susceptible to natural selection because thick enamel may prevent tooth failure. Consequently, it has been suggested that primates consuming stress-limited food on a regular basis would have thick-enameled molars in comparison to primates consuming soft food. Furthermore, the spatial distribution of enamel over a single tooth crown is not homogeneous, and thick enamel is expected to be more unevenly distributed in durophagous primates. Still, a proper methodology to quantitatively characterize enamel 3D distribution and test this hypothesis is yet to be developed. Unworn to slightly worn upper second molars belonging to 32 species of anthropoid primates and corresponding to a wide range of diets were digitized using high resolution microcomputed tomography. In addition, their durophagous ability was scored from existing literature. 3D average and relative enamel thickness were computed based on the volumetric reconstruction of the enamel cap. Geometric estimates of their average and relative enamel-dentine distance were also computed using 3D dental topography. Both methods gave different estimations of average and relative enamel thickness. This study also introduces pachymetric profiles, a method inspired from traditional topography to graphically characterize thick enamel distribution. Pachymetric profiles and topographic maps of enamel-dentine distance are combined to assess the evenness of thick enamel distribution. Both pachymetric profiles and topographic maps indicate that thick enamel is not significantly more unevenly distributed in durophagous species, except in Cercopithecidae. In this family, durophagous species such as mangabeys are characterized by an uneven thick enamel and high pachymetric profile slopes at the average enamel thickness, whereas non-durophagous species such as colobine monkeys are not. These results indicate that the distribution of thick enamel follows different patterns across anthropoids. Primates might have developed different durophagous strategies to answer the selective pressure exerted by stress-limited food.

Keywords: 3DAET, 3DRET, dental topography, enamel thickness, pachymetric profile

OPEN ACCESS

Edited by:
Alexandre Rezende Vieira, University of Pittsburgh, United States

Reviewed by:
Anna Kallistova, Charles University in Prague, Czechia
Mine Koruyucu, Istanbul University, Turkey

***Correspondence:**
Ghislain Thiery
ghislain.thiery@ntymail.com

Specialty section:
This article was submitted to Craniofacial Biology and Dental Research, a section of the journal Frontiers in Physiology

Received: *30 May 2017*
Accepted: *07 July 2017*
Published: *21 July 2017*

Citation:
Thiery G, Lazzari V, Ramdarshan A and Guy F (2017) Beyond the Map: Enamel Distribution Characterized from 3D Dental Topography. Front. Physiol. 8:524. doi: 10.3389/fphys.2017.00524

INTRODUCTION

Teeth are often used by mammals to ingest, reduce, and fragment food that would be difficult or even impossible to digest otherwise (Lucas, 2004; Berthaume, 2016). In turn, the physical and structural properties of the food exert a selective pressure on dental morphology, especially on enamel. As a result, dental enamel is one of the hardest organic tissues found in mammals

(Kallistová et al., 2017). For example, human enamel hardness ranges from 2 to >6 GPa (Cuy et al., 2002; Roy and Basu, 2008; Zhao et al., 2013) depending on whether hardness is measured by indentation depth or by the distance to the enamel-dentine junction. Young's modulus values range from 60 to 130 GPa (Cuy et al., 2002; Braly et al., 2007; Zhao et al., 2013). For a more detailed review, see Zhang et al. (2014). In contrast, Chun et al. (2014) estimated that human dentine was around 4.2 times softer. Also, the energy due to strain dissipates with more ease in enamel compared to solids having a fixed strength, and enamel is capable of self-recovery after unloading (Zhao et al., 2013). All these enamel properties prevent the tooth from fracturing despite repetitively clashing against (sometimes challenging) food objects.

One of these dietary challenges comes from *hard* food i.e., food items that are resistant to plastic deformation in the first place. Primates have been reported to ingest two kinds of hard particles (Rabenold and Pearson, 2011).

(1) Small hard food particles (5–50 μm in size) such as phytoliths, enamel chips, or quartz dust. These "abrasive foods" can be accidentally ingested and are suggested to be one major actor of dental wear (Lucas et al., 2014);
(2) Large hard food particles (2–20 mm), such as nuts and seeds, can resist high global stress before failing, which can expose the tooth to catastrophic fracture. This definition of hardness differs from the one used in mechanical science, in which hard objects would only resist localized plastic deformation (Berthaume, 2016). In order to avoid the confusion, this work refers to large hard food particles as stress-limited foods (Lucas et al., 2000).

While challenging foods are generally avoided by primates (Milton, 1979; Waterman et al., 1988; Hill and Lucas, 1996; Lucas et al., 2000), some species such as *Pithecia*, *Pongo,* or *Cercocebus* are durophagous and are thus expected to show dental adaptations to stress-limited food, including a relatively thicker enamel than non-durophagous species (Vogel et al., 2008; Norconk and Veres, 2011; McGraw et al., 2014). Indeed, a thick enamel lessens the deformation due to strain (Lucas et al., 2008). The higher the stress which enamel is supposed to withstand during the initial power stroke, the thicker the enamel is expected to be. This is consistent with the fact that most durophagous primates have a significantly thicker enamel compared with soft-food consumers of the same size (Molnar and Gantt, 1977; Kay, 1981; Martin, 1983, 1985; Dumont, 1995; Shellis et al., 1998; Lambert et al., 2004; Vogel et al., 2008; Constantino et al., 2011; Strait et al., 2013; McGraw et al., 2014; Smith et al., 2015; but see Pampush et al., 2013).

Furthermore, enamel thickness has been described as an adaptation toward consuming abrasive foods. The thicker the enamel, the longer its lifetime in spite of wear (Maas, 1991; Teaford et al., 1996) and the later dentine will be exposed (Osborn, 1981; Macho and Spears, 1999; Rabenold and Pearson, 2011). This is consistent with the fact that primates consuming very abrasive foods, such as *Daubentonia madagascariensis* or *Sapajus apella*, have a very thick enamel (Rabenold and Pearson, 2011).

It has also been suggested that a thick enamel could emerge as a fast adaptive answer to tough food consumption (Olejniczak et al., 2008; Ungar and Hlusko, 2016). Enamel thickness can indeed change over a few generations (Le Luyer et al., 2014). Still, this assumption requires further investigation.

A large number of studies have dealt with the quantification of enamel thickness, especially in molars, partly because of molar enamel's susceptibility to natural selection but also its importance as a taxonomic trait (Martin, 1985; Macho and Berner, 1993, 1994). Initially, enamel thickness in molars has been measured from 2D transverse cuts at the level of mesial cusps obtained from either actual tooth sections (e.g., Martin, 1983; Macho and Berner, 1993) or scanning methods (e.g., Schwartz et al., 1998). However, assessing enamel thickness from 2D cuts may result in several issues, including a strong dependence on cutting location and orientation (Kimura et al., 1977; Kono, 2004; Kono and Suwa, 2005).

The arrival of non-invasive scanning methods in dental investigation, such as computed tomography, made it easier to estimate molar enamel thickness in three dimensions (Kono et al., 2002; Kono, 2004; Tafforeau et al., 2006). Following Martin (1983), Kono (2004) devised a method to estimate 3D average enamel thickness, defined as the quotient of the enamel cap volume over the dentine surface 3D area. This approach can be described as *volumetric*, as opposed to what we may call a *geometric* approach.

The geometric approach relies on 3D polygonal meshes of the outer enamel surface (OES) and of the enamel-dentine junction (EDJ). These meshes can be used to compute a geometric estimation of enamel thickness, which corresponds to "the minimum Euclidean distance [...] from each OES node to the EDJ closest triangle" (Guy et al., 2013). In contrast to volumetric estimations of enamel thickness, geometric enamel thickness can be used to depict the 3D spatial distribution of enamel, for instance over dental topographic maps (Kono et al., 2002).

Several primates are characterized by a thicker enamel on the distal faces of the molar crowns (Macho and Berner, 1993; Schwartz, 2000; but see Spencer, 1998; Kono et al., 2002). When observed, this mesio-distal gradient has been interpreted as an adaptation to the increase of the loading stress toward the distal end of the dental row (Osborn and Baragar, 1985; Koolstra et al., 1988).

Similarly, enamel is thicker on molars' *functional* cusps i.e., lingual upper cusps and buccal lower cusps, at least in hominoids (Macho and Berner, 1993; Schwartz, 2000; Kono et al., 2002). During mastication, food is crushed on these cusps at the start of the power stroke (Kay, 1975). As a result, hard or stress-limited items expose them to high tensile stress. Blunt cusps better dissipate such stress, while sharp cusps exert higher tensile stress on the food (Berthaume et al., 2013), which might explain why thick enameled, blunt *functional* cusps are associated with sharper, thin-enameled *non-functional* cusps in the molars of primates. This is also consistent with the fact that thick enamel is correlated with a curvature decrease in the molars of primates, which in theory further improves cusp resistance to stress by making them more blunt (Guy et al., 2015). In any case, enamel

distribution is a major dental trait involved in several aspects of the dental form-function relationship.

Regarding the effect of stress-limited food on thick enamel distribution in molars, Lucas et al. (2008) formulated the hypothesis that durophagous primates were characterized by an unevenly thick enamel (**Figure 1**). More specifically, they expected enamel to be thicker at molar cusp tips in durophagous primates than in non-durophagous taxa. This would increase the resistance of enamel by inhibiting crack extension around the region where food enters in contact with the tooth.

To our knowledge, this hypothesis has not been tested yet using quantitative methods. In fact, enamel distribution is usually assessed through qualitative descriptions of topographic maps and no proper quantitative methods have been proposed apart from individual measures on 2D slices. In this study, we introduce new 3D dental topographic methods designed to investigate and quantify the distribution of thick enamel over a single tooth crown. We further test the morphological hypothesis of an unevenly thick enamel in durophagous primates across a large sample of anthropoid primates.

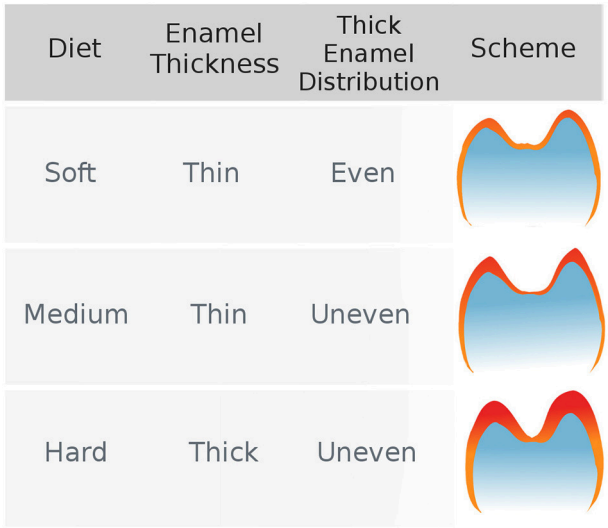

FIGURE 1 | The hypothesis of uneven enamel distribution in durophagous primates (Lucas et al., 2008). Durophagous primates are expected to have unevenly thick enamel, whereas non-durophagous primates are expected to have evenly thin enamel.

MATERIALS AND METHODS

Sample

We collected 70 upper second molars from 32 species of extant anthropoid primates from the following institutions: collections of the iPHEP, Université de Poitiers, France; Muséum National d'Histoire Naturelle, Paris, France; Royal Museum of Central Africa, Tervuren, Belgium; Senckenberg Museum of Frankfurt, Germany. Of course, dental wear would decrease enamel thickness at the tip of the cusps and on dental wear facets. Hence, only juvenile specimens and subadults were selected, so that the enamel was characterized by a minimal level of dental wear.

We included 25 specimens of apes (Hominoidea), 32 specimens of Old World monkeys (Cercopithecoidea), and 13 specimens of New World monkeys (Platyrrhini). Species were selected in order to encompass as wide a range of diets as possible. When possible, they were also classified as stress-limited or soft food eaters *sensu* Lucas et al. (2000). To do so, we followed the methodology presented in Thiery et al. (2017) and combined reports of dietary composition, including seasonal variation in food item consumption, with studies on the physical properties of primates food. Whenever a species was reported to consume stress-limited food on a regular basis, we classified it as a *hard food eater*. If stress-limited food consumption was only reported as marginal despite several reports on diet composition for a given species, we classified it as a *soft food eater*. Species for which data were too scarce or contradictory were classified as *undefined*. This does not necessarily mean no data on their diet could be found. For instance, the diet of chimpanzees (*Pan troglodytes*) is detailed in numerous studies, but it was classified as *undefined* because there are some discrepancies between reports involving forest chimpanzees (Vogel et al., 2008) and savannah chimpanzees (Suzuki, 1969; Peters, 1993).

No living animal was involved in this work, and no animal was killed specifically for this study. Every crania used in this study belong to historical osteological collection gathered, for the most recent specimens, in the beginning of the 20th century. Each specimen has been collected more than one hundred years ago, hence no approval from an ethics committee was required.

Acquisition of Dental 3D Meshes

Computing 3D enamel thickness requires access to the inner part of the tooth and the EDJ. Since the teeth used in this study come from valuable museum specimens of juvenile primates, a non-invasive method was mandatory. The teeth were scanned using x-ray high-resolution micro-computed tomography (HR-μCT) at the Centre de Microtomographie of Poitiers, France. Scans were acquired using an EasyTom HR-microtomograph. Isovoxel resolution spans from 10 to 30 μm depending on tooth size.

The resulting array of 2D slices was stacked to build a 3D reconstruction of the teeth. Both OES and EDJ surfaces were then extracted as polygonal 3D meshes using Avizo. Using Geomagic Studio, these polygonal meshes were re-tesselized into meshes composed of 55,000 triangles of normalized area, which removed scaling effects on triangle geometry. While resulting in a large decrease in the number of polygons used to describe the surface, this level of tessellation has been shown to describe dental surfaces as accurately as surfaces composed of a larger number of triangles (Lazzari and Guy, 2014).

Still using Geomagic Studio, OES, and EDJ surfaces were paired together and their orientation was standardized. The axis formed by the paracone-protocone dentine horn tips was aligned with the x-axis of the 3D space, and the surfaces were translated so that the lowest point of the molar cervix was set to $z = 0$. Following Guy et al. (2015), OES and EDJ occlusal surfaces were subsampled as the regions above a plane parallel to the (xy) reference plane and passing respectively by the lowermost

point of (i) the occlusal enamel basin for the OES, and (ii) the enamel-dentine junction basin for the EDJ (**Figure 2C**).

Computation of Enamel Thickness

Enamel thickness has been measured using both volumetric and geometric approaches. Volumetric average enamel thickness (AET) was computed as the quotient of 3D volume of the enamel cap over 3D area of the EDJ (**Figure 2A**):

$$AET_{Volumetric} = \frac{Volume_{enamel\ cap}}{Area_{EDJ}}$$

For every triangle of the OES, geometric enamel thickness was computed as the minimal euclidean distance between each node of the OES to the closest triangle of the EDJ following normal direction (**Figure 2B**). Afterward, geometric AET was computed as the mean distance for the whole surface:

$$AET_{Geometric} = \frac{\sum distance_{\ [OES-EDJ]}}{N_{Triangles}}$$

Be it volumetric or geometric, AET is a scale-dependant variable. Because our sample includes a wide size range, from the tiny common marmoset *Callithrix jacchus* to the largest living ape *Gorilla gorilla*, comparisons require a standardized estimation of enamel thickness. Following Martin (1985) and Kono (2004), we calculated the relative enamel thickness (RET) as the AET divided by the cubic root of the volume of dentine within the enamel capsule:

$$RET_{Volumetric} = \frac{AET_{Volumetric}}{\sqrt[3]{Volume_{dentine}}} RET_{Geometric} = \frac{AET_{Geometric}}{\sqrt[3]{Volume_{dentine}}}$$

While some authors combined volumetric AET or RET with topographic maps of enamel-dentine distance, a comparison of volumetric and geometric thickness is yet to be done. We thus estimate the correlation between geometric and volumetric approaches for both AET and RET, using both Spearman's and Pearson's coefficients.

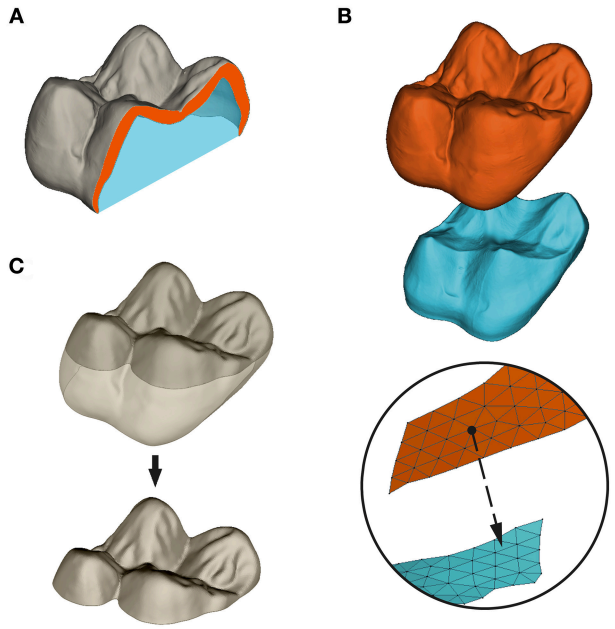

FIGURE 2 | Measure and subsampling of enamel thickness in this paper. **(A)** Volumetric average enamel thickness (3DAET) is measured as the volume of the enamel cap (orange) divided by the square root of the EDJ 3D surface area. Relative enamel thickness (3DRET) is calculated as 3DAET divided by the cubic root of the volume of dentine filling the enamel capsule (blue); **(B)** Geometric AET is computed as the mean of the euclidean shortest distance between points of the OES mesh and the EDJ virtual surface; **(C)** subsampling of the OES occlusal basin as the portion of the OES surface located above the lowermost point of the central basin. All computations of enamel thickness were performed on occlusal subsampled surfaces.

Topographic Analysis of Enamel Distribution

Along with traditional topographic maps, thick enamel distribution has been graphically characterized using pachymetric profiles. A pachymetric profile corresponds to a bivariate plot of enamel-dentine distances for each triangle of the mesh (y-axis) vs. their cumulated frequency (x-axis). To compare teeth regardless of differences in thickness range and/or in the number of triangles, each value is expressed as a percentage of the maximal value for both variables. This approach was inspired by hypsometric curves that are used to characterize the distribution of elevation in traditional topography (Schumm, 1956).

Afterwards, we used pachymetric profiles to characterize the *evenness* of enamel thickness distribution, hereby defined as the proportion of similarly-thick enamel over a tooth surface. While the very notion of *evenness* is qualitative, an evenly thick enamel is expected to have a large proportion of similar enamel-dentine distances. This is precisely this large proportion that would make the enamel look *evenly thick* on topographic maps. In terms of enamel distribution, this would result in a short thickness variation over a large number of triangles. Hence the following proposition: enamel distribution evenness is proportional to the slope of pachymetric profiles, which corresponds to the thickness vs. number of triangle variation. That is, the more evenly thick is enamel, the lower the slope is expected to be.

We computed the slope of the profile at average enamel thickness as the thickness variation between the points located 10 points away at both sides of the geometric AET:

$$Slope_{AET} = \frac{y_{(AET+10)} - y_{(AET-10)}}{x_{(AET+10)} - x_{(AET-10)}}$$

RESULTS

Volumetric vs. Geometric Enamel Thickness

Volumetric 3DAET ranges from 0.0838 to 0.9826 mm. On the other hand, geometric 3DAET ranges from 0.1169 to 1.1960 mm (**Table 1**). Volumetric 3DAET and geometric 3DAET show a significant linear correlation ($\rho = 0.92$; $r^2 = 0.82$; $df = 68$; p-value < 0.001) which is attested graphically by the distribution of

TABLE 1 | Variation of geometric and volumetric Average Enamel Thickness (AET).

Species	N	Vol. AET	Geometric AET				
			mean	min	max	SD	CV
Alouatta sp.	1	0.2620	0.3293	0.0712	0.5132	0.0595	0.1807
Ateles sp.	3	0.1692	0.2997	0.0887	0.5132	0.0882	0.3068
Callicebus cupreus	2	0.1249	0.2254	0.0634	0.3398	0.0387	0.1725
Callithrix jacchus	2	0.0838	0.1169	0.0197	0.2057	0.0359	0.3071
Cebus capucinus	1	0.3418	0.4873	0.2377	0.7576	0.0989	0.2030
Cercocebus galeritus	1	0.5709	0.6918	0.2107	1.0015	0.1622	0.2345
Cercocebus sp.	1	0.5601	0.6768	0.0985	1.0960	0.1680	0.2482
Cercocebus torquatus	1	0.5523	0.7449	0.2158	1.0801	0.1837	0.2466
Cercopithecus campbelli	2	0.3588	0.5120	0.0631	0.7604	0.1266	0.2477
Cercopithecus cephus	1	0.3665	0.4573	0.0374	0.7417	0.0937	0.2049
Cercopithecus diana	2	0.3817	0.5674	0.1634	0.8149	0.1262	0.2244
Cercopithecus nictitans	1	0.3135	0.4461	0.0584	0.6921	0.1245	0.2791
Cercopithecus pogonias	2	0.4132	0.5481	0.0966	0.8430	0.1296	0.2353
Colobus angolensis	3	0.4004	0.5014	0.0961	0.7735	0.1137	0.2251
Colobus guereza	1	0.5205	0.5204	0.0238	0.8661	0.0985	0.1893
Colobus polykomos	2	0.4114	0.4852	0.1469	0.8238	0.0958	0.1998
Erythrocebus patas	1	0.3922	0.5295	0.1940	0.7184	0.0995	0.1879
Gorilla gorilla	6	0.7294	1.0831	0.5388	1.5458	0.1966	0.1803
Hylobates sp.	2	0.4568	0.5292	0.2637	0.7618	0.1106	0.2091
Lagothrix lagotricha	1	0.4640	0.4649	0.1334	0.7239	0.0972	0.2091
Lophocebus albigena	4	0.5517	0.7670	0.1197	1.0887	0.1648	0.2155
Lophocebus atterimus	1	0.5336	0.7016	0.1303	1.0348	0.1518	0.2164
Pan paniscus	7	0.6123	0.7999	0.2810	1.1608	0.1778	0.2222
Pan troglodytes	8	0.7281	0.8272	0.2669	1.2843	0.1987	0.2459
Papio anubis	1	0.7931	1.0730	0.2190	1.4985	0.1826	0.1702
Papio cynocephalus	1	0.9826	1.1960	0.6437	1.5726	0.1610	0.1346
Piliocolobus badius	2	0.4119	0.5084	0.1319	0.7368	0.1035	0.2049
Pithecia pithecia	2	0.1959	0.2660	0.0734	0.4224	0.0518	0.1960
Pongo pygmaeus	2	0.6945	1.1402	0.4919	1.6936	0.2130	0.1864
Procolobus verus	3	0.2528	0.3187	0.0228	0.4748	0.0798	0.2507
Sapajus apella	1	0.2476	0.4646	0.2271	0.7304	0.0994	0.2139
Semnopithecus entellus	2	0.3443	0.6333	0.0243	0.9143	0.1326	0.2140

Vol. AET, volumetric average enamel thickness; CV, coefficient of variation; SD, standard deviation.

the points in the geometric vs. volumetric 3DAET bivariate plot (**Figure 3A**).

Volumetric 3DRET ranges from 0.0890 to 0.2609, while geometric 3DRET ranges from 0.1407 to 0.3672 (**Table 2**). The correlation between volumetric 3DRET and geometric 3DRET is lower though significant ($\rho = 0.84$; $r^2 = 0.67$; df = 68; p-value < 0.001), which is reflected by the dispersion of the points in the bivariate plot of geometric vs. volumetric 3DRET (**Figure 3B**).

Thick Enamel Distribution

In the whole sample, qualitative assessment of thick enamel distribution evenness is strongly consistent with the slope of the pachymetric profile at the mean enamel thickness. When intermediate thickness values (usually green or yellow) are spread on topographic maps, the slope of the profile at mean enamel thickness is typically around 0.2; on the other hand, when the range of colors is wide and when extreme thickness values (dark red) are widespread, the slope of the profile at mean enamel thickness is higher, ranging between 0.6 and up to 1.5 (**Figure 4**).

This result is independent of enamel thickness itself, be it AET or RET, as thick enameled specimens may have a high slope at mean enamel thickness e.g., *Cercocebus torquatus* (**Figure 4A**) but also a low slope at mean enamel thickness e.g., *Pongo pygmaeus* (**Figure 4B**). Conversely, thin-enameled specimens may have a low slope at mean enamel thickness e.g., *Colobus guereza* (**Figure 4A**) but also a high slope at mean enamel thickness e.g., *Ateles* sp. (**Figure 4C**).

Thick enamel distribution does not seem to be more uneven in stress-limited food specialists, except in Old World monkeys (**Figure 5**). Durophagous Old World monkeys have a significantly higher slope (Kruskal-Wallis Analysis of Variance, $H = 11.48$; df = 2; p-value < 0.005). Note that the highest slope

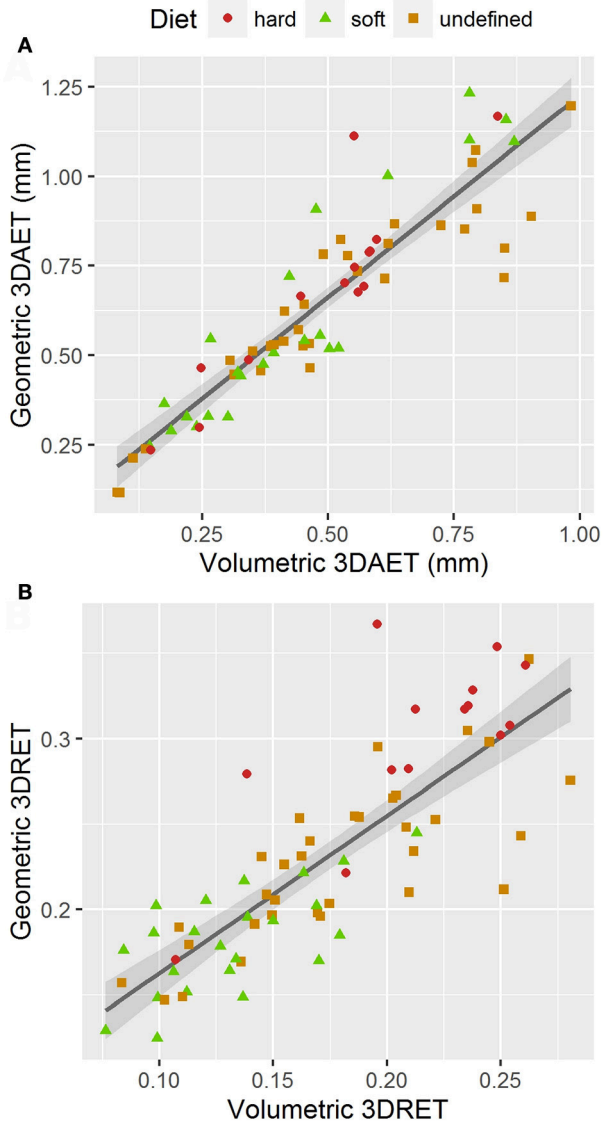

FIGURE 3 | Bivariate plots of volumetric vs. geometric enamel thickness, showing the linear regression model with a 0.95 confidence interval. **(A)** 3DAET in mm; **(B)** 3DRET (dimensionless).

values in the "undefined food hardness" category are assigned to *Cercopithecus diana,* while the lowest values in the "undefined food hardness" category are assigned to *C. cephus, C. pogonias* and both *Papio anubis* and *P. cynocephalus*. In apes, thick enamel distribution is significantly more even in durophagous species ($H = 12.66$; $df = 2$; p-value < 0.05). New World monkeys show no significant difference between durophagous and non-durophagous species.

In addition, pachymetric profile slope was compared with the dispersion of enamel thickness computed as the coefficient of variation (CV) of geometric enamel thickness (**Figure 5**). Based on enamel thickness dispersion alone, stress-limited food consumers could not be separated from soft food consumers in any taxonomic group. Note however that in apes the "undefined" category had a significantly higher CV ($H = 7.76$; $df = 2$; p-value < 0.05).

DISCUSSION

Correlation between Volumetric and Geometric Enamel Thickness

While volumetric and geometric 3DAET are strongly correlated ($r^2 = 0.82$), correlation between volumetric and geometric 3DRET is lower ($r^2 = 0.67$). This lower correlation contrasts with the fact that both variables are expected to measure the same anatomical feature, that is, relative enamel thickness.

Several explanations can account for this difference. Firstly, the amount of enamel involved in the computation of 3DAET differs between the two methods. The volumetric approach divides enamel cap volume by the 3D surface area of the EDJ, which means that it is an estimate of the average volume of enamel per element of EDJ. Martin (1983) postulated that it is a good estimate of average enamel volume synthesized by a single ameloblast, since he expected the size of ameloblasts to be similar between small and large primates. In contrast, the geometric approach consists in measuring a Euclidean distance for only the ~20,000 points that compose the mesh of the occlusal portion. Thus, a portion of the enamel volume is not involved in the computation of geometric 3DAET, which might slightly affect the final result.

Secondly, the two methods do not measure thickness in the same direction. While the geometric approach measures thickness from the OES toward the EDJ, the volumetric approach measures thickness from the EDJ toward the OES. Because OES and EDJ are not perfectly concurrent, this might result in a slight variation of angle for every distance estimation, which in turn would affect average thickness.

Finally, standardization by the cubic root of dentin volume reduces the effects of allometry, which is indeed strong in our sample. This might in turn boost the existing thickness variability between the two methods, which might explain why the difference is more visible for 3DRET.

Nonetheless, since volumetric and geometric 3DRET are not perfectly correlated, the methodology selected to estimate enamel thickness is expected to influence the results. This is corroborated by the fact that the species with the greatest volumetric 3DRET (*Lophocebus aterrimus*) and the one with the greatest geometric 3DRET (*S. apella*) do not match (**Table 2**). The difference is especially visible for the latter (volumetric 3DRET = 0.1956; geometric 3DRET = 0.3672). Hence, the necessity to carefully select the method that is best adapted to one's investigation:

1. For the time being, we recommend choosing a volumetric approach when quantifying enamel thickness as the amount of tissue covering the EDJ. Measuring volumetric enamel thickness can help to characterize the rate and speed of enamel secretion, but also the amount of enamel that is protecting the tooth.
2. On the other hand, we recommend choosing a geometric approach when quantifying the enamel thickness as the depth of tissue underneath the OES. Geometric enamel thickness can

TABLE 2 | Variation of geometric and volumetric Relative Enamel Thickness (RET).

Species	N	Vol. RET	Geometric RET				
			mean	min	max	SD	CV
Alouatta sp.	1	0.1309	0.1644	0.0356	0.2563	0.0297	0.1807
Ateles sp.	3	0.0890	0.1563	0.0457	0.2692	0.0466	0.3068
Callicebus cupreus	2	0.0962	0.1734	0.0491	0.2613	0.0296	0.1725
Callithrix jacchus	2	0.1063	0.1481	0.0251	0.2606	0.0455	0.3071
Cebus capucinus	1	0.2483	0.3540	0.1727	0.5503	0.0718	0.2030
Cercocebus galeritus	1	0.2541	0.3079	0.0938	0.4458	0.0722	0.2345
Cercocebus sp.	1	0.2500	0.3021	0.0440	0.4892	0.0750	0.2482
Cercocebus torquatus	1	0.2095	0.2826	0.0819	0.4097	0.0697	0.2466
Cercopithecus campbelli	2	0.1585	0.2231	0.0300	0.3319	0.0549	0.2477
Cercopithecus cephus	1	0.1358	0.1695	0.0139	0.2749	0.0347	0.2049
Cercopithecus diana	2	0.1754	0.2609	0.0758	0.3745	0.0579	0.2244
Cercopithecus nictitans	1	0.1625	0.2312	0.0303	0.3587	0.0645	0.2791
Cercopithecus pogonias	2	0.1931	0.2552	0.0467	0.3957	0.0614	0.2353
Colobus angolensis	3	0.1582	0.1967	0.0383	0.3027	0.0448	0.2251
Colobus guereza	1	0.1701	0.1701	0.0078	0.2831	0.0322	0.1893
Colobus polykomos	2	0.1529	0.1818	0.0551	0.3107	0.0362	0.1998
Erythrocebus patas	1	0.1419	0.1915	0.0702	0.2599	0.0360	0.1879
Gorilla gorilla	6	0.1388	0.2059	0.1025	0.2934	0.0372	0.1803
Hylobates sp.	2	0.1701	0.1971	0.0982	0.2838	0.0412	0.2091
Lagothrix lagotricha	1	0.2097	0.2101	0.0603	0.3272	0.0439	0.2091
Lophocebus albigena	4	0.2300	0.3206	0.0495	0.4551	0.0690	0.2155
Lophocebus atterimus	1	0.2609	0.3431	0.0637	0.5061	0.0742	0.2164
Pan paniscus	7	0.1826	0.2384	0.0837	0.3459	0.0531	0.2222
Pan troglodytes	8	0.2186	0.2496	0.0798	0.3874	0.0600	0.2459
Papio anubis	1	0.1879	0.2542	0.0519	0.3550	0.0433	0.1702
Papio cynocephalus	1	0.2450	0.2982	0.1605	0.3921	0.0401	0.1346
Piliocolobus badius	2	0.1513	0.1866	0.0486	0.2702	0.0379	0.2049
Pithecia pithecia	2	0.1446	0.1961	0.0541	0.3112	0.0382	0.1960
Pongo pygmaeus	2	0.1703	0.2805	0.1216	0.4165	0.0523	0.1864
Procolobus verus	3	0.1116	0.1407	0.0100	0.2097	0.0352	0.2507
Sapajus apella	1	0.1956	0.3672	0.1795	0.5772	0.0786	0.2139
Semnopithecus entellus	2	0.1095	0.2039	0.007	0.2948	0.0436	0.2140

Vol. RET, volumetric relative enamel thickness; CV, coefficient of variation; SD, standard deviation.

be used in biomechanical models, but also to depict enamel thickness variation over a single tooth crown. This in turn can help to characterize local differences in thick enamel distribution, for instance using pachymetric profiles.

Is Thick Enamel Distribution Related to Durophagy?

At least in the present study and assuming that pachymetric profile slopes are a good estimate of enamel thickness evenness, the hypothesis of an unevenly thick enamel in durophagous primates can be rejected except for Old World monkeys. Durophagous cercopithecids such as *Cercocebus* or *Lophocebus* are all characterized by high slopes and by an unevenly thick enamel (**Figure 5**). Furthermore, *C. diana,* the species from the "undefined" category with the highest pachymetric profile slopes, has been reported to consume a large proportion of seeds in both Bia (Curtin, 2004) and Tai Forest localities (Kane, 2012). In contrast, non-durophagous Old World monkeys such as *Colobus* are characterized by low slopes and by evenly thick enamel (**Figure 5**). This is particularly visible on the topographic map of *C. guereza* (**Figure 4C**). *Cercopithecus cephus,* the species from the "undefined" category with the lowest average pachymetric profile slope, has been reported to consume softer foods in both the localities of Makokou (Gautier-Hion et al., 1980) and Lopé (Tutin et al., 1997; Tutin, 1999). Note however that *C. nictitans*, which is characterized by a high profile slope, and *C. pogonias*, which is characterized by low profile slopes (**Figure 5**), have both been reported to consume a large proportion of seeds at the Makandé location (Brugière et al., 2002). On the other hand, *P. anubis* and *Papio cynocephalus* are also characterized by low profile slopes even though they might regularly consume challenging underground storage organs (Dominy et al., 2008).

Concerning durophagous apes, the orangutan (*P. pygmaeus*) is reported to consume very challenging, stress-limited food such

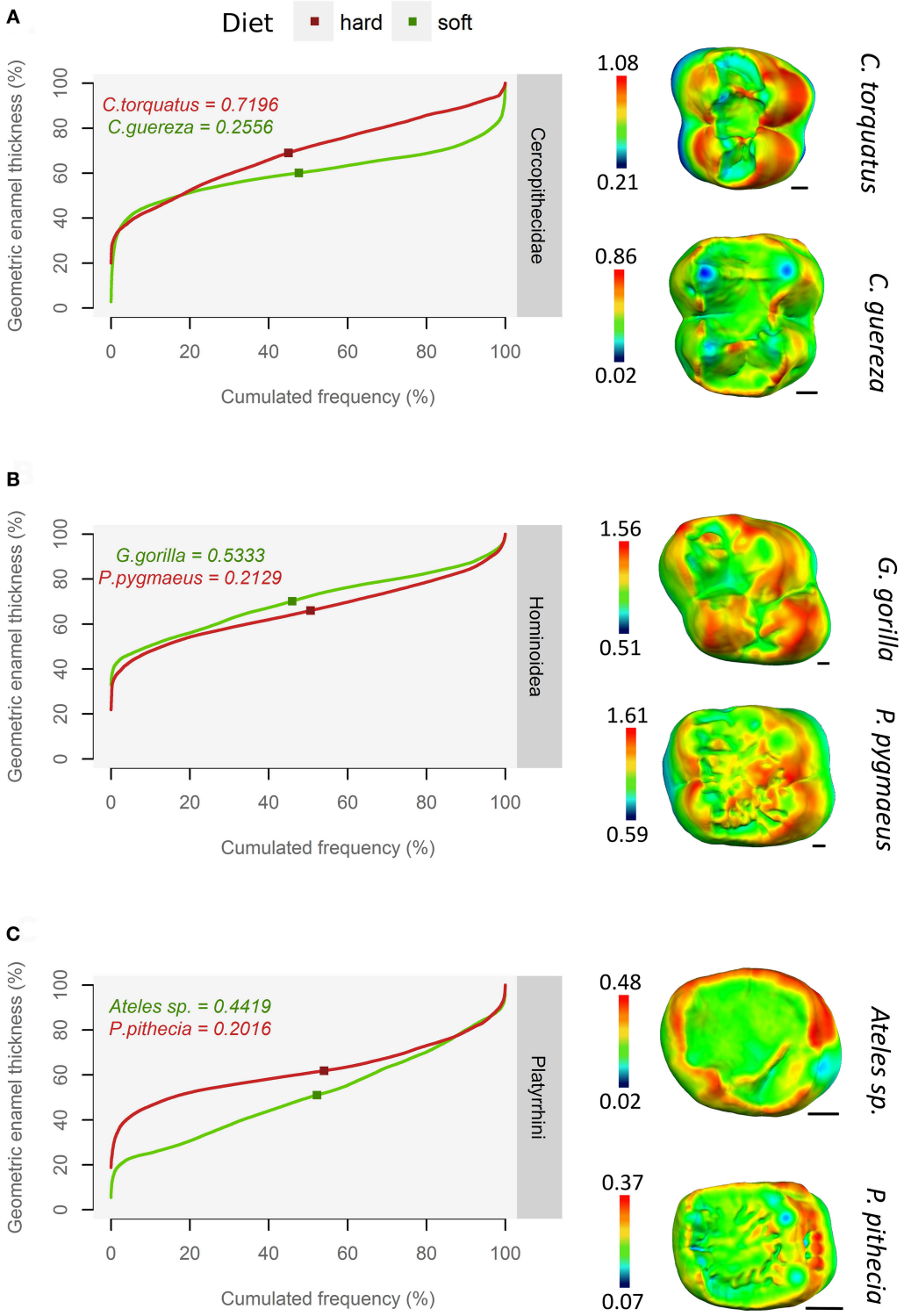

FIGURE 4 | Using pachymetric profile as a graphical estimator of thick enamel distribution. For each group, profiles of a durophagous primate (in red) and a non-durophagous primate (in green) are plotted together and compared with the topographic map of enamel thickness (mm), rendered by a relative color scale ranging from thinnest (dark blue) to thickest (red). The squares on pachymetric curves correspond to the geometric AET and the number above, to the slope of the curve at geometric AET. **(A)** Old World monkeys; **(B)** Apes; **(C)** New World monkeys.

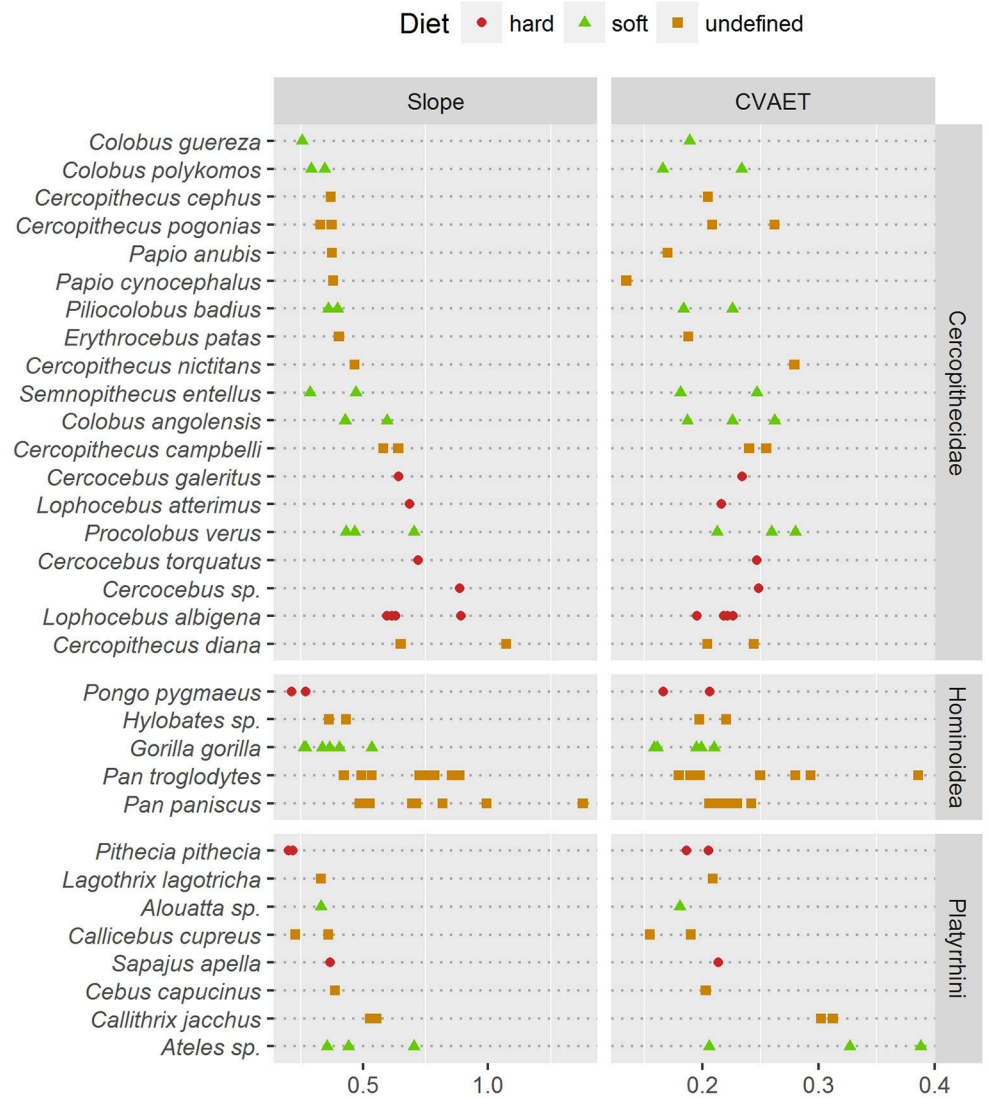

FIGURE 5 | Comparison of two estimates of enamel thickness variation. **(Left)** dotchart of the pachymetric profile slope at geometric AET; **(Right)** dotchart of the intra-specimen coefficient of variation (CV) of geometric enamel thickness.

as the seeds of *Mezzetia parviflora* (Vogel et al., 2008; Lucas et al., 2012). Taking the hypothesis of Lucas et al. (2008) into account, its profile slope is therefore expected to be high, which is not the case (**Figure 5**). The enamel of orangutan appears to be evenly thick. As such, topographic maps of enamel thickness show a large proportion of intermediately-thick enamel (yellow polygons) but a small proportion of very thick enamel (red polygons; **Figure 4B**). In other words, the pachymetric profile drifts toward thicker values, which results in a flatter curve and values closer to the thick 3DAET characteristic of this species (Vogel et al., 2008; this study).

A similar trend is observed in the saki (*Pithecia pithecia*), a notorious seed-eating New World monkey (Norconk and Veres, 2011). Pachymetric profiles of *P. pithecia* are thus characterized by a low slope at mean enamel thickness (**Figure 5**). Topographic maps of enamel thickness for this taxon present, in relative terms, more intermediately-thick enamel (yellow polygons) and less thick enamel (red polygons) than the maps of other New World monkeys (**Figure 4C**). Given its low AET values, the enamel of *P. pithecia* can be thus described as evenly thin.

In orangutan and sakis, the even enamel distribution might result from the presence of crenulations on the occlusal surface of molars (**Figures 4B,C**). Several functional interpretations have been proposed for these crenulations, including a better grip for the manipulation of slippery hard food e.g., seeds of juicy fruit (Lucas and Teaford, 1994) or multiplication of contact points which would improve the ability to fracture fibrous seeds (Lucas and Luke, 1984; Vogel et al., 2008). Our observation is consistent with both interpretations, since a multiplication of contact points with stress-limited food could result in a multiplication

of locally thick-enameled structures, which would ultimately make the whole enamel look evenly thick. Still, this assumption requires further investigation, as both *P. pygmaeus* and *P. pithecia* are only represented by a couple of specimens in the sample.

Similarly, *S. apella* and to a lesser extent *Cebus capucinus* are also characterized by relatively low profile slopes despite being known to consume stress-limited food while having no crenulations (Freese and Oppenheimer, 1981; Terborgh, 1983; Galetti and Pedroni, 1994; but see Mosdossy, 2013). In both species though, topographic maps of the enamel thickness present a very different aspect, with only a small proportion of thick enamel on the hypocone, their enamel being evenly thick over the rest of the tooth crown (G. Thiery, pers. obs.). Enamel is evenly to unevenly thin in the soft food eater *Ateles* sp. (**Figure 5**), although uneven distribution probably comes from a thick lateral enamel on the functional cusps (**Figure 4C**). Overall, several modalities of evenly thick or thin enamel distribution are present in New World monkeys.

Our results imply that the distribution of thick enamel follows different patterns, possibly from one family to another. This might indicate that primates have developed different durophagous strategies to answer the selective pressures exerted by stress-limited food. It also suggests that characterizing enamel thickness distribution requires a phylogenetic context, especially when making dietary inferences for extinct species, since such inferences can not be confronted to behavioral data.

Nonetheless, a feature that was not taken into account is the feeding action performed to access or process stress-limited food, which needs to be considered when evaluating the form-function relationship between diet and dental morphology (Thiery et al., 2017). For instance, *P. pithecia* does not crack open the most challenging food it consumes with its molars, but with its strong and proclive incisors and canines (Kinzey and Norconk, 1993; Norconk and Veres, 2011). The seeds it crushes with its molars might therefore be tough, but they are significantly softer (Kinzey and Norconk, 1993). While this might have affected the results for New World monkeys, we assume this is not the case for apes since *P. pygmaeus* is known to use its molars to crush the shells of stress-limited foods (Lucas et al., 2012).

Enamel decussation was not taken into account either. Indeed, the model proposed by Lucas et al. (2008) mentioned that species consuming large food objects of high modulus which required intermediate or high forces to fracture (i.e., stress-limited foods) were expected to show some decussated enamel. This would require further investigation, as the proportion of decussated enamel might compensate for evenly thick enamel in some durophagous primates. For instance, *P. pithecia* presents an evenly thin enamel (**Figure 4C**), but its enamel is also characterized by narrow, well-defined Hunter-Schreger Bands extending throughout its thickness (Martin et al., 2003). This might increase enamel resistance to the fibrous, possibly stress-limited seeds it masticates on a daily basis and compensate for an evenly thin enamel.

To conclude, this study shows that enamel thickness can be estimated using either a volumetric approach or a geometric approach. The former should be used to assess rate and speed of enamel secretion and more generally the amount of enamel topping the EDJ. The latter should be used to measure enamel thickness as the depth of enamel under OES and is hypothesized to better suit biomechanical models.

Furthermore, topographic maps of geometric enamel thickness and pachymetric profiles combine well for the interpretation of enamel distribution in both qualitative and quantitative terms. Slope of the pachymetric profile appears to be an especially fair estimate of enamel distribution evenness. In contrast, descriptive statistics such as the CV of enamel-dentine distance failed to detect differences in distribution evenness (**Figure 5**).

Overall, the methods introduced in this work make a powerful tool for testing form-function hypotheses related to enamel thickness. They can also be adapted to a wide range of studies focusing on the variation of tissue thickness across a whole surface, be it enamel or not. When investigating enamel however, the phylogenetic context should be taken into account, as enamel distribution patterns seem to depend on the family which is considered.

AUTHOR CONTRIBUTIONS

Specimens were collected by GT, FG, and VL. The scan acquisition, the extraction and the preparation of 3d dental meshes as well as the topographic analysis were performed by GT and FG. All authors participated in the writing of the manuscript.

ACKNOWLEDGMENTS

This work was supported by the Agence Nationale de la Recherche (ANR-09-BLAN-0238), the Ministère de l'Education Nationale, de l'Enseignement Supérieur et de la Recherche, the région Poitou-Charentes (Conventions Région #07/RPC-R-100 and #12/RPC-013) as well as a research grant of the International Primatological Society. Many thanks to E. Gilissen from the Royal Museum of Central Africa (Tervuren, Belgium), J. Cuisin from the Muséum National d'Histoire Naturelle (Paris, France) and K. Krohmann from the Senckenberg Museum of Frankfurt (Frankfurt-am-Main, Germany) for granting us access to the specimen used in this work. We are greatly indebted to A. Mazurier (IC2MP) as well as A. Euriat and J. Surault (iPHEP) for their help in data acquisition. Finally, we are very thankful to the reviewers for their critical comments on earlier versions of the manuscript.

REFERENCES

Berthaume, M. A. (2016). Food mechanical properties and dietary ecology. *Am. J. Phys. Anthropol.* 159, 79–104. doi: 10.1002/ajpa.22903

Berthaume, M. A., Dumont, E. R., Godfrey, L. R., and Grosse, I. R. (2013). How does tooth cusp radius of curvature affect brittle food item processing? *J. R. Soc. Interface* 10:20130240. doi: 10.1098/rsif.2013.0240

Braly, A., Darnell, L. A., Mann, A. B., Teaford, M. F., and Weihs, T. P. (2007). The effect of prism orientation on the indentation testing of human molar enamel. *Arch. Oral Biol.* 52, 856–860. doi: 10.1016/j.archoralbio.2007.03.005

Brugière, D., Gautier, J.-P., Moungazi, A., and Gautier-Hion, A. (2002). Primate diet and biomass in relation to vegetation composition and fruiting phenology in a rain forest in Gabon. *Int. J. Primatol.* 23, 999–1024. doi: 10.1023/A:1019693814988

Chun, K., Choi, H., and Lee, J. (2014). Comparison of mechanical property and role between enamel and dentin in the human teeth. *J. Dent. Biomech.* 5:1758736014520809. doi: 10.1177/1758736014520809

Constantino, P. J., Lee, J. J. W., Morris, D., Lucas, P. W., Hartstone-Rose, A., Lee, W.-K., et al. (2011). Adaptation to hard-object feeding in sea otters and hominins. *J. Hum. Evol.* 61, 89–96. doi: 10.1016/j.jhevol.2011.02.009

Curtin, S. H. (2004). "Diet of the Roloway monkey, *Cercopithecus diana* roloway, in Bia National Park, Ghana," in *The Guenons: Diversity and Adaptation in African Monkeys*, eds M. E. Glenn and M. Cords (New York, NY: Kluwer Academic Publishers), 351–371.

Cuy, J. L., Mann, A. B., Livi, K. J., Teaford, M. F., and Weihs, T. P. (2002). Nanoindentation mapping of the mechanical properties of human molar tooth enamel. *Arch. Oral Biol.* 47, 281–291. doi: 10.1016/S0003-9969(02)00006-7

Dominy, N. J., Vogel, E. R., Yeakel, J. D., Constantino, P., and Lucas, P. W. (2008). Mechanical properties of plant underground storage organs and implications for dietary models of early hominins. *Evol. Biol.* 35, 159–175. doi: 10.1007/s11692-008-9026-7

Dumont, E. R. (1995). Enamel thickness and dietary adaptation among extant primates and chiropterans. *J. Mammal.* 76, 1127–1136. doi: 10.2307/1382604

Freese, C. H., and Oppenheimer, J. R. (1981). "The Capuchin Monkeys, Genus *Cebus*," in *Ecology and Behavior of Neotropical Primates*, eds A. Coimbra-Filho and R. A. Mittermeier (Rio de Janeiro: Academia Brasileira de Ciências), 331–390.

Galetti, M., and Pedroni, F. (1994). Seasonal diet of capuchin monkeys (*Cebus apella*) in a semideciduous forest in south-east Brazil. *J. Trop. Ecol.* 10, 27–39. doi: 10.1017/S0266467400007689

Gautier-Hion, A., Emmons, L. H., and Dubost, G. (1980). A comparison of the diets of three major groups of primary consumers of Gabon (primates, squirrels and ruminants). *Oecologia* 45, 182–189. doi: 10.1007/BF00346458

Guy, F., Gouvard, F., Boistel, R., Euriat, A., and Lazzari, V. (2013). Prospective in (primate) dental analysis through tooth 3D topographical quantification. *PLoS ONE* 8:e66142. doi: 10.1371/journal.pone.0066142

Guy, F., Lazzari, V., Gilissen, E., and Thiery, G. (2015). To what extent is primate second molar enamel occlusal morphology shaped by the enamel-dentine junction? *PLoS ONE* 10:e0138802. doi: 10.1371/journal.pone.0138802

Hill, D. A., and Lucas, P. W. (1996). Toughness and fiber content of major leaf foods of Japanese macaques (*Macaca fuscata yakui*) in Yakushima. *Am. J. Primatol.* 38, 221–231. doi: 10.1002/(SICI)1098-2345(1996)38

Kallistová, A., Horácek, I., Šlouf, M., Skála, R., and Fridrichová, M. (2017). Mammalian enamel maturation: crystallographic changes prior to tooth eruption. *PLoS ONE* 12:e0171424. doi: 10.1371/journal.pone.0171424

Kane, E. E. (2012). *The Context of Dietary Variation in Cercopithecus diana in the Ivory Coast's Tai National Park (Ohio State university)*. Dissertation thesis, Ohio State University, Columbus, OH.

Kay, R. F. (1975). The functional adaptations of primate molar teeth. *Am. J. Phys. Anthropol.* 43, 195–216. doi: 10.1002/ajpa.1330430207

Kay, R. F. (1981). The nut-crackers – a new theory of the adaptations of the Ramapithecinae. *Am. J. Phys. Anthropol.* 55, 141–151. doi: 10.1002/ajpa.1330550202

Kimura, O., Dykes, E., and Fearnhead, R. W. (1977). The relationship between the surface area of the enamel crowns of human teeth and that of the dentine-enamel junction. *Arch. Oral Biol.* 22, 677–683. doi: 10.1016/0003-9969(77)90097-8

Kinzey, W. G., and Norconk, M. A. (1993). Physical and chemical properties of fruit and seeds eaten by *Pithecia* and *Chiropotes* in Surinam and Venezuela. *Int. J. Primatol.* 14, 207–227. doi: 10.1007/BF02192632

Kono, R. T. (2004). Molar enamel thickness and distribution patterns in extant great apes and humans: new insights based on a 3-dimensional whole crown perspective. *Anthropol. Sci.* 112, 121–146. doi: 10.1537/ase.03106

Kono, R. T., and Suwa, G. (2005). Effects of molar crown orientation to measures of lateral enamel thickness in the mesial cusp section. *Bull. Natl. Mus. Nat. Sci. D* 31, 11–22. Available at online: https://www.kahaku.go.jp/english/research/researcher/papers/18078.pdf

Kono, R. T., Suwa, G., and Tanijiri, T. (2002). A three-dimensional analysis of enamel distribution patterns in human permanent first molars. *Arch. Oral Biol.* 47, 867–875. doi: 10.1016/S0003-9969(02)00151-6

Koolstra, J. H., van Eijden, T. M., Weijs, W. A., and Naeije, M. (1988). A three-dimensional mathematical model of the human masticatory system predicting maximum possible bite forces. *J. Biomech.* 21, 563–576. doi: 10.1016/0021-9290(88)90219-9

Lambert, J. E., Chapman, C. A., Wrangham, R. W., and Conklin-Brittain, N. L. (2004). Hardness of cercopithecine foods: implications for the critical function of enamel thickness in exploiting fallback foods. *Am. J. Phys. Anthropol.* 125, 363–368. doi: 10.1002/ajpa.10403

Lazzari, V., and Guy, F. (2014). Quantitative three-dimensional topography in taxonomy applied to the dental morphology of catarrhines. *BMSAP* 26, 140–146. doi: 10.1007/s13219-014-0099-9

Le Luyer, M., Rottier, S., and Bayle, P. (2014). Brief communication: Comparative patterns of enamel thickness topography and oblique molar wear in two early neolithic and medieval population samples. *Am. J. Phys. Anthropol.* 155, 162–172. doi: 10.1002/ajpa.22562

Lucas, P. W. (2004). *Dental Functional Morphology: How Teeth Work*. Cambridge: Cambridge University Press.

Lucas, P. W., Casteren, A. V., Al-Fadhalah, K., Almusallam, A. S., Henry, A. G., Michael, S., et al. (2014). The role of dust, grit and phytoliths in tooth wear. *Ann. Zool. Fenn.* 51, 143–152. doi: 10.5735/086.051.0215

Lucas, P. W., Constantino, P. J., Wood, B. A., and Lawn, B. R. (2008). Dental enamel as a dietary indicator in mammals. *Bioessays* 30, 374–385. doi: 10.1002/bies.20729

Lucas, P. W., Gaskins, J. T., Lowrey, T. K., Harrison, M. E., Morrogh-Bernard, H. C., Cheyne, S. M., et al. (2012). Evolutionary optimization of material properties of a tropical seed. *J. R. Soc. Interface* 9, 34–42. doi: 10.1098/rsif.2011.0188

Lucas, P. W., and Luke, D. A. (1984). "Chewing it Over: Basic Principles of Food Breakdown," in *Food Acquisition and Processing in Primates*, eds D. J. Chivers, B. A. Wood, and A. Bilsborough (New York, NY: Plenum Press), 283–301.

Lucas, P. W., and Teaford, M. F. (1994). "Functional morphology of colobine teeth," in *Colobine Monkeys: Their Ecology, Behaviour and Evolution*, eds G. Davies and J. Oates (Cambridge: Cambridge University Press), 173–203.

Lucas, P. W., Turner, I. M., Dominy, N. J., and Yamashita, N. (2000). Mechanical defences to herbivory. *Ann. Bot.* 86, 913–920. doi: 10.1006/anbo.2000.1261

Maas, M. C. (1991). Enamel structure and microwear: an experimental study of the response of enamel to shearing force. *Am. J. Phys. Anthropol.* 85, 31–49. doi: 10.1002/ajpa.1330850106

Macho, G. A., and Berner, M. E. (1993). Enamel thickness of human maxillary molars reconsidered. *Am. J. Phys. Anthropol.* 92, 189–200. doi: 10.1002/ajpa.1330920208

Macho, G. A., and Berner, M. E. (1994). Enamel thickness and the helicoidal occlusal plane. *Am. J. Phys. Anthropol.* 94, 327–337. doi: 10.1002/ajpa.1330940304

Macho, G. A., and Spears, I. R. (1999). Effects of loading on the biomechanical [correction of biochemical] behavior of molars of *Homo*, *Pan*, and *Pongo*. *Am. J. Phys. Anthropol.* 109, 211–227. doi: 10.1002/(SICI)1096-8644(199906)109

Martin, L. B. (1983). *The Relationships of the Later Miocene Hominoidea*. dissertation thesis, University of London, London.

Martin, L. B. (1985). Significance of enamel thickness in hominoid evolution. *Nature* 314, 260–263. doi: 10.1038/314260a0

Martin, L. B., Olejniczak, A. J., and Maas, M. C. (2003). Enamel thickness and microstructure in pitheciin primates, with comments on dietary adaptations of the middle Miocene hominoid *Kenyapithecus*. *J. Hum. Evol.* 45, 351–367. doi: 10.1016/j.jhevol.2003.08.005

McGraw, W. S., Vick, A. E., and Daegling, D. J. (2014). Dietary variation and food hardness in sooty mangabeys (*Cercocebus atys*): implications for fallback foods and dental adaptation. *Am. J. Phys. Anthropol.* 154, 413–423. doi: 10.1002/ajpa.22525

Milton, K. (1979). Factors influencing leaf choice by howler monkeys: a test of some hypotheses of food selection by generalist herbivores. *Am. Nat.* 114, 362–378. doi: 10.1086/283485

Molnar, S., and Gantt, D. G. (1977). Functional implications of primate enamel thickness. *Am. J. Phys. Anthropol.* 46, 447–454. doi: 10.1002/ajpa.1330460310

Mosdossy, K. (2013). *Insect Abundance in Relation to Capuchin (Cebus capucinus) Foraging: Fallback Foods in a Costa Rican Tropical Dry Forest*. Dissertation thesis, University of Calgary, Calgary, AB.

Norconk, M. A., and Veres, M. (2011). Physical properties of fruit and seeds ingested by primate seed predators with emphasis on sakis and bearded sakis. *Anat. Rec.* 294, 2092–2111. doi: 10.1002/ar.21506

Olejniczak, A. J., Smith, T. M., Wang, W., Potts, R., Ciochon, R., Kullmer, O., et al. (2008). Molar enamel thickness and dentine horn height in *Gigantopithecus blacki*. *Am. J. Phys. Anthropol.* 135, 85–91. doi: 10.1002/ajpa.20711

Osborn, J. W. (ed.). (1981). *Dental Anatomy and Embryology*. Oxford: Blackwell Scientific Publication.

Osborn, J. W., and Baragar, F. A. (1985). Predicted pattern of human muscle activity during clenching derived from a computer assisted model: symmetric vertical bite forces. *J. Biomech.* 18, 599–612. doi: 10.1016/0021-9290(85)90014-4

Pampush, J. D., Duque, A. C., Burrows, B. R., Daegling, D. J., Kenney, W. F., and McGraw, W. S. (2013). Homoplasy and thick enamel in primates. *J. Hum. Evol.* 64, 216–224. doi: 10.1016/j.jhevol.2013.01.009

Peters, C. R. (1993). Shell strength and primate seed predation of nontoxic species in eastern and southern Africa. *Int. J. Primatol.* 14, 315–344. doi: 10.1007/BF02192636

Rabenold, D., and Pearson, O. M. (2011). Abrasive, silica phytoliths and the evolution of thick molar enamel in primates, with implications for the diet of *Paranthropus boisei*. *PLoS ONE* 6:e28379. doi: 10.1371/journal.pone.0028379

Roy, S., and Basu, B. (2008). Mechanical and tribological characterization of human tooth. *Mater. Char.* 59, 747–756. doi: 10.1016/j.matchar.2007.06.008

Schumm, S. A. (1956). Evolution of drainage systems and slopes in badlands at Perth Amboy, New Jersey. *Bull. Geol. Soc.* 67, 597–646. doi: 10.1130/0016-7606(1956)67[597:EODSAS]2.0.CO;2

Schwartz, G. T. (2000). Taxonomic and functional aspects of the patterning of enamel thickness distribution in extant large-bodied hominoids. *Am. J. Phys. Anthropol.* 111, 221–244. doi: 10.1002/(SICI)1096-8644(200002)111

Schwartz, G. T., Thackeray, J. F., Reid, C., and van Reenan, J. F. (1998). Enamel thickness and the topography of the enamel-dentine junction in South African Plio-Pleistocene hominids with special reference to the Carabelli trait. *J. Hum. Evol.* 35, 523–542. doi: 10.1006/jhev.1998.0239

Shellis, R. P., Beynon, A. D., Reid, D. J., and Hiiemae, K. M. (1998). Variations in molar enamel thickness among primates. *J. Hum. Evol.* 35, 507–522. doi: 10.1006/jhev.1998.0238

Smith, A. L., Benazzi, S., Ledogar, J. A., Tamvada, K., Pryor Smith, L. C., Weber, G. W., et al. (2015). The feeding biomechanics and dietary ecology of *Paranthropus boisei*. *Anat. Rec.* 298, 145–167. doi: 10.1002/ar.23073

Spencer, M. A. (1998). Force production in the primate masticatory system: electromyographic tests of biomechanical hypotheses. *J. Hum. Evol.* 34, 25–54. doi: 10.1006/jhev.1997.0180

Strait, D. S., Constantino, P., Lucas, P. W., Richmond, B. G., Spencer, M. A., Dechow, P. C., et al. (2013). Viewpoints: diet and dietary adaptations in early hominins: the hard food perspective. *Am. J. Phys. Anthropol.* 151, 339–355. doi: 10.1002/ajpa.22285

Suzuki, A. (1969). An ecological study of chimpanzees in a savanna woodland. *Primates* 10, 103–148. doi: 10.1007/BF01730979

Tafforeau, P., Boistel, R., Boller, E., Bravin, A., Brunet, M., Chaimanee, Y., et al. (2006). Applications of X-ray synchrotron microtomography for non-destructive 3D studies of paleontological specimens. *Appl. Phys. A* 83, 195–202. doi: 10.1007/s00339-006-3507-2

Teaford, M. F., Maas, M. C., and Simons, E. L. (1996). Dental microwear and microstructure in early oligocene primates from the Fayum, Egypt: implications for diet. *Am. J. Phys. Anthropol.* 101, 527–543. doi: 10.1002/(SICI)1096-8644(199612)101

Terborgh, J. (1983). *Five New World Primates. A Study in Comparative Ecology*. Princeton, NJ: Princeton University Press.

Thiery, G., Guy, F., and Lazzari, V. (2017). Investigating the dental toolkit of primates based on food mechanical properties: feeding action does matter. *Am. J. Primatol.* 79:e22640. doi: 10.1002/ajp.22640

Tutin, C. E. G. (1999). Fragmented living: behavioural ecology of primates in a forest fragment in the Lopé Reserve, Gabon. *Primates* 40, 249–265. doi: 10.1007/BF02557714

Tutin, C. E., Ham, R. M., White, L. J., and Harrison, M. J. (1997). The primate community of the Lopé Reserve, Gabon: diets, responses to fruit scarcity, and effects on biomass. *Am. J. Primatol.* 42, 1–24. doi: 10.1002/(SICI)1098-2345(1997)42

Ungar, P. S., and Hlusko, L. J. (2016). The evolutionary path of least resistance. *Science* 353, 29–30. doi: 10.1126/science.aaf8398

Vogel, E. R., van Woerden, J. T., Lucas, P. W., Utami Atmoko, S. S., van Schaik, C. P., and Dominy, N. J. (2008). Functional ecology and evolution of hominoid molar enamel thickness: *Pan troglodytes schweinfurthii* and *Pongo pygmaeus wurmbii*. *J. Hum. Evol.* 55, 60–74. doi: 10.1016/j.jhevol.2007.12.005

Waterman, P. G., Ross, J., a. M., Bennett, E. L., and Davies, A. G. (1988). A comparison of the floristics and leaf chemistry of the tree flora in two Malaysian rain forests and the influence of leaf chemistry on populations of colobine monkeys in the old world. *Biol. J. Linn. Soc.* 34, 1–32. doi: 10.1111/j.1095-8312.1988.tb01946.x

Zhao, X., O'Brien, S., Shaw, J., Abbott, P., Munroe, P., Habibi, D., et al. (2013). The origin of remarkable resilience of human tooth enamel. *Appl. Phys. Lett.* 103:241901. doi: 10.1063/1.4842015

Zhang, Y.-R., Du, W., Zhou, X.-D., and Yu, H.-Y. (2014). Review of research on the mechanical properties of the human tooth. *Int. J. Oral Sci.* 6, 61–69. doi: 10.1038/ijos.2014.21

Conflict of Interest Statement: The authors declare that the research was conducted in the absence of any commercial or financial relationships that could be construed as a potential conflict of interest.

Copyright © 2017 Thiery, Lazzari, Ramdarshan and Guy. This is an open-access article distributed under the terms of the Creative Commons Attribution License (CC BY). The use, distribution or reproduction in other forums is permitted, provided the original author(s) or licensor are credited and that the original publication in this journal is cited, in accordance with accepted academic practice. No use, distribution or reproduction is permitted which does not comply with these terms.

frontiers in Physiology

PERSPECTIVE
published: 29 June 2017
doi: 10.3389/fphys.2017.00442

Difference in Striae Periodicity of Heilongjiang and Singaporean Chinese Teeth

Sharon H. X. Tan[1], *Yu Fan Sim*[2] *and Chin-Ying S. Hsu*[3]*

[1] Ministry of Health Holdings, Singapore, Singapore, [2] Faculty of Dentistry, National University Health System, National University of Singapore, Singapore, Singapore, [3] Department of Dentistry, Faculty of Dentistry, National University Health System, National University of Singapore, Singapore, Singapore

Striae periodicity refers to the number of cross-striations between successive lines of Retzius in tooth enamel. A regular time dependency of striae periodicity, known as the circaseptan interval, has been proposed. Previous studies on striae periodicity have been carried out on both modern and early humans given its potential applications in forensic age estimations and anthropology. Nevertheless, research comparing striae periodicities across gender groups and populations in different geographical locations, particularly in Asia, is lacking. In this study, we compared the striae periodicities of Heilongjiang and Singaporean Chinese, as well as that of Singaporean Chinese males and females. Results showed that while the median striae periodicity counts of Heilongjiang Chinese and Singaporean Chinese teeth are both 7, Heilongjiang Chinese tend to have lower striae periodicity counts than Singaporean Chinese ($p < 0.01$). No significant gender difference was observed between the median striae periodicity of Singaporean Chinese Female and Singaporean Chinese Male teeth ($p = 0.511$). We concluded that the median striae periodicity may statistically differ with geographical location, but not gender, provided that ethnicity and geographical location are held constant. Further studies are required to examine the causes for variation in striae periodicities between geographical locations, as well as to verify the other bio-environmental determinants of striae periodicity.

Keywords: striae periodicity, striae of Retzius, cross-striations, circaseptan interval, enamel

OPEN ACCESS

Edited by:
Alexandre Rezende Vieira, University of Pittsburgh, United States

Reviewed by:
Juliana Feltrin Souza, Federal University of Paraná, Brazil
Claudio Cantù, University of Zurich, Switzerland

***Correspondence:**
Chin-Ying S. Hsu
denhsus@nus.edu.sg

Specialty section:
This article was submitted to Craniofacial Biology and Dental Research, a section of the journal Frontiers in Physiology

Received: *24 April 2017*
Accepted: *12 June 2017*
Published: *29 June 2017*

Citation:
Tan SHX, Sim YF and Hsu C-YS (2017) Difference in Striae Periodicity of Heilongjiang and Singaporean Chinese Teeth. Front. Physiol. 8:442. doi: 10.3389/fphys.2017.00442

INTRODUCTION

Enamel is the outermost layer of the anatomical crown of the human tooth. It is formed via amelogenesis, a process that comprises of a presecretory stage, secretory stage, transition stage, maturation stage and post-maturation stage (Berkovitz et al., 2009). Incremental lines have been observed in enamel. Cross-striations are seen under light microscope as small transverse lines that run perpendicular to the long axis of enamel prism, and are approximately 4 μm apart (Risnes, 1986). Results from direct experimental studies indicate that cross-striations correlate with a circadian rhythm of ameloblast secretion activity (Schour and Poncher, 1937). In contrast, Striae of Retzius are a manifestation of a long-period incremental growth. Under transmitted light microscope, they appear as dark lines that run at an oblique angle to enamel prisms and cross-striations (Smith, 2006), and emerge on the enamel surface as grooves called perikymata (**Figure 1**). Striae of Retzius occur due to the slowing down of ameloblastic activity at regular intervals (Bromage et al., 2009). Striae periodicity refers to the number of daily increments,

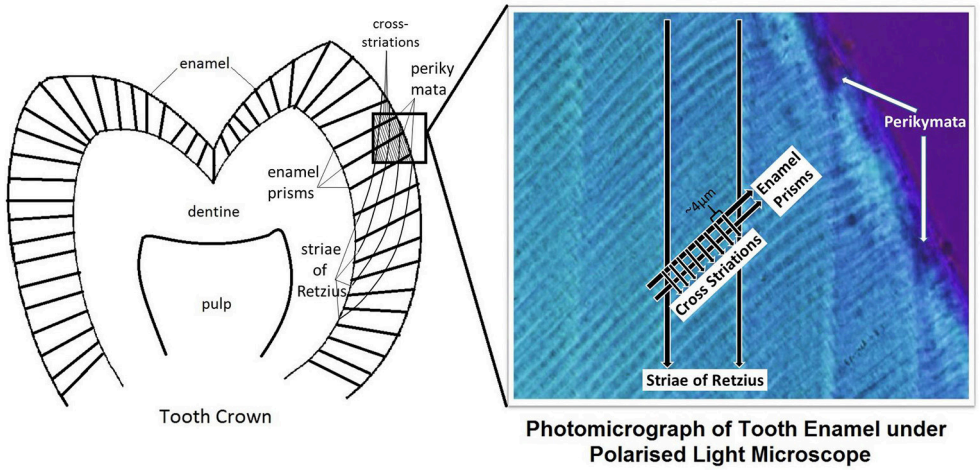

FIGURE 1 | Schematic diagram of tooth.

represented by cross-striations, between two adjacent striae of Retzius. By counting the number of cross striations between striae of Retzius (Berkovitz et al., 2009), by calculation based on a division of the distance between adjacent striae by the average cross striation repeat interval (FitzGerald, 1998), or by estimation (Reid and Ferrell, 2006), striae periodicity has been determined (Supplementary Table 1). A potential explanation for the regular periodicity of striae of Retzius is chronobiology, or the adaptation of cyclic phenomena in living organisms to solar and lunar related rhythms (DeCoursey et al., 2009). Seasons, earth magnetism, solar flares and sunspots appear to have a correlation with human heart rate and melatonin cycles (Cornelissen et al., 2010), and studies suggest that genetically-encoded physiologic circaseptan (7 day) rhythms in humans were evolutionarily adapted to heliogeomagnetic environmental circaseptans (Cornelissen et al., 1998). Although the exact reason remains uncertain, other causes of the regular striae periodicity in enamel could include biologic rhythms controlled by the suprachiasmatic nucleus (Hastings, 1997b), and hormonal controls. Rats with lesions of the suprachiasmatic nucleus have shown disruptions in dentinal incremental lines, while growth and parathyroid hormones known to affect odontoblasts are thought to be responsible for the circadian rhythm of dentin increments (Ohtsuka-Isoya et al., 2001). In addition, melatonin levels increase at night and decrease in the day (Hastings, 1997a), which has been found to correspond with darker stained layers in dentine at night and lighter stained layers in dentine incremental lines of Sprague-Dawley rats (Mishimaa et al., 2012). These suggest the influence of biologic rhythms and hormones on periodic markings in teeth, which may include the Striae of Retzius.

Extensive studies have shown no difference between striae periodicities in different parts of a single tooth (Fukuhara, 1959; Beynon, 1992; FitzGerald, 1998; Mahoney, 2008, 2012). Within an individual, periodicity values are also consistent regardless of the tooth type, or the jaw arch from which the tooth is taken (FitzGerald, 1998; Reid et al., 1998; Mahoney, 2012). Nevertheless, inter-individual variations in striae periodicities have been noted. Proposed factors affecting striae periodicity include gender, ethnicity, body mass and metabolic rate differences (Schwartz et al., 2001; Bromage et al., 2009). However, body mass differences have been said to account more for inter-species or inter-taxa variations in striae periodicity (Schwartz et al., 2001; Smith et al., 2003). Other potential influences include temperature, diet, pH and fluoride levels that affect amelogenesis (Humphrey et al., 2008; Bronckers et al., 2009; Lacruz et al., 2010), although there is currently no direct evidence for these.

With regards to gender effects, a study by Smith et al. (2007) showed inconsistent developmental differences between males and females. While females were found to have a significantly higher periodicity in the South African sample, no significant gender difference was found in the North American sample. No statistical differences in striae periodicity were noted between male and female homo sapiens, despite a faster daily enamel secretion rate in female hominoids (Schwartz et al., 2001). The overall reported range of mean striae periodicity of modern humans is from 6 to 12.3 (FitzGerald, 1998; Reid and Dean, 2006; Supplementary Table 1). The mean striae periodicity values of South African, Northern England, and Northern American populations has been found to be 8.6, 8.1, and 7.9 respectively with South Africans demonstrating a statistically higher mean periodicity than other continental groups (Smith et al., 2007). On the other hand, the mean striae periodicity of early Homo, Australopithecines, and Medieval Danish has been cited as 8, 7 (Lacruz et al., 2006) and 8.5 (Reid and Ferrell, 2006) respectively. Modal periodicity values of early humans range from 7 to 9 (Lacruz et al., 2006).

Given the lack of research comparing striae periodicities across gender groups and populations in different geographical locations, particularly in the Asian context, we sought to examine and compare the striae periodicities of Heilongjiang (China)

Chinese and Singaporean Chinese, as well as that of Singaporean males and females in this study.

MATERIALS AND METHODS

A total of 35 non-carious and non-restored permanent teeth from 35 patients were collected from various dental clinics in Singapore. Another 35 teeth were conveniently collected from various hospitals and clinics in Heilongjiang, China. The teeth were indicated for extraction by dentists for patients' needs. Institution Research Board approval (B-14-004E) was obtained before the start of the study.

Teeth samples were washed in distilled water immediately following extraction, and cleaned thoroughly to remove debris and soft tissues. They were then stored in saline (0.5 Eq/L) in separate labeled containers tagged with a biohazard sign.

A Buehler Isomet Low Speed Saw with a cutting diamond-wafering blade was used to section the teeth longitudinally from cusp tip to cemento-enamel junction with section planes oriented buccolingually and centered through the tips of cusps and the underlying dentine horns. The blade speed was kept at 4 (Marks et al., 1996). Sections were then carefully removed using a cutter blade to obtain two sections per tooth.

Following, the sections were hand ground using a graded series of gradually finer grit Buehler Met-II grinding pads (P800, P1000, P1200, P2500, P4000) with silicon carbide abrasive, on a Buehler Phoenix Beta Grinding/Polishing Machine, until a thickness of 80–100 μm (Reid et al., 1998) was attained and verified with vernier calipers. Each section was then rinsed with distilled water and air-dried for 24 h to remove smear layers and contaminants from the surface of the section. Sections were then mounted onto a glass slide.

Ground sections were examined under an Olympus BX 51 polarized light microscope at 100X magnification. Prior to viewing, a drop of quinoline solution was applied onto each specimen to reduce the optical mismatch of reflective index at enamel-air and enamel-water interfaces (Brodbelt et al., 1981). The outer enamel between lateral and cervical enamel, where striae of Retzius and cross striations are generally most prominent (Lacruz et al., 2006), was first examined. If the striae of Retzius or cross-striations were unclear, the opposite buccal or lingual site was examined. If no results were yielded, adjacent sites were chosen. The section was excluded if enamel imbrication lines could not be clearly visualized at any site of the section. Digital images were produced using a digital microscope camera (Olympus DP25), and captured using imaging software (Olympus Cell D).

Striae periodicity was measured by direct counting of the number of cross-striations between two adjacent striae on captured photomicrographs, by three independent observers. The number of cross-striations was thus measured in whole integers. The median of the striae periodicity values for each tooth based on the six readings from the two sections (or three readings if one section was excluded) was then determined.

To reduce the inaccuracy of results, care was taken to distinguish specimen and optical artefactsfrom cross-striations and striae of Retzius (Mann et al., 1990). All striae counted were traced to their emergence as perikymata (Antoine and Dean, 2009). Only sections with good image quality, without excessive overlap between enamel prisms, and with consistent striae periodicity counts, were included.

All statistical analyses were carried out using STATA Version 14 (StataCrop. 2015. Stata Statistical Software: Release 14. College Station, TX: StataCorp LP). The extent to which each of the three observers gave consistent striae periodicity counts of the same sample (intra-observer reliability) was assessed. Using a random number generator, five sections were selected and an independent repeat count was done by each observer. The repeat striae periodicity counts were then compared with periodicity counts of the corresponding sections recorded in our results, using single-measure intraclass correlation coefficient (ICC) with a one-way random model. To examine for the extent to which the three observers give consistent striae periodicity counts of the same sample (inter-observer reliability), the corresponding readings for the three observers for all sections were assessed using average-measure ICC with a two-way mixed effect model. ICC reflects the degree of agreement between observations by studying the variation of observations from the same sample. The Kolmogorov-Smirnov test was employed for a test of normality, and a non-parametric approach was applied in the event of violation of the normality assumption. The Mann-Whitney U-test was applied to compare the striae periodicities of Heilongjiang Chinese and Singaporean Chinese, as well as that of Singaporean males and females. The significance level for tests was set at 5%.

RESULTS

Out of the 35 Singaporean Chinese teeth, one was excluded as cross-striations and Retzius lines could not be clearly determined from the two sections of the tooth. Seven Heilongjiang Chinese teeth and four Singaporean Chinese teeth had only one section (instead of two) that was determined to be diagnostically acceptable.

Striae periodicity values of the 34 remaining extracted tooth samples from the Singapore population (Supplementary Table 3) and the 35 tooth samples from the Heilongjiang population (Supplementary Table 2) were finalized and analyzed. Within the Singaporean population, the data was further segregated into two groups: striae periodicity values of the 18 teeth from Chinese Male Singaporean residents, and that of the 16 teeth from Chinese Female Singaporean residents.

To first establish that the observations from the two sections from each tooth were similar, a test for homogeneity between the two sections was performed using the Wilcoxon Sign Rank test. No statistically significant differences were observed between the striae periodicity counts of two sections from each tooth ($p = 0.593$). The ICC of average measures on absolute agreement to measure inter-observer reliability was reported at 0.92. On the other hand, the ICC to measure intra-observer reliability for Observer A, Observer B, and Observer C was 0.71, 0.72, and 0.71 respectively. In view of the homogeneity between the sections from each tooth and high degree of inter-observer reliability on striae periodicity counts, the striae periodicity count of each tooth

was summarized using the median reading across sections and observers.

According to the Kolmogorov-Smirnov test for normality, the median striae periodicities of the samples of teeth from both Heilongjiang and Singapore do not follow a normal distribution. Median striae periodicity counts were 7 for both Singapore Chinese group and Heilongjiang Chinese group. However, there is a statistically significant difference in the distribution of striae periodicity counts ($p < 0.001$). As seen in **Figure 2A**, Heilongjiang Chinese teeth tend to have lower striae periodicity counts as compared to Singaporean Chinese teeth. Close to half (49%) of the Heilongjiang Chinese group had striae periodicity counts of 6, while 94% of the Singapore Chinese group had striae periodicity counts of 7 or 8.

Median striae periodicity counts were reported at 7 for both Singaporean Chinese male teeth and Singaporean Chinese female teeth (**Figure 2B**). No statistically significant difference in striae periodicity counts was observed between the teeth from Singapore Chinese males and Singapore Chinese females ($p = 0.511$).

DISCUSSION

Our results suggest that there is a higher striae periodicity of teeth from Singapore than that from Heilongjiang. This is similar to the results published on the striae periodicity of teeth from different geographical locations, which revealed that South Africans have a higher mean periodicity than North

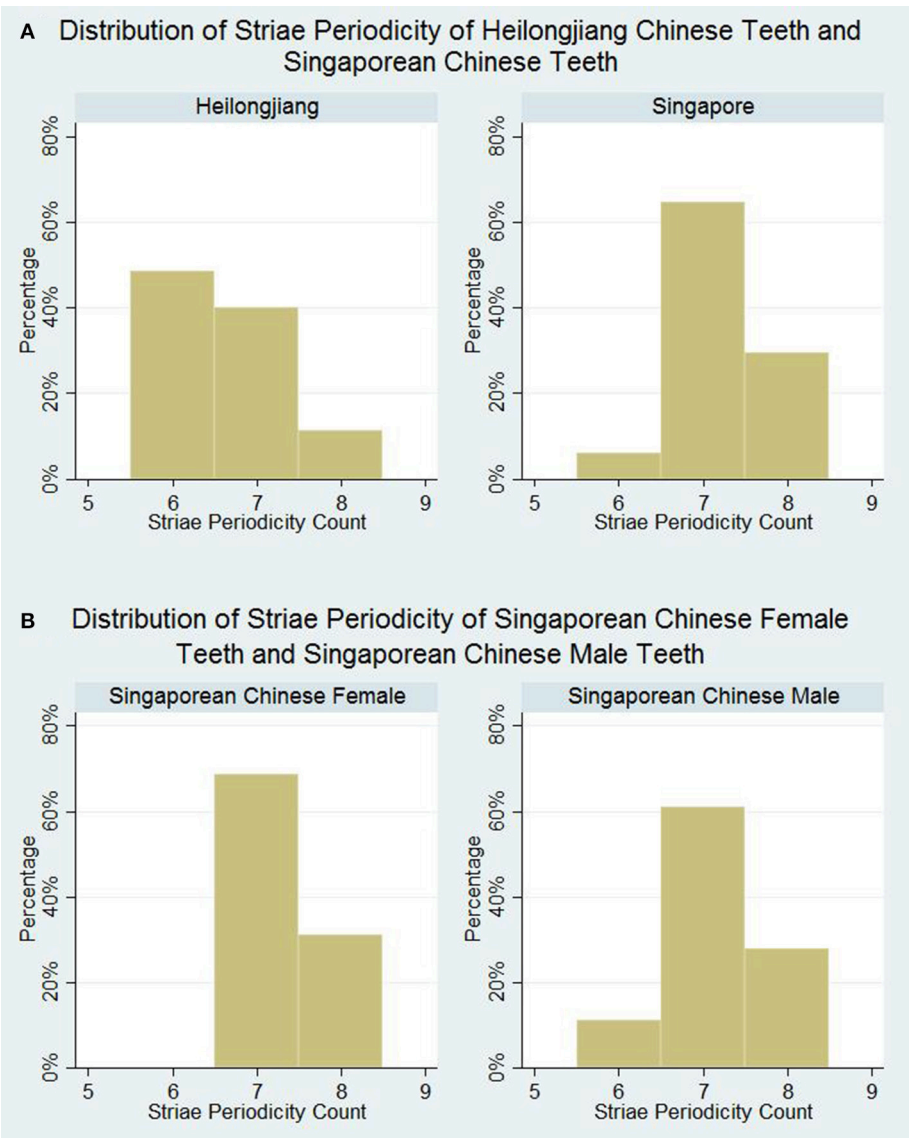

FIGURE 2 | Distribution of striae periodicity. **(A)** Distribution of striae periodicity of Heilongjiang Chinese teeth and Singaporean Chinese teeth. **(B)** Distribution of striae periodicity of Singaporean Chinese female teeth and Singaporean Chinese male teeth.

Europeans and North Americans (Reid and Dean, 2006). While no clear explanations have been given for this difference in the existing literature, one plausible explanation is that people in different geographic locations experience different degrees of light exposure (Burgess, 2009). Assuming the amount of exposure to artificial light in both populations is similar, overall light exposure is higher for Singaporean Chinese than Heilongjiang Chinese due to shorter daytimes in winter for the latter. Given that the human suprachiasmatic nuclei synchronizes internal metabolic circadian rhythms to external light and dark cycles, shorter light hours may alter neuron firing patterns in the suprachiasmatic nuclei via the light sensitive retino-hypothalamic pathway (Brancaccio et al., 2014), resulting in a lower striae periodicity in Heilongjiang teeth. Study data have suggested that circadian clock genes regulate enamel secretion and mineralization by ameloblasts (Zheng et al., 2011), and amelogenin gene expression has been found to be two-fold lower during dark periods compared to light periods (Lacruz et al., 2012). Nevertheless, it is inconclusive if the difference identified in this study is biologically or clinically significant.

In 2012, Bromage et al. (2012) investigated another model of biologic rhythm—the Havers Halberg oscillation (HHO). HHO has been proposed to drive long term biologic rhythms that determine the regular periodicity of Striae of Retzius in enamel, as well as of bone lamella formation. It is generated in the hypothalamus, and regulates growth and body mass through pituitary secretions. The body mass and basal metabolic rates of primates have, in turn, been found to be significantly correlated with striae repeat interval (Bromage et al., 2012). HHO rhythms are said to have evolved in response to selection pressures. Applying the intra-specific HHO (Mahoney et al., 2016), the tropical warm climate of Singapore may favor a different oscillation of the HHO compared to that in the temperate climate of Heilongjiang, leading to higher basal metabolic rates and higher long term striae periodicities. Nevertheless, this argument may be potentially defective due to findings that basal metabolic rates either do not differ between temperate and "hot" climates (Ocobock, 2016), or are lower in tropical climates than temperate climates (Mason and Jacob, 1972).

Furthermore, Newman and Poole hypothesized that a Retzius line is formed when a free running endogenous circadian rhythm is most offset from a more precise 24-h exogenous circadian rhythm (Newman and Poole, 1993). It may be possible that environmental cues such as temperature and climate that vary with geographic location result in variations in the time at which the two cycles are most offset from each other, resulting in a difference in striae periodicity.

Our study showed no statistically significant gender difference in striae periodicity, which is echoed in the study by Schwartz et al. (2001). The lack of disparity between Singaporean Chinese male and female teeth in our study may be cautiously interpreted taking into consideration the following factors. First, the teeth selected in our study were mainly premolars and molars, rather than canines that are thought to be the most sexually dimorphic in terms of size and shape (Plavcan, 2001). Male canines are on average larger and heavier than female canines (Schwartz and Dean, 2005). Nevertheless, this reasoning may be disputed as striae periodicities in different tooth types (incisors, canines, premolars, molars) has been found to be equal in a single individual (FitzGerald, 1998; Reid et al., 1998; Mahoney, 2012). Second, some studies that reported different striae periodicity values between male and female genders did not set geographical location as a constant (FitzGerald, 1998). Since striae periodicity has been shown to vary according to geographical location in our study, the differing results in other studies may be attributed to confounders, such as geographic location. Third, our study is slightly underpowered (power = 78.6%) for the investigation of gender difference at an effect size of 1, based on a *post-hoc* power analysis. Nevertheless, the observed distributions of striae periodicity counts of males and females were similar (**Figure 2B**), suggesting that gender differences may not be clinically relevant.

For reliability testing, the ICC of 0.92 reflects excellent inter-observer reliability. The ICC for all three observers are between 0.5 and 0.75, indicating moderate intra-observer reliability (Cicchetti, 1994; Koo and Li, 2016). The difficulties in striae measurement, due to striae convergence at the tooth surface and the presence of intradian lines and laminations that confound the striae counting process (Smith et al., 2003), may have contributed to the minor differences in final and repeat striae counts by the same observer.

Applications

The total cross-striation count after birth has been found to be highly consistent with those expected from the known ages (Risnes, 1998; Stavrianos et al., 2010). The knowledge of average striae periodicity values of Heilongjiang and Singaporean Chinese populations may thus allow us to make more accurate age estimations in forensic dentistry based on incompletely formed primary and permanent teeth.

The research also adds value in the academic field, particularly in the study of dental histology, by offering an insight into the influence of gender on striae periodicity. The study is one of the first of its kind that examines samples from Asian populations, and investigates the effect of geographical location on striae periodicity, with ethnicity kept constant. As such, this study serves as a stepping-stone for future studies.

Limitations

Logistical limitations prevented the procurement of gender information for the Heilongjiang samples. Further studies with multivariate regression analyses could be conducted to investigate the relationship between demographic and biopsychosocial factors, and striae periodicity counts.

As this study only involved the use of Polarized Light Microscopy, data cannot be confirmed should there be errors due to instrument or measurement limitations. To further improve the study quality, alternative microscopy techniques such as laser confocal scanning microscopy may be explored (Antoine and Dean, 2009).

CONCLUSION

Results show a statistically significant difference between striae periodicity values of Heilongjiang and Singaporean Chinese, but not between gender groups. Further studies with different instruments and methodologies may be required to identify other confounders of striae periodicity values.

AUTHOR CONTRIBUTIONS

ST and CH were involved in the conception and design of the work, data acquisition, analysis, interpretation, and drafting and revision of the manuscript. YS was involved in data analysis and interpretation, and revising the manuscript. All authors are responsible for final approval of the version to be published and agree to be accountable for the content of the work.

FUNDING

This study is funded by the UROP research fund, Department of Dentistry, Faculty of Dentistry, National University of Singapore and partially supported by the Singapore Ministry of Health's National Medical Research Council under its "Clinician Scientist—Individual Research Grant" Scheme, NMRC/CIRG/1341/2012 (grant #R-221-000-059-511).

ACKNOWLEDGMENTS

We would like to thank Florence Limbri, Nicole Thio, and Junhui Yuan for their invaluable contributions and involvement in the research process. We would also like to express our gratitude to Mr. Chan Swee Heng and Dr. Chen Huizhen, for their patient guidance on use of equipments including the microtome, Buehler Isomet machine, and the Polarized Light Microscope.

SUPPLEMENTARY MATERIAL

The Supplementary Material for this article can be found online at: http://journal.frontiersin.org/article/10.3389/fphys.2017.00442/full#supplementary-material

REFERENCES

Antoine, D. H. S., and Dean, M. C. (2009). The developmental clock of dental enamel: a test for the periodicity of prism cross-striations in modern humans and an evaluation of the most likely sources of error in histological studies of this kind. *J. Anat.* 214, 45–55. doi: 10.1111/j.1469-7580.2008.01010.x

Berkovitz, B. K. B., Holland, G. R., and Moxham, B. J. (2009). *Oral Anatomy, Histology and Embryology*. Edinburgh: Elsevier.

Beynon, A. D. (1992). *Circaseptan Rhythms in Enamel Development in Modern Humans and PlioPleistocene Hominids*. London: Freund Publishing House.

Brancaccio, M., Enoki, R., Mazuski, C. N., Jones, J., Evans, J. A., and Azzi, A. (2014). Network-mediated encoding of circadian time: the suprachiasmatic nucleus (SCN) from genes to neurons to circuits, and back. *J. Neurosci.* 34, 15192–15199. doi: 10.1523/JNEUROSCI.3233-14.2014

Brodbelt, R. H. W., O'Brien, W. J., Fan, P. L., Frazer-Dib, J. G., and Yu, R. (1981). Translucency of human dental enamel. *J. Dent. Res.* 60, 1749–1753. doi: 10.1177/00220345810600100401

Bromage, T. G., Hogg, R. T., Lacruz, R. S., and Hou, C. (2012). Primate enamel evinces long period biological timing and regulation of life history. *J. Theor. Biol.* 305, 131–144. doi: 10.1016/j.jtbi.2012.04.007

Bromage, T. G., Lacruz, R. S., Hogg, R., Goldman, H. M., McFarlin, S. C., Warshaw, J., et al. (2009). Lamellar bone is an incremental tissue reconciling enamel rhythms, body size, and organismal life history. *Calcif. Tissue Int.* 84, 388–404. doi: 10.1007/s00223-009-9221-2

Bronckers, A., Lyaruu, D., and DenBesten, P. (2009). The impact of fluoride on ameloblasts and the mechanisms of enamel fluorosis. *J. Dent. Res.* 88, 877–893. doi: 10.1177/0022034509343280

Burgess, P. (2009). "Variation in light intensity at different latitudes and seasons, effects of cloud cover, and the amounts of direct and diffused light," in *Continuous Cover Forestry Group (CCFG) Scientific Meeting* (Westonbirt Arboretum, Gloucestershire).

Cicchetti, D. V. (1994). Guidelines, criteria, and rules of thumb for evaluating normed and standardized assessment instruments in psychology. *Psychol. Assess.* 6:284. doi: 10.1037/1040-3590.6.4.284

Cornelissen, G., Halberg, F., Breus, T. K., Watanabe, Y., Sothern, R. B., Haus, E., et al. (1998). The origin of the biological week from data on the rhythm of cardiac contractions in people during the solar activity cycle. *Biofizika* 43, 666–669.

Cornelissen, G., Halberg, F., Sothern, R., Hillman, D., and Siegelova, J. (2010). Blood pressure, heart rate and melatonin cycles synchronization with the season, earth magnetism and solar flares. *Scr. Med. (Brno).* 83, 16–32.

DeCoursey, P. J., Dunlap, J. C., and Loros, J. J. (2009). *Chronobiology: Biological Timekeeping*. Massachusetts: Sinauer Inc.

FitzGerald, C. M. (1998). Do enamel microstructures have regular time dependency? Conclusions from the literature and a large-scale study. *J. Hum. Evol.* 35, 371–386. doi: 10.1006/jhev.1998.0232

Fukuhara, T. (1959). Comparative anatomical studies of the growth lines in the enamel of mammalian teeth. *Acta Anat. Nipp.* 34, 322–332.

Hastings, M. H. (1997a). Circadian clocks. *Curr. Biol.* 7, R670. doi: 10.1016/S0960-9822(06)00350-2

Hastings, M. H. (1997b). The vertebrate clock: localisation, connection and entrainment. *Handb. Exp. Pharmacol.* 125, 1–28. doi: 10.1016/S0960-9822(06)00350-2

Humphrey, L. T., Dean, M. C., Jeffries, T. E., and Penn, M. (2008). Unlocking evidence of early diet from tooth enamel. *Proc. Natl. Acad. Sci. U.S.A.* 105, 6834–6839. doi: 10.1073/pnas.0711513105

Koo, T. K., and Li, M. Y. (2016). A guideline of selecting and reporting intraclass correlation coefficients for reliability research. *J. Chiropr. Med.* 15, 155–163. doi: 10.1016/j.jcm.2016.02.012

Lacruz, R. S., Hacia, J. G., Bromage, T. G., Boyde, A., Lei, Y., Xu, Y., et al. (2012). The circadian clock modulates enamel development. *J. Biol. Rhythms* 27, 237–245. doi: 10.1177/0748730412442830

Lacruz, R. S., Nanci, A., Kurtz, I., Wright, J. T., and Paine, M. L. (2010). Regulation of pH during amelogenesis. *Calcif. Tissue Int.* 86, 91–103. doi: 10.1007/s00223-009-9326-7

Lacruz, R. S., Rozzi, F. R., and Bromage, T. G. (2006). Variation in enamel development of South African fossil hominids. *J. Hum. Evol.* 51, 580–590. doi: 10.1016/j.jhevol.2006.05.007

Mahoney, P. (2008). Intraspecific variation in M1 enamel development in modern humans: implications for human evolution. *J. Hum. Evol.* 55, 131–147. doi: 10.1016/j.jhevol.2008.02.004

Mahoney, P. (2012). Incremental enamel development in modern human deciduous anterior teeth. *Am. J. Phys. Anthropol.* 147, 637–651. doi: 10.1002/ajpa.22029

Mahoney, P., Miszkiewicz, J. J., Pitfield, R., Schlecht, S. H., Deter, C., and Guatelli-Steinberg, D. (2016). Biorhythms, deciduous enamel thickness, and primary bone growth: a test of the Havers-Halberg Oscillation hypothesis. *J. Anat.* 228, 919–928. doi: 10.1111/joa.12450

Mann, A., Lampl, M., and Monge, J. (1990). Patterns of ontogeny in human evolution: evidence from dental development. *Am. J. Phys. Anthropol.* 33, 111–150. doi: 10.1002/ajpa.1330330507

Marks, M. K., Rose, J. C., and Davenport, W. D. Jr. (1996). Technical note: thin section procedure for enamel histology. *Am. J. Phys. Anthropol.* 99, 493–498.

Mason, E. D., and Jacob, M. (1972). Variations in basal metabolic rate responses to changes between tropical and temperate climates. *Hum. Biol.* 44, 141–172.

Mishimaa, H., Hattori, A., Suzuki, N., Tabata, M., Kakei, M., Miake, Y., et al. (2012). "The connection between the periodicity of incremental lines in the tooth dentin and the regulation by melatonin," in *ECTS 2012, 39th Annual Congress* (Stockholm).

Newman, H. N., and Poole, D. F. (1993). Dental enamel growth. *J. R. Soc. Med.* 86, 61.

Ocobock, C. (2016). Human energy expenditure, allocation, and interactions in natural temperate, hot, and cold environments. *Am. J. Phys. Anthropol.* 161, 667–675. doi: 10.1002/ajpa.23071

Ohtsuka-Isoya, M., Hayashi, H., and Shinoda, H. (2001). Effect of suprachiasmatic nucleus lesion on circadian dentin increment in rats. *Am. J. Physiol. Regul. Integr. Comp. Physiol.* 280, R1364–R1370. Available online at: http://ajpregu.physiology.org/content/280/5/R1364.long

Plavcan, J. M. (2001). Sexual dimorphism in primate evolution. *Am. J. Phys. Anthropol.* 116, 25–53. doi: 10.1002/ajpa.10011

Reid, D. J., Beynon, A. D., and Ramirez Rozzi, F. V. (1998). Histological reconstruction of dental development in four individuals from a medieval site in Picardie, France. *J. Hum. Evol.* 35, 463–477. doi: 10.1006/jhev.1998.0233

Reid, D. J., and Dean, M. C. (2006). Variation in modern human enamel formation times. *J. Hum. Evol.* 50, 329–346. doi: 10.1016/j.jhevol.2005.09.003

Reid, D. J., and Ferrell, R. J. (2006). The relationship between number of striae of Retzius and their periodicity in imbricational enamel formation. *J. Hum. Evol.* 50, 195–202. doi: 10.1016/j.jhevol.2005.09.002

Risnes, S. (1986). Enamel apposition rate and the prism periodicity in human teeth. *Scand. J. Dent. Res.* 94, 394–404. doi: 10.1111/j.1600-0722.1986.tb01779.x

Risnes, S. (1998). Growth tracks in dental enamel. *J. Hum. Evol.* 35, 331–350. doi: 10.1006/jhev.1998.0229

Schour, I., and Poncher, H. (1937). Rate of apposition of enamel and dentin, measured by the effect of acute fluorosis. *Am. J. Dis. Child.* 54, 757–776. doi: 10.1001/archpedi.1937.01980040061005

Schwartz, G. T., and Dean, M. C. (2005). Sexual dimorphism in modern human permanent teeth. *Am. J. Phys. Anthropol.* 128, 312–317. doi: 10.1002/ajpa.20211

Schwartz, G. T., Reid, D. J., and Dean, C. (2001). Developmental aspects of sexual dimorphism in hominoid canines. *Int. J. Primatol.* 22, 837–860. doi: 10.1023/A:1012073601808

Smith, T. M. (2006). Experimental determination of the periodicity of incremental features in enamel. *J. Anat.* 208, 99–113. doi: 10.1111/j.1469-7580.2006.00499.x

Smith, T. M., Martin, L. B., and Leakey, M. G. (2003). Enamel thickness, microstructure and development in Afropithecus turkanensis. *J. Hum. Evol.* 44, 283–306. doi: 10.1016/S0047-2484(03)00006-X

Smith, T. M., Reid, D. J., Dean, M. C., Olejniczak, A. J., Ferrell, R. J., and Martin, L. B. (2007). "New perspectives on chimpanzee and human molar crown development," in *Dental Perspectives on Human Evolution: State of the Art Research in Dental Paleoanthropology*, eds S. Bailey and J.-J. Hublin (Dordrecht: Springer), 177–192.

Stavrianos, C., Papadopoulos, C., Vasiliadis, L., Dagkalis, P., Stavrianou, I., and Petalotis, N. (2010). Enamel structure and forensic use. *Res. J. Biol. Sci.* 5, 650–655. doi: 10.3923/rjbsci.2010.650.655

Zheng, L., Papagerakis, S., Schnell, S. D., Hoogerwerf, W. A., and Papagerakis, P. (2011). Expression of clock proteins in developing tooth. *Gene Expr. Patterns* 11, 202–206. doi: 10.1016/j.gep.2010.12.002

Conflict of Interest Statement: The authors declare that the research was conducted in the absence of any commercial or financial relationships that could be construed as a potential conflict of interest.

Copyright © 2017 Tan, Sim and Hsu. This is an open-access article distributed under the terms of the Creative Commons Attribution License (CC BY). The use, distribution or reproduction in other forums is permitted, provided the original author(s) or licensor are credited and that the original publication in this journal is cited, in accordance with accepted academic practice. No use, distribution or reproduction is permitted which does not comply with these terms.

frontiers in Physiology

ORIGINAL RESEARCH
published: 16 June 2017
doi: 10.3389/fphys.2017.00405

Crystal Initiation Structures in Developing Enamel: Possible Implications for Caries Dissolution of Enamel Crystals

Colin Robinson[1]* *and Simon D. Connell*[2]

[1] School of Dentistry, University of Leeds, Leeds, United Kingdom, [2] Molecular and Nanoscale Physics Group, School of Physics and Astronomy, University of Leeds, Leeds, United Kingdom

OPEN ACCESS

Edited by:
Ariane Berdal,
UMRS 1138 Institut National de la Santé et de la Recherche Médicale (INSERM), Université Paris Diderot, France

Reviewed by:
Janet Moradian-Oldak,
University of Southern California, United States
Lucia Jimenez-Rojo,
University of Zurich, Switzerland
Elia Beniash,
University of Pittsburgh, United States
Pamela DenBesten,
University of California, San Francisco, United States

***Correspondence:**
Colin Robinson
c.robinson@leeds.ac.uk

Specialty section:
This article was submitted to Craniofacial Biology and Dental Research, a section of the journal Frontiers in Physiology

Received: *08 March 2017*
Accepted: *29 May 2017*
Published: *16 June 2017*

Citation:
Robinson C and Connell SD (2017) Crystal Initiation Structures in Developing Enamel: Possible Implications for Caries Dissolution of Enamel Crystals. Front. Physiol. 8:405. doi: 10.3389/fphys.2017.00405

Investigations of developing enamel crystals using Atomic and Chemical Force Microscopy (AFM, CFM) have revealed a subunit structure. Subunits were seen in height images as collinear swellings about 30 nM in diameter on crystal surfaces. In friction mode they were visible as positive regions. These were similar in size (30–50 nM) to collinear spherical structures, presumably mineral matrix complexes, seen in developing enamel using a freeze fracturing/freeze etching procedure. More detailed AFM studies on mature enamel suggested that the 30–50 nM structures were composed of smaller units, ∼10–15 nM in diameter. These were clustered in hexagonal or perhaps a spiral arrangement. It was suggested that these could be the imprints of initiation sites for mineral precipitation. The investigation aimed at examining original freeze etched images at high resolution to see if the smaller subunits observed using AFM in mature enamel were also present in developing enamel i.e., before loss of the organic matrix. The method used was freeze etching. Briefly samples of developing rat enamel were rapidly frozen, fractured under vacuum, and ice sublimed from the fractured surface. The fractured surface was shadowed with platinum or gold and the metal replica subjected to high resolution TEM. For AFM studies high-resolution tapping mode imaging of human mature enamel sections was performed in air under ambient conditions at a point midway between the cusp and the cervical margin. Both AFM and freeze etch studies showed structures 30–50 nM in diameter. AFM indicated that these may be clusters of somewhat smaller structures ∼10–15 nM maybe hexagonally or spirally arranged. High resolution freeze etching images of very early enamel showed ∼30–50 nM spherical structures in a disordered arrangement. No smaller units at 10–15 nM were clearly seen. However, when linear arrangements of 30–50 nM units were visible the picture was more complex but also smaller units including ∼10–15 nM units could be observed.

Conclusions: Structures ∼10–15 nM in diameter were detected in developing enamel.While the appearance was complex, these were most evident when the 30–5 nM structures were in linear arrays. Formation of linear arrays of subunits may be associated with the development of mineral initiation sites and attendant processing of matrix proteins.

Keywords: enamel, crystals, initiation, assembly, caries

INTRODUCTION

Enamel comprises highly ordered crystals of substituted hydroxyapatite. These are of regular size and shape, densely packed with their long c-axes parallel and arranged in bundles, the enamel prisms. The precise mechanism of initiation and growth of these crystals is unclear.

Early transmission electron microscope (TEM) data suggested that crystals formed immediately outside of the ameloblast membrane, immediately after matrix secretion, appearing as thin needles or plates (Leblond and Warshawsky, 1979). However, to avoid the TEM preparation processes of dehydration, fixation and embedding in hydrophobic media which could induce premature precipitation and crystallization, early enamel was viewed using freeze etching which examines fractured surfaces of frozen unfixed tissue (Robinson et al., 1981). This revealed ∼30 nm globular structures arranged both randomly and in linear arrays. Crystals only became visible during maturation after loss of matrix protein. The globules therefore are most likely complexes of amorphous mineral stabilized by protein. The dimensions and arrangement of these globules suggested that they are forerunners of the crystals seen in maturing enamel and delineate both the size, shape, and disposition of the crystals in mature tissue (Robinson et al., 1981). Subsequent investigations have supported the presence of amorphous mineral in early enamel (Aoba and Moreno, 1990; Rey et al., 1991; Diekwisch et al., 1995) which may also explain the very diffuse X ray diffraction patterns reported for early enamel (Nylen et al., 1963).

Globular crystal precursors were also supported by atomic and chemical force microscopy (AFM, CFM) of maturation stage enamel crystals. AFM revealed contiguous regular 30–50 nM globular swellings along maturation stage enamel crystals, redolent of the globules shown by freeze etching but which had subsequently fused and crystallized (Kirkham et al., 2001; Robinson et al., 2004) ultimately giving rise to the regular repeating charge domains on maturing crystals reported by Kirkham et al. (2000).

In addition, however, later high resolution AFM indicated that the 30–50 nM globular structures comprised smaller ∼15 nM subunits arranged in roughly hexagonal or possibly spiral patterns (Robinson et al., 2004, 2006). Since these may represent imprints of original crystal initiation structures, earlier freeze etched data was re-examined at high resolution for their presence. High resolution freeze etched images, did reveal ∼15 nM substructures within the original globules. *These appeared more obviously as the globules formed linear arrays, possibly reflecting matrix processing associated with transition from amorphous mineral to crystals.*

MATERIALS AND METHODS

Freeze etching of early enamel was reported by Robinson et al. (1981). Briefly, early enamel was carefully frozen in liquid nitrogen (−198°C) and fractured under vacuum using a histological knife. The knife was then repositioned over the fractured surface and its temperature lowered to sublime ice from the tissue on to the knife blade. This left a fractured tissue surface unencumbered by ice. The fractured frozen surface was then shadowed, under vacuum, with gold or aluminum. Tissue was dissolved away and the metal replica examined using TEM.

AFM was carried out as described previously (Kirkham et al., 2001; Robinson et al., 2004) using a Nanoscope III AFM (Digital Instruments) equipped with a 16E16-μm scanner and 25 μm silicon nitride cantilevers. Images were obtained in oscillating mode at 0.2 Hz below resonance with drive amplitudes in the range 300–950 mV. Measurements of crystal width and height were made using the software provided.

RESULTS AND DISCUSSION

As previously reported, the data shown illustrates the presence of 30–50 nM diameter globules in secretory enamel, arranged randomly or in linear arrays (Robinson et al., 1981), **Figure 1A**. That these represent crystal forerunners was supported by high resolution AFM height images of deproteinated maturation enamel crystals (Kirkham et al., 2001). AFM images revealed contiguous 30–50 nM diameter swellings along crystal surfaces presumably representing mineralized replacements of original matrix -mineral structures, **Figure 1B**.

However, high resolution AFM images of mature enamel also revealed previously unreported 15 nM substructures within the ∼30 nM globules arranged in roughly hexagonal or perhaps spiral patterns (Robinson et al., 2004, 2006), **Figures 1C,D**. These most likely represent original mineral initiation structures comprising amorphous mineral stabilized by matrix proteins. While the original freeze etching investigation reported 30–50 nM globules, it did not refer to any smaller structures, the images had not, however, been examined at high resolution. When this was carried out smaller globules 15 nM in size were in fact visible, **Figure 1E**. Although it was not possible to discern exactly how these were arranged they are clearly forerunners of the fully mineralized 15 nM subunits seen in mature enamel crystals.

Approximately 15 nM units of enamel structure have also been reported using other techniques. Diekwisch (1998) reported polygonal, possibly mineral particles at about ∼15 nM adjacent to secretory ameloblasts and more recently Beniash et al. (2009) using TEM, showed linear arrays of spherical particles each measuring about 15 nM. This study also used electron diffraction, FITR XPEEM and demonstrated that amorphous mineral was present.

These 15 nM structures may be amorphous mineral *per-se* but are more likely to be mineral matrix complexes. That they appeared more clearly when 30 nM globules lined up suggests that matrix processing may be involved in alignment and mineral precipitation see below (Fang et al., 2011). It is proposed that the ∼15 nM subunits represent mineral initiation sites where mineral nuclei precipitate and subsequently fuse both into long chains and laterally into wider 30–50 nM structures before transforming into hydroxyapatite.

Figure 2 illustrates the proposed formation of enamel crystals from∼15 nM protein mineral complexes to the fully mature crystal. 15 nM structures form comprising mineral ions stabilized

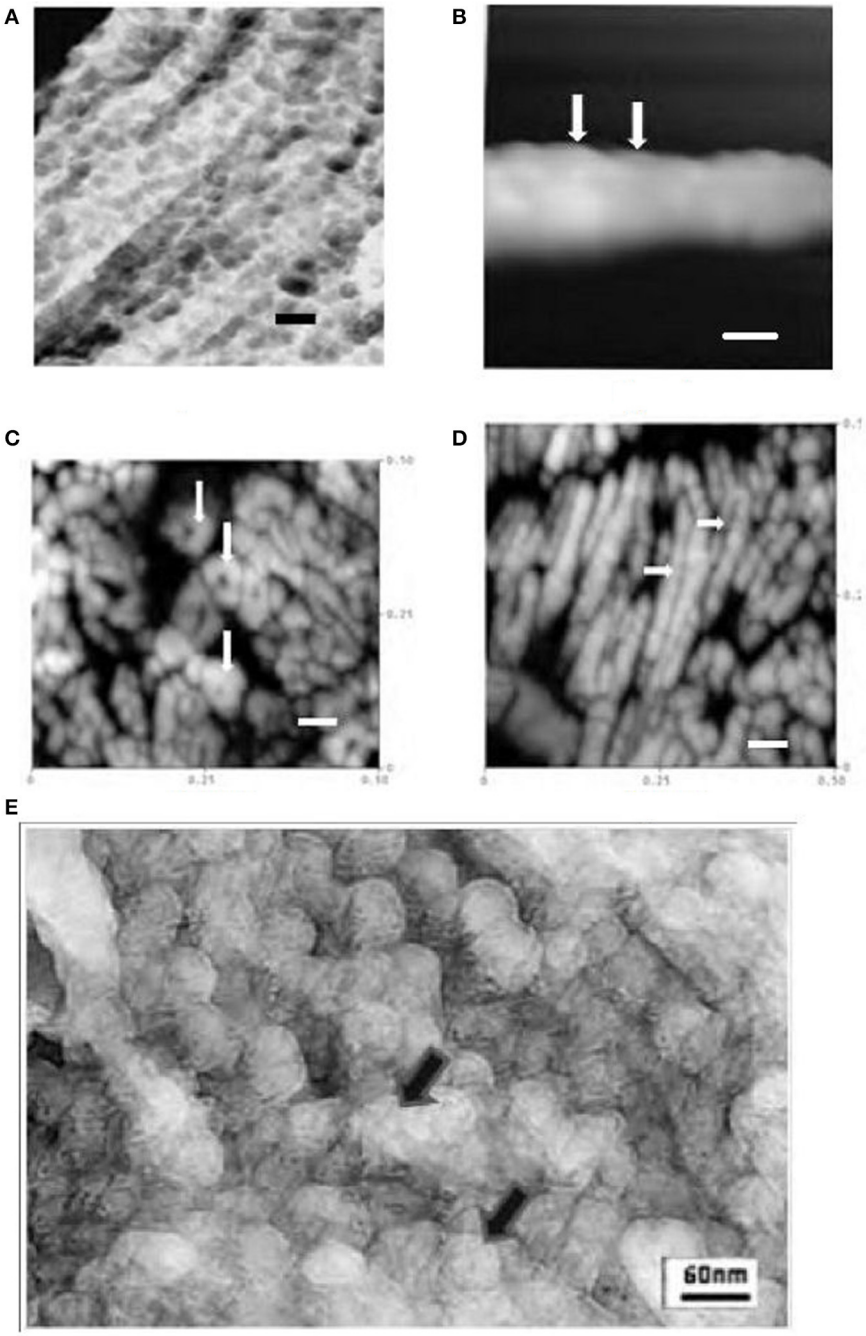

FIGURE 1 | (A) TEM freeze etched enamel showing repeated globular structures ∼30–50 nM dia in linear arrays (rat incisor) (Robinson et al., 1981) (bar = 60 nM). **(B)** AFM tapping mode in air of *maturation stage* enamel crystal showing repeated contiguous globular subunits ∼30 nM diameter (rat incisor, tapping mode in air) (Kirkham et al., 2000; Robinson et al., 2004) arrows (bar=30 nM).**(C)**. AFM image of polished section of mature human enamel. Cross sections of enamel crystals are visible showing ∼15 nM subunits in roughly hexagonal clusters (tapping mode in air) (Robinson et al., 2004) arrows (bar =60 nM). **(D)** AFM image of polished section of mature human enamel. Longitudinal sections of enamel crystals are visible showing 15nm subunits, (human, tapping mode in air) longitudinal interface between subunits can be seen arrows (Robinson et al., 2004) (bar = 60 nM). **(E)** High resolution TEM image of freeze etched rat incisor secretory enamel showing 30–50 nM globules but comprising smaller ∼15 nM subunits, arrows.

by matrix protein. These assemble, either as linear strings which fuse laterally to produce long chains of roughly hexagonal clusters or the hexagonal clusters themselves form and assemble lengthwise to produce long chains of roughly hexagonal clusters. Removal of matrix at some point results in mineral precipitation and transformation to apatite and the clusters fuse to become

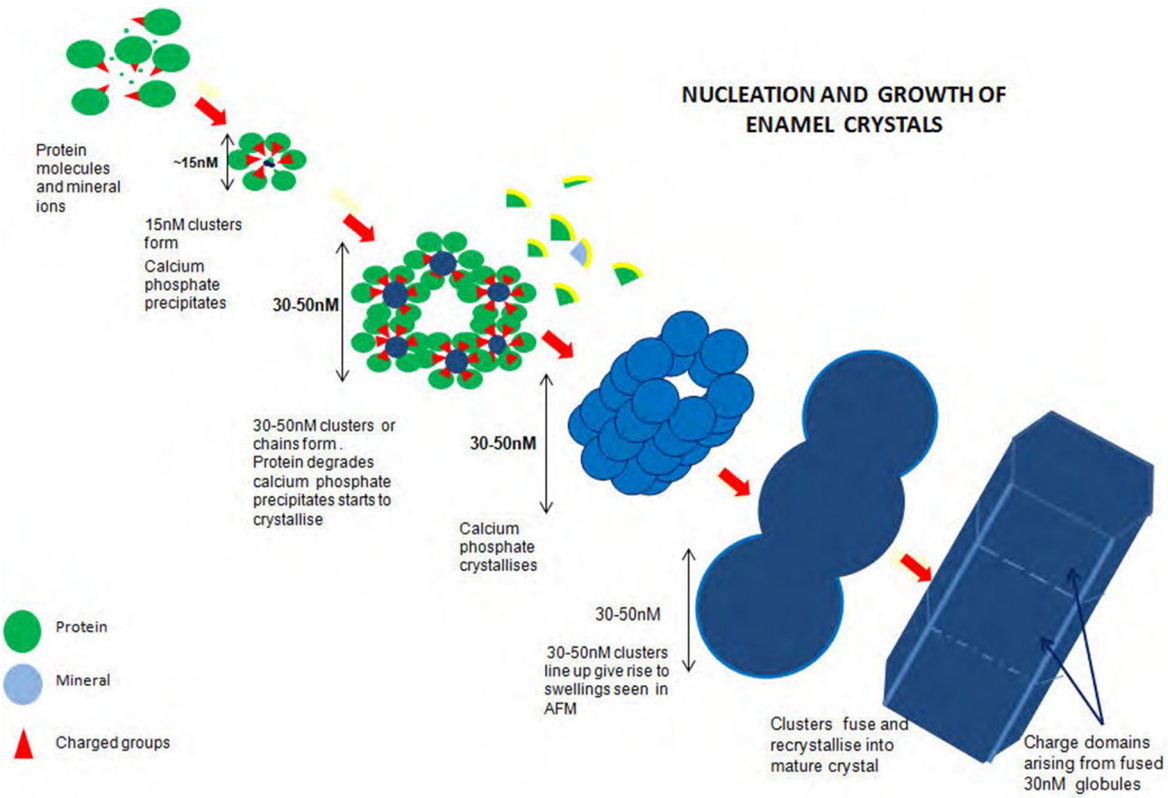

FIGURE 2 | Diagram of proposed formation of enamel crystals from ~15 nM protein mineral complexes to the fully mature crystal. Fifteen nM structures form comprising mineral ions stabilized by matrix protein. These assemble, either as linear strings which fuse laterally to produce long chains of roughly hexagonal clusters or the hexagonal clusters themselves form and assemble lengthwise to produce long chains of roughly hexagonal clusters. Removal of matrix at some point results in mineral precipitation and transformation to apatite and the clusters fuse to become chains of globular structures ~30 nM diameter. Recrystallization results in the mature enamel crystal with crystalline or chemical discontinuities at the fusion interfaces.

chains of globular structures ~30 nM diameter. Recrystallisation results in the mature enamel crystal with crystalline or chemical discontinuities at the fusion interfaces.

It is not yet known precisely how the amorphous material is initiated and temporarily stabilized. Initiation may occur within the 15 nM subunits if ionic peptide side chains, for example, the C terminal peptide of amelogenin and/or its phosphate group are turned inward and the subunits held together by hydrophobic interaction (**Figure 2**).

The rapid loss of the hydrophilic C terminal of amelogenin and loss of the phosphate group have been implicated in the transformation from stabilized amorphous mineral to crystalline phase (see Kwak et al., 2011; Khan et al., 2012). Loss of phosphate may be related to the presence of phosphatase activity reported by Robinson et al. (1990) and Moe et al. (1996). *In vitro* investigations using amelogenin (Fang et al., 2011) have indicated the capacity of amelogenin not only to stabilize amorphous calcium phosphate but also to foster the development of long apatite crystal bundles by oligomeric organization into chains. This does not, however, preclude the effect of further protein processing or a role for other enamel proteins such as enamelin and ameloblastin. It should also be borne in mind that the decrease in the high concentrations of carbonate and magnesium present in early enamel could effect a transformation from amorphous to crystalline phase (Hiller et al., 1975; Aoba and Moreno, 1990; Rey et al., 1991).

The significance of clustering of 15 nM initiation sites is significant from a number of points of view. From the viewpoint of enamel structure, clustering into 30–50 nM units delineates the ultimate crystal width and thickness thus outlining tissue volume to be occupied by crystals. This is important since the matrix is ultimately removed.

This also has implications for enamel caries since the fused interface between these units would lead to increased acid solubility due to crystalline discontinuity (see Robinson et al., 2004). Chemical discontinuity may also occur as high concentrations of carbonate and magnesium may be moved to these interfaces during recrystallization associated with crystal growth. Lateral fusion would lead to a discontinuity along the length of the crystal at its center, while longitudinal fusion would lead to lateral discontinuities perpendicular to the central line. These are the sites at which enamel crystals are known to dissolve preferentially

during carious attack (Johnson, 1967; Yanagisawa and Miake, 2003).

ETHICS STATEMENT

Wistar rats were maintained and killed according to local and national animal regulations. University of Leeds Dental School Animal Committee. Human extracted teeth were obtained from the tissue bank at Leeds dental School. Teeth were obtained according to national and local guidelines permission obtained at source.

AUTHOR CONTRIBUTIONS

CR designed and set up both investigations and was largely responsible for freeze etch studies. SC carried out and advised upon AFM and CFM investigations. Both authors interpreted data and discussed implications, both were involved in writing.

REFERENCES

Aoba, T., and Moreno, E. C. (1990). Changes in the nature and composition of enamel mineral during porcine amelogenesis. *Calcif. Tissue Int.* 47, 356–364. doi: 10.1007/BF02555887

Beniash, E., Metzler, R. A., Lam, R. S., and Gilbert, P. (2009). Transient amorphous calcium phosphate in forming enamel. *J. Struct. Biol.* 166, 133–143. doi: 10.1016/j.jsb.2009.02.001

Diekwisch, T. (1998). Subunit compartments of secretory stage enamel matrix. *Connect. Tissue Res.* 38, 101–111. doi: 10.3109/03008209809017026

Diekwisch, T. G. H., Berman, B. J., Gentner, S., and Slavkin, H. C. (1995). Initial enamel crystals are not spatially associated with mineralized dentine. *Cell Tissue Res.* 279, 149–167.

Fang, P., Conway, J. F., Margolis, H. C., Simmer, J. P., and Beniash E. (2011). Hierarchical self-assembly of amelogenin and the regulation of biomineralization at the nanoscale. *Proc. Nat. Acad. Sci. U.S.A.* 34, 14097–14102. doi: 10.1073/pnas.1106228108

Hiller, C. R., Robinson, C., and Weatherell, J. A. (1975). Variations in the composition of developing rat incisor enamel. *Calcif. Tiss. Res.* 18, 1–12. doi: 10.1007/BF02546222

Johnson, N. W. (1967). Some aspects of the ultrastructure of early human enamel caries seen with the electron microscope. *Archs oral Biol.* 12, l505–1521. doi: 10.1016/0003-9969(67)90186-0

Khan, F., Li, W., and Habelitz, S. (2012). Biophysical characterization of synthetic amelogenin C-terminal peptides. *Eur. J. Oral Sci.* 120, 113–122. doi: 10.1111/j.1600-0722.2012.00941.x

Kirkham, J., Brookes, S. J., Zhang, J., Wood, S. R., Shore, R. C., Smith, D. A., et al. (2001). Effect of experimental fluorosis on the surface topography of developing enamel crystals. *Caries Res.* 35, 50–56. doi: 10.1159/000047431

Kirkham, J., Brookes, S. J., Zhang, J., Wood, S. R., Shore, R. C., Smith, D. A., et al. (2000). Evidence for charge domains on developing enamel crystal surfaces. *J. Dent. Res.* 79, 1943–1947. doi: 10.1177/00220345000790120401

Kwak, S. Y., Green, S., Wiedemann-Bidlack, F. B., Beniash, E., and Yamakoshi, Y. C. (2011). Regulation of calcium phosphate formation by amelogenins under physiological conditions. *Eur. J. Oral Sci.* 119, 103–111. doi: 10.1111/j.1600-0722.2011.00911.x

Leblond, C. P., and Warshawsky, H. (1979). Dynamics of enamel formation in the rat incisor tooth. *J. Dent. Res.* 58, 950–975. doi: 10.1177/00220345790580024901

Moe, D., Kirkeby, S., and Salling, E. (1996). Biochemical characterisation of alkaline phosphatase from partly mineralized bovine enamel. *J. Biol. Buccale* 14, 249–253.

Nylen, M. U., Eanes, E. D., and Omnell, K. A. (1963). Crystal growth in rat enamel. *J. Cell Biol.* 18, 109–123. doi: 10.1083/jcb.18.1.109

Rey, C., Shimizu, M., Collins, B., and Glimcher, M. (1991). Resolution-enhanced Fourier transform infrared spectroscopy study of the environment of phosphate ion in the early deposits of a solid phase of calcium phosphate in bone and enamel and their evolution with age. 2. Investigations in the v3 PO4 domain. *Calcif. Tissue Int.* 49, 383–388. doi: 10.1007/BF025 55847

Robinson, C., Connell, S., Kirkham, J., Shore, R. C., and Smith, A. (2004). Dental enamel, a biological ceramic: regular substructures in enamel hydroxyapatite crystals revealed by atomic force microscopy. *J. Mater. Chem.* 14, 2242–2248. doi: 10.1039/b401154f

Robinson, C., Fuchs, P., and Weatherell, J. A. (1981). The appearance of developing rat incisor enamel using a freeze fracturing technique. *J. Cryst. Growth* 53, 160–165. doi: 10.1016/0022-0248(81)90062-2

Robinson, C., Shore, R. C., Kirkham, J., and Stonehouse, N. J. (1990). Extracellular processing of enamel matrix proteins and the control of crystal growth. *J. Biol. Buccale* 18, 355–361.

Robinson, C., Yamamoto, K., Connell, S., Kirkham, J., Nakagaki, H., and Smith, A. D. (2006). The effects of fluoride on the nanostructure and surface pK of enamel crystals. An atomic force microscopy study of human and rat enamel. *Eur. J Oral Sci.* 114 , 1–10. doi: 10.1111/j.1600-0722.2006.00275.x

Yanagisawa, T., and Miake, Y. (2003). High-resolution electron microscopy of enamel crystal demineralization and remineralization in carious lesions. *J. Electron. Microsc.* 52, 605–613. doi: 10.1093/jmicro/52.6.605

Conflict of Interest Statement: The authors declare that the research was conducted in the absence of any commercial or financial relationships that could be construed as a potential conflict of interest.

Copyright © 2017 Robinson and Connell. This is an open-access article distributed under the terms of the Creative Commons Attribution License (CC BY). The use, distribution or reproduction in other forums is permitted, provided the original author(s) or licensor are credited and that the original publication in this journal is cited, in accordance with accepted academic practice. No use, distribution or reproduction is permitted which does not comply with these terms.

frontiers in Physiology

ORIGINAL RESEARCH
published: 08 June 2017
doi: 10.3389/fphys.2017.00368

Elastin-Like Protein, with Statherin Derived Peptide, Controls Fluorapatite Formation and Morphology

Kseniya Shuturminska[1,2], *Nadezda V. Tarakina*[2,3], *Helena S. Azevedo*[2,3,4], *Andrew J. Bushby*[2,3], *Alvaro Mata*[2,3,4], *Paul Anderson*[1] and *Maisoon Al-Jawad*[1,3]*

[1] *Dental Physical Sciences Unit, Institute of Dentistry, Barts and The London School of Medicine and Dentistry, Queen Mary University of London, London, United Kingdom,* [2] *School of Engineering and Materials Science, Queen Mary University of London, London, United Kingdom,* [3] *Materials Research Institute, Queen Mary University of London, London, United Kingdom,* [4] *Institute of Bioengineering, Queen Mary University of London, London, United Kingdom*

The process of enamel biomineralization is multi-step, complex and mediated by organic molecules. The lack of cells in mature enamel leaves it unable to regenerate and hence novel ways of growing enamel-like structures are currently being investigated. Recently, elastin-like protein (ELP) with the analog *N*-terminal sequence of statherin (STNA15-ELP) has been used to regenerate mineralized tissue. Here, the STNA15-ELP has been mineralized in constrained and unconstrained conditions in a fluoridated solution. We demonstrate that the control of STNA15-ELP delivery to the mineralizing solution can form layered ordered fluorapatite mineral, via a brushite precursor. We propose that the use of a constrained STNA15-ELP system can lead to the development of novel, bioinspired enamel therapeutics.

Keywords: enamel biomimetics, elastin-like proteins, fluorapatite, biomineralization model

OPEN ACCESS

Edited by:
Alexandre Rezende Vieira, University of Pittsburgh, United States

Reviewed by:
Eric Everett, University of North Carolina at Chapel Hill, United States
Yuqiao Zhou, University of Pittsburgh, United States

***Correspondence:**
Maisoon Al-Jawad
m.al-jawad@qmul.ac.uk

Specialty section:
This article was submitted to Craniofacial Biology and Dental Research, a section of the journal Frontiers in Physiology

Received: *10 March 2017*
Accepted: *18 May 2017*
Published: *08 June 2017*

Citation:
Shuturminska K, Tarakina NV, Azevedo HS, Bushby AJ, Mata A, Anderson P and Al-Jawad M (2017) Elastin-Like Protein, with Statherin Derived Peptide, Controls Fluorapatite Formation and Morphology. Front. Physiol. 8:368. doi: 10.3389/fphys.2017.00368

INTRODUCTION

It is well established that enamel biomineralization occurs via a complex, multistep and matrix mediated process. The matrix is made up of many macromolecules including glycoproteins and proteins rich in negatively charged residues, such as amelogenin, enamelin and amelotin (Iijima et al., 2010; Moradian-Oldak and Paine, 2010; Abbarin et al., 2015). These negative residues can bind calcium ions, initiate nucleation and, *via* inhibition and promotion, carefully regulate the crystal growth, morphology and alignment (Mann, 2001). Specifically, biomineralizing proteins have stereochemical matching to crystal surfaces and can inhibit crystal growth in a particular direction. The crystal growth process is further controlled by local pH changes that are said to be crucial in normal enamel development (Lacruz et al., 2010).

The process of dental enamel formation is tightly controlled by ameloblasts and produces a highly organized mineral structure that protects us from infection and mastication forces. However, enamel becomes completely acellular and almost depleted of the proteinaceous matrix when mature. During enamel maturation, the process of enzymatic protein degradation and removal is essential in order to allow for the apatite crystals to fill up the space. The end result is a highly mineralized tissue with a high modulus and hardness arising from 96% by weight mineral content (Deakins and Volker, 1941; Cuy et al., 2002). Although enamel's structure and composition give it its superior mechanical properties, the lack of cells makes it unable to biologically regenerate following damage.

Materials have been developed and used in order to restore enamel tissue when it has been lost after carious infection, removal or trauma. However, these materials lack the intrinsic hierarchical structure and in general have inferior properties compared to enamel, leading to further failure. Today, researchers are looking for new and innovative ways of forming enamel-like structures for repair or remineralization of early carious enamel lesions. Examples of these include the formation of enamel prism-like bundles of apatite needles synthesized in solution (Chen et al., 2005), the use of casein for remineralization (Vashisht et al., 2010), use of a modified hydroxyapatite paste (Yamagishi et al., 2005) and synthetic or natural peptides which promote apatite formation (Brunton et al., 2013; Ruan and Moradian-Oldak, 2014). These examples provide evidence of ordered hydroxyapatite (HAp) formation, epitaxial growth or remineralization.

Often, research looks at including fluoride ions (F^-) into therapeutics such as toothpastes. The F^- ions can incorporate into the apatite structure by replacing the hydroxide ion (OH^-) located in the middle of the hexagonal HAp crystal. This exchange forms fluorapatite (FAp). The F^- causes a reduction in the *a* and *b* unit cell parameters of the apatite structure which directly decreases the crystal energy (Robinson et al., 1995). The reduced crystal energy gives rise to the increased stability of FAp in acids, compared to HAp, deeming it more useful in dental applications. FAp has been synthesized in a variety of ways, for example as a coating on implants (Czajka-Jakubowska et al., 2009; Dunne et al., 2015) or hydrothermally in solution (Chen et al., 2006). However, in order to mimic the natural biomineral formation, we must understand how proteins can be utilized in order to control the nucleation, growth and morphology of FAp.

Recently, elastin-like proteins (ELPs) have been exploited for use in synthetic biomineralization. These are recombinant proteins, produced by genetically modified bacteria, that can be engineered to contain various bioactive sites (Girotti et al., 2004). One such bioactive site is the analog of the 15 amino acid *N*-terminal of statherin (STNA15). Statherin, a 43 amino acid protein present in saliva, aids in remineralization of enamel, on a daily basis, via calcium ion chelation. It is believed that statherin's high affinity to apatite arises from its acidic *N*-terminal domain (Raj and Johnsson, 1992). However, more recent work showed that the basic residues, such as arginine and lysine, also play a crucial role in the interaction of statherin with an apatite surface (Ndao et al., 2010). In the STNA15 sequence, the phosphorylated serines (positions 2 and 3), present in natural statherin, are replaced with aspartic acid (Raj and Johnsson, 1992), removing the need for post-translational modification and still retaining the calcium affinity. Elastin-like protein containing the statherin derived peptide sequence (STNA15-ELP) membranes have already shown potential in bone repair (Tejeda-Montes et al., 2014). Furthermore, we have previously demonstrated the ability of these ELPs to form organized apatite structures (Elsharkawy et al., 2016a,b). The focus of the study presented here is to extend the use of the STNA15-ELP to enamel therapeutics. Here, we utilize the ELPs with the STNA15 sequence in order to study their ability to promote organized fluoridated calcium phosphate formation. The role of STNA15-ELP in different conditions is explored by comparing the effect of mineralizing the protein directly in solution or immobilized on a glass surface.

Abbreviations: STNA15, The analog of the 15 amino acid *N*-terminal of natural human statherin protein; ELP, Elastin-like protein; STNA15-ELP, Elastin-like protein containing the analog of the 15 amino acid *N*-terminal of statherin.

MATERIALS AND METHODS

STNA-15 ELP

The STNA15-ELP was acquired from Technical Proteins Nanobiotechnology (Valladolid, Spain). These recombinant proteins are produced by genetically modified bacteria and extracted at the company (Girotti et al., 2004). The full sequence of the protein used in this study is MESLLP-$[((VPGIG)_2VPGKG(VPGIG)_2)_2$-**DDDEEKFLRRIGRFG**-$((VPGIG)_2VPGKG(VPGIG)_2)_2]_3$-V where the STNA15 sequence is highlighted in bold. It has an inverse transition temperature (ITT) of 23°C and isoelectric point (pI) at pH 9.9 (details provided by the supplier).

To prepare the stock protein solution, 1 mg of STNA15-ELP was dissolved in 1 ml of ultrapure water (18 MΩ·cm). The stock solution was then diluted to yield a 100 μg/ml concentration. To prepare constrained protein samples, 100 μl of the dilute solution was pipetted onto borosilicate glass slides (VWR International Ltd, Lutterworth, UK) and left to completely dry at 21°C overnight.

To prepare the unconstrained STNA15-ELP samples, 100 μl of the 1 mg/ml protein stock solution was pipetted directly into 1 ml of the mineralizing solution. After the mineralization period of either 3 h or 8 days, the samples were frozen in liquid nitrogen and lyophilized. The lyophilized samples were washed with ethanol and dried prior to chemical and morphological analysis.

Mineralizing Solution and Studies

The mineralizing solution was used as previously described by Chen et al. (2006). In short, 104.7 mg sinter grade HAp (Plasma Biotal Ltd., Derbyshire, UK) and 8.49 mg sodium fluoride (Sigma Aldrich, UK) was added to 100 ml of ultrapure water (18 MΩ·cm). Sixty nine percent analytical grade nitric acid (VWR International Ltd., Lutterworth, UK) was added drop-wise until the solution became clear and colorless and a pH of 2.4 was reached. Twenty eight to thirty percent ammonium hydroxide (Sigma Aldrich, UK) was added drop-wise to the solution until

TABLE 1 | Contact angle measured for ultrapure water on uncoated borosilicate glass substrate and on a protein coated borosilicate glass ($n = 3$) are given accompanied with the standard error (σ).

Borosilicate glass property	Value ± σ
Water contact angle/θ (experimental)	70.9° ± 2.0
Water contact angle/θ of protein coated glass (experimental)	18.7° ± 1.25
Isoelectric point/pH	3.62 ± 0.12

The value for the isoelectric point of the glass was obtained from literature (Blass et al., 2013).

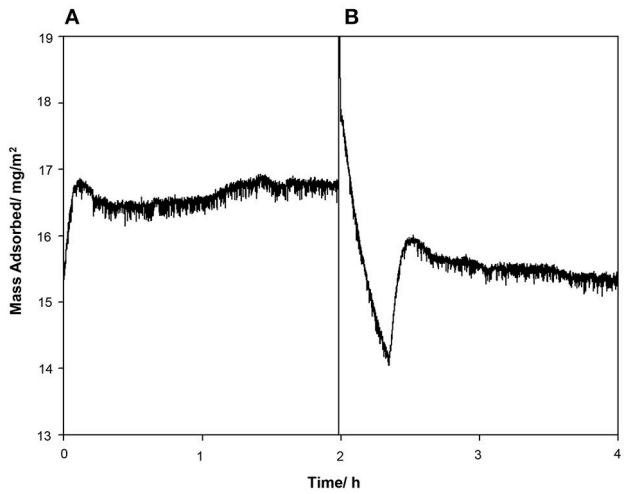

FIGURE 1 | QCM data showing the **(A)** protein injection and **(B)** washing cycles. After the washing cycle the final measured mass adsorbed to the surface was 15.2 mg/m^2.

pH of 6 was reached. The solution was prepared at room temperature and stirred continuously during preparation.

Three milliliters of solution were incubated with each coated sample and 1 ml with STNA15-ELP solution samples. For the coated samples, uncoated borosilicate glass was incubated in the mineralizing solution as a control. Precipitate from pure mineralizing solution, without any protein, was used as a control for unconstrained protein samples. All samples were incubated in the mineralizing solution for either 3 h or 8 days at 37°C in sealed containers.

Quartz Crystal Microbalance (QCM)

Quartz crystal microbalance measurements were carried out in order to check the affinity of the protein to the borosilicate glass. Borosilicate coated quartz sensor crystals (Biolin Scientific Ltd, Stockholm, Sweden) were first washed in a 2% w/v SDS (Sigma Aldrich, UK) solution for 30 min followed by a 10 min UV/ ozone treatment as a cleaning procedure. In the QCM (Q-sense, Biolin Scientific Ltd, Stockholm, Sweden) the crystal was stabilized in ultrapure water then, a solution of STNA15-ELP (100 μg/ml) was added and the QCM measurement was taken until equilibrium was reached. Finally, the crystal was washed again with ultrapure water to remove any unbound or loosely bound protein. The change in resonant frequency of the quartz crystal was converted to mass of protein adsorbed using the Sauerbery equation (Equation 1) where Δm is the change in mass, Δf the measured change in frequency upon protein adsorption, n is the overtone number (3) and C is a constant specific to the crystal.

$$\Delta m = -\frac{C.\Delta f}{n} \quad (1)$$

Contact Angle

A DSA100 Drop Shape Analyzer from Krüss (Hamburg, Germany) was used to measure the contact angle of water on

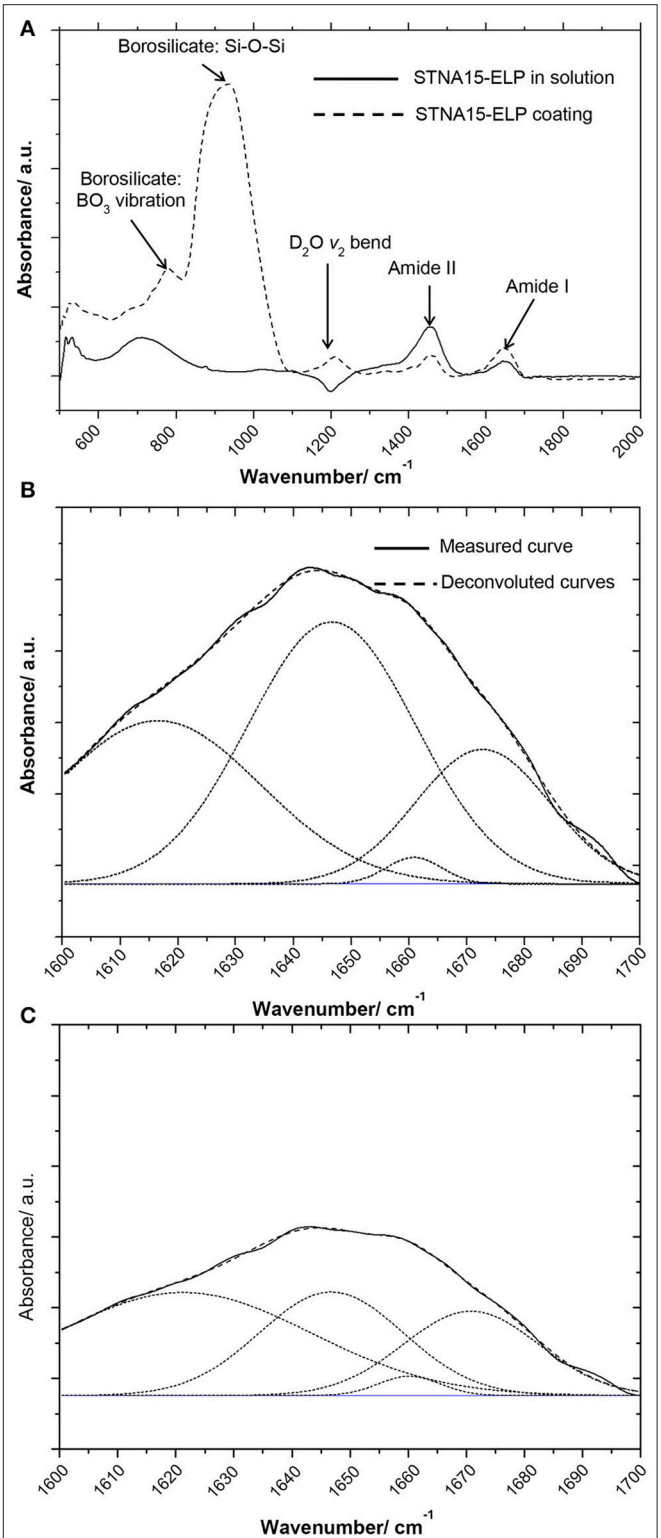

FIGURE 2 | FTIR results of **(A)** coated ELP (dotted line) vs. STNA15-ELP in solution (solid line) showing the difference in the absorbance, especially noticeable difference in the intensity of amide I and II peaks. The Gaussian fit deconvoluted amide I band of **(B)** STNA15-ELP coated on glass and **(C)** protein in solution. The dashed line represents the data and the smooth line is the Gaussian fit.

uncoated and coated borosilicate glass slides. Five microliters of water were pipetted onto the slide and the angle measured immediately. Three repeats were taken and averaged.

Scanning Electron Microscopy (SEM /Energy Dispersive X-Ray Analysis (EDX)

Scanning electron microscopy (SEM) images were recorded, using a secondary electron (SE) and back-scattered electron (BSE) detectors, on an FEI Inspect F SEM (Hillsboro, Oregon, USA) in the NanoVision Centre, Queen Mary University of London. An X-Act Oxford Instruments EDX detector was used for EDX measurements (20 kV accelerating voltage) (Abington, Oxfordshire, UK). The samples were coated with carbon for EDX studies and 20 nm of gold for morphological examination.

Transmission Electron Microscopy (TEM)/Selected Area Electron Diffraction (SAED)

TEM images and SAED patterns were recorded on a JEOL 2010 transmission electron microscope operated at 200 kV (Tokyo, Japan). For the 3 h incubation timepoint of constrained ELP mineralization, the crystals were grown directly on a TEM grid. The 8 day mineralized samples were scraped off the borosilicate glass into ethanol and then pipetted onto grids.

The 3 h and 8 day unconstrained samples were first suspended in ethanol then pipetted onto copper grids and dried prior to TEM inspection.

Attenuated Total Reflection Fourier Transform Infrared Spectroscopy (ATR-FTIR)

ATR-FTIR was carried out using a Bruker Tensor 27 IR spectrometer (Billerica, Massachusetts, USA) to analyze both protein conformation and chemical groups of the mineral precipitate. STNA15-ELP was prepared as previously described with the ultrapure water exchanged for deuterium oxide (D_2O) (VWR International Ltd, Lutterworth, UK).

Before FTIR measurement, an STNA15-ELP coated glass slip was rinsed with D_2O to remove excess protein. The measurements on the coating were taken in a wet condition. Free protein samples were pipetted directly on the ATR window. Eighty scans per measurement, 400–2,000 cm^{-1} range, 3 repeats were acquired and averaged. The FTIR chamber was purged with nitrogen during readings. The amide I region was deconvoluted in Origin Pro using the Gaussian fit and previously reported literature values (Serrano et al., 2007). For the characterization of the mineral precipitate, 60 scans, in the range of 400–4,000 cm^{-1}, were taken for each mineralized sample. All measurements were carried out at 21°C.

TABLE 2 | Wavenumber values of the peak centers and the % area of each assigned peak taken from the deconvolution of the amide I peaks of STNA15-ELP coating and in solution (plotted in **Figure 2**).

Structure	Constrained STNA15-ELP		STNA15-ELP in solution	
	Peak center/cm^{-1}	Area/%	Peak center/ cm^{-1}	Area/%
β-sheet aggregation	1,617	30.2		
β-sheet			1,621	44.3
β-sheet/β-turn	1,647	48.4	1,647	30.2
Random coil	1,661	1.6	1,660	2.4
β-turn	1,673	19.7	1,671	23.1

Raman Spectroscopy

Since the FTIR spectrum of borosilicate glass has large absorptions in the range where calcium phosphate peaks are present, Raman spectroscopy was chosen to analyze the mineral grown on constrained ELP surfaces. A Renishaw inVia Raman Microscope (Wotton-under-Edge, Gloucestershire, UK), equipped with a 633 nm wavelength (20 mW power) laser, was used to record the spectra of the mineral formed in the presence of constrained STNA15-ELP at 3 h and 8 days. A 20x objective was used, giving a spot size of 1.93 μm. The spectra were obtained in the 170–1370 cm^{-1} range with an exposure time of 5 s. Sixty accumulations were recorded for each reading.

RESULTS AND DISCUSSION

STNA15-ELP Adsorption and Conformation

The contact angle of the borosilicate glass surface displayed in **Table 1** is indicative of a surface with low hydrophilicity ($\theta = 70.9°C$). Reports have shown that protein adsorption is favored when $\theta > 65°C$ (Vogler, 2012). Under the given experimental conditions, according to literature value for the isoelectric point (pI), the glass carries a net negative charge (Blass et al., 2013). The protein can arrange itself on the glass surface in such a way that the negative STNA15 (mineralizing) sequence is exposed to the solution due to repulsion from the negatively charged glass surface. The positively charged lysine residues in STNA15-ELP are expected to interact with the negative glass surface. The QCM study confirmed that the STNA15-ELP, in ultrapure water, does bind to the borosilicate glass. The study showed a good binding of STNA15-ELP where 15.2 mg/m^2 remained adsorbed to the substrate after washing with ultrapure water (**Figure 1B**). The contact angle of the coating suggests that the STNA15-ELP coating formed a hydrophilic surface when adsorbed to the glass ($\theta = 18.7°C$, **Table 1**), suggesting the exposure of the hydrophilic mineralizing sequence on the glass surface.

The FTIR spectra of STNA15-ELP in solution vs. STNA15-ELP coating are shown in **Figure 2**. There is a noticeable difference in the amide I (1,600–1,700 cm^{-1}) and amide II (1,400–1,500 cm^{-1}) relative intensities (**Figure 2A**). The amide peaks are normally made up of several components arising due to the stretching vibration of C=O (amide I) and C-N and N-H bending (amide II) (Lenk et al., 1991). The position of the peaks changes depending on the secondary structure of the protein as the hydrogen bonding within the protein alters upon adsorption and/or conformational changes. The dipole moments of the amide I and amide II peaks are almost perpendicular to one another (Miyazawa and Blout, 1961), hence the change in

amide I and amide II intensity is consistent with differences in conformation between the bound and unbound proteins. The overall amide I peak increased in intensity when STNA15-ELP was adsorbed on glass, conversely there was a reduction in the amide II intensity, compared to STNA15-ELP prior to adsorption (**Figure 2A**). Conformational changes of the ELP, upon binding, agree with previous reports of natural elastin structural changes during surface adsorption. Natural elastin is globular in solution and undergoes conformational changes in order to assemble into an ordered structure upon surface adsorption (Subburaman et al., 2006).

To investigate further, the solution (**Figure 2B**) and coated (**Figure 2C**) samples' amide I peaks were deconvoluted using a Gaussian fit. The peak values were chosen according to previous indexed values in literature (Serrano et al., 2007). The results indicate a relative increase in the amount of β-sheet/β-turn structure (at 1,647 cm^{-1}), when the protein was constrained on glass, accompanied with a relative decrease in the random coil component (at 1,660/1,661 cm^{-1}) (**Table 2**). The increase in the amount of β-sheet/β-turn structure and a decrease of the random coil in the amide I band is indicative of an increase in conformation of the secondary structure of STNA15-ELP when adsorbed on a glass substrate.

ELPs are known to have thermoresponsive properties, attributed to their ITT (Urry et al., 1998). It is known that below the ITT the protein is unfolded, mostly with a random

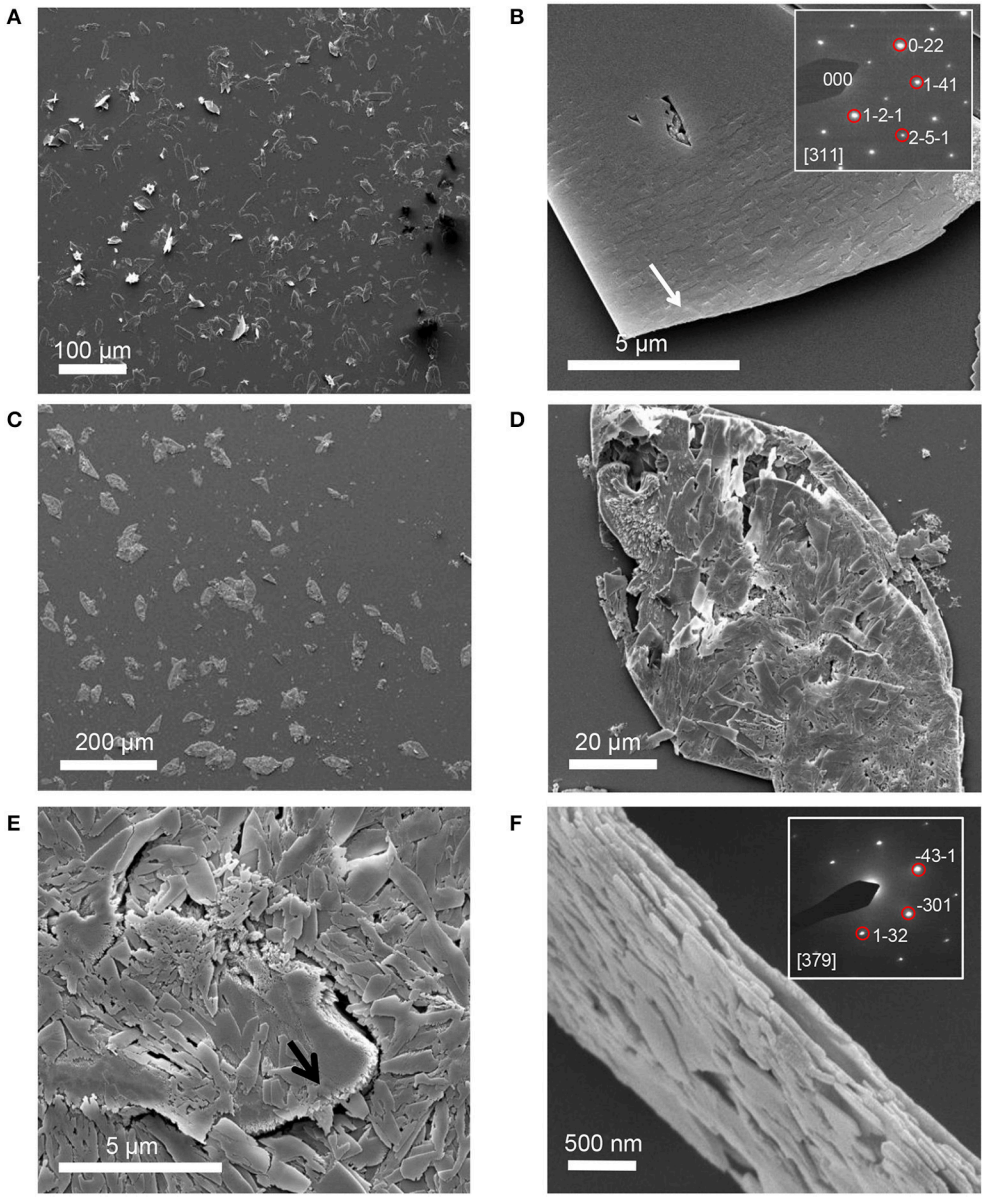

FIGURE 3 | SE images of mineral grown on an STNA15-ELP coated substrate at 3 h **(A,B)** and 8 days **(C–F)**. Single crystal platelets dominate the surface at 3 h with the SAED pattern of brushite, inset of **(B)**. The platelets are polycrystalline FAp at 8 days of incubation. SAED pattern of one of the crystals from the platelet, inset of **(F)**.

coil structure, and the hydrophobic residues are hydrated with clathrate-like water structures (Rodriguez-Cabello, 2004). Above this temperature, the ordered water molecules surrounding the protein are disrupted and the protein becomes dehydrated. The dehydration process causes the protein to fold, via an increase in the β-sheet/β-turn component and simultaneous decrease in random coil, and phase separate. This process is not instantaneous and structural changes occur over a range of temperatures above and below the ITT (for example Reiersen et al., 1998). Previous work by Serrano et al. (2007) investigated ELP structures with FTIR and concluded that below the ITT the protein contains the β-sheet aggregation component (1,616 cm^{-1}), but this completely disappears upon heating above the ITT. The FTIR data presented here shows a similar change between the unconstrained and the constrained STNA15-ELP. From the results presented in **Figure 2** and **Table 2**, it can be expected that upon adsorption on the glass surface the ELP folds into a similar conformation as it would when heated well above the ITT, i.e., the protein loses the random coil component and gains order in its secondary structure.

Protein adsorption is a complex process and can change dramatically with alteration in the surface and solution chemistry. A number of factors that affect adsorption of proteins onto surfaces have been identified. These include pH (pH close to pI promotes adsorption) (Norde, 1986; Norde et al., 1986); substrate hydrophobicity (Shirahama and Suzawa, 1985); dehydration (Lee and Ruckenstein, 1988); and surface-solution equilibrium (Wojciechowski et al., 1986). Although protein adsorption mechanisms can be the result of multiple factors, the adsorption behavior is specific to each protein and the surface it is adsorbing to. In this study, the STNA15-ELP is dissolved in ultrapure water (pH ∼7.0) and is far from its pI. Thus, according to Norde et al. (1986), it would not favorably adsorb to the glass. However, the QCM results (**Figure 1**) confirm that the protein is well bound to the glass surface. Lee and Ruckenstein (1988) proposed that proteins gain entropy upon adsorption to surfaces due to dehydration and structural changes. This explanation is more suitable for the system described here, since STNA15-ELP appears to gain conformation upon adsorption and this is known to occur during the dehydration of the ELP chains and subsequent hydrophobic collapse.

Mineral Morphology and Chemistry

Constrained STNA15-ELP

STNA15-ELP coated on borosilicate glass, incubated in the mineralizing solution at 37°C, produced mineral platelets at both 3 h and 8 days incubation times, as shown in **Figures 3A–F** respectively. EDX analysis (3 hC, **Table 3**) suggests that the platelets at 3 h were brushite [dicalcium phosphate dihydrate (DCPD)], with a Ca/P ratio of approximately 1. Brushite presence was confirmed with SAED (inset **Figure 3B**). Etch pits were visible on the brushite surface due to dissolution of the crystal (arrow, **Figure 3B**). A previous study reported plate-like brushite to grow with a dominant face in the {010} direction (Giocondi et al., 2010). The etch pits typically form on the {010} faces of the brushite crystals. The platelets at day 8 retained their overall platelet shape (**Figure 3D**) but appeared to be a polycrystalline material. EDX analysis of the 8 day sample indicated that the platelets were fluorapatite, with a stoichiometric Ca/P ratio of 1.66 (8 dC, **Table 3**). The SAED of platelets present at 8 days was also indicative of the presence of apatite (inset of **Figure 3F**), agreeing with the EDX analysis.

TABLE 3 | EDX data showing the atomic % of elements present in each sample.

Element	Atomic %				
	Constrained STNA15-ELP		Free STNA15-ELP		CaF_2
	3 hC	8 dC	3 hS	8 dS	
F	–	29.6	38.6	27.9	51.1
P	48.1	26.5	24.7	28.3	2.8
Ca	51.9	43.9	36.7	43.8	46.1
Ca/P Ratio	0.93	1.66	1.48	1.55	16.56

3 hC and 8 dC samples were incubated with the protein adsorbed on the glass for 3 h and 8 days respectively. 3 hS and 8 dS samples were incubated with the protein in solution for 3 h and 8 days respectively. EDX data for calcium fluoride (CaF_2) present in the samples is also given.

The Raman spectra of the mineral formed after 3 h (**Figure 4**) exhibited a strong, sharp peak at 985 cm^{-1}, typical of the ν_2 bending mode of PO_4^{3-} in brushite. The peaks at 381 cm^{-1} (ν_8), 878 cm^{-1} (ν_3) and 1057 cm^{-1} (ν_6) are also indicative of brushite (Casciani and Condrate, 1979; Kim et al., 2002), supporting the SAED and EDX data. The Raman spectrum, of the mineral present in the constrained STNA15-ELP sample after 8 days of incubation, is that of apatite. Raman spectra of apatite are easily characterized by the strong, sharp peak at 961 cm^{-1}, the ν_1 stretching mode of the PO_4^{3-}. Other indicative peaks are visible at 447 and 433 cm^{-1} from the ν_2 bending mode of the PO_4^{3-}; 620, 610, 594, and 582 cm^{-1} form the ν_4 bending mode of the PO_4^{3-}; 1076 and 1054 cm^{-1} from the ν_3 stretching mode of PO_4^{3-}.

SE SEM images of the control sample, uncoated borosilicate glass, show that some mineral is present on the surface after 3 h of incubation (**Figure 5A**). This mineral resembled the shape of the brushite platelets seen in the STNA15-ELP coated samples. However, it appeared to be almost completely dissolved. In contrast to the coated borosilicate glass slide, after 8 days of incubation no mineral platelets were seen on the uncoated substrate (**Figure 5D**). The early dissolution of the mineral and the lack of mineral at the later time suggest that the ELP plays a critical role in stabilizing the early mineral phase.

SEM, EDX and Raman indicate that brushite was the first phase formed in the presence of the constrained STNA15-ELP coating and FAp was present after 8 days of incubation. For instance, brushite typically forms under acidic conditions (Dorozhkin, 2010), such as in this study (pH 6), explaining its presence at early time periods. Even though brushite seems to be the precursor to apatite in this study, brushite and FAp have different crystal structures and therefore are not likely to transform from one to another. Brushite has been reported to have a monoclinic structure (Sainz-Díaz et al., 2004) compared to the hexagonal FAp (Elliott, 1994). These different crystal

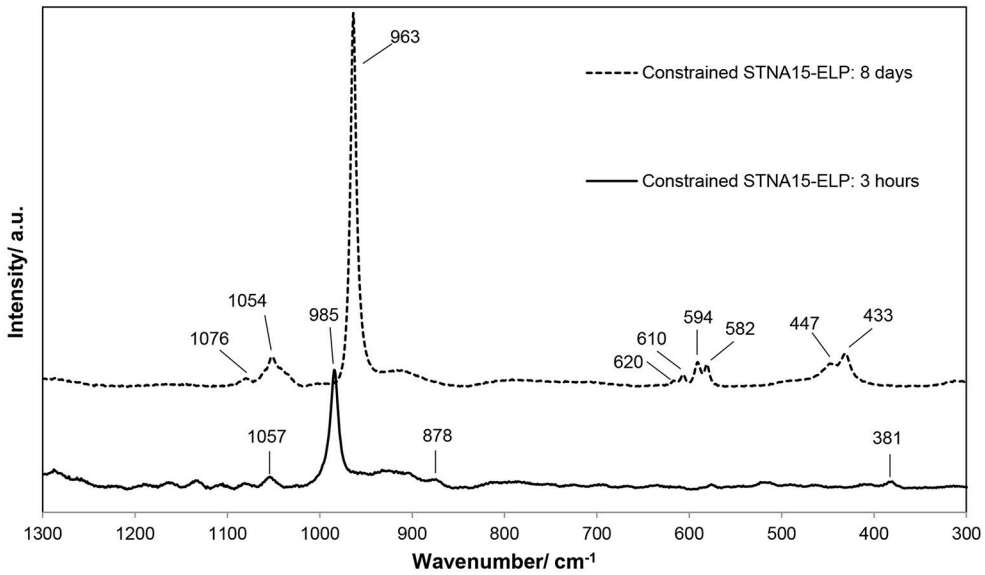

FIGURE 4 | Raman spectroscopic data, in the range of 300–1,300 cm^{-1}, of the mineral formed on the STNA15-ELP coated substrates at 3 h and 8 days of incubation.

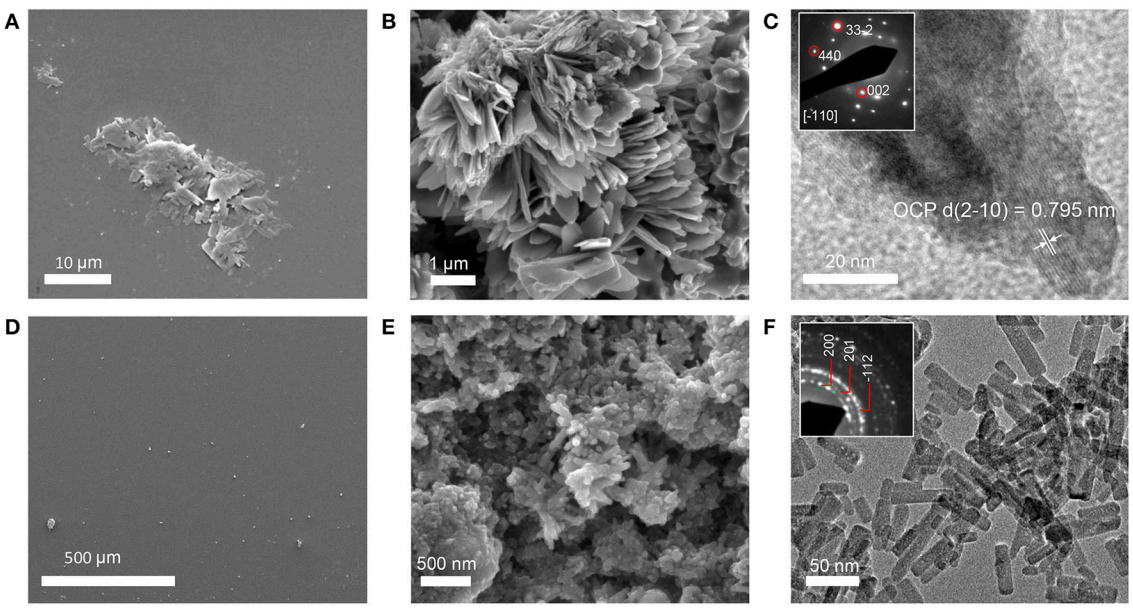

FIGURE 5 | Precipitates formed in control conditions. **(A)** SE image of 3 h non-coated borosilicate glass. **(B)** SE image of precipitate formed in solution without STNA15-ELP. **(C)** High resolution TEM image of precipitate formed in solution with no protein and inset of C showing a typical SAED pattern of the precipitate. **(D)** SE image of the borosilicate surface after 8 days of incubation in mineralizing solution with no platelets present. **(E)** SE image of the precipitate in the control solution with no STNA15-ELP at 8 days. **(F)** TEM image of the precipitate formed in the control solution at 8 days with the inset showing a typical SAED pattern.

structures lead to the conclusion that the change in mineral chemistry and morphology observed between the 3 h and 8 day period, coupled with the etch marks on the brushite surface, occurred due to a dissolution and re-precipitation process. The re-precipitated FAp crystallites were templated by the original brushite crystal, forming a layered ordered structure.

STNA15-ELP in Solution

SE-SEM images of the lyophilized precipitate, formed with STNA15-ELP, are shown in **Figure 6**. After incubation for both 3 h (**Figures 6A,B**) and 8 days (**Figures 6C–F**), needle-like precipitates were visible. However, after 3 h of incubation the needles were only visible when imaged with BSE since they

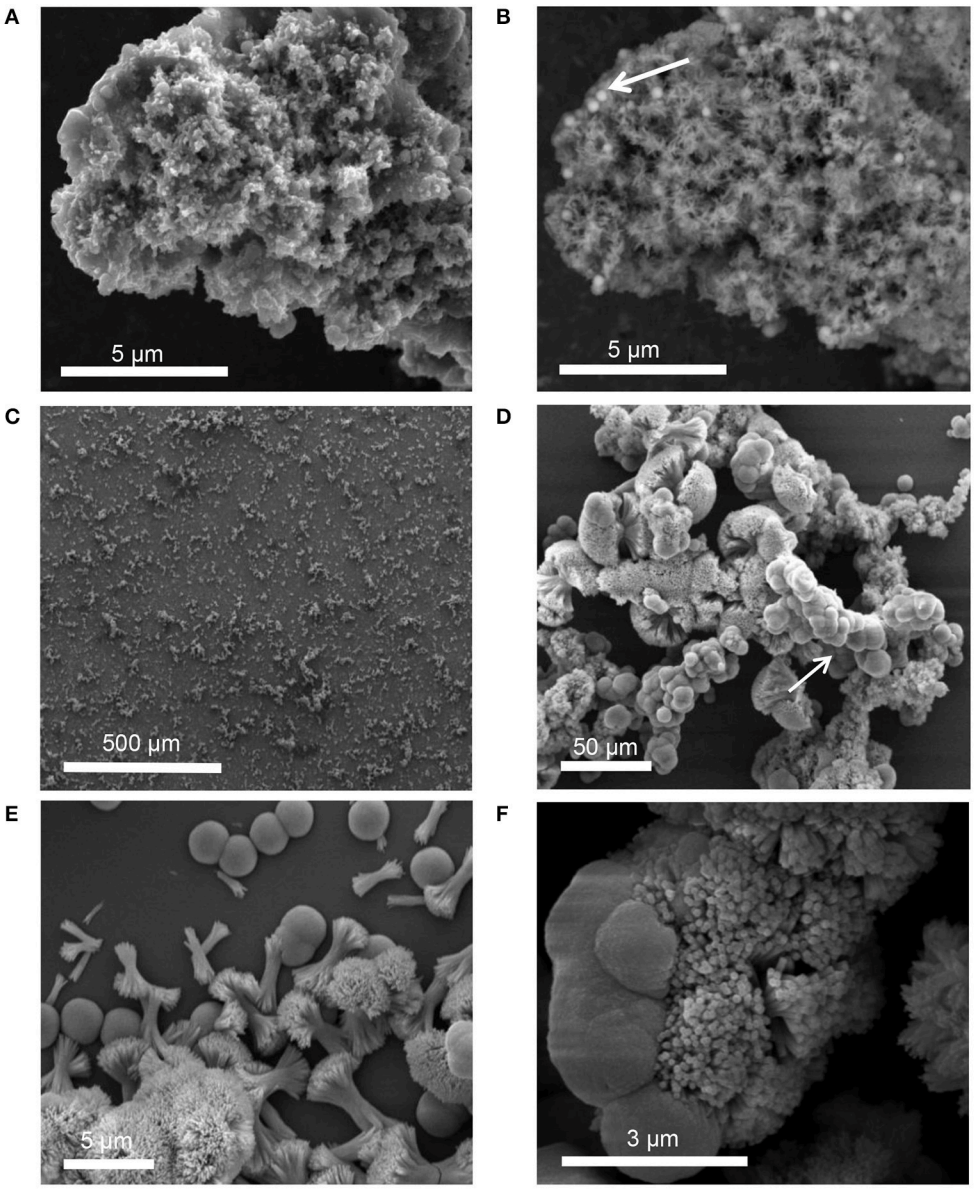

FIGURE 6 | SEM images of precipitate formed in solution containing STNA15-ELP at 3 h [**(A)** SE and **(B)** BSE] and 8 days (SE: **C**–**F**) of incubation.

appeared to be buried within the protein (**Figure 6B**). EDX of the 3 h STNA15-ELP precipitate had a Ca/P ratio of 1.48 (3 hS, **Table 3**). After incubation for 8 days (**Figures 6D–F**) an abundance of spherical and dumbbell structures were observed and the EDX of the mineral suggested that a mixture of calcium fluoride (CaF_2) (CaF_2 in **Table 3**, **Figure 6D** arrow) and fluorapatite (8 dS in **Table 3**) existed. CaF_2-like material has been previously reported to occur in solutions with high fluoride content, such as the one used in this study (Christoffersen et al., 1988; Mohammed et al., 2014). The EDX of the needles present in the 8 day sample gave a Ca/P ratio of 1.55. Since the mineral had a typical FAp needle-like morphology (for example Chen et al., 2006), the non-stoichiometric Ca/P ratio indicates a calcium deficiency in the apatite, analogous to previous literature (Dorozhkin, 2010). Also, the random orientation of the crystals, in both the 3 h and 8 day samples, indicates that the nucleation process in solution is spontaneous and the apatite has no preferred growth direction.

TEM of the 3 h precipitate, formed in the presence of STNA15-ELP, showed nano-crystalline mineral. The high resolution TEM (**Figure 7A**) and SAED (inset of **Figure 7A**) of the early precipitate both indicate FAp was already present at 3 h. The 8 day precipitate was also confirmed to be FAp, both with SAED (inset 1 of **Figure 7B**) and high resolution TEM (inset 2 of

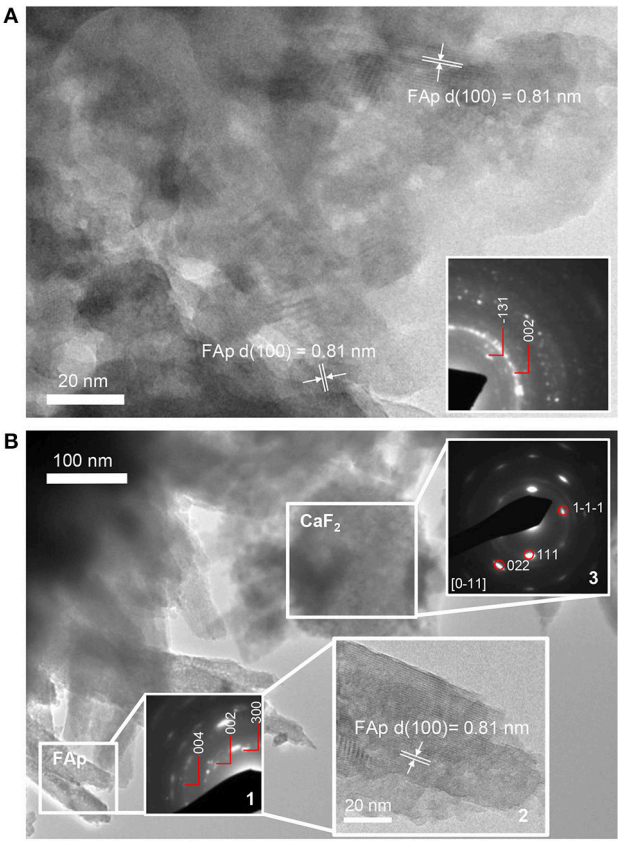

FIGURE 7 | TEM images of precipitate present in solution containing STNA15-ELP at **(A)** 3 h and **(B)** 8 days of incubation (inset 2 showing the high resolution TEM image with FAp planes visible). The 3 h precipitate is a nano-crystalline apatite. At 8 days the apatite has a needle-like form. The needles that were directly in contact had some co-alignment as seen in the SAED pattern (inset 1). The spherical particles, present at 8 days, were confirmed to be CaF_2, from the SAED pattern (inset 3).

Figure 7B). The SAED of the spherical particles confirmed the presence of calcium fluoride (inset 3 of **Figure 7B**).

FTIR analysis of precipitate formed in solution with free STNA15-ELP (**Figure 8**), after 3 h of incubation, shows broad and poorly defined peaks generated by the ν_3 asymmetric stretching mode of the apatitic PO_4^{3-} group (1,000–1,100 cm^{-1}). Further apatitic peaks, generated by the ν_4 bending mode of the PO_4^{3-} group, are visible at 603 and 561 cm^{-1} (Kim et al., 2002). FAp and HAp are crystallographically identical and not distinguishable in many analytical techniques. However, FAp can be characterized in FTIR by the lack of the OH^- liberation peak at 631 cm^{-1}, normally present in the HAp spectra. The traces in **Figure 8** lack this liberation peak, indicating that the apatite precipitate is a fluorapatite. A peak indicative of the HPO_4^{2-} group (527 cm^{-1}) is present in the spectra of both the 3 h and 8 day precipitate formed in the presence of free STNA15-ELP, normally present in octacalcium phosphate (OCP).

FTIR of the control precipitate, formed after 3 h of incubation, has a typical OCP trace with peaks generated by the ν_3 HPO_4^{2-} stretch visible at 1114, 1103 and 1093 cm^{-1}, in addition to the 527 cm^{-1} peak that is visible in the protein containing samples (Berry and Baddiel, 1967; Fowler et al., 1993). SEM of the control precipitate at 3 h shows typical OCP platelets (**Figure 5B**) and its presence was further confirmed with high resolution TEM and SAED (**Figure 5C** and **inset of 5C**). The control precipitate found in the 8 day samples had a typical fluorapatite FTIR spectrum with well-defined apatitic peaks. The apatite crystallites of the control had typical hexagonal needle shapes, seen in SE SEM images (**Figure 5E**) and TEM images (**Figure 5F**). The needles had regular ends, unlike the needle-like precipitate formed in the presence of STNA15-ELP (**Figure 7B**).

The FAp crystals initially formed within an aggregate of STNA15-ELP, where favorable heterogeneous nucleation can occur. The broad peaks of the PO_4 group, seen in the 3 h FTIR traces (**Figure 8**) of the precipitate formed in the presence of ELP, indicate that nano-crystalline apatite had formed, as observed in the TEM image (**Figure 7A**). The low Ca/P ratio of the 3 h precipitate was lower than calcium deficient apatite and was tending toward OCP. Furthermore, the presence of the HPO_4^{2-} peak in the FTIR spectrum is contradicting the presence of apatite. Rey et al. have extensively analyzed nano-crystalline apatite with techniques such as FTIR, NMR and XRD (Eichert et al., 2004; Rey et al., 2007a,b; Drouet et al., 2009). Rey et al. have hypothesized that nano-crystalline apatite is imperfect and is surrounded by a hydration layer. Due to this hydration layer, nano-apatite has a striking likeness to OCP. Firstly, the nano-apatite Ca/P ratio is somewhere in between OCP and apatite, and increases with the maturation of the crystals (Drouet et al., 2009). Similarly, FTIR of nano-apatite can have non-apatitic characteristics, resembling OCP traces, explaining the presence of the HPO_4^{2-} peak in the FTIR. The initial presence of nano-crystalline apatite can further explain the ragged shape of the crystals seen under TEM (**Figure 7B**). Rey et al. (2007b) have hypothesized that during maturation, the nano-crystals fuse together at the expense of the hydrated OCP-like layer.

Protein Conformation and Immobilization Affects Route of Mineral Formation and Mineral Morphology

Differences were observed in the mineralization process and the FAp morphology obtained at the 8 day incubation period between the constrained and unconstrained STNA15-ELP mineralized samples. In the case of the constrained protein, the ordered STNA15-ELP on the glass surface appeared to restrict the formation of the FAp to polycrystalline platelet morphology. The results strongly suggest that there are two reasons for this. Firstly, the brushite platelets exist for longer periods of time in the presence of STNA15-ELP coating. Reports have shown that other proteins, such as bovine serum albumin, can retard the transformation of brushite to apatite (Xie et al., 2001, 2002). Although there is no clear explanation for this, it is speculated that the adsorbed protein prevents water molecules from making direct contact with the surface of the brushite and therefore prevents dissolution.

The second explanation is based on templated mineralization. The stabilized brushite crystals, surrounded by the protein,

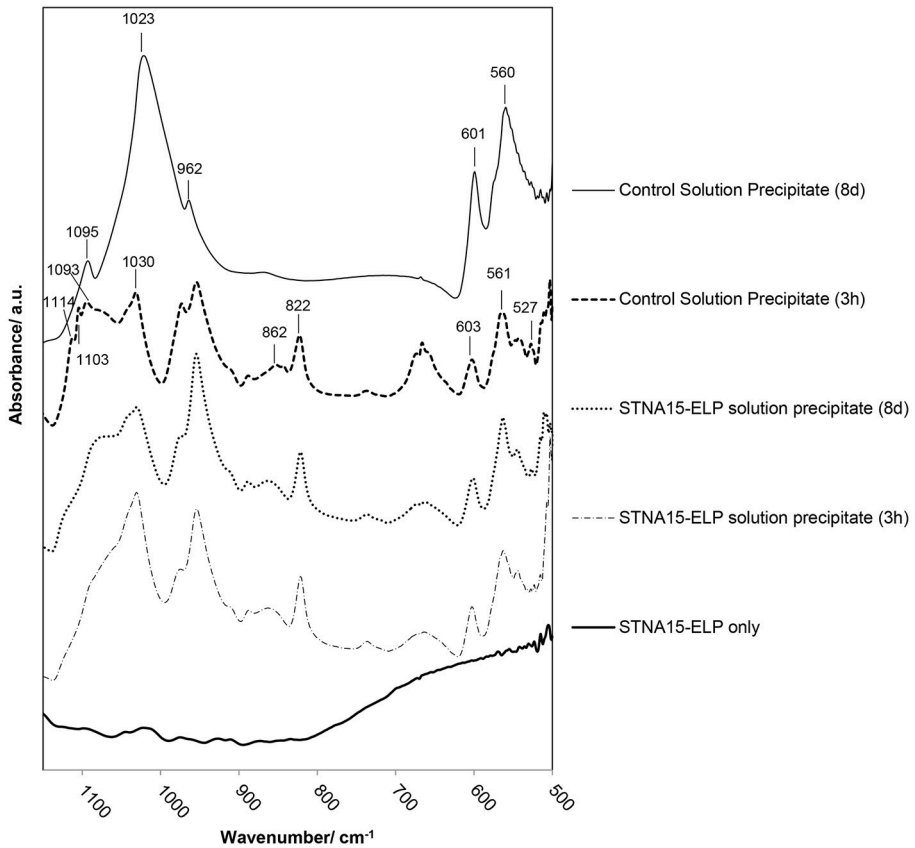

FIGURE 8 | FTIR analysis of precipitate formed in solution with and without STNA15-ELP. Without STNA15-ELP OCP forms at 3 h, transforming to highly crystalline FAp at 8 days. The ELP promotes FAp formation, with the FTIR indicating the presence of nano-crystalline FAp at 3 h and 8 days. (820 cm^{-1}: residual NO_3).

slowly dissolved once formed. The dissolution of the crystals was evidenced by the etch pits visible on the surface (**Figure 3B**). As brushite formed, along with the calcium fluoride precipitate, the calcium-pH isotherm shifts to an area where brushite was no longer stable, causing dissolution. The brushite dissolution created a local supersaturation of calcium that could reprecipitate as FAp, in the presence of fluoride. The slow FAp formation process allowed an ordered structure to form where the FAp crystallites grow along the {010} face of brushite.

A different process occurred when the protein was unconstrained and free in solution. As seen in **Figure 3B**, the nucleation was random and the growth of the crystals had no preferred orientation. The protein aggregates created an environment which favored apatite formation over other phases, even at 3 h of incubation. This may be due to local buffering effects caused by the lysine amino acids in the STNA15-ELP sequence. Since the lysine groups are likely to interact with the borosilicate surface, this effect is not seen with the STNA15-ELP coating. Other mineralizing organic molecules, such as amelogenin, have shown capability of buffering pH and stabilizing precursor phases. Amelogenin has the ability to stabilize amorphous calcium phosphate in a solution which normally precipitates apatite (Kwak et al., 2011).

The specific behavior observed in this study can be further supported by the thermoresponsive properties of ELPs related to their ITT. ELPs are known to fold and aggregate above their transition temperature. In its folded state, the STNA15-ELP can display, when in solution, its nucleating sites on the surface causing FAp nucleation all over the aggregate. The nucleation on ELP aggregates is consistent with other work where needle like apatite grew from spherical ELP particles (Misbah et al., 2016). However, once adsorbed on glass and with an increase in order, the STNA15 sequence of the ELP is no longer concentrated on a surface of a particle but on a flat substrate. In both cases the mineral formation resembled the process of biomineralization where either a precursor phase was present before a stable mineral is formed (for example Johnsson and Nancollas, 1992) or smaller sub-units fused to form larger, imperfect crystals (for example Robinson, 2007). However, only the constrained protein produced mineral that has a preferential growth direction.

These findings provide information that can lead to synthesis of ordered FAp structures that could be used in enamel therapeutics. However, more importantly, this synthetic biomineralizing system has shown that protein constraint and protein conformation both play an extremely important role

in the process of biomineralization. Protein constraint can be related to natural biomineralizing processes, where the mineralizing proteins exist within a gel-like matrix. In fact proteins, such as amelogenin, have been shown to assemble into fibers and nanospheres, rather than existing in a free form (Carneiro et al., 2016).

CONCLUSION

This study has demonstrated the ability of the STNA15-ELP to control the route of formation of FAp and its subsequent morphology. The morphological difference of FAp observed in the two conditions can be attributed to the STNA15-ELP conformation and interaction with a substrate. The addition of STNA15-ELP to a fluoridated mineralizing solution yielded FAp when the protein was both constrained on a surface and free in solution. However, plate-like stoichiometric FAp was found on protein coated borosilicate compared to needle-like calcium deficient FAp with the protein un-constrained in solution. The plate-like FAp was templated by pre-existing brushite platelets forming structures which were organized in a particular direction. The multistep FAp formation presented here resembles the natural biomineralization process, where transient metastable phases precede the final stable calcium phosphate. Ordered FAp formation is preferred for use in enamel therapeutics and therefore the constrained protein will be pursued in further studies in order to optimize and control the mineralization process.

AUTHOR CONTRIBUTIONS

KS, carried out the data collection, data analysis and interpretation and drafted the article; MA, PA, AM, HSA, and AB, are project supervisors and all took part in the critical article revision; MA, PA, and AM, were the initial conception designers; NT, carried out the TEM work and critical revision of the article; Final approval of the article by MA.

ACKNOWLEDGMENTS

We are thankful to the Life Science Initiative, QMUL, for funding the project and providing funding support for this publication. The work was additionally supported by the European Research Council Starting Grant (STROFUNSCAFF) and the Marie Curie Career Integration Grant (BIOMORPH). The authors would like to acknowledge Dr. Carol Crean and Dr. Rachida Bance-Soualhi (Department of Chemistry, University of Surrey) for their help with acquiring the Raman spectroscopy data, funded by EPSRC (grant number EP/M022749/1). KS gratefully acknowledges Dr. Sherif El-Sharkawy for intellectual input and Gastón Agustín Primo for help with FTIR deconvolution, alongside other group members of the Mata, MHAtriCell and DPSU groups.

REFERENCES

Abbarin, N., San Miguel, S., Holcroft, J., Iwasaki, K., and Ganss, B. (2015). The enamel protein amelotin is a promoter of hydroxyapatite mineralization. *J. Bone Miner. Res.* 30, 775–785. doi: 10.1002/jbmr.2411

Berry, E. E., and Baddiel, C. B. C. (1967). Some assignments in the infra-red spectrum of octacalcium phosphate. *Spectrochim. Acta* 23, 1781–1792. doi: 10.1016/0584-8539(67)80061-8

Blass, J., Köhler, O., Fingerle, M., Müller, C., and Ziegler, C. (2013). Properties and characteristics of wet (HF) and dry (RIE) etched borosilicate glass. *Phys. Status solidi* 210, 988–993. doi: 10.1002/pssa.201200769

Brunton, P. A., Davies, R. P. W., Burke, J. L., Smith, A., Aggeli, A., Brookes, S. J., et al. (2013). Treatment of early caries lesions using biomimetic self-assembling peptides–a clinical safety trial. *Br. Dent. J.* 215:E6. doi: 10.1038/sj.bdj.2013.741

Carneiro, K. M. M., Zhai, H., Zhu, L., Horst, J. A., Sitlin, M., Nguyen, M., et al. (2016). Amyloid-like ribbons of amelogenins in enamel mineralization. *Sci. Rep.* 6:23105. doi: 10.1038/srep23105

Casciani, F., and Condrate, R. A. (1979). The vibrational spectra of Brushite, $CaHPO4{\cdot}2H_2O$. *Spectrosc. Lett.* 12, 699–713. doi: 10.1080/00387017908069196

Chen, H., Clarkson, B. H., Sun, K., and Mansfield, J. F. (2005). Self-assembly of synthetic hydroxyapatite nanorods into an enamel prism-like structure. *J. Colloid Interface Sci.* 288, 97–103. doi: 10.1016/j.jcis.2005.02.064

Chen, H., Sun, K., Tang, Z., Law, R. V., Mansfield, J. F., and Clarkson, B. H. (2006). Synthesis of fluorapatite nanorods and nanowires by direct precipitation from solution. *Cryst. Growth Des.* 6, 1504–1508. doi: 10.1021/cg0600086

Christoffersen, J., Christoffersen, M. R., Kibalczyc, W., and Perdok, W. G. (1988). Kinetics of dissolution and growth of calcium fluoride and effects of phosphate. *Acta Odontol. Scand.* 46, 325–336. doi: 10.3109/00016358809004784

Cuy, J. L., Mann, A. B., Livi, K. J., Teaford, M. F., and Weihs, T. P. (2002). Nanoindentation mapping of the mechanical properties of human molar tooth enamel. *Arch. Oral Biol.* 47, 281–291. doi: 10.1016/S0003-9969(02)00006-7

Czajka-Jakubowska, A. E., Liu, J., Chang, S.-R., and Clarkson, B. H. (2009). The effect of the surface characteristics of various substrates on fluorapatite crystal growth, alignment, and spatial orientation. *Med. Sci. Monit.* 15, MT84-88.

Deakins, M., and Volker, J. F. (1941). Amount of organic matter in enamel from several types of human teeth. *J. Dent. Res.* 20, 117–121. doi: 10.1177/00220345410200020201

Dorozhkin, S. V. (2010). Amorphous calcium (ortho)phosphates. *Acta Biomater.* 6, 4457–4475. doi: 10.1016/j.actbio.2010.06.031

Drouet, C., Bosc, F., Banu, M., Largeot, C., Combes, C., Dechambre, G., et al. (2009). Nanocrystalline apatites: from powders to biomaterials. *Powder Technol.* 190, 118–122. doi: 10.1016/j.powtec.2008.04.041

Dunne, C. F., Twomey, B., Kelly, C., Simpson, J. C., and Stanton, K. T. (2015). Hydroxyapatite and fluorapatite coatings on dental screws: effects of blast coating process and biological response. *J. Mater. Sci. Mater. Med.* 26:5347. doi: 10.1007/s10856-014-5347-5

Eichert, D., Sfihi, H., Combes, C., and Rey, C. (2004). Specific characteristics of wet nanocrystalline apatites. Consequences on biomaterials and bone tissue. *Bioceramics* 16, 927–930. doi: 10.4028/www.scientific.net/KEM.254-256.927

Elliott, J. C. (1994). *Structure and Chemistry of the Apatites and Other Calcium Orthophosphates*. London: Elsevier.

Elsharkawy, S., Al-Jawad, M., Agarwal, S., Tejeda-Montes, E., Shuturminska, K., Sanchez, R., et al. (2016a). "1006 - fabrication of hierarchically-ordered enamel-like crystals for novel dental restorative materials," in *35th Annual Meeting of the IADR Korean Division* (Seol).

Elsharkawy, S., Tejeda-Montes, E., Al-Jawad, M., and Mata, A. (2016b). Preferential nucleation and crystal growth on microfabricated topography. *Mater. Today* 19, 478–480. doi: 10.1016/j.mattod.2016.08.002

Fowler, B. O., Markovic, M., and Brown, W. E. (1993). Octacalcium Phosphate. 3. Infrared and Raman vibrational-spectra. *Chem. Mater.* 5, 1417–1423. doi: 10.1021/cm00034a009

Giocondi, J. L., El-Dasher, B. S., Nancollas, G. H., and Orme, C. A. (2010). Molecular mechanisms of crystallization impacting calcium

phosphate cements. *Philos. Trans. A Math. Phys. Eng. Sci.* 368, 1937–1961. doi: 10.1098/rsta.2010.0006

Girotti, A., Reguera, J., Rodríguez-Cabello, J. C., Arias, F. J., Alonso, M., and Testera, A. M. (2004). Design and bioproduction of a recombinant multi(bio)functional elastin-like protein polymer containing cell adhesion sequences for tissue engineering purposes. *J. Mater. Sci. Mater. Med.* 15, 479–484. doi: 10.1023/B:JMSM.0000021124.58688.7a

Iijima, M., Fan, D., Bromley, K. M., Sun, Z., and Moradian-Oldak, J. (2010). Tooth enamel proteins enamelin and amelogenin cooperate to regulate the growth morphology of octacalcium phosphate crystals. *Cryst. Growth Des.* 10, 4815–4822. doi: 10.1021/cg100696r

Johnsson, M. S., and Nancollas, G. H. (1992). The role of brushite and octacalcium phosphate in apatite *Formation* 3, 61–82. doi: 10.1177/10454411920030010601

Kim, J. H., Kim, S. H., Kim, H. K., Akaike, T., and Kim, S. C. (2002). Synthesis and characterization of hydroxyapatite crystals: a review study on the analytical methods. *J. Biomed. Mater. Res.* 62, 600–612. doi: 10.1002/jbm.10280

Kwak, S.-Y., Green, S., Wiedemann-Bidlack, F. B., Beniash, E., Yamakoshi, Y., Simmer, J. P., et al. (2011). Regulation of calcium phosphate formation by amelogenins under physiological conditions. *Eur. J. Oral Sci.* 119(Suppl.), 103–111. doi: 10.1111/j.1600-0722.2011.00911.x

Lacruz, R. S., Nanci, A., Kurtz, I., Wright, J. T., and Paine, M. L. (2010). Regulation of pH during amelogenesis. *Calcif. Tissue Int.* 86, 91–103. doi: 10.1007/s00223-009-9326-7

Lee, S. H., and Ruckenstein, E. (1988). Adsorption of proteins onto polymeric surfaces of different hydrophilicities - a case study with bovine serum albumin. *J. Colloid Interface Sci.* 125, 365–379. doi: 10.1016/0021-9797(88)90001-X

Lenk, T. J., Horbett, T. A., Ratner, B. D., and Chittur, K. K. (1991). Infrared spectroscopic studies of time-dependent changes in fibrinogen adsorbed to polyurethanes. *Langmuir* 7, 1755–1764. doi: 10.1021/la00056a030

Mann, S. (2001). *Biomineralization: Principles and Concepts in Bioinorganic Materials Chemistry*. Oxford: Oxford University Press.

Misbah, M. H., Espanol, M., Quintanilla, L., Ginebra, M. P., and Rodríguez-Cabello, J. C. (2016). Formation of calcium phosphate nanostructures under the influence of self-assembling hybrid elastin-like-statherin recombinamers. *RSC Adv.* 6, 31225–31234. doi: 10.1039/C6RA01100D

Miyazawa, T., and Blout, E. R. (1961). The infrared spectra of polypeptides in various conformations: amide, I., and II Bands. *J. Am. Chem. Soc.* 83, 712–719. doi: 10.1021/ja01464a042

Mohammed, N. R., Lynch, R. J. M., and Anderson, P. (2014). Effects of fluoride concentration on enamel demineralization kinetics *in vitro*. *J. Dent.* 42, 613–618. doi: 10.1016/j.jdent.2013.12.005

Moradian-Oldak, J., and Paine, M. L. (2010). *Mammalian Enamel Formation*. Chichester: John Wiley & Sons, Ltd. doi: 10.1002/9780470986325.ch15

Ndao, M., Ash, J. T., Stayton, P. S., and Drobny, G. P. (2010). The role of basic amino acids in the molecular recognition of hydroxyapatite by statherin using solid state NMR. *Surf. Sci.* 604, L39–L42. doi: 10.1016/j.susc.2010.02.026

Norde, W. (1986). Adsorption of proteins from solution at the solid-liquid interface. *Adv. Colloid Interface Sci.* 25, 267–340. doi: 10.1016/0001-8686(86)80012-4

Norde, W., MacRitchie, F., Nowicka, G., and Lyklema, J. (1986). Protein adsorption at solid-liquid interfaces: reversibility and conformation aspects. *J. Colloid Interface Sci.* 112, 447–456. doi: 10.1016/0021-9797(86)90113-X

Raj, P., and Johnsson, M. (1992). Salivary statherin. Dependence on sequence, charge, hydrogen bonding potency, and helical conformation for adsorption to hydroxyapatite and inhibition of mineralization. *J. Biol.* 267, 5968–5976.

Reiersen, H., Clarke, A. R., and Rees, A. R. (1998). Short elastin-like peptides exhibit the same temperature-induced structural transitions as elastin polymers: implications for protein engineering. *J. Mol. Biol.* 283, 255–264. doi: 10.1006/jmbi.1998.2067

Rey, C., Combes, C., Drouet, C., Lebugle, A., Sfihi, H., and Barroug, A. (2007a). Nanocrystalline apatites in biological systems: characterisation, structure and properties. *Materwiss. Werksttech.* 38, 996–1002. doi: 10.1002/mawe.200700229

Rey, C., Combes, C., Drouet, C., Sfihi, H., and Barroug, A. (2007b). Physico-chemical properties of nanocrystalline apatites: implications for biominerals and biomaterials. *Mater. Sci. Eng. C* 27, 198–205. doi: 10.1016/j.msec.2006.05.015

Robinson, C. (2007). Self-oriented assembly of nano-apatite particles: a subunit mechanism for building biological mineral crystals. *J. Dent. Res.* 86, 677–679. doi: 10.1177/154405910708600801

Robinson, C., Kirkham, J., and Shore, R. (1995). *Chemistry of Mature Enamel in Dental Enamel: Formation to Destruction*. Boca Raton, FL: CRC Press.

Rodriguez-Cabello, J. (2004). *Biomaterials,* eds N. Hasirci and V. Hasirci. Boston, MA: Springer.

Ruan, Q., and Moradian-Oldak, J. (2014). Amelogenin and enamel biomimetics. *J. Mater. Chem. B Mater. Biol. Med.* 3, 3112–3129. doi: 10.1039/C5TB00163C

Sainz-Díaz, C. I., Villacampa, A., and Otálora, F. (2004). Crystallographic properties of the calcium phosphate mineral, brushite, by means of first principles calculations. *Am. Mineral.* 89, 307–313. doi: 10.2138/am-2004-2-308

Serrano, V., Liu, W., and Franzen, S. (2007). An infrared spectroscopic study of the conformational transition of elastin-like polypeptides. *Biophys. J.* 93, 2429–2435. doi: 10.1529/biophysj.106.100594

Shirahama, H., and Suzawa, T. (1985). Adsorption of bovine serum albumin onto styrene/2-hydroxyethyl methacrylate copolymer latex. *J. Colloid Interface Sci.* 104, 416–421. doi: 10.1016/0021-9797(85)90050-5

Subburaman, K., Pernodet, N., Kwak, S. Y., DiMasi, E., Ge, S., Zaitsev, V., et al. (2006). Templated biomineralization on self-assembled protein fibers. *Proc. Natl. Acad. Sci. U.S.A* 103, 14672–14677. doi: 10.1073/pnas.0602952103

Tejeda-Montes, E., Klymov, A., Nejadnik, M. R., Alonso, M., Rodriguez-Cabello, J. C., Walboomers, X. F., et al. (2014). Mineralization and bone regeneration using a bioactive elastin-like recombinamer membrane. *Biomaterials* 35, 8339–8347. doi: 10.1016/j.biomaterials.2014.05.095

Urry, D. W., Peng, S. Q., Hayes, L. C., McPherson, D., Xu, J., Woods, T. C., et al. (1998). Engineering protein-based machines to emulate key steps of metabolism (biological energy conversion). *Biotechnol. Bioeng.* 58, 175–190. doi: 10.1002/(SICI)1097-0290(19980420)58:2/3<175::AID-BIT10>3.0.CO;2-C

Vashisht, R., Kumar, A., Indira, R., Srinivasan, M. R., and Ramachandran, S. (2010). Remineralization of early enamel lesions using casein phosphopeptide amorphous calcium Phosphate: an *ex-vivo* study. *Contemp. Clin. Dent.* 1, 210–213. doi: 10.4103/0976-237X.76385

Vogler, E. A. (2012). Protein adsorption in three dimensions. *Biomaterials* 33, 1201–1237. doi: 10.1016/j.biomaterials.2011.10.059

Wojciechowski, P., Ten Hove, P., and Brash, J. L. (1986). Phenomenology and mechanism of the transient adsorption of fibrinogen from plasma (Vroman effect). *J. Colloid Interface Sci.* 111, 455–465. doi: 10.1016/0021-9797(86)90048-2

Xie, J., Riley, C., and Chittur, K. (2001). Effect of albumin on brushite transformation to hydroxyapatite. *J. Biomed. Mater. Res.* 57, 357–365. doi: 10.1002/1097-4636(20011205)57:3<357::AID-JBM1178>3.0.CO;2-1

Xie, J., Riley, C., Kumar, M., and Chittur, K. (2002). FTIR/ATR study of protein adsorption and brushite transformation to hydroxyapatite. *Biomaterials* 23, 3609–3616. doi: 10.1016/S0142-9612(02)00090-X

Yamagishi, K., Onuma, K., Suzuki, T., Okada, F., Tagami, J., Otsuki, M., et al. (2005). Materials chemistry: a synthetic enamel for rapid tooth repair. *Nature* 433:819. doi: 10.1038/433819a

Conflict of Interest Statement: The authors declare that the research was conducted in the absence of any commercial or financial relationships that could be construed as a potential conflict of interest.

The reviewer YZ and handling Editor declared their shared affiliation, and the handling Editor states that the process nevertheless met the standards of a fair and objective review.

Copyright © 2017 Shuturminska, Tarakina, Azevedo, Bushby, Mata, Anderson and Al-Jawad. This is an open-access article distributed under the terms of the Creative Commons Attribution License (CC BY). The use, distribution or reproduction in other forums is permitted, provided the original author(s) or licensor are credited and that the original publication in this journal is cited, in accordance with accepted academic practice. No use, distribution or reproduction is permitted which does not comply with these terms.

frontiers in Physiology

PERSPECTIVE
published: 24 October 2017
doi: 10.3389/fphys.2017.00823

Co-option of Hair Follicle Keratins into Amelogenesis Is Associated with the Evolution of Prismatic Enamel: A Hypothesis

*Elia Beniash**

Department of Oral Biology, University of Pittsburgh, Pittsburgh, PA, United States

Recent discovery of hair follicle keratin 75 (KRT75) in enamel raises questions about the function of this protein in enamel and the mechanisms of its secretion. It is also not clear how this protein with a very specific and narrow expression pattern, limited to the inner root sheath of the hair follicle, became associated with enamel. We propose a hypothesis that KRT75 was co-opted by ameloblasts during the evolution of Tomes' process and the prismatic enamel in synapsids.

Keywords: enamel, keratin 75, evolution, enamel rod, hair follicle

OPEN ACCESS

Edited by:
Steven Joseph Brookes, Leeds Dental Institute, United Kingdom

Reviewed by:
James P. Simmer, University of Michigan, United States
Michael Lansdell Paine, University of Southern California, United States
Colin Robinson, University of Leeds, United Kingdom

***Correspondence:**
Elia Beniash
ebeniash@pitt.edu

Specialty section:
This article was submitted to Craniofacial Biology and Dental Research, a section of the journal Frontiers in Physiology

Received: *17 April 2017*
Accepted: *06 October 2017*
Published: *24 October 2017*

Citation:
Beniash E (2017) Co-option of Hair Follicle Keratins into Amelogenesis Is Associated with the Evolution of Prismatic Enamel: A Hypothesis. Front. Physiol. 8:823. doi: 10.3389/fphys.2017.00823

Since early days of enamel research the question regarding the presence of keratins in this epithelial tissue intrigued scientists (see Duverger et al., 2016 for review). A number of studies suggested that keratins are present in the insoluble and heavily cross-linked matrix of mature enamel, however due to the extreme insolubility of this material these studies were not able to identify these keratins (Robinson et al., 1975, 1989a,b; Robinson and Hudson, 2011). Recently, Keratin 75 (KRT75) was identified in ameloblasts and the mature enamel matrix (Duverger et al., 2014). Importantly, it was found that a single amino acid substitution in this protein, which causes a hair condition pseudofoliculitis barbae, or barber rush, affects structural and mechanical properties of enamel and increases caries susceptibility (Duverger et al., 2014), suggesting an important functional role for Krt75 in amelogenesis. At the same time a number of critical questions regarding Krt75 need to be investigated. The fact that Krt75 is a cytosolic protein, lacking the signaling peptide, essential for proper sorting of secretory proteins, raises the fundamental question regarding the mechanism of its secretion. One possible scenario is that cytosolic proteins end up in enamel with the vestiges of the Tomes' processes (Warshawsky and Vugman, 1977). Another question is- what role of this highly specialized protein, expressed almost exclusively in the inner root sheath and companion layer of the hair follicle (Winter et al., 1998), plays in enamel? The later question is especially interesting from the evolutionary perspective, since primitive enamel appeared prior to the sea-land transition and the evolutionary explosion of keratins in basal tetrapods.

It is a widely accepted that, ectodermal appendages, such as teeth and hairs evolved independently, but share a common developmental blueprint (Sharpe, 2001). Specifically, the role of epithelial-mesenchymal interactions is absolutely critical for the development of these organs, and their patterning and morphogenesis involve a number of shared regulatory pathways (Biggs and Mikkola, 2014; Lan et al., 2014). These pathways are evolutionary conserved and are involved in morphogenesis of other ectodermal appendages, such as elasmobranch teeth (Rasch et al., 2016) or teleost scales (Sharpe, 2001), which are not direct evolutionary homologs of mammalian teeth or hairs (Qu et al., 2015; Braasch et al., 2016). Although these disparate organs utilize common morphogenetic blueprint, the structural proteins of these appendages differ significantly and in many instances have evolved independently. The presence of Krt75 in the mammalian teeth represents an evolutionary puzzle. It is established that the teeth covered with true enamel appeared in the common ancestors of sarcopterygians prior to the sea to land transition

and that the true enamel present in all classes of tetrapods (Qu et al., 2015; Braasch et al., 2016), while the evolutionary explosion of keratins occurred in basal tetrapods in connection with the sea to land transition and adaptations to multiple land habitats (Vandebergh and Bossuyt, 2012). Intriguingly, in Anura close orthologs of hair and hair follicle keratins are expressed in toe pads and claws, suggesting that the expansion of these genes is associated with the evolution of ectodermal appendages in crown tetrapods (Vandebergh et al., 2013). Although KRT75 gene was not found in amphibians, it is present in all extant amniotes. In birds Krt75 is found in the cells of the feather follicle but not in the feathers themselves, which are made mainly of beta-keratins, a specialized family of proteins found in reptiles and birds (Ng et al., 2012; Greenwold et al., 2014). A mutation of Krt75 in chicken leads to defects in feather rachis, causing so-called frizzle feather phenotype (Ng et al., 2012). These observations draw some interesting commonalities between Krt75 in mammals and birds, namely their localization in the follicles but not in hairs and nails themselves and their control of hair and feather morphology (Ng et al., 2012; Jasterzbski and Schwartz, 2015). This gene also exist in lizards however its tissue localization is unknown (Eckhart et al., 2008).

KRT75 is present in a wide variety of mammals, which is not surprising since it plays a major role in hair formation. Whales (Cetacea), which are hairless, lost a number of hair and hair follicle keratin genes (Nery et al., 2014). Interestingly, a recent study of keratin genes in 6 mammalian species with annotated genomes showed that bottleneck dolphins (which lack hair but retain teeth) retained functional KRT75 gene, while in the toothless and hairless minke whales, this gene is silent (Nery et al., 2014). Similarly, in pangolins which are toothless animals, covered in scales, KRT75 is functional, however there are two single amino acid substitutions in a highly conserved region of the protein (Choo et al., 2016). These findings suggest that KRT75 is important for tooth formation. However, what is the potential role of (Biggs and Mikkola, 2014) this protein in the mammalian teeth? This question remains unclear. There are several major differences

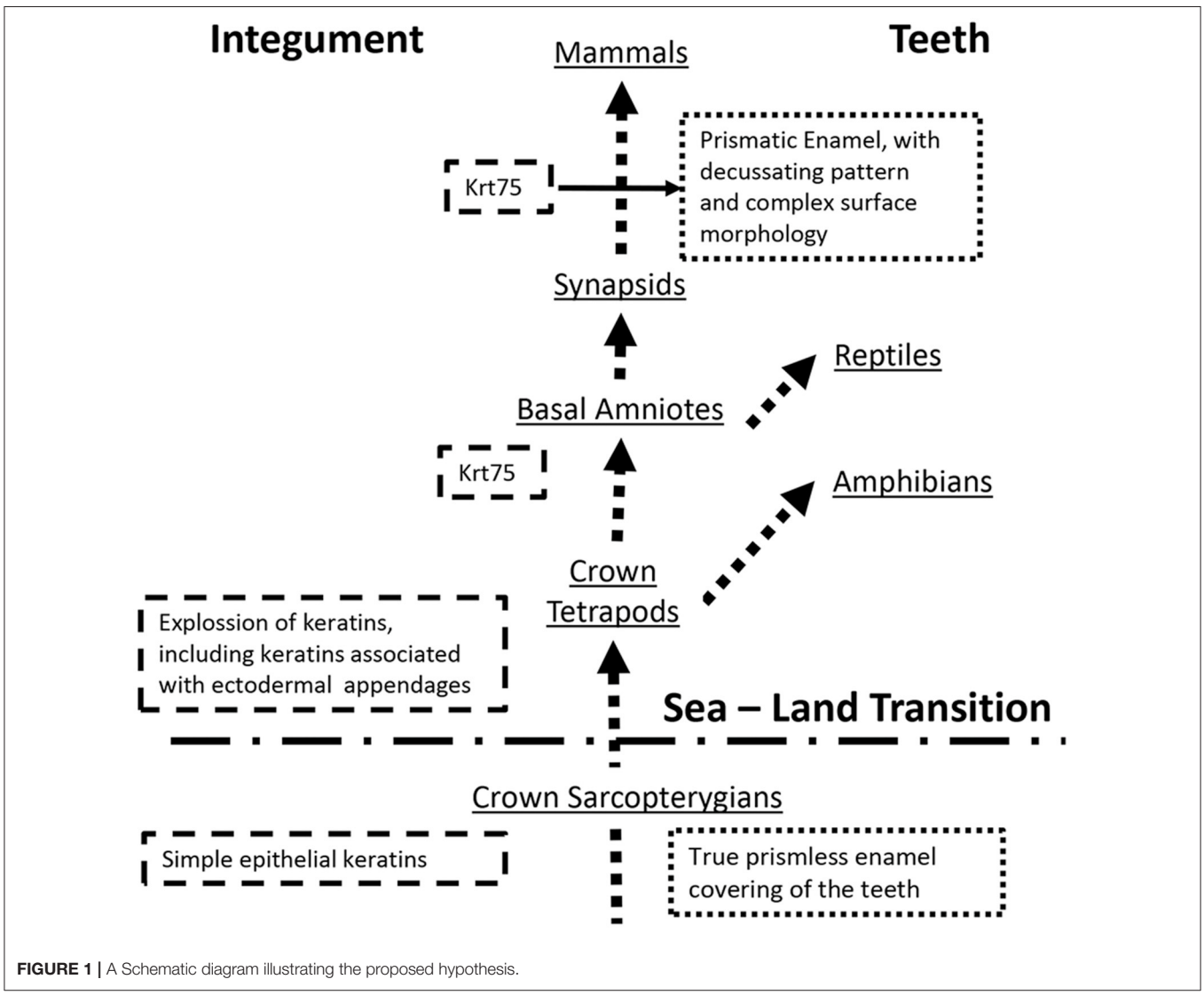

FIGURE 1 | A Schematic diagram illustrating the proposed hypothesis.

in tooth morphology and ultrastructure between mammals and other toothed tetrapods. Among them is the presence of thick prismatic enamel, with a sophisticated decussating pattern, while other extant tetrapods present with prismless enamel (Sander, 2000). According to Sander, development of prismatic enamel occurred after the separation of synapsids from other branches of amniotes (Sander, 1997). Enamel rod, the basic building blocks of the prismatic enamel, is a secretory product of Tomes' process, a highly specialized cellular secretory apparatus (Sander, 1997). Cross-sectional profiles and shapes of the enamel rods are determined by the organization of Tomes' processes and trajectories of ameloblasts movements during the appositional grows of secretory enamel. Importantly, ameloblasts equipped with Tomes' processes are only present in mammals and are not found in other extant toothed tetrapods (Sander, 2000). The facts presented above support a hypothesis that Krt75, and potentially other hair follicle keratins, were co-opted by ameloblasts during the evolution of Tomes' process and the prismatic enamel, which is the major evolutionary innovation (**Figure 1**). The observation that a single amino acid substitution in Krt75 causes malformation of the enamel rods (Duverger et al., 2014) further supports this notion. It has to be pointed out that, as of now, we do not have enough information regarding the exact function of Krt75 in enamel and the evolutionary modifications of the mammalian KRT75 to draw any conclusions. The goal of this essay was to provoke interest in the research community to this intriguing possibility of co-option of a highly specialized hair follicle keratin into enamel.

AUTHOR CONTRIBUTIONS

The author confirms being the sole contributor of this work and approved it for publication.

REFERENCES

Biggs, L. C., and Mikkola, M. L. (2014). Early inductive events in ectodermal appendage morphogenesis. *Semin. Cell Dev. Biol.* 25, 11–21. doi: 10.1016/j.semcdb.2014.01.007

Braasch, I., Gehrke, A. R., Smith, J. J., Kawasaki, K., Manousaki, T., Pasquier, J., et al. (2016). The spotted gar genome illuminates vertebrate evolution and facilitates human-teleost comparisons. *Nat. Genet.* 48, 427. doi: 10.1038/ng.3526

Choo, S. W., Rayko, M., Tan, T. K., Hari, R., Komissarov, A., Wee, W. Y., et al. (2016). Pangolin genomes and the evolution of mammalian scales and immunity. *Genome Res.* 26, 1312–1322. doi: 10.1101/gr.203521.115

Duverger, O., Beniash, E., and Morasso, M. I. (2016). Keratins as components of the enamel organic matrix. *Matrix Biol.* 52–54, 260–265. doi: 10.1016/j.matbio.2015.12.007

Duverger, O., Ohara, T., Shaffer, J. R., Donahue, D., Zerfas, P., Dullnig, A., et al. (2014). Hair keratin mutations in tooth enamel increase dental decay risk. *J. Clin. Invest.* 124, 5219–5224. doi: 10.1172/jci78272

Eckhart, L., Dalla Valle, L., Jaeger, K., Ballaun, C., Szabo, S., Nardi, A., et al. (2008). Identification of reptilian genes encoding hair keratin-like proteins suggests a new scenario for the evolutionary origin of hair. *Proc. Natl. Acad. Sci. U.S.A.* 105, 18419–18423. doi: 10.1073/pnas.0805154105

Greenwold, M. J., Bao, W. E., Jarvis, E. D., Hu, H. F., Li, C., Gilbert, M. T. P., et al. (2014). Dynamic evolution of the alpha (α) and beta (β) keratins has accompanied integument diversification and the adaptation of birds into novel lifestyles. *BMC Evol. Biol.* 14:249. doi: 10.1186/s12862-014-0249-1

Jasterzbski, T. J., and Schwartz, R. A. (2015). Pseudofolliculitis cutis: a vexing disorder of hair growth. *Br. J. Dermatol.* 172, 878–884. doi: 10.1111/bjd.13427

Lan, Y., Jia, S., and Jiang, R. (2014). Molecular patterning of the mammalian dentition. *Semin. Cell Dev. Biol.* 25, 61–70. doi: 10.1016/j.semcdb.2013.12.003

Nery, M. F., Arroyo, J. I., and Opazo, J. C. (2014). Increased rate of hair keratin gene loss in the cetacean lineage. *BMC Genomics* 15:869. doi: 10.1186/1471-2164-15-869

Ng, C. S., Wu, P., Foley, J., Foley, A., McDonald, M. L., Juan, W. T., et al. (2012). The Chicken Frizzle Feather Is Due to an alpha-Keratin (KRT75) Mutation That Causes a Defective Rachis. *PLoS Genet.* 8:e1002748. doi: 10.1371/journal.pgen.1002748

Qu, Q., Haitina, T., Zhu, M., and Ahlberg, P. E. (2015). New genomic and fossil data illuminate the origin of enamel. *Nature* 526, 108–111. doi: 10.1038/nature15259

Rasch, L. J., Martin, K. J., Cooper, R. L., Metscher, B. D., Underwood, C. J., and Fraser, G. J. (2016). An ancient dental gene set governs development and continuous regeneration of teeth in sharks. *Dev. Biol.* 415, 347–370. doi: 10.1016/j.ydbio.2016.01.038.

Robinson, C., and Hudson, J. (2011). Tuft protein: protein cross-linking in enamel development. *Eur. J. Oral Sci.* 119 (Suppl. 1), 50–54. doi: 10.1111/j.1600-0722.2011.00906.x

Robinson, C., Kirkham, J., and Fincham, A. (1989a). The enamelin/non-amelogenin problem. A brief review. *Connect Tissue Res.* 22, 93–100.

Robinson, C., Lowe, N. R., and Weatherell, J. A. (1975). Amino acid composition, distribution and origin of "tuft" protein in human and bovine dental enamel. *Arch Oral. Biol.* 20, 29-IN23. doi: 10.1016/0003-9969(75)90149-1.

Robinson, C., Shore, R. C., and Kirkham, J. (1989b). Tuft protein: Its relationship with the keratins and the developing enamel matrix. *Calcif. Tissue Int.* 44, 393–398. doi: 10.1007/bf02555967

Sander, P. M. (1997). *Non-mammalian Synapsid Enamel and the Origin of Mammalian Enamel Prisms: The Bottom-Up Perspective*. Rotterdam: Balkema, 41–62.

Sander, P. M. (2000). "Prismless enamel in amniotes: terminology, function, and evolution," in *Development, Function and Evolution of Teeth*, eds M. F. Teaford, M. W. J., Ferguson and M. Meredith Smith (Cambridge: Cambridge University Press), 92–106.

Sharpe, P. T. (2001). Fish scale development: Hair today, teeth and scales yesterday? *Curr. Biol.* 11, R751–R752. doi: 10.1016/s0960-9822(01)00438-9

Vandebergh, W., and Bossuyt, F. (2012). Radiation and functional diversification of alpha keratins during early vertebrate evolution. *Mol. Biol. Evol.* 29, 995–1004. doi: 10.1093/molbev/msr269

Vandebergh, W., Maex, M., Bossuyt, F., and Van Bocxlaer, I. (2013). Recurrent functional divergence of early tetrapod keratins in amphibian toe pads and mammalian hair. *Biol. Lett.* 9:20130051. doi: 10.1098/rsbl.2013.0051.

Warshawsky, H., and Vugman, I. (1977). Comparison of protein synthetic activity of pre-secretory and secretory ameloblasts in rat incisors. *Anat Rec* 188, 143–171. doi: 10.1002/ar.1091880203

Winter, H., Langbein, L., Praetzel, S., Jacobs, M., Rogers, M. A., Leigh, I. M., et al. (1998). A novel human type II cytokeratin, K6hf, specifically expressed in the companion layer of the hair follicle. *J. Invest. Dermatol.* 111, 955–962. doi: 10.1046/j.1523-1747.1998.00456.x

Conflict of Interest Statement: The author declares that the research was conducted in the absence of any commercial or financial relationships that could be construed as a potential conflict of interest.

The reviewer CR and handling Editor declared their shared affiliation.

Copyright © 2017 Beniash. This is an open-access article distributed under the terms of the Creative Commons Attribution License (CC BY). The use, distribution or reproduction in other forums is permitted, provided the original author(s) or licensor are credited and that the original publication in this journal is cited, in accordance with accepted academic practice. No use, distribution or reproduction is permitted which does not comply with these terms.

frontiers in Physiology

ORIGINAL RESEARCH
published: 14 June 2017
doi: 10.3389/fphys.2017.00398

Evolutionary Analysis Predicts Sensitive Positions of MMP20 and Validates Newly- and Previously-Identified *MMP20* Mutations Causing Amelogenesis Imperfecta

*Barbara Gasse[1], Megana Prasad[2], Sidney Delgado[1], Mathilde Huckert[2,3], Marzena Kawczynski[3,4], Annelyse Garret-Bernardin[3,5], Serena Lopez-Cazaux[6], Isabelle Bailleul-Forestier[7], Marie-Cécile Manière[3,4], Corinne Stoetzel[2], Agnès Bloch-Zupan[3,4,8,9,10] and Jean-Yves Sire[1]**

[1] Institut de Biologie Paris-Seine, UMR 7138-Evolution Paris-Seine, Sorbonne Universités, Université Pierre et Marie Curie, Paris, France, [2] Laboratoire de Génétique Médicale, Institut National de la Santé et de la Recherche Médicale UMRS_1112, Institut de Génétique Médicale d'Alsace, FMTS, Université de Strasbourg, Strasbourg, France, [3] Faculté de Chirurgie Dentaire, Université de Strasbourg, Strasbourg, France, [4] Pôle de Médecine et Chirurgie Bucco-Dentaires, Centre de Référence des Manifestations Odontologiques des Maladies Rares, O-Rares, Hôpitaux Universitaires de Strasbourg, Strasbourg, France, [5] Unit of Dentistry, IRCCS, Bambino Gesù Children's Hospital, Rome, Italy, [6] Faculté de Chirurgie Dentaire, Département d'Odontologie Pédiatrique, Centre de Compétences Maladies Rares, CHU Hôtel Dieu, Service d'odontologie Conservatrice et Pédiatrique, Nantes, France, [7] Faculté de Chirurgie Dentaire, CHU de Toulouse, Centre de Compétences Maladies Rares, Odontologie Pédiatrique, Université Paul Sabatier, Toulouse, France, [8] Centre Européen de Recherche en Biologie et en Médecine, Centre National de la Recherche Scientifique UMR7104, Institut National de la Santé et de la Recherche Médicale U964, Institut de Génétique et de Biologie Moléculaire and Cellulaire, Université de Strasbourg, Illkirch, France, [9] Institut d'Etudes Avancées, Université de Strasbourg, USIAS, Strasbourg, France, [10] Eastman Dental Institute, University College London, London, United Kingdom*

OPEN ACCESS

Edited by:
Alexandre Rezende Vieira, University of Pittsburgh, United States

Reviewed by:
Elia Beniash, University of Pittsburgh, United States
Rafaela Scariot De Moraes, Universidade Positivo, Brazil

***Correspondence:**
Jean-Yves Sire
jean-yves.sire@upmc.fr

Specialty section:
This article was submitted to Craniofacial Biology and Dental Research, a section of the journal Frontiers in Physiology

Received: *10 March 2017*
Accepted: *26 May 2017*
Published: *14 June 2017*

Citation:
Gasse B, Prasad M, Delgado S, Huckert M, Kawczynski M, Garret-Bernardin A, Lopez-Cazaux S, Bailleul-Forestier I, Manière M-C, Stoetzel C, Bloch-Zupan A and Sire J-Y (2017) Evolutionary Analysis Predicts Sensitive Positions of MMP20 and Validates Newly- and Previously-Identified MMP20 Mutations Causing Amelogenesis Imperfecta. Front. Physiol. 8:398. doi: 10.3389/fphys.2017.00398

Amelogenesis imperfecta (AI) designates a group of genetic diseases characterized by a large range of enamel disorders causing important social and health problems. These defects can result from mutations in enamel matrix proteins or protease encoding genes. A range of mutations in the enamel cleavage enzyme matrix metalloproteinase-20 gene (*MMP20*) produce enamel defects of varying severity. To address how various alterations produce a range of AI phenotypes, we performed a targeted analysis to find *MMP20* mutations in French patients diagnosed with non-syndromic AI. Genomic DNA was isolated from saliva and *MMP20* exons and exon-intron boundaries sequenced. We identified several homozygous or heterozygous mutations, putatively involved in the AI phenotypes. To validate missense mutations and predict sensitive positions in the MMP20 sequence, we evolutionarily compared 75 sequences extracted from the public databases using the Datamonkey webserver. These sequences were representative of mammalian lineages, covering more than 150 million years of evolution. This analysis allowed us to find 324 sensitive positions (out of the 483 MMP20 residues), pinpoint functionally important domains, and build an evolutionary chart of important conserved MMP20 regions. This is an efficient tool to identify new- and previously-identified mutations. We thus identified six functional *MMP20* mutations in unrelated families,

finding two novel mutated sites. The genotypes and phenotypes of these six mutations are described and compared. To date, 13 *MMP20* mutations causing AI have been reported, making these genotypes and associated hypomature enamel phenotypes the most frequent in AI.

Keywords: MMP20, mutations, amelogenesis imperfecta, evolution, phenotype

INTRODUCTION

Amelogenesis imperfecta (AI) describes a group of genetic diseases producing a large range of alterations in enamel structure. Defects include hypoplastic, hypomineralized, or hypomature enamel structure and altered enamel appearance -including rough, pitted, banded, or discolored teeth. These alterations produce severe health problems and impair normal social interactions. Defects can result from mutations either of enamel matrix protein encoding genes [amelogenin (*AMELX*), ameloblastin (*AMBN*), amelotin (*AMTN*), and enamelin (*ENAM*)], or proteases [matrix metalloproteinase-20 (*MMP20*), kallikrein-related peptidase 4 (*KLK4*))]—often displaying specific roles in tooth—and hence at the current stage of our knowledge do not display disorders elsewhere in the body. Other genes encoding proteins having functions in cell attachment, ionic transport, and mineralization processes, when mutated are responsible for AI phenotypes associated with various abnormalities in syndromes (Crawford et al., 2007; reviewed in Bloch-Zupan et al., 2012).

The prevalence of AI can vary from 1:700 to 1:14,000 depending on the country. Although many candidate genes were identified to date, many AI-producing mutations remain to be identified for approximately 50% of diagnosed patients.

Here, we focused on the matrix metalloproteinase-20 gene (*MMP20*), an interesting candidate gene given the numerous identified AI causing mutations (Kim et al., 2005, 2016a; Ozdemir et al., 2005; Papagerakis et al., 2008; Lee et al., 2010; Gasse et al., 2013; Wang et al., 2013; Seymen et al., 2015; Prasad et al., 2016a).

MMPs function in plants, invertebrates, and vertebrates, by their active center possessing a catalytic zinc domain (Gomis-Ruth, 2009; Fanjul-Fernandez et al., 2010). In vertebrates, matrix metalloproteinases (MMPs, also called matrixins) consist of a large family (24 members identified in humans) of endopeptidases, which are phylogenetically related (Fanjul-Fernandez et al., 2010). MMPs were initially thought involved in the degradation and turnover of the extracellular matrix, but recent studies indicate important biological roles regulating cell behavior and signaling pathways (Rodríguez et al., 2010).

MMP20 (also termed enamelysin) is only present in vertebrates. Its origin dates certainly back to an ancestral gnathostome, before the divergence of actinopterygians and sarcopterygians more than 450 million years ago (Kawasaki and Suzuki, 2011). In amniotes, MMP20 is an enamel specific protease. This gene is absent in every species lacking either teeth or enamel (e.g., in turtles, birds, and various mammals -Meredith et al., 2011, 2013).

In toothed mammals, MMP20 was identified first in porcine enamel (Bartlett et al., 1996; Moradian-Oldak et al., 1996) then characterized in humans (Llano et al., 1997). It is expressed both by ameloblasts and odontoblasts, and acts from the enamel secretory to the maturation stages through proteolysis of the enamel organic matrix, required for correct mineralization (Bègue-Kirn et al., 1998). MMP20 cleaves AMEL (Llano et al., 1997; Ryu et al., 1999; Nagano et al., 2009), the enamel matrix protein (EMP) representing more than 90% of the forming enamel matrix in mammals (Fincham et al., 1989). MMP20 also cleaves AMBN, and probably also ENAM, two EMPs with critical functions during enamel mineralization (Iwata et al., 2007; Chun et al., 2010).

Mutations in the *MMP20* gene have been associated with autosomal recessive type 2 amelogenesis imperfecta (AI2A2, MIM #612529, ORPHA100033) also called hypomature AI. In affected patients, enamel displays a normal thickness but is pigmented and hypomineralized as demonstrated by the lack of radio-opacity contrast with dentin (Witkop, 1989).

To find mutations on *MMP20* in French patients diagnosed for AI, we sequenced and identified several new homozygous or heterozygous missense mutations. To validate the potential role of these mutations, hence to predict sensitive positions in MMP20, we analyzed a large set of representative mammalian lineages sequences, covering over 150 million years of evolution. This type of evolutionary analysis has been shown to be an efficient method to validate and predict disease-associated missense mutations (Delgado et al., 2007; Al Hashimi et al., 2009; Bardet et al., 2010; Silvent et al., 2014). This method is termed phylomedicine (Kumar et al., 2011), which is complementary to existing genetic diagnosis.

The aims of the present study were to document MMP20 evolutionary analysis to pinpoint where newly identified mutations act in this evolutionary chart, hence identifying sensitive positions. Collectively this is an efficient tool to functionally validate *MMP20* mutations identified to date.

MATERIALS AND METHODS

Evolutionary Analysis

Data Set

Mammalian *MMP20* sequences were extracted from public databases, *NCBI* [http://www.ncbi.nlm.nih.gov] and *Ensembl* [http://www.ensembl.org]. A total of 75 sequences representative of the main mammalian lineages (55 families distributed within 19 orders) were retained for our analyses (Supplementary Table 1). Identical sequences (such as species from the same genus) were not included in our dataset. *MMP20* being enamel specific the sequences of species lacking either teeth or enamel (i.e., Xenarthra, Pholidota, Mysticeta, and Tubulidentata) were not included in our study because they display various mutations.

Among the selected *MMP20* sequences only five were published in GenBank. Of the 70 other sequences, 65 were computer-predicted from sequenced genomes and six were obtained using Basic Local Alignment Search Tool (BLAST) of the whole genome shotgun (WGS) repository sequences in *NCBI* (Supplementary Table 1). The coding sequences were traduced into amino acid sequences and unpublished sequences were validated through alignment to published ones using *Se-Al v.2.0a11* software [http://tree.bio.ed.ac.uk/software/seal]. The intron-exon boundaries were also carefully checked. The dataset of the 75 MMP20 sequences is available in Supplementary Data 1.

Our final alignment consisted of 483 positions, and no insertions were needed (Supplementary Figure 1). A few residues were missing in some, uncompletely sequenced genomic DNA (i.e., 726 nucleotides, nt, representing <0.7% of the data), and the corresponding positions were treated as "unknown data". In addition, we aligned 21 nucleotides of the intronic region located on both sides of the exons from 12 *MMP20* sequences representative of the main mammalian lineages, known to be important for correct intron splicing (Supplementary Table 2).

Analyses

The putative signal peptide sequence and its cleavage site were predicted using *SignalP 3.0 server* (http://www.cbs.dtu.dk/services/SignalP).

Single Likelihood Ancestor Counting (SLAC) analysis was performed using the Datamonkey webserver (http://www.datamonkey.org/; Delport et al., 2010) to identify amino acids subjected either to purifying or to positive selection, as previously described (Silvent et al., 2014). Biologically significant amino acids (i.e., site-specific selections) in MMP20 were identified in our alignment for the 483 positions and displayed on the human sequence. The analysis was performed according to the substitution preferences of amino acids, i.e., favoring property conservation (see Silvent et al., 2014). We defined three levels of selection throughout mammalian evolution (i.e., 180 Ma): conserved (i.e., unchanged residues), conservative (i.e., substituted residues having similar properties) and variable positions (i.e., substitution with various residues).

Mutation Analyses

Patients

The patients and their families were selected from the pool of patients participating in the French Ministry of Health National Program for Clinical Research, PHRC 2008 HUS (Strasbourg University Hospital) N°4266, Amelogenesis Imperfecta, AI (for further details see Gasse et al., 2013) and in the INTERREG IV Offensive Sciences A27 "Orodental manifestation of rare diseases" EU funded (ERDF) project.

These patients came to The Reference Centre for Orodental Manifestations of Rare Diseases (CRMR Strasbourg, France) or other affiliated Competence Centres (CCMR) for clinical diagnosis and management. Dentists specializing in rare diseases diagnosed amelogenesis imperfecta.

The oral phenotypes were documented using the D[4]/phenodent registry, a Diagnosing Dental Defects Database [see www.phenodent.org, to access assessment form], which is approved by CNIL (French National commission for informatics and liberty, number 908416). This clinical study is registered at https://clinicaltrials.gov: NCT01746121 and NCT02397824, and with the MESR (French Ministry of Higher Education and Research) Bioethics Commission as a biological collection "Orodental Manifestations of Rare Diseases" DC-2012-1677 within DC-2012-1002 and was acknowledged by the CPP (person protection committee) Est IV on the 11 Dec 2012.

Affected and unaffected family members gave informed written consents both for the D4/phenodent registry and for genetic analyses performed on the salivary samples included in the biological collection.

In this study, we selected patients from unrelated families suffering from non-syndromic AI, some of them displaying clinical diagnoses matching possible *MMP20* mutations.

Analyses

Patients spit into an Oragene kit (Oragene DNA®, DNA Genotek, Canada) and genomic DNA was then isolated from saliva according to the manufacturer's protocol. We used previously defined primers (see Gasse et al., 2013). Mutational analysis was performed for the 10 exons of *MMP20* including exon-intron boundaries. PCR products were sent to GATC Biotech for purification and sequencing in both directions in order to minimize sequencing artifacts. The sequences were aligned manually with the reference human *MMP20* sequence NG_012151.1 using *Se-Al v2.0a11* software.

When necessary the sequences were analyzed for splicing site prediction using the NetGene2 server (http://www.cbs.dtu.dk/services/NetGene2/) and MaxEntScan (http://genes.mit.edu/burgelab/maxent/Xmaxentscan_scoreseq.html). The NetGene2 server is a service producing neural network predictions of splice sites in human genes (Hebsgaard et al., 1996) and MaxEntScan is based on the "Maximum Entropy Principle" and generalizes most previous probabilistic models of sequence motifs such as weight matrix models and inhomogeneous Markov models (Yeo and Burge, 2004).

SNPs known to date in the human *MMP20* sequence were found at http://www.ncbi.nlm.nih.gov/snp and at https://www.ncbi.nlm.nih.gov/variation/tools/1000 genomes/(the 1000 genomes project).

RESULTS AND DISCUSSION

Evolutionary Analysis of Functional Constraints in MMP20 Sequence

The alignment of the 75 MMP20 amino acid (aa) sequences indicated a highly conserved protein structure throughout more than 180 million years of mammalian evolution, a finding demonstrating the importance of many regions of this protease as found for the alkaline phosphatase, ALPL (Silvent et al., 2014). The 10 exons encoding the protein do not show insertions and only a limited number of rodent-specific deletions, in which seven MMP20 lack either one codon in exon 1 (*Mus, Rattus, Cricetulus, Mesocricetus, Microtus,* and *Chinchilla*) or two codons in exon 2 (*Octodon*). The MMP20 sequences were therefore mostly composed of 483 residues, from the methionine M^1,

encoded by exon 1, to the cysteine C^{483} encoded by exon 10 and preceding the stop codon (Supplementary Figure 1). At the first glance our alignment indicated that many positions and large domains were conserved throughout the sequence. This is particularly obvious in the large regions encoded by the 3' end of exon 2, by exons 4 and 5, by the 3′ region of exon 6, by most of exons 7 and 8, and by many positions of exons 9 and 10 (Supplementary Figure 1). The alignment of the 21 untranslated nucleotides on both sides of the coding exons indicates that the acceptor sites are either tag or cag, and the donor sites are mostly gta (with the exception of gtt for intron 1 and gtg for intron 9 and in a few other sequences; Supplementary Table 2). This finding is in accordance with the splice site consensus sequences for introns. The other positions are somewhat variable with the exception of the 21 nucleotides of the 5′ region of intron 4 that are unchanged in all species studied (i.e., for 180 MA). We do not know why this region was unchanged during evolution but its conservation suggests functionally important domains otherwise some nucleotide substitutions would have occurred at random. We question whether this intron region could be involved in a regulatory process or was previously encoding region.

The evolutionary analysis using SLAC selected several positions, notably in the N-terminal region, and, in contrast indicated that the MMP20 sequence is globally under strong purifying selection (**Figure 1**). The detailed analysis of each position confirmed the numerous fonctional or structural constraints acting on many amino acids along the sequence (**Figure 2**, Supplementary Figure 2). Out of the 483 amino acids composing the human MMP20 sequence, more than a half (324 aa, 67.08%) were identified as sensitive positions, i.e., that were either conserved (i.e., unchanged residues) (243 aa, 50.31%) or conservative (i.e., substituted with residues having similar properties) (81 aa, 16.77%) during 180 million years of mammalian evolution (**Figure 2**). In contrast, 159 positions (32.92%) were identified as variable (i.e., substituted with various aa). This large number of sensitive positions revealed by our analysis is similar to the values obtained for ALPL (Silvent et al., 2014). These unchanged, conservative and variable positions were reported on the human sequence, resulting in the chart of sensitive positions of human MMP20 (**Figure 2**, Supplementary Figure 2). We predict that any substitution of one of the 243 unchanged positions, or of one of the 81 conservative positions with a residue having a different property, would disrupt MMP20 function and would lead to enamel defects described as amelogenesis imperfecta in patients who unfortunately possess such a mutation in both DNA alleles (homozygous mutation) or an additional mutation in the other allele (counpound heterozygous mutation). Indeed, all missense mutations validated until now in various proteins were located always at conserved positions (Delgado et al., 2007; Kumar et al., 2011).

The boundaries of three, already known, functional domains are also better defined when considering the number of conserved amino acids: the matrixin cystein switch extends from aa98 to aa104, the catalytic domain from aa108 to aa116, and the zinc-binding domain from aa223 to aa232. Similar, accurate definition of the boundaries of functional domains was obtain in various proteins through evolutionary analysis (Al Hashimi et al., 2009; Silvent et al., 2013, 2014). Aside these crucial regions our study highlighted many other evolutionary-conserved residues and domains that have probably a strong functional or structural importance for MMP20. One of these large domains, encoded by the 3′ end of exon 3, exon 4, and most of exon 5, is composed of 109 residues, out of them 102 (93.58%) are either unchanged or conservative. Several, but shorter domains are also encoded by the 3′ region of exons 6 and 7, and by most of the sequence of exons 8–10 (**Figure 2**, Supplementary Figure 2). The only 70 aa located at the N-terminal region are subjected to low selective constraints with 15.71% of sensitive positions detected.

It is worth noting that the percentage of purifying selection is high along the protein sequence, and varies from 7.14% in the region encoded by exon 1–95.24% in the region encoded by exon 4. More precisely, our evolutionary analysis (i) confirmed and accurately defined the boundaries of already known important

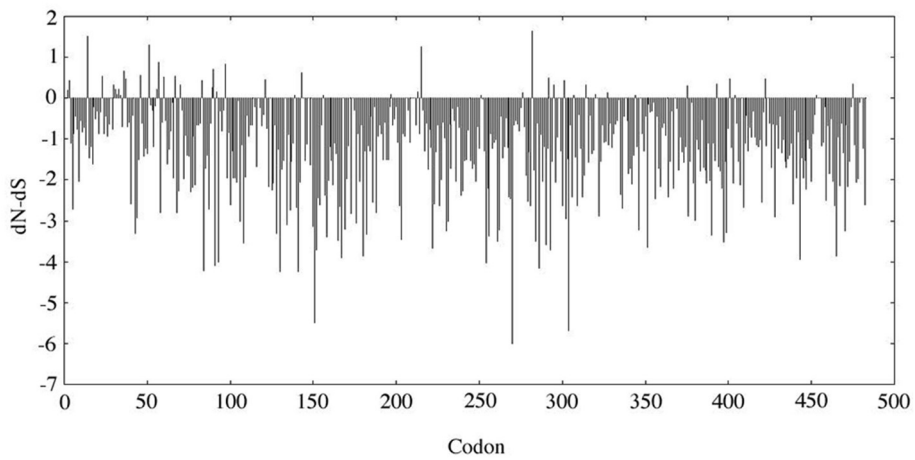

FIGURE 1 | SLAC analysis. The dN-dS value was analyzed along the MMP20 codon sequence. dN, non-synonymous substitution rate; dS, synonymous substitution rate. When dN-dS < 0, the codon is subjected to purifying selection. When dN-dS > 0 (i.e., dN > dS), the codon is considered positively selected.

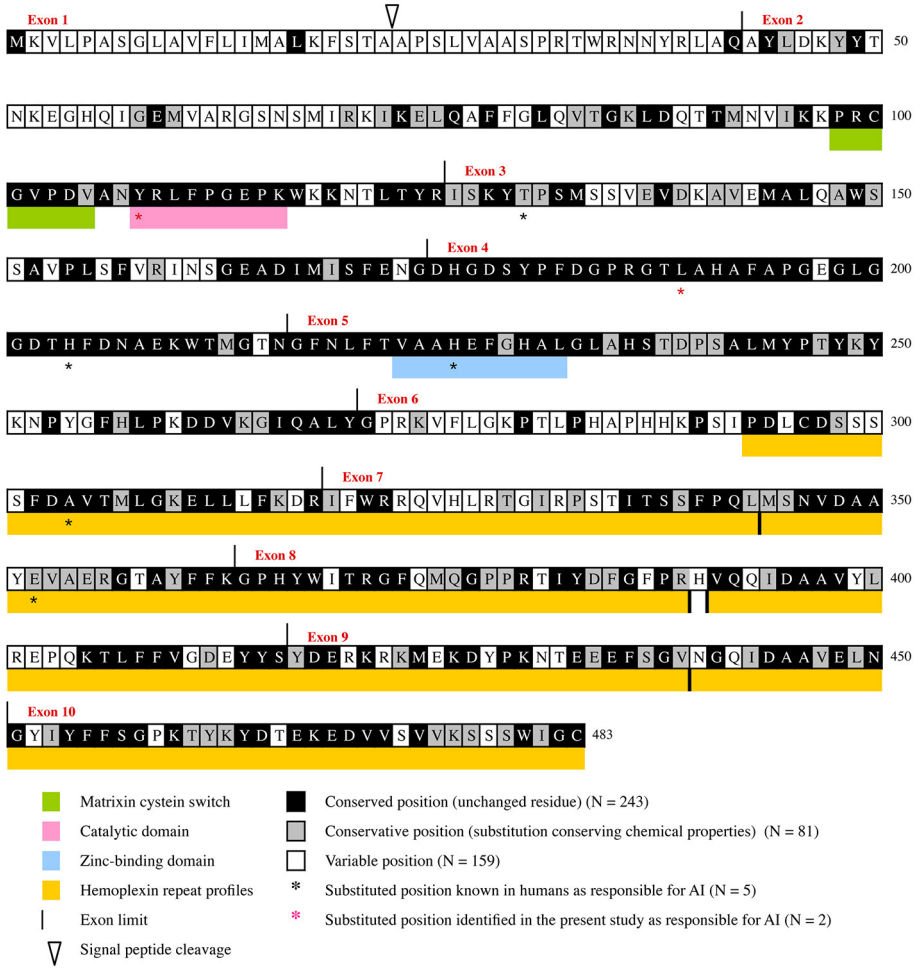

FIGURE 2 | Evolutionary chart of MMP20. This chart was obtained from the alignment of 75 sequences representative of the main mammalian lineages (approx. 180 million years of evolution) and was deduced from the results obtained when dN/dS was calculated at each codon of MMP20 by Consurf (see Supplementary Figures 1, 2). Human sequence is used as a reference. Positions subjected to purifying selecton are on black (conserved positions) and gray (conservative positions) background. Variable positions on white background.

domains of the protein, (ii) highlighted many sensitive residues, and (iii) revealed various domains having putative important roles that should be experimentally studied in the future (**Figure 2**).

Mutation Analyses

Genotypes

Among our patients displaying non-syndromic AI, mutations in the *MMP20* coding gene were diagnosed in six, unrelated families. Clinical diagnoses were confirmed through sequencing as described below. Sequencing DNA of patients 1 and 2 revealed new mutations in the *MMP20* sequence, which are validated as being responsible for the AI phenotype by means of evolutionary analysis. The pedigrees and DNA sequencing chromatograms are presented in **Figure 3**. Moreover, patient 4 displayed two, already reported mutations, but in a new, compound heterozygous context. In patient 3, the compound heterozygous mutations were already described by Prasad et al. (2016a) but not illustrated (see below). Eventually, patients 5 and 6 possessed an already described homozygous mutation. In addition, in these six families we identified several SNPs that change the amino acid but these mutations are not validated by our evolutionary analysis as they occurred in variable positions.

Patient 1: homozygous mutation c.323 A>G

We identified a missense, homozygous mutation in exon 2 of *MMP20* of this male proband. The mutation was not previously reported and is referred to as g.8,470 A>G, c.323 A>G, p.Y108C. Both unaffected parents were heterozygous (**Figures 3A,B**). The mutation occurred at a tyrosine residue of the catalytic domain, a position that is unchanged in the 75 MMP20 mammalian sequences studied and surrounded by a number of conserved residues of this domain (**Figure 2**, Supplementary Figures 1, 2). This finding indicates a putative important function for this amino acid and validates this homozygous mutation as being responsible for the AI phenotype.

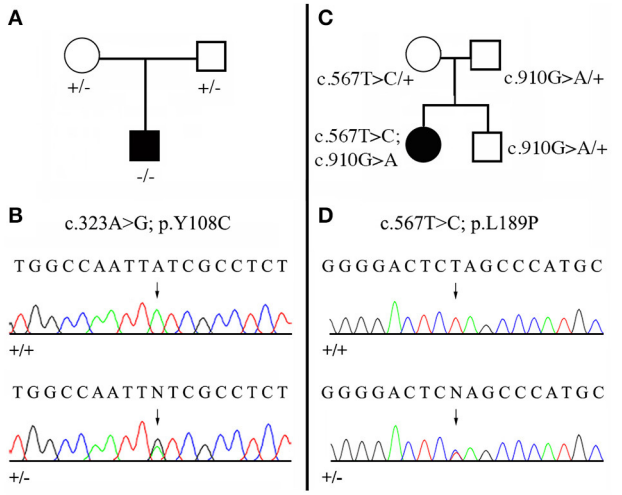

FIGURE 3 | Mutational analysis of the two new *MMP20* mutations. **(A,C)** Pedigree of the AI kindred; **(B,D)** DNA sequencing chromatograms of control (+/+) and of heterozygous (+/−) mutations. Arrows point to the mutation sites. See **Figure 2**, Supplementary Figure 1, Supplementary Table 2 for the validation of these mutations by means of evolutionary analyses. **(A,B)** Patient 1 with the homozygous mutation (c.323 A>G; p.Y108C). **(C,D)** Patient 2 with the compound heterozygous mutation (c.567 T>C; p.L189P / c.910 G>A; p.A304T). The second mutation was already reported as homozygous *MMP20* mutation (Lee et al., 2010).

A second missense, homozygous mutation was identified in exon 1, p.K18T. This frequent mutation in the human population occurred in a variable region of MMP20 and is not responsible for the enamel disorder.

Patient 2: compound heterozygous mutation c.567 T>C and c.910 G>A

In this female proband, we identified two missense, heterozygous mutations that were validated as responsible for AI phenotype in a compound genotype. The mutation on allele 1 is located in exon 6 and referred to as g.18,755 G>A, c.910 G>A, p.A304T. This *MMP20* mutation was already reported in the literature as responsible for the AI phenotype in a patient homozygous for the mutation (Lee et al., 2010). The patient 2 was heterozygous for this mutation, as well as his unaffected father and his brother (**Figure 3C**). The second mutation, on allele 2 was not previously reported and is located in exon 4 and referred to as g.15,345 T>C, c.567 T>C, p.L189P. The patient 2 was heterozygous for this mutation, as well as her unaffected mother (**Figures 3C,D**). The substitution of a leucine with a proline occurred at a conserved position, unchanged in mammals, and surrounded by numerous conserved residues. The substitution of this putative, functionally, or structurally important amino acid validates the mutation as involved in the AI phenotype.

In addition, the MMP20 sequence of patient 2 displayed four other missense mutations of various functional weight when considering our evolutionary analysis (**Figure 2**, Supplementary Figures 1, 2): (i) An uncommon missense mutation, on allele 2, was found in exon 3 and referred to as g.13,560 A>C, c.505 A>C, p.I169L. The mother is heterozygous for this mutation. The substitution of the isoleucine with a leucine occurred at a conservative position, at which isoleucine is substituted with the only valine in a few mammalian species but not with leucine (**Figure 2**, Supplementary Figures 1, 2). These amino acids have, however, similar properties. Also, this mutation occurred in a position surrounded by many conserved residues. The missense mutation p.I169L is present in 3% of the human population (the 1,000 genomes project). The involvement of this missense mutation in the AI phenotype is therefore quite doubtful; (ii) three, common, missense mutations were identified in exon 1, p.K18T (as in patient 1) and p.P31L, and in exon 6, p.T281N, also located in a variable region. These mutations are frequent in the human population occurred in variable regions of MMP20 and are not responsible for the enamel disorder.

The compound heterozygous mutation c.567 T>C (p.L189P) and c.910 G>A (p.A304T) is validated by our evolutionary analysis as the two mutations are located in conserved domains of MMP20, indicating putative important functions for these two amino acids.

Patient 3: compound heterozygous mutation c.126+6 t>g and c.954-2 a>t

The compound heterozygous mutation of *MMP20* in intronic splicing sites identified in this male proband was recently reported in the literature (Prasad et al., 2016a) but was not detailed and not documented with pictures (see below).

The mutation on allele 1 is located at the splicing acceptor site of intron 6 (3′ splice site) and referred to as g.30574 a>t, c.954-2 a>t, p.I319fs338X. This MMP20 mutation disturbing the splice site consensus sequence for introns was already reported in the literature as responsible for the AI phenotype, but in a homozygous context (Kim et al., 2005). Patient 3 was heterozygous for the mutation, as well as his unaffected mother. The mutation on allele 2 is located at the splicing donor site of intron 1 (5′ splice site) and referred to as g.145 t>g, c.126+6 t>g. The male proband was heterozygous for the mutation as well as his unaffected father. This substitution did not occur during 180 million years of mammalian evolution (Supplementary Table 2) and this position is therefore considered of importance for correct intron 1 splicing. In addition, (i) the position +6 belongs to the splice site consensus sequence of the 5′ splice site for introns (A/CAG | gta/gag**t**), (ii) Netgen2 server predicted that the splice donor site in intron 1 does not exist in the mutant sequence and MaxEntScan analysis showed a reduced score of the splicing signal in the mutant compared to the wild sequence (Supplementary Data 2), and (iii) this mutation is not present in the human population (1,000 genomes project).

In addition, three missense mutations, common in the human population (p.K18T, V275A, and p.N281T) were also identified in this patient but are not responsible for the enamel disorder.

Patient 4: compound heterozygous mutation c.389 C>T and c.954-2 a>t<

We identified two already reported mutations in this male proband. These mutations were, however, described as

homozygous *MMP20* mutations in two, unrelated patients, and are reported here to occur as a compound heterozygous mutation in the same patient. The first mutation found on allele 1 and located in exon 3 is referred to as: g.13444 C>T, c.389 C>T, p.T130I (Gasse et al., 2013). Patient 4 was heterozygous for the mutation as well as his unaffected father. The second mutation on allele 2 occurred at the splicing acceptor site of intron 6 and was referred to as g.30574 a>t, c.954-2 a>t, p.I319fs338X (Kim et al., 2005). The male proband was heterozygous for the mutation as well as his unaffecte mother.

Patients 5 and 6: homozygous mutation c.954-2 a>t

Patient 5: The homozygous mutation at the splicing acceptor site of intron 6 identified also in patients 3 and 4 was identified in two sisters of a family, in which the mother, the father, two sisters and a brother were unaffected as heterozygous for thed mutation.

Patient 6: The same mutation was also found in two sisters of this family.

All patients sharing the c.954-2 a>t mutation were from unrelated families, a finding that could indicate a high frequency of this mutation in the human population in an heterozygous context.

Clinical Phenotypes

Here below is a brief description of the features for the six patients displaying non-syndromic hypomature AI and diagnosed as possessing mutations in the *MMP20* coding gene (**Figure 4**).

Patient 1 (Figures 4A–D)

All teeth of this young boy were affected and parents reported damaged teeth since eruption. Enamel was chalky white and opaque. In primary teeth, enamel was either hypoplastic and/or was prematurely shed and worn through mastication and occlusal forces. The panoramic radiograph revealed the poor contrast of enamel compared to dentine, confirming the under-mineralization of enamel.

Patient 2 (Figures 4E,F)

This 5 years old girl was in her primary dentition. The parents reported that primary tooth eruption was delayed as no teeth were present at 1 year. As soon as teeth erupted they showed more opaque enamel and it crumbled. Teeth were small microdont and numerous diastema separated them. Enamel was white, orangy and wore off. On panoramic radiograph, no or very thin enamel was visible on primary teeth. In non-erupted permanent teeth, enamel seemed thicker and more mineralized with a stronger differential contrast with dentine, at least on the first permanent molar germs.

Patient 3 (Figures 4G–J)

In this 5 years old boy, the enamel of primary teeth was more opaque and was prone to disintegration, leaving areas of dentine apparent. In permanent teeth, enamel was also colored and opaque. Erupting teeth were sensitive and the patient experienced difficulties to brush teeth. Dental plaque and gingivitis were clearly visible. On panoramic radiographs limited radiopaque enamel if none was visible, and no contrast existed between enamel and dentine. This patient displayed a severe phenotype.

Patient 4 (Figures 4K,L)

In this 20 year old man, all permanent teeth demonstrated colored, opaque white brownish teeth with hypomature enamel. On the panoramic radiograph enamel is thin and the contrast with dentine is hardly visible.

Patient 5 and patient 6 (Figures 4M,N)

These two girls from unrelated families shared the same mutation and displayed similar phenotypes with colored hypomature amelogenesis imperfecta. The overall tooth contour was respected and enamel chipping was visible at the incisal edge.

Phenotype Comparison

Patient 1 (p.Y108C) was the least affected patient, while the most severe case was patient 3 displaying two mutations in splicing sites, leading to porous enamel and very sensitive teeth. Patient 2′s phenotype was slightly different as it presented additional quantitative defect associated to hypoplastic AI (smaller teeth). The enamel of patients 4, 5, and 6 showed similar mottled appearance of the enamel with more or less irregular staining. In patients 5 and 6 enamel looked rather opaque and uniformly colored.

The comparison of our case series with patients' phenotypes published in the literature led us to the following observations: Patient 1 phenotype was close to the one described for patient 1 by Gasse et al. (2013), characterized by a stronger contrast between enamel and dentine on X-rays. The enamel phenotype of patient 4 was similar to the affected individual described by Kim et al. (2005, **Figure 1**), to patient 2 described by Gasse et al. (2013), and to our patients 5 and 6. However, an anterior openbite was not present. Taurodontism was seen in molars especially in the upper permanent molars.

MMP20 Mutations Known to Date and Validation Using Evolutionary Analysis

When including the two new mutations reported in the present study, there are now 13 different *MMP20* mutations leading to AI reported in the literature. Eight of them are simply missense mutations leading to the only substitution of an amino acid (**Figures 2**, **5**). This finding demonstrates the crucial importance of these residues for the correct function of this protease. With the exception of p.Arg35Arg, which concerns the substitution of a nucleotide only (see discussion in Prasad et al., 2016a), the seven other residue substitutions in MMP20 are validated by our evolutionary analysis as occurring either on a conserved (unchanged residue: 5 cases) or on a conservative (2 cases) position.

To date, 18 other genes have been shown causing non-syndromic AI: *AMELX* (16 different mutations; Kim et al., 2017), *FAM83H* (14, Pourhashemi et al., 2014), *WDR72* (10, Hentschel et al., 2016), *ENAM* (4; Pavlic et al., 2007; Seymen et al., 2014), *ITGB6/4* (4; Poulter et al., 2014; Wang et al., 2014b), *SLC24A4* (3; Wang et al., 2014b), *LAMA3* (3, Gostyńska et al., 2016), *GPR68* (3, Parry et al., 2016b), LTBP3 (3; Huckert et al., 2015), *AMBN*



FIGURE 4 | Hypomature amelogenesis imperfecta encountered in patients with diverse *MMP20* mutations. **(A–D):** Patient 1 (c. 323 A>G). Intraoral clinical views and panoramic radiograph of primary, mixed (**A**: 6 years old; **B**: 7 years old) and permanent (**C,D**: 11 year old) dentitions. Note the limited contrast between enamel and dentine on X-rays. **(E,F)**: Patient 2 (c.567 T>C + c.910 G>A). Primary dentition of a 5 year old girl. No enamel or very thin enamel was visible on X-rays. **(G–J)**: Patient 3 (c.126+6 t>g + c.954-2 a>t). A young boy at 5 (**G,I**: primary teeth) and then at 8 years (**H,J**: permanent teeth). Limited radio-opaque enamel, if none, was seen on X-rays. **(K, L)**: Patient 4 (c.389 C>T + c.954-2 a>t). Permanent teeth of a 20-year old man. Hypomature enamel is clearly visible on X-rays. **(M,N)**: Patient 5 and patient 6 (c.954-2 a>t). Two girls displaying the same mutation leading to similar phenotypes with hypomature amelogenesis imperfecta.

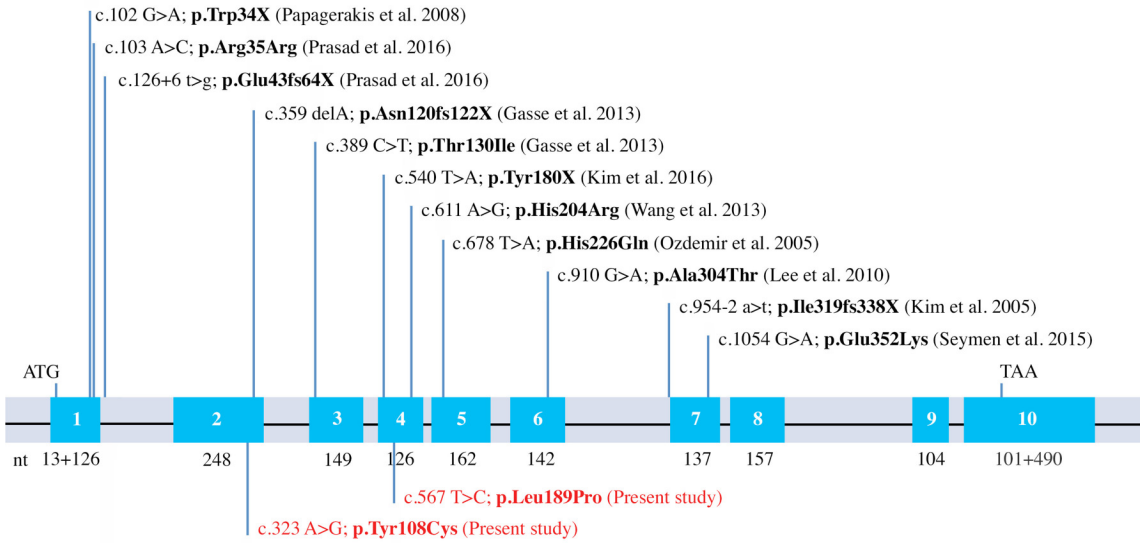

FIGURE 5 | *MMP20* mutations known to date. Schematical representation of the human *MMP20* gene structure with indication of the previously reported mutations and the two new mutations identified in this study (in red).

(2; Prasad et al., 2016a), *KLK4* (2; Lu et al., 2008; Wang et al., 2013), *DLX3* (2; Kim et al., 2016b), *STIM1* (2; Wang et al., 2014b; Parry et al., 2016a), *COL17A1* (1; Prasad et al., 2016b), *C4orf26* (1; Prasad et al., 2016b), *LAMB3* (1; Kim et al., 2016c), *ACPT* (1, Seymen et al., 2016), and *AMTN* (1, Smith et al., 2016). A total of 13 different mutations on the gene sequence causing AI places MMP20 among the top three sensitive proteins involved in non-syndromic AI when mutated.

Providing a clear genetic diagnosis linking genotype and phenotype on the basis of a missense variant can be challenging. A mutation present in a region that is highly conserved in evolution suggests that the amino acid is functionally important. The validated evolutionary analysis is crucial to address these important conserved positions and to facilitate variant analysis leading to disease diagnosis.

AUTHOR CONTRIBUTIONS

BG, MP, SD, AB, and JS have substantially contributed to the conception, design of the work and interpretation of data for the work; MH, MK, AG, SL, IB, and MM have substantially contributed to the acquisition or analysis of data. BG, AB, and JS have drafted the work and MP, SD, MH, MK, AG, SL, IB, and MM revised it critically for important intellectual content. All authors finally approved the version to be published; they all agree to be accountable for all aspects of the work and ensure that questions related to the accuracy or integrity of any part of the work are appropriately investigated and resolved.

ACKNOWLEDGMENTS

We would like to thank the family members for their invaluable contribution and generous help throughout the investigations. We are grateful to colleagues and general dental practitioners (Drs J. M. Schweitzer, A. Froehly, F. Charton, P. Basson) for their collaboration with the Strasbourg Reference Centre for orodental manifestations of rare diseases. This work was supported by grants from the French Ministry of Health (National Program for Clinical Research, PHRC 2008 N°4266 Amelogenesis imperfecta), the EU-funded project (ERDF) A27 "Oro-dental manifestations of rare diseases," supported by the RMT-TMO Offensive Sciences initiative, INTERREG IV Upper Rhine program and the INTERREG V RARENET program, the grant ANR-10-LABX-0030-INRT, a French State fund managed by the Agence Nationale de la Recherche under the frame programme Investissements d'Avenir labeled ANR-10-IDEX-0002-02. This research was funded by the University of Strasbourg Institute for Advanced Study (USIAS) as part of a USIAS Fellowship granted to AB. We would like to thank also Dr K. Niederreither for critical reading and English language editing of the manuscript.

SUPPLEMENTARY MATERIAL

The Supplementary Material for this article can be found online at: http://journal.frontiersin.org/article/10.3389/fphys.2017.00398/full#supplementary-material

REFERENCES

Al Hashimi, N., Sire, J. Y., and Delgado, S. (2009). Evolutionary analysis of mammalian enamelin, the largest enamel protein, supports a crucial role for the 32 kDa peptide and reveals selective adaptation in rodents and primates. *J. Mol. Evol.* 69, 635–656. doi: 10.1007/s00239-009-9302-x

Bardet, C., Delgado, S., and Sire, J. Y. (2010). MEPE evolution in mammals reveals regions and residues of prime functional importance. *Cell. Mol. Life Sci.* 67, 305–320. doi: 10.1007/s00018-009-0185-1

Bartlett, J. D., Simmer, J. P., Xue, J., Margolis, H. C., and Moreno, E. C. (1996). Molecular cloning and mRNA tissue distribution of a novel matrix metalloproteinase isolated from porcine enamel organ. *Gene* 183, 123–128. doi: 10.1016/S0378-1119(96)00525-2

Bègue-Kirn, C., Krebsbach, P. H., Bartlett, J. D., and Butler, W. T. (1998). Dentin sialoprotein, dentin phosphoprotein, enamelysin and ameloblastin: tooth-specific molecules that are distinctively expressed during murine dental differentiation. *Eur. J. Oral Sci.* 106, 963–970. doi: 10.1046/j.0909-8836.1998.eos106510.x

Bloch-Zupan, A., Sedano, H., and Scully, C. (2012). *Dento/Oro/Craniofacial Anomalies and Genetics, 1st Edn*. Boston, MA: Elsevier.

Chun, Y. H., Yamakoshi, Y., Yamakoshi, F., Fukae, M., Hu, J. C., Bartlett, J. D., et al. (2010). Cleavage site specificity of MMP-20 for secretory-stage ameloblastin. *J. Dent. Res.* 89, 785–790. doi: 10.1177/0022034510366903

Crawford, P. J., Aldred, M., and Bloch-Zupan, A. (2007). Amelogenesis imperfecta. *Orphanet J. Rare Dis.* 2:17. doi: 10.1186/1750-1172-2-17

Delgado, S., Ishiyama, M., and Sire, J. Y. (2007). Validation of amelogenesis imperfecta inferred from amelogenin evolution. *J. Dent. Res.* 86, 326–330. doi: 10.1177/154405910708600405

Delport, W., Scheffler, K., Botha, G., Gravenor, M. B., Muse, S. V., and Kosakovsky Pond, S. L. (2010). CodonTest: modeling amino acid substitution preferences in coding sequences. *PLoS Comput. Biol*. 6:e1000885. doi: 10.1371/journal.pcbi.1000885

Fanjul-Fernandez, M., Folgueras, A. R., Cabrera, S., and Lopez-Otin, C. (2010). Matrix metalloproteinases: evolution, gene regulation and functional analysis in mouse models. *Biochim. Biophys. Acta* 1803, 3–19. doi: 10.1016/j.bbamcr.2009.07.004

Fincham, A. G., Hu, Y., Pavlova, Z., Slavkin, H. C., and Snead, M. L. (1989). Human amelogenins: sequences of "TRAP" molecules. *Calcif. Tissue Int.* 45, 243–250. doi: 10.1007/BF02556044

Gasse, B., Karayigit, E., Mathieu, E., Jung, S., Garret, A., Huckert, M., et al. (2013). Homozygous and compound heterozygous MMP20 mutations in amelogenesis imperfecta. *J. Dent. Res.* 92, 598–603. doi: 10.1177/00220345134 88393

Gomis-Ruth, F. X. (2009). Catalytic domain architecture of metzincin metalloproteases. *J. Biol. Chem.* 284, 15353–15357. doi: 10.1074/jbc. R800069200

Gostyńska, K. B., Yan Yuen, W., Pasmooij, A. M., Stellingsma, C., Pas, H. H., Lemmink, H., et al. (2016). Carriers with functional null mutations in LAMA3 have localized enamel abnormalities due to haploinsufficiency. *Eur. J. Hum. Genet.* 25, 94–99. doi: 10.1038/ejhg.2016.136

Hebsgaard, S. M., Korning, P. G., Tolstrup, N., Engelbrecht, J., Rouze, P., and Brunak, S. (1996). Splice site prediction in Arabidopsis thaliana DNA by combining local and global sequence information. *Nucl. Acid Res.* 24, 3439–3452. doi: 10.1093/nar/24.17.3439

Hentschel, J., Tatun, D., Parkhomchuk, D., Kurth, I., Schimmel, B., Heinrich-Weltzien, R., et al. (2016). Identification of the first multi-exonic WDR72 deletion in isolated amelogenesis imperfecta, and generation of a WDR72-specific copy number screening tool. *Gene* 590, 1–4. doi: 10.1016/j.gene.2016.05.040

Huckert, M., Stoetzel, C., Morkmued, S., Laugel-Haushalter, V., Geoffroy, V., Muller, J., et al. (2015). Mutations in the latent TGF-beta binding protein 3 (LTBP3) gene cause brachyolmia with amelogenesis imperfecta. *Hum. Mol. Genet.* 24, 3038–3049. doi: 10.1093/hmg/ddv053

Iwata, T., Yamakoshi, Y., Hu, J. C., Ishikawa, I., Bartlett, J. D., Krebsbach, P. H., et al. (2007). Processing of ameloblastin by MMP-20. *J. Dent. Res.* 86, 153–157. doi: 10.1177/154405910708600209

Kawasaki, K., and Suzuki, T. (2011). Molecular evolution of matrix metalloproteinase 20. *Eur. J. Oral Sci.* 119, 247–253. doi: 10.1111/j.1600-0722.2011.00898.x

Kim, J. W., Simmer, J. P., Hart, T. C., Hart, P. S., Ramaswami, M. D., Bartlett, J. D., et al. (2005). MMP-20 mutation in autosomal recessive pigmented hypomaturation amelogenesis imperfecta. *J. Med. Genet.* 42, 271–275. doi: 10.1136/jmg.2004.024505

Kim, Y. J., Kang, J., Seymen, F., Koruyuku, M., Gencay, K., Hu, J. C., et al. (2016a). "MMP20 mutations causing enamel hypomaturation in two families," in *Enamel 9 Conference,* (Harrogate, UK), Abstract.

Kim, Y. J., Seymen, F., Koruyucu, M., Kasimoglu, Y., Gencay, K., Shin, T. J., et al. (2016b). Unexpected identification of a recurrent mutation in the DLX3 gene causing amelogenesis imperfecta. *Oral Dis.* 22, 297–302. doi: 10.1111/odi. 12439

Kim, Y. J., Shin, T. J., Hyun, H. K., Lee, S. H., Lee, Z. H., and Kim, J. W. (2016c). A novel *de novo* mutation in LAMB3 causes localized hypoplastic enamel in the molar region. *Eur. J. Oral Sci.* 124, 403–435. doi: 10.1111/eos. 12280

Kim, Y. J., Kim, Y. J., Kang, J., Shin, T. J., Hyun, H. K., Lee, S. H., et al. (2017). A novel AMELX mutation causes hypoplastic amelogenesis imperfecta. *Arch. Oral Biol.* 76, 61–65. doi: 10.1016/j.archoralbio.2017.01.004

Kumar, S., Dudley, J. T., Filipski, A., and Liu, L. (2011). Phylomedicine: an evolutionary telescope to explore and diagnose the universe of disease mutations. *Trends Genet.* 27, 377–386. doi: 10.1016/j.tig.2011.06.004

Lee, S. K., Seymen, F., Kang, H. Y., Lee, K. E., Gencay, K., Tuna, B., et al. (2010). MMP20 hemopexin domain mutation in amelogenesis imperfecta. *J. Dent. Res.* 89, 46–50. doi: 10.1177/0022034509352844

Llano, E., Pendas, A. M., Knauper, V., Sorsa, T., Salo, T., Salido, E., et al. (1997). Identification and structural and functional characterization of human enamelysin (MMP-20). *Biochemistry* 36, 15101–15108. doi: 10.1021/bi972120y

Lu, Y., Papagerakis, P., Yamakoshi, Y., Hu, J. C., Bartlett, J. D., and Simmer, J. P. (2008). Functions of KLK4 and MMP-20 in dental enamel formation. *Biol. Chem.* 389, 695–700. doi: 10.1515/BC.2008.080

Meredith, R. W., Gatesy, J., Cheng, J., and Springer, M. S. (2011). Pseudogenization of the tooth gene enamelysin (MMP20) in the common ancestor of extant baleen whales. *Proc. Biol. Sci.* 278, 993–1002. doi: 10.1098/rspb.2010.1280

Meredith, R. W., Gatesy, J., and Springer, M. S. (2013). Molecular decay of enamel matrix protein genes in turtles and other edentulous amniotes. *BMC Evol. Biol.* 13:e20. doi: 10.1186/1471-2148-13-20

Moradian-Oldak, J., Leung, W., Simmer, J. P., Zeichner-David, M., and Fincham, A. G. (1996). Identification of a novel proteinase (ameloprotease-I) responsible for the complete degradation of amelogenin during enamel maturation. *Biochem. J.* 318, 1015–1021. doi: 10.1042/bj3181015

Nagano, T., Kakegawa, A., Yamakoshi, Y., Tsuchiya, S., Hu, J. C., Gomi, K., et al. (2009). Mmp-20 and Klk4 cleavage site preferences for amelogenin sequences. *J. Dent. Res.* 88, 823–828. doi: 10.1177/0022034509342694

Ozdemir, D., Hart, P. S., Ryu, O. H., Choi, S. J., Ozdemir-Karatas, M., Firatli, E., et al. (2005). MMP20 active-site mutation in hypomaturation amelogenesis imperfecta. *J. Dent. Res.* 84, 1031–1035. doi: 10.1177/154405910508401112

Papagerakis, P., Lin, H. K., Lee, K. Y., Hu, Y., Simmer, J. P., Bartlett, J. D., et al. (2008). Premature stop codon in MMP20 causing amelogenesis imperfecta. *J. Dent. Res.* 87, 56–59. doi: 10.1177/154405910808700109

Parry, D. A., Holmes, T. D., Gamper, N., El-Sayed, W., Hettiarachchi, N. T., Ahmed, M., et al. (2016a). A homozygous STIM1 mutation impairs store-operated calcium entry and natural killer cell effector function without clinical immunodeficiency. *J. Allergy Clin. Immun.* 137, 955–957. doi: 10.1016/j.jaci.2015.08.051

Parry, D. A., Smith, C. E., El-Sayed, W., Poulter, J. A., Shore, R. C., Logan, C. V., et al. (2016b). Mutations in the pH-sensing G-protein-coupled receptor GPR68 cause amelogenesis imperfecta. *Am. J. Hum. Genet.* 99, 984–990. doi: 10.1016/j.ajhg.2016.08.020

Pavlic, A., Petelin, M., and Battelino, T. (2007). Phenotype and enamel ultrastructure characteristics in patients with ENAM gene mutations g.13185-13186insAG and 8344delG. *Arch. Oral Biol.* 52, 209–217. doi: 10.1016/j.archoralbio.2006.10.010

Poulter, J. A., El-Sayed, W., Shore, R. C., Kirkham, J., Inglehearn, C. F., and Mighell, A. J. (2014). Whole-exome sequencing, without prior linkage, identifies a mutation in *LAMB3* as a cause of dominant hypoplastic amelogenesis imperfecta. *Eur. J. Hum. Genet.* 22, 132–135. doi: 10.1038/ejhg.2013.76

Pourhashemi, S. J., Ghandehari Motlagh, M., Meighani, G., Ebrahimi Takaloo, A., Mansouri, M., Mohandes, F., et al. (2014). Missense mutation in Fam83H gene in Iranian patients with amelogenesis imperfecta. *Iran J. Public Health* 43, 1680–1687.

Prasad, M. K., Geoffroy, V., Vicaire, S., Jost, B., Dumas, M., Le Gras, S., et al. (2016a). A targeted next-generation sequencing assay for the molecular diagnosis of genetic disorders with orodental involvement. *J. Med. Genet.* 53, 98–110. doi: 10.1136/jmedgenet-2015-103302

Prasad, M. K., Laouina, S., El Alloussi, M., Dollfus, H., and Bloch-Zupan, A. (2016b). Amelogenesis Imperfecta: 1 family, 2 phenotypes, and 2 mutated genes. *J. Dent. Res.* 95, 1457–1463. doi: 10.1177/0022034516663200

Rodríguez, D., Morrison, C. J., and Overall, C. M. (2010). Matrix metalloproteinases: what do they not do? New substrates and biological roles identified by murine models and proteomics. *Biochim. Biophys. Acta* 1803, 39–54. doi: 10.1016/j.bbamcr.2009.09.015

Ryu, O. H., Fincham, A. G., Hu, C. C., Zhang, C., Qian, Q., Bartlett, J. D., et al. (1999). Characterization of recombinant pig enamelysin activity and cleavage of recombinant pig and mouse amelogenins. *J. Dent. Res.* 78, 743–750. doi: 10.1177/00220345990780030601

Seymen, F., Kim, Y. J., Lee, Y. J., Kang, J., Kim, T. H., Choi, H., et al. (2016). Recessive mutations in ACPT, encoding testicular acid phosphatase, cause hypoplastic amelogenesis imperfecta. *Am. J. Hum. Genet.* 99, 1199–1205. doi: 10.1016/j.ajhg.2016.09.018

Seymen, F., Lee, K.-E., Koruyucu, M., Gencay, K., Bayram, M., Tuna, E. B., et al. (2014). ENAM mutations with incomplete penetrance. *J. Dent. Res.* 93, 988–992. doi: 10.1177/0022034514548222

Seymen, F., Park, J. C., Lee, K. E., Lee, H. K., Lee, D. S., Koruyucu, M., et al. (2015). Novel MMP20 and KLK4 mutations in amelogenesis imperfecta. *J. Dent. Res.* 94, 1063–1069. doi: 10.1177/0022034515590569

Silvent, J., Gasse, B., Mornet, E., and Sire, J. Y. (2014). Molecular evolution of the tissue-nonspecific alkaline phosphatase allows prediction and validation of missense mutations responsible for hypophosphatasia. *J. Biol. Chem.* 289, 24168–24179. doi: 10.1074/jbc.M114.576843

Silvent, J., Sire, J. Y., and Delgado, S. (2013). The dentin matrix acidic phosphoprotein 1 (DMP1) in the light of mammalian evolution. *J. Mol. Evol.* 76, 59–70. doi: 10.1007/s00239-013-9539-2

Smith, C. E., Murillo, G., Brookes, S. J., Poulter, J. A., Silva, S., Kirkham, J., et al. (2016). Deletion of amelotin exons 3-6 is associated with amelogenesis imperfecta. *Hum. Mol. Genet.* 25, 3578–3587. doi: 10.1093/hmg/ddw203

Wang, S., Choi, M., Richardson, A. S., Reid, B. M., Seymen, F., Yildirim, M., et al. (2014b). STIM1 and SLC24A4 are critical for enamel maturation. *J. Dent. Res.* 93, 94S–100S. doi: 10.1177/00220345145 27971

Wang, S. K., Hu, Y., Simmer, J. P., Seymen, F., Estrella, N. M., Pal, S., et al. (2013). Novel KLK4 and MMP20 mutations discovered by whole-exome sequencing. *J. Dent. Res.* 92, 266–271. doi: 10.1177/00220345134 75626

Witkop, C. J. (1989). Amelogenesis imperfecta, dentinogenesis imperfecta and dentin dysplasia revisited: problems in classification. *J. Oral Pathol.* 17, 547–553. doi: 10.1111/j.1600-0714.1988.tb01332.x

Yeo, G., and Burge, C. B. (2004). Maximum entropy modeling of short sequence motifs with applications to RNA splicing signals. *J. Comput. Biol.* 11, 377–394. doi: 10.1089/1066527041410418

Conflict of Interest Statement: The authors declare that the research was conducted in the absence of any commercial or financial relationships that could be construed as a potential conflict of interest.

The reviewer EB and handling Editor declared their shared affiliation, and the handling Editor states that the process nevertheless met the standards of a fair and objective review.

Copyright © 2017 Gasse, Prasad, Delgado, Huckert, Kawczynski, Garret-Bernardin, Lopez-Cazaux, Bailleul-Forestier, Manière, Stoetzel, Bloch-Zupan and Sire. This is an open-access article distributed under the terms of the Creative Commons Attribution License (CC BY). The use, distribution or reproduction in other forums is permitted, provided the original author(s) or licensor are credited and that the original publication in this journal is cited, in accordance with accepted academic practice. No use, distribution or reproduction is permitted which does not comply with these terms.

frontiers in Physiology

ORIGINAL RESEARCH
published: 06 December 2017
doi: 10.3389/fphys.2017.00940

No Change in Bicarbonate Transport but Tight-Junction Formation Is Delayed by Fluoride in a Novel Ameloblast Model

*Róbert Rácz[1], Anna Földes[1], Erzsébet Bori[1], Ákos Zsembery[1], Hidemitsu Harada[2], Martin C. Steward[3], Pamela DenBesten[4], Antonius L. J. J. Bronckers[5], Gábor Gerber[6] and Gábor Varga[1]**

[1] Department of Oral Biology, Semmelweis University, Budapest, Hungary, [2] Department of Anatomy, Iwate Medical University, Iwate, Japan, [3] School of Medical Sciences, University of Manchester, Manchester, United Kingdom, [4] Department of Orofacial Sciences, University of California, San Francisco, San Francisco, CA, United States, [5] Department of Oral Cell Biology, Academic Centre for Dentistry Amsterdam (ACTA), Amsterdam, Netherlands, [6] Department of Anatomy, Histology and Embryology, Semmelweis University, Budapest, Hungary

OPEN ACCESS

Edited by:
Catherine Chaussain, Université Paris Descartes, France

Reviewed by:
Christian Morsczeck, University of Regensburg, Germany
Takashi Yamashiro, Osaka University, Japan
Claire Bardet, Université Paris Descartes, France

***Correspondence:**
Gábor Varga
varga.gabor@dent.semmelweis-univ.hu

Specialty section:
This article was submitted to Craniofacial Biology and Dental Research, a section of the journal Frontiers in Physiology

Received: *16 June 2017*
Accepted: *06 November 2017*
Published: *06 December 2017*

Citation:
Rácz R, Földes A, Bori E, Zsembery Á, Harada H, Steward MC, DenBesten P, Bronckers ALJJ, Gerber G and Varga G (2017) No Change in Bicarbonate Transport but Tight-Junction Formation Is Delayed by Fluoride in a Novel Ameloblast Model. Front. Physiol. 8:940. doi: 10.3389/fphys.2017.00940

We have recently developed a novel *in vitro* model using HAT-7 rat ameloblast cells to functionally study epithelial ion transport during amelogenesis. Our present aims were to identify key transporters of bicarbonate in HAT-7 cells and also to examine the effects of fluoride exposure on vectorial bicarbonate transport, cell viability, and the development of transepithelial resistance. To obtain monolayers, the HAT-7 cells were cultured on Transwell permeable filters. We monitored transepithelial resistance (TER) as an indicator of tight junction formation and polarization. We evaluated intracellular pH changes by microfluorometry using the fluorescent indicator BCECF. Activities of ion transporters were tested by withdrawal of various ions from the bathing medium, by using transporter specific inhibitors, and by activation of transporters with forskolin and ATP. Cell survival was estimated by alamarBlue assay. Changes in gene expression were monitored by qPCR. We identified the activity of several ion transporters, NBCe1, NHE1, NKCC1, and AE2, which are involved in intracellular pH regulation and vectorial bicarbonate and chloride transport. Bicarbonate secretion by HAT-7 cells was not affected by acute fluoride exposure over a wide range of concentrations. However, tight-junction formation was inhibited by 1 mM fluoride, a concentration which did not substantially reduce cell viability, suggesting an effect of fluoride on paracellular permeability and tight-junction formation. Cell viability was only reduced by prolonged exposure to fluoride concentrations greater than 1 mM. In conclusion, cultured HAT-7 cells are functionally polarized and are able to transport bicarbonate ions from the basolateral to the apical fluid spaces. Exposure to 1 mM fluoride has little effect on bicarbonate secretion or cell viability but delays tight-junction formation, suggesting a novel mechanism that may contribute to dental fluorosis.

Keywords: HAT-7, ameloblast, bicarbonate, ion transport, pH regulation, fluoride, tight-junction, transepithelial resistance

INTRODUCTION

Dental enamel is the hardest material in the human body and its mineral concentration is also the highest. Its major disorders result from either environmental or genetic conditions. In both cases mineral formation can be greatly impaired. Also dental caries and erosion are important enamel-loss conditions where reconstruction would be the optimal solution. Ameloblasts secrete enamel in a two-stage process. First a slightly mineralized matrix structure is built. Then the remodeling of this matrix results in a high level of mineralization (Robinson, 2014). Ameloblasts have epithelial tight junctions which close the intercellular space allowing the preservation of great concentration gradients between the apical and basal sides of the cells. Calcium and phosphate ions are actively transported into the mineralization space by an only partially understood process.

Acid/base balance is crucial during enamel hydroxyapatite formation since the crystal growth depends upon a delicate cellular control of the ionic composition and pH of the extracellular fluid (Takagi et al., 1998). Hydroxyapatite formation during the maturation stage of amelogenesis liberates an enormous quantity of protons. Thus, sustained crystal growth requires these protons to be neutralized (Smith, 1998; Josephsen et al., 2010; Lacruz et al., 2010) by bicarbonate transported directly into the enamel space. The available information about electrolyte transport by ameloblasts is based almost exclusively on expressional studies, immunohistochemistry, and chemical composition analysis, with little functional support (Schroeder and Listgarten, 1997; Bosshardt and Lang, 2005). Consequently, the mechanistic models have hitherto been purely hypothetical.

We have therefore developed an *in vitro* model, using the HAT-7 rat ameloblast cell line, to study epithelial ion transport during amelogenesis (Bori et al., 2016). HAT-7 is a dental epithelial cell line derived from the cervical loop epithelium of a rat incisor (Kawano et al., 2002). Immunocytochemical studies have shown that HAT-7 cells exhibit several ameloblast characteristics, including the expression of amelogenin and ameloblastin (Kawano et al., 2002) and also maturation-stage ameloblast markers such as kallikrein-4 (Klk4) and amelotin. We have to note, however that further studies are needed to determine how well HAT-7 cells could serve as an optimal model for maturation ameloblast function. In our preliminary, proof-of-concept work (Bori et al., 2016) we demonstrated that our 2D *in vitro* model is suitable for functional investigations of pH regulation, mineral transport, and tight-junction formation. Confluent monolayers of HAT-7 cells grown on permeable supports are functionally polarized, they express ion transporters and tight-junction proteins and they mediate vectorial HCO_3^- transport.

Enamel fluorosis is a developmental disturbance caused by intake of supraoptimal levels of fluoride during early childhood (Aoba and Fejerskov, 2002; Denbesten and Li, 2011). The enamel defects consist of horizontal thin white lines, opacities (subsurface porosities), discolorations, and pits of various sizes. The molecular mechanism underlying enamel fluorosis is still unknown. Possible explanations include direct toxic effects of fluoride on ameloblasts, fluoride-related alterations in the forming enamel matrix, reduced proteolytic activity due to fluoride incorporation into growing enamel crystals, the potential effects of fluoride on matrix pH, and incomplete barrier formation at the mineralization front (Aoba and Fejerskov, 2002; Denbesten and Li, 2011; Lyaruu et al., 2014). None of these hypotheses can be directly proved because there is a lack of appropriate experimental models.

Our newly developed HAT-7 ameloblast monolayer model (Bori et al., 2016) may offer a reasonable basis for such studies. We can hypothesize that fluorosis is due to a combination of direct cytotoxic effects causing cell death, the delayed development of tight junctions, which are necessary to form a sealed barrier between apical and basolateral surfaces, and a direct inhibitory effect of fluoride on vectorial calcium and/or bicarbonate transport. The purpose of the present study was (1) to identify the basolateral acid/base transporters affecting intracellular pH regulation in our polarized HAT-7 cell model, (2) to assess whether acute fluoride exposure disturbs transepithelial HCO_3^- secretion in this model, and (3) to assess viability, development of transepithelial resistance, and gene expression of tight-junction proteins of polarized HAT-7 cells in the presence of fluoride.

MATERIALS AND METHODS

Cell Culture

To obtain polarized monolayers (Bori et al., 2016), HAT-7 cells were seeded on permeable polyester Transwell culture inserts with 0.4 μm pore size and 1.12 cm^2 surface area (Costar, Corning, NY, USA) and were cultured in DMEM/F12 Ham medium (Sigma-Aldrich, St. Louis, MO, USA) supplemented with 10% HyClone fetal bovine serum (Thermo Scientific, Waltham, MA, USA), 100 U/ml penicillin, 10 μg/ml streptomycin (Sigma), $CaCl_2$ (2.1 mM final concentration), and 10^{-5} mM dexamethasone (Sigma) (Arakaki et al., 2012) as described previously (Bori et al., 2016). They were grown in a humidified atmosphere containing 5% CO_2 at 37°C.

Measurement of Transepithelial Electrical Resistance

Transepithelial electrical resistance (TER) values of HAT-7 cells grown on Transwell membranes incubated in 12-well plates were measured using an epithelial volt-ohmmeter (EVOM, World Precision Instruments, Hamden CT, USA) on 5 consecutive days prior to microfluorometric measurements or during NaF treatments. TER values give an indication of the paracellular permeability to electrolytes, and thus tight-junction formation, which are key characteristics of secretory and absorptive epithelia. In multi-day fluoride exposure experiments, 24 h after cell seeding on Transwells, the medium was changed to 0 (control), 0.3, 0.6, or 1 mM NaF-containing medium.

Microfluorometry

Intracellular pH (pH_i) in HAT-7 cells was measured by microfluorometry as described previously (Szucs et al., 2006; Bori et al., 2016). Briefly, the cells were loaded with a fluorescent dye, BCECF-AM, that is sensitive to intracellular pH and

therefore capable of indirectly measuring H^+ and/or HCO_3^- movements through the cell membrane. Particular elements of HCO_3^- transport can be identified by modifying the extracellular environment (e.g., specific ion withdrawal, application of transporter inhibitors).

Cells grown on Transwell membranes were mounted in a minichamber on a Nikon Eclipse TE200 inverted fluorescence microscope and were bilaterally superfused at 3 ml/min. Illumination was alternated between 490 and 440 nm excitation wavelengths. Fluorescence was measured every 5 s at 530 nm using a photomultiplier tube and amplifier (Cairn Research, Faversham, Kent, UK) and data were acquired using DASYLab software (Measurement Computing, Norton, MA). Fluorescence data were corrected for autofluorescence. Using calibration data obtained with the nigericin/high potassium method (Thomas et al., 1979) the ratio of fluorescence signals at the two excitation wavelengths was converted to pH_i.

The following solutions were used for perfusion: standard HEPES-buffered solution containing (in mM) 137 NaCl, 5 KCl, 1 $CaCl_2$, 1 $MgCl_2$, 10 D-glucose, and 10 HEPES (4-(2-hydroxyethyl)-1-piperazineethanesulfonic acid), equilibrated with 100% O_2; standard HCO_3^--containing HEPES-buffered solution containing (in mM) 116 NaCl, 25 $NaHCO_3$, 5 KCl, 1 $CaCl_2$, 1 $MgCl_2$, 10 D-glucose, and 5 HEPES, equilibrated with 5% CO_2/95% O_2. For Na^+ withdrawal, Na^+ was replaced by equimolar N-methyl-D-glucamine (NMDG). For Cl^- withdrawal, Cl^- was replaced with equimolar gluconate. All solutions were adjusted to pH 7.4 at 37°C. For inhibiting specific transport processes 100 μM DIDS was used to block anion exchangers, 300 μM amiloride to block Na^+-H^+ exchange, 500 μM H_2DIDS for Na^+-HCO_3^- cotransport, and 100 μM bumetanide for NKCC. For stimulation of transport, 50 μM ATP was used to elevate intracellular calcium concentrations and 10 μM forskolin, in combination with 500 μM IBMX (3-isobutyl-1-methylxanthine), was used to elevate intracellular cAMP levels. All reagents were purchased from Sigma (Sigma-Aldrich, St. Louis, MO, USA), except H_2DIDS and BCECF-AM (both from Molecular Probes, Eugene, OR, USA) and NaF (Molar Chemicals, Hungary).

Cell Viability Assays

Cell viability was tested by alamarBlue assay (Thermo Scientific, Waltham, MA, USA) according to the manufacturer's protocol. Cells (10^4 per well) were plated in 96-well plates, and experiments started 24 h after plating. At this time the medium was supplemented with various concentrations of NaF. After 48 and 96-h exposures to fluoride, the cells' metabolic activity was evaluated by measuring the alamarBlue fluorescence at 590 nm (with excitation at 560 nm) using a Perkin-Elmer LS50B luminescence spectrometer. Each treatment was applied in six parallel wells.

Quantitative PCR

The expression of tight-junction forming genes was estimated by quantitative RT-PCR as described previously (Hegyesi et al., 2015; Bori et al., 2016). Total RNA was isolated 3 days after seeding from Transwell samples incubated in medium containing 0, 0.6, and 1 mM NaF, by GeneJET RNA Purification Kit (Thermo Scientific, Waltham, MA, USA). Approximately 1–2 μg of total RNA was reverse transcribed by Maxima First Strand cDNA Synthesis Kit for RT-qPCR (Thermo Scientific, Waltham, MA, USA). The cDNA was then used in quantitative PCR reactions. qPCR amplification was performed using the ABI StepOne System with TaqMan Universal Master Mix II and predesigned primers Tjp1: Rn02116071; Cldn1: Rn00581740; Cldn4: Rn01196224; Cldn8: Rn01767199; Cldn16: Rn00590884; and Cldn19: Rn01416537 (Applied Biosystems, Foster City, CA, USA). Acidic ribosomal protein P0 (Rplpo: Rn00821065) was used as internal control and the ΔΔCt method was used to quantify gene expression with ABIPrism 2.3 software. Each sample was measured in three biological replicates and in three technical parallels.

Statistical Analysis

Data are presented as mean ± SEM. Statistical analyses were performed using one-way or repeated-measures ANOVA, followed by Dunnett's *post-hoc* test. Unpaired *t*-tests were applied when only two groups were to be compared. As transepithelial resistance experiments resulted in large differences in SEM values, thus not permitting parametric tests, the non-parametric Kruskal-Wallis test and Dunn's *post-hoc* test were used to compare TER values.

RESULTS

Evidence for Activity of the Major Basolateral Transporters Participating in Intracellular pH Regulation in HAT-7 Cells

In our previous work we showed data suggesting the existence of vectorial, basolateral-to-apical bicarbonate transport in HAT-7 ameloblast cells but we did not identify the individual transporters at the basolateral side (Bori et al., 2016).

Na^+-H^+ Exchanger Activity at the Basolateral Membrane

The ammonium pulse technique (Boron and De Weer, 1976) was used to induce intracellular acidification, and the rate of recovery of pH_i from the acid load was measured in the absence of HCO_3^-/CO_2. Removal of Na^+ from both sides of the epithelium after the NH_4^+ pulse completely blocked the recovery of pH_i from the acidification (**Figure 1A**), indicating the Na^+ dependence of the transporters responsible for pH_i regulation. Na^+ restoration on the basolateral side caused a rapid recovery of pH_i which was sensitive to 300 μM amiloride (**Figures 1A,B**) indicating the existence of basolateral Na^+-H^+ exchanger (NHE) activity, most probably due to NHE1 which is ubiquitously expressed at the basolateral membrane of secretory epithelia.

Na^+-HCO_3^- Cotransporter Activity at the Basolateral Membrane

In the presence of HCO_3^-/CO_2, removal of Na^+ from both sides, after acid load, blocked the recovery of pH_i (**Figure 2A**), suggesting that the HCO_3^- transporters involved in pH_i regulation are also Na^+ dependent and thus likely to include

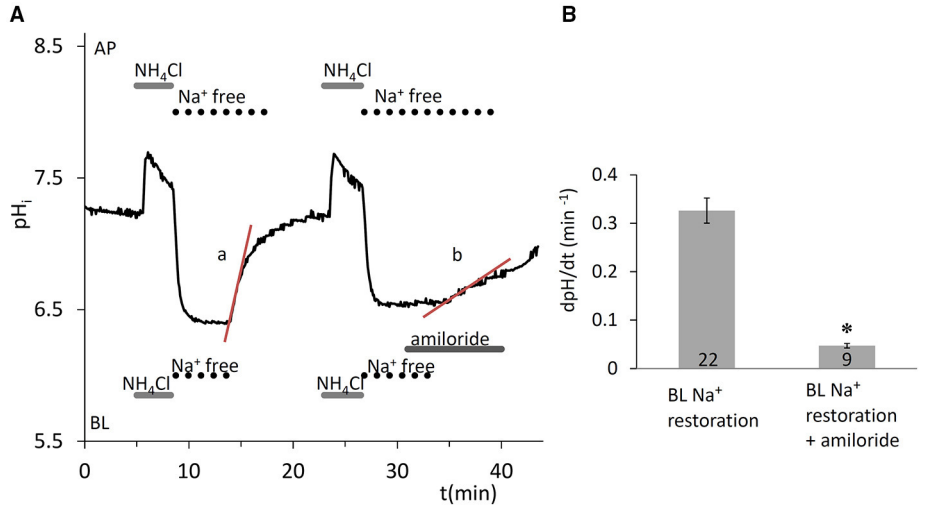

FIGURE 1 | Recovery of pH_i in HAT-7 cells exposed to an acid load in the absence of HCO_3^-/CO_2. **(A)** HAT-7 cells grown on Transwell membranes were exposed bilaterally to 20 mM NH_4Cl followed by bilateral substitution of Na^+ with $NMDG^+$. Recovery of pH_i (a) can be seen following basolateral restoration of external Na^+. Inhibition of pH_i recovery (b) can be seen following restoration of Na^+ in the presence of basolateral (BL) amiloride (300 μM) in order to selectively block the NHE1 exchanger. **(B)** Mean dpH/dt (± SEM) values were calculated from the initial rates of increase in pH_i following restoration of Na^+ in the presence and absence of the inhibitor ($n = 9$–22). *$p < 0.05$ compared with control.

the Na^+-HCO_3^- cotransporter NBCe1. Na^+ restoration on the basolateral side caused a sharp increase in pH_i, which was partially amiloride sensitive (**Figures 2B,D**, $p < 0.05$ vs. control) and therefore only partially attributable to NHE1. Additionally, when the NBCe1 inhibitor H_2DIDS (500 μM) was applied in addition to amiloride, further significant inhibition of pH_i recovery was observed (**Figures 2C,D**, $p < 0.05$ vs. amiloride given alone). Thus, the pH_i regulatory mechanisms following intracellular acidification seem to involve both HCO_3^- uptake by NBCe1, and H^+ extrusion by NHE1 in HAT-7 cells.

Na^+-K^+-$2Cl^-$ Cotransporter Activity at the Basolateral Membrane

A potentially important factor that may contribute to the partial recovery of pH_i from the alkalinization that occurs during the NH_4^+ pulse is the acidifying effect of NH_4^+ uptake. This could be mediated by the Na^+-K^+-$2Cl^-$ cotransporter (NKCC1) which is known to transport NH_4^+ in place of K^+ (Paulais and Turner, 1992b). Basolateral application of the NKCC1 inhibitor bumetanide (100 μM) (Shumaker and Soleimani, 1999), significantly slowed the acidification that occurred during the NH_4^+ pulse ($p < 0.05$, **Figure 3**). This suggests that NKCC1 is present in HAT-7 cells and is consistent with our previous RT-PCR data (Bori et al., 2016).

Anion-Exchanger Activity at the Basolateral Membrane

Since anion secretion by ameloblasts involves Cl^-/HCO_3^- exchange at the basolateral membrane (Lyaruu et al., 2008), the next series of experiments was designed to test the activity of anion exchangers in HAT-7 cells. Extracellular Cl^- was substituted with a non-transported anion, gluconate, and the resulting change in pH_i was recorded. Substitution of Cl^- reverses the normal concentration gradient for Cl^-. If anion exchangers are present, the resulting efflux of Cl^- will be coupled to a rapid uptake of HCO_3^- and this will result in a measurable increase in pH_i. Indeed, removal of basolateral Cl^- from the HEPES-buffered bath solution elicited an increase in pH_i (**Figure 4**), likely due to HCO_3^- influx, which was significantly inhibited by the anion exchange inhibitor DIDS (100 μM) ($p < 0.05$ vs. control). This suggests that a DIDS-sensitive anion exchanger, most probably AE2, is present at the basolateral membrane of HAT-7 ameloblast cells.

Lack of Effect of Acute Fluoride Exposure on Bicarbonate Secretion in HAT-7 Cells

Besides the cotransport of HCO_3^- through the basolateral membrane by NBCe1 (using the Na^+ gradient as a driving force), cells can also accumulate HCO_3^- by the diffusion of CO_2 into the cells, its conversion to HCO_3^- and H^+ by carbonic anhydrases, and subsequent H^+ extrusion by NHE1. We demonstrated in our previous paper that when HCO_3^- uptake is blocked on the basolateral side by NBCe1 and NHE1 inhibitors, the continuing apical efflux of HCO_3^- leads to a slow intracellular acidification. This can be further enhanced by simultaneous application of Ca^{2+}- and cAMP-mobilizing stimuli (ATP and forskolin/IBMX, respectively) (Bori et al., 2016). In the present work we measured this initial acidification rate, an index of HCO_3^- secretion, to test whether acute NaF exposure has any effect on vectorial HCO_3^- transport. We found that fluoride in the concentration range 0.03–1.0 mM did not affect HCO_3^- secretion evoked by simultaneous stimulation with 50 μM ATP, 10 μM forskolin, and 500 μM IBMX (**Figure 5**).

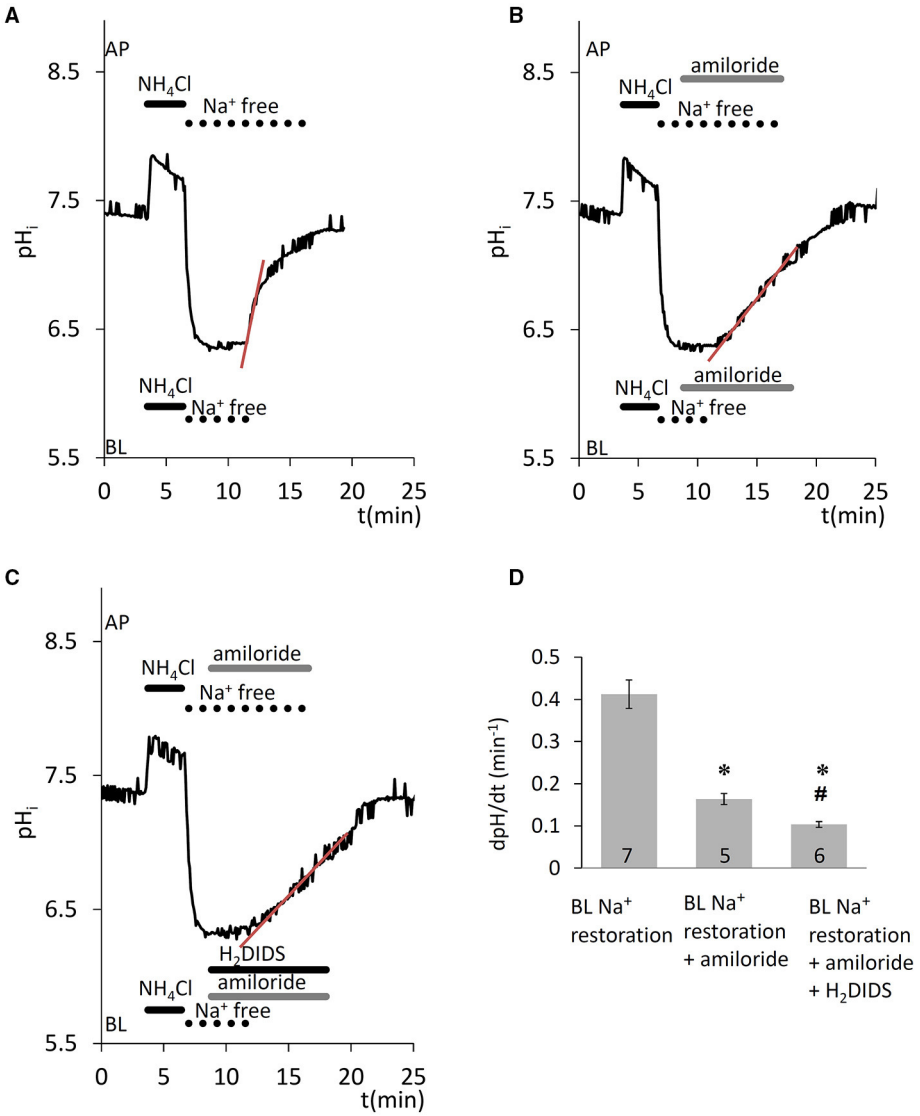

FIGURE 2 | Recovery of pH_i in HAT-7 cells exposed to an acid load in the presence of HCO_3^-/CO_2. HAT-7 cells grown on Transwell membranes were exposed bilaterally to 20 mM NH_4Cl followed by bilateral substitution of Na^+ with $NMDG^+$. **(A)** Recovery of pHi following basolateral restoration of extracellular Na^+. **(B)** Inhibition of pH_i recovery following restoration of Na^+ in the presence of basolateral (BL) amiloride (300 μM). **(C)** As for panel B but with the amiloride-containing BL solution supplemented with H_2DIDS (500 μM) in order to block the NBCe1 cotransporter. **(D)** Mean dpH/dt ± SEM values calculated from the initial rates of increase in pH_i following restoration of Na^+ in the presence and absence of the inhibitors ($n = 5$–7). *$p < 0.05$ compared to control, #$p < 0.05$ compared to amiloride alone.

Development of Transepithelial Resistance, Cell Viability, and Gene Expression in HAT-7 Cells Exposed to Fluoride

The formation of tight junctions is essential for ameloblast polarization and differentiation (Bartlett and Smith, 2013) and it creates an intercellular barrier that separates the apical and basolateral spaces, thus enabling transepithelial ion gradients to exist across the epithelium. We monitored tight-junction formation and polarization by measuring the transepithelial resistance (TER) of HAT-7 cells cultured on Transwell membranes for 5 days, performing daily TER measurements while the cells were exposed to various concentrations of NaF. The cells became confluent, covering the whole surface of the Transwell membranes, after 3–5 days in the presence of fluoride at concentrations up to 1 mM (phase-contrast images in **Figure 6A**). Over the 5-day period TER development was not significantly affected the by presence of 0.3 or 0.6 mM NaF. However, we detected an almost full inhibition of TER development by 1 mM NaF ($p < 0.05$ vs. zero fluoride control, **Figure 6B**).

Tight-junction forming gene expression in HAT-7 cells cultured on Transwell membranes in differentiation medium was evaluated by quantitative RT-PCR (**Figure 6C**). Unexpectedly,

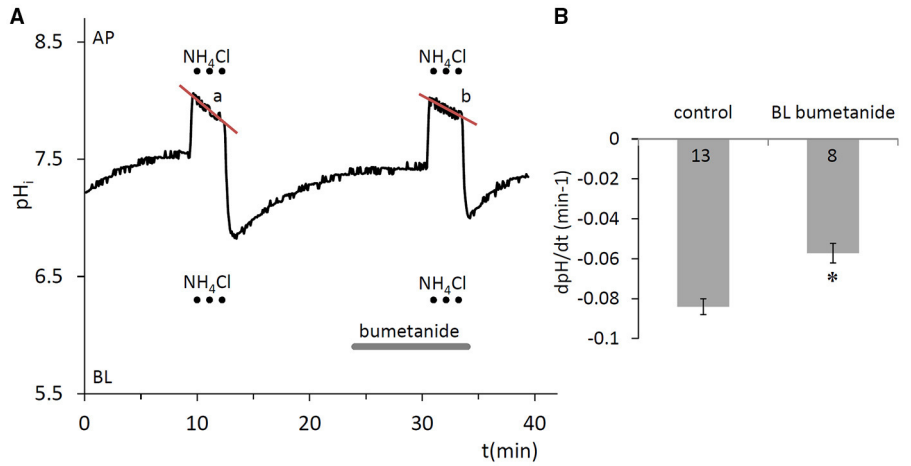

FIGURE 3 | Compensation of pH_i change in HAT-7 cells exposed to an alkali load in the absence of HCO_3^-/CO_2. **(A)** HAT-7 cells grown on Transwell membranes were exposed bilaterally to 20 mM NH_4Cl, during which time partial pHi compensation (a) was observed. Inhibition of pH_i compensation can be seen (b) in the presence of basolateral (BL) bumetanide (100 μM), a selective blocker of the NKCC1 cotransporter. **(B)** Mean dpH/dt ± SEM values were calculated from the rate of pH_i decrease during NH_4Cl exposure in the presence and absence of the inhibitor ($n = 8$–13). *$p < 0.05$ compared to control.

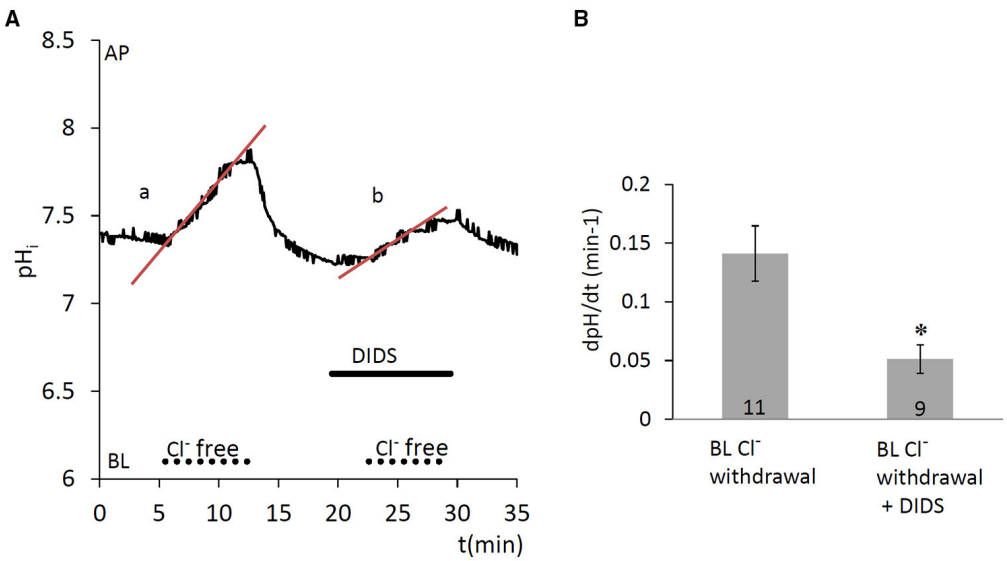

FIGURE 4 | Increase in pH_i in HAT-7 cells upon Cl^- withdrawal in the presence of HCO_3^-/CO_2. **(A)** HAT-7 cells grown on Transwell membranes were exposed basolaterally to Cl^--free HCO_3^--containing HEPES solution. An increase in pH_i (a) can be seen, most probably as a result of HCO_3^- influx. Upon restoration of basolateral Cl^-, pH_i recovers to the baseline. Basolateral administration of DIDS (100 μM) prior to a second Cl^- withdrawal inhibited the increase in pH_i (b) suggesting the presence of a HCO_3^-/Cl^- exchanger. **(B)** Mean dpH/dt (± SEM) values were calculated from the initial rates of increase in pH_i following removal Cl^- in the presence and absence of the inhibitor ($n = 9$–11). *$p < 0.05$ compared to control.

fluoride exposure did not inhibit the expression of the junctional complex genes Tjp1, Cldn1, Cldn4, Cldn8, Cldn16, and Cldn19 at mRNA level at all. Instead, a moderate but significant increase was observed in their expression. These data suggest that fluoride impedes tight junction assembly, rather than the expression of its key protein components.

The cytotoxicity of NaF was determined using the alamarBlue viability assay and this showed that the metabolic activity of HAT-7 cells was not altered by NaF concentrations of up to 0.6 mM (**Figure 6D**). With 1 mM fluoride, the concentration that impeded tight junction formation, metabolic activity was only slightly reduced. However, cell viability was preserved, as judged by the photomicrographs taken at day 5, which show full confluency of the cells (**Figure 6A**). In contrast, 3 mM NaF was totally toxic, killing the cells after just 48 h (**Figure 6D**).

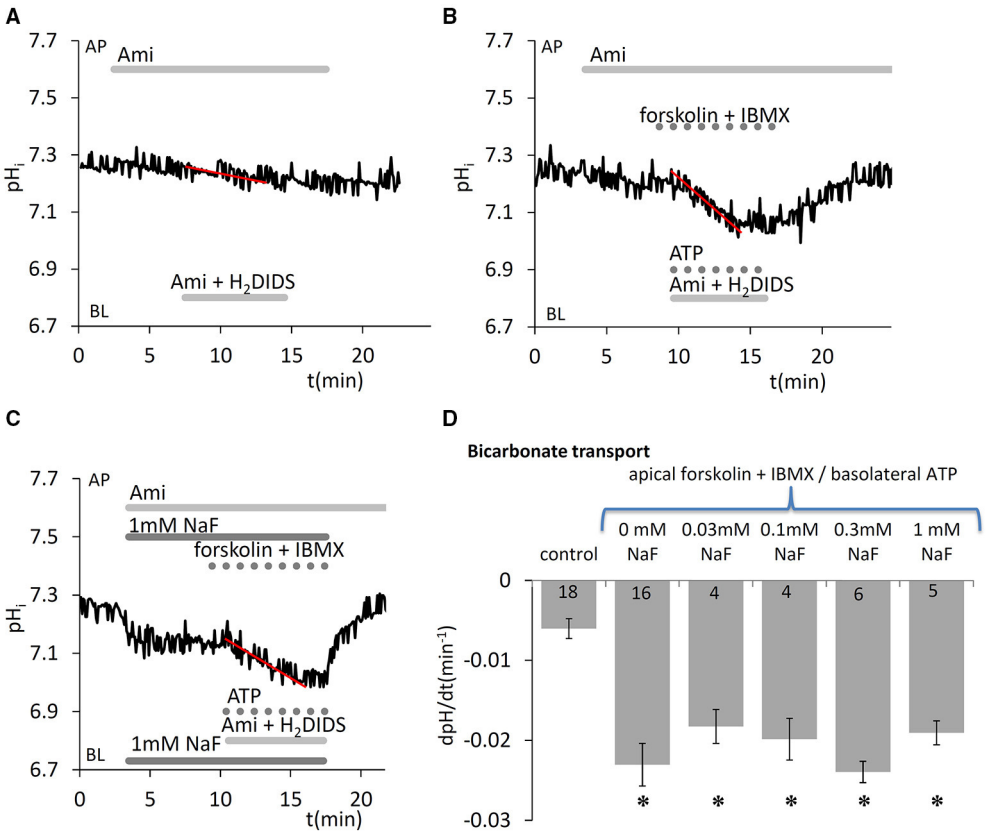

FIGURE 5 | Effects of fluoride on HCO_3^- secretion by HAT-7 cells stimulated with ATP and forskolin**.** Basolateral HCO_3^- uptake in HAT-7 cells grown on Transwell membranes was inhibited by simultaneous basolateral (BL) application of 500 μM H2DIDS and 300 μM amiloride (Ami). Amiloride was also included in the apical (AP) perfusate to inhibit any apical NHE activity. Representative pH_i traces obtained **(A)** in unstimulated control conditions, **(B)** in cells stimulated with ATP (50 μM), forskolin (10 μM), and IBMX (500 μM), and **(C)** in stimulated cells exposed to 1 mM NaF. **(D)** Mean dpH/dt ± SEM values calculated from the initial rates of decrease in pH_i in unstimulated cells (control) and cells stimulated with ATP, forskolin and IBMX, and pretreated with a range of NaF concentrations. *$p < 0.05$ compared with control.

DISCUSSION

The CO_2/HCO_3^- equilibrium is central to the proper regulation of extracellular pH by ameloblasts during enamel mineralization (Lacruz et al., 2010, 2012, 2013; Bronckers et al., 2016). A major finding in our previous work was that HAT-7 cells grown as a monolayer on Transwell membranes are capable of apical-to-basolateral HCO_3^- secretion (Bori et al., 2016). To identify the acid/base transporters responsible for basolateral HCO_3^- accumulation in the cytosol during secretion, we first examined the recovery of pH_i following an acid load in the absence of HCO_3^-/CO_2. This was dependent on basolateral Na^+ and was almost completely blocked by basolateral application of amiloride, suggesting the presence of NHE1 at this membrane. This is consistent with the observation that the presence of a basolateral Na^+/H^+ exchanger, usually NHE1, is an almost universal feature of the epithelial cells of the gastrointestinal tract (Kiela et al., 2006). Under physiological conditions, in the presence of HCO_3^-/CO_2, NHE1 contributes to bicarbonate accumulation within the cells, because it shifts the carbonic-anhydrase catalyzed reaction toward the production of HCO_3^- ions by removing H^+ from the cell. The importance of this mechanism can be clearly seen in other HCO_3^--secreting epithelia such as those of the salivary glands and pancreas (Steward et al., 2005).

Besides H^+ extrusion, Na^+-HCO_3^- co-transporters (NBCs) may also contribute to HCO_3^- uptake. In our study the presence of a basolateral Na^+-HCO_3^- cotransporter was revealed in acid-loading experiments performed in the presence of HCO_3^-/CO_2. The recovery of pH_i was Na^+ dependent, and was only partially inhibited by amiloride. The simultaneous application of amiloride and H_2DIDS resulted in a significantly greater inhibition suggesting that a basolateral NBC also contributes to the cytosolic HCO_3^- supply. Moreover, when NHE activity was measured in HCO_3^--free (HEPES-buffered) medium, the pHi recovery from acidosis (control) and its inhibition by NHE inhibitor was substantially lower than recovery rate and its inhibition by the NHE inhibitor in HCO_3^--containing medium, further suggesting the existence of an NHE-independent mechanism. These data are consistent both with our RT-PCR evidence for NBCe1 expression in HAT-7 cells (Bori et al., 2016) and with previous reports of tissue staining in mid-maturation

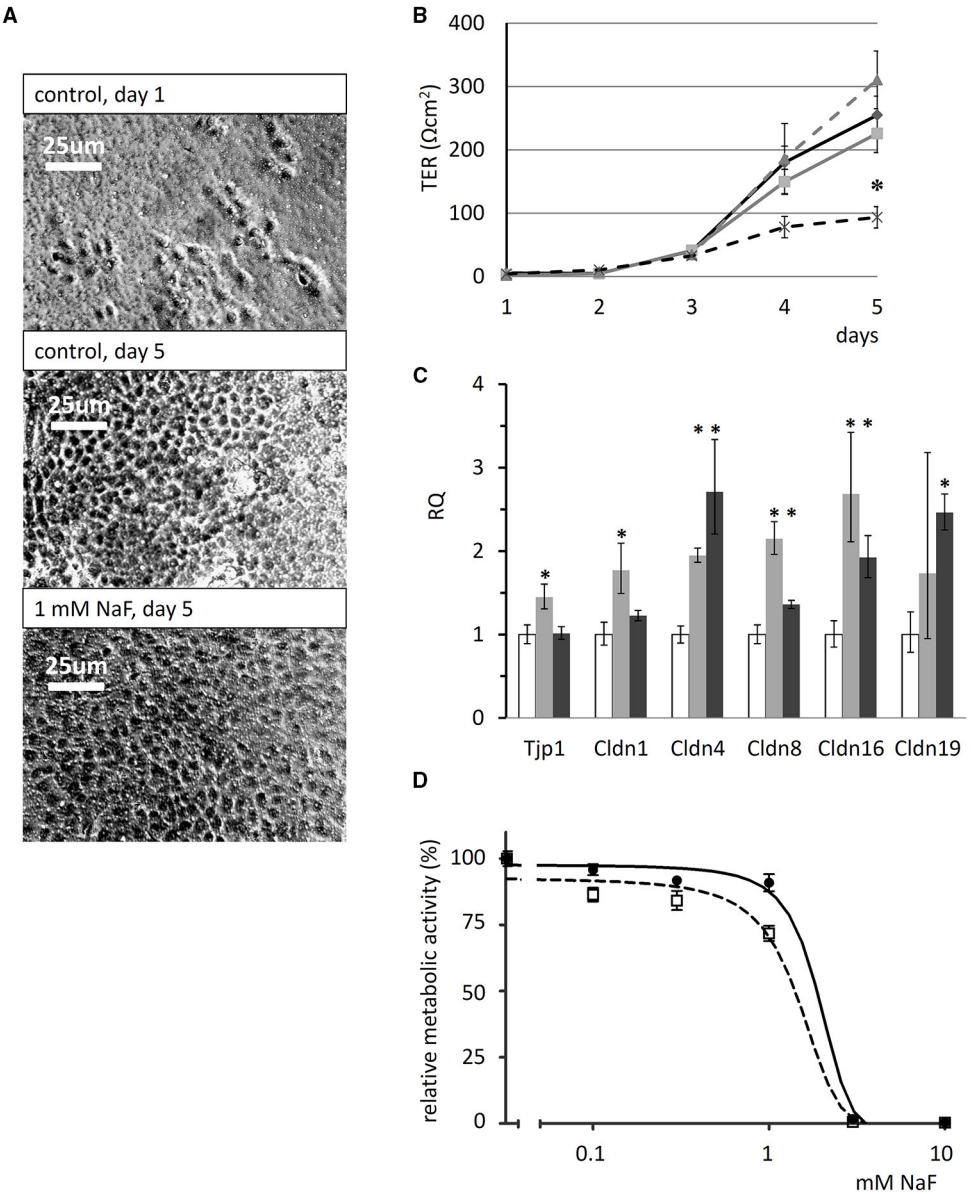

FIGURE 6 | Effects of fluoride on transepithelial resistance, tight-junction protein expression and cell viability of HAT-7 cells**. (A)** Phase-contrast images of HAT-7 cells grown on Transwell membranes in control medium at day1 and 5 (control), or in the same medium supplemented with 1 mM NaF. **(B)** Transepithelial resistance (TER) of the cells cultured on Transwell membranes for 5 days in the absence (solid black) and presence of 0.3 mM (solid gray), 0.6 mM (broken gray), or 1 mM NaF (broken black line). A significant difference in TER was observed after 5 days when cells cultured with 1 mM NaF were compared to controls: $^*p < 0.05$. **(C)** Quantitative RT-PCR data showing expression of tight-junction genes Tjp1, Cldn1, Cldn4, Cldn8, Cldn16, and Cldn19 genes, normalized to mitochondrial Rplpo gene expression in HAT-7 cells treated as described above ($n = 3$ for each gene). Changes in gene expression following treatment with 0.6 mM (gray) and 1 mM (black) NaF are compared to controls (white): $^*p < 0.05$; error bars show 95% confidence intervals. **(D)** Concentration dependence of the effect of NaF on the metabolic activity of HAT-7 cells treated for 48 h (black circles, continuous line) and 96 h (empty rectangles, broken line) ($n = 6$ for each NaF concentration).

ameloblasts (Jalali et al., 2015). The basolateral localization of NBCe1 in these cells is similar to that observed in secretory epithelia in rat (Zhao et al., 1994) and guinea-pig (Ishiguro et al., 2000) pancreatic ducts, and also in rat (Gresz et al., 2002), and guinea-pig (Li et al., 2006) salivary glands.

Chloride ions are usually required for HCO_3^- transport in secretory epithelia (Demeter et al., 2009a), and they are most likely also essential in pH modulation during enamel formation (Bronckers, 2017). There is a strong positive correlation between calcium content and chloride content during ongoing enamel maturation and ameloblast modulation. Lower than normal Cl^- content leads to hypomineralization (Bronckers et al., 2015). CFTR-null and AE2-null mice show strongly affected phenotypes in their enamel structure (Sui et al., 2003; Bronckers et al., 2015). Importantly, cells have to first accumulate Cl^- intracellularly in order to secrete it across the apical membrane. NKCCs are

electroneutral symporters that move Na^+, K^+, and Cl^- ions into the cell by secondary active transport. NKCC activity can be detected by microfluorometry because of its ability to carry NH_4^+ ions in place of K^+ (Paulais and Turner, 1992b). In this study, we observed a bumetanide-sensitive decrease in pH_i during NH_4Cl exposure in HAT-7 cells. Therefore, the cotransporter (most probably NKCC1) may be an important contributor to Cl^- uptake across the basolateral membrane of HAT-7 ameloblast cells, as it is in a number of other secretory epithelia including the pancreatic ductal cell lines Capan-1 and HPAF (Szucs et al., 2006; Demeter et al., 2009a) and salivary acinar cell line Par-C10 (Demeter et al., 2009b), where Cl^- secretion is largely dependent on basolateral NKCC1 activity (Paulais and Turner, 1992a; Melvin et al., 2005). Our study represents the first functional evidence that NKCC1 could have a role in Cl^- accumulation in ameloblasts. Furthermore, it is in line with the recent observation that NKCC1 is expressed during amelogenesis in papillary cells by immunohistochemistry (Jalali et al., 2017).

Another major class of HCO_3^- transporters are the anion exchangers (AEs). The Na^+-independent AEs of the SLC4 family accomplish the electroneutral exchange of Cl^- with HCO_3^- ions. According to our Cl^- substitution experiments, a Cl^-/HCO_3^- exchanger is present at the basolateral membrane of HAT-7 cells, as confirmed by the inhibitory effect of DIDS. This is most likely to be the AE2 exchanger, whose expression we detected previously in polarized HAT-7 cells by immunocytochemistry (Bori et al., 2016) and which is expressed at the basolateral membranes of most epithelial cells (Romero et al., 2004). In salivary acinar cells, the basolateral Cl^-/HCO_3^- exchanger provides an important additional pathway for the accumulation of intracellular Cl^- against its electrochemical gradient (Melvin et al., 2005; Demeter et al., 2009b). This basolateral location in HAT-7 cells is also consistent with previous reports of the basolateral expression of AE2 in maturation ameloblasts (Lyaruu et al., 2008, 2014).

A high level of fluoride exposure is known to impair enamel formation and can result in hypomineralization (Denbesten et al., 1985; Smith et al., 1993; Bronckers et al., 2009). The exact mechanism is unknown and multiple factors might contribute to this phenomenon. Fluoride may affect ion secretion by ameloblasts, the developmental and functional states of ameloblasts unrelated to ion secretion, and it could also contribute to the physical events of mineralization. To test the first possibility, we investigated how fluoride exposure affects transcellular HCO_3^- secretion in HAT-7 cells. We have recently demonstrated that HAT-7 cells can accumulate HCO_3^- ions through the basolateral membrane and in turn secrete them through the apical membrane (Bori et al., 2016). Our present data clearly show that acute exposure to a wide range of fluoride concentrations causes no change in the rate of acidification of the cells when basolateral HCO_3^- uptake is blocked. These data indicate that fluoride has no acute inhibitory effect on HCO_3^- secretion, which we consider to be a crucial requirement for mineralization (Varga et al., 2015).

The investigation of the effect of fluoride on ameloblast monolayer formation and function yielded interesting, and somewhat unexpected results. In our hands fluoride application up to 1 mM resulted in no, or very little, change in HAT-7 cell viability. However, increasing the fluoride concentration to 3 mM resulted in an almost complete loss of the cells, independent of the exposure period (2–5 days). Our findings are consistent with recent observations on HAT-7 cells by other investigators (Zhang et al., 2016) and with studies of the mouse LS8 ameloblast cell line (Kubota et al., 2005; Zhang et al., 2006, 2007; Sharma et al., 2008). Collectively, these studies suggest that ameloblast survival is not seriously affected up to millimolar concentrations, but further increases in the fluoride concentration result in rapid deterioration over a very narrow concentration range.

When we studied the effects of fluoride on the development of transepithelial resistance, we found substantially delayed TER development in doses below those producing cytotoxic levels. We hypothesized that the delay in tight-junction formation might be a consequence of changes in the expression of one or more tight-junction proteins. Thus, we investigated the expressional changes in Tjp1, Cldn1, Cldn4, Cldn8. Importantly, we have shown previously that the expression profiles of these proteins show some relationship with the normal development of TER in HAT-7 cells (Bori et al., 2016). We also evaluated the expression of Cldn16 and Cldn19, since their crucial role in ameloblast tight-junction formation has been recently indicated; their mutation causing familial hypomagnesaemia with hypercalciuria and nephrocalcinosis and amelogenesis imperfecta (Bardet et al., 2016; Yamaguti et al., 2017). To our surprise, fluoride exposure did not inhibit the expression of junctional-complex protein genes Tjp1, Cldn1, Cldn4, Cldn8, Cldn16, and Cldn19 at all. Instead, a moderate but significant increase was observed in their expression. These data suggest that fluoride impedes tight-junction assembly, rather than the expression of its protein constituents. Regarding the mechanism, several types of signaling pathways and proteins have been linked to tight junction assembly. The fluoride-sensitive RhoA-ROCK signaling is crucial in controlling epithelial polarity and adhesion of ameloblasts (Otsu and Harada, 2016), also directly regulating E-cadherin expression (Xue et al., 2013) which is fundamental for tight junction formation (Matter and Balda, 2003). Further studies will determine whether these elements are really linked together. This is particularly important, since the amelogenesis stage mimicked by the proposed polarized HAT-7 model should be better characterized in the future, particularly with respect of tight junctions at protein levels as the lack of this is a major limitation of the present study.

Our present findings indicating delayed tight-junction assembly might offer an alternative, or additional, explanation for dental fluorosis. Our data do not diminish the importance of the many other postulated mechanisms, such as delayed removal of matrix proteins in fluorosed maturation enamel (Denbesten et al., 1985; Smith et al., 1993), increased binding of amelogenins to fluoride-containing hydroxyapatite crystals (Tanimoto et al., 2008), reduced KLK4 expression by ameloblasts (Suzuki et al., 2014), increased SATB1 protein content and enhanced Gαq activity (Zhang et al., 2014), decreased trafficking of NCKX4 Ca^{2+}-transporter to the apical membrane (Bronckers et al., 2017). To some extent, many or all of these mechanisms

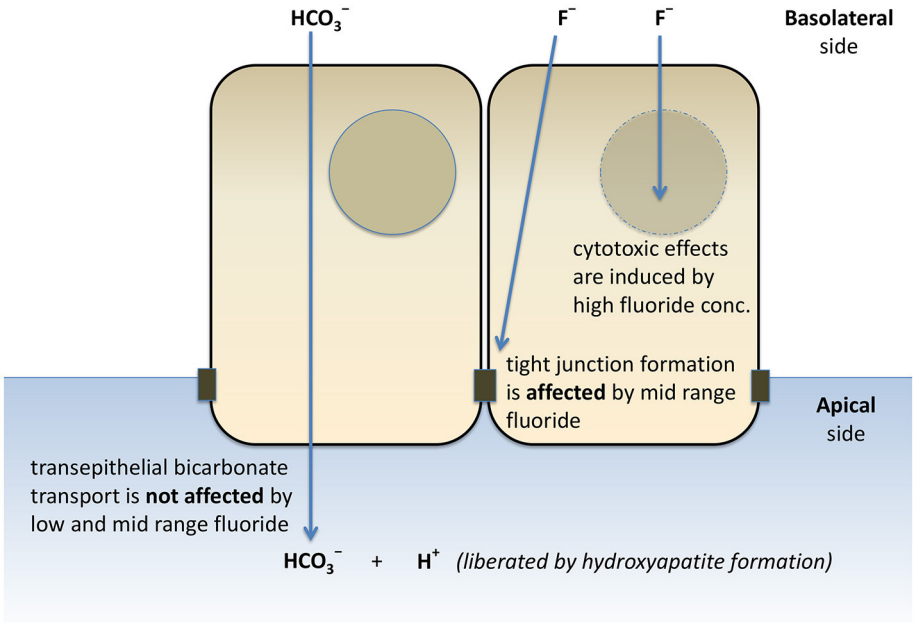

FIGURE 7 | Schematic representation of the effects of fluoride on HCO_3^- secretion, tight junction formation, and cell death of HAT-7 cells**.** Bilateral exposure of 2D monolayers of HAT-7 cells differentiated on Transwell membranes to low-range (0–50 μM), mid-range (100–1,000 μM) fluoride and high fluoride concentration (3 mM) resulted in differential changes in ameloblast function.

may contribute to hypomineralization depending on the actual local concentrations of fluoride. Nonetheless, the delay in tight-junction formation, could also be very important when one considers the structural and functional cycling of ameloblasts. Ruffle-ended ameloblasts cyclically turn into smooth-ended ameloblasts and vice versa during amelogenesis (Smith, 1998; Josephsen et al., 2010). In rats, a cycle lasts about 8 h, during which the cells are in the ruffle-ended state for about 4 h before abruptly changing to the smooth-ended phenotype for about 2 h. Afterwards, the ruffled border of the cell membrane facing the enamel is gradually rebuilt and the tight junctions are translocated and reassembled (Smith, 1998; Josephsen et al., 2010). If the disassembly and reassembly of tight junctions is as important as this model suggests, any delay in their turnover could have serious consequences for the amelogenesis process itself. Since the present observations were obtained in an *in vitro* cellular model, our hypothesis is only tentative, but we certainly believe that it deserves further investigation. However, we have to state that the polarized HAT-7 model needs to be further characterized, and other cellular models, including human ameloblast models have to be developed to support the validity of the above proposed hypothesis.

In conclusion, our HAT-7 model is a useful tool for the functional analysis of ameloblast pH regulation and the associated ion transport mechanisms. We have verified the activity of several key transporters affecting the pH regulation and vectorial HCO_3^- and Cl^- transport by these cells. Furthermore, we have provided evidence that HCO_3^- secretion is not affected by a wide range of fluoride concentrations. However, the formation of tight junctions is severely delayed by 1 mM fluoride, a concentration which does not have substantial cytotoxic effects (**Figure 7**). This hitherto unknown effect of fluoride may prove to be an important factor in the development of dental fluorosis.

AUTHOR CONTRIBUTIONS

RR: contributed to conception and design, data acquisition, analysis, and interpretation, drafted and critically revised manuscript; AF: contributed to data acquisition, analysis, and interpretation, and critically revised manuscript; EB: contributed to conception and design, data acquisition, analysis, and interpretation, and critically revised manuscript; ÁZ and GG: contributed to data analysis and interpretation, and critically revised manuscript; HH: contributed to conception and to data interpretation, and critically revised manuscript; MS: contributed to design, data analysis and interpretation, and critically revised manuscript; PD: contributed to conception and design, data interpretation, and critically revised manuscript; AB: contributed to conception, design, data analysis, and interpretation, and drafted and critically revised manuscript; GV: contributed to conception, design, data analysis and interpretation, and drafted and critically revised the manuscript.

FUNDING

This work was supported by NIH-NIDCR 5R01DE013508 subaward:7743sc, by the Hungarian Human Resources Development Operational Programme (EFOP-3.6.2-16-2017-00006) and by the Hungarian National Research, Development and Innovation Fund (K-125161).

REFERENCES

Aoba, T., and Fejerskov, O. (2002). Dental fluorosis: chemistry and biology. *Crit. Rev. Oral Biol. Med.* 13, 155–170. doi: 10.1177/154411130201300206

Arakaki, M., Ishikawa, M., Nakamura, T., Iwamoto, T., Yamada, A., Fukumoto, E., et al. (2012). Role of epithelial-stem cell interactions during dental cell differentiation. *J. Biol. Chem.* 287, 10590–10601. doi: 10.1074/jbc.M111.285874

Bardet, C., Courson, F., Wu, Y., Khaddam, M., Salmon, B., Ribes, S., et al. (2016). Claudin-16 deficiency impairs tight junction function in ameloblasts, leading to abnormal enamel formation. *J. Bone Miner. Res.* 31, 498–513. doi: 10.1002/jbmr.2726

Bartlett, J. D., and Smith, C. E. (2013). Modulation of cell-cell junctional complexes by matrix metalloproteinases. *J. Dent. Res.* 92, 10–17. doi: 10.1177/0022034512463397

Bori, E., Guo, J., Racz, R., Burghardt, B., Foldes, A., Keremi, B., et al. (2016). Evidence for bicarbonate secretion by ameloblasts in a novel cellular model. *J. Dent. Res.* 95, 588–596. doi: 10.1177/0022034515625939

Boron, W. F., and De Weer, P. (1976). Intracellular pH transients in squid giant axons caused by CO2, NH3, and metabolic inhibitors. *J. Gen. Physiol.* 67, 91–112. doi: 10.1085/jgp.67.1.91

Bosshardt, D. D., and Lang, N. P. (2005). The junctional epithelium: from health to disease. *J. Dent. Res.* 84, 9–20. doi: 10.1177/154405910508400102

Bronckers, A. L. (2017). Ion transport by ameloblasts during amelogenesis. *J. Dent. Res.* 96, 243–253. doi: 10.1177/0022034516681768

Bronckers, A. L., Jalali, R., and Lytton, J. (2017). Reduced protein expression of the $Na^+/Ca^{2+}+K^+$-Exchanger (SLC24A4) in apical plasma membranes of maturation ameloblasts of fluorotic mice. *Calcif. Tissue Int.* 100, 80–86. doi: 10.1007/s00223-016-0197-4

Bronckers, A. L., Lyaruu, D. M., and DenBesten, P. K. (2009). The impact of fluoride on ameloblasts and the mechanisms of enamel fluorosis. *J. Dent. Res.* 88, 877–893. doi: 10.1177/0022034509343280

Bronckers, A. L., Lyaruu, D. M., Guo, J., Bijvelds, M. J., Bervoets, T. J., Zandieh-Doulabi, B., et al. (2015). Composition of mineralizing incisor enamel in cystic fibrosis transmembrane conductance regulator-deficient mice. *Eur. J. Oral Sci.* 123, 9–16. doi: 10.1111/eos.12163

Bronckers, A. L., Lyaruu, D. M., Jalali, R., and DenBesten, P. K. (2016). Buffering of protons released by mineral formation during amelogenesis in mice. *Eur. J. Oral Sci.* 124, 415–425. doi: 10.1111/eos.12287

Demeter, I., Hegyesi, O., Nagy, A. K., Case, M. R., Steward, M. C., Varga, G., et al. (2009a). Bicarbonate transport by the human pancreatic ductal cell line HPAF. *Pancreas* 38, 913–920. doi: 10.1097/MPA.0b013e3181b32c08

Demeter, I., Szucs, A., Hegyesi, O., Foldes, A., Racz, G. Z., Burghardt, B., et al. (2009b). Vectorial bicarbonate transport by Par-C10 salivary cells. *J. Physiol. Pharmacol.* 60(Suppl. 7), 197–204.

Denbesten, P. K., Crenshaw, M. A., and Wilson, M. H. (1985). Changes in the fluoride-induced modulation of maturation stage ameloblasts of rats. *J. Dent. Res.* 64, 1365–1370. doi: 10.1177/00220345850640120701

Denbesten, P., and Li, W. (2011). Chronic fluoride toxicity: dental fluorosis. *Monogr. Oral Sci.* 22, 81–96. doi: 10.1159/000327028

Gresz, V., Kwon, T. H., Vorum, H., Zelles, T., Kurtz, I., Steward, M. C., et al. (2002). Immunolocalization of electroneutral Na^+-HCO cotransporters in human and rat salivary glands. *Am. J. Physiol. Gastrointest. Liver Physiol.* 283, G473–G480. doi: 10.1152/ajpgi.00421.2001

Hegyesi, O., Foldes, A., Bori, E., Nemeth, Z., Barabas, J., Steward, M. C., et al. (2015). Evidence for active electrolyte transport by two-dimensional monolayers of human salivary epithelial cells. *Tissue Eng. C Methods* 21, 1226–1236. doi: 10.1089/ten.tec.2014.0614

Ishiguro, H., Naruse, S., Kitagawa, M., Suzuki, A., Yamamoto, A., Hayakawa, T., et al. (2000). CO_2 permeability and bicarbonate transport in microperfused interlobular ducts isolated from guinea-pig pancreas. *J. Physiol.* 528(Pt 2), 305–315. doi: 10.1111/j.1469-7793.2000.00305.x

Jalali, R., Zandieh-Doulabi, B., DenBesten, P. K., Seidler, U., Riederer, B., Wedenoja, S., et al. (2015). Slc26a3/Dra and Slc26a6 in murine ameloblasts. *J. Dent. Res.* 94, 1732–1739. doi: 10.1177/0022034515606873

Jalali, R., Lodder, J. C., Zandieh-Doulabi, B., Micha, D., Melvin, J. E., Catalan, M. A., et al. (2017). The role of Na:K:2Cl Cotransporter 1 (NKCC1/SLC12A2) in dental epithelium during enamel formation in mice. *Front. Physiol.* 8:924. doi: 10.3389/fphys.2017.00709

Josephsen, K., Takano, Y., Frische, S., Praetorius, J., Nielsen, S., Aoba, T., et al. (2010). Ion transporters in secretory and cyclically modulating ameloblasts: a new hypothesis for cellular control of preeruptive enamel maturation. *Am. J. Physiol. Cell Physiol.* 299, C1299–C1307. doi: 10.1152/ajpcell.00218.2010

Kawano, S., Morotomi, T., Toyono, T., Nakamura, N., Uchida, T., Ohishi, M., et al. (2002). Establishment of dental epithelial cell line (HAT-7) and the cell differentiation dependent on Notch signaling pathway. *Connect. Tissue Res.* 43, 409–412. doi: 10.1080/03008200290000637

Kiela, P. R., Xu, H., and Ghishan, F. K. (2006). Apical NA^+/H^+ exchangers in the mammalian gastrointestinal tract. *J. Physiol. Pharmacol.* 57(Suppl. 7), 51–79.

Kubota, K., Lee, D. H., Tsuchiya, M., Young, C. S., Everett, E. T., Martinez-Mier, E. A., et al. (2005). Fluoride induces endoplasmic reticulum stress in ameloblasts responsible for dental enamel formation. *J. Biol. Chem.* 280, 23194–23202. doi: 10.1074/jbc.M503288200

Lacruz, R. S., Nanci, A., Kurtz, I., Wright, J. T., and Paine, M. L. (2010). Regulation of pH during amelogenesis. *Calcif. Tissue Int.* 86, 91–103. doi: 10.1007/s00223-009-9326-7

Lacruz, R. S., Smith, C. E., Kurtz, I., Hubbard, M. J., and Paine, M. L. (2013). New paradigms on the transport functions of maturation-stage ameloblasts. *J. Dent. Res.* 92, 122–129. doi: 10.1177/0022034512470954

Lacruz, R. S., Smith, C. E., Moffatt, P., Chang, E. H., Bromage, T. G., Bringas, P. Jr., et al. (2012). Requirements for ion and solute transport, and pH regulation during enamel maturation. *J. Cell. Physiol.* 227, 1776–1785. doi: 10.1002/jcp.22911

Li, J., Koo, N. Y., Cho, I. H., Kwon, T. H., Choi, S. Y., Lee, S. J., et al. (2006). Expression of the Na^+-HCO3- cotransporter and its role in pHi regulation in guinea pig salivary glands. *Am. J. Physiol. Gastrointest. Liver Physiol.* 291, G1031–G1040. doi: 10.1152/ajpgi.00483.2005

Lyaruu, D. M., Bronckers, A. L., Mulder, L., Mardones, P., Medina, J. F., Kellokumpu, S., et al. (2008). The anion exchanger Ae2 is required for enamel maturation in mouse teeth. *Matrix Biol.* 27, 119–127. doi: 10.1016/j.matbio.2007.09.006

Lyaruu, D. M., Medina, J. F., Sarvide, S., Bervoets, T. J., Everts, V., Denbesten, P., et al. (2014). Barrier formation: potential molecular mechanism of enamel fluorosis. *J. Dent. Res.* 93, 96–102. doi: 10.1177/0022034513510944

Matter, K., and Balda, M. S. (2003). Signalling to and from tight junctions. *Nat. Rev. Mol. Cell Biol.* 4, 225–236. doi: 10.1038/nrm1055

Melvin, J. E., Yule, D., Shuttleworth, T., and Begenisich, T. (2005). Regulation of fluid and electrolyte secretion in salivary gland acinar cells. *Annu. Rev. Physiol.* 67, 445–469. doi: 10.1146/annurev.physiol.67.041703.084745

Otsu, K., and Harada, H. (2016). Rho GTPases in ameloblast differentiation. *Jpn. Dent. Sci. Rev.* 52, 32–40. doi: 10.1016/j.jdsr.2015.09.001

Paulais, M., and Turner, R. J. (1992a). Activation of the Na(+)-K(+)-2Cl-cotransporter in rat parotid acinar cells by aluminum fluoride and phosphatase inhibitors. *J. Biol. Chem.* 267, 21558–21563.

Paulais, M., and Turner, R. J. (1992b). Beta-adrenergic upregulation of the Na(+)-K(+)-2Cl- cotransporter in rat parotid acinar cells. *J. Clin. Invest.* 89, 1142–1147. doi: 10.1172/JCI115695

Robinson, C. (2014). Enamel maturation: a brief background with implications for some enamel dysplasias. *Front. Physiol.* 5:388. doi: 10.3389/fphys.2014.00388

Romero, M. F., Fulton, C. M., and Boron, W. F. (2004). The SLC4 family of HCO 3 - transporters. *Pflugers Arch.* 447, 495–509. doi: 10.1007/s00424-003-1180-2

Schroeder, H. E., and Listgarten, M. A. (1997). The gingival tissues: the architecture of periodontal protection. *Periodontol 2000* 13, 91–120. doi: 10.1111/j.1600-0757.1997.tb00097.x

Sharma, R., Tsuchiya, M., and Bartlett, J. D. (2008). Fluoride induces endoplasmic reticulum stress and inhibits protein synthesis and secretion. *Environ. Health Perspect.* 116, 1142–1146. doi: 10.1289/ehp.11375

Shumaker, H., and Soleimani, M. (1999). CFTR upregulates the expression of the basolateral Na(+)-K(+)-2Cl(-) cotransporter in cultured pancreatic duct cells. *Am. J. Physiol.* 277(6 Pt 1), C1100–C1110.

Smith, C. E. (1998). Cellular and chemical events during enamel maturation. *Crit. Rev. Oral Biol. Med.* 9, 128–161. doi: 10.1177/10454411980090020101

Smith, C. E., Nanci, A., and Denbesten, P. K. (1993). Effects of chronic fluoride exposure on morphometric parameters defining the stages of

amelogenesis and ameloblast modulation in rat incisors. *Anat. Rec.* 237, 243–258. doi: 10.1002/ar.1092370212

Steward, M. C., Ishiguro, H., and Case, R. M. (2005). Mechanisms of bicarbonate secretion in the pancreatic duct. *Annu. Rev. Physiol.* 67, 377–409. doi: 10.1146/annurev.physiol.67.031103.153247

Sui, W., Boyd, C., and Wright, J. T. (2003). Altered pH regulation during enamel development in the cystic fibrosis mouse incisor. *J. Dent. Res.* 82, 388–392. doi: 10.1177/154405910308200512

Suzuki, M., Shin, M., Simmer, J. P., and Bartlett, J. D. (2014). Fluoride affects enamel protein content via TGF-beta1-mediated KLK4 inhibition. *J. Dent. Res.* 93, 1022–1027. doi: 10.1177/0022034514545629

Szucs, A., Demeter, I., Burghardt, B., Ovari, G., Case, R. M., Steward, M. C., et al. (2006). Vectorial bicarbonate transport by Capan-1 cells: a model for human pancreatic ductal secretion. *Cell. Physiol. Biochem.* 18, 253–264. doi: 10.1159/000097672

Takagi, T., Ogasawara, T., Tagami, J., Akao, M., Kuboki, Y., Nagai, N., et al. (1998). pH and carbonate levels in developing enamel. *Connect Tissue Res.* 38, 181–187; discussion 201–185. doi: 10.3109/03008209809017035

Tanimoto, K., Le, T., Zhu, L., Chen, J., Featherstone, J. D., Li, W., et al. (2008). Effects of fluoride on the interactions between amelogenin and apatite crystals. *J. Dent. Res.* 87, 39–44. doi: 10.1177/154405910808700106

Thomas, J. A., Buchsbaum, R. N., Zimniak, A., and Racker, E. (1979). Intracellular pH measurements in Ehrlich ascites tumor cells utilizing spectroscopic probes generated *in situ*. *Biochemistry* 18, 2210–2218. doi: 10.1021/bi00578a012

Varga, G., Kerémi, B., Bori, E., and Földes, A. (2015). Function and repair of dental enamel - potential role of epithelial transport processes of ameloblasts. *Pancreatology* 15, S55–S60. doi: 10.1016/j.pan.2015.01.012

Xue, H., Li, Y., Everett, E. T., Ryan, K., Peng, L., Porecha, R., et al. (2013). Ameloblasts require active RhoA to generate normal dental enamel. *Eur. J. Oral Sci.* 121, 293–302. doi: 10.1111/eos.12059

Yamaguti, P. M., Neves, F. A., Hotton, D., Bardet, C., de La Dure-Molla, M., Castro, L. C., et al. (2017). Amelogenesis imperfecta in familial hypomagnesaemia and hypercalciuria with nephrocalcinosis caused by CLDN19 gene mutations. *J. Med. Genet.* 54, 26–37. doi: 10.1136/jmedgenet-2016-103956

Zhang, Y., Kim, J. Y., Horst, O., Nakano, Y., Zhu, L., Radlanski, R. J., et al. (2014). Fluorosed mouse ameloblasts have increased SATB1 retention and Galphaq activity. *PLoS ONE* 9:e103994. doi: 10.1371/journal.pone.0103994

Zhang, Y., Li, W., Chi, H. S., Chen, J., and Denbesten, P. K. (2007). JNK/c-Jun signaling pathway mediates the fluoride-induced down-regulation of MMP-20 *in vitro*. *Matrix Biol.* 26, 633–641. doi: 10.1016/j.matbio.2007.06.002

Zhang, Y., Yan, Q., Li, W., and DenBesten, P. K. (2006). Fluoride down-regulates the expression of matrix metalloproteinase-20 in human fetal tooth ameloblast-lineage cells *in vitro*. *Eur. J. Oral Sci.* 114(Suppl. 1), 105–110; discussion 127–109, 380. doi: 10.1111/j.1600-0722.2006.00303.x

Zhang, Y., Zhang, K., Ma, L., Gu, H., Li, J., and Lei, S. (2016). Fluoride induced endoplasmic reticulum stress and calcium overload in ameloblasts. *Arch. Oral Biol.* 69, 95–101. doi: 10.1016/j.archoralbio.2016.05.015

Zhao, H., Star, R. A., and Muallem, S. (1994). Membrane localization of H+ and HCO3- transporters in the rat pancreatic duct. *J. Gen. Physiol.* 104, 57–85. doi: 10.1085/jgp.104.1.57

Conflict of Interest Statement: The authors declare that the research was conducted in the absence of any commercial or financial relationships that could be construed as a potential conflict of interest.

The reviewer CB and handling Editor declared their shared affiliation.

Copyright © 2017 Rácz, Földes, Bori, Zsembery, Harada, Steward, DenBesten, Bronckers, Gerber and Varga. This is an open-access article distributed under the terms of the Creative Commons Attribution License (CC BY). The use, distribution or reproduction in other forums is permitted, provided the original author(s) or licensor are credited and that the original publication in this journal is cited, in accordance with accepted academic practice. No use, distribution or reproduction is permitted which does not comply with these terms.

frontiers in Physiology

ORIGINAL RESEARCH
published: 14 November 2017
doi: 10.3389/fphys.2017.00925

Fluoride Alters Klk4 Expression in Maturation Ameloblasts through Androgen and Progesterone Receptor Signaling

Michael H. Le[1†], *Yukiko Nakano*[1,2†], *Dawud Abduweli Uyghurturk*[1], *Li Zhu*[1] and *Pamela K. Den Besten*[1,2*]

[1] Department of Orofacial Sciences, School of Dentistry, University of California, San Francisco, San Francisco, CA, United States, [2] Center for Children's Oral Health Research, School of Dentistry, University of California, San Francisco, San Francisco, CA, United States

OPEN ACCESS

Edited by:
Sylvie Babajko,
Centre de Recherche des Cordeliers, France

Reviewed by:
Michel Goldberg,
Institut National de la Santé et de la Recherche Médicale, France
Victor E. Arana-Chavez,
University of São Paulo, Brazil
Lucia Jimenez-Rojo,
University of Zurich, Switzerland

***Correspondence:**
Pamela K. Den Besten
pamela.denbesten@ucsf.edu

[†]Co-first authors.

Specialty section:
This article was submitted to Craniofacial Biology and Dental Research, a section of the journal Frontiers in Physiology

Received: 28 April 2017
Accepted: 31 October 2017
Published: 14 November 2017

Citation:
Le MH, Nakano Y, Abduweli Uyghurturk D, Zhu L and Den Besten PK (2017) Fluoride Alters Klk4 Expression in Maturation Ameloblasts through Androgen and Progesterone Receptor Signaling. Front. Physiol. 8:925. doi: 10.3389/fphys.2017.00925

Fluorosed maturation stage enamel is hypomineralized in part due to a delay in the removal of matrix proteins to inhibit final crystal growth. The delay in protein removal is likely related to reduced expression of kallikrein-related peptidase 4 (KLK4), resulting in a reduced matrix proteinase activity that found in fluorosed enamel. *Klk4* transcription is known to be regulated in other cell types by androgen receptor (AR) and progesterone receptors (PR). In this study, we determined the possible role of fluoride in down-regulation of KLK4 expression through changes in AR and PR. Immunohistochemical localization showed that both AR and PR nuclear translocation was suppressed in fluoride exposed mice. However, when AR signaling was silenced in mouse ameloblast-lineage cells (ALCs), expression of both *Pgr* and *Klk4* were increased. Similar to the effect from AR silencing, fluoride also upregulated *Pgr* in ALCs, but downregulated *Klk4*. This finding suggests that though suppression of AR transactivation by fluoride increases *Prg* expression, inhibition of PR transactivation by fluoride has a much greater effect, ultimately resulting in downregulation of *Klk4* expression. These findings indicate that in ameloblasts, PR has a dominant role in regulating *Klk4* expression. We found that when AR was retained in the cytoplasm in the presence of fluoride, that co-localized with heat shock protein 90 (HSP90), a well-known chaperone for steroid hormone receptors. HSP90 also known to regulate TGF-β signaling. Consistent with the effect of fluoride on AR and HSP90, we found evidence of reduced TGF-β signaling activity in fluorosed ameloblasts as reduced immunolocalization of TGFB1 and TGFBR-2 and a significant increase in Cyclin D1 mRNA expression, which also possibly contributes to the reduced AR signaling activity. *In vitro*, when serum was removed from the media, aluminum was required for fluoride to inhibit the dissociation of HSP90 from AR. In conclusion, fluoride related downregulation of *Klk4* is associated with reduced nuclear translocation of AR and PR, and also reduced TGF-β signaling activity, all of which are regulated by HSP90. We suggest that a common mechanism by which fluoride affects AR, PR, and TGF-β signaling is through inhibiting ATP-dependent conformational cycling of HSP90.

Keywords: ameloblasts, enamel, fluoride, KLK4, AR, PR, HSP90, TGF-β

INTRODUCTION

Enamel formed in the presence of high levels of fluoride has a delayed removal of matrix proteins (Den Besten, 1986; DenBesten and Thariani, 1992), most likely due to reduced proteolytic activity in the maturation stage fluorosed enamel (DenBesten et al., 2002). Reduced proteolytic activity in maturation stage fluorosed enamel is consistent with reduced expression of kallikrein-related peptidase 4 (KLK4) (Suzuki et al., 2014), the serine proteinase that is responsible for the final hydrolysis of matrix proteins, which allows enamel hydroxyapatite crystals to reach their full thickness.

KLK4 expression in cancer cell lines, has been shown to be regulated by activation of both androgen receptor (AR) and progesterone receptor (PR) (Lai et al., 2009). AR and PR are members of the nuclear receptor superfamily of transcription factors, residing predominantly in the cytoplasm. Binding of the ligand (i.e., androgenic hormones) promotes nuclear translocation and transactivation for transcription of the target genes (Azad et al., 2015). Jedeon and co-workers have reported that the AR is present in ameloblasts and when activated, regulates KLK4 expression (Jedeon et al., 2016).

Suzuki et al. found that fluoride related downregulation of *Klk4* expression is associated with reduced TGF-β signaling. AR signaling also involves cross-talk with the TGF-β signaling pathway (Gerdes et al., 1998; Bruckheimer and Kyprianou, 2001; Chipuk et al., 2002; Kang et al., 2002; Pratt et al., 2004; Yang et al., 2014), suggesting that possibility that fluoride related effects on TGF-β signaling are also related to effects of the fluoride on AR activation.

To explore the intracellular mechanisms that mediate effects of fluoride on *Klk4* transcription, we used both *in vivo* and *in vitro* experimental models to examine the effects of fluoride on AR, PR, and KLK4 in fluorosed maturation ameloblasts. We found that fluoride related downregulation of *Klk4* was associated with reduced nuclear translocation of AR and PR, and also reduced TGF-β signaling activity, all of which are regulated by heat shock protein 90 (HSP90). *In vitro*, we found that fluoride together with aluminum induced a cytoplasmic retention of AR, suggesting the possibility that fluoride requires aluminum to inhibit the chaperone function of HSP90 to regulate AR nuclear translocation.

MATERIALS AND METHODS

Animals

All animal procedures were carried out with approval by the University of California-San Francisco Institutional Animal Care and Use Committees. The experiments reported herein were conducted in compliance with the Animal Welfare Act and in accordance with the principles set forth in the National Research Council's *Guide for the Care and Use of Laboratory Animals.*

To determine whether the reduced *Klk4* expression in the presence of fluoride resulted in decreased KLK4 activity in the enamel matrix, 3-week-old female Wistar rats (Jackson Laboratory, Sacramento, CA) were divided into two groups, with the groups given either deionized drinking water or deionized drinking water supplemented with 100 ppm (5.3 mM) fluoride as sodium fluoride (Sigma-Aldrich, St. Louis, MO) *ad libitium* for 4 weeks. After 4 weeks, the rats were euthanized, and the mandibular incisors were dissected to allow access to separately dissected the enamel matrix and enamel organ for KLK4 activity assays, and quantitative real-time polymerase chain reaction (qPCR) of the relative expression of *Klk4* mRNA.

Three-week-old C57BL/6J female mice (Jackson Laboratory) were divided into two groups, with the groups given either deionized drinking water or deionized drinking water supplemented with 50 ppm (2.6 mM) fluoride as sodium fluoride (Sigma-Aldrich) *ad libitium* for 4 weeks. After 4 weeks, the mice were euthanized, and mandibles were obtained for morphology, immunohistochemical, and qPCR analyses.

KLK4 Activity Assay

Rat mandibular incisors were removed from the alveolar bone and enamel matrix was dissected from the underlying dentin surface at the early-maturation stage. This includes enamel matrix underlying the distal root of the first molar and continuing until the enamel was too hard to dissect (Stahl et al., 2015). Extracts were homogenized in 100 μl of 5% TCA, and incubated at room temperature for 30 min. After centrifugation at 10,000 × g for 10 min, the supernatants were removed and pellets were re-suspended in 200 μl of ammonium bicarbonate. The total protein concentration of each sample was measured by Bradford assay. KLK4 activity was analyzed by using Boc-Val-Pro-Arg-AMC fluorogenic peptide substrate (R&D Systems Inc., Minneapolis, MN). Each reaction in 96-well black plates contained 150 μl of protein extracts, 5 μl of peptide and 40 μl of 5x reaction buffer (250 mM Tris–HCl, 250 mM NaCl, 50 mM CaCl). The fluorescence signal was detected using a spectrometer at 37°C (excitation at 380 nm and emission at 460 nm), and measured every 20 min for 180 min. For each sample, the fluorescence data was normalized to the protein concentration of a given sample. For each sample, we used R software environment with *drc* package (Ritz and Streibig, 2005; Team, 2014) to generate an averaged 4-parametric regression curve of the treatment groups. Significance of differences at 60, 120, and 180 min were determined by independent Student's *t*-test.

qPCR Analysis

Total RNA was isolated from (rat and mouse) mandibular maturation-stage incisor enamel organs that were dissected according to landmarks described previously (Stahl et al., 2015), and also from ameloblast lineage cells (ALCs; detail in Cell Culture) using RNeasy Mini kit (Qiagen, Germantown, MD). Conversion of mRNA to cDNA was obtained by reverse transcription of the mRNA using Superscript III First-Strand Synthesis Supermix for qRT-PCR (Life Technologies, Carlsbad, CA).

Expression of mRNAs was examined by qPCR with FastStart Universal SYBR Green Master Kit (Roche Diagnostics, Indianapolis, IN) using primer sets for *Klk4, Ccnd1, Ar, Tgfbr2*, and *Tgfb1* (Elim Biopharmaceuticals, Hayward, CA). *Mrpl19* was used as a reference gene for enamel organ samples and *Eef1a1* for ALCs. Primer sequences are listed in **Table 1**. The relative expression level of target genes was analyzed by the

TABLE 1 | Mouse specific primers for qPCR.

Symbol	Accession	Region	
Ar	NM_013476	2506–2596	5′-CCCGTCCCAATTGTGTGAAA–3′ 3′-TCCCTGGTACTGTCCAAACG–5′
Ccnd1	NM_007631	602–724	5′-TTGTGCATCTACACTGACAAC–3′ 3′-GAAGTGTTCGATGAAATCGT–5′
Eef1a1	NM_010106	144–303	5′-CAACATCGTCGTAATCGGACA–3′ 3′-GTCTAAGACCCAGGCGTACTT–5′
Hsp90	NM_010480	1532–1647	5′-TGTTGCGGTACTACACATCTGC–3′ 3′-GTCCTTGGTCTCACCTGTGATA–5′
Klk4	NM_019928	488–617	5′-GAGATACCTGCCTAGTCTCTGG–3′ 3′-AGGTGGTACACAGGGTCATAC–5′
Mrpl19	NM_026490	94–249	5′-ACGGCTTGCTGCCTTCGCAT–3′ 3′-AGGAACCTTCTCTCGTCTTCCGGG–5′
Pgr	NM_008829	1001–1122	5′-CTCCGGGACCGAACAGAGT–3′ 3′-ACAACAACCCTTTGGTAGCAG–5′
Tgfbr2	NM_029575	654–839	5′-GGCTTCACTCTGGAAGATGC–3′ 3′-GCTGACACCCGTCACTTGGA–5′

ΔΔCt method (Livak and Schmittgen, 2001). Expression of each gene was calculated as a relative expression level (fold change) compared with WT (mice samples) or untreated controls (cell culture). Significance of differences was determined using ΔCt values by the two-tailed multiple *t*-test with Benjamini & Hochberg correction following ANOVA (Benjamini and Hochberg, 1995).

Immunohistochemistry

Mouse mandibles were fixed in 4% paraformaldehyde in 0.06 M sodium cacodylate buffer (pH 7.3) at 4°C for 24 h. After decalcification in 8% EDTA (pH 7.3), samples were processed for routine paraffin embedding and sagittally sectioned. The sections were incubated with 10% swine and 5% goat sera followed by incubation with rabbit anti-human AR (1:75; Novus Biologicals, Littleton, CO, NB100-91658), rabbit anti-mouse TGFBR2 (1:100; Santa Cruz Biotech, Santa Cruz, CA, sc-1700), rabbit anti-human TGFB1 (1:50; Abcam PLC, Cambridge, MA, ab92486), and rabbit anti-mouse PR (Santa Cruz Biotech, sc-166170) antibodies respectively overnight at room temperature. A biotinylated swine anti-rabbit IgG F(ab')2 fraction (Dako, Carpinteria, CA) was used as the secondary antibody for 1 h at room temperature incubation. Following incubation with alkaline phosphatase conjugated streptavidin (Vector Laboratories Inc., Burlingame, CA) for 30 min, immunoreactivity was visualized using a Vector® Red kit (Vector Laboratories) resulting in pink/red color for positive staining. Counter-staining was performed with methyl green (Dako). Negative control was done with normal rabbit sera.

Cell Culture

Mouse ameloblast-lineage cells (ALCs, a kind gift from Dr. Toshihiro Sugiyama, Akita University, Japan and Dr. John Bartlett, Forsyth Institute, Boston, Massachusetts) (Nakata et al., 2003) were cultured in DMEM (UCSF Cell Culture Facility, San Francisco, CA) supplemented with 10% Fetal Bovine Serum (FBS) (Gemini Bio-Products, West Sacramento, CA) and 1% penicillin-streptomycin. ALCs were seeded into 6-well plates (2.0×10^5 cells/cm^2) or 8-well chamber slides (1.5×10^5 cells/cm^2). After 24 h, the cells were treated with fluoride (0 or 1 mM) as sodium fluoride (Sigma-Aldrich), followed by total RNA extraction. Other cells, initially cultured in the medium with FBS for 24 h, were exposed to 2% TCM® serum replacement (MP Biomedicals, Santa Ana, CA) for 24 h. After 24 h, cells were transfected with antisense oligonucleotides targeting AR, LNA™ GapmeRs (Exiqon Incorporated, Woburn, MA) to silence *Ar* mRNA, using Lipofectamine 2000 Transfection Reagent (ThermoFisher Scientific, Waltham, MA). Cells were then harvested for total RNA and extracts were analyzed for *Klk4*, *Ar*, *Pgr*, *Tgfb1*, *Tgfbr2*, and *Ccnd1* expression. For immunofluorescent staining, some cells were treated with fluoride as described above. Other cells were initially cultured in FBS containing medium for 24 h. After culturing in the medium with 2% TCM® serum replacement for another 24 h, cells were treated with 0 or 1 μM dihydrotestosterone/DHT (Cerilliant Corporation, Round Rock, TX). Some of the DHT treated cells were further exposed to aluminum (0, 10, or 100 μM) as aluminum chloride (Sigma-Aldrich) and/or fluoride (0 or 1 mM) as sodium fluoride (Sigma-Aldrich). Aluminum concentration was equivalent to the range of those in calf serum (Tomza-Marciniak et al., 2011)

Immunofluorescent Staining

Cells grown in 8-well chamber slides were fixed in 4% paraformaldehyde (Sigma-Aldrich) for 10 min at room temperature and washed with PBS. They were then permeablized with 0.25% Triton-X 100 and incubated with 10% swine and 5% goat sera to block non-specific binding. Cells were then simultaneously incubated with AR (Novus Biologicals) and HSP90 (Santa Cruz Biotech) antibodies that were fluorescently tagged with Zenon Rabbit IgG Labeling Kit (Molecular Probes, Eugene, OR) per manufacturer's instructions. AR antibody was labeled with Alexa Fluor 594 and HSP90 antibody was labeled with Alex Fluor 488. After antibody incubation, cells were washed with PBS, then counterstained with DAPI and mounted with mounting medium.

RESULTS

Fluoride Suppresses KLK4 Activity *in Vivo*

To determine the ultimate effect of fluoride on KLK4 synthesis, we assessed synthesis of KLK4 in fluorosed rat enamel, by comparing KLK4 proteinase activity in the enamel matrix of rats given either 0 or 100 ppm fluoride in drinking water. Enamel matrix protein extracts of rats given 100 ppm F in drinking water had reduced matrix KLK4 proteolytic activity when compared with control rats (**Figure 1A**), and significance of the reduction was confirmed at three different time points of incubation (**Figure 1B**). Consistent with the reduced proteolytic activity in the enamel matrix, *Klk4* mRNA expression was significantly reduced (**Figure 1C**). Similar to rats, fluorosed mice (given

50 ppm F in drinking water) also had reduced *Klk4* expression (data not shown). To further investigate the effect of fluoride on molecular profiles in maturation ameloblasts, we therefore used the mouse model.

Nuclear Translocation of AR is Suppressed in Fluorosed Maturation Ameloblasts *in Vivo* and *in Vitro*

Mice given high levels of fluoride in drinking water had retained enamel matrix (**Figures 2A,B**), with no obvious morphological alteration in ameloblasts (**Figures 2C,D**). To investigate the association of AR with fluorosis, we examined the presence and localization pattern of AR in maturation stage ameloblasts. In control mice, most of the AR immunostaining was in the ameloblast nucleus (**Figure 2E**), whereas in mice ingesting fluoride, immunostaining showed AR mostly remained in the cytoplasm (**Figure 2F**). Similarly, *in vitro*, we found that ALCs grown in serum containing medium with 1 mM fluoride had significantly less *Klk4* expression as compared to ALCs grown in medium without fluoride (**Figure 3A**). Under this condition, *Ar* expression (**Figure 3A**) and cell proliferation (data not shown) were not changed, but visibly less AR localized in the nuclei (**Figure 3B**). These *in vivo* and *in vitro* data together show that nuclear translocation of AR is inhibited by fluoride.

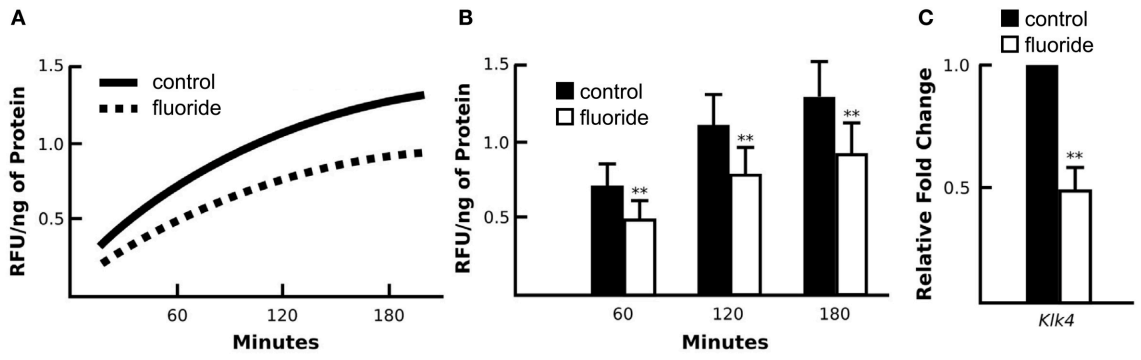

FIGURE 1 | Enamel fluorosis associates with reduced *in vivo* KLK4 activity and *Klk4* expression. **(A)** Averaged profile model of KLK4 activity in early maturation enamel matrix protein extracts (line graph). **(B)** At three time points of measurement (60, 120, and 180 min after the start of incubation), fluorosed enamel showed significantly lower KLK4 activity (bar graph). $^{**}p < 0.01$. **(C)** Relative fold change of *Klk4* expression from maturation-stage enamel organs harvested from control and fluorosed rats shows reduced *Klk4* expression in fluoride exposed ameloblasts. Fold change was calculated relative to the baseline expression of the gene in control mice. Genes were normalized to the expression of *Mrpl19* (mouse ribosomal protein L19). $^{**}p < 0.01$.

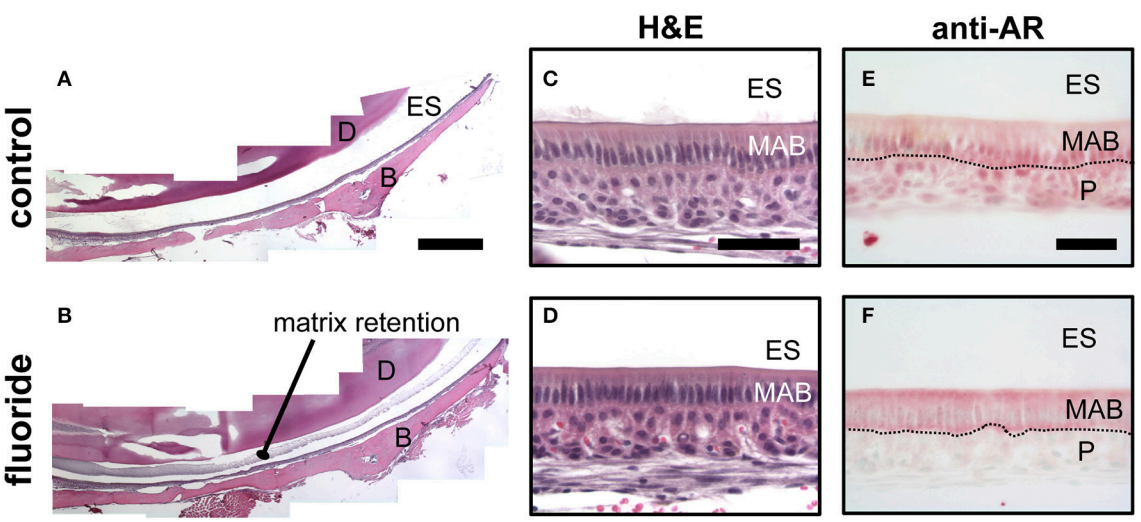

FIGURE 2 | Fluoride related change in the enamel matrix correlates with reduced AR nuclear translocation. **(A–B)** Hematoxylin and eosin-stained mandibular incisors from control **(A)** and fluorosed **(B)** mice. Retained enamel matrix protein is seen in the enamel space of fluorosed but not control mouse enamel. Composite scale bar 1 mm. ES; enamel space, D; dentin, B; bone **(C–D)** Hematoxylin and eosin-stained maturation ameloblasts from control **(C)** and fluorosed **(D)** mice. Bar; 100 um **(E–F)** Maturation-stage ameloblasts immunostained for AR. Control mice have positive AR immunostaining (red color) in the nucleus of maturation ameloblasts (MAB) and papillary layer cells (P). **(E)**. In fluorosed mice, AR immunostaining is mainly seen in the cytoplasm of ameloblasts and absent on the nuclei. Papillary layer cells are negative for AR immunostaining **(F)**. ES; enamel space, Bar; 50 μm.

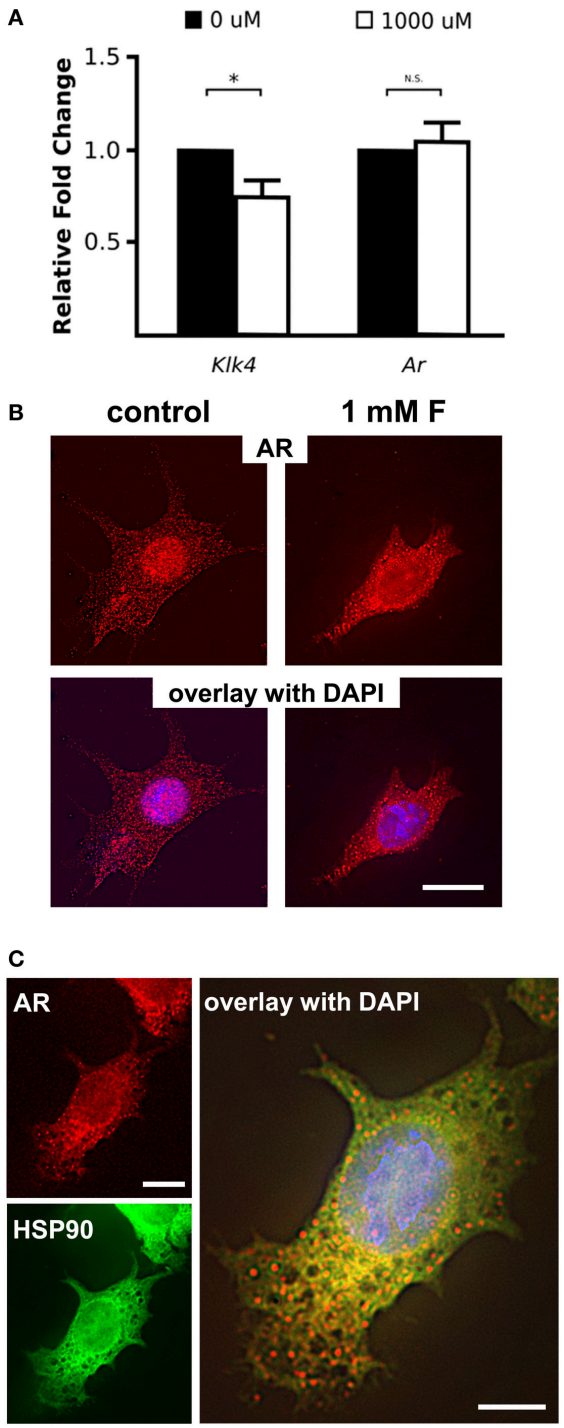

FIGURE 3 | Fluoride reduces *Klk4* expression without altering *Ar* expression. **(A)** Relative fold change of *Klk4* and *Ar* from ALCs exposed to 0 or 1,000 μM fluoride showed significant down regulation of *Klk4* but not *Ar*. Expression of target genes were normalized to the expression of *Mrpl19*. *$p < 0.05$. **(B)** Immunofluorescent staining of AR (red) in ALC showed a relative reduction in AR nuclear translocation in cells exposed to 1 mM fluoride. Scale bar 25 μm. **(C)** Immunofluorescent staining of AR (in red) and HSP90 (in green) in ALC showed that when AR translocation is blocked by 1 mM fluoride, AR and HSP90 are primarily co-localized in the cytoplasm (in yellow). DAPI (in blue), Scale bar 25 μm.

HSP90 Co-localizes with Cytoplasmic AR in Fluorosed Ameloblasts

Nuclear translocation of steroid hormone receptors is well-known to be regulated by the heat shock proteins (HSPs) (Azad et al., 2015). HSP90 plays a major role in the activation process of the steroid hormone receptors by interacting with the unliganded steroid hormone receptors to open the steroid-binding cleft to allow access by a steroid (Pratt et al., 2004). Once the ligand binds to the steroid hormone receptors, HSP90 disassociates from the receptors, allowing the nuclear translocation of the steroid receptors to function as a transcription factor (Azad et al., 2015). To determine if the dissociation of HSP90 from AR is altered by fluoride, we co-immunostained AR and HSP90, and observed co-localization of HSP90 and AR remained in the cytoplasm under the influence of fluoride. We found that HSP90 and AR co-localized in the cytoplasm particularly in the perinuclear region (**Figure 3C**). In the presence of fluoride, mRNA transcription and protein synthesis of HSP90 were unchanged (data not shown).

Decreased AR Activation in Fluorosed Ameloblasts is Related to the TGF-β1-Cyclin D1 Pathway

Previously, Suzuki et al. reported that fluoride treated ALCs had decreased mRNA expression of *Tgfβ1* and *Klk4* (Suzuki et al., 2014). In normal and oncogenic prostate cells, AR signaling is known to cross-talk with the TGF-β signaling pathway (Gerdes et al., 1998; Bruckheimer and Kyprianou, 2001; Chipuk et al., 2002; Kang et al., 2002; Pratt et al., 2004; Yang et al., 2014). Furthermore, activation of TGF-β signaling is also regulated by HSP90, and inhibition of HSP90 induces degradation of TGF-β receptors (Wrighton et al., 2008).

To examine TGF-β signaling in ameloblasts, when fluoride inhibits AR activation *in vivo,* we immunostained maturation ameloblasts from fluoride treated and control mice for TGFB1 and TGF-β1 receptor type II (TGFR-2). In fluorosed ameloblasts, immunostaining for both TGFB1 and TGFR-2 was reduced (**Figure 4A**). *Tgfβr2* transcription was also significantly reduced in fluorosed ameloblasts (**Figure 4B**), indicating a reduced TGF-β signaling activity. Cyclin D1 (CCND1) is a protein commonly known for regulating cell cycle dynamics, and expression of *Ccnd1* is known to be negatively regulated by TGF-β1 signaling in intestinal epithelial cells (Ko et al., 1995). Moreover, CCND1 is known to further negatively regulate the AR function, not only by directly binding to AR to inhibit transactivation of AR, but also by attenuating AR-induced upregulation of *Klk4* in prostate cancer (Knudsen et al., 1999; Comstock et al., 2011). Supporting our findings of reduced TGF-β signaling and inhibited AR activation in maturation ameloblasts, *Ccnd1* expression in fluorosed ameloblast was significantly increased (**Figure 4B**). These results suggest that the previously described effects of fluoride on TGF-β signaling, as related to decreased *Klk4* expression, are also possibly mediated by the effects of fluoride on HSP90.

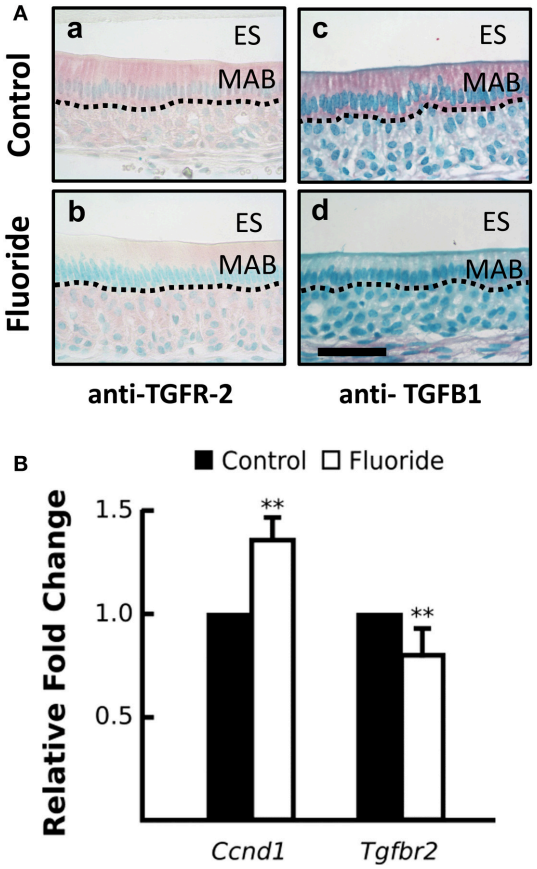

FIGURE 4 | Fluoride altered expression CCND1 and TGFR-2, regulators of androgen receptor activation. **(A)** Images of red TGFR-2 (a–c) and TGFβ1 (b–d) immunostaining show fluoride-exposed maturation ameloblasts have decreased amounts of TGFR-2 (b) and TGFβ1 (d) protein compared to controls (a and c). Scale bar 50 um, ES; enamel space, MAB; maturation ameloblast **(B)** Relative fold change of *Ccnd1* was increased, whereas *Tgfbr2* expression was decreased in maturation-stage ameloblasts harvested from fluorosed as compared to control mice. Genes were normalized to the expression of *Mrpl19*. $^{**}p < 0.01$

Suppression of AR Expression Results in Increased Expression of PR and Klk4

AR is known to regulate *Klk4* expression, but it does not directly interact with the *Klk4* gene (Lai et al., 2009). PR induces *Klk4* expression in breast cancer cells through direct binding to the *Klk4* promoter (Lai et al., 2009). AR suppresses expression of PR-regulated genes in triple negative breast cancer (Tsang et al., 2014; Karamouzis et al., 2016), suggesting negative regulation of AR on *Pgr* expression. To understand how AR regulates *Klk4* transcription in ameloblasts as well as the potential involvement of PR, we silenced *Ar* mRNA in ALCs and examined the expression of *Klk4* and *Pgr*. The antisense oligonucleotides for *Ar* significantly reduced *Ar* mRNA expression in ALCs, but significantly upregulated both *Klk4* and *Pgr* expression (**Figure 5A**). This suggests a negative regulation of *Pgr* by AR, while PR directly upregulates *Klk4* expression.

Fluoride Increases Pgr Expression, but Reduces PR Nuclear Translocation

To further examine the effect of fluoride induced suppression of AR activation on *Pgr* transcription, we examined *Pgr* expression in ameloblasts of fluorosed mice and in ALC culture. In both *in vitro* (**Figure 5B**), and *in vivo* (**Figure 5C**), fluoride exposure resulted in significantly increased *Pgr* expression. As PR nuclear translocation is also chaperoned by HSP90 (Dao-Phan et al., 1997), we examined the change of intracellular localization of PR in fluorosed maturation ameloblasts. Similar to the effects of fluoride on AR, nuclear translocation of PR was reduced in fluorosed ameloblasts as compared to controls (**Figure 5D**). Therefore, though fluoride increased *Pgr* expression, it inhibited nuclear translocation of both PR and AR, resulting in reduced expression of *Klk4* (see diagram shown in **Figure 5E**).

The Inhibitory Effect of Fluoride on AR Translocation Requires Aluminum

Among the nuclear factor family steroid hormone receptors, whose activation strictly depends on the interaction with HSP90, glucocorticoid receptor is the most well-studied steroid hormone receptor (Grad and Picard, 2007). Housley et al. showed that fluoride requires aluminum to stabilize HSP90 binding to glucocorticoid receptor (Housley, 1990). To determine whether aluminum is also required for the fluoride related cytoplasmic stabilization of AR by HSP90 in ameloblasts, we cultured ALCs and examined the intracellular AR localization in presence of fluoride and aluminum. ALCs were grown in serum containing media for 24 h, after which the media was changed to one with an artificial serum substitute (TCM® serum replacement). We found that AR nuclear translocation was stimulated by dihydrotestosterone (DHT) in ALCs (**Figure 6A**). However, when nuclear translocation was stimulated by DHT, the addition of fluoride alone did not alter the intracellular localization of AR, whereas in the presence of both fluoride and aluminum, more AR remained in the cytoplasm (**Figure 6B**). *Ar* transcription was not significantly changed in the presence of aluminum and fluoride (data not shown). Further immunostaining showed that the increased cytoplasmic AR in the presence of both fluoride and aluminum co-localized with HSP90 (**Figure 6B**). An increased AR retention in the cytoplasm was observed in both 10 μM (data not shown) and 100 μM aluminum supplemented culture.

DISCUSSION

The hypomineralized phenotype of severely fluorosed enamel is due in part to a prolonged retention of enamel matrix proteins (Den Besten, 1986; Wright et al., 1996), likely related to the reduced proteinase activity in fluorosed maturation stage enamel (DenBesten et al., 2002). Free fluoride in the enamel matrix is at micromolar levels (Aoba, 1997), which does not significantly alter the matrix proteinase activity (Tye et al., 2011). Therefore, if KLK4 proteinase activity is reduced in the fluorosed enamel matrix, it should be due to reduced KLK4 synthesis. Supporting this possibility, Suzuki et al. found reduced *Klk4* expression in the enamel organ of rats exposed to 50–100 ppm fluoride in the

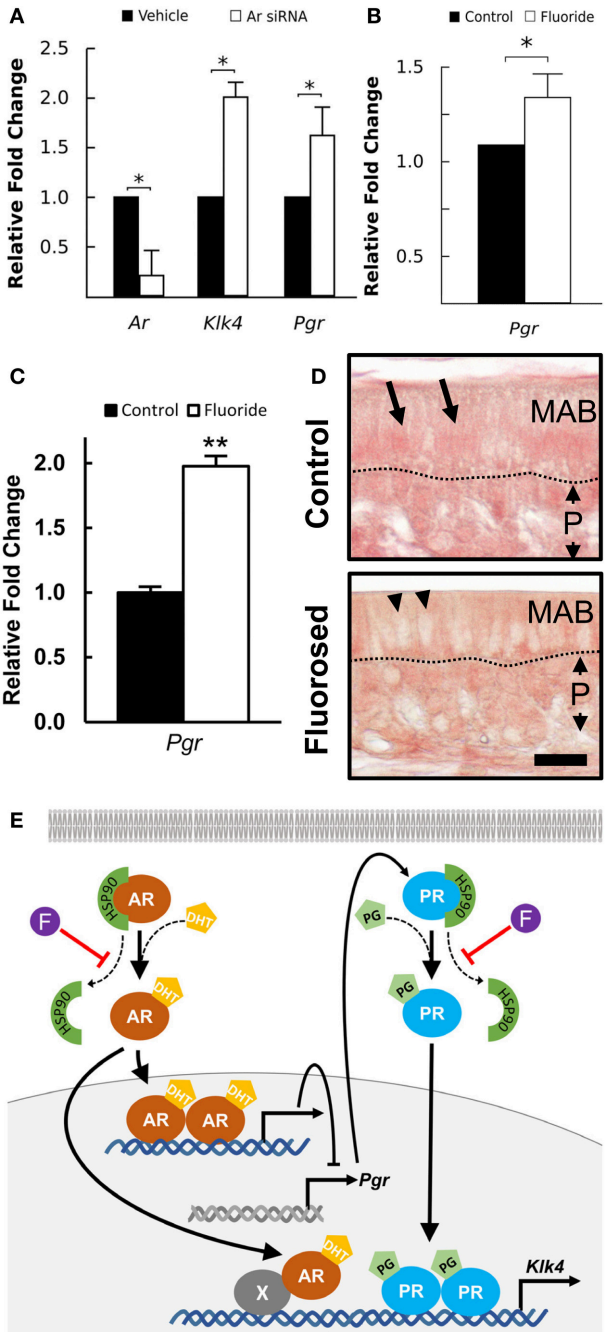

FIGURE 5 | *Klk4* expression is dominantly regulated by PR. **(A)** Relative fold change of *Ar*, *Klk4*, and *Pgr* mRNA expression of ALCs exposed to antisense LNA™ oligonucleotides targeting AR or a vehicle control. The fold change was calculated relative to the baseline expression in control mice. Expression of the target genes is normalized to the expression of *EeF1a1*. $*p < 0.05$. **(B)** Relative fold change of *Pgr* from ALCs exposed to 0 or 1 mM fluoride. Expression of target genes were normalized to the expression of *EeFla1*. $*p < 0.05$, **(C)** Relative fold change of *Pgr* in ameloblast from fluoride exposed mice as compared to controls shows a similar upregulation of *Pgr* expression *in vivo* as compared to *in vitro*. $**p < 0.01$, **(D)** Immunostaining of PR on maturation-stage ameloblasts. In control mice, intense immunostaining (in red) is seen in the nucleus of ameloblast (MAB, arrows). In fluorosed mice,

(Continued)

FIGURE 5 | Continued
immunostaining is mainly seen in the cytoplasm of ameloblasts and is absent from the nucleus (arrow heads). P; papillary layer, Scale bar 25 μm. **(E)** A proposed pathway of AR regulation of *Klk4* transcription: AR indirectly interacts with *Klk4* gene via co-regulator (X), to regulate *Klk4* transcription. AR also negatively regulates *Pgr* expression, and when AR is reduced, *Pgr* expression increases. Nuclear translocation of AR and PR is chaperoned by HSP90. Without fluoride, increased *Pgr* results in an upregulated *Klk4* transcription. With fluoride present, nuclear translocation of PR is inhibited, resulting in a final down regulation of *Klk4* transcription.

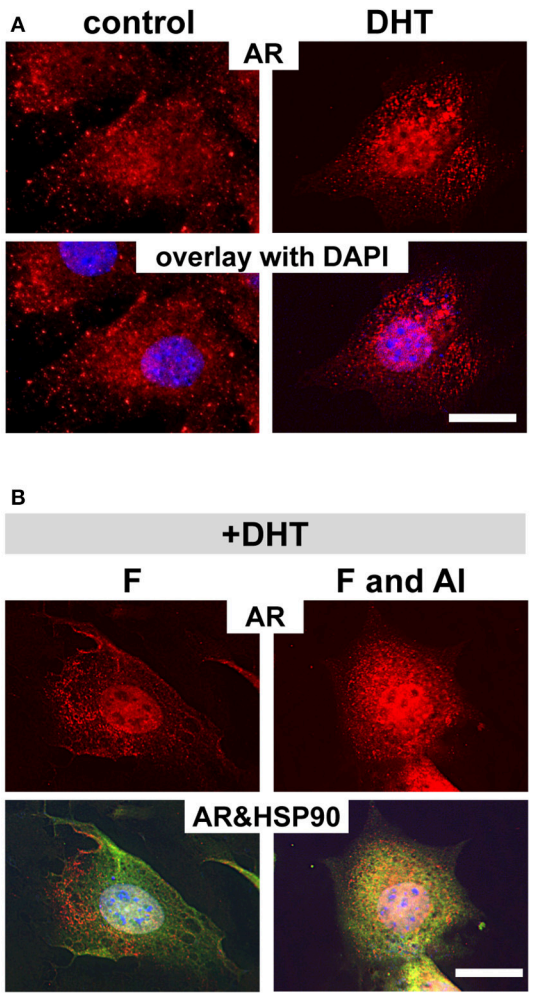

FIGURE 6 | Aluminum is required for fluoride to inhibit AR translocation into nucleus. Immunofluorescent analysis of AR in ALCs cultured in medium containing 2% TCM® serum replacement. **(A)** By adding DHT, increased AR staining (in red) in the nucleus is observed compared with non DHT treated cells (control). **(B)** When cells are treated with DHT, subsequent exposure to 1 mM fluoride does not change the intracellular localization of AR as compared to the control. However, when cells are exposed to 100 μM aluminum, together with fluoride, more AR remains in the cytoplasm. The increased cytoplasmic AR co-localizes with HSP90 (in green), and is seen as the overlaid yellow color. DAPI in blue, Scale bar 25 μm.

drinking water (Suzuki et al., 2014). We also confirmed that *Klk4* expression is reduced in maturation stage enamel organs of rats and mice exposed to high levels of fluoride in drinking water, and

consistent with reduced *Klk4* expression, we found a significant reduction of KLK4 proteolytic activity in fluorosed maturation enamel matrix.

KLK4 is upregulated during ameloblast maturation, but the mechanism by which KLK4 expression is regulated in ameloblasts has not been investigated. KLK4 expression is known to correlate with prostate and ovarian cancer, and AR signaling in association with TGF-β signaling is well-studied in these tissues/cells. In OV-Mz-6 ovarian cancer cells, expression of KLK4–7 leads to elevated TGFβ-1 signaling (Shahinian et al., 2014). In prostate cancer cells, TGF-β induces AR activation of its target genes (Yang et al., 2014), while AR also represses TGF-β signaling through interaction with Smad3 (Chipuk et al., 2002). Furthermore, in prostate smooth muscle cells, TGF-β1 inhibits AR activation (Gerdes et al., 1998). In ameloblasts, Suzuki and co-workers suggested that TGF-β signaling is a target of fluoride to reduce *Klk4* expression (Suzuki et al., 2014). As there is a cross-talk between AR and TGF-β signaling, and more recent studies report the presence of AR in ameloblasts and that AR activation upregulates *Klk4* expression (Houari et al., 2016; Jedeon et al., 2016), our studies were directed to determine whether fluoride inhibits AR activation in ameloblasts to result in the downregulation of *Klk4* expression.

Both AR and PR are transcription factors for *Klk4*, however, Lai et al. reported that AR interactions with the *Klk4* gene is indirect and requires co-regulators, while PR directly binds to the progesterone response element in the *Klk4* gene (Lai et al., 2009). Activation of AR induces *Klk4* transcription in prostate cancer cells, while activation of PR does so in breast cancer cells (Nelson et al., 1999; Lai et al., 2009). Therefore, *Klk4* transcription seems to be driven by AR and/or PR, depending on the circumstance such as availability of co-regulators and cell types. In ALCs, we found that inhibition of AR signaling by *Ar* silencing or fluoride, resulted in upregulation of *Pgr* and *Klk4* expression. However, in presence of fluoride, nuclear translocation PR was also inhibited resulting in the downregulation of *Klk4* expression, indicating that PR has a dominant transactivation role in *Klk4* transcription, rather than AR in our *in vivo* (with C57BL/6 mice) and *in vitro* (with ALCs) experimental system. Indeed, in our ALC culture, DHT induced nuclear translocation of AR, but did not upregulate *Klk4* expression (data not shown). Jedeon et al. showed that in rat HAT-7 ameloblasts, activation of AR by testosterone (a primary androgen) increased expression of both *Klk4* and *Ar* (Jedeon et al., 2016), also in maturation ameloblasts in castrated rats injected with testosterone, *Klk4* expression was also increased (Jedeon et al., 2016). However, we found that the enamel in testicular feminized (Tfm) mouse, in which AR lacks steroid binding domains (He et al., 1994), was not hypomineralized to the extent that we saw in fluorosed mice (unpublished studies), supporting the possibility AR regulates KLK4 expression to a much less extent than PR in mouse ameloblasts. Clearly, further investigation of AR and PR signaling is necessary to understand their role in tooth development.

We did find reduced immunostaining for TGFB1 and TGFR-2 in fluorosed maturation stage ameloblasts. This finding along with increased expression of Cyclin D1 in fluorosed ameloblasts, suggests that fluoride interacts with a regulatory molecule common to TGF-β, AR, and PR signaling. The 90-kDa heat-shock protein (HSP90) is such a candidate molecule. HSP90 is an abundant molecular chaperone that functions by facilitating protein folding and stabilization (Csermely et al., 1998; Li et al., 2012). The chaperone function of HSP90 to TGF-β receptors (TGFR-1 and TGFR-2) is known to regulate TGF-β signaling activity in a range of normal and oncogenic epithelial cells (Wrighton et al., 2008). Loss of HSP90 function by stabilizing conformation of HSP90, results in ubiquitin-mediated degradation of clients, i.e. TGF-β receptors, and blocks TGF-β-induced Smad2/3 activation and transcription (Wrighton et al., 2008). Also, nuclear factor family steroid hormone receptors including AR and PR are well-known clients for HSP90 (Reddy et al., 2006; Azad et al., 2015). Therefore, an effect of fluoride on HSP90 could reduce TGFR-2 levels, which suppress TGF-β signaling activity, resulting in an downregulated AR transactivation likely via upregulated CCND1 (Knudsen et al., 1999). Simultaneously, nuclear translocation of AR and PR would be suppressed.

The ATPase function of HSP90 N-terminal domain has a critical role in the functioning cycle of HSP90 (Li and Buchner, 2013). ATP binding to HSP90 triggers a conformational change to a closed state, forming a "lid" that closes over the nucleotide binding pocket. When HSP90 reaches a fully closed state, ATP hydrolysis occurs to release ADP and inorganic phosphate, and returns again to the open conformation (Sullivan et al., 2002; Colombo et al., 2008; Zhang et al., 2015). Aluminum fluoride is known to occupy the γ-phosphate-binding site on the nucleotide triphosphate binding proteins, and together with bound nucleoside diphosphate, such as ADP and GDP, it stabilizes the transition state of the proteins (Wittinghofer, 1997). If aluminum fluoride complex occupies the γ-phosphate-binding site in the ATP binding pocket of HSP90, similar to the effects of aluminum fluoride on G-proteins (Li, 2003) and nitrogenase (Renner and Howard, 1996; Schindelin et al., 1997), the ATP binding pocket can accept only ADP, not ATP. HSP90 would then take the closed conformation, but be stabilized in that state, preventing release of the client proteins (such as AR and PR) to inhibit their translocation to the nucleus. Our results showing that fluoride in combination with aluminum inhibited AR nuclear translocation in ALCs in serum free media (i.e. in the use of the artificial serum replacement), provides indirect evidence to support this possibility. Aluminum is a trace element in the normal serum (Wang et al., 1991; Murko et al., 2009; Tomza-Marciniak et al., 2011), and it could explain why we see an effect of fluoride inhibiting AR nuclear translocation in serum containing media, but not in serum free media except with the addition of aluminum.

Finally, it is important to mention that studies of the cellular effects of fluoride require attention to biologically relevant levels of fluoride. We do not yet know how fluoride enters ameloblasts, and the effect of the unique process of enamel mineralization, such as changes in the extracellular pH. *In vivo*, rodents ingest ∼10 times the amount of fluoride as humans to obtain similar serum levels and degrees of fluorosis. Humans drinking 3–5 ppm F (1 ppm $F = 52.6$ mM) fluoride supplemented water have a serum fluoride level around 3–5 μM (Guy et al., 1976),

similar to the mouse model used in this study which was given water containing 50 ppm F (Zhang et al., 2014). However, *in vitro*, fluoride levels are required to be much higher to show effects similar to those found *in viv*o (Sharma et al., 2008; Li and Buchner, 2013; Lei et al., 2014; Suzuki et al., 2014). We found that ALCs required 1 mM fluoride to result in reduced AR translocation, similar to what was found *in vivo*, and at these fluoride levels, cell proliferation and morphology of the ALCs were not affected, indicating that the effects of fluoride on the ALCs used for these *in vitro* studies are specific and not due to a generalized effect of fluoride on cell toxicity. The need for higher levels of fluoride in ALC culture may be related to the mechanisms by which fluoride may enter the cell, as compared to *in vivo*.

In conclusion, fluoride targets activation of AR and PR and thus inhibits AR- and PR- driven *Klk4* transcription in maturation ameloblasts. Our data support the possibility that this effect occurs through the action of fluoride in combination with aluminum, possibly through an effect on HSP90. These studies raise many questions related to the regulation of ameloblast maturation, and how fluoride can alter this process at a cellular level, to result in fluorosis. The cellular effect of fluoride may be related to fluoride entry into the cell, which may be unique to ameloblasts, and additional studies will be needed to address this possibility. It should also be noted that the *in vitro* studies were all done using female rats and mice. Though there is no convincing evidence that fluorosis is sex-linked, it is reasonable that future studies of fluorosis mechanisms include both male and female mice.

AUTHOR CONTRIBUTIONS

All authors listed, have made substantial, direct and intellectual contribution to the work, and approved it for publication.

FUNDING

This research was funded by NIDCR grants F30-DE023280 to ML and R01-DE13508 to PD, and funds from the School of Dentistry at UCSF, the Department of Orofacial Sciences at UCSF, and the Center for Children's Oral Health Research at UCSF to YN and PD.

REFERENCES

Aoba, T. (1997). The effect of fluoride on apatite structure and growth. *Crit. Rev. Oral Biol. Med.* 8, 136–153. doi: 10.1177/10454411970080020301

Azad, A. A., Zoubeidi, A., Gleave, M. E., and Chi, K. N. (2015). Targeting heat shock proteins in metastatic castration-resistant prostate cancer. *Nat. Rev. Urol.* 12, 26–36. doi: 10.1038/nrurol.2014.320

Benjamini, Y., and Hochberg, Y. (1995). Controlling the false discovery rate: a practical and powerful approach to multiple testing. *J. R. Stat. Soc.* 57, 289–300.

Bruckheimer, E. M., and Kyprianou, N. (2001). Dihydrotestosterone enhances transforming growth factor-β-induced apoptosis in hormone-sensitive prostate cancer cells. *Endocrinology* 142, 2419–2426. doi: 10.1210/endo.142.6.8218

Chipuk, J. E., Cornelius, S. C., Pultz, N. J., Jorgensen, J. S., Bonham, M. J., Kim, S.-J., et al. (2002). The androgen receptor represses transforming growth factor-β signaling through interaction with smad3. *J. Biol. Chem.* 277, 1240–1248. doi: 10.1074/jbc.M108855200

Colombo, G., Morra, G., Meli, M., and Verkhivker, G. (2008). Understanding ligand-based modulation of the Hsp90 molecular chaperone dynamics at atomic resolution. *Proc. Natl. Acad. Sci. U.S.A.* 105, 7976–7981. doi: 10.1073/pnas.0802879105

Comstock, C. E., Augello, M. A., Schiewer, M. J., Karch, J., Burd, C. J., Ertel, A., et al. (2011). Cyclin D1 is a selective modifier of androgen-dependent signaling and androgen receptor function. *J. Biol. Chem.* 286, 8117–8127. doi: 10.1074/jbc.M110.170720

Csermely, P., Schnaider, T., So″ti, C., Prohászka, Z., and Nardai, G. (1998). The 90-kDa molecular chaperone family: structure, function, and clinical applications. A comprehensive review. *Pharmacol. Ther.* 79, 129–168. doi: 10.1016/S0163-7258(98)00013-8

Dao-Phan, H. P., Formstecher, P., and Lefebvre, P. (1997). Disruption of the glucocorticoid receptor assembly with heat shock protein 90 by a peptidic antiglucocorticoid. *Mol. Endocrinol.* 11, 962–972. doi: 10.1210/mend.11.7.9937

Den Besten, P. K. (1986). Effects of fluoride on protein secretion and removal during enamel development in the rat. *J. Dent. Res.* 65, 1272–1277. doi: 10.1177/00220345860650101401

DenBesten, P. K., and Thariani, H. (1992). Biological mechanisms of fluorosis and level and timing of systemic exposure to fluoride with respect to fluorosis. *J. Dent. Res.* 71, 1238–1243. doi: 10.1177/00220345920710051701

DenBesten, P. K., Yan, Y., Featherstone, J. D., Hilton, J. F., Smith, C. E., and Li, W. (2002). Effects of fluoride on rat dental enamel matrix proteinases. *Arch. Oral Biol.* 47, 763–770. doi: 10.1016/S0003-9969(02)00117-6

Gerdes, M. J., Dang, T. D., Larsen, M., and Rowley, D. R. (1998). Transforming growth factor-β1 induces nuclear to cytoplasmic distribution of androgen receptor and inhibits androgen response in prostate smooth muscle cells. *Endocrinology* 139, 3569–3577. doi: 10.1210/endo.139.8.6138

Grad, I., and Picard, D. (2007). The glucocorticoid responses are shaped by molecular chaperones. *Mol. Cell. Endocrinol.* 275, 2–12. doi: 10.1016/j.mce.2007.05.018

Guy, W. S., Taves, D., R., and Brey, W. S. (1976). Organic fluorocompounds in human plasma: prevalence and characterization in biochemistry involving carbon-fluorine bonds. *Am. Chem. Soc.* 7, 117–134.

He, W. W., Lindzey, J. K., Prescott, J. L., Kumar, M. V., and Tindall, D. J. (1994). The androgen receptor in the testicular feminized (Tfm) mouse may be a product of internal translation initiation. *Receptor* 4, 121–134.

Houari, S., Loiodice, S., Jedeon, K., Berdal, A., and Babajko, S. (2016). Expression of steroid receptors in ameloblasts during amelogenesis in rat incisors. *Front. Physiol.* 7:503. doi: 10.3389/fphys.2016.00503

Housley, P. R. (1990). Aluminum fluoride inhibition of glucocorticoid receptor inactivation and transformation. *Biochemistry* 29, 3578–3585. doi: 10.1021/bi00466a022

Jedeon, K., Loiodice, S., Salhi, K., Le Normand, M., Houari, S., Chaloyard, J., et al. (2016). Androgen receptor involvement in rat amelogenesis: an additional way for endocrine-disrupting chemicals to affect enamel synthesis. *Endocrinology* 157, 4287–4296. doi: 10.1210/en.2016-1342

Kang, H.-Y., Huang, K.-E., Chang, S. Y., Ma, W.-L., Lin, W.-J., and Chang, C. (2002). Differential modulation of androgen receptor-mediated transactivation by smad3 and tumor suppressor smad4. *J. Biol. Chem.* 277, 43749–43756. doi: 10.1074/jbc.M205603200

Karamouzis, M. V., Papavassiliou, K. A., Adamopoulos, C., and Papavassiliou, A. G. (2016). Targeting androgen/estrogen receptors crosstalk in cancer. *Trends Cancer* 2, 35–48. doi: 10.1016/j.trecan.2015.12.001

Knudsen, K. E., Cavenee, W. K., and Arden, K. C. (1999). D-type cyclins complex with the androgen receptor and inhibit its transcriptional transactivation ability. *Cancer Res.* 59, 2297–2301.

Ko, T. C., Sheng, H. M., Reisman, D., Thompson, E. A., and Beauchamp, R. D. (1995). Transforming growth factor-beta 1 inhibits cyclin D1 expression in intestinal epithelial cells. *Oncogene* 10, 177–184.

Lai, J., Myers, S. A., Lawrence, M. G., Odorico, D. M., and Clements, J. A. (2009). Direct progesterone receptor and indirect androgen receptor interactions with the kallikrein-related peptidase 4 gene promoter in breast and prostate cancer. *Mol. Cancer Res.* 7, 129–141. doi: 10.1158/1541-7786.MCR-08-0218

Lei, S., Zhang, Y., Zhang, K., Li, J., and Liu, L. (2014). Effects of Fluoride on the expression of Beclin1 and mTOR in ameloblasts. *Cells Tissues Organs* 200, 405–412. doi: 10.1159/000441052

Li, J., and Buchner, J. (2013). Structure, function and regulation of the hsp90 machinery. *Biomed. J.* 36, 106–117. doi: 10.4103/2319-4170.113230

Li, J., Soroka, J., and Buchner, J. (2012). The Hsp90 chaperone machinery: Conformational dynamics and regulation by co-chaperones. *Biochim. Biophys. Acta* 1823, 624–635. doi: 10.1016/j.bbamcr.2011.09.003

Li, L. (2003). The biochemistry and physiology of metallic fluoride: action, mechanism, and implications. *Crit. Rev. Oral Biol. Med.* 14, 100–114. doi: 10.1177/154411130301400204

Livak, K. J., and Schmittgen, T. D. (2001). Analysis of relative gene expression data using real-time quantitative PCR and the 2−ΔΔCT method. *Methods* 25, 402–408. doi: 10.1006/meth.2001.1262

Murko, S., Milacic, R., Kralj, B., and Scancar, J. (2009). Convective interaction media monolithic chromatography with ICPMS and ultraperformance liquid chromatography-electrospray ionization MS detection: a powerful tool for speciation of aluminum in human serum at normal concentration levels. *Anal. Chem.* 81, 4929–4936. doi: 10.1021/ac9006232

Nakata, A., Kameda, T., Nagai, H., Ikegami, K., Duan, Y., Terada, K., et al. (2003). Establishment and characterization of a spontaneously immortalized mouse ameloblast-lineage cell line. *Biochem. Biophys. Res. Commun.* 308, 834–839. doi: 10.1016/S0006-291X(03)01467-0

Nelson, P. S., Gan, L., Ferguson, C., Moss, P., Gelinas, R., Hood, L., et al. (1999). Molecular cloning and characterization of prostase, an androgen-regulated serine protease with prostate-restricted expression. *Proc. Natl. Acad. Sci. U.S.A.* 96, 3114–3119. doi: 10.1073/pnas.96.6.3114

Pratt, W. B., Galigniana, M. D., Morishima, Y., and Murphy, P. J. (2004). Role of molecular chaperones in steroid receptor action. *Essays Biochem.* 40, 41–58. doi: 10.1042/bse0400041

Reddy, G. P. V., Barrack, E. R., Dou, Q. P., Menon, M., Pelley, R., Sarkar, F. H., et al. (2006). Regulatory processes affecting androgen receptor expression, stability, and function: potential targets to treat hormone-refractory prostate cancer. *J. Cell. Biochem.* 98, 1408–1423. doi: 10.1002/jcb.20927

Renner, K. A., and Howard, J. B. (1996). Aluminum fluoride inhibition of nitrogenase: stabilization of a nucleotide·Fe-Protein·MoFe-protein complex. *Biochemistry* 35, 5353–5358. doi: 10.1021/bi960441o

Ritz, C., and Streibig, J. C. (2005). Bioassay analysis using R. *J. Stat. Softw.* 12, 1–22. doi: 10.18637/jss.v012.i05

Schindelin, H., Kisker, C., Schlessman, J. L., Howard, J. B., and Rees, D. C. (1997). Structure of ADP[middot]AlF4–stabilized nitrogenase complex and its implications for signal transduction. *Nature* 387, 370–376. doi: 10.1038/387370a0

Shahinian, H., Loessner, D., Biniossek, M. L., Kizhakkedathu, J. N., Clements, J. A., Magdolen, V., et al. (2014). Secretome and degradome profiling shows that Kallikrein-related peptidases 4, 5, 6, and 7 induce TGFβ-1 signaling in ovarian cancer cells. *Mol. Oncol.* 8, 68–82. doi: 10.1016/j.molonc.2013.09.003

Sharma, R., Tsuchiya, M., and Bartlett, J. D. (2008). Fluoride induces endoplasmic reticulum stress and inhibits protein synthesis and secretion. *Environ. Health Perspect.* 116, 1142–1146. doi: 10.1289/ehp.11375

Stahl, J., Nakano, Y., Horst, J., Zhu, L., Le, M., Zhang, Y., et al. (2015). Exon4 amelogenin transcripts in enamel biomineralization. *J. Dent. Res.* 94, 836–842. doi: 10.1177/0022034515577412

Sullivan, W. P., Owen, B. A. L., and Toft, D. O. (2002). The influence of ATP and p23 on the conformation of hsp90. *J. Biol. Chem.* 277, 45942–45948. doi: 10.1074/jbc.M207754200

Suzuki, M., Shin, M., Simmer, J. P., and Bartlett, J. D. (2014). Fluoride affects enamel protein content via TGF β1-mediated KLK4 inhibition. *J. Dent. Res.* 93, 1022–1027. doi: 10.1177/0022034514545629

Team, R. C. (2014). *R: A Language and Environment for Statistical Computing*. Vienna: R Foundation for Statistical Computing.

Tomza-Marciniak, A., Pilarczyk, B., Bakowska, M., Pilarczyk, R., and Wojcik, J. (2011). Heavy metals and other elements in serum of cattle from organic and conventional farms. *Biol. Trace Elem. Res.* 143, 863–870. doi: 10.1007/s12011-010-8910-z

Tsang, J. Y., Ni, Y.-B., Chan, S.-K., Shao, M.-M., Law, B. K., Tan, P. H., et al. (2014). Androgen receptor expression shows distinctive significance in ER positive and negative breast cancers. *Ann. Surg. Oncol.* 21, 2218–2228. doi: 10.1245/s10434-014-3629-2

Tye, C. E., Antone, J. V., and Bartlett, J. D. (2011). Fluoride does not inhibit enamel protease activity. *J. Dent. Res.* 90, 489–494. doi: 10.1177/0022034510390043

Wang, S. T., Pizzolato, S., and Demshar, H. P. (1991). Aluminum levels in normal human serum and urine as determined by Zeeman atomic absorption spectrometry. *J. Anal. Toxicol.* 15, 66–70. doi: 10.1093/jat/15.2.66

Wittinghofer, A. (1997). Signaling mechanistics: aluminum fluoride for molecule of the year. *Curr. Biol.* 7, R682–R685. doi: 10.1016/S0960-9822(06)00355-1

Wright, J. T., Chen, S. C., Hall, K. I., Yamauchi, M., and Bawden, J. W. (1996). Protein characterization of fluorosed human enamel. *J. Dent. Res.* 75, 1936–1941. doi: 10.1177/00220345960750120401

Wrighton, K. H., Lin, X., and Feng, X.-H. (2008). Critical regulation of TGFβ signaling by Hsp90. *Proc. Natl. Acad. Sci. U.S.A.* 105, 9244–9249. doi: 10.1073/pnas.0800163105

Yang, F., Chen, Y., Shen, T., Guo, D., Dakhova, O., Ittmann, M. M., et al. (2014). Stromal TGF-β signaling induces AR activation in prostate cancer. *Oncotarget* 5, 10854–10869. doi: 10.18632/oncotarget.2536

Zhang, H., Zhou, C., Chen, W., Xu, Y., Shi, Y., Wen, Y., et al. (2015). A dynamic view of ATP-coupled functioning cycle of Hsp90 N-terminal domain. *Sci. Rep.* 5:9542. doi: 10.1038/srep09542

Zhang, Y., Kim, J. Y., Horst, O., Nakano, Y., Zhu, L., Radlanski, R. J., et al. (2014). Fluorosed mouse ameloblasts have increased SATB1 retention and Galphaq activity. *PLoS ONE* 9:e103994. doi: 10.1371/journal.pone.0103994

Conflict of Interest Statement: The authors declare that the research was conducted in the absence of any commercial or financial relationships that could be construed as a potential conflict of interest.

Copyright © 2017 Le, Nakano, Abduweli Uyghurturk, Zhu and Den Besten. This is an open-access article distributed under the terms of the Creative Commons Attribution License (CC BY). The use, distribution or reproduction in other forums is permitted, provided the original author(s) or licensor are credited and that the original publication in this journal is cited, in accordance with accepted academic practice. No use, distribution or reproduction is permitted which does not comply with these terms.

frontiers in Physiology

REVIEW
published: 08 September 2017
doi: 10.3389/fphys.2017.00653

The Unfolded Protein Response in Amelogenesis and Enamel Pathologies

Steven J. Brookes[1]*, *Martin J. Barron*[2], *Michael J. Dixon*[2] and *Jennifer Kirkham*[1]

[1] Division of Oral Biology, School of Dentistry, University of Leeds, St James's University Hospital, Leeds, United Kingdom, [2] Faculty of Biology, Medicine and Health, Manchester Academic Health Sciences Centre, University of Manchester, Manchester, United Kingdom

During the secretory phase of their life-cycle, ameloblasts are highly specialized secretory cells whose role is to elaborate an extracellular matrix that ultimately confers both form and function to dental enamel, the most highly mineralized of all mammalian tissues. In common with many other "professional" secretory cells, ameloblasts employ the unfolded protein response (UPR) to help them cope with the large secretory cargo of extracellular matrix proteins transiting their ER (endoplasmic reticulum)/Golgi complex and so minimize ER stress. However, the UPR is a double-edged sword, and, in cases where ER stress is severe and prolonged, the UPR switches from pro-survival to pro-apoptotic mode. The purpose of this review is to consider the role of the ameloblast UPR in the biology and pathology of amelogenesis; specifically in respect of amelogenesis imperfecta (AI) and fluorosis. Some forms of AI appear to correspond to classic proteopathies, where pathological intra-cellular accumulations of protein tip the UPR toward apoptosis. Fluorosis also involves the UPR and, while not of itself a classic proteopathic disease, shares some common elements through the involvement of the UPR. The possibility of therapeutic intervention by pharmacological modulation of the UPR in AI and fluorosis is also discussed.

Keywords: ameloblast, ER stress, unfolded protein response, apoptosis, amelogenesis imperfecta, fluorosis

OPEN ACCESS

Edited by:
Petros Papagerakis, University of Michigan, United States

Reviewed by:
Thomas G. H. Diekwisch, Texas A&M University Baylor College of Dentistry, United States
Amel Gritli-Linde, University of Gothenburg, Sweden
Zhi Chen, Wuhan University, China

***Correspondence:**
Steven J. Brookes
s.j.brookes@leeds.ac.uk

Specialty section:
This article was submitted to Craniofacial Biology and Dental Research, a section of the journal Frontiers in Physiology

Received: *16 June 2017*
Accepted: *17 August 2017*
Published: *08 September 2017*

Citation:
Brookes SJ, Barron MJ, Dixon MJ and Kirkham J (2017) The Unfolded Protein Response in Amelogenesis and Enamel Pathologies. Front. Physiol. 8:653. doi: 10.3389/fphys.2017.00653

INTRODUCTION

Amelogenesis involves the incremental secretion of a self-assembling extracellular protein matrix (enamel matrix) on to the pre-existing dentine surface by columnar secretory ameloblasts. The enamel matrix is overwhelmingly (>90%) composed of proteins derived by extracellular proteolysis of alternatively spliced products of the amelogenin gene (*AMELX/Y* in humans; *Amelx* in rodents) (Brookes et al., 1995). Other, far less abundant, matrix proteins that are secreted during the secretory phase of amelogenesis include: enamelin (ENAM), ameloblastin (AMBN) and matrix metallopeptidase 20 (MMP20) (Moradian-Oldak, 2012; Bartlett, 2013). AMELX, ENAM, and AMBN are generally regarded as structural components of the enamel matrix whereas MMP20, present in catalytic amounts, is responsible for the proteolytic processing of AMELX, ENAM, and AMBN. Enamel is partially mineralized during the secretory phase. Extremely elongated crystallites of hydroxyapatite, originating at the enamel-dentine junction, grow in length (c-axis growth) surrounded by enamel matrix proteins that are newly secreted by the ameloblasts as they migrate away from the enamel dentine junction. Secretory stage ameloblasts have the typical characteristics of a specialized secretory cell, including numerous mitochondria and a well-developed endoplasmic

reticulum (ER)/Golgi complex (Reith, 1961). These adaptations allow the ameloblasts to cope with their large secretory load as they incrementally secrete the enamel matrix.

Enamel crystallites are organized into bundles (the so-called enamel prisms or rods) which are interspersed with inter-prismatic enamel crystals that together delineate the enamel ultrastructure; a process directed by the ameloblasts' specialized Tomes' process from which the secretory cargo is elaborated (Smith, 1998). The function of the enamel matrix and its component parts is still not fully understood but the consensus view is that it is involved with the nucleation of the enamel crystallites, the control of their subsequent preferential c-axis growth, and their structural organization into prisms and inter-prismatic enamel. Once the ameloblasts have secreted the required thickness of enamel, matrix secretion ceases. The ameloblasts become shortened and less columnar and lose their Tomes' processes. This marks the end of the secretory phase and the beginning of the maturation phase (Smith, 1998) which is further characterized by ameloblasts up-regulating the expression and secretion of a number of maturation stage-specific proteins including kallikrein-related peptidase 4 (KLK4) (Bartlett, 2013), amelotin (AMTN) (Iwasaki et al., 2005), and odontogenic ameloblast-associated protein (ODAM) (Nishio et al., 2010). KLK4 is a serine protease that quickly degrades the spectrum of proteins comprising the secretory stage matrix, facilitating their ultimate removal from the tissue by ameloblast endocytosis (Lacruz et al., 2013). As the enamel matrix is removed, it is replaced by fluid into which the ameloblasts actively transport mineral ions which drive the growth of the enamel crystallites in width and thickness so that they eventually occlude most of the tissue volume.

The functional importance of the enamel matrix proteins in amelogenesis is evidenced by the effects of mutations in their respective genes on the enamel phenotype, which can result in amelogenesis imperfecta (AI), characterized by biomineralization defects of enamel (Smith et al., 2017). Several studies have examined the potential effects of such mutations on events occurring in the enamel extracellular matrix itself, including protein-protein interactions and enamel matrix self-assembly (Lakshminarayanan et al., 2010; Zhu et al., 2011) and also protein-mineral interactions (Zhu et al., 2011). Certainly, perturbation of these processes would be expected to give rise to enamel biomineralization defects and therefore AI, including, for example, a complete failure to produce enamel, the production of pathologically thin or under-mineralized enamel or enamel in which the ultrastructural arrangement of the crystallites is affected. However, recent data have suggested that intra-cellular events related to the so-called unfolded protein response (UPR) may also play an important role in enamel biology and pathology—including AI and fluorosis.

The UPR is a signaling pathway that has evolved to allow cells to manage their secretory load under normal physiological and pathological conditions to maintain proteostasis in the endoplasmic reticulum (ER) (Hetz et al., 2015). Failure to maintain proteostasis can lead to ER stress which is a factor in many diseases (Kopito and Ron, 2000; Ozcan and Tabas, 2012). Our aim is to review the literature detailing the way in which secretory ameloblasts cope with their large secretory burden by utilizing the UPR in a similar way to other "professional" secretory cells (such as pancreatic islet cells and plasma cells) in order to maintain ER proteostasis and reduce ER stress levels.

We begin with a brief introduction to ER stress and the UPR before moving on to discuss how ameloblasts employ the UPR to cope with ER stress in both the absence and presence of genetic mutations. The evidence supporting the hypothesis that ER stress can be an etiological factor in both AI and fluorosis will be discussed along with possible therapeutic options for targeting ameloblast ER stress to ameliorate associated enamel pathologies.

ER STRESS AND THE UNFOLDED PROTEIN RESPONSE (UPR)

The ER is responsible for trafficking all nascent proteins destined for secretion or insertion into a cellular membrane from their synthesis at the ribosome to the Golgi apparatus. The lumen of the ER contains an assortment of resident ancillary proteins (chaperones) that direct the folding of nascent polypeptides to maximize the probability that a nascent protein attains its correct functional 3-dimensional conformation. In addition, oxidoreducatase enzymes ensure that disulphide bond formation is regulated to inhibit random disulphide bond formation that if allowed could result in mis-folding. However, the molecular policing mechanisms that prevent protein mis-folding can fail. In this case, the protein may be permitted to access and become trapped in some low-energy state with a conformation that may not be biologically active or in some cases may promote pathological intracellular protein aggregation or be frankly cytotoxic (Dobson, 2003; Gregersen et al., 2006). Up to 30% of newly synthesized wild-type (WT) proteins can spontaneously mis-fold and fail to achieve their proper conformation (Schubert et al., 2000). Mutated proteins may show an even greater propensity to mis-fold and aggregate. This is the etiological basis that underpins many so-called proteopathic or conformational diseases (e.g., Parkinson's disease, Alzheimer's disease, cystic fibrosis, Huntington's disease, some cancers, diabetes and myofibrillar myopathies) (Selkoe, 2003; Lin et al., 2008; Valastyan and Lindquist, 2014; Oakes and Papa, 2015). Not surprisingly, cells have therefore evolved an active quality control system that monitors client proteins transiting through the ER. This quality control system recognizes aberrant client proteins, (whether spontaneously mis-folded WT or mis-folded mutated proteins) and acts to restore ER homeostasis thus alleviating ER stress. However, if the stress cannot be alleviated, the cell is directed toward apoptosis. The detection of mis-folded proteins is carried out by three sensor proteins that span the ER membrane: PERK, IRE1, and ATF6 (see below).

ER Stress Can Activate the UPR Which Attempts to Restore Proteostasis

Activation of the trans-ER membrane sensors triggers an integrated signaling pathway that initially attempts to restore ER homeostasis by: (i) reducing the secretory load, (ii) increasing the folding capacity of the ER by up-regulating chaperone expression

and increasing ER volume, and (iii) increasing ER-associated protein degradation (ERAD) (Schroder and Kaufman, 2005). When ER stress is low, the sensors appear to be inactivated by their binding of GRP78 (BiP, HSPA5); present in the ER where it also functions as a chaperone, binding to cargo proteins. Mis-folded proteins in the ER lumen associate with GRP78 such that GRP78 is increasingly dissociated from the sensors, allowing them to become active and trigger the UPR (Schroder and Kaufman, 2005; Malhotra and Kaufman, 2007a). However, GRP78 may not be the main regulator in the case of sensor IRE1, which may be activated by direct interaction with mis-folded proteins (Credle et al., 2005; Gardner and Walter, 2011) that is independent of its GRP78 binding domain (Kimata et al., 2004). The initial UPR is pro-survival in nature, helping cells cope with a heavy secretory load even in the absence of any protein mutations. However, if the ER stress cannot be relieved, then the UPR, acting as a "double edged sword" (Malhotra and Kaufman, 2007b) switches to pro-apoptotic mode (Fribley et al., 2009). The decision to enter apoptosis arises through the integration of the multiple signaling outputs from the UPR; it does not involve a single event or signaling pathway (Rutkowski et al., 2006). In effect, the UPR is a graded response whose effect on the cell appears to depend on cell context, including the nature and duration of the stimulus causing the ER stress and the differential activation of the sensors under specific forms of ER stress, including their differential regulation by protein co-factors other than GRP78. The UPR is further modulated downstream allowing fine-tuning under specific circumstances (Hetz, 2012).

The UPR in Pro-Survival Mode—Adapting to ER Stress

A detailed description of the signaling pathways triggered by ER stress is beyond the scope of this review but the role of the three sensors of the UPR in the pro-survival adaptive response will be discussed briefly below and is summarized in **Figure 1**.

IRE1

On activation, IRE1 oligomerizes and undergoes auto-phosphorylation, activating its endoribonuclease activity to drive the unconventional splicing of XBP1 mRNA (Yoshida et al., 2001; Prischi et al., 2014). Spliced XBP1 mRNA encodes a transcription factor that interacts with ER stress response elements to up-regulate UPR target genes such as chaperones (e.g., GRP78 and GRP94 (Lee et al., 2003), components of the ERAD system, genes associated with ER and Golgi expansion (lipid synthesis) (Lee et al., 2003; Ron and Walter, 2007; Hetz et al., 2011) and IRE1 itself (Tsuru et al., 2016). IRE1 also degrades specific ER-localized mRNAs (regulated Ire1-dependent decay) in an attempt to provide immediate relief from the translational load entering the already stressed ER during the initial phase of ER stress (Hollien and Weissman, 2006; Han et al., 2009).

PERK

On activation, PERK dimerizes and undergoes auto-phosphorylation. Activated PERK phosphorylates its downstream target, eIF2α. Phosphorylated eIF2α binds the guanine nucleotide exchange factor eIF2β, inhibiting assembly of the 43S translation initiation complex. This process effectively reduces general protein translation, thus reducing the secretory load (Harding et al., 2000). However, eIF2α-P selectively *increases* the translation of transcription factor ATF4, which targets a wide range of ER stress response elements including those involved in protein folding, assembly and metabolism (Dey et al., 2010), and as described below, apoptosis.

ATF6

On activation, ATF6 is trafficked to the Golgi where the cytosolic N-terminal domain is proteolytically cleaved (Ron and Walter, 2007). The cleaved ATF6 N-terminal domain is a transcription factor that translocates to the nucleus where it interacts with ER stress response elements to activate multiple UPR target genes coding elements of the ERAD system, chaperones such as GRP78 and the UPR-associated transcription factors AFT4 and Xbp1 (Yoshida et al., 2001). PERK activation enhances ATF6 synthesis and its trafficking to the Golgi for proteolytic activation which is promoted by ATF4 (Teske et al., 2011). The ATF6 pathway appears to overlap functionally to some extent with the PERK and IRE1 pathways (Wu et al., 2007).

The UPR in Pro-Apoptotic Mode—Capitulating to ER Stress

At some point during ER stress, a decision is made to abandon promotion of cell survival in favor of apoptosis. The timing of this decision, and the level of stress required to trigger the switch to pro-apoptotic mode, appear to depend on the specific nature of the stress encountered and the cell context but the decision arises following close scrutiny of the integrated signals originating from the three sensor-led arms of the UPR and the cross-talk between them as the UPR evolves (Tabas and Ron, 2011; Chen and Brandizzi, 2013; Moore and Hollien, 2015).

The IRE1 arm of the UPR appears to be the central player in directing a cell away from survival and toward apoptosis (though all arms of the UPR can activate downstream apoptotic pathways). IRE1 endoribonuclease activity can be used to manipulate the UPR response by finely controlling the degradation of specific target mRNAs (Han et al., 2009); a process enhanced when PERK is activated (Moore and Hollien, 2015), emphasizing the complex cross-talk underpinning the UPR. Under unrelieved ER stress, XBP1 mRNA splicing increases along with the regulated IRE1-dependent decay of ER-localized mRNAs encoding for ER cargo. This depletes the ER cargo including critical cell surface bound traffic (e.g., membrane bound receptors) and ER resident chaperones involved in protein folding. As a result, stress levels are tipped beyond a critical threshold, triggering the pro-apoptotic response (Han et al., 2009; Coelho and Domingos, 2014). In addition, IRE1-dependent decay targets specific microRNAs that repress the translation of caspase-2 (Upton et al., 2012), an executioner caspase implemented in apoptosis and linked to ER stress (Fava et al., 2012).

The molecular details of how the UPR finally brings about apoptosis are still the subject of intense research, driven in part by the fact that the UPR plays a pivotal role in numerous human diseases. A brief, and by no means complete, overview of the

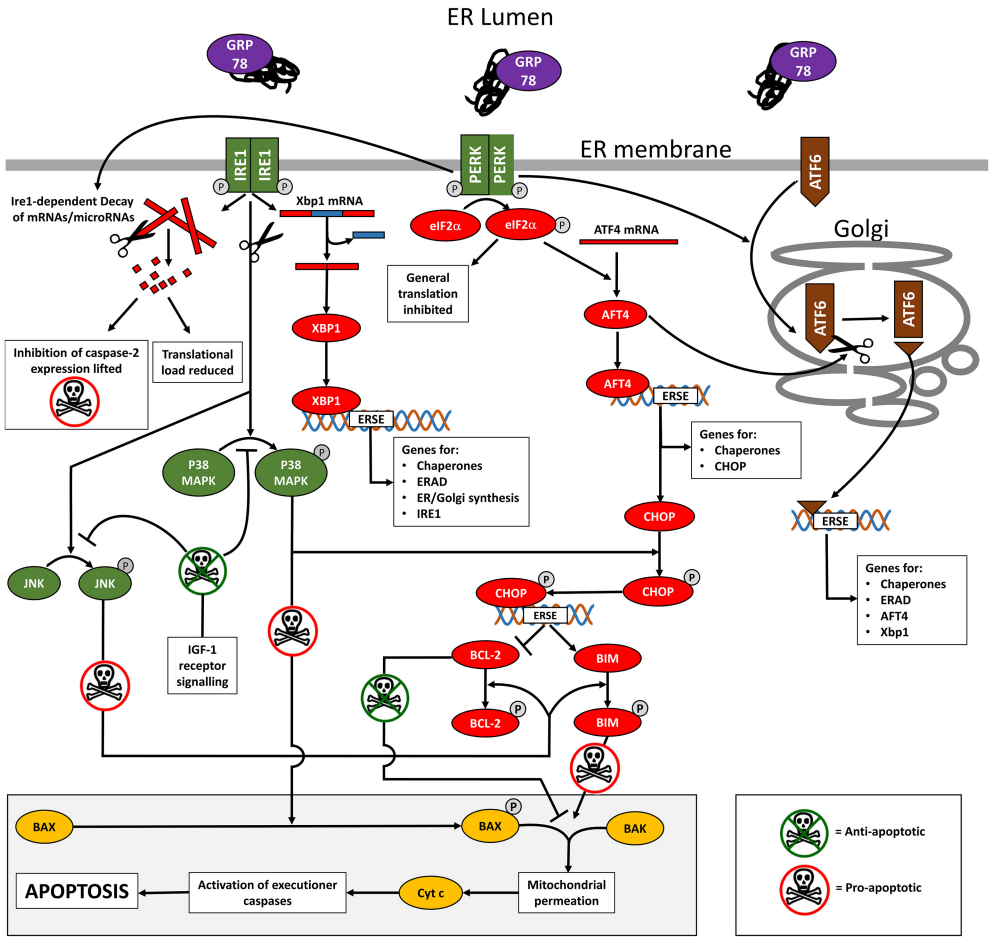

FIGURE 1 | Diagram summarizing an outline of the cell signaling occurring during ER stress and the UPR. Full details are provided in the text but in brief, titration of GRP78 by misfolded proteins in the ER lumen causes phosphorylation (activation) of the ER membrane-spanning stress sensors IRE1, PERK, and AFT6. This unleashes an interconnected downstream signaling cascade of transcription factors that initially reduces the translational load by mRNA degradation and inhibition of translation. A series of ES stress response elements (ERSE) are targeted resulting in the transcription of genes that aid the cell cope with its secretory load and promote cell survival. In cases where the ER stress is unrelieved, the pro-apoptotic transcription factor CHOP is expressed. Together with the concerted activity of P38 MAPK and JNK (activated by IRE1 kinase activity), CHOP promotes apoptosis through the BAX/BAK mediated permeation of mitochondrial outer membranes. IGF-1 receptor signaling inhibits apoptosis by indirectly controlling the activation of P38 MAPK and JNK.

events occurring following the decision to commit to apoptosis is given below.

The transcription factor CHOP is an important UPR target gene. CHOP expression in stress-free cells is almost undetectable but it is upregulated by ATF4 (Su and Kilberg, 2008), which as described previously is itself induced following activation of PERK and AFT6 in cells undergoing ER stress (Tabas and Ron, 2011; Li et al., 2014). CHOP is post-translationally activated by phosphorylation mediated via the stress kinase p38MAPK, which is itself activated by IRE1 kinase activity. Activated CHOP up-regulates expression of pro-apoptotic gene products such as *BIM* (Puthalakath et al., 2007) whilst decreasing expression of anti-apoptotic gene products such as BCL-2 (Li et al., 2014). IRE1 kinase activity also activates a second stress kinase, JNK, which in turn can phosphorylate both BIM and BCL-2 to regulate their activity.

BIM and BCL-2 are exemplar members of a wider family of proteins that facilitate and inhibit the triggering of apoptosis respectively. In their non-phosphorylated states, BCL-2 is actively anti-apoptotic and BIM is inactive. On phosphorylation by JNK, BCL-2 loses its anti-apoptotic properties while BIM becomes actively pro-apoptotic. Under these conditions, the constitutively expressed factors BAX and BAK act in concert to trigger mitochondrial membrane disruption and the release of factors including cytochrome c that initiate the final executioner caspase cascade that leads to cell death (Nomura et al., 1999; Ow et al., 2008; Tabas and Ron, 2011). BAK is usually resident on the outer mitochondrial membrane but BAX translocates from the cytoplasm to the outer mitochondrial membrane following phosphorylation by p38MAPK or JNK (Kim et al., 2006; Ow et al., 2008), linking BAX translocation and apoptosis directly to IRE1. The regulation of BAX and BAK activity is of prime importance

and it is clear even from the simplified account given above that the three arms of the UPR work in concert to tightly regulate BAX and BAK activity with numerous check points and gates in place to ensure that a point of consensus has been reached prior to committing the cell to apoptosis.

WILD-TYPE SECRETORY STAGE AMELOBLASTS RELY ON THE UPR IN PRO-SURVIVAL MODE TO MAINTAIN THEIR SECRETORY OUTPUT

Specialized secretory cells, including plasma cells, pancreatic cells, hepatocytes and osteoblasts face ER stress even under normal conditions simply by virtue of their high secretory load and consequently rely on the UPR acting in pro-survival mode (Moore and Hollien, 2012). Secretory ameloblasts can be regarded as specialized secretory cells and share typical characteristics such as a prominent ER/Golgi network during the secretory stage. An early indication that the UPR is normally active in secretory stage ameloblasts was the finding that IRE was present its activated form (Kubota et al., 2005). As described in previously, a primary outcome of an active UPR is to increase the volume of ER to increase the handling capacity of the cell's secretory pathway. The volume occupied by the ER in WT pre-secretory ameloblasts increases by a factor of around 3.3 by the time the ameloblast has reached the end of the secretory stage (Tsuchiya et al., 2008). Furthermore, there is a dramatic reduction in immunohistological staining for activated phosphorylated IRE1 in maturation-stage ameloblasts compared to secretory-stage ameloblasts which is a reflection of the greatly reduced secretory load transiting the ER in maturation-stage ameloblasts (Tsuchiya et al., 2008). These authors also reported that expression of spliced Xbp1 mRNA was five times greater in secretory enamel organ cells compared to maturation stage enamel organ, indicating that IRE1 activation had indeed triggered the UPR in the secretory ameloblasts (Tsuchiya et al., 2008). These data are important as they indicate that WT secretory ameloblasts are stressed by their secretory load under normal conditions and require the UPR to help manage the situation. The prominent client protein in the secretory ameloblast pathway is amelogenin; a hydrophobic protein that is well known for its propensity to self-assemble/aggregate. Molecular cross-linking studies showed that amelogenin begins to self-assemble during its transit through the ameloblast secretory pathway (Brookes et al., 2006) and the regulation of these intramolecular interactions may well require sustained input from the folding machinery under the influence of UPR signaling.

As described previously, CHOP expression is a marker for UPR-induced apoptosis and is undetectable in stress-free cells. Despite evidence that the UPR operates in pro-survival mode in the secretory stage of amelogenesis, *Chop* expression was detected in secretory stage enamel organs of WT mice by quantitative PCR (Brookes et al., 2014) suggesting that even WT ameloblasts may be on their way toward an apoptotic end-point. It was not clear from this ensemble data whether the level of *Chop* expression represented relatively low level expression in all ameloblasts or whether it reflected relatively high expression in a sub-population of cells. Why is it that WT secretory ameloblasts do not succumb to apoptosis given that they appear to be expressing *Chop* especially as rodent WT ameloblasts have been described as "hard wired" for apoptosis (Joseph et al., 1999)? It has been proposed that activation of IGF-1 receptors, expressed by ameloblasts throughout amelogenesis, except for a short window during the transition from the secretory to maturation stage (Joseph et al., 1994), inhibits pro-apoptotic events by modulating BCL-2 and BAX or by directly inhibiting caspase 3 activation (Joseph et al., 1999). These events are downstream of CHOP (see **Figure 1**) so that even when CHOP is expressed, IGF-1 signaling may prevent the final commitment to apoptosis. Later work confirmed that IGF-1 receptor activation inhibits JNK and P38 MAPK activation (Galvan et al., 2003), both of which are involved in committing the cell to apoptosis by modulating BCL-2, BIM and BAX phosphorylation at a point downstream of CHOP expression (see **Figure 1**). We can therefore hypothesize that the UPR assists WT secretory ameloblasts to cope with their heavy secretory load but also primes the most stressed cells for apoptosis while IGF-1 signaling prevents the cells from taking the final steps that commit to apoptosis. An estimated 25% of ameloblasts abruptly succumb to apoptosis at the end of the secretory stage (Smith and Warshawsky, 1977). We hypothesize that the most stressed secretory stage ameloblasts are prevented from undergoing apoptosis by IGF-1 signaling during secretion, but, during the transition from secretion to maturation, when IGF-1 receptor expression ceases, the brake on apoptosis is released and pre-disposed ameloblasts rapidly undergo apoptosis. However, as IGF-1 receptor expression increases again once ameloblasts enter the maturation stage proper (Joseph et al., 1994), the brake on ameloblast apoptosis is re-applied. IGF-1 signaling also up-regulates the expression of the chaperone GRP78 independently of the UPR which enhances the folding capacity of the ER and provides additional protection against ER stress (Novosyadlyy et al., 2008). The importance of IGF-1 in amelogenesis is emphasized by the fact that ameloblasts express IGF-1 in addition to the IGF-1 receptor, establishing an autocrine signaling loop (Joseph et al., 1996).

Given that WT secretory ameloblasts are already using the UPR to help cope with ER stress generated by their demanding secretory function, the cells are already on a path that can lead to an apoptotic end-point. This raises the question as to whether there is a role for the ameloblast UPR where enamel matrix proteins (or others) are affected by genetic mutations and generate even more intense levels of ER stress. The net effects of the UPR in the presence of an enamel protein mutation may be relatively mild (e.g., due to reduced translation of enamel proteins) or more severe (e.g., due to ameloblast apoptosis). The next section will review the evidence that mutations in enamel matrix proteins can indeed cause AI driven by ER stress.

ER STRESS AND THE UPR AS AN ETIOLOGICAL FACTOR IN AI

Classically, AI has been approached from the perspective that mutations in genes encoding for secreted enamel matrix proteins

would impact on protein functionality and behavior within the extracellular matrix itself. For example, studies have shown that certain AMELX mutations can affect amelogenin self-assembly (Paine et al., 2002; Zhu et al., 2011) and the ability to adsorb onto hydroxyapatite and control crystal growth (Zhu et al., 2011). It is extremely likely therefore that dysfunction of mutated enamel proteins in the extracellular compartment can drive AI. However, in recent years it has become clear that in some specific cases, AI may be associated with the intracellular phenomenon of ameloblast ER stress and UPR activation.

The first evidence that ER stress could drive AI came from detailed phenotyping of a mouse model exhibiting an $Amelx^{p.(Y64H)}$ mutation (Barron et al., 2010; Brookes et al., 2014). More recently mouse $Enam^{p.(S55I)}$ and human $ENAM^{p.(L31R)}$ mutations have also been associated with ameloblast ER stress (Brookes et al., 2017). ENAM is expressed at very low levels compared to AMELX and is biochemically distinct—in mice being over seven times the molecular weight of AMELX and more basic in nature (Hu et al., 1998). The two proteins may have originated from a common ancestral gene (Sire et al., 2006) but no longer share sequence homology, suggesting divergent functional roles. It is therefore somewhat surprising that enamel from female mice heterozygous for $Amelx^{p.(Y64H)}$ (there is no AMELY transcript in rodents) closely phenocopies mice heterozygous for $Enam^{p.(S55I)}$.

Incisor enamel from heterozygous mice of both genotypes revealed an unusual phenotype in which the first 30–50 μm of initially secreted incisor enamel (i.e., the inner enamel adjacent to the dentine) exhibited the decussating prismatic structure characteristic of WT rodent incisor enamel but this was overlaid with subsequently secreted, structurally abnormal, aprismatic enamel (Brookes et al., 2014, 2017). This shared structural phenotype suggests a common underlying etiology despite the presumed functional differences between AMELX and ENAM. Secretory-stage ameloblasts of both genotypes exhibited abnormal retention of enamel matrix proteins, indicating a compromised secretory pathway. Notably, ameloblasts in both $Amelx^{p.(Y64H)}$ and $Enam^{p.(S55I)}$ animals showed a clear upregulation of markers indicative of ER stress and an activated UPR (e.g., *Grp78, Xbp1, Grp94,* and *Atf4*). During the early secretion stage, ameloblasts in affected mice were present as an ordered monolayer characteristic of WT animals and produced a structurally normal inner layer of enamel. However, in the later stages of secretion, the ameloblast monolayer became more disorganized, coincident with the loss of normal prismatic structure. These observations were interpreted in terms of the UPR initially acting in pro-survival mode, which maintained a functional ameloblast monolayer and allowed the cells to produce a structurally normal initial layer of enamel in both mutant genotypes. However, as the UPR signal evolved, ameloblasts from female mice expressing the $Amelx^{p.(Y64H)}$ (comprising ∼50% of the total ameloblast population due to random X-chromosome deactivation) were directed toward apoptosis as evidenced by increased *Chop* expression, which severely disrupted the ameloblast monolayer leading to the production of structurally abnormal enamel. In contrast, *Chop* expression in enamel organs from mice heterozygous for $Enam^{p.(S55I)}$ remained at WT levels and it was assumed that the evolving UPR in these animals was up-regulated but failed to reach the tipping point required to trigger apoptosis. Nevertheless, the response was evidently sufficient to compromise the integrity of the ameloblast monolayer which resulted in the production of a structurally abnormal outer layer of enamel. This section is summarized in **Figure 2**.

Secretory stage ameloblasts in hemizygous male mice carrying the $Amelx^{p.(Y64H)}$ mutation and mice homozygous for $Enam^{p.(S55I)}$ exhibited increased expression of the pro-apoptotic transcription factor *Chop* compared to WT animals. Animals of both mutant genotypes did not produce a recognizable enamel layer. The failure to produce any enamel may have been related to the fact that the UPR evolved more quickly away from a pro-survival mode. However, another possibility is that insufficient mutated AMELX or ENAM molecules were secreted into the matrix to support amelogenesis and even if they were, the mutation could have impacted on their extracellular function.

What about the anti-apoptotic role of IGF-1 in these animals, which should be unaffected by mutations in the *Amelx* and *Enam* genes? We can only assume that if the ER stress reaches a critical intensity, the UPR can circumvent the "protection" provided by IGF-1 receptor signaling. The details of how this can be achieved are unclear but it may be simply due to the significant increase in *Chop* expression in the presence of a mutation that overcomes the anti-apoptotic effects of IGF-1 receptor signaling.

Finally, is there any evidence that ER stress and the UPR are etiological factors in human AI? It is virtually impossible to study amelogenesis in humans due to the obvious issues in obtaining fresh tooth germs to study. However, due to the incremental nature of enamel secretion, mature enamel can provide a temporal record of events that occur during amelogenesis. This is exemplified by the enamel phenotype for mice heterozygous for $Amelx^{p.(Y64H)}$ and $Enam^{p.(S55I)}$ described above. A similar enamel phenotype was recently described in teeth obtained from an AI patient heterozygous for an $ENAM^{p.(L31R)}$ mutation. The mature enamel phenotype from the patient's exfoliated teeth exhibited the same layer of structurally normal inner enamel overlaid by a subsequently secreted, structurally abnormal enamel outer layer (Brookes et al., 2017) comparable to that described in the mouse models. This is not unequivocal evidence that the UPR was responsible for AI in this patient but the developmental record remaining in the enamel indicates that ameloblast function was severely affected after an initial period of near-normal secretory activity, reminiscent of an evolving UPR.

THE ROLE OF THE UPR IN THE PATHOBIOLOGY OF FLUOROSIS

Early indications that excess fluoride may trigger an ER stress–like response in ameloblasts were provided by histological reports suggesting that fluoride disturbs ameloblast intracellular protein trafficking (Matsuo et al., 1996), including the retention of ER cargo and the appearance of a dilated ER (Hassunuma

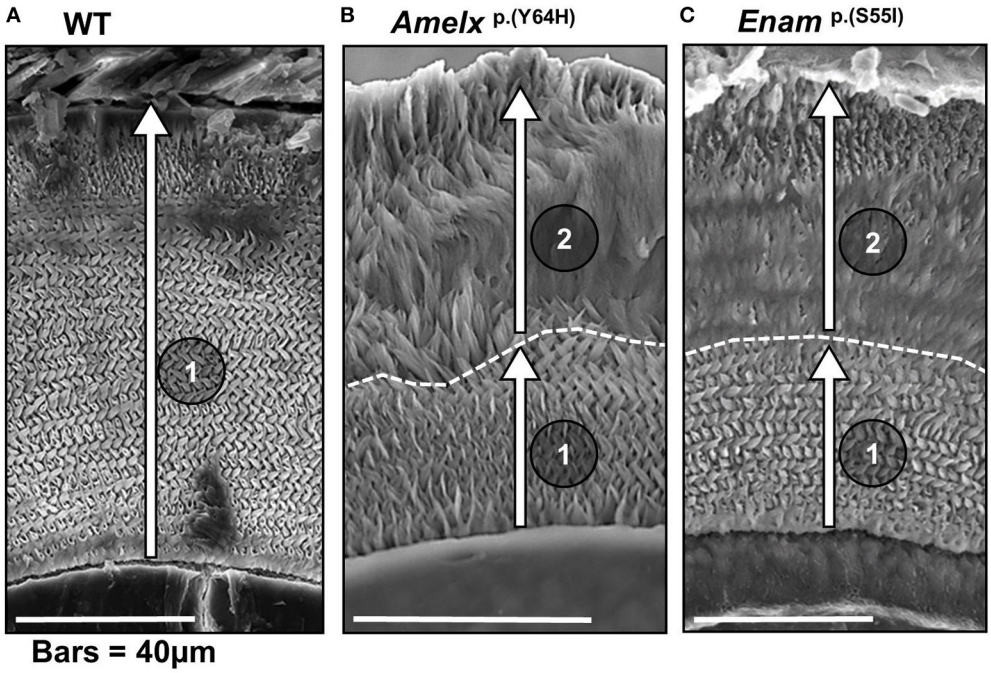

FIGURE 2 | Scanning electron micrographs of transverse sections through mandibular incisors of **(A)** WT mice, **(B)** mice heterozygous for the *Amelx* $^{p.Y64H}$ mutation and **(C)** mice heterozygous for the *Enam*$^{p.S55I}$ mutation at or near the point of eruption (previously reported by Brookes et al., 2014, 2017). **(A)** The incremental secretion of the inner enamel (in the direction indicated by arrow 1) by WT ameloblasts produces the decussating prismatic architecture characteristic of rodent enamel. **(B)** In mice heterozygous for Amelx$^{p.Y64H}$, the ameloblasts begin the incremental secretion of an apparently structurally normal layer of enamel (arrow 1). However, after about 40 μm of enamel is secreted, the ameloblasts continue to secrete enamel (arrow 2) but they lose the ability to produce the characteristic decussating prismatic architecture. **(C)** In mice heterozygous for Enam$^{p.S55I}$, the ameloblasts similarly secrete a structurally normal layer initially (arrow 1) but enamel secreted thereafter is structurally abnormal (arrow 2). We hypothesize that the UPR, initially acting in pro-survival mode, supports normal ameloblast function and allows the ameloblasts to produce an inner layer of decussating enamel. Later, the UPR switches to a more draconian mode and ameloblast function is perturbed resulting in the secretion of structurally abnormal outer layer of enamel. The dotted line marks demarcation between the inner decussating and outer non-decussating enamel. **(B,C)** were derived under Creative Commons CC BY licenses 3.0 and 4.0 (https://creativecommons.org/licenses/) respectively from: Brookes et al. (2014), and phenotypic rescue using 4-phenylbutyrate; and Brookes et al. (2017). Both published by Oxford University press.

et al., 2007). These observations are consistent with ameloblasts suffering ER stress but the up-regulation of UPR components provides unequivocal evidence that the UPR is associated with the ameloblast response to fluoride. The first such evidence suggested that fluoride promoted IRE1 activation in maturation stage ameloblasts *in vivo* and up-regulated *BiP (Grp78)*, *Xbp-1,* and *Chop* expression in the LS8 ameloblast cell line (Kubota et al., 2005). The notion that fluoride may impair protein secretion was further supported when LS8 cells were transfected with secreted alkaline phosphatase. Fluoride decreased the secretion of the phosphatase in a dose-dependent manner while intracellular levels of phosphatase were concomitantly increased, along with increased levels of activated PERK, phosphorylated eIF2α, and BiP (GRP78) (Sharma et al., 2008). Later studies using LS8 cells additionally reported that the third stress sensor, ATF6, is also activated by fluoride (Wei et al., 2013). Increasing levels of phosphorylated eIF2α were also seen in maturation-stage ameloblasts in mice provided with increasing concentrations of fluoride in their drinking water (Sharma et al., 2008, 2010). However, no increase in levels of phosphorylated eIF2α was seen in secretory-stage ameloblasts exposed to fluoride in the same study. The differential effect of fluoride on secretory stage ameloblasts may be explained by the acid hypothesis for fluorosis, in which periodic falls in enamel matrix pH during the maturation stage (but not the secretory stage) lead to protonation of F^- to HF, which greatly increases its ability to diffuse across cell membranes and so enter the cytoplasm. At cytoplasmic pH, HF dissociates, resulting in a HF concentration gradient across the cell membrane. Trapped cytoplasmic F^- would then continue to accumulate intracellularly to levels that trigger a pathological response (Sharma et al., 2010).

The possibility that fluoride can disrupt the intracellular secretory pathway could lead us to conclude that this mechanism alone triggers the three UPR sensors. However, a known cytotoxic effect of fluoride is its ability to promote the accumulation of reactive oxygen species (ROS) by inhibiting free radical scavenging systems such as those based on glutathione peroxidase and superoxide dismutase (Chlubek, 2003). ROS are normally generated by a variety of cellular processes including mitochondrial electron transport and as a byproduct of disulfide bond formation in the lumen of the ER (Santos et al., 2009).

Inability to deal with ROS could lead to redox imbalance in the ER, a situation that can trigger the UPR via the three ER stress sensors and/or via ROS-promoted calcium efflux (Eletto et al., 2014). Evidence that fluoride triggers oxidative stress in ameloblasts was provided by the observation that UCP-2 (an electron transport uncoupler that provides an adaptive defense against oxidative stress; Moukdar et al., 2009), was up-regulated in mice drinking fluoridated water (Suzuki et al., 2014). These authors suggested that in addition to the effect of fluoride on the UPR in maturation stage ameloblasts, their function may be further compromised by energy deficiency caused by the impact of UCP-2 activity uncoupling electron transport from ATP synthesis which could impact on crucial maturation stage processes that require energy, such as the active transport of mineral ions.

Once activated, how does the UPR actually effect extracellular events in the maturation stage enamel matrix under fluorotic conditions? Fluorosis is associated with enamel hypomineralization and abnormal retention of secretory stage matrix proteins in maturation stage enamel, where they could then inhibit secondary crystal growth (Den Besten, 1986; Smith et al., 1993). Under normal circumstances, KLK4, secreted during the maturation stage, degrades residual secretory stage matrix proteins but fluoride does not directly inhibit either KLK4 or its activator proteases (including MMP20) (Tye et al., 2011). Instead, it appears that fluoride inhibits protein expression in maturation stage ameloblasts which reduces the amount of KLK4 available to degrade the residual secretory stage enamel matrix. As described previously, phosphorylation of eIF2α, by PERK during the UPR, decreases general protein translation (Section PERK) and its phosphorylation on exposure to fluoride in rat maturation stage ameloblasts was shown to downregulate KLK4 expression, whereas secretory stage expression of AMELX, AMBN, and MMP20 were unaffected (Sharma et al., 2010). This prompted the suggestion that fluoride reduced KLK4 expression and prevented the efficient degradation and removal of residual secretory stage matrix proteins leading to a pathological retention of protein in the maturation stage tissue. It has been suggested that enamel matrix proteins could have a higher affinity for fluorotic enamel crystals (Tanabe et al., 1988) which could further compromise the removal of residual matrix from maturation stage tissue where KLK4 levels are already depleted.

One final consideration in relation to fluorosis pathobiology and the role of the UPR is the potential effect of fluoride on the expression of IGF-1. Since anti-apoptotic IGF-1 signaling appears to be an important pathway in amelogenesis, it is interesting that when primary mouse osteoblast cultures were treated with fluoride, the resulting oxidative stress led to reduced IGF-1 expression and increased apoptosis (Wang et al., 2011). Maturation-stage ameloblasts undergo apoptosis under high fluoride regimes (Kubota et al., 2005) and it is possible that fluoride not only triggers an apoptotic UPR response but further enhances that response by simultaneously degrading the anti-apoptotic effects of IGF-1. This section is summarized in **Figure 3**.

TARGETING ER STRESS AND THE UPR AS A THERAPEUTIC INTERVENTION IN ENAMEL PATHOLOGIES

ER stress and an up-regulated UPR are now recognized as etiological factors in numerous serious human diseases (Oakes and Papa, 2015). Collectively, these diseases can be classed as proteopathies, or conformational diseases, where protein misfolding and aggregation causes loss of ER homeostasis leading to

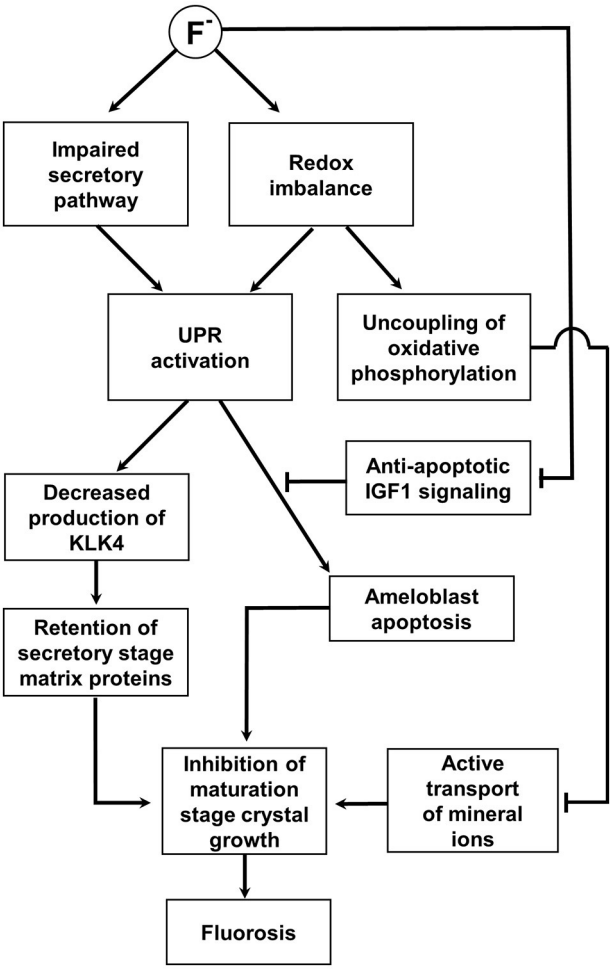

FIGURE 3 | Schematic diagram summarizing the hypothesized role of the UPR in fluorosis as described in the text. This impairs the secretory pathway and promotes a redox imbalance; both can potentially activate the UPR. The UPR decreases the production of KLK4 and degradation and removal of the secretory stage matrix is compromised. Retention of the secretory matrix then inhibits maturation stage crystal growth. In addition, mitochondrial oxidative phosphorylation is uncoupled from electron transport in an attempt to restore redox balance. The resulting reduction in ATP synthesis would limit the active transport of mineral ions into the matrix further compromising maturation stage crystal growth. A severe fluoride challenge induces apoptosis and it is hypothesized that this would be mediated by the UPR. Apoptotic signaling under these circumstances may well be unchecked by anti-apoptotic IGF1 signaling as IGF1 expression is reduced by fluoride. See main text for references.

an up-regulated UPR. Much work is ongoing to find therapeutic strategies to combat proteopathic disease. In general, this is based on identifying molecules (synthetic chaperones) that can prevent protein mis-folding and restore normal protein trafficking, prevent mis-folded proteins activating the three transmembrane ER stress sensors or modulate the UPR to inhibit apoptosis. A typical example where ER stress has been targeted therapeutically is progressive familial intrahepatic cholestasis type 2 caused by a p.T1210P mutation in the canalicular bile salt export pump (BSEP). In cultured cells transfected with $BSEP^{p.T1210P}$, the BSEP $^{p.T1210P}$ protein was retained in the ER, impeding its transportation to the canalicular membrane. Addition of the synthetic chaperone, 4-phenylbutyrate (4-PB), partially corrected the situation. A child homozygous for the $BSEP^{p.T1210P}$ mutation was treated with oral 4-PB with a subsequent improvement in liver function and partial restoration of biliary bile acid secretion. In this case, it appeared that 4-PB restored the trafficking of the mutated bile salt export pump to the canalicular membrane, where, despite the mutation, it was still functional to some degree. Restoring ER trafficking in this case allowed the mutated protein to escape the ERAD system (Gonzales et al., 2012). 4-PB was also able to prevent the aggregation of four different myocilin mutants in the ER of transfected cells and restore the secretion of mutant myocilin. This rescued the cell from ER stress and significantly reduced apoptosis in the transfected cells, leading the authors to propose that 4-PB could be used as a therapeutic agent to treat blindness causing primary open-angle glaucoma (Yam et al., 2007). Topical application of 4-PB eye drops in mice was later shown to restore the secretion of mutant myocilin and return intraocular pressure to WT levels (Zode et al., 2012). In addition to its ability to interact with mis-folded or aggregated proteins in the ER lumen, 4-PB can also influence gene expression by its activity as a histone deacetylase inhibitor that also inhibits the deacetylation of a range of transcription factors, including NF–κβ. This in turn indirectly affects the expression of numerous target genes including those associated with the anti-apoptotic response (Ryu et al., 2005). In short, 4-PB can influence the transcription of wide range of genes by influencing the epigenetic control of gene expression and the covalent regulation of transcription factor activity. This may explain its reported ability to moderate the UPR and UPR-mediated apoptosis (Vilatoba et al., 2005; Basseri et al., 2009; Yue et al., 2016).

Despite this, the specific cellular response to 4-PB depends on cell context. For example, 4-PB can be pro-apoptotic in myeloid leukemia cells (DiGiuseppe et al., 1999) and prostate cancer cells (Melchior et al., 1999). The question as to whether 4-PB might have therapeutic value in treating AI was investigated when female mice heterozygous for the $Amelx^{p.(Y64H)}$ mutation were fed 4-PB in their diet. A dramatic rescue of the AI phenotype resulted (Brookes et al., 2014). In this context, 4-PB did not restore AMELX secretion as might be expected were it to be acting as a synthetic chaperone. Instead, 4-PB appeared to inhibit apoptosis in the 50% of ameloblasts expressing $Amelx^{p.(Y64H)}$. This presumably allowed the remaining ameloblasts expressing WT AMELX to complete amelogenesis. It is possible that AMELX synthesis and secretion was increased in the unaffected ameloblasts and that this compensated for the fact that only half the ameloblasts were secreting matrix.

It is currently unknown whether or not 4-PB treatment can rescue the enamel phenotype in cases of AI other than that in female mice heterozygous for the $Amelx^{p.(Y64H)}$ mutation. However, restoring a stalled secretory pathway or inhibiting the pro-apoptotic actions of the UPR will not rescue the phenotype if the mutated protein in question is dysfunctional when it is secreted into the extracellular matrix.

The suggestion that 4-PB is anti-apoptotic in stressed ameloblasts is further supported by the report that apoptosis triggered by exposure to fluoride in an ameloblast-derived cell line was inhibited by 4-PB, resulting in an anti-apoptotic BCL2/BAX ratio (Suzuki et al., 2017). However, 4-PB was unable to completely prevent fluorosis in mice drinking fluoridated water though it did improve some aspects of the condition compared to control animals who did not receive 4-PB. The failure of 4-PB to rescue fluorosis could be explained if its effect was limited to inhibiting apoptosis whilst having no influence over the effect of fluoride in downregulating KLK4 expression.

An alternative option to treat fluorosis would be to target the oxidative stress that is triggering the UPR in the first place. Numerous studies have shown that antioxidants can counter the oxidative damage caused by fluoride in bone and soft tissues. For example, fisetin, an anti-oxidant polyphenol flavonoid, protects against fluoride-induced oxidative damage in osteoblast cell lines (Inkielewicz-Stepniak et al., 2012) and pretreating rats with the flavonoid silymarin protected against fluoride-induced oxidative stress in the brain. In the case of enamel, Suzuki et al. (2014) reported that a diet enriched with the antioxidant vitamin E had no protective effect against enamel fluorosis in mice drinking 50 ppm fluoride. More recently, it was reported that the antioxidant carotenoid lycopene inhibited fluoride induced ameloblast apoptosis and enamel fluorosis in rats by combating oxidative stress (Li et al., 2017). However, the efficacy of such agents against enamel fluorosis in humans remains unknown.

FUTURE PERSPECTIVE

The phenotypic rescue of female mice heterozygous for $Amelx^{p.(Y64H)}$ proves the principle that AI driven by ER stress and a pro-apoptotic UPR can be treated therapeutically with 4-PB. 4-PB is an approved therapeutic for urea cycle disorders. Acting as an excretable ammonium scavenger, 4-PB is administered orally in high doses from birth. However, 4-PB is contraindicated during pregnancy and so its therapeutic value would be restricted to protecting those permanent teeth whose enamel begins to mineralize after birth.

Clearly, more research is required using relevant mouse models to establish how common ER stress is as an etiological factor in human AI and how appropriate is targeting ER stress and the UPR as a treatment option. There are numerous other compounds under investigation for their therapeutic potential in terms of influencing folding of mutated proteins, inhibiting aggregation of mutated proteins and modulating the UPR. (Schonthal, 2012; Denny et al., 2013) and these may be more

effective than 4-PB for treating specific cases of AI depending on the mutation involved. To treat AI in patients with such compounds, it would first be necessary to establish that ER stress was involved in the etiology in each case and then identify the most effective therapeutic agent able to combat the effects of the specific mutation involved in a personalized medicine approach using cell models.

In summary, ER stress and the UPR play an important role in maintaining ameloblast function and proteostasis under high secretory load during amelogenesis. We also know that it plays a role in the etiology of enamel pathology, and that, at least in some cases, AI can now be added to the growing list of proteopathic diseases. Proteopathies include several of the major diseases of our age and there is intense research underway to identify compounds of therapeutic value. It is an exciting possibility that anti-proteopathic drugs may provide an effective treatment option in amenable cases of AI. Fluorosis is not a classic proteopathic disease but the etiological involvement of the UPR raises the possibility that drugs that can modulate the UPR, or control the oxidative stress triggering the UPR, may be of therapeutic value in areas where fluorosis is endemic.

AUTHOR CONTRIBUTIONS

SB, MB, MD, and JK contributed to the writing of the manuscript and its final approval. All authors agree to be accountable for all aspects of the work in ensuring that questions related to the accuracy or integrity of any part of the work are appropriately investigated and resolved.

FUNDING

We acknowledge the support of the Wellcome Trust (Grant no. 075945).

REFERENCES

Barron, M. J., Brookes, S. J., Kirkham, J., Shore, R. C., Hunt, C., Mironov, A., et al. (2010). A mutation in the mouse Amelx tri-tyrosyl domain results in impaired secretion of amelogenin and phenocopies human X-linked amelogenesis imperfecta. *Hum. Mol. Genet.* 19, 1230–1247. doi: 10.1093/hmg/ddq001

Bartlett, J. D. (2013). Dental enamel development: proteinases and their enamel matrix substrates. *ISRN Dent.* 2013:684607. doi: 10.1155/2013/684607

Basseri, S., Lhotak, S., Sharma, A. M., and Austin, R. C. (2009). The chemical chaperone 4-phenylbutyrate inhibits adipogenesis by modulating the unfolded protein response. *J. Lipid Res.* 50, 2486–2501. doi: 10.1194/jlr.M900216-JLR200

Brookes, S. J., Barron, M. J., Boot-Handford, R., Kirkham, J., and Dixon, M. J. (2014). Endoplasmic reticulum stress in amelogenesis imperfecta and phenotypic rescue using 4-phenylbutyrate. *Hum. Mol. Genet.* 23, 2468–2480. doi: 10.1093/hmg/ddt642

Brookes, S. J., Barron, M. J., Smith, C. E. L., Poulter, J. A., Mighell, A. J., Inglehearn, C. F., et al. (2017). Amelogenesis imperfecta caused by N-terminal enamelin point mutations in mice and men is driven by endoplasmic reticulum stress. *Hum. Mol. Genet.* 26, 1863–1876. doi: 10.1093/hmg/ddx090

Brookes, S. J., Lyngstadaas, S. P., Robinson, C., Shore, R. C., and Kirkham, J. (2006). Intracellular nanosphere subunit assembly as revealed by amelogenin molecular cross-linking studies. *Eur. J. Oral Sci.* 114(Suppl. 1), 280–284. discussion: 285–286, 382. doi: 10.1111/j.1600-0722.2006.00311.x

Brookes, S. J., Robinson, C., Kirkham, J., and Bonass, W. A. (1995). Biochemistry and molecular biology of amelogenin proteins of developing dental enamel. *Arch. Oral Biol.* 40, 1–14. doi: 10.1016/0003-9969(94)00135-X

Chen, Y., and Brandizzi, F. (2013). IRE1: ER stress sensor and cell fate executor. *Trends Cell Biol.* 23, 547–555. doi: 10.1016/j.tcb.2013.06.005

Chlubek, D. (2003). Fluoride and oxidative stress. *Fluoride.* 36, 217–228. Available online at: http://www.fluorideresearch.org/364/files/FJ2003_v36_n4_p217-228.pdf

Coelho, D. S., and Domingos, P. M. (2014). Physiological roles of regulated Ire1 dependent decay. *Front. Genet.* 5:76. doi: 10.3389/fgene.2014.00076

Credle, J. J., Finer-Moore, J. S., Papa, F. R., Stroud, R. M., and Walter, P. (2005). On the mechanism of sensing unfolded protein in the endoplasmic reticulum. *Proc. Natl. Acad. Sci. U.S.A.* 102, 18773–18784. doi: 10.1073/pnas.0509487102

Den Besten, P. K. (1986). Effects of fluoride on protein secretion and removal during enamel development in the rat. *J. Dent. Res.* 65, 1272–1277. doi: 10.1177/00220345860650101401

Denny, R. A., Gavrin, L. K., and Saiah, E. (2013). Recent developments in targeting protein misfolding diseases. *Bioorg. Med. Chem. Lett.* 23, 1935–1944. doi: 10.1016/j.bmcl.2013.01.089

Dey, S., Baird, T. D., Zhou, D., Palam, L. R., Spandau, D. F., and Wek, R. C. (2010). Both transcriptional regulation and translational control of ATF4 are central to the integrated stress response. *J. Biol. Chem.* 285, 33165–33174. doi: 10.1074/jbc.M110.167213

DiGiuseppe, J. A., Weng, L. J., Yu, K. H., Fu, S., Kastan, M. B., Samid, D., et al. (1999). Phenylbutyrate-induced G1 arrest and apoptosis in myeloid leukemia cells: structure-function analysis. *Leukemia* 13, 1243–1253. doi: 10.1038/sj.leu.2401471

Dobson, C. M. (2003). Protein folding and misfolding. *Nature* 426, 884–890. doi: 10.1038/nature02261

Eletto, D., Chevet, E., Argon, Y., and Appenzeller-Herzog, C. (2014). Redox controls UPR to control redox. *J. Cell Sci.* 127(Pt 17), 3649–3658. doi: 10.1242/jcs.153643

Fava, L. L., Bock, F. J., Geley, S., and Villunger, A. (2012). Caspase-2 at a glance. *J. Cell Sci.* 125(Pt 24), 5911–5915. doi: 10.1242/jcs.115105

Fribley, A., Zhang, K., and Kaufman, R. J. (2009). Regulation of apoptosis by the unfolded protein response. *Methods Mol. Biol.* 559, 191–204. doi: 10.1007/978-1-60327-017-5_14

Galvan, V., Logvinova, A., Sperandio, S., Ichijo, H., and Bredesen, D. E. (2003). Type 1 insulin-like growth factor receptor (IGF-IR) signaling inhibits apoptosis signal-regulating kinase 1 (ASK1). *J. Biol. Chem.* 278, 13325–13332. doi: 10.1074/jbc.M211398200

Gardner, B. M., and Walter, P. (2011). Unfolded proteins are Ire1-activating ligands that directly induce the unfolded protein response. *Science* 333, 1891–1894. doi: 10.1126/science.1209126

Gonzales, E., Grosse, B., Cassio, D., Davit-Spraul, A., Fabre, M., and Jacquemin, E. (2012). Successful mutation-specific chaperone therapy with 4-phenylbutyrate in a child with progressive familial intrahepatic cholestasis type 2. *J. Hepatol.* 57, 695–698. doi: 10.1016/j.jhep.2012.04.017

Gregersen, N., Bross, P., Vang, S., and Christensen, J. H. (2006). Protein misfolding and human disease. *Annu. Rev. Genomics Hum. Genet.* 7, 103–124. doi: 10.1146/annurev.genom.7.080505.115737

Han, D., Lerner, A. G., Vande Walle, L., Upton, J. P., Xu, W., Hagen, A., et al. (2009). IRE1alpha kinase activation modes control alternate endoribonuclease outputs to determine divergent cell fates. *Cell* 138, 562–575. doi: 10.1016/j.cell.2009.07.017

Harding, H. P., Zhang, Y., Bertolotti, A., Zeng, H., and Ron, D. (2000). Perk is essential for translational regulation and cell survival during the unfolded protein response. *Mol. Cell.* 5, 897–904. doi: 10.1016/S1097-2765(00)80330-5

Hassunuma, R. M., Zen Filho, E. V., Ceolin, D. S., Cestari, T. M., Taga, R., and de Assis, G. F. (2007). Ultrastructural and immunohistochemical study of the influence of fluoride excess on the development of rat incisor tooth buds. *J. Appl. Oral Sci.* 15, 292–298. doi: 10.1590/S1678-77572007000400010

Hetz, C. (2012). The unfolded protein response: controlling cell fate decisions under ER stress and beyond. *Nat. Rev. Mol. Cell Biol.* 13, 89–102. doi: 10.1038/nrm3270

Hetz, C., Chevet, E., and Oakes, S. A. (2015). Proteostasis control by the unfolded protein response. *Nat. Cell Biol.* 17, 829–838. doi: 10.1038/ncb3184

Hetz, C., Martinon, F., Rodriguez, D., and Glimcher, L. H. (2011). The unfolded protein response: integrating stress signals through the stress sensor IRE1alpha. *Physiol. Rev.* 91, 1219–1243. doi: 10.1152/physrev.00001.2011

Hollien, J., and Weissman, J. S. (2006). Decay of endoplasmic reticulum-localized mRNAs during the unfolded protein response. *Science* 313, 104–107. doi: 10.1126/science.1129631

Hu, C. C., Simmer, J. P., Bartlett, J. D., Qian, Q., Zhang, C., Ryu, O. H., et al. (1998). Murine enamelin: cDNA and derived protein sequences. *Connect. Tissue Res.* 39, 47–61. discussion: 63–47. doi: 10.3109/03008209809023911

Inkielewicz-Stepniak, I., Radomski, M. W., and Wozniak, M. (2012). Fisetin prevents fluoride- and dexamethasone-induced oxidative damage in osteoblast and hippocampal cells. *Food Chem. Toxicol.* 50, 583–589. doi: 10.1016/j.fct.2011.12.015

Iwasaki, K., Bajenova, E., Somogyi-Ganss, E., Miller, M., Nguyen, V., Nourkeyhani, H., et al. (2005). Amelotin–a novel secreted, ameloblast-specific protein. *J. Dent. Res.* 84, 1127–1132. doi: 10.1177/154405910508401207

Joseph, B. K., Harbrow, D. J., Sugerman, P. B., Smid, J. R., Savage, N. W., and Young, W. G. (1999). Ameloblast apoptosis and IGF-1 receptor expression in the continuously erupting rat incisor model. *Apoptosis.* 4, 441–447. doi: 10.1023/A:1009600409421

Joseph, B. K., Savage, N. W., Daley, T. J., and Young, W. G. (1996). *In situ* hybridization evidence for a paracrine/autocrine role for insulin-like growth factor-I in tooth development. *Growth Factors.* 13, 11–17. doi: 10.3109/08977199609034563

Joseph, B. K., Savage, N. W., Young, W. G., and Waters, M. J. (1994). Insulin-like growth factor-I receptor in the cell biology of the ameloblast: an immunohistochemical study on the rat incisor. *Epithelial Cell Biol.* 3, 47–53.

Kim, B. J., Ryu, S. W., and Song, B. J. (2006). JNK- and p38 kinase-mediated phosphorylation of Bax leads to its activation and mitochondrial translocation and to apoptosis of human hepatoma HepG2 cells. *J. Biol. Chem.* 281, 21256–21265. doi: 10.1074/jbc.M510644200

Kimata, Y., Oikawa, D., Shimizu, Y., Ishiwata-Kimata, Y., and Kohno, K. (2004). A role for BiP as an adjustor for the endoplasmic reticulum stress-sensing protein Ire1. *J. Cell Biol.* 167, 445–456. doi: 10.1083/jcb.200405153

Kopito, R. R., and Ron, D. (2000). Conformational disease. *Nat. Cell Biol.* 2, E207–E209. doi: 10.1038/35041139

Kubota, K., Lee, D. H., Tsuchiya, M., Young, C. S., Everett, E. T., Martinez-Mier, E. A., et al. (2005). Fluoride induces endoplasmic reticulum stress in ameloblasts responsible for dental enamel formation. *J. Biol. Chem.* 280, 23194–23202. doi: 10.1074/jbc.M503288200

Lacruz, R. S., Brookes, S. J., Wen, X., Jimenez, J. M., Vikman, S., Hu, P., et al. (2013). Adaptor protein complex 2-mediated, clathrin-dependent endocytosis, and related gene activities, are a prominent feature during maturation stage amelogenesis. *J. Bone Miner. Res.* 28, 672–687. doi: 10.1002/jbmr.1779

Lakshminarayanan, R., Bromley, K. M., Lei, Y. P., Snead, M. L., and Moradian-Oldak, J. (2010). Perturbed amelogenin secondary structure leads to uncontrolled aggregation in amelogenesis imperfecta mutant proteins. *J. Biol. Chem.* 285, 40593–40603. doi: 10.1074/jbc.M110.131136

Lee, A. H., Iwakoshi, N. N., and Glimcher, L. H. (2003). XBP-1 regulates a subset of endoplasmic reticulum resident chaperone genes in the unfolded protein response. *Mol. Cell. Biol.* 23, 7448–7459. doi: 10.1128/MCB.23.21.7448-7459.2003

Li, W., Jiang, B., Cao, X., Xie, Y., and Huang, T. (2017). Protective effect of lycopene on fluoride-induced ameloblasts apoptosis and dental fluorosis through oxidative stress-mediated Caspase pathways. *Chem. Biol. Interact.* 261, 27–34. doi: 10.1016/j.cbi.2016.11.021

Li, Y., Guo, Y., Tang, J., Jiang, J., and Chen, Z. (2014). New insights into the roles of CHOP-induced apoptosis in ER stress. *Acta Biochim. Biophys. Sin.* 46, 629–640. doi: 10.1093/abbs/gmu048

Lin, J. H., Walter, P., and Yen, T. S. (2008). Endoplasmic reticulum stress in disease pathogenesis. *Annu. Rev. Pathol.* 3, 399–425. doi: 10.1146/annurev.pathmechdis.3.121806.151434

Malhotra, J. D., and Kaufman, R. J. (2007a). The endoplasmic reticulum and the unfolded protein response. *Semin. Cell Dev. Biol.* 18, 716–731. doi: 10.1016/j.semcdb.2007.09.003

Malhotra, J. D., and Kaufman, R. J. (2007b). Endoplasmic reticulum stress and oxidative stress: a vicious cycle or a double-edged sword? *Antioxid. Redox Signal.* 9, 2277–2293. doi: 10.1089/ars.2007.1782

Matsuo, S., Inai, T., Kurisu, K., Kiyomiya, K., and Kurebe, M. (1996). Influence of fluoride on secretory pathway of the secretory ameloblast in rat incisor tooth germs exposed to sodium fluoride. *Arch. Toxicol.* 70, 420–429. doi: 10.1007/s002040050294

Melchior, S. W., Brown, L. G., Figg, W. D., Quinn, J. E., Santucci, R. A., Brunner, J., et al. (1999). Effects of phenylbutyrate on proliferation and apoptosis in human prostate cancer cells *in vitro* and *in vivo*. *Int. J. Oncol.* 14, 501–508. doi: 10.3892/ijo.14.3.501

Moore, K. A., and Hollien, J. (2012). The unfolded protein response in secretory cell function. *Annu. Rev. Genet.* 46, 165–183. doi: 10.1146/annurev-genet-110711-155644

Moore, K., and Hollien, J. (2015). Ire1-mediated decay in mammalian cells relies on mRNA sequence, structure, and translational status. *Mol. Biol. Cell.* 26, 2873–2884. doi: 10.1091/mbc.E15-02-0074

Moradian-Oldak, J. (2012). Protein-mediated enamel mineralization. *Front. Biosci.* 17, 1996–2023. doi: 10.2741/4034

Moukdar, F., Robidoux, J., Lyght, O., Pi, J., Daniel, K. W., and Collins, S. (2009). Reduced antioxidant capacity and diet-induced atherosclerosis in uncoupling protein-2-deficient mice. *J. Lipid Res.* 50, 59–70. doi: 10.1194/jlr.M800273-JLR200

Nishio, C., Wazen, R., Kuroda, S., Moffatt, P., and Nanci, A. (2010). Expression pattern of odontogenic ameloblast-associated and amelotin during formation and regeneration of the junctional epithelium. *Eur. Cell. Mater.* 20, 393–402. doi: 10.22203/eCM.v020a32

Nomura, M., Shimizu, S., Ito, T., Narita, M., Matsuda, H., and Tsujimoto, Y. (1999). Apoptotic cytosol facilitates Bax translocation to mitochondria that involves cytosolic factor regulated by Bcl-2. *Cancer Res.* 59, 5542–5548.

Novosyadlyy, R., Kurshan, N., Lann, D., Vijayakumar, A., Yakar, S., and LeRoith, D. (2008). Insulin-like growth factor-I protects cells from ER stress-induced apoptosis via enhancement of the adaptive capacity of endoplasmic reticulum. *Cell Death Differ.* 15, 1304–1317. doi: 10.1038/cdd.2008.52

Oakes, S. A., and Papa, F. R. (2015). The role of endoplasmic reticulum stress in human pathology. *Annu. Rev. Pathol.* 10, 173–194. doi: 10.1146/annurev-pathol-012513-104649

Ow, Y. P., Green, D. R., Hao, Z., and Mak, T. W. (2008). Cytochrome c: functions beyond respiration. *Nat. Rev. Mol. Cell Biol.* 9, 532–542. doi: 10.1038/nrm2434

Ozcan, L., and Tabas, I. (2012). Role of endoplasmic reticulum stress in metabolic disease and other disorders. *Annu. Rev. Med.* 63, 317–328. doi: 10.1146/annurev-med-043010-144749

Paine, M. L., Lei, Y. P., Dickerson, K., and Snead, M. L. (2002). Altered amelogenin self-assembly based on mutations observed in human X-linked amelogenesis imperfecta (AIH1). *J. Biol. Chem.* 277, 17112–17116. doi: 10.1074/jbc.M110473200

Prischi, F., Nowak, P. R., Carrara, M., and Ali, M. M. (2014). Phosphoregulation of Ire1 RNase splicing activity. *Nat. Commun.* 5:3554. doi: 10.1038/ncomms4554

Puthalakath, H., O'Reilly, L. A., Gunn, P., Lee, L., Kelly, P. N., Huntington, N. D., et al. (2007). ER stress triggers apoptosis by activating BH3-only protein Bim. *Cell* 129, 1337–1349. doi: 10.1016/j.cell.2007.04.027

Reith, E. J. (1961). The ultrastructure of ameloblasts during matrix formation and the maturation of enamel. *J. Biophys. Biochem. Cytol.* 9, 825–839. doi: 10.1083/jcb.9.4.825

Ron, D., and Walter, P. (2007). Signal integration in the endoplasmic reticulum unfolded protein response. *Nat. Rev. Mol. Cell Biol.* 8, 519–529. doi: 10.1038/nrm2199

Rutkowski, D. T., Arnold, S. M., Miller, C. N., Wu, J., Li, J., Gunnison, K. M., et al. (2006). Adaptation to ER stress is mediated by differential stabilities of pro-survival and pro-apoptotic mRNAs and proteins. *PLoS Biol.* 4:e374. doi: 10.1371/journal.pbio.0040374

Ryu, H., Smith, K., Camelo, S. I., Carreras, I., Lee, J., Iglesias, A. H., et al. (2005). Sodium phenylbutyrate prolongs survival and regulates expression of anti-apoptotic genes in transgenic amyotrophic lateral sclerosis mice. *J. Neurochem.* 93, 1087–1098. doi: 10.1111/j.1471-4159.2005.03077.x

Santos, C. X., Tanaka, L. Y., Wosniak, J., and Laurindo, F. R. (2009). Mechanisms and implications of reactive oxygen species generation during the unfolded protein response: roles of endoplasmic reticulum oxidoreductases, mitochondrial electron transport, and NADPH oxidase. *Antioxid. Redox Signal.* 11, 2409–2427. doi: 10.1089/ars.2009.2625

Schonthal, A. H. (2012). Endoplasmic reticulum stress: its role in disease and novel prospects for therapy. *Scientifica* 2012:857516. doi: 10.6064/2012/857516

Schroder, M., and Kaufman, R. J. (2005). ER stress and the unfolded protein response. *Mutat. Res.* 569, 29–63. doi: 10.1016/j.mrfmmm.2004.06.056

Schubert, U., Anton, L. C., Gibbs, J., Norbury, C. C., Yewdell, J. W., and Bennink, J. R. (2000). Rapid degradation of a large fraction of newly synthesized proteins by proteasomes. *Nature* 404, 770–774. doi: 10.1038/35008096

Selkoe, D. J. (2003). Folding proteins in fatal ways. *Nature* 426, 900–904. doi: 10.1038/nature02264

Sharma, R., Tsuchiya, M., and Bartlett, J. D. (2008). Fluoride induces endoplasmic reticulum stress and inhibits protein synthesis and secretion. *Environ. Health Perspect.* 116, 1142–1146. doi: 10.1289/ehp.11375

Sharma, R., Tsuchiya, M., Skobe, Z., Tannous, B. A., and Bartlett, J. D. (2010). The acid test of fluoride: how pH modulates toxicity. *PLoS ONE* 5:e10895. doi: 10.1371/journal.pone.0010895

Sire, J. Y., Delgado, S., and Girondot, M. (2006). The amelogenin story: origin and evolution. *Eur. J. Oral Sci.* 114(Suppl. 1), 64–77. discussion: 93–65, 379–380. doi: 10.1111/j.1600-0722.2006.00297.x

Smith, C. E. (1998). Cellular and chemical events during enamel maturation. *Crit. Rev. Oral Biol. Med.* 9, 128–161. doi: 10.1177/10454411980090020101

Smith, C. E., Nanci, A., and Denbesten, P. K. (1993). Effects of chronic fluoride exposure on morphometric parameters defining the stages of amelogenesis and ameloblast modulation in rat incisors. *Anat. Rec.* 237, 243–258. doi: 10.1002/ar.1092370212

Smith, C. E. L., Poulter, J. A., Antanaviciute, A., Kirkham, J., Brookes, S. J., Inglehearn, C. F., et al. (2017). Amelogenesis imperfecta; genes, proteins, and pathways. *Front. Physiol.* 8:435. doi: 10.3389/fphys.2017.00435

Smith, C. E., and Warshawsky, H. (1977). Quantitative analysis of cell turnover in the enamel organ of the rat incisor. Evidence for ameloblast death immediately after enamel matrix secretion. *Anat. Rec.* 187, 63–98. doi: 10.1002/ar.1091870106

Su, N., and Kilberg, M. S. (2008). C/EBP homology protein (CHOP) interacts with activating transcription factor 4 (ATF4) and negatively regulates the stress-dependent induction of the asparagine synthetase gene. *J. Biol. Chem.* 283, 35106–35117. doi: 10.1074/jbc.M806874200

Suzuki, M., Everett, E. T., Whitford, G. M., and Bartlett, J. D. (2017). 4-phenylbutyrate mitigates fluoride-induced cytotoxicity in ALC cells. *Front. Physiol.* 8:302. doi: 10.3389/fphys.2017.00302

Suzuki, M., Sierant, M. L., Antone, J. V., Everett, E. T., Whitford, G. M., and Bartlett, J. D. (2014). Uncoupling protein-2 is an antioxidant that is up-regulated in the enamel organ of fluoride-treated rats. *Connect. Tissue Res.* 55(Suppl. 1), 25–28. doi: 10.3109/03008207.2014.923854

Tabas, I., and Ron, D. (2011). Integrating the mechanisms of apoptosis induced by endoplasmic reticulum stress. *Nat. Cell Biol.* 13, 184–190. doi: 10.1038/ncb0311-184

Tanabe, T., Aoba, T., Moreno, E. C., and Fukae, M. (1988). Effect of fluoride in the apatitic lattice on adsorption of enamel proteins onto calcium apatites. *J. Dent. Res.* 67, 536–542. doi: 10.1177/00220345880670030301

Teske, B. F., Wek, S. A., Bunpo, P., Cundiff, J. K., McClintick, J. N., Anthony, T. G., et al. (2011). The eIF2 kinase PERK and the integrated stress response facilitate activation of ATF6 during endoplasmic reticulum stress. *Mol. Biol. Cell.* 22, 4390–4405. doi: 10.1091/mbc.E11-06-0510

Tsuchiya, M., Tye, C. E., Sharma, R., Smith, C. E., and Bartlett, J. D. (2008). XBP1 may determine the size of the ameloblast endoplasmic reticulum. *J. Dent. Res.* 87, 1058–1062. doi: 10.1177/154405910808701115

Tsuru, A., Imai, Y., Saito, M., and Kohno, K. (2016). Novel mechanism of enhancing IRE1alpha-XBP1 signalling via the PERK-ATF4 pathway. *Sci. Rep.* 6:24217. doi: 10.1038/srep24217

Tye, C. E., Antone, J. V., and Bartlett, J. D. (2011). Fluoride does not inhibit enamel protease activity. *J. Dent. Res.* 90, 489–494. doi: 10.1177/0022034510390043

Upton, J. P., Wang, L., Han, D., Wang, E. S., Huskey, N. E., Lim, L., et al. (2012). IRE1alpha cleaves select microRNAs during ER stress to derepress translation of proapoptotic Caspase-2. *Science* 338, 818–822. doi: 10.1126/science.1226191

Valastyan, J. S., and Lindquist, S. (2014). Mechanisms of protein-folding diseases at a glance. *Dis. Model. Mech.* 7, 9–14. doi: 10.1242/dmm.013474

Vilatoba, M., Eckstein, C., Bilbao, G., Smyth, C. A., Jenkins, S., Thompson, J. A., et al. (2005). Sodium 4-phenylbutyrate protects against liver ischemia reperfusion injury by inhibition of endoplasmic reticulum-stress mediated apoptosis. *Surgery* 138, 342–351. doi: 10.1016/j.surg.2005.04.019

Wang, Z., Yang, X., Yang, S., Ren, G., Ferreri, M., Su, Y., et al. (2011). Sodium fluoride suppress proliferation and induce apoptosis through decreased insulin-like growth factor-I expression and oxidative stress in primary cultured mouse osteoblasts. *Arch. Toxicol.* 85, 1407–1417. doi: 10.1007/s00204-011-0697-y

Wei, W., Gao, Y., Wang, C., Zhao, L., and Sun, D. (2013). Excessive fluoride induces endoplasmic reticulum stress and interferes enamel proteinases secretion. *Environ. Toxicol.* 28, 332–341. doi: 10.1002/tox.20724

Wu, J., Rutkowski, D. T., Dubois, M., Swathirajan, J., Saunders, T., Wang, J., et al. (2007). ATF6alpha optimizes long-term endoplasmic reticulum function to protect cells from chronic stress. *Dev. Cell* 13, 351–364. doi: 10.1016/j.devcel.2007.07.005

Yam, G. H., Gaplovska-Kysela, K., Zuber, C., and Roth, J. (2007). Sodium 4-phenylbutyrate acts as a chemical chaperone on misfolded myocilin to rescue cells from endoplasmic reticulum stress and apoptosis. *Invest. Ophthalmol. Vis. Sci.* 48, 1683–1690. doi: 10.1167/iovs.06-0943

Yoshida, H., Matsui, T., Yamamoto, A., Okada, T., and Mori, K. (2001). XBP1 mRNA is induced by ATF6 and spliced by IRE1 in response to ER stress to produce a highly active transcription factor. *Cell* 107, 881–891. doi: 10.1016/S0092-8674(01)00611-0

Yue, Z. S., Zeng, L. R., Quan, R. F., Tang, Y. H., Zheng, W. J., Qu, G., et al. (2016). 4Phenylbutyrate protects rat skin flaps against ischemiareperfusion injury and apoptosis by inhibiting endoplasmic reticulum stress. *Mol. Med. Rep.* 13, 1227–1233. doi: 10.3892/mmr.2015.4636

Zhu, L., Uskokovic, V., Le, T., Denbesten, P., Huang, Y., Habelitz, S., et al. (2011). Altered self-assembly and apatite binding of amelogenin induced by N-terminal proline mutation. *Arch. Oral Biol.* 56, 331–336. doi: 10.1016/j.archoralbio.2010.10.017

Zode, G. S., Bugge, K. E., Mohan, K., Grozdanic, S. D., Peters, J. C., Koehn, D. R., et al. (2012). Topical ocular sodium 4-phenylbutyrate rescues glaucoma in a myocilin mouse model of primary open-angle glaucoma. *Invest. Ophthalmol. Vis. Sci.* 53, 1557–1565. doi: 10.1167/iovs.11-8837

Conflict of Interest Statement: The authors declare that the research was conducted in the absence of any commercial or financial relationships that could be construed as a potential conflict of interest.

Copyright © 2017 Brookes, Barron, Dixon and Kirkham. This is an open-access article distributed under the terms of the Creative Commons Attribution License (CC BY). The use, distribution or reproduction in other forums is permitted, provided the original author(s) or licensor are credited and that the original publication in this journal is cited, in accordance with accepted academic practice. No use, distribution or reproduction is permitted which does not comply with these terms.

frontiers in Physiology

PERSPECTIVE
published: 03 August 2017
doi: 10.3389/fphys.2017.00546

Molar Hypomineralisation: A Call to Arms for Enamel Researchers

Michael J. Hubbard[1,2]*, *Jonathan E. Mangum*[2], *Vidal A. Perez*[2,3], *Garry J. Nervo*[2] and *Roger K. Hall*[2]

[1] Department of Paediatrics, University of Melbourne, Melbourne, VIC, Australia, [2] Department of Pharmacology and Therapeutics, University of Melbourne, Melbourne, VIC, Australia, [3] Department of Pediatric Stomatology, University of Talca, Talca, Chile

Developmental dental defects (DDDs, hereafter "D3s") hold significance for scientists and practitioners from both medicine and dentistry. Although, attention has classically dwelt on three other D3s (amelogenesis imperfecta, dental fluorosis, and enamel hypoplasia), dental interest has recently swung toward Molar Hypomineralisation (MH), a prevalent condition characterised by well-delineated ("demarcated") opacities in enamel. MH imposes a significant burden on global health and has potential to become medically preventable, being linked to infantile illness. Yet even in medico-dental research communities there is only narrow awareness of this childhood problem and its link to tooth decay, and of allied research opportunities. Major knowledge gaps exist at population, case and tooth levels and salient information from enamel researchers has sometimes been omitted from clinically-oriented conclusions. From our perspective, a cross-sector translational approach is required to address these complex inadequacies effectively, with the ultimate aim of prevention. Drawing on experience with a translational research network spanning Australia and New Zealand (The D3 Group; *www.thed3group.org*), we firstly depict MH as a silent public health problem that is generally more concerning than the three classical D3s. Second, we argue that diverse research inputs are needed to undertake a multi-faceted attack on this problem, and outline demarcated opacities as the central research target. Third, we suggest that, given past victories studying other dental conditions, enamel researchers stand to make crucial contributions to the understanding and prevention of MH. Finally, to focus geographically diverse research interests onto this nascent field, further internationalisation of The D3 Group is warranted.

Keywords: enamel defects, enamel opacities, dental caries, amelogenesis imperfecta, dental fluorosis, enamel hypoplasia, translational research, networked research

OPEN ACCESS

Edited by:
Sylvie Babajko,
Centre de Recherche des Cordeliers, France

Reviewed by:
Charles F. Shuler,
University of British Columbia, Canada
Michel Goldberg,
Institut National de la Santé et de la Recherche Médicale (INSERM), France
Javier Catón,
CEU San Pablo University, Spain

***Correspondence:**
Michael J. Hubbard
mike.hubbard@unimelb.edu.au

Specialty section:
This article was submitted to Craniofacial Biology and Dental Research, a section of the journal Frontiers in Physiology

Received: *07 April 2017*
Accepted: *14 July 2017*
Published: *03 August 2017*

Citation:
Hubbard MJ, Mangum JE, Perez VA, Nervo GJ and Hall RK (2017) Molar Hypomineralisation: A Call to Arms for Enamel Researchers. Front. Physiol. 8:546. doi: 10.3389/fphys.2017.00546

Developmental dental defects (DDDs), hereafter termed D3s per recent translational usage[1], hold significance for scientists and practitioners from both medicine and dentistry. Dentally, D3s are commonly associated with increased risk for toothache, decay (caries) and concerns about appearance, each of which may require non-standard approaches to management. Medically, although childhood illness clearly underlies many D3s, the lack of specific causalities and prognostics precludes doctors from taking preventive measures. And scientifically, despite evidence that many D3s involve disruption of the enamel-forming cells (ameloblasts), today's scant pathomechanistic understanding carries little in the way of clinical value. These knowledge gaps hold importance not only for naturally-formed teeth, but also for future aspirations to bioengineer replacement teeth free of D3s. Classically, the collective attention of dentists, doctors, and scientists has dwelt mostly on three types of D3 that affect enamel, namely amelogenesis imperfecta, dental

[1] www.thed3group.org/what-is-d3.html

fluorosis, and enamel hypoplasia. Multiple victories have arisen from these research efforts which have spanned more than a century (see **Box 1**). Over the past decade however, dental attention has swung toward a condition primarily affecting back teeth and which we term Molar Hypomineralisation (or "chalky molars" in public settings[2]).

MOLAR HYPOMINERALISATION, A SILENT PUBLIC HEALTH PROBLEM

Molar Hypomineralisation (MH) is emerging as a costly, yet largely silent, challenge to public health. Several key aspects can be identified, as summarised in the first column of **Table 1**. Foremost, the prevalence of MH is disturbingly high, with the commonest variant affecting 1-in-6 children worldwide (i.e., 17% averaged from 59 studies)[3]. In this presentation which is commonly termed "Molar-Incisor Hypomineralisation," one or more of the permanent first-molars ("6-year molars") are affected, sometimes with co-involvement of contemporaneous front teeth (i.e., "adult" incisors and canines). Deciduous second-molars ("baby" or "2-year molars") are also commonly afflicted, perhaps half as frequently as 6-year molars, and some children suffer both presentations in succession. A diagnostic hallmark of MH, that distinguishes it from amelogenesis imperfecta and classical chronological D3s including fluorosis, is the sporadic occurrence of distinctively well-delineated hypomineralised enamel lesions (termed "demarcated opacities") on anywhere between one and all-four teeth of each type[4]. With molars the main victim, MH brings considerable risk for dental breakdown and caries. Such carious lesions often manifest atypically, both in their unusually rapid progression through abnormal enamel and by being located in areas usually devoid of dental plaque (e.g., cusps and upper smooth surfaces). Toothache (dental pain) is another frequent manifestation of MH and often causes sufficient discomfort to trigger oral hygiene avoidance, exacerbating caries risk. Unsurprisingly, these fundamentally weakened teeth introduce treatment challenges for dentist and patient alike, including difficulty obtaining local anaesthesia, higher failure rates for restorations, and premature extractions with allied orthodontic need[5]. So for individual sufferers and their families, MH often inflicts significant longterm costs in financial and quality-of-life terms (e.g., dental costs, toothache, disrupted bite, and poor appearance). At population level, MH implicitly poses a substantial socioeconomic burden given its high prevalence and overlap with conventional risk factors for childhood caries (Casamassimo et al., 2009), but these costs remain to be properly quantified[6]. Regards causation, MH has been broadly linked with illnesses at the time developing enamel is being hardened (i.e., infancy in the case of 6-year molars), but specific or multifactorial causes have yet to be proven. Indeed, it still remains to be determined whether such causes relate to childhood diseases *per-se*, or instead to therapeutics commonly used in their treatment or environmental toxins. These uncertainties aside however, it does seem reasonable to anticipate that, once these research questions are answered, MH may well become largely preventable through medical or public-health interventions (Mangum et al., 2010).

When MH is compared against the three classical types of D3, it stands out as having the most impact overall at population level (**Figure 1**). Notably, amelogenesis imperfecta can be quite devastating for the families concerned, as often all teeth are severely malformed leading to extreme risk for poor appearance, toothache, caries, and failed dental restorations (Parekh et al., 2014; Sneller et al., 2014). Yet, because of its rarity, this genetic disorder poses a comparatively small burden for society (**Table 1**). Likewise, in developed countries at least, fluorosis and (true) enamel hypoplasia are generally less prevalent than MH and don't carry as much risk for caries and toothache. MH-related decay may also be wrongly attributed to hypoplasia due to ignorance that the latter term describes enamel missing before eruption and not enamel loss that has occurred post-eruptively[7]. With such high burdens on individuals and society, it is quite remarkable that MH is not better recognised and understood. Although its key features were reported decades ago (Hurme, 1949; Suckling et al., 1976, 1987; Koch et al., 1987), MH has only come to prominence in the past 15 years and, even then, awareness resides mainly with specialists in children's dentistry. A likely reason is that, due to inadequate education about the diagnostic differentiators noted above, MH is widely misdiagnosed as regular caries (particularly in high-caries-risk situations). Consequently, MH remains a largely silent public health problem and its considerable socioeconomic costs may be misassigned to caries. With few researchers currently engaged on this topic, MH offers numerous opportunities for worthy investigation.

A MULTI-FACETED RESEARCH ATTACK IS NEEDED FOR MOLAR HYPOMINERALISATION

As MH is a complex problem from both aetiological and healthcare perspectives, a multi-faceted research approach should prove beneficial. Research needs can be divided into two broad areas, namely better dental care for now and avenues toward medical prevention in the future. Within each area there are opportunities for several disciplines including public health, dentistry, medicine, and basic science. To understand the idiosyncrasies of MH (**Table 1**), investigations are needed at population, individual case and tooth levels. For example, respective enigmas include reasons behind (1) the large variations in MH prevalence reported from studies of nominally similar populations;[8] (2) the asymmetric attack pattern at mouth level,

Abbreviations: AI, amelogenesis imperfecta; D3, developmental dental defect; MH, Molar Hypomineralisation.

[2]http://www.chalkyteeth.org

[3]www.thed3group.org/prevalence.html

[4]www.thed3group.org/the-basics-2.html

[5]www.thed3group.org/health-risks.html

[6]www.thed3group.org/economic-cost.html

[7]www.thed3group.org/the-basics.html

[8]www.thed3group.org/prevalence.html

BOX 1 | Past Victories Involving Enamel Research

"Tetracycline-Stained Teeth"

From the mid-1950s, many children were found to have abnormally coloured teeth at the time of eruption. Such "enamel staining" generally worsened with age, progressing from yellow to grey/brown. Researchers soon linked this problem to paediatric use of tetracycline, a newly available antibiotic. This side-effect, which also affected dentine and bone, was exploited scientifically to elucidate the developmental timing of enamel formation and allied defects. With few exceptions, tetracycline-stained teeth are now consigned to history thanks to evidence-based interventions at multiple levels (medical, pharmacy, industry, government).

Dental Fluorosis ("Mottled Enamel")

In the 1920s, research across the USA led to evidence that populations exposed to low amounts of fluoride in drinking water had lesser amounts of dental decay. Higher fluoride exposures were linked to "fluorosis" (i.e., enamel with defects ranging from white flecks through to brown pits). A century of research has since delivered comprehensive understanding of the effects of fluoride on populations, individuals, teeth, cells, and minerals. Enamel has been at the heart of this research. Today's evidence-base enables fluoride to be used safely and effectively in a variety of dental, medical and public-health settings. A global decrease in tooth decay has occurred consequently.

Tooth Decay (Dental Caries)

By the 1960s and with rates of tooth decay plummeting, attention turned to the earliest stages of dental caries in superficial enamel (i.e., so-called "white-spot lesions") with the aim of preventing or reversing the disease process. Researchers elucidated how enamel is attacked by acids from dental plaque and established various procedures for reversing or arresting such damage. These developments have led to a new generation of dentistry whereby surgical "drilling and filling" (dental restorations) may be preempted by various preventive and non-surgical early interventions.

Amelogenesis Imperfecta ("AI")

Early in the twentieth century it was recognised that some types of enamel defect were inheritable, leading to recognition of a complex genetic disorder termed AI (meaning "imperfect enamel formation"). Recently researchers have identified many of the genes involved and aligned these with different types of enamel abnormality. AI enamel has been characterised in animal models and humans. Genetic testing is now becoming available for some types of AI and improved dental treatments have arisen from understanding the peculiarities of AI enamel.

Enamel Hypoplasia ("Pits and Grooves")

By the late nineteenth century, enamel hypoplasias (meaning "thin enamel") were linked with childhood illness, poor appearance, and increased risk of decay. Researchers found that hypoplasia has many causes and occurs at an earlier stage of enamel formation than hypomineralisation. Thanks to better paediatric health today, enamel hypoplasias are generally less prevalent but remain of concern in some situations (e.g., high-caries-risk, vitamin D insufficiency).

TABLE 1 | Comparing molar hypomineralisation with other major D3s.

	Molar hypomin (MH)	Dental fluorosis	Enamel hypoplasia	Amelogenesis imperfecta
Child prevalence (permanent teeth)	1-in-6 (≈17%)[a]	1-in-10 (≈10%)[b]	1-in-20 (≈5%)[c]	1-in-10,000 (≈0.01%)[d]
Commonest teeth affected	6-year molars[e]	Any tooth	Any tooth	All teeth
How many teeth affected	1 to all 4 of each tooth type	All front teeth often	Several teeth often	Front and back teeth
Adds risk for	Toothache, decay, cosmetic issues	Cosmetic issues mostly	Decay, cosmetic issues	Toothache, decay, cosmetic issues
Dental consequences	Fillings, extractions, orthodontic need	Cosmetic dentistry	Cosmetic dentistry, fillings	Fillings, extractions, tooth replacement
Cost to family	Medium[f]	Low	Low	High
Costs to society	High[g]	Low	Low	Low
Cause	Infantile illness	Fluoride excess	Infantile illness	Genetic mutation
Preventable?	Potentially	Yes	Largely	No

[a] *Average value from 59 prevalence studies worldwide; www.thed3group.org/prevalence.html*

[b] *Prevalence of dental fluorosis is often lower and sometimes much higher than 10% (e.g., due to dietary habits in some communities or exposure to naturally high levels of fluoride in drinking water).*

[c] *Prevalence of enamel hypoplasia ranges from 1% in developed countries (e.g., 0.7% in New Zealand; Mahoney and Morrison, 2011) to much higher levels in communities with suboptimal paediatric healthcare [e.g., 11% in Brazil (Lunardelli and Peres, 2005) and 99% in Australian aboriginals (Pascoe and Seow, 1994)]. Accordingly an arbitrary value of 5% is used here.*

[d] *Global prevalence of amelogenesis imperfecta remains poorly characterised, but a range from 1-in-700 to 1-in-14,000 is often cited (Sneller et al., 2014).*

[e] *Permanent first molars ("6-year molars") are affected most commonly, followed by incisors, second molars ("12-year" molars) and primary second molars ("2-year" molars). All other teeth in the primary and permanent dentitions are affected more rarely.*

[f] *Lacking normal hardness, MH teeth are often difficult to treat and so restorations frequently don't last as long as usual. Extractions are common and can lead to costly orthodontic needs.*

[g] *www.thed3group.org/economic-cost.html*

To strengthen comparison, a typical version of each disorder as seen in the recently-erupted permanent teeth of healthy schoolchildren was used. Representative prevalence values are given for developed countries, realising that significant differences exist in some other parts of the world. The family and social costs were ranked arbitrarily (as high, medium, low), taking into account prevalence, health risks and presumptive economic cost. High-impact features are shaded (orange) and reportrayed comparatively in ***Figure 1****.*

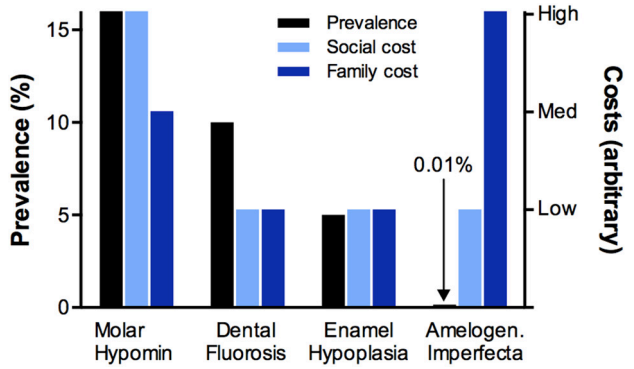

FIGURE 1 | Relative impacts of the four major D3s. Prevalence, and (arbitrary) family costs and social costs were taken from **Table 1** and represented comparatively in different colours as indicated. It is apparent that MH is the commonest D3, the most costly to society, and often burdensome for families (in terms of suffering, time and money). In contrast, although amelogenesis imperfecta can be quite devasting for the families concerned, this genetic disorder is relatively rare and so poses a low burden for society. Dental fluorosis and enamel hypoplasia also have lesser impacts than MH under the general population settings of **Table 1**.

whereby anywhere from one to all-four 6-year molars can be affected; and (3) the biophysical properties of demarcated opacities, whose discoloured enamel varies from having chalk-like softness to near-normal hardness. Given their past victories informing a variety of clinical issues (see **Box 1**), enamel researchers are well-positioned to advance the understanding of demarcated opacities and MH. Much potential exists for established enamel-research methodologies to be deployed on MH, both de novo and in comparison with the better understood classical D3s (**Table 1**).

SCIENTIFIC DRILLING INTO DEMARCATED OPACITIES

Being the defining pathology of MH, demarcated enamel opacities occupy centre stage not only clinically but also as a potential goldmine for aetiology. By 1949, it was recognised that these sharply-bordered opacities are clinicopathologically distinct, differing from the so-called "diffuse opacities" (the signature lesion of dental fluorosis) and the early stages of caries termed "white-spot lesions" (Hurme, 1949). Thirty years later in New Zealand, animal studies provided experimental verification and established that demarcated opacities arise during the hardening (maturation) stage of enamel formation, unlike enamel hypoplasias which occur in the preceeding secretory stage. A hypothesised link with infectious disease was supported in an infantile sheep model, but parallel epidemiology on children failed to reveal any concrete medical associations[9]. Perplexingly, this causal enigma persists today despite more than 30 aetiological studies of childhood populations around the globe (Suckling et al., 1987; Silva et al., 2016). Much potential exists for enamel researchers to refine these and other past findings, for example by using modern understanding of enamel maturation to narrow down the developmental period when immature enamel is at risk of MH (Suckling, 1980; Smith, 1998; Lacruz et al., 2011; Robinson, 2014).

Recently, a possible breakthrough has come from proteomic investigation of "chalky" demarcated opacities (Mangum et al., 2010). Such opacities, which are found in moderate and severe cases of MH, present clinically as being unusually soft and discoloured in shades of cream, yellow, and brown. By comparing normal enamel with chalky opacities bearing intact and broken surfaces, a unique correlation was found between chalky enamel and albumin—a protein normally found in blood, tissue fluid, and saliva. This observation, which we have since verified using additional methodology and specimens (VP, JM, MH; unpublished data), resonates with an earlier speculation that albumin may have an inhibitory effect on enamel mineralisation during the development of so-called "white spot hypoplasias" (Robinson et al., 1992). However support at that time was controversial, coming from post-mortem animal specimens and being contradicted by albumin-transcript and human-derived data (Couwenhoven et al., 1989; Mangum et al., 2010). Moreover, another group's proteomic investigation produced somewhat different results by revealing albumin in both normal enamel and demarcated opacities, along with other proteins usually associated with saliva (Farah et al., 2010). Clearly, further work is required to verify the hypothesised developmental link between albumin and chalky enamel and to rule out alternative explanations such as post-eruptive contamination with blood or saliva. A second finding from proteomic profiling was nearly complete absence of the principal enamel protein, amelogenin, from chalky opacities which in turn led to MH being categorised as a hypocalcification defect by analogy to the various phenotypes of amelogenesis imperfecta. This result argued against abnormal retention of amelogenin being primarily responsible for chalky enamel (as holds for some types of amelogenesis imperfecta and fluorosis), and instead added support to the albumin hypothesis (Mangum et al., 2010). Provocatively, these proteomic findings suggest that other aetiological clues might remain preserved within chalky enamel. Complementing the proteomic approach, murine toxicology models have been used to investigate whether antibiotics and environmental toxins cause MH (Laisi et al., 2009; Jedeon et al., 2013; see also Kirkham et al., 2017). Although various effects on enamel development were reported, it is uncertain how closely these animal models emulate the human situation in terms of opacity characteristics and typical childhood exposures. Regardless, much potential exists for enamel researchers to pursue such avenues and develop rigorous animal models for demarcated opacities and MH (Suckling et al., 1983; see also Kirkham et al., 2017).

Considering past gains (see **Box 1**), enamel researchers could sensibly tackle many other questions in this area besides those related to pathomechanism and causation. For example, of particular clinical relevance are correlations between physicochemical properties and opacity appearance, and also the notion of using allied chemical and molecular information to assist diagnosis and treatment (Mahoney et al., 2004; Mangum et al., 2010; Natarajan et al., 2015). Currently dentists have

[9]www.thed3group.org/grace-suckling.html

little other than hard-won experience to go on when deciding whether a moderate-grade opacity might be preserved using remineralisation strategies, or will instead break down under chewing forces and progress rapidly to severe decay. The role of genetics in MH risk is another area yet to be clarified, including by use of twin studies. It is noteworthy in this regard that, although not primarily genetic in origin (unlike amelogenesis imperfecta), fluorosis and caries-risk both appear to have underlying genetic contributions (Everett et al., 2002; Shaffer et al., 2011; Vieira and Kup, 2016).

To maximise research traction, it will be important to amalgamate clinical and scientific viewpoints on demarcated opacities, and to develop cross-compatible research frameworks and terminologies[10]. And in deciding how best to move forward, it will also be valuable to reevaluate historic data which in many cases remains pertinent to what is today described as MH, despite diagnostic and terminological differences[11]. It follows from such ambitions that further scientific drilling into the medical origins, clinical properties and treatment of demarcated opacities will best be done collaboratively by cross-disciplinary teams. Moreover, while as in the past there remains an important role for individual contributions, it seems that an expansive medico-dental research problem of this nature will benefit from a networked research approach whereby various participatory groups are brought together into a more powerful whole.

THE NEED FOR A CROSS-SECTOR, TRANSLATIONAL APPROACH TO MOLAR HYPOMINERALISATION

Simply put, "the MH problem" can be seen to comprise three aspects—(1) the health issues surrounding MH, (2) the under-recognition of this silent health problem, and (3) the paucity of research-based understanding of MH. If MH is to be treated better in the near-term and ultimately prevented, improvements to research and awareness are required. Key topics for awareness-building include the socioeconomic gravity of MH, its common misdiagnosis as regular dental caries, and the worthiness of preventive research. These messages need to be delivered across the sector, thereby informing the at-risk public and politicians serving them, the healthcare providers and their educators, the supporting industry, and the medico-dental research community. With so many unknowns and so much at stake, researchers need encouragement to address not just the amount of research they do, but also its quality as seen through translational eyes. It follows that a cross-sector, translational network approach to the MH problem stands to benefit research, education, and public-health policy. For such an approach to work, diverse research capabilities must be attracted to this nascent field, particularly from basic science, paediatric medicine, dentistry, public health, and allied industry. Many strategic advantages would accrue if such a network was to have global reach, recognising for example that, as for childhood caries, the MH problem will have socio-geographic variations. Likewise, educational benefits will flow from consistent messaging, and a "networked research army" should act as a high-capability magnet for the requisite major resourcing. With these ideas in mind, a translational network was recently piloted across Australia and New Zealand. Using cross-sector inputs, this initiative (The D3 Group) has launched a public awareness campaign[12], a children's storybook[13], and a comprehensive online-education resource serving diverse target audiences (i.e., affected children and families, public health sector and politicians, medical and dental practitioners, researchers)[14]. A key element of these initial steps was the drafting of a translational lexicon that embraces diverse needs including public-friendliness ("chalky teeth"), ease of speech ("D3s"), and a public-health focus on decay-prone molars whilst respecting the clinicopathological importance that any tooth can be affected by demarcated opacities ("Molar Hypomineralisation"). Realising the enamel-science community is small and scattered, it is hoped that further internationalisation of The D3 Group network will provide an empowering vehicle that attracts more enamel researchers (amongst many others) to join the worthy fight against MH.

AUTHOR CONTRIBUTIONS

MH conceived, designed and drafted the article and figures. VP and JM helped conceive the D3 comparisons and Past Victories sections, respectively, and added other intellectual content. As originators of "D3 Dad's Army" (i.e., senior practitioners contributing hands-on to basic research in the Hubbard group), GN and RH have made numerous intellectual contributions to the perspective outlined here. All authors refined and reviewed the final manuscript.

FUNDING

Support from the Melbourne Research Unit for Facial Disorders, Department of Pharmacology & Therapeutics (MH, JM, VP), Department of Paediatrics and Faculty of Medicine, Dentistry and Health Science (MH) at the University of Melbourne is gratefully acknowledged. JM holds a Peter Doherty early career fellowship from NHMRC Australia. VP additionally received PhD scholarship support in Melbourne from Becas Chile and the University of Talca where he now holds a faculty position.

ACKNOWLEDGMENTS

We thank our numerous colleagues from the enamel research community, The D3 Group and the Hubbard group for their valuable inputs over many years that have inspired the translational viewpoint expressed here. Susan Parekh and Alan Mighell are thanked for their critique of the manuscript.

[10] www.thed3group.org/the-basics.html
[11] www.thed3group.org/grace-suckling.html
[12] www.chalkyteeth.org
[13] www.thed3group.org/sam-has-molar-hypomin.html
[14] www.thed3group.org

REFERENCES

Casamassimo, P. S., Thikkurissy, S., Edelstein, B. L., and Maiorini, E. (2009). Beyond the dmft: the human and economic cost of early childhood caries. *J. Am. Dent. Assoc.* 140, 650–657. doi: 10.14219/jada.archive.2009.0250

Couwenhoven, R. I., Davis, C., and Snead, M. L. (1989). Mouse ameloblasts do not transcribe the albumin gene. *Calcif. Tissue Int.* 45, 367–371. doi: 10.1007/BF02556008

Everett, E. T., Mchenry, M. A., Reynolds, N., Eggertsson, H., Sullivan, J., Kantmann, C., et al. (2002). Dental fluorosis: variability among different inbred mouse strains. *J. Dent. Res.* 81, 794–798. doi: 10.1177/0810794

Farah, R. A., Monk, B. C., Swain, M. V., and Drummond, B. K. (2010). Protein content of molar-incisor hypomineralisation enamel. *J. Dent.* 38, 591–596. doi: 10.1016/j.jdent.2010.04.012

Hurme, V. O. (1949). Developmental opacities of teeth in a New England community; their relation to fluorine toxicosis. *Am. J. Dis. Child* 77, 61–75. doi: 10.1001/archpedi.1949.02030040068005

Jedeon, K., De La Dure-Molla, M., Brookes, S. J., Loiodice, S., Marciano, C., Kirkham, J., et al. (2013). Enamel defects reflect perinatal exposure to bisphenol A. *Am. J. Pathol.* 183, 108–118. doi: 10.1016/j.ajpath.2013.04.004

Kirkham, J., Brookes, S. J., Diekwisch, T. G. H., Margolis, H. C., Berdal, A., and Hubbard, M. J. (2017). Enamel research: priorities and future directions. *Front. Physiol.* 8:513. doi: 10.3389/fphys.2017.00513

Koch, G., Hallonsten, A. L., Ludvigsson, N., Hansson, B. O., Holst, A., and Ullbro, C. (1987). Epidemiologic study of idiopathic enamel hypomineralization in permanent teeth of Swedish children. *Community Dent. Oral Epidemiol.* 15, 279–285. doi: 10.1111/j.1600-0528.1987.tb00538.x

Lacruz, R. S., Smith, C. E., Chen, Y. B., Hubbard, M. J., Hacia, J. G., and Paine, M. L. (2011). Gene-expression analysis of early- and late-maturation-stage rat enamel organ. *Eur. J. Oral Sci.* 119(Suppl. 1), 149–157. doi: 10.1111/j.1600-0722.2011.00881.x

Laisi, S., Ess, A., Sahlberg, C., Arvio, P., Lukinmaa, P. L., and Alaluusua, S. (2009). Amoxicillin may cause molar incisor hypomineralization. *J. Dent. Res.* 88, 132–136. doi: 10.1177/0022034508328334

Lunardelli, S. E., and Peres, M. A. (2005). Prevalence and distribution of developmental enamel defects in the primary dentition of pre-school children. *Braz. Oral Res.* 19, 144–149. doi: 10.1590/S1806-83242005000200013

Mahoney, E. K., and Morrison, D. G. (2011). Further examination of the prevalence of MIH in the Wellington region. *N. Z. Dent. J.* 107, 79–84.

Mahoney, E. K., Rohanizadeh, R., Ismail, F. S., Kilpatrick, N. M., and Swain, M. V. (2004). Mechanical properties and microstructure of hypomineralised enamel of permanent teeth. *Biomaterials* 25, 5091–5100. doi: 10.1016/j.biomaterials.2004.02.044

Mangum, J. E., Crombie, F. A., Kilpatrick, N., Manton, D. J., and Hubbard, M. J. (2010). Surface integrity governs the proteome of hypomineralized enamel. *J. Dent. Res.* 89, 1160–1165. doi: 10.1177/0022034510375824

Natarajan, A. K., Fraser, S. J., Swain, M. V., Drummond, B. K., and Gordon, K. C. (2015). Raman spectroscopic characterisation of resin-infiltrated hypomineralised enamel. *Anal. Bioanal. Chem.* 407, 5661–5671. doi: 10.1007/s00216-015-8742-y

Parekh, S., Almehateb, M., and Cunningham, S. J. (2014). How do children with amelogenesis imperfecta feel about their teeth? *Int. J. Paediatr. Dent.* 24, 326–335. doi: 10.1111/ipd.12080

Pascoe, L., and Seow, W. K. (1994). Enamel hypoplasia and dental caries in Australian aboriginal children: prevalence and correlation between the two diseases. *Pediatr. Dent.* 16, 193–199.

Robinson, C. (2014). Enamel maturation: a brief background with implications for some enamel dysplasias. *Front. Physiol.* 5:388. doi: 10.3389/fphys.2014.00388

Robinson, C., Kirkham, J., Brookes, S. J., and Shore, R. C. (1992). The role of albumin in developing rodent dental enamel: a possible explanation for white spot hypoplasia. *J. Dent. Res.* 71, 1270–1274. doi: 10.1177/00220345920710060101

Shaffer, J. R., Wang, X., Feingold, E., Lee, M., Begum, F., Weeks, D. E., et al. (2011). Genome-wide association scan for childhood caries implicates novel genes. *J. Dent. Res.* 90, 1457–1462. doi: 10.1177/0022034511422910

Silva, M. J., Scurrah, K. J., Craig, J. M., Manton, D. J., and Kilpatrick, N. (2016). Etiology of molar incisor hypomineralization - A systematic review. *Community Dent. Oral Epidemiol.* 44, 342–353. doi: 10.1111/cdoe.12229

Smith, C. E. (1998). Cellular and chemical events during enamel maturation. *Crit. Rev. Oral Biol. Med.* 9, 128–161. doi: 10.1177/10454411980090020101

Sneller, J., Buchanan, H., and Parekh, S. (2014). The impact of amelogenesis imperfecta and support needs of adolescents with AI and their parents: an exploratory study. *Int. J. Paediatr. Dent.* 24, 409–416. doi: 10.1111/ipd.12086

Suckling, G. (1980). Defects of enamel in sheep resulting from trauma during tooth development. *J. Dent. Res.* 59, 1541–1548. doi: 10.1177/00220345800590092701

Suckling, G. W., Herbison, G. P., and Brown, R. H. (1987). Etiological factors influencing the prevalence of developmental defects of dental enamel in nine-year-old New Zealand children participating in a health and development study. *J. Dent. Res.* 66, 1466–1469. doi: 10.1177/00220345870660091101

Suckling, G. W., Pearce, E. I., and Cutress, T. W. (1976). Developmental defects of enamel in New Zealand children. *N. Z. Dent. J.* 72, 201–210.

Suckling, G., Elliott, D. C., and Thurley, D. C. (1983). The production of developmental defects of enamel in the incisor teeth of penned sheep resulting from induced parasitism. *Arch. Oral Biol.* 28, 393–399. doi: 10.1016/0003-9969(83)90134-6

Vieira, A. R., and Kup, E. (2016). On the etiology of molar-incisor hypomineralization. *Caries Res.* 50, 166–169. doi: 10.1159/000445128

Conflict of Interest Statement: The authors declare that the research was conducted in the absence of any commercial or financial relationships that could be construed as a potential conflict of interest.

Copyright © 2017 Hubbard, Mangum, Perez, Nervo and Hall. This is an open-access article distributed under the terms of the Creative Commons Attribution License (CC BY). The use, distribution or reproduction in other forums is permitted, provided the original author(s) or licensor are credited and that the original publication in this journal is cited, in accordance with accepted academic practice. No use, distribution or reproduction is permitted which does not comply with these terms.

frontiers in Physiology

OPINION
published: 26 May 2017
doi: 10.3389/fphys.2017.00343

Disruption of Steroid Axis, a New Paradigm for Molar Incisor Hypomineralization (MIH)

Sylvie Babajko[1,2]*, *Katia Jedeon*[1,2], *Sophia Houari*[1,2], *Sophia Loiodice*[1,2] and *Ariane Berdal*[1,2,3]

[1] Laboratory of Molecular Oral Pathophysiology, Centre de Recherche des Cordeliers, Institut National de la Santé et de la Recherche Médicale UMRS 1138, University Paris-Descartes, University Pierre et Marie Curie-Paris, Paris, France, [2] Unité de Formation et de Recherche en Odontologie, University Paris-Diderot, Paris, France, [3] Centre de Référence des Maladies Rares de la face et de la Cavité Buccale MAFACE, Rothschild Hospital, Paris, France

Keywords: amelogenesis, MIH, steroid receptors, steroid hormones, endocrine disrupting chemicals, enamel mineralization

OVERVIEW

Molar-Incisor Hypomineralization (MIH) is a common developmental enamel defect characterized by asymmetric demarcated opacities in permanent molars and incisors. MIH was first described in 2001–2003 (Weerheijm et al., 2001; Weerheijm and Merjare, 2003). It was previously called cheese molars, idiopathic enamel hypomineralization in permanent teeth, included in developmental enamel defects other than that caused by fluoride but the prevalence of these defects was poorly documented except in Sweden where it was first investigated (Koch et al., 1987). It affects now 15–20% of 6–9 year-old children worldwide but its etiology still remains unclear. MIH is certainly a non-hereditary multifactorial pathology even though an individual hereditary susceptibility to MIH is not excluded as suggested by enamelin gene polymorphism (Jeremias et al., 2013). Several causal factors have been proposed such as prematurity, long breastfeeding, viral or bacterial infections, respiratory diseases, asthma (Alaluusua et al., 2002; Alaluusua, 2010; Serna et al., 2016; Silva et al., 2016; Tourino et al., 2016). None of these factors is satisfactory to explain MIH recent emergence nor its selective enamel lesions on the first mineralizing permanent teeth, mainly permanent first molars and incisors. Despite the fact that mineralization of the other permanent teeth may be delayed, they are rarely affected by MIH. Given that MIH affects those teeth undergoing mineralization around the time of birth, it is clear that the enamel forming ameloblasts are sensitive to the causative agent(s) in a specific time window only. It is noteworthy that MIH emergence is overlaying to increased prevalence of pathologies related to the currently changing environmental conditions with increasing amounts of pollutants. Indeed, our environment and lifestyle are dramatically changing and exposure to novel molecules or combination of factors during the period of amelogenesis may be a possible track. Among environmental toxicants, Endocrine Disrupting Chemicals (EDCs) are exogenous substances or mixtures that alter function(s) of the endocrine system and consequently cause adverse health effects in an intact organism, or its progeny, or (sub) populations (EDC definition established by the World Health organization in 2002). EDCs are small molecules that may share structural homologies with steroid hormones, and are thus able to disrupt steroid axes. Steroid hormones (such as estrogens, androgens, or corticoids for example) mediate their effects through intracellular steroid receptors that modulate transcription of their target genes. Most of steroid receptors are expressed by ameloblasts and thus possibly involved in amelogenesis (Houari et al., 2016). The present paper explores the hypothesis of their involvement in amelogenesis and delineates one mechanistic path that would account for MIH.

OPEN ACCESS

Edited by:
Petros Papagerakis, University of Michigan, United States

Reviewed by:
Yong-Hee Patricia Chun, University of Texas Health Science Center at San Antonio, United States
Harald Osmundsen, University of Oslo, Norway

***Correspondence:**
Sylvie Babajko
sylvie.babajko@crc.jussieu.fr

Specialty section:
This article was submitted to Craniofacial Biology and Dental Research, a section of the journal Frontiers in Physiology

Received: *20 March 2017*
Accepted: *10 May 2017*
Published: *26 May 2017*

Citation:
Babajko S, Jedeon K, Houari S, Loiodice S and Berdal A (2017) Disruption of Steroid Axis, a New Paradigm for Molar Incisor Hypomineralization (MIH). Front. Physiol. 8:343. doi: 10.3389/fphys.2017.00343

EVIDENCE

EDCs have often been proposed to contribute to hormone-dependent cancers, decreased fertility, diabetes, obesity, and cognitive disorders over the past 50 years (Gore et al., 2015). This hypothesis is supported by a number of recent epidemiological and experimental studies. Among the thousands of EDCs, bisphenol A (BPA) is one of the most active and widely used by the plastic industry and also for dental materials. It may be leached as an active monomer under several conditions (Cooper et al., 2011). Sensitivity to BPA is the greatest during the perinatal period and many pathologies diagnosed during adulthood would result from fetal and perinatal exposure to these molecules (Poimenova et al., 2010; Varayoud et al., 2014; Braun, 2017). Interestingly, this period of time corresponds to the temporal window when the enamel of the human permanent teeth is being formed.

Our recent data showed that human MIH and BPA exposed rat teeth present similar structural and biochemical characteristics (Jedeon et al., 2013). Both series of teeth present broken enamel in areas where the teeth occlude. In addition, the prismatic structure in human MIH enamel as well as BPA exposed rat enamel was obscured by a covering organic layer (Jedeon et al., 2013) similar to the one reported previously (Jälevik et al., 2005). Among the main enamel matrix proteins, enamelin expression was higher in BPA exposed ameloblasts. Enamelin amount is a central parameter for enamel synthesis as demonstrated by an experimental genetic approach (Hu et al., 2014). Indeed, *ENAM* mutations have been reported in Amelogenesis Imperfecta (AI) (Lindemeyer et al., 2010; Chan et al., 2011), and have been associated with MIH (Jeremias et al., 2013). Specific alleles of *ENAM* are also associated with high susceptibility to dental caries (Chaussain et al., 2014) and the expression level of enamelin appears to be determinant for the structure and quality of enamel (Hu et al., 2014). Too much or too little enamelin abolishes the formation of enamel crystals and prism structure. BPA has also been shown to decrease KLK4 expression which is involved in the degradation of enamel matrix proteins (Jedeon et al., 2013). KLK4 is a serine-protease that cleaves enamel matrix proteins to permit enamel full and correct enamel mineralization (Bartlett and Simmer, 2014). *KLK4* mutations have also been reported in AI (Chan et al., 2011). When KLK4 activity and/or level of expression is reduced, remaining enamel proteins after the maturation process of enamel inhibit normal apatite crystal growth. This second event strengthens the first one by additionally increasing the amount of remaining enamelin in mature enamel. In such case, extraneous proteins such as serum albumin are able to accumulate in the poor quality enamel (Farah et al., 2010) worsening the hypomineralization, finally diagnosed as white opaque spots (Denis et al., 2013).

Human and animal populations are exposed to many EDCs simultaneously. BPA certainly acts in combination with other EDCs or hypomineralizing agents. These molecules do not necessarily share the same structural properties, and act through different signaling pathways and receptors. Consequently, the effects of EDCs combinations are unpredictable. For example, combination of low doses of BPA with low doses of genistein and vinclozolin, two other EDCs, didn't lead to a greater phenotype (Jedeon et al., 2014a) whereas combination of BPA with fluoride increased enamel hypomineralization (Jedeon et al., 2016a). Enamel defects have also been associated to exposure to dioxin (Alaluusua et al., 2004) and PCBs (Jan et al., 2007), two groups of pollutants presenting EDC activity. Interestingly, dioxin and amoxicillin exposures have been proposed as a causal factor of Molar Incisor Hypomineralisation (MIH) (Alaluusua et al., 1999; Laisi et al., 2009). It is noteworthy that both factors increase enamel hypomineralization in the presence of fluoride (Salmela et al., 2011; Sahlberg et al., 2013) and the importance of the perinatal exposure to these agents has been underlined (Alaluusua et al., 2002). Even if fluoride is probably not a causal factor of MIH, experimental fluoride in combination with EDCs was shown to increase enamel hypomineralization (Salmela et al., 2011; Sahlberg et al., 2013; Jedeon et al., 2016a).

A number of EDCs are known to disrupt the steroid axis. BPA, for example, binds ERs (Delfosse et al., 2012), GPR30 (Pupo et al., 2012), and ERRγ with high affinity (Liu et al., 2012; abbreviations in **Table 1**). BPA is also able to, directly or indirectly, modulate the activity of AR, PR, GR, RXR, and PPARγ receptors (Li et al., 2015; Rehan et al., 2015). Except PPARγ and ERβ, rodent ameloblasts express all these receptors and their expression levels vary depending on the ameloblast differentiation stage (Houari et al., 2016; **Figure 1**). Furthermore, we have shown that ERα is involved in pre-ameloblast proliferation (Jedeon et al., 2014b), and AR in the enamel terminal mineralization process (Jedeon et al., 2016b). Thus, mediated by these receptors, EDCs such as BPA and vinclozolin may disrupt amelogenesis. GR and VDR are classically associated to amelogenesis and enamel mineralization (Pawlicki et al., 1992; Berdal et al., 1993) and might also play a role in the transmission of EDC effects.

All these data argue for the steroid axis playing a central role in the physiological as well as pathological process of amelogenesis.

TABLE 1 | List of abbreviations cited in the text.

AhR	Aryl hydrocarbon Receptor
AI	Amelogenesis Imperfecta
AR	Androgen Receptor
BPA	Bisphenol A
EDC	Endocrine Disrupting Chemical
ER	Estrogen Receptor
ERRγ	Estrogen Related Receptor γ
GPR30	G-Protein-Coupled Receptor 30
GR	Glucocorticoid Receptor
KLK4	Kallikrein-related peptidase 4
MIH	Molar Incisor Hypomineralization
PCB	PolyChlorinated Biphenyl
PPARγ	Peroxisome Proliferator-Activated Receptor γ
PR	Prolactin Receptor
RAR	Retinoic Acid Receptor
RXR	Retinoid X Receptor
VDR	Vitamin D receptor

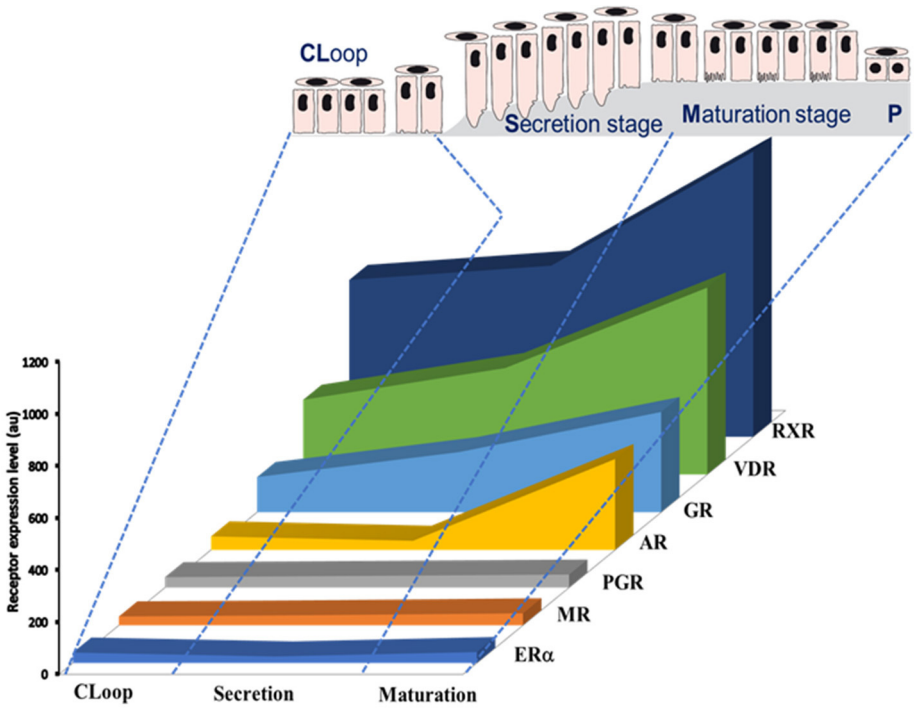

FIGURE 1 | Schematic representation of expression profiles of steroid receptors during amelogenesis based on data published by Houari et al. (2016). The relative level of expression of each mRNA was determined by microarray analysis of RNAs extracted from maturation-stage enamel organ.

The presence of these receptors which expression vary during amelogenesis suggests a stage-specific susceptibility to the corresponding ligands. These may be endogenous molecules like hormones, or exogenous such as vitamins, drugs and EDCs. Otherwise, data reported in the literature showed that many if not all MIH causal factors hypothesized are associated, directly or indirectly, with steroid axis:

Indeed, prematurity and long breastfeeding have been associated to MIH but seem controversial (Alaluusua, 2010; Sönmez et al., 2013). If so, it's worthy to note that milk may accumulate pollutants such as dioxin and PCBs, acting through AhR sharing signaling pathway with ERs (Solomon and Weiss, 2002). On the other hand, premature babies were reported to be contaminated with BPA and phthalates essentially due to medical devices (Calafat et al., 2009; Duty et al., 2013). And, both class of EDCs act via steroid receptors, ERs and AR, reported to modulate enamel key genes like KLK4 (Jedeon et al., 2016b).

MIH is also associated to infections, otitis, bronchitis, pneumonia, fever and asthma (Tourino et al., 2016). These pathologies are often treated with antibiotics combined to anti-inflammatory molecules as corticoids, acting through GR, which may lead to enamel hypomineralization. There are typical responsive elements to GR in the amelogenin promoter which is a key component of enamel matrix (Gibson et al., 1997) and exposure to corticoids was associated to enamel hypomineralization in rats (Pawlicki et al., 1992).

Deficiency in vitamin A acting through RAR/RXR pathway has been recently associated to MIH (Mishra and Pandey, 2016). Ameloblasts express retinoid receptors and binding proteins (Bloch-Zupan et al., 1994; Houari et al., 2016) and excess of retinoids disrupt amelogenesis leading to enamel hypomineralization (Morkmued et al., 2017), meaning that the right concentration of retinoids is required at the right moment of amelogenesis. Another vitamin which deficiency was associated to MIH is vitamin D (Kühnisch et al., 2015). It is well-known that vitamin D binds to the heterodimer VDR/RXR which are the most highly expressed steroid receptors in maturation-stage ameloblasts (**Figure 1**). Vitamin D and VDR are tightly associated to enamel mineralization (Berdal et al., 1993). And, the steady-state mRNA levels of enamel matrix peptides were shown vitamin-dependant in vitamin D deficient rats which harbored malformed enamel (Papagerakis et al., 2002). In addition, levels of vitamin D were inversely correlated to BPA contamination (Johns et al., 2016) suggesting a protective role of vitamin D against EDC adverse effects and reinforcing the idea of the importance of steroid axis during the pathophysiology of amelogenesis.

CONCLUSION

Many of the proposed causal factors for MIH, including EDCs, anti-inflammatory corticoids, vitamin deficiency involve the large family of the steroid receptors. Most of the steroid receptors are expressed in ameloblasts and their levels of expression are dependent on their stage of differentiation. The steroid receptors thus appear as the common elements able to modulate the

expression of enamel key genes controlling enamel synthesis or leading to enamel hypomineralization in case of disruption.

AUTHOR CONTRIBUTIONS

SB raised the hypothesis of the paper, drafted and wrote the paper. KJ, SH, and SL did experiments, obtained the results and wrote the corresponding published papers cited in the text. AB drafted, read the paper and made helpful suggestions to improve the paper. All authors approved the final version to be published.

FUNDING

This work was funded by the University Paris-Diderot, the French National Institute of Health and Medical Research (INSERM).

REFERENCES

Alaluusua, S. (2010). Aetiology of molar-incisor hypomineralisation: a systematic review. *Eur. Arch. Paediatr. Dent.* 11, 53–58. doi: 10.1007/BF03262713

Alaluusua, S., Calderara, P., Gerthoux, P. M., Lukinmaa, P. L., Kovero, O., Needham, L., et al. (2004). Developmental dental aberrations after the dioxin accident in Seveso. *Environ. Health Perspect.* 112, 1313–1318. doi: 10.1289/ehp.6920

Alaluusua, S., Kiviranta, H., Leppaniemi, A., Hölttä, P., Lukinmaa, P. L., Lope, L., et al. (2002). Natal and neonatal teeth in relation to environmental toxicants. *Pediatr. Res.* 52, 652–655. doi: 10.1203/00006450-200211000-00008

Alaluusua, S., Lukinmaa, P. L., Torppa, J., Tuomisto, J., and Vartiainen, T. (1999). Developing teeth as biomarker of dioxin exposure. *Lancet* 353, 206. doi: 10.1016/S0140-6736(05)77214-7

Bartlett, J. D., and Simmer, J. P. (2014). Kallikrein-related peptidase-4 (KLK4): role in enamel formation and revelations from ablated mice. *Front. Physiol.* 5:240. doi: 10.3389/fphys.2014.00240

Berdal, A., Hotton, D., Pike, J. W., Mathieu, H., and Dupret, J. M. (1993). Cell- and stage-specific expression of vitamin D receptor and calbindin genes in rat incisor: regulation by 1,25-dihydroxyvitamin D3. *Dev. Biol.* 155, 172–179. doi: 10.1006/dbio.1993.1016

Bloch-Zupan, A., Décimo, D., Loriot, M., Mark, M. P., and Ruch, J. V. (1994). Expression of nuclear retinoic acid receptors during mouse odontogenesis. *Differentiation* 57, 195–203. doi: 10.1046/j.1432-0436.1994.5730195.x

Braun, J. M. (2017). Early-life exposure to EDCs: role in childhood obesity and neurodevelopment. *Nat. Rev. Endocrinol.* 13, 161–173. doi: 10.1038/nrendo.2016.186

Calafat, A. M., Weuve, J., Ye, X., Jia, L. T., Hu, H., Ringer, S., et al. (2009). Exposure to bisphenol A and other phenols in neonatal intensive care unit premature infants. *Environ. Health Perspect.* 117, 639–644. doi: 10.1289/ehp.0800265

Chan, H. C., Estrella, N. M., Milkovich, R. N., Kim, J. W., Simmer, J. P., and Hu, J. C. (2011). Target gene analyses of 39 amelogenesis imperfecta kindreds. *Eur. J. Oral Sci.* 119(Suppl. 1), S311–S323. doi: 10.1111/j.1600-0722.2011.00857.x

Chaussain, C., Bouazza, N., Gasse, B., Laffont, A. G., Opsahl Vital, S., Davit-Béal, T., et al. (2014). Dental caries and enamelin haplotype. *J. Dent. Res.* 93, 360–365. doi: 10.1177/0022034514522060

Cooper, J. E., Kendig, E. L., and Belcher, S. M. (2011). Assessment of bisphenol A released from reusable plastic, aluminium and stainless steel water bottles. *Chemosphere* 85, 943–947. doi: 10.1016/j.chemosphere.2011.06.060

Delfosse, V., Grimaldi, M., Pons, J. L., Boulahtouf, A., le Maire, A., Cavailles, V., et al. (2012). Structural and mechanistic insights into bisphenols action provide guidelines for risk assessment and discovery of bisphenol A substitutes. *Proc. Natl. Acad. Sci. U.S.A.* 109, 14930–14935. doi: 10.1073/pnas.12035 74109

Denis, M., Atlan, A., Vennat, E., Tirlet, G., and Attal, J. P. (2013). White defects on enamel: diagnosis and anatomopathology: two essential factors for proper treatment (part 1). *Int. Orthod.* 11, 139–165. doi: 10.1016/j.ortho.2013.02.014

Duty, S. M., Mendonca, K., Hauser, R., Calafat, A. M., Ye, X., Meeker, J. D., et al. (2013). Potential sources of bisphenol A in the neonatal intensive care unit. *Pediatrics* 131, 483–489. doi: 10.1542/peds.2012-1380

Farah, R. A., Monk, B. C., Swain, M. V., and Drummond, B. K. (2010). Protein content of molar-incisor hypomineralisation enamel. *J. Dent.* 38, 591–596. doi: 10.1016/j.jdent.2010.04.012

Gibson, C. W., Collier, P. M., Yuan, Z. A., Chen, E., Adeleke-Stainback, P., Lim, J., et al. (1997). Regulation of amelogenin gene expression. *Ciba Found. Symp.* 205, 187–97; discussion 197–9.

Gore, A. C., Chappell, V. A., Fenton, S. E., Flaws, J. A., Nadal, A., Prins, G. S., et al. (2015). EDC-2: the endocrine society's second scientific statement on endocrine-disrupting chemicals. *Endocr. Rev.* 36, E1–E150. doi: 10.1210/er.2015-1093

Houari, S., Loiodice, S., Jedeon, K., Berdal, A., and Babajko, S. (2016). Expression of steroid receptors in ameloblasts during amelogenesis in rat incisors. *Front. Physiol.* 7:503. doi: 10.3389/fphys.2016.00503

Hu, J. C., Hu, Y., Lu, Y., Smith, C. E., Lertlam, R., Wright, J. T., et al. (2014). Enamelin is critical for ameloblast integrity and enamel ultrastructure formation. *PLoS ONE* 9:e89303. doi: 10.1371/journal.pone.0089303

Jälevik, B., Dietz, W., and Norén, J. G. (2005). Scanning electron micrograph analysis of hypomineralized enamel in permanent first molars. *Int. J. Paediatr. Dent.* 15, 233–240. doi: 10.1111/j.1365-263X.2005.00644.x

Jan, J., Sovcikova, E., Kocan, A., Wsolova, L., and Trnovec, T. (2007). Developmental dental defects in children exposed to PCBs in eastern Slovakia. *Chemosphere* 67, S350–S354. doi: 10.1016/j.chemosphere.2006.05.148

Jedeon, K., De la Dure-Molla, M., Brookes, S. J., Loiodice, S., Marciano, C., Kirkham, J., et al. (2013). Enamel defects reflect perinatal exposure to bisphenol A. *Am. J. Pathol.* 83, 108–118. doi: 10.1016/j.ajpath.2013.04.004

Jedeon, K., Houari, S., Loiodice, S., Thuy, T. T., Le Normand, M., Berdal, A., et al. (2016a). Chronic exposure to bisphenol A exacerbates dental fluorosis in growing rats. *J. Bone Miner. Res.* 31, 1955–1966. doi: 10.1002/jbmr.2879

Jedeon, K., Loiodice, S., Le Normand, M., Houari, S., Chaloyard, J., Salhi, K., et al. (2016b). Androgen receptor involvement in rat amelogenesis: an additional way for endocrine disrupting chemicals to affect enamel synthesis. *Endocrinology* 157, 4287–4296. doi: 10.1210/en.2016-1342

Jedeon, K., Loiodice, S., Marciano, C., Vinel, A., Canivenc Lavier, M. C., Berdal, A., et al. (2014b). Estrogen and bisphenol A affect male rat enamel formation and promote ameloblast proliferation. *Endocrinology* 155, 3365–3375. doi: 10.1210/en.2013-2161

Jedeon, K., Marciano, C., Loiodice, S., Boudalia, S., Canivenc Lavier, M.-C., Berdal, A., et al. (2014a). Enamel hypomineralization due to endocrine disruptors. *Conn. Tiss. Res.* 55, 1–5. doi: 10.3109/03008207.2014.923857

Jeremias, F., Koruyucu, M., Küchler, E. C., Bayram, M., Tuna, E. B., Deeley, K., et al. (2013). Genes expressed in dental enamel development are associated with molar-incisor hypomineralization. *Arch. Oral Biol.* 58, 1434–1442. doi: 10.1016/j.archoralbio.2013.05.005

Johns, L. E., Ferguson, K. K., and Meeker, J. D. (2016). Relationships between urinary phthalate metabolite and bisphenol A concentrations and vitamin D levels in U.S. Adults: National Health and Nutrition Examination Survey (NHANES), 2005–2010. *J. Clin. Endocrinol. Metab.* 101, 4062–4069. doi: 10.1210/jc.2016-2134

Koch, G., Hallonsten, A. L., Ludvigsson, N., Hansson, B. O., Holst, A., and Ullbro, C. (1987). Epidemiologic study of idiopathic enamel hypomineralization in permanent teeth of Swedish children. *Commun. Dent. Oral Epidemiol.* 15, 279–285. doi: 10.1111/j.1600-0528.1987.tb00538.x

Kühnisch, J., Thiering, E., Kratzsch, J., Heinrich-Weltzien, R., Hickel, R., and Heinrich, J. (2015). GINIplus study group; LISAplus study group. Elevated serum 25(OH)-vitamin D levels are negatively correlated with molar-incisor hypomineralization. *J. Dent. Res.* 94, 381–387. doi: 10.1177/0022034514561657

Laisi, S., Ess, A., Sahlberg, C., Arvio, P., Lukinmaa, P. L., and Alaluusua, S. (2009). Amoxicillin may cause molar incisor hypomineralization. *J. Dent. Res.* 88, 132–136. doi: 10.1177/0022034508328334

Li, L., Wang, Q., Zhang, Y., Niu, Y., Yao, X., and Liu, H. (2015). The molecular mechanism of bisphenol A (BPA) as an endocrine disruptor by interacting with nuclear receptors: insights from molecular dynamics (MD) simulations. *PLoS ONE* 10:e0120330. doi: 10.1371/journal.pone.0120330

Lindemeyer, R. G., Gibson, C. W., and Wright, T. J. (2010). Amelogenesis imperfecta due to a mutation of the enamelin gene: clinical case with genotype-phenotype correlations. *Pediatr. Dent.* 32, 56–60.

Liu, X., Matsushima, A., Nakamura, M., Costa, T., Nose, T., and Shimohigashi, Y. (2012). Fine spatial assembly for construction of the phenol pocket to capture bisphenol A in the human nuclear receptor estrogen related receptor γ. *J. Biochem.* 151, 403–415. doi: 10.1093/jb/mvs008

Mishra, A., and Pandey, R. K. (2016). Molar incisor hypomineralization: an epidemiological study with prevalence and etiological factors in Indian pediatric population. *Int. J. Clin. Pediatr. Dent.* 9, 167–171. doi: 10.5005/jp-journals-10005-1357

Morkmued, S., Laugel-Haushalter, V., Mathieu, E., Schuhbaur, B., Hemmerlé, J., Dollé, P., et al. (2017). Retinoic acid excess impairs amelogenesis inducing enamel defects. *Front. Physiol.* 7:673. doi: 10.3389/fphys.2016.00673

Papagerakis, P., MacDougall, M., and Berdal, A. (2002). Differential epithelial and mesenchymal regulation of tooth-specific matrix proteins expression by 1,25-dihydroxyvitamin D3 *in vivo*. *Connect. Tissue Res.* 43, 372–375. doi: 10.1080/03008200290000655

Pawlicki, R., Knychalska-Karwin, Z., Stankiewicz, D., Jakób-Dolezal, K., and Karwan, T. (1992). Disturbances of mineral metabolism in teeth of rats receiving corticosteroids for 3 generations. *Folia Histochem. Cytobiol.* 30, 75–78.

Poimenova, A., Markaki, E., Rahiotis, C., and Kitraki, E. (2010). Corticosterone-regulated actions in the rat brain are affected by perinatal exposure to low dose of bisphenol A. *Neuroscience* 167, 741–749. doi: 10.1016/j.neuroscience.2010.02.051

Pupo, M., Pisano, A., Lappano, R., Santolla, M. F., De Francesco, E. M., Abonante, S., et al. (2012). Bisphenol A induces gene expression changes and proliferative effects through GPER in breast cancer cells and cancer-associated fibroblasts. *Environ. Health Perspect.* 120, 1177–1182. doi: 10.1289/ehp.1104526

Rehan, M., Ahmad, E., Sheikh, I. A., Abuzenadah, A. M., Damanhouri, G. A., Bajouh, O. S., et al. (2015). Androgen and progesterone receptors are targets for Bisphenol A (BPA), 4-methyl-2,4-bis-(P-Hydroxyphenyl)Pent-1-Ene–A potent metabolite of BPA, and 4-Tert-Octylphenol: a computational insight. *PLoS ONE* 10:e0138438. doi: 10.1371/journal.pone.0138438

Sahlberg, C., Pavlic, A., Ess, A., Lukinmaa, P. L., Salmela, E., and Alaluusua, S. (2013). Combined effect of amoxicillin and sodium fluoride on the structure of developing mouse enamel *in vitro*. *Arch. Oral Biol.* 58, 1155–1164. doi: 10.1016/j.archoralbio.2013.03.007

Salmela, E., Lukinmaa, P. L., Partanen, A. M., Sahlberg, C., and Alaluusua, S. (2011). Combined effect of fluoride and 2,3,7,8-tetrachlorodibenzo-p-dioxin on mouse dental hard tissue formation *in vitro*. *Arch. Toxicol.* 85, 953–963. doi: 10.1007/s00204-010-0619-4

Serna, C., Vicente, A., Finke, C., and Ortiz, A. J. (2016). Drugs related to the etiology of molar incisor hypomineralization: a systematic review. *J. Am. Dent. Assoc.* 147, 120–130. doi: 10.1016/j.adaj.2015.08.011

Silva, M. J., Scurrah, K. J., Craig, J. M., Manton, D. J., and Kilpatrick, N. (2016). Etiology of molar incisor hypomineralization - A systematic review. *Commun. Dent. Oral Epidemiol.* 44, 342–353. doi: 10.1111/cdoe.12229

Solomon, G. M., and Weiss, P. M. (2002). Chemical contaminants in breast milk: time trends and regional variability. *Environ. Health Perspect.* 110, A339–A347. doi: 10.1289/ehp.021100339

Sönmez, H., Yıldırım, G., and Bezgin, T. (2013). Putative factors associated with molar incisor hypomineralisation: an epidemiological study. *Eur. Arch. Paediatr. Dent.* 14, 375–380. doi: 10.1007/s40368-013-0012-0

Tourino, L. F., Corrêa-Faria, P., Ferreira, R. C., Bendo, C. B., Zarzar, P. M., and Vale, M. P. (2016). Association between molar incisor hypomineralization in schoolchildren and both prenatal and postnatal factors: a population-based study. *PLoS ONE* 11:e0156332. doi: 10.1371/journal.pone.0156332

Varayoud, J., Ramos, J. G., Munoz-de-Toro, M., and Luque, E. H. (2014). Long-lasting effects of neonatal bisphenol A exposure on the implantation process. *Vitam. Horm.* 94, 253–275. doi: 10.1016/B978-0-12-800095-3.00010-9

Weerheijm, K. L., Jalevik, B., and Alaluusua, S. (2001). Molar-incisor hypomineralisation. *Caries Res.* 35, 390–391. doi: 10.1159/000047479

Weerheijm, K. L., and Merjare, I. (2003). Molar incisor hypomineralisation: a questionnaire inventory on its occurrence in member countries of the European Academy of Paediatric Dentistry (EAPD). *Int. J. Paediatr. Dent.* 13, 411–416. doi: 10.1046/j.1365-263X.2003.00498.x

Conflict of Interest Statement: The authors declare that the research was conducted in the absence of any commercial or financial relationships that could be construed as a potential conflict of interest.

Copyright © 2017 Babajko, Jedeon, Houari, Loiodice and Berdal. This is an open-access article distributed under the terms of the Creative Commons Attribution License (CC BY). The use, distribution or reproduction in other forums is permitted, provided the original author(s) or licensor are credited and that the original publication in this journal is cited, in accordance with accepted academic practice. No use, distribution or reproduction is permitted which does not comply with these terms.

frontiers in Physiology

ORIGINAL RESEARCH
published: 11 May 2017
doi: 10.3389/fphys.2017.00302

4-phenylbutyrate Mitigates Fluoride-Induced Cytotoxicity in ALC Cells

Maiko Suzuki[1], *Eric T. Everett*[2], *Gary M. Whitford*[3] *and John D. Bartlett*[1]*

[1] Division of Biosciences, College of Dentistry, The Ohio State University, Columbus, OH, USA, [2] Department of Pediatric Dentistry and The Carolina Center for Genome Sciences, University of North Carolina, Chapel Hill, NC, USA, [3] Department of Oral Biology, College of Dental Medicine, Georgia Regents University, Augusta, GA, USA

Chronic fluoride over-exposure during pre-eruptive enamel development can cause dental fluorosis. Severe dental fluorosis is characterized by porous, soft enamel that is vulnerable to erosion and decay. The prevalence of dental fluorosis among the population in the USA, India and China is increasing. Other than avoiding excessive intake, treatments to prevent dental fluorosis remain unknown. We previously reported that high-dose fluoride induces endoplasmic reticulum (ER) stress and oxidative stress in ameloblasts. Cell stress induces gene repression, mitochondrial damage and apoptosis. An aromatic fatty acid, 4-phenylbutyrate (4PBA) is a chemical chaperone that interacts with misfolded proteins to prevent ER stress. We hypothesized that 4PBA ameliorates fluoride-induced ER stress in ameloblasts. To determine whether 4PBA protects ameloblasts from fluoride toxicity, we analyzed gene expression of *Tgf-β1*, *Bcl2*/*Bax* ratio and cytochrome-c release *in vitro*. *In vivo*, we measured fluorosis levels, enamel hardness and fluoride concentration. Fluoride treated Ameloblast-lineage cells (ALC) had decreased *Tgf-β1* expression and this was reversed by 4PBA treatment. The anti-apoptotic *Blc2*/*Bax* ratio was significantly increased in ALC cells treated with fluoride/4PBA compared to fluoride treatment alone. Fluoride treatment induced cytochrome-c release from mitochondria into the cytosol and this was inhibited by 4PBA treatment. These results suggest that 4PBA mitigates fluoride-induced gene suppression, apoptosis and mitochondrial damage *in vitro*. *In vivo,* C57BL/6J mice were provided fluoridated water for six weeks with either fluoride free control-chow or 4PBA-containing chow (7 g/kg 4PBA). With few exceptions, enamel microhardness, fluorosis levels, and fluoride concentrations of bone and urine did not differ significantly between fluoride treated animals fed with control-chow or 4PBA-chow. Although 4PBA mitigated high-dose fluoride toxicity *in vitro*, a diet rich in 4PBA did not attenuate dental fluorosis in rodents. Perhaps, not enough intact 4PBA reaches the rodent ameloblasts necessary to reverse the effects of fluoride toxicity. Further studies will be required to optimize protocols for 4PBA administration *in vivo* in order to evaluate the effect of 4PBA on dental fluorosis.

Keywords: fluoride, dental fluorosis, enamel, ameloblast, 4-phenylbutyrate, ER stress, apoptosis, TGF-β1

OPEN ACCESS

Edited by:
Steven Joseph Brookes, Leeds Dental Institute, UK

Reviewed by:
Pierfrancesco Pagella, University of Zurich, Switzerland
Michael Lansdell Paine, University of Southern California, USA
Bo Han, China Agricultural University, China
Mike Hubbard, University of Melbourne, Australia

***Correspondence:**
John D. Bartlett
bartlett.196@osu.edu

Specialty section:
This article was submitted to Craniofacial Biology and Dental Research, a section of the journal Frontiers in Physiology

Received: *16 February 2017*
Accepted: *25 April 2017*
Published: *11 May 2017*

Citation:
Suzuki M, Everett ET, Whitford GM and Bartlett JD (2017) 4-phenylbutyrate Mitigates Fluoride-Induced Cytotoxicity in ALC Cells. Front. Physiol. 8:302. doi: 10.3389/fphys.2017.00302

INTRODUCTION

Dental caries remains the most common chronic disease in which acid produced by bacteria dissolves tooth enamel (Dye et al., 2017). Dental caries is a largely preventable condition and fluoride has proven an effective caries prophylactic. The U.S. Public Health Service (PHS) recommends public water fluoridation at an optimal fluoride concentration of 0.7 ppm (corresponding to 0.04 mM NaF) in order to prevent dental caries (Health and Human Services Federal Panel on Community Water, 2015). On the other hand, fluoride is an environmental health hazard and acute or chronic over-exposure can result in enamel fluorosis (Denbesten, 1999), skeletal fluorosis (Boivin et al., 1989), and reproductive toxicity in animal models (Sm and Mahaboob Basha, 2017).

The prevalence of dental fluorosis among the population in the USA, India, and China is increasing. Predominantly mild dental fluorosis among children aged 12–15 in USA is about 41% and represents an increase compared to the 1980s when it was 23% (Beltrán-Aguilar et al., 2010).

However, other than avoiding excessive intake during enamel development, treatments to prevent dental fluorosis remain unknown. Fluoride exerts diverse cellular effects in a dose, cell type, and tissue dependent manner. We and others have shown in several rodent tissues, including the enamel organ, that high-dose fluoride causes cell stress, such as endoplasmic reticulum (ER) stress (Kubota et al., 2005; Sharma et al., 2008; Ito et al., 2009) and oxidative stress (Sun et al., 2011; Suzuki et al., 2014b, 2015).

Enamel development occurs in stages, as defined by the morphology of the ameloblasts responsible for enamel formation. Secretory-stage ameloblasts secrete matrix metalloproteinase 20 (MMP20) and enamel proteins that combine to form a mineralization front that promotes appositional growth until the enamel layer reaches full thickness (Simmer et al., 2012; Bartlett and Smith, 2013). Maturation-stage ameloblasts secrete kallikrein related peptidase 4 (KLK4), reabsorb protein degradation products, and promote mass mineral deposition as the enamel hardens into its final form (Hu and Simmer, 2007). During the maturation stage ameloblasts are in direct contact with the acidic (pH $<$ 6.0) mineralizing enamel matrix (Smith et al., 1996). Therefore, maturation stage ameloblasts are exposed to fluoride under low pH conditions. The low extracellular pH surrounding the maturation stage ameloblasts promotes the conversion of F^- to HF. When the pKa value for HF (3.45) is substituted in the Henderson-Hasselbalch equation (pH = pKa+log $[F^-]/[HF]$), we observe that at pH 7.4, the $[F^-]$: [HF] ratio is 8913:1. However, at pH 6.0, this ratio decreases to 355:1. Therefore, approximately 25-fold more HF is formed at pH 6.0 as compared to pH 7.4. The low pH environment of maturation stage facilitates entry of toxic HF into ameloblasts to enhance fluoride-induced cell stress (Sharma et al., 2010). This suggests that compared to the secretory stage (pH $\sim$ 7.2), the low pH environment of the maturation stage reduces the threshold dose required to induce fluoride-mediated cytotoxicity *in vivo*. In contrast, the *in vitro* cell culture environment (culture media) is neutral (pH $\sim$ 7.3) which requires a higher fluoride dose than does a low pH environment to induce fluoride-mediated cytotoxicity. This suggests that the neutral cell culture environment *in vitro* requires a higher dose of fluoride than is present in serum to induce fluoride toxicity *in vitro*. It has previously been demonstrated that 100 fold disparity exists between fluoride sensitivity *in vitro* and *in vivo* (Bronckers et al., 2009).

The ER functions as a quality control organelle and prevents misfolded proteins from traversing the secretory pathway (Zhang et al., 1997). ER stress is caused by the accumulation of unfolded proteins. The response to this stress is known as the unfolded protein response (UPR) (Doyle et al., 2011). UPR activation results in transient suppression of protein translation, enabling cells to cope with the existing misfolded protein load. The UPR increases ER chaperone gene expression including GRP78/Bip to augment the folding capacity of the ER (Claudio et al., 2013).

Accumulated proteins may also be removed via the ER-associated degradative pathway (Bonifacino and Weissman, 1998). UPR-mediated alleviation of ER stress may allow the cell to survive, whereas prolonged ER stress can result in apoptosis (Gow and Sharma, 2003).

High-dose fluoride can trigger ER stress, which compromises ameloblast function during enamel development. Fluoride decreases KLK4 and TGF-β1 transcript and protein levels that are necessary for enamel formation (Suzuki et al., 2014a).

Chemical chaperones are small molecules and can eliminate aggregation and/or accumulation of misfolded proteins (Zhao et al., 2007) to cope with the ER stress. One such molecule is sodium 4-phenylbutyrate (4PBA). As a chemical chaperone, 4PBA helps with the correct folding of proteins to reduce ER stress (Kolb et al., 2015). 4PBA is a known inhibitor of histone deacetylase (HDAC) that could also affect gene expression (Daosukho et al., 2007). 4PBA is FDA-approved and is licensed for the treatment of urea cycle disorders (Iannitti and Palmieri, 2011), sickle cell disease (Odievre et al., 2007), and thalassemia (Collins et al., 1995). Amelogenesis imperfecta (AI) is an inherited disorder of enamel development with an incidence as high as 1 in 700 live births (Backman and Holm, 1986). A recent study demonstrated that AI pathogenesis is associated with ameloblast apoptosis induced by ER stress and 4PBA treatment rescued the AI enamel phenotype by inhibiting ER stress-mediated apoptosis in rodent model (Brookes et al., 2014).

To study dental fluorosis, rodent models have been employed because rodent incisors erupt continuously and every stage of enamel development is present along the length of the rodent incisor.

Here we assessed whether 4PBA protects against fluoride-mediated gene repression, apoptosis, and mitochondrial damage *in vitro*, and we analyzed 4PBA efficacy in the mouse dental fluorosis model.

MATERIALS AND METHODS

Reagents

Sodium fluoride (NaF) Cat. S299-100 was obtained from Fisher Scientific, (Pittsburgh, PA). 4-phenylbutyric acid sodium salt (4PBA) was purchased from Scandinavian Formulas, Cat. 1716-12-7 (Sellerville, PA).

Animals

C57BL/6 mice (6-week-old) were purchased from Charles River Laboratories (Wilmington, MA). Mice (N=5/group) were provided water containing 0, 50, 100 ppm fluoride as NaF *ad libitum* for 6 weeks. Animals were fed with either fluoride-free control-chow (F1515, rodent standard diet, AIN-76A, Bio-Sev, Frenchtown, NJ) or 4PBA-chow (same as control-chow containing 7 g/kg 4PBA, rodent custom diet, Bio-Sev). Mice were kept on these different chows beginning 1 week prior to fluoride water treatment until fluoride treatment termination. After fluoride treatment for 6 weeks, animals were euthanized and incisors were extracted for quantitative fluorescence (QF) analysis, Vickers microhardness measurments and measurement of fluoride concentration in bone, serum, and urine. All animals were treated humanely and all handling procedures were approved by the Institutional Animal Care Use Committee (IACUC) at The Forsyth Institute. The Forsyth Institute is accredited by the Association for Assessment and Accreditation of Laboratory Animal Care International (AAALAC) and follows the Guide for the Care and Use of Laboratory Animals (NRC1996). Note that the first and senior authors were employed by The Forsyth Institute through October 2015 when the animal experiments were completed.

Cell Culture

Mouse ameloblast-lineage cell line (ALC) Cells (Nakata et al., 2003) were grown in Dulbecco's modified Eagle's medium supplemented with 10% fetal bovine serum, 4.5 g/l of D-glucose, 4 mM L-glutamine, and 110 mg/l of sodium pyruvate (Invitrogen, Carlsbad, CA, USA) without antibiotics. Cells were treated with or without NaF (1–5 mM) in the presence or absence of 4PBA as indicated. 4PBA was present throughout the fluoride exposure. NaF 5 mM is corresponding to F^- 95 ppm.

Real-Time Quantitative PCR (qPCR) Analysis

Total RNA was extracted from cells using Direct-zol RNA Mini Prep (Zymo Research Corp., Irvine, CA).

Total RNA was reverse-transcribed into cDNA using a Transcriptor First Strand cDNA Synthesis Kit (Roche Diagnostics, Minneapolis, MN). The cDNA was subjected to qPCR amplification on a LightCycler 480 Real Time PCR System (Roche Diagnostics). The relative expression of target genes was determined by the $2^{-\Delta\Delta CT}$ method (Pfaffl, 2001). The internal reference control gene was *B2m*. Primers (Invitrogen) and their sequences were;

Bcl2 (Gene ID 12043),

forward: 5′-TCAGGCTGGAAGGAGAAGATG-3′ reverse: 5′-TGTCACAGAGGGGCTACGAGT-3′,

Bax (Gene ID 12028),

forward: 5′-AGCTGCCACCCGGAAGAAGACCT-3′ reverse: 5′-CCGGCGAATTGGAGATGAACTG-3′

Tgf-β1 (Gene ID 21803),

forward: 5′-AGGACCTGGGTTGGAAGTGGAT-3′ reverse: 5′-AAGCGCCCGGGTTGTGTT-3′

B2m (Gene ID 12010),

forward: 5′- GGTCTTTCTGGTGCTTGTCTC -3′ reverse: 5′-CGTAGCAGTTCAGTATGTTCG G -3′.

Three biological replicates were analyzed. Data were presented as the mean ± standard deviation (SD).

Western Blot Analysis

Western blots were performed as described previously (Suzuki et al., 2015). Briefly, mitochondrial fractions and cytosolic fractions were isolated using a mitochondria isolation kit for cultured cells (Thermo Scientific, Rockford, IL). Equal amounts of protein per lane (5–20 μg) were loaded onto Mini-Protean® TGX™ gels (Biorad, Hercules, CA), transferred to Trans-Blot Turbo Transfer nitrocellulose membranes (Biorad) and probed with primary antibodies. Primary antibodies included: rabbit anti-cytochrome-c, rabbit anti-VDAC1/Porin (Abcam, Inc., Cambridge, MA), and rabbit anti-β-actin (Cell Signaling Technology, Danvers, MA). The secondary antibody was HRP-conjugated goat anti-rabbit IgG (Biorad). Enhanced chemiluminescence was performed with SuperSignal West Pico (Thermo Scientific). Signal was detected by myECL imager (Thermo Scientific) and band density was quantified using myimageAnalysis™ Software (Thermo Scientific).

Photographs of Mouse Incisors

After fluoride water treatment with control-chow or 4PBA-chow for 6 weeks, animals were euthanized. Heads were cleaned of fur and skin. Photographs of the maxillary and mandibular incisors were taken using a Nikon SMZ745T microscope and Leica DFC400 digital camera under standard white balance and lighting conditions.

QF Assay and Measurement of Fluoride Concentration

Quantitative fluorescence (QF) has been used to evaluate the severity of fluorosis in mice (Everett et al., 2002). Mandibular incisors were dissected as pairs and subjected to QF using a Nikon epifluorescence micro camera equipped with a Chroma Gold 11006v2 set cube (exciter D360/40x, dichroic 400DCLP, and emitter E515LPv2). Fluorescence images of teeth were converted to grayscale values and intensities were analyzed using Image J software (http://imagej.nih.gov/ij/). Samples of mouse chow, serum, urine and bone (femurs) were assessed for fluoride concentration as previously described (Sharma et al., 2011).

Vickers Microhardness Testing of Mouse Incisor Enamel

Erupted portions of mandibular and maxillary incisors from mice were washed and dehydrated with graded alcohol and acetone. Incisors were embedded sagittally in hard-formulation epoxy embedding medium (EpoFix, EMS, Hatfield, PA) and samples were ground and polished to 0.25 μm with diamond suspensions (EMS) as previously described (Shin et al., 2014). The polished samples were tested for enamel microhardness on an M 400 HI testing machine (Leco, St. Joseph, Michigan). Testing was performed with a load of 25 g for 5 s with a Vickers tip. Twelve indentations per sample were performed on five teeth per group

and averaged. Data are presented as the mean ± standard deviation (SD).

Statistical Analysis

Quantitative analysis between two groups was performed by Student's *t*-test. Multiple group comparison was performed by one-way analysis of variance with Fisher's protected least significant difference post hoc test. Significance was assessed at $P < 0.05$.

RESULTS

4PBA Reversed Fluoride-Induced *Tgf-β1* Suppression in ALC Cells

Previously we reported fluoride treatment decreased *Tgf-β1* transcript and protein levels, which is associated with enamel malformation (Suzuki et al., 2014a). Here we asked if 4PBA prevents fluoride-induced *Tgf-β1* repression. ALC cells were treated with 4PBA for 1 h followed by addition of 5 mM (95 ppm) fluoride treatment for 24 h. *Tgf-β1* mRNA expression was decreased by fluoride treatment, but this was reversed by 4PBA treatment in a dose-dependent manner ($P < 0.01$; **Figure 1**).

4PBA Increased Anti-Apoptotic Gene Expression Ratio (*Blc2/Bax*) in ALC Cells

High-dose fluoride induces apoptosis in ameloblast-derived cell line (LS8) cells (Suzuki and Bartlett, 2014) and in rodent ameloblasts (Kubota et al., 2005). Anti-apoptotic Bcl-2 protein can repress apoptotic death programs, while pro-apoptotic Bax protein can accelerate cell death. The Bcl2/Bax ratio determines survival or death following an apoptotic stimulus (Oltvai et al., 1993). Next, we assessed the 4PBA effect on the *Bcl2/Bax* expression ratio in ALC cells. The qPCR results showed that fluoride treatment alone did not significantly alter the anti-apoptotic *Blc2/Bax* ratio compared to the non-fluoride-treated control, however 4PBA treatment significantly increased the *Blc2/Bax* ratio compared to fluoride alone ($P < 0.01$; **Figure 2**). Previously we demonstrated that fluoride treatment alone induces apoptosis with accompanying caspase-3 cleavage (Suzuki and Bartlett, 2014) and DNA fragmentation (Kubota et al., 2005). In the current study, contrary our expectation, fluoride treatment alone did not significantly alter the Blc2/Bax ratio. Since there are several apoptotic pathways and apoptotic factors besides Bcl2 and Bax, we interpret that Bcl2 and Bax may not be main factors in fluoride-induced pro-apoptotic pathways in ALC cells. However, 4PBA can counteract fluoride-induced apoptosis by increasing anti-apoptotic Bcl2/Bax ratio.

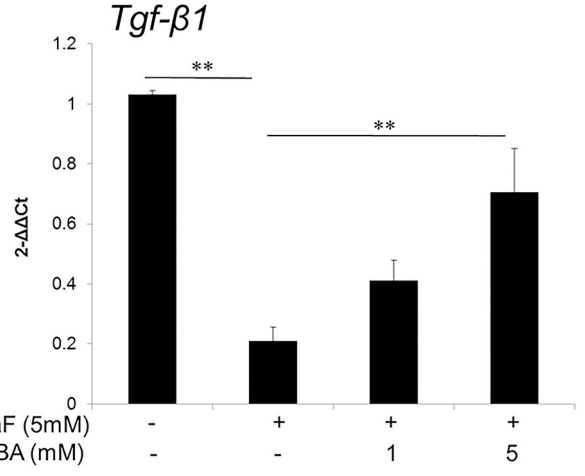

FIGURE 1 | 4PBA reversed fluoride-induced *Tgf-β1* suppression in ALC cells. ALC cells were treated with 4PBA (0–5 mM) for 1 h followed by the addition of 5 mM (95 ppm) fluoride for 24 h. *Tgf-β1* mRNA was quantified by qPCR. Fluoride decreased *Tgf-β1* expression and 4PBA treatment significantly reversed the suppression of *Tgf-β1* expression. Three biological replicates were analyzed. Data are presented as the mean ± standard deviation (SD). Results were analyzed by one-way analysis of variance with Fisher's protected least significant difference *post hoc* test. $^{**}P < 0.01$.

Fluoride-Induced Cytochrome-c Release was Inhibited by 4PBA Treatment in ALC Cells

High-dose fluoride induces oxidative stress (Suzuki et al., 2014b) followed by mitochondrial damage (Suzuki et al., 2015). Here, we asked if 4PBA mitigates fluoride-induced cytochrome-c release in ALC cells. Cells were treated with 4PBA for 1 h followed by 5 mM (95 ppm) fluoride for 24 h. Western blot results showed that fluoride treatment alone increased cytochrome-c in the cytosol fraction (Cyto) and decreased it in the mitochondrial fraction (Mito). In contrast, 4PBA treatment prevented fluoride-induced cytochrome-c release into cytosol fraction (**Figure 3**). This result indicates that 4PBA protects ameloblasts from fluoride-induced mitochondrial damage.

Effects of Fluoride and 4PBA on Rodent Tissues

Next we evaluated the 4PBA efficacy in a rodent dental fluorosis model. After fluoride treatment, animals were euthanized and incisor phenotype (**Figure 4**), fluorosis level (**Figure 5**), enamel microhardness (**Figure 6**), and fluoride concentrations in serum, urine and bone (**Figure 7**) were assessed.

Incisor Phenotype of Mice Treated with Fluoride Water with Either Control-chow or 4PBA-chow

Figure 4 shows five mouse incisors for each treatment group. Left panels show control-chow groups and right panels show 4PBA-chow groups. Among control-chow groups, compared to the 0 ppm fluoride group (upper row), tooth color was changed to chalky white opaque in both 50 ppm (middle) and 100 ppm (bottom) fluoride groups. Attrition (indicated by arrow) was observed in 50 ppm and 100 ppm groups and white spots (indicated by arrow head) were detected in the 100 ppm group. Among 4PBA-chow groups (right panels), fluoride treatment (50 ppm and 100 ppm) changed tooth color to chalky white opaque, however attrition and white spots were not seen in 4PBA-chow groups. In addition, in the 100 ppm fluoride/4PBA chow group (bottom in right panel), there was a mouse with pale creamy

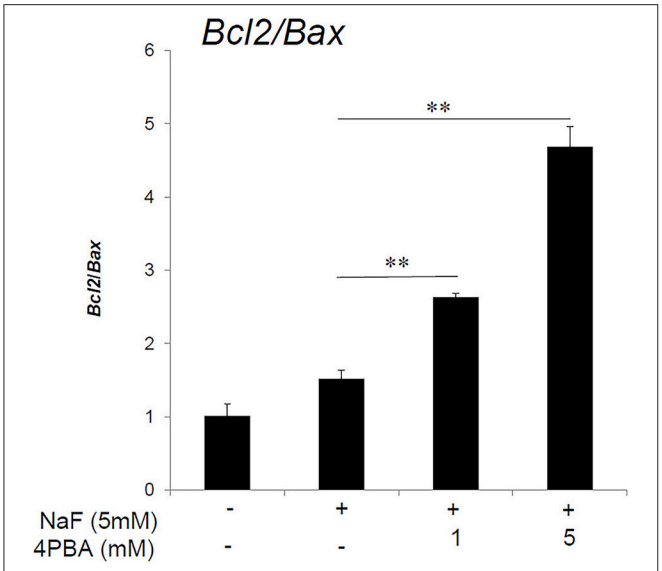

FIGURE 2 | Anti-apoptotic *Blc2/Bax* expression ratio increased by 4PBA treatment of ALC cells. ALC cells were treated with 4PBA (0–5 mM) for 1 h followed by the addition of 5 mM (95 ppm) fluoride for 24 h. *Blc2* and *Bax* mRNA were quantified by qPCR. The ratio of *Blc2/Bax* was significantly increased with NaF/4PBA treatment compared to NaF treatment alone. Three biological replicates were analyzed. Data are presented as the mean ± standard deviation (SD). Results were analyzed by one-way analysis of variance with Fisher's protected least significant difference *post hoc* test. $^{**}P < 0.01$.

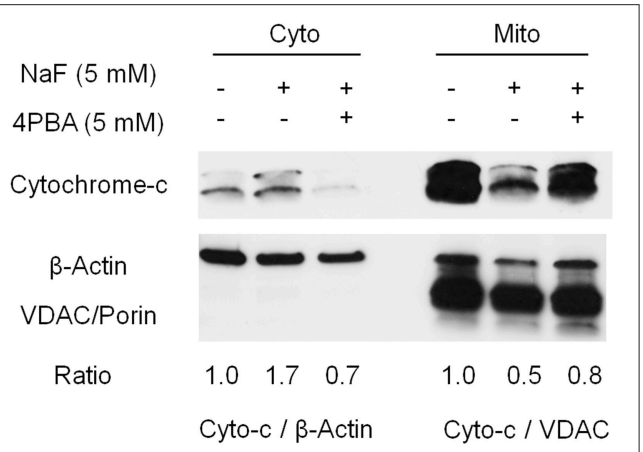

FIGURE 3 | Fluoride-induced cytochrome-c release was inhibited by 4PBA in ALC cells. ALC cells were treated with 5 mM 4PBA for 1 h followed by the addition of 5 mM (95 ppm) of fluoride for 24 h. Cytochrome-c (12 kDa) in the cytosol (Cyto) and in the mitochondria (Mito) was detected by Western blots. Fluoride induced cytochrome-c release from Mito into Cyto, which was reversed by 4PBA pretreatment. β-Actin (42 kDa) and VDAC/Porin (31 kDa) were used as loading controls for Cyto and Mito respectively. Figure shows the representative result of three biological experiments. Numbers indicate cytochrome-c/β-actin expression ratio (for cytosol) or cytochrome-c/VDAC expression ratio (for mitochondria).

colored teeth (indicated by ∗) similar to teeth in the 0 ppm group.

Fluorosis Level Quantified by QF Assay

Figure 5 shows fluorosis level as measured by QF assay. Data are presented as scatter plots from five mice in each group. Numbers indicate the mean ± standard deviation (SD). Fluoride treatment increased QF in a dose-dependent manner in both control-chow groups (−) and in 4PBA-chow groups (+). Between control-chow (−) and 4PBA-chow (+), the 4PBA-chow significantly ($**P < 0.01$) decreased QF in the 50 ppm fluoride treatment but not in the 100 ppm group.

Measurement of Enamel Hardness

Previously we demonstrated that fluorosed mouse incisor enamel is significantly softer than normal (Bartlett et al., 2004; Tye et al., 2009). Microhardness of fluoride-treated enamel significantly decreased as compared with control enamel (Sharma et al., 2011). Here we assessed the 4PBA effect on enamel hardness as a function of fluoride treatment. **Figure 6** shows Vickers microhardness values from mouse mandibular (A) and maxillary (B) incisors. Each bar represents hardness measurements for incisors from 5 mice in each group. Between control-chow (open columns) and 4PBA-chow (filled columns), the 4PBA-chow significantly ($P < 0.01$) increased enamel hardness compared to control-chow in only maxillary incisors treated with 100 ppm fluoride (**Figure 6B**).

Fluoride Concentrations in Mouse Urine, Serum, and Bone

After fluoride treatment, fluoride concentrations (ppm) in urine (A), serum (B), and bone (C) were measured (**Figure 7**). Compared to control-chow (open columns), 4PBA-chow (filled columns) had no effect on the quantity of fluoride that accumulated in the urine or bone (**Figures 7A,C**). However, 4PBA-chow significantly decreased fluoride concentration ($P < 0.05$) in serum exposed to 100 ppm fluoride treatment (**Figure 7B**). Trace amounts of fluoride were found in control-chow (1.16 ppm), 4PBA-chow (1.36 ppm) and control water (0.01 ppm). For fluoride at 50 ppm and at 100 ppm in water, we directly measured concentrations of 51.69 and 105.26 ppm respectively.

DISCUSSION

In the present study, we hypothesized that 4PBA is an effective treatment for dental fluorosis and tested if 4PBA ameliorates fluoride toxicity in ALC cells and in mouse dental fluorosis. Previously we demonstrated that high-dose fluoride induces ER stress and oxidative stress in ameloblasts that results in *Klk4* and *Tgf-β1* repression (Sharma et al., 2010; Suzuki et al., 2014a), mitochondrial damage (cytochrome-c release), DNA damage and apoptosis (Suzuki et al., 2015). In the present study, we demonstrated that 4PBA pretreatment reversed fluoride-induced *Tgf-β1* repression (**Figure 1**), increased the anti-apoptotic *Bcl2/Bax* expression ratio in ALC cells (**Figure 2**) and inhibited cytochrome-c release (**Figure 3**). However, the mechanism of how 4PBA alleviated fluoride toxicity in ALC

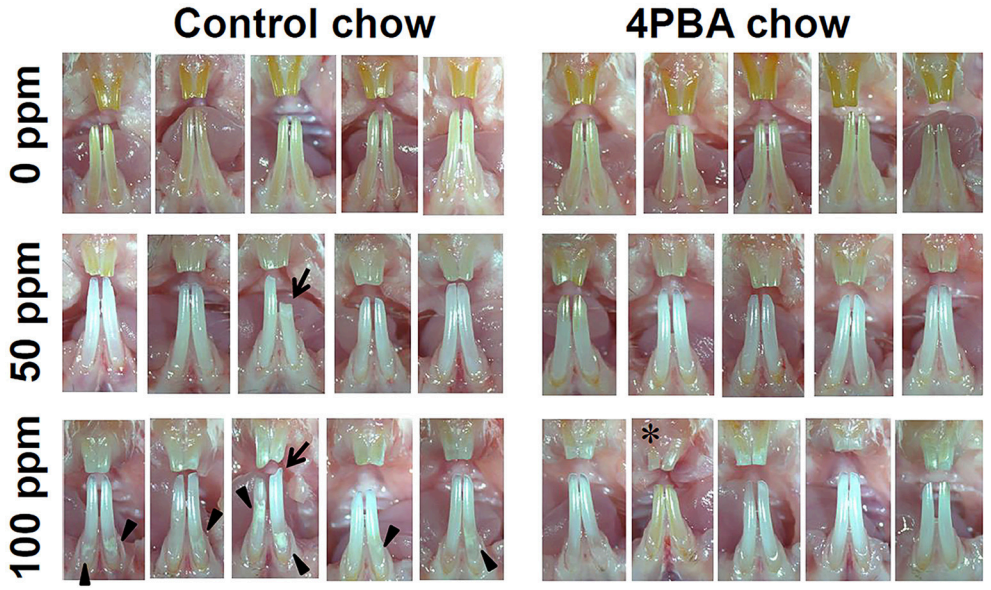

FIGURE 4 | Incisor phenotype of mice treated with fluoride with either control-chow or 4PBA-chow. C57BL/6 mice ($N = 5$/group) were provided water *ad libitum* containing 0 (upper row), 50 (middle row) or 100 (bottom row) ppm fluoride and were fed for 6 weeks with either control-chow (left panels) or 4PBA-containing chow (7 g/kg) (right panels). After 6 weeks, animals were euthanized. Pictures are of five mouse incisors for each group.

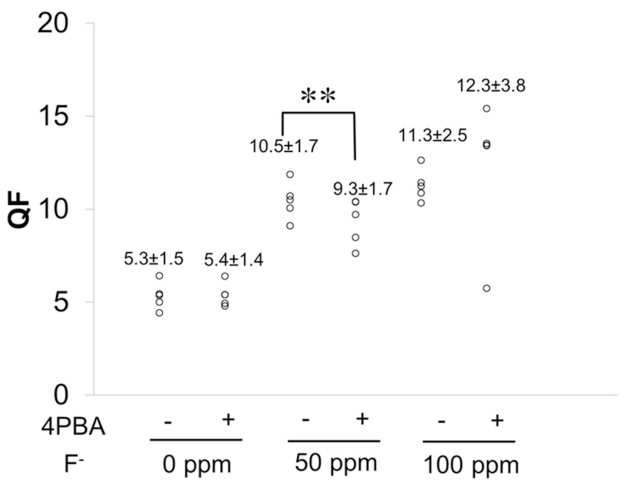

FIGURE 5 | QF analysis of enamel. C57BL/6 mice ($N = 5$/group) were provided water *ad libitum* containing fluoride (0, 50, or 100 ppm) with either control-chow or 4 PBA-chow for 6 weeks. After 6weeks, fluorescence of mandibular incisors was quantified by QF assay. Data are presented as scatter plots from five mice in each group. Numbers indicate the mean ± standard deviation (SD). Results between control-chow and 4-PBA chow were analyzed by Student's *t*-test. $P < 0.05$ was considered significant. $^{**}P < 0.01$.

cells remained to be elucidated. Since 4PBA is a chemical chaperone and helps with the correct folding of proteins to reduce ER stress (Kolb et al., 2015), 4PBA could attenuate fluoride-induced ER stress to alleviate gene repression, apoptosis and mitochondrial damage. On the other hand, 4PBA is a known inhibitor of histone deacetylase (HDAC) (Daosukho et al., 2007). 4PBA is a short chain fatty acid derivative that inhibits class I and class IIa HDACs, but not IIb HDACs (Bolden et al., 2006; Chuang et al., 2009). HDAC inhibitors increase the acetylation of histone and non-histone proteins to activate transcription, enhance gene expression, and modify the function of target proteins. HDAC inhibitors provide protection against not only ER stress but also oxidative stress to promote survival over cell stress (Fessler et al., 2013). Although it is largely unknown if and how 4PBA targets class I and class IIa HDACs during the pathology of dental fluorosis, the results *in vitro* suggest that 4PBA may ameliorate fluoride-induced *Tgf-β1* repression, apoptosis, and mitochondrial damage in ALC cells.

Next we asked if 4PBA mitigates dental fluorosis in a rodent model. **Figure 4** shows the phenotype of mouse incisors treated with fluoride and fed with either control-chow or 4PBA-chow. Contrary to our expectation, fluoride treatment changed tooth color to a chalky white opaque color in both control-chow and 4PBA-chow groups. However, attrition and white spots were observed only in the fluoride/control-chow groups but not in the fluoride/4PBA-chow groups. Moreover, in the 100 ppm fluoride/4PBA-chow group, we observed a mouse with incisors of a color similar to non-fluoride treated mice. Statistical analysis shows that 4PBA-chow significantly decreased fluorosis levels in the 50 ppm fluoride treatment group (**Figure 5**) and reversed microhardness in maxillary incisors treated with 100 ppm fluoride (**Figure 6B**) and also decreased serum fluoride concentrations in the 100 ppm fluoride treatment group (**Figure 7B**). Taken together, 4PBA might act to avert fluoride toxicity, but results were not consistent across *in vivo* analyses. In contrast to *in vitro* results, with few exceptions, 4PBA did not ameliorate dental fluorosis in our mouse model. Perhaps, not enough intact 4PBA reaches the rodent ameloblasts

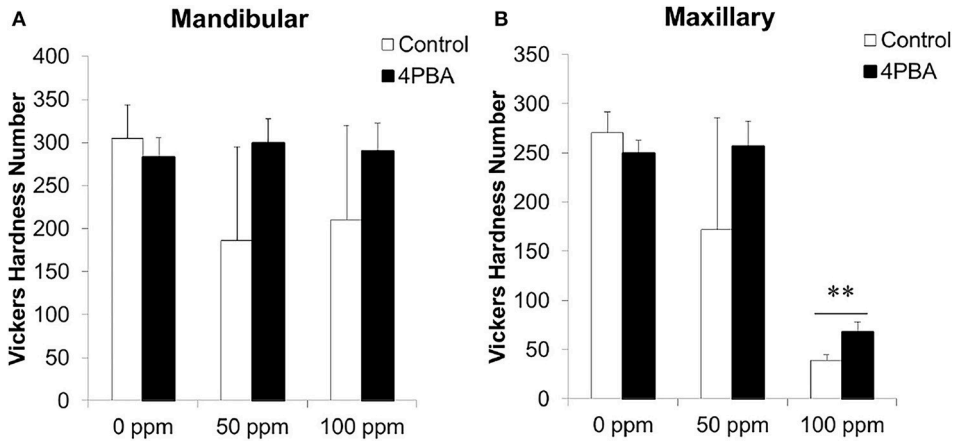

FIGURE 6 | Microhardness measurement on incisor longitudinal sections. C57BL/6 mice ($N = 5$/group) were provided water *ad libitum* containing fluoride (0, 50, or 100 ppm) with either control-chow (open columns) or 4 PBA-chow (filled columns) for 6 weeks. After 6weeks, microhardness of mandibular **(A)** and maxillary **(B)** incisors was measured. Data are presented as the mean ± standard deviation (SD). Results between control-chow and 4PBA chow were analyzed by Student's *t*-test. $P < 0.05$ was considered significant.**$P < 0.01$.

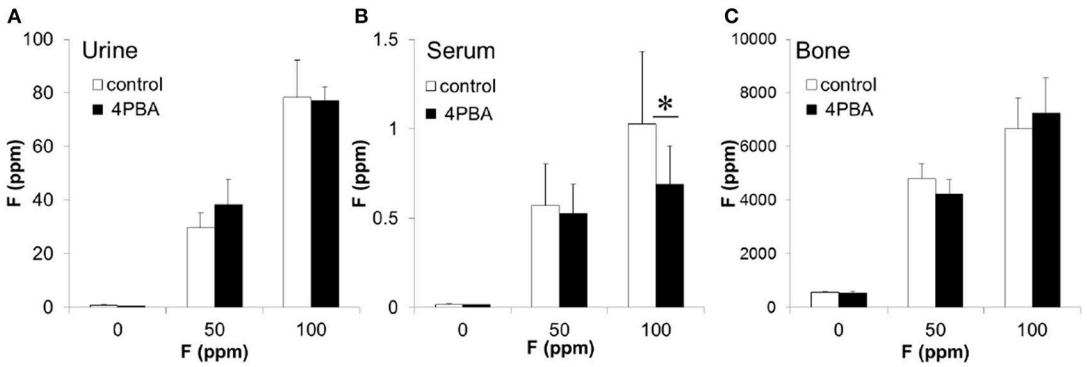

FIGURE 7 | The concentration of fluoride in mouse urine, serum and bone. C57BL/6 mice ($N = 5$/group) were provided water *ad libitum* containing fluoride (0, 50, or 100 ppm) with either control-chow (open columns) or 4 PBA-chow (filled columns) for 6 weeks. After 6 weeks, fluoride concentrations (ppm) in urine **(A)**, serum **(B)** and bone **(C)** were measured. Data are presented as the mean ± standard deviation (SD). Results between control-chow and 4-PBA chow were analyzed by Student's *t*-test. $P < 0.05$ was considered significant. *$P < 0.05$.

to reverse the effects of fluoride toxicity. In addition, careful consideration should be given to the HDAC inhibitor function of 4PBA. Recently, we demonstrated that fluoride activates SIRT1 in ameloblasts as an adaptive response and pharmacological SIRT1 activation protects ameloblasts from fluoride-induced cell stress (Suzuki and Bartlett, 2014; Suzuki et al., 2015). SIRT1 is a highly conserved NAD^+-dependent class III HDAC. By deacetylating target substrates, SIRT1 promotes cell survival by modulating cellular processes involved in stress adaptation (Michan and Sinclair, 2007). Even though it has not been reported if 4PBA can affect SIRT1 (class III HDAC), it seems prudent to assess the effect of 4PBA on SIRT1 function in dental fluorosis.

In conclusion, we show that 4PBA mitigated fluoride toxicity *in vitro*, while in general, a diet rich in 4PBA did not attenuate dental fluorosis in rodents. Further studies will be required to optimize protocols for 4PBA administration *in vivo* in order to evaluate the effect of 4PBA on dental fluorosis.

ETHICS STATEMENT

This study was carried out in accordance with the recommendations of Institutional Animal Care Use Committee (IACUC) at the Forsyth Institute. The Forsyth Institute is accredited by the Association for Assessment and Accreditation of Laboratory Animal Care International (AAALAC) and follows the Guide for the Care and Use of Laboratory Animals (NRC1996).The protocol was approved by the IACUC at the Forsyth Institute. Note that the first and senior authors were employed by The Forsyth Institute through October 2015 when the animal experiments were completed.

AUTHOR CONTRIBUTIONS

MS and JB designed experiments. MS, EE, and GW performed the experiments. MS prepared the figures and wrote the main manuscript text. JB reviewed and modified the manuscript text. All authors reviewed the manuscript.

FUNDING

Research reported in this publication was supported by the National Institute of Dental and Craniofacial Research of the National Institutes of Health under Award R01DE018106 (JB).

ACKNOWLEDGMENTS

The authors thank Dr. Toshihiro Sugiyama for his generous gift of ALC cells, Cheryl Bandoski for help with breeding mice and the assessment of enamel hardness and Kathleen Ryan with incisor imaging and QF.

REFERENCES

Backman, B., and Holm, A. K. (1986). Amelogenesis imperfecta: prevalence and incidence in a northern Swedish county. *Community Dent. Oral Epidemiol.* 14, 43–47. doi: 10.1111/j.1600-0528.1986.tb01493.x

Bartlett, J. D., Beniash, E., Lee, D. H., and Smith, C. E. (2004). Decreased mineral content in MMP-20 null mouse enamel is prominent during the maturation stage. *J. Dent. Res.* 83, 909–913. doi: 10.1177/154405910408301204

Bartlett, J. D., and Smith, C. E. (2013). Modulation of cell-cell junctional complexes by matrix metalloproteinases. *J. Dent. Res.* 92, 10–17. doi: 10.1177/0022034512463397

Beltrán-Aguilar, E. D., Barker, L., and Dye, B. A. (2010). Prevalence and severity of dental fluorosis in the United States, 1999-2004. *NCHS Data Brief* 53, 1–8.

Boivin, G., Chavassieux, P., Chapuy, M. C., Baud, C. A., and Meunier, P. J. (1989). Skeletal fluorosis: histomorphometric analysis of bone changes and bone fluoride content in 29 patients. *Bone* 10, 89–99. doi: 10.1016/8756-3282(89)90004-5

Bolden, J. E., Peart, M. J., and Johnstone, R. W. (2006). Anticancer activities of histone deacetylase inhibitors. *Nat. Rev. Drug Discov.* 5, 769–784. doi: 10.1038/nrd2133

Bonifacino, J. S., and Weissman, A. M. (1998). Ubiquitin and the control of protein fate in the secretory and endocytic pathways. *Annu. Rev. Cell Dev. Biol.* 14, 19–57. doi: 10.1146/annurev.cellbio.14.1.19

Bronckers, A. L., Lyaruu, D. M., and Denbesten, P. K. (2009). The impact of fluoride on ameloblasts and the mechanisms of enamel fluorosis. *J. Dent. Res.* 88, 877–893. doi: 10.1177/0022034509343280

Brookes, S. J., Barron, M. J., Boot-Handford, R., Kirkham, J., and Dixon, M. J. (2014). Endoplasmic reticulum stress in amelogenesis imperfecta and phenotypic rescue using 4-phenylbutyrate. *Hum. Mol. Genet.* 23, 2468–2480. doi: 10.1093/hmg/ddt642

Chuang, D. M., Leng, Y., Marinova, Z., Kim, H. J., and Chiu, C. T. (2009). Multiple roles of HDAC inhibition in neurodegenerative conditions. *Trends Neurosci.* 32, 591–601. doi: 10.1016/j.tins.2009.06.002

Claudio, N., Dalet, A., Gatti, E., and Pierre, P. (2013). Mapping the crossroads of immune activation and cellular stress response pathways. *EMBO J.* 32, 1214–1224. doi: 10.1038/emboj.2013.80

Collins, A. F., Pearson, H. A., Giardina, P., Mcdonagh, K. T., Brusilow, S. W., and Dover, G. J. (1995). Oral sodium phenylbutyrate therapy in homozygous beta thalassemia: a clinical trial. *Blood* 85, 43–49.

Daosukho, C., Chen, Y., Noel, T., Sompol, P., Nithipongvanitch, R., Velez, J. M., et al. (2007). Phenylbutyrate, a histone deacetylase inhibitor, protects against Adriamycin-induced cardiac injury. *Free Radic. Biol. Med.* 42, 1818–1825. doi: 10.1016/j.freeradbiomed.2007.03.007

Denbesten, P. K. (1999). Biological mechanisms of dental fluorosis relevant to the use of fluoride supplements. *Community Dent. Oral Epidemiol.* 27, 41–47. doi: 10.1111/j.1600-0528.1999.tb01990.x

Doyle, K. M., Kennedy, D., Gorman, A. M., Gupta, S., Healy, S. J., and Samali, A. (2011). Unfolded proteins and endoplasmic reticulum stress in neurodegenerative disorders. *J. Cell. Mol. Med.* 15, 2025–2039. doi: 10.1111/j.1582-4934.2011.01374.x

Dye, B. A., Vargas, C. M., Fryar, C. D., Ramos-Gomez, F., and Isman, R. (2017). Oral health status of children in Los Angeles County and in the United States, 1999-2004. *Community Dent. Oral Epidemiol.* 45, 135–144. doi: 10.1111/cdoe.12269

Everett, E. T., Mchenry, M. A., Reynolds, N., Eggertsson, H., Sullivan, J., Kantmann, C., et al. (2002). Dental fluorosis: variability among different inbred mouse strains. *J. Dent. Res.* 81, 794–798. doi: 10.1177/0810794

Fessler, E. B., Chibane, F. L., Wang, Z., and Chuang, D. M. (2013). Potential roles of HDAC inhibitors in mitigating ischemia-induced brain damage and facilitating endogenous regeneration and recovery. *Curr. Pharm. Des.* 19, 5105–5120. doi: 10.2174/1381612811319280009

Gow, A., and Sharma, R. (2003). The unfolded protein response in protein aggregating diseases. *Neuromolecular Med.* 4, 73–94. doi: 10.1385/NMM:4:1-2:73

Health, U. S. D. O., and Human Services Federal Panel on Community Water, F. (2015). U.S. Public Health Service Recommendation for Fluoride Concentration in Drinking Water for the Prevention of Dental Caries. *Public Health Rep.* 130, 318–331. doi: 10.1177/003335491513000408

Hu, J. C.-C., and Simmer, J. P. (2007). Developmental biology and genetics of dental malformations. *Orthod. Craniofac. Res.* 10, 45–52. doi: 10.1111/j.1601-6343.2007.00384.x

Iannitti, T., and Palmieri, B. (2011). Clinical and experimental applications of sodium phenylbutyrate. *Drugs R D* 11, 227–249. doi: 10.2165/11591280-000000000-00000

Ito, M., Nakagawa, H., Okada, T., Miyazaki, S., and Matsuo, S. (2009). ER-stress caused by accumulated intracistanal granules activates autophagy through a different signal pathway from unfolded protein response in exocrine pancreas cells of rats exposed to fluoride. *Arch. Toxicol.* 83, 151–159. doi: 10.1007/s00204-008-0341-7

Kolb, P. S., Ayaub, E. A., Zhou, W., Yum, V., Dickhout, J. G., and Ask, K. (2015). The therapeutic effects of 4-phenylbutyric acid in maintaining proteostasis. *Int. J. Biochem. Cell Biol.* 61, 45–52. doi: 10.1016/j.biocel.2015.01.015

Kubota, K., Lee, D. H., Tsuchiya, M., Young, C. S., Everett, E. T., Martinez-Mier, E. A., et al. (2005). Fluoride induces endoplasmic reticulum stress in ameloblasts responsible for dental enamel formation. *J. Biol. Chem.* 280, 23194–23202. doi: 10.1074/jbc.M503288200

Michan, S., and Sinclair, D. (2007). Sirtuins in mammals: insights into their biological function. *Biochem. J.* 404, 1–13. doi: 10.1042/BJ20070140

Nakata, A., Kameda, T., Nagai, H., Ikegami, K., Duan, Y., Terada, K., et al. (2003). Establishment and characterization of a spontaneously immortalized mouse ameloblast-lineage cell line. *Biochem. Biophys. Res. Commun.* 308, 834–839. doi: 10.1016/S0006-291X(03)01467-0

Odievre, M. H., Brun, M., Krishnamoorthy, R., Lapoumeroulie, C., and Elion, J. (2007). Sodium phenyl butyrate downregulates endothelin-1 expression in cultured human endothelial cells: relevance to sickle-cell disease. *Am. J. Hematol.* 82, 357–362. doi: 10.1002/ajh.20709

Oltvai, Z. N., Milliman, C. L., and Korsmeyer, S. J. (1993). Bcl-2 heterodimerizes *in vivo* with a conserved homolog, Bax, that accelerates programmed cell death. *Cell* 74, 609–619. doi: 10.1016/0092-8674(93)90509-O

Pfaffl, M. W. (2001). A new mathematical model for relative quantification in real-time RT-PCR. *Nucleic Acids Res.* 29:e45. doi: 10.1093/nar/29.9.e45

Sharma, R., Tsuchiya, M., and Bartlett, J. D. (2008). Fluoride induces endoplasmic reticulum stress and inhibits protein synthesis and secretion. *Environ. Health Perspect.* 116, 1142–1146. doi: 10.1289/ehp.11375

Sharma, R., Tsuchiya, M., Skobe, Z., Tannous, B. A., and Bartlett, J. D. (2010). The acid test of fluoride: how pH modulates toxicity. *PLoS ONE* 5:e10895. doi: 10.1371/journal.pone.0010895

Sharma, R., Tye, C. E., Arun, A., Macdonald, D., Chatterjee, A., Abrazinski, T., et al. (2011). Assessment of dental fluorosis in Mmp20 +/− mice. *J. Dent. Res.* 90, 788–792. doi: 10.1177/0022034511398868

Shin, M., Hu, Y., Tye, C. E., Guan, X., Deagle, C. C., Antone, J. V., et al. (2014). Matrix metalloproteinase-20 over-expression is detrimental

to enamel development: a Mus musculus model. *PLoS ONE* 9:e86774. doi: 10.1371/journal.pone.0086774

Simmer, J. P., Richardson, A. S., Hu, Y.-Y., Smith, C. E., and Ching-Chun Hu, J. (2012). A post-classical theory of enamel biomineralization... and why we need one. *Int. J. Oral Sci.* 4, 129–134. doi: 10.1038/ijos.2012.59

Sm, S., and Mahaboob Basha, P. (2017). Fluoride exposure aggravates the testicular damage and sperm quality in diabetic mice: protective role of ginseng and banaba. *Biol. Trace Elem. Res.* 177, 331–344. doi: 10.1007/s12011-016-0893-y

Smith, C. E., Issid, M., Margolis, H. C., and Moreno, E. C. (1996). Developmental changes in the pH of enamel fluid and its effects on matrix-resident proteinases. *Adv. Dent. Res.* 10, 159–169. doi: 10.1177/08959374960100020701

Sun, Z., Niu, R., Wang, B., Jiao, Z., Wang, J., Zhang, J., et al. (2011). Fluoride-induced apoptosis and gene expression profiling in mice sperm *in vivo*. *Arch. Toxicol.* 85, 1441–1452. doi: 10.1007/s00204-011-0672-7

Suzuki, M., Bandoski, C., and Bartlett, J. D. (2015). Fluoride induces oxidative damage and SIRT1/autophagy through ROS-mediated JNK signaling. *Free Radic. Biol. Med.* 89, 369–378. doi: 10.1016/j.freeradbiomed.2015.08.015

Suzuki, M., and Bartlett, J. D. (2014). Sirtuin1 and autophagy protect cells from fluoride-induced cell stress. *Biochim. Biophys. Acta* 1842, 245–255. doi: 10.1016/j.bbadis.2013.11.023

Suzuki, M., Shin, M., Simmer, J. P., and Bartlett, J. D. (2014a). Fluoride affects enamel protein content via TGF-beta1-mediated KLK4 inhibition. *J. Dent. Res.* 93, 1022–1027. doi: 10.1177/0022034514545629

Suzuki, M., Sierant, M. L., Antone, J. V., Everett, E. T., Whitford, G. M., and Bartlett, J. D. (2014b). Uncoupling protein-2 is an antioxidant that is up-regulated in the enamel organ of fluoride-treated rats. *Connect Tissue Res* 55(Suppl. 1), 25–28. doi: 10.3109/03008207.2014.923854

Tye, C. E., Pham, C. T., Simmer, J. P., and Bartlett, J. D. (2009). DPPI may activate KLK4 during enamel formation. *J. Dent. Res.* 88, 323–327. doi: 10.1177/0022034509334240

Zhang, J. X., Braakman, I., Matlack, K. E., and Helenius, A. (1997). Quality control in the secretory pathway: the role of calreticulin, calnexin and BiP in the retention of glycoproteins with C-terminal truncations. *Mol. Biol. Cell* 8, 1943–1954. doi: 10.1091/mbc.8.10.1943

Zhao, J. H., Liu, H. L., Lin, H. Y., Huang, C. H., Fang, H. W., Chen, S. S., et al. (2007). Chemical chaperone and inhibitor discovery: potential treatments for protein conformational diseases. *Perspect. Medicin. Chem.* 1, 39–48.

Conflict of Interest Statement: The authors declare that the research was conducted in the absence of any commercial or financial relationships that could be construed as a potential conflict of interest.

Copyright © 2017 Suzuki, Everett, Whitford and Bartlett. This is an open-access article distributed under the terms of the Creative Commons Attribution License (CC BY). The use, distribution or reproduction in other forums is permitted, provided the original author(s) or licensor are credited and that the original publication in this journal is cited, in accordance with accepted academic practice. No use, distribution or reproduction is permitted which does not comply with these terms.

frontiers in Physiology

REVIEW
published: 26 June 2017
doi: 10.3389/fphys.2017.00435

Amelogenesis Imperfecta; Genes, Proteins, and Pathways

Claire E. L. Smith[1,2], James A. Poulter[2], Agne Antanaviciute[3], Jennifer Kirkham[1], Steven J. Brookes[1], Chris F. Inglehearn[2] and Alan J. Mighell[2,4]*

[1] Division of Oral Biology, School of Dentistry, St. James's University Hospital, University of Leeds, Leeds, United Kingdom,
[2] Section of Ophthalmology and Neuroscience, St. James's University Hospital, University of Leeds, Leeds, United Kingdom,
[3] Section of Genetics, School of Medicine, St. James's University Hospital, University of Leeds, Leeds, United Kingdom,
[4] Oral Medicine, School of Dentistry, University of Leeds, Leeds, United Kingdom

Amelogenesis imperfecta (AI) is the name given to a heterogeneous group of conditions characterized by inherited developmental enamel defects. AI enamel is abnormally thin, soft, fragile, pitted and/or badly discolored, with poor function and aesthetics, causing patients problems such as early tooth loss, severe embarrassment, eating difficulties, and pain. It was first described separately from diseases of dentine nearly 80 years ago, but the underlying genetic and mechanistic basis of the condition is only now coming to light. Mutations in the gene *AMELX,* encoding an extracellular matrix protein secreted by ameloblasts during enamel formation, were first identified as a cause of AI in 1991. Since then, mutations in at least eighteen genes have been shown to cause AI presenting in isolation of other health problems, with many more implicated in syndromic AI. Some of the encoded proteins have well documented roles in amelogenesis, acting as enamel matrix proteins or the proteases that degrade them, cell adhesion molecules or regulators of calcium homeostasis. However, for others, function is less clear and further research is needed to understand the pathways and processes essential for the development of healthy enamel. Here, we review the genes and mutations underlying AI presenting in isolation of other health problems, the proteins they encode and knowledge of their roles in amelogenesis, combining evidence from human phenotypes, inheritance patterns, mouse models, and *in vitro* studies. An LOVD resource (http://dna2.leeds.ac.uk/LOVD/) containing all published gene mutations for AI presenting in isolation of other health problems is described. We use this resource to identify trends in the genes and mutations reported to cause AI in the 270 families for which molecular diagnoses have been reported by 23rd May 2017. Finally we discuss the potential value of the translation of AI genetics to clinical care with improved patient pathways and speculate on the possibility of novel treatments and prevention strategies for AI.

Keywords: amelogenesis, amelogenesis imperfecta, ameloblasts, enamel, biomineralization, Leiden Open Variant Database, LOVD, amelogenesis genetics

OPEN ACCESS

Edited by:
Agnes Bloch-Zupan, University of Strasbourg, France

Reviewed by:
Lucia Jimenez-Rojo, University of Zurich, Switzerland
Bernhard Ganss, University of Toronto, Canada

****Correspondence:***
Claire E. L. Smith
c.e.l.smith@leeds.ac.uk

Specialty section:
This article was submitted to Craniofacial Biology and Dental Research, a section of the journal Frontiers in Physiology

Received: *26 April 2017*
Accepted: *08 June 2017*
Published: *26 June 2017*

Citation:
Smith CEL, Poulter JA, Antanaviciute A, Kirkham J, Brookes SJ, Inglehearn CF and Mighell AJ (2017) Amelogenesis Imperfecta; Genes, Proteins, and Pathways. Front. Physiol. 8:435. doi: 10.3389/fphys.2017.00435

INTRODUCTION

Mature enamel is the hardest, most mineralized tissue in the human body, comprising >95% by weight crystals of substituted calcium hydroxyapatite (HA; $Ca_{10}[PO_4]_6[OH]_2$). Enamel consists of a highly organized structure of interwoven prisms and inter-prismatic material, both made up of HA crystals (**Figure 1**). This structural organization and chemical composition provide the

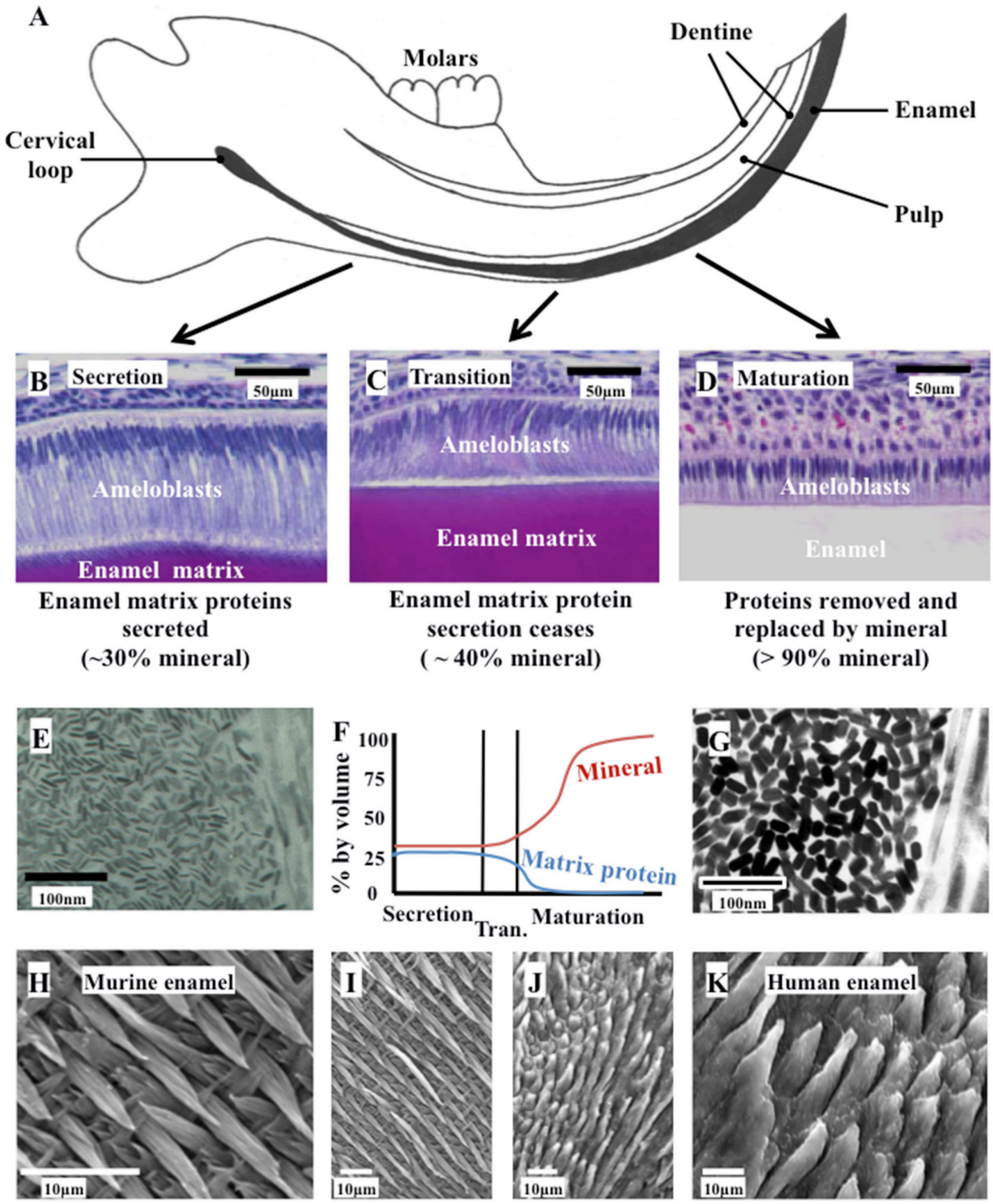

FIGURE 1 | Ameloblast morphology, crystal development, and the final structure of the enamel. **(A)** Schematic cross section of the murine incisor. **(B–D)** Histology of the murine incisor. **(B)** During secretion, ameloblasts exhibit an elongated morphology with a cellular extension (the Tomes' process); **(C)** during transition the Tomes' process degenerates and the ameloblasts begin to reduce in height; **(D)** during maturation, the ameloblasts remove nearly all protein from the developing enamel and supply mineral ions to support crystallite growth; **(E)** immature enamel crystalites form during secretion by growth in their long axis; **(F)** by the end of secretion, the developing enamel is around 30% mineral and 25% matrix protein, with the remainder tissue fluid. By the end of maturation, the enamel is nearly 100% mineral; **(G)** the enamel crystallites grow in width and thickness during enamel maturation; **(H)** and **(I)** murine enamel has a decussating arrangement of enamel prisms; **(J)** and **(K)** human enamel is also arranged in a prismatic structure. Elements from this figure have been adapted from previously published figures and we acknowledge the following publications and publishers for the elements specified: Panels **(A–D)** were previously published by Barron et al. (2010). Panel **(E)** was previously published by Robinson (2014).

mechanical strength to withstand long-term use. The enamel-forming cells, the ameloblasts, are lost upon tooth eruption. Consequently enamel lacks any capacity for cellular repair and once formed, must function over a lifetime.

Amelogenesis

Amelogenesis is the process of enamel formation. It takes place in three, well-defined stages known as the secretory, transition and maturation phases (**Figure 1**). The initial differentiation, positioning and orientation of ameloblasts, as well as their coordinated functioning as a cohort, are also crucial to amelogenesis.

Amelogenesis involves the secretion of a proteinaceous matrix in which immature enamel HA crystallites are deposited. The matrix is then degraded and concurrently replaced, almost entirely, with HA mineral (**Figure 2**). During the secretary phase, the ameloblasts move away from the dentino-enamel junction (DEJ), secreting a soft extracellular protein matrix by exocytosis from cellular extensions (known as Tomes' processes) to fill the space they leave behind (Skobe, 1976). During the transition stage, which begins as the matrix achieves the thickness of the future enamel, matrix protein secretion decreases and the ameloblasts restructure (Reith, 1970). During the maturation stage, the matrix proteins are degraded by proteases and replaced with tissue fluid. Maturation stage ameloblasts increase their active transport of mineral ions into the fluid, which drives the growth of the pre-existing enamel crystallites in width and thickness (Robinson et al., 1995). During this stage, ameloblasts alternate between a ruffle ended and smooth ended morphology in groups of coordinated cells (Warshawsky and Smith, 1974). These different morphologies reflect cyclical changes in ameloblast function related to the regulation of pH and the control of ion transport so that the enamel becomes progressively more mineralized until the crystallites occlude the tissue volume. The matrix is transformed into mature enamel that is almost devoid of protein (Smith, 1998).

Throughout the transition and maturation stages, around 50% of the ameloblasts undergo apoptosis (Smith and Warshawsky, 1977). Post maturation, the surviving ameloblasts either apoptose or go on to contribute to the junctional epithelium of mature teeth (Bosshardt and Lang, 2005).

Amelogenesis Imperfecta

Definition and Phenotypes

Amelogenesis imperfecta (AI) is a heterogeneous group of genetic conditions characterized by defects in the formation of enamel in all teeth of both dentitions. In an effort to classify the disease, particular phenotypes have been defined but this approach can be confounded by mixed phenotypes (**Figure 3**). *Hypoplastic AI* describes thin but mineralized enamel, or in extreme cases, the complete absence of enamel, that results from failure during the secretory stage. *Hypomineralized AI* is caused by maturation stage failure, giving rise to enamel that is of full thickness but is weak and fails prematurely. The hypomineralized phenotype can be further subdivided into *hypomaturation* and *hypocalcified AI*. The former is caused by incomplete removal of protein from the enamel matrix and produces brittle enamel, while the latter is characterized by insufficient transport of calcium ions (Ca^{2+}) into the developing enamel and produces soft enamel.

Phenotyping of teeth from AI patients is complicated by post-eruptive changes that occur during the time spent in the mouth. Obtaining unerupted genotyped human embryonic teeth would be difficult and ethically questionable, while the study of erupted teeth precludes the direct study of amelogenesis (though enamel composition and ultrastructure can provide some form of record of the events occurring during amelogenesis). Therefore, mouse models have proved invaluable to AI research. Murine phenotyping of AI disease models can utilize the continuously erupting incisor to view all stages of amelogenesis at once, or gain a snapshot of amelogenesis via analysis of embryonic/neonatal unerupted molar teeth. **Figure 1** shows the histology of the murine incisor and Supplementary Table 1 summarizes a selection of the AI-relevant mouse models that have been well characterized to date. The table also highlights genes for which murine models have not yet been described or for which an abnormal dental phenotype has not been reported.

Prevalence, Impact, and Treatment

AI is reported to range in frequency in different populations from 1 in 700 to 1 in 14,000 (Witkop and Sauk, 1976; Backman and Holm, 1986; Crawford et al., 2007), and has a significant impact upon patients and healthcare provision (Coffield et al., 2005). AI enamel is abnormally thin, soft, fragile, pitted and/or discolored, causing patients severe embarrassment, eating difficulties and pain. It is also associated with negative social outcomes and poor aesthetics (Hashem et al., 2013). AI is very difficult to treat and there is a weak evidence base to inform clinical decision-making and management choices (Dashash et al., 2013). Interventions focus on aesthetics and maintaining occlusal height and tooth function, whilst maintaining the natural dentition for as long as possible. Diagnostically it is necessary to distinguish AI from more common enamel defects such as fluorosis, molar incisor hypomineralization (Gotler and Ratson, 2010) and those caused by time-limited events, such as serious systemic illness (Salanitri and Seow, 2013).

THE GENETICS OF AMELOGENESIS IMPERFECTA

AI was first described as a separate clinical entity to dentinogenesis imperfecta in 1938 (Finn, 1938) and its study has helped to define the processes and genes involved in amelogenesis. Since the discovery, over 25 years ago, that mutations in amelogenin, X linked (*AMELX*) lead to AI (Lagerstrom et al., 1991), many other genes have been shown to be defective in AI. The falling costs of next generation sequencing (NGS) have accelerated the identification of new genes for AI. These discoveries have also expanded the known functions of proteins mutated in AI from solely the structural enamel matrix proteins and their proteolytic processing enzymes, to a range of other proteins, involved in diverse functions, such as vesicle transport, pH sensing and cell adhesion.

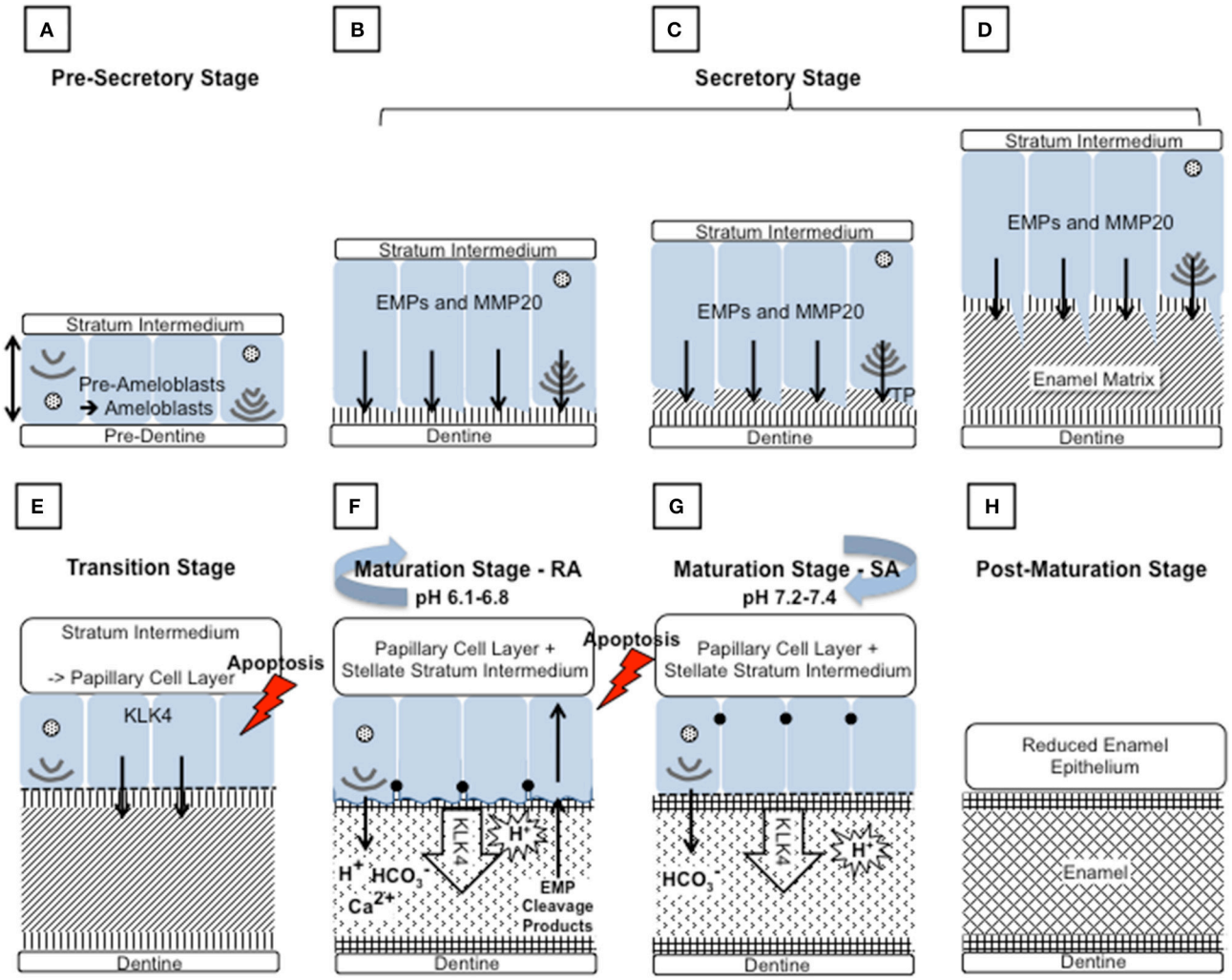

FIGURE 2 | Schematic diagram depicting the main events during amelogenesis. **(A)** Pre-secretory stage: Ameloblasts (blue) differentiate from the cells of the inner enamel epithelium (IEE), in response to reciprocal signaling between the IEE and the dental papilla. The basal lamina between the IEE and dental papilla breaks down so that the cells are in contact with the pre-dentine. The ameloblasts elongate and their nuclei shift to the proximal side of the cell, nearest the stratum intermedium (SI), resulting in reversal of the ameloblasts' polarity. At the distal end, closest to the pre-dentine, the Golgi apparatus and rough endoplasmic reticulum increase in size to increase the capacity for protein production, post translational modification and secretion. The non-dividing cell becomes further polarized as it forms a distal extension that will go on to form the Tomes' process (TP). Each ameloblast develops and maintains anchoring junctions to hold the ameloblast layer in alignment and to control what passes between them. **(B–D)** Secretory stage: During the secretory stage, a proteinaceous extracellular matrix is secreted from the ameloblast TP, as the ameloblast layer retreats from the dentine layer. To achieve this, ameloblasts produce large amounts of membrane bound, secretory granules containing enamel matrix proteins (EMPs). EMPs are constitutively secreted via exocytosis into the extracellular space at the distal end of the cell, on to the newly formed dentine. **(B)** Mineral immediately forms in this initial enamel matrix and forms a close association with the dentine mineral. This will form the aprismatic enamel. **(C)** The ameloblasts begin to move away from the dentine and further develop their TP at the distal end. EMPs are secreted from two aspects of the ameloblasts to produce enamel matrix that will go on to form the prismatic and interprismatic enamel. **(D)** As secretion progresses the TP lengthens and thins. The portion secreting the prismatic enamel is reduced before secretion ceases, therefore the final enamel formed will be aprismatic. **(E)** Transition stage: The transition stage is characterized by reduced EMP secretion and internal reorganization of the ameloblasts. Ameloblasts shorten to around half their original height and reduce in volume. Their nuclei become more central and the ER is reduced in size. The TP is completely lost and an atypical basal lamina is formed against the enamel matrix. Ameloblasts adhere to the enamel matrix via hemidesmosomes. The cells of the SI, stellate reticulum and the outer enamel epithelium form the papillary layer (PL). Capillaries invaginate into this layer and overlay the ameloblasts. The cells of the PL may assist ameloblasts in the maturation stage by participating in ion transport and removal of enamel protein products and water from the developing enamel. The ameloblast population reduces by around 25% at this stage through apoptosis. **(F)** and **(G)** Maturation stage: During the maturation stage the partially mineralized enamel matrix becomes fully mineralized by the breakdown and removal of residual EMPs, and the growth in width and thickness of enamel crystallites. These processes are achieved through repeated cyclical processes. The ameloblasts act as a gated barrier for the movement of ions and degraded proteins between the SI and the developing enamel and vice versa. To achieve this, the ameloblast membrane facing the enamel matrix modulates between ruffle ended **(F)** and smooth ended **(G)** morphologies. This is achieved in coordinated groups of ameloblasts across the developing enamel. Ruffle ended ameloblasts (RA) form membrane invaginations and tight junctions at the apical end, near the enamel surface, whereas smooth ended ameloblasts (SA) are more leaky. Enamel crystal growth generates large amounts of protons but it has also been shown that protons are pumped into the enamel by RA. Both RA and SA release bicarbonate ions into the enamel that act as a buffer to increase pH. A mildy acidic pH is found in enamel at RA regions and a more

(Continued)

FIGURE 2 | Continued
neutral pH in SA regions. During maturation around 25% of ameloblasts apoptose. **(H)** Post-maturation stage: The ameloblasts and other cells of the enamel organ, form the reduced enamel epithelium, which eventually contributes to the junctional epithelium of mature teeth. However, many of the ameloblasts apoptose before the formation of the junction epithelium is completed.

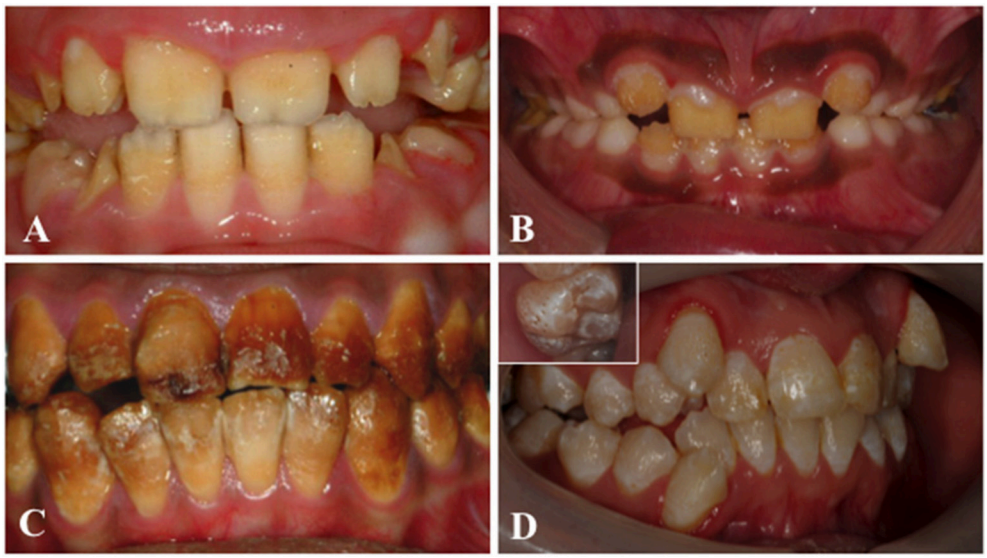

FIGURE 3 | Clinical images that illustrate the variability of AI. **(A)** Hypoplastic AI is characterized by teeth without the curves associated with a normal enamel volume. **(B)** In hypomaturation AI enamel volume can be near-normal, but opaque with structural weaknesses that result in rapid post-eruptive enamel loss with enamel fracturing away to exposure the underlying dentine. **(C)** Brown discolouration and early post-eruptive enamel loss is typical of hypomineralised forms of AI. **(D)** Mixed AI phenotypes are frequently encountered. In this example a near-normal enamel volume is characterized by multiple focal pits that are most evident on the inset image, with variable colouration that includes focal opacities, but without premature fracturing of the enamel to reveal dentine.

Here we review advances in our understanding of the molecular basis of AI presenting in isolation of other health problems with recognition that co-segregating health problems may present later in life. For some of the genes included, other mutations can cause more widespread health problems beyond AI. We focus on the more recently identified AI genes, but include all reported genes, reviewing the functions of the proteins that they encode, the mutations identified and the resulting enamel phenotypes. We also summarize the murine models available and document any enamel phenotypes observed in these. Furthermore, we highlight a new online resource (http://dna2.leeds.ac.uk/LOVD/), detailing nearly two hundred published AI-causing mutations identified in two hundred and seventy families reported by 23rd May 2017. This resource represents an open repository for all interested in advancing the understanding of amelogenesis. We conclude by considering how these advances might impact on clinical care in future.

The Enamel Matrix Proteins

The first AI-causing mutations were identified in the genes encoding the enamel matrix proteins (EMPs), known to make up the bulk of the secreted enamel organic matrix. The EMP genes evolved from a common ancestral gene (Sire et al., 2007) and form part of the secretory calcium-binding phosphoprotein gene cluster. Their encoded proteins have a distinctive architecture of a signal peptide and a conserved casein kinase 2 phosphorylation domain likely to be targeted by family with sequence similarity 20, member C (FAM20C, MIM *611061) (Yang et al., 2016).

The enamel matrix proteins include amelogenin (AMELX, MIM *300391), which makes up around 90% of the EMPs secreted by ameloblasts (Termine et al., 1980), with the remaining 10% comprising ameloblastin (AMBN, MIM *610259) and enamelin (ENAM MIM *606585), in order of abundance (Smith, 1998). The alternative splicing and extracellular proteolytic processing of amelogenin, ameloblastin and enamelin have been reviewed elsewhere (Brookes et al., 1995; Iwata et al., 2007; Kobayashi et al., 2007; Moradian-Oldak, 2012). However, it is becoming increasingly clear that it is not only perturbation of the proteins' extracellular roles as part of the enamel matrix that is important in AI, but also the proteins' aberrant intracellular processing and the outcome of the unfolded protein response (UPR; Brookes et al., 2014).

AMELX

Amelogenin is a hydrophobic, proline and histidine rich protein, thought to act as an enamel matrix pH buffer (Guo et al., 2015) and as a scaffold for the spacing and growth of enamel crystallites (Chen et al., 2011). It is subject to extensive extracellular proteolytic processing following its secretion (Brookes et al., 1995). It is regarded as a tooth specific protein since it has not

been detected elsewhere in human tissues (Chan et al., 2011). However, in murine tissues, it has been detected in dentine-forming, cementum-forming and bone-forming cells, as well as in the developing eye and brain (Fong and Hammarstrom, 2000; Janones et al., 2005; Haze et al., 2007).

AMELX mutations cause X-linked AI (MIM #301200) (Lagerstrom et al., 1991). Heterozygous mutations tend to present in female AI patients as stripes of normal and AI affected enamel due to lyonization (Berkman and Singer, 1971). In males, a copy of *AMELX* exists as *AMELY* on the Y chromosome, but *AMELY* transcription is around 10% of that of *AMELX* (Aldred et al., 1992; Salido et al., 1992) and hence cannot compensate for loss of *AMELX* expression. The AI phenotype in males is determined by the type and position of the mutation. Large deletions and N-terminal variants cause a hypomaturation AI defect with variable focal hypoplasia while mutations in the signal peptide and toward the C terminus cause smooth hypoplastic AI (Hart et al., 2002).

Over twenty *AMELX* mutations have been reported, including large deletions, frameshifts, nonsense and missense variants. For the majority of variants, pathology is thought to be due to loss of function, though an *Amelx* mutation in mice has been linked to toxic gain of function via activation of the pro-apoptotic UPR (Brookes et al., 2014). Altered splicing, due to variants such as the silent c.120T>C (NM_182680.1) change, has also been shown to result in enamel pathology (Cho et al., 2014). This particular variant prevents the excision of exon 4 from the majority of *AMELX* transcripts, thus preventing the formation of a miRNA from the normally excised exon 4 (Le et al., 2016). These examples show that further study, within the context of *AMELX* alternative splicing and its roles in signaling, is required to accurately define disease mechanisms.

ENAM

Enamelin, the largest of the EMPs, is a tooth specific acidic protein expressed primarily by secretory stage ameloblasts (Hu and Yamakoshi, 2003). It is successively cleaved from its C terminus, resulting in numerous products (Fukae et al., 1993; Hu and Yamakoshi, 2003; Lu et al., 2008). Like amelogenin and ameloblastin, the uncleaved protein is found only within the newly secreted, outermost layer of the enamel matrix and is thought to be involved in enamel crystal extension (Hu et al., 2008). Some ENAM cleavage products, such as the 32 kDa fragment identified in pigs, have high affinity for HA crystals and accumulate within and between the enamel prisms (Hu and Yamakoshi, 2003).

The first mutation identified in *ENAM* caused an autosomal dominant AI with a severe, smooth hypoplastic phenotype (MIM #104500) as a result of a dominant-negative effect of aberrant splicing (Rajpar et al., 2001) and a milder, local hypoplastic phenotype (MIM #204650) caused by missense mutations (Mardh et al., 2002). Autosomal recessive inheritance has also been documented for *ENAM* mutations (Hart et al., 2003; Ozdemir et al., 2005a; Chan et al., 2010); homozygotes and heterozygotes present with a severe and a milder, local form, respectively (Ozdemir et al., 2005a). Severity based on zygosity is more often seen with nonsense or frameshift variants that escape nonsense mediated decay (NMD).

AMBN

AMBN is rich in glycine, leucine and proline and, in addition to within the enamel matrix, localizes to the Tomes' processes and the DEJ (Krebsbach et al., 1996; MacDougall et al., 2000), but has also been detected in pre-odontoblasts, developing tooth roots and craniofacial bone (Fong et al., 1996, 1998; Spahr et al., 2006). AMBN is expressed throughout amelogenesis (Lee et al., 1996) but peaks during the secretory stage (Fukumoto et al., 2004). *AMBN* transcripts undergo alternative splicing to form two isoforms (Krebsbach et al., 1996; Hu et al., 1997). Porcine ameloblastin is extensively modified and is cleaved upon secretion by MMP20 to form a number of protein products that accumulate within different compartments of the enamel matrix. For example, N-terminal products accumulate between the enamel prisms throughout the matrix (Bartlett and Simmer, 1999). Although, it is known that AMBN can influence the differentiation and proliferation of ameloblasts (Fukumoto et al., 2004), it is also important in extracellular signaling to induce osteoblast differentiation (Iizuka et al., 2011), cell adhesion, via heparin and fibronectin (Beyeler et al., 2010), and mineralization (Yamakoshi et al., 2001; Zhang et al., 2011).

Only two mutations have been reported in *AMBN* in AI patients, both discovered through NGS. The first *AMBN* mutation reported, a large, in-frame deletion encompassing exon 6, segregated with recessive hypoplastic AI (MIM #616270) in a consanguineous Costa Rican family (Poulter et al., 2014c). Scanning electron microscopy showed both reduced mineral density and enamel thickness, mirroring the murine $Ambn^{-5,6/-5,6}$ model. The second homozygous mutation, thought to alter splicing, was identified in one patient in a large cohort with oro-dental disease, using a targeted NGS assay (Prasad et al., 2016a).

The Enamel Matrix Proteases

Another group of genes for which a candidate approach identified AI-causing mutations are those encoding the enamel matrix proteases. These enzymes include matrix metallopeptidase 20 (MMP20, MIM *604629), which specifically cleaves the enamel matrix proteins during the secretory stage to produce functional peptides, and kallikrein related peptidase 4 (KLK4, MIM *603767) that proteolytically degrades the enamel matrix proteins to facilitate their removal by endocytosis during the maturation stage.

MMP20

Matrix metallopeptidases (MMPs) influence cell motility by regulating cell interactions and matrix degradation, crucial processes in many aspects of development (VanSaun and Matrisian, 2006). Like other MMPs, MMP20 is a zinc dependent endopeptidase that is secreted in an inactive precursor form that requires cleavage for its activation (Llano et al., 1997). MMP20 is secreted by ameloblasts concurrent with the EMPs, and is responsible for cleavage of EMP at specific residues, shortly after their secretion (Simmer and Hu, 2002). This generates

products with specific, diverse roles during amelogenesis. MMP20 has been shown to be necessary for controlling HA crystal morphology (Prajapati et al., 2016) and through its action on amelogenin, may regulate mineralization (Kwak et al., 2016). MMP20 is also capable of cleaving the extracellular domains of cadherins that mediate cell-cell interactions as part of adherens junctions to allow ameloblast cell movement (Guan and Bartlett, 2013; Guan et al., 2016). This may affect amelogenesis since ameloblasts must move in synchronous groups in order to form typical enamel architecture. Since cadherins are linked to the actin cytoskeleton via catenins, cadherin cleavage releases β-catenin, which can act as a transcription factor and may be important for ameloblast differentiation (Bartlett et al., 2011; Guan et al., 2016).

Mutations in *MMP20* lead to autosomal recessive hypomaturation AI (MIM #612529) (Kim et al., 2005). Eleven missense, nonsense, frameshift and splice site mutations have been described, all resulting in a similar phenotype (Ozdemir et al., 2005b; Papagerakis et al., 2008; Lee et al., 2010a; Gasse et al., 2013; Wang et al., 2013b). All five of the missense variants reported lie within either the catalytic peptidase domain or the hemopexin domain, which, through homology, is thought to influence substrate specificity or to bind inhibitors or activators of the pro-enzyme.

KLK4

KLK4 encodes a serine protease that is expressed and secreted by ameloblasts in both the transition and maturation stages of amelogenesis (Hu et al., 2000, 2002; Simmer et al., 2009). Like MMP20, newly secreted KLK4 must be cleaved for its activation. *In vitro* experiments have shown that MMP20 can activate newly secreted KLK4 and that KLK4 can inactivate MMP20, potentially explaining the shift in proteinase activity during the transition stage (Yamakoshi et al., 2013).

KLK4 acts to further degrade the enamel proteins already cleaved by MMP20 during secretion and is capable of functioning over the wide pH range that occurs during maturation (Smith, 1998; Bartlett, 2013). Such activity aids removal of protein from the developing enamel by maturation stage ameloblasts, allowing the enamel crystallites to grow in width and thickness (Simmer et al., 2009; Bartlett, 2013).

KLK4 mutations cause autosomal recessive hypomaturation AI (Hart et al., 2004). All four *KLK4* variants reported so far are either nonsense or frameshift mutations (Hart et al., 2004; Wright et al., 2011; Wang et al., 2013b; Smith et al., 2017a). However, only two of the four are predicted to lead to NMD. Of the two frameshift mutations affecting codons in the final exon, and therefore not expected to undergo NMD, one alters one of the three catalytic residues, p.S207, essential to the function of all kallikrein enzymes. This mutation has been shown to result in greatly reduced protein expression and proteolytic function (Seymen et al., 2015). Prior to the identification of the frameshift variant, c.632delT only three *KLK4* variants in four families had been identified. However, the c.632delT variant, reported to occur at a frequency of 0.15% in the South Asian population, has been reported in five Pakistani families with hypomaturation AI and is predicted to disrupt three of six structurally important disulphide bonds (Smith et al., 2017a). Characterization of the human enamel phenotype revealed that overall the enamel was hypomineralized but that the deeper (inner) enamel was more seriously affected than the more superficial (outer) enamel (Smith et al., 2017a).

Cell-Cell and Cell-Matrix Adhesion

For amelogenesis to proceed, the ameloblasts must function as a coordinated cohort and must maintain their contact with the secreted extracellular matrix (ECM) not only as they retreat from the dentine surface during secretion, but also during transition and maturation. These contacts require specific molecules, including integrins, laminins and collagens, and structures such as desmosomes and hemidesmosomes. The basal lamina degrades as the pre-ameloblasts undergo their terminal differentiation and an atypical basal lamina is then reformed during the transition stage. During the secretory stage, the Tomes' processes act as the contact point between the ameloblast and the enamel matrix.

ITGB6

Integrin, β6 (ITGB6; MIM *147558) is a member of a large family of cell surface-adhesion receptors that mediate cell-cell and cell-ECM interactions by facilitating interaction with the cytoskeleton (Alberts et al., 2002). ITGB6 is predominantly found in epithelial cells and forms a heterodimer with integrin subunit alpha V (Busk et al., 1992; Breuss et al., 1993). Within the developing tooth, ITGB6 localizes predominantly in maturation stage ameloblasts (Wang et al., 2014b).

ITGB6 is known to bind to arginine-glycine-aspartic acid (RGD) motifs which are found in ECM proteins such as fibronectin, as well as the latency associated peptide of transforming growth factor-β1 (TGF-β1) (Breuss et al., 1993; Weinacker et al., 1994; Munger et al., 1999; Annes et al., 2002). Via this interaction and other mechanisms, ITGB6 is able to activate TGF-β1 (Munger et al., 1999).

An *Itgb6* null mouse exhibited a hypomineralized AI phenotype, with the loss of any ordered enamel prism arrangement (Mohazab et al., 2013). Accumulation of amelogenin in the enamel matrix and the presence of enamel pits were also noted (Mohazab et al., 2013). Patients with mutations in *ITGB6* have since been reported (MIM #616221) with either hypomineralized pitted enamel, similar to that reported in the *Itgb6* null mouse (Poulter et al., 2014a), or hypoplastic enamel with a rough surface (Wang et al., 2014b), both recessively inherited. More recently, Ansar et al. (2015) reported a consanguineous family with a homozygous *ITGB6* mutation with adolescent alopecia, intellectual disability and dentogingival abnormalities with rough, discolored enamel. However, it is unclear if these additional phenotypes result from the *ITGB6* variant or are co-segregating, for example, due to an undetected copy number variant. The *ITGB6* missense mutations identified so far lie within the β1 domain of the protein involved in binding to α integrin subunits, activity-modifying cations and ligands (Xiong et al., 2001, 2002). Wang et al. (2014b) also reported a patient with a homozygous *ITGB6* nonsense mutation, but phenotyping of the enamel was complicated by the co-presence

of a hemizygous Nance-Horan syndrome (congenital cataracts and dental anomalies) mutation (MIM *300457).

LAMA3, LAMB3, and COL17A1

Laminin, alpha 3 (*LAMA3*; MIM *600805), laminin, beta 3 (*LAMB3*; MIM *150310) and laminin gamma 2 (*LAMC2*; MIM *150292) encode the three subunits of the heterotrimeric protein laminin 332 (LM332), which localizes to epithelial basement membranes of the ECM (Aberdam et al., 1994a). LM332 has a central role in the assembly and stability of hemidesmosomes, structures that mediate attachment between cells and the ECM (Nievers et al., 1999). Collagen type XVII, alpha-1 (COL17A1; MIM *113811) is a constituent of hemidesmosomes and is a ligand for LM332 (Nishie et al., 2011; Van den Bergh et al., 2011). Mutations in the genes encoding COL17A1 or the subunits of LM332 cause the autosomal recessive condition junctional epidermolysis bullosa (JEB; MIM #226700, #226650), in which failure to form hemidesmosomes between skin layers leads to extensive skin blistering (Aberdam et al., 1994b; Pulkkinen et al., 1994a,b; Kivirikko et al., 1995; McGrath et al., 1995). In addition, JEB patients often present with hypoplastic, pitted enamel (Wright et al., 1993), and it has been noted that heterozygous carriers of some mutations in these genes sometimes have AI in the absence of any skin phenotype (McGrath et al., 1996; Yuen et al., 2012; Kim et al., 2013; Poulter et al., 2014b).

LM332 has been implicated in ameloblast adhesion to the enamel surface via interaction with integrin alpha 6 beta 4 within hemidesmosomes; and in cell migration via binding of integrin alpha 3 beta 1 (Carter et al., 1991; Marchisio et al., 1993). Mature ameloblasts and Tomes' processes show particularly strong staining for mature LM332 protein (Yoshiba et al., 1998), which is thought to participate in the control of ameloblast differentiation and adhesion to the enamel matrix. This is supported by analysis of tooth buds from JEB patients, which show ameloblast disorganization and subsequent reduction in enamel volume (Brain and Wigglesworth, 1968). Enamel in JEB patients also has a number of changes in chemical composition, suggesting that mineral transport or ameloblast metabolism is affected (Kirkham et al., 2000).

No enamel phenotype has been reported for *Lamb3* null mice since they die in early post-natal life (Kuster et al., 1997). In contrast, for *Lama3* null mice, ameloblasts were smaller than those in wild-type (WT) mice, suggesting that LM332 is required for normal ameloblast differentiation (Ryan et al., 1999). Enamel deposition was described as abnormal and the enamel epithelium was disorganized (Ryan et al., 1999).

COL17A1 is expressed throughout enamel formation (Asaka et al., 2009). *Col17*$^{-/-}$ mice have fewer hemidesmosomes than WT mice and exhibit thin, disorganized Tomes' processes (Asaka et al., 2009). This may be the result of alterations in ameloblast differentiation due to lack of contact with, and signals from, mesenchymal tissues. Mineralization is delayed in *Col17*$^{-/-}$ mice. The enamel formed lacks the typical regular prism structure and the prisms themselves are malformed, a phenotype reminiscent of the *Lama3*$^{-/-}$ mouse but not as severe (Asaka et al., 2009). Enamel proteins such as AMELX, AMBN, and ENAM are expressed by ameloblasts at a significantly lower level in *Col17*$^{-/-}$ mice than WT, whereas expression of the pre-secretory protein tuftelin is increased, again suggesting that ameloblast differentiation is incomplete in *Col17*$^{-/-}$ mice (Asaka et al., 2009).

Heterozygous carriers of some *LAMA3*, *LAMB3,* and *COL17A1* mutations present with hypoplastic AI (MIM #104530) (Murrell et al., 2007; Pasmooij et al., 2007; Yuen et al., 2012; Kim et al., 2013; Poulter et al., 2014b). Initial reports of the tooth phenotype simply mentioned that the relatives of some JEB patients had poor enamel, without recognition that the phenotype was truly AI (Murrell et al., 2007; Pasmooij et al., 2007). It was not until later that families segregating AI with autosomal dominant inheritance, and without any family members with JEB, were recognized and the phenotype more accurately described as AI (Poulter et al., 2014b).

The enamel of *LAMA3* and *LAMB3* patients is similarly described as hypoplastic, with grooving and pitting often present (Kim et al., 2013; Lee et al., 2014; Poulter et al., 2014b). Carriers of the JEB-causing *LAMA3* frameshift mutation c.488delG were found to have rough, pitted enamel due to haploinsufficiency of the protein (Yuen et al., 2012). One report of a patient carrying a *LAMB3* mutation highlighted that the multi-cusped teeth were more severely affected by AI than the anterior teeth (Kim et al., 2016b), although further study is required to determine whether this is a general trend.

AI-causing mutations in *LAMA3* and *LAMB3* present somewhat of a dichotomy. *LAMA3* variants that cause AI in heterozygous carriers, also cause JEB in biallelic individuals but the majority of AI-causing *LAMB3* variants have not been reported in JEB patients. Most *LAMB3* variants identified in AI patients are either frameshift or nonsense mutations predicted to escape NMD. The variants are consistent with a dominant gain of function disease mechanism, unlike the loss of function variants associated with recessively inherited JEB. However, Prasad et al. (2016a) did identify two AI patients carrying *LAMB3* mutations that do not fit this pattern of pathogenesis. These mutations have also been identified in JEB patients as recurrent mutations at hypermutable CpG sites (Kivirikko et al., 1996). Nevertheless, the pathogenicity of these variants in AI remains to be confirmed since segregation of one of the variants with the dental phenotype was inconsistent, and for the other, no segregation was possible, since only one affected individual was recruited to the study.

COL17A1 mutation carriers with an AI phenotype harbor glycine substitutions, as well as nonsense, frameshift and splicing mutations (McGrath et al., 1996; Murrell et al., 2007). The nonsense and frameshift mutations identified would be expected to lead to NMD, suggesting that the cause of the phenotype is haploinsufficiency. The glycine substitutions are predicted to disrupt an extracellular collagenous triple helix, potentially affecting both the susceptibility of the protein to degradation and its secretion (McGrath et al., 1996).

No patients with AI and heterozygous *LAMC2* mutations have yet been reported although it seems likely that these exist. In addition, other genes which are known to be involved in the etiology of JEB, such as integrin, alpha 6 (MIM *147556) (Ruzzi et al., 1997) and integrin, beta 4 (MIM *147557) (Vidal et al., 1995), may harbor heterozygous mutations that cause

dental defects in the absence of skin blistering since homozygous patients with a number of different JEB sub-types present with enamel hypoplasia (Fine et al., 2008).

AMTN

Amelotin (AMTN; MIM *610912) is a proline, leucine, threonine and glutamine rich protein secreted by transition and maturation stage ameloblasts (Iwasaki et al., 2005; Moffatt et al., 2006). The protein localizes to the ameloblast basal lamina where it known to bind to itself, to ODAM (odontogenic, ameloblast associated) and to SCPPPQ1 (secretory calcium-binding phosphoproteins proline-glutamine rich 1) (Holcroft and Ganss, 2011; Fouillen et al., 2017). It is hypothesized to form large aggregates (Holcroft and Ganss, 2011; Bartlett and Simmer, 2015). These aggregates are thought to mediate attachment between the maturation stage ameloblasts and the mineralizing enamel (Moffatt et al., 2014). AMTN is also expressed at the junctional epithelium, a structure partially formed from maturation stage ameloblasts that mediates the attachment of the gingiva to the tooth (Bosshardt and Lang, 2005; Moffatt et al., 2006).

Murine models of amelotin function include an *Amel* promoter driven *Amtn* overexpressing mouse (p*Amel:Amtn*$^{+/+}$) and a knockout (*Amtn*$^{-/-}$) model (Lacruz et al., 2012a; Nakayama et al., 2015). The p*Amel:Amtn*$^{+/+}$ model had thin brittle enamel with an irregular surface layer (Lacruz et al., 2012a). The *Amtn*$^{-/-}$ model had mandibular incisors with a chalky appearance and enamel in which mineralization was delayed and organic material retained (Nakayama et al., 2015). The surface enamel easily chipped away and was found to be softer than the inner and middle enamel (Nakayama et al., 2015; Nunez et al., 2015). These phenotypes and an *in vitro* study that found that AMTN promotes HA precipitation, suggested a critical role for AMTN in the formation of compact surface aprismatic enamel during maturation (Abbarin et al., 2015). Therefore, AMTN could be bi-functional, with roles in both cell-matrix attachment and mineral nucleation.

In humans, only one *AMTN* mutation has been associated with AI; an in-frame deletion spanning exons 3 to 6 (Smith et al., 2016). The family exhibited hypomineralized AI with autosomal dominant inheritance. Phenotypic analysis of teeth revealed that the enamel was of a lower mineral density when compared to WT and the typical prismatic enamel structure was disturbed throughout the enamel layer.

FAM83H

Family with sequence similarity 83, member H (FAM83H; MIM *611927), is an intracellular protein with ubiquitous expression (Lee et al., 2008a). In oral tissues, the ameloblasts show the highest expression of FAM83H, especially in pre-secretory and secretory stages (Lee et al., 2008a). Lower expression is seen in maturation stage ameloblasts as well as in the odontoblasts and alveolar bone (Lee et al., 2008a).

Through homology, FAM83H was suggested to be involved in membrane vesicle trafficking or cytoskeletal reorganization (Foster and Xu, 2003; Ding et al., 2009). FAM83H has now been shown, via binding to casein kinase 1 (CK1), to regulate the organization of the keratin cytoskeleton and therefore also to be involved in desmosome formation (Kuga et al., 2016).

Human mutations identified in *FAM83H* cause autosomal dominant hypocalcified AI (MIM #130900) (Mendoza et al., 2007; Kim et al., 2008). Analysis of teeth from individuals with *FAM83H* mutations identified defects in enamel rods, especially at the DEJ, with increased organic content within the enamel (El-Sayed et al., 2010; Zhang et al., 2015a).

All of the mutations identified so far have been located in the final, largest exon and all but two are nonsense or frameshift variants predicted to lead to premature translation termination (Kim et al., 2008; Lee et al., 2008a, 2011; Ding et al., 2009; Hart et al., 2009; Hyun et al., 2009; Wright et al., 2009, 2011; El-Sayed et al., 2010; Chan et al., 2011). As terminating mutations in the last exon are generally not subject to NMD (Nagy and Maquat, 1998), the truncated products may cause AI through a dominant gain of function effect.

In vitro analysis of three of the reported AI-causing *FAM83H* mutations suggests that the mutations alter the localization of the FAM83H protein, leading to an increased concentration within the nucleus rather than its typical cytoplasmic location (Lee et al., 2011). Analysis of the shortest of the truncated mutant proteins reported, p.S287* (NP_198488.3), revealed that it bound and inhibited CK1 (Kuga et al., 2016). All of the twenty-seven *FAM83H* mutations identified reside within the first 1343 bp of the final exon (up to Glu694) with the final 1460 bp devoid of known mutations, suggesting that this region may not be critical to FAM83H function. In addition, some degree of phenotypic variation has been reported in patients, with mutations predicted to produce longer truncation products having a milder phenotype confined to just the cervical areas of the teeth (Wright et al., 2009).

Interestingly, *Fam83h* knockout mice and a mouse overexpressing FAM83H do not show an AI enamel phenotype (Kweon et al., 2013) supporting a dominant negative effect as the disease mechanism.

Transport

The formation of enamel requires both the transport of large volumes of protein from ameloblasts via exocytic vesicles during the secretory stage and the removal of degraded protein via endocytic pathways during the maturation stage. During maturation, ameloblasts must also increase the active transport of mineral ions into the enamel space to support crystallite growth. Efficient and effective transport of cellular cargo is therefore critical in enamel formation.

WDR72

WD repeat domain 72 (WDR72; MIM *613214) is believed to form a beta propeller structure (Jawad and Paoli, 2002; Valeyev et al., 2008) and is predicted by protein homology to be an intracellular vesicle coat protein (El-Sayed et al., 2009; Katsura et al., 2014). WDR72 expression is widespread, and is highest in bladder and kidney (Lee et al., 2010b). Immunolocalization of WDR72 in mouse incisors revealed more intense staining in maturation stage than secretory stage ameloblasts (El-Sayed et al.,

2009), with a specific increase in expression noted to occur at the initiation of enamel maturation (Katsura et al., 2014).

Wdr72 null mouse models exhibit hypomaturation AI (Katsura et al., 2014; Wang et al., 2015). In one model, maturation stage ameloblasts were shorter compared with WT mice, whereas there was no difference for secretory stage ameloblasts (Katsura et al., 2014). Affected enamel appeared stained and opaque and had retained proteins within it, including amelogenin. In another null mouse model, attachment between the ameloblasts and the enamel matrix was found to be disrupted (Wang et al., 2015). Ruffle ended maturation stage ameloblasts, thought to be responsible for protein removal, did not appear to be present and uptake of processed enamel matrix proteins by maturation stage ameloblasts was affected (Wang et al., 2015). In addition, the localization of putative Ca^{2+} transporter SLC24A4 was altered in $Wdr72^{-/-}$ mice.

Originally, three truncating *WDR72* mutations were identified in patients with autosomal recessive hypomaturation AI (MIM #613211) (El-Sayed et al., 2009). Subsequently, other truncating mutations have been described, all causing an identical enamel phenotype and likely to be subject to NMD (Lee et al., 2010b; Chan et al., 2011; El-Sayed et al., 2011; Wright et al., 2011; Kuechler et al., 2012; Katsura et al., 2014). Patients with mutations affecting the region between the two beta propeller clusters have also been reported to exhibit hypodontia and delayed tooth eruption (Kuechler et al., 2012; Katsura et al., 2014). Additionally there have been reports of short stature in families with *WDR72* variants; however, given the consanguineous nature of the majority of the families studied and the lack of adequate controls, it is difficult to directly associate the phenotype with *WDR72* variants and to exclude the possibility that this is caused by an additional co-segregating variant.

SLC24A4

Solute carrier family 24 (Sodium/potassium/calcium exchanger), member 4 (SLC24A4; MIM *609840) is one of a family of potassium dependent sodium/calcium exchangers. Members of this protein family share highly conserved hydrophobic regions, termed alpha-1 and alpha-2 repeats, which interact to form ion-binding pockets and lie within two clusters of five transmembrane helices (Iwamoto et al., 2000; Parry et al., 2013). SLC24A4 is highly expressed in a wide range of tissues including brain, aorta, lung and thymus (Li et al., 2002). Within the developing tooth, it is expressed by maturation stage ameloblasts and localizes to the membrane in contact with the developing enamel (Hu et al., 2012). In rat, *Slc24a4* transcripts are highly upregulated during the shift from secretion to maturation in the enamel organ (Lacruz et al., 2012b) and it is suggested that SLC24A4 is responsible for the active transport of Ca^{2+} ions from ameloblasts into the enamel matrix during maturation (Wang et al., 2014a). In mice, SLC24A4 expression is restricted to ruffle-ended maturation stage ameloblasts (Bronckers et al., 2015).

Mutations in *SLC24A4* cause a hypomaturation/hypomineralized AI phenotype with autosomal recessive inheritance (Parry et al., 2013; Seymen et al., 2014; Wang et al., 2014a; Herzog et al., 2015; Prasad et al., 2016a). Missense mutations affecting both alpha repeats and the cytoplasmic domain, as well as a nonsense mutation and a multi-exonic deletion, have been detected. Subsequent to the identification of *SLC24A4* mutations in human AI, incisors from *Slc24a4* null mice (Stephan et al., 2012) were examined using SEM and a similar phenotype was observed. The enamel was poorly mineralized and quickly wore away to expose the underlying dentine (Parry et al., 2013).

Others: pH Sensing, Crystal Nucleation, and Unknown Functions

Some of the genes known to be mutated in AI have protein products with functions that cannot be grouped easily. In other cases, their function is debated or is simply unknown. It is becoming ever more apparent that discovery of the causative mutations in AI is only the first step and that experiments to discover the functions of the encoded proteins through creation of murine models or *in vitro* study, will be crucial in the understanding of amelogenesis and the pathology of AI.

GPR68

G protein-coupled receptor 68 (GPR68; MIM *601404) is a proton-sensing protein known to function in a wide range of cells including osteoblasts and osteocytes (Ludwig et al., 2003; Yang et al., 2006). Its activation leads to inositol phosphate formation and calcium release from intracellular stores (Ludwig et al., 2003). The protein contains seven transmembrane helices, with the histidine residues responsible for its pH sensing properties on the extracellular surface of the protein (Ludwig et al., 2003). GPR68 has been shown to be expressed in ameloblasts throughout all stages of amelogenesis, with strong expression at the ameloblast pole in contact with the enamel matrix (Parry et al., 2016). GPR68 activation is known to result in inositol phosphate formation that is associated with cytoplasmic re-organization and membrane ruffling (Honda et al., 1999; Czech, 2000; Parry et al., 2016). Therefore, Parry et al. (2016) proposed that GPR68 acts as a pH sensor in amelogenesis, directing ameloblasts to switch between the ruffle ended and smooth ended conformations during the maturation stage.

Three families with autosomal recessive hypomineralized AI have been reported with mutations in the single exon *GPR68* gene (MIM #617217) (Parry et al., 2016). All are predicted to result in loss of function. Two of the families carried deletions expected to remove histidine residues shown to be crucial to the pH sensitivity or the structural integrity of the protein. The third carried a missense variant predicted to destabilize the second transmembrane helix.

In light of mutations in *GPR68* leading to AI in humans, the incisors of $Gpr68^{-/-}$ mice (Mogi et al., 2009) were assessed for enamel defects (Parry et al., 2016). A limited phenotype, of retarded formation of enamel with minor structural differences, was reported. This phenotype partially mirrors *GRP68*-associated AI in humans but may also reflect temporal differences in human and murine amelogenesis, the genetic strain of the $Gpr68^{-/-}$ model or the possibility that mutant protein persists in cases of human AI.

C4orf26

The chromosome 4 open reading frame 26 (*C4orf26*; MIM *614829) gene encodes a proline rich protein containing a signal peptide, two highly conserved but unknown motifs and ten predicted phosphorylation sites (Parry et al., 2012). It has been suggested, based on its amino acid sequence, that C4orf26 belongs to the acidic phosphoprotein family of proteins. These are known to promote HA crystallization, and C4orf26 peptide with a phosphorylated C-terminus was shown to promote HA nucleation and support crystal growth *in vitro* (Parry et al., 2012). Analysis of *C4orf26* expression in rat revealed transcripts in both secretory and maturation stage enamel organs but not in heart or kidney, and in a human cDNA panel lacking any dental tissues, expression was highest in placenta but was also evident in many other tissues (Parry et al., 2012).

Six mutations have been identified in *C4orf26* in ten families with autosomal recessive hypomineralized AI (MIM #614832) (Parry et al., 2012; Prasad et al., 2016b). These include only nonsense, frameshift and splice site variants predicted to escape NMD. However, the resulting proteins are predicted to be non-functional. Enamel from affected individuals contained thin crystallites more typical of the early maturation stage of enamel development rather than of mature enamel. To date no mouse model has been characterized.

ACPT

Acid phosphatase, testicular (ACPT; MIM *606362) is one of a group of enzymes capable of hydrolysing esters of orthophosphoric acid in acidic conditions (Romas et al., 1979). It is expressed by secretory, but not maturation stage, ameloblasts (Seymen et al., 2016) and it has been suggested to elicit odontoblast differentiation and mineralization by supplying phosphate during dentine formation (Choi et al., 2016). *ACPT* was first identified as a gene immediately centromeric to the kallikrein gene cluster within a region of chromosome 19q13.3-q13.4 that is differentially expressed in solid tumors (Yousef et al., 2001). *ACPT* is itself known to show lower expression in testicular cancer tissues compared to normal tissues and is regulated by steroid hormones (Yousef et al., 2001). Its chromosomal location, around 111 kb proximal to *KLK4*, is notable, although *Acpt* was first associated with amelogenesis through the differential analysis of ameloblast gene expression in rats (Lacruz et al., 2011). However, the function of ACPT during amelogenesis is currently unclear and no mouse model has been characterized to date.

ACPT is also expressed in the brain, where it is enriched at post-synaptic sites, and is thought to dephosphorylate the ErbB4 receptor (Fleisig et al., 2004). The ErbB4 receptor has important roles in neuronal differentiation and synaptogenesis, and ACPT acts as a tyrosine phosphatase to modulate signals mediated by ErbB4 that are important for neuronal development and synaptic plasticity (Fleisig et al., 2004).

Mutations in *ACPT* were recently identified in eight families with autosomal recessive hypoplastic AI (MIM #617297) (Seymen et al., 2016; Smith et al., 2017b). All seven variants identified are missense changes predicted to affect residues within the extracellular domain that makes up the majority (residues 29–390; NP_149059.1) of the 426 amino acid protein. Assessment of an affected tooth by X-ray computed tomography revealed that the enamel, where present, was around one tenth of the thickness of control enamel, but was well mineralized (Smith et al., 2017b). The authors found that the underlying dentine was hypermineralized compared to control, although no abnormalities were evident upon clinical examination (Smith et al., 2017b). Assessment of additional samples will be required to confirm this.

Master Controllers of Amelogenesis

These genes control gene expression or the modification of a subset of AI- and other- proteins to influence enamel development. Both members of this group are involved in the development and/or maintenance of other organs and therefore disease can present as both isolated and syndromic AI, although enamel symptoms are usually the first to develop and can serve as an early warning for the development of other pathology.

FAM20A

Family with sequence similarity 20, member A (FAM20A) is one of a family of three human homologs of the *Drosophila* four jointed (fj) protein kinase. Additional family member FAM20C is a Golgi casein kinase responsible for phosphorylating many secreted proteins involved in biomineralization (Tagliabracci et al., 2012). *In vitro* expression of FAM20A has shown that it is also located in the Golgi (Ishikawa et al., 2012; Wang et al., 2013a). FAM20A has been shown to control FAM20C localization and to potentiate its extracellular action *in vitro* (Ohyama et al., 2016). The protein is therefore designated a pseudokinase (Cui et al., 2015).

Mutations in *FAM20A* have been shown to cause autosomal recessive AI and gingival fibromatosis syndrome (AIGFS; O'Sullivan et al., 2011) and enamel renal syndrome (ERS; Jaureguiberry et al., 2012; Wang et al., 2013a). Both syndromes have since been recognized as phenotypic variants of the same condition and are now collectively termed ERS (MIM #204690) (de la Dure-Molla et al., 2014). Patients with *FAM20A* mutations have hypoplastic AI which, in extreme cases, may present as a complete absence of enamel (de la Dure-Molla et al., 2014) or characteristic "glassy" incisor teeth. There are a variety of associated ERS oral defects that may include delayed tooth eruption, hyperplastic dental follicles, pulp stones and gingival overgrowth with ectopic calcification (de la Dure-Molla et al., 2014). Calcification of other organs, most frequently nephrocalcinosis, is variably reported. This may be due to a combination of age, genetic modifiers, and exposure to Ca^{2+} channel blocking drugs (Poulter et al., 2015).

The symptoms associated with ERS suggest that FAM20A phosphorylates proteins involved in enamel formation and other aspects of tooth development, as well as those critical to Ca^{2+} regulation within the kidney. Analysis of developing murine oral tissues showed the presence of FAM20A within ameloblasts, odontoblasts and at consistently high levels within the oral epithelium (Wang et al., 2014c). Ameloblasts expressed FAM20A only during the secretory stage, consistent with the hypoplastic AI phenotype (Wang et al., 2014c). Analysis of

teeth from *Fam20a*$^{-/-}$ mice showed that the ameloblast layer was disorganized and detached from the DEJ, leading to pitted and thin enamel (Vogel et al., 2012). A similar phenotype was observed in an epithelial specific (K14-cre) *Fam20a*$^{-/-}$ model, along with reduced levels of ENAM and MMP20 proteins in ameloblasts but increased levels of AMBN (Li et al., 2016). The authors suggest that reduced levels of ENAM may be due to a lack of phosphorylation by FAM20C due to the absence of FAM20A. However, the authors do not explain the increased and decreased levels of AMBN and MMP20, respectively.

DLX3

Distal-less homeobox 3 (DLX3; MIM *600525) is one of a family of six DLX transcription factors essential to the development of placental, epidermal and ectodermal appendages (Beanan and Sargent, 2000). DLX3 is also expressed in skin, bone and dental tissues including both the odontoblasts and ameloblasts, with greatest expression in ameloblasts during the late secretory stage (Zhang et al., 2015b). Murine whisker and hair follicles strongly express DLX3 before birth but expression decreases after birth. DLX3 is expressed in the placenta during early embryonic development and *Dlx3*$^{-/-}$ mice die around embryonic day 10 due to placental defects, whereas *Dlx3*$^{+/-}$ mice appear phenotypically normal (Morasso et al., 1999). Although, the role of DLX3 has been studied in dentine, bone and hair, through the creation of conditional knockouts of *Dlx3*, (Hwang et al., 2008; Duverger et al., 2012, 2013) no study has reported the creation of a conditional knockout of *Dlx3* in ameloblasts.

Mutations in *DLX3* are known to cause the autosomal dominantly-inherited trichodentoosseous syndrome (TDO; MIM #190320) and amelogenesis imperfecta hypomaturation-hypoplastic type with taurodontism (AIHHT; MIM #104510). TDO is defined as AIHHT with additional features such as kinky hair, especially in infancy, and increased bone density/thickening of the craniofacial cortical bones (Lichtenstein and Warson, 1971). Other variably associated features include flattened fingernails and altered craniofacial morphology, including dolichocephaly and prognathism (Price et al., 1998).

A mutation was first associated with AIHHT in patients carrying a 2 bp deletion (c.561_562delCT; NM_005220.2) in *DLX3* (Dong et al., 2005). Other families of different ethnicities have since been described with the same *DLX3* mutation, potentially highlighting the position as a mutational hotspot. However, the phenotype varies from AI with only mild taurodontism (Kim et al., 2016a) to TDO (Lee et al., 2008b) suggesting that there may be wide phenotypic variation in presentation, even for identical *DLX3* mutations.

DLX3, like all DLX proteins, contains a homeobox domain flanked by N- and C-terminal transactivation domains. The homeobox domain directly binds to target DNA sequences but the transactivation domains have also been shown to be crucial to this binding. DLX3 has been shown to bind to the enhancer regions of *Amelx*, *Enam* and *Odam* in a murine ameloblast cell lineage and to positively regulate their expression (Zhang et al., 2015b).

Only six *DLX3* variants have been reported so far, including two frameshift variants predicted to escape NMD but to result in an altered C-terminal transactivation domain and four missense variants predicted to affect residues (spanning residues 133–182; NP_005211.1) within the central DNA binding homeodomain (residues 129–188). Disease has been postulated to result from haploinsufficiency (Nieminen et al., 2011) but other effects, including dominant negative through binding to WT DLX3 (Duverger et al., 2008), as well as gain of function, through interactions of the mutant protein with other transcription factors, have not been ruled out.

Frequency of Mutations Identified in AI Cohorts

Given the paucity of epidemiological data on AI, the difficulty in estimating its prevalence and the recent advances in knowledge of the underlying genetic causes, we assessed the frequencies of variants in each gene recorded in the AI Leiden Open Variant Database (LOVD) resource (http://dna2.leeds.ac.uk/LOVD/). These findings are biased by studies focusing on particular populations or the specific recruitment of consanguineous families with recessively inherited AI for ease of study. The targeted sequencing of AI cohorts for variants in particular genes and the time since discovery of causality of each of the AI genes will also influence reported relative contributions to disease burden. It is also likely that variants that cause AI as a dominant trait but JEB as a recessive trait, i.e. those in *LAMA3*, *COL17A1*, and potentially also *LAMB3*, are underreported. JEB carriers are often only mentioned in passing in reports as having poor enamel. A larger AI-focused study of carriers of *LAMA3*, *LAMB3,* and *COL17A1* variants would help to clarify the frequency of enamel defects in these individuals and whether the same variants cause both isolated AI and JEB in the case of *LAMB3* variants.

However, with all of these caveats, as of 23rd May 2017, the AI LOVD resource (http://dna2.leeds.ac.uk/LOVD/) details 192 different, published AI gene variants identified in 270 families with AI (**Table 1**). Analysis of these variants shows that just four genes account for the cause of AI in 163 families (60.4%). Variants were most commonly identified in *FAM83H* (19.3% of cases), followed by *FAM20A* (15.2%), *ENAM* (14.2%), and *AMELX* (11.5%). Of the AI families reported with a known mutation, 132 (48.9%) have autosomal dominant AI, with autosomal recessive (109 families; 40.4%) and X linked inheritance (31 families; 11.5%) less frequently reported.

Analysis has also shown that there are a number of variants that have been repeatedly identified in families with AI and that may represent founder mutations or reside at mutational hotspots. These include *ENAM* c.92T>G, p.(L31R) (Brookes et al., 2017) and *KLK4* c.632delT, p.(L211Rfs*37) (Smith et al., 2017a). Some genes, for example *FAM83H* and *WDR72*, show clear trends in the types and positions of AI-causing variants reported, giving clues as to how these variants cause disease.

From a recent focused clinical exome study, molecular diagnoses were obtained in only 18 of 65 syndromic and non-syndromic AI cases (27.7%) (Prasad et al., 2016a). Earlier studies using Sanger sequencing of candidate genes identified variants in 36.6–48.7% of families (Chan et al., 2011; Wright et al., 2011). This suggests that additional AI genes remain to be identified

TABLE 1 | Summary of the variants reported in individuals with AI and entered in the AI LOVD.

Gene (Refseq refs)	No. of variants	Families no. (%)	Variants identified in ≥3 families; number of families: reported nationality/ethnicity	Mode of inheritance and trends in variants identified
FAM83H NM_198488.3 NP_940890.3	26	52 (19.3)	c.973C>T, p.(L31R), 3: Korean and Chinese; c.1192C>T, 5: Korean, Turkish, Caucasian, N/R; c.1354C>T, p.(Q452*), 5: Korean, Danish, Chinese, Jewish, Caucasian; c.2029C>T, p.(Q677*), 5: Korean, Caucasian, N/R.	AD. All within final exon. All except c.1669G>T, p.(G557C), are frameshift/nonsense variants predicted to escape NMD.
FAM20A NM_017565.3 NP_060035.2	42	41 (15.2)	c.34_35delCT, p.(L12Afs*67), 5: Pakistani, Moroccan, Korean/Turkish, N/R; c.406C>T, p.(R136*), 3: Brazilian, Omani, Iranian.	AR. Most are nonsense/frameshift. Three missenses reported: c.518T>G, p.(L173R), c.992T>G, p.(G331D), c.1207G>A, p.(D403N).
ENAM NM_031889.2 NP_114095.2	18	39 (14.4)	c.92T>G, p.(L31R), 5 families: British; c.157A>T, p.(K53*), 7: Swedish; c.588+1delG, p.?, 5: Japanese, Lebanese, Slovenian, N/R; c.1259_1260insAG, p.(V422Pfs*27), 7: Turkish, Slovenian, N/R.	AD (AR also reported). Most are protein-truncating. In-frame indels and missense variants also identified.
AMELX NM_182680.1 NP_872621.1	22	31 (11.5)	c.208C>A, p.(P70T), 6: North American, N/R; c.473delC, p.(P158Hfs*31), 3: North American, British.	XLD. Most are protein-truncating variants. Missense variants affect the N-terminus.
DLX3 NM_005220.2 NP_005211.1	6	15 (5.6)	c.561_562delCT, p.(Y166Qfs*13), 4: Australian, Korean, Caucasian, Turkish; c.571_574delGGGG, p.(G191Rfs*66), 7: North American.	AD. Most are missenses in homeodomain, other two are frameshifts predicted to escape NMD and to affect C-terminal transactivation domain.
MMP20 NM_004771.3 NP_004762.2	11	13 (4.8)	c.389C>T, p.T130I, 3: French, N/R c.678T>A, p.H226Q, 3: Turkish, North American, N/R. c.954-2A>T, p.?, 4: North American, French/German/Moroccan.	AR. Variety of missense, frameshift, splice and nonsense variants reported.
WDR72 NM_182758.3 NP_877435.3	10	12 (4.4)	c.1467_1468delAT, p.(V491Dfs*8), 3: Mexican, Turkish, unknown.	AR. All are nonsense/frameshift predicted to under-go NMD, except missense variant c.182A>G, p.(H61R).
COL17A1 NM_000494.3 NP_000485.3	10	12*^ (4.4)	N/A	AD. Nonsense/frameshift variants predicted to undergo NMD, and missense variants affecting glycine residues.
C4orf26 NM_178497.3 NP_848592.2	6	10* (3.7)	c.51_56delGGTAACinsATGCTGGTTACTGGTA, p.(V18Cfs*23), 3: North American; c.229C>T, p.(R77*), 4: Omani.	AR. All nonsense/frameshift/splice variants. Nonsense/frameshifts predicted to escape NMD.
LAMB3 NM_000228.2 NP_000219.2	9	9 (3.3)	N/A	AD. Majority frameshift/nonsense. Most lead to stop codon in penultimate/final exon. Two variants within other exons identified.
KLK4 NM_004917.4 NP_004908.4	4	9 (3.3)	c.632delT, p.(L211Rfs*37), 5: Pakistani.	AR. All are nonsense/frameshift. Not all are predicted to undergo NMD.
ACPT NM_033068.2 NP_149059.1	7	8 (3.0)	c.713C>T, p.(S238L), 3: Turkish.	AR. All missense variants within the extracellular domain.

(Continued)

TABLE 1 | Continued

Gene (Refseq refs)	No. of Variants	Families No. (%)	Variants identified in ≥3 families; number of families: reported nationality/ethnicity	Mode of inheritance and trends in variants identified
SLC24A4 NM_153646.3 NP_705932.2	5	6 (2.2)	N/A	AR. Variety reported, including a multi-exon deletion, a nonsense and missense variants.
ITGB6 NM_000888.*4* NP_000879.2	6	5 (1.9)	N/A	AR. All missense variants except one nonsense variant, c.1846C>T, p.(R616*).
LAMA3 NM_000227.3 NP_00218.2	4	4^ (1.5)	N/A	AD. All frameshift, nonsense or splice variants.
GPR68 NM_001177676.1 NP_001171147.1	3	3 (1.1)	N/A	AR. One frameshift, one in-frame deletion, one missense variant.
AMBN NM_016519.5 NP_057603.1	2	2 (0.7)	N/A	AR. One in-frame exon deletion, one splice variant.
AMTN NM_212557.3 NP_997722.1	1	1 (0.4)	N/A	AD. One variant: a multi-exon, in-frame deletion.
Total	192	270^		

*Genes are ordered in decreasing number of families reported. No. of variants denotes the number of unique variants reported for each gene within the AI LOVD. Nationality/ethnicity is as reported, in some cases, multiple families are reported within one study with only details of the nationalities/ethnicities of the cohort included but with no specific nationality/ethnicity assigned to each individual/family. In such cases, all nationalities/ethnicities have been listed. The inheritance of disease due to ENAM variants has been reported to be AR in some instances, however heterozygous and biallelic individuals for ENAM variants were reported to have a milder and more severe phenotype, respectively. *one family carries variants in both COL17A1 and C4orf26. ^one family carries variants in both COL17A1 and LAMA3. Therefore, total number of families is 270 not 272. AD, autosomal dominant; AR, autosomal recessive; NMD, nonsense mediated decay; N/A, not applicable; N/R, not reported; XLD, X-linked dominant. Data obtained from AI LOVD: http://dna2.leeds.ac.uk/LOVD/ 23rd May 2017.*

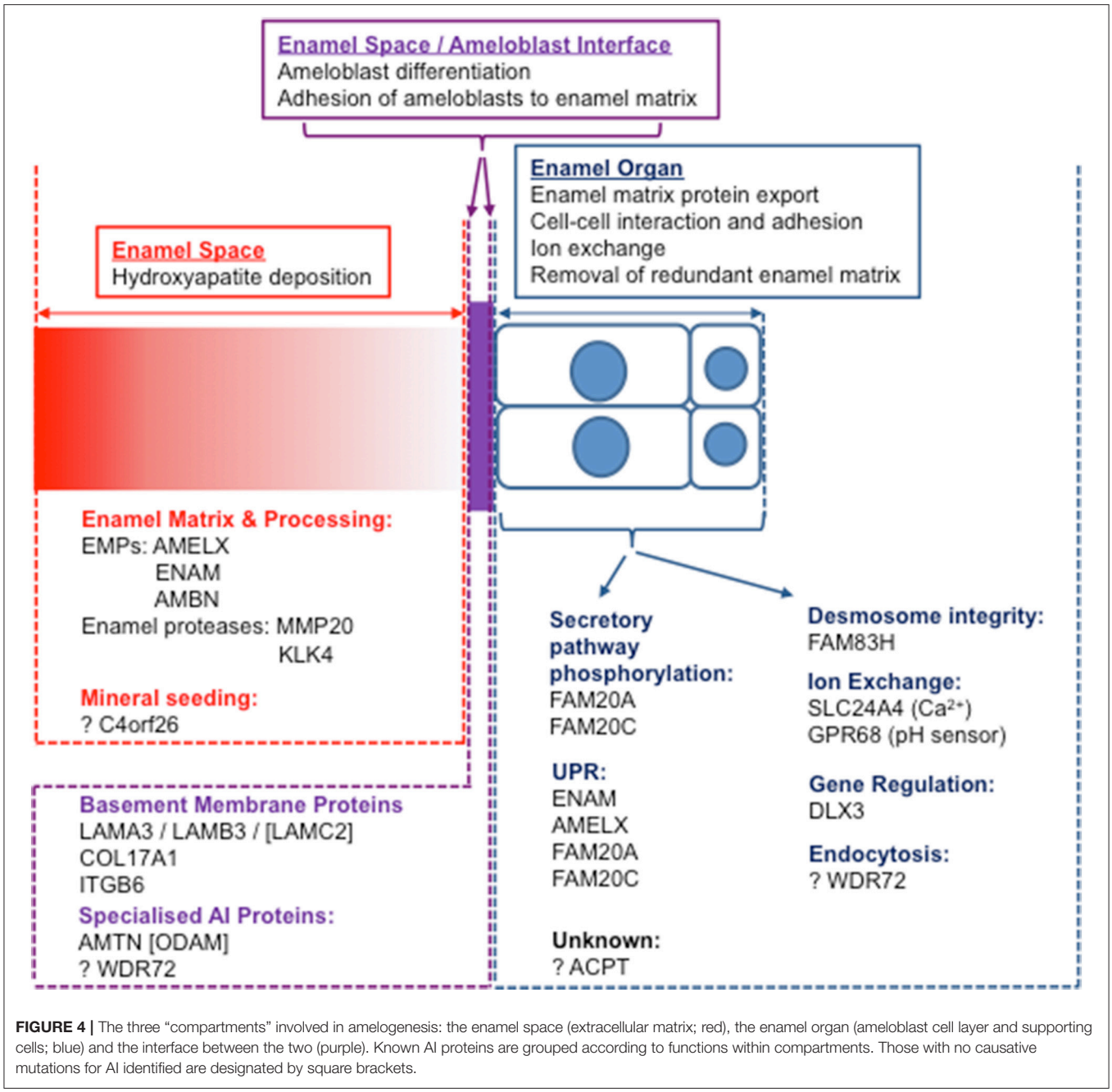

FIGURE 4 | The three "compartments" involved in amelogenesis: the enamel space (extracellular matrix; red), the enamel organ (ameloblast cell layer and supporting cells; blue) and the interface between the two (purple). Known AI proteins are grouped according to functions within compartments. Those with no causative mutations for AI identified are designated by square brackets.

and/or that variants in known AI genes, such as intronic, regulatory, and larger structural alterations, are being missed by current analysis pipelines. For example, particular variant types, such as heterozygous copy number changes larger than an exon, are likely to be under-represented in reports since they would not have been identified by Sanger sequencing or WES data without specific downstream analysis (Poulter et al., 2015; Smith et al., 2016).

DISCUSSION

This article reviews the genes and proteins where variants cause AI presenting in isolation of other health problems and also reviews current knowledge of their functions. Potential mechanisms of disease were explored with reference to evidence from mouse models and human pathology. Finally, the prevalence of reports of families with AI with mutations in each gene was explored through the development and interrogation of an AI LOVD resource.

It is evident that some proteins with roles in amelogenesis can be classified into clear functional groups, with obvious examples including the EMPs: AMELX, ENAM and AMBN; the enamel matrix proteases: MMP20 and KLK4; as well as those involved in cell-cell and cell-matrix adhesion: ITGB6, LAMB3, LAMA3, COL17A1, AMTN, and FAM83H, transport: WDR72 and SLC24A4 and master controllers of amelogenesis: FAM20A

and DLX3. However, there is also an emerging group of proteins that exhibit diverse functions in enamel development. These include proteins thought to be involved in activities as wide-ranging as crystal nucleation (C4orf26), proton sensing (GPR68) and those with unknown roles (ACPT). Further investigation is required to define the role of each protein in amelogenesis and to identify interacting partners, mechanisms, and functional pathways.

To understand the events of amelogenesis and how mutations can impact on the enamel formed, it is important to consider three linked but distinct compartments, namely the cellular enamel organ, including both the ameloblast cell layer and its supporting cells, the extracellular enamel space and the interface between sites (**Figure 4**). Initial mutation discovery focused on EMPs and the events in the extracellular enamel space. However, it is becoming clear that intracellular events in the ameloblast, ameloblast cell-cell interactions and ameloblast attachment to the enamel matrix also play critical roles in amelogenesis. Even disease previously considered to be entirely the result of perturbations in extracellular events, such as that resulting from EMP mutations, has, in some cases, been shown to result in catastrophic intracellular effects. For example, some mutations in *Amelx* (Barron et al., 2010) and *Enam* (Brookes et al., 2017) lead to activation of the unfolded protein response and to apoptosis of ameloblasts. Therefore, it is important to consider pathology in the context of all three compartments and to study the roles of the affected proteins through the production of murine models with AI specific mutations. Assessment of the variants identified in human AI to date suggests that for many AI genes, trends indicate that protein absence may not be the mechanism of disease.

Classification of AI by phenotype and pattern of Mendelian inheritance has been modified since the first description of AI as a separate condition to dentinogenesis imperfecta in 1938 (Finn, 1938; Aldred et al., 2003). In recent years, the narrow definition of AI as an isolated enamel pathology has expanded to include diverse syndromes with generalized developmental enamel defects indistinguishable from AI in isolation (Aldred et al., 2003). The ability to identify the underlying genetic cause in individuals with AI has informed a more meaningful classification. Nevertheless, recognition of characteristic phenotypes remains useful. For example, patients with *FAM20A* variants can be readily identified upon oral examination. Patients with *FAM20A* variants should be referred for specialist renal evaluation and follow-up, to better understand the natural history of this feature and for development of intervention strategies to limit development of ectopic calcification. The contribution of this gene to the variant load reported for AI, described in the LOVD resource, is 15.2%. Therefore, *FAM20A* variants are the second most commonly reported cause of AI overall and the most commonly reported cause for autosomal recessive AI, at least in the AI LOVD of published reports. This finding highlights the real need for genetic diagnosis for AI patients. Knowledge of AI genetics has already prompted the development of a targeted diagnostic AI genetic screen within the UK National Healthcare Service that will help to inform improved patient pathways and to raise standards of care (Holland, 2017).

WES has expedited the identification of new genetic variants that cause AI (O'Sullivan et al., 2011; Jaureguiberry et al., 2012; Poulter et al., 2014a,b) but it is likely that more genes, not currently known to be critical for enamel formation, remain to be identified. As costs continue to fall, whole genome sequencing is also facilitating the discovery of mutations that cannot be found by conventional WES analysis (Poulter et al., 2015). For many human conditions, greater awareness of the importance of non-coding mutations is leading to an increase in the study of patient mRNA. However, for AI this approach is hampered by the enamel specific expression of many of the genes so far implicated. Transcript profiling in mammalian models can overcome this difficulty and highlight potential candidate genes, such as *SLC24A4*, where genetic variants were subsequently confirmed as causing of AI (Lacruz et al., 2012b).

The identification of AI genes will allow clinical and molecular diagnoses to be matched. This will in turn help clinicians to improve patient pathways and offer a more accurate prognosis and clearer risk information to patients and other family members. Genotyping of AI cohorts will facilitate participant recruitment to future clinical trials to develop improved clinical decision-making for AI, consistent with an increasingly personalized precision approach to care. To further support the development of diagnostic screening and variant interpretation in AI, we have created a dedicated LOVD resource recording all published mutations causing AI presenting in the absence of other health problems (http://dna2.leeds.ac.uk/LOVD/). The improved understanding of AI resulting from identification of the causative mutations and their pathogenesis also highlights new avenues for possible therapeutic intervention to improve outcomes for those with AI. ER stress is now recognized as a mechanism of AI pathogenesis (Brookes et al., 2014, 2017) and represents a possible therapeutic opportunity through *in utero*/early post-natal use of protein chaperoning/anti-apoptotic drugs such as 4-phenylbutyrate (Brookes et al., 2014). Biomimetic technologies that repair carious lesions to enamel have also been reported (Brunton et al., 2013) although it remains to be seen whether these will be effective in treating selective forms of AI. A thorough understanding of the molecular mechanisms underlying biomineralization, obtained through a genetic dissection of AI, will inform the development of new interventions for enamel defects.

In summary, recent increases in our understanding of the genetic variants that cause AI offer us new insights into the varied cellular and extracellular biological processes that are essential for enamel formation. Collation of published genetic variants causing AI presenting in the absence of other health problems in one LOVD resource will support this process. New genetic insight can translate into improved patient care in the short-term and will inform the development of new therapeutic strategies for enamel pathologies that are not expected to be restricted to AI in the future.

AUTHOR CONTRIBUTIONS

CELS drafted the manuscript, figures and tables, deposited variants in the AI LOVD and curates the AI LOVD. AA hosts the AI LOVD. JAP, CFI and AJM revised early drafts of the

manuscript. JK, SJB and AJM drafted figures. All authors read, critically revised and gave approval for the manuscript. All authors agree to be accountable for all aspects of the work.

FUNDING

This work was supported by the Wellcome Trust [grant numbers 093113 and 075945]. CS is funded by a Wellcome Trust Institutional Strategic Support award. JK is supported by the NIHR Leeds Musculoskeletal Biomedical Research Unit. Funding to pay the Open Access publication charges for this article were provided by the Wellcome Trust.

ACKNOWLEDGMENTS

The authors thank all of the families with AI that have provided DNA and teeth for research. Data from this article was presented at the Ninth Enamel Symposium, Harrogate, England, UK 30th October to 3rd November 2016.

SUPPLEMENTARY MATERIAL

The Supplementary Material for this article can be found online at: http://journal.frontiersin.org/article/10.3389/fphys.2017.00435/full#supplementary-material

REFERENCES

Abbarin, N., San Miguel, S., Holcroft, J., Iwasaki, K., and Ganss, B. (2015). The enamel protein amelotin is a promoter of hydroxyapatite mineralization. *J. Bone Miner. Res.* 30, 775–785. doi: 10.1002/jbmr.2411

Aberdam, D., Aguzzi, A., Baudoin, C., Galliano, M. F., Ortonne, J. P., and Meneguzzi, G. (1994a). Developmental expression of nicein adhesion protein (laminin-5) subunits suggests multiple morphogenic roles. *Cell Adhes. Commun.* 2, 115–129. doi: 10.3109/15419069409004431

Aberdam, D., Galliano, M. F., Vailly, J., Pulkkinen, L., Bonifas, J., Christiano, A. M., et al. (1994b). Herlitz's junctional epidermolysis bullosa is linked to mutations in the gene (LAMC2) for the gamma 2 subunit of nicein/kalinin (LAMININ-5). *Nat. Genet.* 6, 299–304. doi: 10.1038/ng0394-299

Alberts, B. J., Lewis, J., Raff, M., and Roberts, K., Walter, P. (2002). *Molecular Biology of the Cell*. New York, NY: Garland Science.

Aldred, M. J., Crawford, P. J., Roberts, E., Gillespie, C. M., Thomas, N. S., Fenton, I., et al. (1992). Genetic heterogeneity in X-linked amelogenesis imperfecta. *Genomics* 14, 567–573. doi: 10.1016/S0888-7543(05)80153-3

Aldred, M. J., Savarirayan, R., and Crawford, P. J. (2003). Amelogenesis imperfecta: a classification and catalogue for the 21st century. *Oral Dis.* 9, 19–23. doi: 10.1034/j.1601-0825.2003.00843.x

Annes, J. P., Rifkin, D. B., and Munger, J. S. (2002). The integrin alphaVbeta6 binds and activates latent TGFbeta3. *FEBS Lett.* 511, 65–68. doi: 10.1016/S0014-5793(01)03280-X

Ansar, M., Jan, A., Santos-Cortez, R. L., Wang, X., Suliman, M., Acharya, A., et al. (2015). Expansion of the spectrum of ITGB6-related disorders to adolescent alopecia, dentogingival abnormalities and intellectual disability. *Eur. J. Hum. Genet.* 24, 1223–1227 doi: 10.1038/ejhg.2015.260

Asaka, T., Akiyama, M., Domon, T., Nishie, W., Natsuga, K., Fujita, Y., et al. (2009). Type XVII collagen is a key player in tooth enamel formation. *Am. J. Pathol.* 174, 91–100. doi: 10.2353/ajpath.2009.080573

Backman, B., and Holm, A. K. (1986). Amelogenesis imperfecta: prevalence and incidence in a northern Swedish county. *Commun. Dent. Oral Epidemiol.* 14, 43–47. doi: 10.1111/j.1600-0528.1986.tb01493.x

Barron, M. J., Brookes, S. J., Kirkham, J., Shore, R. C., Hunt, C., Mironov, A., et al. (2010). A mutation in the mouse Amelx tri-tyrosyl domain results in impaired secretion of amelogenin and phenocopies human X-linked amelogenesis imperfecta. *Hum. Mol. Genet.* 19, 1230–1247. doi: 10.1093/hmg/ddq001

Bartlett, J. D. (2013). Dental enamel development: proteinases and their enamel matrix substrates. *ISRN Dent.* 2013:684607. doi: 10.1155/2013/684607

Bartlett, J. D., and Simmer, J. P. (1999). Proteinases in developing dental enamel. *Crit. Rev. Oral Biol. Med.* 10, 425–441. doi: 10.1177/10454411990100040101

Bartlett, J. D., and Simmer, J. P. (2015). New perspectives on amelotin and amelogenesis. *J. Dent. Res.* 94, 642–644. doi: 10.1177/0022034515572442

Bartlett, J. D., Yamakoshi, Y., Simmer, J. P., Nanci, A., and Smith, C. E. (2011). MMP20 cleaves E-cadherin and influences ameloblast development. *Cells Tissues Organs* 194, 222–226. doi: 10.1159/000324205

Beanan, M. J., and Sargent, T. D. (2000). Regulation and function of Dlx3 in vertebrate development. *Dev. Dyn.* 218, 545–553. doi: 10.1002/1097-0177(2000)9999:9999<::AID-DVDY1026>3.0.CO;2-B

Berkman, M. D., and Singer, A. (1971). Demonstration of the lyon hypothesis in X-linked dominant hypoplastic amelogenesis imperfecta. *Birth Defects Orig. Artic. Ser.* 7, 204–209.

Beyeler, M., Schild, C., Lutz, R., Chiquet, M., and Trueb, B. (2010). Identification of a fibronectin interaction site in the extracellular matrix protein ameloblastin. *Exp. Cell Res.* 316, 1202–1212. doi: 10.1016/j.yexcr.2009.12.019

Bosshardt, D. D., and Lang, N. P. (2005). The junctional epithelium: from health to disease. *J. Dent. Res.* 84, 9–20. doi: 10.1177/154405910508400102

Brain, E. B., and Wigglesworth, J. S. (1968). Developing teeth in epidermolysis bullosa hereditaria letalis. A histological study. *Br. Dent. J.* 124, 255–260.

Breuss, J. M., Gillett, N., Lu, L., Sheppard, D., and Pytela, R. (1993). Restricted distribution of integrin beta 6 mRNA in primate epithelial tissues. *J. Histochem. Cytochem.* 41, 1521–1527. doi: 10.1177/41.10.8245410

Bronckers, A. L., Lyaruu, D., Jalali, R., Medina, J. F., Zandieh-Doulabi, B., and DenBesten, P. K. (2015). Ameloblast modulation and transport of Cl-, Na+, and K+ during amelogenesis. *J. Dent. Res.* 94, 1740–1747. doi: 10.1177/0022034515606900

Brookes, S. J., Barron, M. J., Boot-Handford, R., Kirkham, J., and Dixon, M. J. (2014). Endoplasmic reticulum stress in amelogenesis imperfecta and phenotypic rescue using 4-phenylbutyrate. *Hum. Mol. Genet.* 23, 2468–2480. doi: 10.1093/hmg/ddt642

Brookes, S. J., Barron, M. J., Smith, C. E. L., Poulter, J. A., Mighell, A. J., Inglehearn, C. F., et al. (2017). Amelogenesis imperfecta caused by N-Terminal enamelin point mutations in mice and men is driven by endoplasmic reticulum stress. *Hum. Mol. Genet.* 26, 1863–1876. doi: 10.1093/hmg/ddx090

Brookes, S. J., Robinson, C., Kirkham, J., and Bonass, W. A. (1995). Biochemistry and molecular biology of amelogenin proteins of developing dental enamel. *Arch. Oral Biol.* 40, 1–14. doi: 10.1016/0003-9969(94)00135-X

Brunton, P. A., Davies, R. P., Burke, J. L., Smith, A., Aggeli, A., Brookes, S. J., et al. (2013). Treatment of early caries lesions using biomimetic self-assembling peptides–a clinical safety trial. *Br. Dent. J.* 215:E6. doi: 10.1038/sj.bdj.2013.741

Busk, M., Pytela, R., and Sheppard, D. (1992). Characterization of the integrin alpha v beta 6 as a fibronectin-binding protein. *J. Biol. Chem.* 267, 5790–5796.

Carter, W. G., Ryan, M. C., and Gahr, P. J. (1991). Epiligrin, a new cell adhesion ligand for integrin alpha 3 beta 1 in epithelial basement membranes. *Cell* 65, 599–610. doi: 10.1016/0092-8674(91)90092-D

Chan, H. C., Estrella, N. M., Milkovich, R. N., Kim, J. W., Simmer, J. P., and Hu, J. C. (2011). Target gene analyses of 39 amelogenesis imperfecta kindreds. *Eur. J. Oral Sci.* 119(Suppl. 1), 311–323. doi: 10.1111/j.1600-0722.2011.00857.x

Chan, H. C., Mai, L., Oikonomopoulou, A., Chan, H. L., Richardson, A. S., Wang, S. K., et al. (2010). Altered enamelin phosphorylation site causes amelogenesis imperfecta. *J. Dent. Res.* 89, 695–699. doi: 10.1177/0022034510365662

Chen, C. L., Bromley, K. M., Moradian-Oldak, J., and DeYoreo, J. J. (2011). *In situ* AFM study of amelogenin assembly and disassembly dynamics on charged surfaces provides insights on matrix protein self-assembly. *J. Am. Chem. Soc.* 133, 17406–17413. doi: 10.1021/ja206849c

Cho, E. S., Kim, K. J., Lee, K. E., Lee, E. J., Yun, C. Y., Lee, M. J., et al. (2014). Alteration of conserved alternative splicing in AMELX causes enamel defects. *J. Dent. Res.* 93, 980–987. doi: 10.1177/0022034514547272

Choi, H., Kim, T. H., Yun, C. Y., Kim, J. W., and Cho, E. S. (2016). Testicular acid phosphatase induces odontoblast differentiation and mineralization. *Cell Tissue Res.* 364, 95–103. doi: 10.1007/s00441-015-2310-9

Coffield, K. D., Phillips, C., Brady, M., Roberts, M. W., Strauss, R. P., and Wright, J. T. (2005). The psychosocial impact of developmental dental defects in people with hereditary amelogenesis imperfecta. *J. Am. Dent. Assoc.* 136, 620–630. doi: 10.14219/jada.archive.2005.0233

Crawford, P. J., Aldred, M., and Bloch-Zupan, A. (2007). Amelogenesis imperfecta. *Orphanet J. Rare Dis.* 2:17. doi: 10.1186/1750-1172-2-17

Cui, J., Xiao, J., Tagliabracci, V. S., Wen, J., Rahdar, M., and Dixon, J. E. (2015). A secretory kinase complex regulates extracellular protein phosphorylation. *Elife* 4:e06120. doi: 10.7554/eLife.06120

Czech, M. P. (2000). PIP2 and PIP3: complex roles at the cell surface. *Cell* 100, 603–606. doi: 10.1016/S0092-8674(00)80696-0

Dashash, M., Yeung, C. A., Jamous, I., and Blinkhorn, A. (2013). Interventions for the restorative care of amelogenesis imperfecta in children and adolescents. *Cochrane Database Syst. Rev.* 6:CD007157. doi: 10.1002/14651858.CD007157.pub2

de la Dure-Molla, M., Quentric, M., Yamaguti, P. M., Acevedo, A. C., Mighell, A. J., Vikkula, M., et al. (2014). Pathognomonic oral profile of enamel renal syndrome (ERS) caused by recessive FAM20A mutations. *Orphanet J. Rare Dis.* 9:84. doi: 10.1186/1750-1172-9-84

Ding, Y., Estrella, M. R., Hu, Y. Y., Chan, H. L., Zhang, H. D., Kim, J. W., et al. (2009). Fam83h is associated with intracellular vesicles and ADHCAI. *J. Dent. Res.* 88, 991–996. doi: 10.1177/0022034509349454

Dong, J., Amor, D., Aldred, M. J., Gu, T., Escamilla, M., and MacDougall, M. (2005). DLX3 mutation associated with autosomal dominant amelogenesis imperfecta with taurodontism. *Am. J. Med. Genet. A* 133A, 138–141. doi: 10.1002/ajmg.a.30521

Duverger, O., Isaac, J., Zah, A., Hwang, J., Berdal, A., Lian, J. B., et al. (2013). *In vivo* impact of Dlx3 conditional inactivation in neural crest-derived craniofacial bones. *J. Cell. Physiol.* 228, 654–664. doi: 10.1002/jcp.24175

Duverger, O., Lee, D., Hassan, M. Q., Chen, S. X., Jaisser, F., Lian, J. B., et al. (2008). Molecular consequences of a frameshifted DLX3 mutant leading to Tricho-Dento-Osseous syndrome. *J. Biol. Chem.* 283, 20198–20208. doi: 10.1074/jbc.M709562200

Duverger, O., Zah, A., Isaac, J., Sun, H. W., Bartels, A. K., Lian, J. B., et al. (2012). Neural crest deletion of Dlx3 leads to major dentin defects through down-regulation of Dspp. *J. Biol. Chem.* 287, 12230–12240. doi: 10.1074/jbc.M111.326900

El-Sayed, W., Parry, D. A., Shore, R. C., Ahmed, M., Jafri, H., Rashid, Y., et al. (2009). Mutations in the beta propeller WDR72 cause autosomal-recessive hypomaturation amelogenesis imperfecta. *Am. J. Hum. Genet.* 85, 699–705. doi: 10.1016/j.ajhg.2009.09.014

El-Sayed, W., Shore, R. C., Parry, D. A., Inglehearn, C. F., and Mighell, A. J. (2010). Ultrastructural analyses of deciduous teeth affected by hypocalcified amelogenesis imperfecta from a family with a novel Y458X FAM83H nonsense mutation. *Cells Tissues Organs* 191, 235–239. doi: 10.1159/000252801

El-Sayed, W., Shore, R. C., Parry, D. A., Inglehearn, C. F., and Mighell, A. J. (2011). Hypomaturation amelogenesis imperfecta due to WDR72 mutations: a novel mutation and ultrastructural analyses of deciduous teeth. *Cells Tissues Organs* 194, 60–66. doi: 10.1159/000322036

Fine, J. D., Eady, R. A., Bauer, E. A., Bauer, J. W., Bruckner-Tuderman, L., Heagerty, A., et al. (2008). The classification of inherited epidermolysis bullosa (EB): report of the third international consensus meeting on diagnosis and classification of EB. *J. Am. Acad. Dermatol.* 58, 931–950. doi: 10.1016/j.jaad.2008.02.004

Finn, S. B. (1938). Hereditary opalescent dentin. I. an analysis of the literature on hereditary anomalies of tooth color. *JADA* 25, 1240–1249. doi: 10.14219/jada.archive.1938.0205

Fleisig, H., El-Din El-Husseini, A., and Vincent, S. R. (2004). Regulation of ErbB4 phosphorylation and cleavage by a novel histidine acid phosphatase. *Neuroscience* 127, 91–100. doi: 10.1016/j.neuroscience.2004.04.060

Fong, C. D., and Hammarstrom, L. (2000). Expression of amelin and amelogenin in epithelial root sheath remnants of fully formed rat molars. *Oral Surg. Oral Med. Oral Pathol. Oral Radiol. Endod.* 90, 218–223. doi: 10.1067/moe.2000.107052

Fong, C. D., Cerny, R., Hammarstrom, L., and Slaby, I. (1998). Sequential expression of an amelin gene in mesenchymal and epithelial cells during odontogenesis in rats. *Eur. J. Oral Sci.* 106(Suppl. 1), 324–330. doi: 10.1111/j.1600-0722.1998.tb02193.x

Fong, C. D., Slaby, I., and Hammarstrom, L. (1996). Amelin: an enamel-related protein, transcribed in the cells of epithelial root sheath. *J. Bone Miner. Res.* 11, 892–898. doi: 10.1002/jbmr.5650110704

Foster, D. A., and Xu, L. (2003). Phospholipase D in cell proliferation and cancer. *Mol. Cancer Res.* 1, 789–800.

Fouillen, A., Dos Santos Neves, J., Mary, C., Castonguay, J. D., Moffatt, P., Baron, C., et al. (2017). Interactions of AMTN, ODAM and SCPPPQ1 proteins of a specialized basal lamina that attaches epithelial cells to tooth mineral. *Sci. Rep.* 7:46683. doi: 10.1038/srep46683

Fukae, M., Tanabe, T., Uchida, T., Yamakoshi, Y., and Shimizu, M. (1993). Enamelins in the newly formed bovine enamel. *Calcif. Tissue Int.* 53, 257–261. doi: 10.1007/BF01320911

Fukumoto, S., Kiba, T., Hall, B., Iehara, N., Nakamura, T., Longenecker, G., et al. (2004). Ameloblastin is a cell adhesion molecule required for maintaining the differentiation state of ameloblasts. *J. Cell Biol.* 167, 973–983. doi: 10.1083/jcb.200409077

Gasse, B., Karayigit, E., Mathieu, E., Jung, S., Garret, A., Huckert, M., et al. (2013). Homozygous and compound heterozygous MMP20 mutations in amelogenesis imperfecta. *J. Dent. Res.* 92, 598–603. doi: 10.1177/0022034513488393

Gotler, M., and Ratson, T. (2010). Molar incisor hypomineralization (MIH)–a literature review. *Refuat Hapeh Vehashinayim* 27, 10–18, 60.

Guan, X., and Bartlett, J. D. (2013). MMP20 modulates cadherin expression in ameloblasts as enamel develops. *J. Dent. Res.* 92, 1123–1128. doi: 10.1177/0022034513506581

Guan, X., Xu, M., Millar, S. E., and Bartlett, J. D. (2016). Beta-catenin is essential for ameloblast movement during enamel development. *Eur. J. Oral Sci.* 124, 221–227. doi: 10.1111/eos.12261

Guo, J., Lyaruu, D. M., Takano, Y., Gibson, C. W., DenBesten, P. K., and Bronckers, A. L. (2015). Amelogenins as potential buffers during secretory-stage amelogenesis. *J. Dent. Res.* 94, 412–420. doi: 10.1177/0022034514564186

Hart, P. S., Aldred, M. J., Crawford, P. J., Wright, N. J., Hart, T. C., and Wright, J. T. (2002). Amelogenesis imperfecta phenotype-genotype correlations with two amelogenin gene mutations. *Arch. Oral Biol.* 47, 261–265. doi: 10.1016/S0003-9969(02)00003-1

Hart, P. S., Becerik, S., Cogulu, D., Emingil, G., Ozdemir-Ozenen, D., Han, S. T., et al. (2009). Novel FAM83H mutations in Turkish families with autosomal dominant hypocalcified amelogenesis imperfecta. *Clin. Genet.* 75, 401–404. doi: 10.1111/j.1399-0004.2008.01112.x

Hart, P. S., Hart, T. C., Michalec, M. D., Ryu, O. H., Simmons, D., Hong, S., et al. (2004). Mutation in kallikrein 4 causes autosomal recessive hypomaturation amelogenesis imperfecta. *J. Med. Genet.* 41, 545–549. doi: 10.1136/jmg.2003.017657

Hart, P. S., Michalec, M. D., Seow, W. K., Hart, T. C., and Wright, J. T. (2003). Identification of the enamelin (g.8344delG) mutation in a new kindred and presentation of a standardized ENAM nomenclature. *Arch. Oral Biol.* 48, 589–596. doi: 10.1016/S0003-9969(03)00114-6

Hashem, A., Kelly, A., O'Connell, B., and O'Sullivan, M. (2013). Impact of moderate and severe hypodontia and amelogenesis imperfecta on quality of life and self-esteem of adult patients. *J. Dent.* 41, 689–694. doi: 10.1016/j.jdent.2013.06.004

Haze, A., Taylor, A. L., Blumenfeld, A., Rosenfeld, E., Leiser, Y., Dafni, L., et al. (2007). Amelogenin expression in long bone and cartilage cells and in bone marrow progenitor cells. *Anat. Rec. (Hoboken).* 290, 455–460. doi: 10.1002/ar.20520

Herzog, C. R., Reid, B. M., Seymen, F., Koruyucu, M., Tuna, E. B., Simmer, J. P., et al. (2015). Hypomaturation amelogenesis imperfecta caused by a novel SLC24A4 mutation. *Oral Surg. Oral Med. Oral Pathol. Oral Radiol.* 119, e77–e81. doi: 10.1016/j.oooo.2014.09.003

Holcroft, J., and Ganss, B. (2011). Identification of amelotin- and ODAM-interacting enamel matrix proteins using the yeast two-hybrid system. *Eur. J. Oral Sci.* 119(Suppl. 1), 301–306. doi: 10.1111/j.1600-0722.2011.00870.x

Holland, C. (2017). Special feature: Gene genie. *Br. Dent. J.* 222:74. doi: 10.1038/sj.bdj.2017.66

Honda, A., Nogami, M., Yokozeki, T., Yamazaki, M., Nakamura, H., Watanabe, H., et al. (1999). Phosphatidylinositol 4-phosphate 5-kinase alpha is a downstream effector of the small G protein ARF6 in membrane ruffle formation. *Cell* 99, 521–532. doi: 10.1016/S0092-8674(00)81540-8

Hu, C. C., Fukae, M., Uchida, T., Qian, Q., Zhang, C. H., Ryu, O. H., et al. (1997). Sheathlin: cloning, cDNA/polypeptide sequences, and immunolocalization of porcine enamel sheath proteins. *J. Dent. Res.* 76, 648–657. doi: 10.1177/00220345970760020501

Hu, J. C., and Yamakoshi, Y. (2003). Enamelin and autosomal-dominant amelogenesis imperfecta. *Crit. Rev. Oral Biol. Med.* 14, 387–398. doi: 10.1177/154411130301400602

Hu, J. C., Hu, Y., Smith, C. E., McKee, M. D., Wright, J. T., Yamakoshi, Y., et al. (2008). Enamel defects and ameloblast-specific expression in Enam knock-out/lacz knock-in mice. *J. Biol. Chem.* 283, 10858–10871. doi: 10.1074/jbc.M710565200

Hu, J. C., Sun, X., Zhang, C., Liu, S., Bartlett, J. D., and Simmer, J. P. (2002). Enamelysin and kallikrein-4 mRNA expression in developing mouse molars. *Eur. J. Oral Sci.* 110, 307–315. doi: 10.1034/j.1600-0722.2002.21301.x

Hu, J. C., Zhang, C., Sun, X., Yang, Y., Cao, X., Ryu, O., et al. (2000). Characterization of the mouse and human PRSS17 genes, their relationship to other serine proteases, and the expression of PRSS17 in developing mouse incisors. *Gene* 251, 1–8. doi: 10.1016/S0378-1119(00)00203-1

Hu, P., Lacruz, R. S., Smith, C. E., Smith, S. M., Kurtz, I., and Paine, M. L. (2012). Expression of the sodium/calcium/potassium exchanger, NCKX4, in ameloblasts. *Cells Tissues Organs* 196, 501–509. doi: 10.1159/000337493

Hwang, J., Mehrani, T., Millar, S. E., and Morasso, M. I. (2008). Dlx3 is a crucial regulator of hair follicle differentiation and cycling. *Development* 135, 3149–3159. doi: 10.1242/dev.022202

Hyun, H. K., Lee, S. K., Lee, K. E., Kang, H. Y., Kim, E. J., Choung, P. H., et al. (2009). Identification of a novel FAM83H mutation and microhardness of an affected molar in autosomal dominant hypocalcified amelogenesis imperfecta. *Int. Endod. J.* 42, 1039–1043. doi: 10.1111/j.1365-2591.2009.01617.x

Iizuka, S., Kudo, Y., Yoshida, M., Tsunematsu, T., Yoshiko, Y., Uchida, T., et al. (2011). Ameloblastin regulates osteogenic differentiation by inhibiting Src kinase via cross talk between integrin beta1 and CD63. *Mol. Cell. Biol.* 31, 783–792. doi: 10.1128/MCB.00912-10

Ishikawa, H. O., Xu, A., Ogura, E., Manning, G., and Irvine, K. D. (2012). The Raine syndrome protein FAM20C is a Golgi kinase that phosphorylates bio-mineralization proteins. *PLoS ONE* 7:e42988. doi: 10.1371/journal.pone.0042988

Iwamoto, T., Uehara, A., Imanaga, I., and Shigekawa, M. (2000). The Na^+/Ca^{2+} exchanger NCX1 has oppositely oriented reentrant loop domains that contain conserved aspartic acids whose mutation alters its apparent Ca^{2+} affinity. *J. Biol. Chem.* 275, 38571–38580. doi: 10.1074/jbc.M003788200

Iwasaki, K., Bajenova, E., Somogyi-Ganss, E., Miller, M., Nguyen, V., Nourkeyhani, H., et al. (2005). Amelotin–a novel secreted, ameloblast-specific protein. *J. Dent. Res.* 84, 1127–1132. doi: 10.1177/154405910508401207

Iwata, T., Yamakoshi, Y., Hu, J. C., Ishikawa, I., Bartlett, J. D., Krebsbach, P. H., et al. (2007). Processing of ameloblastin by MMP-20. *J. Dent. Res.* 86, 153–157. doi: 10.1177/154405910708600209

Janones, D. S., Massa, L. F., and Arana-Chavez, V. E. (2005). Immunocytochemical examination of the presence of amelogenin during the root development of rat molars. *Arch. Oral Biol.* 50, 527–532. doi: 10.1016/j.archoralbio.2004.10.004

Jaureguiberry, G., De la Dure-Molla, M., Parry, D., Quentric, M., Himmerkus, N., Koike, T., et al. (2012). Nephrocalcinosis (enamel renal syndrome) caused by autosomal recessive FAM20A mutations. *Nephron Physiol.* 122, 1–6. doi: 10.1159/000349989

Jawad, Z., and Paoli, M. (2002). Novel sequences propel familiar folds. *Structure* 10, 447–454. doi: 10.1016/S0969-2126(02)00750-5

Katsura, K., Horst, J., Chandra, D., Le, T., Nakano, Y., Zhang, Y., et al. (2014). WDR72 models of structure and function: a stage-specific regulator of enamel mineralization. *Matrix Biol.* 38, 48–58.doi: 10.1016/j.matbio.2014.06.005

Kim, J. W., Lee, S. K., Lee, Z. H., Park, J. C., Lee, K. E., Lee, M. H., et al. (2008). FAM83H mutations in families with autosomal-dominant hypocalcified amelogenesis imperfecta. *Am. J. Hum. Genet.* 82, 489–494. doi: 10.1016/j.ajhg.2007.09.020

Kim, J. W., Seymen, F., Lee, K. E., Ko, J., Yildirim, M., Tuna, E. B., et al. (2013). LAMB3 mutations causing autosomal-dominant amelogenesis imperfecta. *J. Dent. Res.* 92, 899–904. doi: 10.1177/0022034513502054

Kim, J. W., Simmer, J. P., Hart, T. C., Hart, P. S., Ramaswami, M. D., Bartlett, J. D., et al. (2005). MMP-20 mutation in autosomal recessive pigmented hypomaturation amelogenesis imperfecta. *J. Med. Genet.* 42, 271–275. doi: 10.1136/jmg.2004.024505

Kim, Y. J., Seymen, F., Koruyucu, M., Kasimoglu, Y., Gencay, K., Shin, T. J., et al. (2016a). Unexpected identification of a recurrent mutation in the DLX3 gene causing amelogenesis imperfecta. *Oral Dis.* 22, 297–302. doi: 10.1111/odi.12439

Kim, Y. J., Shin, T. J., Hyun, H. K., Lee, S. H., Lee, Z. H., and Kim, J. W. (2016b). A novel de novo mutation in LAMB3 causes localized hypoplastic enamel in the molar region. *Eur. J. Oral Sci.* 124, 403–405. doi: 10.1111/eos.12280

Kirkham, J., Robinson, C., Strafford, S. M., Shore, R. C., Bonass, W. A., Brookes, S. J., et al. (2000). The chemical composition of tooth enamel in junctional epidermolysis bullosa. *Arch. Oral Biol.* 45, 377–386. doi: 10.1016/S0003-9969(00)00003-0

Kivirikko, S., McGrath, J. A., Baudoin, C., Aberdam, D., Ciatti, S., Dunnill, M. G., et al. (1995). A homozygous nonsense mutation in the alpha 3 chain gene of laminin 5 (LAMA3) in lethal (Herlitz) junctional epidermolysis bullosa. *Hum. Mol. Genet.* 4, 959–962. doi: 10.1093/hmg/4.5.959

Kivirikko, S., McGrath, J. A., Pulkkinen, L., Uitto, J., and Christiano, A. M. (1996). Mutational hotspots in the LAMB3 gene in the lethal (Herlitz) type of junctional epidermolysis bullosa. *Hum. Mol. Genet.* 5, 231–237. doi: 10.1093/hmg/5.2.231

Kobayashi, K., Yamakoshi, Y., Hu, J. C., Gomi, K., Arai, T., Fukae, M., et al. (2007). Splicing determines the glycosylation state of ameloblastin. *J. Dent. Res.* 86, 962–967. doi: 10.1177/154405910708601009

Krebsbach, P. H., Lee, S. K., Matsuki, Y., Kozak, C. A., Yamada, K. M., and Yamada, Y. (1996). Full-length sequence, localization, and chromosomal mapping of ameloblastin. A novel tooth-specific gene. *J. Biol. Chem.* 271, 4431–4435. doi: 10.1074/jbc.271.8.4431

Kuechler, A., Hentschel, J., Kurth, I., Stephan, B., Prott, E. C., Schweiger, B., et al. (2012). A Novel Homozygous WDR72 mutation in two siblings with amelogenesis imperfecta and mild short stature. *Mol. Syndromol.* 3, 223–229. doi: 10.1159/000343746

Kuga, T., Sasaki, M., Mikami, T., Miake, Y., Adachi, J., Shimizu, M., et al. (2016). FAM83H and casein kinase I regulate the organization of the keratin cytoskeleton and formation of desmosomes. *Sci. Rep.* 6:26557. doi: 10.1038/srep26557

Kuster, J. E., Guarnieri, M. H., Ault, J. G., Flaherty, L., and Swiatek, P. J. (1997). IAP insertion in the murine LamB3 gene results in junctional epidermolysis bullosa. *Mamm. Genome* 8, 673–681. doi: 10.1007/s003359900535

Kwak, S. Y., Yamakoshi, Y., Simmer, J. P., and Margolis, H. C. (2016). MMP20 proteolysis of native amelogenin regulates mineralization *in vitro*. *J. Dent. Res.* 95, 1511–1517. doi: 10.1177/0022034516662814

Kweon, Y. S., Lee, K. E., Ko, J., Hu, J. C., Simmer, J. P., and Kim, J. W. (2013). Effects of Fam83h overexpression on enamel and dentine formation. *Arch. Oral Biol.* 58, 1148–1154. doi: 10.1016/j.archoralbio.2013.03.001

Lacruz, R. S., Nakayama, Y., Holcroft, J., Nguyen, V., Somogyi-Ganss, E., Snead, M. L., et al. (2012a). Targeted overexpression of amelotin disrupts the microstructure of dental enamel. *PLoS ONE* 7:e35200. doi: 10.1371/journal.pone.0035200

Lacruz, R. S., Smith, C. E., Bringas, P. Jr., Chen, Y. B., Smith, S. M., Snead, M. L., et al. (2012b). Identification of novel candidate genes involved in mineralization of dental enamel by genome-wide transcript profiling. *J. Cell Physiol.* 227, 2264–2275. doi: 10.1002/jcp.22965

Lacruz, R. S., Smith, C. E., Chen, Y. B., Hubbard, M. J., Hacia, J. G., and Paine, M. L. (2011). Gene-expression analysis of early- and late-maturation-stage rat enamel organ. *Eur. J. Oral Sci.* 119(Suppl. 1), 149–157. doi: 10.1111/j.1600-0722.2011.00881.x

Lagerstrom, M., Dahl, N., Nakahori, Y., Nakagome, Y., Backman, B., Landegren, U., et al. (1991). A deletion in the amelogenin gene (AMG) causes X-linked amelogenesis imperfecta (AIH1). *Genomics* 10, 971–975. doi: 10.1016/0888-7543(91)90187-J

Le, M. H., Warotayanont, R., Stahl, J., Den Besten, P. K., and Nakano, Y. (2016). Amelogenin Exon4 Forms a Novel miRNA that directs ameloblast and osteoblast differentiation. *J. Dent. Res.* 95, 423–429. doi: 10.1177/0022034515622443

Lee, K. E., Ko, J., Tran Le, C. G., Shin, T. J., Hyun, H. K., Lee, S. H., et al. (2014). Novel LAMB3 mutations cause non-syndromic amelogenesis imperfecta with variable expressivity. *Clin. Genet.* 87, 90–92. doi: 10.1111/cge.12340

Lee, S. K., Hu, J. C., Bartlett, J. D., Lee, K. E., Lin, B. P., Simmer, J. P., et al. (2008a). Mutational spectrum of FAM83H: the C-terminal portion is required for tooth enamel calcification. *Hum. Mutat.* 29, E95–E99. doi: 10.1002/humu.20789

Lee, S. K., Krebsbach, P. H., Matsuki, Y., Nanci, A., Yamada, K. M., and Yamada, Y. (1996). Ameloblastin expression in rat incisors and human tooth germs. *Int. J. Dev. Biol.* 40, 1141–1150.

Lee, S. K., Lee, K. E., Jeong, T. S., Hwang, Y. H., Kim, S., Hu, J. C., et al. (2011). FAM83H mutations cause ADHCAI and alter intracellular protein localization. *J. Dent. Res.* 90, 377–381. doi: 10.1177/0022034510389177

Lee, S. K., Lee, Z. H., Lee, S. J., Ahn, B. D., Kim, Y. J., Lee, S. H., et al. (2008b). DLX3 mutation in a new family and its phenotypic variations. *J. Dent. Res.* 87, 354–357. doi: 10.1177/154405910808700402

Lee, S. K., Seymen, F., Kang, H. Y., Lee, K. E., Gencay, K., Tuna, B., et al. (2010a). MMP20 hemopexin domain mutation in amelogenesis imperfecta. *J. Dent. Res.* 89, 46–50. doi: 10.1177/0022034509352844

Lee, S. K., Seymen, F., Lee, K. E., Kang, H. Y., Yildirim, M., Tuna, E. B., et al. (2010b). Novel WDR72 mutation and cytoplasmic localization. *J. Dent. Res.* 89, 1378–1382. doi: 10.1177/0022034510382117

Li, L. L., Liu, P. H., Xie, X. H., Ma, S., Liu, C., Chen, L., et al. (2016). Loss of epithelial FAM20A in mice causes amelogenesis imperfecta, tooth eruption delay and gingival overgrowth. *Int. J. Oral Sci.* 8, 98–109. doi: 10.1038/ijos.2016.14

Li, X. F., Kraev, A. S., and Lytton, J. (2002). Molecular cloning of a fourth member of the potassium-dependent sodium-calcium exchanger gene family, NCKX4. *J. Biol. Chem.* 277, 48410–48417. doi: 10.1074/jbc.M210011200

Lichtenstein, J. R., and Warson, R. W. (1971). Syndrome of dental anomalies, curly hair and sclerotic bones. *Birth Defects Orig. Artic. Ser.* 7, 308–311.

Llano, E., Pendas, A. M., Knauper, V., Sorsa, T., Salo, T., Salido, E., et al. (1997). Identification and structural and functional characterization of human enamelysin (MMP-20). *Biochemistry* 36, 15101–15108. doi: 10.1021/bi972120y

Lu, Y., Papagerakis, P., Yamakoshi, Y., Hu, J. C., Bartlett, J. D., and Simmer, J. P. (2008). Functions of KLK4 and MMP-20 in dental enamel formation. *Biol. Chem.* 389, 695–700. doi: 10.1515/BC.2008.080

Ludwig, M. G., Vanek, M., Guerini, D., Gasser, J. A., Jones, C. E., Junker, U., et al. (2003). Proton-sensing G-protein-coupled receptors. *Nature* 425, 93–98. doi: 10.1038/nature01905

MacDougall, M., Simmons, D., Gu, T. T., Forsman-Semb, K., Mardh, C. K., Mesbah, M., et al. (2000). Cloning, characterization and immunolocalization of human ameloblastin. *Eur. J. Oral Sci.* 108, 303–310. doi: 10.1034/j.1600-0722.2000.108004303.x

Marchisio, P. C., Cremona, O., Savoia, P., Pellegrini, G., Ortonne, J. P., Verrando, P., et al. (1993). The basement membrane protein BM-600/nicein codistributes with kalinin and the integrin alpha 6 beta 4 in human cultured keratinocytes. *Exp. Cell Res.* 205, 205–212. doi: 10.1006/excr.1993.1078

Mardh, C. K., Backman, B., Holmgren, G., Hu, J. C., Simmer, J. P., and Forsman-Semb, K. (2002). A nonsense mutation in the enamelin gene causes local hypoplastic autosomal dominant amelogenesis imperfecta (AIH2). *Hum. Mol. Genet.* 11, 1069–1074. doi: 10.1093/hmg/11.9.1069

McGrath, J. A., Gatalica, B., Christiano, A. M., Li, K., Owaribe, K., McMillan, J. R., et al. (1995). Mutations in the 180-kD bullous pemphigoid antigen (BPAG2), a hemidesmosomal transmembrane collagen (COL17A1), in generalized atrophic benign epidermolysis bullosa. *Nat. Genet.* 11, 83–86. doi: 10.1038/ng0995-83

McGrath, J. A., Gatalica, B., Li, K., Dunnill, M. G., McMillan, J. R., Christiano, A. M., et al. (1996). Compound heterozygosity for a dominant glycine substitution and a recessive internal duplication mutation in the type XVII collagen gene results in junctional epidermolysis bullosa and abnormal dentition. *Am. J. Pathol.* 148, 1787–1796.

Mendoza, G., Pemberton, T. J., Lee, K., Scarel-Caminaga, R., Mehrian-Shai, R., Gonzalez-Quevedo, C., et al. (2007). A new locus for autosomal dominant amelogenesis imperfecta on chromosome 8q24.3. *Hum. Genet.* 120, 653–662. doi: 10.1007/s00439-006-0246-6

Moffatt, P., Smith, C. E., St-Arnaud, R., Simmons, D., Wright, J. T., and Nanci, A. (2006). Cloning of rat amelotin and localization of the protein to the basal lamina of maturation stage ameloblasts and junctional epithelium. *Biochem. J.* 399, 37–46. doi: 10.1042/BJ20060662

Moffatt, P., Wazen, R. M., Dos Santos Neves, J., and Nanci, A. (2014). Characterisation of secretory calcium-binding phosphoprotein-proline-glutamine-rich 1: a novel basal lamina component expressed at cell-tooth interfaces. *Cell Tissue Res.* 358, 843–855. doi: 10.1007/s00441-014-1989-3

Mogi, C., Tobo, M., Tomura, H., Murata, N., He, X. D., Sato, K., et al. (2009). Involvement of proton-sensing TDAG8 in extracellular acidification-induced inhibition of proinflammatory cytokine production in peritoneal macrophages. *J. Immunol.* 182, 3243–3251. doi: 10.4049/jimmunol.0803466

Mohazab, L., Koivisto, L., Jiang, G., Kytomaki, L., Haapasalo, M., Owen, G. R., et al. (2013). Critical role for alphavbeta6 integrin in enamel biomineralization. *J. Cell Sci.* 126(Pt 3), 732–744. doi: 10.1242/jcs.112599

Moradian-Oldak, J. (2012). Protein-mediated enamel mineralization. *Front. Biosci.* 17, 1996–2023. doi: 10.2741/4034

Morasso, M. I., Grinberg, A., Robinson, G., Sargent, T. D., and Mahon, K. A. (1999). Placental failure in mice lacking the homeobox gene Dlx3. *Proc. Natl. Acad. Sci. U.S.A.* 96, 162–167. doi: 10.1073/pnas.96.1.162

Munger, J. S., Huang, X., Kawakatsu, H., Griffiths, M. J., Dalton, S. L., Wu, J., et al. (1999). The integrin alpha v beta 6 binds and activates latent TGF beta 1: a mechanism for regulating pulmonary inflammation and fibrosis. *Cell* 96, 319–328. doi: 10.1016/S0092-8674(00)80545-0

Murrell, D. F., Pasmooij, A. M., Pas, H. H., Marr, P., Klingberg, S., Pfendner, E., et al. (2007). Retrospective diagnosis of fatal BP180-deficient non-Herlitz junctional epidermolysis bullosa suggested by immunofluorescence (IF) antigen-mapping of parental carriers bearing enamel defects. *J. Invest. Dermatol.* 127, 1772–1775. doi: 10.1038/sj.jid.5700766

Nagy, E., and Maquat, L. E. (1998). A rule for termination-codon position within intron-containing genes: when nonsense affects RNA abundance. *Trends Biochem. Sci.* 23, 198–199. doi: 10.1016/S0968-0004(98)01208-0

Nakayama, Y., Holcroft, J., and Ganss, B. (2015). Enamel hypomineralization and structural defects in amelotin-deficient mice. *J. Dent. Res.* 94, 697–705. doi: 10.1177/0022034514566214

Nieminen, P., Lukinmaa, P. L., Alapulli, H., Methuen, M., Suojarvi, T., Kivirikko, S., et al. (2011). DLX3 homeodomain mutations cause tricho-dento-osseous syndrome with novel phenotypes. *Cells Tissues Organs* 194, 49–59. doi: 10.1159/000322561

Nievers, M. G., Schaapveld, R. Q., and Sonnenberg, A. (1999). Biology and function of hemidesmosomes. *Matrix Biol.* 18, 5–17. doi: 10.1016/S0945-053X(98)00003-1

Nishie, W., Kiritsi, D., Nystrom, A., Hofmann, S. C., and Bruckner-Tuderman, L. (2011). Dynamic interactions of epidermal collagen XVII with the extracellular matrix: laminin 332 as a major binding partner. *Am. J. Pathol.* 179, 829–837. doi: 10.1016/j.ajpath.2011.04.019

Nunez, S. M., Chun, Y. P., Ganss, B., Hu, Y., Richardson, A. S., Schmitz, J. E., et al. (2015). Maturation stage enamel malformations in Amtn and Klk4 null mice. *Matrix Biol.* 52–54:219–233. doi: 10.1016/j.matbio.2015.11.007

Ohyama, Y., Lin, J. H., Govitvattana, N., Lin, I. P., Venkitapathi, S., Alamoudi, A., et al. (2016). FAM20A binds to and regulates FAM20C localization. *Sci. Rep.* 6:27784. doi: 10.1038/srep27784

O'Sullivan, J., Bitu, C. C., Daly, S. B., Urquhart, J. E., Barron, M. J., Bhaskar, S. S., et al. (2011). Whole-Exome sequencing identifies FAM20A mutations as a cause of amelogenesis imperfecta and gingival hyperplasia syndrome. *Am. J. Hum. Genet.* 88, 616–620. doi: 10.1016/j.ajhg.2011.04.005

Ozdemir, D., Hart, P. S., Firatli, E., Aren, G., Ryu, O. H., and Hart, T. C. (2005a). Phenotype of ENAM mutations is dosage-dependent. *J. Dent. Res.* 84, 1036–1041. doi: 10.1177/154405910508401113

Ozdemir, D., Hart, P. S., Ryu, O. H., Choi, S. J., Ozdemir-Karatas, M., Firatli, E., et al. (2005b). MMP20 active-site mutation in hypomaturation amelogenesis imperfecta. *J. Dent. Res.* 84, 1031–1035. doi: 10.1177/154405910508401112

Papagerakis, P., Lin, H. K., Lee, K. Y., Hu, Y., Simmer, J. P., Bartlett, J. D., et al. (2008). Premature stop codon in MMP20 causing amelogenesis imperfecta. *J. Dent. Res.* 87, 56–59. doi: 10.1177/154405910808700109

Parry, D. A., Brookes, S. J., Logan, C. V., Poulter, J. A., El-Sayed, W., Al-Bahlani, S., et al. (2012). Mutations in C4orf26, encoding a peptide with *in vitro* hydroxyapatite crystal nucleation and growth activity, cause amelogenesis imperfecta. *Am. J. Hum. Genet.* 91, 565–571. doi: 10.1016/j.ajhg.2012.07.020

Parry, D. A., Poulter, J. A., Logan, C. V., Brookes, S. J., Jafri, H., Ferguson, C. H., et al. (2013). Identification of mutations in SLC24A4, encoding a potassium-dependent sodium/calcium exchanger, as a cause of amelogenesis imperfecta. *Am. J. Hum. Genet.* 92, 307–312. doi: 10.1016/j.ajhg.2013.01.003

Parry, D. A., Smith, C. E. L., El-Sayed, W., Poulter, J. A., Shore, R. C., Logan, C. V., et al. (2016). Mutations in the pH Sensing G-protein coupled receptor GPR68 cause Amelogenesis Imperfecta. *Am. J. Hum. Genet.* 99, 984–990. doi: 10.1016/j.ajhg.2016.08.020

Pasmooij, A. M., Pas, H. H., Jansen, G. H., Lemmink, H. H., and Jonkman, M. F. (2007). Localized and generalized forms of blistering in junctional epidermolysis bullosa due to COL17A1 mutations in the Netherlands. *Br. J. Dermatol.* 156, 861–870. doi: 10.1111/j.1365-2133.2006.07730.x

Poulter, J. A., Brookes, S. J., Shore, R. C., Smith, C. E. L., Abi Farraj, L., Kirkham, J., et al. (2014a). A missense mutation in ITGB6 causes pitted hypomineralized amelogenesis imperfecta. *Hum. Mol. Genet.* 23, 2189–2197. doi: 10.1093/hmg/ddt616

Poulter, J. A., El-Sayed, W., Shore, R. C., Kirkham, J., Inglehearn, C. F., and Mighell, A. J. (2014b). Whole-exome sequencing, without prior linkage, identifies a mutation in LAMB3 as a cause of dominant hypoplastic amelogenesis imperfecta. *Eur. J. Hum. Genet.* 22, 132–135. doi: 10.1038/ejhg.2013.76

Poulter, J. A., Murillo, G., Brookes, S. J., Smith, C. E. L., Parry, D. A., Silva, S., et al. (2014c). Deletion of ameloblastin exon 6 is associated with amelogenesis imperfecta. *Hum. Mol. Genet.* 23, 5317–5324. doi: 10.1093/hmg/ddu247

Poulter, J. A., Smith, C. E. L., Murrillo, G., Silva, S., Feather, S., Howell, M., et al. (2015). A distinctive oral phenotype points to FAM20A mutations not identified by Sanger sequencing. *Mol. Genet. Genomic Med.* 3, 543–549. doi: 10.1002/mgg3.164

Prajapati, S., Tao, J., Ruan, Q., De Yoreo, J. J., and Moradian-Oldak, J. (2016). Matrix metalloproteinase-20 mediates dental enamel biomineralization by preventing protein occlusion inside apatite crystals. *Biomaterials* 75, 260–270. doi: 10.1016/j.biomaterials.2015.10.031

Prasad, M. K., Geoffroy, V., Vicaire, S., Jost, B., Dumas, M., Le Gras, S., et al. (2016a). A targeted next-generation sequencing assay for the molecular diagnosis of genetic disorders with orodental involvement. *J. Med. Genet.* 53, 98–110. doi: 10.1136/jmedgenet-2015-103302

Prasad, M. K., Laouina, S., El Alloussi, M., Dollfus, H., and Bloch-Zupan, A. (2016b). Amelogenesis Imperfecta: 1 Family, 2 Phenotypes, and 2 mutated genes. *J. Dent. Res.* 95, 1457–1463. doi: 10.1177/0022034516663200

Price, J. A., Wright, J. T., Kula, K., Bowden, D. W., and Hart, T. C. (1998). A common DLX3 gene mutation is responsible for tricho-dento-osseous syndrome in Virginia and North Carolina families. *J. Med. Genet.* 35, 825–828. doi: 10.1136/jmg.35.10.825

Pulkkinen, L., Christiano, A. M., Airenne, T., Haakana, H., Tryggvason, K., and Uitto, J. (1994a). Mutations in the gamma 2 chain gene (LAMC2) of kalinin/laminin 5 in the junctional forms of epidermolysis bullosa. *Nat. Genet.* 6, 293–297. doi: 10.1038/ng0394-293

Pulkkinen, L., Christiano, A. M., Gerecke, D., Wagman, D. W., Burgeson, R. E., Pittelkow, M. R., et al. (1994b). A homozygous nonsense mutation in the beta 3 chain gene of laminin 5 (LAMB3) in Herlitz junctional epidermolysis bullosa. *Genomics* 24, 357–360. doi: 10.1006/geno.1994.1627

Rajpar, M. H., Harley, K., Laing, C., Davies, R. M., and Dixon, M. J. (2001). Mutation of the gene encoding the enamel-specific protein, enamelin, causes autosomal-dominant amelogenesis imperfecta. *Hum. Mol. Genet.* 10, 1673–1677. doi: 10.1093/hmg/10.16.1673

Reith, E. J. (1970). The stages of amelogenesis as observed in molar teeth of young rats. *J. Ultrastruct. Res.* 30, 111–151. doi: 10.1016/S0022-5320(70)90068-7

Robinson, C., Kirkham, J., Brookes, S. J., Bonass, W. A., and Shore, R. C. (1995). The chemistry of enamel development. *Int. J. Dev. Biol.* 39, 145–152.

Robinson, C. (2014). Enamel maturation: a brief background with implications for some enamel dysplasias. *Front. Physiol.* 5:388. doi: 10.3389/fphys.2014.00388

Romas, N. A., Rose, N. R., and Tannenbaum, M. (1979). Acid phosphatase: new developments. *Hum. Pathol.* 10, 501–512. doi: 10.1016/S0046-8177(79)80094-5

Ruzzi, L., Gagnoux-Palacios, L., Pinola, M., Belli, S., Meneguzzi, G., D'Alessio, M., et al. (1997). A homozygous mutation in the integrin alpha6 gene in junctional epidermolysis bullosa with pyloric atresia. *J. Clin. Invest.* 99, 2826–2831. doi: 10.1172/JCI119474

Ryan, M. C., Lee, K., Miyashita, Y., and Carter, W. G. (1999). Targeted disruption of the LAMA3 gene in mice reveals abnormalities in survival and late stage differentiation of epithelial cells. *J. Cell Biol.* 145, 1309–1323. doi: 10.1083/jcb.145.6.1309

Salanitri, S., and Seow, W. K. (2013). Developmental enamel defects in the primary dentition: aetiology and clinical management. *Aust. Dent. J.* 58, 133–140; quiz 266. doi: 10.1111/adj.12039

Salido, E. C., Yen, P. H., Koprivnikar, K., Yu, L. C., and Shapiro, L. J. (1992). The human enamel protein gene amelogenin is expressed from both the X and the Y chromosomes. *Am. J. Hum. Genet.* 50, 303–316.

Seymen, F., Kim, Y. J., Lee, Y. J., Kang, J., Kim, T.-H., Choi, H., et al. (2016). Recessive mutations in testicular acid phosphatase (ACPT) cause hypoplastic amelogenesis imperfecta. *Am. J. Hum. Genet.* 99, 1199–1205. doi: 10.1016/j.ajhg.2016.09.018

Seymen, F., Lee, K. E., Tran Le, C. G., Yildirim, M., Gencay, K., Lee, Z. H., et al. (2014). Exonal deletion of SLC24A4 causes hypomaturation amelogenesis imperfecta. *J. Dent. Res.* 93, 366–370. doi: 10.1177/0022034514523786

Seymen, F., Park, J. C., Lee, K. E., Lee, H. K., Lee, D. S., Koruyucu, M., et al. (2015). Novel MMP20 and KLK4 Mutations in Amelogenesis Imperfecta. *J. Dent. Res.* 94, 1063–1069. doi: 10.1177/0022034515590569

Simmer, J. P., and Hu, J. C. (2002). Expression, structure, and function of enamel proteinases. *Connect. Tissue Res.* 43, 441–449. doi: 10.1080/03008200290001159

Simmer, J. P., Hu, Y., Lertlam, R., Yamakoshi, Y., and Hu, J. C. (2009). Hypomaturation enamel defects in Klk4 knockout/LacZ knockin mice. *J. Biol. Chem.* 284, 19110–19121. doi: 10.1074/jbc.M109.013623

Sire, J. Y., Davit-Beal, T., Delgado, S., and Gu, X. (2007). The origin and evolution of enamel mineralization genes. *Cells Tissues Organs* 186, 25–48. doi: 10.1159/000102679

Skobe, Z. (1976). The secretory stage of amelogenesis in rat mandibular incisor teeth observed by scanning electron microscopy. *Calcif. Tissue Res.* 21, 83–103. doi: 10.1007/BF02547385

Smith, C. E. (1998). Cellular and chemical events during enamel maturation. *Crit. Rev. Oral Biol. Med.* 9, 128–161. doi: 10.1177/10454411980090020101

Smith, C. E., and Warshawsky, H. (1977). Quantitative analysis of cell turnover in the enamel organ of the rat incisor. Evidence for ameloblast death immediately after enamel matrix secretion. *Anat. Rec.* 187, 63–98. doi: 10.1002/ar.1091870106

Smith, C. E. L., Kirkham, J., Day, P. F., McDerra, E. J., Poulter, J. A., Inglehearn, C. F., et al. (2017a). A fourth KLK4 mutation is associated with enamel hypomineralisation and structural abnormalities. *Front. Physiol.* 8, 1–11. doi: 10.3389/fphys.2017.00333

Smith, C. E. L., Murillo, G., Brookes, S. J., Poulter, J. A., Silva, S., Kirkham, J., et al. (2016). Deletion of amelotin exons 3-6 is associated with amelogenesis imperfecta. *Hum. Mol. Genet.* 25, 3578–3587. doi: 10.1093/hmg/ddw203

Smith, C. E. L., Whitehouse, L. L. E., Poulter, J. A., Brookes, S. J., Day, P. F., Soldani, F., et al. (2017b). Defects in the acid phosphatase ACPT cause recessive hypoplastic amelogenesis imperfecta. *Eur. J. Hum. Genet.* doi: 10.1038/ejhg.2017.79. [Epub ahead of print].

Spahr, A., Lyngstadaas, S. P., Slaby, I., and Pezeshki, G. (2006). Ameloblastin expression during craniofacial bone formation in rats. *Eur. J. Oral Sci.* 114, 504–511. doi: 10.1111/j.1600-0722.2006.00403.x

Stephan, A. B., Tobochnik, S., Dibattista, M., Wall, C. M., Reisert, J., and Zhao, H. (2012). The Na^+/Ca^{2+}) exchanger NCKX4 governs termination and adaptation of the mammalian olfactory response. *Nat. Neurosci.* 15, 131–137. doi: 10.1038/nn.2943

Tagliabracci, V. S., Engel, J. L., Wen, J., Wiley, S. E., Worby, C. A., Kinch, L. N., et al. (2012). Secreted kinase phosphorylates extracellular proteins that regulate biomineralization. *Science* 336, 1150–1153. doi: 10.1126/science.1217817

Termine, J. D., Belcourt, A. B., Christner, P. J., Conn, K. M., and Nylen, M. U. (1980). Properties of dissociatively extracted fetal tooth matrix proteins. I. Principal molecular species in developing bovine enamel. *J. Biol. Chem.* 255, 9760–9768.

Valeyev, N. V., Downing, A. K., Sondek, J., and Deane, C. (2008). Electrostatic and functional analysis of the seven-bladed WD beta-propellers. *Evol. Bioinform.* 4, 203–216.

Van den Bergh, F., Eliason, S. L., and Giudice, G. J. (2011). Type XVII collagen (BP180) can function as a cell-matrix adhesion molecule via binding to laminin 332. *Matrix Biol.* 30, 100–108. doi: 10.1016/j.matbio.2010.10.005

VanSaun, M. N., and Matrisian, L. M. (2006). Matrix metalloproteinases and cellular motility in development and disease. *Birth Defects Res. C Embryo Today* 78, 69–79. doi: 10.1002/bdrc.20061

Vidal, F., Aberdam, D., Miquel, C., Christiano, A. M., Pulkkinen, L., Uitto, J., et al. (1995). Integrin beta 4 mutations associated with junctional epidermolysis bullosa with pyloric atresia. *Nat. Genet.* 10, 229–234. doi: 10.1038/ng0695-229

Vogel, P., Hansen, G. M., Read, R. W., Vance, R. B., Thiel, M., Liu, J., et al. (2012). Amelogenesis imperfecta and other biomineralization defects in Fam20a and Fam20c null mice. *Vet. Pathol.* 49, 998–1017. doi: 10.1177/0300985812453177

Wang, S., Choi, M., Richardson, A. S., Reid, B. M., Seymen, F., Yildirim, M., et al. (2014a). STIM1 and SLC24A4 Are critical for enamel maturation. *J. Dent. Res.* 93(Suppl. 7), 94S–100S doi: 10.1177/0022034514527971

Wang, S. K., Aref, P., Hu, Y., Milkovich, R. N., Simmer, J. P., El-Khateeb, M., et al. (2013a). FAM20A mutations can cause enamel-renal syndrome (ERS). *PLoS Genet.* 9:e1003302. doi: 10.1371/journal.pgen.1003302

Wang, S. K., Choi, M., Richardson, A. S., Reid, B. M., Lin, B. P., Wang, S. J., et al. (2014b). ITGB6 loss-of-function mutations cause autosomal recessive amelogenesis imperfecta. *Hum. Mol. Genet.* 23, 2157–2163. doi: 10.1093/hmg/ddt611

Wang, S. K., Hu, Y., Simmer, J. P., Seymen, F., Estrella, N. M., Pal, S., et al. (2013b). Novel KLK4 and MMP20 mutations discovered by whole-exome sequencing. *J. Dent. Res.* 92, 266–271. doi: 10.1177/0022034513475626

Wang, S. K., Hu, Y., Yang, J., Smith, C. E., Nunez, S. M., Richardson, A. S., et al. (2015). Critical roles for WDR72 in calcium transport and matrix protein removal during enamel maturation. *Mol. Genet. Genomic Med.* 3, 302–319. doi: 10.1002/mgg3.143

Wang, S. K., Reid, B. M., Dugan, S. L., Roggenbuck, J. A., Read, L., Aref, P., et al. (2014c). FAM20A mutations associated with enamel renal syndrome. *J. Dent. Res.* 93, 42–48. doi: 10.1177/0022034513512653

Warshawsky, H., and Smith, C. E. (1974). Morphological classification of rat incisor ameloblasts. *Anat. Rec.* 179, 423–446. doi: 10.1002/ar.1091790403

Weinacker, A., Chen, A., Agrez, M., Cone, R. I., Nishimura, S., Wayner, E., et al. (1994). Role of the integrin alpha v beta 6 in cell attachment to fibronectin. Heterologous expression of intact and secreted forms of the receptor. *J. Biol. Chem.* 269, 6940–6948.

Witkop, C. J., and Sauk, J. J. (1976). *Heritable Defects of Enamel*. St. Louis, MO: CV Mosby Company.

Wright, J. T., Frazier-Bowers, S., Simmons, D., Alexander, K., Crawford, P., Han, S. T., et al. (2009). Phenotypic variation in FAM83H-associated amelogenesis imperfecta. *J. Dent. Res.* 88, 356–360. doi: 10.1177/0022034509333822

Wright, J. T., Johnson, L. B., and Fine, J. D. (1993). Development defects of enamel in humans with hereditary epidermolysis bullosa. *Arch. Oral Biol.* 38, 945–955. doi: 10.1016/0003-9969(93)90107-W

Wright, J. T., Torain, M., Long, K., Seow, K., Crawford, P., Aldred, M. J., et al. (2011). Amelogenesis imperfecta: genotype-phenotype studies in 71 families. *Cells Tissues Organs* 194, 279–283. doi: 10.1159/000324339

Xiong, J. P., Stehle, T., Diefenbach, B., Zhang, R., Dunker, R., Scott, D. L., et al. (2001). Crystal structure of the extracellular segment of integrin alpha Vbeta3. *Science* 294, 339–345. doi: 10.1126/science.1064535

Xiong, J. P., Stehle, T., Zhang, R., Joachimiak, A., Frech, M., Goodman, S. L., et al. (2002). Crystal structure of the extracellular segment of integrin alpha Vbeta3 in complex with an Arg-Gly-Asp ligand. *Science* 296, 151–155. doi: 10.1126/science.1069040

Yamakoshi, Y., Simmer, J. P., Bartlett, J. D., Karakida, T., and Oida, S. (2013). MMP20 and KLK4 activation and inactivation interactions *in vitro*. *Arch. Oral Biol.* 58, 1569–1577. doi: 10.1016/j.archoralbio.2013.08.005

Yamakoshi, Y., Tanabe, T., Oida, S., Hu, C. C., Simmer, J. P., and Fukae, M. (2001). Calcium binding of enamel proteins and their derivatives with emphasis on the calcium-binding domain of porcine sheathlin. *Arch. Oral Biol.* 46, 1005–1014. doi: 10.1016/S0003-9969(01)00070-X

Yang, M., Mailhot, G., Birnbaum, M. J., MacKay, C. A., Mason-Savas, A., and Odgren, P. R. (2006). Expression of and role for ovarian cancer G-protein-coupled receptor 1 (OGR1) during osteoclastogenesis. *J. Biol. Chem.* 281, 23598–23605. doi: 10.1074/jbc.M602191200

Yang, X., Yan, W., Tian, Y., Ma, P., Opperman, L. A., and Wang, X. (2016). Family with sequence similarity member 20C is the primary but not the only kinase for the small-integrin-binding ligand N-linked glycoproteins in bone. *FASEB J.* 30, 121–128. doi: 10.1096/fj.15-273607

Yoshiba, N., Yoshiba, K., Aberdam, D., Meneguzzi, G., Perrin-Schmitt, F., Stoetzel, C., et al. (1998). Expression and localization of laminin-5 subunits in the mouse incisor. *Cell Tissue Res.* 292, 143–149. doi: 10.1007/s004410051044

Yousef, G. M., Diamandis, M., Jung, K., and Diamandis, E. P. (2001). Molecular cloning of a novel human acid phosphatase gene (ACPT) that is highly expressed in the testis. *Genomics* 74, 385–395. doi: 10.1006/geno.2001.6556

Yuen, W. Y., Pasmooij, A. M., Stellingsma, C., and Jonkman, M. F. (2012). Enamel defects in carriers of a novel LAMA3 mutation underlying epidermolysis bullosa. *Acta Derm. Venereol.* 92, 695–696. doi: 10.2340/00015555-1341

Zhang, C., Song, Y., and Bian, Z. (2015a). Ultrastructural analysis of the teeth affected by amelogenesis imperfecta resulting from FAM83H mutations and review of the literature. *Oral Surg. Oral Med. Oral Pathol. Oral Radiol.* 119, e69–e76. doi: 10.1016/j.oooo.2014.09.002

Zhang, X., Diekwisch, T. G., and Luan, X. (2011). Structure and function of ameloblastin as an extracellular matrix protein: adhesion, calcium binding, and CD63 interaction in human and mouse. *Eur. J. Oral Sci.* 119(Suppl. 1), 270–279. doi: 10.1111/j.1600-0722.2011.00889.x

Zhang, Z., Tian, H., Lv, P., Wang, W., Jia, Z., Wang, S., et al. (2015b). Transcriptional factor DLX3 promotes the gene expression of enamel matrix proteins during amelogenesis. *PLoS ONE* 10:e0121288. doi: 10.1371/journal.pone.0121288

Conflict of Interest Statement: The authors declare that the research was conducted in the absence of any commercial or financial relationships that could be construed as a potential conflict of interest.

Copyright © 2017 Smith, Poulter, Antanaviciute, Kirkham, Brookes, Inglehearn and Mighell. This is an open-access article distributed under the terms of the Creative Commons Attribution License (CC BY). The use, distribution or reproduction in other forums is permitted, provided the original author(s) or licensor are credited and that the original publication in this journal is cited, in accordance with accepted academic practice. No use, distribution or reproduction is permitted which does not comply with these terms.

frontiers in Physiology

ORIGINAL RESEARCH
published: 29 May 2017
doi: 10.3389/fphys.2017.00333

A Fourth *KLK4* Mutation Is Associated with Enamel Hypomineralisation and Structural Abnormalities

Claire E. L. Smith[1,2]*, *Jennifer Kirkham*[1], *Peter F. Day*[3,4], *Francesca Soldani*[4], *Esther J. McDerra*[3,5], *James A. Poulter*[2], *Christopher F. Inglehearn*[2], *Alan J. Mighell*[2,3] and *Steven J. Brookes*[1]

[1] Department of Oral Biology, School of Dentistry, St James's University Hospital, University of Leeds, Leeds, United Kingdom, [2] Section of Ophthalmology and Neuroscience, St James's University Hospital, University of Leeds, Leeds, United Kingdom, [3] School of Dentistry, University of Leeds, Leeds, United Kingdom, [4] Bradford District Care NHS Foundation Trust, Community Dental Service, Horton Park Health Centre, Bradford, United Kingdom, [5] Locala Dental Care, Dental Department, Batley Health Centre, Batley, United Kingdom

"Amelogenesis imperfecta" (AI) describes a group of genetic conditions that result in defects in tooth enamel formation. Mutations in many genes are known to cause AI, including the gene encoding the serine protease, kallikrein related peptidase 4 (*KLK4*), expressed during the maturation stage of amelogenesis. In this study we report the fourth *KLK4* mutation to be identified in autosomal recessively-inherited hypomaturation type AI, c.632delT, p.(L211Rfs*37) (NM_004917.4, NP_004908.4). This homozygous variant was identified in five Pakistani AI families and is predicted to result in a transcript with a premature stop codon that escapes nonsense mediated decay. However, the protein may misfold, as three of six disulphide bonds would be disrupted, and may be degraded or non-functional as a result. Primary teeth were obtained from one affected individual. The enamel phenotype was characterized using high-resolution computerized X-ray tomography (CT), scanning electron microscopy (SEM), energy dispersive X-ray spectroscopy (EDX), and microhardness testing (MH). Enamel from the affected individual (referred to as KLK4 enamel) was hypomineralised in comparison with matched control enamel. Furthermore, KLK4 inner enamel was hypomineralised compared with KLK4 outer enamel. SEM showed a clear structural demarcation between KLK4 inner and outer enamel, although enamel structure was similar to control tissue overall. EDX showed that KLK4 inner enamel contained less calcium and phosphorus and more nitrogen than control inner enamel and KLK4 outer enamel. MH testing showed that KLK4 inner enamel was significantly softer than KLK4 outer enamel ($p < 0.001$). However, the hardness of control inner enamel was not significantly different to that of control outer enamel. Overall, these findings suggest that the *KLK4* c.632delT mutation may be a common cause of autosomal recessive AI in the Pakistani population. The phenotype data obtained mirror findings in the *Klk4*$^{-/-}$ mouse and suggest that KLK4 is required for the hardening and mineralization of the inner enamel layer but is less essential for hardening and mineralization of the outer enamel layer.

Keywords: KLK4, enamel, phenotype, mutation, amelogenesis imperfecta

OPEN ACCESS

Edited by:
Agnes Bloch-Zupan, University of Strasbourg, France

Reviewed by:
Karina Carneiro, University of Toronto, Canada
Petros Papagerakis, University of Michigan, United States

***Correspondence:**
Claire E. L. Smith
c.e.l.smith@leeds.ac.uk

Specialty section:
This article was submitted to Craniofacial Biology and Dental Research, a section of the journal Frontiers in Physiology

Received: *20 March 2017*
Accepted: *08 May 2017*
Published: *29 May 2017*

Citation:
Smith CEL, Kirkham J, Day PF, Soldani F, McDerra EJ, Poulter JA, Inglehearn CF, Mighell AJ and Brookes SJ (2017) A Fourth KLK4 Mutation Is Associated with Enamel Hypomineralisation and Structural Abnormalities. Front. Physiol. 8:333. doi: 10.3389/fphys.2017.00333

INTRODUCTION

Formation of the complex structure of tooth enamel is remarkable. Enamel is both extremely hard and very dense. These properties enable tooth enamel to withstand the large forces experienced during mastication and make it the hardest tissue in the human body.

Amelogenesis, the process of enamel formation, can be broadly subdivided into three stages: secretion, transition and maturation. During secretion, an extracellular matrix (ECM) of enamel proteins, including amelogenin (AMELX as well as AMELY for males), enamelin (ENAM), and ameloblastin (AMBN), is secreted by the enamel secreting cells, the ameloblasts. Except for initial and final layers of enamel secreted, the bulk of the enamel is secreted via an apical cellular extension on each ameloblast, termed the Tomes' process. During secretion, the ameloblasts retreat away from the forming dentine to produce a layer of enamel matrix containing immature enamel crystals that span the full thickness of the future enamel that are organized into rod and inter rod enamel (Skobe, 1976). Following their secretion, enamel proteins are specifically cleaved by the secretory stage proteinase, matrix metallopeptidase 20 (MMP20), to produce peptides with seemingly specific roles in enamel formation (Simmer and Hu, 2002). During the transition stage, the ameloblasts reduce secretion of enamel proteins and MMP20, lose their Tomes' processes and undergo phenotypic remodeling, reflecting their reduced rate of secretion (Reith, 1970). At this stage, the ameloblasts also begin to secrete the enamel serine protease, kallikrein related peptidase 4 (KLK4), which reaches maximal secretion during the maturation stage (Hu et al., 2000, 2002). The maturation stage involves the complete breakdown of the enamel protein matrix and its removal, concurrent with secondary mineralization of the enamel ECM. KLK4 acts to degrade the remaining enamel matrix peptides to facilitate their removal by endocytosis. The removal of matrix protein from the forming enamel and its replacement with tissue fluid provides space for the enamel crystals to grow in width. At the same time, mineral ions are pumped into the enamel to support mineral growth. Once formed, enamel is around 96% mineral by weight, 3% protein, and 1% water (Deakins and Burt, 1944).

Perturbed amelogenesis can result in amelogenesis imperfecta (AI), a collection of genetic conditions resulting in defective tooth enamel. AI has been broadly classified into hypoplastic and hypomineralised types (Gadhia et al., 2012). Hypoplastic AI results from failure during the secretory stage and is characterized by thin enamel that is variably mineralized. Hypomineralised AI can be further subdivided into hypocalcified and hypomaturation sub-types, where the enamel is soft and brittle, respectively. AI can show autosomal dominant, recessive or X-linked inheritance and is associated with mutations in a number of genes. These include, but are not limited to, genes encoding the enamel proteins, AMELX (Lagerstrom et al., 1991), ENAM (Rajpar et al., 2001), and AMBN (Poulter et al., 2014) as well as the secretory stage metalloproteinase, MMP20 (Kim et al., 2005) and the maturation stage serine proteinase, KLK4 (Hart et al., 2004).

Mutations in *KLK4* have been shown to result in recessively-inherited hypomaturation AI (MIM #204700) (Hart et al., 2004). To date, only three *KLK4* mutations have been reported in a total of four families (Hart et al., 2004; Wright et al., 2011; Wang et al., 2013; Seymen et al., 2015), suggesting that *KLK4* mutations are a relatively rare cause of AI. Mutations described to date include a frameshift and a nonsense mutation for which the resulting transcript is likely to be subject to nonsense mediated decay (NMD). The most recently reported mutation was a frameshift in the final exon, predicted to escape NMD. However, *in vitro* expression showed that a lower level of protein was produced with a lower level of enzymatic activity compared to controls. The human enamel phenotype resulting from *klk4* mutations remains uncharacterized outside of the mouth, but a *Klk4* knockout mouse model ($Klk4^{-/-}$) has been extensively characterized (Simmer et al., 2009, 2011; Smith et al., 2011; Yamakoshi et al., 2011; Nunez et al., 2016). The enamel was reported to be of a similar thickness and decussating structure to wild-type (WT) controls but was hypomineralised (Simmer et al., 2009), at levels of around 80 % compared with WT enamel (Smith et al., 2011). The defect was shown to be more severe in the inner enamel layer [toward the dentino-enamel junction (DEJ)] compared with the outer enamel (toward the surface) in these animals, suggesting that KLK4 is needed more for the mineralization of inner enamel than outer enamel (Smith et al., 2011). Microhardness values also mirrored these findings, with softer enamel overall for $Klk4^{-/-}$ mice compared with WT, but increasingly soft enamel from the surface to the DEJ (Nunez et al., 2016).

Here we report the fourth *KLK4* mutation, identified in five UK families of Pakistani origin, and characterize the phenotype of the enamel of teeth from one individual.

MATERIALS AND METHODS

Patients

Individuals from each of the five families were recruited following informed consent in accordance with the principles outlined in the declaration of Helsinki and with local ethical approval. Genomic DNA was obtained from saliva using Oragene® DNA Sample Collection kits (DNA Genotek, ONT, Canada) according to the manufacturer's instructions. Deciduous teeth were obtained following natural exfoliation.

Genotyping

Whole-Exome Sequencing and Analysis

Genomic DNA from a single individual from families 1, 2, 3, and 5 (marked with an arrow on each pedigree, **Figure 1**) was subjected to whole exome sequencing (WES). Three micrograms (families 1, 2, and 3) or 200 nanograms (family 5) of genomic DNA were processed using the Agilent SureSelect XT Library Prep according to the manufacturer's protocol (Agilent Technologies, CA, USA). Sequencing was performed on an Illumina HiSeq 2500 using a 100 bp paired-end protocol (families 1, 2, and 3) or an Illumina HiSeq 3000 using a 150 bp paired-end protocol (family 5). The fastq files were aligned to the human reference genome (GRCh37) using the Burrows Wheeler aligner (Li and Durbin, 2009). The resulting alignment was processed in the SAM/BAM format using the SAMtools, Picard

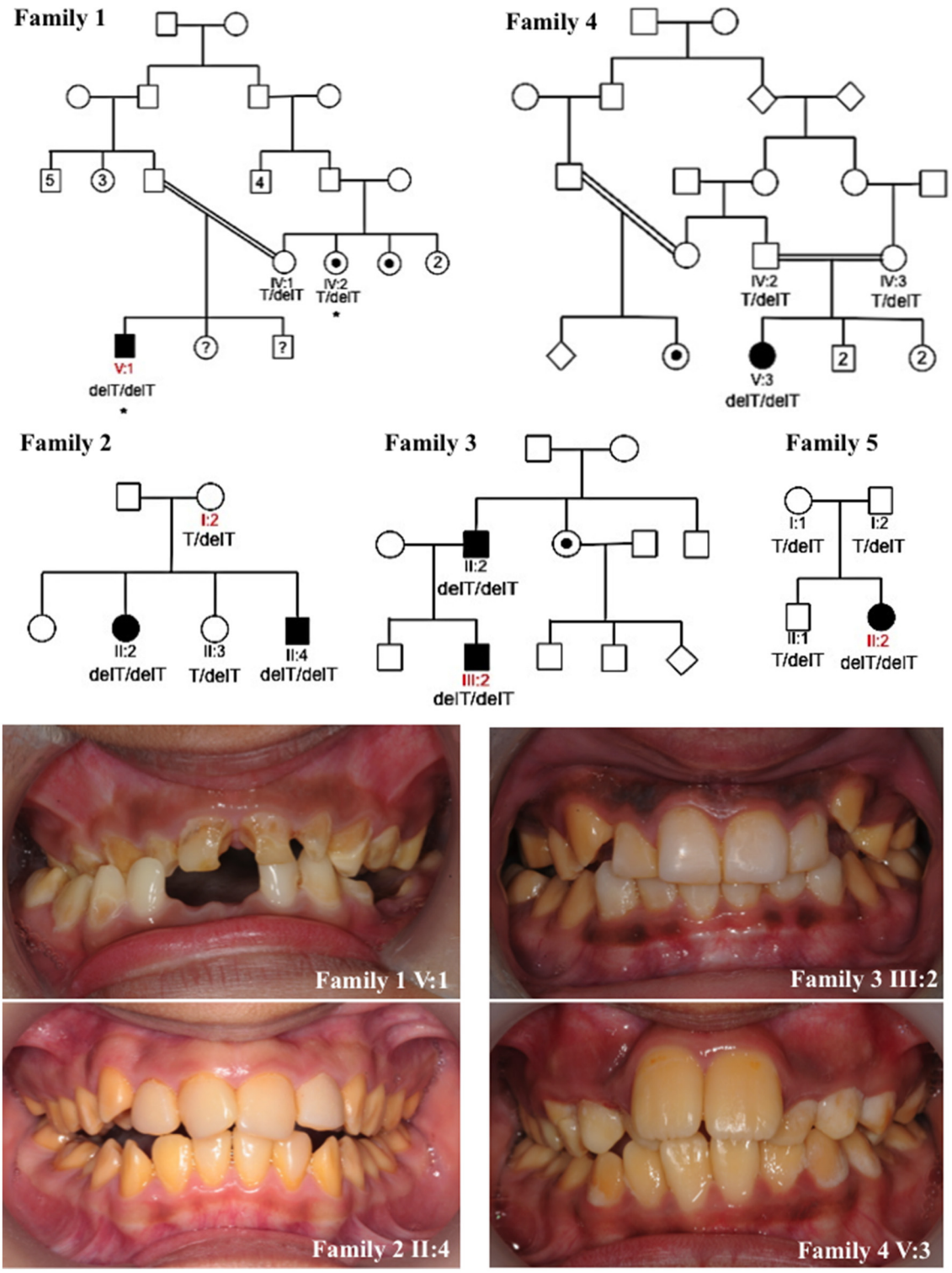

FIGURE 1 | Pedigrees and clinical images of families 1–5. Red labels indicate the individuals for which DNA was subjected to whole exome sequencing for families 1–3 and 5. Asterisks mark individuals in family 1 whose DNA underwent SNP genotyping analysis. Dots indicate individuals that self-reported as affected with AI or were reported by other family members to be affected with AI. However these individuals were not themselves clinically assessed by a dental practitioner. Question marks indicate individuals for which details of their AI phenotype were unavailable. The genotypes of the *KLK4* c.632delT variant (NM_004917.4) for each individual for which DNA was available for analysis are marked on each pedigree. Clinical images show hypomaturation AI in families 1–4. Clinical images were unavailable for family 5.

(http://picard.sourceforge.net) and the Genome Analysis Toolkit (GATK) in order to correct alignments around indel sites and mark potential PCR duplicates (McKenna et al., 2010; DePristo et al., 2011).

Indel and single-nucleotide variants were called in the VCF format using the Haplotype Caller function of the GATK program. Using the VCFhacks package (freely available at https://github.com/gantzgraf/vcfhacks) variants present in NCBI's dbSNP142 or the Exome Aggregation Consortium database (ExAC; v0.3.1) with a minor allele frequency (MAF) $\geq$1% were excluded. The remaining variants were annotated using NCBI's Variant Effect Preditor. Variants with a Combined Annotation Dependent Depletion (CADD) score of $\geq$15 were prioritized and variants in genes already known to cause AI were highlighted for segregation analysis.

PCR and Sanger Sequencing

Variants identified by WES were confirmed and segregation performed for all available members of each family. For family 4, variants were identified and segregation performed for all available family members by direct Sanger sequencing of the *KLK4* gene. Primer sequences can be found in Supplementary Table 1. Sanger sequencing was performed using the BigDye Terminator v3.1 kit (Life Technologies, CA, USA) according to manufacturer's instructions and resolved on an ABI3130xl sequencer (Life Technologies, CA, USA). Results were analyzed using SeqScape v2.5 (Life Technologies, CA, USA).

SNP Genotyping

DNA from two affected individuals, IV:2 and V:1 was genotyped using Affymetrix 6.0 SNP microarrays by AROS Applied Biotechnology (Aarhus, Denmark). The resulting birdseed files were annotated and analyzed using SnpViewer (freely available at https://github.com/gantzgraf/snpviewer) to identify shared regions of homozygosity between both the affected individuals.

Microsatellite Analysis

Standard primers for markers D11S217, D11S902, D11S246, D11S907, D11S1553, D11S397, and D11S601 were used to assess the flanking haplotypes of the *KLK4* gene for families 1–4 (Supplementary Table 2). Products were sized using GeneScan 500 ROX (Life Technologies, CA, USA) according to the manufacturer's instructions and resolved on an ABI3130xl sequencer (Life Technologies, CA, USA). Results were analyzed using Genemapper v4.0 (Life Technologies, CA, USA).

Enamel Phenotyping

Computerized X-ray Tomography

Teeth were analyzed by high resolution X-ray microCT using a Skyscan 1172 (Bruker, Coventry, UK) operated at 100 kV with a source current of 100 μA and an aluminum/copper filter to reduce beam hardening. CT slices were reconstructed using Skyscan Recon software (Bruker). The CT images were calibrated using a two point standard of hydroxyapatite mineral of known densities [0.25 and 0.75 g/cm^3 (Bruker)]. Matched control teeth were obtained from the Skeletal Tissues Research Tissue Bank (School of Dentistry, University of Leeds; NRES REC ref: 07/H1306/95+5). These were obtained with written consent from patients attending clinics at Leeds Dental Hospital, and analyzed during the same scan as their test counterpart. Tooth slices of 500 μm, prepared from both control and KLK4 teeth, were also scanned to ensure that whole tooth results were representative.

Calibrated color contour maps of mineral density were generated using ImageJ and the 3D interactive surface plot plugin. Videos were created using CTVox software (Bruker).

Tooth Sectioning

Control and KLK4 teeth were sectioned in similar planes using an Accutom-5 cutter (Struers, Ballerup, Denmark) fitted with a peripheral diamond cutting disc and cooled with minimal water.

Scanning Electron Microscopy

After sectioning, the cut edge of the tooth was polished using 600 and 2000 grade carborundum paper (3M, Maplewood, MN, USA), followed by a nail buffer. Sections were etched by immersion in 30 % phosphoric acid, followed by thorough rinsing in excess distilled water and dried overnight under vacuum. Sections were mounted on aluminum stubs and sputter coated with gold using an auto sputter coater (Agar Scientific, Elektron Technology, Stansted, UK). Microstructural analysis was undertaken using a Hitachi S-3400N scanning electron microscope (Hitachi, Tokyo, Japan), fitted with a 123 eV Nano XFlash® Detector 5010 (Bruker) and operated at an accelerating voltage of 20 kV using secondary electron detection.

Microhardness Testing

Microhardness measurements were carried out on incisor and molar teeth halves. Sections were immobilized on glass slides (cut side up) using superglue adhesive (Loctite, Düsseldorf, Germany). Sections were polished plano-parallel with 1000 grade then 2000 grade carborundum paper (3M, Maplewood, MN, USA) and then finely polished with 5 μm aluminum oxide suspension (Struers). Tooth surfaces were thoroughly cleaned with a cotton bud to remove polishing debris prior to indentation. The buccal enamel was examined for both incisors and molars. Microhardness measurements were carried out using a Duramin Microhardness Tester (Struers) using Duramin 5 software. The indentations were made using a Knoop diamond under a 100 g load for 15 s. A minimum of 10 indentations spaced at least 50 μm apart were made for each tooth region. Enamel 50–70 μm from the tooth surface or enamel 50–70 μm from the DEJ was examined for both control and KLK4 teeth. In addition, enamel from a region between these measurements was also examined in KLK4 teeth in order to compare with readings closer to the DEJ. The length of each indent was measured by image analysis and the microhardness reading was automatically calculated by the Duramin 5 software. Statistical testing used unpaired 2-tailed *T*-tests to compare results between regions within the same tooth. No tests were conducted to compare microhardness values between different teeth due to the small sample size.

Energy-Dispersive X-Ray Spectroscopy

Energy- dispersive X-ray spectroscopy (EDX) elemental analysis was performed on selected regions of the enamel of control and KLK4 teeth using a detector fitted with an ultrathin window using Bruker Quantax Espirit software version 1.9.4 (Bruker). A minimum of five measurements were obtained for each specified enamel region. The mean composition of each enamel region was then calculated using atomic mass percentage measurements.

RESULTS

Clinical Presentation and Genotyping

We identified five families living in the UK but originating from Pakistan, presenting with autosomal recessive AI in the absence of any clinically-obvious co-segregating disease. Each of the families exhibited a similar hypomaturation AI phenotype (**Figure 1**). None of the families were known to be related. A total of 16 individuals from the five families were recruited to the study for genotyping. WES was carried out using DNA from one individual from families 1, 2, 3 and 5. Depth of coverage indicated that mean coverage was 54.5, 57.7, 80.8 and 59.7 × for individuals from families 1, 2, 3, and 5 respectively (Supplementary Table 3). For families 1, 2, 3, and 5, an identical homozygous frameshift mutation in *KLK4*, c.632delT, p.(L211Rfs*37) (NM_004917.4), was identified in affected individuals after filtering of WES data. The mutation was confirmed by Sanger sequencing (Supplementary Figure 1) and segregated with the AI phenotype in all available family members except for family 1 IV:2. This individual self-reported as affected with AI but was never examined, and was heterozygous for the variant (**Figure 1**). SNP genotyping data for both IV:2 and V:1 confirmed that the two affected individuals did not share a homozygous region over *KLK4* (Supplementary Tables 4–6). Sequencing of the remaining coding exons of *KLK4* for IV:2 did not identify any additional variants. The cause of AI in family 1, IV:2 therefore remains unknown.

Due to the similar phenotype, mode of inheritance and ethnicity of individual V:3 of family 4, Sanger sequencing was used to check for the presence of an identical mutation in *KLK4*. This revealed that family 4 also carried the *KLK4* c.632delT variant that segregated with disease for all family members for which DNA was available. Due to the presence of the same c.632delT variant in five families originating from Pakistan, microsatellite markers flanking the variant were genotyped for four of these families to check the surrounding haplotype. Families 1 and 4 shared an identical haplotype surrounding the *KLK4* c.632delT variant over a genetic distance of at least 13.4 cM (approximately 7.27 Mb in this case; Supplementary Tables 2, 7). Families 2 and 3 did not share an identical haplotype flanking the *KLK4* variant.

Interrogation of publically available databases of variation, such as dbSNP147, ExAC v0.3.1 and Exome Variant Server, found that the variant was present in all three databases, although at very low frequencies and always as a heterozygous variant (Supplementary Table 8). The *KLK4* variant was assigned as variant ID #0000000189 in the University of Leeds AI LOVD (http://dna2.leeds.ac.uk/LOVD/) and was submitted to ClinVar, accession SCV000494588.

Enamel Phenotyping

Deciduous teeth were made available from male V:1 (family 1) through either natural exfoliation or clinical extraction (hereafter referred to as KLK4 teeth; Supplementary Figure 2). In total five deciduous KLK4 teeth and five deciduous and type matched control teeth were examined. The control teeth were obtained from an anonymised tissue bank therefore the teeth could not be age or sex matched. Two whole KLK4 teeth (a canine and a molar) and two type matched control teeth were analyzed by high-resolution CT. SEM and EDX analysis were carried out on one KLK4 incisor tooth and a type matched control tooth. Mineral density measurements were also made from these slices of incisor teeth after high-resolution CT analysis. Two KLK4 teeth (an incisor and a molar) and two type matched control teeth were subjected to microhardness testing.

Structural analysis of the enamel was undertaken to characterize the detailed phenotype. High-resolution CT scans were carried out for two whole KLK4 teeth, including one canine and one molar, as well a 500 μm slice taken from a KLK4 incisor tooth (to reduce beam hardening), alongside dentition and type matched controls. CT scanning revealed that the enamel of the teeth from the *KLK4* c.632delT patient exhibited two distinct layers of different enamel density (**Figure 2** and **Supplementary Videos 1–4**). For all tooth types, the outer layer extended a small distance from the surface and was consistently present except in those regions affected by, or lost as a result of, decay. This layer was most clearly visible in the regions of thicker enamel found at the enamel cusps and was not evident in control teeth.

Enamel mineral density measurements were taken from the 500 μm KLK4 and control tooth slices rather than from the whole teeth, since measurements from the tooth slices would be less affected by CT beam hardening artifacts. These errors could have led to artificial inflation of the outer enamel mineral density compared to the inner enamel mineral density. Therefore, to quantify the enamel mineral density in the outer and inner layers of the KLK4 tooth slice, specific regions were selected by application of mineral density thresholds. In this way, the entire enamel thickness and none of the dentine could be specifically selected by thresholding both samples at $\geq$2.13 g/cm^3 (Supplementary Figure 3, Supplementary Table 9). For control enamel, the mean mineral density was 2.93 g/cm^3, whereas the mean enamel mineral density for the KLK4 enamel was 2.64 g/cm^3. By thresholding at a mineral density of $\geq$2.75 g/cm^3, only the outer enamel layer in the KLK4 tooth slice was selected. However, the entire enamel thickness was selected in the control tooth slice, suggesting that the inner enamel layer seen in the KLK4 teeth was of reduced mineral density compared with both KLK4 outer enamel and the full width of enamel in control teeth. The mean enamel mineral values obtained for the control and the KLK4 tooth slice were 3.04 and 2.92 g/cm^3 respectively. By thresholding at a mineral density of 2.13–2.75 g/cm^3, only the inner enamel was selected in the KLK4 tooth slice and a mean value of 2.58 g/cm^3 was obtained. No comparable data was

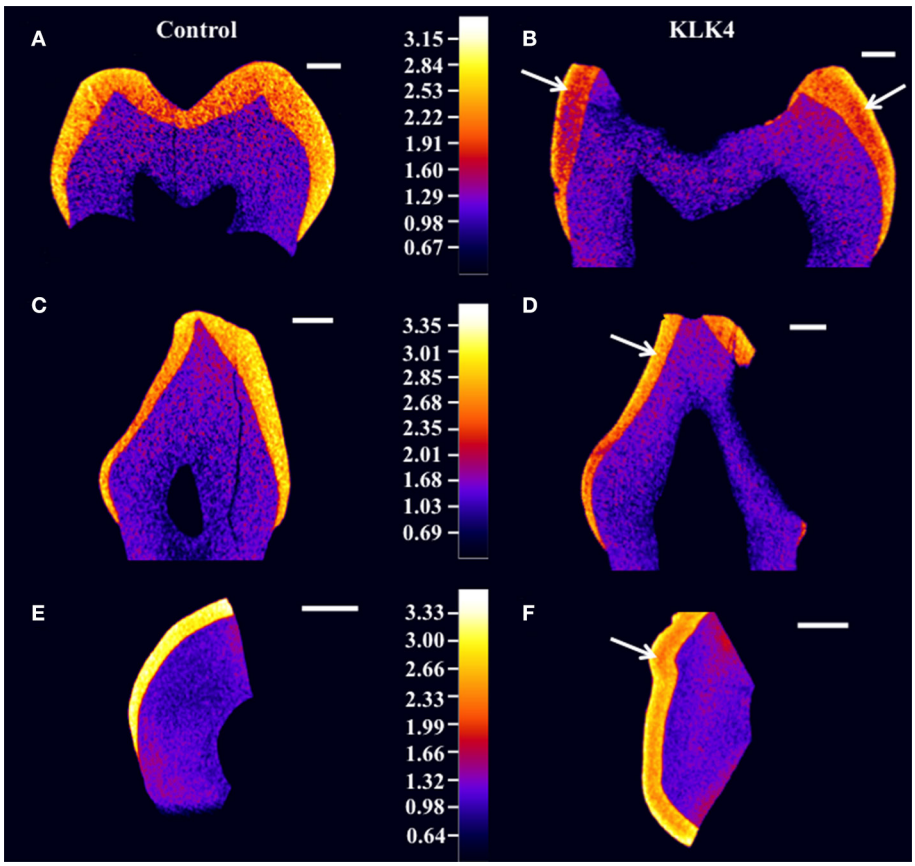

FIGURE 2 | High resolution X-ray CT analysis of WT control and KLK4 teeth from individual V:1 (family 1). (A,B): molar teeth, **(C,D)**: canine teeth, **(E,F)**: incisal tooth slices. Arrows indicate the presence of an inner layer of enamel of lower mineral density not seen in control teeth. Scale bars represent 1 mm.

obtainable for the control tooth slice as so little of the enamel had a mineral density value in this lower range. Whilst the enamel density of the control tooth showed a general trend of decreasing mineral density when moving from the outer enamel surface toward the DEJ, there were no clear divisions to demarcate sudden changes in enamel density, such as those seen in the KLK4 teeth (**Figure 2**).

For SEM, one KLK4 incisor tooth and one type matched control tooth were sectioned planar to the bucco-lingual axis. SEM revealed that a clear demarcation boundary between the outer and the inner enamel was visible for the KLK4 tooth, most especially on the lingual face, but no such boundary was evident for the control tooth (**Figure 3**). In addition, the outer enamel of the KLK4 incisor tooth had the appearance of a more densely packed mineral compared with the inner enamel of the KLK4 incisor tooth.

Knoop microhardness (KM) testing was carried out to determine whether the lower mineral density detected in the inner layer of KLK4 teeth resulted in lower KM values compared to control teeth. One KLK4 incisor tooth and one KLK4 molar tooth and two type matched controls were analyzed along the buccal faces of the enamel in each section. Measurements revealed that the outer enamel of control incisor and molar teeth had a mean KM value of 298.3 ± 32.7 (2x standard error of the mean) and 323.4 ± 24.0 respectively. Control inner enamel had mean KM values of 283.0 ± 14.6 (incisor) and 298.9 ± 13.8 (molar) (**Figure 3**). These data agree with previous investigations of control human deciduous teeth, showing that microhardness decreases from the surface enamel toward the DEJ (He et al., 2010) with reported KM values ranging from 304.5 to 326.6 for incisors (25 g load for 30 s, Scatena et al., 2014) and 271–320 for molars (50 g load for 10 s, Mirkarimi et al., 2012; Mudumba et al., 2014). For the KLK4 teeth, the KM of the outer enamel layer was 264.1 ± 23.1 for the incisor and 310.9 ± 15.2 for the molar, representing 88.5 and 96.1 % of the values obtained for matched control teeth respectively. KM values for the inner enamel of the KLK4 teeth however, were much reduced, at 127.1 ± 20.3 (incisor) and 87 ± 13.9 (molar) and were significantly lower (incisor: $t = -8.9486$ $p < 0.001$; molar: $t = -18.2654$, $p < 0.001$) than the values obtained for the KLK4 outer enamel (**Figure 3M**). Comparison of the KM values for the inner and outer enamel of both the matched control incisor and molar teeth showed that the KM of the inner enamel was not significantly different to that of the outer enamel in each case (incisor: $t = -0.854$ $p > 0.05$; molar: $t = -1.7642$, $p > 0.05$).

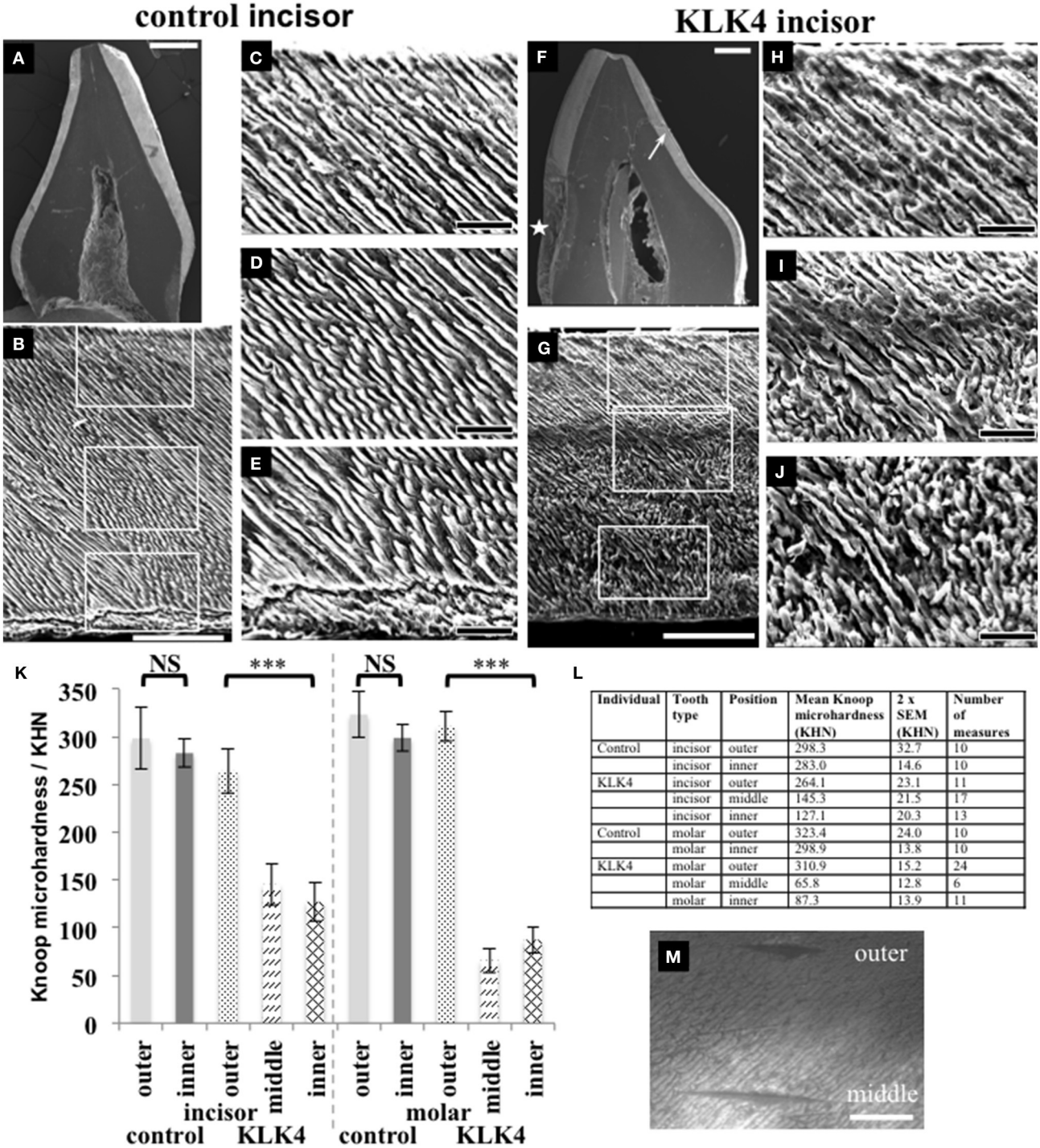

Individual	Tooth type	Position	Mean Knoop microhardness (KHN)	2 x SEM (KHN)	Number of measures
Control	incisor	outer	298.3	32.7	10
	incisor	inner	283.0	14.6	10
KLK4	incisor	outer	264.1	23.1	11
	incisor	middle	145.3	21.5	17
	incisor	inner	127.1	20.3	13
Control	molar	outer	323.4	24.0	10
	molar	inner	298.9	13.8	10
KLK4	molar	outer	310.9	15.2	24
	molar	middle	65.8	12.8	6
	molar	inner	87.3	13.9	11

FIGURE 3 | SEM and microhardness testing of control and KLK4 teeth from individual V:1 (family 1). (A–E): Control tooth; **(F–J)**: KLK4 tooth. **(A)**: Whole tooth longitudinal section. **(B)**: The enamel layer with the enamel surface shown at the top and the enamel-dentine junction at the bottom. White boxes indicate the positions of magnified images **(C,D)** and **(E)** respectively (top to bottom). **(C–E)**: outer **(C)**: close to the surface; middle **(D)** and inner **(E)**: close to the EDJ, enamel. **(F)**: Whole tooth longitudinal section—note the clear demarcation in the enamel layer between the inner and outer enamel on the lingual side of the tooth (arrow). An area of decay is present on the one side of the tooth (star). **(G)**: The enamel layer with surface at the top and the enamel-dentine junction at the bottom. White boxes indicate the positions of magnified images **(H–J)** respectively (top to bottom). **(H–J)**: outer **(H)**: close to the surface: middle **(I)** and inner **(J)**: close to the EDJ, enamel. **(K)**: Knoop microhardness testing for control and KLK4 incisor and molar teeth. Error bars represent 2x standard error of the mean. Brackets indicate the conditions for which unpaired, two-tailed *T*-tests were undertaken. Results are abbreviated as follows: NS; not significant, i.e., $p > 0.05$; *** significant at $p < 0.001$. **(L)**: Knoop microhardness testing results in table form. **(M)**: Light microscopy image showing two indentations made around 100 μm apart on the KLK4 incisor tooth, one in the outer enamel layer and the other in the middle enamel layer. Scale bars represent **(A,F)**: 1 mm; **(B,G)**: 100 μm; **(C–E)** and **(H–J)**: 25 μm; **(M)**: 50 μm.

EDX analysis was undertaken on the lingual and buccal outer and inner enamel for the KLK4 incisor tooth and the type matched control tooth previously analyzed using SEM. Compared to the control tooth, the inner enamel of the KLK4 tooth contained a lower atomic percentage of both calcium and phosphorus (**Figure 4**, Supplementary Table 10). KLK4 inner enamel also contained a larger atomic percentage proportion of nitrogen although this was more evident for the enamel on the lingual side of the tooth than the buccal side. The atomic percentage content of both oxygen and carbon appeared to vary across both teeth while the atomic percentage contribution of fluoride, sodium and magnesium were all found to be lower in the KLK4 tooth compared with the control tooth.

DISCUSSION

The *KLK4* variant, identified here in five unrelated families of Pakistani origin, was associated with a hypomaturation AI clinical phenotype, as previously described for the three other *KLK4* variants reported so far (Hart et al., 2004; Wright et al., 2011; Wang et al., 2013; Seymen et al., 2015). The *KLK4* c.632delT variant is predicted to produce a transcript that escapes NMD as it is predicted to lead to a frameshift variant in the final exon. RNA was unavailable from any of the families for study to confirm this. Of the *KLK4* variants previously identified, only the c.620_621delCT, p.S207Wfs*38 variant leads to a frameshift, generating a premature stop codon within the final exon (Seymen et al., 2015), whereas the other two reported mutations (a frameshift and a nonsense variant) are predicted to produce a transcript that is subject to NMD (Hart et al., 2004; Wang et al., 2013). Seymen et al. (2015) analyzed the effect of the *KLK4* c.620_621delCT, p.(S207Wfs*38) variant via an *in vitro* expression assay and found reduced protein expression compared with a WT construct and no catalytic activity. This was unsurprising since the frameshift affected the p.S207 residue, one of the catalytic triad of residues crucial to the function of all kallikrein enzymes.

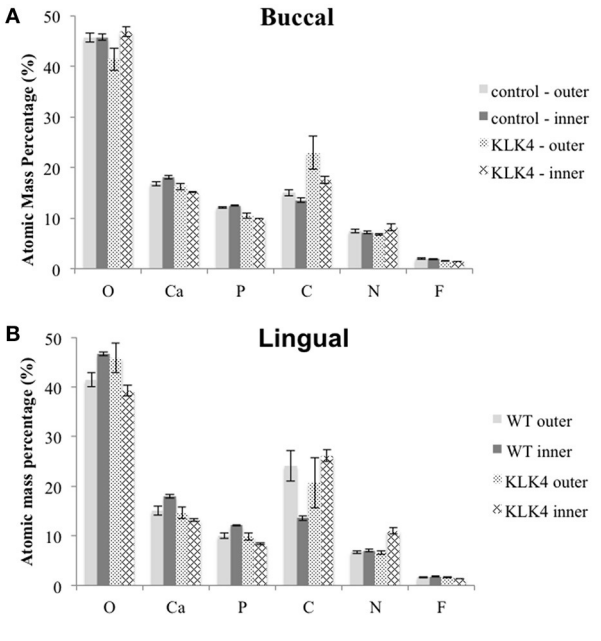

FIGURE 4 | Elemental analysis by energy dispersive X-ray spectroscopy (EDX). Measurements are detailed in Supplementary Table 10. Note that Mg and Na content were also analyzed but are not included here. Measurements were taken from both sides of the tooth: **(A)**: buccal, **(B)**: lingual.

A truncated protein may potentially be produced as a result of the *KLK4* c.632delT variant reported here. If this were indeed the case, the catalytic triad of residues essential to the function of KLK4 (residues His71, Asp116, and Ser207) would be preserved but three of six structurally important disulphide bonds would be precluded due to loss of cysteine residues at positions 213, 228, and 241 (Debela et al., 2006) (Supplementary Figure 4). The protein is therefore likely to be misfolded and may be degraded or non-functional.

The recognition of an identical *KLK4* variant within five families not known to be related but of the same Pakistani origin, suggests that the mutation may be the result of a common ancestral founder mutation. Analysis of the haplotype that surrounded the *KLK4* c.632delT variant in four of the families (1–4) found that families 1 and 4 shared a relatively large common haplotype extending at least 13.4 cM (approximately 7.27 Mb), but there was no evidence of a shared haplotype for families 2 and 3. This, together with the relative frequency of the variant within the South Asian population (0.146 %) and the lack of the variant in other populations (other than in one individual of African origin) as shown by the ExAC browser (v0.3.1), all suggest that the c.632delT variant may have arisen in the Pakistani population a long time ago and may have been maintained in several isolated endogamous sub-populations. Overall, these findings suggest that the *KLK4* c.632delT variant may be a common cause of autosomal recessive AI in the Pakistani population.

Phenotypic analysis of teeth from individual V:1 from family 1 using CT showed that the enamel was hypomineralised in comparison to control enamel but that the hypomineralisation was greatest in the deeper enamel, away from the surface and toward the DEJ. Microhardness readings also showed that the surface enamel was harder than the inner enamel layer and a clearly demarcated outer enamel layer was visible upon SEM. EDX revealed decreased oxygen and phosphorus content, and hinted at increased nitrogen content for the inner enamel of the KLK4 tooth compared with the WT control. This latter may suggest the presence of retained protein but this remains to be confirmed.

This apparent difference in the mineralization, elemental content and hardness of KLK4 inner compared with outer enamel may reflect a number of different factors acting during enamel formation.

During the transition and maturation stages, ameloblasts secrete KLK4 into the enamel matrix to further degrade enamel matrix proteins already processed by the secretory stage proteinase, MMP20. *KLK4* has been shown to be a relatively recent evolutionary development that is suggested to be concurrent with the development of thicker enamel and earlier tooth eruption (Kawasaki et al., 2014). Prior to *KLK4* evolution,

ameloblast endocytosis of enamel matrix protein fragments was the primary mechanism for elimination of residual protein from the maturing tissue, though residual MMP20 secreted during the secretory stage may have also remained active to cleave enamel peptides. It has been shown *in vitro* that MMP20 is able to activate KLK4 and is itself inactivated by the action of KLK4, thus potentially explaining the shift in proteinase activity from MMP20 to KLK4 observed during the transition stage of enamel development (Yamakoshi et al., 2013). If mutant KLK4 were unable to inactivate MMP20, MMP20 may remain active during the maturation stage as reported in *Klk4*$^{-/-}$ mice (Yamakoshi et al., 2011). However this alone would not explain the greater mineralization of the outer enamel layer compared to the inner enamel in the KLK4 teeth. It has been suggested that cleavage by KLK4 enables the movement of enamel matrix protein degradation products from the deeper enamel (Bartlett and Simmer, 2014) and an absence or reduced activity of KLK4 would preclude or hinder this. In such a case, residual protein fragments would remain in the inner depths of the tissue, inhibiting secondary mineral growth of the enamel crystallites and leading to reduced mineral density. *Klk4*$^{-/-}$ mouse studies support this theory as the enamel has been shown to be less mineralized and softer with depth whilst the overall enamel thickness is similar to that of WT mice (Simmer et al., 2011; Smith et al., 2011; Nunez et al., 2016).

The mean enamel mineral density reported for *Klk4*$^{-/-}$ mice was 2.5 g/cm^3 compared with 3.1 g/cm^3 reported for WT controls, a reduction of 19 % (Nunez et al., 2016). The figures reported here for enamel density measurements in the human *KLK4* c.632delT tooth are equivalent to a 10% reduction, although it is important to stress that this is based on measurements at only one plane in one tooth slice. Microhardness readings for *Klk4*$^{-/-}$ mice indicated a 77 and 39 % reduction in microhardness between the inner and outer enamel respectively (Nunez et al., 2016). This compares with 55–71% and 4–11% reductions in microhardness between the inner and outer enamel of our human *KLK4* c.632delT teeth vs. matched control teeth. It must be noted that the loads used, and the time for which they were applied during microhardness testing may account for some of the differences in absolute values obtained in mouse compared with human teeth. However, there are a number of other differences in amelogenesis between the two species, including the speed of enamel formation, the thickness of the enamel formed, the architecture of the two tissues and the fact that enamel formed in the null mouse model may not be comparable to enamel from an individual with a *KLK4* mutation predicted to escape NMD. Nevertheless, our data clearly demonstrate a difference in hardness between inner and outer enamel of KLK4 teeth that is not apparent in human control teeth and is similar to that seen in the *Klk4*$^{-/-}$ mouse, suggesting that the inner enamel is preferentially affected by perturbations in KLK4 function.

During maturation, ameloblasts employ endocytosis to remove residual enamel matrix proteins/peptides diffusing to the surface/outer enamel layer from deeper enamel layers. Reduced proteolysis due to compromised KLK4 activity may hinder diffusion from deeper layers and may result in retention of proteins/peptide within the deeper enamel. This may, in turn, inhibit maturation stage crystal growth. The visible demarcation between the outer and inner enamel in our KLK4 teeth and the observed differences in physical properties between inner and outer enamel in both the *Klk4*$^{-/-}$ mouse model and the KLK4 human teeth could represent the extent to which ameloblast endocytosis alone is effective in removing residual matrix protein. Given the more rapid time to eruption in the mouse compared with the human, this might also explain the differences in absolute hardness values between our KLK4 human enamel and the *Klk4*$^{-/-}$ mouse teeth, with the longer maturation time in the case of human enamel development resulting in (relatively) harder tissue. It is difficult to explain the developmental origin of the clear demarcation line present between the outer and inner enamel, but it may actually be a preparation artifact reflecting some subtle difference in the physiochemical properties of the enamel involved.

In addition, post-eruptive mineralization of surface enamel by ions from saliva may have contributed to the outer enamel being harder than the inner enamel of the KLK4 teeth. The extent to which post-eruptive mineralization can compensate for hypomineralisation in the outer enamel of human teeth is unknown but cannot be discounted.

In conclusion, the data presented here adds a fourth *KLK4* mutation to those already reported and challenges the notion that *KLK4* mutations are a rare cause of AI, at least in the Pakistani population. The c.632delT variant may represent a founder mutation within the Pakistani population and may prove to be a common cause of autosomal recessive AI in this cohort. Analysis of human enamel affected by the *KLK4* c.632delT mutation has shown common features with those described for enamel in the *Klk4*$^{-/-}$ mouse model, suggesting that KLK4 is essential for protein removal from, and the mineralization of, the inner enamel matrix.

ETHICS STATEMENT

This study was carried out in accordance with the recommendations of the principles outlined in the declaration of Helsinki and with local ethical approval from the National Research Ethics Service Committee, UK with written informed consent from all subjects. All subjects gave written informed consent in accordance with the Declaration of Helsinki. The protocol was approved by the National Research Ethics Service Committee, UK: Yorkshire and The Humber-South Yorkshire Research Ethics Committee reference 13/YH/0028.

AUTHOR CONTRIBUTIONS

CS contributed to study design, conducted all experimental work, except that stated below, and drafted the manuscript. JK contributed to study design and edited the manuscript. CI and AM contributed to study design. PD, FS, EM, and AM recruited the families. JP contributed to study design, carried out SNP genotyping analysis, and prepared WES libraries for family 1. SB contributed to study design and advised on enamel phenotyping.

All authors read and critically revised the manuscript. All authors gave final approval and agree to be accountable for all aspects of the work.

FUNDING

This work was supported by the Wellcome Trust [grant numbers 093113 and 075945]. CS is funded by a Wellcome Trust Institutional Strategic Support award. JK is supported by the NIHR Leeds Musculoskeletal Biomedical Research Unit. Funding to pay the Open Access publication charges for this article were provided by the Wellcome Trust.

ACKNOWLEDGMENTS

The authors thank the families involved in this study and Dr. Simon M. Strafford, University of Leeds, for his assistance with microhardness testing. Data from this article was presented at the Ninth Enamel Symposium, Harrogate, England, UK 30th October to 3rd November 2016.

SUPPLEMENTARY MATERIAL

The Supplementary Material for this article can be found online at: http://journal.frontiersin.org/article/10.3389/fphys.2017.00333/full#supplementary-material

Supplementary Video 1 | Control canine.

Supplementary Video 2 | KLK4 canine.

Supplementary Video 3 | Control molar.

Supplementary Video 4 | KLK4 molar.

REFERENCES

Bartlett, J. D., and Simmer, J. P. (2014). Kallikrein-related peptidase-4 (KLK4): role in enamel formation and revelations from ablated mice. *Front. Physiol.* 5:240. doi: 10.3389/fphys.2014.00240

Deakins, M., and Burt, R. L. (1944). The deposition of calcium, phosphorus, and carbon dioxide in calcifying dental enamel. *J. Biol. Chem.* 156, 77–83.

Debela, M., Magdolen, V., Grimminger, V., Sommerhoff, C., Messerschmidt, A., Huber, R., et al. (2006). Crystal structures of human tissue kallikrein 4: activity modulation by a specific zinc binding site. *J. Mol. Biol.* 362, 1094–1107. doi: 10.1016/j.jmb.2006.08.003

DePristo, M. A., Banks, E., Poplin, R., Garimella, K. V., Maguire, J. R., Hartl, C., et al. (2011). A framework for variation discovery and genotyping using next-generation DNA sequencing data. *Nat. Genet.* 43, 491–498. doi: 10.1038/ng.806

Gadhia, K., McDonald, S., Arkutu, N., and Malik, K. (2012). Amelogenesis imperfecta: an introduction. *Br. Dent. J.* 212, 377–379. doi: 10.1038/sj.bdj.2012.314

Hart, P. S., Hart, T. C., Michalec, M. D., Ryu, O. H., Simmons, D., Hong, S., et al. (2004). Mutation in kallikrein 4 causes autosomal recessive hypomaturation amelogenesis imperfecta. *J. Med. Genet.* 41, 545–549. doi: 10.1136/jmg.2003.017657

He, B., Huang, S., Jing, J., and Hao, Y. (2010). Measurement of hydroxyapatite density and Knoop hardness in sound human enamel and a correlational analysis between them. *Arch. Oral Biol.* 55, 134–141. doi: 10.1016/j.archoralbio.2009.12.005

Hu, J. C., Sun, X., Zhang, C., Liu, S., Bartlett, J. D., and Simmer, J. P. (2002). Enamelysin and kallikrein-4 mRNA expression in developing mouse molars. *Eur. J. Oral Sci.* 110, 307–315. doi: 10.1034/j.1600-0722.2002.21301.x

Hu, J. C., Zhang, C., Sun, X., Yang, Y., Cao, X., Ryu, O., et al. (2000). Characterization of the mouse and human PRSS17 genes, their relationship to other serine proteases, and the expression of PRSS17 in developing mouse incisors. *Gene* 251, 1–8. doi: 10.1016/S0378-1119(00)00203-1

Kawasaki, K., Hu, J. C., and Simmer, J. P. (2014). Evolution of Klk4 and enamel maturation in eutherians. *Biol. Chem.* 395, 1003–1013. doi: 10.1515/hsz-2014-0122

Kim, J. W., Simmer, J. P., Hart, T. C., Hart, P. S., Ramaswami, M. D., Bartlett, J. D., et al. (2005). MMP-20 mutation in autosomal recessive pigmented hypomaturation amelogenesis imperfecta. *J. Med. Genet.* 42, 271–275. doi: 10.1136/jmg.2004.024505

Lagerstrom, M., Dahl, N., Nakahori, Y., Nakagome, Y., Backman, B., Landegren, U., et al. (1991). A deletion in the amelogenin gene (AMG) causes X-linked amelogenesis imperfecta (AIH1). *Genomics* 10, 971–975. doi: 10.1016/0888-7543(91)90187-J

Li, H., and Durbin, R. (2009). Fast and accurate short read alignment with burrows-wheeler transform. *Bioinformatics* 25, 1754–1760. doi: 10.1093/bioinformatics/btp324

McKenna, A., Hanna, M., Banks, E., Sivachenko, A., Cibulskis, K., Kernytsky, A., et al. (2010). The genome analysis toolkit: a mapreduce framework for analyzing next-generation DNA sequencing data. *Genome Res.* 20, 1297–1303. doi: 10.1101/gr.107524.110

Mirkarimi, M., Bargrizan, M., Eskandarion, S., and Shahsavari, M. (2012). Effect of zinc sulfate on human primary enamel microhardness: an *in vitro* study. *J. Clin. Pediatr. Dent.* 36, 369–371. doi: 10.17796/jcpd.36.4.92q7971127v210r1

Mudumba, V. L., Muppa, R., Srinivas, N., and Kumar, D. M. (2014). Evaluation and comparison of changes in microhardness of primary and permanent enamel on exposure to acidic center-filled chewing gum: an *in vitro* study. *Int. J. Clin. Pediatr. Dent.* 7, 24–29. doi: 10.5005/jp-journals-10005-1228

Nunez, S. M., Chun, Y. H., Ganss, B., Hu, Y., Richardson, A. S., Schmitz, J. E., et al. (2016). Maturation stage enamel malformations in Amtn and Klk4 null mice. *Matrix Biol.* 52–54, 219–233. doi: 10.1016/j.matbio.2015.11.007

Poulter, J. A., Murillo, G., Brookes, S. J., Smith, C. E., Parry, D. A., Silva, S., et al. (2014). Deletion of ameloblastin exon 6 is associated with amelogenesis imperfecta. *Hum. Mol. Genet.* 23, 5317–5324. doi: 10.1093/hmg/ddu247

Rajpar, M. H., Harley, K., Laing, C., Davies, R. M., and Dixon, M. J. (2001). Mutation of the gene encoding the enamel-specific protein, enamelin, causes autosomal-dominant amelogenesis imperfecta. *Hum. Mol. Genet.* 10, 1673–1677. doi: 10.1093/hmg/10.16.1673

Reith, E. J. (1970). The stages of amelogenesis as observed in molar teeth of young rats. *J. Ultrastruct. Res.* 30, 111–151. doi: 10.1016/S0022-5320(70)90068-7

Scatena, C., Galafassi, D., Gomes-Silva, J. M., Borsatto, M. C., and Serra, M. C. (2014). *In vitro* erosive effect of pediatric medicines on deciduous tooth enamel. *Braz. Dent. J.* 25, 22–27. doi: 10.1590/0103-64402013002344

Seymen, F., Park, J. C., Lee, K. E., Lee, H. K., Lee, D. S., Koruyucu, M., et al. (2015). Novel MMP20 and KLK4 mutations in amelogenesis imperfecta. *J. Dent. Res.* 94, 1063–1069. doi: 10.1177/0022034515590569

Simmer, J. P., and Hu, J. C. (2002). Expression, structure, and function of enamel proteinases. *Connect. Tissue Res.* 43, 441–449. doi: 10.1080/03008200290001159

Simmer, J. P., Hu, Y., Lertlam, R., Yamakoshi, Y., and Hu, J. C. (2009). Hypomaturation enamel defects in Klk4 knockout/LacZ knockin mice. *J. Biol. Chem.* 284, 19110–19121. doi: 10.1074/jbc.M109.013623

Simmer, J. P., Hu, Y., Richardson, A. S., Bartlett, J. D., and Hu, J. C. (2011). Why does enamel in Klk4-null mice break above the dentino-enamel junction? *Cells Tissues Organs* 194, 211–215. doi: 10.1159/000324260

Skobe, Z. (1976). The secretory stage of amelogenesis in rat mandibular incisor teeth observed by scanning electron microscopy. *Calcif. Tissue Res.* 21, 83–103. doi: 10.1007/BF02547385

Smith, C. E., Richardson, A. S., Hu, Y., Bartlett, J. D., Hu, J. C., and Simmer, J. P. (2011). Effect of kallikrein 4 loss on enamel mineralization: comparison with mice lacking matrix metalloproteinase 20. *J. Biol. Chem.* 286, 18149–18160. doi: 10.1074/jbc.M110.194258

Wang, S. K., Hu, Y., Simmer, J. P., Seymen, F., Estrella, N. M., Pal, S., et al. (2013). Novel KLK4 and MMP20 mutations discovered by whole-exome sequencing. *J. Dent. Res.* 92, 266–271. doi: 10.1177/0022034513475626

Wright, J. T., Torain, M., Long, K., Seow, K., Crawford, P., Aldred, M. J., et al. (2011). Amelogenesis imperfecta: genotype-phenotype studies in 71 families. *Cells Tissues Organs* 194, 279–283. doi: 10.1159/000324339

Yamakoshi, Y., Richardson, A. S., Nunez, S. M., Yamakoshi, F., Milkovich, R. N., Hu, J. C., et al. (2011). Enamel proteins and proteases in Mmp20 and Klk4 null and double-null mice. *Eur. J. Oral Sci.* 119(Suppl. 1), 206–216. doi: 10.1111/j.1600-0722.2011.00866.x

Yamakoshi, Y., Simmer, J. P., Bartlett, J. D., Karakida, T., and Oida, S. (2013). MMP20 and KLK4 activation and inactivation interactions *in vitro*. *Arch. Oral Biol.* 58, 1569–1577. doi: 10.1016/j.archoralbio.2013.08.005

Conflict of Interest Statement: The authors declare that the research was conducted in the absence of any commercial or financial relationships that could be construed as a potential conflict of interest.

Copyright © 2017 Smith, Kirkham, Day, Soldani, McDerra, Poulter, Inglehearn, Mighell and Brookes. This is an open-access article distributed under the terms of the Creative Commons Attribution License (CC BY). The use, distribution or reproduction in other forums is permitted, provided the original author(s) or licensor are credited and that the original publication in this journal is cited, in accordance with accepted academic practice. No use, distribution or reproduction is permitted which does not comply with these terms.

frontiers in Physiology

ORIGINAL RESEARCH
published: 03 May 2017
doi: 10.3389/fphys.2017.00267

FAM20A Gene Mutation: Amelogenesis or Ectopic Mineralization?

Guilhem Lignon[1†], Fleur Beres[1†], Mickael Quentric[1†], Stephan Rouzière[2], Raphael Weil[2], Muriel De La Dure-Molla[3], Adrien Naveau[1], Renata Kozyraki[1], Arnaud Dessombz[1‡] and Ariane Berdal[1,3‡]*

[1] Molecular Oral Pathophysiology, Cordeliers Research Center, UMRS 1138 Institut National de la Santé et de la Recherche Médicale, Paris-Descartes, Pierre-et-Marie-Curie, Paris-Diderot Universities, Paris, France, [2] Laboratoire de Physique des Solides, Centre National de la Recherche Scientifique, Univ. Paris-Sud, Université Paris-Saclay, Orsay Cedex, France, [3] Reference Center of Rare Buccal and Facial Malformations MAFACE-Rothschild Hospital, APHP, Paris, France

OPEN ACCESS

Edited by:
Petros Papagerakis, University of Michigan, USA

Reviewed by:
Jung-Wook Kim, Seoul National University, South Korea
Hidemitsu Harada, Iwate Medical University, Japan
Amel Gritli-Linde, University of Gothenburg, Sweden

***Correspondence:**
Arnaud Dessombz
arnaud.dessombz@crc.jussieu.fr

[†]Co-first-authors.
[‡]Co-last-authors.

Specialty section:
This article was submitted to Craniofacial Biology and Dental Research, a section of the journal Frontiers in Physiology

Received: *22 February 2017*
Accepted: *11 April 2017*
Published: *03 May 2017*

Citation:
Lignon G, Beres F, Quentric M, Rouzière S, Weil R, De La Dure-Molla M, Naveau A, Kozyraki R, Dessombz A and Berdal A (2017) FAM20A Gene Mutation: Amelogenesis or Ectopic Mineralization? Front. Physiol. 8:267. doi: 10.3389/fphys.2017.00267

Background and objective: *FAM20A* gene mutations result in enamel renal syndrome (ERS) associated with amelogenesis imperfecta (AI), nephrocalcinosis, gingival fibromatosis, and impaired tooth eruption. FAM20A would control the phosphorylation of enamel peptides and thus enamel mineralization. Here, we characterized the structure and chemical composition of unerupted tooth enamel from ERS patients and healthy subjects.

Methods: Tooth sections were analyzed by Scanning Electron Microscopy (SEM), Energy Dispersive Spectroscopy (EDS), X-Ray Diffraction (XRD), and X-Ray Fluorescence (XRF).

Results: SEM revealed that prisms were restricted to the inner-most enamel zones. The bulk of the mineralized matter covering the crown was formed by layers with varying electron-densities organized into lamellae and micronodules. Tissue porosity progressively increased at the periphery, ending with loose and unfused nanonodules also observed in the adjoining soft tissues. Thus, the enamel layer covering the dentin in all ERS patients (except a limited layer of enamel at the dentino-enamel junction) displayed an ultrastructural globular pattern similar to one observed in ectopic mineralization of soft tissue, notably in the gingiva of *Fam20a* knockout mice. XRD analysis confirmed the existence of alterations in crystallinity and composition (vs. sound enamel). XRF identified lower levels of calcium and phosphorus in ERS enamel. Finally, EDS confirmed the reduced amount of calcium in ERS enamel, which appeared similar to dentin.

Conclusion: This study suggests that, after an initial normal start to amelogenesis, the bulk of the tissue covering coronal dentin would be formed by different mechanisms based on nano- to micro-nodule aggregation. This evocated ectopic mineralization process is known to intervene in several soft tissues in FAM20A gene mutant.

Keywords: amelogenesis imperfecta, *FAM20A*, rare disease, mineral, matrix biology

INTRODUCTION

Hereditary amelogenesis imperfecta (AI) is caused by mutations in genes encoding a number of effectors of amelogenesis such as enamel matrix proteins (amelogenin, ameloblastin, enamelin), peptidases (*MMP20, KLK4*), transcription factors (*DLX3*), and membrane-anchoring polypeptides (laminin 5, collagen 16 laminin; Salido et al., 1992; Barron et al., 2010; Poulter et al., 2014; Seymen et al., 2015; Kim et al., 2016) as well as other polypeptides (ACPT, GPR68, CLDN19; Parry et al., 2016; Seymen et al., 2016; Yamaguti et al., 2017) of unknown function (Prasad et al., 2016). AI can be isolated or syndromic. Recessive *FAM20A* mutations were initially discovered by a whole-exome sequencing of AI patient DNA (O'Sullivan et al., 2011), suggesting an important role of the encoded polypeptide during amelogenesis and in ERS. AI associated with gingival fibromatosis (AIGF MIM#614253; O'Sullivan et al., 2011) or enamel renal syndrome (ERS, MIM#204690; Jaureguiberry et al., 2012; Cabral et al., 2013; Wang et al., 2014; Jaouad et al., 2015; Poulter et al., 2015; Volodarsky et al., 2015) arise due to mutation of one same *FAM20A* gene (Jaureguiberry et al., 2012; Vogel et al., 2012; Chaitanya et al., 2014; de la Dure-Molla et al., 2014; Bhesania et al., 2015). Patients carrying FAM20A mutations present a very distinctive phenotype (de la Dure-Molla et al., 2014): marked hypoplastic AI, important eruption impairment with dental retention and ectopic mineralization in several tissues, including the gingiva, follicular sac, dental pulp, periodontal ligament, and the kidney. Variable semi-lacunar defects at the occlusal edge of permanent upper central incisors have been described. Posterior teeth were reported with a flat cuspid relief wich might be related to either congenital defects or secondary abrasion (Wang et al., 2013). On the other hand, in a number of soft tissues, *FAM20A* loss of function was shown to cause ectopic mineralization (de la Dure-Molla et al., 2014).

The *Fam20a* gene (the name refers to "family with sequence similarity 20") was initially discovered in mouse hematopoietic cells (Nalbant et al., 2005). Two other members (*Fam20b* and *Fam20c*) were identified by sequence homology, and the proteins they encode (FAM20A, B, and C) are structurally conserved in mice and humans. The most studied member, FAM20C, which was independently identified in odontoblasts as Dentin Matrix Protein 4 (DMP4; Hao et al., 2007), was revealed to be the long-sought Golgi casein kinase (Tagliabracci et al., 2012). This kinase phosphorylates proteins containing canonical Ser-x-Glu/pSer motifs, including a number of matrix phosphoproteins of bone and teeth such as the three major enamel polypeptides, amelogenin, Ameloblastin, enamelin, and osteopontin (Cui et al., 2015; Ma et al., 2016). FAM20B controls glycosaminoglycan assembly by phosphorylating xylose in its elongation common linkage region (Koike et al., 2009). Finally, FAM20A, is considered a pseudokinase due to a mutation within its catalytic site; however, it partners with FAM20C to enhance the latter's Golgi kinase activity. Aberrant tooth phenotypes of null mutant mice reflect the important roles of *Fam20* members in enamel development (Li et al., 2016). Similarly, human *FAM20C* mutations result in AI with hypoplastic enamel (Vogel et al., 2012; Acevedo et al., 2015; Elalaoui et al., 2016), underscoring the importance of the FAM20A-FAM20C interactions in promoting enamel mineralization (Ohyama et al., 2016).

To date, micro CT and scanning electron microscopy of human teeth from patients carrying *FAM20A* mutations revealed crown and root resorption and hypercementosis (Wang et al., 2013, 2014). Increased enamel fragility was suggested, the tissue being quickly worn down by mastication forces after eruption. The chemical composition and ultrastructure of enamel from patients carrying *FAM20A* mutations are still unknown.

This study aimed to characterize the ultrastructure and mineral composition of human enamel of unerupted teeth in a cohort of patients carrying *FAM20A* gene mutations and to compare the findings with those of healthy enamel. We exploited recently developed technological interfaces between physics, chemistry, and biomedical science to analyze biomineralization and map ectopic mineral accretion, as reported previously (Dessombz et al., 2015; Berès et al., 2016). We characterized the enamel from ERS patients using scanning electron microscopy (SEM), X-ray diffraction (XRD), X-ray fluorescence (XRF), and SEM-energy-dispersive spectroscopy (EDS).

MATERIALS AND METHODS

Patients Recruitment

Twenty-five loss of functions mutations have been reported in the *FAM20A* gene (deletions and base substitutions leading to premature stop codon). Patients carrying FAM20 gene mutations ($n = 6$) is a cohort recruited in the Reference Center of rare dental disease in Paris (Rothschild hospital) being part of previously published cases of ERS (Jaureguiberry et al., 2012). Diagnosis of ERS was based on clinical and radiological features (enamel hypoplasia, eruption impairment, and pulp mineralization) and *FAM20A* mutations as previously published (de la Dure-Molla et al., 2014). Affected individuals and controls were recruited following informed consent in accordance with the principles outlined in the declaration of Helsinki. According to the French law, the samples were considered as operating waste and used under patient informed consent. Erupted ($n = 3$) and unerupted teeth ($n = 9$) from 3 differents ERS patients and permanent teeth from healthy subjects ($n = 6$) were collected after their extraction, based on the treatment plan.

Sample Preparation

Teeth were rinsed with PBS (Invitrogen, Carlsbad, CA) and fixed in 4% paraformaldehyde (Electron Microscopy Sciences, Hatfield, PA). Samples were then dehydrated in alcohol, embedded into light-cured methacrylate resin (Technovit 7200 VLC; Heraeus Kulzer, Hanau, Germany) and cut into 100–150 µm thick slices using a low-speed diamond saw under irrigation (Isomet Low Speed Cutter; Buehler, Dusseldorf, Germany). Finally, the samples were polished using graded grit polisher disks.

Scanning Electron Microscopy

Sections were sputter-coated with a 6-nm layer of platinum (SC7640 sputter coater; Quorum Technologies, Guelph, ON,

Canada). A SUPRA 40 Scanning Electron Microscope (SEM; Carl Zeiss, Oberkochen, Germany) was used to observe the microstructure of the teeth. This field-effect gun microscope operates at 0.5–30 kV. Observations of sectioned samples were made by using an Everhart-Thornley Secondary Electron (SE) detector at 20 keV and with a backscattered electrons (BSE) detector at 20 keV.

X-Ray Diffraction

Chemical phase and crystallinity of the enamel mineral were evaluated by X-ray diffraction (XRD). Experiments were carried out with a Molybdenum rotating anode X-ray generator (Rigaku RU-H2R; Rigaku, Tokyo, Japan) coupled with multilayer W/Si optics (Xenocs, Grenoble, France) delivering a focalized and monochromated ($\lambda = 0.711$ Å) X-ray beam of 800 μm × 1 mm onto the sample. X-ray images were recorded with a MAR345 (marXperts, Hamburg, Germany) detector placed 150 mm from the sample. The acquisition time for each measurement was 30 min. Diffraction diagrams were obtained by processing radial intensity integration of each image with in-house software. Then, the positions of the diffraction peaks were compared with reference files from the International Center for Diffraction Data (ICDD).

X-Ray Fluorescence

X-ray fluorescence (XRF) experiments were carried out with Molybdenum rotating anode X-ray generator (Rigaku RU200) coupled with multilayer W/Si optics (Xenocs) delivering a focalized and monochromated ($\lambda = 0.711$ Å) X-ray beam of 150 × 150 μm. Fluorescence spectra were measured with an energy-dispersive detector (SDD detector, Ketek), with a time acquisition of 240 min. XRF analysis was performed with PyMca software (Solé et al., 2007).

Energy Dispersive Spectroscopy

A SUPRA 55 SEM (Carl Zeiss, Oberkochen, Germany) equipped with an energy-dispersive X-ray spectrometer (Bruker SDD detector) was used to perform the observations and chemical analyses. This field-effect "gun" microscope (FE-SEM) operates at 0.5–30 kV with an energy of 25 kV. High-resolution observations were obtained by 2 secondary electron detectors: an in-lens SE detector and an Everhart-Thornley SE detector. The acquisition mode only permits qualitative analysis because no control sample was used.

RESULTS

Scanning Electron Microscopic Analysis Reveals Dramatic Enamel Hypoplasia in ERS

SEM images (**Figure 1**) were obtained using the BSE mode to analyze chemical contrast and the SE mode to visualize morphology. Healthy enamel displayed a normal thickness and a high level of mineralization in comparison to dentin (**Figure 1A**). Moreover, at the Dentino-Enamel Junction (DEJ), using BSE mode, sound enamel showed a uniform electron density (**Figure 1B**), suggesting the presence of a homogeneous chemical phase.

All ERS erupted teeth presented enamel breakdown (data non-shown) suggesting their decreased mechanical resistance as described by other studies (Wang et al., 2013). Representative features for enamel and ectopic mineral present in all ERS unerupted teeth are shown in **Figures 1C–G**. There, the enamel displayed a severe reduction in thickness It should be noted that the images in panels A and C are at the same magnification, thus highlighting the dramatic native enamel hypoplasia in ERS. Samples appeared to be fractured, suggesting their low resistance (**Figures 1C–E**), in contrast with controls (**Figures 1A,B**).

At the DEJ, enamel from an ERS patient (**Figure 1D**) exhibited layers of alternating dark and light areas (arrows), signifying differences in electron density (in BSE mode). This finding raised three non-exclusive hypotheses for the observed differences between healthy and ERS enamel: (1) differences in chemical phase, (2) differences in qualitative composition, and/or (3) differences in mineral density, which we investigated in turn in the subsections below. Indeed, BSE electrons result from elastic interactions with the nuclei of atoms. The higher the atomic number (Z), the higher the probability of an elastic interaction, and the brighter the contrast.

Fused nodules of varying sizes were found throughout the enamel thickness (**Figures 1C,E,F,G**). Most of the enamel layers from ERS patients were composed of micro- and nano-nodules (**Figure 1E**, asterisks—white boxes). In the major part of enamel, enamel prisms tended to be restrained to the most inner zones (**Figures 1C,F**). Nodules ranged from 1 to 50 μm in diameter, separated poorly electron dense frontiers and embedded in more or less regular lamellae (arrows; **Figure 1E**). Nanonodules with a concentric organization of varying sizes were present at the surface of ERS enamel and also within the enamel organ bordering the enamel [**Figure 1F** (white box) with enlargement in **Figure 1G**].

X-Ray Diffraction Reveals Small and Disoriented Crystallites in ERS Enamel

XRD was used to determine if differences in the crystalline phase exist between sound enamel (**Figure 2A**) and ERS enamel (**Figure 2B**). The general features of both two-dimensional XRD patterns were similar, with the same number and position of diffraction rings. However, several differences were observed: first, the ERS enamel displayed continuous powder-like diffraction rings, indicating a loss of texture compared to sound enamel. This corresponded to an isotropic crystalline orientation in ERS enamel. Conversely, in sound enamel, the ring patterns were textured according to the anisotropic orientation of the prisms. Radial integration profiles (**Figure 2C**) provided diffraction diagrams as a function of 2θ diffraction Bragg angles. The diffraction diagrams from both enamels showed similar characteristics, with significant peaks located at identical 2θ angles; however, the diffraction diagram of ERS enamel displayed broader and overlapping peaks. These results indicate the same crystalline phase, but with smaller and disoriented crystallites in ERS enamel. Phase identification confirmed the presence of

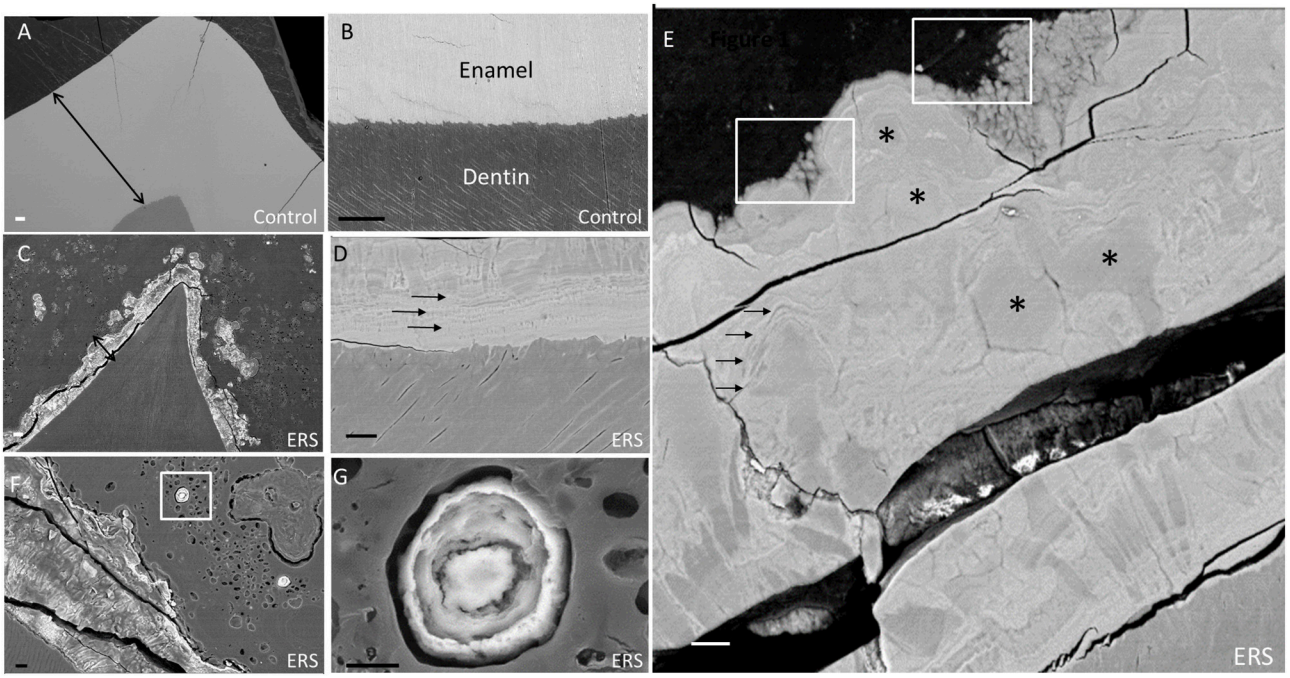

FIGURE 1 | SEM images of enamel from erupted teeth of a healthy subject and unerupted teeth from an ERS patient (mutated for *FAM20A*). (A) Sound enamel of a healthy tooth. **(B)** Sound dentino-enamel junction. Double arrows underlining a reference and identical scale in **(A,C)**. **(C)** Enamel from an ERS patient. **(D)** Dentino-enamel junction from an ERS patient. Single arrows highlighting the presence of an enamel organized in different layers. **(E)** Enamel outer layer from an ERS patient. Asterisks and white boxes show the presence of micro- and nano-nodules in enamel layers and arrows highlighting the presence of enamel organized in different layers. **(F)** Enamel organ from an ERS patient. Nodule calcification in box is represented at higher magnification in G. **(G)** Higher magnification of nodule calcification in the enamel organ shown in **(F)**. Scale bar: **(A–C)**, 100 μm; **(D–G)**, 20 μm.

carbonated apatite (ICDD 09-432) in all tested samples, which is a normal constituent of healthy enamel.

X-Ray Fluorescence Analysis Indicates a Calcium-Phosphate Mineral Phase in ERS Enamel

XRF was used to analyze chemical composition in healthy and ERS enamel. The XRF spectra identified phosphorus, argon, calcium, zinc, and strontium in both enamel samples (**Figure 3**). The presence of Ca and P further supported that the mineral phase is a calcium phosphate, in accordance with the XRD results shown in **Figure 2**. Presence of Zn and Sr, two trace elements, is related to calcium substitution. Ar is present in the atmosphere along the path of the incident X-ray beam.

Energy Dispersive Spectroscopy Reveals Reduced Mineralization in ERS Enamel

EDS was used to analyze mineral density. The results are shown in **Figure 4** and present the EDS elemental mapping (Spectral imaging mode) of phosphorus, calcium and oxygen in sound enamel (**Figures 4A–D**) and ERS enamel (**Figures 4E–H**). In sound enamel, P (**Figure 4B**) and Ca (**Figure 4C**) were present in higher amounts in comparison to dentin. This result underlines the high degree of mineralization in sound enamel. In contrast, there was no such difference between the enamel and dentin from an ERS patient (**Figures 4E–H**), demonstrating the reduction of enamel mineralization in ERS. Furthermore, spectra of Ca and P in ERS patient enamel showed significant variations through the enamel (**Figure 4I**).

DISCUSSION

Amelogenesis is a complex process which results in the secretion of an acellular matrix by ameloblasts. In the first secretion stage, ameloblasts export enamel matrix proteins (EMPs) required for the deposition of the different enamel layers (Lignon et al., 2015). After the deposition of a first internal aprismatic enamel, the ameloblasts produce internal prismatic enamel. Finally, external prismatic and outer aprismatic enamels are deposited. The organized patterns of crystal directions in these specific aprismatic and prismatic layers confer on enamel its anisotropic structure (Simmons et al., 2011; Al-Jawad et al., 2012). Then after, ameloblasts produce extracellular proteases such as metalloproteinase (MMP20) or kallikrein 4 (KLK4) which cleave EMPs. During the maturation, their proteolysis and removal from the matrix allow the lateral growth of the crystal. The constitutive components of intraprismatic and interprismatic enamel are hexagonal hydroxyapatite crystals (Lignon et al., 2015). Several EMPs play a germinal role in enamel formation, mainly the amelogenins (AMEL) which

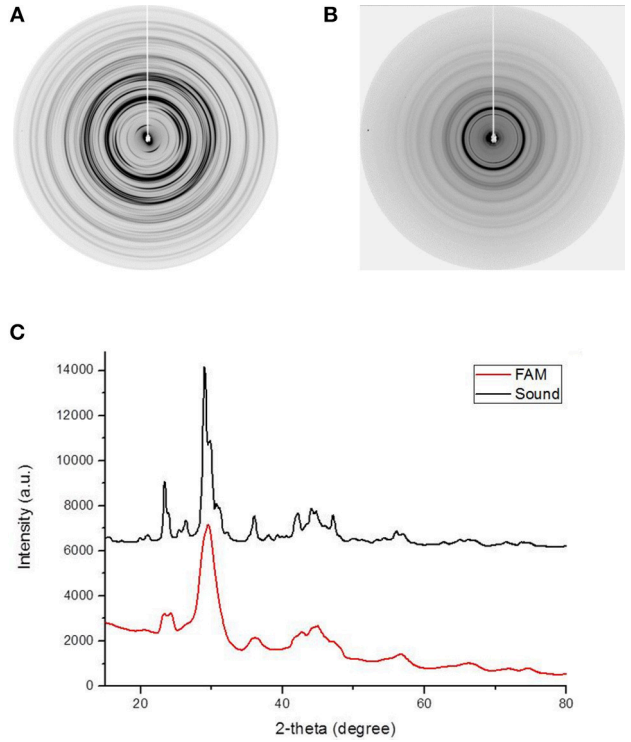

FIGURE 2 | Two-dimensional XRD patterns produced by (A) healthy enamel and **(B)** enamel from an ERS patient. **(C)** Diffraction diagram obtained by radial intensity integration of the diffraction images in **(A,B)**.

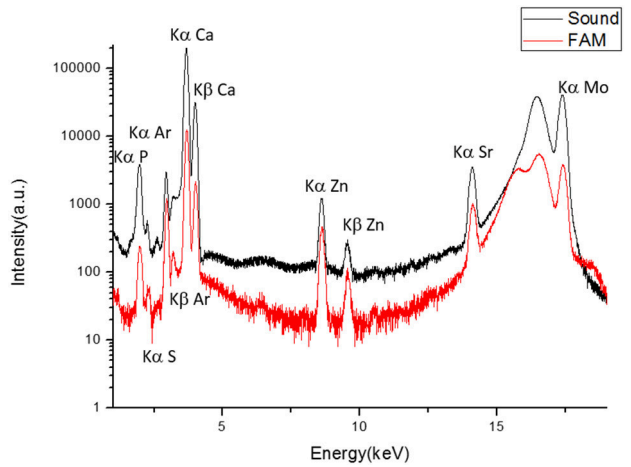

FIGURE 3 | XRF spectra of sound enamel and enamel from an ERS patient. Contributions of P (Kα = 2.014 keV), S (Kα = 2.307 keV), atmospheric Ar (Kα = 2.958 keV), Ca (Kα = 3.692 keV, Kβ = 4.012 keV), Zn (Kα = 8.638 keV, Kβ = 9.572 keV), Sr (Kα = 14.165 keV), and Mo (17.48 keV). The peaks at 16.534 and 17.48 keV are Compton scattering and irradiation, respectively.

regulate mineralization by controlling enamel thickness. Their supramolecular organization sets up the crystal elongation axis and the prism pattern. Ameloblastin (AMBN) is located between intra- and inter-prismatic enamel and establishes the supra-crystalline organization of enamel. Enamelin (ENAM) is required for crystal growth and elongation. FAM20A is produced by ameloblasts (Wang et al., 2014), and by interacting with the FAM20C kinase would help phosphorylate these EMPs (Vogel et al., 2012).

Mutation of EMP genes leads to AI, which may be hypoplastic, hypomature, or hypomineralized (Lignon et al., 2015). Autosomal dominant AI comprises 46–67% of all AI. The most frequently affected genes are *ENAM* and *FAM83H* (involved in ameloblast differentiation). In 2014, Poulter et al. identified a mutation in *AMBN* which also gives rise to AI (Poulter et al., 2014). AI associated with *AMELX* gene mutations (located on the X chromosome) is involved in 5% of cases, all of which feature a striated enamel appearance. Autosomal recessive forms involving six genes, but mainly kalikrein 4 (*KLK4*) and metalloprotease-20 (*MMP20*), are the scarcest. In these latter forms of AI, enamel exhibits a normal thickness but is more fragile and frequently worn. More recently, *FAM20A* gene mutations have been identified in hypoplastic AI associated with gingival fibromatosis (O'Sullivan et al., 2011) and with nephrocalcinosis (Jaureguiberry et al., 2012; Wang et al., 2013). The present data support and extend previous studies on teeth from ERS patients (Wang et al., 2013, 2014) by furnishing details of the ultrastructure of the tissue covering the dentin as well as its physicochemical properties.

XRD diffractograms proved the presence of the same crystalline phase in sound enamel and ERS enamel. Differences were, however, observed in the width and intensity of the diffraction rings, suggesting some morphological and structural changes. Concerning diffractograms, the broader the peaks, the smaller the diffracting crystallites. ERS enamel therefore displays smaller size crystals. Moreover, the powder-like diffractograms indicates a loss of structural organization between the crystallites, in contrast with the prismatic organization in sound enamel. In this study, it should be kept in mind that this technique presented some limitations due to the resolution. The major limitation of a smaller-diameter beam is the reduction in luminous flux. A superior alternative would be to use a synchrotron beam, which provides better resolution.

As the crystalline phase was found to be the same in sound and ERS enamel, we then investigated, by XRF, possible differences in the presence of trace elements. The XRF data revealed a similar elemental composition for both samples, including the presence of Ca and P. The Ar detected originated from gas in the atmosphere. Moreover, two trace elements were detected, Zn and Sr, which correspond to Ca substitution. Indeed, Zn is an essential trace element for living organisms. It takes part in many aspects of metabolism and may be inserted into hydroxyapatite. In apatite, Zn may substitute for up to 5% of Ca (Bazin et al., 2009). This substitution does not induce modification in lattice parameters (Ren et al., 2009). Moreover, Zn may also be a marker of inflammation (Dessombz et al., 2013). As observed here, Sr is also commonly found in biological apatite as a substitute for Ca (Schroeder et al., 1972). In long bones, Sr promotes biomineralization and is used as a preventive in osteoporosis (Bone et al., 2013; Bazin et al., 2014). Other research groups have applied XRF to detect other trace elements in tooth enamel

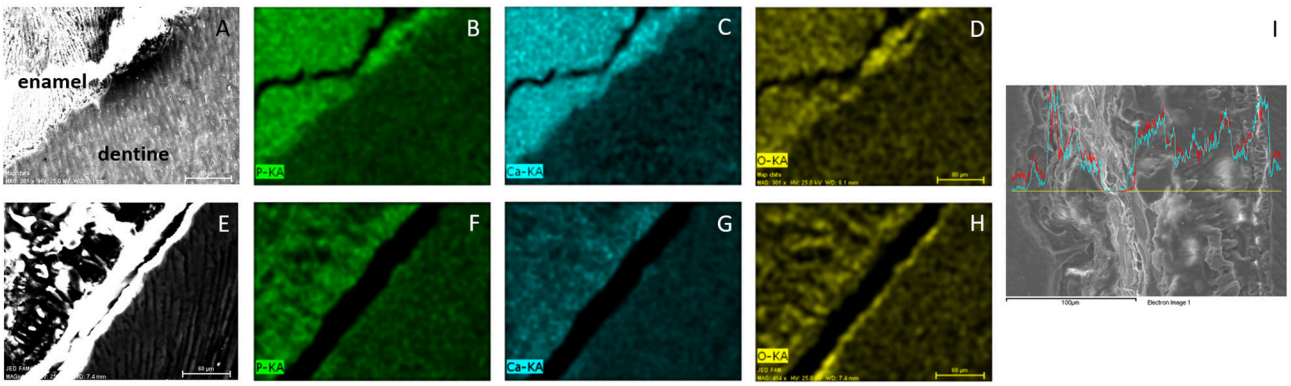

FIGURE 4 | EDS mapping of enamel and dentine from healthy donors (A–D) and from FAM20A patient **(E–H)**. Images are first viewed in SEM **(A,E)**. Contributions of P **(B,F)**, Ca **(C,G)** and O **(D,H)** are then analyzed. **(I)** Enamel section with variation of Ca (blue) and P (red) across the section. Scale bar: 80 μm, except for **(I)** 100 μm.

(Oprea et al., 2009; Zimmerman et al., 2015), also resulting from Ca substitution. The other elements we identified were As, Ti, Li, Be, Mg, Al, Mn, Fe, Cu, Zr, Sn, Au, Hg, Pb, Ac. Additionally, phosphate and hydroxyl groups may be substituted by F and Cl (Oprea et al., 2009; Zimmerman et al., 2015), which was also what we found here.

On the other hand, XRF did reveal differences in the intensity of elemental composition between sound and ERS enamel. The increased intensity observed for trace elements in ERS enamel was probably due to the enamel's reduced thickness and exchanges with the environment. Indeed, in 1989, Frank et al. showed by ED-XRF a higher concentration of Zn and Sr in outer enamel vs. inner enamel (Frank et al., 1989).

Finally, we used EDS to analyze mineral proportion in tissue. Our results showed higher calcium concentration in enamel compared with dentin in healthy teeth, underlining the important proportion of mineral in this calcified tissues. In contrast, ERS enamel and dentin showed similar levels of mineralization, indicating a weakly mineralized enamel. The deficiency left by the lower Ca level in ERS enamel is probably filled by organic species, like proteins. The XRF and EDS methods are complementary owing to their different detection thresholds. Indeed, low-Z elements like oxygen cannot be detected by XRF, whereas the concentrations of the trace elements Sr and Zn were probably too low to be detected by EDS.

The present study evidenced alterations in patients carrying *FAM20A* mutations, with major disturbances in enamel morphogenesis and biomineralization. SEM and physicochemical methods highlighted specific mineral morphology or composition, suggesting some pathological mechanisms and revealing conditions of the mineral formation. In ERS enamel, we observed a prismatic-like structure exclusively in the most internal enamel, suggesting normal initiation of the amelogenesis process. In contrast, in the rest of the enamel, our SEM data highlight the heterogeneity of ERS enamel structure. SEM imaging revealed nano- to micro-meter nodules, increasing in size from the outer to the inner zones. This would suggest that, in contrast to normal enamel in which enamel crystals continuously elongate throughout the enamel thickness, independent nanonodules would be produced which fuse to form micronodules. This process, also observed in the adjoining soft tissues shows some similarities with ectopic mineralization described in the gingiva (Vogel et al., 2012). The produced tissue remains highly heterogeneous and the spatial distribution of atomic mineralization's markers (Ca and P) is strongly disturbed.

The role of FAM20A in amelogenesis may be indirect, as FAM20A binds FAM20C kinase to promote phosphorylation of secreted polypeptides *in vitro* (Ohyama et al., 2016). Indeed, the three major enamel matrix proteins (AMEL, AMBN, and ENAM) contain the amino-acid motif enabling phosphorylation by FAM20C. Furthermore, several studies have demonstrated the essential role of EMP phosphorylation during amelogenesis. First, in 2010, Chan et al. showed that, in humans, lack of ENAM phosphorylation gives rise to AI (Chan et al., 2010); in cases where only one allele was affected, minor pitting or enamel hypoplasia was observed. In patients where both alleles were affected, severe enamel malformations were observed, with little or no mineralize material covering the dentin. In 2016, Ma et al., using transgenic mice with a phosphorylation-defective AMBN polypeptide, found severe enamel defects such as hypoplasia, severely disturbed enamel rods and interrod structure, and enamel matrix invading the ameloblast layer (Ma et al., 2016). Thus, it may be hypothesized that FAM20A loss of function would result in reduced phosphorylation of EMPs, thus disrupting amelogenesis beyond the first stages of inner enamel deposition, and leading to a poorly mineralized matrix.

A second physiological role for FAM20A would be to inhibit ectopic mineralization. Indeed, *FAM20A* mutations in humans (this report) or *Fam20A* deficiency in mouse knockout (KO) models are associated with ectopic mineralization in the gingiva and enamel organ, suggesting that some mineralization inhibitors may be additional FAM20A targets. Among many potential candidates, fetuin may be one such putative inhibitor.

Indeed, fetuin deficiency results in an ectopic calcification phenotype, resembling that in *Fam20a* KO mice (Schäfer et al., 2003; Vogel et al., 2012; Ohyama et al., 2016).

In order to define more definitively this sequence of enamel formation and/or ectopic mineral deposition in the context of *FAM20A* gene mutations, an ultrastructural analysis of enamel, of the produced EMPs and extracellular peptides in the available animal models would be of great interest.

AUTHOR CONTRIBUTIONS

Conceived and designed the experiments: GL, FB, AD, and AB. Performed the experiments: GL, FB, AD, SR, and RW. Analyzed the data: GL, FB, AB, and AD. Wrote the paper: GL, FB, RK, and AD. Teeth were collected by MQ, MD and AN.

ACKNOWLEDGMENTS

The authors thank Ludovic Mouton for his technical assistance during SEM observations, Veronique Brouet and David Montero for their technical assistance during EDS implementations. The SU-70 Hitachi SEM-FEG instrumentation was provided by the IMPC FR2482 (Institut des Matériaux de Paris Centre) and financially supported by the C'Nano projects of the Region Ile-de-France. This study was supported by grant Idex SPC "Once upon a tooth" (grant number: ANR-11-IDEX-0005-02; AB and AD) for its financial support.

REFERENCES

Acevedo, A. C., Poulter, J. A., Alves, P. G., De Lima, C. L., Castro, L. C., Yamaguti, P. M., et al. (2015). Variability of systemic and oro-dental phenotype in two families with non-lethal raine syndrome with FAM20C mutations. *BMC Med. Genet.* 16:5. doi: 10.1186/s12881-015-0154-5

Al-Jawad, M., Addison, O., Khan, M. A., James, A., and Hendriksz, C. J. (2012). Disruption of enamel crystal formation quantified by synchrotron microdiffraction. *J. Dent.* 40, 1074–1080. doi: 10.1016/j.jdent.2012.08.020

Barron, M. J., Brookes, S. J., Kirkham, J., Shore, R. C., Hunt, C., Mironov, A., et al. (2010). A Mutation in the Mouse Amelx Tri-Tyrosyl domain results in impaired secretion of amelogenin and phenocopies human X-linked amelogenesis imperfecta. *Hum. Mol. Genet.* 19, 1230–1247. doi: 10.1093/hmg/ddq001

Bazin, D., Carpentier, X., Brocheriou, I., Dorfmuller, P., Aubert, S., Chappard, C., et al. (2009). Revisiting the Localisation of Zn^{2+} cations sorbed on pathological apatite calcifications made through X-Ray absorption spectroscopy. *Biochimie* 91, 1294–1300. doi: 10.1016/j.biochi.2009.05.009

Bazin, D., Dessombz, A., Nguyen, C., Ea, H. K., Lioté, F., Rehr, J., et al. (2014). The status of strontium in biological apatites: an XANES/EXAFS investigation. *J. Synchrotron Radiat.* 21, 136–142. doi: 10.1107/S1600577513023771

Berès, F., Isaac, J., Mouton, L., Rouzière, S., Berdal, A., Simon, S., et al. (2016). Comparative physicochemical analysis of pulp stone and dentin. *J. Endod.* 42, 432–438. doi: 10.1016/j.joen.2015.11.007

Bhesania, D., Arora, A., and Kapoor, S. (2015). Enamel renal syndrome with associated amelogenesis imperfecta, nephrolithiasis, and hypocitraturia: a case report. *Imaging Sci. Dent.* 45, 181–185. doi: 10.5624/isd.2015.45.3.181

Bone, H. G., Chapurlat, R., Brandi, M. L., Brown, J. P., Czerwiński, E., Krieg, M. A., et al. (2013). The effect of three or six years of denosumab exposure in women with postmenopausal osteoporosis: results from the freedom extension. *J. Clin. Endocrinol. Metab.* 98, 4483–4492. doi: 10.1210/jc.2013-1597

Cabral, R. M., Kurban, M., Rothman, L., Wajid, M., Shimomura, Y., Petukhova, L., et al. (2013). Autosomal recessive gingival hyperplasia and dental anomalies caused by a 29-base pair duplication in the FAM20A gene. *J. Hum. Genet.* 58, 566–567. doi: 10.1210/jc.2013-1597

Chaitanya, V., Sangeetha, B., Sandeep, P., Varalaxmi, B., Sridhar, A. V., Aparna, G., et al. (2014). Amelogenesis imperfecta and nephrocalcinosis syndrome. *Indian J. Nephrol.* 24, 260–261. doi: 10.4103/0971-4065.133043

Chan, H. C., Mai, L., Oikonomopoulou, A., Chan, H. L., Richardson, A. S., Wang, S. K., et al. (2010). Altered enamelin phosphorylation site causes amelogenesis imperfecta. *J. Dent. Res.* 89, 695–699. doi: 10.1210/jc.2013-1597

Cui, J., Xiao, J., Tagliabracci, V. S., Wen, J., Rahdar, M., and Dixon, J. E. (2015). A secretory kinase complex regulates extracellular protein phosphorylation. *Elife* 4:e06120. doi: 10.7554/elife.06120

de la Dure-Molla, M., Quentric, M., Yamaguti, P. M., Acevedo, A. C., Mighell, A. J., Vikkula, M., et al. (2014). Pathognomonic oral profile of Enamel Renal Syndrome (ERS) caused by recessive FAM20A mutations. *Orphanet J. Rare Dis.* 9:84. doi: 10.1186/1750-1172-9-84

Dessombz, A., Lignon, G., Picaut, L., Rouzière, S., and Berdal, A. (2015). Mineral studies in enamel, an exemplary model system at the interface between physics, chemistry and medical sciences. *C. R. Chim.* 19, 1656–1664. doi: 10.1016/j.crci.2015.03.009

Dessombz, A., Nguyen, C., Ea, H. K., Rouzière, S., Foy, E., Hannouche, D., et al. (2013). Combining μX-Ray fluorescence, μXANES and μXRD to shed light on Zn^{2+} cations in cartilage and meniscus calcifications. *J. Trace Elem. Med. Biol.* 27, 326–333. doi: 10.1016/j.jtemb.2013.02.001

Elalaoui, S. C., Al-Sheqaih, N., Ratbi, I., Urquhart, J. E., O'Sullivan, J., Bhaskar, S., et al. (2016). Non lethal raine syndrome and differential diagnosis. *Eur. J. Med. Genet.* 59, 577–583. doi: 10.1016/j.ejmg.2016.09.018

Frank, R. M., Sargentini-Maier, M. L., Turlot, J. C., and Leroy, M. J. (1989). Zinc and strontium analyses by energy dispersive X-Ray fluorescence in human permanent teeth. *Arch. Oral Biol.* 34, 593–597. doi: 10.1016/0003-9969(89)90012-5

Hao, J., Narayanan, K., Muni, T., Ramachandran, A., and George, A. (2007). Dentin matrix protein 4, a novel secretory calcium-binding protein that modulates odontoblast differentiation. *J. Biol. Chem.* 282, 15357–15365. doi: 10.1074/jbc.M701547200

Jaouad, I., El Alloussi, M., El Alaoui, S., Laarabi, F. Z., Lyahyai, J., and Sefiani, A. (2015). Further evidence for causal FAM20A mutations and first case of amelogenesis imperfecta and gingival hyperplasia syndrome in morocco: a case report. *BMC Oral Health* 15:14. doi: 10.1186/1472-6831-15-14

Jaureguiberry, G., De la Dure-Molla, M., Parry, D., Quentric, M., Himmerkus, N., Koike, T., et al. (2012). Nephrocalcinosis (Enamel Renal Syndrome) caused by autosomal recessive FAM20A mutations. *Nephron. Physiol.* 122, 1–6. doi: 10.1159/000349989

Kim, Y. J., Seymen, F., Koruyucu, M., Kasimoglu, Y., Gencay, K., Shin, T. J., et al. (2016). Unexpected identification of a recurrent mutation in the DLX3 gene causing amelogenesis imperfecta. *Oral Dis.* 22, 297–302. doi: 10.1111/odi.12439

Koike, T., Izumikawa, T., Tamura, J., and Kitagawa, H. (2009). FAM20B is a kinase that phosphorylates xylose in the glycosaminoglycan-protein linkage region. *Biochem. J.* 421, 157–162. doi: 10.1042/BJ20090474

Li, L. L., Liu, P. H., Xie, X. H., Ma, S., Liu, C., Chen, L., et al. (2016). Loss of epithelial FAM20A in mice causes amelogenesis imperfecta, tooth eruption delay and gingival overgrowth. *Int. J. Oral Sci.* 8, 98–109. doi: 10.1038/ijos.2016.14

Lignon, G., de la Dure-Molla, M., Dessombz, A., Berdal, A., and Babajko, S. (2015). Enamel: a unique self-assembling in mineral world. *Méd. Sci.* 31, 515–521. doi: 10.1051/medsci/20153105013

Ma, P., Yan, W., Tian, Y., He, J., Brookes, S. J., and Wang, X. (2016). The importance of serine phosphorylation of ameloblastin on enamel formation. *J. Dent. Res.* 95, 1408–1414. doi: 10.1177/0022034516661513

Nalbant, D., Youn, H., Nalbant, S. I., Sharma, S., Cobos, E., Beale, E. G., et al. (2005). FAM20: an evolutionarily conserved family of secreted proteins expressed in hematopoietic cells. *BMC Genomics* 6:11. doi: 10.1186/1471-2164-6-11

O'Sullivan, J., Bitu, C. C., Daly, S. B., Urquhart, J. E., Barron, M. J., Bhaskar, S. S., et al. (2011). Whole-exome sequencing identifies FAM20A mutations as a cause

of amelogenesis imperfecta and gingival hyperplasia syndrome. *Am. J. Hum. Genet.* 88, 616–620. doi: 10.1016/j.ajhg.2011.04.005

Ohyama, Y., Lin, J. H., Govitvattana, N., Lin, I. P., Venkitapathi, S., Alamoudi, A., et al. (2016). FAM20A binds to and regulates FAM20C localization. *Sci. Rep.* 6:27784. doi: 10.1038/srep27784

Oprea, C., Szalanski, P. J., Gustova, M. V., Oprea, I. A., and Buzguta, V. (2009). Multivariate comparison of elemental concentrations in human teeth. *Appl. Radiat. Isot.* 67, 2142–2145. doi: 10.1016/j.apradiso.2009.04.017

Parry, D. A., Smith, C. E., El-Sayed, W., Poulter, J. A., Shore, R. C., Logan, C. V., et al. (2016). Mutations in the pH-sensing G-protein-coupled receptor GPR68 cause amelogenesis imperfecta. *Am. J. Hum. Genet.* 99, 984–990. doi: 10.1016/j.ajhg.2016.08.020

Poulter, J. A., Murillo, G., Brookes, S. J., Smith, C. E., Parry, D. A., Silva, S., et al. (2014). Deletion of ameloblastin exon 6 is associated with amelogenesis imperfecta. *Hum. Mol. Genet.* 23, 5317–5324. doi: 10.1093/hmg/ddu247

Poulter, J. A., Smith, C. E., Murrillo, G., Silva, S., Feather, S., Howell, M., et al. (2015). A distinctive oral phenotype points to FAM20A mutations not identified by sanger sequencing. *Mol. Genet. Genomic Med.* 3, 543–549. doi: 10.1002/mgg3.164

Prasad, M. K., Geoffroy, V., Vicaire, S., Jost, B., Dumas, M., Le Gras, S., et al. (2016). A targeted next-generation sequencing assay for the molecular diagnosis of genetic disorders with orodental involvement. *J. Med. Genet.* 53, 98–110. doi: 10.1136/jmedgenet-2015-103302

Ren, F., Xin, R., Ge, X., and Leng, Y. (2009). Characterization and structural analysis of zinc-substituted hydroxyapatites. *Acta Biomater.* 5, 3141–3149. doi: 10.1016/j.actbio.2009.04.014

Salido, E. C., Yen, P. H., Koprivnikar, K., Yu, L. C., and Shapiro, L. J. (1992). The human enamel protein gene amelogenin is expressed from both the X and the Y chromosomes. *Am. J. Hum. Genet.* 50, 303–316.

Schäfer, C., Heiss, A., Schwarz, A., Westenfeld, R., Ketteler, M., Floege, J., et al. (2003). The serum protein α2–heremans-schmid glycoprotein/fetuin-A is a systemically acting inhibitor of ectopic calcification. *J. Clin. Invest.* 112, 357–366. doi: 10.1172/JCI17202

Schroeder, H. A., Tipton, I. H., and Nason, A. P. (1972). Trace metals in man: strontium and barium. *J. Chronic Dis.* 25, 491–517. doi: 10.1016/0021-9681(72)90150-6

Seymen, F., Kim, Y. J., Lee, Y. J., Kang, J., Kim, T. H., Choi, H., et al. (2016). Recessive mutations in ACPT, encoding testicular acid phosphatase, cause hypoplastic amelogenesis imperfecta. *Am. J. Hum. Genet.* 99, 1199–1205. doi: 10.1016/j.ajhg.2016.09.018

Seymen, F., Park, J. C., Lee, K. E., Lee, H. K., Lee, D. S., Koruyucu, M., et al. (2015). Novel MMP20 and KLK4 mutations in amelogenesis imperfecta. *J. Dent. Res.* 94, 1063–1069. doi: 10.1177/0022034515590569

Simmons, L. M., Al-Jawad, M., Kilcoyne, S. H., and Wood, D. J. (2011). Distribution of enamel crystallite orientation through an entire tooth crown studied using synchrotron X-Ray diffraction. *Eur. J. Oral Sci.* 19(Suppl. 1), 19–24. doi: 10.1111/j.1600-0722.2011.00909.x

Solé, V. A., Papillon, E., Cotte, M., Walter, P., and Susini, J. (2007). A multiplatform code for the analysis of energy-dispersive X-Ray fluorescence spectra. *Spectrochim. Acta Part B Atom. Spectrosc.* 62, 63–68. doi: 10.1016/j.sab.2006.12.002

Tagliabracci, V. S., Engel, J. L., Wen, J., Wiley, S. E., Worby, C. A., Kinch, L. N., et al. (2012). Secreted kinase phosphorylates extracellular proteins that regulate biomineralization. *Science* 336, 1150–1153. doi: 10.1126/science.1217817

Vogel, P., Hansen, G. M., Read, R. W., Vance, R. B., Thiel, M., Liu, J., et al. (2012). Amelogenesis imperfecta and other biomineralization defects in FAM20A and FAM20C null mice. *Vet. Pathol.* 49, 998–1017. doi: 10.1177/0300985812453177

Volodarsky, M., Zilberman, U., and Birk, O. S. (2015). Novel FAM20A mutation causes autosomal recessive amelogenesis imperfecta. *Arch. Oral Biol.* 60, 919–922. doi: 10.1016/j.archoralbio.2015.02.018

Wang, S. K., Aref, P., Hu, Y., Milkovich, R. N., Simmer, J. P., El-Khateeb, M., et al. (2013). FAM20A mutations can cause Enamel-Renal Syndrome (ERS). *PLoS Genet.* 9:e1003302. doi: 10.1371/journal.pgen.1003302

Wang, S. K., Reid, B. M., Dugan, S. L., Roggenbuck, J. A., Read, L., Aref, P., et al. (2014). FAM20A mutations associated with enamel renal syndrome. *J. Dent. Res.* 93, 42–48. doi: 10.1177/0022034513512653

Yamaguti, P. M., Neves, F. A., Hotton, D., Bardet, C., de La Dure-Molla, M., Castro, L. C., et al. (2017). Amelogenesis imperfecta in familial hypomagnesaemia and hypercalciuria with nephrocalcinosis caused by CLDN19 gene mutations. *J. Med. Genet.* 54, 26–37. doi: 10.1136/jmedgenet-2016-103956

Zimmerman, H. A., Meizel-Lambert, C. J., Schultz, J. J., and Sigman, M. E. (2015). Chemical differentiation of osseous, dental, and non-skeletal materials in forensic anthropology using elemental analysis. *Sci. Justice* 55, 131–138. doi: 10.1016/j.scijus.2014.11.003

Conflict of Interest Statement: The authors declare that the research was conducted in the absence of any commercial or financial relationships that could be construed as a potential conflict of interest.

Copyright © 2017 Lignon, Beres, Quentric, Rouzière, Weil, De La Dure-Molla, Naveau, Kozyraki, Dessombz and Berdal. This is an open-access article distributed under the terms of the Creative Commons Attribution License (CC BY). The use, distribution or reproduction in other forums is permitted, provided the original author(s) or licensor are credited and that the original publication in this journal is cited, in accordance with accepted academic practice. No use, distribution or reproduction is permitted which does not comply with these terms.

frontiers in Physiology

ORIGINAL RESEARCH
published: 20 April 2017
doi: 10.3389/fphys.2017.00229

Analyses of *MMP20* Missense Mutations in Two Families with Hypomaturation Amelogenesis Imperfecta

*Youn Jung Kim[1], Jenny Kang[2], Figen Seymen[3], Mine Koruyucu[3], Koray Gencay[3], Teo Jeon Shin[2], Hong-Keun Hyun[2], Zang Hee Lee[4], Jan C.-C. Hu[5], James P. Simmer[5] and Jung-Wook Kim[1,2]**

[1] Department of Molecular Genetics and Dental Research Institute, School of Dentistry, Seoul National University, Seoul, Korea, [2] Department of Pediatric Dentistry and Dental Research Institute, School of Dentistry, Seoul National University, Seoul, Korea, [3] Faculty of Dentistry, Department of Pedodontics, Istanbul University, Istanbul, Turkey, [4] Department of Cell and Developmental Biology and Dental Research Institute, School of Dentistry, Seoul National University, Seoul, Korea, [5] Department of Biologic and Materials Sciences, University of Michigan School of Dentistry, Ann Arbor, MI, USA

OPEN ACCESS

Edited by:
Ariane Berdal, UMRS 1138 INSERM University Paris-Diderot Team POM, France

Reviewed by:
Flavia Martinez De Carvalho, Oswaldo Cruz Foundation, Brazil
Rafaela Scariot De Moraes, Universidade Positivo, Brazil
Agnes Bloch-Zupan, University of Strasbourg, France

***Correspondence:**
Jung-Wook Kim
pedoman@snu.ac.kr

Specialty section:
This article was submitted to Craniofacial Biology and Dental Research, a section of the journal Frontiers in Physiology

Received: *10 February 2017*
Accepted: *31 March 2017*
Published: *20 April 2017*

Citation:
Kim YJ, Kang J, Seymen F, Koruyucu M, Gencay K, Shin TJ, Hyun H-K, Lee ZH, Hu JCC, Simmer JP and Kim J-W (2017) Analyses of MMP20 Missense Mutations in Two Families with Hypomaturation Amelogenesis Imperfecta. Front. Physiol. 8:229. doi: 10.3389/fphys.2017.00229

Amelogenesis imperfecta is a group of rare inherited disorders that affect tooth enamel formation, quantitatively and/or qualitatively. The aim of this study was to identify the genetic etiologies of two families presenting with hypomaturation amelogenesis imperfecta. DNA was isolated from peripheral blood samples obtained from participating family members. Whole exome sequencing was performed using DNA samples from the two probands. Sequencing data was aligned to the NCBI human reference genome (NCBI build 37.2, hg19) and sequence variations were annotated with the dbSNP build 138. Mutations in *MMP20* were identified in both probands. A homozygous missense mutation (c.678T>A; p.His226Gln) was identified in the consanguineous Family 1. Compound heterozygous *MMP20* mutations (c.540T>A, p.Tyr180∗ and c.389C>T, p.Thr130Ile) were identified in the non-consanguineous Family 2. Affected persons in Family 1 showed hypomaturation AI with dark brown discoloration, which is similar to the clinical phenotype in a previous report with the same mutation. However, the dentition of the Family 2 proband exhibited slight yellowish discoloration with reduced transparency. Functional analysis showed that the p.Thr130Ile mutant protein had reduced activity of MMP20, while there was no functional MMP20 in the Family 1 proband. These results expand the mutational spectrum of the *MMP20* and broaden our understanding of genotype-phenotype correlations in amelogenesis imperfecta.

Keywords: amelogenesis imperfecta, enamelysin, proteinase, enamel, matrix, hypomaturation

INTRODUCTION

Non-syndromic amelogenesis imperfecta (AI), hereditary enamel defects, can be divided into 3 major categories based on the quantity and quality of the enamel (Witkop, 1988). In hypoplastic AI, the enamel is thin with interdental spacing and the affected individuals are often sensitive to thermal changes and possess an increased tendency of anterior open bite (Ravassipour et al., 2005). In hypocalcification AI, the affected enamel is extremely soft with normal thickness

prior to tooth eruption, which may be lost rapidly after eruption leaving the remaining enamel rough, discolored, and thin. Hypomaturation AI is caused by failures during the maturation stage of amelogenesis. The resulting phenotype is characteristically (dark) brown or yellowish discolored less mineralized enamel with normal thickness. But because the enamel is not matured well, prolonged attrition can result in excessive enamel wear facets or localized enamel fractures (Wright et al., 2011). However, definitive characterization of the phenotype may be challenging in some cases. Therefore, a broader classification scheme with two categories has been used: hypoplastic AI and hypomineralized AI. The hypomineralized AI includes hypocalcification AI and hypomaturation AI (Prasad et al., 2016).

To date, mutations in more than 17 genes are involved in non-syndromic AI. Hypoplastic AI can be caused by mutations in *AMELX* (MIM: 300391), *ENAM* (MIM: 606585), *AMBN* (MIM: 601259), *LAMB3* (MIM: 150310), *LAMA3* (MIM: 600805), *COL17A1* (MIM: 113811), *ITGB6* (MIM: 147558), and *ACPT* (MIM: 606362) (Lagerstrom et al., 1991; McGrath et al., 1996; Rajpar et al., 2001; Yuen et al., 2012; Kim et al., 2013; Wang et al., 2014; Poulter et al., 2014a,b,c; Seymen et al., 2016). Autosomal dominant hypocalcification AI is caused by mutations in *FAM83H* (MIM: 611927) (Kim et al., 2008). Some *AMELX* mutations can cause hypomaturation AI with enamel hypoplasia (Hart et al., 2000). Recessive mutations in *SLC24A4* (MIM: 609840), *WDR72* (MIM: 613214), *MMP20* (MIM: 604629), *KLK4* (MIM: 603767), and *GPR68* (MIN: 601404) cause hypomaturation AI (Wright et al., 2003; Hart et al., 2004; Kim et al., 2005; El-Sayed et al., 2009; Parry et al., 2013, 2016). Clinical phenotype caused by autosomal recessive mutations of *C4orf26* (MIM: 614829) and autosomal dominant mutation of *AMTN* (MIM: 610912) were reported as hypomineralization AI (Parry et al., 2012; Smith et al., 2016).

Two proteinases secreted by ameloblasts during mammalian enamel formation are matrix metalloproteinase 20 (MMP20, enamelysin) and kallikrein 4 (KLK4) (Hu et al., 2002). MMP20 is the early protease expressed by ameloblasts throughout the secretory stage and early maturation stage of amelogenesis. KLK4 is the late protease expressed by ameloblasts from the transition stage to the maturation stage. Lack of proteinase function in the maturing enamel matrix prevents proper degradation and removal of the enamel matrix proteins resulting in enamel hypomaturation AI.

Here we report the identification of *MMP20* mutations in two Turkish families with hypomaturation AI by whole exome sequencing and the mutational effect on the protein secretion and proteolytic activity.

MATERIALS AND METHODS

Identification and Enrollment of AI Families

Clinical and radiographic examinations of the probands and their available family members were performed, and blood samples were collected with the understanding and written consent of each participant according to the Declaration of Helsinki. Affected individuals were healthy, except hypomaturation enamel defects. The study protocol was independently reviewed and approved by the Institution Review Board at the Seoul National University Dental Hospital, the University of Istanbul and the University of Michigan.

DNA Isolation and Whole-Exome Sequencing

Genomic DNA was isolated from peripheral whole blood. The purity and concentration of the DNA were quantified by spectrophotometry measurement and the OD_{260}/OD_{280} ratio obtained. Whole-exome sequencing was performed with the DNA sample of the probands using Illumina HiSeq 2000 platform. The NimbleGen (Roche Diagnostics, Indianapolis, IL, USA) exome capture reagent was used for exome capturing.

Autozygosity Mapping

The affected individuals in family 1 (IV:3 and IV:4) were genotyped with the Affymetrix Genome-Wide Human SNP array 6.0 (DNALINK INC., Seoul, Korea). The annotated SNP files were analyzed with HomozygosityMapper (http://www.homozygositymapper.org/) (Seelow et al., 2009) to identify the shared regions of homozygosity in the affected individuals.

Segregation Analysis by Polymerase Chain Reaction (PCR)

The sequence variations in the *MMP20* gene and segregation within each family was confirmed by Sanger sequencing with primers and conditions described previously (Kim et al., 2005). PCR amplifications were done with the HiPi DNA polymerase premix (Elpis Biotech, Daejeon, Korea), and DNA sequencing was performed at a DNA sequencing center (Macrogen, Seoul, Korea).

Cloning and Mutagenesis of the *MMP20* cDNA

Human *MMP20* cDNA, previously cloned into the pcDNA3.1 vector, was used to introduce the identified mutations using PCR mutagenesis (sense: 5′-TACCGTTGCTGCTCAAGAATT TGGCCATGC, antisense: 5′-GCATGGCCAAATTCTTGAGCA GCAACGGTA for the p.His226Gln and sense: 5′-GAATATCTA AATACATACCTTCCATGAGTT, antisense: 5′-AACTCATGG AAGGTATGTATTTAGATATTC for the p.Thr130Ile) (Lee et al., 2010). Sequences of normal and mutant *MMP20* pcDNA3.1 vectors were confirmed by direct plasmid sequencing.

Transfection

HEK293T cells were grown and maintained in DMEM supplemented with 10% FBS and antibiotics in a 5% CO_2 atmosphere at 37°C. Cells at $\sim 2 \times 10^5$ quantity were seeded in each well of the 6-well culture dish. Each plasmid construct at 2 ug quantity was transiently transfected into HEK293T cells with Genjet *in vitro* DNA transfection reagent (SigmaGen Laboratories, Ijamsville, MD, USA). The culture medium of each well was harvested after 30 h of incubation and concentrated using Amicon ultra-4 centrifugal filter units (Millipore, Bedford, MA, USA).

Zymography

Four ml of conditioned medium from the culture was collected and concentrated to 50 ul. The concentrated media of 20 ul was mixed with 4 ul of 5x non-reducing buffer, then loaded onto the 11% SDS-polyacrylamide gel with β-casein (Sigma-Aldrich, St. Louis, MO, USA) as a substrate. The zymogram was developed, stained with Coomassie brilliant blue R-250 staining solution (Bio-rad, Hercules, CA, USA) for 20 min, and visualized after incubation in a destaining solution (10% MeOH, 10% acetic acid) for 3 h.

Western Blot

Concentrated media and cell lysates were run on the 11% SDS-polyacrylamide gel and subjected to Western blotting. Specifically, 50 ug cell lysate from each sample and 10 ul of concentrated media were used. After gel transfer to the PVDF membrane and blocking, MMP20 was detected by incubating the membrane with primary antibody overnight at 4°C and with secondary antibody for 2 h at room temperature. The primary antibodies used were a rabbit polyclonal anti-MMP20 antibody (ab39038, abcam plc., Cambridge, UK) and a mouse monoclonal anti-ACTB antibody (A2228, Sigma-Aldrich, St. Louis, MO, USA); both of which were diluted in 1:10,000.

RESULTS

Clinical Phenotype

The proband of Family 1 (IV:4) was an 11-year-old girl from a consanguineous marriage of first cousins (**Figure 1A**). Her prenatal and perinatal history was uneventful and her parents reported no other medical problem. Her teeth exhibited generalized brown discoloration with exogenous black pigmentation mainly on occlusal surface of the posterior teeth (**Figures 1B–D**). Maxillary left central incisor was lost due to trauma. The radiopacity of enamel did not contrast well with dentin in the panoramic radiograph, consistent with hypomineralization (**Figure 1E**). Her 24-year-old brother (IV:3) was also affected and almost all of his teeth have been reconstructed with full-coverage prosthodontics. His remaining natural teeth exhibited dark brown discoloration with exogenous pigmentation (Figure S1).

The proband of the family 2 (III:1) was a 10-year-old girl from a non-consanguineous family (**Figure 2A**). Her past medical history was unremarkable. Her anterior permanent teeth were not severely discolored, but slightly yellow and less transparent than normal teeth (**Figures 2B,C**). Her right second premolar was congenitally absent based on the panoramic radiograph (**Figure 2D**).

Mutational Analysis

Sequencing reads were aligned to the UCSC human reference genome (hg19) with Burrow-Wheeler Aligner, and the sequence variations were annotated by referencing dbSNP build 138, which preceded variant calling with SAMtools and GATK (Table S1). Annotated variants were filtered with the criteria of minor allele frequency of 0.01.

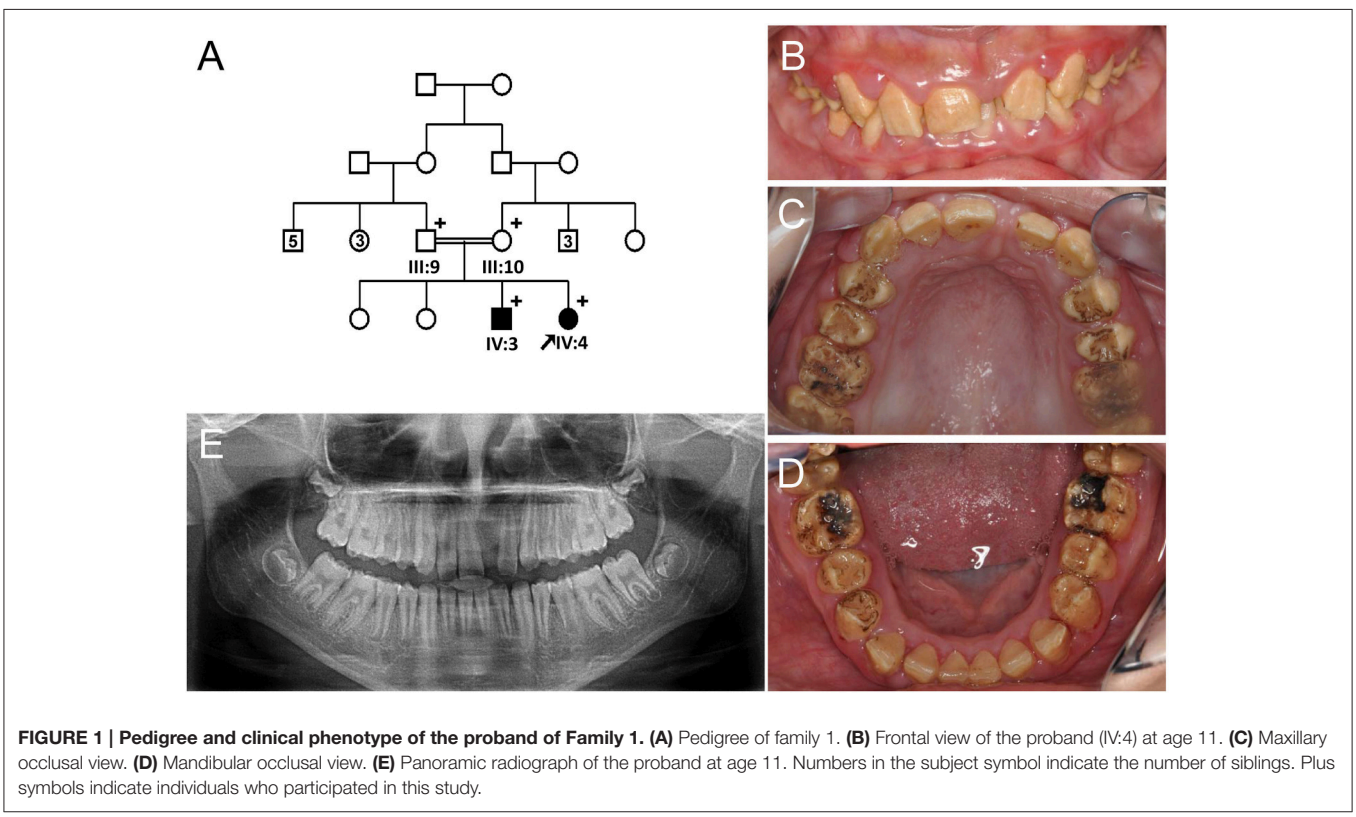

FIGURE 1 | Pedigree and clinical phenotype of the proband of Family 1. (A) Pedigree of family 1. **(B)** Frontal view of the proband (IV:4) at age 11. **(C)** Maxillary occlusal view. **(D)** Mandibular occlusal view. **(E)** Panoramic radiograph of the proband at age 11. Numbers in the subject symbol indicate the number of siblings. Plus symbols indicate individuals who participated in this study.

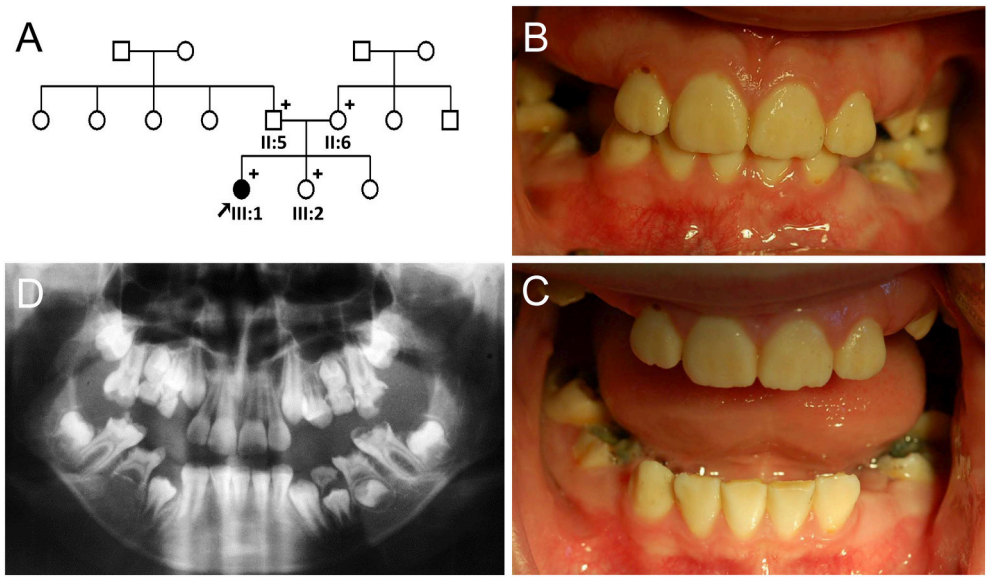

FIGURE 2 | Pedigree and clinical phenotype of the proband of Family 2. (A) Pedigree of family 2. **(B)** Frontal view of the proband (III:1) at age 10. **(C)** Frontal view with bite open. **(D)** Panoramic radiograph of the proband at age 10. Plus symbols indicate individuals who participated in this study.

Autozygosity mapping of the family 1 revealed 3 shared regions of loss of heterozygosity: chr4:65,904,881–82,427,846, chr11:83,358,629–113,318,007, and chr21:11,039,570–17,728,224 (Figure S2). The exome data in the shared regions of the proband in family 1 revealed a homozygous variant in exon 5 of the *MMP20* gene (NM_004771.3: c.678T>A). This transversion of thymine to adenine changed histidine to glutamine at amino acid position 226 (p.His226Gln). There was no other variation in the known AI-causing genes and the *MMP20* mutation (c.678T>A, p.His226Gln) was previously reported as an AI-causing mutation (Ozdemir et al., 2005; Wright et al., 2011).

Whole exome sequencing of the Family 2 proband revealed compound heterozygous *MMP20* mutations (c.389C>T and c.540T>A). There was no other variation in the known AI-causing genes. A cytosine to thymine transition in exon 3 changed threonine to isoleucine at amino acid position 130 (p.Thr130Ile). This variation was listed in the Exome Aggregation Consortium (ExAC) database (rs61730849) with an allele frequency of 0.00165 (200/121176). But the frequency was relatively high (0.0294) in a certain subset of small population (ss86247256, AGI_ASP_population; Coriell Apparently Healthy Collection). In addition, it was previously reported as a disease-causing mutation (Gasse et al., 2013). The other variation, a transversion of thymine to adenine in exon 4, would introduce a premature stop codon (p.Tyr180∗) and the mutant transcript would be degraded by the nonsense-mediated decay system. This variant was not listed in any database.

Segregation within the families by Sanger sequencing confirmed that the nonsense mutation (c.540T>A, p.Tyr180∗) was transmitted paternally and the missense mutation (c.389C>T, p.Thr130Ile) was transmitted maternally to the proband (**Figure 3A**, Figure S3). These amino acids at the mutation sites (Thr130, Tyr180, and His226) are strictly conserved among eutherian mammal orthologs (**Figure 3B**).

Western blotting and zymography determining the function of the MMP20 mutants demonstrated that the p.Thr130Ile mutant protein was secreted at a reduced amount and had proteolytic activity. Western blot of cell lysate revealed that the p.His226Gln mutant protein was retained in the cell and likely not able to be secreted (**Figures 3C,D**).

DISCUSSION

MMP20 is one of 23 human matrix metalloproteinases. It processes structural enamel matrix proteins into functional fragments in the secretory stage and facilitates the removal of those proteins during the maturation stage. *MMP20* gene is located in a cluster with 7 other MMPs on chromosomal location 11q22.3. *MMP20* encodes a 483-amino-acid protein, which has a signal peptide (Met1 to Ala22), a prodomain (Ala23 to Asn107), a catalytic domain (Tyr108 to Gly271), a linker (Pro272 to Leu295) and a hemopexin domain (Cys296 to Cys483) (Llano et al., 1997).

The homozygous missense mutation (c.678T>A, p.His226Gln) identified in Family 1 was previously reported (Ozdemir et al., 2005; Wright et al., 2011). His226 is one of the three histidine residues involved in the coordination of zinc ion at the active site (Llano et al., 1997). This study showed that the p.His226Gln mutant protein cannot be secreted into the developing extracellular matrix, probably due to a structural change in the core area of the protein.

The Family 2 proband had a paternal nonsense mutation (c.540T>A, p.Tyr180∗) and a maternal missense mutation (c.389C>T, p.Thr130Ile) (Gasse et al., 2013). This novel nonsense mutation would introduce a premature stop codon in exon 4, so the mutant mRNA transcript would be degraded by the nonsense-mediated decay system. This study

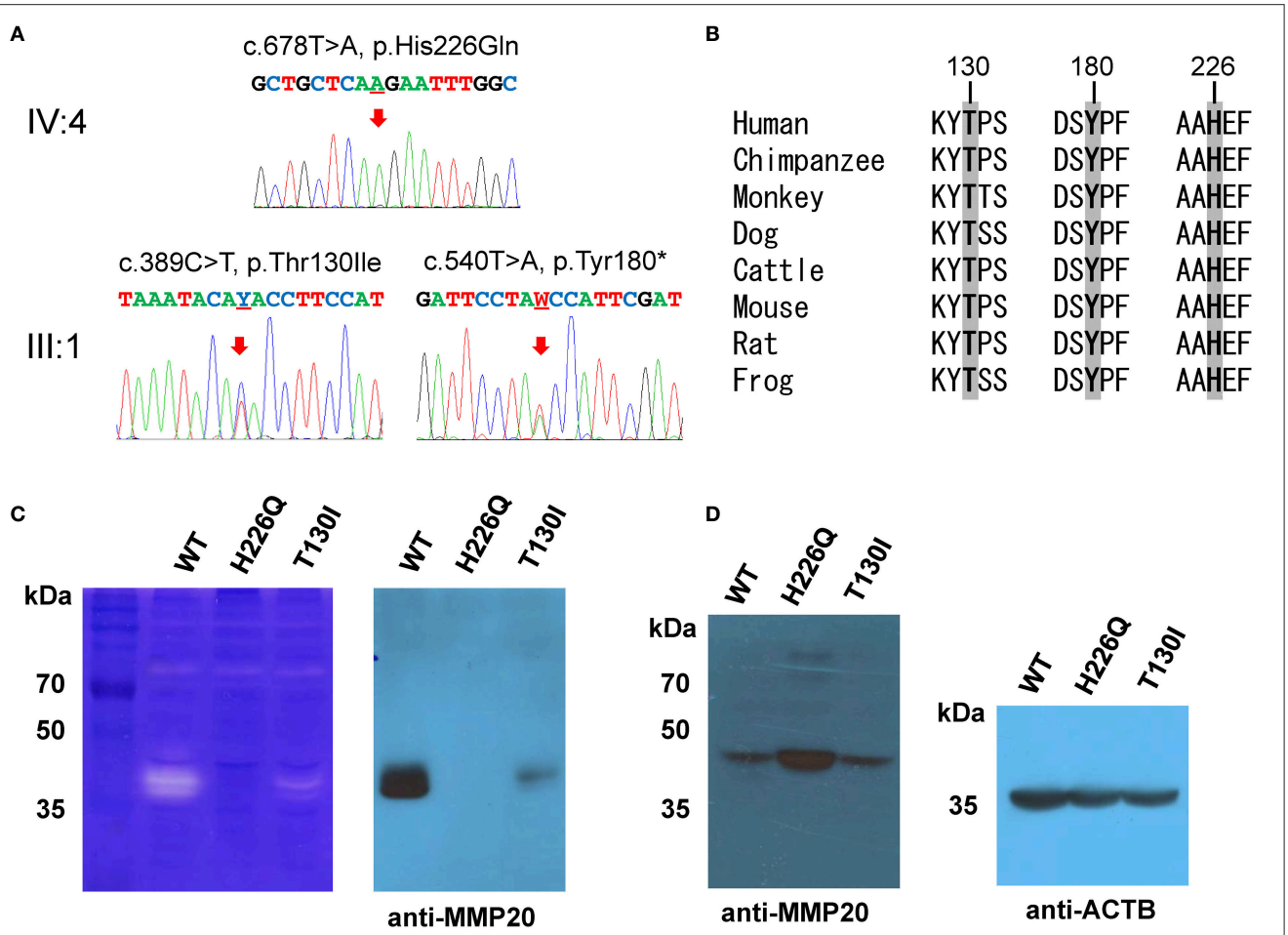

FIGURE 3 | Orthologs alignment, sequencing chromatograms and *in vitro* translation. (A) Sanger sequencing chromatograms of the probands (IV:4 of family 1 and III:1 of family 2). The mutated nucleotide is indicated by a red arrow and underlined (Y; C or T and W; A or T). **(B)** Sequence alignment of vertebrate orthologs. Amino acids affected by the mutations are indicated with bold character and gray highlight. Numbers above the amino acids are based on the human MMP20 sequence. **(C)** Casein zymography indicated that the p.Thr130Ile mutant protein retains proteolytic function, but the p.His226Gln mutant protein has no proteolytic activity. Western blot of the conditioned media revealed that the secretion of the p.Thr130Ile mutant protein into the culture media was greatly reduced, but the p.His226Gln mutant protein cannot be secreted at all. **(D)** Western blot of the cell lysate demonstrated that the p.His226Gln mutant protein remained in the cell. (ACTB: beta actin).

TABLE 1 | Disease-causing mutations of the MMP20 gene.

Location	cDNA	Protein	Mode of inheritance	References
Exon 1	c.102G>A	p.Trp34*	AR homo	Papagerakis et al., 2008; Chan et al., 2011
Exon 2	c.359delA	p.Asn120Ilefs*3	AR paternal	Gasse et al., 2013
Exon 3	c.389C>T	p.Thr130Ile	AR maternal / AR homo	Gasse et al., 2013
Exon 4	c.540T>A	p.Tyr180*	AR paternal	This report
Exon 4	c.611A>G	p.His204Arg	AR homo	Wang et al., 2013
Exon 5	c.678T>A	p.His226Gln	AR homo	Ozdemir et al., 2005; Wright et al., 2011
Exon 6	c.910G>A	p.Ala304Thr	AR homo	Lee et al., 2010
Intron 6	c.954-2A>T	p.0 or p.Ile319* or p.Ile319Serfs*20	AR homo	Kim et al., 2005; Wright et al., 2011
Exon 7	c.1054G>A	p.Glu352Lys	AR homo	Seymen et al., 2015

*Sequences based on the reference sequence for mRNA (NM_004771.3) and protein (NP_004762.2), where the A of the ATG translation initiation codon is designated as nucleotide 1.

showed that the p.Thr130Ile mutant protein could be secreted into the developing enamel matrix and retained proteolytic function.

The functional analysis suggested that the Family 2 proband would have reduced MMP20 activity, while there's no functional MMP20 in the Family 1 proband. This reduced functional

activity of MMP20 potentially explains the difference in clinical phenotype between the probands of these two families. Among nine mutations in *MMP20* gene reported to date (Kim et al., 2005; Ozdemir et al., 2005; Papagerakis et al., 2008; Lee et al., 2010; Wright et al., 2011; Gasse et al., 2013; Wang et al., 2013; Seymen et al., 2015), mutations presumed to have retained functional activity would likely present less severe discoloration compared to nullifying mutations (**Table 1**). The degree of discoloration could be an indicator of the enamel porosity and reflects an altered level of maturation. Therefore, such clinical feature reflecting enamel quality should be considered by clinicians when devising a treatment plan for the patient.

As mutations of the *MMP20* gene are characterized, their functional impact investigated, and clinical features of the affected individuals documented, it will enhance our ability to establish genotype and phenotype correlation and provide the needed evidence to improve clinical diagnosis and management of patients with AI.

AUTHOR CONTRIBUTIONS

Study design: FS, JH, JS, and JWK. Data collection: MK, KG, TS, HH, and ZL. Data analysis: YK, MK, KG, TS, HH, and JWK. Drafting manuscript: YK, JH, JS, and JWK. Revising manuscript content: JK, JH, JS, and JWK. Approving final version of manuscript: YK, JK, FS, MK, KG, TS, HH, ZL, JH, JS, and JWK. JWK takes responsibility for the integrity of the data analysis.

FUNDING

This work was supported by grants from the National Research Foundation of Korea (NRF) grant funded by the Korea government (2014R1A2A1A11049931) and the National Institute for Dental and Craniofacial Research (DE015846).

ACKNOWLEDGMENTS

The authors sincerely thank all the family members for their participation in this study.

SUPPLEMENTARY MATERIAL

The Supplementary Material for this article can be found online at: http://journal.frontiersin.org/article/10.3389/fphys.2017.00229/full#supplementary-material

REFERENCES

Chan, H. C., Estrella, N. M., Milkovich, R. N., Kim, J. W., Simmer, J. P., and Hu, J. C. (2011). Target gene analyses of 39 amelogenesis imperfecta kindreds. *Eur. J. Oral Sci.* 119(Suppl 1), 311–323. doi: 10.1111/j.1600-0722.2011.00857.x

El-Sayed, W., Parry, D. A., Shore, R. C., Ahmed, M., Jafri, H., Rashid, Y., et al. (2009). Mutations in the beta propeller WDR72 cause autosomal-recessive hypomaturation amelogenesis imperfecta. *Am. J. Hum. Genet.* 85, 699–705. doi: 10.1016/j.ajhg.2009.09.014

Gasse, B., Karayigit, E., Mathieu, E., Jung, S., Garret, A., Huckert, M., et al. (2013). Homozygous and compound heterozygous MMP20 mutations in amelogenesis imperfecta. *J. Dent. Res.* 92, 598–603. doi: 10.1177/0022034513488393

Hart, P. S., Hart, T. C., Michalec, M. D., Ryu, O. H., Simmons, D., Hong, S., et al. (2004). Mutation in kallikrein 4 causes autosomal recessive hypomaturation amelogenesis imperfecta. *J. Med. Genet.* 41, 545–549. doi: 10.1136/jmg.2003.017657

Hart, S., Hart, T., Gibson, C., and Wright, J. T. (2000). Mutational analysis of X-linked amelogenesis imperfecta in multiple families. *Arch. Oral Biol.* 45, 79–86. doi: 10.1016/S0003-9969(99)00106-5

Hu, J. C. C., Sun, X., Liu, S., Zhang, C., Bartlett, J. D., and Simmer, J. P. (2002). Enamelysin and kallikrein-4 expression in developing mouse molars. *Eur. J. Oral Sci.* 110, 307–315. doi: 10.1034/j.1600-0722.2002.21301.x

Kim, J. W., Lee, S. K., Lee, Z. H., Park, J. C., Lee, K. E., Lee, M. H., et al. (2008). FAM83H mutations in families with autosomal-dominant hypocalcified amelogenesis imperfecta. *Am. J. Hum. Genet.* 82, 489–494. doi: 10.1016/j.ajhg.2007.09.020

Kim, J. W., Seymen, F., Lee, K. E., Ko, J., Yildirim, M., Tuna, E. B., et al. (2013). LAMB3 Mutations Causing Autosomal-dominant Amelogenesis Imperfecta. *J. Dent. Res.* 92, 899–904. doi: 10.1177/0022034513502054

Kim, J. W., Simmer, J. P., Hart, T. C., Hart, P. S., Ramaswami, M. D., Bartlett, J. D., et al. (2005). MMP-20 mutation in autosomal recessive pigmented hypomaturation amelogenesis imperfecta. *J. Med. Genet.* 42, 271–275. doi: 10.1136/jmg.2004.024505

Lagerstrom, M., Dahl, N., Nakahori, Y., Nakagome, Y., Backman, B., Landegren, U., et al. (1991). A deletion in the amelogenin gene (AMG) causes X-linked amelogenesis imperfecta (AIH1). *Genomics* 10, 971–975. doi: 10.1016/0888-7543(91)90187-J

Lee, S. K., Seymen, F., Kang, H. Y., Lee, K. E., Gencay, K., Tuna, B., et al. (2010). MMP20 hemopexin domain mutation in amelogenesis imperfecta. *J. Dent. Res.* 89, 46–50. doi: 10.1177/0022034509352844

Llano, E., Pendas, A. M., Knauper, V., Sorsa, T., Salo, T., Salido, E., et al. (1997). Identification and structural and functional characterization of human enamelysin (MMP-20). *Biochemistry* 36, 15101–15108. doi: 10.1021/bi972120y

McGrath, J. A., Gatalica, B., Li, K., Dunnill, M. G., McMillan, J. R., Christiano, A. M., et al. (1996). Compound heterozygosity for a dominant glycine substitution and a recessive internal duplication mutation in the type XVII collagen gene results in junctional epidermolysis bullosa and abnormal dentition. *Am. J. Pathol.* 148, 1787–1796.

Ozdemir, D., Hart, P. S., Ryu, O. H., Choi, S. J., Ozdemir-Karatas, M., Firatli, E., et al. (2005). MMP20 active-site mutation in hypomaturation amelogenesis imperfecta. *J. Dent. Res.* 84, 1031–1035. doi: 10.1177/154405910508401112

Papagerakis, P., Lin, H. K., Lee, K. Y., Hu, Y., Simmer, J. P., Bartlett, J. D., et al. (2008). Premature stop codon in MMP20 causing amelogenesis imperfecta. *J. Dent. Res.* 87, 56–59. doi: 10.1177/154405910808700109

Parry, D. A., Brookes, S. J., Logan, C. V., Poulter, J. A., El-Sayed, W., Al-Bahlani, S., et al. (2012). Mutations in C4orf26, encoding a peptide with *in vitro* hydroxyapatite crystal nucleation and growth activity, cause amelogenesis imperfecta. *Am. J. Hum. Genet.* 91, 565–571. doi: 10.1016/j.ajhg.2012.07.020

Parry, D. A., Poulter, J. A., Logan, C. V., Brookes, S. J., Jafri, H., Ferguson, C. H., et al. (2013). Identification of mutations in SLC24A4, encoding a potassium-dependent sodium/calcium exchanger, as a cause of amelogenesis imperfecta. *Am. J. Hum. Genet.* 92, 307–312. doi: 10.1016/j.ajhg.2013.01.003

Parry, D. A., Smith, C. E., El-Sayed, W., Poulter, J. A., Shore, R. C., Logan, C. V., et al. (2016). Mutations in the pH-Sensing G-protein-Coupled Receptor GPR68 Cause Amelogenesis Imperfecta. *Am. J. Hum. Genet.* 99, 984–990. doi: 10.1016/j.ajhg.2016.08.020

Poulter, J. A., Brookes, S. J., Shore, R. C., Smith, C. E., Abi Farraj, L., Kirkham, J., et al. (2014a). A missense mutation in ITGB6 causes pitted hypomineralized amelogenesis imperfecta. *Hum. Mol. Genet.* 23, 2189–2197. doi: 10.1093/hmg/ddt616

Poulter, J. A., El-Sayed, W., Shore, R. C., Kirkham, J., Inglehearn, C. F., and Mighell, A. J. (2014b). Whole-exome sequencing, without prior linkage, identifies a mutation in LAMB3 as a cause of dominant hypoplastic amelogenesis imperfecta. *Eur. J. Hum. Genet.* 22, 132–135. doi: 10.1038/ejhg.2013.76

Poulter, J. A., Murillo, G., Brookes, S. J., Smith, C. E., Parry, D. A., Silva, S., et al. (2014c). Deletion of ameloblastin exon 6 is associated with amelogenesis imperfecta. *Hum. Mol. Genet.* 23, 5317–5324. doi: 10.1093/hmg/ddu247

Prasad, M. K., Laouina, S., El Alloussi, M., Dollfus, H., and Bloch-Zupan, A. (2016). Amelogenesis Imperfecta: 1 Family, 2 Phenotypes, and 2 Mutated Genes. *J. Dent. Res.* 95, 1457–1463. doi: 10.1177/0022034516663200

Rajpar, M. H., Harley, K., Laing, C., Davies, R. M., and Dixon, M. J. (2001). Mutation of the gene encoding the enamel-specific protein, enamelin, causes autosomal-dominant amelogenesis imperfecta. *Hum. Mol. Genet.* 10, 1673–1677. doi: 10.1093/hmg/10.16.1673

Ravassipour, D. B., Powell, C. M., Phillips, C. L., Hart, P. S., Hart, T. C., Boyd, C., et al. (2005). Variation in dental and skeletal open bite malocclusion in humans with amelogenesis imperfecta. *Arch. Oral Biol.* 50, 611–623. doi: 10.1016/j.archoralbio.2004.12.003

Seelow, D., Schuelke, M., Hildebrandt, F., and Nurnberg, P. (2009). HomozygosityMapper–an interactive approach to homozygosity mapping. *Nucleic Acids Res.* 37, W593–W599. doi: 10.1093/nar/gkp369

Seymen, F., Kim, Y. J., Lee, Y. J., Kang, J., Kim, T. H., Choi, H., et al. (2016). Recessive mutations in ACPT, encoding testicular acid phosphatase, cause hypoplastic amelogenesis imperfecta. *Am. J. Hum. Genet.* 99, 1199–1205. doi: 10.1016/j.ajhg.2016.09.018

Seymen, F., Park, J. C., Lee, K. E., Lee, H. K., Lee, D. S., Koruyucu, M., et al. (2015). Novel MMP20 and KLK4 mutations in amelogenesis imperfecta. *J. Dent. Res.* 94, 1063–1069. doi: 10.1177/0022034515590569

Smith, C. E., Murillo, G., Brookes, S. J., Poulter, J. A., Silva, S., Kirkham, J., et al. (2016). Deletion of amelotin exons 3-6 is associated with amelogenesis imperfecta. *Hum. Mol. Genet.* 25, 3578–3587. doi: 10.1093/hmg/ddw203

Wang, S. K., Choi, M., Richardson, A. S., Reid, B. M., Lin, B. P., Wang, S. J., et al. (2014). ITGB6 loss-of-function mutations cause autosomal recessive amelogenesis imperfecta. *Hum. Mol. Genet.* 23, 2157–2163. doi: 10.1093/hmg/ddt611

Wang, S. K., Hu, Y., Simmer, J. P., Seymen, F., Estrella, N. M., Pal, S., et al. (2013). Novel KLK4 and MMP20 mutations discovered by whole-exome sequencing. *J. Dent. Res.* 92, 266–271. doi: 10.1177/00220345134 75626

Witkop, C. J. Jr. (1988). Amelogenesis imperfecta, dentinogenesis imperfecta and dentin dysplasia revisited: problems in classification. *J. Oral Pathol.* 17, 547–553. doi: 10.1111/j.1600-0714.1988.tb01332.x

Wright, J. T., Hart, P. S., Aldred, M. J., Seow, K., Crawford, P. J., Hong, S. P., et al. (2003). Relationship of phenotype and genotype in X-linked amelogenesis imperfecta. *Connect Tissue Res.* 44(Suppl. 1), 72–78. doi: 10.1080/03008200390152124

Wright, J. T., Torain, M., Long, K., Seow, K., Crawford, P., Aldred, M. J., et al. (2011). Amelogenesis imperfecta: genotype-phenotype studies in 71 families. *Cells Tissues Organs* 194, 279–283. doi: 10.1159/0003 24339

Yuen, W. Y., Pasmooij, A. M., Stellingsma, C., and Jonkman, M. F. (2012). Enamel defects in carriers of a novel LAMA3 mutation underlying epidermolysis bullosa. *Acta Derm. Venereol.* 92, 695–696. doi: 10.2340/000155 55-1341

Conflict of Interest Statement: The authors declare that the research was conducted in the absence of any commercial or financial relationships that could be construed as a potential conflict of interest.

Copyright © 2017 Kim, Kang, Seymen, Koruyucu, Gencay, Shin, Hyun, Lee, Hu, Simmer and Kim. This is an open-access article distributed under the terms of the Creative Commons Attribution License (CC BY). The use, distribution or reproduction in other forums is permitted, provided the original author(s) or licensor are credited and that the original publication in this journal is cited, in accordance with accepted academic practice. No use, distribution or reproduction is permitted which does not comply with these terms.

frontiers in Physiology

ORIGINAL RESEARCH
published: 21 September 2017
doi: 10.3389/fphys.2017.00714

A Novel Kinetic Method to Measure Apparent Solubility Product of Bulk Human Enamel

Linda Hassanali[1], Ferranti S. Wong[1], Richard J. M. Lynch[2] and Paul Anderson[1]**

[1] *Dental Physical Sciences Unit, Institute of Dentistry, Queen Mary University of London, London, United Kingdom,*
[2] *Innovation Research and Development, Oral Healthcare, GlaxoSmithKline, Weybridge, United Kingdom*

Introduction: Tooth enamel mineral loss is influenced by its solubility product value, which is fundamental to the understanding of de- and remineralization resulting from a carious or erosive challenge. Published pKsp values for human enamel and hydroxyapatite range from 110 to 126 suggesting a heterogeneous nature of enamel solubility. However, this range of values may also result from the variety of methods used, e.g., some authors reporting values for suspensions of enamel powder and others for bulk enamel. The aim of this study was to develop a method to measure the solubility of bulk human enamel under controlled *in vitro* conditions simulating demineralization behavior of enamel within the oral environment using scanning microradiography (SMR). SMR was used to monitor real-time changes in enamel demineralization rates at increasing calcium concentrations in a caries simulating demineralization solution until the concentration at which thermodynamic equilibrium between enamel and solution was achieved.

Method: 2 mm thick caries free erupted human enamel slabs with the natural buccal surfaces exposed were placed in SMR cells exposed to circulating caries-simulating 2.0 L 0.1 M pH = 4.0 acetic acid, at 25°C. SMR was used to continuously measure in real-time the decrease in mineral mass during the demineralization at 5 different points from on each slab. Demineralization rates were calculated from a linear regression curve of projected mineral mass against demineralization time. Changes in the demineralization rates were monitored following a series of successive increases in calcium (and phosphate at hydroxyapatite stoichiometric ratios of Ca:P 1.67) were added to the demineralizing solution, until demineralization ceased. The pH was maintained constant throughout.

Results: Demineralization halted when the calcium concentration was ~30 mM. At higher calcium concentrations, mineral deposition (remineralization) occurred. By comparison with results from speciation software calculations for the calcium phosphate ternary system, this result suggests that the bulk solubility product of enamel ($pKsp_{BEnamel}$) under the conditions used is 121.

OPEN ACCESS

Edited by:
Steven Joseph Brookes, Leeds Dental Institute, United Kingdom

Reviewed by:
Frederico Barbosa De Sousa, Federal University of Paraíba, Brazil
Pierfrancesco Pagella, University of Zurich, Switzerland

****Correspondence:***
Linda Hassanali
l.hassanali@qmul.ac.uk
Paul Anderson
p.anderson@qmul.ac.uk

Specialty section:
This article was submitted to Craniofacial Biology and Dental Research, a section of the journal Frontiers in Physiology

Received: *31 March 2017*
Accepted: *04 September 2017*
Published: *21 September 2017*

Citation:
Hassanali L, Wong FS, Lynch RJM and Anderson P (2017) A Novel Kinetic Method to Measure Apparent Solubility Product of Bulk Human Enamel. Front. Physiol. 8:714. doi: 10.3389/fphys.2017.00714

Discussion: The apparent $pKsp_{BEnamel}$ under these conditions was higher than many previous reported values, and much closer to those previously reported for HAp. However, this is a bulk value, and does not reflect that enamel is a heterogeneous material, nor the influence of ionic inclusions.

Keywords: enamel, demineralization, solubility, calcium, phosphate, scanning microradiography, solubility product

INTRODUCTION

Tooth decay is a multifactorial process which is influenced by genetic and environmental factors (Keyes, 1962; Borutta et al., 2010). For example, caries related illnesses have become a cause for concern within the UK according to a recent LGA 2013 report (Brunton, 2014; Local Government Authority Report, 2016). Such factors include those associated with the host tissue such as the structure and composition of enamel (Robinson et al., 1995), the pellicle and saliva (Leung and Darvell, 1991) as well as environmental factors such as diet and socioeconomic status (Lalloo and Myburgh, 1999; Hobdell et al., 2003). The kinetics of mineral loss and precipitation is influenced by many factors (Gibbs, 1873; Arends, 1981; DeVoe, 2016), including its physical (Nancollas, 2005) and chemical structure, and the composition and pH, and, also the chemical equilibria between enamel and solution (Dorozhkin, 2012), i.e., the solubility product constant (Ksp). Thus, the dissolution of bulk enamel is significantly influenced by its solubility product (which is defined as the mathematical product of its ion activities raised to the power of their stoichiometric coefficients). Enamel is a calcium deficient form of HAp (Elliott et al., 1994). The Ksp of HAp (Ksp_{HAp}) is defined, from the stoichiometry:

$$Ca_{10}(PO_4)_6OH_2 \leftrightarrows 10Ca^{2+} + 6PO_4^{3-} + 2OH^- \quad (1)$$

and therefore:

$$Ksp_{HAP} = \{Ca^{2+}\}^{10}\{PO_4^{3-}\}^6\{OH^-\}^2 \quad (2)$$

where {} denotes ionic activities at equilibrium raised by the power according to the stoichiometry. In this study the negative logarithm to the base 10 of the Ksp is used (pKsp).

Solubility is the propensity for a solute to dissolve in a solvent and arrive at an end point where the potential energy of the system is at its lowest (Smith, 2015). pKsp is a function of the amount of dissolved solid in solution at equilibrium. **Table 1** shows published pKsp values for bulk enamel, and for HAp, which are within the range 110–126. This range suggests uncertainties in the precise value, and as to whether the solubility of bulk enamel is similar to that of HAp, and, if it is influenced by chemical inclusions. The range also suggests incongruent dissolution behavior of both enamel and hydroxyapatite. However, the range in the measured pKsp values of both enamel and HAp also suggests that the values may also be dependent on the choice of experimental protocol, such as the types of materials used (e.g., whether powdered or bulk samples); the methodology; and the analysis/calculations used to calculate the pKsp value.

Conventional methods of the measurement of solubility product of enamel use chemical equilibrium conditions, with the concentration of solute in the solution at saturation determined by an analytical procedure (Chen et al., 2004; Brittain, 2014). In this study, the aim was to develop a method to measure the rate of bulk enamel demineralization at increasing calcium concentrations in the demineralizing solution (and therefore increasing degrees of saturation) until dissolution stopped and equilibrium achieved. No chemical analyses of solutions was required.

The dissolution rate of enamel can be expressed as a function of the degree of saturation with respect to enamel (Margolis and Moreno, 1985, 1992):

$$R = k\bar{A}(C_{eq} - C_b)^n \quad (3)$$

where;
R = rate;
k = rate constant;
$\bar{A}$ = specific surface area of dissolving surface;
C_{eq} = equilibrium concentration of solvent;
C_b = undersaturated concentration of solvent;
n = integer.

Equation (3) indicates that the addition and/or presence of ionizable solutes will influence the rate (Berner, 1978). It is therefore important to ensure that all ionic concentrations are accounted for and controlled. Previous studies have highlighted that caution is required to ensure that the monitoring device used to measure dissolution rates is sensitive enough to identify the point at which equilibrium is reached, and must not mistake extremely low rates that are undetectable for the condition of equilibrium (Zhang et al., 2000).

In this study, a real-time methodology scanning microradiography (SMR) was used to accurately measure the rate of bulk enamel mineral loss in demineralizing solutions that contained increasing concentration of calcium. The calcium concentration at which the rate ceased (i.e., equilibrium) was then compared with calculated results of degree of saturation at a range solubility products of hydroxyapatite. These values were calculated using a ionic speciation program (Chemist) incorporating the chemical conditions used in the SMR experiment, to calculate the different species that would be present in the dissolution media. The SMR methodology provides a precise means of measuring real-time dissolution of enamel blocks under controlled conditions that simulate caries. Further, the methodology is directly quantitative achieved using an X-ray photon counting system with minimum error (for a

TABLE 1 | Published $pKsp_{enamel/HAp}$ values with references and summary of methodologies.

pKsp	References	Substrate and method
106–116	Patel and Brown, 1975	Human powdered enamel. pH range 4.5–7.6. Measured the amounts dissolved to calculate Ksp.
110 (*Apparent* solubility product 116)	Zhang et al., 2000	Contact Microradiography assessed the demineralization of sections of enamel in lactic acid solutions ranging pH 5–5.07 over a range of DS_{en} values (0.28–0.79) that were based on a $pKsp_{enamel}$ of 110. Suggest that enamel may have an *apparent* solubility product of 116 based on experimental findings.
116	Shellis et al., 1993	Enamel powder equilibrated with 4 or 17 mM of H_3PO_4 at 37°C. Amounts dissolved were measured and used to calculate the ion activity product at equilibrium = Ksp.
117	Dawes, 2003	HAp Ksp cited in special feature article
118	McDowel et al., 1977	4 g synthetic hydroxyapatite. Ion concentrations at equilibrium then measured. Ksp determined as a function of temperature.
Enamel: 117.6 HAp: 121.82 (Pooled from pH 4.5–5.5)	Shellis and Wilson, 2004	Powdered synthetic HAp. Premolar enamel powder. 5 mg equilibrated with acetic buffers at pH 4.5, 5.0 (0.15 M) 5.5 (0.2 M) in a range of degrees of saturation (range of pI_{HA}) at 37°C. Mass fraction dissolved plotted against pI_{HA} to give distribution curves at each pH. No statistical difference in pH differences.
126	Pan and Darvell, 2007	Solid HAP titrated with KCl solutions at pH 3.2, 3.6, and 4.1 at 37°C. Dissolution monitored using a semiconductor-diode laser scattering system that peaked each time solid was added and disappeared when all solid dissolved. Same solution was adjusted to a decreasing pH using 1M HCl.

full description of SMR and calculation of statistical errors of the photon counting system see Anderson et al., 1998).

For the solubility product to be accurately calculated, all phases and ion-pairs present during dissolution need to be accounted for. Chemical speciation of a solution describes the chemical form and concentrations of each species present, and can be derived using the thermodynamic principals of mass balance (Quinn and Taylor, 1992). Speciation software can be used to calculate the chemical speciation of complex systems. In this study, we describe a novel kinetic method to measure the *apparent*-$pKsp_{BEnamel}$ under conditions relevant to caries, in conjunction with a speciation program so that the *apparent*-$pKsp_{BEnamel}$ value could be calculated at conditions of pH = 4.0 and 25°C. The rate of demineralization of natural unaltered surfaces of human permanent enamel blocks was measured using SMR to determine the effective solubility in an inorganic caries-like demineralizing solution with a decreasing degree of undersaturation with respect to HAp.

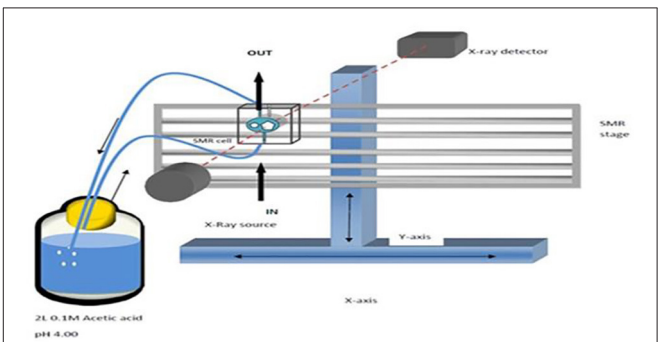

FIGURE 1 | Schematic diagram of SMR experimental set up showing X-rays parallel to the direction of acid attack and perpendicular to the enamel surface.

MATERIALS AND METHODS

Scanning Microradiography

SMR is an X-ray absorption technique that enables the monitoring of mineral loss (and eventually gain once equilibrium is surpassed) in thin sections of enamel samples during demin/remineralization studies (Anderson et al., 1998). Developed to overcome some of the limitations of conventional (contact) microradiography which required samples to be in contact with a photographic film, SMR can measure mineral changes in real time as solutions can be circulated through SMR cells, within which samples are mounted, at a controlled rate simulating salivary flow.

In this study, the integrated mode of SMR (**Figure 1**) was used whereby the direction of acid attack was parallel to a 15 μm diameter X-ray beam so that changes in the projected mineral mass from the surface could be measured as mineral was lost from the surface and receded to the enamel dentine junction (Anderson and Elliott, 2000). The X-ray generator was operated at a maximum voltage of 41 kV and a current of 0.7 mA. The transmitted X-ray intensity for energies selected at 22.1 keV at each point was measured and the mass of absorbing mineral determined. Since demineralization is nearly linear with time under constant chemical conditions (Elliott et al., 1994; Wang et al., 2006), the rate of projected mineral mass loss of the same enamel sample at decreasing degrees of undersaturation with respect to HAp could be measured (Margolis et al., 1999).

Enamel Sample Preparation for SMR

Eleven different permanent enamel blocks were prepared from teeth extracted for orthodontic purposes, with the roots removed and discarded and stored in methylated ethanol solution at room temperature were analyzed. Teeth were cut parallel to the tooth face into 2 mm enamel blocks with the natural buccal surfaces intact using a diamond cutting saw (Microslice 2, Malvern Instruments, UK). Ethical approval was granted by Queen Mary Research Ethics Committee (QMREC 2011/99).

The enamel blocks were mounted in SMR cells with the natural surfaces exposed (**Figure 2**). Each was scanned with X-ray Microtomography (XMT) (Elliott et al., 1994) to identify caries free (unaffected) areas suitable for analysis with SMR. The

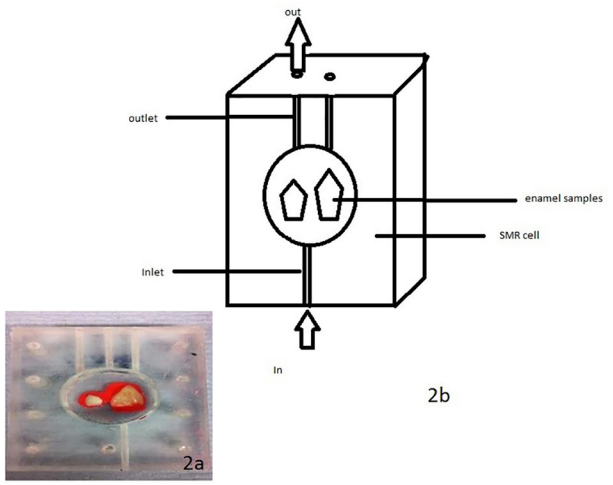

FIGURE 2 | (a,b) A photo and schematic diagram of human enamel blocks in an SMR cell with figure **(b)** showing the flow of acid into and out of the cell.

SMR cells were then mounted on the XY stage of the SMR apparatus. The samples were initially immersed in deionized water circulated using a peristaltic pump as previously described in Mishra et al. (2009) for 48 h in order to ensure the samples were fully hydrated prior to the commencement of the dissolution experiment. The temperature was maintained at 25.0 ± 1.0°C throughout the experiment, as solubility is highly dependent on temperature.

Calculation of Integrated Mineral Mass Using SMR

The mineral mass of enamel was calculated using the mass absorption coefficient (μ_m) of pure hydroxyapatite as previously described in Anderson et al. (1998), for AgKα radiation at 22.1 keV (4.69 cm^2 g^{-1}). The integrated mineral mass per unit area (m) at each data point is:

$$m = \frac{1}{\mu_m} \ln \frac{No}{N} \quad (4)$$

where;
μ_m is mass attenuation coefficient of HAp for AgKα radiation at 22.1 keV.
N_0 is number of incident photons.
N is number of transmitted photons.

Identification of SMR Scanning Points

Before the dissolution experiment, SMR area scans were carried out in order to locate the samples on the XY stage, and to select the coordinates of ∼5 points suitable for measuring mineral mass changes as identified using XMT (see section Enamel Sample Preparation for SMR). The selected points were located horizontally across the buccal enamel surface from distal to mesial.

Preparation of Demineralization Solution

2.0 L of pH = 4.0 acetic acid 0.1 M (Anderson et al., 2004) was prepared using 12 g of pure acetic acid, diluted with deionized water and adjusted to a pH of 4.0 with a 1.0 M stock solution of KOH using a pH meter (Orion-pH/ISE meter Model 710).

Calculation of Demineralization Rates

Mean demineralization rates were calculated using linear regression from the projected mineral mass curves obtained from SMR analysis of selected points on the enamel surface (**Figure 3**). The rate of mineral loss was determined from the gradient in units of grams per unit exposed area per hour. Typical times between successive data points on the same sample was about 10 min.

Calculation of Equilibrium Conditions

Thermodynamic equilibrium was assumed to be when demineralization rate was zero. The calcium concentration at thermodynamic equilibrium was determined by plotting demineralization rates against calcium concentration (**Figure 6**) and determining the x-intercept (calcium concentration) from the line equation of the polynomial regression curve (of order 2) using MATLAB (MathWorks).

Preparation of Calcium and Phosphate Increments

0.66 g increments of $CaCl_2$ and 0.822 g increments of K_2HPO_4 were weighed so that any additions of each increment into the 2.0 L of acetic acid solution would give a concentration of 3.0 mM calcium and 1.8 mM phosphate (Ca/P 1.67).

The concentration of calcium and phosphate in the demineralizing solution was increased incrementally by 3.0 mM calcium and 1.8 mM phosphate, respectively (Ca/P 1.67) every 48 h. Steps were taken to ensure pH was maintained constant throughout. The rate of demineralization of the enamel sample was measured at each increase in calcium/phosphate concentration increment using SMR.

CALCULATION OF DEGREE OF SATURATION OF DEMINERALIZING SOLUTIONS USED

An ionic speciation program, Chemist (MicroMath, Missouri, USA) was used to calculate the degree of saturation with respect to hydroxyapatite (DS_{HAp}) for a solution at pH = 4.0 in a range of solutions with increasing calcium concentrations identical to those used in the SMR measurements. This calculation was repeated for a range of pKsp values from 116 to 126, and the degree of saturation as a function of calcium concentration was then plotted for each pKsp value (**Figure 4**). The calcium concentration at equilibrium (i.e., when the saturation was 1) was determined from each plot, and then these were then plotted for each pKsp value (**Figure 5**). The corresponding calcium concentration required to halt demineralization from the SMR data (**Figure 3**) was then used to determine the pKsp for the calcium concentration required to reach equilibrium (**Figure 7**).

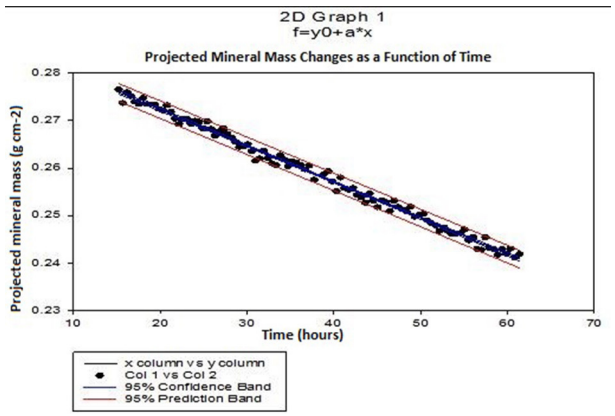

FIGURE 3 | Typical SMR showing the linear changes in projected mineral mass of enamel with time and the 95% confidence intervals ($p \leq 0.0001$) in 0.1 M acetic acid solution at pH = 4.0.

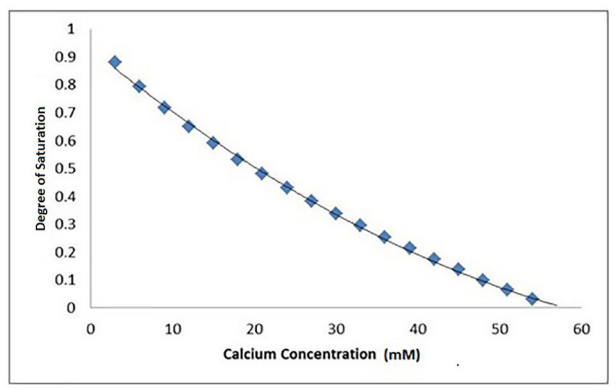

FIGURE 4 | A typical Chemist plot for a pKsp of 118 showing thermodynamic equilibrium is reached at 57 mM of calcium at the x-intercept, under pH = 4.0 at 25°C conditions. The degree of saturation with respect to HAp was calculated based on the conditions and calcium and phosphate concentrations used in the SMR experiment.

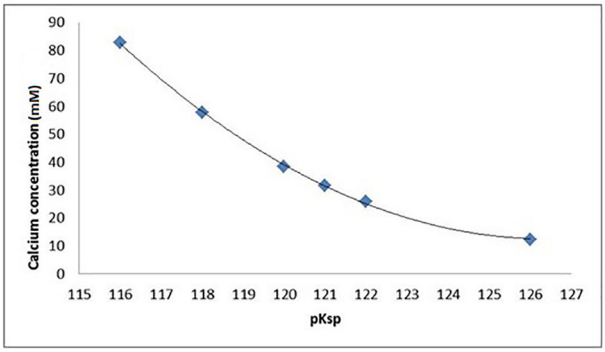

FIGURE 5 | Calcium and phosphate concentration (mM) in equilibrium with HAp as a function of the pKsp assumed for HAp, assuming pH = 4.0, 0.1 M acetic acid, and 25°C as calculated by Chemist.

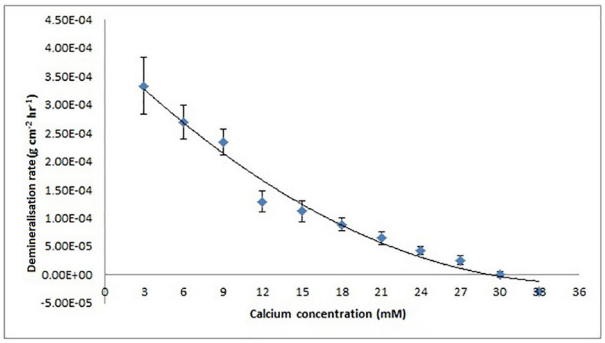

FIGURE 6 | Enamel demineralization rate as a function of increasing calcium concentration at pH = 4.0 and 25°C based on results from the SMR experiment. Rate is zero at a calcium concentration of 30 mM calculated using MATLAB from the x-intercept of the regression curve ($R^2 = 9.8$).

RESULTS

Enamel Demineralization Rate As a Function of Increasing Calcium Concentration

Figure 3 shows a typical plot of mineral mass changes of bulk enamel with time during demineralization with 0.1 M acetic acid at pH = 4.0 at 25°C (confidence intervals of 95%, $p \leq 0.0001$). Similar results showing a linear rate of mineral loss with time were obtained at each incremental additional calcium concentration. Mean enamel demineralization rates were calculated from a total of 33 points on 11 different permanent enamel blocks (see section Calculation of Demineralization Rates for calculation of demineralization rates procedure).

The mean demineralization rates were then plotted as a function of calcium concentration (**Figure 6**), which showed a decreasing, but non-linear, trend (SE ranged from $\pm$ 2.90 $\times$ 10^{-06} to $\pm$ 1.09 $\times$ 10^{-05}). This result shows that under the conditions used, the calcium concentration required to achieve thermodynamic equilibrium was 30 mM as determined from the horizontal intercept (regression curve $R^2 = 0.98$), calculated using MATLAB.

Identifying the pKsp of Bulk Enamel using Ion Speciation Software

Data fitting of the SMR data shows that calcium concentration required for demineralization of bulk enamel to cease (at conditions of pH = 4.0 and 25°C), i.e. that equilibrium is achieved is 30 mM. under the same conditions. Fitting to the speciation software data suggests a pKsp of 121 corresponds to a calcium concentration of 30 mM to reach thermodynamic equilibrium for pH = 4.0 and 25°C conditions. This result suggests that the $pKsp_{BEnamel}$ is 121 (**Figure 7**).

DISCUSSION

It is important to measure the solubility of enamel under caries like conditions using a precise measuring system in order to

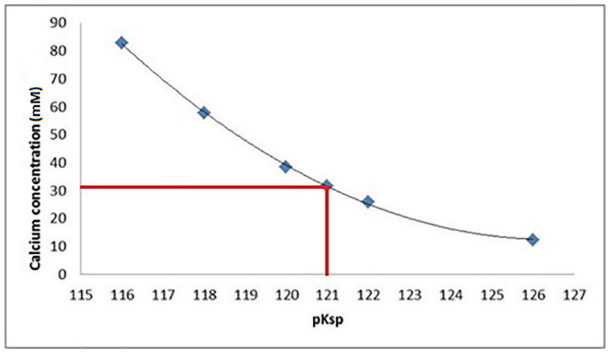

FIGURE 7 | At a pKsp of 121, a calcium concentration of 30 mM is required for saturation of a solution with respect to HAp at pH = 4.0.

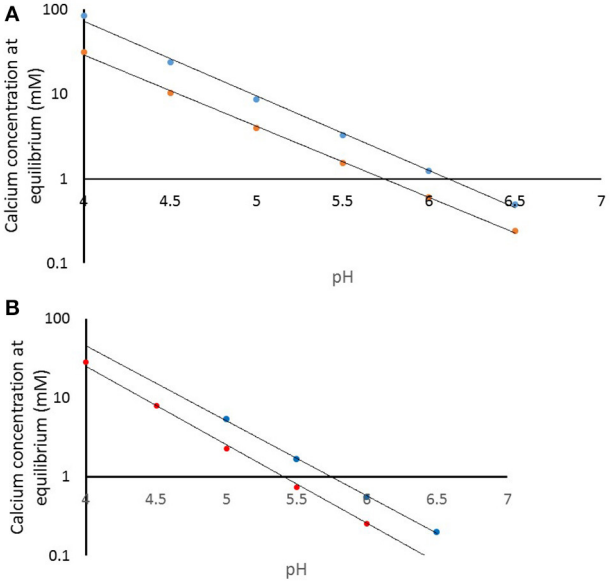

FIGURE 8 | (A) Calculated calcium concentration required for equilibrium at pKsp values of 116 (blue) and 121 (red) for a demineralization solution of 100 mmol/L acetic acid. **(B)** Calculated calcium concentration required for equilibrium at pKsp values of 116 (blue) and 121 (red) with only that acid or base required for pH condition.

accurately derive the solubility product. This information is relevant to the development of our understanding of caries and erosion and to develop preventative measures such as to screen anticaries agents.

The SMR data showed that the bulk human enamel demineralization at pH = 4.0 was reduced to zero at a calcium concentration of 30 mM. Correlation with the speciation software calculations shows this corresponds to a pKsp value of 121. **Figures 4**, **6** show a consistency between the speciation software of degree of saturation (proportional to chemical driving force) and the SMR kinetic data, indicating that the method was appropriate.

Figure 6 shows that the decrease in demineralization rate was non-linear (rather than linear as would be expected from simple first-order dissolution kinetics) similar to that obtained from speciation calculations for all pKsp values (**Figure 4**). This is consistent with what would be predicted for the calcium phosphate ternary system (Leaist et al., 1990).

As discussed earlier it is important to account for all possible phase transformations, and equilibria, as a lack of information on the resulting equilibria results in imperfect calculations (Pan and Darvell, 2007). Ion speciation programs rely on databases that report experimental results for speciation constants as well as the methods and conditions of the experiments reported (VanBriesen et al., 2010). The similarities observed in the data from the SMR method and the speciation software (**Figures 4**, **6** respectively) confirm the methodology. The small standard errors (**Figure 6**) also indicate that there was little variation in the demineralization rates between samples.

The *apparent*-$pKsp_{BEnamel}$ value of 121 measured in this study is higher than many previously reported values (see **Table 1**), and higher than many values reported for pure HAp. As mentioned above, the methodology may influence the values reported for enamel and hydroxyapatite (Dorozhkin, 2012, Liu et al., 2013).

How does this impact on the clinical situation? We have used the speciation software to model the equilibrium conditions as a function of pH for the pKSp values under the conditions used in the experiment. **Figure 8A** shows the calcium concentration required for equilibrium under the conditions used, including acid concentration and temperature (plotted on a log scale) for a pKSp value of 116 (blue), and for pKsp of 121 (red). This shows that at pH 4.0, the calcium concentration required for equilibrium for a pKSp = 116 would be 85 mM, whereas for pKSp = 121 this would only be 31 mmol/L. However, let us consider a calcium concentration of 1 mmol/L, cited as the value of free calcium concentration in saliva (Lagerlof, 1983). Then, from **Figure 8A**, this would suggest that the saturation would occur only at pH above 6.0. This is often called the "critical pH" (Dawes, 2003). However, using a value of pKSp of 121, then this would suggest a much lower "critical pH" (at a calcium concentration of 1 mM). Of course, these calculations were performed with an acid concentration of 0.1 M, which is high for oral conditions. **Figure 8B** is a repeat of this calculation, but with no fixed acetic concentration (and is therefore not necessarily repeatable in a laboratory), but represents the opposite extreme with a zero acetic concentration. This reduces the critical pH value, assuming a free calcium ion concentration of 1.0 mM (Lagerlof, 1983). The oral environment acid concentration is likely to be somewhere between these extremes, but this calculation confirms that a pKSp value of 116 is too low, and that is likely to be nearer to 121, otherwise there would be insufficient calcium in the oral environment to prevent enamel being undersaturated. It is also likely that other factors including salivary proteins (Kosoric et al., 2010) also play in role in the protective function of enamel, and will modify the apparent solubility product.

Whilst these results provide an insight into the dynamics of enamel dissolution under pH = 4.0 conditions at 25°C, the

result is for bulk enamel only, and based on an *in vitro* design, and so it is important to acknowledge that any conclusions made are limited to these conditions only. For instance, further similar SMR studies are required to determine the effect pH (Ito et al., 1996). An increase in dissolution rate is observed when pH is reduced (Gao et al., 2001). Furthermore, published data on the effect of pH on the solubility product of enamel is contradictory, e.g., Shellis and Wilson (2004) found no statistical difference in the solubility product of powdered enamel at different pH values between 4.5 and 5.5 whereas the earlier studies of Patel and Brown (1975) reported lower solubility product values of 106–116 over a pH range of 4.5–7.6. The inconsistency in results is in spite of both experiments using powdered enamel as the substrate which again highlights the advantage of using bulk enamel as the substrate rather than powdered. Such measurements will also confirm or otherwise the marked change in slope of the solubility isotherm for HAp at around pH 3.9 as reported by Pan and Darvell (2009a,b).

Also, further similar SMR studies are required to study the influence of different ionic substitutions on both enamel and HAp powder, including carbonate, Mg^{2+}, F^{-}, etc. would provide significant further information on the chemistry of demineralization process. Also, similar studies are required too for a comparison of bulk enamel values with values obtained for powdered hydroxyapatite, similar to the studies reported in **Table 1.**

Further, the physical and chemical heterogeneities within enamel should not be ignored (Arends and Jongebloed, 1977; Zhang et al., 2000; Bechtle et al., 2012). For example, demineralization rates of prismatic, interprismatic and aprismatic enamel are not the same due to differences between the organization of crystals, the presence of more soluble material, and the porosity (Avery et al., 1961; Boyde, 1967; Shellis, 1996; Shellis and Dibdin, 2000). On a chemical compositional level, enamel is a substituted calcium hydroxyapatite (Neel et al., 2016). Its composition varies with ions such as F^{-}, CO_3^{2-} and Mg^{2+} replacing OH^{-}, PO_4^{3-} and Ca^{2+} within the stoichiometry allegedly altering the solubility of enamel (Aoba, 1997; Elliott, 2003; West and Joiner, 2014; Liu et al., 2016). Thus, the site of source material may be a critical factor. Further solubility measurements are also needed to investigate the influence of the structural or chemical heterogeneities of enamel on the demineralization rate. As the enamel is etched away and moves toward the enamel dentine junction there are changes in demineralization rate resulting from gradients in ionic substitutions within enamel structure (Anderson and Elliott, 2000). In addition, within enamel, the processes of demineralization and remineralization may not be co-localized, with ions diffusing in different directions (Anderson and Elliott, 1992).

In conclusion, the SMR method described here provides greater insight into bulk enamel dissolution by measuring the *effect* of calcium concentration on the dissolution kinetics of bulk enamel demineralization under standardized caries-like conditions. The measured $pKsp_{BEnamel}$ value of ∼121 is similar to that reported by Shellis and Wilson (2004) for pure HAp, and is in agreement with recent suggestions that $pKsp_{BEnamel}$ is higher than that reported previously in literature, and may be much closer to the value for pure HAp. However, further similar kinetic studies will be needed to measure enamel solubility at a range of pH conditions, temperatures, and, for example, the influence of salivary proteins, in order to replicate the changing conditions of the oral environment.

ETHICS STATEMENT

Written informed consent was obtained from patients who agreed to give their teeth anonymously for research. Ethical approval was granted to use that pool of teeth by Queen Mary Research Ethics Committee (QMREC 2011/99). The site license is in the name of the author FW.

AUTHOR CONTRIBUTIONS

LH, contribution toward the conception and design of the work. Acquisition, interpretation and analysis of all data. Drafting and revising the work and ensuring the integrity and accuracy of the work. FW, contributions include the interpretation and analysis of data. Revising work and ensuring the integrity and accuracy of the work. RL, contributions include the interpretation and analysis of data. Revising work and ensuring the integrity and accuracy of the work. PA, contributions include the design and conception of the work. Interpretation and analysis of data. Drafting and revising the work and ensuring the integrity and accuracy of the work.

FUNDING

LH is the recipient of a PhD studentship from BBSRC (grant number BB/L502091/1).

ACKNOWLEDGMENTS

This study was supported by the Biotechnology and Biological Sciences Research Council and GlaxoSmithKline. The authors are thankful to the staff and students in the Dental Physical Sciences Unit at Queen Mary University of London.

REFERENCES

Anderson, P., Bollet-Quivogne, F. R. G., Dowker, S. E. P., and Elliott, J. C. (2004). Demineralization in enamel and hydroxyapatite aggregates at increasing ionic strengths. *Arch. Oral Biol.* 49, 199–207. doi: 10.1016/j.archoralbio.2003.10.001

Anderson, P., and Elliott, J. C. (1992). Subsurface demineralization in dental enamel and other permeable solids during acid dissolution. *J. Dent. Res.* 71, 1473–1481. doi: 10.1177/00220345920710080301

Anderson, P., and Elliott, J. C. (2000). Rates of mineral loss in human enamel during *in vitro* demineralization perpendicular and parallel to the natural surface. *Caries Res.* 34, 33–40. doi: 10.1159/000016567

Anderson, P., Levinkind, M., and Elliott, J. C. (1998). Scanning microradiographic studies of rates of *in vitro* demineralization in human and bovine dental enamel. *Arch. Oral Biol.* 43, 649–656. doi: 10.1016/S0003-9969(98)00052-1

Aoba, T. (1997). The effect of fluoride on apatite structure and growth. *Crit. Rev. Oral Biol. Med.* 8, 136–153. doi: 10.1177/10454411970080020301

Arends, J. K. (1981). "Mechanism of dental caries," in *Biological Mineralisation and Demineralisation, Life Sciences Research Report 23, Dahlem Konferenzen Berlin,* ed Nancollas (Berlin; Heidelberg; New York, NY: Springer–Verlag). 303–327.

Arends, J. K., and Jongebloed, W. L. (1977). Dislocations and dissolution in apatites: theoretical considerations. *Caries Res.* 11, 186–188. doi: 10.1159/000260266

Avery, J. K., Visser, R. L., and Knapp, D. E. (1961). The pattern of the mineralization of enamel. *J. Dent. Res.* 40, 1004–1019. doi: 10.1177/00220345610400050101

Bechtle, S., Ozcoban, H., Lilleodden, E. T., Huber, N., Schreyer, A., Swain, M. V., et al. (2012). Hierarchical flexural strength of enamel: transition from brittle to damage-tolerant behaviour. *J. R. Soc. Interface* 9, 1265–1274. doi: 10.1098/rsif.2011.0498

Berner, R. A. (1978). Rate control of mineral dissolution under earth surface conditions. *Am. J. Sci.* 278, 1235–1252. doi: 10.2475/ajs.278.9.1235

Borutta, A., Wagner, M., and Kneist, S. (2010). Early childhood caries: a multifactorial disease. *OHDMBSC.* 9, 32–38.

Boyde, A. (1967). The development of enamel structure. *Proc. R. Soc. Med.* 60, 923–928.

Brittain, H. G. (2014). Thermodynamic vs. kinetic solubility: knowing which is which. *Am. Pharmaceut. Rev.* 17, 10–15.

Brunton, P. (2014). Summary of: continuing development of an oral health score for clinical audit. *Br. Dent. J.* 216, 526–527. doi: 10.1038/sj.bdj.2014.380

Chen, Z. F., Darvell, B. W., and Leung, V. W. H. (2004). Hydroxyapatite solubility in simple inorganic solutions, *Arch. Oral Biol.* 49, 359–367. doi: 10.1016/j.archoralbio.2003.12.004

Dawes, C. (2003). What is the critical pH and why does a tooth dissolve in acid? *J. Can. Dent. Assoc.* 69, 722–724.

DeVoe, H. (2016). *Thermodynamics and Chemistry, 2nd Edn Version 8.* Maryland, MD; Pearson Education, Inc.

Dorozhkin, S. V. (2012). Dissolution mechanism of calcium apatites in acids: a review of literature. *World. J. Methodol.* 2, 1–17. doi: 10.5662/wjm.v2.i1.1

Elliott, J. C. (ed.). (2003). "Structure and chemistry of the apatites and other calcium orthophosphates," in *Studies in Inorganic Chemistry,* Vol. 18 (London, UK: Elsevier), 259–295.

Elliott, J. C., Anderson, P., Gao, X. J., Wong, F. S. L., Davis, G. R., and Dowker, S. E. P. (1994). Application of scanning microradiography and X-Ray microtomography to studies of bones and teeth. *J. X-ray Sci. Technol.* 4, 102–111.

Gao, X. J., Fan, Y., Kent, R. L. Jr., Van Houte, J., and Margolis, H. C. (2001). Association of caries activity with the composition of dental plaque fluid. *J. Dent. Res.* 80, 1834–1839. doi: 10.1177/00220345010800091201

Gibbs, J. W. (1873). A method of geometrical representation of the thermodynamic properties of substances by means of surfaces. *Trans. Conn. Acad. Arts Sci.* 2, 382–404.

Hobdell, M. H., Oliveira, E. R., Bautista, R., Myburgh, N. G., Lalloo, R., Narendran, S., et al. (2003). Oral diseases and socio-economic status (SES). *Br. Dent. J.* 194, 91–96. doi: 10.1038/sj.bdj.4809882

Ito, A., Maekawa, K., Tsutsumi, S., Ikazaki, F., and Tateishi, T. (1996). Solubility product of OH-carbonated hydroxyapatite. *J. Biomed. Mater. Res.* 36, 522–528. doi: 10.1002/(SICI)1097-4636(19970915)36:4<522::AID-JBM10>3.0.CO;2-C

Keyes, P. H. (1962). Recent advances in dental caries research. *Int. Dent. J.* 12, 443–464.

Kosoric, J., Hector, M. P., and Anderson, P. (2010). The influence of proteins on demineralization kinetics of hydroxyapatite aggregates. *J. Biomed. Mater. Res. A* 94, 972–977. doi: 10.1002/jbm.a.32759

Lagerlof, F. (1983). Effects of flow-rate and pH on calcium-phosphate saturation in human-parotid saliva. *Caries Res.* 17, 403–411. doi: 10.1159/000260694

Lalloo, R., and Myburgh, N. G. (1999). Dental caries, socio-economic development and national oral health policies. *Int. Dent. J.* 49, 196–202. doi: 10.1111/j.1875-595X.1999.tb00522.x

Leaist, D. G., Anderson, P., and Elliott, J. C. (1990). Diffusion coefficients for the ternary system $Ca(OH)_2$-H_3P0_4-Water. *J. Chem. Soc. Faraday Trans.* 86, 3093–3095. doi: 10.1039/FT9908603093

Leung, V. W. H., and Darvell, B. W. (1991). Calcium phosphate system in saliva-like media. *J. Chem. Soc. Faraday Trans.* 87, 1759–1764. doi: 10.1039/ft9918701759

Liu, Q., Chen, Z., Pan, H., Darvell, B. W., and Matinlinna, J. P. (2016). Effect of magnesium on the solubility of hydroxyapatite. *Eur. J. Inorg. Chem.* 2016, 5623–5629. doi: 10.1002/ejic.201601056

Liu, Q., Huang, S., Matinlinna, P. J., Chen, Z., and Pan, H. (2013). Insight into biological apatite: physiological properties and preparation approaches. *Biol. Med. Res. Int.* 2013, 1–13. doi: 10.1155/2013/929748

Local Government Authority Report (2016), *Tackling Poor Oral Health in Children, Local Governments Public Health Role*. London, UK: Public Health England.

Margolis, H. C., and Moreno, E. C. (1985). Kinetic and thermodynamic aspects of enamel demineralization. *Caries Res.* 19, 22–35. doi: 10.1159/000260826

Margolis, H. C., and Moreno, E. C. (1992). Kinetics of hydroxyapatite dissolution in acetic, lactic, and phosphoric acid solutions. *Calcif. Tissue Int.* 50, 137–143. doi: 10.1007/BF00298791

Margolis, H. C., Zhang, Y. P., Lee, C. Y., Kent, R. L. Jr., and Moreno, E. C. (1999). Kinetics of enamel demineralisation *in vitro*. *J. Dent. Res.* 78, 1326–1335. doi: 10.1177/00220345990780070701

McDowel, H., Gregory, T. M., and Brown, W. E. (1977). Solubility of $Ca_5(P0_4)_3OH$ in the system $Ca(OH)_2$- H_3P0_4- H_20 at 5, 15, 25, and 37°C. *J. Res. Natl. Bur. Stand. A Phys. Chem.* 81A, 273–281. doi: 10.6028/jres.081A.017

Mishra, S., Thomas, H. F., Fearne, J. M., Boyde, A., and Anderson, P. (2009). Comparison of demineralisation rates in pre- and postnatal enamel and at the neonatal line. *Arch. Oral Biol.* 54, 101–106. doi: 10.1016/j.archoralbio.2008.09.013

Nancollas, G. H. (2005). A new model for nanoscale enamel dissolution. *J. Phys. Chem. B* 109, 999–1005. doi: 10.1021/jp046451d

Neel, E. A. A., Aljabo, A., Strange, A., Ibrahim, S., Coathup, M., Young, A. M., et al. (2016). Demineralization–remineralization dynamics in teeth and bone. *Int. J. Nanomedicine* 11, 4743–4763. doi: 10.2147/IJN.S107624

Pan, H. B., and Darvell, B., W (2009a). Calcium phosphate solubiliy; the need for re-evaluation. *Cryst. Growth Des.* 4, 639–645. doi: 10.1021/cg801118v

Pan, H. B., and Darvell, B. W. (2007). Solubility of hydroxyapatite by solid titration at pH 3–4. *Arch. Oral Biol.* 52, 618–624. doi: 10.1016/j.archoralbio.2006.12.007

Pan, H. B., and Darvell, B. W. (2009b). Solid titration of octacalcium phosphate. *Caries Res.* 43, 322–330. doi: 10.1159/000226231

Patel, P. R., and Brown, W. P. (1975). Thermodynamic solubility product of human tooth enamel, powdered sample. *J. Dent. Res.* 54, 728–736. doi: 10.1177/00220345750540040601

Quinn, G. W., and Taylor, D. M. (1992). NSPEC: a chemical speciation program for personal computers. *Analyst* 117, 689–691. doi: 10.1039/an9921700689

Robinson, C., Kirkham, J., Brookes, S. J., and Shore, R. C. (1995). "Chemistry of mature enamel," in *Dental Enamel: Formation to Destruction,* eds C. Robinson, J. Kirkham, and S. J. Brookes (Leeds: CRC Press), Chapter 8, 167–191.

Shellis, R. P. (1996). A scanning electron microscopic study of solubility variations in human enamel and dentine. *Arch. Oral Biol.* 41, 473–484. doi: 10.1016/0003-9969(96)00140-9

Shellis, R., and Dibdin, G. (2000). "Enamel microporosity and its functional implications," in *Development, Function and Evolution of Teeth,* eds M. Teaford, M. Meredith Smith, and M. Ferguson (Cambridge: Cambridge University Press), 242–251. doi: 10.1017/CBO9780511542626.017

Shellis, R. P., Wahab, F. K., and Heywood, B. R. (1993). The Hydroxyapatite Ion Activity Product in Acid Solutions Equilibrated with Human Enamel. *Caries Res.* 27, 365–372. doi: 10.1159/000261566

Shellis, R. P., and Wilson, R. M. (2004). Apparent solubility distributions of hydroxyapatite and enamel apatite. *Adv. Colloid Interface Sci.* 278, 325–332. doi: 10.1016/j.jcis.2004.06.016

Smith, B. T. (2015). *Remington Education: Physical Pharmacy, 1st Edn.* London, UK: Pharmaceutical Press.

VanBriesen, J. M., Small, M., Weber, C., and Wilson, J. (2010). "Modelling chemical speciation: thermodynamics, kinetics and uncertainty," in *Modelling of Pollutants in Complex Environmental Systems*, ed G. Hanrahan (St. Albans: ILM Publications), 133–149.

Wang, L. J., Tang, R., Bonstein, T., Bush, P., and Nancollas, G. H. (2006). Enamel demineralization in primary and permanent teeth. *J. Dent. Res.* 85, 359–363. doi: 10.1177/154405910608500415

West, N., and Joiner, A. (2014). Enamel mineral loss. *J. Dent.* 42, 2–11. doi: 10.1016/S0300-5712(14)50002-4

Zhang, Y. P., Kent, R. L. Jr., and Margolis, H. C. (2000). Enamel demineralization under driving forces found in dental plaque fluid. *Eur. J. Oral Sci.* 108, 207–213. doi: 10.1034/j.1600-0722.2000.108003207.x

Conflict of Interest Statement: Author RL is employed by GlaxoSmithKline and LH is the recipient of a studentship from BBSRC and stipend from GlaxoSmithKline.

The other authors declare that the research was conducted in the absence of any commercial or financial relationships that could be construed as a potential conflict of interest.

Copyright © 2017 Hassanali, Wong, Lynch and Anderson. This is an open-access article distributed under the terms of the Creative Commons Attribution License (CC BY). The use, distribution or reproduction in other forums is permitted, provided the original author(s) or licensor are credited and that the original publication in this journal is cited, in accordance with accepted academic practice. No use, distribution or reproduction is permitted which does not comply with these terms.

frontiers in Physiology

ORIGINAL RESEARCH
published: 12 July 2017
doi: 10.3389/fphys.2017.00461

In-vitro Thermal Maps to Characterize Human Dental Enamel and Dentin

Paula Lancaster[1], David Brettle[2], Fiona Carmichael[3] and Val Clerehugh[1]*

[1] Restorative Department, School of Dentistry, University of Leeds, Leeds, United Kingdom, [2] Department of Medical Physics and Engineering, St. James's University Hospital, Leeds, United Kingdom, [3] Department of Dental and Maxillofacial Radiology, Leeds Dental Institute, University of Leeds, Leeds, United Kingdom

The crown of a human tooth has an outer layer of highly-mineralized tissue called enamel, beneath which is dentin, a less-mineralized tissue which forms the bulk of the tooth-crown and root. The composition and structure of enamel and dentin are different, resulting in different thermal properties. This gives an opportunity to characterize enamel and dentin from their thermal properties and to visually present the findings as a thermal map. The thermal properties of demineralized enamel and dentin may also be sufficiently different from sound tissue to be seen on a thermal map, underpinning future thermal assessment of caries. The primary aim of this novel study was to produce a thermal map of a sound, human tooth-slice to visually characterize enamel and dentin. The secondary aim was to map a human tooth-slice with demineralized enamel and dentin to consider future diagnostic potential of thermal maps for caries-detection. Two human slices of teeth, one sound and one demineralized from a natural carious lesion, were cooled on ice, then transferred to a hotplate at 30°C where the rewarming-sequence was captured by an infra-red thermal camera. Calculation of thermal diffusivity and thermal conductivity was undertaken, and two methods of data-processing used customized software to produce thermal maps from the thermal characteristic-time-to-relaxation and heat-exchange. The two types of thermal maps characterized enamel and dentin. In addition, sound and demineralized enamel and dentin were distinguishable within both maps. This supports thermal assessment of caries and requires further investigation on a whole tooth.

Keywords: dental enamel, dental dentin, dental caries, demineralization, thermal imaging, thermal map

OPEN ACCESS

Edited by:
Alexandre Rezende Vieira, University of Pittsburgh, United States

Reviewed by:
Victor E. Arana-Chavez, University of São Paulo, Brazil
Pamela DenBesten, University of California, San Francisco, United States

****Correspondence:***
Paula Lancaster
p.e.lancaster@leeds.ac.uk

Specialty section:
This article was submitted to Craniofacial Biology and Dental Research, a section of the journal Frontiers in Physiology

Received: *19 April 2017*
Accepted: *16 June 2017*
Published: *12 July 2017*

Citation:
Lancaster P, Brettle D, Carmichael F and Clerehugh V (2017) In-vitro Thermal Maps to Characterize Human Dental Enamel and Dentin. Front. Physiol. 8:461. doi: 10.3389/fphys.2017.00461

INTRODUCTION

The portion of tooth visible within the human mouth, known as the crown, has two main layers of mineralized tissue: enamel and dentin. Tooth enamel is produced by ameloblasts and has the highest mineral content of any tissue within the human body at approximately 96% mineral by weight, compared to dentin which is produced by odontoblasts at approximately 70% mineral by weight (Goldberg et al., 2012; Kunin et al., 2015). Enamel is primarily made of hydroxyapatite, the crystals of which can vary in shape from rods and needles to rhombohedral. They can have a variety of orientations and form enamel prisms. Between the prisms, inter-prismatic crystals, organic material such as proteins, lipids and carbohydrates can be found, as well as water. Enamel mineralization can vary between teeth and within the same tooth. The surface layer of enamel

has the greatest level of mineralization, with the layer closest to dentin having the least (Kunin et al., 2015). There are different types of dentin in teeth. The outer layer, mantle dentin, is made of calcospheritic globules with interglobular spaces. Tubules may be found in mantle dentin but is usually void of them. The next layer is circumpulpal dentin, which forms the bulk of the tooth-tissue. It is initially deposited as a cellular layer which matures to predentin and then undergoes mineralization. Tubules are present to house the odontoblast process, with mineralized intertubular dentin between. The circumference of the tubule is made of peritubular dentin, which has a higher mineral content (≈95%) compared to the circumpulpal dentin (≈30%). This peritubular mineral is deposited from the tubular amorphous material. Continuous production of dentin occurs throughout the life of the tooth and, if the tooth is exposed to caries or erosion for example, defensive mechanisms are available, producing either reactionary dentin usually from an odontoblast, or reparative dentin from other cells, e.g., pulp progenitor cells, which is usually void of tubules. Dentin also has an organic matrix (20%) which includes collagens (Types I, III, and V) and non-collagenous proteins, in addition to its water (10%) (Pashley, 1996; Goldberg et al., 2012). Both the mineral layers (enamel and dentin) are heterogeneous and provide protection to the vital soft-tissue - the pulp - centrally. These mineralized tissues are susceptible to dental decay—dental caries—one of the commonest, preventable diseases affecting the human population (Marcenes et al., 2013) where mineral is lost from the tissues and can lead to irreversible cavitation.

Imaging techniques aid detection of dental caries, the simplest being produced from the sensory organ of the eye, which uses the visible light of the electromagnetic spectrum. Light can interact with the mineralized tooth-tissue in a number of ways, such as reflection, scattering, transmission, or absorption. Absorption can produce heat or fluorescence. These interactions can contribute to optical detection methods, such as transillumination, optical coherence tomography and quantitative light-induced fluorescence. There are no health-risks from these methods, which are non-ionizing. Digital imaging fiber optic transillumination (DiFOTI) has limited penetration depth of dental caries but can be improved by using longer wavelengths of near-infrared (780–1550 nm), especially 1,310 nm, due to enamel transparency at these wavelengths. Penetration-depth of optical coherence tomography (OCT) can also be limited but detection of lesions just beyond the dentin-enamel junction have been reported. Mineralized tooth-tissue possesses the ability to auto-fluoresce and quantitative light-induced fluorescence (QLF) uses this property, whereas DIAGNOdent (Kavo) and the LF-pen is thought to use fluorescence from protoporphyrin IX and associated bacterial products, not the mineralized tissue (Hall and Girkin, 2004; Karlsson, 2010; Park et al., 2017).

Over a century ago, the first acceptable dental radiographs for clinical use were reported by Harrison (1896), utilizing X-rays from the electromagnetic spectrum. X-rays have limitations - such as the extent of demineralization needed before caries can be detected (Whaites, 2007) and its location, e.g., occlusal caries (Bader et al., 2002; Bader and Shugars, 2006). Occlusal lesions are positioned in the center of the biting-surface of the tooth and are less easily detected due to the bulk of sound mineralized tissue which surrounds them. This surrounding sound tissue reduces penetration of the X-ray beam, compared to the demineralized lesion which would allow a greater proportion of X-rays to pass onto the image receptor, providing contrast between the lesion and sound tissue. This results in the occlusal lesion being masked by the sound surrounding tissue. X-rays are also ionizing in nature with associated biological risks, e.g., somatic deterministic, somatic stochastic and genetic stochastic effects (Whaites, 2007).

An infra-red thermal camera captures naturally-emitted electromagnetic radiation from the infra-red region. Infra-red radiation has longer wavelengths (700 nm to 1mm) than X-rays (0.01–10 nm), is non-ionizing and totally harmless. The Herschel family were central in discovering infra-red radiation and William Herschel was credited in 1800, and John Herschel produced the first Thermogram in 1840 (Holst, 2000). By the mid-1900s, the military was maximizing the heat-seeking capacity of thermal imaging. Technological advancement in recent years provides accessible and affordable thermal cameras with potential for clinical diagnostic application in medicine. Currently, thermal imaging is not used to detect dental caries but warrants further investigation.

In Kaneko et al. (1999) and Zakian et al. (2010) assessed caries-detection with thermal imaging based on a drop in temperature due to the evaporation of moisture from the porous demineralized tissue compared to sound tissue. Their findings were positive but the thermal properties of the mineralized tissue were not considered. The two mineralized tissues, enamel and dentin, have different compositions and structures (as described earlier) which result in a range of values for thermal diffusivity (enamel $\approx 2.27–4.69 \times 10^{-7} m^2/s$, dentin $\approx 1.83–2.6 \times 10^{-7} m^2/s$) and thermal conductivity (enamel ≈0.45–0.93 W/mK, dentin ≈ 0.11–0.96 W/mK), as shown in **Table 1** (Lin et al., 2010a). These values were obtained from the use of thermocouples, a thermometer, a thermistor, a pulse-laser and infra-red thermography (Lisanti and Zander, 1950; Phillips et al., 1956; Soyenkoff and Okun, 1958; Craig and Peyton, 1961; Braden, 1962; Brown et al., 1989; Panas et al., 2003; Lin et al., 2010b).

A map provides spatial information from co-ordinates on two axes, such as X and Y. The use of a thermal value for each co-ordinate corresponding to a pixel of tooth-tissue could be represented from a grayscale, producing a thermal map specific to that tooth-tissue. This could show the spatial relationship of the thermal properties of the tooth-tissue as an image, rather than a series of numerical values. This may be more clearly understood from the map providing a 2-dimensional relationship of the thermal properties across the whole surface of the tooth-tissue. The thermal properties of enamel and dentin may be sufficiently different to visually distinguish enamel from dentin. Demineralized areas within both tissues may also

have different thermal properties due to tissue-changes, such as mineral loss from caries, which may be seen in the thermal map.

The primary aim of this study was to produce a thermal map of a sound, human tooth-slice to visually characterize human enamel and dentin. The secondary aim was to map a human tooth-slice with demineralized enamel and dentin to consider future diagnostic potential of thermal maps in caries-detection.

MATERIALS AND METHODS

Materials

Two lower-third molar teeth were ethically sourced from Leeds Dental Institute Research Tissue Bank. Both teeth were cut bucco-lingually with an Accutom-5 (Struers, Copenhagen, Denmark) into 1 mm-thick tooth-slices and then polished with an 800-grit abrasive sheet, with the addition of distilled water as needed. Slice-thickness was measured with a digimatic micrometer (IP65 Quantumike Mitutoyo). Photographs and radiographs of each tooth-slice were taken.

Method

A purpose-built thermal cube provided a stable thermal environment at 22°C (**Figure 1**) with macro-regulation from the room air-conditioning and micro-control from a thermal sensor (TD100 Temperature-Controller Auber Instruments) which activated heat-reduction from two thermoelectric cooling units (ActiveCool AC4G TE), or heat-addition from a heating-pad (25 × 35 cm, 2 amp, 15 W, Warmeplatte, BioGreen). A period of 35 min stabilization was allowed prior to commencing data-collection.

A fixed camera-mounting held the FLIR SC305 thermal camera with a x4 lens (resolution of 100 μm) at a focal distance of 8 cm. The parameters used with the camera were: Emissivity 0.96, Reflective Apparent Temperature 27.2°C and Humidity 50%. The recording-rate was 9-frames-per-second and data-collection was with ThermaCAM Researcher Professional 2.10 Software.

An aluminum hotplate (Bibby Techne DB-2TC) was positioned within the cube and stabilized at 30°C. Thermocouples (Omega Type-K SA1XL) were attached to the 0.5 mm thermal pad (thermal conductivity 6 W/mK) of the copper-based specimen-carrier.

Each tooth-slice was paper-dried, placed on the thermal pad and cooled on a block of ice until a temperature of 2°C was recorded on a Fluke 52 II thermometer. The carrier was manually transferred to the aluminum hotplate.

Data-capture by the thermal camera commenced prior to transfer of the carrier. Processing of data from selected areas-of-interest circled in blue (**Figure 2**) occurred initially in a macro-enabled Microsoft Excel File (Microsoft®) to provide time-temperature-curves according to frame-rate. This was followed by selection of the last half of data for curve-fitting to an exponential equation to ascertain the characteristic-time-to-relaxation (τ_c), which required bespoke software for use in Matlab (MathWorks®).

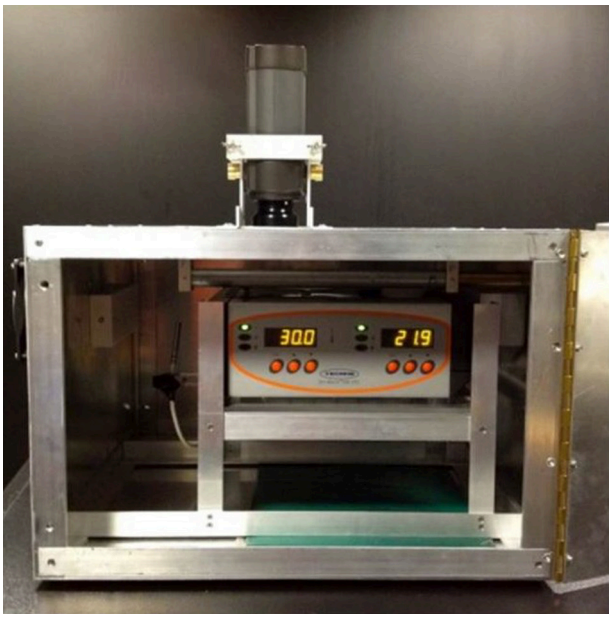

FIGURE 1 | Thermal cube with hotplate and heating-mat (green) in position, with camera secured on the cube by a fixed-mounting normal to the samples.

$$f(x) = C0 * \exp(-1 * x/\tau_c) + C1$$

The difference in value of characteristic-time-to-relaxation (τ_c) of the thermal pad and the tissue area-of-interest was applied to the formulae below to calculate the thermal diffusivity:

$$\alpha = \frac{4H^2}{\pi^2 \tau_c Diff}$$

$\alpha =$ Thermal Diffusivity(10^{-7}m^2/Sec)
$H =$ Half the thickness of the tissue (m)
$\tau_c Diff =$ τ_cTissue $-$ τ_cThermal Pad (Seconds)

Once the value of thermal diffusivity was known, thermal conductivity could be calculated:

$$\kappa = \alpha * \sigma * C_p$$

$\kappa =$ Thermal Conductivity (W/mK)
$\alpha =$ Thermal Diffusivity(10^{-7}m^2/Sec)
$\sigma =$ Density (Kg/m^3) $= 2800$ for enamel and 2248 for dentin (Lin et al., 2010b)
$C_p =$ Specific Heat Capacity (J/Kg k) $= 710$ for enamel and 1066.4 for dentin (Lin et al., 2010b)

The τ_c and the integral of the curve were calculated for each pixel of the image through the thermal sequence in Matlab (MathWorks®) software, from which two thermal maps were produced.

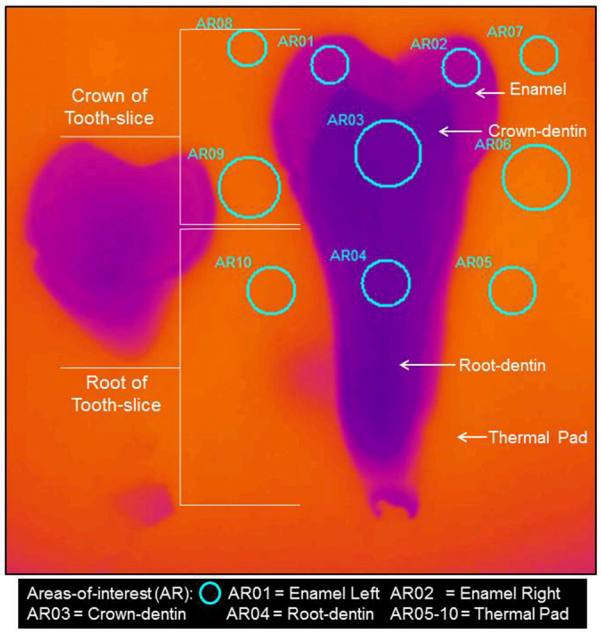

FIGURE 2 | Thermograph of Sample 1–Sound tooth-slice, with circular areas-of-interest shown to enable calculation of the characteristic-time-to-relaxation used in the computation of the thermal diffusivity of the tissues.

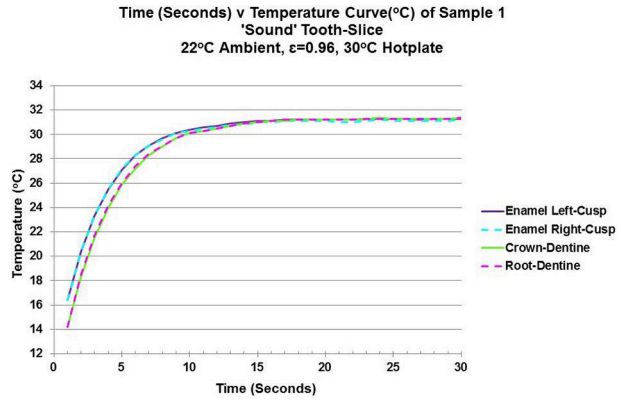

FIGURE 3 | Line Graph of Time (Seconds) v Temperature (°C) showing the data used for curve fitting the exponential equation - $f(x) = C0*\exp(-1*x/\tau_C) + C1$ - to calculate the characteristic-time-to-relaxation (τ_C) for enamel and dentin.

RESULTS

Tooth-Slice-Thickness

The thickness of the sound tooth-slice measured less than a millimeter in all areas, with the greatest enamel-thickness in the middle at 0.78 mm, the greatest crown-dentin-thickness recorded was on the left at 0.784 mm and the single measurement of the root-dentin was 0.785 mm. The carious tooth-slice was thicker in all areas, with the maximum thickness of enamel at 1.227 mm in the middle, similarly for crown-dentin at 1.223, and the thickest root-dentin was 1.166 mm on the left (see **Table 2** for all measurements).

Thermal Properties

The initial rewarming temperatures for the sound tooth-slice in both crown- and root-dentin (green and pink broken-lines) were lower than the two areas of enamel (purple and blue broken-lines). It took circa 30 s to reach thermal equilibrium of all tissues (**Figure 3**). The rate of rewarming in both regions of enamel are the same and marginally quicker (i.e., a steeper gradient) compared to both crown- and root-dentin which are also the same. The results for the right-hand side enamel and crown-dentin respectively, show differences in characteristic-times-to-relaxation: enamel at 3.655 s (95% CI 3.472, 3.838) compared to crown-dentin at 4.018 s (95% CI 3.855, 4.181), with no overlap in the confidence-intervals for either of these samples. The characteristic-time-to-relaxation (τ_c) is used to calculate the thermal properties of diffusivity and conductivity in conjunction with tissue-thickness. The results indicate from the sound tooth-slice that enamel has a higher value of thermal diffusivity (3.79–4.15 $\times$ $10^{-7}m^2/s$) and thermal conductivity (0.75–0.83 W/mK) than dentin thermal diffusivity (1.89–2.81 $\times$ $10^{-7}m^2/s$) and thermal conductivity (0.45–0.67 W/mK) except for one outlier for root dentin with thermal diffusivity of 7.71 $\times$ $10^{-7}m^2/s$ and thermal conductivity of 1.85 W/mK. All values are provided in **Table 3**. These values fall mainly within the accepted range for thermal diffusivity of enamel at 2.27–4.69 $\times$ $10^{-7}m^2/s$ and dentin at 1.83–2.6 $\times$ $10^{-7}m^2/s$ and thermal conductivity of enamel at 0.45–0.93 W/mK and dentin at 0.11–0.96 W/mK, as previously quoted in **Table 1**.

Within the carious tooth-slice, the rate of rewarming in the two sound enamel areas-of-interest (purple and blue broken-lines) are similar, whereas the enamel carious lesion is slower (red solid-line) (**Figure 4**). Carious enamel fails to reach equilibrium in the 30 s time-period. Crown-dentin (green broken-line) warms quicker than root-dentin (pink broken-line). The carious dentin (mustard solid-line) is the slowest of all tissues to rewarm and fails to reach equilibrium within the time-frame. The characteristic-time-to-relaxation for carious enamel is 5.381 s, which is slower than the crown dentin at 5.329 s. This is the only occassion where enamel has a slower characteristic-time-to-relaxation than dentin. All other values give enamel (4.78–4.902 s) a quicker time than dentin (5.521–6.001 s). The enamel has a lower value of thermal diffusivity, ranging from 1.13 $\times$ $10^{-7}m^2/s$ for the carious region to 1.85 $\times$ $10^{-7}m^2/s$ for the right-hand-side sound enamel, than others' findings. Thermal diffusivity shows the crown-dentin (0.77 $\times$ $10^{-7}m^2/s$) and root-dentin (0.57 $\times$ $10^{-7}m^2/s$) are reduced, compared to others' findings of 1.83–2.6 $\times$ $10^{-7}m^2/s$. The carious area of dentin has an increased value of 1.01 $\times$ $10^{-7}m^2/s$ which is comparable to the carious area of the enamel (1.13 $\times$ $10^{-7}m^2/s$). The thermal conductivity of carious enamel (0.22 W/mK) is similar to carious dentin (0.24 W/mK). All other values of thermal conductivity for enamel and dentin within the carious tooth-slice are lower than others' findings. All values are provided in **Table 3**.

TABLE 1 | Thermal diffusivity and thermal conductivity values of human enamel and dentin.

	Enamel	Dentin	Technique	Author	Year
α Thermal Diffusivity ($x10^{-7}m^2/s$)	4.2	2.6	Thermocouple	Braden	1964
	4.69	1.87-1.83	Thermometer	Brown, Dewey, Jacobs	1970
	2.27	1.92	Pulse Laser and Thermocouple	Panas, Żmuda, Terpilowski, Preiskorn	2003
	4.08	2.01	IR Thermography	Lin, Liu, Kim, Xu, Bai, Lu	2010
κ Thermal Conductivity (W/mK)		0.96	Thermocouple	Lisanti, Zander	1950
		0.11	Thermocouple	Phillips, Johnson, Phillips	1956
		0.45	Thermistor	Soyenkoff, Okun	1958
	0.93	0.58	Thermocouple	Craig, Peyton	1961
	0.92	0.63	Thermocouple	Braden	1964
	0.81	0.48	IR Thermography	Lin, Liu, Kim, Xu, Bai, Lu	2010

TABLE 2 | Dimensions of tooth-slices as recorded with a calibrated digimatic micrometer.

	Thickness of Teeth-Slices (mm)								
Sample	Enamel			Crown-Dentin			Root-Dentin		
	Left	Middle	Right	Left	Middle	Right	Left	Middle	Right
1	0.776	0.78	0.778	0.784	0.782	0.781		0.785	
2	1.174	1.227	1.161	1.169	1.223	1.166	1.166	1.157	1.164

Thermal Maps

The two thermal maps distinguish the mineralized tissues of enamel, dentin and the carious areas of both tissues using the thermal properties of characteristic-time-to-relaxation and heat-exchange during rewarming (**Figure 5**).

DISCUSSION

Infra-red thermal imaging is a technique which is yet to be maximized within the field-of-medicine and its subsidiary specialty - dentistry. Published work for determining the thermal properties of tooth-tissue (Panas et al., 2007; Lin et al., 2010b), was adapted to provide the current methodology. The provision of a stable environment in this study removed environmental temperature-confounders (unlike the previous investigations) and 22°C provided a realistic ambient room-temperature. Tooth-slice thicknesses of 2.2–3.15 mm were used in the previous studies, increasing the three-dimensional heat-transfer compared to the maximum thickness of 1.23 mm within this study. Lin et al. (2010b), applied heat to the occlusal surface of the samples and heat-transfer was recorded along the length of the tooth. Simultaneous heat-application to the irregular occlusal surface would be unlikely, compared to the application of vertical heat to the flat surface of the samples within this study and Panas et al. (2007). The tooth-slices within this study were viewed directly—unlike Lin et al. (2010b), who had applied a black layer of paint. They were also heated directly—unlike Panas et al. (2007), who used a dental cement to attach the samples to the baseplate. Neither of these additional layers was considered in their final calculations. Heat at 30°C was applied in this study to replicate the temperature of the anterior teeth in a living human being (Fanibunda, 1986).

Despite these variations, a single-sample (Lin et al., 2010b), shows comparable results with values reported, as does this study. Multiple samples from different teeth have not previously been reported from this technique, nor have areas of demineralization or caries. All samples are from different donors with inherent anomalies in the tissue-types, as previously described. Investigation of a point location or a single line of a single tissue-sample with any temperature-recording-method, e.g., thermal imaging (Panas et al., 2007; Lin et al., 2010b) or a single thermocouple (Panas et al., 2003) is not ideal. The larger the area-of-interest used for each tissue and the greater the sample-size, the more valid and reliable any inference from the findings. Within this study, two samples, one sound and one carious with a demineralized area, were investigated with multiple areas-of-interest for each tissue. Enamel values of thermal diffusivity and conductivity fall within proximity of known-ranges for the sound tooth-slice but do differ slightly between the two sides examined. Greater variation is seen within the demineralized enamel, where the carious area-of-interest returns the lowest values. This could be explained by the loss of mineral, but caution is needed as the range of values for the sound areas-of-interest differ by a similar proportion within the same sample. These findings appear appropriate to the nature of the tissues being investigated and a more general outcome (as described by Panas et al., 2003) is accepted. That is, following the application of heat and analysis with thermal imaging, a difference between the thermal response of enamel and dentin was detectable, with enamel tending to conduct heat quicker than dentin. The data from this study agrees with that baseline principle and within the two samples presented - sound and demineralized - the thermal properties indicate that enamel conducts heat quicker than dentin within each sample. Two exceptions are seen - one for carious enamel and one for the root-dentin outlier. The carious lesion will have a reduced mineral content - not quantified in this study - and returns a thermal conductivity

TABLE 3 | Compilation of sample-thickness as H (m), characteristic-time-to-relaxation (τ_C in Seconds), enabling the difference of τ_C to be calculated between the thermal pad and area-of-interest, leading to calculation of the thermal diffusivity and, hence, thermal conductivity of enamel and dentin in two slices of tooth - one sound and one carious.

	H = 0.5 Thickness (m)	Tc (Sec)	Tc Thermal Pad (Sec)		Tc Difference (Sec)		Thermal Diffusivity ($10^{-7}m^2$/Sec) ($4H^2/\pi^2$Tc Diff) α		Density (Kg/m^3) σ	Specific Heat Capacity (J/kg K) cp	Thermal Conductivity (W/mK) (α*σ*cp) k	
1-Sound tooth-slice			Left	Right	Left	Right	Left	Right			Left	Right
Lin value enamel								4.08				0.81
Panas value enamel								2.27				0.45
Enamel left	0.000388	3.719	3.572		0.147		4.15		2800	710	0.83	
Enamel right	0.000389	3.655		3.493		0.162		3.79	2800	710		0.75
Lin value dentin								2.01				0.48
Panas value dentin								1.92				0.46
Crown-dentin	0.000391	4.018	3.69	3.705	0.328	0.313	1.89	1.98	2248	1066.4	0.45	0.47
Root-dentin	0.0003925	3.918	3.696	3.837	0.222	0.081	2.81	7.71	2248	1066.4	0.67	1.85
2-Carious tooth-slice			Left	Right	Left	Right	Left	Right			Left	Right
Lin value enamel								4.08				0.81
Panas value enamel								2.27				0.45
Enamel right	0.000587	4.78		4.027		0.753		1.85	2800	710		0.37
Enamel left	0.0005805	4.902	4.027		0.875		1.56		2800	710	0.31	
Enamel caries	0.0006135	5.381	4.027		1.354		1.13		2800	710	0.22	
Lin value dentin								2.01				0.48
Panas value dentin								1.92				0.46
Crown-dentin	0.0005845	5.329	3.528		1.801		0.77		2248	1066.4	0.18	
Root-dentin	0.000582	6.001		3.609		2.392		0.57	2248	1066.4		0.14
Dentin caries	0.0006115	5.521	4.027		1.494		1.01		2248	1066.4	0.24	

which lies between the crown-dentin and carious dentin of the same tooth-slice. Comparison between sample-values does not agree with this principle and may be due to the natural variation of the samples from different people, the age of the teeth, the orientation of enamel prisms and dentinal tubules or the carious process. Further work is needed to investigate these relationships.

The purpose of this study was to see if enamel and dentin could be visualized from their individual thermal properties within a map. A thermal map provides a 2-dimensional diagram of the spatial relationship of every thermal value per pixel calculated across the whole tooth-slice. This advances the techniques previously described and adds to the information of an optical image. The thermal maps are produced from the gradient of the rewarming curve - characteristic-time-to-relaxation - and the integral of the curve - heat-exchange. As seen in **Figure 5**, the two types of thermal map do characterize enamel and dentin.

The characteristic-time-to-relaxation map of sample one, the sound tooth-slice, shows a diffuse boundary between enamel and dentin and is sensitive to the tissue-thickness, as shown from the sloping-sides of the tooth-slice in the root-area. In the second sample, the carious tooth-slice, the slope of the root makes no contact with the thermal pad and is seen clearly as a "white" area at the bottom of the root. This is radiolucent on the X-ray. The thermal map does detect the thin tooth-tissue in the pulp-chamber and produces the outline of the "true" pulp-chamber as seen in the photograph, but this is not seen in the radiographic image where there is insufficient tooth-tissue to attenuate the X-rays. The heat-exchange thermal map shows distinct contrast between enamel and dentin and the carious change within the enamel and dentin is clearly visible, compared to the characteristic-time-to-relaxation thermal map, where there is less contrast of the carious lesion within enamel

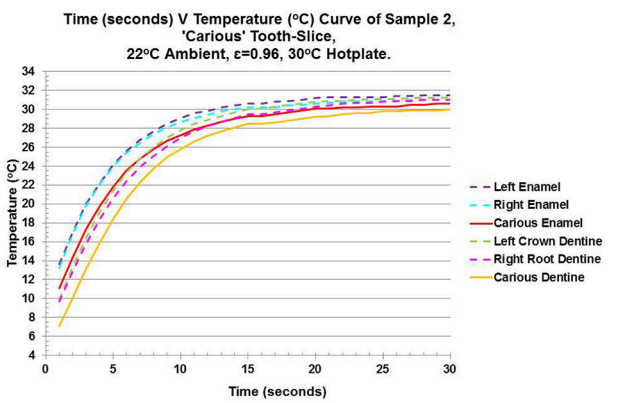

FIGURE 4 | Line Graph of Time (Seconds) v Temperature (°C) showing the data used for curve fitting the exponential equation - $f(x) = C0*\exp(-1*x/\tau_C) + C1$ - to calculate the characteristic-time-to-relaxation (τ_C) for enamel, dentin and carious tissue of both enamel and dentin.

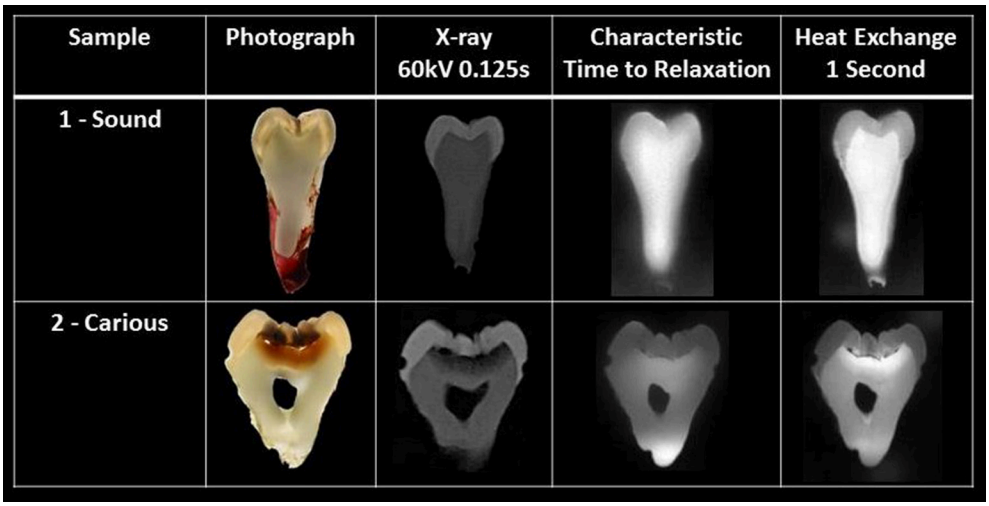

FIGURE 5 | Sample 1- Sound tooth-slice and Sample 2 - Carious tooth-slice. Initially, a photograph is shown, followed by an X-ray, then the characteristic-time-to-relaxation thermal map and, finally, the heat-exchange thermal map depicting enamel, dentin and carious areas of enamel and dentin.

and diffuse change is seen in dentin. All the advantages of the characteristic-time-to-relaxation thermal map are retained by the heat-exchange thermal map.

The thermal camera and lens used within this study had a spatial resolution of 100 μm producing 5 line-pairs per mm (lp/mm) which was confirmed with a USAF1951 Positive Test Target. OCT has a higher resolution at 5–15 μm (from ≈33 lp/mm), as does DiFOTI at 43 pixels/mm (≈ 21 lp/mm) (Lancaster et al., 2013). The spatial resolution of intra-oral bitewing radiographs has improved from spatial resolutions not dissimilar to those of this thermal camera, up to 20 lp/mm. Unaided human vision is claimed to detect 11 lp/mm on film (Künzel et al., 2003). Phosphor plates can deliver approximately 6–20 lp/mm depending on the age of the plate (Buchanan et al., 2017) and the machine used, e.g., VistaScan or Digora (Li et al., 2008). The spatial resolution defines the ability to distinguish two separate points but this does not necessarily transfer to diagnostic ability for the human operator. The 5 lp/mm available with the thermal camera used produces an acceptable image not dissimilar to that of the digital radiograph from phosphor plates. The lesion shown within the demineralized tooth-slice is large, and the minimum size and level of demineralization detectable with this system is currently unknown and requires additional work with suitable test-objects. Spatial resolution can be limited due to equipment and the infra-red wavelength (700 nm to 1 mm) which will always be less than that of X-rays (0.01 to 10 nm) but may not be a restricting factor for diagnostic ability. This study has viewed slices of teeth *in-vitro*, not a whole tooth, and the findings can underpin future models on whole teeth. Two studies have investigated carious lesions in whole human teeth *in-vitro* - one looking at artificially-created lesions on the smooth labial surface of incisors (Kaneko et al., 1999), and the other viewing naturally-occurring occlusal caries on the surface of molar teeth (Zakian et al., 2010). The theory of a thermal difference between sound tooth-tissue and carious tissue was based on evaporative cooling due to an increase in moisture-content within the micro-pores of the carious lesion. This was found to provide a positive outcome in both studies. Consideration of the thermal properties of the tissues, as seen in this study, were not presented in either of the whole-tooth studies, but their outcomes positively reinforce the need for further work. Cooling by ice to 2°C and rewarming of the samples was observed in this study and there are clinical cooling-methods, such as cryogesic sprays, already in use within dentistry. Water stored in a domestic fridge is approximately 5°C, and the surface-temperature of ice immediately following removal from a domestic freezer is approximately −15°C and, when combined, could provide suitable cooling. This is being investigated for comfort and time-of-application.

The use of thermal imaging to detect approximal caries is unlikely as it cannot penetrate tissues in the way X-rays do. However, detection of early smooth-surface lesions and occlusal lesions would allow preventive measures to be prescribed. X-rays have limitations, as previously mentioned, as do optical detection methods. Thermal imaging may complement our current armamentarium. Detection of active and arrested caries remains uninvestigated with thermal imaging and consideration will be needed for other potential causes of difference in tooth structure and composition, e.g., amelogenesis imperfecta and molar incisor hypomineralization.

CONCLUSIONS

The enamel and dentin of tooth-slices can be characterized *in-vitro* from their thermal properties, as seen in the thermal maps of heat-exchange and characteristic-time-to-relaxation. The heat-exchange map produces better contrast between enamel and dentin than the characteristic-time-to-relaxation map. Within enamel and dentin, demineralized tissue can be detected in both maps, with heat-exchange providing the greatest contrast within

both tissues. These thermal maps support further investigation of thermal imaging to complement diagnosis of caries.

AUTHOR CONTRIBUTIONS

PL, DB, designed the Study, undertook the acquisition, analysis and interpretation of data, wrote the first draft of the manuscript, provided contribution to revision and final approval of the manuscript and are accountable for the work presented. FC, VC, were involved with conception of the design, revision and approval of the manuscript.

ACKNOWLEDGMENTS

Some data within this manuscript was presented at the Enamel 9 Conference, 30th October to 3rd November, 2016 and PL's attendance at the Conference was supported by an Early Career Research Award from Enamel 9, which was gratefully received.

REFERENCES

Bader, J. D., and Shugars, D. A. (2006). The evidence supporting alternative management strategies for early occlusal caries and suspected occlusal dentinal caries. *J. Evid. Based Dent. Pract.* 6, 91–100. doi: 10.1016/j.jebdp.2005.12.004

Bader, J. D., Shugars, D. A., and Bonito, A. J. (2002). A systematic review of the performance of methods for identifying carious lesions. *J. Public Health Dent.* 62, 201–213. doi: 10.1111/j.1752-7325.2002.tb03446.x

Braden, M. (1962). Heat conduction in teeth and the effect of lining materials. *J. Dent. Res.* 43, 315–322. doi: 10.1177/00220345640430030201

Brown, W. S., Dewey, W. A., and Jacobs, H. (1989). Thermal properties of teeth. *J. Dent. Res.* 49, 752–755. doi: 10.1177/00220345700490040701

Buchanan, A., Benton, B., Carraway, A., Looney,S., and Kalathingal, S. (2017). Perception versus reality–findings from a phosphor plate quality assurance study. *Oral Surg. Oral Med. Oral Pathol. Oral Radiol.* 123, 496–501. doi: 10.1016/j.oooo.2016.12.004

Craig, R. G., and Peyton, F. A. (1961). Thermal conductivity of tooth structure, dental cements and amalgam. *J. Dent. Res.* 40, 411–418. doi: 10.1177/00220345610400030501

Fanibunda, K. B. (1986). The feasibility of temperature measurement as a diagnostic procedure in human teeth. *J. Dent.* 14, 126–129. doi: 10.1016/0300-5712(86)90077-1

Goldberg, M., Kulkarni, A. B., Young, M., and Boskey, B. (2012). Dentin:structure, composition and mineralization: the role of dentin ecm in dentin formation and mineralization. *Front. Biosci. (Elite. Ed).* 3, 711–735. doi: 10.2741/e281

Hall, A., and Girkin, J. M. (2004). A review of potential new diagnostic modalities for caries lesions. *J. Dent. Res.* 83, C89–C94. doi: 10.1177/154405910408301s18

Harrison, F. (1896). The 'X' rays in the practice of dental surgery. *Br. Dent. J.* 17, 624–628.

Holst, G. C. (2000). Common Sense Approach to Thermal Imaging First. Winter Park, FL: JCD Publishing and SPIE Optical Engineering Press.

Kaneko, K., Matsuyama, K., and Nakashima, S. (1999). "Quantification of early carious enamel lesions by using an infrared camera *in-vitro*," in *4th Annual Indiana Conference,* ed G. K. Stookey (Indianapolis), 83–100.

Karlsson, L. (2010). Caries detection methods based on changes in optical properties between healthy and carious tissue. *Int. J. Dent.* 2010:270729. doi: 10.1155/2010/270729

Kunin, A. A., Evdokimova, A. Y., and Moiseeva, N. S. (2015). Age-related differences of tooth enamel morphochemistry in health and dental caries. *EPMA J.* 6:3. doi: 10.1186/s13167-014-0025-8

Künzel, A., Scherkowski, D., Willers, R., and Becker, J. (2003). Visually detectable resolution of intraoral dental films. *Dentomaxillofacial Radiol.* 32, 385–389. doi: 10.1259/dmfr/22478778

Lancaster, P., Carmichael, F., Britton, J., Craddock, H., Brettle, D., and Clerehugh, V. (2013). Surfing the spectrum–what is on the horizon? *Br. Dent. J.* 215, 401–409. doi: 10.1038/sj.bdj.2013.994

Li, G., Berkhout, W. E. R., Sanderink, G. C. H., Martins, M., and van der Stelt, P. F. (2008). Detection of *in-vitro* proximal caries in storage phosphor plate radiographs scanned with different resolutions. *Dentomaxillofacial Radiol.* 37, 325–329. doi: 10.1259/dmfr/62591340

Lin, M., Xu, F., Lu, T. J., and Bai, B. F. (2010a). A review of heat transfer in human tooth-experimental characterization and mathematical modelling. *Dental Mater.* 26, 501–513. doi: 10.1016/j.dental.2010.02.009

Lin, M., Liu, Q. D., Kim, T., Xu, F., Bai, B. F., and Lu, T. J. (2010b). A new method for characterization of thermal properties of human enamel and dentin: influence of microstructure. *Infrar. Phys. Technol.* 53, 457–463. doi: 10.1016/j.infrared.2010.09.004

Lisanti, V. F., and Zander, H. A. (1950). Thermal conductivity of dentin. *J. Dent. Res.* 29, 493–497. doi: 10.1177/00220345500290041201

Marcenes, W., Kassebaum, N. J., Bernabe, E., Flaxman, A., Naghavi, M., Lopez, A., et al. (2013). Global burden of oral conditions in 1990-2010: a systematic analysis. *J. Dent. Res.* 92, 592–597. doi: 10.1177/0022034513490168

Panas, A. J., Preiskorn, M., Dabrowski, M., and Zmuda, S. (2007). Validation of hard tooth tissue thermal diffusivity measurements applying an infrared camera. *Infrar. Phys. Technol.* 49, 302–305. doi: 10.1016/j.infrared.2006.06.021

Panas, A. J., Zmuda, S., Terpilowski, J., and Preiskorn, M. (2003). Investigation of the thermal diffusivity of human tooth hard-tissue. *Int. J. Thermophys.* 24, 837–848. doi: 10.1023/A:1024004803596

Park, K.-J., Haak, R., Ziebolz, D., Krause, F., and Schneider, H. (2017). OCT assessment of non-cavitated occlusal carious lesions by variation of incidence angle of probe light and refractive index matching. *J. Dent.* 62, 31–35. doi: 10.1016/j.jdent.2017.05.005

Pashley, D. H. (1996). Dynamics of the pulpo-dentin complex. *Crit. Rev. Oral Biol. Med.* 7, 104–133. doi: 10.1177/10454411960070020101

Phillips, R. W., Johnson, R. J., and Phillips, L. J. (1956). An improved method for measuring the coefficient of thermal conductivity of dental cement. *J. Am. Dent. Assoc.* 53, 577–583. doi: 10.14219/jada.archive.1956.0217

Soyenkoff, B. C., and Okun, J. H. (1958). Thermal conductivity measurements of dental tissues with the aid of thermistors. *J. Am. Dent. Assoc.* 57, 23–30. doi: 10.14219/jada.archive.1958.0234

Whaites, E. (2007). *Essentials of Dental Radiography and Radiology*, 4th *Edn*. Edinburgh: Churchill, Livingstone.

Zakian, C. M., Taylor, A. M., Ellwood, R. P., and Pretty, I. A. (2010). Occlusal caries detection by using thermal imaging. *J. Dent.* 38, 788–795. doi: 10.1016/j.jdent.2010.06.010

Conflict of Interest Statement: The authors declare that the research was conducted in the absence of any commercial or financial relationships that could be construed as a potential conflict of interest.

Copyright © 2017 Lancaster, Brettle, Carmichael and Clerehugh. This is an open-access article distributed under the terms of the Creative Commons Attribution License (CC BY). The use, distribution or reproduction in other forums is permitted, provided the original author(s) or licensor are credited and that the original publication in this journal is cited, in accordance with accepted academic practice. No use, distribution or reproduction is permitted which does not comply with these terms.

frontiers in Physiology

ORIGINAL RESEARCH
published: 22 February 2017
doi: 10.3389/fphys.2017.00104

In Vitro Acid-Mediated Initial Dental Enamel Loss Is Associated with Genetic Variants Previously Linked to Caries Experience

Alexandre R. Vieira[1,2]*, *Merve Bayram*[3], *Figen Seymen*[4], *Regina C. Sencak*[1], *Frank Lippert*[5] and *Adriana Modesto*[1,2]

[1] Department of Oral Biology, School of Dental Medicine, University of Pittsburgh, Pittsburgh, PA, USA, [2] Department of Pediatric Dentistry, School of Dental Medicine, University of Pittsburgh, Pittsburgh, PA, USA, [3] Department of Pedodontics, School of Dentistry, Medipol Istanbul University, Istanbul, Turkey, [4] Department of Pedodontics, School of Dentistry, Istanbul University, Istanbul, Turkey, [5] Department of Cariology, Operative Dentistry and Dental Public Health, School of Dentistry, Indiana University, Indianapolis, IN, USA

OPEN ACCESS

Edited by:
Thimios Mitsiadis, University of Zurich, Switzerland

Reviewed by:
Claudio Cantù, University of Zurich, Switzerland
Aris N. Economides, Regeneron Pharmaceuticals, Inc., USA
Catherine Chaussain, Université Paris Descartes, France

***Correspondence:**
Alexandre R. Vieira
arv11@pitt.edu

Specialty section:
This article was submitted to Craniofacial Biology and Dental Research, a section of the journal Frontiers in Physiology

Received: *20 December 2016*
Accepted: *08 February 2017*
Published: *22 February 2017*

Citation:
Vieira AR, Bayram M, Seymen F, Sencak RC, Lippert F and Modesto A (2017) In Vitro Acid-Mediated Initial Dental Enamel Loss Is Associated with Genetic Variants Previously Linked to Caries Experience. Front. Physiol. 8:104. doi: 10.3389/fphys.2017.00104

We have previously shown that *AQP5* and *BTF3* genetic variation and expression in whole saliva are associated with caries experience suggesting that these genes may have a functional role in protecting against caries. To further explore these results, we tested *ex vivo* if variants in these genes are associated with subclinical dental enamel mineral loss. DNA and enamel samples were obtained from 53 individuals. Enamel samples were analyzed for Knoop hardness of sound enamel, integrated mineral loss after subclinical carious lesion creation, and change in integrated mineral loss after remineralization. DNA samples were genotyped for single nucleotide polymorphisms using TaqMan chemistry. Chi-square and Fisher's exact tests were used to compare individuals above and below the mean sound enamel microhardness of the cohort with alpha of 0.05. The A allele of *BTF3* rs6862039 appears to be associated with harder enamel at baseline ($p = 0.09$), enamel more resistant to demineralization ($p = 0.01$), and enamel that more efficiently regain mineral and remineralize ($p = 0.04$). Similarly, the G allele of *AQP5* marker rs3759129 and A allele of *AQP5* marker rs296763 are associated with enamel more resistant to demineralization ($p = 0.03$ and 0.05, respectively). *AQP5* and *BTF3* genetic variations influence the initial subclinical stages of caries lesion formation in the subsurface of enamel.

Keywords: dental caries, dental enamel, dental erosion, transcription factors, aquaporins

INTRODUCTION

Dental caries is a complex multifactorial disease and historically the biological factors operating within the host have been less explored. Our group has, for the last decade, investigated the possible role of genetic variation in the individual susceptibility to caries. Our results suggest, as expected, that several genes underlying multiple mechanisms (i.e., enamel formation, immune response, saliva composition, and quantity) are associated with dental caries (reviewed in Nibali et al., 2016).

One methodological challenge has been the use of past and current caries experience as a measure of disease. We believe that caries experience indicators do not capture fully the underlying

mechanisms modulating the pathogenesis of dental caries in an individual, which may hinder discovery if one is trying to identify factors increasing or decreasing individual susceptibility to disease. With that idea in mind, we started to define the disease based on subclinical enamel loss (Shimizu et al., 2012; Weber et al., 2014; Bayram et al., 2015; Vieira et al., 2015) or presence of periapical pathology related to deep caries lesions in dentin (Menezes-Silva et al., 2012; Dill et al., 2015; Maheshwari et al., 2016). Typically, sound enamel microhardness is a poor indicator for susceptibility to demineralization (Lippert and Lynch, 2014). A myriad of factors are involved in the caries process and focusing only on enamel, structural (e.g., pore size and volume, ratio between interprismatic and prismatic enamel fractions) and compositional differences (e.g., Mg, Na, CO_3, F contents) are likely the predetermining factors for caries susceptibility. We studied sound enamel microhardness presently to gain further insight into potential genetic factors predetermining susceptibility to demineralization and to explain variations in sound enamel microhardness. Here we are expanding this work to two loci that we previously showed are associated with caries experience, 5q13.2 and 12q13.12, to verify if we can still detect associations when a different phenotypical definition for dental caries is used.

METHODS

This study was approved by the Ethics Committee of the Istanbul University, Medical Faculty, Istanbul, Turkey and the University of Pittsburgh Institutional Review Board (IRB# 11070236). Written informed consent was obtained from all participating individuals and parents/legal guardians. Fifty-three orthodontic patients from Istanbul University, Faculty of Dentistry, Department of Orthodontics, participated in this study during the period 5 September 2011 to 30 November 2012. Participants had an indication for extraction of pre-molars for orthodontic reasons and were consecutively invited to participate in the study during the period described above. They agreed to donate their extracted tooth (teeth). One first premolar, extracted for orthodontic reasons, was used from each participant as a source of enamel.

Unstimulated saliva samples were obtained from all participants and stored in Oragene DNA Self-Collection kits (DNA Genotek, ON, Canada) at room temperature until processed. DNA was extracted according to the manufacturer's instructions. Ten single nucleotide polymorphisms (SNPs) were selected, including six in the aquaporin locus 12q13.2 (rs3759129, rs10875989, rs1996315, rs2878771, rs296763, and rs467323) and four located in 5q13.2 (rs27565, rs4700418, rs875459, and rs6862039). These SNPs were chosen based on the results of our previous fine mapping studies on the two loci (Shimizu et al., 2013; Anjomshoaa et al., 2015). Polymerase chain reactions with TaqMan (hydrolysis probes that are designed to increase the specificity of quantitative PCR) SNP Genotyping Assays from Applied Biosystems (Valencia, CA, USA), with a total volume of 3 μl per reaction and 3.0 ng of DNA per reaction, were used for genotyping all selected markers in a Tetrad PTC225 thermocycler from MJ Research (Waltham, MA, USA). Genotype detection and analysis were performed using the ABI 7900HT with ABI SDS software (Applied Biosystems, Valencia, CA, USA).

Fifty-three caries-free premolar teeth (one from each participant), extracted for orthodontic reasons, were studied. **Figure 1** summarizes the study design. Caries experience of this cohort was high, with a mean DMFT score of 5.19.

The tissue remnants were cleaned from the teeth and then teeth were stored in 10% buffered formalin (pH 7.0) solution at 4°C until required for initial laboratory manipulation. The crowns were separated from the roots, and then each tooth was cut into 3 × 3-mm specimens using a low-speed saw (Isomet, Buehler, Lake Bluff, IL, USA). The teeth were stored in thymol during the sample preparation process. The specimens were embedded individually in acrylic resin (Varidur, Buehler) and polished to create flat surfaces to facilitate surface microhardness testing using Struers Rotopol 31/Rotoforce 4 polishing unit (Struers Inc., Cleveland, PA, USA). Specimens were ground flat and polished with water-cooled abrasive disks (500-, 1,200-, 2,400-, and 4,000-grit SiC papers; MDFuga, Struers Inc., Cleveland, Ohio, USA) and polishing cloth with diamond suspension (1 μm; Struers Inc.). After the polishing procedures, specimens were sonicated in neutral detergent solution and rinsed with deionized water. As a final cleaning step, the specimens were sonicated in a detergent solution (Micro-90 concentrated cleaning solution with 2 % dilution) for 3 min. The specimens were finally assessed under Nikon SMZ 1500

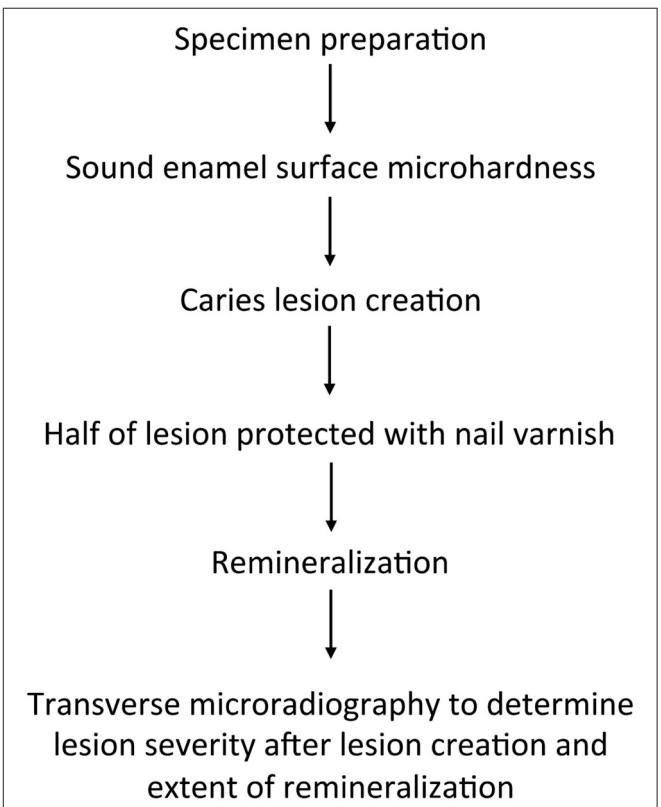

FIGURE 1 | Summary of the study design.

stereomicroscope at ×10 magnification. Accepted specimens had no obvious cracks, areas of hypomineralization, or other flaws in the enamel surface.

Initial hardness of each specimen was determined using a Knoop microhardness indenter (2100 HT; Wilson Instruments, Norwood, MA, USA) at a load of 50 g for 15 s. The average specimen surface microhardness was determined from five indentations placed in the center of the surface of each specimen, ∼100 μm apart from one another.

Early carious lesions were created in the specimens utilizing a demineralization protocol based on that by White (1987), which has been extensively studied using a variety of techniques over the years (White, 1987; Churchley et al., 2011). Artificial lesions were formed in the enamel specimens of each disk by a 5-day immersion into a solution containing 0.1 M lactic acid, 4.1 mM $CaCl_2 \times 2\ H_2O$, 8.0 mM KH_2PO_4, and 0.2% w/v Carbopol 907 (BF Goodrich Co., USA), pH adjusted to 5.0 using KOH, for 5 days at 37°C. Demineralization was performed at a ratio of 10 ml of solution per specimen. The resulting lesions were early, shallow, subsurface[1] lesions with a typical, average depth of approximately 50 μm. After lesion creation, approx. half of the lesion surface area was covered with colored, acid-resistant nail varnish to preserve a baseline lesion for future analysis.

All lesions were then remineralized for 4 days at 37°C using "resting plaque fluid" (Lynch et al., 2007) with the following composition: 10 mM acetic acid, 1.0 mM $CaCl_2 \times 2\ H_2O$, 12.7 mM KH_2PO_4, 130 mM KCl, 20 mM HEPES, 0.1 ppm F (NaF), pH adjusted to 6.5 using KOH.

Sections, approximately 100 μm in thickness and two per specimen, were cut from the center of the specimens across the varnish-covered lesion area and remineralized lesion window using a Silverstone-Taylor Hard Tissue Microtome (Scientific Fabrications Laboratories, USA). The sections were mounted, with an aluminum step wedge, on high resolution glass plate Type I A (Microchrome Technology Inc., San Jose, CA) and X-rayed at 20 kV and 30 mA at a distance of 42 cm for 65 min. The film was developed in Kodak D-19 developer for 3 min, placed in a stop bath (Kodak 146-4247) for 45 s, and then fixed (Kodak 146-4106) for 3 min. All plates were then rinsed in deionized water for 15 min and air-dried. Microradiographs were examined with a Zeiss EOM microscope in conjunction with the TMR software v.3.0.0.11. Sound enamel was assumed to be 87% v/v mineral. Integrated mineral loss (ΔZ) was recorded for both the varnish-covered lesion baseline area and the remineralized lesion. The difference was calculated (pre–post data) to assess the extent of remineralization.

Based on sound enamel hardness values, subjects were classified into dichotomous groups (baseline values or rate changes above or below the average of the group). Subjects were classified as having "softer enamel" (below the average of the group) and "harder enamel" (above the average of the group) for determination of hardness phenotypes. Chi-square and Fisher's exact tests were used to assess association between the SNPs and hardness values by the use of the PLINK software package (Purcell et al., 2007) with an established alpha of 0.05.

[1]The chosen demineralization procedure will result in the formation of early caries lesions. The most prominent feature of these lesions is that demineralization is primarily confined to enamel mineral below the surface. Hence, the term "subsurface" demineralization has been introduced into the literature to differentiate to surface loss such as that occurring during dental erosion.

RESULTS

Table 1 shows the mean values of hardness and **Table 2** summarizes all genotyping frequencies and comparisons were made between individuals that showed levels of enamel loss above or below the mean loss of the studied sample. The A allele of *BTF3* rs6862039 appears to be associated with harder enamel at baseline ($p = 0.09$), enamel more resistant to demineralization ($p = 0.01$), and enamel that more efficiently regain mineral and remineralize ($p = 0.04$). Similarly, the G allele of *AQP5* marker rs3759129 and A allele of *AQP5* marker rs296763 are associated with enamel more resistant to demineralization ($p = 0.03$ and 0.05, respectively). No other markers studied showed statistical evidence of association.

DISCUSSION

Our data confirm the association between dental caries and genetic variation in *BTF3* and *AQP5* we have previously reported (Shimizu et al., 2013; Anjomshoaa et al., 2015). When we reported the association between caries experience and *BTF3* (Shimizu et al., 2013), we tested if *BTF3* was expressed in whole saliva and if expression that correlated with caries experience. We suggested based on our initial findings that BTF3 may be involved in caries susceptibility acting through saliva. This gene encodes the basic transcription factor 3, a protein that forms a stable complex with RNA polymerase IIB and is required for transcriptional initiation. Alternative splicing results in multiple transcript variants encoding different isoforms. *BTF3* has multiple pseudogenes (https://www.ncbi.nlm.nih.gov/gene, Gene ID = 689). In gastric cancer, BTF3 expression is associated with enhanced cell proliferation, reduced cell cycle regulation, and apoptosis and its silencing inhibits proliferation of gastric cancer cells (Liu et al., 2013). Our data may suggest that *BTF3* may be involved in the formation of the enamel, possibly acting as a transcription factor controlling cell proliferation.

Aquaporin 5 (AQP5) is a water channel protein expressed in salivary and lacrimal glands, various types of epithelial cells, and during tooth development (Ishida et al., 1997; Nielsen et al., 1997; Funaki et al., 1998; Hamann et al., 1998; Felszeghy

TABLE 1 | Mean hardness of studied specimens.

Study phase	Baseline	After creation of artificial lesion	After remineralization
Mean Enamel Hardness	45.95	64.92	76.62

TABLE 2 | Genotyping frequencies and summary results of the association studies.

Locus	Marker (rs#) and gene	Genotype/ allele	Number of Individuals (Genotypes) or Alleleswith less enamel loss	Number of Individuals (Genotypes) or Alleleswith more enamel loss	*p*-value	Number of Individuals (Genotypes) or Alleleswith less enamel loss	Number of Individuals (Genotypes) or Alleleswith more enamel loss	*p*-value	Number of Individuals (Genotypes) or Alleleswith less enamel loss	Number of Individuals (Genotypes) or Alleleswith more enamel loss	*p*-value
			Baseline			After creation of artificial lesion			After remineralization		
5q13.2	27565 (*PART1*)	CC	3	4	0.68#	2	6	0.77#	5	5	0.89#
		CT	13	14		11	19		16	18	
		TT	1	3		1	3		4	3	
		C	19	22	0.76##	15	31	0.88##	26	28	0.85##
		T	15	20		13	25		24	24	
	4700418 (*ZSWIM6*)	CC	5	7	0.71#	3	9	0.64#	7	7	0.98#
		CG	7	6		7	10		11	11	
		GG	5	8		4	9		7	8	
		C	17	20	0.84##	13	28	0.76##	25	25	0.85##
		G	17	22		15	28		25	27	
	875459 (*CCNB1*)	GG	5	5	0.69#	2	8	0.3#	5	0	0.32#
		GT	11	13		9	18		18	2	
		TT	1	3		3	2		2	17	
		G	21	23	0.84##	13	34	0.21##	28	26	0.54##
		T	13	19		15	22		22	26	
	6862039 (*BTF3*)	AA	1	0	0.22#	1	0	0.1#	2	0	0.32#
		AT	2	1		2	1		4	2	
		TT	8	17		7	22		17	17	
		A	4	1	0.04##	4	1	0.01##	8	2	0.09##
		T	18	35		16	45		38	36	
Aquaporin 12q13.12	467323 (*AQP2*)	AA	2	3	0.88#	1	4	0.5#	1	4	0.32#
		AG	8	11		6	15		12	13	
		GG	7	7		7	9		12	9	
		A	12	17	0.64##	8	23	0.26##	14	21	0.19##
		G	22	25		20	33		36	31	
	2878771 (*AQP2*)	AA	2	0	0.26#	1	1	0.83#	2	0	0.3#
		AG	5	8		5	9		7	7	
		GG	10	13		8	18		15	19	
		A	9	8	0.44##	7	11	0.57##	11	7	0.22##
		G	25	34		21	45		37	45	
	10875989 (*AQP2*)	AA	2	3	0.9#	1	4	0.26#	1	4	0.18#
		AG	9	12		6	17		12	15	
		GG	6	6		7	7		12	7	

(Continued)

TABLE 2 | Continued

Locus	Marker (rs#) and gene	Genotype/ allele	Number of Individuals (Genotypes) or Alleleswith less enamel loss	Number of Individuals (Genotypes) or Alleleswith more enamel loss	*p*-value	Number of Individuals (Genotypes) or Alleleswith less enamel loss	Number of Individuals (Genotypes) or Alleleswith more enamel loss	*p*-value	Number of Individuals (Genotypes) or Alleleswith less enamel loss	Number of Individuals (Genotypes) or Alleleswith more enamel loss	*p*-value
			Baseline			After creation of artificial lesion			After remineralization		
		A	13	18	0.68##	8	25	0.16##	14	23	0.09##
		G	21	24		20	31		36	29	
	3759129 (*AQP5*)	AA	8	13	0.36#	5	19	0.07#	14	14	0.91#
		AG	6	5		6	6		6	8	
		GG	1	0		1	0		1	1	
		A	22	31	0.19##	16	44	0.03##	34	36	0.75##
		G	8	5		8	6		8	10	
	296763 (*AQP5*)	AA	2	0	0.25#	1	1	0.12#	0	2	0.21#
		AG	6	7		7	6		11	7	
		GG	9	14		6	21		14	17	
		A	10	7	0.18##	9	8	0.05##	11	11	1.0#
		G	24	35		19	48		39	41	
	1996315 (*AQP6*)	AA	0	0	0.52#	0	0	0.93#	0	0	0.23#
		AG	3	2		3	5		3	6	
		GG	12	15		11	17		20	16	
		A	3	2	0.54##	3	5	0.93##	3	6	0.26##
		G	27	32		25	39		43	38	

#*p-value of the comparison of genotyping frequencies between individuals with enamel loss below and above the mean of the studied group. Chi-square or Fisher's exact tests with 2 degrees of freedom.*

##*p-value of the comparison of allele frequencies between individuals with enamel loss below and above the mean of the studied group. Chi-square or Fisher's exact tests with 1 degree of freedom.*

et al., 2004). AQP5 interactions during dental development may impact the formation of dental enamel and susceptibility to dental caries (Anjomshoaa et al., 2015). Since the AQP locus was not associated with enamel hardness, we thought the role of AQP5 in caries was through salivation rather than influencing enamel development. We decided to reassess our microhardness experiments and this time we tested the specimens, instead directly at the treated surface, in the subsurface. These analyses suggested that genetic variants in AQP5 are associated with initial enamel loss, which is a surrogate for the development of early caries lesions. These data support the idea that *AQP5* impacts enamel development possibly making it more susceptible to caries.

While concerned about multiple testing, we avoided to apply the strict Bonferroni correction and increase type II error. If we had used Bonferroni correction, we would have lowered the alpha to 0.005 (0.05/10). We have demonstrated previously (Vieira et al., 2008) that known true associations are missed when correction for multiple testing is implemented. The results of our work should be considered with caution and serve to generate a hypothesis to be directly tested in larger and more homogeneous samples. On the other hand, simply disregarding the nominal associations presented here may delay discovery by misleading the field to believe that no true biological relationships exist. Another limitation of our study is that our phenotype reflects subclinical caries lesions that cannot be detected by the naked eye (Shimizu et al., 2012). The SNPs we report here as associated with caries do not have known functional roles. Our work continues to support that individuals susceptibility is a factors in dental caries susceptibility, with some individuals more susceptible to mineral losses when pH lowers.

AUTHOR CONTRIBUTIONS

ARV designed the study, obtained support, analyzed and interpreted data, and wrote the first draft of the manuscript. MB and FS (Istanbul University) helped design the study facilitated DNA and sample collections, Kathleen Deeley (University of Pittsburgh) managed samples and generated genotypes, FL (Indiana University) helped design the study and generated enamel microhardness measurements, and RS (University of Pittsburgh) statistically analyzed the data. AM helped design the study and obtained support. All authors critical revised the manuscript.

ACKNOWLEDGMENTS

Part of the data of this manuscript was presented during the Enamel 9 Conference, between October 30th and November 3rd 2016. The Enamel 9 Conference was supported in part by the NIH/NIDCR grant R13-DE026647, awarded to ARV. ARV's attendance to the conference was supported by Colgate Palmolive.

REFERENCES

Anjomshoaa, I., Briseño-Ruiz, J., Deeley, K., Poletta, F. A., Mereb, J. C., Leite, A. L., et al. (2015). Aquaporin 5 interacts with fluoride and possibly protects against caries. *PLoS ONE* 10:e0143068. doi: 10.1371/journal.pone.0143068

Bayram, M., Deeley, K., Reis, M. F., Trombetta, V. M., Ruff, T. D., Sencak, R. C., et al. (2015). Genetic influences on dental enamel that impact caries differ between the primary and permanent dentitions. *Eur. J. Oral Sci.* 123, 327–334. doi: 10.1111/eos.12204

Churchley, D., Lynch, R. J., Lippert, F., Eder, J. S., Alton, J., and Gonzalez-Cabezas, C. (2011). Terahertz pulsed imaging study to assess remineralization of artificial caries lesions. *J. Biomed. Opt.* 16, 026001. doi: 10.1117/1.3540277

Dill, A., Letra, A., Chaves de Souza, L., Yadlapati, M., Bigueti, C. C., Garlet, G. P., et al. (2015). Analysis of multiple cytokine polymorphisms in individuals with untreated deep carious lesions reveals IL1B (rs1143643) as a susceptibility factor for periapical lesion development. *J. Endod.* 41, 197–200. doi: 10.1016/j.joen.2014.10.016

Felszeghy, S., Módis, L., Németh, P., Hagy, G., Zelles, T., Agre, P., et al. (2004). Expression of aquaporin isoforms during human and mouse tooth development. *Arch. Oral Biol.* 49, 247–257. doi: 10.1016/j.archoralbio.2003.09.011

Funaki, H., Yamamoto, T., Koyama, Y., Kondo, D., Yaoita, E., Kawasaki, K., et al. (1998). Localization and expression of AQP5 in cornea, serous salivary glands, and pulmonary epithelial cells. *Am. J. Physiol.* 275, C1151–C1157.

Hamann, S., Zeuthen, T., LaCour, M., Nagelhus, E. A., Ottersen, O. P., Agre, P., et al. (1998). Aquaporins in complex issues: distribution of aquaporins 1–5 in human and rat eye. *Am. J. Physiol.* 274, C1332–C1345.

Ishida, N., Hirai, S. I., and Mita, S. (1997). Immunolocalization of aquaporin homologs in mouse lacrimal glands. *Biochem. Biophys. Res. Commun.* 238, 891–895. doi: 10.1006/bbrc.1997.7396

Lippert, F., and Lynch, R. J. (2014). Comparison of knop and Vickers surface microhardness and transverse microradiography for the study of early caries lesion formation in human and bovine enamel. *Arch. Oral Biol.* 59, 704–710. doi: 10.1016/j.archoralbio.2014.04.005

Liu, Q., Zhou, J. P., Li, B., Huang, Z. C., Dong, H. Y., Li, G. Y., et al. (2013). Basic transcription factor 3 is involved in gastric cancer development and progression. *World J. Gastroenterol.* 19, 4495–4503. doi: 10.3748/wjg.v19.i28.4495

Lynch, R. J., Mony, U., and ten Cate, J. M. (2007). Effect of lesion characteristics and mineralizing solution type on enamel remineralization *in vitro*. *Caries Res.* 41, 257–262. doi: 10.1159/000101914

Maheshwari, K., Silva, R. M., Guajardo-Morales, L., Garlet, G. P., Vieira, A. R., and Letra, A. (2016). Heat shock 70 protein genes and genetic susceptibility to apical periodontitis. *J. Endod.* 42, 1467–1471. doi: 10.1016/j.joen.2016.07.010

Menezes-Silva, R., Khaliq, S., Deeley, K., Letra, A., and Vieira, A. R. (2012). Genetic susceptibility to periapical disease: conditional contribution of MMP2 and MMP3 genes to the development of periapical lesions and healing response. *J. Endod.* 38, 604–607. doi: 10.1016/j.joen.2012.02.009

Nibali, L., Di Iorio, A., Tu, Y. K., and Vieira, A. R. (2016). Host genetics role in the pathogenesis of periodontal disease and caries. *J. Clin. Periodontol.* doi: 10.1111/jcpe.12639. [Epub ahead of print].

Nielsen, S., King, L. S., Christensen, B. M., and Agre, P. (1997). Aquaporins in complex tissues. II. Subcellular distribution in respiratory and glandular tissues of rat. *Am. J. Physiol.* 273, C1549–C1561.

Purcell, S., Neale, B., Todd-Brown, K., Thomas, L., Ferreira, M. A., Bender, D., et al. (2007). PLINK: a toolset for whole-genome association and population-based linkage analysis. *Am. J. Hum. Genet.* 81, 559–575. doi: 10.1086/519795

Shimizu, T., Deeley, K., Briseño-Ruiz, J., Faraco, I. M. Jr., Poletta, F. A., Brancher, J. A., et al. (2013). Fine-mapping of 5q12.1-13.3 unveils new genetic contributors to caries. *Caries Res.* 47, 273–283. doi: 10.1159/000346278

Shimizu, T., Ho, B., Deeley, K., Briseño-Ruiz, J., Faraco, I. M. Jr., Schupack, B. I., et al. (2012). Enamel formation genes influence enamel

microhardness before and after cariogenic challenge. *PLoS ONE* 7:e45022. doi: 10.1371/journal.pone.0045022

Vieira, A. R., Gibson, C. W., Deeley, K., Xue, H., and Li, Y. (2015). Weaker enamel explains dental decay. *PLoS ONE* 10:e0124236. doi: 10.1371/journal.pone.0124236

Vieira, A. R., McHenry, T. B., Daack- Hirsch, S., Murray, J. C., and Marazita, M. L. (2008). Candidate gene/loci studies in cleft lip/palate and dental anomalies finds novel susceptibility genes for clefts. *Genet. Med.* 10, 668–674. doi: 10.1097/GIM.0b013e3181833793

Weber, M. L., Hsin, H. Y., Kalay, E., Brožková, D. S., Shimizu, T., Bayram, M., et al. (2014). Role of estrogen related receptor beta (ESRRB) in DFN35B hearing impairment and dental decay. *BMC Med. Genet.* 15:81. doi: 10.1186/1471-2350-15-81

White, D. J. (1987). Reactivity of fluoride dentifrices with artificial caries. I. Effects on early lesions: F *uptake, surface hardening and remineralization.* Caries Res. 21, 126–140. doi: 10.1159/000261013

Conflict of Interest Statement: The authors declare that the research was conducted in the absence of any commercial or financial relationships that could be construed as a potential conflict of interest.

The reviewer CC and handling Editor declared their shared affiliation, and the handling Editor states that the process nevertheless met the standards of a fair and objective review.

Copyright © 2017 Vieira, Bayram, Seymen, Sencak, Lippert and Modesto. This is an open-access article distributed under the terms of the Creative Commons Attribution License (CC BY). The use, distribution or reproduction in other forums is permitted, provided the original author(s) or licensor are credited and that the original publication in this journal is cited, in accordance with accepted academic practice. No use, distribution or reproduction is permitted which does not comply with these terms.

frontiers in Physiology

ORIGINAL RESEARCH
published: 09 February 2018
doi: 10.3389/fphys.2018.00071

A microCT Study of Three-Dimensional Patterns of Biomineralization in Pig Molars

Susanna S. Sova[1,2]*, *Leo Tjäderhane*[3,4], *Pasi A. Heikkilä*[2] and *Jukka Jernvall*[1]

[1] Developmental Biology Program, Institute of Biotechnology, University of Helsinki, Helsinki, Finland, [2] Department of Geoscience and Geography, University of Helsinki, Helsinki, Finland, [3] Department of Oral and Maxillofacial Diseases, Helsinki University Hospital, University of Helsinki, Helsinki, Finland, [4] Institute of Dentistry and Medical Research Center Oulu, Oulu University Hospital, University of Oulu, Oulu, Finland

Domestic pig molars provide an interesting system to study the biomineralization process. The large size, thick enamel and complex crown morphology make pig molars relatively similar to human molars. However, compared to human molars, pig molars develop considerably faster. Here we use microCT to image the developing pig molars and to decipher spatial patterns of biomineralization. We used mineral grains to calibrate individual microCT-scans, which allowed an accurate measure of the electron density of the developing molars. The microCT results show that unerupted molars that are morphologically at the same stage of development, can be at markedly different stage of enamel biomineralization. Erupted molars show increased electron density, suggesting that mineralization continues in oral cavity. Yet, our comparisons show that human enamel has slightly higher electron density than pig enamel. These results support the relatively low hardness values and calcium level values that have been reported earlier in literature for pig teeth. The mineral calibration was an efficient method for the microCT-absorption models, allowing a relatively robust way to detect scanning artifacts. In conclusions, whereas thin sections remain the preferred way to analyze enamel features, such as incremental lines and crystal orientation, the microCT allows efficient and non-destructive comparisons between different teeth and species.

Keywords: teeth, tooth maturation, biomineralization, sus scrofa, 3D-imaging, microtomography, beam hardening artifacts

OPEN ACCESS

Edited by:
Steven Joseph Brookes, Leeds Dental Institute, United Kingdom

Reviewed by:
Michel Goldberg, Institut National de la Santé et de la Recherche Médicale (INSERM), France
Marianna Bei, Harvard Medical School, United States
Colin Robinson, University of Leeds, United Kingdom

***Correspondence:**
Susanna S. Sova
susanna.sova@helsinki.fi

Specialty section:
This article was submitted to Craniofacial Biology and Dental Research, a section of the journal Frontiers in Physiology

Received: *19 June 2017*
Accepted: *19 January 2018*
Published: *09 February 2018*

Citation:
Sova SS, Tjäderhane L, Heikkilä PA and Jernvall J (2018) A microCT Study of Three-Dimensional Patterns of Biomineralization in Pig Molars. Front. Physiol. 9:71. doi: 10.3389/fphys.2018.00071

INTRODUCTION

The domestic pig (*Sus scrofa domesticus*) is a plant-dominated omnivore with low-crowned, multi-cusped molars. The relatively fast development of teeth together with their large size and thick enamel makes pig teeth an interesting model for biomineralization studies. The general morphology and tissue structure of pig teeth is closer to human teeth than that of rodent teeth (Robinson et al., 1987; Mlakar et al., 2014). The large size and complex tooth morphology of pig molars, however, makes them also challenging to investigate.

We use x-ray microtomography (microCT)-imaging to document the maturation of domestic pig molars, and compare the microCT models with photomicrographs from polished thin sections of the molars. According to Kirkham et al. (1988), pig enamel is relatively immature at the time of the tooth eruption, and the surface hardness of erupted pig teeth is "astonishingly low" compared to other domestic animal teeth and human teeth (Karlström, 1931).

Computational microCT is becoming an increasingly used method in paleontological, biological and medical studies (e.g., Ortiz et al., 2012; Tafforeau et al., 2012; Schmitz et al., 2014). MicroCT is a relatively rapid and non-destructive method to image different size of specimens, and to create a precise 3D-model of specimens surface and internal structure. One of our methodological interests is to test if mineral grains can be used in microCT as internal reference for relative calibration of absorption models. Different absorption models, even of similar samples, are difficult to compare because absorption values are not absolute and are affected by several scanning variables. So-called phantoms are normally used in microCT calibration, but when working with highly mineralized samples such as tooth enamel, the electron densities of the phantoms are below the electron densities of the samples (e.g., Farah et al., 2010). Due to the large size of pig molars, individual teeth need to be scanned one at a time in most commercial microCT instruments, necessitating reliable methods to normalize each scan. Apatite single crystal is the best comparable to the hydroxylapatite of the teeth. Siderite is an iron carbonate mineral with the highest electron density of our standard samples, and quartz is a pure silicon dioxide mineral, whose electron density is comparable to less mineralized tooth material, for example dentin.

MATERIALS AND METHODS

Samples

The permanent molars were extracted from half-mandibles of approximately 6 months old healthy production pigs (breed unknown). The first molars (M1) were in occlusion, the second and third molars (M2 and M3) were not erupted. The M2 crowns were fully formed but the root formation had not started yet. The third molars (M3) were still very small relative to their final size. The unerupted teeth were extracted in their dental sacs and all tooth samples were stored in 70% ethanol at 4°C. All the procedures of this study involving animals were reviewed and approved by relevant Animal Welfare and Research Committees.

Human third molars were extracted as part of a normal dental treatment and used for the study with the patients' informed consent. Immediately after the extraction, the teeth were stored in phosphate-buffered saline—containing 0.02% sodium azide, and transferred into 70% ethanol within 1 week after the extraction.

microCT

The microCT measurements of the pig molars were performed at the Laboratory of X-ray Microtomography at the Department of Physics, University of Helsinki, Finland. The imaging set-up is a custom-built microtomography system, which is manufactured by phoenix|X-ray System and Service GmbH (General Electric, Wunstorf, Germany). The x-ray source is a fixed-target transmission type x-ray tube with a tungsten filament cathode and a tungsten transmission anode, target that is fused onto a 400 μm thick beryllium window.

The following parameters were used in the study: source voltage of 120 kV, source current of 170 μA, imaging voxel size was 10 to 24 μm (or 2 to 4 enamel rods) 5 mm Al-filter, projection images were taken over rotation step of (360°/1200 rotation, exposure time 500 to 750 ms, and frame averaging of 8). Tomography reconstructions were obtained using the program Datos |X by phoenix|X-ray System and Service GmbH (General Electric). Human and pig molars comparison was obtained using SkyScan 1272 desktop micro-CT system, Bruker microCT N.V., Kontich, Belgium. All absorption models were down-sampled to 44 μm voxel size for the analyzes.

For the microCT-imaging, we selected three single-crystal mineral grains to be used as internal reference samples: fluorapatite ($Ca_5(PO_4)_3F$), quartz (SiO_2) and siderite ($FeCO_3$). Each molar was scanned together with three mineral grains that were used as an internal reference for relative calibration for the microCT absorption models. The gray-scale values of the mineral grains in the absorption models were measured from a 1 mm^2 homogenous area at the center of each mineral grain (**Figure 1A**). The gray-scale measurement was repeated five times from non-overlapping areas within each mineral grain and the results were averaged. The gray-scale values of each mineral were correlated with its (theoretical) electron density values (Barthelmy, 2014) to produce a calibration line for each model. The calibrated values were used to convert the gray-scale values of each model to relative electron density values (RED). Comparison of the calibration lines between the reconstructions reveals the initial gray-scale value discrepancies between the scans. The slopes of each calibration line are relatively equal, however, showing that the electron density range that was covered by the mineral reference standards, can be used to convert the gray-scale value ranges of each tooth measurement to comparable RED-values (**Figure 1B**). The analyses were done using Fiji (https://fiji.sc/).

Polarized Light Microscopy

One cross-section from each pig molar (M1, M2, M3) was prepared for microscopic examinations. Prior to the thin section preparation, the teeth were covered with epoxy to avoid fracturing. The polished thin sections (thickness 30 μm) were studied and photographed using Leica DM2500P polarized light microscope equipped with Leica DFC450C camera.

RESULTS

MicroCT Absorption Models of Pig Molars

The absorption models of the molars show small differences in development between pig individuals, here referred as the younger and the older pigs for brevity (**Figure 2**). The first molars of both pigs appear equal electron density (degree of mineralization), but the dentin layer is slightly thicker in the older pig individual. The second molars are morphologically similar and the enamel thickness is roughly equal, but the enamel maturation is more advanced in older pig than in the younger one. In the older pig M2, the electron density of enamel is higher than that of dentin in the cusps, but not in the neck. In the younger pig, the electron density of enamel is relatively uniform, but distinctly lower than that of the dentin. As a

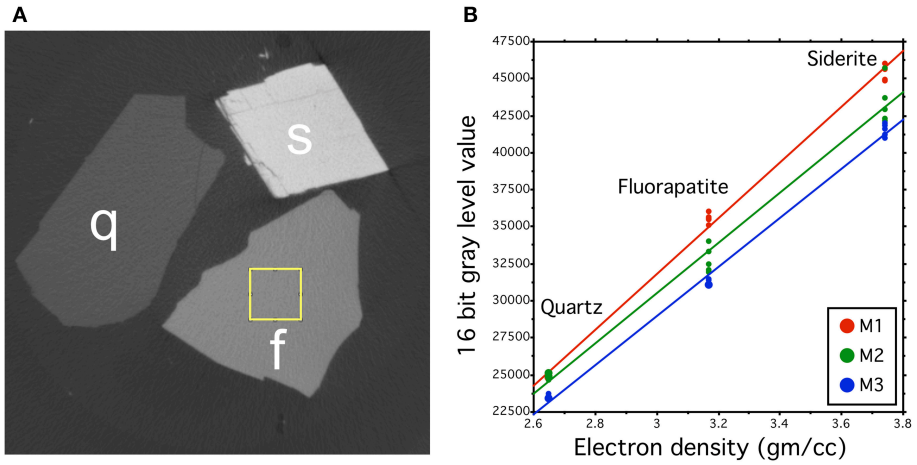

FIGURE 1 | Calibration method for the microCT absorption models. **(A)** Cross-sections of the mineral standards quartz (Q), siderite (S), and fluorapatite (F) in one microCT model, showing different gray values that correlate with the electron density of the material. The rectangle in F represents one area, from where the gray value of the grain was measured. **(B)** Comparison of the calibration lines of three different samples (M1, M2, M3). The slopes of each calibration line are relatively equal, but slightly spreading toward higher electron density values. Each point represents one gray value measurement of the mineral standard and its theoretical electron density value.

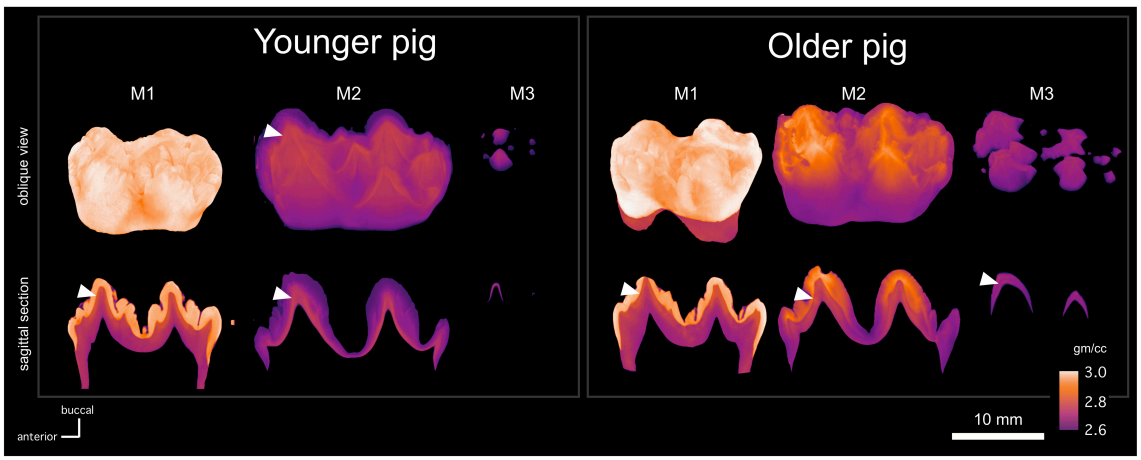

FIGURE 2 | MicroCT absorption models of the molars (M1, M2, M3) of two pig individuals (younger and older), showing the shape (**upper row**) of each tooth, where the maturation stage is represented by reduced transparency, and the electron density by calibrated false color scale. Sagittal cross sections (**lower row**) of each tooth show mutually comparable electron density variation across each profile with EDJ marked with the white arrow heads.

consequence, the morphology of the enamel-dentin-junction (EDJ) is distinguishable through the enamel in the absorption model (**Figure 2**).

Robinson et al. (1987) described enamel maturation using a partially visual classification scheme. Stages 1 and 2 enamel is translucent whereas stage 3 enamel is white and opaque. Stage 4 enamel is hard and translucent. Compared to stage 1, stage 2 enamel cracks vertically when let to dry. These stages correspond to chemical and histological changes related to maturation (Robinson and Kirkham, 1984; Robinson et al., 1987, 1988), and some of the stages can also be distinguished from our absorption models. Based on our visual inspection of the molars, the first molars were at the stage 4 and the third molars were at the stage 1, whereas the second molars showed differences. The whole crown of the younger pig M2 was at stage 1, whereas the top 57% (of 14 mm total) of the older pig crown was at stage 3. In our absorption models, the stage 1 and 2 enamel correspond to electron densities that are lower than that of dentin, and the stage 3 enamel of the older pig M2 shows higher than dentine electron density values (**Figure 2**).

The pig M2 reveal distinctly different morphologies between EDJ and enamel surface: The EDJ has sharp cusp tips and ridges with concave valleys between them, but the enamel surface has convex cusps with narrow fissures in between the cusps. A similar EDJ-morphology is visible in the M1 absorption model, when the enamel layer is digitally removed (**Figures 3A,B**). As in M1, the

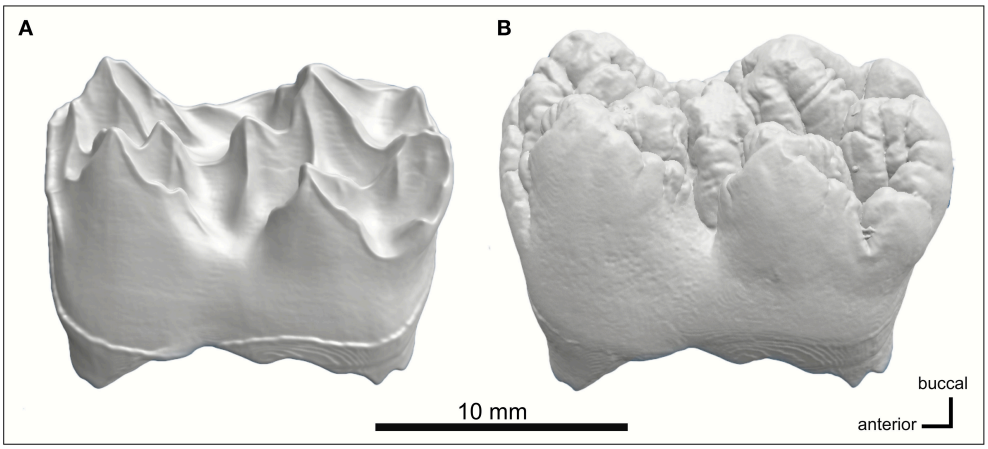

FIGURE 3 | MicroCT models of **(A)** EDJ morphology and **(B)** tooth surface of the younger pig M1. The enamel is digitally removed using its electron density threshold. Enamel surface shows rounded, convex cusps with narrow intervening fissures, whereas the EDJ is characterized by sharp cusp tips and ridges with concave valleys in between them.

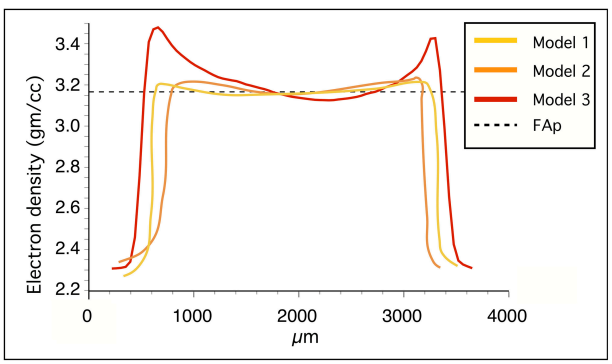

FIGURE 4 | Electron density profiles of the fluorapatite standard in three microCT absorption models. Models 1 and 2 have consistent values whereas model 3 shows higher electron density at the sample surface due to beam-hardening.

dentin of M2 is thicker in the older pig than in the younger pig. In the third molars, the mineralization has only begun at the tips of the principal cusps. The order of development from the anterior to posterior parts of the molars, is well visible in the younger M3 in which the mineralized tips of talonid cusps are barely visible and still close to each other, indicating that the growth of the valley separating the cusps has not yet been completed (**Figure 2**). With the older pig M3, more cusps are distinguishable than in the younger pig M3 and the valleys between the principal cusps are larger.

Because mineral grains used for calibration have reasonably uniform electron densities, we discovered that an additional benefit of the minerals is their suitability for detecting beam-hardening artifacts from the microCT models (**Figure 4**). Beam hardening makes the sample appear artificially denser at or near its surface, and less dense in its central parts (Boas and Fleischmann, 2012). The x-rays produced in laboratory x-ray sources are polychromatic and have mixed x-ray photon energy. As this mixed beam of x-rays passes through the sample, the lower energy x-rays will be attenuated more rapidly than the higher energy x-rays, resulting in brighter edges if beam attenuation is considered linear. The hardening effects can be reduced during scanning or with specific algorithms that are used during reconstruction. However, these artifacts can be particularly challenging to recognize in tooth samples: teeth usually have a thin layer of highly mineralized enamel on the surface that can be difficult to distinguish from the hardening artifact as thick as the whole enamel layer, especially in small teeth with thin enamel. In our scans, the relatively large apatite crystal shows a flat electron density profile in microCT models without hardening artifacts, but a concave profile in a microCT model with hardening artifacts (**Figure 4**).

Comparison of the microCT Absorption Models and Thin Sections

Physical thin sections of teeth and virtual sections made from the microCT absorption models show similar patterns of maturation (**Figures 5A–C**). However, thin sections also show details that are not visible in microCT absorption models. For example, the cross-polarized light and additional gypsum plate allow the direct observation of the principal crystal orientation (**Figures 6A,B**). In the M1 thin section, the neonatal line is optically more coherent than the surrounding enamel. Contrary to the neonatal line, the most pronounced incremental lines observed in M2 are opaque.

Electron Density Comparison of Pig and Human Molars

Comparison of the calibrated microCT models of pig M1, human P1 and M3 show that human enamel has slightly higher electron

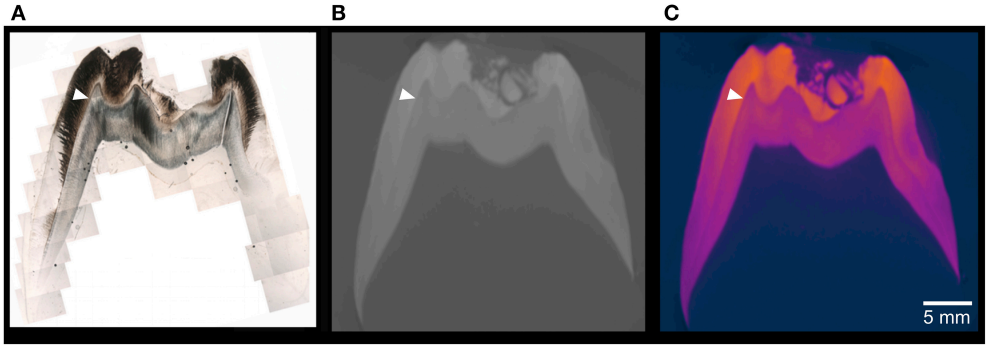

FIGURE 5 | Cross sections of the older pig M2. **(A)** Combined photomicrograph of a thin section and **(B)** Cross section of the microCT model in electron-density-calibrated in gray scale, and false colors **(C)**. The ultrastructure of enamel and dentin under polarized light microscope is superior to the microCT model and false colors aid the detection of differences in electron density.

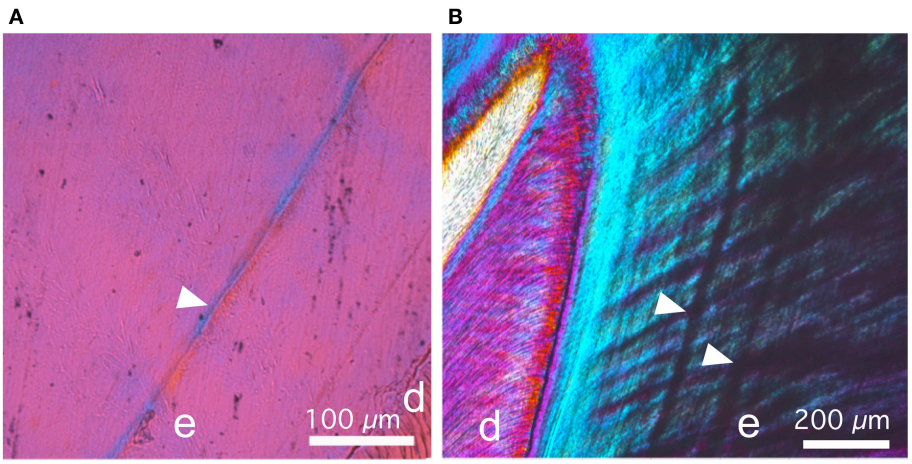

FIGURE 6 | Details of thin sections of the older stage pig, photographed using cross-polarized light and gypsum accessory plate. **(A)** In M1, the neonatal line (arrow head) is optically more coherent than the surrounding enamel, as evidenced by the stronger blue and yellow interference colors. **(B)** In M2, the most pronounced incremental lines appear opaque, and therefore distinct from the neonatal line.

density values than pig enamel (**Figures 7A–C**). The differences in the electron density of dentin are small.

DISCUSSION

The microCT absorption models provide a good overall view of the developing pig molars. 3D-models show the timeline of tooth maturation in two directions: in anterior-posterior axis, and from the tooth cusps toward the tooth neck. MicroCT-models also show how the maturation of enamel takes longer than that of the dentin. The transition point when the electron density of enamel exceeds that of dentin, appears to correspond to the transition from stage 1-2 enamel to stage 3 enamel in the classification scheme used by Robinson et al. (1987). This suggests that microCT could potential be used for non-invasive classification of enamel maturation.

The mineral calibration of the microCT model proved to be an efficient method to re-scale the electron density values to comparable semi-quantitative scale. In addition, mineral grains are useful for the detection of beam hardening artifacts when the properties of the investigated samples are unknown. The electron density of fluorapatite is higher than that of hydroxylapatite that is again slightly higher than the electron density of enamel. Accordingly, it could be sufficient to use fluorapatite as the highest electron density standard in bio-apatite research instead of siderite. In addition to fluorapatite and quartz, diamond could be utilized as the lowest electron density reference. Diamond and quartz are also available as pure synthetic phases. An obvious future extension of our calibration method is to compare the absorption of the minerals to hydroxyapatite phantoms (Schweizer et al., 2007).

Whereas the microstructure of tooth and the orientation of crystals (e. g. enamel rods and their decussation) are not visible in absorption models, they are detectable in thin sections. However, 3D detection of enamel microstructure is possible using synchrotron x-ray imaging (e.g., Tafforeau et al., 2012).

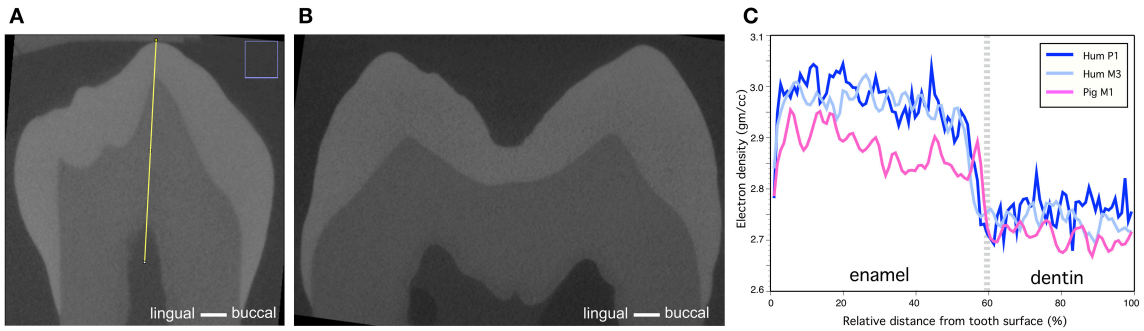

FIGURE 7 | Comparison of human and pig molar electron density. **(A)** Cross-section of human P1 (Yellow line denotes the line of measurements) **(B)** Cross-section of human M3. **(C)** Comparison of electron density of human and older stage pig M1 show that human molar has slightly higher electron density in enamel and the difference is negligible in dentin.

The polarized light microscopy observations showed the different appearance of the neonatal line and other incremental lines. The higher optical coherence indicates more parallel crystal orientation in neonatal line than elsewhere in enamel, and could indicate that the crystal nucleation was arrested at the time of the birth.

Kirkham et al. (1988) studied the mineral content of pig enamel. Their results showed that the mineral content of pig enamel at eruption is 50–60% per volume, which is near or equal to the mineral content of human dentin and considerably lower than the mineral content of human enamel (Jenkins, 1976). In the pig molars that we studied, the electron density of enamel is higher than that of dentin before the tooth eruption (**Figure 2**). According to our microCT models, the electron density of human enamel is slightly higher than that of pig enamel, whereas the differences in the electron densities of dentin are negligible (**Figure 7C**). Kirkham et al. (1988) state that the characteristics of mature mammal enamel could be achieved in pig teeth considerably later after tooth eruption. In our samples, the first molars of pigs had been in oral cavity approximately for 2 months whereas the human M3s were extracted from adults. In human teeth, the enamel surface still hardens in oral cavity at least for 2–3 years (Lynch, 2013).

One possible reason for the low electron density values of erupting pig molars could be the relatively fast development of pig teeth. Pig M1 develops from the beginning of the bud stage to the eruption in approximately 6.5 months whereas with human this takes 6 years (Kraus and Jordan, 1965; Tonge and McCance, 1973; Berkovitz et al., 2009; Wang et al., 2014). In other words, pig tooth development is almost 10 times faster than human tooth development, even though the pig M1 size is almost twice that of human M1. Studies on rat incisor eruption suggest that incisors compensate for artificially accelerated eruption by having wider zone of secreting ameloblasts (Robinson et al., 1988). Whereas, it is not known how molars that develop rapidly regulate their development, the low electron density values of erupting pig molars could indicate the maturation stage as a limiting factor. Another consideration is that in most ungulates, the secondary morphology of molars is functionally more important than the primary morphology, and immature enamel in erupting molars may help to quickly acquire the functional morphology. In the domestic pig, both primary and secondary morphologies are functional. Nevertheless, despite the differences between pig and human molars, they have comparable tooth replacement patterns and bunodont crown features such as thick enamel with deep furrows between cusps.

Finally, Limeback et al. (1992) reported difficulties in detecting the effects of Vitamin-D deficiency in pig enamel radiographically, and it remains to be tested whether mineralization defects can be detected in pigs using calibrated microCTs. The difficulty in detecting vitamin D defects may also be connected to the fast tooth development in pigs. With the increasing efficiency of genome editing of large animals (Whitelaw et al., 2016), it is conceivable that new pig-models suitable for dental studies will be available in the future.

In conclusion, microCT is a valuable starting point for the traditional destructive methods used in the study of biomineralization, but does not substitute for them. Thin sections still provide valuable information about the tooth structure. The optical differences between neonatal line and other incremental lines were clear under polarized light microscope, warranting further study. Mineral grains as internal standards can be used to calibrate microCT scans, allowing the detection of scanning artifacts and comparisons between developmental stages and species. Our results show that the fast developing pig molars complete their enamel matrix deposition over the whole crown prior to the maturation. Considering that pig enamel is very thick, the combination of microCT imaging and pig molars is a useful model system in the study of biomineralization.

AUTHOR CONTRIBUTIONS

SS, PH, and JJ designed the project. SS acquired the data and performed the imaging and analyses. LT provided material, observations and scientific interpretations. SS wrote the initial manuscript and all authors discussed the results and provided input on the manuscript.

ACKNOWLEDGMENTS

We thank Teemu Mattila from HK-Ruokatalo, Mikael Fortelius, Helena Korkka, Heikki Suhonen, Aki Kallonen and Juha Laakkonen for help or comments. This work was presented at the Enamel 9 Symposium held in Leeds, UK. We thank three reviewers for their suggestions that improved the manuscript.

REFERENCES

Barthelmy, D. (2014). *Mineralogy Database*. Available online at: http://www.webmineral.com/

Berkovitz, B. K. B., Holland, G. R., and Moxham, B. J. (2009). *Oral anatomy, Histology and Embryology, 4th Edn*. Edinburgh: Mosby/Elsevier.

Boas, F. E., and Fleischmann, D. (2012). CT artifacts: causes and reduction techniques. *Imaging Med*. 4, 229–240. doi: 10.2217/iim.12.13

Farah, R. A., Swain, M. V., Drummond, B. K., Cook, R., and Atieh, M. (2010). Mineral density of hypomineralized enamel. *J. Dent.* 38, 50–58. doi: 10.1016/j.jdent.2009.09.002

Jenkins, N. G. (1976). *The Physiology and Biochemistry of the Mouth*, *4th Edn,* (Oxford: Blackwell Scientific Publications), 54–112.

Karlström, S. (1931). *Physical, Physiological and Pathological Studies of Dental Enamelwith Special References to the Question of its Vitality*. Stockholm: A. B. Fahlcrantz' Boktryckeri.

Kirkham, J., Robinson, C., Weatherell, J. A., Richards, A., Fejerskov, O., and Josephsen, K. (1988). Maturation in developing permanent porcine enamel. *J. Dent. Res.* 67, 1156–1160. doi: 10.1177/00220345880670090301

Kraus, B. S., and Jordan, R. E. (1965). *The Human Dentition Before Birth* Philadelphia, PA: Lea and Febiger.

Limeback, H., Schlumbohm, C., Sen, A., and Nikiforuk, G. (1992). The effects of hypocalcemia hypophosphatemia on porcine bone and dental hard tissues in an inherited form of type-1 pseudo-vitamin-d deficiency rickets. *J. Dent. Res.* 71, 346–352. doi: 10.1177/00220345920710020101

Lynch, R. J. M. (2013). The primary and mixed dentition, post eruptive enamel maturation and dental caries: review. *Int. Dent. J.* 63, 3–13. doi: 10.1111/idj.12076

Mlakar, N., Pavlica, Z., Petelin, M., Štrancar, J., and Zrimšek, P. (2014). Animal and human dentin microstructure and elemental composition. *Cent. Eur. J. Med.* 9, 468–476. doi: 10.2478/s11536-013-0295-x

Ortiz, A., Skinner, M. M., Baileya, S. E., and Hublin, J.-J. (2012). Carabelli's trait revisited: an examination of mesiolingual features at the enamel-dentin junction and enamel surface of Pan and Homo sapiens upper molars. *J. Hum. Evol.* 63, 586–596. doi: 10.1016/j.jhevol.2012.06.003

Robinson, C., and Kirkham, J. (1984). Is the rat incisor typical. *INSERM* 125, 377–388.

Robinson, C., Kirkham, J., and Nutman C. A. (1988). Relationship between enamel formation and eruption rate in rat mandibular incisors. *Cell Tissue Res.* 254, 655–658.

Robinson, C., Kirkham, J., Weatherell, J. A., Richards, A., Josepsen, K., and Fejerskov, O. (1987). Developmental stages in permanent porcine enamel. *Acta Anatomica* 128, 1–10. doi: 10.1159/000146306

Schmitz, J. E., Teepe, J. D., Hu, Y., Smith, C. E., Fajardo, R. J., and Chun, Y.-H. P. (2014). Estimating mineral changes in enamel formation by ashing BSE and MicroCT. *J. Dent. Res.* 20, 1–7. doi: 10.1177/0022034513520548

Schweizer, S., Hattendorf, B., Schneider, P., Aeschlimann, B., Gauckler, L., Müller, R., et al. (2007). Preparation and characterization of calibration standards for bone density determination by micro-computed tomography. *Analyst* 132, 1040–1045. doi: 10.1039/b703220j

Tafforeau, P., Zermeno, J., and Smith, T. (2012). Tracking cellular-level enamel growth and structure in 4D with synchrotron imaging. *J. Hum. Evol.* 62, 424–428. doi: 10.1016/j.jhevol.2012.01.001

Tonge, C. H., and McCance, R. A. (1973). Normal development of the jaws and teeth in pigs, and the delay and malocclusion produced by calorie defiencies. *J. Anat.* 155, 1–22.

Wang, F., Xiao, J., Cong, W., Li, A., Song, T., Wei, F., et al. (2014). Morphology and chronology of diphyodont dentition in miniature pigs, Sus Scrofa. *Oral Disease* 20, 367–379. doi: 10.1111/odi.12126

Whitelaw, C. B., Sheets, T. P., Lillico, S. G., and Telugu, B. P. (2016). Engineering large animal models of human disease. *J. Pathol.* 238, 247–256. doi: 10.1002/path.4648

Conflict of Interest Statement: The authors declare that the research was conducted in the absence of any commercial or financial relationships that could be construed as a potential conflict of interest.

Copyright © 2018 Sova, Tjäderhane, Heikkilä and Jernvall. This is an open-access article distributed under the terms of the Creative Commons Attribution License (CC BY). The use, distribution or reproduction in other forums is permitted, provided the original author(s) and the copyright owner are credited and that the original publication in this journal is cited, in accordance with accepted academic practice. No use, distribution or reproduction is permitted which does not comply with these terms.

frontiers in Physiology

OPINION
published: 20 July 2017
doi: 10.3389/fphys.2017.00513

Enamel Research: Priorities and Future Directions

Jennifer Kirkham[1], Steven J. Brookes[1], Thomas G. H. Diekwisch[2], Henry C. Margolis[3], Ariane Berdal[4] and Michael J. Hubbard[5]*

[1] Division of Oral Biology, School of Dentistry, St James's University Hospital, University of Leeds, Leeds, United Kingdom, [2] Texas A&M University College of Dentistry, Dallas, TX, United States, [3] Center for Biomineralization, The Forsyth Institute, Cambridge, MA, United States, [4] Centre de Recherche des Cordeliers, INSERM UMRS 1138, University Paris-Diderot, Paris, France, [5] Department of Paediatrics, University of Melbourne, Melbourne, VIC, Australia

Keywords: enamel, research priorities, amelogenesis, odontogenesis, future directions

OPEN ACCESS

Edited by:
Agnes Bloch-Zupan, University of Strasbourg, France

Reviewed by:
Michel Goldberg, Institut National de la Santé et de la Recherche Médicale, France
Jung-Wook Kim, Seoul National University, South Korea
Jan Hu, University of Michigan, United States
Bernhard Ganss, University of Toronto, Canada
Colin Robinson, University of Leeds, United Kingdom

****Correspondence:***
Jennifer Kirkham
j.kirkham@leeds.ac.uk

Specialty section:
This article was submitted to Craniofacial Biology and Dental Research, a section of the journal Frontiers in Physiology

Received: *28 April 2017*
Accepted: *05 July 2017*
Published: *20 July 2017*

Citation:
Kirkham J, Brookes SJ, Diekwisch TGH, Margolis HC, Berdal A and Hubbard MJ (2017) Enamel Research: Priorities and Future Directions. Front. Physiol. 8:513. doi: 10.3389/fphys.2017.00513

At the close of the 2016 Enamel 9 International Symposium, the collective wisdom and views of enamel researchers were sought and discussions held in order to provide a consensus view of the priorities and future directions in enamel research. Researchers considered progress in the field since the Enamel VIII conference held in 2011, together with the research strengths and strategic gaps in our current knowledge portfolio, synthesizing this information toward recommendations for future advancement. We aim to present these recommendations and identified priorities here, drawing upon the Closing Session discussions and those held throughout the Symposium as presented in the Supplemental data.

It is clear that significant advancements have been made in enamel research over the last 5 years since Enamel VIII. Despite these advances, it is equally clear that many issues highlighted there as future priorities (Scientific Advisory Board, 2011) are still pressing. The greater our technical capabilities and knowledge base, the more questions and unknowns we uncover and the more we realize what we do not know. More than 100 researchers from 28 countries attended Enamel 9 and their reported findings provide indisputable evidence of the quality, breadth and vigor of enamel research across the globe. Attendance at the Symposium by >30 early career researchers gives us confidence of the continuing vibrance and sustainability of the enamel field. In addition, it was particularly gratifying to see so many examples of interdisciplinary effort used to address increasing numbers of research questions in an integrated way, as was prioritized at Enamel VIII. Our first priority reflects the need to encourage and hasten the development of this valuable trend.

PRIORITY 1—STRONGER OUTCOMES THROUGH INTERDISCIPLINARY, INTEGRATIVE AND TRANSLATIONAL APPROACHES

Future advancements will be made at the interfaces of disciplinary boundaries (Nature News, 2015) and we encourage such collaborations as the preferred models for future working.

We propose positioning enamel within the context of the whole organism and not viewing this tissue in isolation. Enamel is unique but the cells that are central to its formation respond to equivalent signals and insults and share common pathways with cells throughout the body. For example, we need to improve our understanding of the regulatory/signaling pathways that contribute toward enamel development and how these align with, or differ from, those in other systems. These are important issues in framing our future research questions as we move toward translating findings from bench to chairside to population. We note the greatly increased participation by clinicians at Enamel 9 and recommend clinical involvement in framing translational research questions through identification of the clinical challenges and by

contextualization of existing research. This is particularly important if we wish to remain responsive to advances and shifts in the direction of clinical treatment (e.g., minimally interventive dentistry, biomimetics) and open up new frontiers such as regenerative therapies and tissue engineering.

PRIORITY 2—BETTER INTERFACING OF BIOLOGY WITH PATHOLOGY

Research into the dysregulation of amelogenesis and biomineralization defects has significantly expanded over the past 5 years, adding vastly to classical understanding obtained from studies of normal tissue. Enamel VIII predicted that the extraordinary pace of technical advancement in genetics with concomitant decreases in costs for whole exome sequencing would see all genes underlying *amelogenesis imperfecta* (AI) identified by Enamel 9. We now know that this is far from reality, despite the fact that >18 genes have been identified where mutations underlie AI, with new variants—and new genes—being reported regularly (Smith et al., 2017) Each finding brings new pointers to direct our lines of enquiry in to the normal mechanisms of enamel formation, the basis of its highly complex architecture and the pathogenesis of disease. There are clearly many more AI-associated genes to be discovered but we face a significant lag in our understanding of pathological mechanisms and phenotyping of affected tissues.

Increased awareness of the high prevalence of Molar Hypomineralization (MH)[1], (Hubbard et al., in press) highlights both a significant public health challenge and the need to better understand the pathology (and ultimately the prevention) of enamel opacities. It is likely that MH has multi-factorial causation, with environmental/lifestyle factors playing an important role but potentially with an underlying genetic component increasing individuals' susceptibility. Given suggestions that MH prevalence has increased in recent times, there may be parallels with other "lifestyle" related diseases that have seen greatly increased prevalence over relatively short timescales, such as cardiovascular disease and diabetes, where prevalence patterns reflect both patients' lifestyle and their genetic background. Individuals' susceptibility to enamel caries has already been linked to specific genetic polymorphisms (Bayram et al., 2015) and it seems likely that this paradigm could also account for variable susceptibility to fluorosis. Improved understanding of the relationship between genes and environmental factors in the patterns of normal and abnormal enamel development should be a major priority.

PRIORITY 3—BETTER STANDARDIZATION OF EXPERIMENTAL VARIABLES

Attendees identified the urgent need for standardization of enamel phenotyping, both in AI and MH and also in animal models more generally. This includes the need to consider effects in different tooth types (molars as well as incisors) and in different tissues and compartments (including non-dental). The need to standardize phenotyping at each level, including detailed histological, ultrastructural, and molecular phenotyping in animal models and, wherever possible, of affected human teeth is paramount.

PRIORITY 4—BETTER USE OF ANIMAL MODELS

Animal models have added greatly to our understanding of the fundamental biology, chemistry and physical properties of enamel and will continue to do so but it is important that we understand the disadvantages and limitations of any models (and this applies equally *in vitro* and *in vivo*) when using them to better understand pathobiology and draw conclusions in comparisons with human teeth. We recommend that a standardized (and updatable) "check list" for phenotyping would greatly facilitate our combined understanding of the effects of gene mutations and knock-outs and enable cross-comparisons to be made with wild-type animals and "equivalent" human teeth. It would also mean that we could understand the limitations of our models and increase the rigor of our findings. For example, the recent reports of ER stress as a pathomechanism in AI and the view of AI as a proteopathy (Brookes et al., 2014) signals that we should be aware that confounded observations could arise from inadvertent stressing of the ameloblasts in *in vivo* models. Major differences in fluoride metabolism between rodents and humans (Angmar-Mansson and Whitford, 1984) is another important example.

PRIORITY 5—BETTER COLLABORATION FOR STRONGER COLLECTIVE VOICE AND OUTPUTS

Compared with many others areas of scientific endeavor, enamel researchers are generally few and far between, making it difficult to be competitive at both topic and individual-performance levels. For example, it is likely that the "low hanging fruit" of gene discovery in AI has been picked by small groups in multiple countries but we know that for many AI patients, no causative gene has yet been identified. At Enamel 9, the proposal was made to establish an enamel genetics research network to support effective international collaboration by sharing findings in a community of trust ("GEnamel": "Genetics for understanding Enamel"). We hope that GEnamel will provide a paradigm for further inter-group collaborations and data sharing. In turn, it was agreed that this network might usefully interface with a translational research and education network recently established to promote issues associated with developmental dental defects (The D3 Group)[2]. Together with the potential for more frequent Enamel Symposia (see below), such combined initiatives would move toward an identifiable international community with a strong collective voice without inhibiting the independent

[1]http://www.thed3group.org/prevalence.html

[2]http://www.thed3group.org

approaches to enamel research that often generate new growth points.

PRIORITY 6—HARNESSING NEW TECHNOLOGIES

Furthering our understanding of pathology and the fundamental processes of normal enamel development can be accelerated by adopting new ways of looking at old problems. Recent advances in computational evolutionary genetics and molecular paleobiology bring new perspectives on the role of specific molecules in enamel formation (Qu et al., 2015). Additional materials science perspectives on enamel and its bio-inspired analogs would enormously benefit translational research seeking to develop new biomimetic materials and regenerative approaches to dental diseases. The need for greater inclusion of materials scientists in enamel research was recognized at Enamel VIII but this remains a strategic gap that has yet to be closed. Computer modeling of the complex data sets now being generated across multiple physiological compartments is also poorly represented in the enamel field. There is an urgent need to pro-actively recruit scientists from these disciplines to join us in both framing and answering questions.

New techniques in imaging and high resolution sample interrogation, such as focussed ion beam microscopy (Smith et al., 2016) and neutron reflectometry (Tarasevich et al., 2013) are yielding previously unobtainable insights, for example in elucidating the earliest stages of amelogenesis, the elusive "mineralization front" and the physico-chemical nature of the earliest enamel minerals. We predict that improved imaging techniques will help provide answers to outstanding questions in respect of our understanding of the mineralization front and the complex four dimensional movements of ameloblasts in dictating enamel structure. However, we still lack technical capability in tissue culture, notably three dimensional (3D) *in vitro* models and long term organoculture for investigating the relationship between ameloblasts, the enamel matrix and the other constituents of the enamel organ. We have long recognized that ameloblasts and the stratum intermedium form a functional syncytium (Skobe et al., 1995) and that studying ameloblasts in isolation seriously curtails both scope and significance of findings but a 3D culture system eludes us still and remains a much needed priority.

PRIORITY 7—INCREASED ATTRACTIVENESS TO FUNDING BODIES

Funding for enamel research remains a problem world-wide despite the fact that dental disease is a major public health burden. Affecting about 3 billion people, untreated caries in adults was the number one disease reported in the last Global Burden of Disease study (Murray et al., 2012). The international dearth of "programme grant" funding schemes that support multi-disciplinary teams and enable the integrated science approach we favor here (Priority 1) is a serious problem. We urge all colleagues to impress upon funders the advantages of such an approach. Increased attractiveness to funders should follow from improvements to our research quality, quantity, utility and visibility (Priorities 1–6). We acknowledge the continued support for the Enamel Symposia from NIH and the participation at Enamel 9 by Dr Jason Wan (NICDR), illustrating a working relationship that we should aspire to emulate with research funders across the globe. The classical funding envelope might also be expanded through translational initiatives involving industry, professional bodies and government. Enamel is the most highly mineralized mammalian tissue and its exquisitely ordered structure confers unique mechanical properties of significance to a broad audience, inside and outside of the health sciences. There is much we and others can learn from this tissue in the design of new materials and therapeutics. Opportunities therefore arise for generating research funding from our national research councils (e.g., for fundamental discovery, applied and translational research), industry (e.g., oral healthcare, orthobiologics, pharmaceutical) and charitable foundations (e.g., Wellcome Trust, Gates Foundation).

PRIORITY 8—INCREASED AND MORE EFFECTIVE COMMUNICATION

Given how rapidly recent findings have impacted our thinking plus the ongoing emergence of new technologies, our final recommendation is that due consideration be given to holding the Enamel Symposia more frequently and/or that additional short, sharply focussed meetings be held alongside larger events (e.g., the IADR global congress). We also need to ask how we might help researchers, especially those new to our field, access recommendations from previous Enamel Symposia and find key work published between meetings. These challenges might be met through an easily accessible website, increasing our currency and ensuring that past knowledge and thinking are not lost.

In conclusion, the Enamel Symposia uniquely bring together researchers from across the world, engendering a sense of community that fosters collaboration and exchange of ideas to accelerate research. We look forward to the next Symposium, Enamel 10, where progress against these identified priorities—and advances currently unforeseen—will be considered.

AUTHOR CONTRIBUTIONS

JK drafted the paper; all co-authors added intellectual content. All authors agreed to the final manuscript.

ACKNOWLEDGMENTS

We gratefully acknowledge the excellent work of Greg Baugh and Julie McDermott in transcribing the Q&A and Panel Discussions and Claire Smith for her help in proof reading. We are indebted to the Session Moderators at the Enamel 9 Symposium for their contributions toward editing the transcripts, including Ophir

Klein (Session1); Ariane Berdal (Session 2); Janet Moradian-Oldak (Session 3); Jim Simmer (Session 4); Michael Hubbard (Session 5); Agnès Bloch-Zupan (Session 6); John Bartlett (Session 7); Elia Beniash (Session 8); Henry Margolis (Session 9), and Steven Brookes (Session 10).

SUPPLEMENTARY MATERIAL

The Supplementary Material for this article can be found online at: http://journal.frontiersin.org/article/10.3389/fphys.2017.00513/full#supplementary-material

REFERENCES

Angmar-Mansson, B., and Whitford, G. M. (1984). Enamel fluorosis related to plasma F levels in the rat. *Caries Res.* 18, 25–32. doi: 10.1159/000260743

Bayram, M., Deeley, K., Reis, M. F., Trombetta, V. M., Ruff, T. D., Sencak, R. C., et al. (2015). Genetic influences on dental enamel that impact caries differ between the primary and permanent dentitions. *Eur. Oral Sci.* 123, 327–334. doi: 10.1111/eos.12204

Brookes, S. J., Barron, M. J., Boot-Handford, R., Kirkham, J., and Dixon, M. J. (2014). Endoplasmic reticulum stress in amelogenesis imperfecta and phenotypic rescue using 4-phenylbutyrate. *Hum. Mol. Genet.* 23, 2468–2480. doi: 10.1093/hmg/ddt642

Hubbard, M. J., Mangum, J. E., Perez, V. A., Nervo, G. J., and Hall, R. K. (in press). Molar hypomineralisation: a call to arms for enamel researchers. *Front. Physiol.* doi: 10.3389/fphys.2017.00546

Murray, C. J., Vos, T., Lozano, R., Naghavi, M., Flaxman, A. D., Michaud, C., et al. (2012). Disability-adjusted life years (DALYs) for 291 diseases and injuries in 21 regions, 1990–2010: a systematic analysis for the Global Burden of Disease Study 2010. *Lancet* 380, 2197–2223. doi: 10.1016/S0140-6736(12)61689-4

Nature News (2015). Why interdisciplinary research matters. *Nature* 525:305. doi: 10.1038/525305a

Qu, Q., Haitina, T., Zhu, M., and Ahlberg, P. E. (2015). New genomic and fossil data illuminate the origin of enamel. *Nature* 526, 108–111. doi: 10.1038/nature15259

Scientific Advisory Board, M. (2011). Enamel biology and future research directions. *Eur. J. Oral Sci.* 119, 377–379. doi: 10.1111/j.1600-0722.2011.00934.x.

Skobe, Z., Stern, D. N., and Prostak, K. S. (1995). "The cell biology of amelogenesis," in *Dental Enamel: Formation to Destruction,* eds C. Robinson, J. Kirkham, and R. Shore (Boca Raton, FL: CRC Press), 23–57.

Smith, C. E., Hu, Y., Hu, J. C., and Simmer, J. P. (2016). Ultrastructure of early amelogenesis in wild-type, Amelx−/−, and Enam−/− mice: enamel ribbon initiation on dentin mineral and ribbon orientation by ameloblasts. *Mol. Genet. Genomic Med.* 4, 662–683. doi: 10.1002/mgg3.253

Smith, C. E. L., Poulter, J. A., Antanaviciute, A., Kirkham, J., Brookes, S. J., Inglehearn, C. F., et al. (2017). Amelogenesis imperfecta; genes, proteins, and pathways. *Front. Physiol.* 8:435. doi: 10.3389/fphys.2017.00435

Tarasevich, B. J., Perez-Salas, U., Masica, D. L., Philo, J., Kienzle, P., Krueger, S., et al. (2013). Neutron reflectometry studies of the adsorbed structure of the amelogenin, LRAP. *J. Phys. Chem. B* 117, 3098–3109. doi: 10.1021/jp311936j

Conflict of Interest Statement: The authors declare that the research was conducted in the absence of any commercial or financial relationships that could be construed as a potential conflict of interest.

The reviewer CR declared a shared affiliation, though no other collaboration, with the authors JK and SB to the handling Editor, who ensured that the process met the standards of a fair and objective review.

Copyright © 2017 Kirkham, Brookes, Diekwisch, Margolis, Berdal and Hubbard. This is an open-access article distributed under the terms of the Creative Commons Attribution License (CC BY). The use, distribution or reproduction in other forums is permitted, provided the original author(s) or licensor are credited and that the original publication in this journal is cited, in accordance with accepted academic practice. No use, distribution or reproduction is permitted which does not comply with these terms.

Advantages of publishing in Frontiers

OPEN ACCESS
Articles are free to read for greatest visibility and readership

FAST PUBLICATION
Around 90 days from submission to decision

HIGH QUALITY PEER-REVIEW
Rigorous, collaborative, and constructive peer-review

TRANSPARENT PEER-REVIEW
Editors and reviewers acknowledged by name on published articles

Frontiers
Avenue du Tribunal-Fédéral 34
1005 Lausanne | Switzerland

Visit us: www.frontiersin.org
Contact us: info@frontiersin.org | +41 21 510 17 00

REPRODUCIBILITY OF RESEARCH
Support open data and methods to enhance research reproducibility

DIGITAL PUBLISHING
Articles designed for optimal readership across devices

FOLLOW US
@frontiersin

IMPACT METRICS
Advanced article metrics track visibility across digital media

EXTENSIVE PROMOTION
Marketing and promotion of impactful research

LOOP RESEARCH NETWORK
Our network increases your article's readership